ASNR22/SNR XXII

ABSTRACT PROCEEDINGS

SCIENTIFIC PODIUM PRESENTATIONS

Monday, May 16, 2022
8:00-9:15 AM
Cervical and Intracranial Vessel Wall Imaging Study Group Programming

1255

Multi-Center MRI Radiomics Analysis Differentiate Between Primary Central Nervous System Lymphoma, Glioblastoma, and Brain Metastasis

M Ak[1], M Pease[1], P Mamindla[1], M Ayoub[2], M Yilmaz[1], V Peddagangireddy[1], A Kamal[1], N Ak[1], S Zenkin[1], P Zinn[1], F Moron[3], R Colen[1]

[1]University of Pittsburgh Medical Center, Pittsburgh, PA, [2]Rush University Medical Center, Chicago, IL, [3]BCM, Houston, TX

Purpose

To investigative the diagnostic performance of radiomics-based machine learning in differentiating glioblastoma (GBM), primary central nervous system lymphoma (PCNSL) and brain metastasis (BM).

Materials and Methods

We retrospectively identified 1075 patients from three institutions with untreated solitary, pathologically proven cases of PCNSL (133), GBM (433), and breast or lung BM (509). For each tumor, we segmented edema, contrast enhancement, necrosis, and contralateral white matter (cWM) volume of interest (VOI) for T2 FLAIR and T1 post-contrast sequences. A total of 205 texture features were extracted from each sequence's VOI including 10 histogram based first-order features and 195 second-order features using gray-level co-occurrence matrices. After feature normalization using cWM, we divided the 195 second level features by the volumes of each VOI to generate another 195 volume-independent features per VOI and 2,400 features per MRI. We performed feature selection with Least Absolute Shrinkage and Selection Operator (LASSO). We split the cohort into 70% training and 30% testing sets. We used XGBoost (eXtreme Gradient Boosting) algorithm to perform three-way classification and generate the radiomics model. The predictive performance of the models for classifying each tumor type against all others (i.e., BM versus PCNSL and GBM) was estimated using the receiver operating characteristic (ROC) curve, summarized as the area under the curve (AUC).

Results

LASSO identified 216 independent features, of which 20 most relevant used for model building. Our three-classification model robustly differentiated ($p < 0.001$) between PCNSL (AUC 0.95), GBM (AUC 0.97), and BM (AUC 0.96) and achieved 88% accuracy. The model obtained 76.9% sensitivity and 98.2% specificity for PCNS prediction, 86% sensitivity and 94.7% specificity for the GBM prediction and 92.7% sensitivity 86.3% specificity for the BM prediction.

Conclusions

This study presents radiomics-based signature that can successfully differentiate between PCNSL, GBM, and BM. Although further independent validation is warranted the proposed predictive radiomics-based signature is cost-effective, non-invasive and enable better patient stratification, management, and clinical decision-making.

831

Systematic literature review on noninvasive predicting O6 Methylguanine-DNA Methyltransferase status in Glioblastoma, using machine learning algorithms on Pre-therapy MR Imaging

J Lost[1], T Verma[2], N Tillmanns[1], R Bahar[1], I Ikuta[3], W Zucconi[1], M Lin[4], M Johnson[5], J Cui[5], A Malhotra[6], S Abi Fadel[7], M Aboian[7], H Subramanian[1], R Bronen[3], K Bousabarah[8], M Sabel[9]

[1]Yale School of Medicine, New Haven, CT, [2]Yale School of Medicine, Ossining, NY, [3]Yale University School of Medicine, New Haven, CT, [4]Yale University School of Medicine and Visage Imaging, Inc., New Haven, CT, [5]Yale University, New Haven, CT, [6]Yale University School of Medicine, New Canaan, CT, [7]Yale University, Woodbridge, CT, [8]Visage Imaging GmbH, Berlin, CT, [9]University Hospital Dusseldorf, Dusseldorf, NRW

Purpose

Glioblastomas are the most common malignant primary brain tumors in adults, with a median survival rate of 15 months.1 Standard of care besides surgical resection and radiation involves chemotherapeutic treatment with temozolomide (TMZ). O6 Methylguanine-DNA Methyltransferase (MGMT) is a protein associated with DNA repair and therefore with resistance against alkylating agents like TMZ. Methylation of the MGMT promotor thus is a prognostic indicator for survival prognosis, but standard diagnosis requires biopsy and invasive surgery to extract small portions of tumor, which are analyzed at a neuropathological lab. Recent advances report molecular and genetic alterations of GBM manifest as macroscopical changes, which can be quantified by clinical imaging.2,3 We performed a systematic review of recent literature on predicting molecular alterations pre-treatment using machine learning methods on MR Images.

Materials and Methods
Literature review was done conforming to PRISMA guidelines for publications prior to February 2021 using Ovid Embase, Ovid MEDLINE, Cochrane trials (CENTRAL) and Web of Science core-collection as databases. The Keywords included artificial intelligence, machine learning, deep learning, radiomics, magnetic resonance imaging, glioma and glioblastoma. Non-human, non-machine learning studies were excluded. Bias analysis was done using TRIPOD guidelines and screening was performed using Covidence software.
Results
After retrieving 11,727 abstracts, we applied initial screening criteria that identified 1,135 articles for full text reviews resulting in 82 publications meeting our inclusion criteria. Out of these papers eleven specifically analyzed MGMT status prediction, excluding studies which analyzed low grade glioma MGMT status and multiple subtypes. Mean prediction accuracy was 82.5%, while three paper did not report specific accuracy results. Out of all analyzed papers, nine used internal cross validation and only two an external validation cohort. Random forest machine learning classifier turned out best for predicting MGMT Methylation with an accuracy of 87%.
Conclusions
Major limitations include use of small datasets and incoherent accuracy measurement (based on different analyzed features) resulting in limited generalizability. Due to a lack of explanation of missing data in all eleven papers, we recommend including this information to improve reliability of the results.

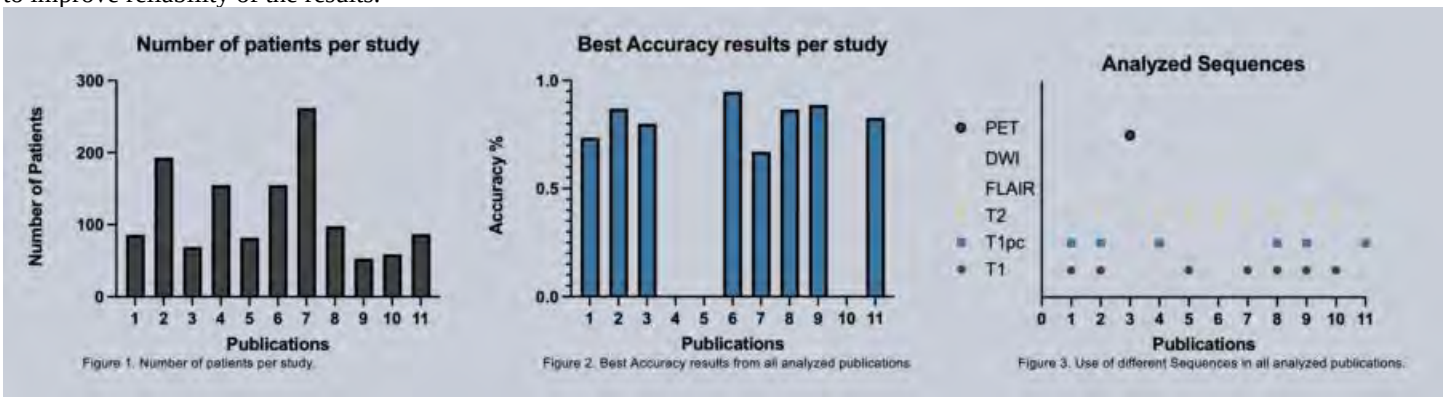

(Filename: TCT_831_ASNR_Grapchis_JanLost.jpg)

316

The Radiomics based MRI Analysis could Classify the Juvenile Myoclonic Epilepsy from Healthy Control

B Sohn[1], K Kim[2], S Ahn[1]
[1]Department of Radiology, Severance Hospital, Yonsei University College of Medicine, Seoul, Korea, Republic of, [2]Department of Neurology, Severance Hospital, Yonsei University College of Medicine, Seoul, Korea, Republic of

Purpose
The aim of this study is to build and validate radiomics prediction models for patients with juvenile myoclonic epilepsy (JME) from healthy controls (HC) with MRI.
Materials and Methods
A total of 129 subjects (97 JME patients and 32 HC) were assigned to the training (n=90) and test-validation (n=39) sets. We used FreeSurfer 6.0.0 to obtain subject-specific masks of brain regions. Radiomics features were extracted from 20 regions of interest in T1-weighted MRI image. Machine learning models for identifying JME from HC were trained with radiomics features of training sets and validated with test-validation sets. In order to explore a way with high performance, grid search method was done for the multiple machine learning methods. Models were trained on training set and hyperparameter tuning was done. After training, the performance of models was compared with respect to the test-validation set, and this was shown as Receiver operating characteristics (ROC) curve. To examine which feature played important roles in prediction, we calculated the mean absolute Shapley value for each of the selected input features using the Shapley additive explanations (SHAP) algorithm with the models.
Results
Seven radiomics models – light gradient boosting machine, support vector classifier, random forest, logistic regression, extreme gradient boosting, gradient boosting machine, decision tree – showed AUCs of 0.82, 0.81, 0.78, 0.78, 0.77, 0.76, 0.67, respectively. The best performance model, light gradient boosting machine, demonstrated an accuracy, precision, recall, and F1 score of 0.79, 0.82, 0.93, and 0.87, respectively. Radiomics features with putamen and cerebral peduncle ranked highest important features of the best performance model.
Conclusions
Radiomics models with multiple regions of interest in routine brain MRI could be an auxiliary tool in the identification of JME from HC.

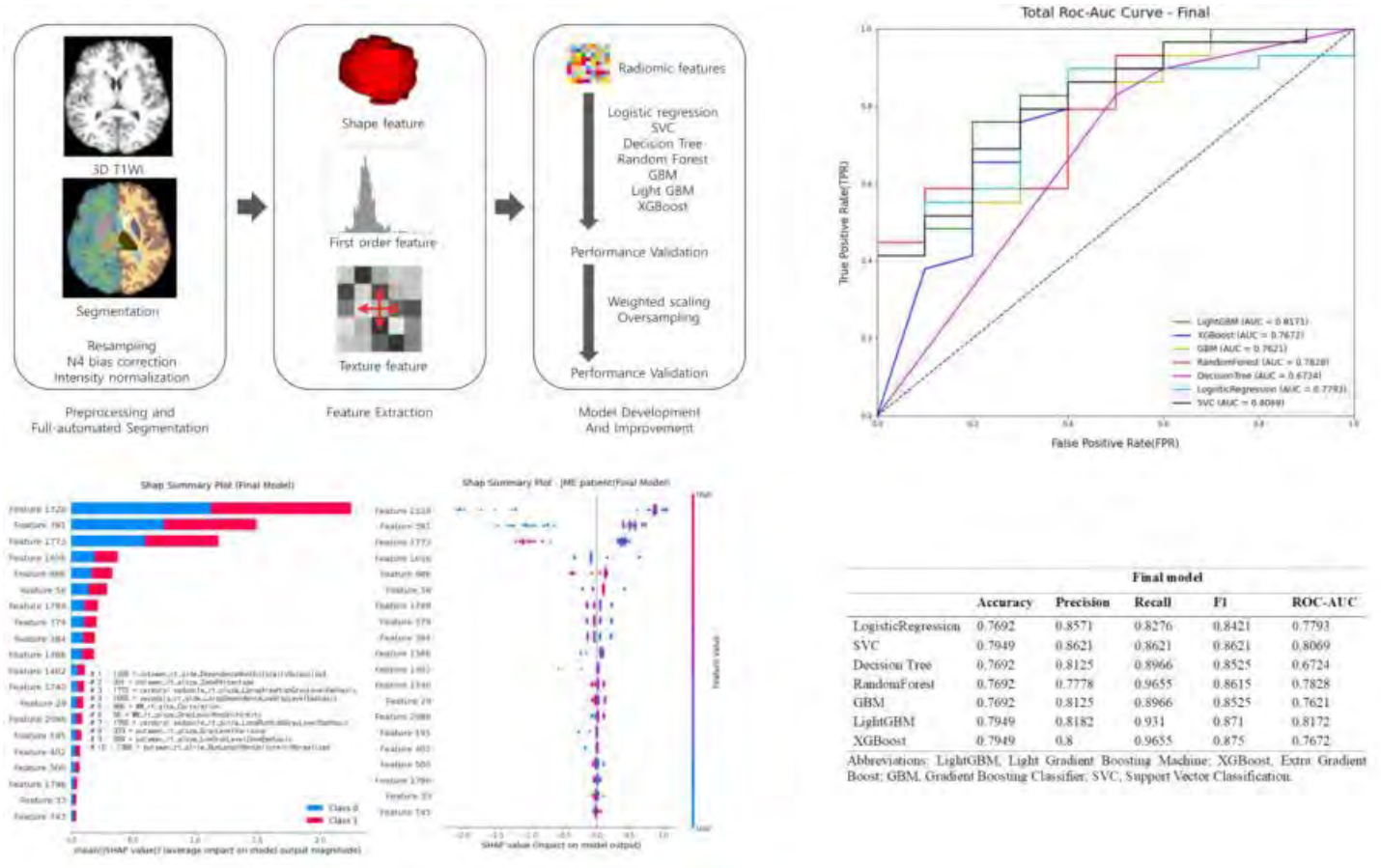

Final model					
	Accuracy	Precision	Recall	F1	ROC-AUC
LogisticRegression	0.7692	0.8571	0.8276	0.8421	0.7793
SVC	0.7949	0.8621	0.8621	0.8621	0.8069
Decision Tree	0.7692	0.8125	0.8966	0.8525	0.6724
RandomForest	0.7692	0.7778	0.9655	0.8615	0.7828
GBM	0.7692	0.8125	0.8966	0.8525	0.7621
LightGBM	0.7949	0.8182	0.931	0.871	0.8172
XGBoost	0.7949	0.8	0.9655	0.875	0.7672

Abbreviations: LightGBM, Light Gradient Boosting Machine; XGBoost, Extre Gradient Boost; GBM, Gradient Boosting Classifier; SVC, Support Vector Classification.

(Filename: TCT_316_figure.jpg)

Monday, May 16, 2022
3:30-5:00 PM
ASPNR Programming: Essentials of Neuroradiology: Pediatric Core, Tell Me More!

561

Conventional and Advanced MR Imaging Findings in a Cohort of Pathology-Proven Dermoid Cysts of the Pediatric Scalp and Skull

B Serrallach[1], G Orman[1], J Hicks[1], N Desai[1], S Kralik[1], T Huisman[1]
[1]*Texas Children's Hospital and Baylor College of Medicine, Houston, TX*

Purpose
In the pediatric population, dermoid cysts are among the most frequent lesions of the scalp and skull (1). Imaging plays a key role in characterizing scalp and skull lesions in order to narrow the differential diagnosis. In general, dermoids are described as heterogeneous T1-/T2-hypo- to hyperintense lesions on MRI. The goal of this retrospective study is to evaluate the DWI findings while reviewing the conventional T1-/T2-/T1+C-weighted MR characteristics in a pathology-proven series of 14 dermoids of the pediatric scalp and skull.
Materials and Methods
The inclusion criteria for this study were (1) pathology-proven diagnosis of a scalp or skull dermoid, (2) MRI data without artifacts and (3) patient age between 0-18 years. MR protocols typically included axial T1- and T2-weighted images, axial T1+C-weighted images and axial DWI. Apparent diffusion coefficient (ADC) maps were automatically calculated. The MRI studies were subsequently evaluated for the T1W and T2W signal intensity of the dermoid (hypo-, iso- or hyperintense compared to the cortical gray matter; homogeneous vs. heterogeneous), for the pattern of contrast enhancement (no contrast enhancement vs. rim enhancement) and for the signal intensity on DWI and corresponding ADC map (diffusion increase vs. diffusion restriction with reference to the brain).
Results
In our pediatric cohort (eight boys, six girls, age range 3-95 months), half of the dermoids were homogeneous T1-hypointense and

homogeneous T2-hyperintense. We found a mixture of restricted (45.5 %) and increased diffusion (54.5 %) in dermoids. The vast majority of dermoids (91.7 %) showed rim enhancement. Most dermoids (57.1 %) were located at the midline and adjacent to one of its sutures.

Conclusions

Imaging plays a key role in characterizing pediatric scalp and skull lesions in order to narrow the differential diagnosis. With our cohort of pathology-proven dermoids of the pediatric scalp and skull, we showed that dermoids may have variable imaging appearances (Figure 1 and 2). In general, dermoids are described as heterogeneous hypo- to hyperintense on T2W and on non-contrast TW images. Notably in our cohort, half of the dermoids were homogeneous hypointense on T1W and hyperintense on T2W images, resembling the imaging features of epidermoids. Restricted or increased diffusion can be seen in dermoids. The vast majority of dermoids showed rim enhancement. Most dermoids were located in the midline and frequently overlaid the anterior fontanelle.

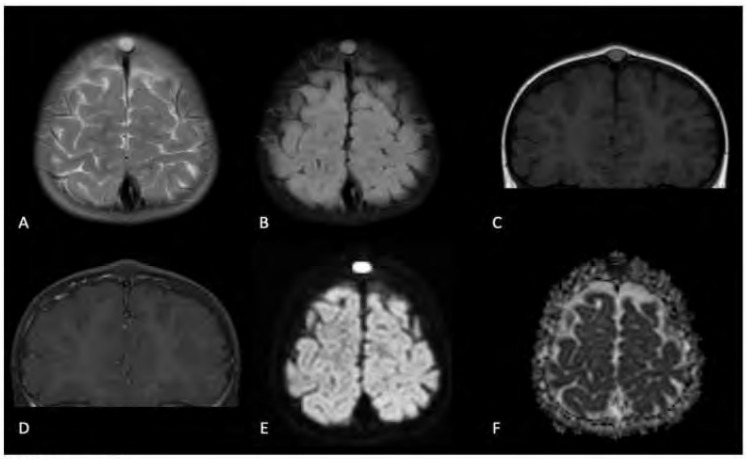

Figure 1

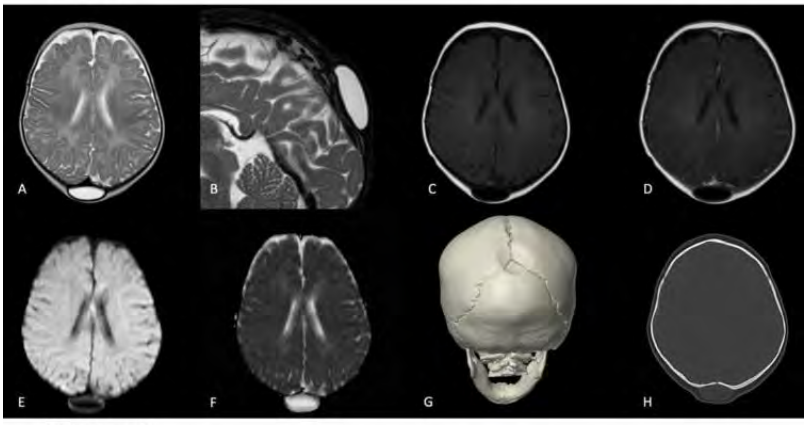

Figure 2

(Filename: TCT_561_abstract-dermoid-asnr_300.jpg)

1415

Cortical Myelin Maturation during Adolescence using the Human Connectome Project Development Study

C Filippi[1], N Madan[2], R Watts[3]

[1]Tufts University Medical Center, Boston, MA, [2]Tufts Medical Center, Boston, MA, [3]Yale University, New Haven, CT

Purpose

Enhanced sensitivity to cortical myelin detection on MR can be achieved via division of T1W/T2W, which minimizes effects of SI inhomogeneity (1,2). The purpose of this study was to quantify cortical myelin maturation across adolescence using Human Connectome Project (HCP) Development study (3) data to assess for gender differences and age dependency.

Materials and Methods

HCP Development data from 652 participants (299 male, 353 female) aged from 5 to 22 years (mean 14.4 +/- 4.0 years) were used in this study. The acquisition (3) and analysis (4,5) protocols are described elsewhere. The non-bias field corrected myelin maps are used in this analysis so that low spatial frequency variations in cortical myelin would not be removed by this processing (5). The CIFTI format myelin data on the Conte69 mesh (2) were concatenated, and vertex-wise general linear model was applied using FSL PALM with age and sex and their interaction as covariates. Cortical maps were parcellated using the Desikan atlas to further investigate the developmental trajectories of cortical development.

Results

Group average myelin map (Figure 1) is similar to adults. Widespread increases in cortical myelin with age were observed over almost

the entire cortex (Figure 2), but were concentrated in regions of high baseline myelination such as the motor and visual cortices. Correlation between cortical myelin and age was exceptionally low in the rostral anterior cingulate (left: r=0.02, right: r=0.04), averaged 0.48 over the entire cortex, and highest values in superior parietal (left: r=0.72, right: r=0.74 and precentral (left: r=0.71, right: r=0.69) regions. In these areas, about 50% of the variance in cortical myelination can be explained by age. In the superior and medial-orbitofrontal cortex, males show higher myelination (Figure 3). Investigating developmental trajectories for multiple regions suggested some divergence between the sexes around the onset of puberty (Figure 4).

Conclusions

Cortical myelin maturation across adolescence shows gender differences between males and females; and, cortical myelination increases during adolescence but levels off later in adolescence. Areas of higher cortical myelination are noted in primary motor cortex and somatosensory cortices as well as visual cortices indicative of higher efficiency/speed and less plasticity/flexibility. Further work could combine data from the HCP Young Adult study and HCP Aging to better characterize cortical development over the entire lifespan.

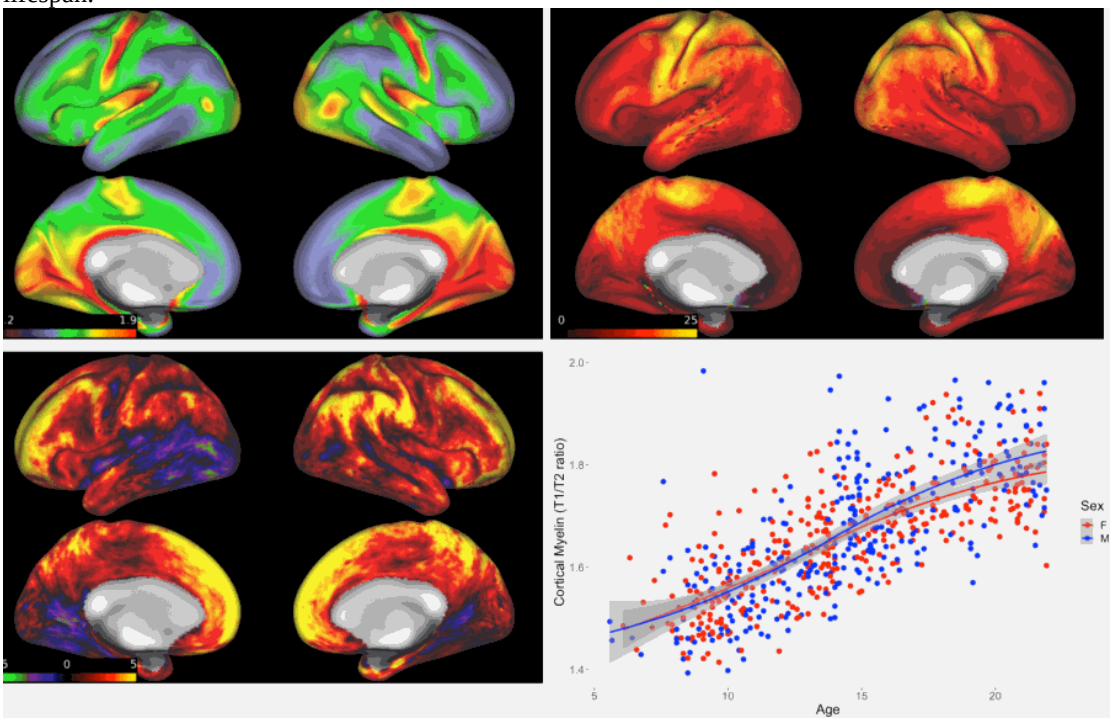

(Filename: TCT_1415_image001.gif)

306

Neurodevelopmental Patterns of Early Postnatal White Matter Maturation Represent Distinct Underlying Microstructure and Histology

A Nazeri[1], Ž Krsnik[2], I Kostovic[3], S Ha[4], D Barch[4], J Luby[4], C Rogers[4], B Warner[4], J Shimony[5], R McKinstry[4], J Neil[4], C Smyser[4], A Sotiras[4]

[1]Washington University in St. Louis, Saint Louis, MO, [2]University of Zagreb, Zagreb, -, [3]University of Zagreb, Zagreb, ., [4]Washington University in St. Louis, St. Louis, MO, [5]Washington University School of Medicine, St. Louis, MO

Purpose

During the early postnatal period, cerebral white matter (WM) undergoes rapid maturation through complex cellular and histogenetic processes, which affect its signal characteristics on MRI [1]. Here, we aimed to identify the spatial patterns of early postnatal WM MRI signal evolution and examine the underlying WM microstructural and histological features they represent.

Materials and Methods

We capitalized on a large sample of newborns, the Developing Human Connectome Project (dHCP; n=342; 35-44wk post-menstrual age) [2] and leveraged advances in unsupervised multivariate pattern analysis to analyze the ratio of T2w/T1w image intensities (Fig. 1). We delineated spatial patterns of WM maturation using non-negative matrix factorization (NMF) [3]. Using multi-shell diffusion-weighted MRI and neurite orientation dispersion and density imaging (NODDI) modeling [4], we explored how changes in WM free water content and neurite density differentially contribute to patterns of T2w/T1w signal changes. We compared our findings with postmortem late fetal/early postnatal brain specimens from the Zagreb Collection of Human Brains.

Results

Using NMF, we identified 9 newborn WM maturation patterns (NeWMaPs, Fig. 2). The NeWMaPs were remarkably symmetric, demonstrated a characteristic distance distribution with respect to the cortex and/or the lateral ventricles (3 superficial, 3 periventricular, and 3 intermediate WM NeWMaPs), and showed divergent maturational trajectories. Furthermore, we showed that T2w/T1w signal variations in WM maturational patterns are explained by differential contributions of WM microstructure indices

derived from NODDI (i.e., free water content and neurite density index, which were associated with higher and lower T2w/T1w signal ratio, respectively; Fig. 3). Finally, we demonstrated how distinct histological features (i.e., extracellular matrix, astroglial density, and myelination) correlate with NeWMaPs by comparing our findings with postmortem late fetal/early postnatal brain specimens (Fig. 4).

Conclusions

Our study provides insights into early postnatal WM organization and maturation using conventional T2w and T1w MRI sequences coupled with advanced image processing and analysis techniques. We reveal distinct WM maturation patterns, which follow distinct developmental trajectories and align well with underlying microstructure and histology. The identified early postnatal maturational patterns may provide an alternative to existing tract-based atlas definitions.

Figure 1

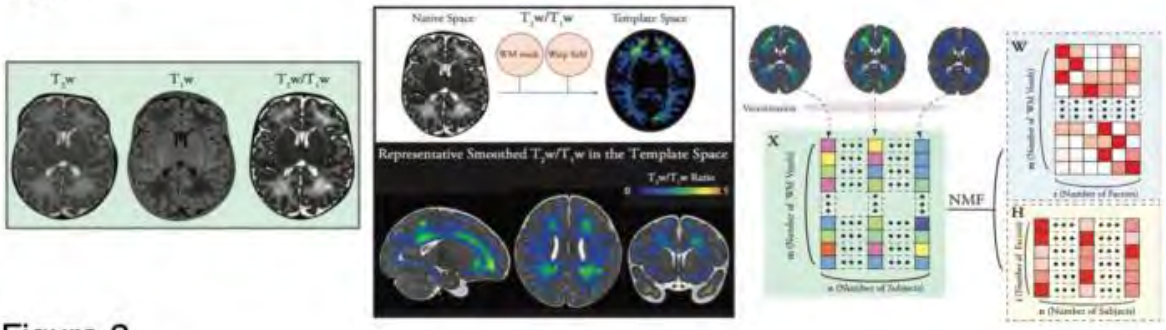

Figure 2

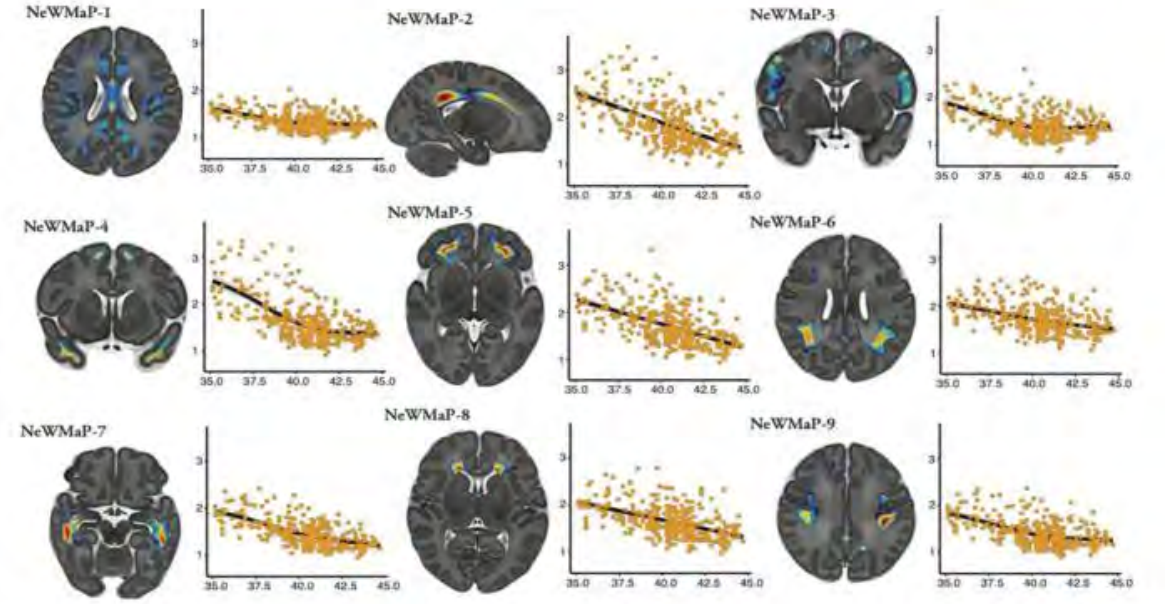

Figure 3

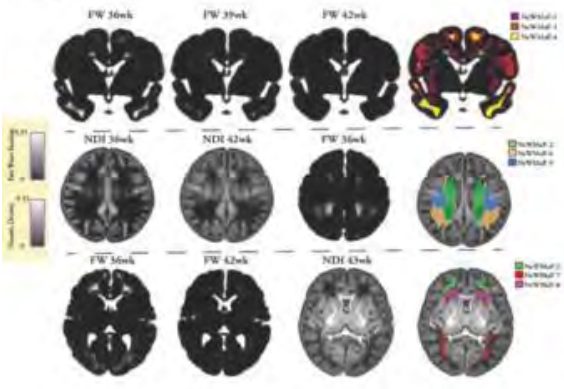

Figure 4

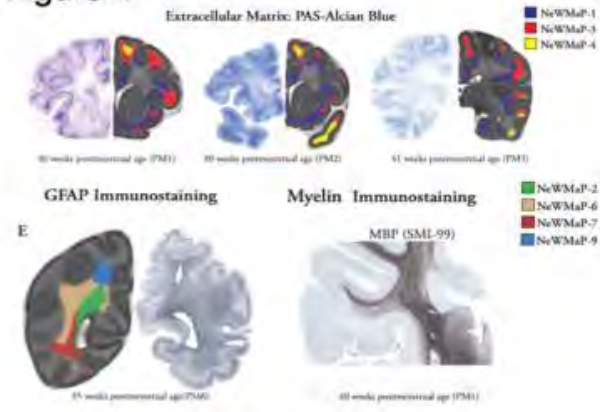

(Filename: TCT_306_Figure.jpg)

Monday, May 16, 2022
3:30-5:00 PM
Late-Breaking Abstracts

1576

Automatic Detection, Segmentation, and Radiomic-based Characterization of Gliomas for Prediction of Biomarker Status, Prognosis, and Treatment Response

S KIHIRA[1], X Mei[1], S Dogra[1], P Belani[2], Z Fayad[3], A Doshi[4], K Nael[5]
[1]Icahn School of Medicine at Mount Sinai, New York, NY, [2]Mount Sinai Hospital, new york, NY, [3]Icahn School of Medicine at Mount Sinai Hospital, New York, NY, [4]Mount Sinai Hospital, New York, NY, [5]UCLA, Los Angeles, CA

Purpose
To develop a machine learning based framework for detection, segmentation, and radiomic-based characterization of gliomas in initial evaluation for prediction of biomarker status and prognosis and for serial follow-up imaging.
Materials and Methods
This is a retrospective study with an initial cohort of roughly 500 patients with 1) a diagnosis of glioma (grade II-IV) with known surgical histopathology and 2) preoperative MR with FLAIR sequence. The entire tumor volume including FLAIR hyperintense infiltrative component and necrotic and cystic components will be manually segmented on FLAIR images to be used as ground truth masks. Deep learning-based U-Net framework will be developed based on symmetric architecture from these segmented maps. Dice similarity coefficient (DSC) will be calculated to assess the deep learning-based masks against ground truth segmentation. Volumetric analysis utility would be assessed in serial follow-up imaging.
Results
Our preliminary data on a small subset of patients (n=116) showed DSC of up to 0.9 for auto-detection and segmentation of gliomas (grades II-IV). Initial attempt at texture extraction from the segmentation maps showed IDH-1 prediction of AUC 0.82 and ATRX of 0.78. Survival prediction of <18 months demonstrated AUC of 0.67. We hope with increased cohort size and further optimization of our algorithm to improve AUCs for prediction of biomarker status and prognosis. We are also including MGMT and TP53 statuses in our prediction algorithm with data pending at this time.
Conclusions
An automated pipeline that can predict treatment response and prognosis in patients with glioma can guide treatment options and surgical/chemotherapy management, serving as a non-invasive alternative to brain biopsy and tissue resection. This algorithm can also be used in serial follow-up in glioma patients.

1587

Benefits of 3D deep learning reconstruction on image quality: cases study in neuroradiology.

P ROUX[1], S CANTIN[2], S Banerjee[3], R Lebel[4]
[1]CIN, Saint Denis, PARIS IDF, [2]C, Grenoble, FRANCE, [3]GE Healthcare, Menlo Park, CA, [4]GE Healthcare, Calgary, Alberta

Purpose
3D AIRTM Recon DL (3D ARDL) is a novel deep learning-based MRI reconstruction pipeline to address fundamental image quality limitations of conventional reconstruction to provide high-resolution, low noise MR images and free from standard Gibbs truncation artifacts. The aim of this early study is to demonstrate the benefits of this new reconstruction pipeline in neuroradiology.
Materials and Methods
Several brain MR examinations were performed on a 3T MR system (Signa PREMIER, GE Healthcare, Waukesha, WI) according to clinical standards in our institution. Different MR sequence types (3D Gradient echo and 3D Fast spin Echo) and contrast (T1w, T1w FatSat with Gadolinium injection or T2w) were acquired to have an overview of ARDL reconstruction algorithm performance on standard sequences used in neuroradiology. 3D AIRTM Recon DL reconstructions were performed offline with medium noise reduction and then compared with conventional reconstruction produced by the MR scanner. Qualitative criteria were used for images comparison such as, anatomical and lesions depiction, SNR assessment and artifacts presence in images. Particular attention has been paid to reformat image quality as 3D isotropic MR sequences are gold standard in neuro MR Exam.
Results
3D AIRTM Recon DL reconstruction leads to reduced truncation artifacts, higher SNR and improved sharpness. First, we will present some cases that demonstrate how 3D ARDL can help better depict pathological features. In those cases, 3D ARDL leads to a better spatial resolution, a better contrast, and a better outlining of the lesions especially in reformatted planes. Then, we will discuss about different protocol optimization strategies that take advantage of improved image quality to reduce scan time.
Conclusions
3D AIRTM Recon DL is a new deep learning-based reconstruction pipeline for MRI that substantially improves image quality. With some protocol optimizations, 3D AIRTM Recon DL can potentially increase diagnostic performance and confidence but also operational performance of MRI scanner. Compatible with clinically relevant MR sequences and contrast weightings, 3D AIRTM Recon DL opens new perspectives and new possibilities in every field of neuroradiology.

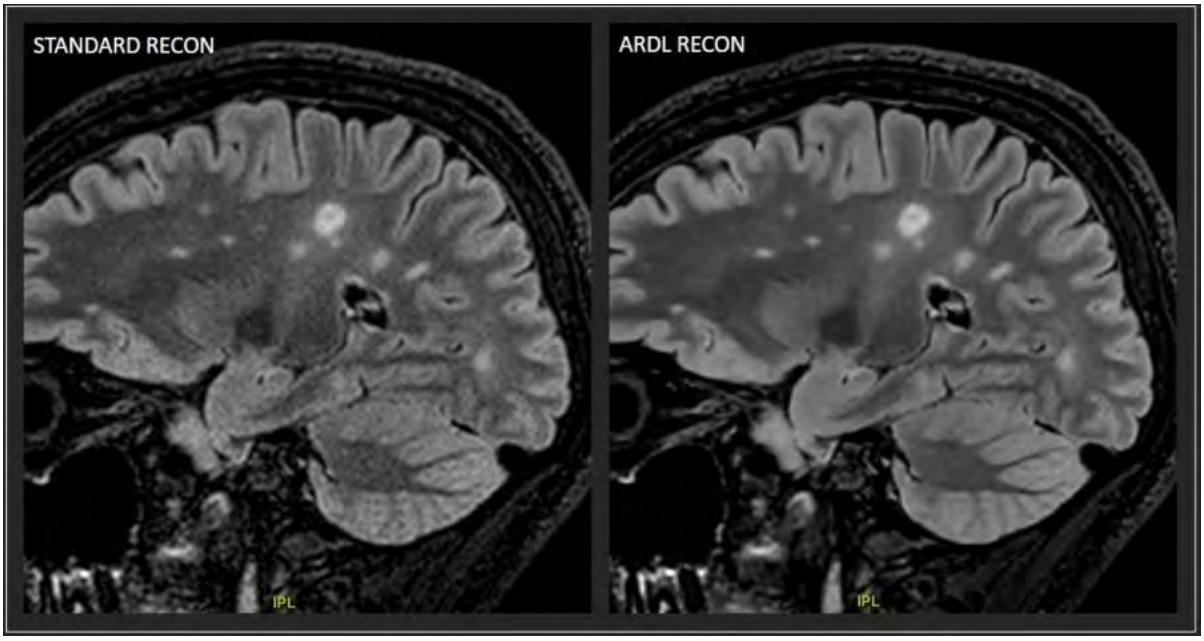

(Filename: TCT_1587_CaptureARDL.jpg)

1584

Brain Parenchymal Injury and Outcomes of Fetuses with Vein of Galen Malformations and Non-Galenic Arteriovenous Fistulas

F Machado-Rivas[1], C Jaimes[2], K Chen[3], E Yang[4], D Orbach[4]

[1]Boston Childrens Hospital, Boston, MA, [2]Boston Children's Hospital, BOSTON, MA, [3]Texas Children's Hospital, Houston, TX, [4]Boston Children's Hospital, Boston, MA

Purpose

To evaluate the presentation of brain parenchymal injury, injury progression, and outcomes in fetuses with Vein of Galen Malformations (VOGMs) and Non-Galenic Arteriovenous Fistulas (NGAVFs).

Materials and Methods

The EHR was queried for patients with VOGM or NG-AVF and at least one fetal brain MRI between 2007-2022. Subjects with non-diagnostic image quality, or with other CNS/ body abnormalities not attributable to VOGM/ NG-AVF were excluded. Gestational age (GA), sex and postnatal outcome (good or adverse) were recorded. Postnatal outcome was categorized as adverse if intubation, emergent embolization, or death occurred by postnatal day 2. Two board certified pediatric neuroradiologists evaluated each case for brain parenchymal injury: structural images (T2 HASTE, SSFP, and T1-VIBE) were evaluated for (a) signal abnormality (T2 hyperintensity, T2 hypointensity, and T1 hyperintensity), (b) low volume, and (c) ventriculomegaly; DWI acquisitions for restricted diffusion; and for T2*gradient/echo sequences for abnormal parenchymal blooming. Additionally, the progression of parenchymal injury was evaluated in all subjects with a repeat fetal scan or an immediate postnatal scan.

Results

49 fetal MRI exams corresponding to 31 subjects (27 VOGM, 4 AVF) were analyzed (18M, 13F). The mean GA for the first exam was 32.3w±SD 4.7, and 14 subjects underwent at least one additional fetal MRI exam (mean interval 3.9w±SD 3.2). Brain parenchymal injury were observed in 8 subjects (26%). The mean GA at the time of identification of brain injury (presenting MRI) was 32.2w±SD 4.9. Abnormalities on structural imaging were identified in all fetuses with brain injury (n=8). Restricted diffusion was identified in 5/7 fetuses who had available data (71%). Abnormalities in the T2* weighted sequences were identified in 5/5 cases that had available data. Progression of the brain parenchymal injury was seen in all cases that that had at least one abnormality (mean interval 3.1w±SD 2.1) [Fig 1]. All subjects (8/8) who had brain parenchymal injury on fetal MRI had an adverse outcome at 2 days of life, while this was the case for only 30% of subjects (7/23) who did not present with injury. These findings indicate a tripling of the risk of having the adverse outcome in patients with fetal brain parenchymal injury (RR 3.29, 95%CI 1.77-6.10, P<.001).

Conclusions

Findings of brain parenchymal injury appear to predict a poor prognosis, with relentless progression and a significant association with adverse neonatal outcomes.

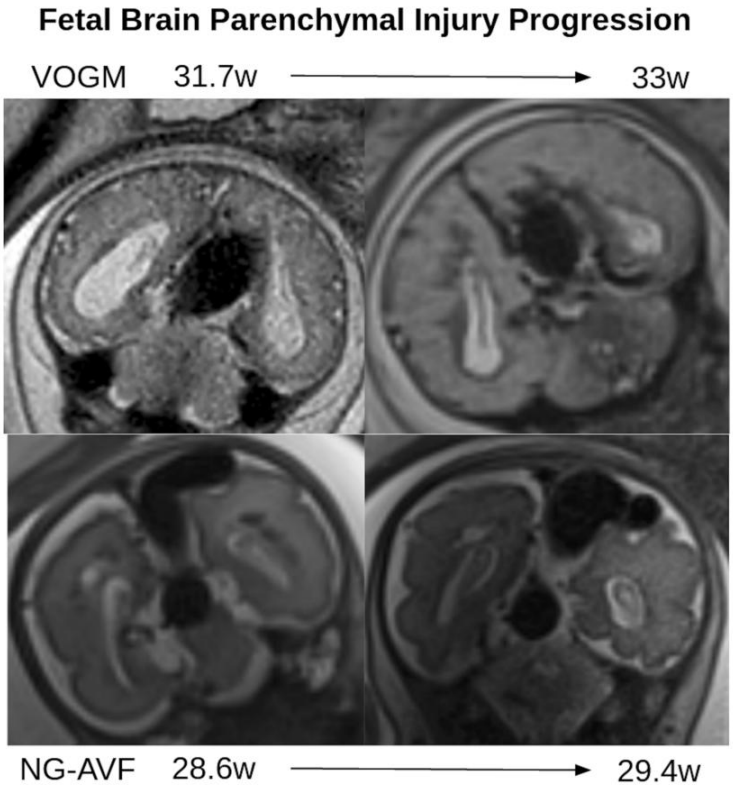

(Filename: TCT_1584_FIGURE1_ASNR.jpg)

1589

Comparison of Common Carotid, Internal Carotid and Vertebral Arterial Compliance in Young Healthy Controls and Elderly Subjects with Mild Cognitive Impairment Measured with Cardiac-Gated 3D Time of Flight MRA and Ultrasound

R Obid[1], F Mihlon[2], K Hildreth[3], K Moreau[3], R Bert[1]

[1]University of Louisville, Louisville, KY, [2]HAMPTON ROADS RADIOLOGY ASSOCIATES, VIRGINIA BEACH, VA, [3]University of Colorado, Aurora, CO

Purpose

We have shown that common carotid artery (CCA) and internal carotid arterial (ICA) pulsatilities strongly correlate with CSF pulsatility at the foramen magnum and upper spine. CSF and interstitial space pulsatility may help clear potential waste products such as beta amyloid. CCA compliance has been shown to be decreased in patients with mild cognitive impairment (MCI) but less is known about ICA and Vertebral artery (VA) contributions, as direct ultrasound measurements are difficult at these vessels and not possible intracranially. We have devised a MRI method using cardiac-gated 3D time of flight (CG3DToF) MRI for measuring both the extracranial and intracranial ICA and VA. We present compliance measurements using this technique for the CCA, ICA and VA in cohorts of young healthy subjects and older subjects with known MCI, along with correlated US measurements in the CCA.

Materials and Methods

After IRB approval. Two selected cohorts consisted of 12 young healthy controls (ages 24-30) without cardiovascular disease and older volunteers (59-77) with established MCI. Standard US compliance measurements were recorded for each CCA in each subject 1 cm below the bifurcation, followed by CG3DToF measurements (details to be presented). Post processing of both US and MRI was performed offline with standard commercial software. Vascular volumes were measured both with seeding software and hand-drawn ROI to confirm repeatability. Measurements were placed in standard spreadsheet software for calculating and charting compliance and distensibility.

Results

Direct distensibility CCA measurements using US and CG3DToF were comparable with a correlation coefficient of 0.734 (Fig. 1A). CCA, ICA and VA mean cohort compliances measured with CG3DToF for MCI subjects were: 0.69(0.26), 0.20(0.06), 0.18(0.10). Values for younger subjects were: 1.86(0.4), 0.34(0.17), 0.33(0.10) (Fig. 1B). The CCA were significantly more compliant than the ICA and VA. The decreased compliance in the MCI population was about 2/3, compared to about 1/3 for the ICA and VA. Image examples are shown in Fig. 1C. Gate selection is shown in Fig. 1D.

Conclusions

CG3DToF provides a means of accurately determining arterial compliance that can be used in CCA and VA, perhaps including intracranially. Additionally, it has demonstrated significant decreases in compliance in CCA, ICA and VA in the MCI population. This may have a significant impact on CSF pulsations that in turn may impact beta amyloid removal.

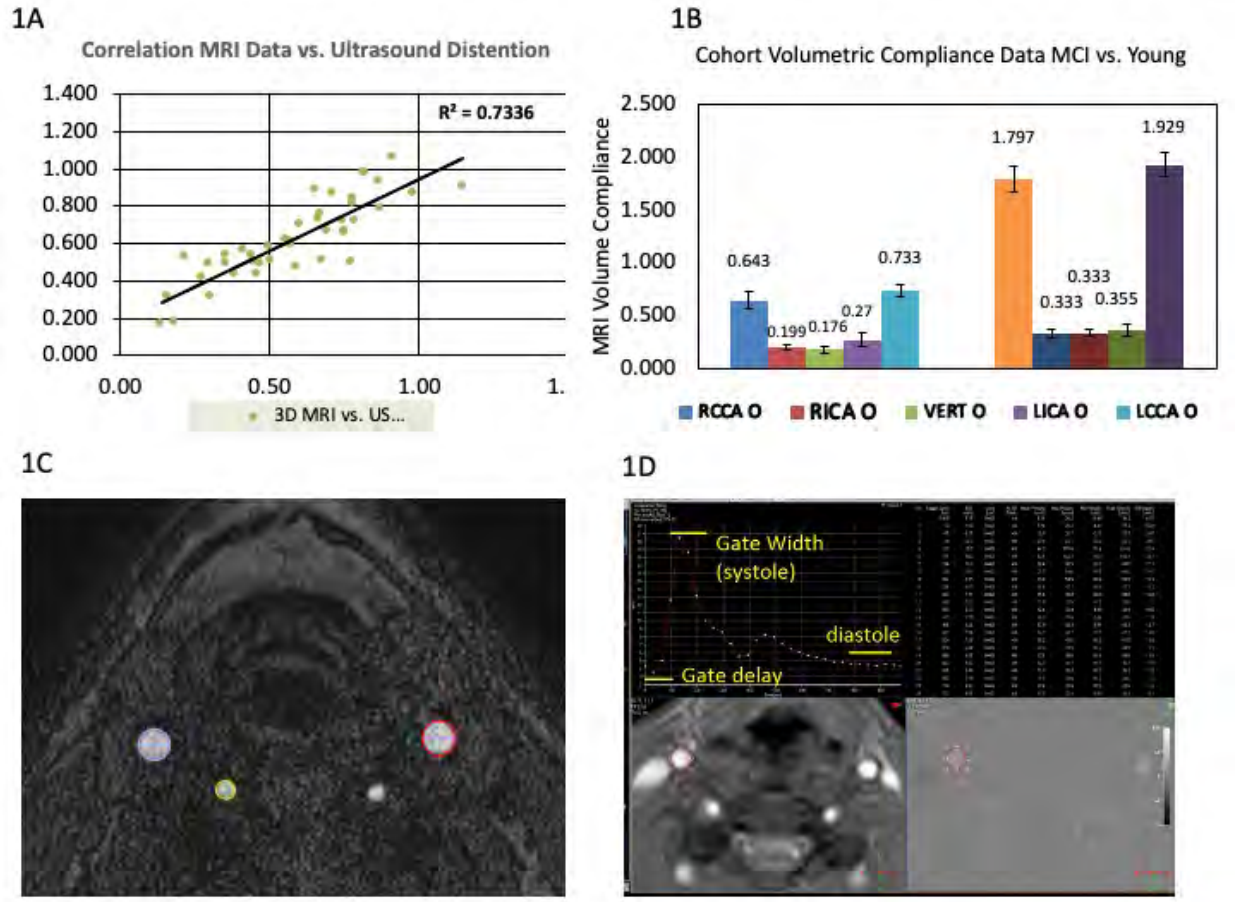

(Filename: TCT_1589_ASNR_2022.jpg)

1625

Differential Atrophy Profiles Related to APOE4 Genetic Variant: An ENIGMA-VBM Multicohort Analysis in Alzheimer's Disease

P Rajagopalan[1], V Tennant[2], S Thomopoulos[2], P Thompson[3]

[1]University of Southern California, South Pasadena, CA, [2]University of Southern California, Marina del Rey, , CA, [3]University of Southern California, Los Angeles, CA

Purpose

Alzheimer's disease (AD) is the most common neurodegenerative disorder and apolipoprotein E (APOE) ε4 allele is the greatest common genetic risk factor for late-onset AD. Patients with dementia demonstrate a strong pattern of cortical brain volume deficits in medial temporal lobes, notably the bilateral hippocampus, entorhinal cortex, amygdala and fusiform gyrus, as shown in our recent work (Figure 1). In a large multi-cohort VBM analysis in AD, we aimed to investigate how atrophy patterns in AD were modulated by carrying the APOE4 genotype.

Materials and Methods

The ENIGMA voxel based morphometry (VBM; https://sites.google.com/view/enigmavbm) pipeline was used to perform a mega-analysis and a multicohort meta-analysis on T1-weighted brain MRI data from 488 subjects across four different cohorts, namely the Alzheimer's Disease Neuroimaging Initiative (ADNI) 1, ADNIGO/2, ADNI3, and the Open Access Series of Imaging Studies (OASIS3). All participants were diagnosed with dementia and had APOE genotype data, with 316 being carriers of the APOE ε4 (ε3/ε4, ε4/ε4) and 172 being non-carriers (ε3/ε3). Protective APOE ε2 carriers were excluded. Within the 488 participants with dementia, effects of carrying the APOE ε4 allele were tested using a VBM analysis adjusting for age, sex, intracranial volumes and differences in cohorts.

Results

In participants with dementia, APOE4 carriers demonstrated relatively higher gray matter volumes in the primary motor cortex, medial frontal gyrus and posterior middle temporal gyrus, compared to non-carriers (k100, $P<0.001$, uncorrected; Figure 2). As expected, APOE ε4 carriers demonstrated lower medial temporal lobe and precuneal gray matter volumes.

Conclusions

Interestingly, within the dementia group, APOE ε4 carriers showed higher gray matter density in the primary motor cortex, a region not routinely associated with AD nor with amyloid deposition, as shown in a smaller prior study. APOE ε4 carriers showed typical medial temporal and precuneal volume reductions which commonly show amyloid deposition, consistent with the notion that APOE

ε4 mediates atrophy mainly via an amyloid dependent mechanism. Further studies in additional AD cohorts will clarify if this effect reflects a survivor bias, or relative preservation of the areas detected.

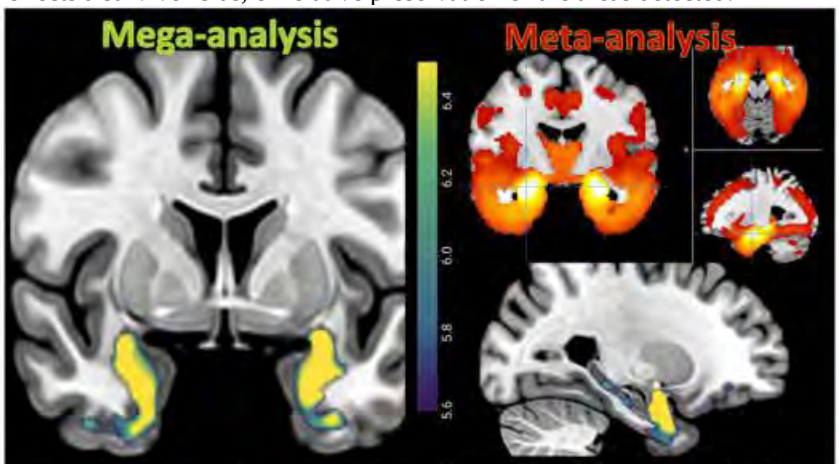

Figure 1: Z maps of Mega-analysis (Green-Purple scale with uncorrected P<0.001) and Meta-analysis (Red-Orange scale with uncorrected P <0.001) demonstrating voxel-wise cortical brain volume reductions in dementia versus controls (n=1,893) adjusted for age, sex, intracranial volumes and cohort differences.

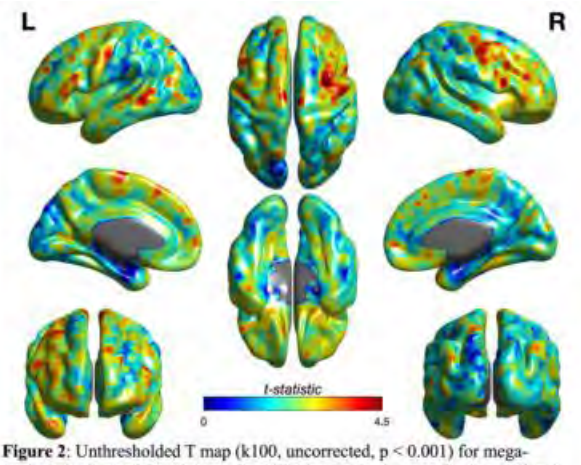

Figure 2: Unthresholded T map (k100, uncorrected, p < 0.001) for mega-analysis in dementia participants (n=488) demonstrating genetically mediated voxel-wise cortical brain volume deficits in APOE ε4 non-carriers versus carriers, after adjusting for age, sex, intracranial volumes and cohort differences.

(Filename: TCT_1625_LBCombined.jpg)

1624

Differentiation of Keratin Containing Cholesteatoma Using Dual Energy Computed Tomography

k samadi[1], C Rouse[1], R Danrad[1], D Casey[1]

[1]Louisiana State University Health Sciences Center, New Orleans, LA

Purpose

Soft tissue density lesions are frequently encountered within the middle ear on temporal bone computed tomography examinations. Differentiation of the etiology on CT has proven difficult. For instance, cholesteatoma, otitis media, and post operative granulation tissue can have similar appearance on both soft tissue and bone windows using conventional CT. In recent years, non-echo planar diffusion weighted imaging (DWI) has proven helpful in identifying DWI hyperintense cholesteatomas. However, anatomic structures, especially in the post-operative patient, are poorly delineated with this sequence. Recently, dual energy CT has been utilized for the detection of monosodium urate crystals in patients with gout 1, due to the unique attenuation profile of uric acid at two kVp peaks. Multiple authors have found a similar attenuation of uric acid and keratin containing nail beds and have drawn an assumption that keratin and uric acid demonstrate similar dual energy attenuation. Therefore, based on these attenuation characteristics of keratin, dual energy CT may be used to identify cholesteatomas in a pre-operative and/or post-operative basis and differentiate them from masses with a similar appearance on conventional CT.

Materials and Methods

Temporal bone dual-energy CT images were obtained using a Philips IQon Dual Energy Spectral CT. Peak kilovoltages of 80 and 120 kVp were utilized. Post processing was performed on a Philips Intellispace Portal. Temporal bone CT of pre-operative and post-operative patients with known cholesteatomas were retrospectively analyzed using the Uric Acid Hounsfield unit preset function. Attenuation map and subtraction images were obtained.

Results

Conventional temporal bone CT in patients with known cholesteatomas demonstrated soft tissue density within the middle ear with Hounsfield units measuring approximately 60 HU. Patients with otitis media, otomastoiditis, and post-operative granulation tissue also demonstrated similar Hounsfield units. However, dual energy CT using a set uric acid attenuation protocol was able to subtract out areas of similar attenuation in patients with known cholesteatomas.

Conclusions

Dual energy CT attenuation of keratin may be useful in differentiating keratin containing cholesteatomas from other etiologies with a similar appearance on conventional CT. This can be especially useful in the post-operative patient, using dual energy CT to distinguish recurrent or residual cholesteatomas from granulation or scar tissue.

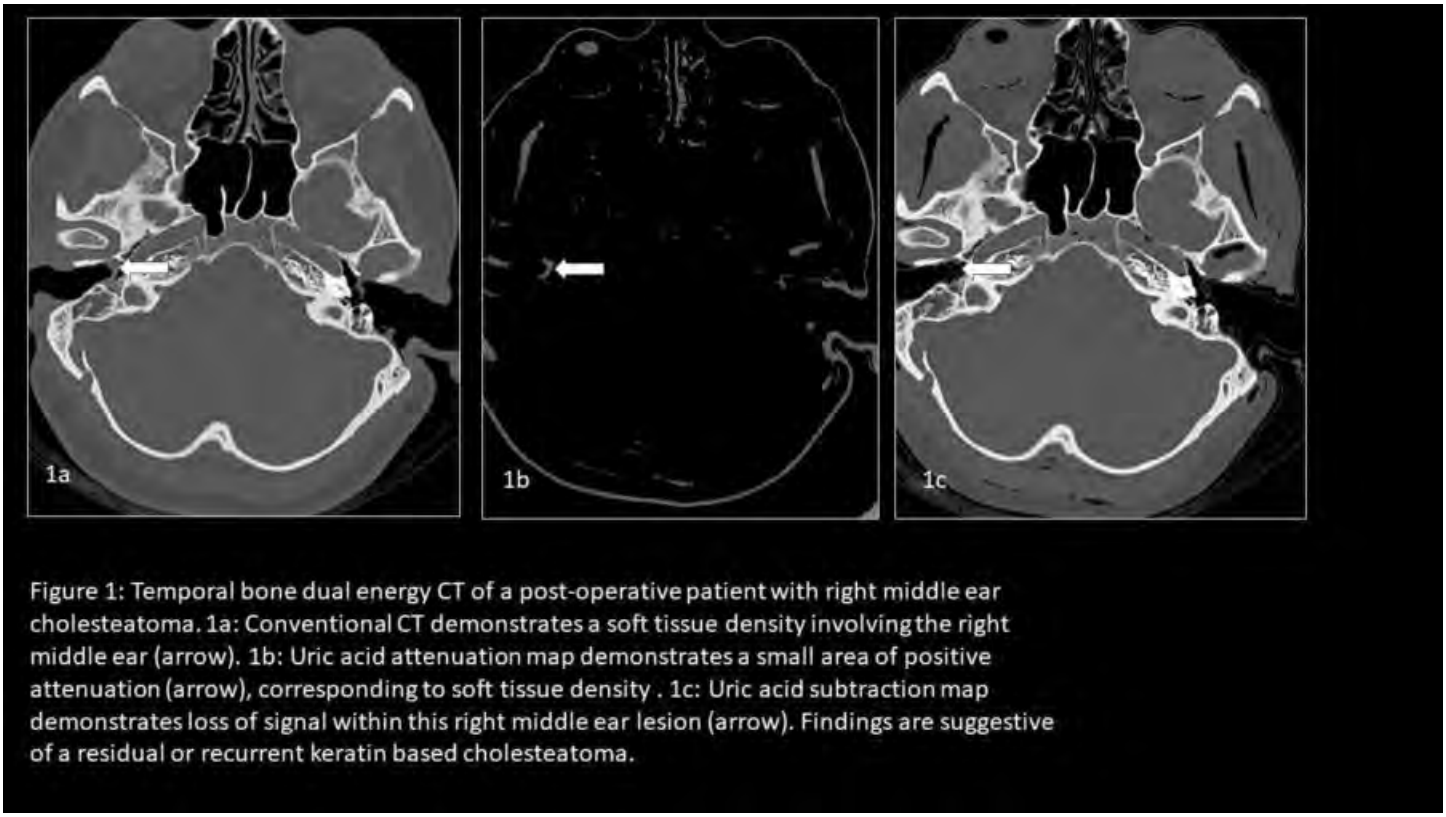

Figure 1: Temporal bone dual energy CT of a post-operative patient with right middle ear cholesteatoma. 1a: Conventional CT demonstrates a soft tissue density involving the right middle ear (arrow). 1b: Uric acid attenuation map demonstrates a small area of positive attenuation (arrow), corresponding to soft tissue density . 1c: Uric acid subtraction map demonstrates loss of signal within this right middle ear lesion (arrow). Findings are suggestive of a residual or recurrent keratin based cholesteatoma.

(Filename: TCT_1624_Slide1.JPG)

1599

Non-invasive assessment of tissue microstructure using neurite orientation dispersion and density index (NODDI) and diffusion kurtosis MR imaging (DKI) in preclinical and prodromal stages of dementia

P Srivastava[1], E Davenport[2], A Proskovec[2], H Rossetti[2], J Berry[2], J Maldjian[3], F Yu[4]

[1]University of Texas Southwestern Medical Center, dallas, TX, [2]University of Texas Southwestern, Dallas, TX, [3]University of Texas Southwestern Medical Center, Dallas, TX, [4]UT Southwestern, Dallas, TX

Purpose

NODDI is a clinically-feasible diffusion MRI-based technique that can non-invasively assess axonal integrity. The purpose of this study is to investigate the potential of NODDI to detect white matter (WM) tissue microstructural changes in preclinical and early-stages of dementia. We focused on the parietal lobe as prior histopathologic studies have shown it to be involved early in Alzheimer's Disease and other dementias [1,2].

Materials and Methods

Our analysis included age, sex, and race matched mild cognitive impairment (MCI; 34 subjects) and 34 healthy controls (HC) (mean age 61 years, 42/26 females/males, 36/32 Black/White), as well as 33 subjects with subjective memory complaints (SMC) and 33 matched HC (mean age 62 years, 47/19 females/males, 26/40 Black/White) from the Dallas Heart and Minds Study. Multi-shell diffusion MRI was performed on a 3 T scanner. NODDI and DKI maps were calculated and normalized to MNI template space. Intracellular volume fraction (ICVF [NODDI]) and mean kurtosis (Kmean [DKI]) were then measured within the parietal AAL atlas regions. Additionally, whole brain WM voxel-wise analysis of ICVF was performed using TBSS.

Results

Two sample t-tests showed significant WM ICVF differences between HC and MCI throughout the parietal lobe, and to a lesser extent between HC and SMC (Table 1). Kmean also showed significant differences between HC and MCI but not between HC and SMC (Table 2). We also found significant correlations between ICVF and processing speed (Table 3). Voxel-wise analysis showed significantly decreased ICVF in MCI compared to HC after correcting for multiple comparisons (Fig1a), whereas group differences between SMC and HC were not significant. However, in uncorrected analysis, group differences between SMC and HC trended towards significance (p=0.07) as shown in Fig1(b).

Conclusions

NODDI outperformed DKI in detecting WM tissue microstructural changes in MCI as well as SMC subjects. Additionally, more brain regions were significantly correlated with processing speed using NODDI. Significant voxel-wise group differences in ICVF were seen between MCI and HC. This study highlights the potential of NODDI to assist in the diagnosis and monitoring of patients presenting with pre-clinical and prodromal stages of dementia, facilitating early intervention.

Table 1.	NODDI in MCI vs HC				NODDI in SMC vs HC			
Parietal AAL regions	Mean HC N=34	Mean MCI N=34	p value	fdr p value	Mean HC N=33	Mean SMC N=33	p value	fdr p value
Postcentral L	0.449	0.430	**0.007**	**0.007**	0.450	0.434	**0.010**	**0.025**
Postcentral R	0.443	0.428	**0.015**	**0.013**	0.445	0.431	**0.007**	**0.025**
Parietal_Sup_L	0.442	0.421	**0.001**	**0.003**	0.441	0.424	**0.002**	**0.012**
Parietal_Sup_R	0.424	0.400	**0.003**	**0.003**	0.423	0.405	**0.002**	**0.012**
Parietal_Inf_L	0.428	0.412	**0.005**	**0.01**	0.428	0.415	**0.017**	**0.025**
Parietal_Inf_R	0.417	0.399	**0.001**	**0.003**	0.419	0.403	**0.011**	**0.025**
SupraMarginal_L	0.442	0.427	**0.012**	**0.013**	0.440	0.428	**0.028**	**0.034**
SupraMarginal_R	0.435	0.420	**0.013**	**0.013**	0.434	0.422	**0.019**	**0.025**
Angular_L	0.444	0.430	**0.024**	**0.034**	0.444	0.433	**0.057**	**0.057**
Angular_R	0.440	0.426	**0.017**	**0.015**	0.441	0.427	**0.017**	**0.025**
Precuneus_L	0.451	0.430	**0.000**	**0.001**	0.449	0.436	**0.013**	**0.025**
Precuneus_R	0.453	0.437	**0.003**	**0.004**	0.453	0.443	**0.049**	**0.054**

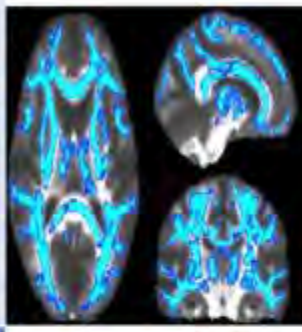

Fig 1(a): TBSS results of ICVF group differences between MCI and HC (after correcting for multiple comparisons, P=0.05). Lighter blue represents more statistically significant areas where HC>MCI ICVF.

Table 2. DKI in MCI vs HC					DKI in SMC vs HC			
Parietal AAL regions	Mean HC N=34	Mean MCI N=34	p value	fdr p value	Mean HC N=33	Mean SMC N=33	p value	fdr p value
Postcentral L	0.449	0.430	**0.006**	**0.009**	0.762	0.745	**0.032**	0.096
Postcentral R	0.443	0.428	**0.005**	**0.009**	0.760	0.741	**0.017**	0.092
Parietal Sup L	0.442	0.421	**0.001**	**0.004**	0.755	0.739	**0.023**	0.092
Parietal Sup R	0.424	0.400	**0.004**	**0.009**	0.729	0.709	**0.023**	0.092
Parietal Inf L	0.428	0.412	**0.004**	**0.009**	0.737	0.726	0.113	0.136
Parietal Inf R	0.417	0.399	**0.008**	**0.011**	0.717	0.701	0.075	0.111
SupraMarginal L	0.442	0.427	**0.005**	**0.009**	0.750	0.744	0.334	0.334
SupraMarginal R	0.435	0.420	**0.011**	**0.012**	0.744	0.729	0.061	0.111
Angular L	0.444	0.430	**0.014**	**0.014**	0.760	0.753	0.238	0.260
Angular R	0.440	0.426	**0.009**	**0.011**	0.751	0.737	0.082	0.111
Precuneus L	0.451	0.430	**0.001**	**0.004**	0.768	0.756	0.069	0.111
Precuneus R	0.453	0.437	**0.000**	**0.004**	0.769	0.755	0.083	0.111

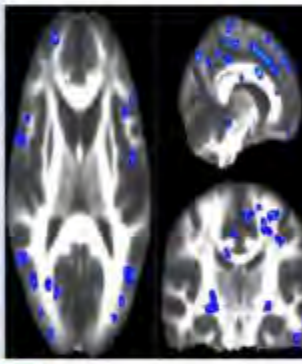

Fig 1(b): TBSS results of ICVF group differences between SMC and HC (not corrected for multiple comparisons, p=0.07). Lighter blue represents areas where HC>SMC ICVF.

Table 3. Pearson Correlation with mental processing speed (Digit symbol coding test) in MCI						
Parietal AAL regions	NODDI ICVF			DKI Kmean		
	r^2	p value	fdr p value	r^2	p value	fdr p value
Postcentral_L	0.390	**0.023**	**0.023**	0.362	**0.036**	0.053
Postcentral_R	0.476	**0.004**	**0.012**	0.354	**0.040**	0.053
Parietal_Sup_L	0.573	**0.000**	**0.005**	0.562	**0.001**	**0.006**
Parietal_Sup_R	0.522	**0.002**	**0.009**	0.518	**0.002**	**0.010**
Parietal_Inf_L	0.454	**0.007**	**0.012**	0.466	**0.006**	**0.016**
Parietal_Inf_R	0.459	**0.006**	**0.012**	0.467	**0.005**	**0.016**
SupraMarginal_L	0.454	**0.007**	**0.012**	0.396	**0.020**	**0.035**
SupraMarginal_R	0.443	**0.009**	**0.013**	0.342	**0.048**	0.054
Angular_L	0.394	**0.021**	**0.023**	0.334	0.054	0.054
Angular_R	0.472	**0.005**	**0.012**	0.421	**0.013**	**0.026**
Precuneus_L	0.437	**0.010**	**0.013**	0.455	**0.007**	**0.016**
Precuneus_R	0.427	**0.012**	**0.014**	0.335	0.053	0.054

(Filename: TCT_1599_asnrabstract.jpg)

1613

Quantitative Permeability Mapping (QPM)-MRI of Water Exchange at the Blood-Brain-Barrier: Correlation with Cortical β-Amyloid Plaque Deposition in APOE4-Positive Subjects.

J Ivanidze[1], Q Zhang[2], J Ford[3], H Bowe[4], P Leopold[4], R Crystal[5], Y Wang[4], T Nguyen[2]

[1]Weill Cornell Medicine Radiology, Larchmont, NY, [2]Weill Cornell Medical College, New York, NY, [3]Massachusetts General Hospital, Boston, MA, [4]Weill Cornell Medicine, New York, NY, [5]Weill Cornell Medicine, New York City, NY

Purpose

Impaired waste clearance across the defective BBB is an early pathophysiological mechanism in AD, preceding β-amyloid (Aβ) accumulation and cognitive impairment (CI). We recently demonstrated the feasibility and reproducibility of quantitative permeability mapping (QPM) MRI, a high-resolution 3D spiral DW-ASL pulse sequence, for kW mapping. We further demonstrated global and regional kW decrease in cognitively normal subjects across the age spectrum. The purpose of this study was correlation between between kW and cortical Aβ burden quantified on PET in APOE4 homozygous patients with preclinical AD. We hypothesized that kW decrease would correlate with increased cortical Aβ given preclinical findings of Aquaporin-4 (AQP4 depolarization) in AD.

Materials and Methods

We prospectively enrolled subjects with pre-clinical AD. We performed QPM MRI and analyzed Florbetaben PET in 3 APOE4/E4 positive subjects who had genetic testing, basic cognitive assessment including mini mental state exam (MMSE). PET segmentation was performed in AAL space using syngo.via MI neurology workflow (Siemens Healthineers). MRI segmentation was performed on 3D T1 images using FreeSurfer analysis pipeline. We a priori defined vulnerable regions (5 bilateral regions involved early in the course of AD: hippocampus, precuneus, posterior cingulate, middle frontal gyrus, cuneus). We performed Pearson correlation analysis to determine statistical significance.

Results

100% (3/3) of subjects were female (age range: 52-65 years). Cognitive scores were normal in subjects 1 and 2 (MMSE 29-30) while subject 3 had mild-moderate CI (MMSE 22). Florbetaben PET was negative in Subject 1, moderately positive in Subject 2, and diffusely positive in Subject 3. Region-specific analysis demontrated a moderate negative correlation between kW and Florbetaben PET SUV by region across Aβ PET-positive subjects (r = -0.66, p = 0.0017).

Conclusions

We found a moderate negative correlation between region-specific kW and Aβ load in APOE4+ individuals. Our findings are in direct support of our hypothesis that kW decline reflects AQP4 depolarization, a central pathophysiologic mechanism in AD, and can be measured non-invasively and sensitively with QPM.

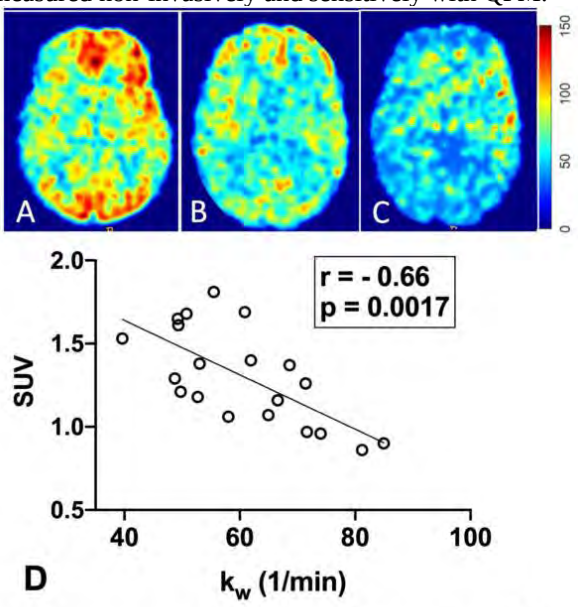

k_W decreases with increasing cortical Aβ in APOE4/4+ subjects. k_W maps (A-C) in 3 subjects (all APOE4/E4+), 52F, MMSE30, Aβ- (A), 65F, MMSE29, Aβ+ (B), 65F, MMSE22, Aβ+++ (C). Correlation plot (D): 10 ROI per subject were selected a priori: left and right hippocampus, precuneus, posterior cingulate, middle frontal, cuneus.

(Filename: TCT_1613_ASNR-late-breaking-kw-SUV.jpg)

1632

Radiomic Signature and Machine Learning Modeling of Outcomes in Cerebral Cavernous Malformations

M Jabal[1], W Brinjikji[1]
[1]Mayo Clinic, Rochester, MN

Purpose

With intracranial hemorrhage having the most impact on clinical outcome in cerebral cavernous malformations (CCM), it remains difficult to identify, with certainty, which lesions will bleed if left untreated. There has been increasing need for novel prognostic tools and predictive biomarkers to help in clinical decisions. We aimed to develop explainable radiomic-based machine learning models from MR images in a large cohort of patients with CCM to demonstrate the value of artificial intelligence (AI) and radiomics in complementing natural history studies for hemorrhage and functional outcome prediction.

Materials and Methods

One-hundred-eighty-one patients from a prospectively registered cohort of 366 adults with CM were included. FLAIR T2-weighted brain images were preprocessed, and CCM and surrounding edema were segmented before radiomic feature computation. Minority class oversampling, dimensionality reduction and feature selection methods were applied. Various machine learning models were built, cross-validated, and compared using clinical, radiomic, and combined features. SHAP was used for interpretation to determine the radiomic features with most contribution to hemorrhage prediction.

Results

The highest performances in hemorrhage predictions on the test set were combining radiomic and clinical features with a ROC-AUC of 83% using LR and MRMR selected features, and an F1 score of 61% and 85% sensitivity using KNN model with PCA. MLP had the best performance predicting mRS≥2 with ROC-AUC of 74% using PCA derived features. For interpretation of the selected radiomic signature XGB model, SHAP highlighted 6 radiomic features contributing the most to hemorrhage prediction.

Conclusions

Radiomic-based modeling using machine learning has the potential to highlight novel imaging biomarkers that predict hemorrhagic and functional outcomes, ensuring more precise and personalized care for CM patients.

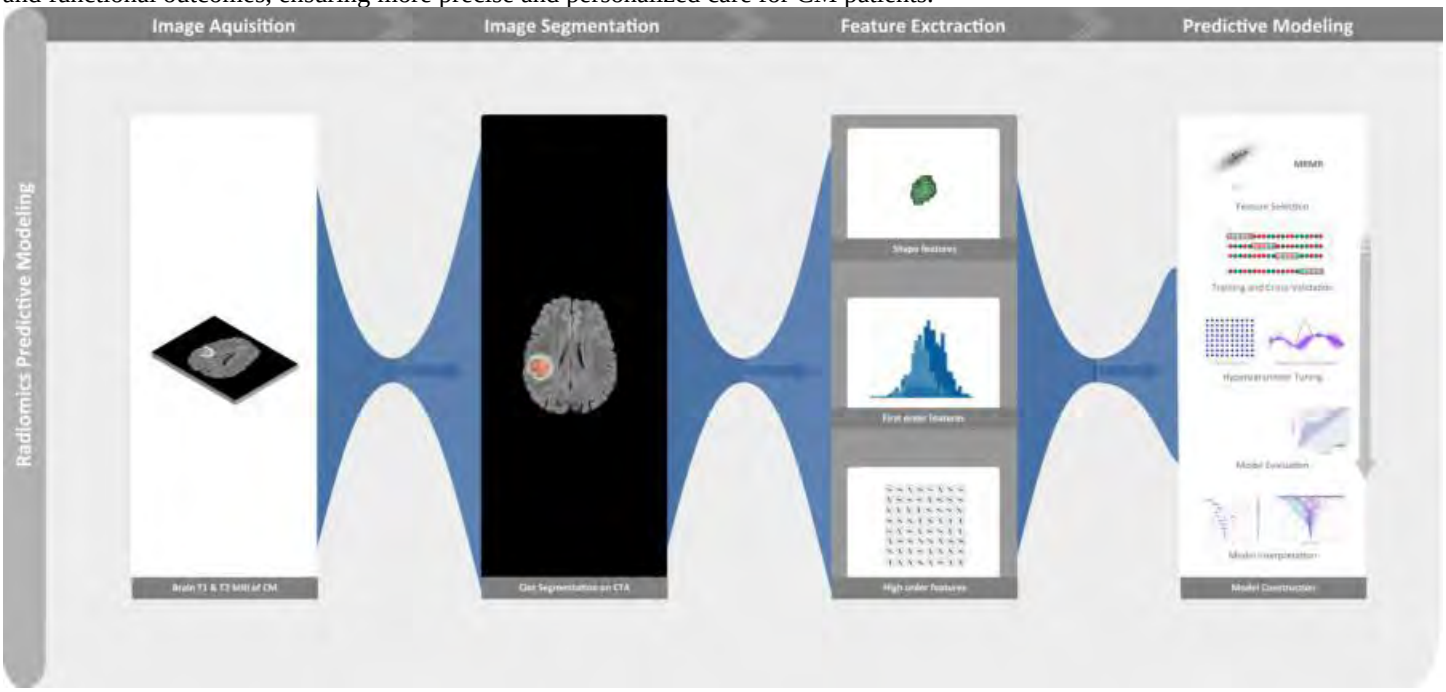

(Filename: TCT_1632_Untitled-21.jpg)

1578

Radiosurgical Treatment Planning and Response Assessment in Meningiomas Using [Ga68]DOTATATE PET/MRI

S Chang[1], S Kim[2], M Roytman[1], A Haghdel[1], R Ramakrishna[1], S Pannullo[2], T Schwartz[3], J Osborne[2], R Magge[3], E Lin[1], J Knisely[1], J Ivanidze[4]
[1]Weill Cornell Medicine, New York, NY, [2]New York-Presbyterian Hospital/Weill Cornell Medicine, New York, NY, [3]Weill Cornell Medicine/NewYork-Presbyterian Hospital, New York, NY, [4]Weill Cornell Medicine Radiology, Larchmont, NY

Purpose

Somatostatin receptor 2 (SSTR2)-targeted PET imaging using [68Ga]-DOTATATE can assist in distinguishing residual meningioma from postsurgical change in the postoperative setting [1-4]. We have previously shown that DOTATATE-PET/MRI assisted postoperative target delineation for patients with intracranial meningiomas reduce planning target volume (PTV) and decrease organ-

at-risk dose [5]. This study aims to demonstrate utility of DOTATATE PET/MR for radiosurgical treatment (RT) response assessment in meningiomas.

Materials and Methods

Following resection and histopathological confirmation of WHO Grade, 17 patients underwent postoperative radiation treatment planning using DOTATATE PET/MRI according to our published protocol. Both DOTATATE PET and gadolinium-enhanced T1 weighted MR imaging were incorporated in RT planning. All patients underwent follow-up DOTATATE PET/MRI at 6-12 months following completion of stereotactic radiosurgery (SRS). Maximum absolute standardized uptake value (SUV) and SUV ratio (SUVR) of lesion relative to superior sagittal sinus SUV were obtained. MRI size product was available in 15/17 patients. Paired t-test and linear regression were performed for statistical analysis.

Results

Across the cohort of 17 patients, 42 meningiomas were treated. Clinical and demographic characteristics of the cohort are summarized in Figure 1. Following SRS, DOTATATE PET/MRI demonstrated on average a 35.2% decrease in SUV (p=0.0002) and a 49% decrease in SUVR (p<0.0001). MRI on average demonstrated at 41.2% decrease in size product. However, there was a wide range, and some subjects demonstrated an increase in size product. SUV/SUVR of meningioma were significantly correlated with lesion size product (p=0.002, p=0.0006, respectively). The rate of SUVR decrease post-RT was found to significantly predict percent size product decrease (p=0.0292).

Conclusions

DOTATATE PET SUV and SUVR demonstrated significant decrease post-RT that correlated with decrease in lesion size. Of note, the rate of change in SUVR was found to predict percent change of lesion size. DOTATATE PET/MR is thus a promising, complementary adjunct modality in radiation treatment planning and response assessment for atypical and anaplastic meningiomas. We plan to perform further correlative analyses with lesion-specific follow up clinical outcomes data to determine if the degree of post-RT SUV and/or SUVR decrease can predict progression-free-survival.

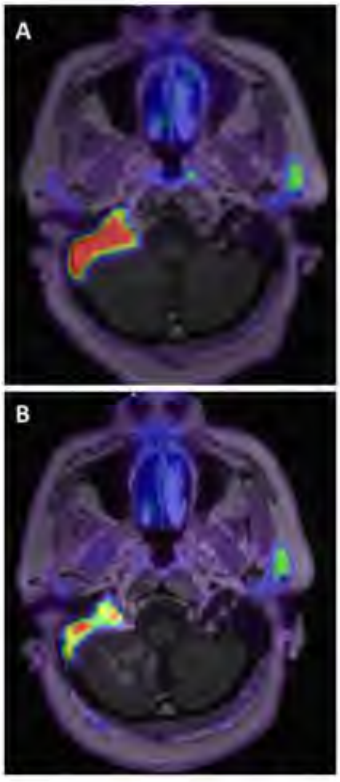

C

N Patients	17
Age	55.5 (21 – 74)
Sex	70.6% F (12/17)
N meningiomas identified on 1st PET	70
N treated meningiomas	42
N meningiomas per patient	Median: 4, Range: 1-9 (17.5% with 1, 41.2% with 2-4, 41.2% with >4)
N treated meningiomas per patient	Median: 2, Range: 1-7 (41.2% with 1, 11.8% with 2, 29.4% with 3, 17.6% with >3)
WHO grade	11.8% (2/17) WHO grade unknown
	11.8% (2/17) WHO grade 1
	52.9% (9/17) WHO grade 2
	23.5% (4/17) WHO grade 3
Surgical history	88.2% (15/17)
Mean time from Surgery to 1st PET	21.2 mos (1.4-94.1 mos)
Mean SRS Radiation Dose	29.6 Gy (7-35 Gy)
SRS Radiation Fractions	Median: 5 fx (1-5), Mean: 4.5 fx
Progression Free Survival (PFS)	6 months: 11/17 (64.7%); 12 months: 8/12 (66.7%); 18 months: 7/9 (77.8%)
Mean Post-RT follow up	14.2 months (6 - 18 months)

D

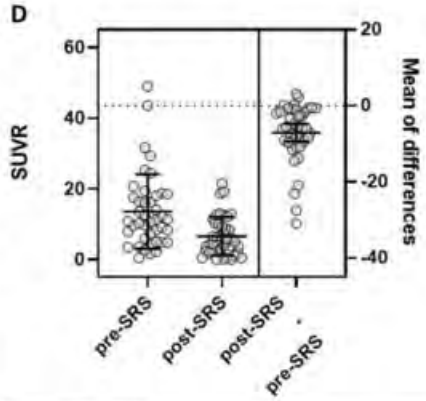

Figure 1. A + B) Example images from a representative subject, a 71-year-old man whose follow-up DOTATATE PET/MR demonstrated **A)** an intensely avid expansile enhancing mass centered in the right sigmoid sinus/internal jugular vein. **B)** 20.5 months after SRS (35 Gy in 5 fractions), the mass demonstrated a mild increase in size (7.48 cm^2 → 8.75 cm^2) but a marked decrease in SUV (58.7 → 30.1) and SUVR (48.92 → 21.50). Note partially visualized new irregular enhancement in right cerebellar hemisphere which was a new early subacute infarct the patient had developed in the interim. **C)** Clinical and demographic characteristics of the study population. **D)** DOTATATE-PET derived SUVR decrease ($p < 0.0001$) visualized with respective estimation plot on the right.

(Filename: TCT_1578_SJCHANG_ASNRLateBreakingFigure_03142022.jpg)

1579

RAPID Aneurysm: Artificial Intelligence for Unruptured Cerebral Aneurysm Detection on CT Angiography

J Heit[1], J Honce[2], V Yedavalli[3], C Baccin[4], R Tatit[4], K Copeland[5], V Timpone[6]

[1]Stanford University, Los Altos, CA, [2]Unviersity of Colorado School of Medicine, Aurora, CO, [3]Johns Hopkins School of Medicine/Johns Hopkins Hospital, Baltimore, MD, [4]Albert Einstein Hospital, São Paulo, Brazil, São Paulo, NA, [5]Boulder Statistics, Steamboat Springs, CO, [6]University of Colorado Hospital, Denver, CO

Purpose

Cerebral aneurysms may result in significant morbidity and mortality. Identification of these aneurysms on CT Angiography (CTA) studies is critical to guide patient treatment. We determined the performance of a semi-automated artificial intelligence software program (RAPID Aneurysm) for the detection of cerebral aneurysms on CTA.

Materials and Methods
RAPID Aneurysm was used to detect the presence of cerebral aneurysms in CTA studies. The gold standard was aneurysm presence and location as determined by the consensus of three expert neuroradiologists. Aneurysm detection accuracy, sensitivity, specificity, positive predictive value, negative predictive value, and positive and negative likelihood ratios by RAPID Aneurysm were determined.
Results
53 studies with a total of 62 aneurysms were evaluated. RAPID Aneurysm had a sensitivity of 0.839 (95% CI: 0.728-0.910), specificity of 0.995 (95% CI: 0.988-0.998), a positive predictive value (PPV) of 0.912 (95% CI: 0.811-0.962), and a negative predictive value (NPV) of 0.989 (95% CI: 0.981-0.994) for cerebral aneurysm detection. Accuracy ranged from 94.3-100% depending upon aneurysm location. False negative aneurysms were smaller than correctly detected aneurysms in each vessel segment.
Conclusions
RAPID Aneurysm is highly accurate for the detection of cerebral aneurysms on CTA.

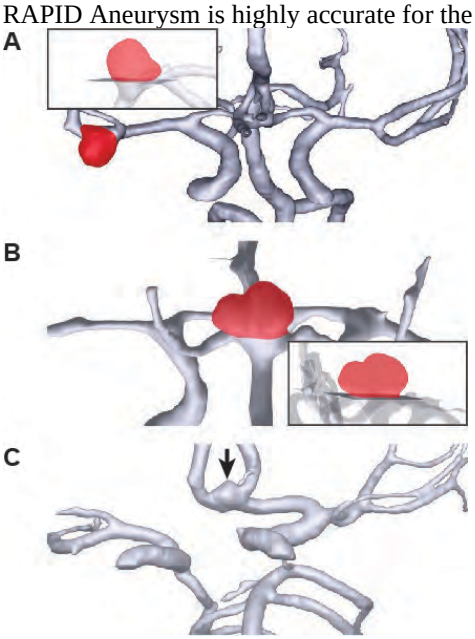

(Filename: TCT_1579_Figure1.jpg)

1608

Unravelling the neuropathogenesis in COVID associated minor neurocognitive disorder- Imaging of excitotoxic brain injury.

J Chaganti[1]
[1]St Vincent's Hospital, Sydney, Australia

Purpose
SARS-COV-2 infection has been implicated in multi-system injury much after the virus is completely eliminated. Brain fog is a term which is used to describe the constellation of symptoms that are ascribed to patients who had COVID and subsequently feel lethargic, apathy and lack of motivation persisting much after they are aviremic. This cohort is put under the broad term "long COVID". Neuron has been implicated as one of the likely causes for this long COVID and is potentially play a role in the pathogenesis of the in this neurocognitive disorder akin to the findings described with MERS-CoV. We hypothesized that the neuron is likely to have been initiated by an excitotoxic injury and consequent disturbance in the blood brain barrier.
Materials and Methods
In this prospective study, we have recruited fourteen patients who had recovered from acute COVID infection, but continue to struggle from minor neurocognitive disorder and 10 sex and age matched controls. All of them underwent DCE perfusion, Diffusion Tensor Imaging and single voxel MR spectroscopy of the frontal cortex and white matter as well as Brain stem in addition to the standard MR imaging protocols. MRS derived metabolites, DTI metrics were correlated with K trans to identify if there is any relationship between the permeability and neuronal integrity with metabolites associated with neuroinflammation.
Results
As compared with the normal controls the permeability metric has significantly increased in several areas of the brain indicating diffuse disturbance in the BBB (p=0.005). The MR spectroscopy showed marked reduction in NAA and moderate reduction in the Glx (Glutamate + Glutamine) (as compared with the controls particularly in the frontal white matter (p=0.004). The radial diffusivity has positively correlated with the increased k trans.
Conclusions
Patients with brain fog from Long COVID is associated with diffuse increase in the permeability possibly as a result of excitotoxic injury as suggested by increased Glx compounds. Positive correlation of radial diffusivity with K trans indicate that there is likely loss of myelin integrity at least temporarily in these patients.

1321
Cost Effectiveness of Perfusion imaging in patients with low ASPECT score
A Malhotra[1], M Khunte[2], X Wu[3], S Bajaj[4], S Payabvash[5], P Sanelli[6], D Gandhi[7]
[1]Yale University School of Medicine, New Canaan, CT, [2]Yale University, New Haven, CT, [3]University of California (San Francisco), San Francisco, CA, [4]Yale School of Medicine, New Haven, CT, [5]Yale, New Haven, CT, [6]Northwell Health, Manhasset, NY, [7]University of Maryland School of Medicine, Baltimore, MD

Purpose
Imaging may identify a subset of patients with large-vessel-occlusion (LVO) and a large volume of irreversibly injured tissue who might benefit from endovascular thrombectomy (EVT). The objective of this study was to determine the health outcomes and cost effectiveness of imaging selection for EVT in patients with acute ischemic stroke with LVO and low Alberta Stroke Program CT score (ASPECTS).
Materials and Methods
A decision-analytical study was performed with Markov modeling to estimate the lifetime quality-adjusted life years (QALYs) and associated costs of patients selected with imaging versus no-imaging selection for EVT. The study was performed over a lifetime horizon with a societal perspective in the US setting. One-way, two-way and probabilistic sensitivity analyses were performed.
Results
Base Case Analysis The base case calculation showed perfusion imaging to be the dominant strategy compared to no imaging in patients presenting with LVO and large core infarct size. Perfusion imaging yielded 6.27 QALYs (95% confidence interval (CI): 5.15 – 7.39 QALY) at a cost of $529,309 (95% CI: $442,376 - $630,444); no-imaging yielded 5.23 QALYs (95% CI: 4.44 – 6.03 QALY) at a cost of $603,400 (95% CI: $511,704 - $706,588). Perfusion imaging resulted in 1.04 QALYs incremental health benefit at a lower cost. The difference in health benefit per patient was equivalent to 380 days in perfect health and 479 days in mRS 0-2. For our additional subgroup analysis for 55-year-old patients presenting with LVO and large core infarct size, perfusion imaging yielded 9.16 QALYs (95% CI: 7.50 – 10.79 QALYs) at a cost of $962,530 (95% CI: $780,172 - $1,170,684) and IVT yielded 7.69 QALYs (95% CI: 6.52 – 8.89 QALYs) at a cost of $1,083,789 (95% CI: $893,835 - $1,298,606). Perfusion imaging resulted in a 1.47 QALYs incremental health benefit, equivalent to 537 days in perfect health and 603 days in mRS 0-2. Perfusion imaging remained the dominant strategy. Monte Carlo simulation with 10,000 sampling showed imaging to be the cost-effective strategy in 98.04% of iterations using a WTP threshold of $100,000/QALY.
Conclusions
Perfusion imaging is cost-effective in management of acute stroke patients with low ASPECTS, both by appropriately selecting patients with mismatch for EVT, and by avoiding EVT and resultant complications and poor outcomes in patients with no mismatch

1285
Covid-19 viral vector vaccine : A spectrum of neurological manifestations
H Haseeb[1], J Jen[2], M Patel[2], M Al-Tibi[3], V Sawlani[2]
[1]Queen Elizabeth Hospital-University Hospitals Birmingham, Birmingham, West midlands, [2]Queen Elizabeth Hospital-University Hospitals Birmingham, Birmingham, West Midlands, [3]Queen Elizabeth Hospital- University Hospitals Birmingam, Birmingham, West Midlands

Purpose
There is a globally well documented evidence of neurological manifestations secondary to Covid-19 infection, however vaccine-induced immune thrombocytopenia and thrombosis (VITT) , although a rare complication, is associated with ChAdOx1 adenoviral vector vaccine and has been seen in up to 15.1 per million doses. We report and discuss a case series (n=16) of vaccine-induced neuroimaging manifestations.
Materials and Methods
Data Collection Patients presented between March-June 2021; all had recent COVID vaccination with overall onset of symptoms 1-3 weeks post vaccination, half following the second dose, and all were COVID PCR negative. VITT was seen in 75% of the cases (n=12). Cerebral venous sinus thrombosis (CVST) was the most common presenting feature (n=10), some complicated by venous bleeds (n=3). Six patients required mechanical thrombectomy and made a good recovery. One patient developed ischemic infarct and subarachnoid hemorrhage, requiring long term rehabilitation and anticoagulation. The second most common finding was acute disseminated encephalomyelitis (ADEM, n=3), treated with IV immunoglobulins, one requiring prolonged hospitalization.
Results
Outcomes: In our cohort, the majority of patients with vaccine-induced neuroradiological complications made a good recovery (n=11), however there was death (n=3) and severe morbidity (n=2).
Conclusions
Against the backdrop of a successful vaccination program in the United Kingdom, VITT has emerged as a rare complication and can

have serious consequences. Up to 6 October 2021, 151 cases of CVST were reported in UK following the AstraZeneca COVID-19 vaccination. The cases discussed represent rare complications. Timely recognition and rationalized treatment decisions offer a reasonably good prognosis and add to the evolving understanding of the etiopathogenesis of these complications.

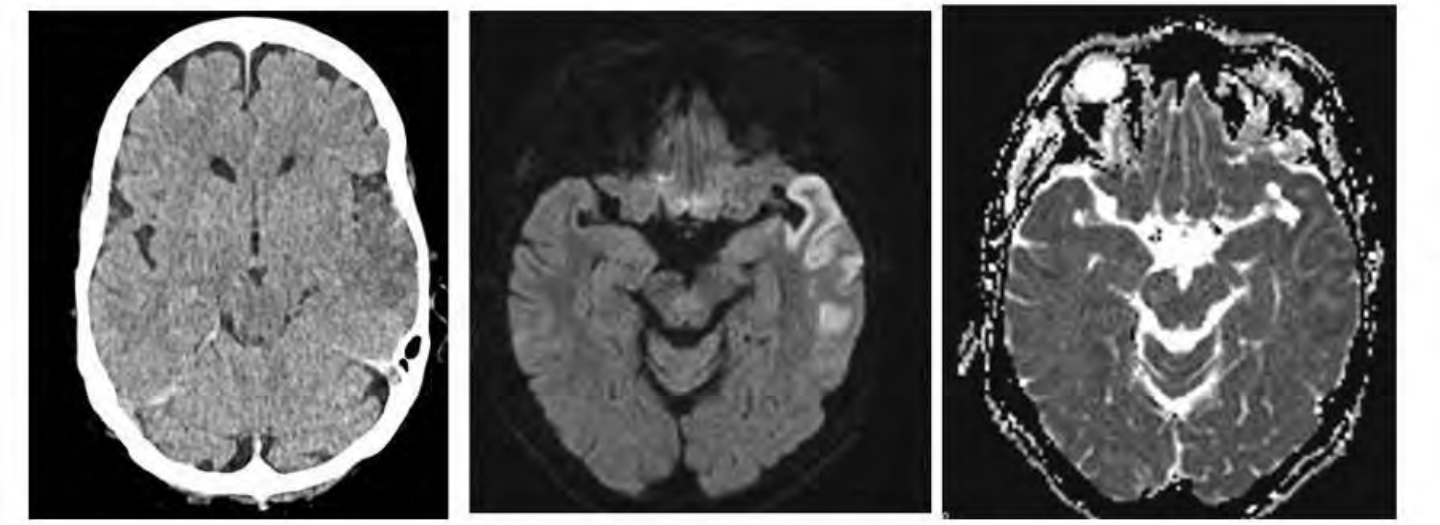

(Filename: TCT_1285_title.jpg)

1139

Current Status of Clinical and Academic Productivity Bonus Proportions

S Ameli[1], M Motaghi[2], D Yousem[3]
[1]UAMS, Little rock, AR, [2]Johns Hopkins, Baltimore, MD, [3]Johns Hopkins Medical Institution, Evergreen, CO

Purpose
Many academic and private radiology practices incentivize clinical productivity. However, studies have shown less widespread incentives dedicated to academic productivity. We investigated the current state of incentive plans in neuroradiology practices in the United States.
Materials and Methods
An electronic survey was emailed to the program directors (PD) of Neuroradiology fellowship Neuroradiology fellowship (N=87) programs. The survey queried the proportion of salary appropriated to various types of bonuses, changes over time, and satisfaction with incentive plans.
Results
The survey response rate was 57/87 (65.5%). Of 57 PDs responding, 51 (89.5%) were from university programs. On average a greater percentage of the total annual bonus was devoted to academic productivity than clinical productivity (51.3% vs. 28.6%, p-Value = 0.03). However, within the past 5-10 years the size of the academic bonuses decreased more than increased (13% vs 27%). Inversely, clinical productivity bonuses increased more than decreased over time (33% vs. 18%). The maximum overall value of bonus money that was incentivized each year was mostly within the 0- $20K category (29%), or $21-$40K (22%). While 47% of PDs were satisfied with their current incentive plan, 42% of PDs were dissatisfied and wanted a change in their incentive plans.
Conclusions
37 out of 57 (65%) neuroradiology programs incentivize academic productivity. Although a greater percentage of the total annual bonus is devoted to academic productivity than RVU productivity in neuroradiology, our survey showed that within the past 5-10 years, the incentives dedicated to academic productivity were more likely to have decreased than increased.

493

Diagnostic Errors in Brain Pathology: Retrospective Analysis of a Large Tertiary Academic Medical Center Attending Neuroradiologist Database

I Brown[1], L Hacein-Bey[1], O Raslan[1], R Assadsangabi[1], V Ivanovic[1]
[1]UC Davis Medical Center, Sacramento, CA

Purpose
We conducted a retrospective analysis of diagnostic neuroradiology attending errors in brain pathology at a single tertiary academic institution to evaluate association of errors and daily volume of interpreted studies.
Materials and Methods
Database spanning from 2014 - 2020 was searched for attending physician errors in brain pathology on CT and MR neuroradiology studies. Data was collected on missed findings, study types, interpretation setting, and further categorized by location. Welch's t-test

evaluated for significant differences between mean volume of interpreted studies per shift for the groups with and without documented error.

Results

A total of 245,762 Neuroradiology CT and MRI studies were interpreted with a mean volume of 35.24 (+/-21.59) interpreted studies per shift. A total of 282 studies contained a diagnostic error, with a mean of 45.29 (+/-24.04) interpreted studies on shifts when errors were made. Shifts without documented errors had a mean volume of 34.88 (+/-21.59) interpreted studies per shift. The results suggest a highly significant difference, $t(282) = 12.45$, $p<0.0001$, with a higher mean volume of interpreted studies per shift when an error was documented. 74.8% of errors were perceptual and 25.2% were interpretive; 92.1% were clinically significant (RADPEER 2b or 3b). The most common locations of errors included brain parenchyma 37.3%, extra-axial 19.7%, skull base 19.0%, and vascular 11.6%. The two most common missed pathologies were tumor (35.8%) and vascular etiologies (33.0%).

Conclusions

Diagnostic errors were associated with higher interpretation volumes, majority were perceptual and clinically significant. Most common errors were tumors and vascular etiologies.

1189

Diversity, Equity and Inclusion: Analysis of IMG Applicants Experience in the 2020 Diagnostic Radiology Residency Match

M Hosseiny[1], P Khoshpouri[2], S Ramezanpour[3], D Yousem[4]

[1]UCSD, Los Angeles, CA, [2]None, Vancouver, British Columbia, [3]None, San Francisco, CA, [4]Johns Hopkins Medical Institution, Evergreen, CO

Purpose

1) analyze the proportion of the Diagnostic Radiology (DR) residency positions filled by International Medical School Graduates (IMG), American Medical School Graduates (AMG MD), and Doctor of Osteopathic Medicine (DO) applicants, 2) compare these values with other specialties and 3) analyze DR residency match results for IMGs in each state.

Materials and Methods

The official published data of national residency match program (NRMP) for the 2020 Main Residency Match were accessed and reviewed from NRMP website (https://www.nrmp.org/main-residency-match-data/). The proportions of DR residency positions filled by US citizen and non-US citizen IMGs were compared with the overall match results for all applicants and all specialties. Match data were reviewed state-wise to assess the distribution of IMGs ranked into DR residency spots.

Results

Overall, 990 PGY2 and 123 PGY1 DR residency positions were offered, of which 967 PGY2 and 116 PGY1 spots were filled. Of filled PGY2 spots, the proportion of AMG MD, DO, non-US IMGs and US IMG applicants were 72.1%,14.8%, 8%, and 5.1%, respectively. The share of IMG applicants from the filled DR spots was lower compared to the average of all specialties. (Fig. 1a) Among applicants who ranked DR as their only choice, 60.4% of non-US and 67.9% of US IMGs were matched, compared to a match rate of 97.8% for AMG MD and 97% for DO applicants whose only choice for specialty was DR. (Fig. 1b) At state-wise level, the ratio of matched IMGs/total DR residency spots was highest at AZ (62.5%, 5/8) followed by MI (38%, 8/21), MA (25%, 15/60), FL (25%, 13/52) and NY (19.1%, 26/136). There were 19 states who did not have any IMGs match into their DR Residency spots. Of these, NC (28), GA (23), VA (21) had the highest number of eligible DR residency spots.

Conclusions

IMGs filled 14.8% of the DR residency positions in 2020 main residency match, compared to 21.7% of total residency positions filled by IMGs in all specialties. Overall, AZ, MI, MA, FL and NY were the most IMG-friendly states, while in 19 states with DR residency spots, no IMG applicants were matched. The findings have implications on the goals of diversity, equity and inclusion in the Radiology specialty.

Specialty	#Total positions	#Filled positions	#AMG MD	#DO	#US IMG	#Non-US IMG
DR PGY2	990	967	72.1% (697/967)	14.8% (143/967)	5.1% (49/967)	8% (78/967)
All Specialties	37008	35048	58.8% (20634/35048)	18.9% (6630/35048)	9.3% (3277/35048)	12.4% (4349/35048)

Figure 1a: Proportions of filled positions in DR compared to the positions for all specialties, per type of applicant

Specialty	# AMG MD matched	#DO matched	#US IMG matched	#Non-US IMG matched
DR	97.8% (441/451)	97% (98/101)	67.93% (19/28)	60.4% (32/53)
All specialties	94% (15034/15989)	91.3% (4558/4991)	58% (1817/3134)	59.7% (2744/4597)

Figure 1b: Successful match rate among applicants who ranked a single specialty as their only choice, per type of applicant

(Filename: TCT_1189_Figure1.jpg)

1019

Meet the symmetricals. A lesson to trainees

A Hussien[1]
[1]*UT southwestern, Dallas, TX*

Purpose

Neuroradiology is unique in its anatomical nature in comparison to the rest of the radiology subspecialties. There are many types of disease entities that are bilateral and symmetrical and easy to overlook by radiologists, particularly the trainees and less experienced radiologists. We think that our eyes have tendency to dismiss the abnormalities that are not unilateral , and they require more mental effort to be able to notice. Some of these entities are of significant importance to recognize in patient management and decision making. This presentation focuses on discussing the various disease entities that may have bilateral and symmetrical imaging abnormalities, and the best imaging clue to identify them.

Materials and Methods

A list of disease entities will be provided and classified based on the anatomical location. The focus will be mainly on the entities that are easy to miss on imaging, based on 10 years of experience in at three different institutions. For example: Basal ganglia bilateral symmetrical disease Brain cortex bilateral symmetrical disease Bilateral symmetrical disease in the ear

Results

With this exhibit the audiences will have more awareness of the subtle but important disease entities that may be missed because of the symmetrical appearance.

Conclusions

Some neurological disease entities can present with symmetrical imaging appearance. A special attention in image evaluation search pattern needs to be paid to avoid missing them.

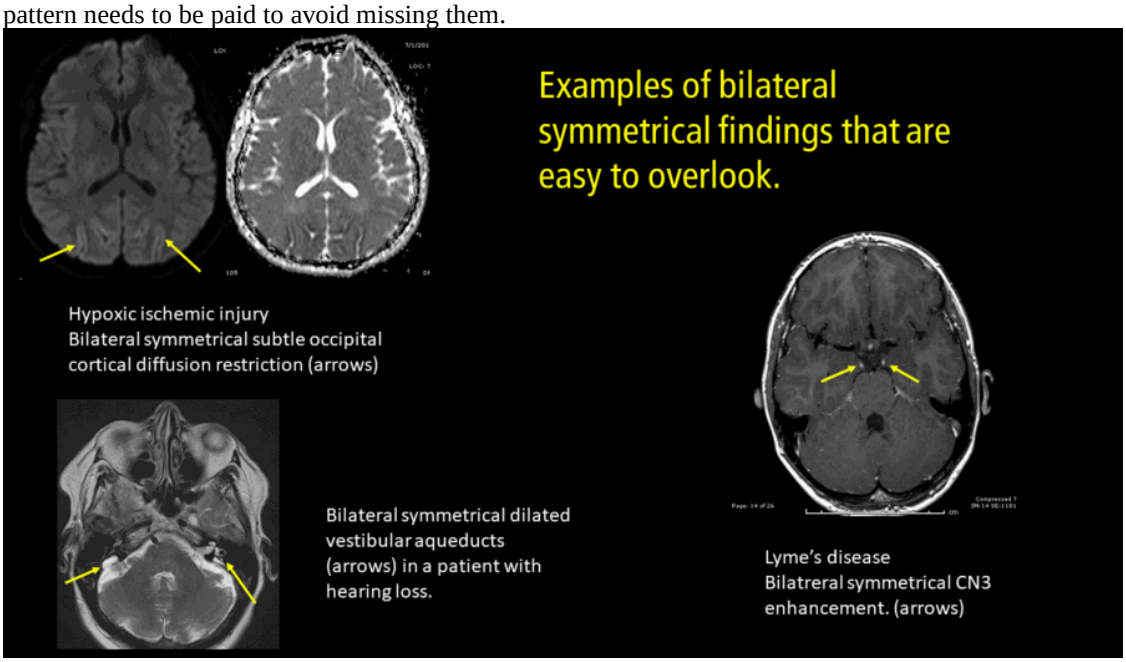

(Filename: TCT_1019_Symmetricals.gif)

1429

Patterns of Responsiveness among Radiologists Receiving AI Reports of Potentially Missed Findings

B Delman[1], P Belani[1], N Kagetsu[1], D Mendelson[1], A Doshi[1]
[1]*Icahn School of Medicine at Mount Sinai, New York, NY*

Purpose

Our system runs Aidoc software, which detects and prioritizes CTs with high likelihood of abnormalities. The software also emails advisories to alert radiologists when it detects a critical value that is not found in the associated written report. The purpose of this study was to characterize how radiologists respond to these emails, including patterns of notification and reporting.

Materials and Methods

All post-hoc emails in our health system advising of possible misses from 6/23/20 and 11/1/21 were included in this review. Population was limited to neuroimaging findings, including intracranial hemorrhage and C-spine fractures. For each email, imaging was reviewed to determine true or false positivity, radiologists' response or lack thereof in the report, and timeliness of provider notification and report addenda. Accuracy and responsiveness were tallied and summarized.

Results

Nineteen advisory emails were reviewed. 63% (12/19) were adjudicated as true positive alerts (i.e., algorithm correctly identified a finding not mentioned in the report) and 37% were false positive (adjudication did not agree). True positives included 7 hemorrhages

and 5 cervical fractures. Among the 12 positive cases, formal addenda were dictated in 10 (83%); exceptions included stable trace intraventricular and subarachnoid blood and a dens fracture on cervical CTA which was subsequently shown on MRI less than 1 hour later. Notification of provider about a change of interpretation was found in 6/10 cases with addenda, with an average time between email and notification of 29.6 hours (-10.8 to 121.1 hrs).

Conclusions

This retrospective review on advisory emails characterized how radiologists respond to discrepant findings. Although software may alert radiologists to findings in realtime, failure to detect or realize these alerts can result in missed diagnostic opportunities. We found that radiologists generated addenda on 10/12 (83%) of cases where the AI email advisory did correctly reveal an abnormality that was initially overlooked. However, even when email correctly suggests a finding, in 4/10 cases (40%) the radiologist dictated an addendum without documenting notification of the provider. In those cases where notification was documented, this occurred on average 29.6 hours after the email. These findings suggest that targeted advisory to one radiologist may not be a time-effective way to advise of potential diagnostic errors.

1081

Persistent Abnormal Cerebrovascular Reactivity and Vessel Wall Enhancement in Individuals Recovered from COVID-19 Infection

A Callen[1], A Thaker[1], R Pollard[2], B Sauer[3], W Jones[3], J Pattee[1], B Steach[1], J Tanabe[1], V Timpone[1]

[1]University of Colorado School of Medicine, Department of Radiology, Aurora, CO, [2]University of Pittsburgh School of Medicine, Department of Neurology, Pittsburgh, PA, [3]University of Colorado School of Medicine, Department of Neurology, Aurora, CO

Purpose

The extrapulmonary, vascular effects of COVID-19, have emerged as one of the most devastating components of the disease. Viral tropism to the vascular endothelium and resultant endothelial dysfunction has emerged as a putative mechanism for vascular pathology. It is unknown whether acquired endothelial dysfunction and inflammation persists after the acute infectious phase. The purpose of this study is to assess basal cerebral blood flow (CBF), cerebral vasoreactivity (CVR), and arterial wall imaging (AWI) in patients previously infected with COVID-19.

Materials and Methods

Individuals who received neuroimaging during or after documented COVID infection were invited to participate. Never-infected individuals were recruited as control subjects through hospital fliers. CBF and CVR were measured using a PCASL MRI perfusion technique, with an acetazolamide (ACZ) stimulus. CBF maps were coregistered to T1-weighted structural images, and then normalized to a standard atlas to generate regions of interest. CVR was defined as the absolute difference in CBF before and after ACZ. AWI was performed using a post-gadolinium 3D high resolution variable flip angle black blood post contrast sequence. Two neuroradiologists identified and characterized the presence of any AWI abnormalities by consensus decision in a blinded fashion. Data is available for 13 subjects: 8 COVID+ and 5 COVID-. Basal CBF and CVR were assessed for the whole cortex and 5 sub-regions: deep grey nuclei, frontal, occipital, parietal, and temporal lobes. Two-sample t-tests were used to assess whether infection was associated with changes in basal CBF. Linear mixed models were used to assess whether CVR differences were associated with infection. Confidence intervals for the sub-regions incorporate a Bonferroni correction for multiple testing.

Results

There is a statistically significant association between COVID status and whole cortex CVR (mean difference -9.0, 95% CI -17.6, to -0.5, p = .04). Regional subanalysis accounting for multiple comparisons demonstrated no statistically significant difference in lobar subregions. COVID positive subjects tended to have lower global and regional basal CBF, although this tendency was not statistically significant. Of the 8 COVID- subjects, 4 had AWI abnormalities. None of the 5 COVID- subjects had AWI abnormalities.

Conclusions

CVR and AWI abnormalities suggest persistent endothelial dysfunction in some adults in the post-infectious period. This should be further interrogated in larger populations.

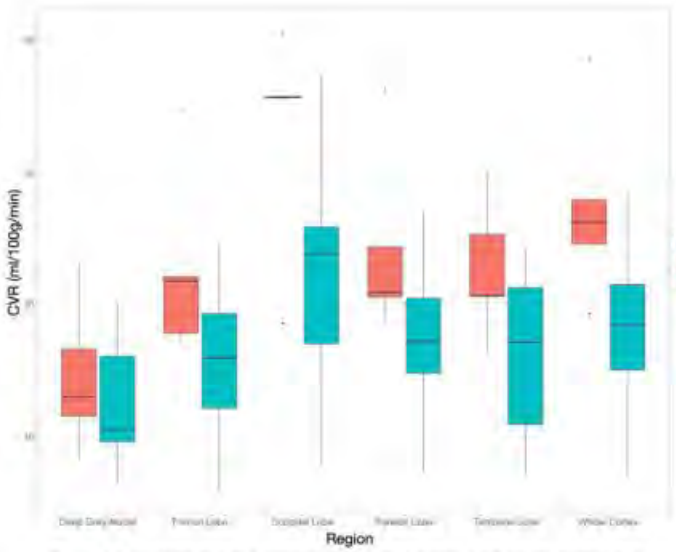

Figure 1a: CVR for the entire cortex (far right) and each of the five sub-regions, stratified by whether or not subjects had a prior documented COVID infection. CVR of the whole brain cortex was significantly different between groups (mean difference -9.0, 95% CI -17.6, to -0.5, p = .04). Regional subanalysis accounting for multiple comparisons demonstrated no statistically significant difference in lobar subregions.

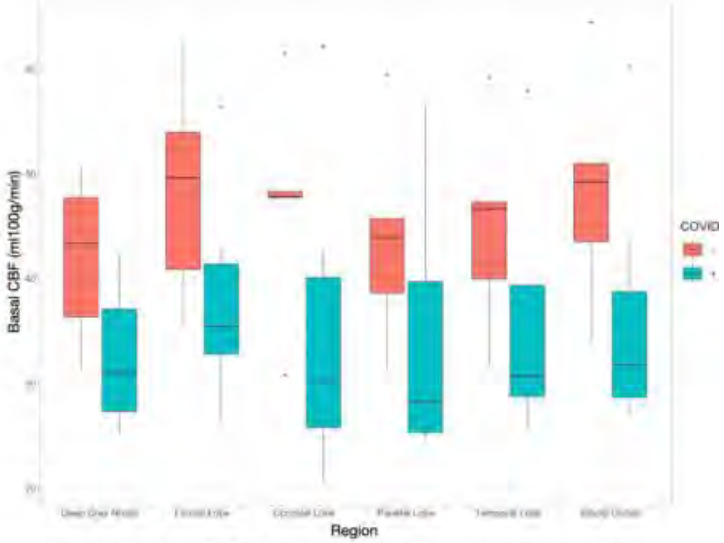

Figure 1b: Basal CBF for the entire cortex (far right) and each of the five sub-regions, stratified by whether or not subjects had a prior documented COVID infection.

(Filename: TCT_1081_AbstractFigure.jpg)

1447

Prevalence of Neuroimaging Findings in Patients with COVID-19 and Correlation with Common Chest Imaging Patterns

R Scott[1], M Lund[1], A Achiriloaie[1]
[1]*Loma Linda University Medical Center, Loma Linda, CA*

Purpose
The clinical manifestations of COVID-19 are broad, including multifactorial involvement of the central nervous system related primarily to inflammatory response, prolonged illness or hospitalization, and rarely direct viral infection. Common neuroradiologic manifestations include acute infarct in the setting of large vessel occlusion, intracranial hemorrhage, and microhemorrhages. The purpose of this study is to further describe and assess the prevalence of positive findings on neuroimaging for patients diagnosed with COVID-19, particularly in relation to the presence of commonly reported radiographic and CT findings of the chest.
Materials and Methods
A retrospective review of all COVID-19 positive patients who received imaging of the head and chest at Loma Linda University Medical Center between April 2020 and April 2021 was performed. A total of 249 patients were reviewed (132 male, 117 female, 3 pediatric). The type and distribution of any intracranial findings on CT and/or MRI were recorded. Chest radiographs and chest CT, if available, were reviewed and documented utilizing the RSNA and BSTI standardized reporting criteria for COVID-19 pneumonia.
Results
197 of the 249 patients (79%) had normal or chronic/unrelated findings on head imaging. The remaining 52 patients (21%) had positive intracranial findings, the most common being acute stroke (60%), intracranial hemorrhage (15%), microhemorrhages (13%), and hypoxic-ischemic encephalopathy (13%), some of which occurred in combination. Less common findings included posterior reversible encephalopathy syndrome (PRES)-like changes, leukoencephalopathy, optic neuritis, olfactory nerve atrophy and suspected supratentorial demyelinating disease. 71% of the patients with positive intracranial findings, including 24 of the 31 patients with infarcts (77%) and 6 of the 8 patients with intracranial hemorrhage (75%) demonstrated typical chest findings of acute COVID-19 pneumonia i.e., bilateral peripheral-predominant groundglass opacification/consolidation.
Conclusions
A significant fraction of patients with moderate to severe COVID-19 treated at our institution had positive findings on neuroimaging, likely related to underlying thrombotic/coagulopathic states, as infarct and hemorrhage were the most common intracranial abnormalities. A large majority of these patients also had typical radiographic or CT chest findings of COVID-19 pneumonia.

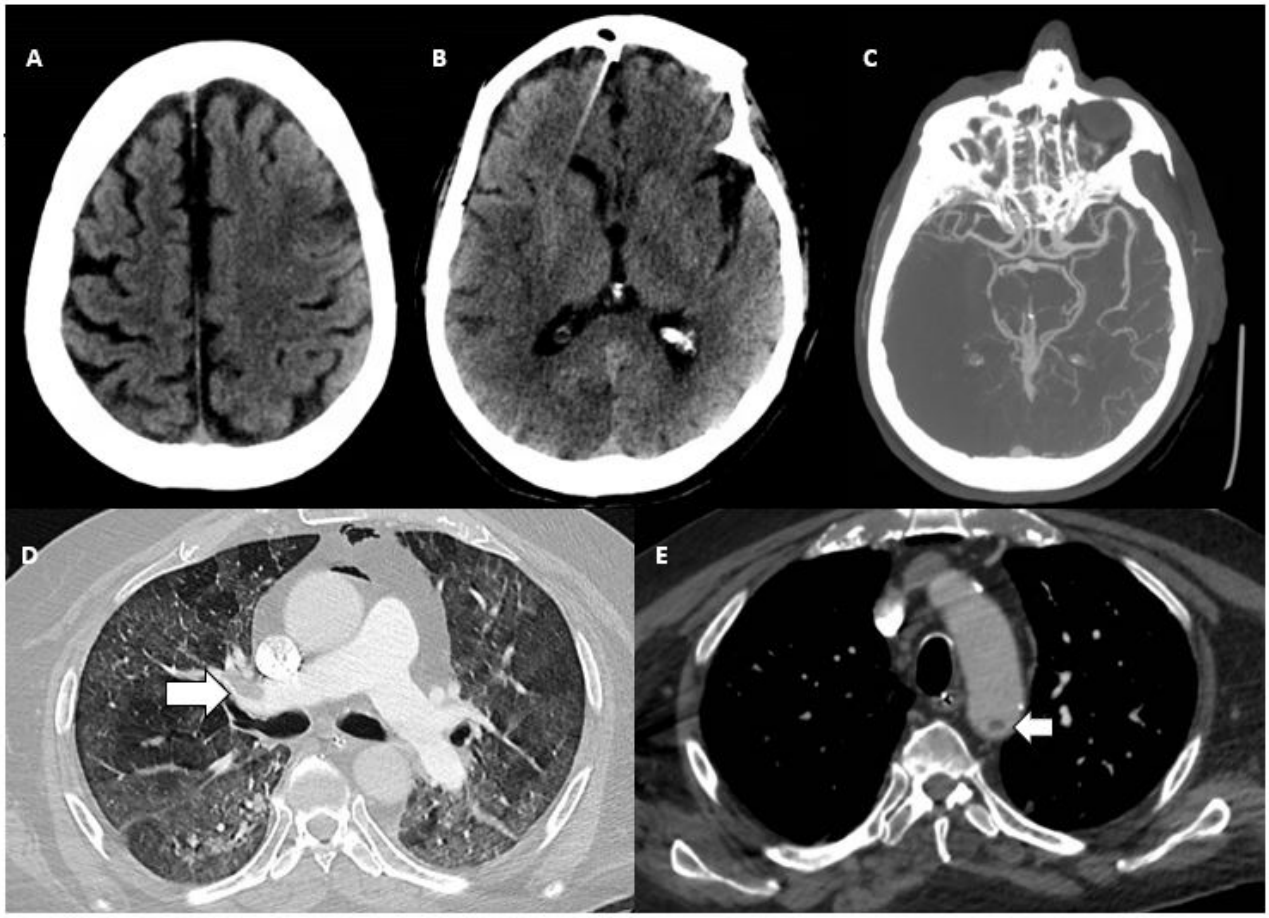

Figure 1. 74-year-old male with COVID-19 pneumonia found to have bilateral cerebral infarcts **(a,b)** and multifocal thrombi involving the right M2 middle cerebral artery **(c)**, right main pulmonary artery **(d)**, and aortic arch **(e)**.

	n	Average Age	Median Age	Classic/typical Chest Findings	Indeterminate Chest Findings	Non-COVID/atypical Chest Findings	Negative Chest Imaging
Acute stroke	31	67.9	67	24 (77%)*	3 (10%)	3 (10%)	1 (3%)
Intracranial hemorrhage	8	59.4**	44	6 (75%)	2 (25%)	0	0
Microhemorrhage	7	49.3	53	4 (57%)	3 (43%)	0	0
Hypoxic-ischemic encephalopathy	7	57.1	56	5 (71%)	2 (29%)	0	0
Other	10	60.3	65.5	5 (50%)	2 (20%)	2 (20%)	1 (10%)
Normal chronic/unrelated	197	67.8	70	102 (52%)	57 (29%)	25 (13%)	13 (6%)

Table 1. Intracranial findings relative to patient age and chest imaging findings. *p < 0.05 **p < 0.01

(Filename: TCT_1447_nCV-19_figure.JPG)

532

Question format for trainees. Are there more ways to tackle the memory and consolidate knowledge in Neuroradiology?

A Hussien[1]

[1]UT southwestern, Dallas, TX

Purpose

Trainees may benefit from reversing the way they practice questions to enhance the learning process. In daily practice, sometimes we may need to recall or mentally formulate expected imaging findings before opening a specific case based on the clinical history. Also we may see a typical imaging signature of a specific disease and we should be able to recall which one it should be from a list of differential diagnosis with no multiple choices to pick from. The aim of this review is to describe a suggested way of formulating practice questions to the trainees (residents or fellows) using a specific diagnosis or a clinical scenario in the question stem followed by a multiple imaging sets. The potential benefits of this technique in the learning process of neuroradiology will be discussed and

compared with the classic multiple choice questions method. For example, a question stem of an acute stroke with aphasia, the trainee would be expecting to find a CT hypodensity in Broca's or Wernicke's areas, those images can be put between multiple other images to choose from. Another example of CNS lymphoma which has specific imaging characteristics that can be put in a question and the trainee chooses from multiple image sets the correct one.

Materials and Methods

A couple of examples of suggested questions using the same concept and the suggested benefits of it in consolidating memory about disease process and their role of engraving the radiological fingerprint of a disease . The examples will include; stroke, CNS lymphoma, petrous apex lesions, skull base / clival lesions , jugular foramen lesions and white matter disease.

Results

The use of more than one question format and different ways of recalling information is expected to enhance trainees knowledge and consolidate memory especially when it comes to disease process imaging fingerprint.

Conclusions

In preparation to practice radiology especially in Neuroradiology, the trainees would need to perform more than one type of question format and different ways of recalling information, formulating an accurate diagnosis and differential diagnosis. The classic MCQ type of questions are definitely effective, but what about multiple choices of imaging sets to reach a specific diagnosis or clinical scenario in question? This way would stimulate memorizing the disease process in a different way, which would inquire a more focused way of preparation for the exam and future clinical practice. "Now I know the diagnosis, what am I expecting to find?"

446

Repurposing CME Funds During COVID Provides Opportunity for New Radiology Staffing Models at an Academic Medical Center

M Keiper[1], S Kelly[2], J Cramer[3], C Johnson[3], C Walker[4]

[1]University of Nebraska Mecial Center, Omaha, NE, [2]UNMC, papillion, NE, [3]University of Nebraska Medical Center, Omaha, NE, [4]UNMC, Omaha, NE

Purpose

To display the impact on staffing models of the voluntary use of CME funds to purchase remote workstations at an academic university medical center.

Materials and Methods

As a result of travel bans and cancellation of national radiology society meetings and other work-related travel during the COVID era, CME funds for individual radiology staff members were underutilized. A significant accumulation of these funds provided a resource for the voluntary purchase of home workstations as a contingency plan to mitigate potential staff shortages during COVID. Standardized workstations with remote access points (RAP) certified by medical center PACS and IT personnel were selected to ensure uniformity of quality and service by PACS personnel. Requests for medical center purchase of workstations were first submitted prior to the alternative solution of the use of CME funds.

Results

After medical center administration declined the purchase of workstations citing financial constraints, standardized workstations were purchased and installed for all staff volunteers (26 of 32, 81% of staff) using individual CME funds. The workstations were successfully utilized for staff quarantine shortages providing a model to ensure full staffing during COVID and other unforeseen events. Experience with remote reading during COVID allowed for innovation with remote resident education, the use of similar workstations in satellite offices thereby decreasing the number of staff required to cover clinical work, and, ultimately, the confidence to apply the use of remote workstations to more progressive staffing models in the setting of a sparse radiologist candidate market. The models allowed the department to advertise and successfully attract remote radiology candidates to cover swing shift and after-hours positions and will also likely provide a method to attract high level remote candidates to fill vacant daytime positions in the future.

Conclusions

A COVID contingency staffing plan incorporating the voluntary purchase of remote workstations provided a vehicle to accommodate unexpected staff shortages in the short term. However, this model was also successfully applied to develop a more comprehensive and innovative staffing solution to sustain and grow a radiology department in a difficult job market with a more modern approach catering to the preferences of high-quality remote radiology candidates thereby fulfilling the clinical mission of a radiology department in a large academic medical center.

1469

Anatomy of the Artery of von Haller

J Small[1], V Perez[2]

[1]Lahey Hospital and Medical Center, Burlington, MA, [2]Instituto de Ciencias Forenses, Mexico City, Mexico

Purpose

Although dominant radiculomedullary arteries such as the artery of Adamkiewicz (AKA) and great posterior radiculomedullary artery (GPRA) (1) are well documented, marked variability exists as to the size, number and location of other anterior radiculomedullary arteries contributing supply to the anterior spinal artery (ASA). The artery of von Haller (AVH) has attracted little attention in the literature with a single spinal angiography study conducted in 50 patients (2). The aim of this anatomic study was to document the presence and characteristics of the AVH in cadaveric specimens.

Materials and Methods

Microsurgical dissection on formaldehyde-fixed cadaveric human spinal cord specimens (n = 50) was conducted. The AKA was injected with colored latex until the small-caliber arterial vessels were filled. The course, diameter, and location of the AVH was documented.

Results

The AKA was identified between T3 and L2 in all 50 patients (100%). At least 1 AVH distinct from the AKA was identified between T1 and T8 in 47 of the 50 patients (94%). An AVH was not identified in 3 patients (6%). A single AVH was identified in 33 patients (66%). Two AVH were identified in 13 patients (26%). Three AVH were identified in a single patient (2%) with 3 arising on the left at the level of T3, T7 y T9. The most frequent origin of the artery of Von Haller was at the level of T4. The average size of the AVH was .446 mm.

Conclusions

An AVH is present in 94% of individuals. These findings are similar to those of Gailloud (2013) in which an AVH was evident in 86% of angiograms. We describe the microsurgical anatomy of the AVH with important implications for anterior thoracic spinal cord blood supply. Variations of the arterial supply to the anterior thoracic cord are of great importance due to their implications for ischemic events as well as surgical and endovascular procedures. Figure 1. Arteries of Von Haller. Anterior view of the spinal cord (A) clearly reveals evidence of the artery of Adamkiewicz (black arrow) as well as two left sided upper thoracic anterior radiculomedullary arteries consistent with arteries of Von Haller (white arrows) supplying the anterior spinal artery. REFERENCES 1. Perez Perez VH, Hernesniemi J, Small JE. Anatomy of the Great Posterior Radiculomedullary Artery. AJNR Am J Neuroradiol. 2019 Dec;40(12):2010-2015. 2. Gailloud P. The artery of von Haller: a constant anterior radiculomedullary artery at the upper thoracic level. Neurosurgery. 2013 Dec;73(6):1034-43.

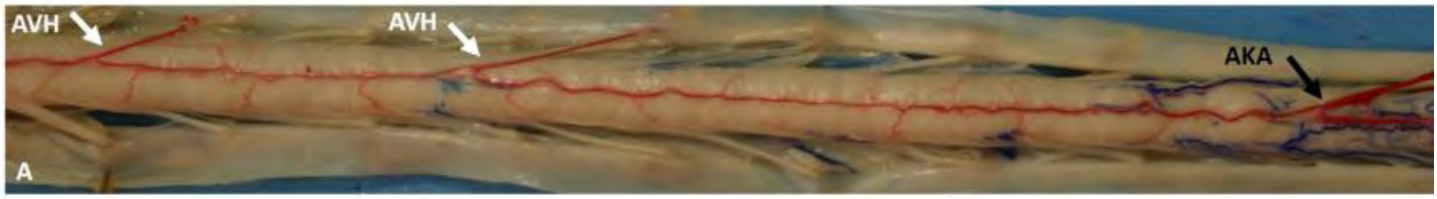

(Filename: TCT_1469_AVH.jpg)

1333

Cerebello-Thalamo-Cortical MR Spectroscopy in patients with essential tremor (ET) undergoing MRgFUS thalamotomy: pilot study

F Bruno[1], E Tommasino[2], A Splendiani[3]

[1]University of L'Aquila, L'Aquila, Abruzzo, [2]University of L'Aquila, L'aquila, Italy, [3]University of L'Aquila, L'AQUILA, l'aquila

Purpose

Previous literature studies explored the association between brain neurometabolic changes detected by MR spectroscopy and symptoms in patients with tremor, as well as outcome after deep brain stimulation (DBS) treatment. The purpose of our study was to evaluate the possible association between cerebello-thalamo-cortical neurometabolic findings and procedural/clinical outcome in patients submitted to MRgFUS thalamotomy.

Materials and Methods

For this pilot study we prospective enrolled 12 ET patients (8 males, 4 females, mean age 71.3 years) eligible for MRgFUS thalamotomy. All patients were preoperatively submitted to 3T MR spectroscopy. Single voxel MRS measurements were performed at the level of the thalamus contralateral to the treated side and the ipsilateral cerebellar dentate nucleus. Multivoxel acquisition was used for MRS at the level of the contralateral motor cortex. NAA/Cr and GABA/Cr ratio values were calculated and recorded. Clinical

examination, performed before and after treatment, was assessed using the Clinical Rating Scale for Tremor (CRST). Procedural parameters recorded included the number of sonications and target movements. Correlation and regression analysis were performed for the evaluation of MRS and clinical/procedural parameters.
Results
We found a significant positive correlation between cortical NAA/Cr and clinical improvement (i.e. tremor reduction) after treatment. A significant negative correlation was found between clinical improvement and thalamic and cerebellar NAA/Cr. Thalamic GABA/Cr correlated inversely with the number of target shifts during treatment.
Conclusions
Confirming some previous literature observations, our preliminary results suggest a possible prognostic role of the neurometabolic assessment using MR spectroscopy in patients with ET treated by MrgFUS.

1338

Clinical And Radiologic Weight Bearing MRI Outcome After Percutaneous Interspinous Spacer Insertion For Lumbar Spinal Canal Stenosis: A Preliminary Study.

A De Vivo[1], A Araùjo[2], F Ventura[3], L Manfre[4]
[1]I.O.M., Catania, ITALY, [2]Centro Hospitalar de Vila Nova de Gaia/Espinho., Vila Nova de Gaia, EU, [3]Mediterranean Institute for Oncology, Catania, Italy, [4]Mediterranean Institute for Oncology, Viagrande, Catania

Purpose
To evaluate clinical and radiologic weight bearing MRI outcome of a series of patients treated with a percutaneous interspinous process spacer for symptomatic degenerative lumbar spinal stenosis.
Materials and Methods
All patients treated with this IPS for lumbar spinal canal stenosis were retrospectively reviewed. Patients with incomplete clinical or radiological documentation and patients with foraminal stenosis were not included. Patients were clinically evaluated before intervention and at 3-month follow-up with Visual Analog Scale for pain (VAS), Oswestry Disability Index (ODI) and radiologically with weight bearing and non-weight bearing MRI. Minimum Spinal Canal area was assessed with a semi-automatic measurement for each patient on pre- and post-procedural MRI scan.
Results
36 patients were treated and 32 were included in this study. No procedural complications were reported. Clinical follow-up at 3 months showed a significant reduction of pain and an improvement in functionality. There was one case of posterior migration at 3-month follow-up. Mean spinal canal area increased after intervention with a higher improvement observed in weight bearing scans.
Conclusions
This study showed a good clinical outcome at 3 months, associated with radiologic increase of spinal canal minimum area, with high improvement in weight bearing scans.

1220

Diagnostic yield of MR myelography in patients with newly diagnosed spontaneous intracranial hypotension: a systematic review and meta-analysis

C Suh[1], S Lee[2], S Kim[1], D Kim[3]
[1]Asan Medical Center, Seoul, Seoul, [2]Asan medical center, Seoul, Seoul, [3]University of Ulsan College of Medicine, Seoul, Seoul

Purpose
To investigate the pooled diagnostic yield of MR myelography in patients with newly diagnosed spontaneous intracranial hypotension.
Materials and Methods
A literature search of the MEDLINE/PubMed and Embase databases was conducted until July 25, 2021, including studies meeting the following inclusion criteria: (a) population: patients with newly diagnosed SIH; (b) diagnostic modality: MR myelography or MR myelography with intrathecal gadolinium for evaluation of CSF leakage; (c) outcomes: diagnostic yield of MR myelography or MR myelography with intrathecal gadolinium. The risk of bias was evaluated using the Assessment of Diagnostic Accuracy Studies-2 tool. DerSimonian–Laird random-effects modeling was used to calculate the pooled estimates. Subgroup analysis regarding epidural fluid collection and meta-regression were additionally performed.
Results
Fifteen studies with 604 patients were included. Six studies were conducted using MR myelography with intrathecal gadolinium and 11 using MR myelography. The overall quality of the included studies was high. The pooled diagnostic yield of MR myelography was 87% (95% CI, 80–92%) and the pooled diagnostic yield of MR myelography with intrathecal gadolinium was 82% (95% CI, 40–97%). There was no significant difference between MR myelography and MR myelography with intrathecal gadolinium (P = 0.526). In subgroup analysis, the pooled diagnostic yield of epidural fluid collection was 91% (95% CI, 84–94%). In meta-regression, the diagnostic yield was unaffected regardless of consecutive enrollment, magnet strength, or 2D/3D.
Conclusions
MR myelography had high diagnostic yield in patients with SIH. MR myelography is non-invasive and not inferior to MR myelography with intrathecal gadolinium.

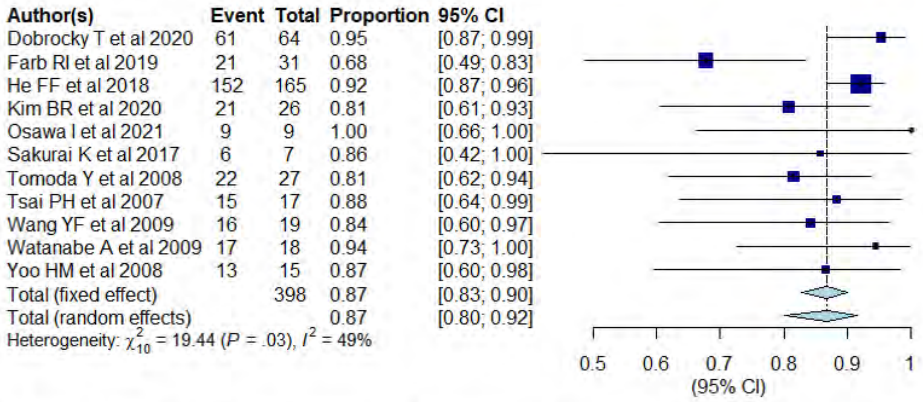

Figure 1. The pooled diagnostic yield of MR myelography in SIH patient. Numbers are pooled estimates with 95% confidence intervals (CIs) in parentheses and indicated as horizontal lines.

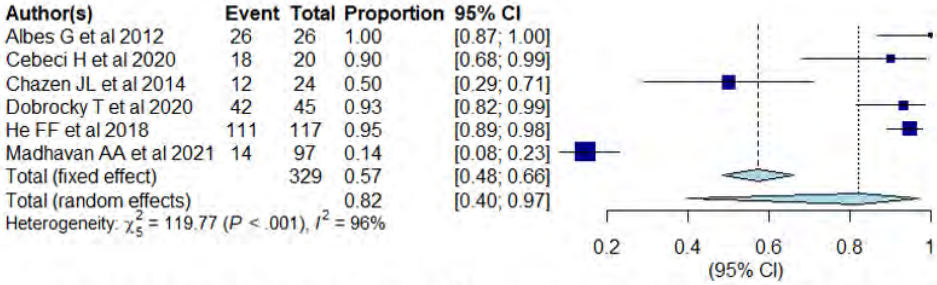

Figure 2. The pooled diagnostic yield of MR myelography with intrathecal gadolinium in SIH patient. Numbers are pooled estimates with 95% confidence intervals (CIs) in parentheses and indicated as horizontal lines.

(Filename: TCT_1220_meta_figure.jpg)

1350

Evolution and prognostic value of intervertebral disc T2-mapping values after ozone chemonucleolysis in patients with lumbar disc herniation"

F Bruno[1], E Tommasino[2], A Splendiani[3]

[1]University of L'Aquila, L'Aquila, Abruzzo, [2]University of L'Aquila, L'aquila, Italy, [3]University of L'Aquila, L'AQUILA, l'aquila

Purpose

To assess the validity of the MR T2-mapping sequence in estimating the modifications of the intervertebral disc (IVD) treated by O2 - O3 chemodiscolysis and its possible role in predicting clinical outcomes.

Materials and Methods

40 patients with Low Back Pain (LBP) (22 males, 18 females; mean age 46.15 years) were enrolled for percutaneous CT-guided O2-O3 chemodiscolysis. Thirty-one sex- and age-matched patients, served as controls and were treated by CT-guided periradicular injections. All patients were assessed clinically trough the Visual Analogue Scale (VAS) and the Oswestry Disability Index (ODI), and radiologically, by using a 3Tscanner, for evaluating the intervertebral disc area (IDA) and the T2-mapping values of the IVD before, at 1-month, and 6-months follow-up.

Results

The mean pre-treatment T2 relaxation time values were 38.80 ± 4.51 ms, 44.05 ± 0.91 ms, and 45.45 ± 14.11 ms for the anterior annulus fibrosus (aAF), nucleus pulposus (NP), and posterior annulus fibrosus (pAF), respectively, with a significant increase at the level of the NP ($p < 0,05$) at the 1-month follow-up. The 6-months follow-up showed a reduction with normalization of intradiscal T2 relaxation time values showed a significant correlation of NP values with both the reduction of IDA (0.81, $p < 0.001$) and the improvement of clinical scores (0.86, $p < 0.001$). In the control group, despite the clinical improvement, we did not find significant IVA reduction nor significant T2 values changes after treatment.

Conclusions

T2-mapping may be a useful indicator to predict disc chrinkage and the clinical response to CT-guided 02 - 03 injection.

832

Intracranial Findings and Clinical Presentation of Patients with Type I/II CSF Leaks Compared to Type III CSF Leak

W Mehan[1], K Buch[1]
[1]Massachusetts General Hospital, Boston, MA

Purpose

Spinal CSF leaks are an underdiagnosed cause of neurologic symptoms and headaches in patients. Type I (dural tears) and type II (meningeal diverticula) CSF leaks are most common while type III leaks (CSF-venous fistulas) are less common and underrecognized. The purpose of this study was to evaluate the intracranial findings and clinical presentations of patients with types I/II CSF leaks compared to type III leaks.

Materials and Methods

This was a retrospective, IRB-approved study. Inclusion criteria were 1) adults with a surgically confirmed type I/II/III CSF leak, 2) pre-operative brain MRI 3) pre-operative spine MRI, and 4) medical record documentation of symptom onset, spectrum of symptoms, and initial diagnosis provided at the time of symptoms onset. Exclusion criteria were patients with non-diagnostic brain and/or spine MRI exams and incomplete records. Brain MRIs were evaluated for presence of extra-axial collections, pachymeningeal thickening, brain sagging, inferior cerebellar tonsillar descent, uncal herniation, and ponto-mamillary distance was recorded. Spine MRIs were reviewed for presence of extra-dural collections. Demographic and clinical information was correlated with brain MRI findings.

Results

7 patients with type III leak and 16 patients with type I/II leak were included. Patients with type III leaks were significantly older than those with type I/II leaks (P=0.0003). Patients with type III leaks had a higher frequency of misdiagnosis (100%) vs type I/II leaks (31%) and had longer symptom duration (1,111 days vs 280 days, P=0.03). Extra-axial collections were not seen in any patient with a type III leak compared to 50% of patients with type I/II leak. Extradural spinal collections were never seen in patients with type III leaks compared to 100% with type I/II leaks. Pachymeningeal thickening, brainstem sagging, and uncal herniation was seen with nearly equal frequency between patients with type III and type I or II leaks (50% vs 57%). Patients with type III leaks had smaller ponto-mamillary distances (mean 3.06mm) compared to type I/II leaks (mean 4.83mm)(P=0.047).

Conclusions

Important demographic and MRI brain differences may be seen in patients with type III leaks compared to type I/II leaks noting absence of extra-axial collections, smaller ponto-mamillary distance and increased patient age. These differences may be helpful when assessing patients with suspected CSF leak.

1001

MR-guided Focused Ultrasound of the Dorsal Root Ganglion for the Treatment of Low Back Pain: Preclinical Study in a Peripheral Nerve Injury Model

L Shah[1], A Payne[2], H Odeen[2], C Floyd[2], M Kline[2], Y Xiong[2], V Rieke[2]
[1]University of Utah Health Care, Salt Lake Cty, UT, [2]University of Utah, Salt Lake City, UT

Purpose

Focused ultrasound (FUS) is a lower risk, completely non-invasive alternative treatment modality. In vivo animal models have suggested dorsal root ganglia (DRG) to play a role in pain propagation and neuropathic modulation. We developed a large animal chronic LBP model, induced by peripheral nerve injury (PNI), and evaluated the response to several stimuli with quantitative sensory testing (QST). Here we investigate the ability to decrease neuropathic LBP in the pig PNI model with FUS neuromodulation of the spinal DRG with MR-guided FUS (MRgFUS) without permanent surrounding tissue damage.

Materials and Methods

Pigs (N=4, 2 controls) underwent weekly QST, using a porcine pain scale that uses vocalization and facial expression as quantifiable measures indicative of a supra-spinal pain response. QST was performed 4 wks before and 6 wks after MRgFUS. Two animals underwent surgery (unilateral ligation of the common peroneal nerve with complete Freund's adjuvant) to create neuropathic radicular LBP. For MRgFUS, the animals were positioned dorsal recumbent over the FUS transducer (Image Guided Therapy) and imaged with a custom built 3-channel coil at 3T (Siemens, PrismaFIT). The transducer was positioned to target unilateral DRGs (L1-L6). Two different sonication protocols were used: continuous FUS sonication for the control animals and pulsed sonications for the PNI animals. MR temperature imaging (3D segmented EPI, FOV=192x180x30 mm, Res=1.5x1.5x2.5 mm, TR/TE=23/11 ms, FA=14°, BW=1004 Hz/px, ETL=7) was used to measure temperature at the location of the DRG and surrounding areas. Post-treatment 3D SPACE T2w (to visualize edema) and 3D VIBE CE-T1w (to visualize non-perfused volume) was performed to assess FUS effects.

Results

We used QST outcome metrics that parallel highly quantitative clinical assessments of neuropathic pain and were able to demonstrate expected increase in pain with PNI that was ameliorated for 4 weeks following MRgFUS treatment. Similar to Hellman et al, we show that MRgFUS can ameliorate pain. We further demonstrate that our QST techniques are sensitive indicators of pain in a large animal model and are clinically translatable.

Conclusions

We demonstrated the ability to target the spinal DRG with MRgFUS without damage to the surrounding tissue. Furthermore, our

study shows that the QST techniques are sensitive indicators of pain in a large animal model and that MRgFUS-effects on pain reduction can be detected using this clinically relevant evaluation method.

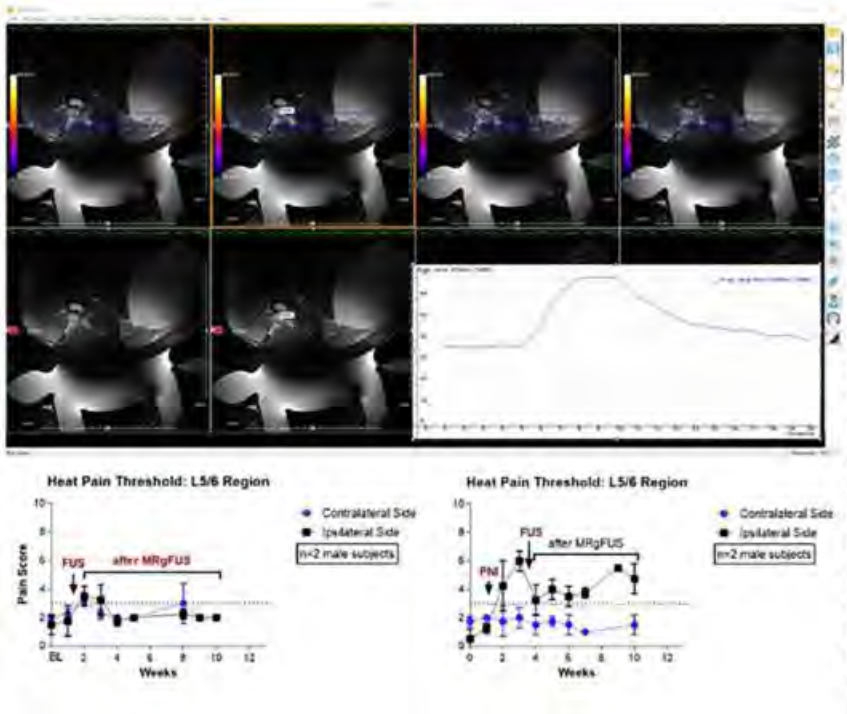

Top: 3D MR temperature imaging (MRTI) during MRgFUS treatment of a porcine DRG using continuous sonication over 4 slices (top row). Associated cumulative thermal dose for two of the slices is shown (bottom row). For better visualization of the heating, the 3D temperature volume is reformatted and overlaid on the high-resolution T2w anatomical images. The insert shows the absolute temperature (°C) over time (# of acquisition) for a selected pixel in the target area.

Bottom: Pigs (N=4) were trained to stand in a testing arena equipped with cameras and microphones. A thermode was applied in the dermatome associated with L5/6. **Left:** In control animals (high temperature ablation) pain score to the heat pain threshold increased over baseline directly after MRgFUS and remained elevated for two weeks before returning to baseline. **Right:** Prior to peripheral nerve injury (PNI) responses were below the pain threshold of 3 (dotted line). After PNI, pain responses were elevated. Acutely following MRgFUS, pain scores were markedly reduced, followed by a later resumption of pain scores.

(Filename: TCT_1001_FUS.jpg)

1327

MRgFUS thalamotomy for the treatment of tremor: evaluation of learning curve and operator's experience impact on the procedural and clinical outcome

F Bruno[1], E Tommasino[2], A Splendiani[3]
[1]University of L'Aquila, L'Aquila, Abruzzo, [2]University of L'Aquila, L'aquila, Italy, [3]University of L'Aquila, L'AQUILA, l'aquila

Purpose
To evaluate the impact of the operator's experience and learning curve on procedural and clinical outcome of MRgFUS thalamotomy
Materials and Methods
90 MRgFUS thalamotomy procedures (38 ET, 52 PD) performed by the same interventional neuroradiologist were retrospectively evaluated. Three groups were identified according to the time of execution (Group A: 30 patients treated from February 2018 to January 2019; Group B: 30 patients, January 2019 -September 2019; C: 30 patients, September 2019 to July 2020). In each group, demographic/clinical parameters (age, sex, pathology, days of hospitalization, complications, tremor relapses), and procedural parameters (SDR, preparation time, planning time, treatment time, number of sonications, target shifts) were recorded and compared.
Results
In group C procedures we found significantly shorter preparation and treatment times (101.9min vs 120min and 105.5min of group A and B respectively, p-value 0.04), with a significant reduction in the number of sonications in group B and C (mean 13.2 and 10.6 compared to 15.1 of group A). Mean hospitalization days were 3.8 in group A and 3.2 (p-value 0.02) and 3.5 (p-value 0.04) in group B and C, respectively. Patients with complications were 9 in group A, 2 in group B (p-value 0.03) and 4 in group C. Tremor relapsed in 7 patients of group A and 3 and 2 patients of groups B and C, respectively.
Conclusions
MRgFUS thalamotomy is a novel technique, transversal between the disciplines of neurology, neurosurgery, and interventional radiology. The learning curve for the radiologist is rapid, with significant improvements in procedural management and the clinical outcome already after the first treatments.

436

MRI-guided Focused Ultrasound-Enabled Release of Brain-derived Biomarkers in a Mouse Model of Tauopathy

A Nazeri[1], C Pacia[2], J Yuan[2], M Manis[2], Y Yue[2], M Finn[2], T Benzinger[3], H Chen[2]
[1]Washington University in St. Louis, Saint Louis, MO, [2]Washington University in St. Louis, St. Louis, MO, [3]Washington University in St.louis, Saint Louis, MO

Purpose
Tauopathies are a diverse class of neurodegenerative disorders characterized by the deposition of pathogenic forms of tau protein in the brain, which include Alzheimer's disease and frontotemporal lobar degeneration, among others. Given the variety of post-

translational modifications of tau protein and their associations with disease stage and their effect on tau pathogenicity[1], non-invasive detection of tau modifications in each patient has critical implications in diagnosis and personalized patient care. However, direct examination of these tissue markers requires invasive tissue biopsy, as many of these biomarkers do not readily cross the blood-brain barrier (BBB)[2]. In this proof-of-principle study, we sought to determine the capability of focused ultrasound (FUS)-enabled liquid biopsy (sonobiopsy)[3,4] to release phosphorylated tau and NFL (neurofilament light chain, a marker of neurodegeneration) into the bloodstream by opening the BBB.

Materials and Methods

MRI-guided sonication experiments were performed on a transgenic mouse model of tauopathy (PS19) using a 4.7T small animal MRI system and an MRI-compatible FUS transducer. Sonications were performed in conjunction with intravenous administration of microbubbles. Post-contrast T1-weighted MR images were obtained to confirm BBB opening. In the first experiment, both the right cerebral cortex and hippocampus were targeted in 2-month-old PS19 and wild type mice. For the second experiment, either the right cerebral cortex or hippocampus were sonicated in 6-month-old PS19 mice. Post-sonication plasma levels of mouse tau (mTau), phosphorylated tau (p181), and NFL were measured.

Results

FUS in conjunction with microbubbles resulted in consistent BBB opening in the targeted brain area. In the first experiment, there was a significant 1.7-fold increase in normalized plasma pTau-181 (pTau-181/mTau ratio) in the FUS-treated PS19 mice compared to the control PS19 mice (Fig. 2; p=0.006). In the second experiment, we observed a 2-fold increase in plasma NFL following sonication of the cerebral cortex, but not hippocampus, among 6-month-old PS19 mice (Fig. 2; p=0.05).

Conclusions

Our study demonstrated the feasibility of sonobiopsy to enable sensitive detection of post-translational modifications of the tau protein and a key marker of neurodegeneration in the blood of a transgenic mouse model of tauopathy. This proof-of-principle study was the first to expand the utility of sonobiopsy from brain cancer to neurodegenerative disorders.

Figure 1

Figure 2

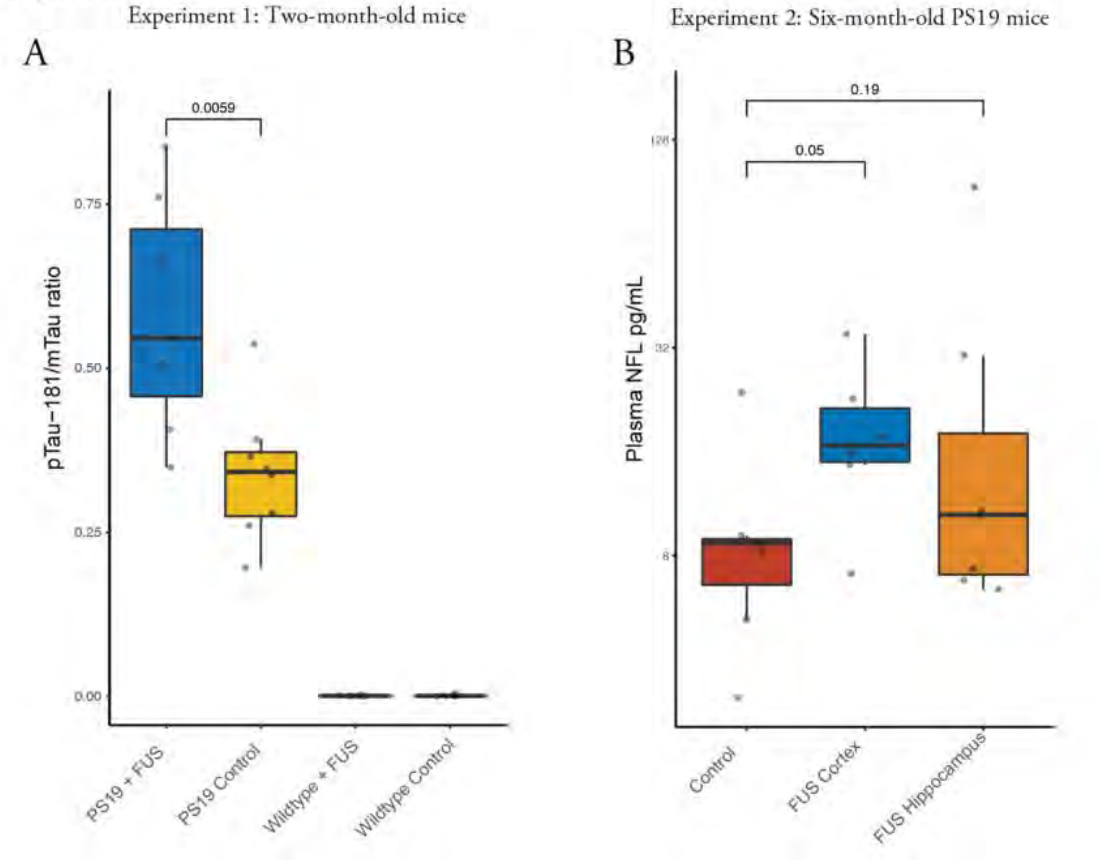

(Filename: TCT_436_image.jpg)

367

Novel Imaging Target for Noninvasive Thalamotomy in Treatment of Tremor Using FGATIR MRI

L Okromelidze[1], J Mendez[1], E Middlebrooks[1]
[1]Mayo Clinic, Jacksonville, FL

Purpose

Stereotactic radiosurgery (SRS) thalamotomy is an alternative, noninvasive treatment for tremor. To date, outcomes are variable due to variances in targeting and lack of any reliable biomarker. We propose a novel, imaging-based target using fast gray matter acquisition T1 inversion recovery (FGATIR) to identify a hypointense area corresponding to the prelemniscal radiations and dentato-rubro-thalamic tract (DRTT) and hypothesize that overlap with this region will result in greater tremor improvement.

Materials and Methods

Twenty patients were enrolled in a prospective clinical trial and retrospectively reviewed. Prior to SRS, patients underwent FGATIR and high-resolution DTI imaging on a 3T Siemens Prisma. The treatment lesion was segmented on 6-month follow-up postcontrast MRI. Overlap between the lesion and the FGATIR hypointensity (Fig 1A) was calculated, as well as overlap with the DRTT derived from probabilistic tractography. Volume of overlap was correlated with improvement in TRS between preoperative assessment and 6-12 months follow-up using nonparametric Spearman correlation. All lesions were also normalized to MNI space and the group mean center-of-gravity (COG) was calculated for responders (>=50% tremor improvement) versus nonresponders (<50% tremor improvement).

Results

Mean improvement in TRS was 40.3% (range: -14.8 to 88%) at a mean follow-up of 6.9 months (range: 6 to 12 months). The COG for the responder group (MNI = -13.5/-16.5/0.5) was closer to the FGATIR hypointensity (Fig 1B) and was anterior and slightly inferior to the nonresponder group (MNI = -13.5/-19/1.5). Increasing overlap of the lesion and FGATIR hypointensity (Fig 1C) was significantly correlated with TRS improvement ($r = 0.84$; $p < 0.0001$) and explained 70.6% of variance in tremor improvement. Increasing overlap of lesion and DRTT (Fig 1D) was also a significant predictor of improvement ($r = 0.58$, $p = 0.01$), but only explained 33.6% of variance.

Conclusions

We have shown a novel targeting approach in noninvasive thalamotomy using FGATIR MRI. Increasing interest in preoperative DTI presents issues with modeling crossing fibers, requires substantial expertise for processing, and subject to distortions that can be significant given the required precision. These issues are reduced or eliminated by the more easily implemented FGATIR sequence. The identified FGATIR hypointensity was a significant predictor of outcome, explaining 70.6% of outcome variance, while DTI of DRTT only explained 33.6% of variance in outcome.

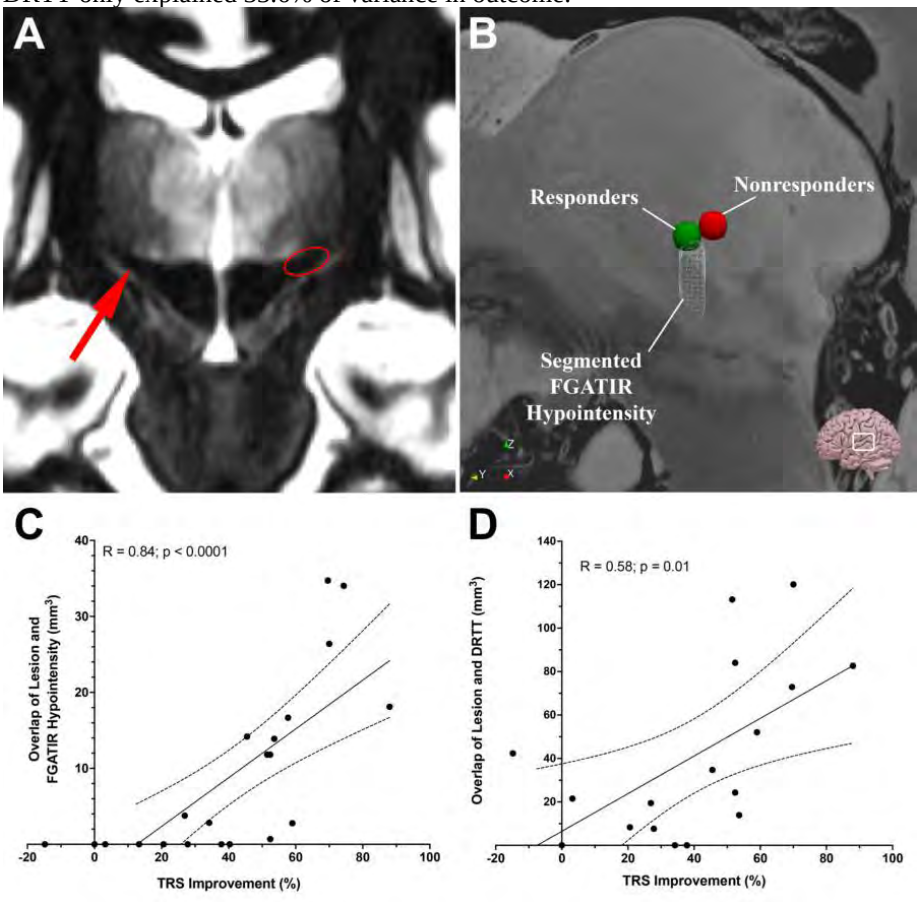

(Filename: TCT_367_asnr.jpg)

789

Percutaneous Laser Disc Decompression for the Treatment of Lumbar Disc Herniation: A new approach

a biagelli[1], r pantaleoni[2], l bellantonio[3], a fiacca[4], p floridi[5]

[1]azienda ospedaliera di perugia, perugia, italia, [2]azienda ospedaliera Perugia, perugia , italy, [3]azienda oospedaliera perugia, perugia, Italy, [4]azienda ospedaliera perugia, perugia , italy, [5]azienda ospedliera perugia, perugia , italy

Purpose

Uncontained hernias represent a contraindication for percutaneous laser discolysis standardly executed under fluoroscopic guide. In our experience we introduced the probe directly in the hernial fragment assuming a better clinical outcome compared to standad discal decompression and widening the indications to uncontained hernial fragments. The purpose of our study is to evaluate efficiency, safety and tolerance of laser discolysis throught a new approach: the introduction of laser probe, under TC guidance, directly into the hernial fragment (contained or not), obtaining its vaporization.

Materials and Methods

70 patients (34 men and 36 women), aged 21-84 years, with low back pain and or lombosciatalgy-cruralgy who failed conservative therapy carried out for at least 3 months and with TC and/or MRI evidence of herniated discs that justify symptoms without migration, sequestration or severe degenerative disc changes, were included in our study. Evaluated Clinical outcome were: pain related disability, measured by Oswestry disability index (ODI); pain intensity, measured on visual-analogical scale (VAS) and patient satisfaction related to the procedure, evaluated by McNab modified criteria. Data have been obtained by oral or written questionnaire, considering patient conditions before, 6 months after and 1 year after treatment. Statistical analysis through ANOVA, and related Tukey's test, and Wilcoxon's matched-pairs signed rank test has been executed. P-value < 0.01 has been considered statistically significant in all the analysis.

Results

There has been a reduction of ODI values from before procedure and 1 year after in 95% of patients, with a reduction of ODI values median of 13 points and a decrease of VAS values between before treatment and 1 year after in 91.67% of patients with a reduction of VAS score median of 6 points ($p < 0,01$). Procedure safety is proved by lack of major complications in most of the analyzed sample and by presence of only 3 cases of liquoral hypotension. 95% of patients defined the procedure as tolerable and barely painful. Procedure was considered on average as 'good' according to McNab modified criteria.

Conclusions

Laser TC guided dyscolisis with introduction of laser probe inside the herniated fragment could be considered as effective, safe and tolerable procedures in treatment of lumbar disc hernias even in uncontained or greater dimension hernias.

827

Utility of the ‘Crossing Collection Sign’ for Localizing Cerebrospinal Fluid Leaks

K Buch[1], W Mehan[1]

[1]Massachusetts General Hospital, Boston, MA

Purpose

To determine if the site of 'cross' between ventral and dorsal spinal epidural collections seen on MRI during initial workup of patients with suspected CSF leaks can predict the subsequently confirmed leakage site on CT myelography and surgical repair.

Materials and Methods

This was an IRB-approved, retrospective study performed from 2006 to 2021. Patients with longitudinally extensive spinal epidural fluid collections who underwent total spine MRI at our institution followed by myelography and/or surgical repair for CSF leak were included in our study. Patients with incomplete workup at our institution including lack of CT myelography and surgical repair, as well as patients who had severe artifact degradation on spine MRI were excluded from our study. The site of crossing between the ventral and dural epidural collections was determined as the 'crossing collection sign' and was selected as the site of suspected CSF leak. The frequency of this site as determined on MRI was compared to the leakage site confirmed on myelography and/or at the time of surgical repair.

Results

The crossing collection sign was seen in 76% of 29 patients who met inclusion criteria. This study included 18 females and 11 males ranging in age from 27-60 years (median=40 years, IQR= 14 years). The anatomic distribution of confirmed CSF leak were: the cervical (n=9), thoracic (n=17), and lumbar spine (n=3). The crossing collection sign predicted the site of CSF leak in 12/29 patients (41%) and within 3-vertebral body segments in 86% of cases.

Conclusions

By helping to prospectively identify on MRI the spinal regions with highest likelihood for being the site of CSF leakage, the 'crossing collection sign' can potentially help optimize the more invasive subsequently steps in the workup of patients with suspected CSF leak including myelography and surgical exploration for repair.

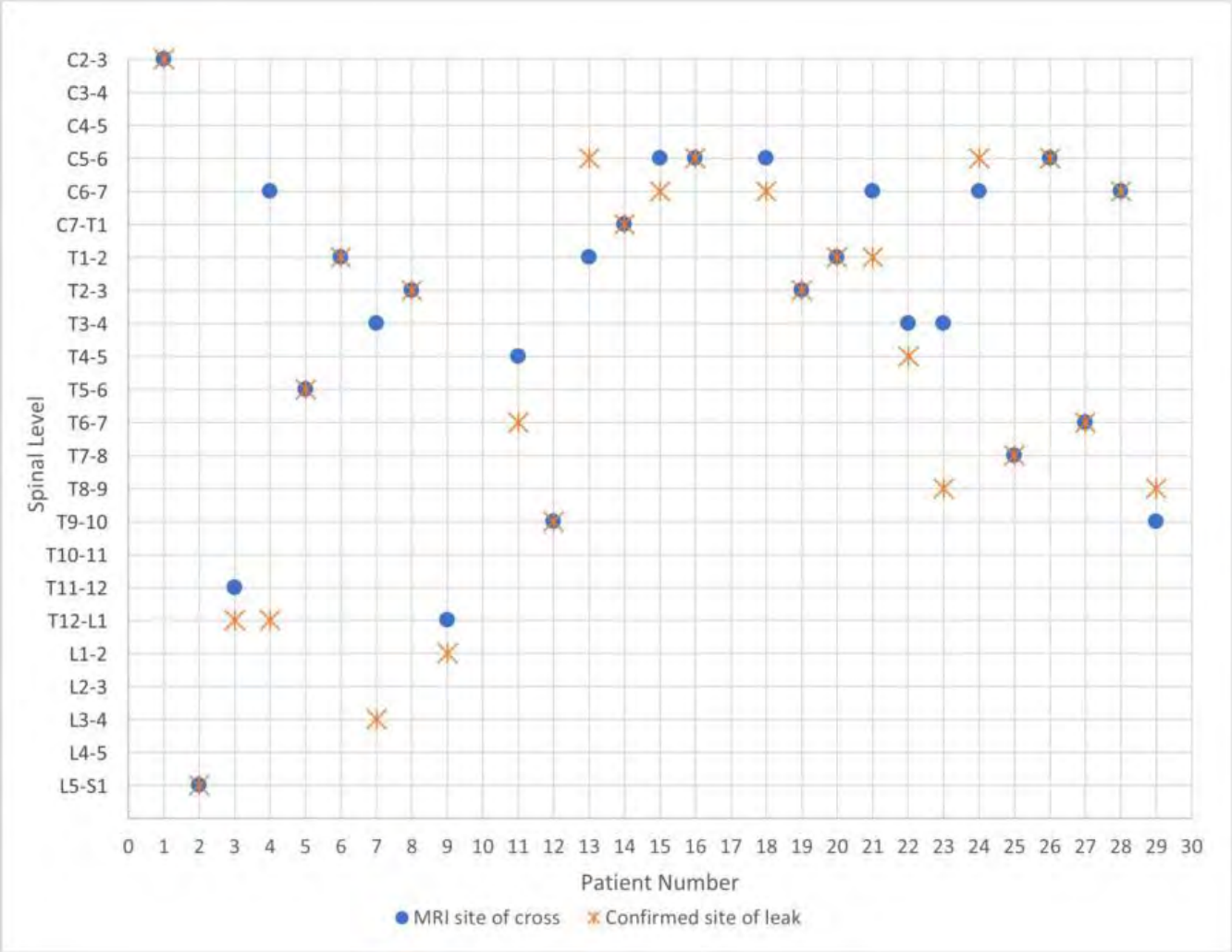

(Filename: TCT_827_Table1.jpg)

Monday, May 16, 2022
3:30-5:00 PM
Scientific Podium Presentations: Stroke

270

Association Between High-risk Extracranial Carotid Plaque and Covert Brain Infarctions and Cerebral Microbleeds

H Baradaran[1], S Culleton[1], M Alexander[1], S Kim[1], D Parker[1], J McNally[1]
[1]*University of Utah, Salt Lake City, UT*

Purpose

Covert brain infarctions (CBIs) and cerebral microbleeds (CMBs) are clinically silent infarctions and microhemorrhages respectively, discovered on brain imaging. There is evidence that carotid atherosclerosis is associated with CBIs and CMBs, though the exact association with specific high-risk plaque features, including intraplaque hemorrhage (IPH) and plaque ulceration is unclear. We sought to evaluate the association between two high-risk plaque features, IPH and ulceration, to the presence of CBIs and CMBs.

Materials and Methods

In this retrospective cross-sectional study, 394 patients (698 arteries) with both brain MR and extracranial carotid MRA were available for analysis after exclusion criteria were applied. IPH and plaque ulceration was recorded on carotid MRA and total, cortical, and lacunar subtype CBIs and CMBs were recorded on brain MR. Multivariable Poisson regression was performed to test high-risk plaque features to CBIs and CMBs. Within-subject analysis in those with unilateral IPH and ulceration was performed with Poisson regression.

Results
We found that both IPH and plaque ulceration were associated with total CBI with prevalence ratios (PR) of 3.33 (95% CI: 2.16-5.15, p <0.001) and 1.91(1.21-3.00, p=0.005), respectively, after adjusting for degree of stenosis and demographic and vascular risk factors. In subjects with unilateral IPH, we found PR of 2.83 (CI:1.76-4.55, p<0.001) for having CBI in the hemisphere downstream from IPH after adjusting for degree of stenosis. Among those with unilateral plaque ulceration, we found PR of 1.82 (1.18-2.81, p=0.007) for total CBI in the hemisphere downstream from ulceration after adjusting for degree of stenosis. We found no statistically significant association between plaque features and CMBs.
Conclusions
We found that both IPH and plaque ulceration are associated with total, cortical, and lacunar type CBIs but not CMBs. These results support the potential role of advanced atherosclerosis in markers of subclinical vascular injury which are independently associated with cognitive impairment.

Total Cohort (n=349)						
IPH						
	PR (95% CI)	**p-value**	**PR adjusted for degree of stenosis**	**p-value**	**PR adjusted for Stenosis and additional demographics and vascular risk factors**	**p-value**
Total CBI	5.31 (3.69-7.66)	p<0.001	3.30 (2.14-5.09)	p<0.001	3.33 (2.16-5.15)	p<0.001
Cortical CBI	8.81 (3.43 to 22.6)	p<0.001	4.43 (1.39-14.2)	p=0.012	6.73 (1.72-26.3)	P=0.006
Lacunar CBI	4.33 (2.71 to 6.90)	p<0.001	2.55 (1.59-4.09)	p<0.001	2.68 (1.74-4.14)	P<0.001
Total CMB	1.17 (0.56 to 2.42)	p=0.68	N/A	N/A	N/A	N/A
Ulceration						
Total CBI	3.47 (2.23-5.41)	p<0.001	1.39 (1.06-1.83)	P=0.02	1.91(1.21-3.00)	P=0.005
Cortical CBI	5.09 (1.30 - 19.9)	P=0.02	3.14 (1.12-8.76)	p=0.03	2.73 (1.12-6.66)	P=0.03
Lacunar CBI	4.04 (2.51 - 6.50)	p<0.001	2.40 (1.35-4.26)	P=0.003	2.23 (1.32-3.76)	P=0.003
Total CMB	1.66 (0.83 - 3.36)	p=0.15	N/A	N/A	N/A	N/A

(Filename: TCT_270_FigureASNRabstract2022.jpg)

1082

Bobby Balloon Guide Catheter Thrombectomy For Acute Ischemic Stroke: Initial Experience

K Topiwala[1], C Quinn[2], K Masood[3], U Okafo[3], T Mehta[4], L Qi[3], B Jagadeesan[5]
[1]University Of Minnesota School Of Medicine, Minneapolis, MN, [2]Carolina Spine and Neurosurgery Center, Asheville, NC, [3]University Of Minnesota, Minneapolis, MN, [4]Hartford Hospital, Hartford, CT, [5]University of Minnesota, Minneapolis, MN

Purpose
Balloon Guide Catheters (BGC) have been shown to improve recanalization rates, increase first-pass effect, reduce new territory embolization and independently predict functional outcome in patients undergoing mechanical thrombectomy for acute ischemic stroke regardless of the type of first-line endovascular modality.
Materials and Methods
We performed a retrospective analysis on prospectively collected data of consecutive ischemic stroke patients undergoing mechanical thrombectomy at our institution (December 2020-October 2021). Interventions where Bobby BGC (MicroVentionTM, Aliso Viejo, CA) was used were identified. Baseline demographics, NIH Stroke Scale (NIHSS), modified Rankin Score (mRS), aortic arch type, occlusion site, first-pass effect (FPE), modified Thrombolysis in Cerebral Infarction (mTICI) score, trackability, and use of adjunct devices were collected and analyzed.
Results
A total of 43 patients received Bobby BGC guided mechanical thrombectomy (M:F=26:16, median age 72 years [IQR 62-82]). Thrombo-embolic occlusions occurred in the middle cerebral artery (M1 34.9%, M2 23.2%, M3 2.3%), internal carotid artery 9.3%, tandem (internal carotid/M1) 21%, anterior cerebral artery (A1 2.3%), and posterior circulation (7%). Fifty-one percent received intravenous thrombolytics. The median last-known-well-to-arteriotomy and arteriotomy-to-perfusion times were 266.5 minutes (IQR 150-430) and 29 minutes (IQR 20-46) respectively. All thrombectomies were performed by the same neurointerventionalist (BDJ), using thromboaspiration (69.7%) or aspiration plus stentretriever (30.3%) as first-pass modality. The Bobby BGC tracked well over tortuous aortic arches (type II 34.8%, type III 16.3%), and was inflated under fluoroscopic guidance within the internal carotid artery

(74.4%), common carotid artery (18.6%), and vertebral artery (6.9%). The median number of thrombectomy passes was 1 (IQR 1-2), with final recanalization rates: mTICI 3 (74.4%), mTICI 2b (20.9%), mTICI 2b/3 (95.3%). Our first-pass-effect and modified first-pass-effect rates were 51.1% and 79.1% respectively. Among survivors, the discharge NIHSS reduced by a median 9 points (IQR 4-15, p<0.0001). At median follow-up of 3.5 months (IQR 1-6), the median 90-day mRS score was 1.5 (IQR 0-2).
Conclusions
Bobby BGC use in patients undergoing mechanical thrombectomy was found to be associated with a high rate of first-pass effect, overall recanalization, and resulted in good functional outcomes.

645

Crowd-sourced Deep Learning for Intracranial Hemorrhage Detection: Wisdom of Crowds or Laissez Faire Information Corruption

E Hofmeijer[1], C Tan[2], F van der Heijden[1], R Gupta[3]
[1]University of Twente, Enschede, Overijssel, [2]Harvard Medical School / Massachusetts General Hospital, Cambridge, MA, [3]Massachusetts General Hospital and Harvard Medical School, BOSTON, MA

Purpose
Intracerebral hemorrhage (ICH) poses substantial burden on healthcare systems world-wide and can lead to long-term functional disability.1-3 Convolutional neural networks (CNNs) have been developed to automatically detect, classify or segment ICH from a Computed Tomography (CT) scan.4 Such evaluation has been shown to improve clinical workflow, but CNNs are still not accepted as fully-autonomous "assistants". To further improve classification performance and robustness, Ensemble Learning (EL) may appear to be an attractive technique. Overall accuracy of classification may be boosted by crowd sourcing over a set of separate CNNs that were trained to detect the presence of ICH in CT scans. In this study, we assess this hypothesis.
Materials and Methods
A dataset of 134 anonymized and deidentified CT scans was provided by the Massachusetts General Hospital for a graduate-level course in Technical Medicine at the University of Twente, Netherlands. Five different EL approaches were employed to derive conditions under which crowd sourcing can improve ensemble accuracy over any individual CNN. The assessment was conducted using 70 CNNs developed and trained by 140 students divided into teams. Each team started with a base CNN architecture and independently modified it, trained it, and measured its performance. From the 134 CT scans, 4287 slices were extracted of which 34.4% slices were positive for ICH. The dataset was sub-divided, at the patient level, into 4 sets: 2 for training and validating the 70 CNNs, 1 for training the EL networks, and 1 for independently testing both the 70 CNNs and EL networks.
Results
The base architecture achieved a 62.67% accuracy. The performance of EL algorithms roughly spanned a normal distribution curve with mean accuracy and standard deviation of 67.83% and 3.94%, respectively (Fig. 1). Majority Voting (accuracy=71.83%), Decision Tree (70.13%) and Support Vector Machine (74.10%) performed better than the average, with SVM ranking above the 95th percentile of all CNNs. Multi Input Deep Neural Network performed worse than the average. The accuracy of all EL techniques was lower than the best individual CNN (75.99%). Minimum Redundancy Maximum Relevance algorithm revealed that 2 of the individual CNNs together provide almost as much information as all 70 CNNs together.
Conclusions
Variations in model architecture are not enough to benefit from ensemble learning and the assumption of holistic performance from crowd sourcing may not hold if the individual CNNs are correlated.

Figure1: Accuracy of Individual CNNs and Ensemble Learning

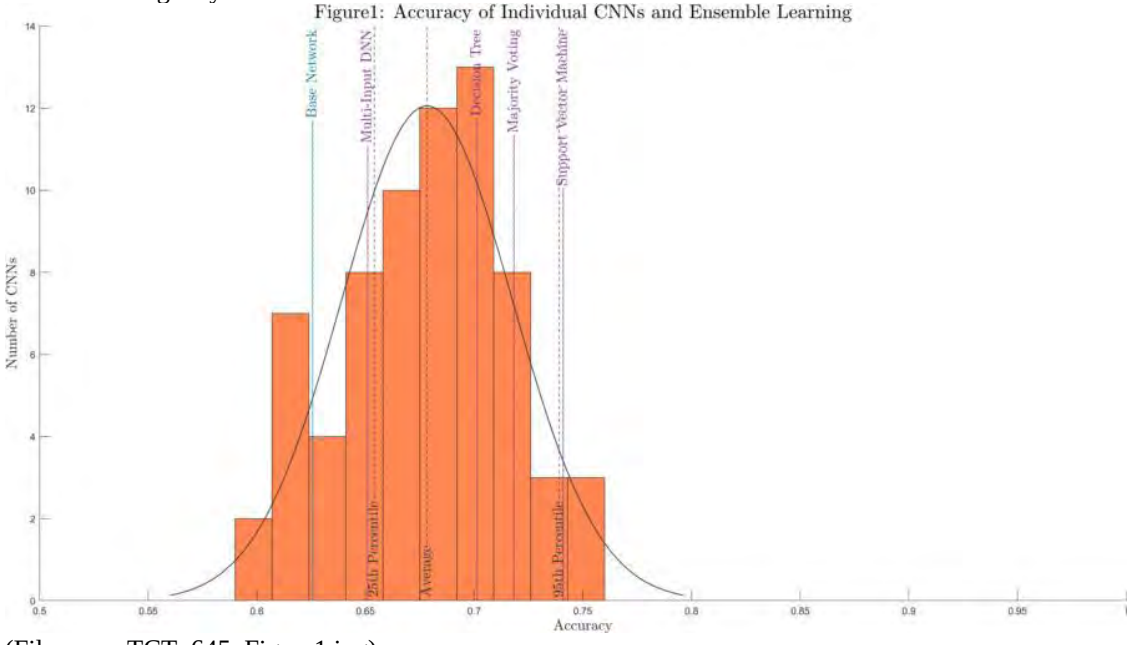

(Filename: TCT_645_Figure1.jpg)

594

Detection of Early Ischemic Changes with Virtual Non-contrast Dual-energy CT in Acute Ischemic Stroke: a Non-inferiority Analysis

F Kauw[1], V Ding[2], J Dankbaar[1], F van Ommen[1], G Zhu[2], D Wolman[3], L Molvin[4], H de Jong[1], L Kappelle[1], B Velthuis[1], J Heit[5], M Wintermark[6]

[1]University Medical Center Utrecht, Utrecht, Utrecht, Netherlands, [2]Stanford University, Stanford, CA, [3]Stanford University Hospital, Palo Alto, CA, [4]Duke University, Durham, NC, [5]Stanford University, Los Altos, CA, [6]Stanford University School of Medicine, Stanford, CA

Purpose

Dual-energy virtual non contrast (VNC) CT has the potential to replace conventional non-contrast CT (NCCT) acquisition to reduce the radiation dose, but it is unclear whether VNC CT of the brain is non-inferior to conventional NCCT to detect early ischemic changes in patients with acute ischemic stroke.1,2 In this study, we evaluated whether dual-energy VNC CT is non-inferior compared to conventional NCCT regarding detection of early ischemic changes with the Alberta stroke program early CT score (ASPECTS).

Materials and Methods

Adult patients who presented with suspected acute ischemic stroke and who underwent NCCT, dual-energy CT angiography and brain MRI within 48 hours as part of routine care were included. VNC images were reconstructed from CT angiography. Early ischemic changes were evaluated with ASPECTS on NCCT and VNC images by two independent reviewers in a blinded manner. In case of disagreement a third reviewer was consulted to reach consensus. The reference standard was ASPECTS on diffusion weighted imaging MRI, which was assessed by one independent reviewer blinded for CT imaging. Interobserver agreement between the CT reviewers was assessed with weighted kappa. Agreement between CT assessments and the reference standard was evaluated with the Lin's concordance correlation coefficient. Non-inferiority was assessed with bootstrapped estimates (5000 iterations) of the differences in ASPECTS between NCCT and VNC CT with 95% confidence intervals (CI). The pre-specified non-inferiority margin was 0.1.

Results

Of the 193 included patients (mean age 67, 53% male), 100 patients (52%) had ischemia on diffusion weighted imaging MRI. Interobserver agreement regarding ASPECTS was fair for VNC (weighted kappa 0.27, 95% CI 0.14-0.4) and NCCT (weighted kappa 0.38, 95% CI 0.23-0.54). Compared to the reference standard, the ASPECTS concordance correlation coefficient for NCCT and VNC was 0.23 (0.15-0.32) and 0.44 (95% CI 0.33-0.53), respectively. The difference in concordance correlation coefficient between VNC and conventional CT was 0.20 (95% CI 0.01-0.39) and did not cross the non-inferiority margin.

Conclusions

Dual-energy VNC CT is non-inferior compared to NCCT for detection of early ischemic changes with ASPECTS.

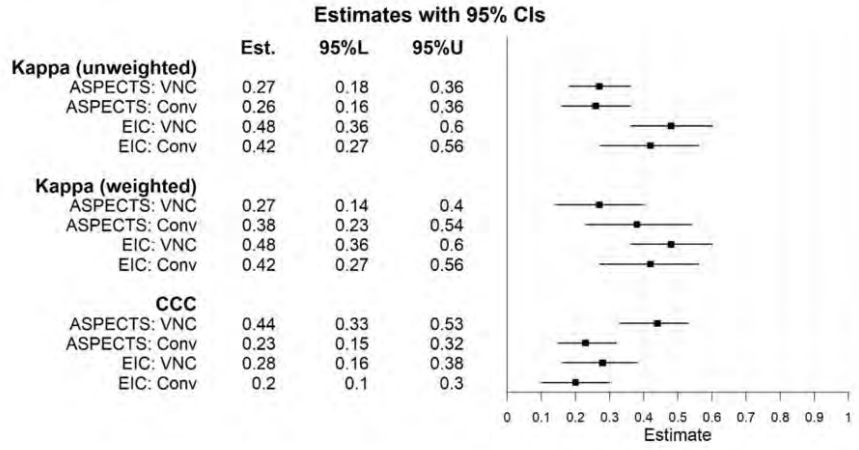

(Filename: TCT_594_Figure1.jpg)

900

Dual-module Velocity-Selective ASL (dm-VSASL) with improved SNR efficiency and doubled temporal SNR for perfusion imaging

J Guo[1]

[1]Bioengineering, University of California, Riverside, Riverside, CA

Purpose

Velocity-selective arterial spin labeling (VSASL) [1] is insensitivity to inhomogeneous arterial transit times (ATT) [1, 2], and holds great promises in clinical imaging of perfusion when ATT is concerned [3]. Recently dual-module (dm-) VS saturation (dm-VSS) [2] and VS inversion (VSI) preparation [4] have been developed to improve the SNR efficiency. However, its temporal SNR (tSNR) was typically unsatisfactory in practice. A novel dm-VSASL strategy is developed to further improve the SNR efficiency and the tSNR.

Materials and Methods

The new dm-labeling strategy uses VS pulses with inversion as the first VS module, and switches the label/control condition in the second VS module. This results in a more balanced utility of VS gradients under the label/control conditions than conventional single-module (sm-) VSASL. We hypothesize that this should reduce noise and artefacts from sources such as motion, eddy currents (ECs) and diffusion. Four healthy human subjects (1F, age 23-38) were studied on a 3T MRI scanner (Siemens Prisma, Erlangen, Germany). The ASL scans with background suppression (BS) included: 1) Pulsed ASL (PASL); 2) VSSinv; 3) VSS+VSSinv; 4) VSSinv+VSS; 5) VSI; and 6) VSI+VSI. Sinc-VSI [5] and symmetric BIR-8 (sBIR8) with built-in inversion (VSSinv) [2] were used for dm-VSI and dm-VSS labeling.

Results

Examples of ASL signal, tSNR and CBF maps are shown in Figure 1. Averaged ASL signal, tSNR and CBF in gray and white matter (GM/WM) ROIs are summarized in Table 1. Figure 2 shows examples time series of the ASL scans. ATT artefacts with PASL were observed in Sub. 3 (Figure 3), while all VSASL methods demonstrated excellent ATT insensitivity. Dm-VSI produced the highest signal in GM and WM, and showed a trend of increase by 6.6% (p=0.062) compared to sm-VSI; VSS+VSSinv increased the signal by 24.4% (p=0.025) compared to sm-VSS, consistent with previous findings [2, 5]. Dm-VSI and sm-VSI increased ASL signal by 50% (p≤0.01) compared to sm-VSS. There was no significant difference in CBF between labeling methods (p=0.19 in GM, and p=0.070 in WM). Compared to the single-module counterparts, VSSinv+VSS improved the tSNR by 142.2% (GM, p=0.011) and 55.2% (WM, p=0.044); and dm-VSI improved the tSNR by 165.6% (GM, p=0.003) and 90.5% (WM, p=0.010).

Conclusions

Dm-VSASL significantly improves the SNR performance of VSASL. Combined with the SNR advantage of VSI, dm-VSI should be an excellent tool for imaging baseline and functional changes of perfusion.

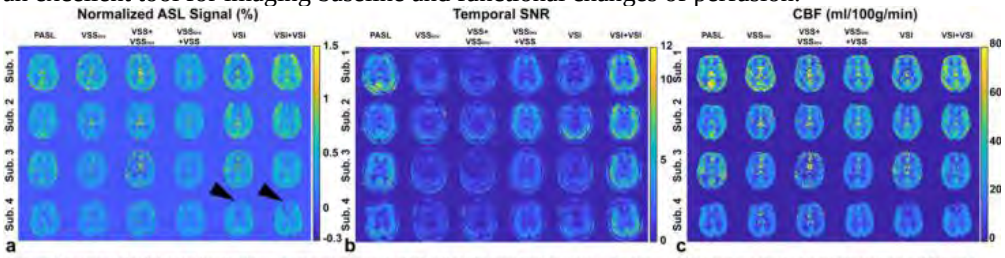

Figure 1. Examples of a) ASL signal (normalized to the reference images), b) tSNR, and c) CBF maps from the subjects. A reduction of ASL signal was observed in the anterior regions of Subject 4 using VSI labeling (black arrows), but not with sBIR8 VSS labeling, possibly due to VSI's sensitivity to field inhomogeneities.

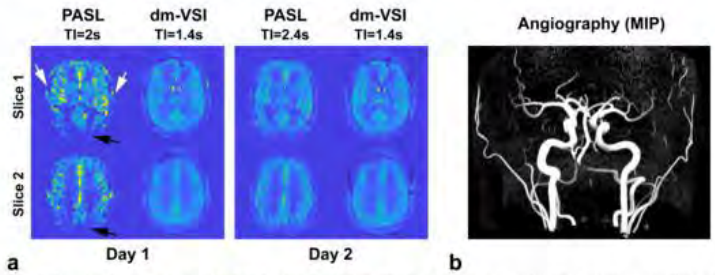

Figure 2. Examples of transit artefacts with PASL in Sub. 3 (a, TI1 = 0.8s and TI = 2s on Day 1, delayed perfusion and strong intravascular signals are labeled with black and white arrows, respectively), but none of the VS labeling methods showed such artefacts (only dm-VSI is shown). A later PASL scan with a longer TI of 2.4s (Day 2, most of the artefacts were gone) and angiography (b) confirmed that the flow was delayed due to tortuous routes in the vertebral arteries.

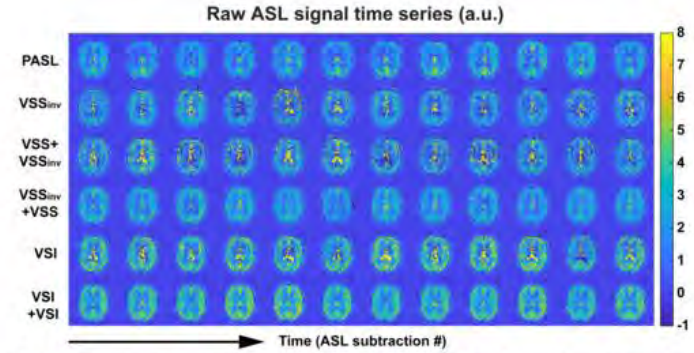

Figure 3. Examples of the raw ASL time series using different labeling methods in Subject 2. For VSASL, each time point corresponds to 20s of acquisition time, all 12 time points are shown; for PASL, each time point corresponds to 16s of acquisition time and only the first 12 (out of 15) time points are shown.

	Gray Matter						White Matter					
Sequence	PASL	VSS_{inv}	$VSS+VSS_{inv}$	$VSS_{inv}+VSS$	VSI	VSI+VSI	PASL	VSS_{inv}	$VSS+VSS_{inv}$	$VSS_{inv}+VSS$	VSI	VSI+VSI
ASL Signal w/ BS correction (%, n=4, mean±SEM)	0.52±0.11	0.41±0.12	0.51±0.11	0.42±0.10	0.61±0.17	0.65±0.19	0.18±0.02	0.19±0.07	0.13±0.02	0.17±0.03	0.24±0.04	0.28±0.08
tSNR w/ BS correction (n=4, mean±SEM)	4.45±0.98	1.45±0.43	1.34±0.44	3.52±1.12	2.18±0.96	5.80±1.05	1.48±0.29	0.77±0.15	0.55±0.16	1.20±0.36	1.11±0.33	2.12±0.45
CBF (n=4, ml/100g/min)	38.43±10.44	34.11±11.09	35.12±7.8	33.35±8.71	35.54±9.18	38.74±12.69	10.16±1.66	12.80±5.00	9.55±1.71	10.40±2.24	11.21±1.84	13.25±4.13

Table 1. Averaged ASL signal, tSNR and CBF in GM and WM ROIs across subjects. Note that the ASL signal and tSNR were corrected for BS attenuation.

(Filename: TCT_900_all_pic_mid_quality.jpg)

978

Edinburgh CT criteria in patients with lobar intracerebral hemorrhage: interobserver agreement and prognostic utility

E Tommasino[1], F Bruno[2], A Splendiani[3]

[1]University of L'Aquila, L'aquila, Italy, [2]University of L'Aquila, L'Aquila, Abruzzo, [3]University of L'Aquila, L'AQUILA, l'aquila

Purpose

We aimed to assess interobserver agreement and prognostic utility of the Edinburgh CT criteria in patients with ICH.

Materials and Methods

We retrospectively evaluated 186 patients hospitalized for a first-ever lobar ICH from 2015 to 2020 applying the Edinburgh criteria to the brain CT's done at admission. ICH characteristics and outcomes were compared according to the presence of the Edinburgh CT criteria, including associated subarachnoid hemorrhage (aSAH) and finger-like projections (FLPs). The outcome of ICH in-hospital mortality was assessed with multivariate logistic regression analysis. Two neuroradiologist (with respectively 8 and 20 years of experience) evaluated the brain CT's images.

Results

52/186 patients (28%) had aSAH+FLPs, 68 (36.6%) aSAH only, 1 (0.5%) FLPs, and 65 (34.9%) none. Interrater agreement was almost perfect for both aSAH ($k = 0.860$; $P < 0.001$) and FLPs ($k = 0.905$; $P < 0.001$). Patients with aSAH+FLPs were older (80.0 ± 8.7 years) than those with only one criterion or none (73.0 ± 14.3 and 71.2 ± 12.8 years, respectively; $P = 0.020$). Patients with aSAH+FLPs also had more severe ICH at onset, higher in-hospital case-fatality (log rank test $P = 0.003$) and higher mRS scores at discharge ($P < 0.001$).

Conclusions

Our data shows that the CT-based radiological Edinburgh criteria are easily applicable in the routine evaluation of patients with lobar ICH. The presence of those criteria directly reflects ICH clinical severity.

299

Functional Outcomes of Patients 85 Years or Older with Acute Ischemic Stroke Following Endovascular Treatment – Results from a HERMES Subgroup Analysis

R McDonough[1], J Ospel[2], B Campbell[3], M Hill[4], J Saver[5], D Dippel[6], A Demchuk[7], C Majoie[8], S Brown[9], P Mitchell[10], S Bracard[11], F Guillemin[11], T Jovin[12], K Muir[13], P White[14], M GOYAL[15]

[1]University of Calgary, Calgary, Alberta, [2]University Hospital Basel, Basel, Basel, [3]Royal Melbourne Hospital, University of Melbourne, Melbourne, Melbourne, [4]Cumming School of Medicine, University of Calgary, Caglary, Alberta, [5]UCLA, Los Angeles, CA, [6]Erasmus Medical Center, Rotterdam, Zuid-Holland, [7]Cumming School of Medicine, University of Calgary, Calgary, Alberta, [8]Amsterdam University Medical Centers, Amsterdam, Noord-Holland, [9]BRIGHT Research Partners, Mooresville, NC, [10]Royal Melbourne Hospital, Melbourne, Melbourne, [11]Université de Lorraine, Nancy, na, [12]University of Pittsburgh, Pittsburgh, PA, [13]University of Glasgow, Glasgow, na, [14]Newcastle University, Newcastle, Tyne & Wear, [15]University of Calgary, CALGARY, ALBERTA

Purpose

Observational studies have shown endovascular treatment (EVT) for acute ischemic stroke to be effective in the elderly, despite resulting in poorer outcomes and higher rates of mortality compared to younger patients. Randomized data on the effect of advanced age on outcomes following EVT are however lacking. Our aim was to assess the influence of age on outcome and EVT effect for ischemic stroke in patients aged ≥85 years in a large, randomized trial dataset.

Materials and Methods

Data were from the HERMES collaboration, a meta-analysis of 7 randomized trials that tested the efficacy of EVT. A possible multiplicative interaction effect of age on the relationship between treatment and outcome was investigated. Ordinal logistic regression tested the association between EVT and 90-day functional outcome (modified Rankin Scale [mRS], primary outcome) in patients ≥85 years. Multivariable binary regression was performed to compare primary and secondary outcomes (mRS 0-2/5-6) of patients ≥85 years versus those <85 years.

Results

We included 1764 patients in the analysis, of whom 77 (4.4%) were ≥85 years old. A significant interaction of age and treatment on poor outcome (mRS5-6, p=0.020) and mortality (p=0.031) was observed, with older adults having worse functional outcomes at 90 days compared to younger patients (adjusted common[ac]OR:0.20, 95%CI:0.13-0.33). However, a benefit of EVT was observed in the ≥85-year-old patient subgroup (cOR:4.20 (95%CI:1.56-11.32, Figure). Age ≥85 years was not significantly associated with differing rates of symptomatic intracerebral hemorrhage or reperfusion (aOR:1.92, 95%CI:0.71-5.15 and aOR:0.91, 95%CI:0.40-2.06, respectively).

Conclusions

Patients ≥85 years old with independent premorbid function more often achieve good functional outcomes and have lower rates of mortality when treated with EVT compared to conservative management, with an observed treatment effect modification of age on outcome. EVT should therefore not be withheld in this subgroup.

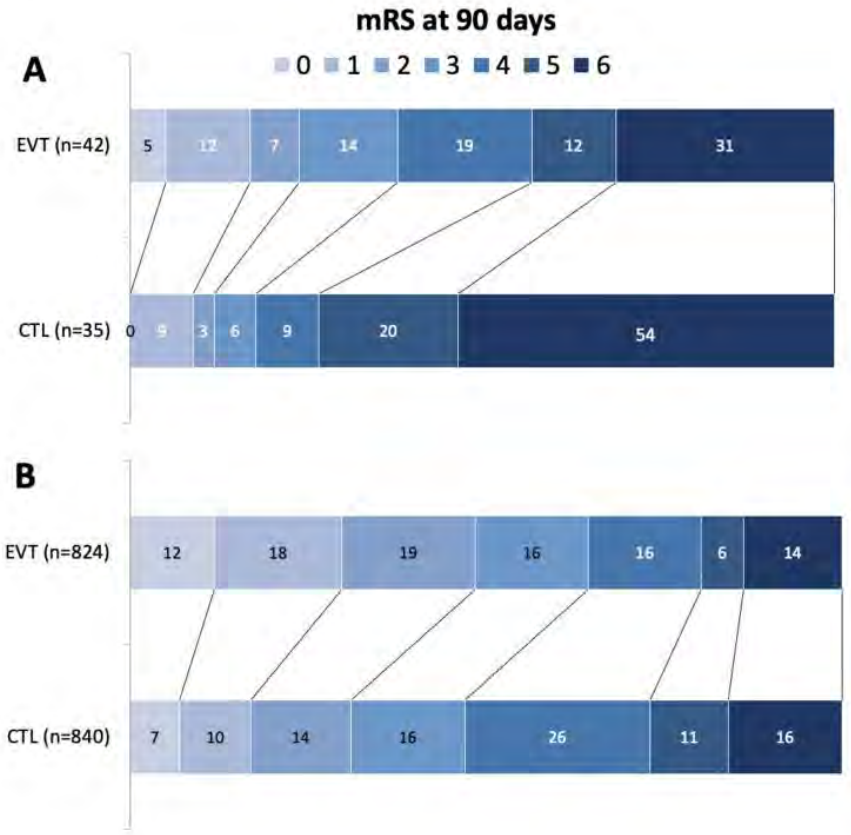

Figure 1. Distribution (in percentage) of mRS scores at 90 days in the intervention and control arms for patients aged ≥85 years (A) and those <85 years (B). *mRS: modified Rankin Scale; EVT: endovascular treatment; CTL: control*

(Filename: TCT_299_age_fig_2.jpg)

394

New Imaging Score for Outcome Prediction in Basilar Artery Occlusion Stroke

G BROOCKS[1], L Meyer[2], S Elsayed[2], A Kemmling[3], U Hanning[2]

[1]University Hamburg, Hamburg, NA, [2]University Hamburg, Hamburg, Hamburg, [3]University Marburg, Marburg, Hessen

Purpose

In ischemic posterior circulation stroke, the utilization of standardized image scores is not established in daily clinical practice. In contrast, rating of early ischemic changes or status of the collateral circulation is well recognized in anterior circulation stroke, and is used for outcome prediction, or treatment selection. We aimed to test a novel imaging score that combines the collateral status with rating of the posterior circulation Acute Stroke Prognosis Early CT score (pcASPECTS). We hypothesized that this score (pcASCO) predicts functional outcome and malignant cerebellar edema (MCE).

Materials and Methods

Ischemic stroke patients with acute BAO who received multimodal-CT and underwent thrombectomy on admission at two comprehensive stroke centers were analyzed. pcASCO was defined as a 20-point score adding the posterior circulation collateral score to the pcASPECTS. Endpoints were functional independence at day 90 assessed using modified Rankin Scale (mRS) scores, and occurrence of MCE in follow-up CT using the established Jauss scale score.

Results

118 patients were included, of which 84 (71%) achieved successful thrombectomy. Based on receiver operating characteristic curve analysis, pcASCO ≥14 classified functional independence with higher discriminative power (AUC: 0.83, 95%CI: 0.71-0.91) than pcASPECTS (AUC: 0.74). In multivariable logistic regression analysis, pcASCO was significantly and independently associated with functional independence (aOR: 1.91, 95%CI: 1.25-2.92, p=0.003), and MCE (aOR: 0.71, 95%CI: 0.53-0.95, p=0.02).

Conclusions

The pcASCO could serve as a simple and feasible imaging tool to assess BAO stroke patients on admission and might be tested as a complementary tool to select patients for thrombectomy in uncertain situations, or to predict clinical outcome.

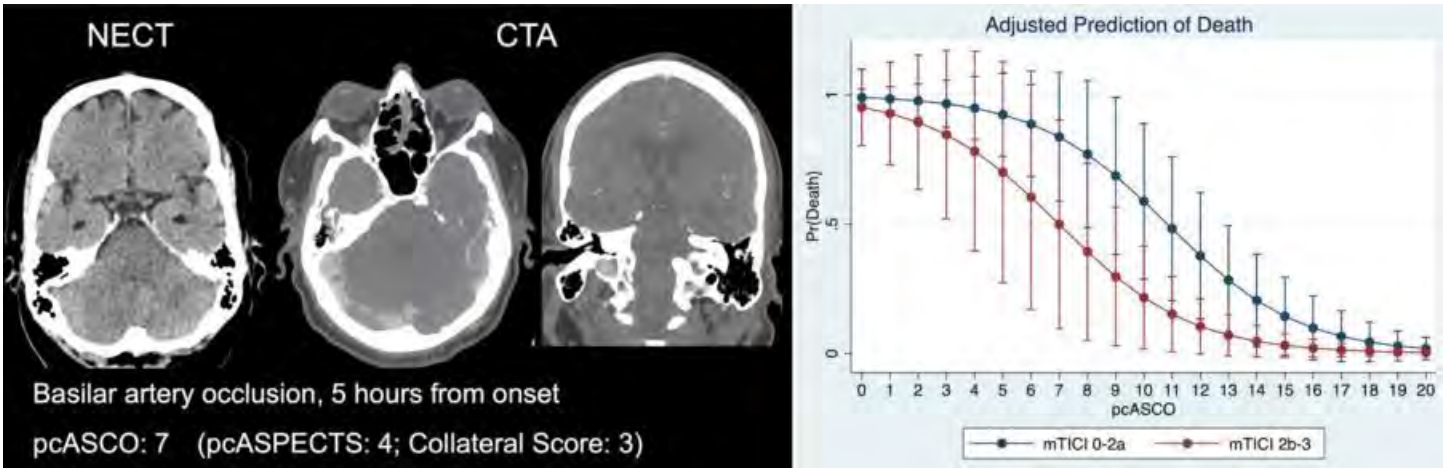

(Filename: TCT_394_ASNR_PCASCO_FIG.jpg)

1310

Noncontrast Computed Tomography Markers as Predictors of Intraventricular Hemorrhage Growth in Acute Intracerebral Hemorrhage

J Nawabi[1], F Schlunk[2], D Desser[1], F Mazzacane[3], P Sporns[4], J Fiehler[5], U HANNING[6], A Morotti[7]

[1]Charité Berlin, Berlin, NA, [2]Charité Belin, Berlin, NA, [3]ASST Valcamonica, Esine, NA, [4]Clinic for Radiology and Nuclear Medicine, Basel, NA, [5]University Hospital Hamburg-Eppendorf, Hamburg, Hamburg, [6]UNIVERSITY MEDICAL CENTER HAMBURG-EPPENDORF, HAMBURG, Germany, [7]University of Brescia, Brescia, NA

Purpose

Noncontrast computed tomography (NCCT) markers are the emerging predictors of hematoma expansion in intracerebral hemorrhage. The aim of this study was to assess the associations of NCCT markers with intraventricular hemorrhage growth and how the concurrent presence of each sign independently contributes to the predictive power of IVH growth.

Materials and Methods

We included patients with intracerebral hemorrhage admitted from two large tertiary stroke centers in Europe from January 2014 to July 2019. ICH volumes and intraventricular hemorrhage (IVH) volumes were measured using a semiautomatically. NCCT markers were rated for hypodensity, black hole sign, swirl sign, blend sign, fluid level, heterogeneous density, irregular shape, island sign, and satellite sign. A binary definition for IVH growth and revised hematoma growth (rHE) was defined by incorporating the original definition of hematoma expansion into IVH growth. Receiver operating characteristic (ROC) curve analysis was used to compare the performance of the NCCT markers in predicting the IVH growth and rHE.

Results

455 out of 720 consecutive patients were included in our multicenter study. 92 (20.2%) had IVH growth and 149 (32.7%) had rHE. Hypodensity was found in 138 (30.3%), black hole in 98 (21.5%), swirl sign in 273 (60.0%), blend sign in 55 (12.1%), fluid level sign in 37 (8.1%), heterogeneous density in 86 (18.9%), irregular shape in 246 (54.1%), island sign in 43 (9.5%), satellite sign in 173 (38.0%). After adjustment for potential confounding variables, swirl sign and heterogeneous density could independently predict IVH growth in the multivariate logistic regression analysis (OR 2.54, 95%CI 1.10-5.82; p=0.028 and OR 1.55, 95% CI 1.03-2.34; p=0.035) versus black hole sign and swirl sign for predicting rHE (OR 2.37, 95%CI 1.04-5.41; p=0.04 and OR 2,81, 95% CI 1.26-6.29; p=0.012). Hypodensity had the highest diagnostic value for predicting IVH growth (ROC AUC 0.591) and swirl sign for rHE (ROC AUC 0.623).

Conclusions

The NCCT markers are independently associated with IVH growth and rHE. Swirl sign and heterogeneous density were the most reliable NCCT markers for predicting IVH growth. These findings may assist in improved risk stratification of NCCT signs for predicting active bleeding.

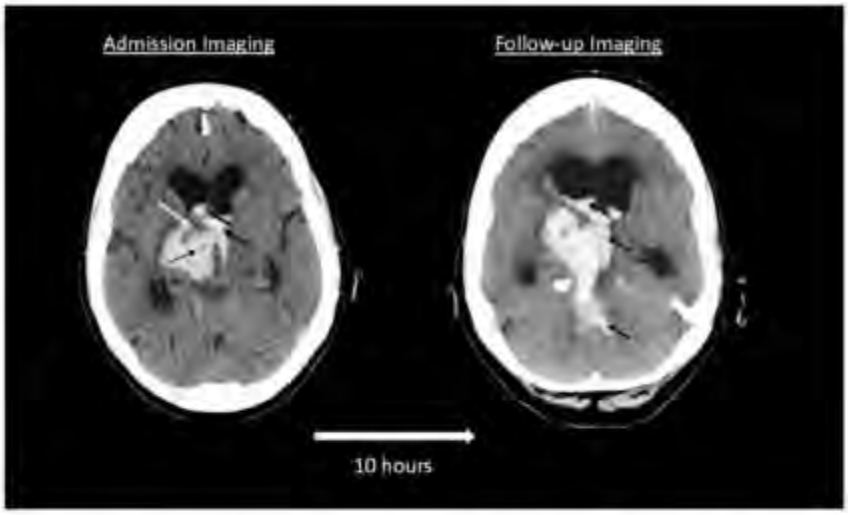

Figure 1: Representative example of a patient with intracerebral hemorrhage (ICH) on the admission Computed Tomography (CT) scan (left) and intraventricular hemorrhage growth and ICH expansion according revised hematoma expansion presented on the follow-up CT scan (right), respectively. Illustration of noncontrast computed tomographic markers of intracerebral hemorrhage expansion with swirl sign (both arrows), hypodensity (dashed arrow only), irregular shape (grade III) and heterogeneous density (grade II). The interval time from ICH onset to follow-up CT scan was 10 hours.

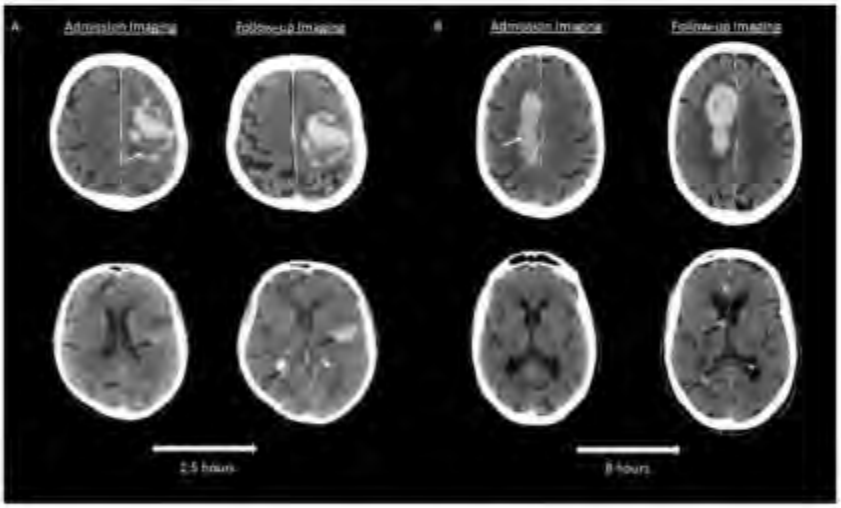

Figure 2: Representative example of a patients with intracerebral hemorrhage (ICH) on the admission Computed Tomography (CT) scan (A and B; left side) and both intraventricular hemorrhage and ICH expansion according revised hematoma expansion presented on the follow-up CT scan (A and B; right side), respectively. **A:** Illustration of noncontrast computed tomographic markers of intracerebral hemorrhage expansion with swirl sign (white arrow), and fluid sign (black arrow), hypodensity (dashed arrow only) and irregular shape (grade IV) and heterogeneous density (grade III). The interval time from ICH onset to follow-up CT scan was 2,5 hours. **B:** Hypodensity, swirl sign and black hole sign (white arrow), irregular shape (grade III) and heterogeneous density (grade IV), intraventricular hemorrhage expansion (black arrow), and subarachnoid hemorrhage (white star). The interval time from ICH onset to follow-up CT scan was 8 hours.

(Filename: TCT_1310_Figures.jpg)

628

Pre-Existing Small Vessel Disease Burden is Associated with the Degree of Early Neurological Worsening in Acute Ischemic Stroke: Results from the APRISE study

A Mahammedi[1], P Khatri[1], L Wang[1], H Sucharew[2], P Horn[2], D Wang[3], M Gaskill-Shipley[1], T Tomsick[1], R Cornelius[1], B Williamson[1], V Khandwala[1], S Gangatirkar[1], M Haverbusch[1], B Kissela[1], A Vagal[1]

[1]University of Cincinnati, Cincinnati, OH, [2]Cincinnati Children's Hospital Medical Center, Cincinnati, OH, [3]I-MED Radiology, Melbourne, Australia

Purpose

Small vessel disease (SVD) including white matter hyperintensity, enlarged perivascular spaces, microbleeds and lacunes are frequently seen in stroke patients. A total SVD score provides a more comprehensive assessment rather than individual markers. Our objective was to determine whether total SVD score is associated with the amount of early neurological worsening of acute ischemic stroke from initial to 24 hours, as measured by the NIH Stroke Scale score (NIHSS).

Materials and Methods

All hospitilized ischemic stroke patients were ascertained and characterized in a metropolitan population of 1.3 million served by 15 different inpatient hospitals for the calendar year of 2015, as part of the NIH-funded Greater Cincinnati/Northern Kentucky Stroke Study. We then collected and characterized all associated MR brain imaging through the ancillary NIH-funded Assessing Population-based Radiological brain health in Stroke Epidemiology (APRISE) study. MRIs were evaluated by trained, central neuroradiologists using STRIVE criteria for assessing small vessel disease burden. We calculated the total SVD score, ranging from 0-4 where one point is allocated to each of the following: (1) presence of lacunes, (2) presence of microbleeds, (3) moderate to severe (>10) basal ganglia perivascular spaces, and (4) severe periventricular or moderate to severe deep white matter hyperintensity. We collected the initial and 24-hour NIHSS. Linear regression was used to evaluate the association between total SVD score and change in NIHSS score (24h minus initial) (Tables 1 and 2).

Results

Of the 2478 ischemic stroke events identified during 2015, we anticipate 70% will have associated MRIs. We currently report results from 1128 events with associated MRIs (45% of projected total MRIs) with a mean (SD) age of 68 (15) years and 53% women. The mean (SD) SVD score was 1.9 (1.0), and NIHSS scores were 5.0 (6.8) at baseline and 5.1 (6.8) at 24 hours. We observed a significant positive chronic SVD-by-initial NIHSS score interaction ($p<0.01$), with a mean increase in the change in NIHSS of 0.48 points (95% CI 0.01, 0.94) per point increase in SVD at initial NIHSS of 15, but no association at initial NIHSS of 5 (-0.08, 95% CI -0.35, 0.19) (Figure 1).

Conclusions

Greater pre-existing SVD burden is associated with increased early neurological worsening in patients with acute ischemic stroke, and with greater amount of worsening for strokes that were more clinically severe initially.

Figure 1. Graphical representation of the SVD-by-initial NIHSS interaction on change in NIHSS. Estimated effects are relative to a patient with a SVD score of 0 (gray line).

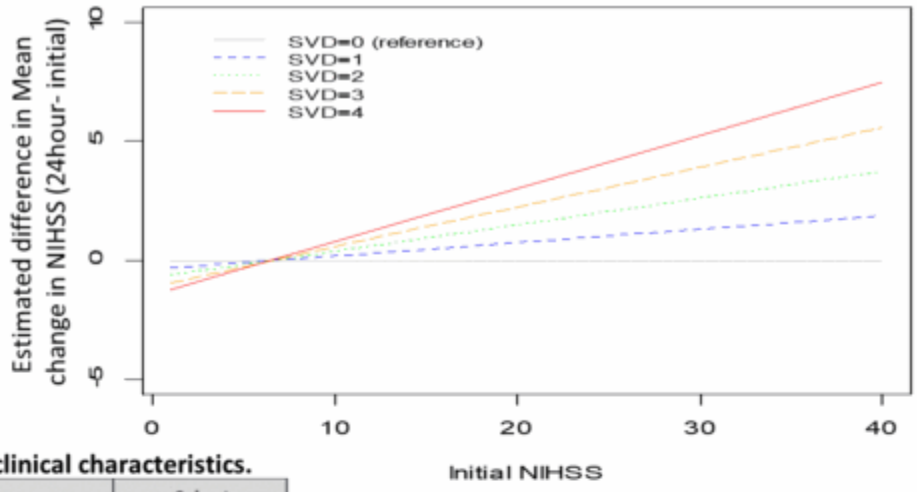

Table 1. Demographic and clinical characteristics.

	Cohort N=1128 N (%) or mean (SD)
Demographics:	
Age, mean (SD)	69 (14)
Black (%)	276 (24%)
Female (%)	608 (54%)
Risk factors and clinical characteristics:	
History of HTN (%)	943 (84%)
History of DM (%)	440 (39%)
History of coronary artery disease (%)	370 (33%)
History of atrial fibrillation (%)	209 (19%)
History of HF (%)	184 (16%)
History of dementia (%)	118 (10%)
History of previous stroke (%)	306 (27%)
Current smoker (%)	310 (27%)
Pre-stroke mRS, mean (SD)	1.6 (1.4)
Initial NIHSS, mean (SD)	5.1 (6.8)
Imaging Characteristics:	
WMH periventricular	
0	124 (11%)
1	351 (31%)
2	312 (28%)
3	341 (30%)
WMH deep	
0	154 (14%)
1	591 (52%)
2	228 (20%)
3	155 (14%)
Sum periventricular and deep WMH, mean (SD)	3.1 (1.7)
Microbleed present	235 (21%)
Perivascular spaces in basal ganglia	
None	130 (12%)
1-10	593 (53%)
11-20	284 (25%)
21-40	92 (8%)
>40	29 (3%)
Total SVD score	1.9 (1.0)

Table 2. Multivariable linear regression model for SVD and change in NIHSS score (24hour-initial)

	Change in NIHSS Score Points coefficient (95% CI)	p-value
Age, per year	0.02 (-0.01, 0.04)	0.16
Black	0.10 (-0.55, 0.75)	0.76
Female	-0.44 (-0.98, 0.09)	0.11
History of HTN	-0.23 (-1.01, 0.55)	0.56
History of DM	0.08 (-0.49, 0.65)	0.78
History of coronary artery disease	-1.10 (-1.73, -0.47)	<0.01
History of atrial fibrillation	0.33 (-0.41, 1.07)	0.38
History of HF	0.64 (-0.15, 1.42)	0.11
History of dementia	-0.08 (-1.01, 0.85)	0.87
History of previous stroke	1.00 (0.37, 1.64)	<0.01
Current smoker	0.29 (-0.36, 0.93)	0.39
Pre-stroke mRS	0.59 (0.36, 0.82)	<0.01
Initial NIHSS – Imaging effects, p-value for interaction	**<0.01**	
SVD, per point		
at initial NIHSS = 5	-0.08 (-0.35, 0.19)	0.55
at initial NIHSS = 10	0.20 (-0.13, 0.53)	0.24
at initial NIHSS = 15	0.48 (0.01, 0.94)	0.046
at initial NIHSS = 25	1.03 (0.23, 1.84)	0.01
at initial NIHSS = 35	1.59 (0.42, 2.76)	<0.01
Initial NIHSS, per point		
at SVD=0	-0.39 (-0.47, -0.31)	<0.01
at SVD=1	-0.33 (-0.38, -0.28)	<0.01
at SVD=2	-0.27 (-0.32, -0.23)	<0.01
at SVD=3	-0.22 (-0.28, -0.16)	<0.01
at SVD=4	-0.16 (-0.26, -0.07)	<0.01

(Filename: TCT_628_ASNRSVDNIHSS2022.gif)

1217

Predictors of Early Neurological Improvement in Patients with Anterior Large Vessel Occlusion and Successful Recanalization Following Endovascular Thrombectomy – Does CT Perfusion Imaging matter?

C Deuschl[1], Y Li[2], M Köhrmann[3], A Demircioglu[1], N van Landeghem[3], E Kellner[4], L Milles[5], K Wrede[6], i wanke[7], B Frank[8]
[1]University Hospital Essen, Essen, NRW, [2]Institute of Diagnostic and Interventional Radiology and Neuroradiology, University Hospital Essen, 45147, Germany, [3]University Essen, Essen, NRW, [4]University Medical Center Freiburg, Freiburg, BW, [5]UniversityHospital Essen, Essen, NRW, [6]Department of Neurosurgery, University Hospital Essen, Essen, Germany, [7]Neuroradiologie Hirslanden, Zurich, zurich, [8]Department of Neurology, Universitiy Hospital Essen, Essen, Germany

Purpose
Since 2015 multiple randomised trials showed efficacy of endovascular thrombectomy (EVT) over standard medical therapy alone regarding improvement of functional outcomes in patients with acute ischemic stroke (AIS) caused by anterior large vessel occlusion (LVO) within 7.3 hours from stroke onset to arterial access [1]. We aimed to assess predictors of early neurological improvement (ENI) in acute ischemic stroke (AIS) patients with anterior large vessel occlusion and successful reperfusion following endovascular thrombectomy (EVT). The treatment effect of EVT on National Institutes of Health Stroke Scale (NIHSS) scores was additionally investigated every 24 hours.
Materials and Methods
Stroke data from January 2018 to December 2020 in a tertiary care centre were retrospectively analysed. Inclusion criteria were 1) occlusion of internal carotid artery and/or M1/M2 branch of middle cerebral artery; 2) successful reperfusion by Thrombolysis in Cerebral Infarction Scale (TICI) 2b/3. A reduction of at least 8 NIHSS points at 24 hours after EVT or an extremely low NIHSS score ≤ 1 at discharge was defined as ENI. Twenty variables were tested in a smoothed ridge regression for their association with ENI.
Results
172 out of 211 patients experienced successful recanalization with 54 patients achieving ENI. Impact of successful reperfusion on NIHSS scores reduction grew continuously on a daily basis up to the date of discharge. 105 out of 172 patients with available CT perfusion (CTP) imaging were included in the regression model. Short time from onset to admission and from groin-puncture to recanalization, young age, low pre-stroke disability, high baseline CTP ASPECTS and high follow-up CT ASPECTS at 24 hours were significantly associated with ENI.
Conclusions
CT perfusion ASPECTS outperformed non-contrast CT ASPECTS at baseline. Neither the volume of the pneumbra nor the size of the ischemic core were associated with ENI.

1031

Quantification of cerebral small vessel disease lesions using ex-vivo magnetic resonance imaging in Alzheimer's disease.

E Fadaee[1], K Li[1], T Rashid[1], J Walker[1], K Bieniek[1], T Richardson[1], V Ganapathy[1], H Katragadda[1], J Toledo[2], S Seshadri[1], M Habes[1]
[1]The Glenn Biggs Institute for Alzheimer's and Neurodegenerative Diseases, San Antonio, TX, [2]Department of Neurology, University of Florida, Gainesville, FL

Purpose
This study provides feasibility data and a methodological approach for manual segmentation of cerebral small vessel disease (CSVD) lesions in magnetic resonance imaging (MRI) of postmortem brains that will serve as the gold standard for applying machine learning segmentation methods(1) currently under development. The end goal is to create an automated tissue and image processing pipeline to identify and localize lesions in order to analyze the relationship between CSVD and dementia and to use CSVD as a predictor for the degree of severity in AD and other dementia categories(2-4).
Materials and Methods
From 2019 to 2021, 38 hemispheres of participants (15 female, 23 male) with Alzheimer's Disease (AD) were fixed and submerged in formalin postmortem and were scanned in a 3T Siemens TIM Trio scanner with an 8-channel knee transmit/receive coil. Scans included T1- and T2-weighted images (T1w and T2w, respectively). T1w images were 144 x 448 x 308 voxels in dimension with an isotropic resolution of 0.5 mm, and T2w images were 55 x 320 x 256 voxels in dimension with an in-plane resolution of 0.62 mm x 0.62 mm (sagittal) and a slice thickness of 1.5 mm. Following image acquisition and preprocessing (reorientation and inhomogeneity correction), white matter hyperintensities (WMH), enlarged perivascular spaces (ePVS), and infarctions were manually segmented by three expert raters (EF, KL, and TR) using ITK-SNAP software (http://www.itksnap.org). The T1w and T2w images were visually inspected simultaneously to detect and verify lesions (see Table 1).
Results
Visual examination revealed numerous WMH, ePVS, and infarctions in the brains. Through manual segmentation, we found that the average WMH volume was (± standard error) 13772 ± 2046 mm^3. The average number of infarctions was 4.91 ± 0.79 per participant with an average volume of 312 ± 177 mm^3. There were 81 ± 22 ePVS per hemisphere with a mean total volume of 95 ± 161 mm^3. Figure 1 shows an example of WMH and small infarction (Panel A), and ePVS (Panel B).
Conclusions
CSVD is prevalent with aging. CSVD affects the small arteries, arterioles, venules, and capillaries and has been associated with vascular risk factors of cognitive impairment such as hypertension and diabetes mellitus. Neuroimaging plays an essential role in

evaluating CSVD by quantifying WMH, ePVS, and infarctions. Our study manually quantified these three lesion types on MRI scans of postmortem brains. Acknowledgments NIH grant P30AG066546, JBT is supported by the Edmond J. Safra Fellowship in Movement Disorders.

	White Matter Hyperintensities (WMH)	Enlarged Perivascular Spaces (ePVS)	Infarctions
Appearance on T1w	Hypo- to isointense	Hypointense	Variably isointense
Appearance on T2w	Hyperintense	Hyperintense	Variably hyperintense
Typical Location	Periventricular and deep white matter	Basal ganglia and subcortical white matter	Variable, most commonly in basal ganglia and cerebellum
Shape	Ring around ventricles, small round spots that can join into large confluences	Small, curvilinear or ellipsoidal	Irregular shape depending on etiology

Table. Physical characteristics of cerebral small vessel disease lesions.

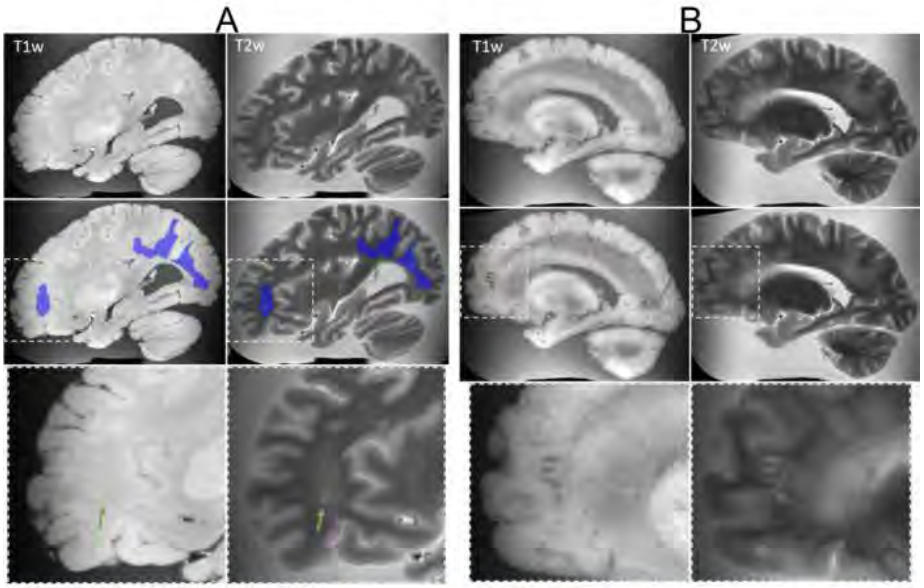

Figure. Panel A: (top row) T1w and T2w MRI showing white matter hyperintensities and an infarction. (Middle row) Manual segmentation of the lesions (blue for white matter hyperintensities, green for infarction). (Bottom row) Magnified view of the infarction, indicated by the green arrow. Panel B: (top row) T1w and T2w MRI showing enlarged perivascular spaces. (Middle row) Manual segmentation of ePVS lesions (red). (Bottom row) Magnified view of the ePVS.

(Filename: TCT_1031_Fig_and_Table.jpg)

Monday, May 16, 2022

3:30-5:00 PM

SNIS Programming: Complex NIR Treatments: What Am I Supposed to Do With This?

1249

Endovascular Treatment of Acute Tandem Lesions in Patients with Mild Anterior Circulation Stroke

L Meyer[1], U Hanning[2], G BROOCKS[3], M Bechstein[1], J Fiehler[4], P Papanagiotou[5]

[1]University Medical Center Hamburg-Eppendorf, Hamburg, Hamburg, [2]University Hamburg, Hamburg, Hamburg, [3]University Hamburg, Hamburg, NA, [4]University Hospital Hamburg-Eppendorf, Hamburg, Hamburg, [5]Neuroradiology, Central Hospital Bremen Mitte, Bremen, Bremen

Purpose

The risk-benefit ratio of endovascular treatment (EVT) for tandem lesions has yet not been evaluated outside of current guideline

recommendations of patients with mild anterior circulation strokes. This study investigates the frequency as well as the clinical and safety outcomes in this subgroup treated in daily clinical practice.
Materials and Methods
All currently available data of patients from the German Stroke Registry-Endovascular Treatment with anterior circulation stroke due to tandem lesions were analyzed if they presented with mild deficits defined as National Institutes of Health Stroke Scale (NIHSS) scores of 0-5. Successful recanalization was assessed with the Thrombolysis in cerebral infarction scale (mTICI) defined as mTICI 2b/3. Early neurological and long-term functional outcome at day 90 were assessed with the NIHSS change and modified Rankin scale (mRS), respectively. Safety assessment included periprocedural complications and the rate of symptomatic intracerebral hemorrhage (sICH).
Results
A total of 61 patients met the inclusion criteria and were treated endovascularly for tandem lesions in the anterior circulation. The median age was 68 (IQR, 59-76) and 32.9% (20) were female. Patients were admitted to the hospital with a median NIHSS score of 4 (IQR, 2–5) and a median ASPECTS of 9 (IQR, 8-10). Successful recanalization (mTICI 2b-3) was observed in 86.9% (53). NIHSS decreased non-significantly (p=0.382) from baseline to 2 points (IQR, 1-9) at discharge. Excellent and favorable long-term functional outcome at day 90 was 55.8% (29) and 69.2% (36), respectively. Mortality rates at 90-days were 9.6% (5) and sICH occurred in 8.3% (5).
Conclusions
EVT for tandem lesions in patients with mild anterior circulation stroke seems to be a technically feasible therapy option. Further studies comparing endovascular with best medical treatment, especially investigating the risk of periprocedural hemorrhage complications, are needed.

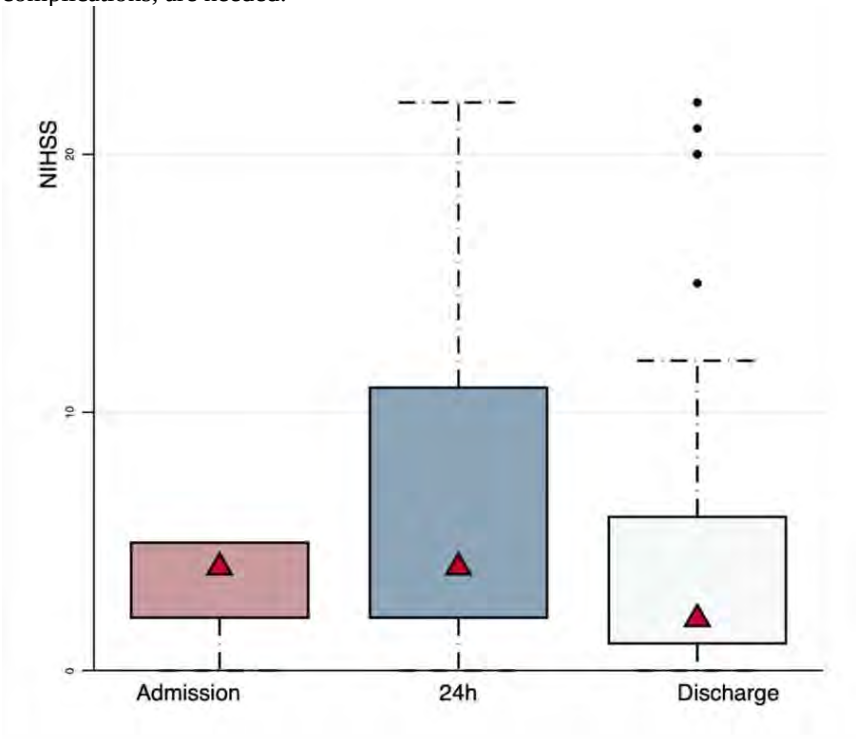

(Filename: TCT_1249_LowNIHSS_Tand.jpg)

1024
Spinal Arteriovenous Shunts in Children: Spectrum of Clinical and Angiographic Phenotypes and Implications for Endovascular Treatment
M Caton[1], A Baker[1], O Nnabue[1], C Reynolds[2], E Smith[1], M Amans[3], R Higashida[4], D COOKE[1], C Dowd[1], S Hetts[5]
[1]UCSF, San Francisco, CA, [2]JPS Health Network, Fort Worth, TX, [3]Ucsf, San Francisco, CA, [4]University of California, San Francisco, San Francisco, CA, [5]UCSF, San Fransico, CA

Purpose
Pediatric spinal arteriovenous shunts (pSAVS) are rare lesions with heterogenous ontogenesis and clinical manifestations [1, 2]. The purpose of this study is to present a large single institutional experience with pSAVS through the lens of pathophysiology and angioarchitecture to guide optimal treatment strategy.
Materials and Methods
An IRB-approved, retrospective review of a neurointerventional database was performed to identify children (< 20 years) who underwent spinal angiography for pSAVS. Lesion characteristics on MRI, angioarchitecture (DSA), and therapeutic strategy

(endovascular, surgical, conservative) were compiled. Clinical data were extracted to establish modified Aminoff-Logue (mAL) and McCormick (MC) disability indices pre- and post-treatment.

Results

Between 1996 and 2021, 30 pSAVS were identified in 28 children, mean age at diagnosis was 12 years (range 1.5 – 20), and 17/28 (60.1%) were female. pSAVS phenotypes included perimedullary arteriovenous fistula (PMF, n=10, 33.3%), metameric AVM with spinal involvement (n=5, 16.7%), glomus-type intramedullary AVM (n=5, 16.7%, Fig 1A, 1B), epidural AVF (n =3, 10.0%), paraspinal AVF/AVM (n=2, 6.7%), dural AVF (n=1, 3.3%), and diffuse spinal vasculopathy (n=1, 3.3%). Treatment was combined endovascular and microsurgical in 9/30 (30%), conservative in 8/30(26.7%), exclusively endovascular in 8/30 (26.7%) or microsurgical in 4/30 (13.3%). One patient was treated with immunotherapy. Mean follow-up was 5.8 years. Sufficient data were available to ascertain disability indices in 22/28 78.6% of patients; post-treatment improvement averaged 1.2 and 1.5 units on the MC and mAL indices, respectively. Glomus-type AVM had the most severe clinical presentation (mean MC = 3 and mAL = 5) and epidural AV fistulas had the most benign presentation (none with functional disability). The pSAVS subtype with greatest clinical improvement with intervention was PMF (mean MC and mAL index improvement 1.5 and 1.75, respectively); a demonstrative PMF case is shown in Fig 1B and 1C (pre- and post-embolization).

Conclusions

This represents one of the largest cumulative neurointerventional experiences with pSAVS including long-term clinical follow up [3,4]. Insights on angioarchitectural differences and their relation to relative clinical risk and treatment options will inform decision-making for pediatric neurointerventionalists.

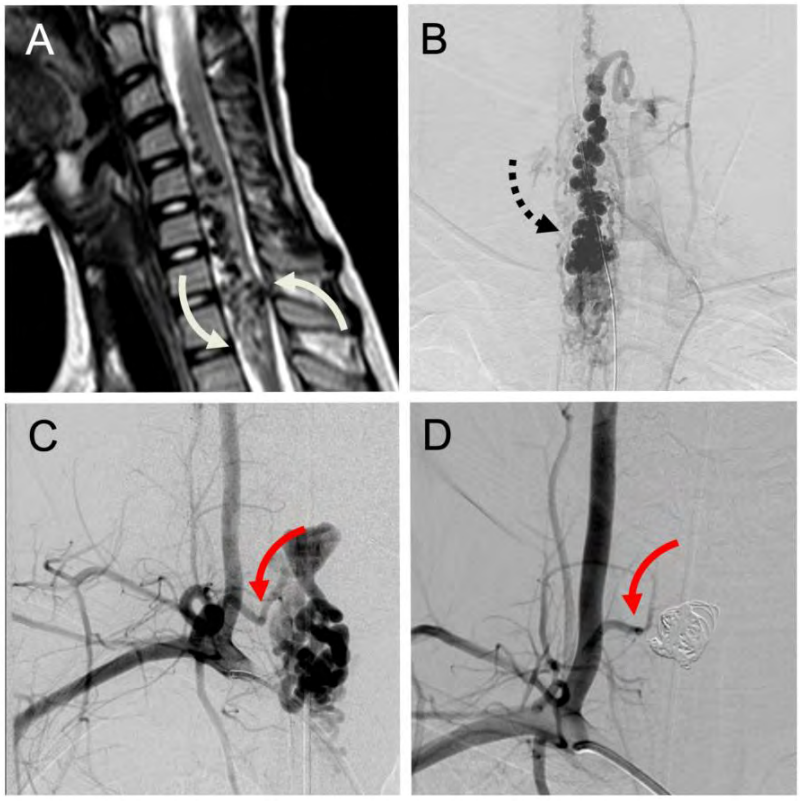

(Filename: TCT_1024_Ped_spinal_angio_Fig1.jpg)

Monday, May 16, 2022

5:15-6:15 PM

ASHNR Programming: What You Need to Know to Go with the Flow: A Primer on Head and Neck Vascular Lesions

287

Imaging Of Head And Neck Cancer Patients During Covid-19: Implications Of Changing Imaging Patterns During The Expansion Of Virtual Care

M Chen[1], A Tam[1], M Gule-Monroe[1], K Learned[1], D Kaya[2], S Calle[3], T Vu[4], V Kumar[5], K Shah[6]

[1]MD Anderson Cancer Center, Houston, TX, [2]UT Texas MD Anderson Cancer Center, Houston, TX, [3]The University of Texas MD Anderson Cancer Center, Houston, TX, [4]MD Anderson Cancer Center, Houston, Tx, [5]University of Texas MD Anderson Cancer Center, Houston, TX, [6]UT MD Anderson Cancer Center, Houston, TX

Purpose

The COVID-19 pandemic prompted profound change in healthcare delivery with expansion of telehealth and normalization of remote care. Destination travel to access care at tertiary cancer centers dropped and surveillance imaging studies were performed at facilities near patients' homes. The purpose of this study was to review the image quality and reporting of CT neck studies performed on head and neck cancer patients by non-oncologic imaging centers.

Materials and Methods

269 outside CT neck images (4/1/20-11/30/20) with 110 available reports were uploaded into the PACS for second review by our neuroradiologists. Image quality was assessed for: soft tissue contrast enhancement timing, slice thickness of axial images, whether angled images at the level of the mandible or larynx was performed when appropriate, and whether the "puffed cheek" technique appropriately. Imaging reports were reviewed to determine if the outside facility compared current to prior imaging, if there were reporting discrepancies, and whether these discrepancies resulted in changes to care management.

Results

During fiscal year 2020, overall volume of CT soft tissue of the neck performed at our institution for our follow-up head neck cancer patients declined by 20% relative to the prior year. During the study period, up to 6% of the CT neck studies interpreted by our neuroradiologists were from outside facilities. 46% (122/269) of CT neck images were rated inadequate (Table 1), with at least 51% of studies having at least one protocol issue and 24% of studies having multiple protocol issues. The most common protocol issues were: inadequate slice thickness (35%) and IV contrast bolus timing not optimized for enhancement of mucosal surfaces and soft tissues (25%).For patients with reports available, 56% (62/110) of reports did not compare to prior imaging. 35% (38/107) of reports had discrepancies between the outside radiologist and our neuroradiologists. 20% of patients had change in management.

Conclusions

During the height of the pandemic, we saw a change in patient care delivery with the increase in virtual visits also leading to imaging performed closer to home. In the majority of outside studies, imaging parameters were not optimized for the detection of recurrence or new head and neck cancers and comparison to prior imaging did not occur. Discrepancies in reporting changed patient care 20% of the time.

	Overall (N=269)			Inadequate image quality (N=122)		
		95% CI			95% CI	
	%	LL	UL	%	LL	UL
Protocol Issues						
Incorrect bolus timing	25.3%	20.1%	30.5%	45.9%	37.1%	54.7%
Inadequate slice thickness	35.3%	29.6%	41.0%	59.0%	50.3%	67.7%
No angled images	19.0%	14.3%	23.6%	33.6%	25.2%	42.0%
No IV contrast	2.6%	0.1%	4.5%	5.7%	1.6%	9.9%
No puffed cheek	0.7%	0.0%	1.8%	1.6%	0.0%	3.9%
At least 1 protocol issue	51.3%	45.3%	57.3%	82.8%	76.1%	89.5%
Multiple protocol issues	24.2%	19.1%	29.3%	48.4%	39.5%	57.2%

(Filename: TCT_287_Table1.JPG)

Monday, May 16, 2022

5:15-6:15 PM

Scientific Podium Presentations: Head & Neck

1471

3D deep learning model for predicting Pituitary Macroadenoma Cavernous Sinus Invasion

F Behzadi[1], M Nuru[2], J Kus[3], S Ramasamy[3], B Ploussard[3], J Cunningham[4], S Bajwa[5], M Kim[6], A Germanwala[7], A Mallik[8]

[1]Loyola Medical Center, Maywood , IL, [2]Loyola Medical Center, Chicago, IL, [3]Loyola University Medical Center, Maywood, IL, [4]BS, Maywood, IL, [5]Loyola University Chicago, Maywood, IL, [6]Loyola Medical Center, Maywood, IL, [7]Loyola University Chicago Stritch School of Medicine, Maywood, IL, [8]Loyola University Medical Center - Strich School of Medicine, Maywood, IL

Purpose

Pituitary imaging is a crucial tool for pituitary macroadenoma (PA) resection planning. MRI is used for current clinical criteria to

assess difficulty of cases and resectability, such as the Knosp criteria for assessing cavernous sinus invasion (CSI). We apply a 3D deep learning model to predict CSI that is comparable to current tools used by clinicians. This approach uses a more complex, modern architecture than a recent promising model (2) and is validated with endoscopic intraoperative findings, a more accurate gold standard than used for another promising model (3).

Materials and Methods

Data from 64 patients was extracted after inclusion and exclusion criteria were applied to consecutive PA patients operated on by a single Neurosurgeon (AG). Pre-operative images and operative data were reviewed, and the Knosp criteria and percent encasement of the internal carotid artery (PEICA) were assessed. Presence of CSI during endoscopic surgery was used as ground truth. Tensorflow (Python) was used to design a 3D convolutional neural network (CNN) CSI predictive model (8 convolutional layers). A training cohort (70%) was used to fit the model on a Linux GPU workstation (nVidia GTX 3080). A testing cohort (30%) was used to validate the model.

Results

Our 3D CNN model for CSI converged with 15 iterations and yielded sensitivity of 66% ± 33%, specificity of 100%± 1%, accuracy of 91%±10% (AUC 0.67). Knosp Criteria yielded sensitivity of 63%, specificity of 85% and accuracy of 85%. PEICA yielded sensitivity of 100%, specificity of 87%, and accuracy of 89%.

Conclusions

The comparable performance of this streamlined deep learning model to current clinical criteria with relatively few cases is promising for a rapid, accurate tool that can be used for operative planning. This also lays the groundwork for more robust 3D models, which can be validated with larger, multisite data sets, and may be applied to predict other outcomes such as gross total resection.

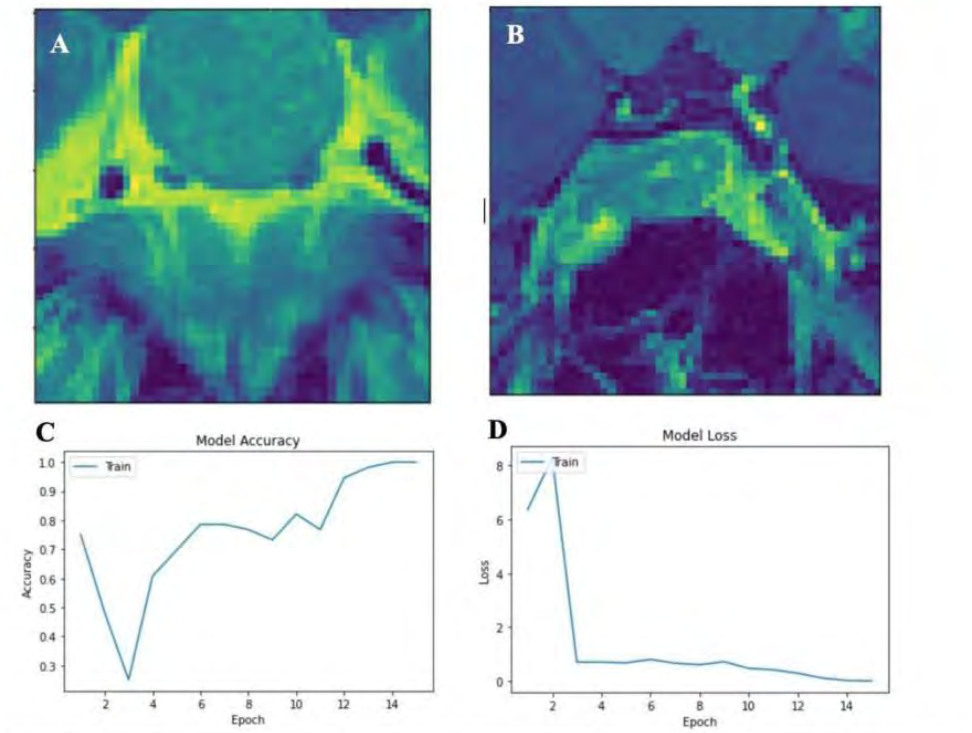

Figure. Grayscale, normalized, cropped (50X50 pix) stereotactic post-contrast MRI slices of **(A)** a larger pituitary macroadenoma without CSI and **(B)** a pituitary macroadenoma with CSI. Additionally, statistical evidence of the model converging over 15 iterations is shown in **(C)** graph of consistent increase in accuracy reaching close to 90% at iteration 12 and **(D)** Graph of relative categorical loss over iterations; showing plateau at iteration 3.

(Filename: TCT_1471_ffe4ea9f0974c7d9e58be920ab6fba2d.jpg)

950

Comparative Study of Utility of 3D Double Inversion Recovery (DIR) Versus 3D Fluid Attenuated Inversion Recovery (FLAIR) in Precise Diagnosis of Acute Optic Neuritis

V MURUMKAR[1], K Kulanthaivelu[1], J Saini[2]

[1]National Instituite of Mental Health and Neurosciences, Bangalore, Karnataka, [2]NATIONAL INSTITUTE OF MENTAL HEALTH & NEURO SCIENCES, BANGALORE, India

Purpose

Relevant clinical features and abnormalities in visual evoked potentials (VEP) are sufficient to diagnose ON (1). However, in the presence of atypical clinical features or an inconclusive VEP probe, imaging of the optic nerve may serve as a useful adjunct (2). 3D Double Inversion Recovery (DIR) employs two inversion pulses to nullify signal emanating from cerebrospinal fluid (CSF) and

normal-appearing white matter (3)(4). The contrast between optic nerve and sheath on 3D Fluid Attenuated Inversion Recovery (FLAIR) remains sub-optimal even in normal baseline-state that subtle signal changes stand the risk of being overlooked. Small size of nerve, intraorbital fat, periotic CSF sheath and air-bone interface are main hurdles for optic nerve imaging. Objectives: To compare diagnostic accuracy of 3-dimensional Fluid Attenuation Inversion Recovery (3D FLAIR) and 3-dimensional double Inversion Recovery 3D DIR in cases of acute optic neuritis (AON).

Materials and Methods

In this prospective, observational study, clinically suspected cases of AON with VEP abnormality were recruited for the case cohort while healthy control with normal visual acuity constituted control. MRI examination consists of 3D FLAIR and 3D DIR in addition to routine sequences. Images were analysed by novice, blinded radiologist. Inter-modality agreement, odds ratio, receiver operator characteristics (ROC) curve and inter observer agreement between two experienced neuroradiologists for two sequences was performed. Contrast ratio was calculated for the radiologically unilateral AON cases.

Results

Fair intermodally agreement was found between 3D-FLAIR & 3D-DIR (P-value <0.001). Odds ratio (OR) for the predictive power of a diagnosis of optic neuritis was higher for the 3D-DIR sequence compared to 3D-FLAIR (P-value <0.001). The area under the ROC curve for DIR was larger (p<0.001). Contrast ratio was higher for the 3 DIR (p<0.001).

Conclusions

3D DIR, by virtue of its unique contrast-generating schemes, demonstrates a greater contrast for lesions when compared to 3D FLAIR and it confers a greater degree of confidence for the diagnosis of AON even for novice readers.

Table 1: Table showing ICC between DIR & FLAIR

	ICC [95% Confidence interval (CI)]	P-value
Overall	0.537 (0.47 - 0.597)	0.000
Intracanalicular segment	0.491 (0.342 - 0.615)	0.000
Intraorbital segment	0.42 (0.261 - 0.557)	0.000
Optic chiasm	0.503 (0.357 - 0.626)	0.000
Prechiasmatic segment	0.63 (0.509 - 0.727)	0.000

Table 2: Table comparing odds ratio of DIR & FLAIR

	FLAIR	P-value	DIR	P-value
Overall	1.28 (1.1 - 1.5)	0.001	1.96 (1.66 - 2.39)	0.000
Intracanalicular segment	1.34 (1 - 1.82)	0.053	2.14 (1.56 - 3.27)	0.000
Intraocular segment	1.2 (0.86 - 1.67)	0.285	2.06 (1.55 - 2.91)	0.000
Optic chiasm	1.92 (1.12 - 4.38)	0.047	1.74 (1.16 - 3.22)	0.023
Prechiasmatic segment	1.37 (1.01 - 1.92)	0.051	1.98 (1.41 - 3.1)	0.000

Table 3: Table comparing the ROC of FLAIR & DIR for different optic nerve segments

	FLAIR	DIR	P-value
Overall	0.558 (0.512 - 0.605)	0.663 (0.628 - 0.699)	<0.001
Introrbital	0.538 (0.436 - 0.64)	0.716 (0.638 - 0.795)	<0.001
Intracanalicular	0.576 (0.478 - 0.673)	0.703 (0.634 - 0.773)	0.004
Optic chiasm	0.559 (0.504 - 0.615)	0.577 (0.523 - 0.631)	0.595
Prechiasmatic	0.572 (0.488 - 0.656)	0.667 (0.596 - 0.738)	0.0125

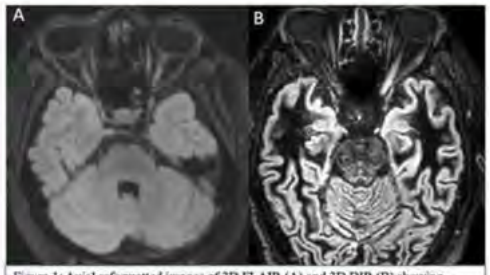

Figure 1: Axial reformatted images of 3D FLAIR (A) and 3D DIR (B) showing abnormal hyperintense signal of the left optic nerve in IO, IC segments on 3D DIR while 3D FLAIR appears to be normal.

(Filename: TCT_950_ONFLAIRDIR.jpg)

613

Comparison of diagnostic utility of coronal STIR and fat-suppressed 3D FLAIR on orbital MRI of acute and chronic optic neuritis

S Chang[1], M Labowsky[1], H Sharma[1], P Belani[1], M Schecht[1], M Kupersmith[1], B Delman[1]

[1]Icahn School of Medicine at Mount Sinai Hospital, New York, NY

Purpose

Coronal STIR is the standard of care for diagnosing optic neuritis (ON) on a noncontrast MRI. Fat-suppressed 3D-FLAIR (FS-FLAIR) may demonstrate similar or better diagnostic utility. We aim to compare STIR and FS-FLAIR in the detection of lesions in acute and chronic ON patients.

Materials and Methods

Orbital MRIs were retrospectively analyzed in 57 patients (females, 56%; mean years of age, 50.8 ± 16.7). Subjects consisted of 15 acute ON, 31 chronic ON, and 11 clinically normal cases. Image sets included paired coronal STIR and FS-FLAIR sequences and were randomly assessed by 2 blinded neuroradiologists for presence of lesion, lesion region of interest normalized to ipsilateral normal frontal white matter (ROI), and lesion length.

Results

Inter-rater reliability on presence of lesion was moderate (Cohen's $\kappa = 0.52$). On STIR, diagnostic accuracy for acute and chronic ON were 73-100% and 58-71%, respectively. On FS-FLAIR, diagnostic accuracy for acute and chronic ON were 87-100% and 48-71%, respectively. Diagnostic accuracy for chronic ON was lower than acute ON for one reader on STIR and both readers on FS-FLAIR ($p = 0.02$). Intraclass correlation coefficients (ICC) for ROI measurements were excellent (> 0.90) for acute and chronic ON. ICC for length measurements was poor for acute ON cases on FS-FLAIR (0.32; 95% CI, -1.02 to 0.78) but good to excellent (> 0.60) for acute and chronic ON cases on STIR and chronic ON cases on FS-FLAIR. Average ROI of acute and chronic ON lesions were higher than

clinically normal cases on STIR (p = 0.01 and < 0.01, respectively) and FS-FLAIR (p = 0.07 and 0.08, respectively). Nonsignificant trend for higher ROI was observed for both STIR and FS-FLAIR in acute ON cases compared to chronic ON cases.
Conclusions
FS-FLAIR demonstrated similar diagnostic utility to STIR for detecting ON lesions. Both methods exhibited decreased efficacy for chronic lesions. ROI methods appear useful for distinguishing affected optic nerves from normal white matter. Adoption of FS-FLAIR in clinical practice can be limited by inconsistency in measuring lesion characteristics, particularly lesion length.

1329

Comparison of Optic Nerve Sheath Diameter Measurements Using MRI Versus CT

F Ucisik[1], L Nunez-Rubiano[2], R Riascos[2], A Kamali[3]
[1]University of Texas Health Science Center at Houston, Houston, TX, [2]The University of Texas Health Science Center at Houston, Houston, TX, [3]University of Texas Health Science Center Houston, Houston, TX

Purpose
Optic nerve sheath dilation (ONSD) on magnetic resonance imaging (MRI) is a relatively sensitive imaging marker of intracranial hypertension. CT is generally the first-line imaging tool to evaluate for an acute intracranial pathology. Although, CT is commonly available before MRI in patients with symptoms of intracranial hypertension, its role in optic nerve sheath measurement has not been studied or established. In this study, we opted to see whether there is an agreement between CT and MRI for the measurement of optic nerve sheath diameter in patients with intracranial hypertension and healthy controls.
Materials and Methods
This is an IRP approved retrospective study. We studied 40 patients with confirmed diagnosis of idiopathic intracranial pressure (opening pressure > 25 cm of water) between the age of 20-40 years old. 40 age and sex matched patients with complaint of syncope were selected as healthy controls with documented normal cerebrospinal fluid (CSF) opening pressures. All patients had a head CT and brain MRI performed within few days. The diameter of the retrobulbar optic nerves were measured on T2 coronal planes of MRI brain and coronal CT sequences. The CT and MRI measurements were performed by a neuroradiology fellow and a research associate physician. Both were blinded to the measurements from one modality while performing the measurements for the other. The statistical analysis was performed by in-house statistician.
Results
The statistic analysis showed that using cut-off value of 6 mm for optic nerve sheath diameter, MRI is slightly more accurate than CT to diagnose IIH with sensitivity values of 78.8% (62.3%−89.3%) for MRI versus 66.7% (49.6%−80.3%) for CT (p-value of 0.25) and specificity values of 59.5% (43.5%−73.7%) for MRI versus 62.2% (46.1%−75.9%) for CT (p-value of 0.8). Although MRI was slightly more superior than CT, there was a good agreement between CT and MRI measurements for both study groups.
Conclusions
Although MRI appears to be slightly more accurate modality compared to CT in evaluation for ONSD, CT is more readily available and relatively accurate imaging modality to evaluate for ONSD, rendering it a favorable alternative to MRI.

Table 1. Accuracy of MRI and CT based on rater 1 (ONSD ≥ 6.0mm was used as criterion for IIH diagnosis)

Parameter	MRI	CT	P value
Sensitivity	79.4% (63.2% – 89.7%)	76.5% (60.0% – 87.6%)	0.76
Specificity	70.3% (54.2% – 82.5%)	48.7% (33.5% – 64.1%)	0.046

Estimates and 95% score confidence intervals are shown in the table. McNemar's test was used to compare sensitivities (and specificities) of MRI and CT.

Table 2. Accuracy of MRI and CT based on rater 2 (ONSD ≥ 6.0mm was used as criterion for IIH diagnosis)

Parameter	MRI	CT	P value
Sensitivity	78.8% (62.3% – 89.3%)	66.7% (49.6% – 80.3%)	0.25
Specificity	59.5% (43.5% – 73.7%)	62.2% (46.1% – 75.9%)	0.80

Estimates and 95% score confidence intervals are shown in the table. McNemar's test was used to compare sensitivities (and specificities) of MRI and CT.

Table 3. Inter-rater agreement (Cohen's kappa) for using MRI and CT (ONSD ≥ 5.5mm was used as criterion for IIH diagnosis)

Cohort	MRI	CT	P value
IIH	-0.053 (-0.138 – 0.033)	0.216 (-0.230 – 0.661)	0.24
Normal	0.446 (0.161 – 0.731)	0.377 (0.113 – 0.641)	0.70
Whole	0.426 (0.183 – 0.669)	0.376 (0.148 – 0.604)	0.74

Cohen's kappa statistic and 95% confidence interval are shown in the table. Wald test was performed to evaluate difference of kappa statistics of MRI and CT, where standard error of the difference was estimated by the bootstrap method.

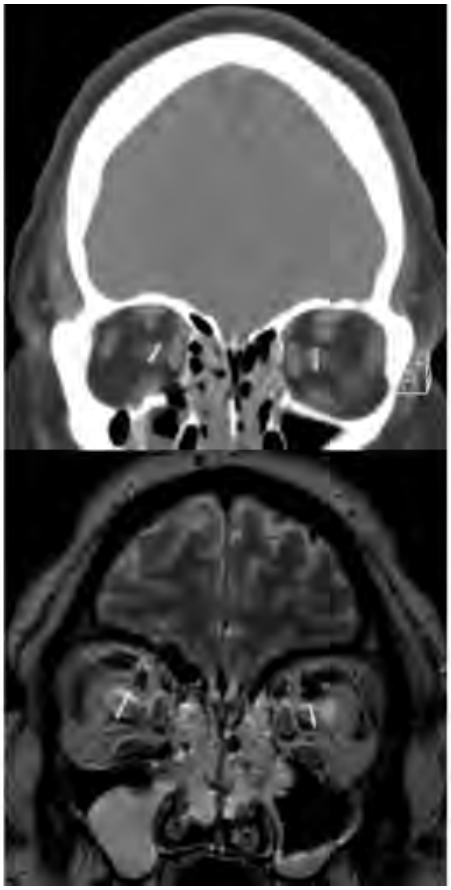

Figure 1. Measurement of the optic nerve sheath diameters on CT and MRI in a patient with IIH. The statistic analysis showed that MRI is slightly more accurate than CT for this purpose, however CT is a good screening tool by 6mm cut-off value

(Filename: TCT_1329_FIGURE.jpg)

910

MRI-Based Radiomics and Radiogenomics Classification of Genetic and Clinical Information in Skull Base Chordoma

S Zenkin[1], M Ak[1], Z Gersey[2], P Mamindla[3], V Peddagangireddy[1], E Wang[4], C Snyderman[4], P Gardner[2], G Zenonos[2], R Colen[1]

[1]Department of Radiology; University of Pittsburgh, Pittsburgh, PA, [2]Department of Neurological Surgery, University of Pittsburgh, Pittsburgh, PA, [3]Hillman Cancer Center; University of Pittsburgh Medical Center, Pittsburgh, PA, [4]Department of Otolaryngology, University of Pittsburgh, Pittsburgh, PA

Purpose

To classify genetic alterations and clinical outcomes in skull base chordoma by using radiomics imaging biomarker.

Materials and Methods

We studied radiomics signatures in a cohort of 252 primary and recurrent SBC pre-operative MRI scans. The lesions were segmented using 3D slicer to create a volume of interest for radiomics texture analysis from T1 post-contrast and T2 MRI sequences. We extracted 800 features from each volume of interest. Supervised analysis using training and testing method through eXtreme Gradient Boosting algorithm for classification and Least Absolute Shrinkage (LASSO) and Selection Operator regularization for feature selection was performed to identify radiomic signatures that differentiate groups of 9p21 and 1p36 deletions. Unsupervised analysis through consensus clustering techniques was performed to identify distinct groups based on radiomics texture features. The identified cluster groups were then correlated with progression free survival after surgery (PFSS), as well as the cell percentages with homozygous 9p21 deletions and 1p36 deletions on Fluorescent In Situ Hybridization.

Results

Supervised analysis resulted in a three-way classification radiomic model using 28 LASSO features and a two-way classification model using 18 lasso features to predict groups of 9p21 and 1p36 deletions, respectively. Three-way classification model for 9p21 deletions achieved accuracy of 75% with high sensitivity and specificity in 0-3 (82% and 78%, respectively), 4-24 (69% and 93%, respectively) and >25 (73% and 91%, respectively). Two-way classification model for 1p36 deletions differentiated between 0-15 and >15 groups with accuracy (76%), sensitivity (77%) and specificity (73%). Tumors were grouped into 4 radiomics-based clusters using unsupervised analysis. These clusters had distinct PFSS curves on Kaplan-Meier graphs (p-value < 0.0001), suggesting a strong association with clinical outcomes. In addition, significant differences were observed in the percentages of 1p36 (p-value <0.00072) and homozygous 9p21 deletions (p-value=0.026), suggesting a strong correlation with the tumor's genetic alterations.

Conclusions

This study presents MRI-based radiomics signatures that are strongly associated with clinical outcomes and genetic markers

commonly used to guide clinical decision-making in SBC. Radiomics based imaging biomarkers may prove to be a non-invasive, cost and time-effective means of pre-operative individualization of care for patients with SBC.

999

Optic chiasm morphometry in radiologically isolated syndrome

F Zaccagna[1], S Suthiphosuwan[1], M Guenette[2], J Glaister[2], J Oh[2], T Massoud[3], A Bharatha[1]

[1]Division of Neuroradiology, University of Toronto and St. Michael's Hospital, Toronto, Ontario, [2]Division of Neurology, University of Toronto and St. Michael's Hospital, Toronto, Ontario, [3]Division of Neuroimaging and Neurointervention, Stanford University School of Medicine, Stanford, CA

Purpose

Radiologically isolated syndrome (RIS) is associated with an increased risk of progression to multiple sclerosis (MS)1. There is no consensus on how to manage RIS, and a reliable predictive imaging biomarker would be useful. The optic pathway is atrophied in MS2, and retinal neuroaxonal degeneration correlates with brain atrophy, disease activity, and prognosis in RIS3,4. Thus, we studied optic pathway morphometry and degeneration in RIS to establish potentially useful quantifiable structural MRI prognostic biomarker, which may have clinical utility in treatment decision-making.

Materials and Methods

In a subgroup analysis of a prospective cohort study of RIS5, 22 RIS subjects (37±10yr) were age-matched with 22 healthy volunteers (HVs). A neuroradiologist blinded to clinical data performed morphometric analysis of the optic chiasm (OC), intracranial segment of the optic nerves (ONs) and proximal optic tracts (OTs) using Horos (horosproject.org) on 3T MRI 3D isotropic T1W MPRAGE images, as described previously2 (fig.1). We measured the Evans' index (EI) on axial T2W FLAIR images to assess for brain atrophy. For statistical evaluation we used Matlab, unpaired sample t test and the Mann-Whitney test, according to data distribution. P<0.05 indicated a statistically significant difference, which was corrected for multiple comparisons using the Benjamini-Hochberg correction.

Results

Clinical characteristics and morphometrics are shown in table 1. One RIS subject was excluded (EI>0.3). The antero-posterior (AP) diameter and the height of the OC were significantly smaller in the RIS group vs. HVs (p<0.005 and p=0.003, respectively). The OC volume was smaller in the RIS group, but not significant after correction (p = 0.03). After correction, there were no significant differences in ON diameters (right p=0.02, left p=0.06). The right OT was significantly smaller in the RIS group (p=0.006); but no significant difference was found for the left OT (p=0.13).

Conclusions

Optic chiasm AP diameter, OC height and the right proximal OT tract are significantly smaller in RIS patients compared to age-matched controls, confirming white matter tract atrophy in RIS. The OC AP diameter may be a convenient predictive imaging biomarker to measure on MR images that may have clinical utility with respect to treatment initiation. In ongoing and future longitudinal studies, we will validate the potential utility of the OC AP diameter as a prognostic biomarker of conversion to MS in subjects with RIS.

Table

	Radiologically isolated syndrome (n=21)	Healthy volunteers (n=22)	p value
Age	36.8 ± 9.6 yrs (95% CI 32.7-40.9)	36.5 ± 9.5 yrs (95% CI 32.6 – 40.5)	0.54
Evans' index	0.26 ± 0.02 (95% CI 0.25-0.27)	0.25 ± 0.02 (95% CI 0.25–0.26)	0.53
Optic chiasm morphometrics			
Width	12.1 ± 1.7 mm (95% CI 11.4-12.9)	12.2 ± 1.2 mm (95% CI 11.6-12.7)	0.72
AP diameter	4.1 ± 0.5 mm (95% CI 3.9-4.3)	4.9 ± 0.8 mm (95% CI 4.54-5.21)	< 0.005 *
Height	2.1 ± 0.3 mm (95% CI 2-2.2)	2.4 ± 0.3 mm (95% CI 2.2-2.5)	0.003 *
OC volume	132 ± 12.7 mm³ (95% CI 127-138)	144 ± 17.8 mm³ (95% CI 136-151)	0.03 ~
Intracranial segment of the optic nerves			
Diameter - right	3.5 ± 0.5 mm (95% CI 3.2-3.7)	3.9 ± 0.5 mm (95% CI 3.7-4.0)	0.02 ~
Diameter - left	3.6 ± 0.5 mm (95% CI 3.4-3.8)	3.9 ± 0.5 mm (95% CI 3.7-4.1)	0.06
Angle between the ONs	74.3° ± 7.5° (95% CI 71.1-77.5)	69.6° ± 7.8° (95% CI 66.4-72.9)	0.07
Optic tracts			
Proximal OT - right	3.1 ± 0.3 mm (95% CI 2.9-3.2)	3.5 ± 0.4 mm (95% CI 3.3-3.6)	0.006 *
Proximal OT - left	3.2 ± 0.4 mm (95% CI 3.1-3.4)	3.5 ± 0.3 mm (95% CI 3.3-3.6)	0.13
Angle between the OTs	70.9° ± 9.3° (95% CI 66.9-74.8)	72.2° ± 10.4° (95% CI 67.9-76.5)	0.61

Table 1: the table shows clinical characteristics and morphometrics for the radiologically isolated syndrome group and the age matched healthy volunteers' group. Normality of data distribution was tested using the Shapiro–Wilk test. Continuous values are shown as mean ± standard (95% confidence interval (CI)). Clinical data were compared using unpaired sample t test. Differences in the morphometric data between the two study groups were explored using a Mann–Whitney test for independent samples. A *p* value < 0.05 was chosen to indicate of a statistically significant difference and corrected for multiple comparisons by using the Benjamini-Hochberg correction with a False Discovery Rate of 5%25. Raw p values are shown, and significance is based on Benjamini-Hochberg correction.
* Statistically significant difference after correction. ~ Not statistically significant difference after correction.

Figure

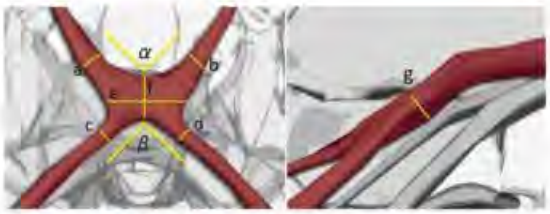

Figure 1: Schematic diagram showing axial and sagittal depiction of the OC, distal parts of ONs, and proximal parts of OTs. The diameters of the ONs (a and b) were measured 2 mm anterior of the ventral margin of the OC, perpendicular to the long axis of the nerve. The diameters of the proximal parts of OTs (c and d) were measured 2 mm posterior to the dorsal border of the OC, perpendicular to the long axis of the tracts. The width of the OC was measured at its narrowest part (e), and similarly for the AP diameter (f). The angles between both ONs and both OTs (α and β, respectively) were measured by drawing lines through the middle of the nerves or tracts and taking the angle at the crossing point of these two lines. The OC height (g) was measured perpendicular to the long axis on the sagittal plane images.
Adapted from ref. 2.

(Filename: TCT_999_OCRIS_FZ_ASNR.jpg)

437

Postoperative Temporalis Muscle Findings and the Mayfield Skull Clamp: A Potential Pitfall in Surveillance Imaging of the Head

B Budigi[1], K Hiatt[2], M Benayoun[3], J Sachs[4], P Bunch[3]

[1]Wake Forest Baptist medical center, Winston Salem, NC, [2]Wake Forest Baptist Medical Center, Winston Salem, NC, [3]Wake Forest School of Medicine, Winston-Salem, NC, [4]Wake Forest School of Medicine, Winston Salem, NC

Purpose

Recognized complications of the Mayfield skull clamp include skull fracture, epidural hematoma, and air embolism (1). Following surgery using the Mayfield skull clamp, we have observed temporalis muscle signal abnormality and enhancement initially interpreted as extracranial metastasis (Figure) that subsequently spontaneously resolved. We hypothesize that these findings are attributable to Mayfield skull clamp pin insertion. Our purposes are to evaluate temporalis muscle findings occurring after use of the Mayfield skull clamp and to increase radiologist awareness of this previously undescribed interpretation pitfall.

Materials and Methods

Patients undergoing craniotomy for brain tumor between February 2018 and September 2019 were retrospectively reviewed. The following inclusion criteria were applied: 1) Mayfield skull clamp used and 2) pre- and at least 1 post-operative brain MRI performed. Patient demographics and operative details were collected from the electronic health record. Pre- and post-operative brain MR examinations were reviewed by a second-year neuroradiology fellow for the presence of temporalis muscle findings (e.g., T2/FLAIR hyperintensity, gadolinium enhancement) potentially corresponding to pin insertion sites (i.e., separable from the craniotomy site). Mean, standard deviation (SD), and range are reported for continuous variables. Proportions were compared by Fisher exact test, and continuous variables were compared by Student t-test.

Results

A total of 49 patients (26 male, 23 female, mean age 62 years) formed the study cohort. The most common locations of resected tumors were the frontal (n=23), temporal (n=9), and parietal (n=6) lobes. Mean operation duration was 204 minutes (SD 47; range 108-324). Temporalis muscle signal abnormality was present on pre-operative brain MR in zero patients and on immediate post-operative brain MR in 19/49 (39%) patients, more commonly bilateral (13/19; 68%) than unilateral (6/19; 32%). Among 12 patients with temporalis muscle signal abnormality and multiple available post-operative brain MRs, the temporalis muscle findings resolved at a mean of 3.3 months (SD 1.0, range 1-5). There was no significant association between the presence of temporalis muscle findings and sex (p=1.00), age (p=0.95), or operation duration (p=0.69).

Conclusions

Temporalis muscle abnormalities are identifiable on brain MR following Mayfield skull clamp-aided craniotomy in 39% of patients and should not be mistaken for soft tissue metastasis.

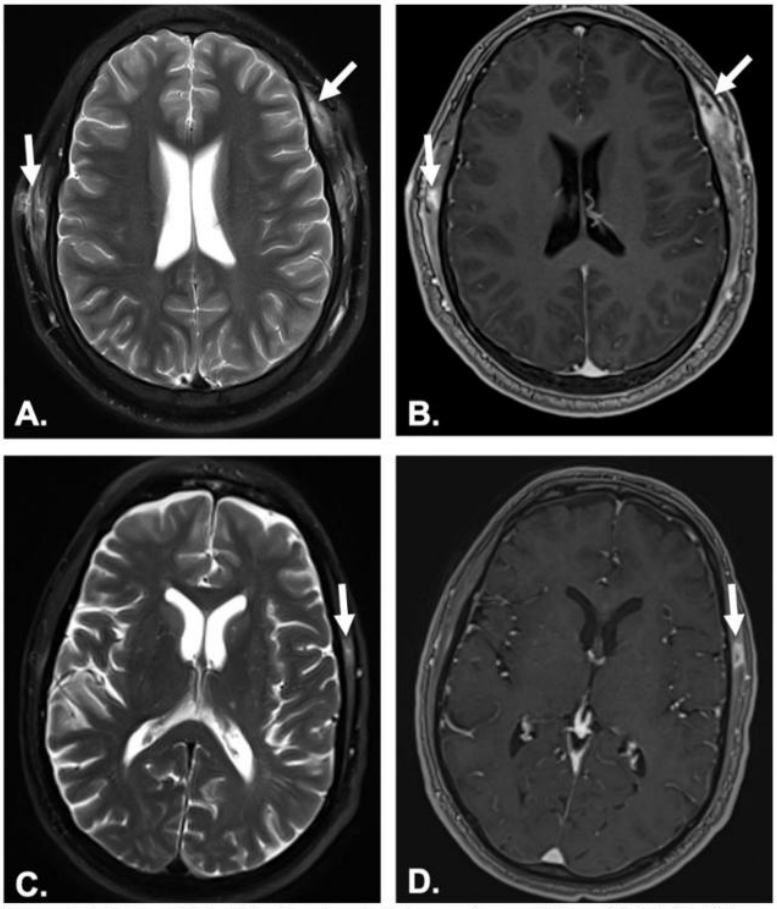

Figure: Axial T2-weighted (A, C) and gadolinium-enhanced T1-weighted (B, D) images obtained in 2 different patients following recent surgery demonstrate T2-hyperintense, enhancing temporalis muscle abnormalities (arrows, A-D) initially interpreted as suspicious for metastasis but which spontaneously resolved on follow-up imaging. Patient 1 (A and B) recently underwent suboccipital craniotomy, and Patient 2 (C, D) recently underwent cervical laminectomy, both for tumor resection and both aided by the Mayfield skull clamp.

(Filename: TCT_437_Capture300.JPG)

1077

Radiomic Analysis For Differentiating Cystic and Cystic-appearing Jaw Lesions

L Acosta Barrios[1], M Gomez Alonso[2], D Calvo Gijón[3], D Roman Moya[4], B Asenjo Garcia[5], A Pérez-Lara[6], J Pérez-Lara[7], E Briceño[8], J Martínez Barbero[9]

[1]Hospital Regional Universitario de Malaga, Malaga, Malaga, [2]Hospital regional universitario de Malaga, Malaga, Malaga, [3]Hospital Virgen de Valme, Sevilla, Sevilla, [4]Hospital Regional universitario de Malaga, Malaga, Malaga, [5]Hospital Regional Universitario de Málaga, MALAGA, Malaga, [6]Hospital Regional Universitario de Málaga, Málaga, Malaga, [7]Universidad de Málaga, Málaga, Málaga, [8]Hospital Regional Universitario de Málaga, Málaga, Málaga, [9]Hospital Virgen de las Nieves, Granada, Granada

Purpose

There are multiple cystic and cystic-appearing lesions that involve the jaw. An accurate diagnosis of these lesions using different imaging modalities is essential to determine the therapeutic approach. However, these entities may share different radiological features which makes their diagnosis particularly challenging. The aim of this study is to evaluate the utility of radiomic analysis in the differentiation of the most common cyst and cystic-like tumoral lesions of the jaw (ameloblastoma, dentigerous cyst, periapical cyst and odontogenic keratocyst).

Materials and Methods

We performed a retrospective study by selecting 15 patients with ameloblastoma, 15 with dentigerous cyst, 15 with periapical cyst, and 15 with odontogenic keratocyst. All patients underwent a CT scan of the jaw without contrast injection prior to surgical treatment, and had a histological confirmation of the lesion. Radiomic analysis was performed using 3D Slicer. The whole lesion was segmented by a radiology resident and supervised by a neuroradiologist with specific training in head and neck radiology. The radiomic data (first and second order features) were extracted from each case. Subsequently, an algorithm with Machine Learning methods was created to predict the histology of each lesion based on the data obtained.

Results
Cystic-appearing tumoral lesions of the jaw demonstrate a complex structure, with high entropy values and high variability of attenuation data and extreme values of kurtosis and skewness. The periapical and dentigerous cyst demonstrated more homogeneous characteristics in the radiomic analysis, which can be helpful for their detection.
Conclusions
Radiomic analysis may be a useful tool to facilitate the differentiation between cystic jaw lesions and tumoral lesions with cystic appearance, improving the diagnostic approach and the therapeutic management of these patients.

Monday, May 16, 2022
5:15-6:15 PM
Scientific Podium Presentations: MRI

886

Body Mass Index is Associated with Hippocampal Subfield Volume in Autosomal Dominant Alzheimer Disease

F Rahmani[1], D Hobbs[2], N McKay[1], C Chen[3], N Joseph-Mathurin[2], R Hornbeck[2], S Flores[2], S Keefe[1], T Benzinger[1], C Raji[4]
[1]Washington University in St.louis, Saint Louis, MO, [2]Washington University in St.louis, saintlouis, MO, [3]Washington University in St. Louis, St. Louis, MO, [4]Mallinckrodt Institute of Radiology Washington University in St. Louis, ST LOUIS, MO

Purpose
Increased body mass index (BMI) is associated with hippocampal atrophy (1). Hippocampal atrophy begins up to 8 years prior to the average age of symptom onset in autosomal dominant Alzheimer disease (ADAD) (2). We investigated the association of body mass index (BMI) and hippocampal subfield volume in young adults with a family history of ADAD.
Materials and Methods
We studied 111 cognitively normal participants with a family history of ADAD from the Dominantly Inherited Alzheimer Network (DIAN) cohort in a cross-sectional study at their baseline visit. Participants were between -15 to -5 estimated years to symptom onset (EYO) including 59 mutation carriers, 44 men/67 women (BMI of 27.3±5.8 kg/m2 & age of 37.7±6.8 years). The FreeSurfer v6.0. hippocampal subfield segmentation was used to obtain hippocampal subfield volumes for CA1, CA2/3, CA4/DG, and subiculum, which were then normalized to the total intracranial volume. Linear mixed models were used to investigate the association of hippocampal subfield volume and the interaction of EYO and mutation status with BMI.
Results
Neither mutation status nor EYO were independently associated with hippocampal subfield volume (Figure 1.a and 1.b). The interaction between EYO and mutation carrier status was associated with a significant decrease in the volume of parasubiculum and the granule cell and molecular layers of the dentate gyrus (GC-ML-DG) (corrected P <0 .001 for all models) (Figure 1.c and 1.d). Increased BMI was associated with larger volume in the hippocampal tail (β(CI95%):7.2(2.6-11.9)), body (β(CI95%):9.8(1.7-18.1)), parasubiculum ((β(CI95%):0.87(0.28-1.47)), the CA4 part of the body ((β(CI95%):1.05(0.13-1.47)), and the GC-ML-DG ((β(CI95%):1.3(0.33-2.3)) (corrected P <0 .001 for all models)). The positive association between subfield volume and BMI persisted in the parasubiculum and GC-ML-DG regions even after controlling for the interaction between mutation status and EYO, as well as the random effect at subject and family level (subfield volume ~ BMI + EYO*mutation + random=list(~1 | subject, ~1 | family)) (Figure 1.e and 1.f).
Conclusions
We observed a positive association between BMI and the volume of the parasubiculum and the dentate gyrus independent of mutation status and Alzheimer disease stage in individuals with a family history of ADAD. This contrasts with existing literature suggesting an inverse association of BMI and hippocampal volume (3), and could suggest a transient compensatory phase in the ADAD population.

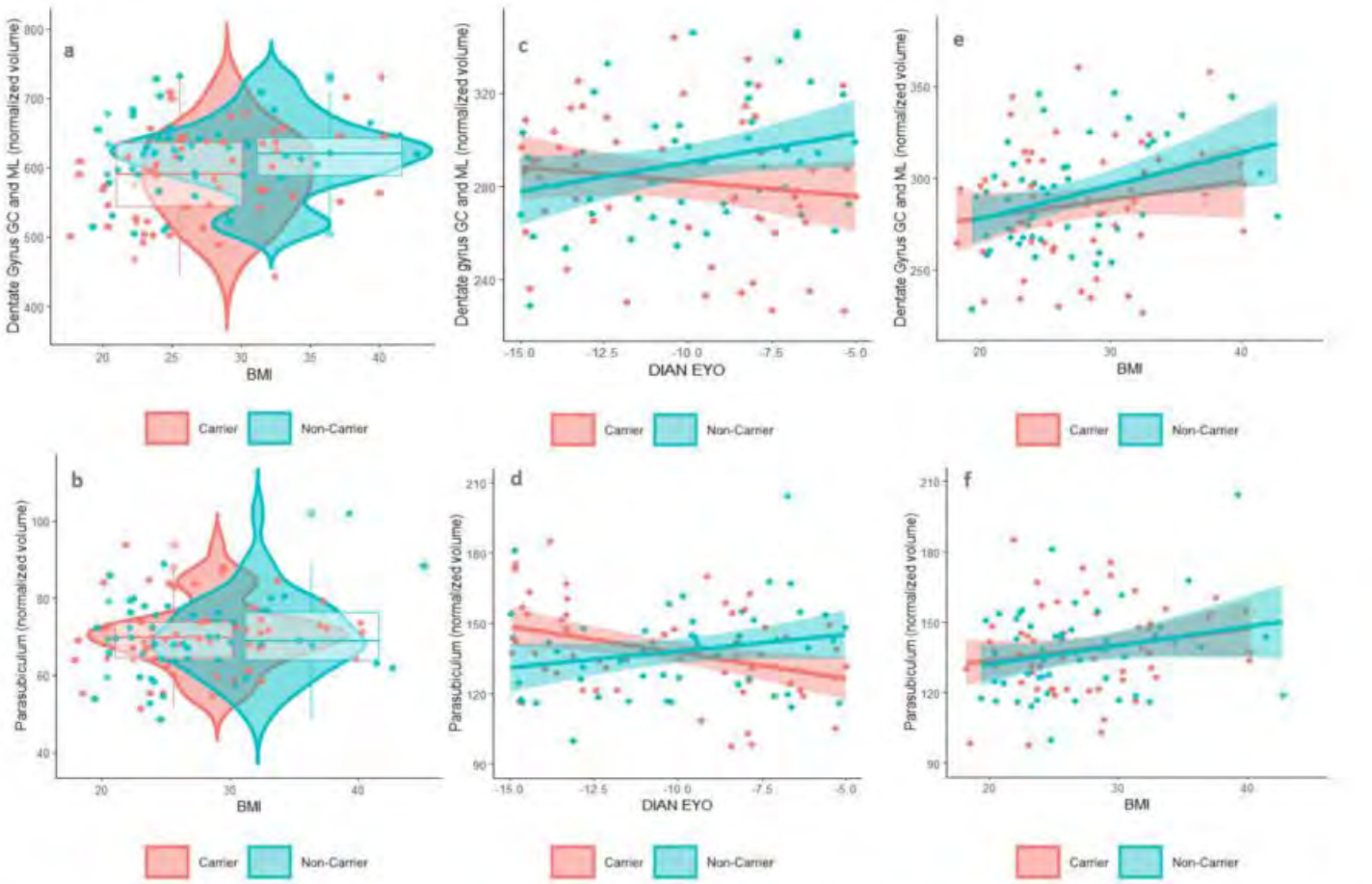

Figure 1. Summary of models for the parasubiculum and the granular cell and molecular layers of the dentate gyrus subfields of the hippocampus. a-b: Mutation carrier and non-carrier participants in the DIAN cohort are not different in their BMI or subfields volume. c-d mutation carriers demonstrate a steeper decline in subfields volume compared to non-carriers. e-f BMI is paradoxically associated with larger subfields volume, an association that is unaffected by mutation or pre-clinical ADAD status.
** BMI: body-mass index; ADAD: autosomal-dominant Alzheimer disease*

(Filename: TCT_886_Fig1_diana.jpg)

514

Comparison of image quality and detection of contrast-enhancing intra-and extra-cranial lesions between MPRAGE and CS-VIBE accelerates MRI techniques.

Y Yim[1]
[1]*Chung Ang University Hospital, Seoul, Korea, Republic of*

Purpose
To compare the diagnostic performance of post-contrast 3D compressed-sensing volume-interpolated breath-hold examination (CS-VIBE) and 3D T1 magnetization-prepared rapid-acquisition gradient-echo (MPRAGE) in detecting enhancing intra- and extra-cranial lesions. We also examined and compared image quality between both sequences.
Materials and Methods
Between January 2020 and June 2021, 347 patients who underwent contrast-enhanced brain MRI using ProHance, 0.2ml/kg to evaluate intracranial lesion with both conventional MPRAGE and CS-VIBE (scan time: 5 minutes 48 seconds vs. 2 minutes 44 seconds) were included in this retrospective study. All images were independently reviewed by two radiologists for the presence of enhancing intra- and extra-cranial lesions. Signal-to-noise ratio (SNR) of the pons, both centrum semiovale, cerebellum, temporal lobe was compared between two sequences. In patients with intracranial enhancing lesions, enhancement degree and contrast-to-noise ratio (CNR parenchyma-enhancing lesion) of the lesion were measured. For qualitative analysis, overall SNR, image quality, white-gray matter discrimination and enhancing lesion conspicuity were analyzed.
Results
In qualitative analysis, SNR and enhancing lesion conspicuity, overall image quality, artifact and gray-white matter differentiation showed moderate to excellent agreement between MPRAGE and CS-VIBE (k=0.75 – 0.97) in two observations. Both MPRAGE and

CS-VIBE equally detected enhancing lesions. Total 66 patients had enhancing lesions and CNR (27.41 ± 27.1 vs. 25.78 ± 18.4) and contrast rate of MPRAGE (85.6 ± 117.6 vs. 77.9± 63.8) showed significantly higher than that of CS-VIBE. Overall SNR of temporal region, centrum semiovale, pons showed significantly higher while both cerebellum showed lower in MPRAGE. Overall, MPRAGE showed more best image quality than that of CS-VIBE (30.4% vs. 26.7%), but CS-VIBE showed less blurred images than that of MPRAGE (15.0% vs. 20.4%).
Conclusions
CS-VIBE postcontrast technique achieved comparable image quality and visualization compared to the conventional MPRAGE, with the scan time being half of that of MPRAGE.

1443

Explainability Through Architecture Design - a Multi-path Branched Deep Learning Network with Explainability for Brain MRI Dose Reduction

S Pasumarthi[1], B Duffy[2], E Gong[3], G Zaharchuk[4], K Datta[1]
[1]Subtle Medical, Menlo Park, CA, [2]Subtle Medical Inc., menlo park, CA, [3]Subtle Medical Inc., Menlo Park, CA, [4]Stanford University, Stanford, CA

Purpose
Deep learning (DL) has been used to derive intrinsic contrast information from non-contrast images to reduce[1,2] or eliminate[4] gadolinium contrast dose in brain MRI. But these are black-box models that lack explainability and interpretability - a limitation to widespread clinical adoption. Explainable AI systems are desired or fair and trustable clinical decision making and prognosis. We propose an explainable DL model for brain MRI contrast dose reduction.
Materials and Methods
With IRB approval and informed consent, 185 patient scans were obtained where each patient underwent three pre-contrast scans: T2-w, FLAIR and T1-w. This was followed by two post-contrast scans: 10% of standard dose (0.01mmol/kg) and with remaining 90% dose. The first four images were used as model input to predict the T1-w full-dose post-contrast image. Train/validation split was 150/35 patient scans. An unsupervised anomaly detection (UAD) scheme was used as described in[3], to make the model pay more attention to hyper-intense anomalies found in FLAIR images. The DL architecture design is shown in FigA. Each branch is processed by a UNet-like encoder-decoder structure to extract features and produce "synthesized pseudo T1Gd images" - images with enhancement derived from the respective inputs in the branch. The corresponding branch outputs are then combined through a convolution layer and boosted again to produce the final synthesis. The DL model was trained with a combination of L1+SSIM+VGG-19 losses. The L1-loss was weighted with the UAD mask as an anomaly-aware attention mechanism.
Results
FigB depicts the explainable nature of the model for a patient with glioblastoma. FLAIR has the maximum contribution to the enhancement in the GBM ring in the synthesized post-Gad image. These kinds of supporting explanatory information can be used in assessing the kind of tumor, stage and the rate of progression. Several studies[4] have evaluated the importance of different input contrasts in synthesizing post-gad images; but the relative weightage is calculated over an entire dataset. In contrast, the proposed DL model can provide a case-by-case assessment of the contribution of each multi-contrast input.
Conclusions
We have demonstrated the feasibility of using an explainable DL model for contrast dose reduction in brain MRI. The unique explainability aspect is by virtue of the architecture design and has broader scope and potential in various clinical applications.

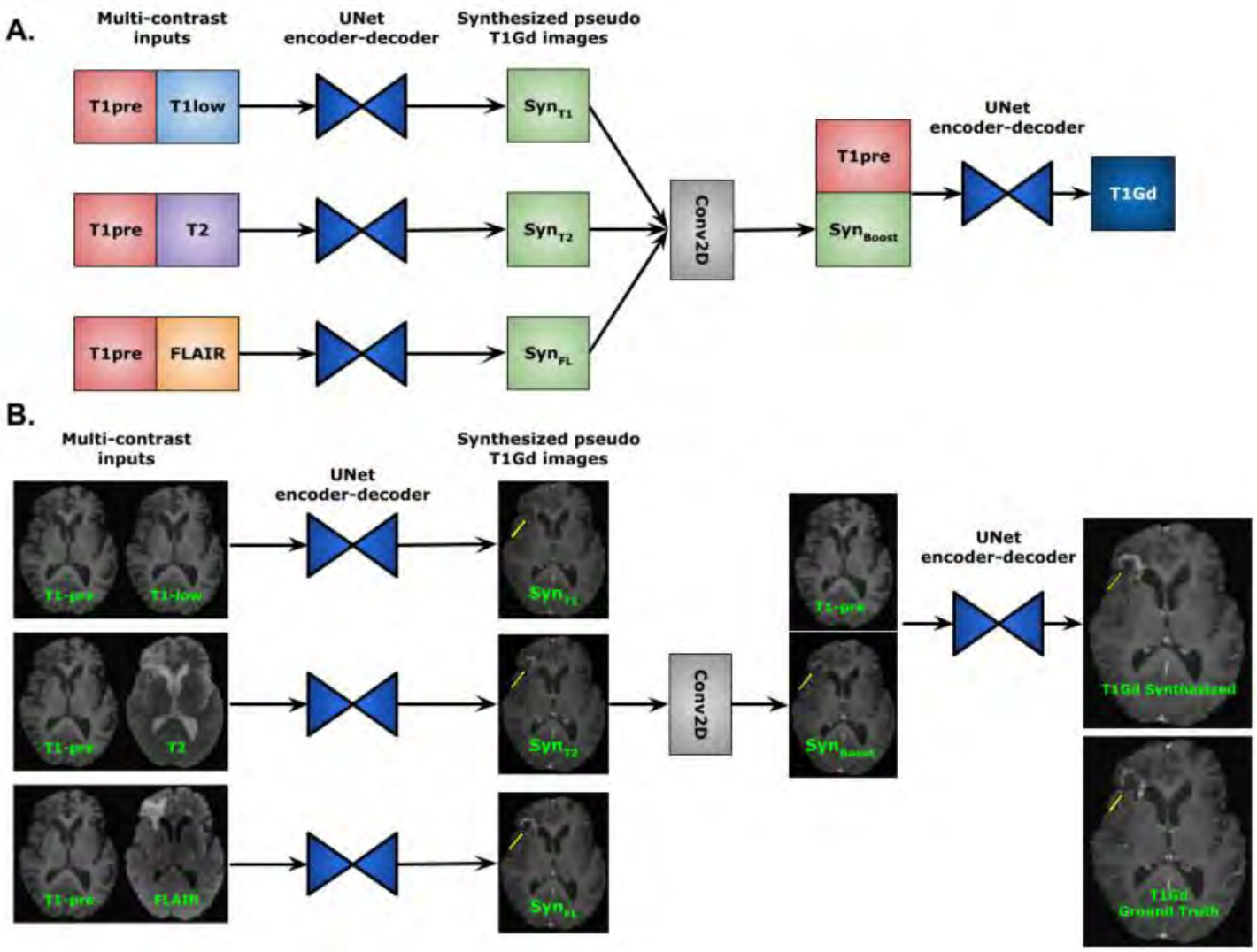

(Filename: TCT_1443_Figure_MC.jpg)

1514

Fast and Accurate Brain MRI Affine Registration Using Unsupervised Deep Learning

S Pasumarthi[1], B Duffy[2], K Datta[1]

[1]Subtle Medical, Menlo Park, CA, [2]Subtle Medical Inc., menlo park, CA

Purpose

Registration of inter/intra-patient multimodal MRI images is a crucial step in analysis tasks such as segmentation, mapping structural changes and quantifying clinically relevant parameters such as cortical thickness. Existing software solutions for image registration[1] based on iterative optimization, are slow - a bottleneck to existing analysis pipelines. We propose a deep learning (DL) model for fast and accurate affine registration.

Materials and Methods

The proposed work is based on an existing framework for deformable registration [5]. We used the pre-registered BRATS 2021 dataset[2] consisting of 1251 cases with T1, T1-CE, T2 & FLAIR images plus the tumor segmentation masks. The train/validation split was 1126/125. FigA shows the training pair generation scheme where the target image was subject to random affine transformations. FigB shows the network architecture and the training scheme based on the architecture from [3]. The spatial transformer layer is from [4]. Four models were trained with T1 vs T1-CE input pairs and MSE, normalized cross-correlation (NCC), normalized mutual information (NMI) & NCC+NMI as loss functions. The same scheme was extended to train a model to register T2 & FLAIR images with T1 as the template. The model was quantitatively evaluated on (1) MSE between DL predicted affine matrix and inverse of simulated affine matrix, (2) SSIM & PSNR between predicted image and pre-registered BRATS image, (3) tumor segmentation mask before and after registration.

Results

The MSE, SSIM, PSNR (dB) and Dice scores before (after) registration for the best model respectively are: 0.00030, 0.971(0.873), 39.631(31.683), 0.940(0.595). When compared to SimpleElastix [1] (with default settings) which took 24 secs for registering a 128x256x256 volume, the proposed model clocked ~0.8 secs. FigD shows sample qualitative results of multimodal registration.

Conclusions

Here, we have demonstrated that DL algorithms can be used for fast and accurate affine registration of multi-modal brain MRI images which can also be extended for registering cross modal (PET/CT, PET/MR, MR/CT) image volumes.

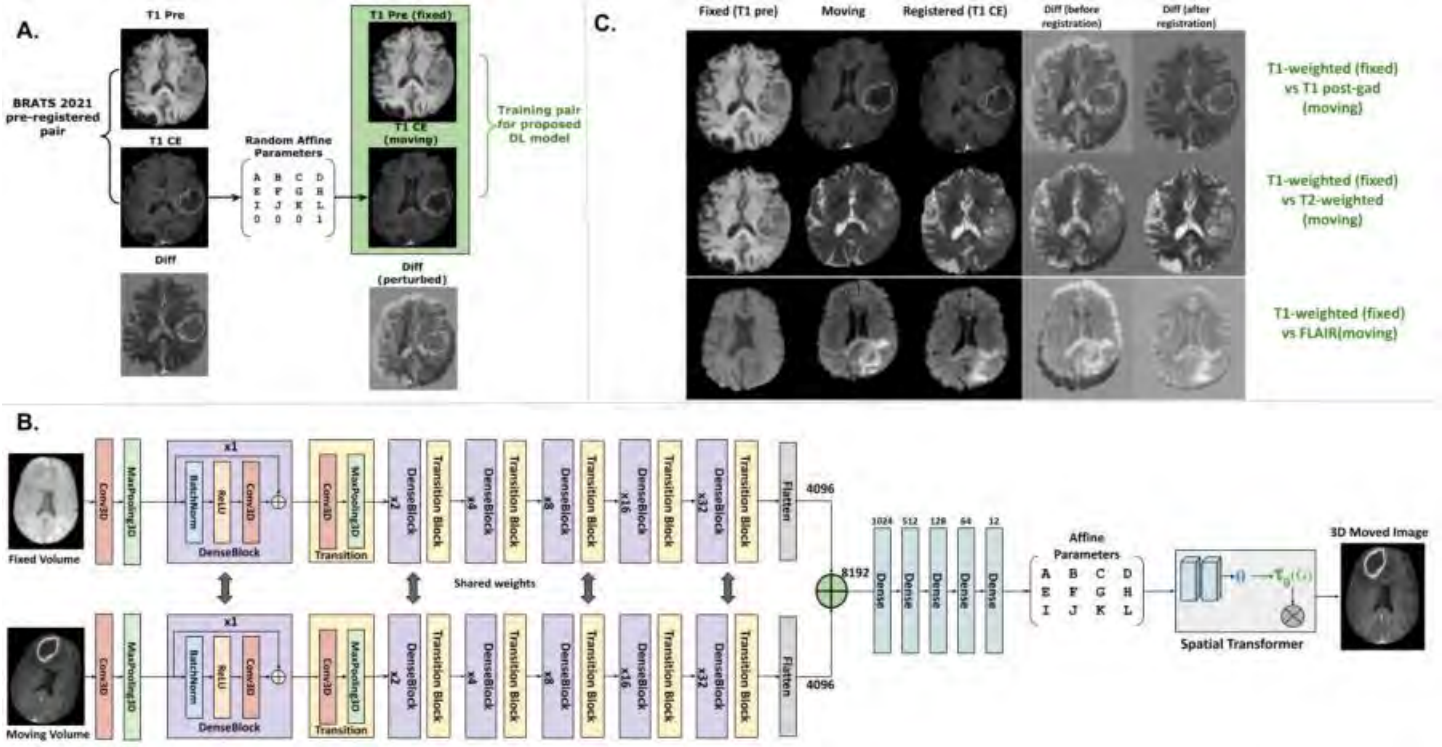

(Filename: TCT_1514_Figure_Vmorph.jpg)

304

Image discretization of quantitative multi-compartment diffusion MRI

V Jain[1], A Singh[1], J Yu[1]

[1]*University of Wisconsin School of Medicine and Public Health, Madison, WI*

Purpose

Multi-compartment diffusion weighted imaging (MC-DWI) techniques such as neurite orientation dispersion and density imaging (NODDI) have been used to gain insight into brain microstructure. However, while MC-DWI techniques like NODDI are sensitive to disease pathology, there is non-specificity to changes in underlying neurobiology (1). A radiomics-based approach incorporating texture analyses of NODDI images could potentially add specificity to capture these changes. As radiomic studies of NODDI have not been performed before, the parameters used for radiomic extraction must first be defined. One such parameter is image discretization, which converts original pixel intensities into a series of bins used for texture feature calculations. This project seeks to test and identify viable image discretization parameters for NODDI using a well-characterized and validated murine model of microglial depletion (1).

Materials and Methods

12-week-old C57BL/6J male mice (n=12) were randomly assigned to CSF1R-inhibited (microglia depleted) and control groups, with treatment conditions administered for 8 days and euthanization 1 day thereafter. Ex vivo imaging, preprocessing, segmentation and parameter calculations were then performed. Texture features were extracted using Pyradiomics to yield 792 features across original and 8 wavelet-transformed groups (2). 8 fixed bin widths were tested, ranging from 0.01 to 25. Statistically significant differences in texture features between control and microglia-depleted animals were identified using Student's t-tests followed by multiple testing correction (FDR $p<0.05$) with Python SciPy, NumPy, and Pandas libraries.

Results

It was observed for NODDI parameters of ODI and NDI that bin widths of 1 or greater yielded a similar and an unvarying number of significant features, suggestive of low sensitivity to neuropathology at these bin widths. The number of significantly different texture features notably spiked at a bin width of 0.1, where a total of 443 ODI and 248 NDI significant features were identified. At smaller tested bin widths, no significant trends were apparent, thus suggestive of signal noise.

Conclusions

This project is the first to test and characterize the effect of image discretization on texture analyses of NODDI data. By extracting radiomic features across multiple bin widths, a specific fixed bin width (0.1) was identified as a leading candidate parameter setting for texture analyses of NODDI imaging data.

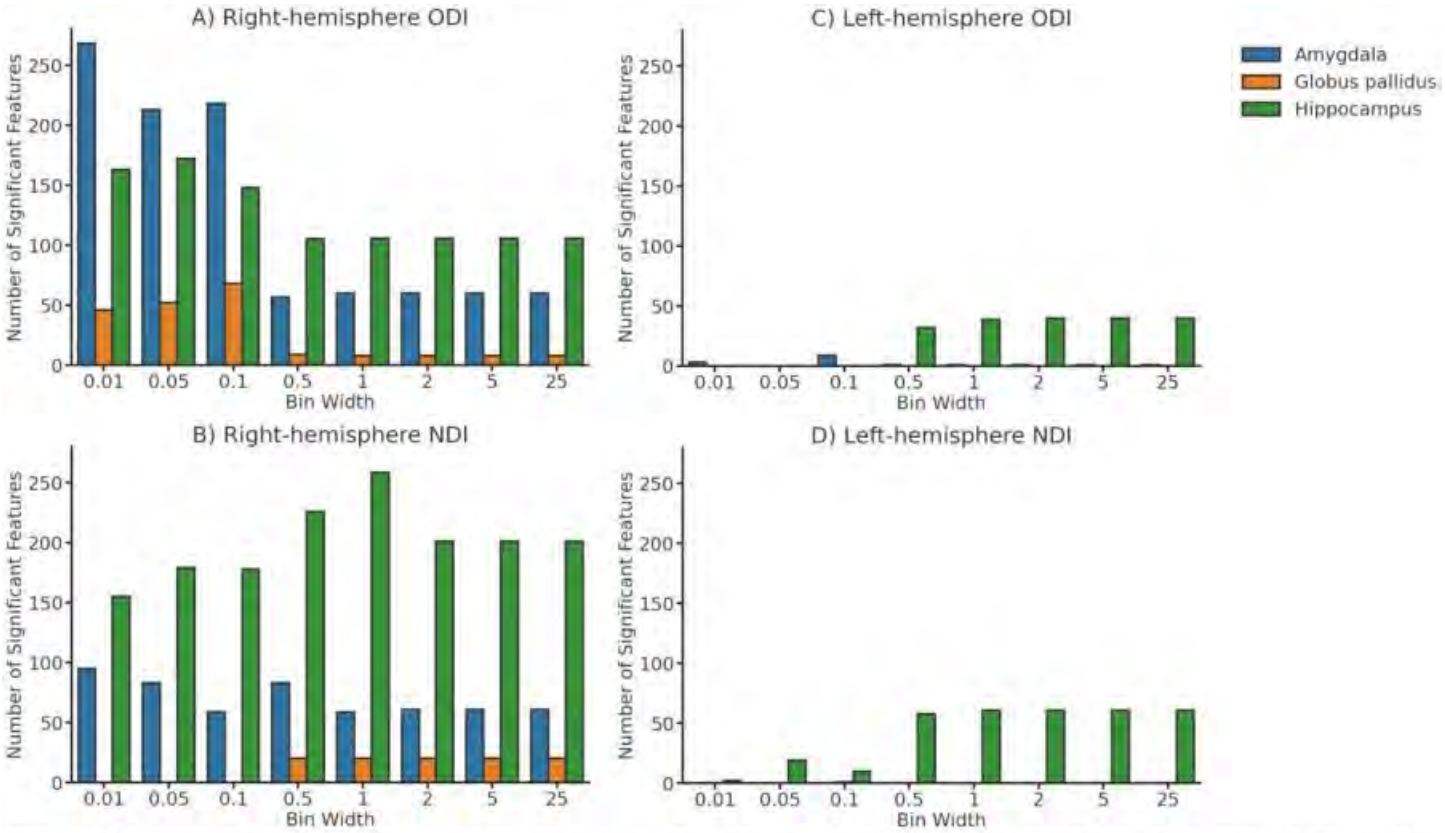

Figure 1: Number of significant features (experimental versus control) for right and left hemisphere ROIs across 8 bin widths ranging from 0.01 to 25 following Student's *t*-test and multiple comparisons correction for ODI and NDI ($p < 0.05$).

(Filename: TCT_304_Figure1.jpg)

597

K-space Based Deep Learning Reconstruction Empowers 60-70% Acceleration of MR Imaging of the Spine

L Tanenbaum[1], S Bash[2], M Thomas[3], R Lebel[4], M Fung[5]

[1]RadNet, New York, NY, [2]RadNet, Woodland Hills, CA, [3]GE, Hillsborough, NJ, [4]GE Healthcare, Calgary, Alberta, [5]GE Healthcare, Waukesha, NJ

Purpose

This prospective, multireader study evaluates the impact on perceived image quality of highly scan-time reduced cervical (72%) and lumbar (64%) spine MRI reconstructed with deep learning (DL).

Materials and Methods

With IRB approval and patient consent, 26 consecutive patients underwent standard-of-care (SOC) and accelerated (FAST) spine MRI exams acquired from a GE 3T Architect scanner. DL processing of the FAST scan data set (FAST-DL) was performed using an FDA-cleared CNN based, DL image enhancement product - Air Recon DLTM. The k-space based tool offers powerful denoising, sharpness enhancement and elimination of some artifacts such as truncation ringing. Two neuroradiologists were presented were presented with the different image series as paired side-by-side datasets. Datasets were blinded and randomized in sequence and left-right display order. Image features were preference rated on a 5-point Likert scale.

Results

FAST-DL was qualitatively better than SOC and FAST for perceived signal-to-noise ratio (SNR) sharpness and artifacts. Inter-rater agreement was high and no image aberrations were detected.

Conclusions

DL enables 64-72% spine MRI scan time reduction as well as what radiologists perceive as enhanced image quality with benefits in SNR, image sharpness and artifact reduction over SOC and FAST images without DL processing, providing gains in efficiency and portending practice utility for routine use.

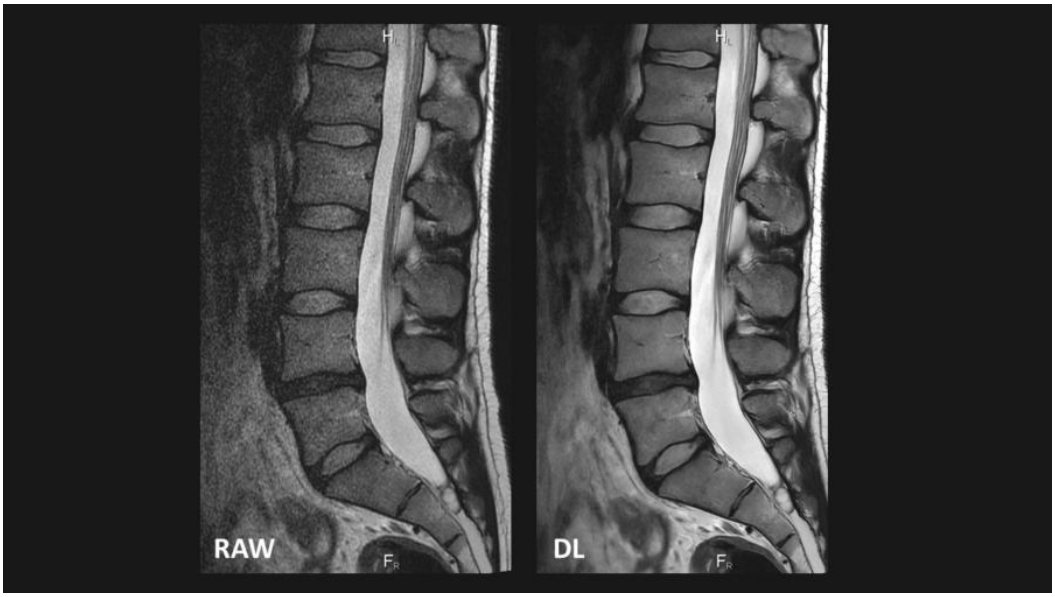

(Filename: TCT_597_DL_trialandimagesASNR.jpg)

1411

MP-PCA Denoising of Complex Imaging Data for Direct Visualization of the Dentatorubrothalamic Tract Using Diffusion MRI at 3T

B Ades-Aron[1], G Lemberskiy[1], S Coelho[1], A Mogilner[2], D Novikov[3], T Shepherd[4], E Fieremans[5]

[1]NYU School of Medicine, Center for Advanced Imaging and Research, New York, NY, [2]NYU Lagone Health, New York, NY, [3]New York University School of Medicine, New York, NY, [4]New York University, New York, NY, [5]NYU Grossman School of Medicine, New York, NY

Purpose

The brainstem, basal ganglia and thalamus are complex configurations of small nuclei and pathways that are challenging to localize in-vivo using MRI. Diffusion MRI (dMRI) may be highly sensitive to early pathological processes in these small structures yet suffers from low signal-to-noise ratio. We demonstrate the high resolution needed to directly visualize these structures, and compare complex, magnitude, and no denoising to show the benefits for visualization, precision and accuracy of diffusion parameter estimates.

Materials and Methods

A healthy 38-y/o woman underwent MRI on a 3-T Siemens Prisma. The protocol included 1-mm isotropic resolution FGATIR (TR/TE/TI=3/0.019/0.41s, 256x256 matrix, 144 slices), and dMRI (b=0(6),1000(20 dirs),2000(60 dirs)) with either 1-mm isotropic resolution (TR/TE:20/0.093s 210x210, 126 slices), or 2-mm isotropic resolution (TR/TE:8/0.063s, 106x106, 76 slices). Denoising was performed using MPPCA with eigenvalue shrinkage and nonlocal patching. Preprocessed was done in 3 ways for comparison: 1) Complex dMRI phase denoising and unwinding, then denoising of phase-unwound signal using a nonlocal patch. 2) Denoised magnitude data. 3) Non-denoised data. dMRI for all resolutions and denoising levels were processed using DESIGNER. Fiber tracking was performed using probabilistic tensor tracking. Quantitative comparisons were done based on mean diffusivity (MD), mean kurtosis (MK) and fractional anisotropy (FA) over all white matter.

Results

Figure 1 shows histograms of MD, MK, and FA, Table 1 shows quantitative comparisons using non-denoised 2mm iso data as an index standard. Complex denoising resulted in the lowest variance overall and reduced bias to just 3.0% in MD, 10.5% for MK, and 5.6% for FA, along with decreased parameter variance caused by noise (Fig. 1). Figure 2 shows results of fiber tracking in the lateral thalamus, where the terminations of the medial lemniscus and dentarubrothalamic tract are not seen at 2-mm resolution, and only visualized after magnitude and complex denoising of the 1-mm resolution images respectively.

Conclusions

State-of-art clinical practice and investigations often use 2-mm isotropic resolution to study subcortical anatomy. However, 1-mm isotropic resolution appears essential for directly visualizing the dentatorubrothalamic tract (a key structure of interest for functional neurosurgery), yet without denoising the resulting parametric maps are effectively useless (Fig 2).

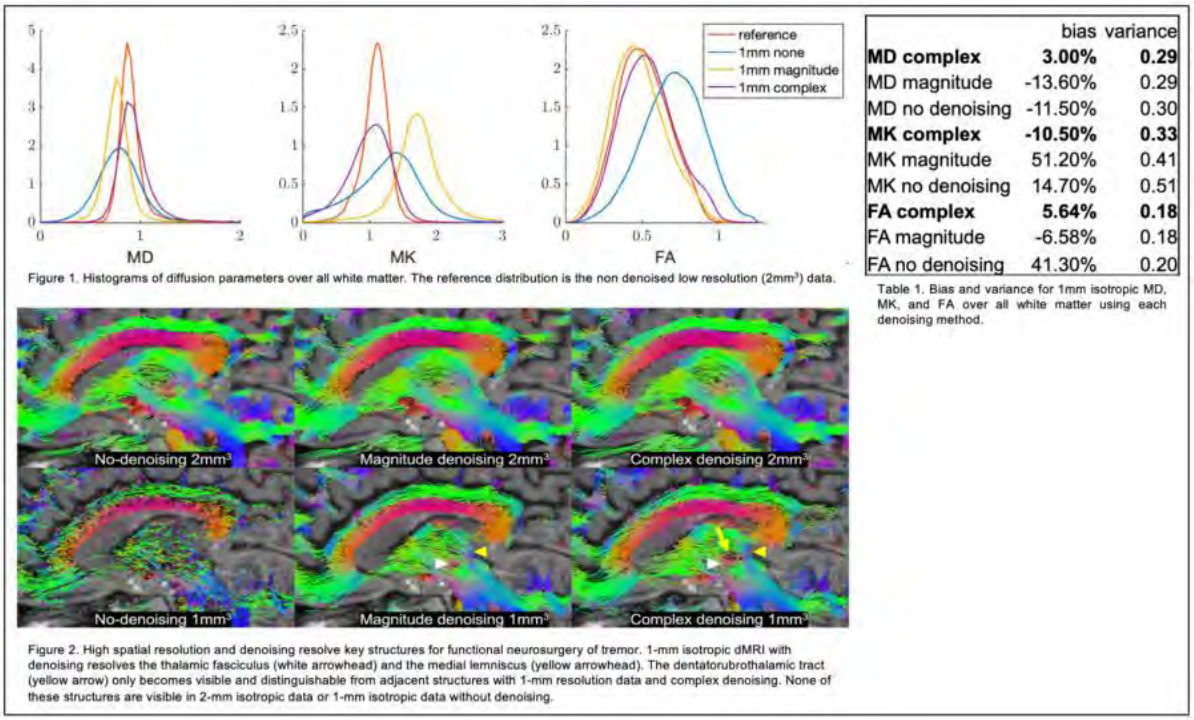

Figure 1. Histograms of diffusion parameters over all white matter. The reference distribution is the non denoised low resolution (2mm³) data.

	bias	variance
MD complex	**3.00%**	**0.29**
MD magnitude	-13.60%	0.29
MD no denoising	-11.50%	0.30
MK complex	**-10.50%**	**0.33**
MK magnitude	51.20%	0.41
MK no denoising	14.70%	0.51
FA complex	**5.64%**	**0.18**
FA magnitude	-6.58%	0.18
FA no denoising	41.30%	0.20

Table 1. Bias and variance for 1mm isotropic MD, MK, and FA over all white matter using each denoising method.

Figure 2. High spatial resolution and denoising resolve key structures for functional neurosurgery of tremor. 1-mm isotropic dMRI with denoising resolves the thalamic fasciculus (white arrowhead) and the medial lemniscus (yellow arrowhead). The dentatorubrothalamic tract (yellow arrow) only becomes visible and distinguishable from adjacent structures with 1-mm resolution data and complex denoising. None of these structures are visible in 2-mm isotropic data or 1-mm isotropic data without denoising.

(Filename: TCT_1411_fig1_asnr.jpg)

761

Rater Study Comparing CNN and Model-Based Denoising Approaches to Denoised FGATIR Images for Functional Neurosurgery Planning

M Elsayed[1], B Ades-Aron[2], M Hoch[3], E Fieremans[4], T Shepherd[5]

[1]NYU, Brooklyn, NY, [2]NYU school of medicine, center for advanced imaging and research, Brooklyn, NY, [3]University of Pennsylvania School of Medicine, Philadelphia, PA, [4]NYU Grossman School of Medicine, New York, NY, [5]New York University, New York, NY

Purpose

The 3D Fast Gray Matter Acquisition T1 Inversion Recovery (FGATIR) sequence can provide excellent discrimination of subcortical anatomy for functional neurosurgery targets. FGATIR however is signal-to-noise limited which reduces its feasibility and utility for multiple clinical applications. We used an MRI training dataset to develop a supervised convolutional neural network (PS-CNN) for FGATIR. There are limited objective measurements of image improvement and there is limited data comparing CNN to state-of-art model based denoising approaches. We conducted a rater study to determine if the CNN improved image quality to skilled observers and compared the results to an alternative denoising approach using 4D filtering (bm4d).

Materials and Methods

Two board-certified neuroradiologists blindly and independently evaluated axial FGATIR images of the midbrain through the red nucleus parallel to the commissural plane from 12 subjects. Images were derived with 1, 2, 4 & 8 averages, the 8-average image with added noise, and the 3 randomly selected 1 average images processed using single-input channel CNN (PS-CNN-1c), two-input channel CNN (PS-CNN-2c) and bm4d denoising methods (14 images per subject or 168 images total). Raters assessed 3 specific features (Contrast Resolution, Signal Quality, and Artificiality) using ordinal scores (3 = good, 2 = average, 1 = poor). The raters also assessed overall Clinical Quality on a 4-point ordinal scale (where 1= nondiagnostic and 4 = excellent).

Results

As expected simply increasing averages increased rater scores for all features. PS-CNN-2c was rated modestly better than PS-CNN-1c for signal and overall quality. PS-CNN-2c and bm4d appeared relatively equivalent – both improved single average data to rater scores for true 4 average data. Raters agreed most when the data quality was low (ICC=0.91) and tended to disagree more when rating artificiality. (Figure 1)

Conclusions

CNN denoising made 1-average FGATIR images look like 4-averages to expert neuroradiologists. The 2-channel CNN (PS-CNN-2c) may be better suited for dynamic changes in image noise across different patients and FGATIR acquisition protocols (e.g. 1.5T or different resolutions). The PS-CNN-2c appeared equivalent to bm4d, but processes data faster. Effective denoising should increase the utility of FGATIR for future investigations in functional neurosurgery.

A

ICC	contrast resolution	signal homogeneity	artificiality	overall quality
one average	0.91	0.89	0.58	0.91
two averages	0.91	1.00	0.86	0.86
four averages	0.91	0.33	0.83	0.73
eight averages	0.78	0.30	0.64	0.75
simulated noi	0.86	0.69	0.59	0.87
bm4d	0.84	0.69	0.31	0.85
cnn 2channel	0.83	0.73	0.76	0.84
cnn 1 channel	0.86	0.61	0.62	0.76
average	0.86	0.66	0.65	0.82

B

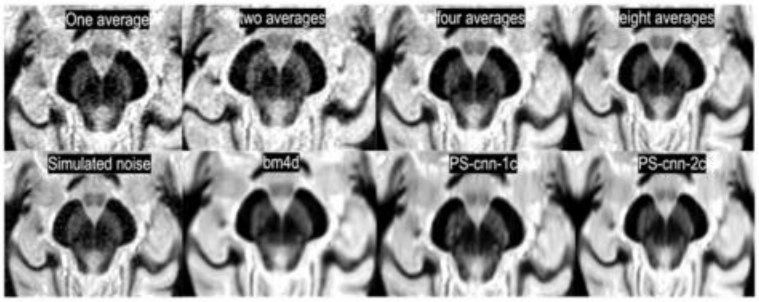

Figure 1 (A) Intra-class correlation coefficients (ICC) between the two raters over each metric. Values closer to 1 indicate a strong agreement between raters and zero indicate poor agreement **(B)** Example images from a healthy single subject (30-year-old female) used in the rater study

(Filename: TCT_761_ASNR2022Figure.jpg)

Monday, May 16, 2022
5:15-6:15 PM
Scientific Podium Presentations: Stroke Artificial Intelligence

358

Automated Detection of Arterial Landmarks and Vascular Occlusions in Acute Stroke Patients on Digital Subtraction Angiography Using Deep Learning

J Khankari[1], Y Yu[1], J Ouyang[1], G Zaharchuk[1], R Hussein[1]
[1]Stanford University, Stanford, CA

Purpose

Digital subtraction angiography (DSA) is the gold-standard for assessing blood flow in endovascular thrombectomy. Reading DSA may be challenging due to vessel tortuosity, vessel overlap in the imaging plane, and the presence of multiple occlusions. We aim to explore if convolutional neural networks (CNN) can be used to detect occlusions and landmarks on DSA.

Materials and Methods

We reviewed 96 patients from Imaging Collaterals in Acute Stroke (NCT02225730) who underwent DSA. We used arterial and parenchymal views. Experienced neurointerventionalists annotated occluded arteries (ICA, M1, M2 segment) and ICA terminus. We removed 14 patients whose ICA terminus was not visible (n=82 patients). Patient data in Table 1. We divided this study into 2 tasks: occlusion detection and ICA terminus detection. Details of data preprocessing for both tasks in Figure I. In task 1, we trained 3 CNNs (ResNet-50 trained from scratch, ResNet-50 pre-trained on ImageNet, and CNN with 3 convolutional and 2 max-pooling layers). Six-fold cross validation was performed with a train:test:val split of 3:2:1. Models were evaluated on AUC-ROC, mean pixel distance from ground truth, and accuracy. We calculated AUC-ROC using each model's predicted probability that a patch contains the ICA terminus. We found mean pixel distance by calculating distance between maximal probability for ICA terminus ("predicted" location) and ground truth. We found accuracy by calculating percentage of model predictions within 100 pixels from ground-truth. In task 2, a similar training and evaluation approach was used, taking into account that some cases had multiple occlusions.

Results

A ResNet-50 trained from scratch best detected the ICA terminus (AUC 0.998, 95% CI [0.997, 0.999], $p < 0.00001$) and occlusions (AUC 0.973, 95% CI [0.971, 0.975], $p < 0.0001$). Predicted ICA terminus location was 63±45 pixels (~1.26 cm) from ground truth (corresponding to ~5% of linear field-of-view of DSA images). Accuracy was 93%. Predicted occlusion location(s) were 98±84 pixels (~1.96 cm) from ground truth. Accuracy was 84%. Model predictions for both tasks in Figures II and III.

Conclusions

A ResNet-50 trained from scratch can localize the ICA terminus and arterial occlusions with high confidence. Ultimately combining occlusion locations with a map of arterial vasculature on DSA could improve rapid evaluation of occlusion status and "real-time" TICI scores. This may enable more standardized assessment for clinical trials requiring DSA analysis.

Mean [STD]	
Unique patients	82
Age (yrs)	67±14
Sex (F, %)	52%
NIHSS	14 [8-20]
TICI (0/1/2a/3b/3)	10/20/30/40/10
Onset to treatment time (hours)	6.6±5.6
Initial vascular occlusion site (ICA/ACA/M1/M2)	14/3/1/50/14
Number of individual DSA runs	382
Number of ICA terminus patches (positive/negative)	17,500/17,500
Number of patches with occlusion (positive/negative)	17,500/17,500

Table I. Demographics and Characteristics of the Patient Population

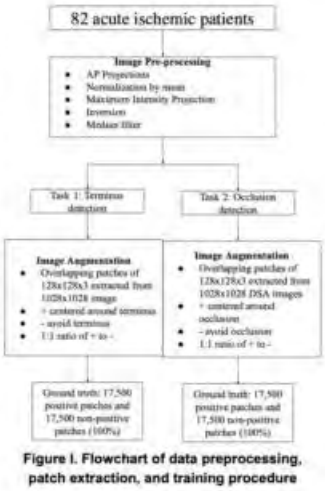

Figure I. Flowchart of data preprocessing, patch extraction, and training procedure

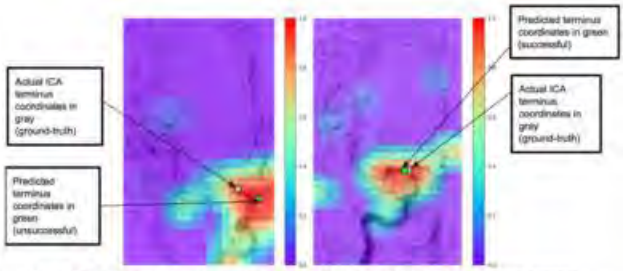

Figure II. Left: Relatively poor terminus prediction (>100 pixel error). Right: Relatively good terminus prediction (<100 pixel error). Gray dot signifies ground truth.

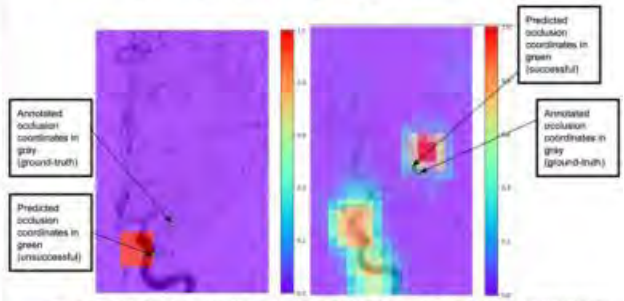

Figure III. Left: Relatively poor occlusion prediction (>100 pixel error). Right: Relatively good occlusion prediction (<100 pixel error). Gray dot signifies ground truth.

(Filename: TCT_358_DSAASNRAbstractTablesFigures.jpg)

268

Automated Detection Of Intracranial Hemorrhage Using Artificial Intelligence (RAPID-ICH): Initial Clinical Experience

W CHANG[1], A Rajan[1], C LI[1], B Weston[1], T Tragon[1], P Annigeri[1], L Eisenmenger[2], M Goldberg[1]

[1]Allegheny Health Network, Pittsburgh, PA, [2]University of Wisconsin - Madison, Middleton, WI

Purpose

Intracranial hemorrhage (ICH) has high morbidity and mortality with nearly 50% 30 day mortality for patients admitted to the ICU and as few as 20% of survivors demonstrating full neurologic recovery. Early intervention has been shown to improve clinical outcomes. Given high mortality and morbidity, prompt identification of ICH has high clinical utility. Several applications have emerged using artificial intelligence (AI) for automated detection of ICH, including RAPID ICH (iSchemaView, Menlo Park, CA). We present our initial clinical experience with RAPID ICH in a busy Level 1 trauma center.

Materials and Methods

The study was supervised by the local institutional review board. Patients presenting to the emergency department (ED) receiving CT scans of the brain and inpatients (IP) scanned on the ED scanner at one level 1 trauma center were included in the study. The RAPID ICH output ("no ICH" or "suspected ICH") was recorded for each study. The initial interpreting emergency radiologist or neuroradiologist had access to the RAPID ICH output. Radiology reports reporting ICH were considered positive and those reporting no ICH were considered negative. A board certified neuroradiologist reviewed each case who had access to the initial report, RAPID ICH output, and all subsequent examinations. In cases with disagreement between the readers, a third reader adjudicated the result and their decision was considered final. The expert reads were used as the gold standard and sensitivity, specificity, negative predictive value (NPV) and positive predictive value (PPV) were calculated.

Results

A total of 1388 patients were included in the study, 1251 from the ED and 137 IP. For ED patients, 139 had ICH and 1112 did not, where as in the IP cohort, 100 had ICH and 37 did not. RAPID ICH demonstrated overall sensitivity of 79% (73% ED, 88% IP), overall specificity of 95% (96% ED, 84% IP), overall PPV of 76% (65% ED, 94% IP) and overall NPV of 96% (97% ED, 72% IP).

Conclusions

RAPID ICH demonstrated relatively high sensitivity and very high specificity for ICH, with lower sensitivity and higher specificity in the ED, and higher sensitivity but lower specificity in the inpatient setting. Using AI applications such as RAPID ICH for active worklist reprioritization may allow timely triage of potentially positive studies, allowing early intervention and potentially leading to improved clinical outcomes, especially in the inpatient setting with longer average turnaround times for routine studies.

	Overall	RAPID +	RAPID -	ED	RAPID +	RAPID -	Inpatient	RAPID +	RAPID -
ICH present		189	50		101	38		88	12
ICH absent		61	1088		55	1057		6	31
Sensitivity	79%			73%			88%		
Specificity	95%			95%			84%		
PPV	76%			65%			94%		
NPV	96%			97%			72%		

(Filename: TCT_268_rapidich.GIF)

267

Automated Detection of Large Vessel Occlusion (RAPID-LVO) Using Relative Vessel Density Improved Clinical and Stroke Workflow Outcomes in a Large Health System: One Year Retrospective Analysis

W CHANG[1], J Adhya[1], C LI[1], R Cerejo[1], B Weston[1], P Annigeri[1], L Eisenmenger[2], M Goldberg[1]
[1]Allegheny Health Network, Pittsburgh, PA, [2]University of Wisconsin - Madison, Middleton, WI

Purpose

RAPID LVO (RLVO) automatically detects anterior circulation large vessel occlusion (LVO) by comparing MCA territory relative vessel density (RVD) to the contralateral side, allowing early mobilization of treatment teams. Previous studies investigating the use of LVO detection algorithms have typically been single center studies, used patients from thrombectomy trials, or had little clinical follow-up. We present our one year experience with RLVO in a large health hub/spoke health system and report its accuracy, effect on stroke workflow outcomes, and effect on clinical outcomes.

Materials and Methods

All patients presenting with stroke symptoms at six network hospitals who received CTAs w/RLVO from November 1, 2019 to November 1, 2020 were included, totaling 1207 patients. RLVO exams were considered positive at RVD <60% and negative at RVD >60%. Radiology exams were positive if LVO (ICA/M1 or M2 occlusion) or high grade stenosis (HGS) was detected. All positive cases were reviewed by a second reader with 100% concordance. Expert reads were considered the gold standard and sensitivity, specificity, PPV (positive predictive value) and NPV (negative predictive value) were calculated. Mechanical thrombectomy (MT) was performed at a comprehensive stroke center, after patient transfer, if imaging was obtained at a primary stroke center. CTA to groin puncture time for patients receiving MT was calculated from 11/1/2018 to 11/1/2019 (before RLVO installation) and 11/1/2019-11/1/2020 (after RLVO installation) for patients undergoing MT. 90 day Modified Rankin Scores (mRS) were obtained for the same cohort of patients receiving MT.

Results

126 patients had M1/ICA occlusion, 71 had M2 occlusion, and 134 had HGS of the ICA or MCA. RLVO had sensitivities of 90%, 82%, and 82%, specificities of 82%, 85%, and 95%, PPV of 37%, 52%.and 87% and NPV of 99%, 96%, and 93% for detection of M1 occlusion, LVO, or HGS/LVO, respectively. CTA to groin puncture time significantly decreased after deployment of RLVO (93 minutes vs 68 minutes, $p<0.05$). Average 90-day mRS significantly improved (3.65 vs 4.44) improved with a higher percentage of functional independence (mRS ≤ 2 in 41% of patients compared to 23%) ($p<0.05$) after RVLO deployment.

Conclusions

RLVO detected HGS or LVO in patients presenting with stroke symptoms with high accuracy. After RLVO installation, clinical and stroke workflow outcomes significantly improved. This study demonstrates the efficacy of AI-based LVO detection software in a real-world environment.

Pathology present	RAPID <45% (red)	RAPID 45-60% (yellow)	RAPID >60% (negative)
M1 or ICA occlusion	101	13	12
M2 occlusion	28	19	24
High grade stenosis	34	75	25
No high grade stenosis or occlusion	9	31	832
Total	172	138	893

Detection of pathology at different thresholds of MCA territory relative vessel density (RVD) (compared to contralateral side) on RAPID CTA. RVD <60% (red and yellow categories) was considered positive, where RVD >60% was considered negative.

	Sensitivity	Specificity	Positive Predictive Value	Negative Predictive Value
M1 or ICA occlusion	90%	82%	37%	99%
M1/ICA or M2 occlusion (LVO)	82%	85%	52%	96%
High grade stenosis or LVO	82%	95%	87%	93%

Sensitivity, specificity, positive predictive value, and negative predictive value of RAPID CTA for ICA/M1 occlusion, ICA/M1 and MCA occlusions (LVO), and high grade stenosis or LVO. RVD < 60% was considered positive and RVD > 60% was considered negative.

Time Period	Number of Patients	CTA to groin puncture (min)
Nov 2018-2019 (no RAPID CTA)	74	92
Nov 2019-2020 (w/RAPID CTA)	72	68

The difference was statistically significant ($p<0.05$)

Time Period	Number of Patients	Average mRS	% Patients with mRS ≤ 2
Nov 2018-2019 (no RAPID CTA)	74	4.47	23
Nov 2019-2020 (w/RAPID CTA)	67	3.90	34

The difference was statistically significant ($p<0.05$)

(Filename: TCT_267_rctafigure4.JPG)

1251

Automated Measurement of Final Infarct Volume in Acute Ischemic Stroke

L Pisani[1], M Bouslama[2], G Harston[3]

[1]St Vincent Hospital, Worcester, MA, [2]New York University, New York City, NY, [3]Oxford University Hospitals NHSFT, Oxford, Oxfordshire

Purpose

Final infarct volume (FIV) is a commonly used imaging endpoint in stroke trials. The aim of this study was to investigate the potential of an automated masking pipeline (Brain Intensity AbNormality Classification Algorithm - BIANCA) for the measurement of ischemic stroke lesions on follow-up imaging of acute ischemic stroke patients treated with mechanical thrombectomy (MT).

Materials and Methods

Patients were retrospectively selected from a prospectively acquired MT database from January to July 2019, and were included if they had a follow-up Diffusion-weighted MRI within 72h post procedure. Masks were generated on B1000 imaging by clinical stroke research personnel and then compared with volumes delineated by a fully automated method for lesion detection, based on a k-nearest neighbor (k-NN) algorithm. Anatomical distortion (AD) was quantified using a previously published registration-based approach. Follow-up MRI were registered to the baseline MRI or to a template image in MNI152 space using FMRIB's Linear Image Registration Tool (FLIRT), and FMRIB's Non-Linear Image Registration Tool (FNIRT).

Results

A total of 100 patients were included. Thirty were used for training. The remaining seventy (validation cohort) had the mean FIV volumes for the human-derived and BIANCA measurements comparable [67.7±73.2 vs 71.8±67 mL ($p<0.05$)]. Use of multiple MRI parameter maps improved overlap agreement, with optimum results using both b=1000 DWI and ADC imaging to segment stroke lesions, compared to using b=1000 imaging alone. Lesions in the lower volume quantiles benefitted from higher probability thresholds, higher numbers of non-lesion training points and lower patch sizes. Dice similarity index showed to be 0.710 whilst the ICC was 0.960 ($p<0.05$).

Conclusions

The automated masking pipeline measurement showed to be highly similar to a standardized human reading protocol of FIV estimation at a high volume stroke center. This is a promising technology that may significantly facilitate data analysis in large registries and trials.

1414

Head-to-Head Comparison of Commercial Artificial Intelligence Solutions for Detection of Large Vessel Occlusion at a Comprehensive Stroke Center

D Ro[1], S Kang[2], S Salehi[3], J Schlossman[3], L Groysman[1], P Chang[3], J Soun[1]

[1]University of California Irvine Medical Center, Orange, CA, [2]Hallym University Medical Center, Seoul, South Korea, [3]University of California Irvine School of Medicine, Irvine, CA

Purpose

While there is data supporting the benefit of using Artificial Intelligence (AI) tools for large vessel occlusion (LVO) detection, there is paucity of data regarding head-to-head comparison of commercially available software. Here, we compared performance of RAPID (a traditional Machine Learning model) and CINA (a Deep Learning model) for LVO detection in anterior circulation stroke.

Materials and Methods

This was a retrospective, single center study using anonymized data from December 2020 to June 2021. 255 CTA cases for suspected stroke were analyzed using both LVO detection tools. Ground truth was based off interpretation from a board-certified neuroradiologist. Performance metrics were analyzed by location of LVO: intracranial internal carotid artery (ICA), middle cerebral artery M1 segment, or both.

Results

There were 31 positive and 224 negative LVO cases. For overall performance, RAPID demonstrated an accuracy of 0.86, sensitivity of 0.90, specificity of 0.86, PPV of 0.45, and NPV of 0.98, while CINA demonstrated an accuracy of 0.96, sensitivity of 0.76, specificity of 0.98, PPV of 0.85, and NPV of 0.97. For ICA LVOs, RAPID demonstrated an accuracy of 0.86, sensitivity of 0.82, and specificity of 0.86, while CINA demonstrated an accuracy of 0.96, sensitivity of 0.55, and specificity of 0.98. For M1 LVOs, RAPID demonstrated an accuracy of 0.86, sensitivity of 0.91, and specificity of 0.86, while CINA demonstrated an accuracy of 0.97, sensitivity of 0.87, and specificity of 0.98.

Conclusions

This is the first study to compare the performance of traditional and deep learning LVO detection tools in the clinical setting. RAPID had overall higher sensitivity while CINA had overall higher accuracy and specificity. Common reasons for false positives for RAPID included stenosis or other vessel caliber change. Both tools missed cases of ICA occlusion that reconstituted at the carotid terminus and moyamoya steno-occlusive disease with prominent leptomeningeal collaterals. Interestingly, both tools were able to detect some, but not all M2 MCA occlusions. Both automated LVO detection tools offer advantages in that RAPID may serve as the initial screening tool while CINA may serve as complimentary tool in reducing false positive cases for the purpose of providing timely diagnosis of LVO. As more automated LVO detection tools become commercially available, it will be paramount to conduct comparison studies to evaluate their performance in the clinical setting.

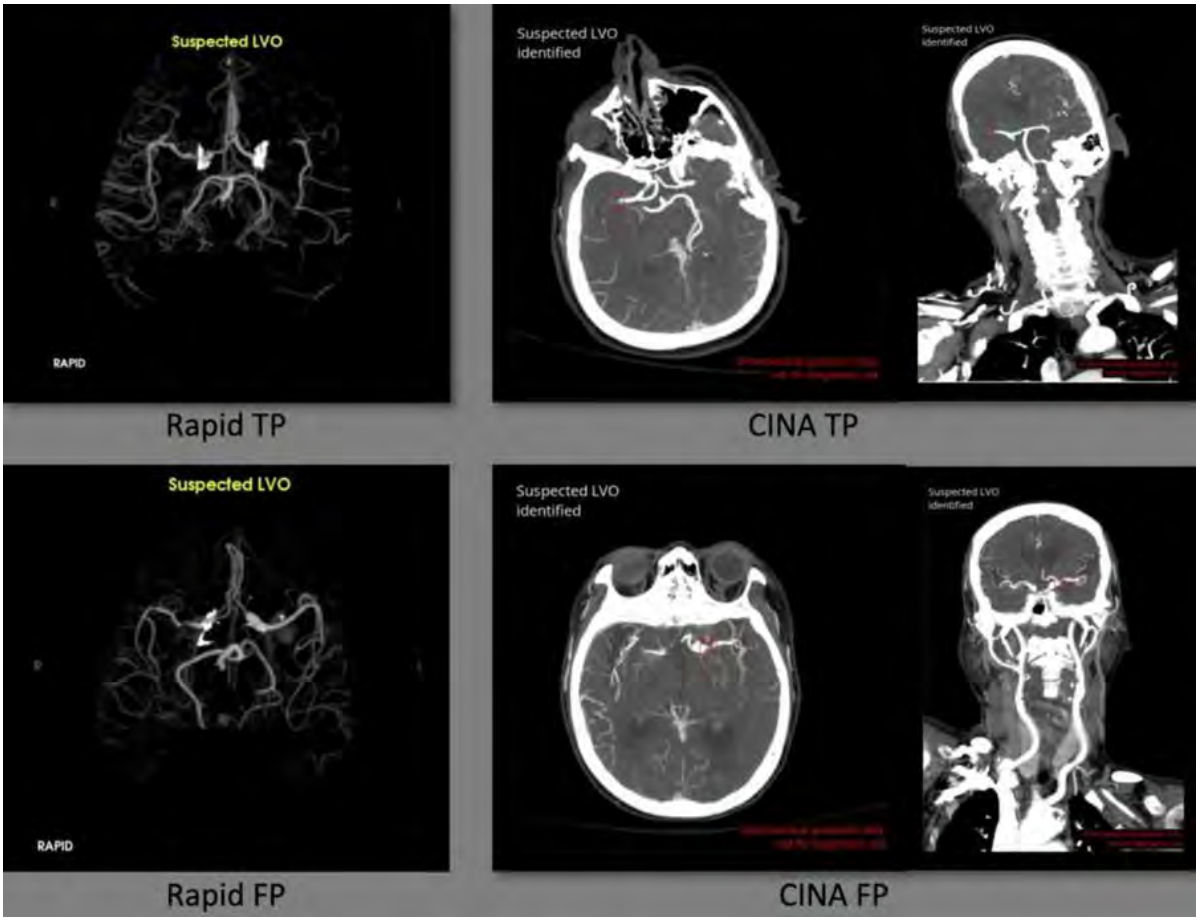

(Filename: TCT_1414_RapidvCINAv3.jpg)

942

Head-To-Head Comparison of Two Artificial Intelligence (AI) Solutions for Large Vessel Occlusion and Perfusion Deficits in Acute Ischemic Stroke

A Udare[1], C Ko[1], P Mondel[1], V Rao[2], A Flanders[1]
[1]Thomas Jefferson University Hospital, Philadelphia, PA, [2]Thomas Jefferson University, Philadelphia, PA

Purpose

1. To compare the performance of two FDA approved AI solutions in the automated detection of large vessel occlusion (LVO) using CT angiography (CTA) datasets in a series of patients being evaluated for acute ischemic stroke (AIS). 2. To determine whether the automated CT Perfusion (CTP) AI estimation of ischemic core and penumbra are significantly different using the two solutions.

Materials and Methods

Retrospective review of all consecutive head and neck CTA with complementary CTP performed from April 2020-Sept 2021 for evaluation of AIS meeting the following inclusion criteria: 1)Adequate quality thin-section CTA and CTP imaging DICOM dataset of anterior circulation AIS, 2)Complete processing by both AI software solutions 3)Complete/near-complete endovascular reperfusion and/or follow-up MRI. Exclusion criteria: posterior circulation strokes, ICH, vascular malformations and tumors. Ground truth for LVO detection was by consensus with two neuroradiologists. The sensitivity, specificity, PPV, NPV and accuracy for LVO detection of the two AI packages were compared to the consensus reads. Paired t-test comparisons ($p<0.05$) for affected brain volumes where Tmax>6s (hypoperfused brain), CBF<30% (infarct core) and mismatch volumes (ischemic penumbra i.e. difference between Tmax>6s and rCBF<30% volumes) as established in the DAWN and DEFUSE3 stroke trials.

Results

From a total of 684 AIS CTA head and neck exams performed during this time period, 165 met inclusion criteria. 33(20%) patients of the 165 had a confirmed LVO and 132(80%) had confirmed no LVO. The sensitivity, specificity, PPV, NPV & accuracy of AI software#1 (93%, 84%, 61%, 98%, 87%) were higher than AI software#2 (91%, 83%,57%, 97%, 84%) for all types of LVO, but not significantly($p < 0.64, 0.73$). Both solutions demonstrated lower sensitivity (77%) for specifically M2 occlusions. There was statistically significant difference ($t(162) = 2.4$, $p = 0.015$) for the means of Tmax>6s volumes and no statistically significant difference ($t(162) = 1.1$, $p = 0.27$) for means of rCBF<30% volumes. The mismatch volumes (ischemic penumbra) between the two software were significantly different ($p<0.05$).

Conclusions

Both AI solutions had comparable accuracy for predicting LVOs. Both had good sensitivity and specificity for detection of ICA and

M1 LVOs, but lower sensitivity for detection of M2 LVOs. There was a statistically significant difference between the means of Tmax>6s and mismatch volumes and no statistically significant difference for rCBF<30%.

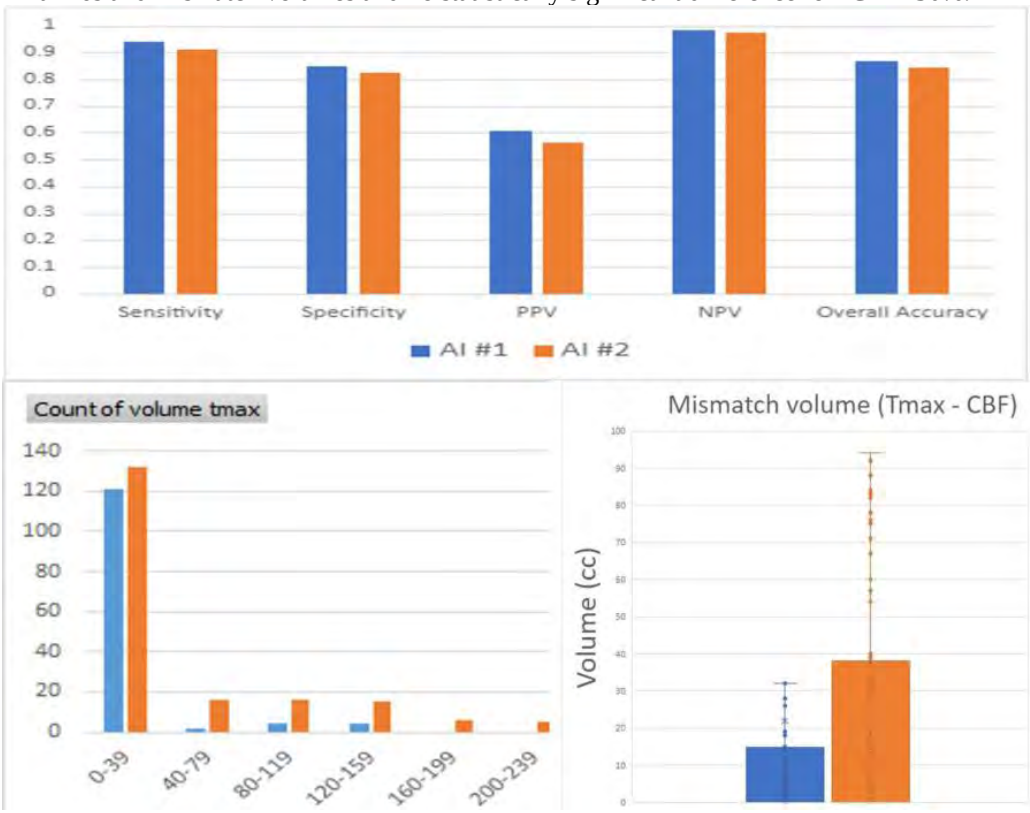

(Filename: TCT_942_figurefinal.jpg)

888

Identification of Intracranial Hemorrhage and Its Subtypes on Head CT Scans Using Transfer Learning and Weakly-supervised Networks

Y Wu[1], A Adate[1], D Cantrell[2], V HILL[3]

[1]Northwestern University, Evanston, IL, [2]Northwestern University, Chicago, IL, [3]Neuroradiology Section, Department of Radiology, Northwestern University Feinberg School of Medicine, Chicago, IL

Purpose

To develop a weakly-supervised deep learning application trained with scan-level labels using transfer learning and attention-based Long Short Term Memory (LSTM) to automatically detect and localize intracranial hemorrhage (ICH) at the slice-level in real-time in order to improve patient safety.

Materials and Methods

A total of 15,904 CT scans from 10,089 subjects were included in this study. The scan-based labels were extracted from the radiology reports [1] and used as the gold standard (normal or ICH). 80% of the dataset was used for five-fold cross-validation training and 20% for independent testing. Three window levels were applied to each slice to enhance the brain, soft tissues and ischemic infarct using the window width and center pairs of [80,40], [400,80] and [30,30] respectively, which were concatenated as the input to the network (Fig. A). The training process has three stages: 1) the EfficientNet-B2 [2] Network, pre-trained on RSNA dataset [3], extracts features on each slice of our data and predicts confidence scores of ICH and its subtypes. 2) Attention-based bidirectional LSTM networks further extract spatial connections among the slice features from the same scan. 3) A fully-connected layer predicts the outcome. The model was fine-tuned by training in an end-to-end manner (Fig. B). Gradient-based class activation mapping (Grad-CAM) [4] was applied to each slice to map the locations that were most likely used to predict ICH and provide the likelihood of the ICH subtypes. The average and the ensemble model performance across five-folds were evaluated on the independent testing data.

Results

This weakly supervised LSTM model achieves the performance of detecting ICH at scan-level averaged across all five-folds with an overall accuracy of 0.913 ± 0.004, f1 score of 0.851 ± 0.008, and ROC-AUC score of 0.952 ± 0.001. The ensemble of five-folds improves the performance with accuracy of 0.918 and f1 score of 0.857 (Table 1). GRAD-CAM successfully localized all types of ICH, provided the subtype probability per slice (Fig. C) and generated subtype specific maps (Fig. D). The fully trained model takes less than 1s to analyze a full head CT scan.

Conclusions

The model was trained with scan-level labels of ICH but produced subtype detection and per-slice identification. This real-time

diagnosis and visual presentation of ICH can be used by radiologists to automatically detect ICH and prioritize reading for improved clinical workflow and, most importantly, improved patient safety.

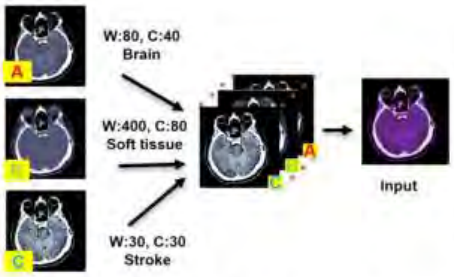

Fig. A. Windowing pre-processing

Table 1. Model evaluations on testing dataset (mean ± standard deviation)

Metrics	LSTM-testing (average)	LSTM-testing (ensemble)
Accuracy	0.913 ± 0.004	0.918
F1	0.851 ± 0.008	0.857
Precision	0.871 ± 0.009	0.884
Recall	0.834 ± 0.011	0.835
AUC	0.952 ± 0.001	0.952

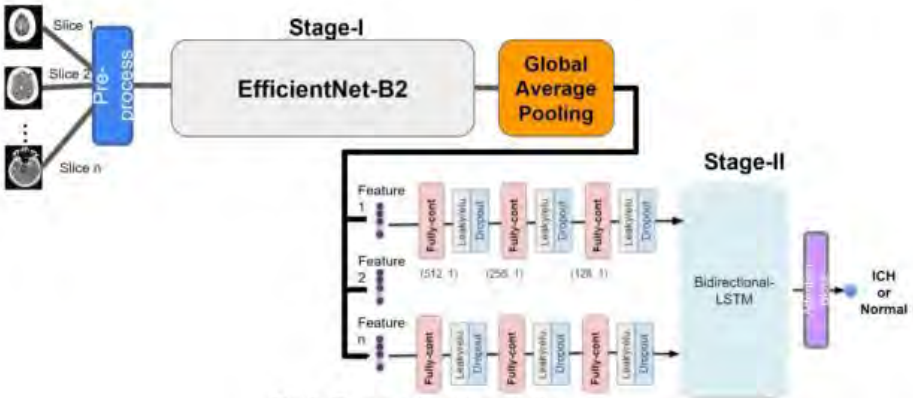

Fig. B. The model training pipeline

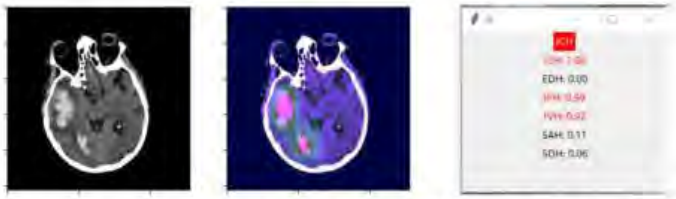

Fig. C: Grad-CAM highlights possible ICH locations. The raw CT image (left), the Grad-CAM map (middle), and the confidence score if ICH and prediction of subtypes (right). The redder the mapping, the stronger the prediction.

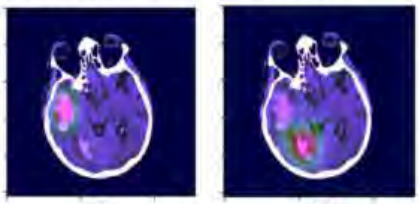

IPH IVH

Fig. D: Grad-CAM indicates possible ICH. Intraparenchymal hemorrhage (left). Intraventricular hemorrhage (right).

(Filename: TCT_888_figure.jpg)

952

Real-World Integration of an Automated Tool for Intracranial Hemorrhage Detection in Emergency Department Patients – an External Validation Study

R Antulov[1], M Weber Kusk[1], G Knudsen[1], S Lynggaard[1], S Lysdahlgaard[1], V Antonov[1]
[1]Hospital South West Jutland, Esbjerg, Denmark

Purpose

Intracranial hemorrhage (ICH) is a life-threating medical event that can be reliably and rapidly detected by non-contrast head computed tomography (NCCT). Several commercially available artificial intelligence (AI) tools showed promising results in automated ICH detection.1 The aim of this study was to validate the implementation of an automated tool for ICH detection in emergency patients.

Materials and Methods

This retrospective study included 880 consecutive NCCTs done at the Emergency Department during a three months period. All

NCCTs were acquired on the same Somatom FORCE CT (Siemens) with the following parameters: tube voltage 120 kV, single collimation width 0.6 mm, reconstructed slice thickness 5 mm, reconstruction method ADMIRE level 3 and reconstruction kernel HR32. Resulting images were automatically sent to RAPID ICH (iSchemaView), a commercially available AI-based automated ICH detection tool, for analysis. All NCCTs were reviewed by a 2nd-year radiology resident (RR) who excluded 36 NCCTs due to significant motion and metal artifacts. The remaining 844 NCCTs were analyzed by two senior neuroradiologists (SN) for ICH presence and type which was considered the reference standard. Discrepancies in interpretation between SN were resolved by consensus. The included NCCTs were also assessed for ICH presence by a 1st-year RR who underwent training in neuroradiology. All readers were blinded to RAPID ICH results.

Results

Out of 844 NCCTs, 63 (7.5%) ICH-positive examinations were confirmed by the SN. RAPID ICH detected 258 possibly ICH-positive NCCTs of which 203 (78.7%) were false positives (FP) and out of 586 ICH-negative NCCTs there were 8 (1,4%) false negatives (FN) (Fig 1A). The 1st-year RR found 132 possibly ICH-positive NCCTs of which 72 (54,6%) were FP and from 712 ICH-negative NCCTs there were 3 (0,4%) FN (Fig 1B). The diagnostic performance of RAPID ICH showed 87.3% sensitivity, 74% specificity, 21.3% positive predictive value (PV) and 98.6% negative PV. The 8 FN RAPID ICH NCCTs were with bleedings measuring up to 6 mm (Fig 1C). Of the 203 FP RAPID ICH NCCTs most were related to dural thickening (Fig 1D).

Conclusions

Compared with other commercially available AI tools, RAPID ICH showed similar results in actual ICH detection, while a substantial discrepancy was found in the number of flagged FP ICH examinations which could impair clinical workflow. 2 3 4 Therefore, further real-world studies with external validation are needed.

A

RAPID ICH results	Examination validation	Number of examinations (Percentage of positive or negative ICH examinations)	Percentage of all included examinations (844)
Positive for ICH (258 examinations)	True positive	55 (21,32%)	6,52%
	False positive	203(78,68%)	24,05%
Negative for ICH (586 examinations)	True negative	578 (98,63%)	68,48%
	False negative	8 (1,37%)	0,95%

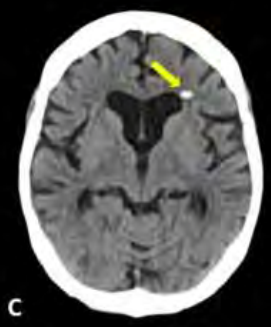

C

B

1st year radiology resident results	Examination Validation	Number of examinations (Percentage of positive or negative ICH examinations)	Percentage of all included examinations (844)
Positive for ICH (132 examinations)	True positive	60 (45,45%)	7,11%
	False positive	72 (54,55%)	8,53%
Negative for ICH (712 examinations)	True negative	709 (99,67%)	84,00%
	False negative	3 (0,42%)	0,36%

D

Classification of false positive RAPID ICH examinations according to findings	Number of examinations (Percentage of total false positive RAPID ICH examinations)
Dural thickening (thick falx cerebri of thick tentorium cerebelli)	71 (34.97%)
Calcification of the choroid plexus	58 (28.57%)
Other calcified structures (basal ganglia, pineal gland)	18 (8.86%)
Basilar artery or middle cerebral artery	12 (5.91%)
Venous sinus	6 (2.95%)
Streak or beam hardening artifacts	14 (6.89%)
Post-surgical / tumor / other	24 (11.82%)

(Filename: TCT_952_952-slide.jpg)

Tuesday, May 17, 2022

10:30-11:30 AM

ASSR Programming: Essentials of Neuroradiology: Basics to Advanced: Spinal Anatomy Through Cases

1460

INTRODUCING A NOVEL HIGH-RESOLUTION PROTON DENSITY WEIGHTED SEQUENCE FOR ASSESSMENT OF THE CRANIO-CERVICAL JUNCTION

R Riascos[1], S Khanpara[2], L Nunez-Rubiano[1], O Arevalo[3], Y Cai[4], R Gabr[5]

[1]The University of Texas Health Science Center at Houston, Houston, TX, [2]University of Texas MD Anderson Cancer Center, Houston, TX, [3]LSU Health Shreveport, Shreveport, LA, [4]University of Texas Health Science Center at Houston, Houston, TX, [5]UTHSC-Houston, Houston, TX

Purpose
The Cranio-Cervical Junction (CCJ) is a unique anatomical structure comprised by multiple bony and ligamentous elements. Current imaging modalities utilized to evaluate the CCJ demonstrate inadequate sensitivity to detect traumatic injuries at this level. In the search of an ideal imaging acquisition MR protocol, we developed a novel high-resolution (HR) proton density weighted sequence for a better visualization of the CCJ.
Materials and Methods
Subjects with a history of trauma and clinical suspicion of CCJ injury underwent imaging evaluation with both a conventional MR protocol and the HR sequence. A board certified neuroradiologist graded the imaging quality using the following scale: 1, complete obscuration of anatomical detail; 2, partial obscuration of anatomical detail; 3, impaired depiction of only some anatomical detail; 4, partial impairment but preservation of all anatomical detail; and 5, unimpaired depiction of all anatomical detail. The 3D HR MRI was performed on a 3.0-Tesla system with an 8-channel SENSE head coil. 3D proton density weighted images were acquired in a coronal plane. Scan parameters were as follows: TR/TE, 1000/36 ms; FOV, 150 mm x 150 mm x 50 mm; acquisition matrix, 288 x 288 x 80; acquired resolution, 0.52 mm x 0.52 mm x 1.0 mm; reconstructed resolution, 0.5 mm isotropic; flip angle, 90˚; TSE factor, 60; refocusing angle, 65˚; echo spacing, 5.2 ms; no parallel imaging; number of signal averages, 2; scan time, 5:02 min.
Results
A total of 34 patients were included in the study. In the conventional cervical spine protocol, there was limited visualization of the alar ligaments, the C0-C1 capsule, and the C1-C2 capsule on 15 (44%) studies. In contrast, the visualization of these structures in the HR sequence was only limited on 4 (12%) studies. Visualization of the transverse ligament and the tectorial membrane was similar in both protocols. When assessing image quality, a greater proportion of alar ligaments were graded 5 in the HR sequence compared to the standard protocol (47 to 41% in the right; 47 to 35% in the left). Similarly, the C0-C1 capsule achieved a score of 5 in 50% of the HR studies, compared to 25% of the conventional studies. In addition, a greater proportion of alar ligament injuries were detected when using the HR sequence.
Conclusions
The 3D proton density weighted sequence is a feasible approach to image the CCJ, and successfully demonstrated a higher image quality to visualize the C0-C1 and C1-C2 capsules, as well as the alar ligaments.

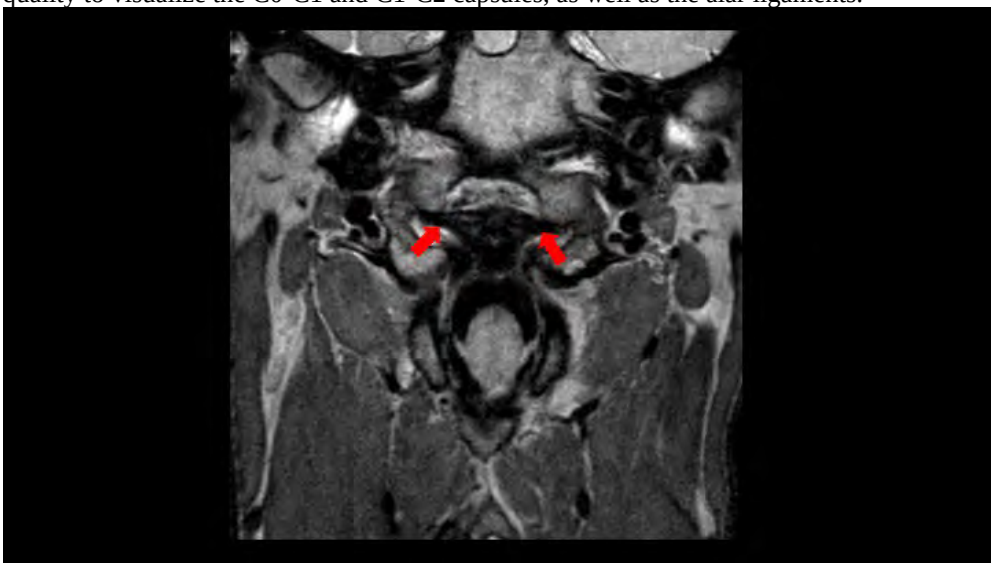

(Filename: TCT_1460_CCJ.gif)

Tuesday, May 17, 2022
10:30AM - 11:30AM
Scientific Podium Presentations: Multiple Sclerosis

277

Assessment of Automatic Decision-Support Systems for Detecting Active T2 Lesions in Multiple Sclerosis Patients

A Rovira[1], J Corral[2], C Auger[3], S Valverde[4], A Oliver[5], K Ng Wong[2], F Aymerich[2], X Lladó[5], J Alonso[2]
[1]Hospital Universitari Vall d'Hebron, Barcelona, Barcelona, [2]Hospital Universitari Vall d'Hebron, Barcelona, Spain, [3]Hospital Universitari Vall d´Hebron, Barcelona, Barcelona, [4]TENSOR MEDICAL s.l., Girona, Spain, [5]University of Girona, Girona, Spain

Purpose
Active (new/enlarging) T2 lesion counts are routinely used in the clinical management of multiple sclerosis. Thus, automated tools

able to accurately identify active T2 lesions would be of high interest to neuroradiologists for assisting in their clinical activity. The objective of this study is to compare the accuracy in detecting active T2 lesions and of radiologically active patients based on different visual and automated methods.

Materials and Methods

One hundred multiple sclerosis patients underwent two magnetic resonance imaging examinations within 12 months. Four approaches were assessed for detecting active T2 lesions: V1) conventional neuroradiological reports; V2) prospective visual analyses performed by an expert; A1) automated unsupervised tool; and A2) supervised convolutional neural network (CNN). As a gold standard, a reference outcome (RONL) was created by the consensus of two observers.

Results

The automated methods detected a higher number of active T2 lesions, and a higher number of active patients, but a higher number of false positive active patients than visual methods. The convolutional neural network model was more sensitive in detecting active T2 lesions and active patients than the other automated method.

Conclusions

The results of this study show that the automated methods have greater sensitivity but slightly lower specificity in detecting new/enlarging T2 lesions and active MS patients than conventional neuroradiological reports and expert visual analysis. This indicates that the automated tools should be further developed to allow their fully unsupervised use in clinical practice. From the comparison of both automated tools, we show that the one based on the application of a CNN model, is more promising than automated unsupervised approaches in detecting MR disease activity. Finally, although not specifically assessed in this study, visually supervised automated tools likely provide a higher level of confidence in the detection of radiological activity than the standard radiological report and show potential as an aid to neuroradiological visual assessment in clinical practice.

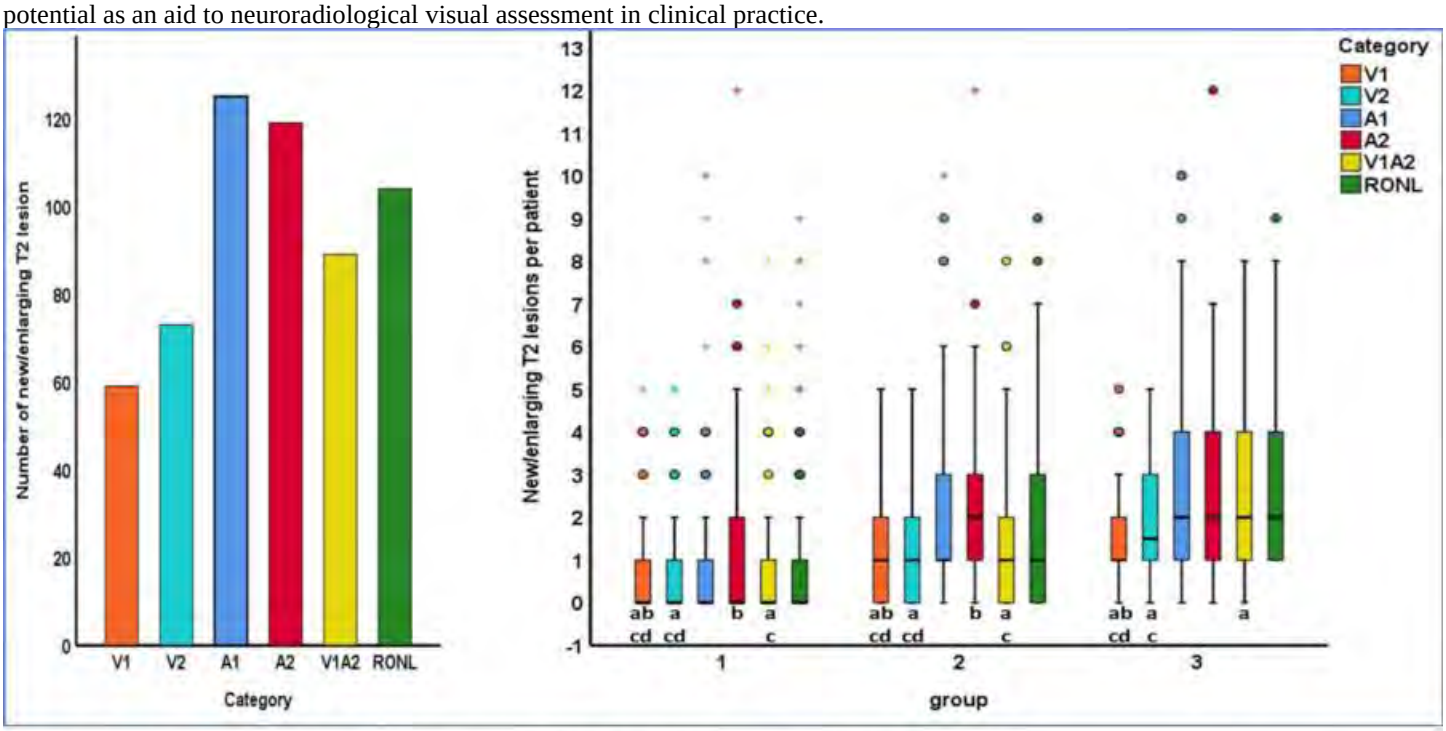

Boxplots comparing the mean number of new/enlarging T2 lesions per patient for the different methods and the reference outcome of new/enlarging lesions (RONL).

Left: Number of new/enlarging T2 lesions for the different methods and the reference outcome of new/enlarging lesions (RONL). Right: Comparison of the new/enlarging T2 lesions per patient for the different methods considering the whole cohort (group 1), the 53 patients for whom at least one new/enlarging T2 lesion was detected by one method (group 2) and the 38 patients with truly new/enlarging T2 lesion (group 3).

V1, standard radiological report method; V2, visual review of the MR scans by an expert nonblinded to the radiological report; A1, automated unsupervised approach; A2, automated supervised convolutional neural network-based approach; V1A2, A2 method corrected with the report information; RONL, reference outcome of new/enlarging lesions.

[a] Significantly different with respect to RONL. [b] Significantly different with respect to V1A2. [c] Significantly different with respect to A2. [d] Significantly different with respect to A1.

(Filename: TCT_277_Imagen1.jpg)

148

Characterization of Demyelinating Lesions in Multiple Sclerosis Using Highly Accelerated 3D Wave-CAIPI Susceptibility-Weighted Imaging and FLAIR

N Grinspan[1], A Goncalves Filho[1], A Tabari[1], C Ngamsombat[2], D Splitthoff[3], P Schaefer[4], J Conklin[1], S HUANG[1]

[1]Massachusetts General Hospital, Boston, MA, Athinoula A. Martinos Center for Biomedical Imaging, Charlestown, MA, [2]Athinoula A. Martinos Center for Biomedical Imaging, Charlestown, MA, [3]Siemens Healthineers, Erlangen, Germany, [4]Massachusetts General Hospital, Boston, MA

Purpose

We assessed the frequency of paramagnetic rims and central vein signs (CVS) associated with multiple sclerosis (MS) lesions using highly accelerated 3D Wave-CAIPI susceptibility-weighted imaging (Wave-SWI) and FLAIR (Wave-FLAIR) sequences for

characterization of demyelinating lesions in MS within clinically feasible scan times. The sensitivity and specificity of central vein sign lesion criteria using the Wave-CAIPI accelerated images was evaluated.

Materials and Methods

67 patients undergoing MRI for the clinical evaluation of demyelinating disease from June 2020-January 2021 were scanned on 3T MRI systems (MAGNETOM Prisma and Vida, Siemens Healthcare, Erlangen, Germany). The imaging protocol included accelerated prototype 3D Wave-SWI (acceleration factor [R]=6, acquisition time [TA]=1:58min, 0.8x0.8x1.8mm) and 3D Wave-FLAIR (R=4, TA=2:30min, 1x1x1mm) sequences. The Wave-FLAIR and Wave-SWI sequences shortened the clinical MS protocol from 30 min to <20 min. Wave-FLAIR and Wave-SWI images were co-registered using built-in 3D registration software within the PACS (Visage). Two radiologists blinded to clinical diagnosis independently reviewed the co-registered image series and determined the number of lesions with paramagnetic rims and CVS. Discrepancies between raters were discussed, and a consensus was reached. We calculated the proportion of MS or clinically isolated syndrome (CIS) patients with paramagnetic rim lesions and/or CVS. We assessed agreement between raters in their independent review. Sensitivity and specificity were assessed on Wave-SWI and Wave-FLAIR for a CVS criteria for MS diagnosis, defined by an absolute number of lesions with CVS.

Results

Of the 67 patients evaluated, 46 patients (68.7%) had confirmed MS by 2017 McDonald criteria, 7 had clinically isolated syndrome (CIS) (10.4%), and 14 had a non-MS diagnosis (20.9%). Of the 53 patients with MS or CIS, paramagnetic rims were identified in 22 cases (41.5%). 39 cases had at least one lesion with CVS (73.6%). There was substantial agreement between raters (91.04% - Cohen $k=0.78$, $p < 0.01$) before consensus. The CVS criteria had a sensitivity of 0.63 and a specificity of 0.90. This is consistent with reported calculations for the same CVS diagnosis criteria using longer encoding techniques.

Conclusions

Highly accelerated Wave-CAIPI allows for a more comprehensive protocol for characterization of demyelinating lesions and provides additional information to improve confidence in the diagnosis of MS and assessment of disease progression.

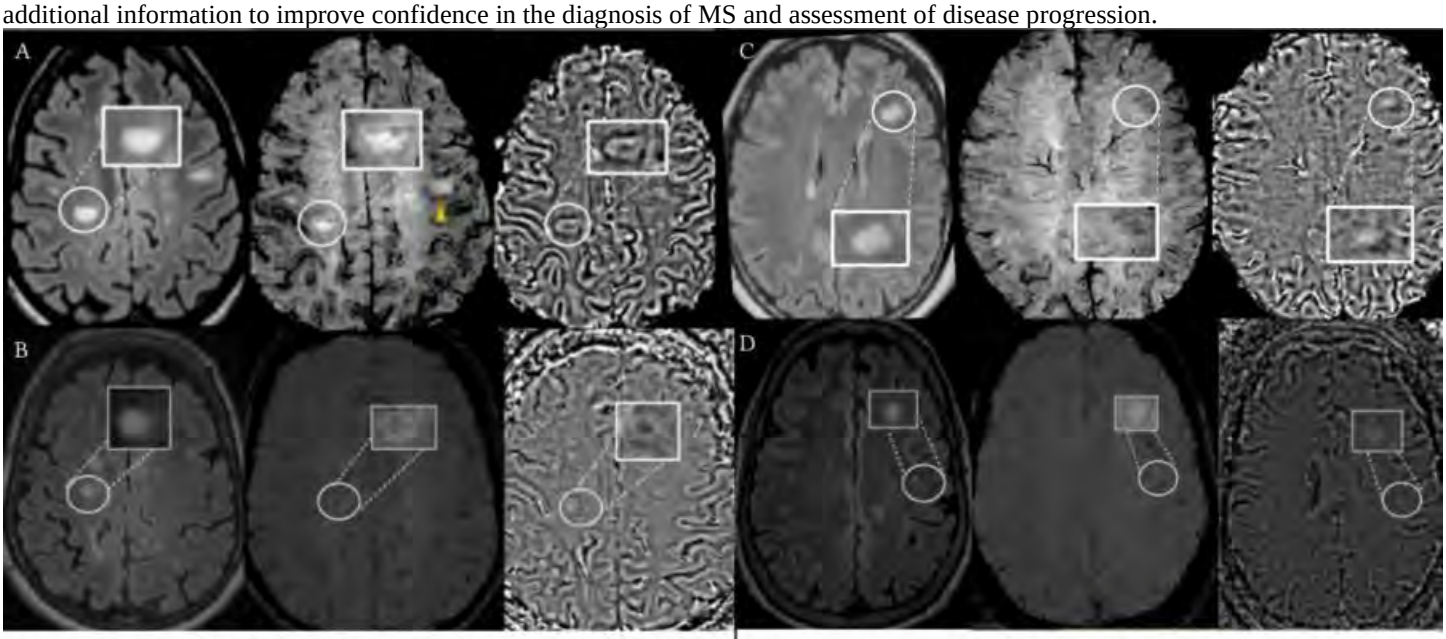

Fig 1: Representative examples of MS patients with central vein sign and paramagnetic rims.

A. Axial Wave-SPACE-FLAIR (left), Wave-SWI (middle), and phase images (right) in a patient with confirmed MS showing the presence of paramagnetic rims corresponding to lesions visible on FLAIR (highlighted).

B. Axial Wave-SPACE-FLAIR (left), Wave-SWI (middle), and phase images (right) in a patient with confirmed MS showing the presence of paramagnetic rims.

Fig 2: Representative examples of non-MS patients without lesions containing paramagnetic rims or central vein signs.

C. Axial Wave-SPACE-FLAIR (left), Wave SWI (middle), and phase images (right) in a patient with confirmed anti-MOG disease with no visible paramagnetic rim around the lesion visible on FLAIR. No lesions with a central vein sign were identified on Wave-FLAIR and Wave-SWI.

D. Axial Wave-SPACE-FLAIR (left), Wave SWI (middle), and phase images (right) in a chronic migraine patient with no visible lesions with a paramagnetic rim or a central vein sign.

(Filename: TCT_148_Figure1_ASNR.jpg)

1118

Correlation between post-contrast SWI and post-contrast T1 sequences for detection and active search of active lesions in Multiple Sclerosis

A Lima Júnior[1], P Coimbra[2], A Brandão Nascimento[3], J Rodrigues[4]

[1]Mount Sinai Hospital, New York, NY, [2]Antonio Prudente Hospital, Fortaleza, Ceara, [3]UNIRIO(UNIVERSIDADE FEDERAL DO ESTADO DO RIO DE JANEIRO), RIO DE JANEIRO, RIO DE JANEIRO, [4]Antonio Prudente Hospital, Fortaleza, Fortaleza

Purpose

Multiple slerosis is characterized as a multifactorial demilienizing disease that affects several areas of the central nervous system. Among the main ways of evaluating acute/subacute and chronic multiple sclerosis involvement is the cranial magnetic resonance. Usually, the diagnosis is eminently clinical, however the post-contrast T1-weighted sequences have great sensitivity for detecting active foci/inflammation resulting from multiple sclerosis activity. Lately, the post-contrast magnetic susceptibility (SWI) sequences

(Amaral et al.) for the detection of active multiple sclerosis plaques in the breakdown of the blood-brain barrier have been gaining strength. The present study aims to determine the post-contrast SWI accuracy for active multiple sclerosis lesions using the standard T1 spin sequence
Materials and Methods
Retrospective analyzes of 51 patients were performed, the two independent observers (the first neuroradiologist with 12 years of experience and the second neuroradiologist with 5 years of experience) in a 3T MRI machine, with patients undergoing an additional sequence of post-contrast swi that is not part of the standard protocols for studying multiple sclerosis. Correlation between observers was described by the Cohen K score. The standard sequence adopted was the post contrast T1 spin echo. Thus, the specified sensitivity, positive predictive value and negative predictive value were calculated for the post-contrast SWI sequence
Results
The post-contrast swi sequence showed similar sensitivity to post-contrast T1 in method detection in detecting active demyelinating lesions. Some lesions were observed in the post-contrast swi sequence, not being noticed in the post-contrast T1 spin-echo sequence, and it is not possible in this study to characterize whether such lesions are false negatives or active lesions that were not characterized by the post-contrast T1-spin echo sequence. New retrospective cohorts with the realization of a sequence of the "gadolinium T1 magnetization transfer contrast" sequence (sequence considered more sensitive for the detection of demyelinating lesions) may clarify these questions. The interobserver agreement was high evaluating the cohen score.
Conclusions
The incorporation of the studied sequence in protocols for screening for active demyelinating multiple sclerosis lesion can benefit the patient with a small burden of increasing the examination time. Additional studies are needed to strengthen the evidence for such a benefit.

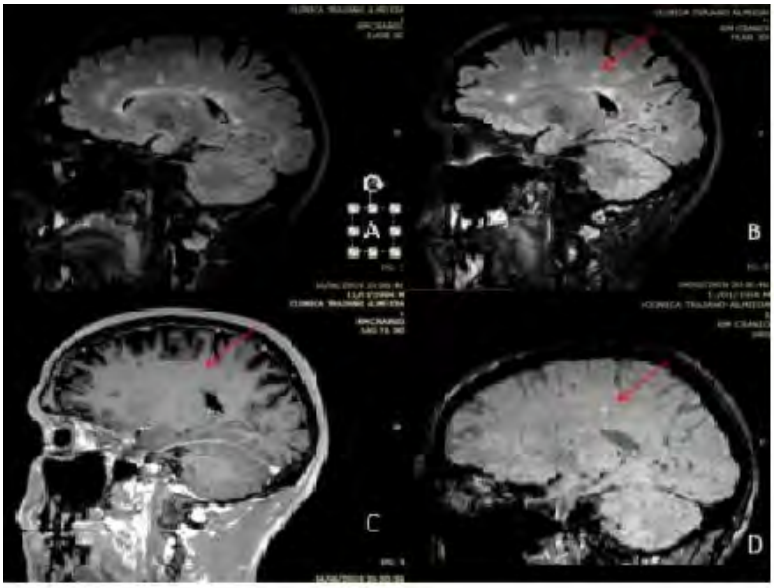

(Filename: TCT_1118_imagem1asterisco.jpg)

757

Domain Knowledge and Uncertainty Maps Improve Synthetic MRI in Multiple Sclerosis: A Multicenter Validation Study

B Wiestler[1], T Finck[1], S Schlaeger[1], H Li[1], B Bender[2], M Mühlau[1], B Menze[1]
[1]TU Munich University Hospital, Munich, Germany, [2]Tuebingen University Hospital, Tuebingen, Germany

Purpose
Generative adversarial networks (GANs) enable to synthesize high-contrast MR images from lower-contrast input. We here investigate the generalizability of a novel GAN designed to synthesize high-contrast double inversion recovery (DIR) images using a novel lesion attention loss and additionally evalute the use of uncertainty maps to further enhance the clinical utility and trustworthiness of synthetic images.
Materials and Methods
A GAN was trained to synthesize DIR images from input fluid-attenuated inversion recovery (FLAIR) and T1w data of 50 MS patients (training data). A novel lesion attention loss was incorporated into the training, forcing the network to pay specific attention to MS lesions. In another 50 patients (test data), two blinded readers (R1&R2) independently quantified lesions in synthetic DIR (synthDIR), acquired DIR (trueDIR) and FLAIR. Of the 50 test patients, 20 were acquired on the same scanner as the training data (internal data), while 30 were scanned at different scanners with heterogeneous field strengths and protocols (external data). Lesion-to-Background ratios (LBR) and image quality parameters were calculated for quantitative comparison. Uncertainty maps were generated to visualize model confidence in the synthetic images.
Results
Significantly more MS-specific lesions were found in synthDIR compared to FLAIR (R1: 26.7 ± 2.6 vs. 22.5 ± 2.2 $p<0.0001$; R2: 22.8

± 2.2 vs. 19.9 ± 2.0, p=0.0005). While trueDIR remained superior to synthDIR in R1 [28.6 ± 2.9 vs. 26.7 ± 2.6 (p=0.0021)], both sequences showed comparable lesion conspicuity in R2 [23.3 ± 2.4 vs. 22.8 ± 2.2 (p=0.98)]. Importantly, improvements in lesion counts were comparable in internal and external data, demonstrating the generalizability of the network. LBR confirmed that targeted translation through attentional learning improves lesion conspicuity compared to a network trained without lesion attention (2.80 ± 0.67 vs. 2.69 ± 0.66, p<0.001). Uncertainty maps supported the discrimination between correctly translated lesions and false-positive hyperintensities by highlighting these false-positive hyperintensities as areas of high variance.

Conclusions

This multicenter study confirms the external validity of a Deep Learning tool for synthetic DIR generation. By including lesion attention, the translation of MS lesions is further improved. Uncertainty maps are promising to increase the trustworthiness of synthetic images. The model is freely available at https://figshare.com/articles/software/synthDIR/16607831.

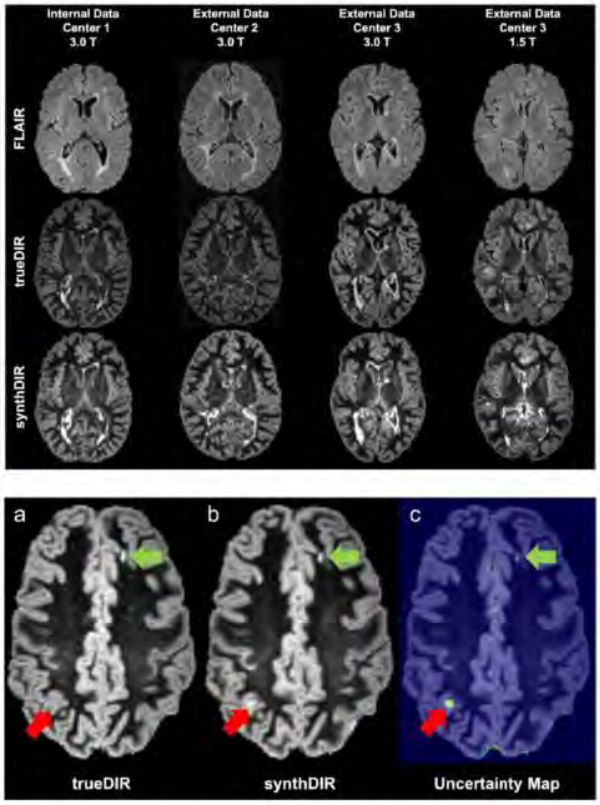

Top panel: Exemplary images of FLAIR, trueDIR and synthDIR for all centers and scanners.

Bottom panel: Uncertainty maps provide relevant information regarding the validity of image-to-image translation. In the synthDIR (b), a false-positive lesion (red arrow) is easily recognized by the high model uncertainty (c) as opposed to a true lesion (green arrow).

(Filename: TCT_757_figure1.jpg)

1170

Free-water diffusion tensor imaging detects occult periependymal abnormality in the AQP4-IgG-seropositive neuromyelitis optica spectrum disorder

K Choi[1], M Kim[2], J Kim[1], I Hwang[1]

[1]Seoul National University Hospital, Seoul, Republic of Korea, [2]Kangbuk Samsung Hospital, Seoul, Republic of Korea

Purpose

To compare free-water corrected diffusion tensor imaging (DTI) measures in the normal-appearing periependymal area between AQP4-IgG-seropositive NMOSD and multiple sclerosis (MS) to investigate occult pathophysiology

Materials and Methods

This prospective study included 44 patients (mean age, 39.52±11.90 years; 14 men) with AQP4-IgG-seropositive NMOSD (n = 20) and MS (n = 24) who underwent DTI between April 2014 and April 2020. Based on free-water corrected DTI measures obtained from

normal-appearing periependymal voxels of (1) lateral ventricles and (2) the 3rd and 4th ventricles as dependent variables, MANCOVA was conducted to compare the two groups, using clinical variables as covariates.
Results
A significant difference was found between AQP4-IgG-seropositive NMOSD and MS in the 3rd and 4th periependymal voxels (λ = 0.462, P = 0.001). Fractional anisotropy, axial diffusivity was significantly decreased and radial diffusivity was increased in AQP4-IgG-seropositive NMOSD in post-hoc analysis, compared with MS (F=27.616, P < 0.001, F=7.336, P = 0.011, and F=5.800, P = 0.022, respectively).
Conclusions
Free-water corrected DTI measures differ in the periependymal area surrounding the diencephalon and brain stem/cerebellum between MS and NMOSD, which may suggest occult white matter injury in areas with distribution of AQP-4 in NMOSD.

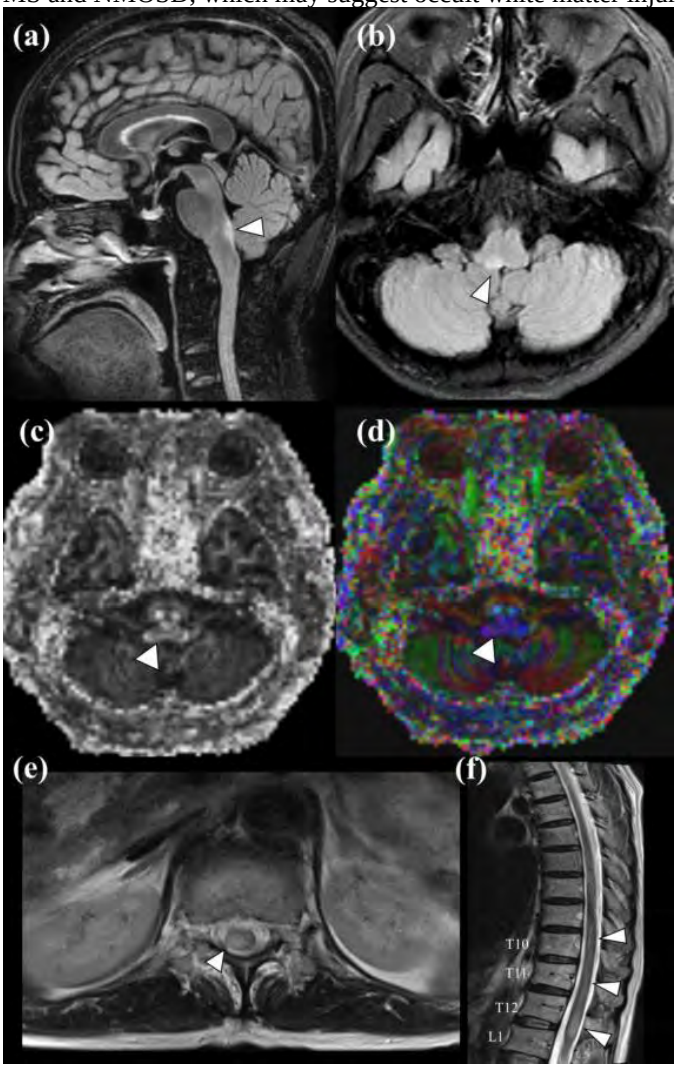

(Filename: TCT_1170_Fig2.jpg)

1195
Improved Detection of New Multiple Sclerosis Lesions on Routine Longitudinal Brain MRI by Human Readers Using Statistical Detection of Change Algorithm
M Homssi[1], E Sweeney[1], E Demmon[1], W Mannheim[1], M Sakirsky[1], Y Wang[1], A GUPTA[1], S Gauthier[1], T Nguyen[1]
[1]*Weill Cornell Medicine, New York, NY*

Purpose
Multiple sclerosis (MS) patients often undergo regular brain MRI for lesion activity monitoring. Detecting lesion incidence on non-coregistered high-resolution (typically 1mm isotropic) images from two scans is time-consuming and prone to error. The statistical detection of change (SDC) algorithm, which identifies new lesions from the subtraction image of two coregistered images [1], has shown potential in a pilot study [2]. Our objective was to evaluate the improvement in the detection performance of human readers when assisted by SDC in image review in a large patient cohort.
Materials and Methods
This was a retrospective cohort study of 200 consecutive MS patients who had two brain MRIs approximately one year apart. T2W FLAIR images were brain-extracted, bias-field corrected using FSL, and coregistered to a half-space using ANTs. SDC was applied to

the subtraction image to detect areas of lesion growth, which were shown to a board certified neuroradiologist during review of the coregistered images (Figure 1). The performance of this Reader+SDC method for new lesion detection on a per patient basis was compared to that of the traditional neuroradiologist reader only (Reader) method as captured in the neuroradiology reports.

Results

Of the total 200 patients, Reader+SDC found new lesions in 42 patients (21%), while Reader detected new lesions in only 20 patients (10%%) (Table 1). The agreement between the two methods was found to be 87%. Figure 1 shows an example of a small periventricular MS lesion not definitively detected during routine image review, which was captured by readers with the use of SDC.

Conclusions

Our results showed that SDC can improve detection of new lesions by human readers on longitudinal T2W FLAIR images. Designed to achieve high detection sensitivity with moderate positive predictive value [1], SDC is well suited for a semi-automated workflow where human readers can quickly eliminate false positives among the potential new lesions. Future works will focus on increasing SDC performance and exploring its application in other brain diseases.

	Review by reader and SDC		
	No	Yes	All
Total	159 (100)	42 (100)	200
Review by reader only (radiology reports)			
No	156 (98.7)	24 (57.1)	180 (90)
Yes	2 (1.3)	18 (42.9)	20 (10)

Table 1. Contingency table showing agreement between review by reader only with review by reader and SDC.

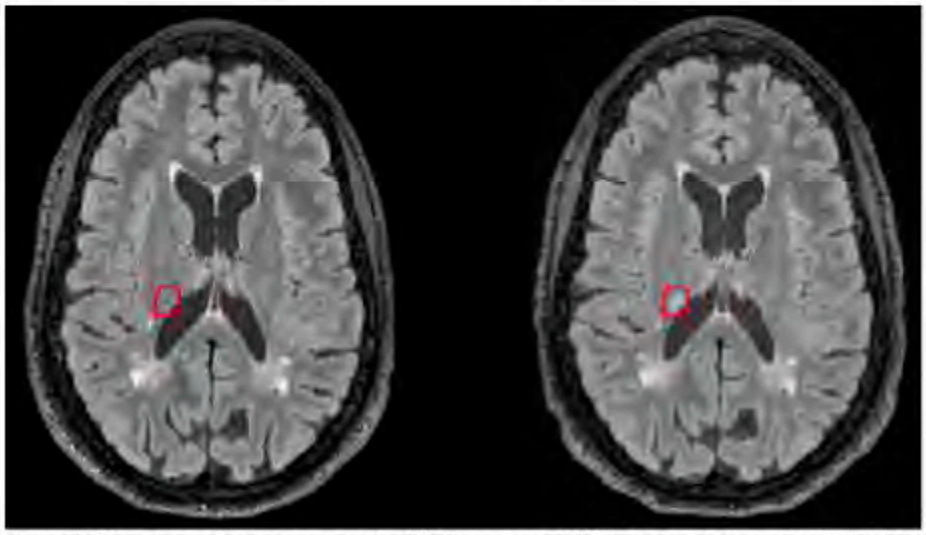

Figure 1. New interval lesion outlined by SDC generated ROI. This lesion was detected by SDC with reader review and not identified on radiology report.

(Filename: TCT_1195_ASNRfigures.jpg)

1111

Improved Detection, Description and Efficiency of Multiple Sclerosis Lesions' Assessment using a Semi-Automatic Dedicated Deep-Learning Based Software

C Federau[1], G Zhu[2], N Hainc[3], S Paganucci[1], L Kipp[4], M Wintermark[4]

[1]AI Medical AG, Zollikon, CA, [2]Stanford University, Stanford, CA, [3]University Hospital Zurich, Zürich, WY, [4]Stanford, Stanford, CA

Purpose

Multiple sclerosis (MS) requires yearly follow-up controls with MRIs, 1 which involves the tedious, time-consuming, and error-prone manual comparing and counting of the patient's demyelinating lesions. We evaluate the software Jazz, 2 a semi-automatic, deep-learning based software for the efficient assessment of MS images, wherein "semi-automatic" refers to the fact that each process gets verified by a radiologist. The software optimizes the reading time of the radiologist, by preprocessing the images before displaying them, including contrast recognition and image coregistration. Jazz permits efficient navigation with single-click switches to images of previous exams and to different contrasts of the same exam, and includes lesion pre-segmentation using a deep learning networks, and efficient correction tools to verify and modify these segmentations.

Materials and Methods

Two sets of respectively 40 and 20 MS follow-up examinations were collected, including 3D FLAIR, and pre- and post-Gad T1-weighted 3D images, and processed through the Jazz software. The cases were read by two experienced neuroradiologists and reading

time was recorded. Ground truth was defined by reevaluating all described lesions in all reports. In the first set, a standard report was produced and compared to the standard report. In the second set, a full quantification of the lesion load was performed, by correcting the deep-learning lesion segmentation, and the clinical performance of the network was assessed.
Results
In the first set, reading using Jazz took on average 2m8s±59s per case. The ground truth reported 30 new lesions (NL), and 44 slowly evolving lesions (SEL). No gadolinium-enhancing lesions were described in any report. The standard report reported a total of 5 NL and no SEL, missing 25 NL. Using Jazz, an average of 24 NL and 24 SEL were reported, missing 11 NL. In the second set, neuroradiological reading including volumetric correction took on average 10m26s±7m45s. The deep learning predictions required corrections in all cases by both readers, with on average 28±20 true positive lesions, 3±4 false negative lesions, 8±8 false positive lesions, and a lesion volume correction of 0.5±1.3mL. Interreader cohen's kappa was 0.9.
Conclusions
A significant larger number of NL are reported with Jazz, in a very time efficient manner, permitting significant gain in productivity. A neuroradiologically controlled, quantitative load assessment with numerization of a structured report can be obtained in 10 minutes per case.

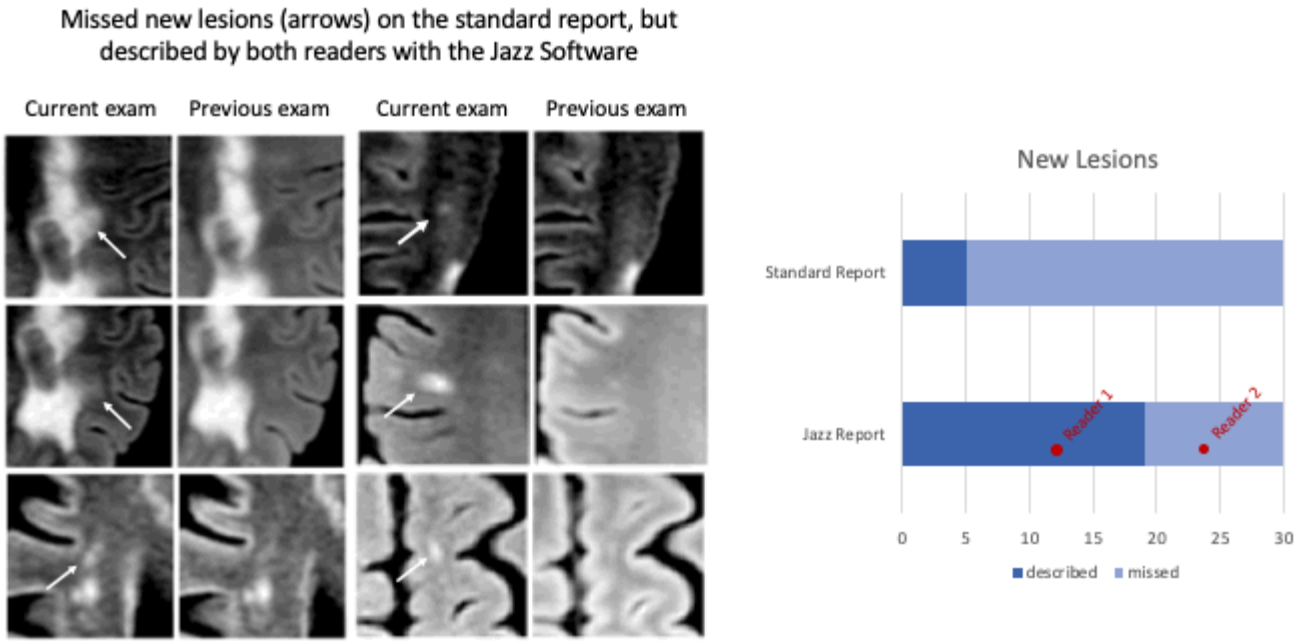

(Filename: TCT_1111_figures.gif)

337
Quantitative Analysis of MS Lesion in Cervical Spinal Cord (CSC) using Ultrahigh-b DWI (UHb-DWI)
L Shah[1], K Jeong[1], Y Lee[1], B Thapa[2], N Sapkota[2], E Bisson[1], N Carlson[3], E Jeong[4], J Rose[4]
[1]University of Utah, Salt Lake Cty, UT, [2]University of Utah, SALT LAKE CITY, UT, [3]Wahlen Veteran Administration Hospital, SALT LAKE CITY, UT, [4]University of Utah, Salt Lake City, UT

Purpose
Spinal cord injury in multiple sclerosis (MS) can cause major disabilities due to varying degrees of axonal demyelination and/or damage. Unfortunately, current conventional MRI has limited ability to detect MS with high specificity. Our Ultrahigh-b DWI (UHb-rDWI) quantitatively observes water diffusivity in intra-/extra-axonal spaces in cervical spinal cord (CSC) white matter (WM) of MS patients, providing greater insight into CSC pathology with respect to demyelination, inflammation, and axonal damage. The purpose of this project is to compare quantitative values obtained from UHb-rDWI in CSC WM of healthy controls and in both MS normal appearing WM and MS WM lesions.
Materials and Methods
Seven patients (five relapsing remitting (RRMS), two 2 primary progressive (PPMS)) and seven healthy controls were selected with consent to participate in this IRB-approved study. RRMS patients had relapses, corticosteroid therapy, and clinical MRI scans of the CSC. Two patients (MS1: 48-yr-old male, MS2: 22-yr-old female) are presented in this abstract. UHb-DWI data were acquired with bmax8800 s/mm2 at a 3T MRI system using 2D ss-DWSTEPI-rFOV pulse sequence and a CSC-dedicated 8-channel array coil. Monte Carlo Simulation (MCS) was used to estimate the degree of demyelination.

Results
The diffusion coefficient (DH) showed high-b diffusivity was measured (0.767±0.297)x10-3 mm2/s in the posterior column lesions, averaged over 6 MS patients, and 0.587x10-3 mm2/s in the corticospinal tracts of another patient. The averaged DH of the 7 healthy volunteers was (0.0312±0.0306)x10-3 and (0.0505±0.0205)x10-3 mm2/s in the posterior and lateral columns, respectively. Monte Carlo Simulation suggested approximately 30% and 15% demyelination in MS1, and 40% and 15% demyelination in MS2, in the lesion and NAWM, respectively.
Conclusions
UHb-DWI of the CSC reveals a marked difference in signal-b-curves and DH values in MS lesions compared to NAWM and healthy control WM. Therefore, our UHb-rDWI method can be a powerful tool to provide quantitative evaluation of the degree of axonal damage in MS lesions.

Tuesday, May 17, 2022
10:30-11:30 AM
Scientific Podium Presentations: TBI

696

7T MRI versus 3T MRI of the Brain in Professional Fighters and Traumatic Brain Injury Patients

J Lee[1], C Bernick[2], A Ritter[3], S Stephen[4], J Joyce[5], A Mangat[6], S Jones[7]
[1]Cleveland Clinic, Brecksville, OH, [2]Cleveland Clinic Foundation, Cleveland, OH, [3]Cleveland Clinic, Las Vegas, NV, [4]University of Rochester School of Medicine, Rochester, NY, [5]UC Health, Cincinnati, OH, [6]N/A, N/A, [7]Cleveland Clinic, Cleveland, OH

Purpose
Prior study with a large cohort of fighters in the Professional Fighters Brain Health Study (PFBHS) showed no statistical difference in the number of nonspecific WM changes (NSWMC) and cerebral microhemorrhages (CMH) at 3T MRI compared to controls. Additionally, there is controversy whether traumatic brain injury patients (TBI) have different changes in the brain compared to repetitive trauma that fighters are exposed to. Recently, the 7T MRI has become a new tool used for potentially greater accuracy in neurological diagnosis, and provides greater signal to noise ratio, smaller voxel size, and greater sensitivity to susceptibility effects. This study utilizes 7T MRI in order to evaluate whether more NSWMC changes and CMH can be seen in fighters at 7T versus controls, and to compare any differences with traumatic brain injury patients.
Materials and Methods
MRI scans of 19 professional fighters, 16 TBI patients, and 10 controls were examined by two board certified neuroradiologists with 5 years (JL) and 14 years (SJ) experience.
Results
The two readers agreed on the presence/absence of white matter changes for 79% (27/34) of patients with 3T (Cohen's kappa: 0.48) and for 93% (41/44) of patients with 7T (Cohen's kappa: 0.69). The two readers agreed on the presence/absence of hemorrhages for 91% (31/34) of patients with 3T (Cohen's kappa: 0.72) and for 96% (43/45) of patients with 7T (Cohen's kappa: 0.86). For both readers and in both patient subgroups (fighter and TBI), the number of white matter changes detected tended to be greater with 7T MRI compared to 3T. There was, however, no statistically significant difference in the number of hemorrhages detected with 7T MRI versus 3T MRI. For both readers, there was no statistically significant difference in the number of white matter changes (using 7T) for fighters compared to either controls or TBI patients. There was also no statistically significant difference in the number of hemorrhages detected among the patient groups.
Conclusions
There is increased prevalence of NSWMC on 7T as compared to 3T MRI for fighters and TBI patients, which may indicate that many NSWMC are missed by conventional 3T imaging, but this was not statistically different than controls in our small patient population. No differences in microhemorrhages were found on either 3T or 7T images likely due to low prevalence, which supports the earlier at 3T.

816

A Comprehensive Approach to Resting-State Functional Connectivity in Patients with Mild Traumatic Brain Injury

S Arabshahi[1], S Chung[2], P Amorapanth[2], A Laine[1], S Flanagan[2], Y Lui[2]
[1]Columbia University, New York, NY, [2]NYU Grossman School of Medicine, New York, NY

Purpose
Sequalae of Mild Traumatic Brain Injury (MTBI) include a broad group of symptoms, and several studies suggest there is altered connectivity within functional networks after injury. Unfortunately, reports within this body of literature are difficult to synthesize, with small cohorts and different statistical approaches to protect against false discoveries. Here, we take an unbiased, broad, and comprehensive approach to investigating resting-state functional connectivity (rsFC) in MTBI without a priori assumptions, employing rigorous statistical methods.

Materials and Methods

100 subjects were studied (55 MTBI within a month of injury; 45 normal controls (NC), Table 1) using conventional closed-eyes rs-fMRI sequence performed on 3T MRI scanners (Skyra/Prisma, Siemens). Pearson's correlation coefficient between each pair of 32 ROIs within 10 major brain networks in each group was calculated to measure rsFC after preprocessing/denoising, were transformed to Fisher's Z-scores and controlled for age, gender, and scanner type. Functionally connected ROIs were identified (one-sample t-test), and between-group differences were revealed by using independent Welch's t-test. Benjamini-Hochberg's false discovery rate (FDR) correction was employed for multiple comparisons.

Results

Out of 496 connections, 86 (MTBI) and 120 (NC) significant connections are identified in each group (corrected $p < 0.05$, Fig. 1). However, only 13 connections showed significant differences between MTBI and NC groups (Welch's t-test, corrected $p < 0.05$, Fig. 2); among them, 4 exhibited hyperconnectivity (MTBI > NC) and 9 exhibited hypoconnectivity (MTBI < NC).

Conclusions

It appears that there are fewer functional connections in MTBI subjects compared with NCs, suggesting that the graph of functionally connected regions in resting-state differs as a consequence of MTBI. In particular, there appear to be differences in within-network rsFC between the two groups. However, between-group analysis identifies 13 significantly different connections (2.6% of 496 connections), falling within the FDR marginal allowance of false discoveries of 5%. This could be improved by using advanced harmonization methods, larger sample size, and methods such as independent component analysis and dynamic functional connectivity. In addition, a more directed hypotheses to minimize the statistical dimensionality of the problem could help yield further insights.

Table 1 Subjects' demographics.

	MTBI (55 subjects)	NC (45 subjects)	Statistic
Age (year)	18 – 65 (35.52 ± 12.48)	19 – 65 (34.15 ± 11.40)	$t = -0.56$, $p = 0.57$
Gender (M/F)	20/35	18/27	$\chi^2 = 0.005$, $p = 0.94$
Scanner (Skyra/Prisma)	30/25	26/19	$\chi^2 = 0.004$, $p = 0.94$

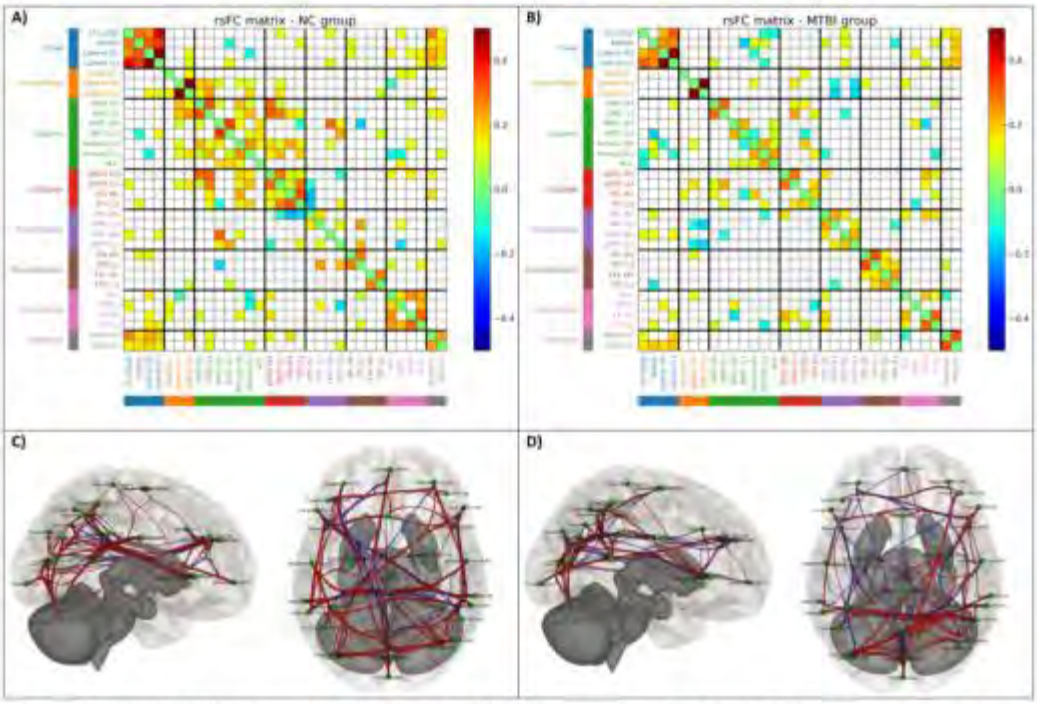

Figure 1. Resting-stat functional connectivity (rsFC) matrix of 32 ROIs within 10 major brain networks (Visual Sensorimotor, Salience, Language, Frontoparietal, Dorsal Attention, Default Mode, and Cerebellar): among a total of 495 connections, (A) 120 connections in the NC group and (B) 86 connections in the MTBI group are identified as significant (FDR-corrected, $p < 0.05$). The color map indicates the Fisher's Z-score of correlation coefficient, ranging from -0.5 to 0.5. The corresponding significant connections are shown in MNI template space as edges for (C) NC and (D) MTBI groups. The red and blue links indicate positively and negatively correlated ROIs, respectively.

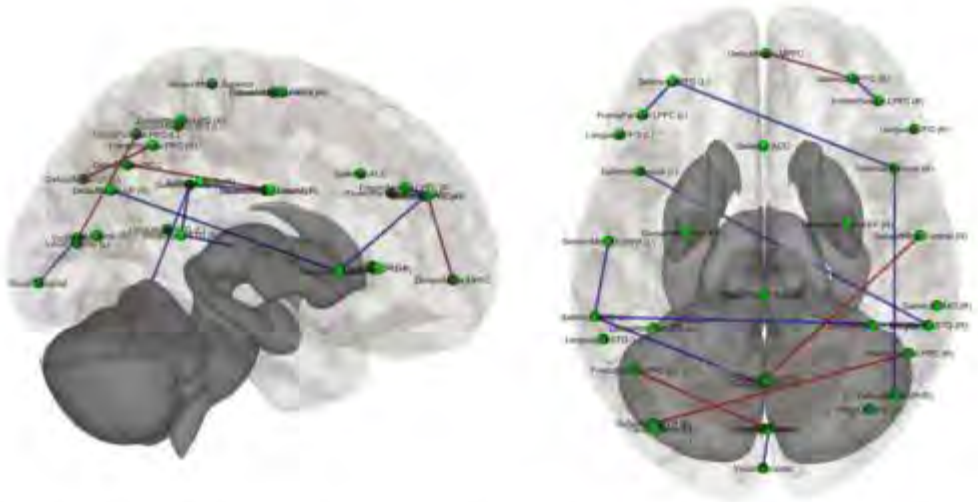

Figure 2. 13 significantly different connections between NC and MTBI groups that survive multiple comparison (FDR-corrected, $p < 0.05$), including 4 hyperconnectivity (MTBI > NC; Red) and 9 hypoconnectivity (MTBI < NC; Blue).

(Filename: TCT_816_GraphicFile3.jpg)

796

Deep Neural Network Analysis of CT Scans to Predict Long-term risk of Post-traumatic Epilepsy after Severe Traumatic Brain Injury

M Pease[1], C Liu[1], A Dooman[1], J Elmer[1], A Puccio[1], J Castellano[1], J Gonzalez-Martinez[1], D Okonkwo[1], S Wu[1]
[1]*UPMC, Pittsburgh, PA*

Purpose
Post-traumatic epilepsy (PTE) occurs in 10-20% of patients with severe traumatic brain injury (TBI) and accounts for 20% of symptomatic epilepsy. Known risk factors include penetrating injury, depressed skull fractures, and cerebral contusions. Despite the outsized impact of PTE, no validated model exists to predict which patients will develop PTE. We hypothesized that a deep learning analysis of CT scans and clinical information could predict long-term risk of PTE.
Materials and Methods
We reviewed severe TBI patients treated from November 2002 to December 2018 at a single level 1 trauma center, excluding those with prior seizure history, missing clinical information, or unusable CT head scan. Using definitions from the International League Against Epilepsy, a seizure was defined as a witnessed clinical event confirmed to be a seizure by the treating healthcare team or electroencephalography, and PTE as two or more seizures. We applied a convolutional neural network (CNN) to build a model using admission CT head scans to predict long-term risk for PTE (Imaging Model). The Imaging Model used an AlexNet backbone and was pre-trained with ImageNet. Next, we developed a machine-learning model with clinical variables available during the index hospitalization (Clinical Model). We then augmented the Imaging Model with the Clinical Model using the stacking ensemble technique to create a comprehensive, Fusion Model (Figure 1). The cohort was chronologically split into 70%, 10%, and 20% for training, validation, and independent testing.
Results
Of the 393 patients who survived to discharge, 257 remained after exclusions and removal of patients for missing information (Table 1). Fifty patients developed PTE and 207 had no seizure activity. Our CNN Imaging Model had an area under the receiver operating curve (AUC) of 0.71 (95% Confidence Interval [CI]: 0.55 – 0.84) for predicting PTE. The Clinical Model had an AUC of 0.73 (95% CI: 0.51 – 0.88). The combined, Fusion Model with CT head and clinical inputs performed best with an AUC of 0.77 (95% CI: 0.58 – 0.89; Figure 2).
Conclusions
Deep learning models can successfully predict the long-term risk for post-traumatic epilepsy after severe TBI using information available during the index hospitalization. This type of AI model could guide care through identifying at-risk TBI patients. Our study is limited as a single-center study and requires external validation.

Table 1. Patient Characteristics

	Description		No Seizure	Seizure
Demographic	Age		38 +/- 16	32 +/- 14
	Race	American Indian	0.4%	2%
		Asian/Indian	1%	0%
		Black	9%	3%
		White	89%	95%
		Other	0.4%	0%
Clinical	GCS	3	12%	14%
		4	7%	7%
		5	11%	8%
		6	17%	22%
		7	41%	44%
		8	11%	5%
	Hypoxia		12%	16%
	Hypotension		24%	18%
	Major extracranial injury		16%	11%
	EVD hemorrhage		12%	11%
	CNS Infection		7%	19%
	DHC		20%	55%
	Craniotomy		30%	65%
	Shunt		12%	29%
	Lobectomy		2%	16%
	LOS		24 +/- 15	27 +/- 13
	ICU LOS		17 +/- 9	21 +/- 9
Laboratory	Glucose		155 +/- 60	160 +/- 64
	Hemoglobin		13.2 +/- 2.11	13.3 +/- 2.1
	INR		1.1 +/- 0.2	1.2 +/- 0.3
	Intoxicated		49%	46%
Radiographic	SDH		35%	53%
	EDH		11%	13%
	tSAH		77%	80%
	IVH		19%	20%
	Contusion		55%	63%
	Depressed Skull Fracture		12%	77%
	Petechial hemorrhage		68%	68%
	Obliteration of the 3rd ventricle		13%	68%
	Midline Shift		26%	31%
	MLS > 5mm		15%	30%
	Marshall CT score	1	7%	1%
		2	66%	48%
		3	6%	10
		4	5%	8%
		5	14%	32%
		6	2%	1%

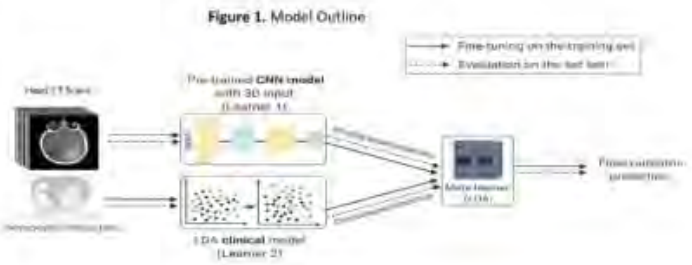

Figure 1. Model Outline

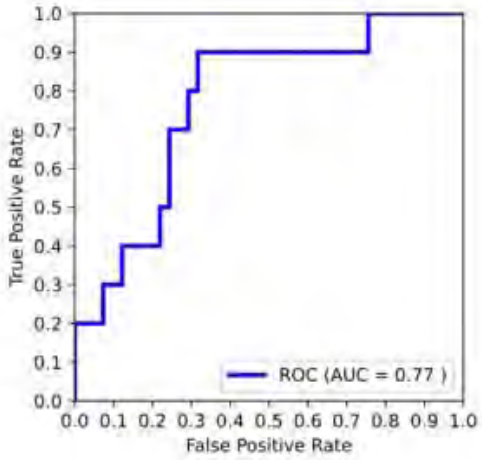

Figure 2. Receiver Operating Curve predicting rates of PTE

(Filename: TCT_796_0001.jpg)

811

Effect of Resolution on Quantifying Susceptibility and R2* of Cerebral Microbleeds in Traumatic Brain Injury

S Gharabaghi[1], M Jokar[1], S Buch[2], L Latour[3], A Griffin[4], E Haacke[2]

[1]SpinTech MRI, Inc., Bingham Farms, MI, [2]Wayne State University, Detroit, MI, [3]National Institutes of Health, Bethesda, MD, [4]Center for Neuroscience and Regenerative Medicine, Bethesda, MD

Purpose

To study the effect of resolution on quantitative susceptibility mapping (QSM) and transverse relaxation rate, R2* mapping of cerebral microbleeds (CMBs) using MRI.

Materials and Methods

The accuracy of localization and assessing CMBs in QSM and R2* depends on the imaging resolution. There is a systematic underestimation of susceptibility when the CMB is on the order of or smaller than several pixels [1,2]. To evaluate the dependence of the QSM and R2* values of the CMBs, we used a simulated model and ex vivo imaging at 7T of post-mortem brain data and its histopathological data for a TBI subject. The model includes a sphere with different radii (1-5,10,15,20,25 and 30 pixels) and susceptibility (0.5,1,1.5,2,2.5, and 3 ppm) in the center representing a CMB surrounded by white matter. After simulating the isotropic (0.1mm)3 magnitude and phase images [3], low resolution (LR) data was derived by doubling slice thickness (ST) in steps from 0.1 to 1.6mm with fixed in-plane resolution followed by doubling both ST and in-plane resolution up to (1.6mm)3. After reconstructing QSM images at different resolutions, the susceptibility of CMBs were measured. For the ex vivo data with resolution=(0.42mm)3, k-space was truncated to simulate LR data by increasing the ST to 0.84, 1.26, 1.68, 2.1, and 3.36mm with fixed in-plane resolution and then the in-plane spacing was increased from (0.42mm)2 to (0.84mm)2, with ST of 0.84 and 1.68mm. Local QSM and R2* maps were reconstructed and mean R2* and susceptibility values of 11 punctuate (spherical) CMBs were measured.

Results

Based on the simulated data results (Figure 1), a CMB with radius r (mm) effectively vanishes in the QSM data when the ST is around 4r. Also, there is a drastic reduction in the measured susceptibility when the ST is greater than or equal to r. For the ex vivo data, both

measured R2* and susceptibility values decrease as the ST increases and resolution decreases. However, the magnetic moment (susceptibility×volume) is less affected by the resolution changes. Figure 2 shows smaller CMBs in the R2* map that have either disappeared in the QSM data (yellow arrow) or appear as a single CMB (red arrow). Furthermore, histopathological data suggests more wide-spread local vascular injury than can be resolved on MRI.

Conclusions

This work showed that CMBs great than 1/4 (1/8) the size of a voxel can be detected using QSM (R2*). Further, a single CMB seen in QSM may actually be multiple physically close small bleeds as revealed in the R2* map.

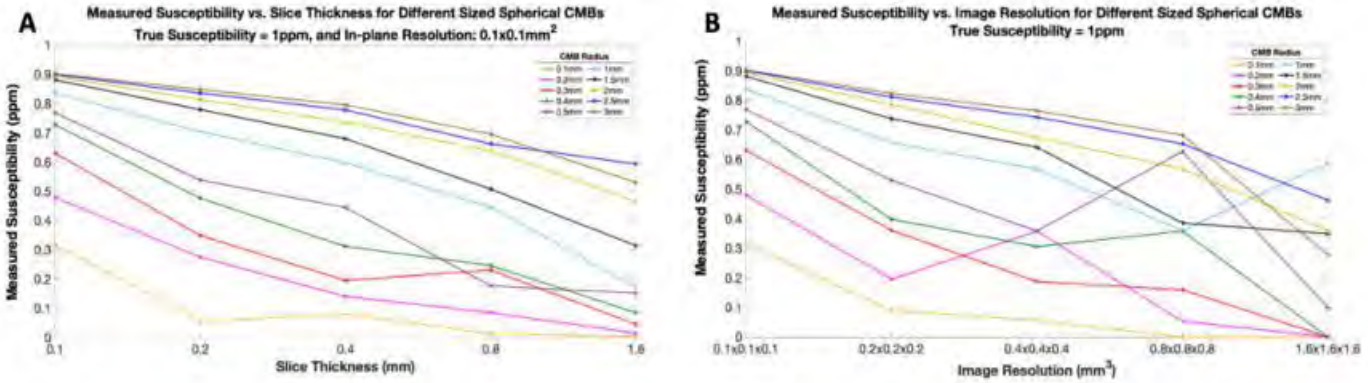

Figure 1. This figure compares the measured susceptibility versus slice thickness while in-plane resolution ($0.1\times0.1mm^2$) is fixed with variable slice thickness (A) and variable image resolution (B) for different sized spheres in the simulated CMB model with a true susceptibility value of 1ppm. The imaging parameters used for this simulation were: B_0=7T, FA=10°, TEs=1/6.09/15.99ms, TR=60ms, and the susceptibility measurements were performed in the TE=6.09ms.

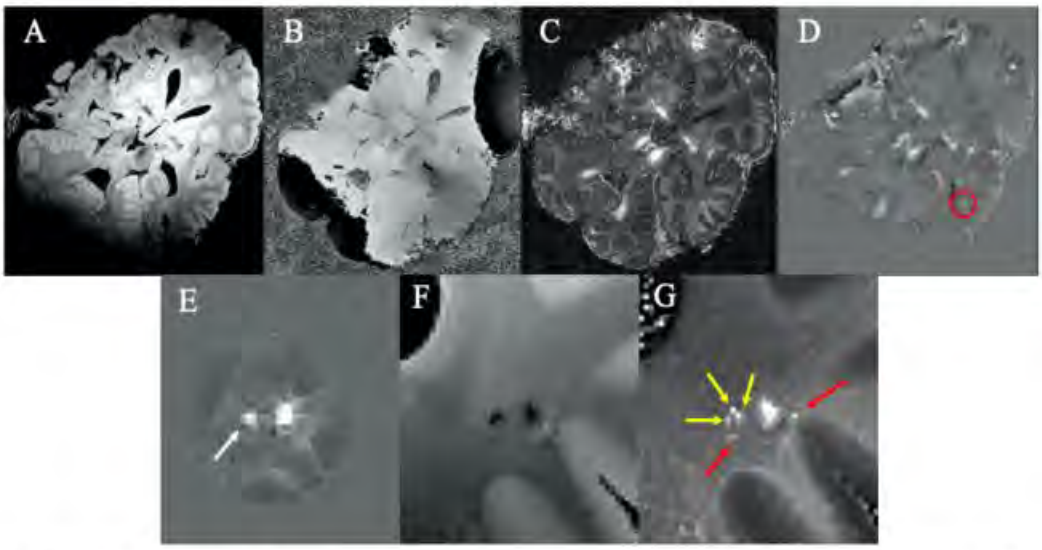

Figure 2. Original magnitude (A), phase (B), R2* (C), and QSM (D) images for the whole brain *ex vivo* dataset. The local QSM in the region defined by the red circle in (D) in the original image resolution of $(0.42mm)^3$ is shown in (E). The magnitude images (F) and R2* maps (G) for the corresponding local QSM are also shown. Comparing the QSM and R2* maps in the original resolution (E, G), it seems that the smaller CMB (shown by white arrow) is composed of three smaller CMBs shown by the yellow arrow in (G). There are also a few smaller CMBs in the R2* map shown by the red arrows in (G) that are not even visible in the local QSM image of the original resolution (E). All these images are from the first echo except the R2* maps that are generated from the first two echoes. The *ex vivo* post-mortem data was acquired with a 7T Siemens scanner (Siemens Healthcare, Erlangen, Germany) with: FA=10°, TR=60ms, TEs=6.09/15.99/25.89/35.79ms, bandwidth=150Hz/pixel, matrix size=384×384×88, FOV=256×192×139mm^3 and voxel resolution=$(0.42mm)^3$

(Filename: TCT_811_Latour_ASNR2022_15Nov2021_Figures_V3_SG.jpg)

1120

How Often is an MRI positive in Acutely Encephalopathic Patients, and Can the Presenting History Contribute to Predictive Analytics?

A McKinney[1], Y Koksel[2], J Rykken[3], T Braga[4], A Martin[5]

[1]University of Miami & Jackson Memorial Hospital, Miami, FL, [2]N/A, N/A, [3]University of Minnesota, Minneapolis, MN, [4]University of Miami, Miami, FL, [5]University of Miami, miami, FL

Purpose

MRI's are often ordered in acutely encephalopathies, but the diagnoses can be difficult due to insufficient history or a vague reason for examination (RFE). Scant literature exists on how often they are positive, and whether a more detailed RFE increases that likelihood; such data could lead to predictive algorithms. As such, this study's goals were to determine: 1) how often such MRI's are positive, and 2) if the data provided in a RFE's order affects the likelihood that a brain MRI will be positive.

Materials and Methods

Using a report search algorithm (VITREA Intelligence, Canon Medical, Minnetonka, MN, USA), 2475 MRI reports were identified over 3.5 years, using the terms "altered mental status", "confusion", "obtunded", "encephalopathy", and "level of consciousness". Children, followups, known tumors, and chronic conditions were excluded. Each report's RFE was graded as one of 3 probability categories for an MRI-identifiable syndrome: 1) "high probability/likelihood", 2) "medium", or 3) "low", based on the RFE's level of detail, which included evaluating whether an underlying condition was specified and/or specific symptomatology. A consensus review of two staff neuroradiologists and clinical data ensued as the "ground truth" as to whether an MRI was positive, with statistical calculations of sensitivity, specificity, likelihood ratios (LR), and odds ratios.

Results

The analysis included 1986/2475 reports (mean age 63.9 years), including both ED/inpatients (n=1373) and outpatients (n=614). Overall, 545/1986 (27.4%) were positive, and 1441 (72.6%) were negative; the 5 most common etiologies were infarct (n=251, 46.1%), PRES (n=69, 12.7%), tumor/carcinomatosis (n=50, 9.2%), hepatic encephalopathy (n=43, 7.9%), and infectious (n=31, 5.7%). There were 155/345 (44.9%) positives within the "high probability" category, 32.7% (n=374/1144) in the "medium", and 3.22% (16/497) in the "low " category. There was moderate sensitivity (78.9%), specificity (83.0%) and LR's (LR+=4.64, LR- =0.255) of the MRI being positive (based solely on the RFE) only in the outpatient group; the inpatient/ED group had less robust results.

Conclusions

A minority of encephalopathic patients are positive, being more frequent in ED/inpatients, as expected. However, the LR's, sensitivity, and specificity correspond better to the RFE in outpatients. Thus, the RFE itself can augment future predictive algorithms in outpatients, but further clinical data is likely necessary for such a predictive approach to apply to ED/inpatients.

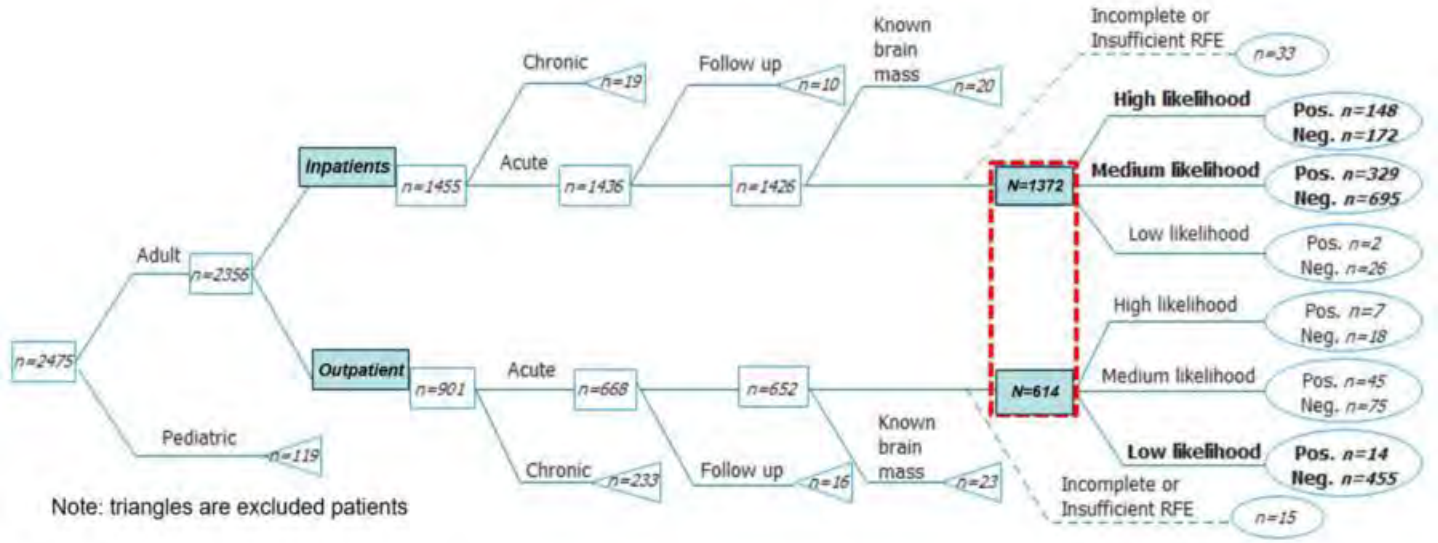

Statistic	All Patients	ED/Inpatient Group	Outpatient Group
Sensitivity	97.1%	99.6%	78.8%
Specificity	32.4%	01.1%	83.0%
LR^+	1.44	1.07	**4.64**
LR^-	**0.09**	0.38	**0.26**

LR > 10: Large, conclusive increase in likelihood of disease
5 – 10: Moderate increase in the likelihood of disease
2 – 5: Small increase in the likelihood of disease
1 – 2: Minimal increase in the likelihood of disease
1.0 : No change in the likelihood of disease
0.5 - 1.0: Minimal decrease in the likelihood of disease
0.2 - 0.5: Small decrease in the likelihood of disease
0.1 - 0.2: Moderate decrease in the likelihood of disease
LR < 0.1: Large, conclusive decrease in likelihood of disease

(Filename: TCT_1120_2022EncephalopathyASNRfigure.jpg)

1048

Prognostic Value of Initial Diagnostic Imaging Findings for Patient Outcomes in Adult Patients with Traumatic Brain Injury: A Systematic Review and Meta-Analysis

H Yu[1], S Ande[1], D Batoo[1], J Linton[1], J Shankar[1]
[1]*University of Manitoba, Winnipeg, Manitoba*

Purpose

Traumatic brain injury (TBI) is a significant cause of death and disability in the United States (1). NECT is a widely available imaging tool that can accurately and promptly diagnose catastrophic intracranial injuries post-TBI. Classification systems such as the Rotterdam CT score have been developed to prognosticate TBI patients based on CT findings (2). This review, however, aims to evaluate the prognostic value of features seen on initial imaging—completed within 24 hours of presentation—in adult TBI patients, particularly in those with severe TBI (GCS ≤8).

Materials and Methods

A comprehensive search was done in the databases Ovid MEDLINE and EMBASE for studies published on and before 2020. All imaging modalities were accepted. Studies were included if sample size ≥5 and all patients ≥18 years. Studies were excluded if imaging was not performed within 24 hours, if there were no outcome measures, and if the mechanism of insult was non-traumatic.

Results

19 of 4027 studies with 10,733 patients were eligible for inclusion; 7 studies with 603 patients solely investigated severe TBI patients. Modalities included NECT, perfusion CT (CTP), CT angiography, and transcranial doppler (TCD) ultrasound. GOS was the most common patient outcome measure, with GOS 1-3 generally defined as poor outcome and GOS 4-5 as good outcome. In all TBI patients, the presence of intracranial hemorrhage of any kind, midline shift, basal cistern compression, cerebral edema, MCA velocity ≤50 cm/s and pulsatility index (PI) >1, and decreased whole brain CBF and CBV on CTP were associated with poorer in- and out-of hospital outcomes. In the combined data for severe TBI patients, the presence of subarachnoid hemorrhage had a sensitivity of 67.7% (95% CI: 58.9 to 75.4) and a specificity of 62.5% (95% CI: 52.0 to 72.0) for predicting poor outcome. Intraventricular hemorrhage had high specificity (88.1%; 95% CI: 77.3 to 94.3) but very poor sensitivity (5.0%; 95% CI: 2.0 to 10.9) for predicting mortality, and midline shift had a 75.2% (95% CI: 66.4 to 82.4) sensitivity and a 71.9% (95% CI: 58.3 to 82.6) specificity for predicting mortality.

Limitations include study heterogeneity and the small number of studies that solely evaluated severe TBI patients and initial imaging findings.
Conclusions
Multiple initial imaging findings on NECT, TCD, and CTP are associated with poorer outcomes in both TBI patients in general and severe TBI patients. Awareness of these findings can aid in identifying patients at high-risk for morbidity.

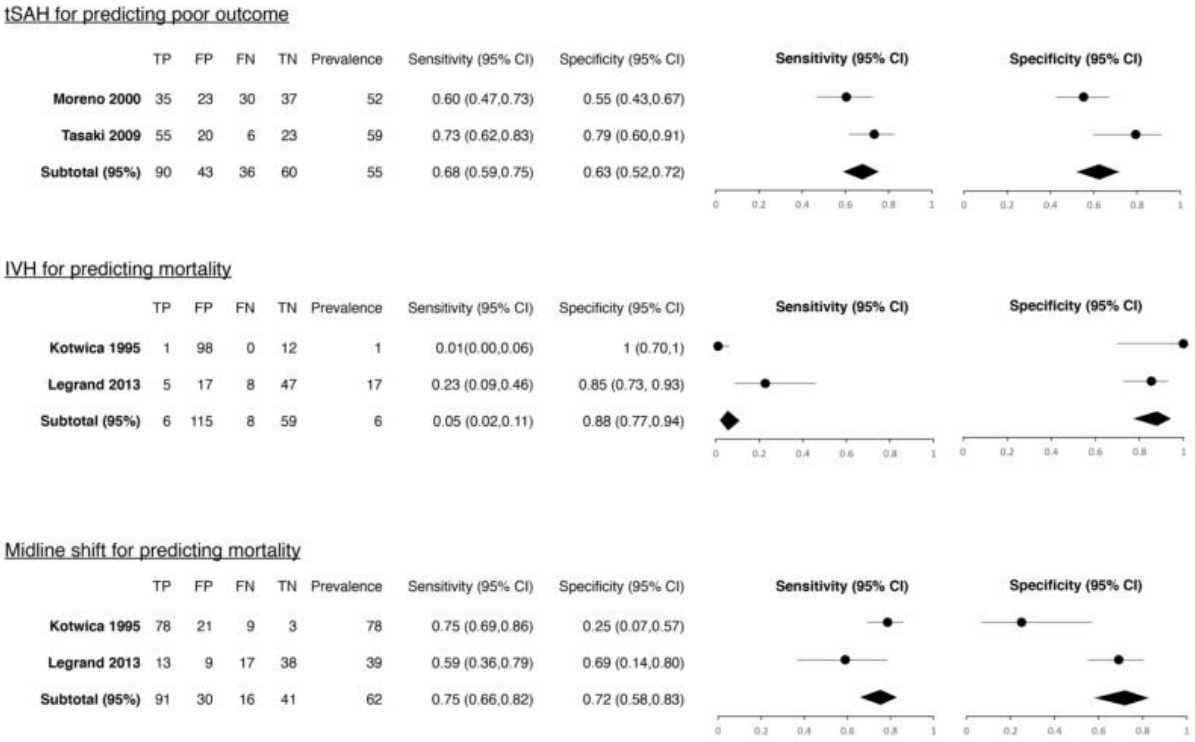

(Filename: TCT_1048_FigureASNR2022.jpg)

854

Resting-State Connectivity Between the Insula and Prefrontal Cortex Is Sensitive to Acute Injury and Symptom Persistence After Sport-Related Concussion

C Sheridan[1], W Flood[2], C Whitlow[1]
[1]Wake Forest School of Medicine, Winston-Salem, NC, [2]Wake Forest University, Winston-Salem, NC

Purpose
Autonomic, affective, and nociceptive symptoms are common after sport-related concussion (SRC) and have well-established relationships with central autonomic network (CAN) structures. We previously found that symptom persistence was positively correlated with hyperconnectivity between the medial amygdala and vmPFC/sgACC. We hypothesized that the insula might also display similar symptom-relevant hyperconnectivity. We investigated the relationship between symptoms and rsfMRI connectivity between the insula and PFC in SRC.
Materials and Methods
We computed whole-brain seed-to-voxel connectivity from BOLD rsfMRI acquisitions at 3 timepoints after SRC (T1=1-4days, T2=10-14days, T3=2-3months) in collegiate athletes (N=31,female=14) and for two groups of healthy age- and gender-matched controls (in-sport, N=36,female=17; non-contact sport N=37,female=15). Twelve insula seed regions were selected from the Brainnetome 264 Atlas (voxel threshold uncorrected $p<0.001$, two-sided; cluster threshold FDR-corrected $p<0.001$). ANOVA followed by Tukey's HSD was used to assess differences across group and time. Subject-level insula-PFC connectivity values (Fisher's Z) were correlated with SCAT-3 graded symptom checklist (GSC) and Brief Symptom Inventory 18 (BSI-18) scores at each timepoint.
Results
Compared to controls, SRC subjects displayed hyperconnectivity between 8 of 13 insula-PFC pairs at T1, hyperconnectivity between 2 of 13 insula-PFC pairs at T2, and hypoconnectivity between 8 of 13 insula-PFC pairs at T3. Among SRC subjects at T1, connectivity between right dorsal dysgranular insula and left frontal pole was negatively correlated with GSC and BSI-18 severity. Among SRC subjects at T3, connectivity between left ventral dysgranular/granular insula and right mPFC/dlPFC was positively

correlated with GSC severity and the GSC cognitive subscale; connectivity between right ventral dysgranular/granular insula and left lateral frontal pole was negatively correlated with BSI-18 severity and BSI-18 depression and anxiety subscales.

Conclusions

Acute hyperconnectivity between insula and PFC may be protective or compensatory after SRC. Chronic hyperconnectivity with the left insula may signal persistent cognitive symptoms; chronic hypoconnectivity with the right insula may signal persistent affective symptoms.

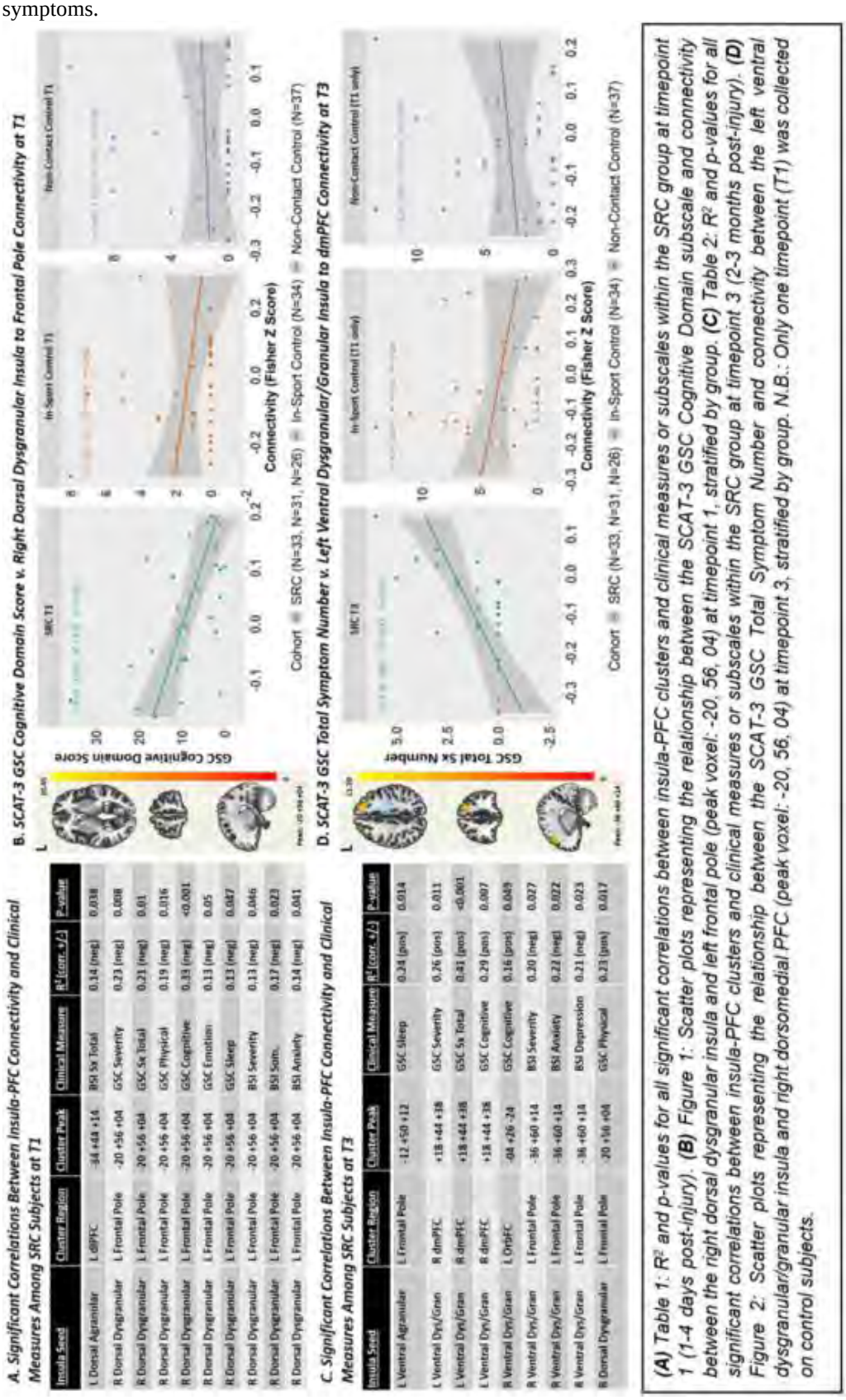

Insula Seed	Cluster Region	Cluster Peak	Clinical Measure	R^2 (corr. +/-)	P-value
L Dorsal Agranular	L dlPFC	-34 +44 +14	BSI Sx Total	0.14 (neg)	0.038
R Dorsal Dysgranular	L Frontal Pole	-20 +56 +04	GSC Severity	0.23 (neg)	0.008
R Dorsal Dysgranular	L Frontal Pole	-20 +56 +04	GSC Sx Total	0.21 (neg)	0.01
R Dorsal Dysgranular	L Frontal Pole	-20 +56 +04	GSC Physical	0.19 (neg)	0.016
R Dorsal Dysgranular	L Frontal Pole	-20 +56 +04	GSC Cognitive	0.33 (neg)	<0.001
R Dorsal Dysgranular	L Frontal Pole	-20 +56 +04	GSC Emotion	0.13 (neg)	0.05
R Dorsal Dysgranular	L Frontal Pole	-20 +56 +04	GSC Sleep	0.13 (neg)	0.047
R Dorsal Dysgranular	L Frontal Pole	-20 +56 +04	BSI Severity	0.13 (neg)	0.046
R Dorsal Dysgranular	L Frontal Pole	-20 +56 +04	BSI Som.	0.17 (neg)	0.023
R Dorsal Dysgranular	L Frontal Pole	-20 +56 +04	BSI Anxiety	0.14 (neg)	0.041

Insula Seed	Cluster Region	Cluster Peak	Clinical Measure	R^2 (corr. +/-)	P-value
L Ventral Agranular	L Frontal Pole	-12 +50 +12	GSC Sleep	0.24 (pos)	0.014
L Ventral Dys/Gran	R dmPFC	+18 +44 +38	GSC Severity	0.26 (pos)	0.011
L Ventral Dys/Gran	R dmPFC	+18 +44 +38	GSC Sx Total	0.41 (pos)	<0.001
L Ventral Dys/Gran	R dmPFC	+18 +44 +38	GSC Cognitive	0.29 (pos)	0.007
R Ventral Dys/Gran	L OrbFC	-04 +26 -24	GSC Cognitive	0.16 (pos)	0.049
R Ventral Dys/Gran	L Frontal Pole	-36 +60 +14	BSI Severity	0.20 (neg)	0.027
R Ventral Dys/Gran	L Frontal Pole	-36 +60 +14	BSI Anxiety	0.22 (neg)	0.022
R Ventral Dys/Gran	L Frontal Pole	-36 +60 +14	BSI Depression	0.21 (neg)	0.023
R Dorsal Dysgranular	L Frontal Pole	-20 +56 +04	GSC Physical	0.23 (pos)	0.017

***(A)** Table 1: R^2 and p-values for all significant correlations between insula-PFC clusters and clinical measures or subscales within the SRC group at timepoint 1 (1-4 days post-injury). **(B)** Figure 1: Scatter plots representing the relationship between the SCAT-3 GSC Cognitive Domain subscale and connectivity between the right dorsal dysgranular insula and left frontal pole (peak voxel: -20, 56, 04) at timepoint 1, stratified by group. **(C)** Table 2: R^2 and p-values for all significant correlations between insula-PFC clusters and clinical measures or subscales within the SRC group at timepoint 3 (2-3 months post-injury). **(D)** Figure 2: Scatter plots representing the relationship between the SCAT-3 GSC Total Symptom Number and connectivity between the left ventral dysgranular/granular insula and right dorsomedial PFC (peak voxel: -20, 56, 04) at timepoint 3, stratified by group. N.B.: Only one timepoint (T1) was collected on control subjects.*

(Filename: TCT_854_SheridanChristopher_11Nov2021_ASNRAbstract_CBFInsula_Figure.jpg)

1030

Symptom Burden-related White Matter Microstructural Changes in Mild Traumatic Brain Injury: a Harmonized Multi-scanner Diffusion MRI Study

S Chung[1], P Amorapanth[1], E Fieremans[1], D Novikov[2], J Rath[1], S Flanagan[1], Y Lui[3]

[1]NYU Grossman School of Medicine, New York, NY, [2]New York University School of Medicine, New York, NY, [3]NYU Langone Health, New York, NY

Purpose

Mild traumatic brain injury (MTBI) is a major public health problem with serious clinical sequelae. Here we study white matter (WM) microstructural changes in high and low symptom burden MTBI, using DTI, DKI, WM tract integrity (WMTI) [1] metrics. Inter-scanner harmonization was performed using the ComBat [2] while maintaining biological variability associated with age, gender, and disease.

Materials and Methods

We studied 23 MTBI patients with high (36±12 yrs; SCAT3 total, 72±18) and 24 MTBI patients with low symptom burden (30±11 yrs; SCAT3 total, 10±3) within a month of injury and 46 normal controls (NC) (35±11 yrs). Multi-shell diffusion imaging was performed on 3T MR scanners (Skyra/Prisma, Siemens) (5 b-values=0.25-2.5ms/μm2, FOV=220×220mm2, 2.5mm-isotropic resolution). We calculated 11 parametric maps of DTI (fractional anisotropy [FA], mean/axial/radial diffusivities [MD/AD/RD]), DKI (mean/axial/radial kurtosis [MK/AK/RK]), and WMTI metrics (axonal water fraction [f], intra-axonal diffusivity [Daxon], extra-axonal axial/radial diffusivities [De,par/De,perp]). To minimize scanner variability, ComBat [2] was used for harmonization of diffusion parametric maps. Tract-based spatial statistics (TBSS) was performed with age and gender as covariates to test between-group differences with corrected $p<0.05$ considered significant.

Results

Substantial differences between scanners (Fig.1,top) were reduced after ComBat (Fig.1,bottom). TBSS revealed diffusely decreased FA and increased De,perp in high symptom burden MTBI as well as more focally decreased AK mainly in anterior thalamic radiation (Fig.2). No differences were detected between the low symptom burden MTBI and NC groups.

Conclusions

Our findings highlight the microstructural effects on WM of high symptom burden MTBI within a month of injury. Increased De,perp has previously been shown to reflect changes in myelination [3], and increased radial diffusivity to be associated with tau pathology in WM regions [4] in the setting of TBI [5]. Decreased AK in focal areas reflects decreased microstructural complexity along the axial direction and has been previously associated with disrupted axonal integrity. Our findings showing no differences in low symptom burden MTBI, suggest that the reported diffusion metrics might specifically serve as good biomarkers for the clinically important group of symptomatic MTBI. Further study on the relationship between symptom recovery and microstructural recovery would be important.

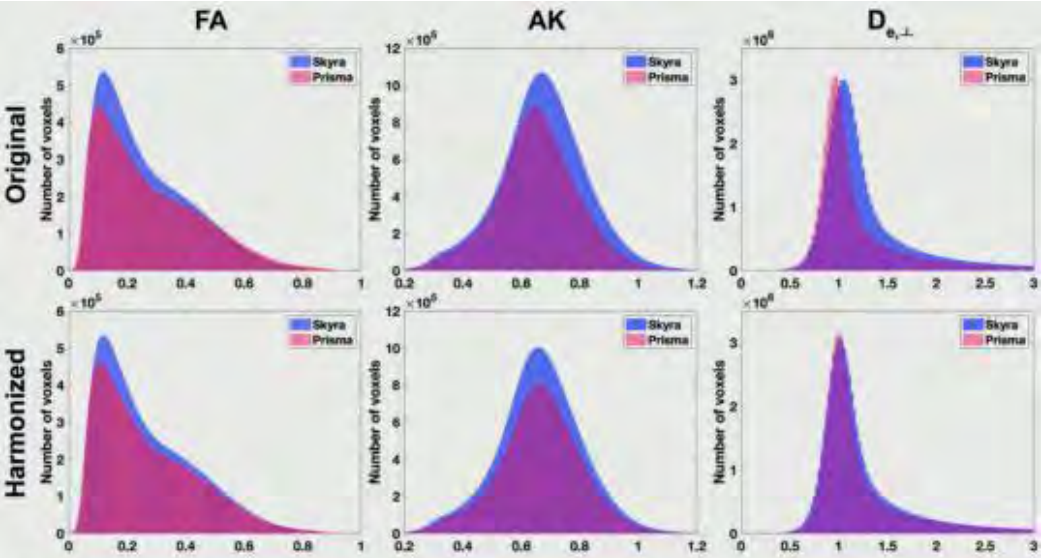

Figure 1. Harmonization of the diffusion parametric maps using Combat. (Top) Histograms showing variability on different scanners in representative diffusion maps which were harmonized using ComBat **(bottom)**. The harmonization process corrects the variance in scanner without altering the biological variance expected with age, gender and disease.

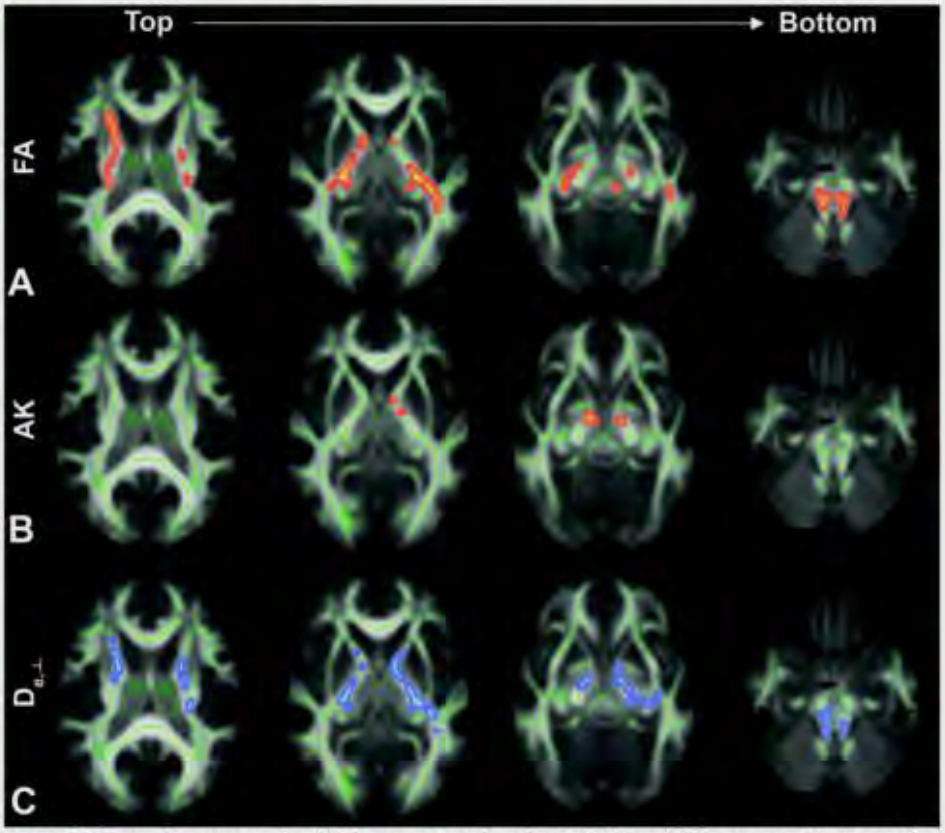

Figure 2. TBSS results comparing high symptom burden MTBI and NC groups. Clusters of voxels demonstrating **(A)** significantly decreased FA and **(B)** AK, and significantly increased $D_{e,\perp}$ in the high symptom burden MTBI group are present mainly in anterior/posterior limb of internal capsule, anterior thalamic radiation, cerebral peduncle, inferior longitudinal fasciculus, inferior fronto-occipital fasciculus, and superior cerebellar peduncle.

(Filename: TCT_1030_figures_submitted.jpg)

Tuesday, May 17, 2022
1:00-2:30 PM
Late-Breaking Abstracts

1612

A Regression Analysis: Magnetoencephalography (MEG) and Diffusion Kurtosis Imaging (DKI) Measured Structural and Functional Brain Changes Regressed with Head Impact Exposure in American Youth Football Players

N Bell[1], F Yu[2], J Urban[3], C Whitlow[3], J Stitzel[4], J Maldjian[5], E Davenport[6]

[1]UT Southwestern Medical Center, Dallas, TX, [2]UT Southwestern, Dallas, TX, [3]Wake Forest School of Medicine, Winston-Salem, NC, [4]Wake Forest University, Winston-Salem, NC, [5]University of Texas Southwestern Medical Center, Dallas, TX, [6]University of Texas Southwestern, Dallas, TX

Purpose

Recent retrospective studies have postulated that multiple concussions, in addition to years of exposure to subconcussive head impacts, are associated with later-life disease development. In order to interrogate these findings our group conducted a prospective study in a high contact sport, football. Our previous findings in the high school football player age group found significant increases in the delta frequency band related with increased Risk Weighted Exposure (RWE), a head impact exposure metric. The objective of this analysis was to investigate the role of cumulative head impact exposure (HIE) on MEG and MRI-measured brain metrics in youth football players.

Materials and Methods

103 youth football players (all male; mean age = 13.23y) and 22 non-contact athlete control participants (all male; mean age = 11.6y) were included in this analysis. Football players wore sensor-embedded helmets that detected HIE throughout the season. From this data, RWE was calculated per subject, and control participants were assumed to have a 0 RWE value. Diffusion Kurtosis Imaging (DKI), and 8 minutes of eyes-opened resting state MEG data were acquired pre- and post-season for all participants. MEG data underwent standard pre-processing and source localization in Brainstorm. The relative power per frequency band and mean kurtosis (kmean) images were normalized to MNI template brain space. Voxel-wise difference (post-pre) maps were computed for all imaging metrics per subject. Voxel-wise z-scores were computed and thresholded at 2 standard deviations above the mean. A linear regression model was performed on these metrics.

Results

The number of abnormal voxels in high gamma (60-90Hz) band showed a positive association ($p<0.05$) with RWE (Figure 1). No other bands showed significant associations. Additionally, the number of abnormal voxels for kmean and the number of abnormal voxels for all frequency bands showed a strong positive association ($p<0.001$ Bonferroni).

Conclusions

This study found increased high gamma power significantly associated with increased HIE in youth football players, which is in agreement with other TBI studies. However, it is not concordant with the high school group, where delta power was significantly associated with HIE.

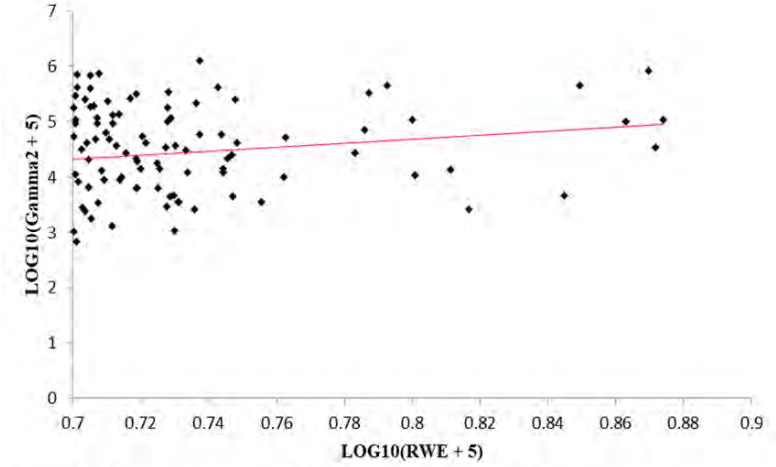

Figure 1. Linear Regression of RWE on High Gamma Response.
Utilizing high gamma (60-90 Hz) as the dependent variable and RWE as the independent variable (n=127). Both high gamma and RWE were log normalized and a value of 5 was added following standard normalization methods from the literature. This high gamma value was the number of abnormal voxel clusters after applying a 2 SD threshold to the z-score (zmaps) that were created.

(Filename: TCT_1612_Regression_Figure_1.jpg)

1559

Abnormalities of Hemispheric Specialization in Drug-Naïve and Drug-Receiving Children with Rolandic Epilepsy

Y Yin[1]

[1]*Affiliated Hospital of Zunyi Medical University, Zunyi, Guizhou*

Purpose

To explore hemispheric specialization measured by resting-state functional magnetic resonance imaging (rs-fMRI) functional connectivity in children with Rolandic epilepsy (RE).

Materials and Methods

Hemispheric specialization was quantified in three groups of children, including 21 drug-naïve RE (DNRE), 34 drug-receiving RE (DRRE) and 36 demographically matched typical development (TD).

Results

Compared with TD, DNRE group exhibited significantly higher hemispheric specialization in right precentral gyrus and right inferior temporal gyrus, while DRRE demonstrated significantly higher hemispheric specialization in the left postcentral gyrus and right hippocampus. In addition, both DNRE and DRRE groups exhibited significantly higher specialization in left superior temporal gyrus, right parahippocampus, left putamen and right caudate. Notably, bilateral cerebellum_6 showed opposite trends of hemispheric specialization in the two RE groups.

Conclusions

Our findings showed that children with RE exhibited altered hemispheric specialization in the language processing areas, suggesting both abnormal local segregation and interhemispheric integration in these children.

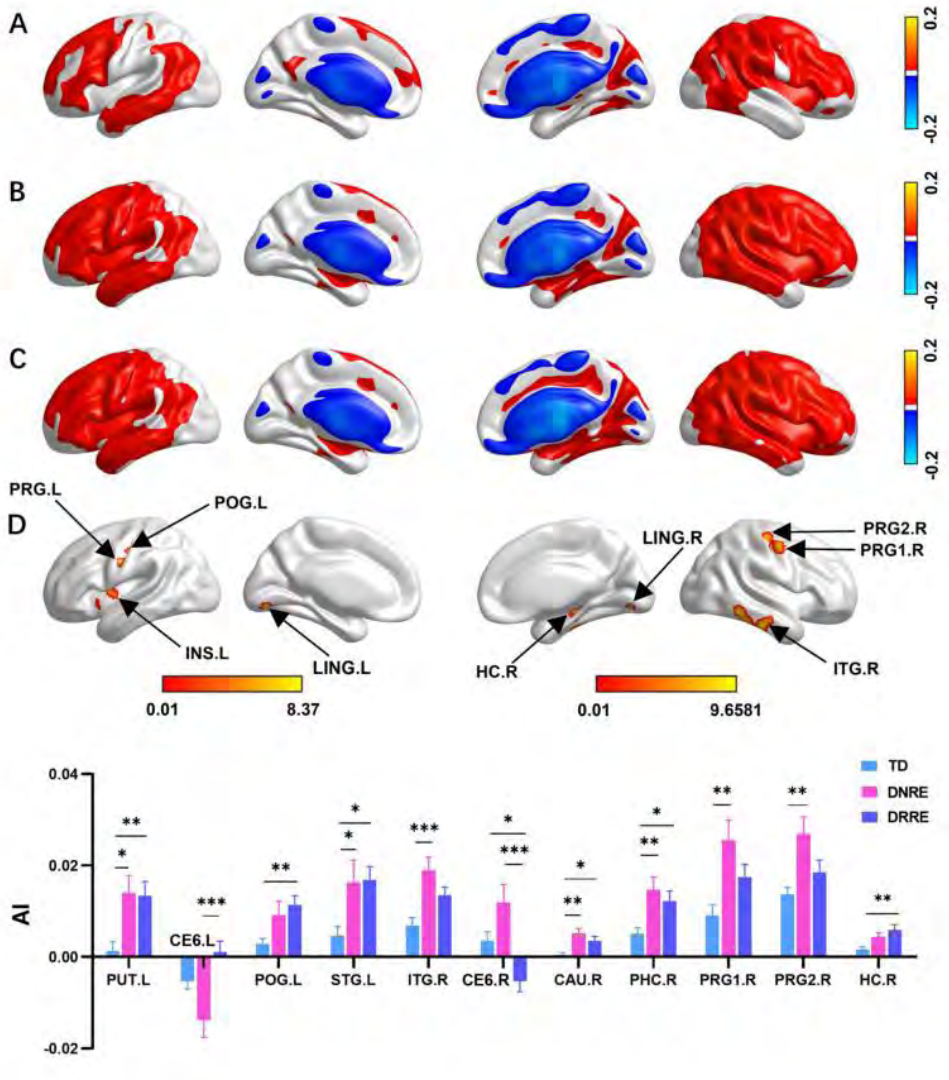

(Filename: TCT_1559_Fig1.jpg)

1575

Association Of CT Perfusion Ischemic Core With Effect of Intravenous Alteplase Prior To Endovascular Treatment In Acute Ischemic Stroke: Results From The MR CLEAN-NO IV Trial

J Hoving[1], H van Voorst[1], D Peerlings[2], J Daems[3], M Koopman[1], A Wouters[1], M Kappelhof[1], N LeCouffe[1], K Treurniet[1], A Bruggeman[1], L Rinkel[1], I van den Wijngaard[4], J Coutinho[1], H Lingsma[3], A van der Lugt[3], H Marquering[1], Y Roos[1], C Majoie[1], B Emmer[1]

[1]Amsterdam UMC, University of Amsterdam, Amsterdam, Noord-Holland, [2]UMC Utrecht, Utrecht, Utrecht, [3]Erasmus University Medical Center, Rotterdam, Zuid-Holland, [4]Haaglanden Medical Center, The Hague, Zuid-Holland

Purpose

The MR CLEAN-NO IV trial showed that intravenous alteplase (IVT) prior to endovascular treatment (EVT) was neither superior nor inferior to EVT alone in acute ischemic stroke (AIS) patients.(1) CT perfusion (CTP) could potentially identify patients with reduced benefit from IVT. We aim to assess whether the effect of IVT prior to EVT differs according to CTP-estimated ischemic core volume.

Materials and Methods

We included patients from the MR CLEAN-NO IV trial with available baseline CTP. CTP data were processed using syngo.via (version VB40). We performed multivariable ogistic regression on the ordinal modified Rankin Scale (mRS) at 90 days and functional independence (i.e., mRS 0-2). We report the adjusted (common) odds ratio (a[c]OR) for better outcome on the 90-day mRS and for functional independence.

Results

CTP results were available for 226/540(42%) patients. Median baseline CTP core volume at presentation was 13 (IQR 5-35) mL. The a(c)OR for CTP core volume on outcome was 0.98 (95% CI 0.97-0.99). The a(c)OR for IVT on outcome was 1.01 (95% CI 0.62-1.64). The effect of IVT prior to EVT on outcome did not differ by CTP core volume (pfor interaction=0.8). The association between CTP core volume and functional independence is shown in Figure 1.

Conclusions

In this post-hoc analysis of a randomized trial of IVT prior to EVT, CTP-estimated ischemic core volume did not alter the treatment effect of IVT prior to EVT in terms of functional outcome at 90 days. These results should be confirmed in a pooled meta-analysis of trials of IVT prior to EVT.

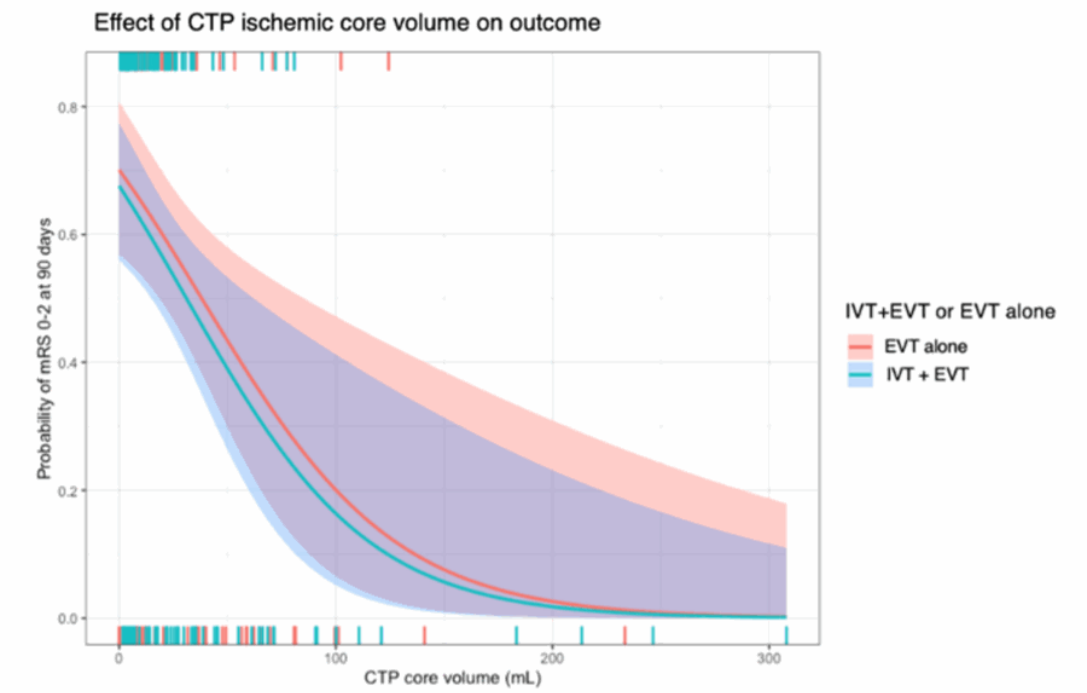

(Filename: TCT_1575_Fig1.gif)

1598

Cerebral Blood Flow Patterns in Preterm and Term Neonates Assessed with Pseudo-Continuous Arterial Spin Labeling Perfusion MRI

E Piccirilli[1], A Chiarelli[1], D Mascali[1], D Calvo Garcia[1], C Sestieri[1], R Wise[1], A Ferretti[1], M Caulo[1]

[1]University of Chieti, Chieti, Italy

Purpose

Structural and functional modifications of the brain in the 3rd trimester are affected by preterm birth and abnormalities in CBF

distribution may play a role. Our aim was to evaluate modifications of CBF patterns assessed with pCASL in preterm (PT) and full-term (FT) infants using a data-driven model.
Materials and Methods
82 PT (<37 weeks GA at birth, GAB) and 55 FT (>37 weeks GAB) with no major neonatal morbidity were scanned within 7 days of TEA and of birth, respectively; they underwent the same standardized MR protocol on a 3T, including a pCASL. The presence of prematurity-related brain injury (GMH and PVL) was also evaluated, and PT infants were stratified into those without (PTh, further divided in: Early PT, PThe: <=28 weeks; Moderate PT, PThm: 29-32 weeks; Late PT, PThl: 33-36 weeks) and those with prematurity-related brain injury (PTpvl and PTgmh, respectively). The grey matter CBF (CBFgm) was extracted from 90 ROIs of the UNC Infant Atlas, and normalized through z-scoring (computing nCBFgm, expressed in units of SD from the global CBFgm). The ROIs were then combined using hierarchical clustering (HC) applied on nCBFgm of healthy neonates. Differences in nCBFgm within the clusters as a function of prematurity and prematurity-related brain injuries were evaluated by multiple one-way ANOVAs.
Results
The HC identified 4 main clusters of ROIs:Fronto-Temporal,Parieto-Occipital,Insular-Deep Grey Matter and SensoriMotor. SensoriMotor and Insular-DGM had the highest CBF (13.2 and 11.9 ml/100g/min), while Parietal-Occipital and Fronto-Temporal were the least perfused (10.2 and 8.5 ml/100g/min).nCBFgm was above 0 in SensoriMotor and Insular-DMG (.94 and .48; p<10^-4),and below 0 in Fronto-Temporal (-.78; p<10^-4). In Fronto-Temporal,nCBFgm was higher in FT compared to all PTh subgroups (p<.05), with a positive association between nCBFgm and GAB (r=.37; p<.01) and higher in PTpvl compared to PTH (p<.05).In SensoriMotor, nCBFGM was lower in FT compared to all PTh subgroups (p<10^-3) with a negative association between nCBFGM and GAB (r=.42, p<10^-3).In Insular-DMG,nCBFGM was higher in PTh compared to PTpvl (p<.05) and to PTgmh (p<0.1).
Conclusions
CBFgm at TEA distributes heterogeneously within 4 clusters of ROIs both as a function of GAB between PTh and PT with brain injuries, suggesting different metabolic demands and developmental trajectories of brain regions among these groups

1574

Extreme undersampling applied to clinical brain MRI and qualitative assessment of deep learning-based reconstruction at up to 100-fold acceleration

E Lindsey[1], M Muckley[2], A Radmanesh[1], Y Lui[1], T Murrell[3], F Knoll[4], D Sodickson[1]
[1]NYU Langone Health, New York, NY, [2]Facebook AI Research, New York, NY, [3]Shaped AI, New York, NY, [4]Friedrich-Alexander Universität Erlangen-Nürnberg, Erlangen, Germany

Purpose
To perform expert qualitative evaluation of deep learning-based brain MR reconstruction of undersampled image data across a broad range of accelerations and assess acceleration rates acceptable for clinical diagnosis as well as level for potential screening examination.
Materials and Methods
A neural network was trained to reconstruct clinical 2D brain MR images using 5,847 imaging volumes from the fastMRI data set across a wide range (from 2-fold up to 100-fold along a single phase-encoded direction). T1-weighted, T2-weighted, and T2 FLAIR reconstructions from a subset of 69 cases from the held-out test set were then qualitatively evaluated by two radiologists to identify two thresholds:1) highest acceleration yielding image quality useful for current clinical practice and 2) highest acceleration yielding quality for potential use as a screening tool for major intracranial pathology.
Results
Radiologists rated 100% of studies as diagnostic image quality for clinical practice at up to 4X acceleration and 90% of studies as having sufficient image quality for screening up to 14X acceleration, with some pathologies present even at 100X acceleration.
Conclusions
For 2D brain images using a state-of-the-art deep learning-based reconstruction, 100% of studies were considered to be diagnostic quality at 4x acceleration with potential use for screening of major intracranial abnormalities 3-4 times higher.

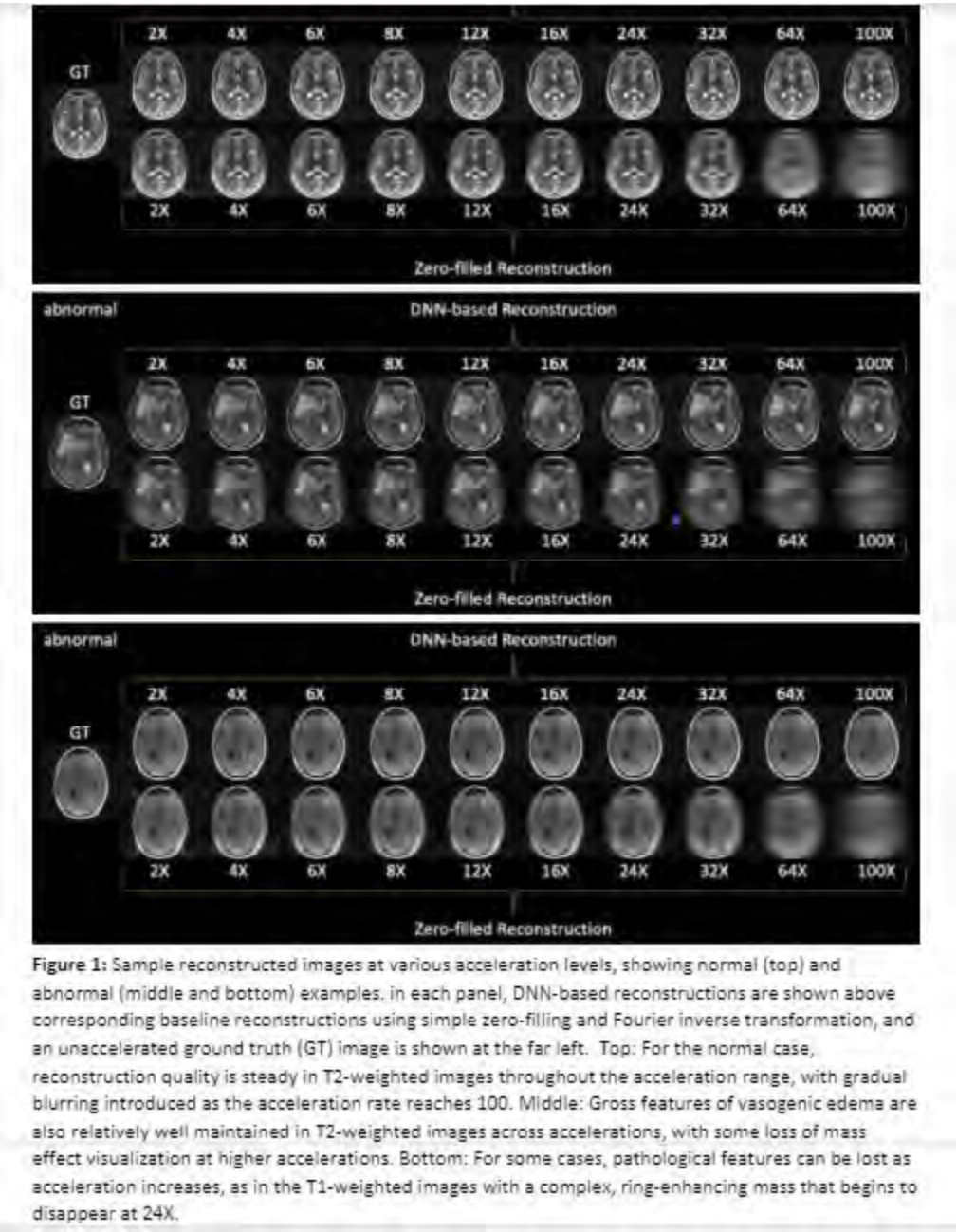

Figure 1: Sample reconstructed images at various acceleration levels, showing normal (top) and abnormal (middle and bottom) examples. in each panel, DNN-based reconstructions are shown above corresponding baseline reconstructions using simple zero-filling and Fourier inverse transformation, and an unaccelerated ground truth (GT) image is shown at the far left. Top: For the normal case, reconstruction quality is steady in T2-weighted images throughout the acceleration range, with gradual blurring introduced as the acceleration rate reaches 100. Middle: Gross features of vasogenic edema are also relatively well maintained in T2-weighted images across accelerations, with some loss of mass effect visualization at higher accelerations. Bottom: For some cases, pathological features can be lost as acceleration increases, as in the T1-weighted images with a complex, ring-enhancing mass that begins to disappear at 24X.

(Filename: TCT_1574_Figure1forabstract.jpg)

1588

Imaging Features Predictive of Poor Endovascular Thrombectomy Results Using Machine Learning

J Salameh[1], B Wylynko[1], A Simpson[1], J Ortiz Jimenez[1], O Islam[1], D Tampieri[2]
[1]Queen's University, Kingston, Ontario, [2]Queen's University KHSC, Kingston, Ontario

Purpose

To accurately predict poor or incomplete recanalization after endovascular thrombectomy (EVT) using imaging features on CT Angiography (CTA) in patients with anterior large vessel occlusion (LVO) using a 3D convolutional neural network (CNN) based algorithm.

Materials and Methods

Patients presenting to our Institution between April 2018 and May 2020 were identified for inclusion. Large vessel occlusions included internal carotid artery (ICA), and M1 and M2 segments of the middle cerebral artery (M1-MCA and M2-MCA) occlusions. The outcome measure of interest in this study is poor or incomplete recanalization after EVT defined as a TICI score of 2A or less. A Multivariable logistic regression model was fit to evaluate the association of the outcome of interest with various clinical variables (i.e., location of LVO, hyperdensity of the clot, presence of tortuous parent artery, etc). Segmentations were performed manually in consultation with an experienced interventional neuroradiologist. Ten epochs were used with a train-test split of 70% / 30%. In each training / validation step, 8 training samples and 4 validation samples are selected. The model loss was computed via binary cross

entropy, which updates the model weights based on the model's confidence in its predictions of each training / validation sample. The performance was evaluated using the area under the curve (AUC).
Results
Our sample was comprised of 81 CTA images from 31 females and 47 males. The mean age (± SD) was 71.7 (±13.6) years old. Multivariable logistic regression evaluating the association between the TICI score and various clinical variables demonstrated significant association between successful recanalization after EVT and location of the clot (LVO at M1 – P=0.01, at M2 – P=0.01) and the hyperdensity of the clot (P=0.02). The 3D CNN algorithm built using segmentations of the LVO achieved an AUC of 0.77
Conclusions
Our 3D convolutional neural network algorithm demonstrated a moderate accuracy in predicting outcomes of EVT in patients with anterior arterial circulation occlusion.

1627

Reflections on supporting the young democracy of Ukraine through Ukrainian-language Radiology education

L Wolansky[1]
[1]UCONN, Farmington, CT

Purpose
N/A
Materials and Methods
N/A
Results
N/A
Conclusions
The Friends Of Radiology in Ukraine (Friends) was founded as a nonprofit charitable organization in 1992 by M. Paul Capp, who was at the time the executive director of the ABR. "Friends" supported publication of Ukrainian language Radiology educational resources. In 1996, a conference program was founded by Friends member Leo Wolansky in collaboration with the Lviv Med Institute as a "Radiology school." After its inception, the course, typically three days in length, took place every two years, excepting 2014 which was postponed due to the Russian invasion of Crimea, Luhansk & Donetsk. Around that time, Dr. Walter Kucharczyk then chair of the ASNR International Outreach Professor program reached out to Dr. Wolansky, and informed him that he would like to provide one or two professors to Ukraine on an annual basis for a period of approximately two weeks. The course was modified to accommodate this resource of professors, and an expanded version took place annually until 2020 when the COVID pandemic intervened. A downsized virtual version of the course took place in 2021 and a face to face course had been planned for 2022. Over the years more than 3500 Ukrainian health professionals have attended. The majority has been from western Ukraine, but representatives from numerous distant regions have attended, including Kharkiv, Kyiv, Poltava, Dnipro, Odessa, even Luhansk, Donetsk, and Crimea. The program has also been the subject of multiple news articles and television news reports, which profiled the high educational value of the course and patriotic mission. In the Spring of 2019 the ASNR International Imaging Series partnered with "Friends" and the Association of Radiologists of Ukraine (ARU), which was holding an international congress of Radiology. Seven ASNR professors presented. Acting Minister of Health for Ukraine, Ulana Suprun, who had been one of the founding members of "Friends," gave opening remarks. Unlike the first International Congress of Radiology in independent Ukraine in 1995, for which the official language was Russian, by 2019 the official language was Ukrainian! With the help of Webmaster Ivan Wolansky, a library of over sixty Ukrainian language lectures are posted on two websites as a free resource. https://www.friendsofradiologyinukraine.org https://www.facebook.com/friendsofradiologyinukraine It takes decades to build...

1569

Synthetic Lumbar Spine CT from MRI Imaging for Surgical Navigation: Proof-of-concept

G Gong[1], H Wang[2]
[1]Johns Hopkins University, Baltimore, MD, [2]Shandong Provincial Hospital Affiliated to Shandong First Medical University, Jinana, MD

Purpose
CT imaging-assisted navigation has greatly improved the accuracy in screw placement during spine surgery due to CT's superior visualization of bony details. However, MRI is often the imaging modality of choice for diagnosing soft tissue related disease of the spine. Current MRI images lack the ability of revealing bony anatomy which is required for intraoperative surgical navigation. The possibility of using MRI to eliminate CT scanning would have great clinical implication in reducing radiation and cost. To date, the feasibility of MR-generated synthetic CT (SCT) on few body parts has been demonstrated, however, no study has been conducted on the SCT clinical application. This study aims to illustrate the feasibility of using SCT generated from clinical MRI data by AI algorithm to guide spine surgery.
Materials and Methods
This is a proof-of-concept prospective study. Adult patients who underwent lumbar spine surgery for spinal stenosis were selected. MRI and CT of the lumbar spine were performed on the same patient within two months. A customized 3D (0.8 mm) radiofrequency-spoiled T1-weighted multiple gradient echo MRI (T1SGRE) scan was added to the regular clinical MRI scan sequence, performed on

a Siemens 3.0T scanner. The T1SGRE data were used to generate corresponding synthetic CT images using a deep learning-based image synthesis method with a proprietary software. The synthetic CT images were transferred to intraoperative surgical navigation system.

Results

We found the MR-based SCT could reliably depict overall lumbar spine morphology and bony details of the lumbar spine by using MRI voxel-based radiodensity representation as illustrated in case 1. SCT is equivalent to conventional CT in geometrical accurate visualization of lumbar spine vertebral body, disc space, pedicle width and orientation, spinous process, and soft tissue calcifications. Those SCT data could be utilized by the intraoperative navigation system to successfully guide screw placement by the neurosurgeon, as seen in case 2.

Conclusions

This study demonstrated satisfactory imaging fidelity of MR-generated SCT and its imaging equivalency to conventional CT in imaging and surgical evaluation of lumbar spine. In combination with the soft tissue information of the conventional MRI, SCT provides new possibilities in diagnosing and surgical planning of lumbar spine disorders with the added potential benefits of reducing workflow complexity, radiation exposure, and costs associated with adjunctive CT scanning.

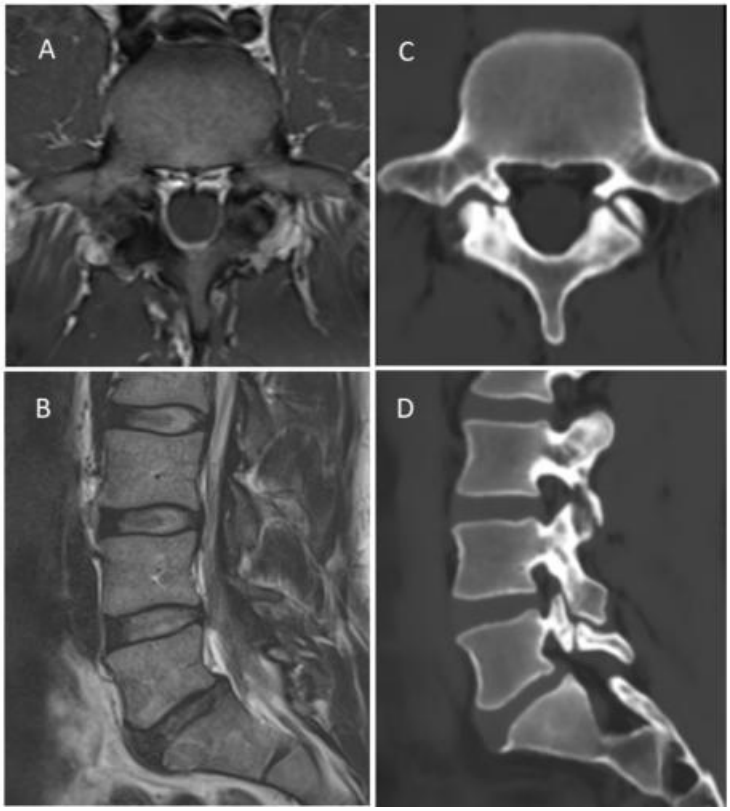

FIG. Axial T1-weighted (A) and sagittal (B) T2-weighted lumbar spine MRI images from Case 1. Same patient MR-generated SCTs in corresponding axial (C) and sagittal (D) Better depicting pars defect and Adequate bony details.

(Filename: TCT_1569_FIG1.jpg)

1577

The Paramaxillary Approach for CT-Guided Biopsy of Head and Neck Masses: A Single Institution Review of Technique, Safety, and Yield

d wang[1], S Strauss[2]

[1]Weill Cornell Medicine, New York, NY, [2]New York Presbyterian Hospital-Weill Cornell, New York, NY

Purpose

CT-guided biopsy of deep-seated head and neck lesions can be a less invasive and equally effective alternative to surgical techniques. There are multiple approaches for needle biopsy that target varying deep spaces within the head and neck while successfully avoiding critical anatomy. In the paramaxillary approach, the needle is advanced through the infrazygomatic buccal space, in between the maxilla medially and mandible laterally. This trajectory allows access to the parapharyngeal, retropharyngeal, parotid, and carotid spaces. Cranial needle angulation can allow further access to the skull base and upper cervical vertebrae. Although the general safety and efficacy of CT-guided biopsy of the deep spaces of the head and neck have been previously explored, to our knowledge, the paramaxillary approach in specific has not yet been studied. The purpose of this retrospective study is to evaluate the histopathologic yield and complication rate of CT-guided fine needle aspiration performed via paramaxillary approach.

Materials and Methods

This is an IRB-approved, HIPAA compliant retrospective review of 18 patients undergoing 19 fine needle aspirates and 4 core needle biopsies of the head and neck via CT-guided paramaxillary approach from May 2014 to November 2021. Patient demographic,

clinical diagnosis, mass location and size, diagnostic histopathologic yield, biopsy result, and post-operative outcome were recorded for all patients.
Results
A total of 19 fine needle aspirates and 4 core needle biopsies were collected from 18 patients . Needle gauges used ranged from 20 to 25 gauge for fine needle aspirates and 18 to 20 for core needle biopsies. Average age of the patients was 57.8 with 27.8% (5/18) males. Of the fine needle aspirates, 84.2% (16/19) were diagnostic with an average of three passes performed on an average lesion size of 2.2 ± 1.0 cm. Concordant histopathologic diagnosis to final pathology was obtained in 100% (16/16) diagnostic fine needle aspirates. Diagnostic rate for core needle biopsies was 100% (4/4) with 100% (4/4) concordant with fine needle aspirates and final pathology. There were no post-procedural complications.
Conclusions
CT-guided paramaxillary approach is a safe and effective method for diagnosing deep-seated, poorly accessible lesions of the face, even when it is known a priori that core biopsy cannot be performed due to small lesion size or risk of vascular or nerve injury.

1633

Transvenous Embolization of CSF-Venous Fistulas Associated with Spontaneous Intracranial Hypotension

T Huynh[1], D Parizadeh[2]
[1]Mayo Clinic, Jacksonville, FL, [2]Mayo Clinic Florida, Jacksonville, FL

Purpose
Endovascular transvenous embolization is a novel treatment for patients with spontaneous intracranial hypotension (SIH) secondary to CSF-venous fistulas (CVF)[1]. The technique was introduced recently at a single center promising results [1,2]. We sought to perform the first independent validation of this procedure to evaluate its efficacy and safety.
Materials and Methods
Data were collected prospectively. Inclusion criteria was: 1) clinical diagnosis of SIH, 2) definitive diagnosis of CVF on either digital subtraction myelogram or CT myelogram[3], 3) transvenous embolization for treatment of CVF at Mayo Clinic, Florida, between December 2020 - March 2022, 4) available clinical and imaging follow-up after the procedure. Clinical symptoms pre and post-embolization were assessed using standardized scores including the Headache Impact Test (Hit-6)[4] and Patient Global Impression of Change (PGIC)[5] score. Features of SIH pre and post-embolization were assessed using the Bern SIH score6 on brain MRI. Procedural and post-procedural complications were recorded.
Results
Eleven patients (mean [SD] age 59 [8] years, 73% female), underwent transvenous embolization. Orthostatic/valsalva headache was the most common symptom (73%). Median (IQR) follow-up was 4 (3) months for clinical and 3.5 (1) months for imaging outcome. Headache severity decreased significantly post-embolization (mean [SD] HIT-6 score of 62.8 [11] pre-embolization and 39.3 [10] post-embolization, p = 0.010) and 91% of cases were headache free after treatment. PGIC post-embolization demonstrated 91% were "very much improved" (PGIC score of 1). Concordant with clinical improvement, post-operative Bern SIH Score significantly improved post-embolization in 91%. There were no neurological complications. Side effects were localized back pain (64%) and rebound headache (73%) which resolved within one month with medical treatment in all cases.
Conclusions
Transvenous embolization is a highly efficacious and safe treatment for CVF in patients with SIH.

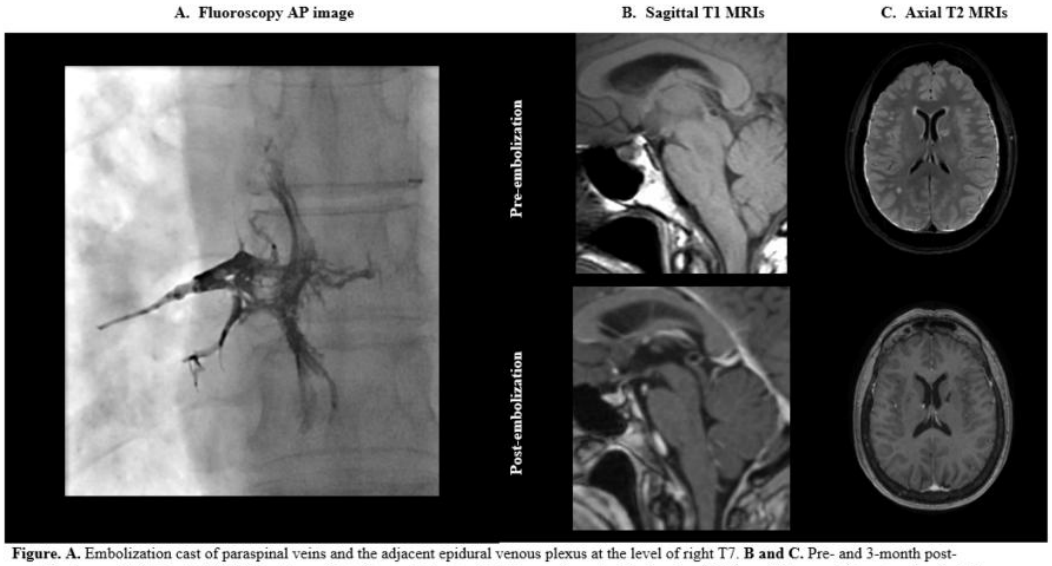

Figure. A. Embolization cast of paraspinal veins and the adjacent epidural venous plexus at the level of right T7. **B and C.** Pre- and 3-month post-embolization sagittal T1 axial T2 MRIs of the patient. Pre-embolization MRI shows characteristic imaging findings of intracranial hypotension including diffuse pachymeningeal enhancement, pontine belly flattening and narrowing of the mamillary pontine distance. Post-embolization MRI shows marked improvement of the previous findings, including resolution of diffuse pachymeningeal thickening, increase in the size of ventricles, increase in the suprasellar cistern and prepontine cistern volumes, as well as improved pontomedullary distance and midbrain pontine angle.

(Filename: TCT_1633_161163_figure_1.jpg)

1571

Use of 3D and Augmented Reality Facial Tracking for Visualization of Intracranial, Head, and Neck pathology

L Lin[1], Z Wilseck[2], N Chaudhary[3], J Gemmete[3]

[1]University of Michigan Hospital, Ann Arbor, MI, [2]UNIVERSITY OF MICHIGAN HEALTH SYSTEMS, CANTON, MI, [3]University of Michigan, Ann Arbor, MI

Purpose

Three-dimensional (3D) segmentation of images, virtual reality (VR), and augmented reality (AR) tools are used for education and surgical planning. We describe methods for 3D and AR visualization using available platforms that are readily accessible using a computer or mobile device without requiring installation of specialized software.

Materials and Methods

The 3D models were created from imaging using Vitrea (Vital Images, Minnetonka, MN). The segmentations were exported in the stereolithography (STL) file format and imported into Blender (blender.org) to combine multiple STL files and assignment material properties. The final 3D figure can be exported to a variety of file formats. MeshLab (meshlab.net) was used to reduce the polygon count and convert the model to an universal 3D (U3D) file, which can be inserted to a portable document format (PDF) file using Acrobat (Adobe Inc, San Jose, CA). The full 3D PDF functions are available with using Acrobat Reader. 3D models can also be imported on web-based interactive 3D viewing platforms such as Sketchfab (sketchfab.com). The models can also be registered to a face model on AR platforms such as ZapWorks (Zappar, London, UK) which will allow visualization of the pathology on the user's face. These platforms are accessible on all modern computers or mobile devices.

Results

3D segmentations of a tumor at the carotid bifurcation, osseous, and vascular structures was created. 3D figures embedded in PDF documents (figure A) can be controlled using mouse commands. Web-based 3D visualization (Figure B) has similar interactive elements with more customization. Interactive AR visualization of this tumor can be accessed by scanning the quick response (QR) code allowing for access with the front facing camera of a mobile device (Figure C) This platform tracks facial features and tracks important structures onto the user's head (Figure D).

Conclusions

We describe a method and pipeline for converting 3D segmentation from medical imaging to formats that are easily viewable on any modern device. This can be useful for education and clinical planning.

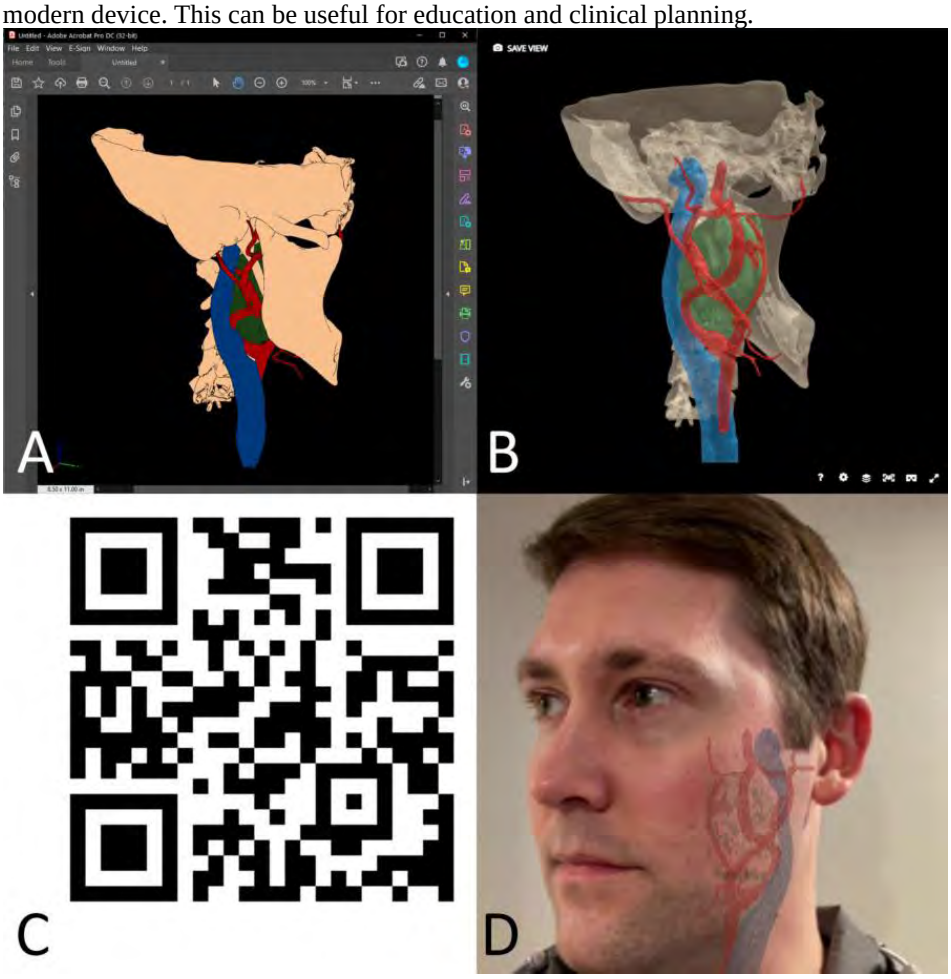

(Filename: TCT_1571_Figure.jpg)

1602

Viable Allograft Supplemented Disc Regeneration in the Treatment of Patients With Low Back Pain (VAST Trial): 36-month Interim Results of an Open-label Extension Study

D Beall[1], T Phillips[2], T Davis[3], S Gershon[4], M Langhorst[5], M DePalma[6]

[1]Comprehensive Specialty Care, Edmond, OK, [2]Clinical Radiology of Oklahoma, Edmond, OK, [3]Source Healthcare, Santa Monica, CA, [4]Gershon Pain, Virginia Beach, VA, [5]OrthoIndy, Indianapolis, IN, [6]Virginia iSpine Physicians, Richmond, VA

Purpose

The Viable Allograft Supplemented Disk Regeneration in the Treatment of Patients With Low Back Pain (VAST) trial (NCT03709901) evaluated the safety and efficacy of disc tissue allograft injection (VIA Disc®) into degenerated lumbar discs in patients with discogenic chronic low back pain (N=218; Beall et al. Pain Physician 2021). At 12 months, clinically meaningful improvements in pain, assessed via a visual analog scale (VAS), and in function, based on Oswestry Disability Index (ODI) score, were achieved in both the investigational allograft and saline groups. An open-label extension study is in progress. Here, for the first time, we report outcomes in patients treated with allograft who completed the 36-month follow-up.

Materials and Methods

The prospective, randomized, controlled VAST trial was conducted in patients with 1- or 2-level degenerative lumbar disc disease and chronic low back pain refractory to nonoperative treatments. At 12 months, patients could continue in an open-label extension study for up to 36 months, with an interim visit at 24 months. In this interim analysis, we assessed mean change from baseline in VAS Average LBP. To minimize confounding, we compared these 36-month data with results from prior timepoints in this completer population only

Results

Nine of 12 sites participated in the VAST extension; outcome data were entered for 45 patients at 36 months. The 36-month completer population was similar to the intent-to-treat population in age, sex, race, ethnicity, body mass index, and smoking status. For these patients, the baseline VAS average LBP was 65.98. LBP scores improved at 6 months (36 pts or 55%); at 12 months (39.9 pts or 60.4%); at 24 months (32 pts or 48%) and 36 months (35.9 pts or 55%). 16 patients were re-injected at 24 months. Further analysis is on-going and will be available for the 60th Annual Meeting.

Conclusions

This interim analysis of an open-label extension of the VAST trial suggests that viable disc tissue allograft might be a beneficial nonsurgical treatment for patients with chronically painful degenerated lumbar discs. These 36-month data showed durable pain relief and functional improvement in treated patients.

Tuesday, May 17, 2022

1:00-2:30 PM

Scientific Podium Presentations: Brain Tumors 1

851

Analyzing Trends in the Utilization of Machine Learning Algorithms for Glioma Molecular Subtype Classification using Pre-Therapy MR Imaging: A Systematic Literature Review

T Verma[1], J Lost[2], N Tillmanns[2], I Ikuta[3], R Bronen[3], W Zucconi[2], K Bousabarah[4], M Lin[3], M Sabel[5], M Aboian[6]

[1]Yale School of Medicine, Ossining, NY, [2]Yale School of Medicine, New Haven, CT, [3]Yale University School of Medicine, New Haven, CT, [4]Visage Imaging GmbH, Berlin, CT, [5]University Hospital Dusseldorf, Dusseldorf, NRW, [6]Yale University, Woodbridge, CT

Purpose

The classification of molecular subtypes in gliomas provides insight for prognosis and clinical treatment. Recent advances in artificial intelligence (AI) has shown promise in providing non-invasive pre-operative characterization of glioma molecular subtypes. To identify the best algorithms for clinical implementation, we performed a systematic review on AI applications that characterize molecular subtypes of WHO grade I-IV gliomas.

Materials and Methods

Following PRISMA guidelines, we performed a literature review using the Ovid Embase, Ovid MEDLINE, Cochrane trials (CENTRAL), and Web of Science core-collection databases for articles published prior to February 2021. Literature search keywords included artificial intelligence, machine learning, deep learning, radiomics, MRI, glioma, and glioblastoma. Non-human and non-machine learning studies were excluded. Screening was performed using the Covidence software and the bias analysis was performed following TRIPOD guidelines.

Results

11,727 abstracts were identified and based on the predefined inclusion/exclusion criteria, 1,135 full text articles were reviewed and 82 were selected for data extraction. It was found that 57% of these studies used retrospective single center hospital data, 31.6% used TCIA and BraTS, and 11.4% analyzed multicenter hospital data. These studies included an average sample size of 146 patients (range

34-462 patients) and 60.2% of studies examined ≤150 patients. AI algorithms were used to predict IDH status in 52.4% of studies and MGMT in 19.5%. Overall, support vector machine (32.1%) and random forest (28.2%) presided as the most common algorithms. Interestingly, convolutional neural network was used in 17.9% of studies, and over the past 4 years, use of deep learning algorithms has been on the rise. Mean prediction accuracy was 76.6%.
Conclusions
Classical machine learning, in particular SVM, was the most common method for glioma molecular subtype classification. In recent years, the use of deep learning, specifically CNN, is rising. However, small sample sizes remain one of the major limitations of this field. Identification of the best algorithms for clinical implementation requires testing of algorithms in diverse and large datasets with balanced numbers of different molecular subtypes. Current literature is focused on identification of algorithms that predict individual molecular subtypes of gliomas; therefore, further research on universal and generalizable implementation of algorithms is needed.

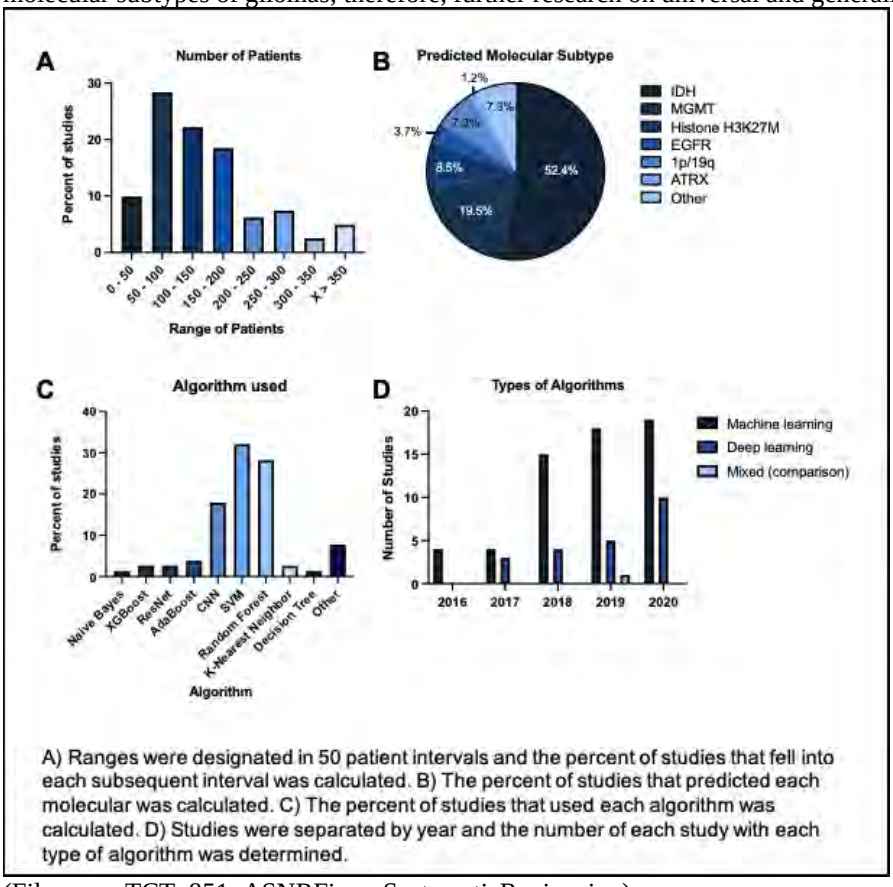

A) Ranges were designated in 50 patient intervals and the percent of studies that fell into each subsequent interval was calculated. B) The percent of studies that predicted each molecular was calculated. C) The percent of studies that used each algorithm was calculated. D) Studies were separated by year and the number of each study with each type of algorithm was determined.
(Filename: TCT_851_ASNRFigureSystematicReview.jpg)

1057
Automated color-coding of lesion changes in contrast-enhanced 3D T1-weighted sequences for MRI follow-up of brain metastases
D Zopfs[1], K Laukamp[1], R Reimer[1], N Große Hokamp[1], C Kabbasch[1], J Borggrefe[2], L Pennig[1], A Bunck[1], M Schlamann[1], S Lennartz[1]
[1]University Hospital Cologne, Cologne, NRW, [2]Johannes Wesling University Hospital, Minden, NRW

Purpose
Contrast-enhanced MRI is the imaging modality of choice for evaluation of therapy response in patients with brain metastases. However, follow-up assessment is often time-consuming and error-prone, especially in studies with multiple metastases or subtle changes. In particular in patients with multiple metastatic lesions who show a mixed response to treatment on follow-up MRI, the radiologist may be prone to a statisfaction of search bias, resuting in an inaccurate diagnosis (1-4). The aim of this study was to compare the diagnostic accuracy and certainty between conventional and automated co-registration and color-coding (AC)-assisted MRI follow-up assessments in patients with brain metastases.
Materials and Methods
121 consecutive MRI datasets from 95 patients with brain metastases were retrospectively included in this monocentric study. Contrast-enhanced 3D-T1 sequences from each of two consecutive examinations were assessed by two radiologists using conventional reporting and AC software (LOBI, IntelliSpace, Philips) assisted reporting with respect to the following criteria: a) progress, b) regress, c) mixed response, or d) stable. There was an interval of eight weeks between both reporting times to minimize a potential recall bias. Reference diagnoses were independently determined by two additional radiologists, taking into account all available data.
Results
The percentage of correct diagnoses increased from 74.0% (179/242) to 91.3% (221/242) when supported by the AC software

($p<0.01$), with a corresponding increase in subjective diagnostic certainty (4 (3-5) vs. 2 (2-3); $p<0.05$). Interrater agreement between both radiologists increased from moderate ($\kappa = 0.46$ (95%CI: 0.34-0.58)) to excellent ($\kappa = 0.80$ (95%CI: 0.71-0.89)) when the assessment of brain metastases was supported by AC.

Conclusions

Compared with conventional reporting, evaluators achieved a significantly higher percentage of correct diagnoses with higher diagnostic confidence when AC-assisted reporting was used. Therefore, automated co-registration and color coding appears beneficial in follow-up assessment of brain metastases and should be further clinically evaluated.

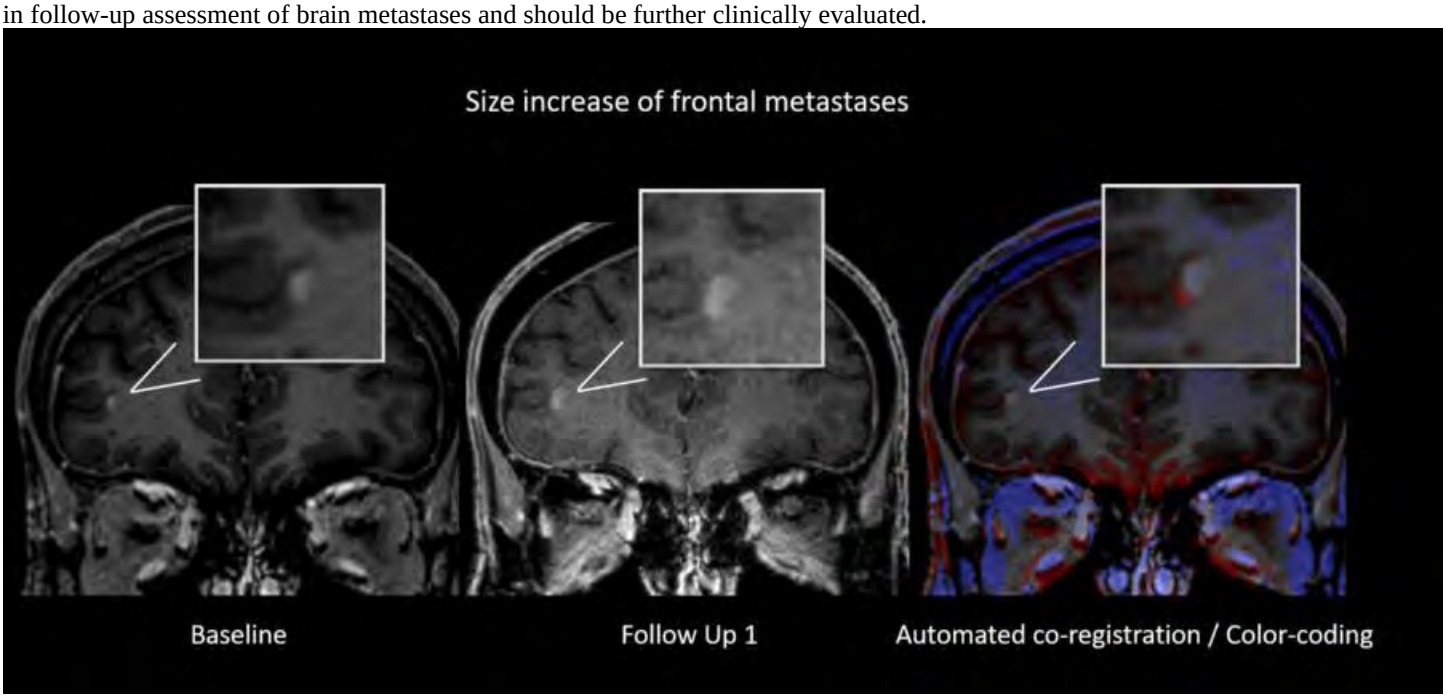

(Filename: TCT_1057_FIgure1ASNR.jpg)

1233

Evaluating the Efficacy of Regorafenib Treatment in Brain Tumors: Should We Rely on RANO Criteria Alone?

G Savini[1], F Garoli[2], L Giordano[3], P Persico[4], R Levi[5], E Clerici[6], P Navarria[6], F Pessina[7], M Grimaldi[8], M Simonelli[4], L Politi[9]

[1]Humanitas research Hospital, Rozzano, Milano, [2]Humanitas University, Rozzano, Milano (Italy), [3]Humanitas Research Hospital, Rozzano, Milan, [4]Humanitas University, Pieve Emanuele, Milan, [5]Humanitas University, Pieve Emanuele, Italy, [6]Humanitas Research Hospital, rozzano, italy, [7]Humanitas University, pieve emanuele, italy, [8]Humanitas Research Hospital, Rozzano, Milano, [9]Humanitas University, Pieve Emanuele, Milano

Purpose

Standard-of-care treatment of high-grade brain tumors includes maximal safe resection followed by radiotherapy and adjuvant chemotherapy with temozolomide. Disease recurrence frequently occurs and Regorafenib has been proposed as a second-line therapy (1). However, from a radiological point of view, RANO criteria may not be suitable to distinguish true progression from treatment-induced pseudo-progression (2,3) upon Regorafenib administration. This work aimed at identifying radiological features able to predict the clinical outcome of second-line treatment with Regorafenib in patients with high-grade brain tumors, and to distinguish between true disease progression and treatment-induced modifications.

Materials and Methods

In this preliminary study, we analyzed MR images from 17 patients with recurrent high-grade IDH wild-type brain tumors (15 glioblastomas, 2 anaplastic astrocytomas), who were scanned before, during and after Regorafenib treatment, with a minimum follow-up of 3 months. For each scan we manually segmented the tumor on an axial post-contrast T1-weighted (gdT1w) image and measured the tumor area. Upon co-registration with the 3D gdT1w, the area of intra-tumoral restricted diffusivity was measured on the ADC map. Matching slices were selected for the measurement of tumor size in the following time points. Tumor size measure on gdT1w and area of restricted diffusivity was used to perform a survival analysis with overall survival (OS) as primary endpoint.

Results

We found that the relative lesion growth alone, as measured on gdT1w, was not predictive of the OS. The same was also true for the lesion area measured on ADC maps. However, a high ratio between ADC and gdT1w lesion extent showed a remarkable protective effect, even when the lesion size on gdT1w images was increased. On the contrary, a small value of the ratio was a strong predictor of poor prognosis.

Conclusions

Our results showed that in high-grade brain tumors the response to treatment with Regorafenib can lead to apparent tumor growth on gdT1w images. Therefore, the contrast-enhancing lesion size alone is not a reliable marker of disease progression or treatment

response for these patients; on the contrary, the ratio between the area measured on ADC maps and gdT1w images is a promising marker of disease response and should be considered in the treatment decision process.

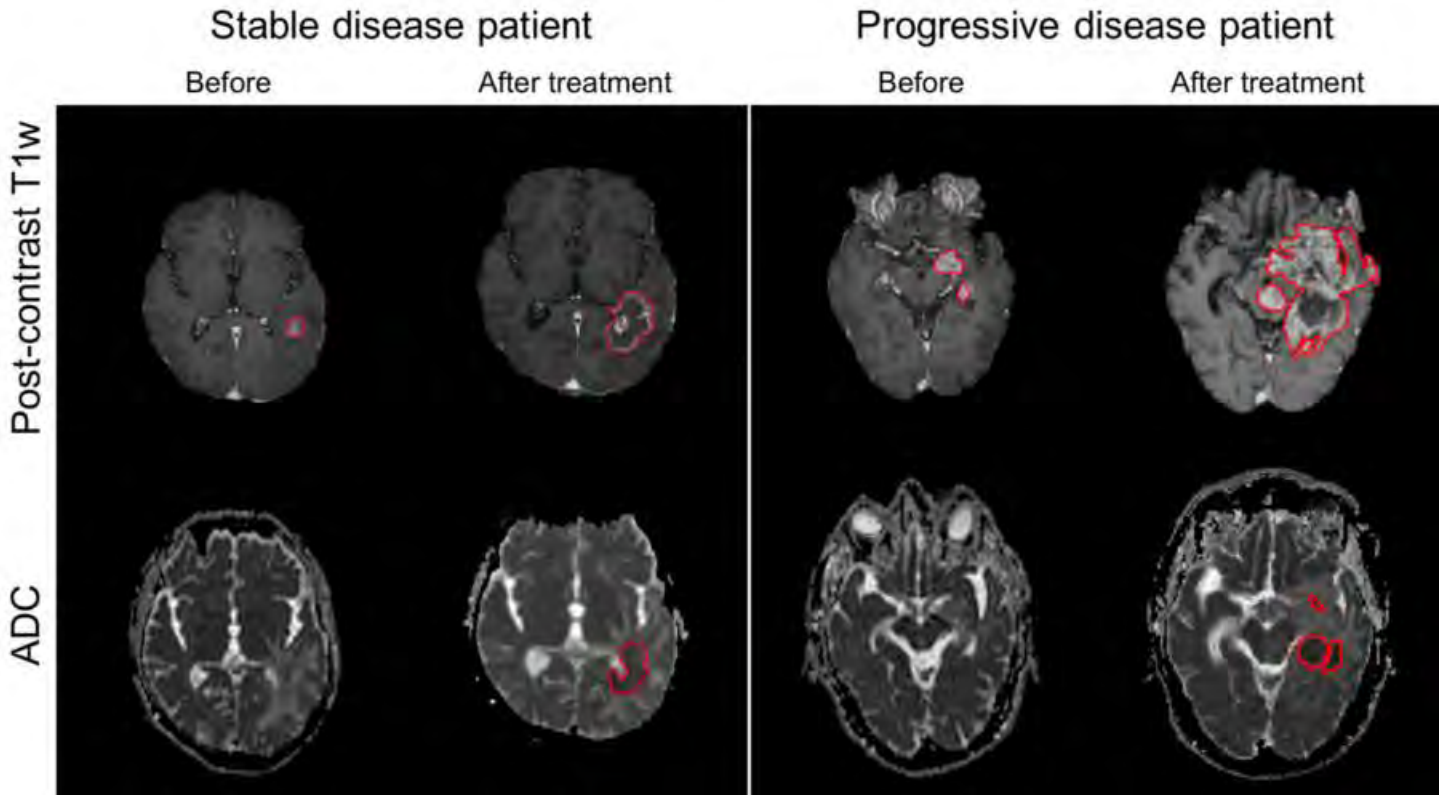

(Filename: TCT_1233_rego.jpg)

1005

Hybrid 18F-FET PET MRI: Multi-Modality Feature Analysis for Post-Treatment Malignant Brain Tumor Diagnosis at a US Institution.

N Smith[1], T Deaton[2], W Territo[1], M Green[1], G Hutchins[1], S Snyder[1], A KAMER[1], B Graner[1], M Veronesi[1]
[1]Indiana University School of Medicine, Indianapolis, IN, [2]Indiana University Purdue University Indianapolis, Indianapolis, IN

Purpose

18F-Fluoro-Ethyl-Tyrosine positron emission tomography (18F-FET PET) is rarely implemented in routine clinical care in the U.S. despite its high utility (1-3) and standardized international use recommendations (EANO/RANO) (4). Multimodal 18F-FET PET/MR image analysis metrics were analyzed within routine clinical care in the U.S. for post-treatment evaluation of high-grade gliomas (HGG) and brain metastases (BM).

Materials and Methods

51 patients with treated HGG or BM were evaluated over 62 imaging sessions on a Siemens 3T Biograph mMR PET/MRI unit from Aug 6th, 2020 through Apr 29th, 2021. The acquired perfusion-weighted MRI images (PWI), 18F-FET PET, and textural analysis metrics were analyzed for their capacity to differentiate treatment-related changes (TRC) from progression of disease (POD). Semiquantitative assessment metrics included: rCBV, Ktrans, and Ve for PWI; Tumor-to-Brain Ratio (TBR) max and mean, Standard Uptake Value (SUV), time-to-peak (TTP), slope, and Total Lesion FET Uptake (TLU) for 18F-FET PET metrics, and; Grey-Level Zone Length Matrix (GLZLM), Grey-Level Co-Occurrence Matrix (GLCM), and Neighborhood Grey-Level Difference Matrix (NGLDM) for 18F-FET PET textural features (5). Textural features were evaluated at the lesion center and edge for each patient. All patients were monitored beyond 6 months and subsequent pathology, imaging, and clinical reports established a final diagnosis via a panel of three Neuroradiologists. 45 of 51 patients were included in the sensitivity analysis because 4 patients died before final analysis and 2 patients were lost to follow-up. Of these 45 patients, 39 patients were included in the regression analysis since 6 patients had at least 1 non-diagnostic PWI parameter. All metrics were evaluated with receiver operating characteristic (ROC) analysis, and metrics with an AUC > 0.6 were implemented into a decision tree regression model.

Results

Refer to Table 1 for dataset characteristics, Table 2 for ROC analysis, and Figure 1 for decision tree regression. Figure 1 supports diagnostic confirmatory roles for TLU and GLCM metrics. Multimodal imaging improves the sensitivity and specificity for discriminating TRC from POD over PWI alone.

Conclusions

Reliable diagnosis of malignant brain tumor treatment response is limited with current imaging options in the US. This project

synthesized hybrid FET PET/MR analysis metrics at our institution for superior sensitivity, specificity, and reader confidence over single modality imaging.

Table 1. Data Acquisition and Patient Characteristics

	TOTAL	HGG	BM
TOTAL IMAGING SESSIONS (AUG 6, 2020 – APR 29, 2021)	62	35	27
PATIENTS WITH REPEAT ^{18}F-FET PET STUDIES	11	7	4
PATIENTS WHO DIED DURING STUDY	4	0	4
PATIENTS LOST TO FOLLOW-UP	2	1	1
PATIENTS INCLUDED IN SENSITIVITY ANALYSIS	45	27	18
PATIENTS WITH NON-DIAGNOSTIC PERFUSION MRI	6	1	5
PATIENTS INCLUDED IN REGRESSION ANALYSIS	39	26	13
FINAL DX POD	24	20	4
FINAL DX TRC	15	6	9

Table 1: Description of the total number of acquired datasets. Of 62 imaging sessions, 17 were excluded due to lack of 6-month follow-up or because of repeat studies. Further, 6 additional patients had corrupted MRI PWI values and were excluded from the regression analysis. In total, 45 patients were included in the sensitivity analysis, and 39 patients were included in the regression analysis.

Table 2. Sensitivity, Specificity, and Accuracy of Metrics by Modality

	ALL ACC N=45	ALL SN N=45	ALL SP N=45	HGG ACC N=26	BM ACC N=26	HGG SN N=26	BM SN N=19	HGG SP N=19	BM SP N=19
COMBINED MULTI-MODALITY (PET/MR)	91%	92%	90%	88%	95%	90%	100%	83%	93%
rCBV	72%	83%	56%	77%	62%	80%	100%	67%	50%
K_{TRANS}	67%	84%	45%	85%	44%	90%	75%	67%	36%
V_E	64%	80%	45%	85%	39%	90%	50%	67%	36%
TBR_{MAX}	89%	88%	90%	88%	89%	85%	100%	100%	86%
TBR_{MEAN}	82%	79%	85%	81%	83%	80%	75%	83%	86%
DISCRETIZED TLU	85%	80%	68%	88%	59%	85%	75%	100%	54%
GLCM DISSIMILARITY	60%	54%	68%	65%	56%	55%	67%	100%	54%

Table 2: Accuracy (ACC), sensitivity (SN), and specificity (SP) of high-performing metrics for distinguishing TRC from POD. High-grade glioma (HGG) and brain metastasis (BM) cases were evaluated individually and in combination using high-performing perfusion MRI (rCBV, K_{TRANS}, V_E) metrics, ^{18}F-FET PET (TBR_{MAX}, TBR_{MEAN}, Discretized TLU) metrics, and ^{18}F-FET PET textural analysis (GLCM Dissimilarity)

Figure 1:

Figure 1: Decision tree regression using factors with individual AUC >0.6 in ROC analysis (N=39). The data-driven primary cutoff (TBR_{max} > 2.42) demonstrates strong concordance with the established EANO/RANO criteria (TBR_{max} > 2.5). The data also suggests that ^{18}F-FET PET metrics (TLU and GLCM) are useful toward secondary confirmation of TRC and POD, respectively. In the above decision tree, Total Lesion Glycolysis (TLG) is an equivalent calculation for TLU in the ^{18}F-FET PET scan.

(Filename: TCT_1005_ASNRAbstract2021supplementhoriz.jpg)

524

Longitudinal evaluation of brain plasticity in glioma: graph-theory provides biomarkers of language reorganization on post-surgical fMRI

L Pasquini[1], K Peck[2], A Tao[3], G Del Ferraro[4], M jenabi[5], D Correa[5], E Kobylarz[6], C Brennan[5], A Holodny[7]

[1]Memorial Sloan Kettering Cancer Center, New York, NY, [2]Department of Radiology, Memorial Sloan Kettering Cancer Center, New York, NY, [3]Weill Cornell University, New York City, NY, [4]New York University, New York City, NY, [5]Memorial Sloan Kettering Cancer Center, New York City, NY, [6]Weill Medical College of Cornell University, New York City, NY, [7]MEMORIAL SLOAN KETTERING CANCER CENTER, NEW YORK, NY

Purpose

Language reorganization is an adaptive phenomenon to tumor invasion of the dominant hemisphere1. Plastic changes of eloquent areas may affect treatment planning; however, their dynamics are unknown. K-coreness is a graph-theoretical measure capable of pointing out the most important components of a network (core)2, whose reorganization may represent a biomarker of plastic changes. Our aim was to evaluate glioma patients before and after surgery with functional MRI (fMRI) and graph theory. We hypothesized that this longitudinal evaluation will unravel connectivity changes underlying language reorganization.

Materials and Methods

Inclusion criteria: right-handedness; left-hemispheric glioma; no tumor progression; task-based language fMRI at 4 timepoints: pre-op, post-op1(4-8months), post-op2(8-15months), post-op3(14-24months). Language ability was evaluated at every timepoint by cognitive tests. Starting from fMRI clusters, we computed individual functional networks as previously shown, by applying optimal percolation thresholding3,4. Language dominance was quantified via voxel count on fMRI with a laterality index (LI) defined as (L-R)/(L+R)4. We run k-core centrality measure to characterize changes of the language network over time.

Results

Five patients (4M, mean 47.6Y) were recruited. Individual networks showed increased inter- and right-hemispheric connections over time, involving eloquent language areas homologues: BA (5/5), WA (3/5), Exner's (2/5), middle frontal gyrus (5/5), insula (3/5). We found two main patterns of language reorganization: LI demonstrated left-to-codominant shift from pre-op to post-op3 in 3/5 patients (type1); K-coreness confirmed this trend, with increased high-rank occupancy of right-sided areas after surgery. On the other hand, 2/5 patients started as co-dominant on pre-op and remained the same at post-op3 (type2). Language ability remained stable over time.

Conclusions

Plastic changes follow surgical resection of LGG. fMRI maps showed increased activation in the right hemisphere over time. Connectivity maps showed increased inter-hemispheric connections involving language areas-homologues. K-coreness confirmed this trend and showed complete right-shift of the network core in one case. We found two patterns of language reorganization: type1 changes may be surgery-related; type2 may be tumor-induced, since already present at baseline. Language plasticity may help compensating post-surgical deficits, as demonstrated by stable language ability.

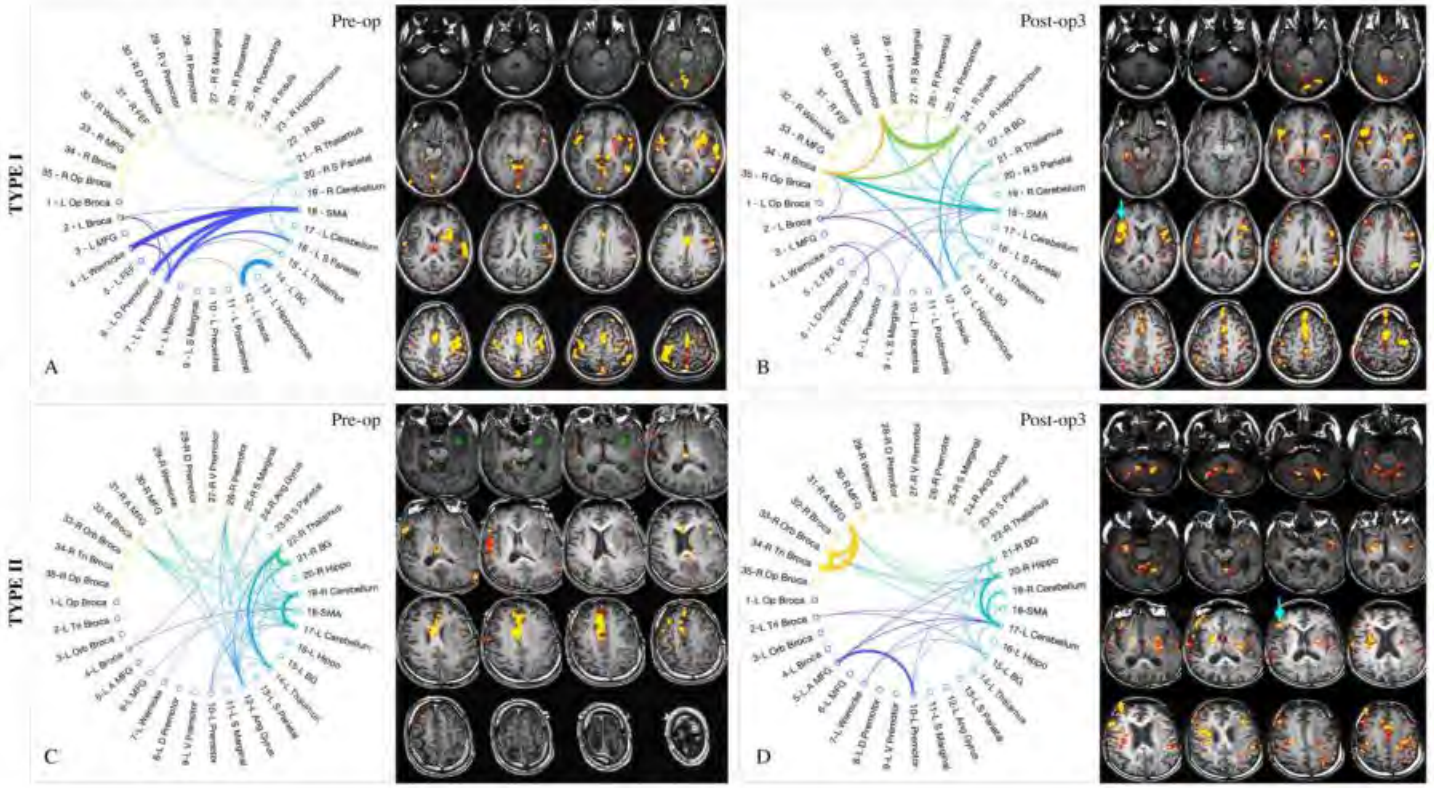

The panels above (A and B) display a case of "type I" plasticity in a patient with left frontal glioma (green asterisk in A): before surgery (panel A) the brain connectivity diagram and task-based language fMRI maps show prevalent left-sided connections and left dominance. In the post-operative timepoint #3 (20 months after surgery in this case, panel B), the connectivity diagram shows increased inter-hemispheric and right-sided connections, while fMRI maps show right-sided activation, including Broca's area homologous (light blue arrow in B). K-coreness confirmed this trend and showed complete right-shift of the network core in this case.

The panels below (C and D) display a case of "type II" plasticity in a patient with left temporal-insular glioma (green asterisks in C): before surgery (panel C) the brain connectivity diagram shows inter-hemispheric connections between eloquent language areas at baseline; fMRI maps show right-sided Broca's area (red arrow in C). In the post-operative timepoint #3 (16 months after surgery in this case, panel D), the connectivity diagram and fMRI maps show persistent inter-hemispheric and right-sided connections, including Broca's area homologous activation (light blue arrow in D).

(Filename: TCT_524_figure.jpg)

398

MGMT combined with post-CRT perfusion MRI-derived Fractional Tumor Burden informs overall survival in newly diagnosed glioblastoma.

M Prah[1], J Connelly[1], K Schmainda[1]
[1]*Medical College of Wisconsin, Milwaukee, WI*

Purpose

To evaluate whether image stratification by fractional tumor burden (FTB) [1,2] of newly diagnosed glioblastoma (nGBM) informs a survival benefit beyond MGMT promoter methylation status [3].

Materials and Methods

Consented subjects were identified from a database of nGBM brain tumors following standard upfront therapy including surgical diagnosis followed by irradiation with concomitant (CRT) and adjuvant temozolomide. Only subjects with measurable disease, known MGMT promoter methylation status, and pre- and post-contrast T1w and dynamic susceptibility contrast (DSC: TE/TR=30/1500 ms, FA=60 degrees, 0.1 mmol/kg preload + 0.1 mmol/kg bolus) MRI acquired within 6 wks following completion of CRT were included. Subjects with known IDH1 mutation were not considered for analysis. FTB maps (using thresholds previously established from MRI spatially co-localized to tumor histology) were generated using leakage corrected and standardized relative cerebral blood volume (sRCBV) and standardized deltaT1 maps (Imaging Biometrics, Elm Grove, WI) [1,4,5]. Twenty-four month overall survival (OS) was evaluated for MGMT methylation status alone and in combination with FTB volume above or below 5 ml (empirically chosen). For comparison, OS was also estimated for mean sRCBV within the enhancing lesion (stratified by the cohort mean of 1.3 a.u.). OS was estimated using Kaplan-Meier and measured from the date of post-CRT imaging (P<.05 is significant).

Results

Results are shown in Figure 1. A total of 43 subjects (male/female=21/22) met inclusion criteria, with n=15 MGMT methylated and n=28 MGMT unmethylated. All but one subject was older than 40 y/o (mean=57, range=23-74). Imaging was acquired an average of 29 (range=12-42) days following CRT. MGMT methylated had significant OS benefit compared to unmethylated subjects (OS=19.08 vs 10.18 months; P=.0129; HR=2.5). When further stratified by FTB volume, those with methylated MGMT showed no further distinction in OS (P=.64). However, those with unmethylated MGMT status had significant benefit in OS when FTB volume was less

than 5 ml (OS=16.15 vs 8.39 months; P=.0054, HR=2.8). Mean sRCBV did not reveal any significant OS advantages for those with MGMT methylated (P=.9275) or unmethylated (P=.2986) tumors.

Conclusions

FTB volume in combination with unmethylated MGMT informs survival outcomes in nGBM patients in the early post-CRT time-period, potentially identifying those who might respond better to treatment or for whom more aggressive treatment approaches are warranted.

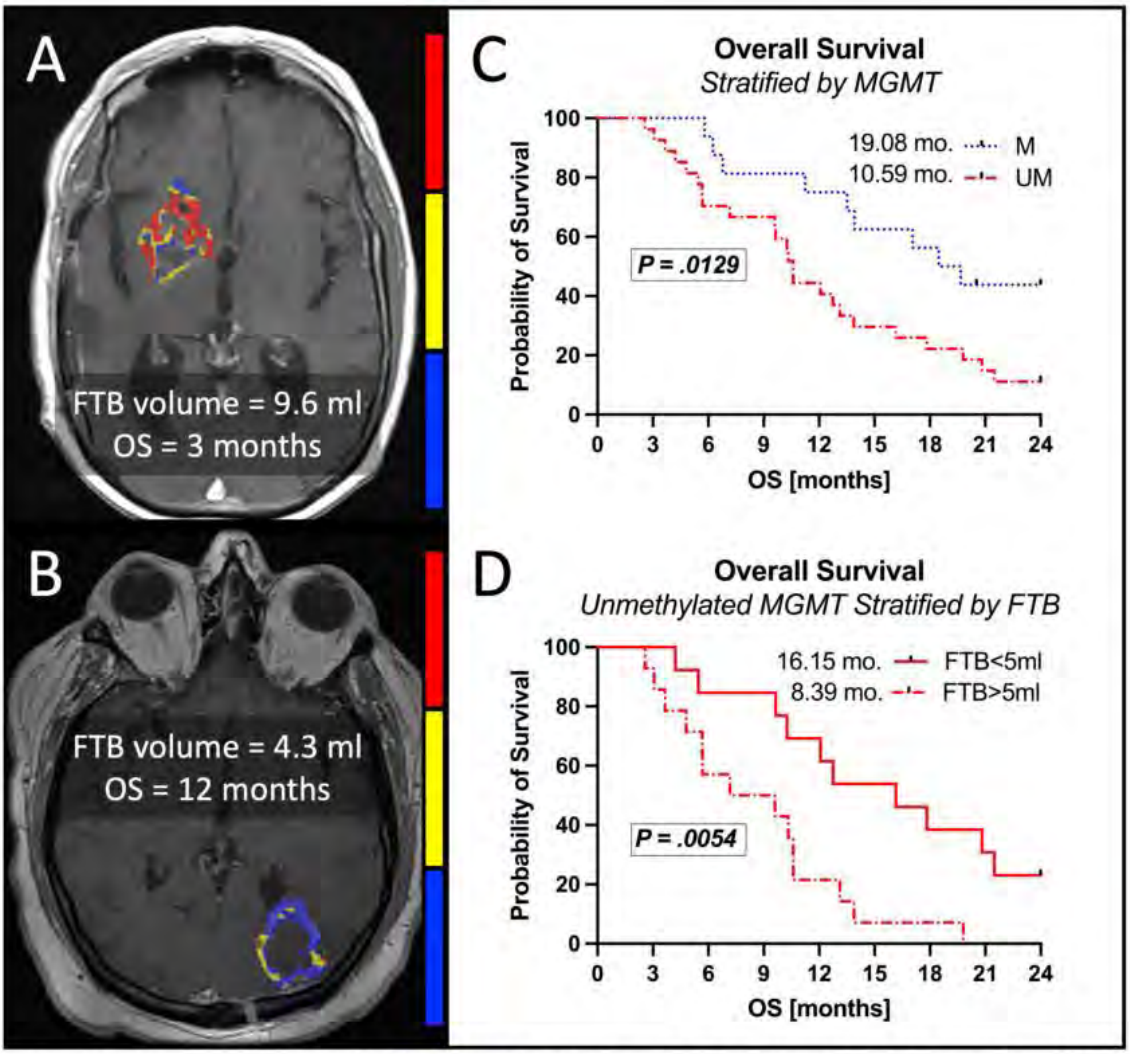

Figure 1: *Representative FTB maps (A, B) and overall survival curves (C, D). Representative FTB maps from MGMT unmethylated nGBM patients following CRT in a 61 y/o male with FTB volume > 5 ml (A) and in a 43 y/o male with FTB volume < 5 ml (B). 24-month overall survival stratified by MGMT methylation status alone (C) and FTB volume in combination with unmethylated MGMT (D). Note: nGBM=newly diagnosed glioblastoma, M=MGMT methylated, UM=MGMT unmethylated, FTB = fractional tumor burden, FTB volume includes red and yellow regions*

(Filename: TCT_398_ASNR_FigureUpdated.jpg)

690

PET/CT in Predicting Lymph Node Metastasis With Early-Stage Oral Cavity Cancer

J Lee[1], S Stock[2], S Campbell[3], B Prendes[3], J Geiger[3], J Scharpf[3], E Yilmaz[3], N Woody[3], J Ku[3], E Lamarre[3], S Koyfman[3]

[1]Cleveland Clinic, Brecksville, OH, [2]Cleveland Clinic Foundation, Cleveland, OH, [3]Cleveland Clinic, Cleveland, OH

Purpose

The use of sentinel lymph node biopsy is growing in early stage (T1-T2) oral cavity squamous cell carcinoma (OC-SCC). The ongoing NRG-HN006 trial seeks to de-intensify treatment in the early stage OC-SCC clinical N0 group with sentinel lymph node sampling instead of neck dissection. HN006 uses a SUVmax cutoff of 3.5, while most radiologists use SUVmax of 2.5 in clinical practice to identify suspicious lymph nodes. We retrospectively reviewed pre-operative PET/CTs for early stage OC-SCC N0 patients (SUVmax<3.5) to validate using a SUVmax >3.5 rather than 2.5 for stratification of patients into a de-intensified treatment course.

Materials and Methods

This is an IRB approved retrospective review of our head and neck cancer database queried for early stage (T1-T2) clinical N0 initial diagnosis OC-SCC with pre-operative PET/CT within 30 days of surgery, which included local excision and at least ipsilateral lymph

node dissection. A neuroradiologist with 6 years experience evaluated the PET/CT and CT neck for ipsilateral level I/II lymph node Max SUV.

Results

50 patients were included, 12 (25%) patients were clinical T1, and 38 were clinical T2 (75%). In total, 11 (22%) clinical N0 patients with SUVmax<3.5 had pathologically positive lymph node metastasis. Using a SUVmax cutoff of 2.5, 8 (16%) out of the 50 patient would have had at least one lymph node clinically suspicious for metastasis. 3 (27%) out of 11 patients with pathologically positive lymph nodes had level III (2) or level IV (1) metastasis which all had SUVmax <2.5, and the rest had level I or II lymph node metastasis. In the 39 patients with no lymph node metastasis, 5 (13%) had a SUVmax between 2.5 and 3.5.

Conclusions

Based on this retrospective review of early stage OC- SCC with clinically negative lymph nodes (SUVmax<3.5) treated with surgery, the overall incidence of lymph node metastasis on neck dissection is low at 22%, so elective neck dissection would have been negative in 78% of these patients, or almost 4 out of 5. If a SUVmax<2.5 was used, 16% had lymph node metastasis, which is a small absolute difference from 22%. Therefore, enrolling early stage OC-SCC clinically N0 patients with a SUVmax<3.5 in a sentinel lymph node trial seems appropriate, although HN006 trial results for outcomes will be needed for confirmation.

947

Regional correlates of GBM cancer hallmarks using the DSC-MRI Consensus Protocol

D Malik[1], M Kong[1], R Patel[1], T Dondlinger[2], K Singleton[1], J Urcuyo[3], L Curtin[1], E Lewis[4], G Mazza[1], K Donev[1], L Wang[5], H Wang[5], J Li[5], K Swanson[1], N Tran[1], J Boxerman[6], C Quarles[7], K Schmainda[8], Y Zhou[9], C Plaisier[4], L Hu[1]

[1]Mayo Clinic, Arizona, Phoenix, AZ, [2]Imaging Biometrics, LLC, Elm Grove, WI, [3]Mayo Clinic, Phoenix, AZ, [4]Arizona State University, Tempe, AZ, [5]Georgia Tech, Atlanta, GA, [6]Rhode Island Hospital / Brown University, Providence, RI, [7]Barrow Neurological Institute, Phoenix, AZ, [8]Medical College of Wisconsin, Milwaukee, WI, [9]Mayo Clinic, Scottsdale, AZ

Purpose

The 2020 DSC-MRI consensus recommendations offer a pathway for widespread clinical adoption (1). Neuro-oncologic applications have focussed on the metric relative cerebral blood volume (rCBV) and the diagnosis of histologic identity (e.g., high-grade vs. low-grade glioma, recurrence vs. post-treatment effect) (2). While other DSC metrics, such as percent signal recovery (PSR) and cerebral blood flow (CBF), have remained understudied, they offer potentially complementary insights to tumor biology and molecular characterization (3, 4). We correlate various DSC metrics (rCBV, PSR, CBF) from consensus acquisitions with cancer hallmark pathways in GBM (angiogenesis, proliferation, invasion) (5), as defined through gene expression from spatially matched image-localized biopsies.

Materials and Methods

We recruited patients undergoing presurgical MRI for suspected GBM, including conventional MRI and Dynamic Susceptibility Contrast (DSC-MRI) using the consensus protocol with 2 separate, sequential single dose contrast bolus injections: the first (0+1) with flip angle (FA) 30 degrees, and the second (1+1) with FA 60 degrees. We measured parametric maps for PSR, relative CBF, and both normalized (norm-rCBV) and standardized (std-rCBV) rCBV from FA30 and FA60 acquisitions. We spatially coregistered regions of interest with recorded stereotactic locations of corresponding biopsies. For each biopsy, we performed RNA sequencing to define gene set enrichment scores for key hallmark pathways: angiogenesis, proliferation, invasion. We determined Pearson correlations ($p < 0.05$) between spatially matched data pairs, using mixed effect models for multiple samples from each patient.

Results

We collected 78 biopsies from 22 patients. Both PSR (FA30 and FA60) and relative CBF (FA30 and FA60) positively correlated with proliferation ($p<0.05$), while PSR (FA60) also correlated positively with invasion and angiogenesis pathways ($p<0.05$). None of the hallmark pathways correlated positively with rCBV. Surprisingly, angiogenesis (receptor expression) negatively correlated with std-rCBV (t value = -2.1) and norm rCBV (t value = -2.0) on FA30 ($p<0.05$).

Conclusions

To our knowledge, this study is the first to report correlations between consensus protocol DSC metrics and cancer hallmark pathways using image-localized stereotactic biopsies. Our results suggest the utility of complementary DSC metrics such as PSR and CBF, and also challenge conventional wisdom regarding rCBV and angiogenesis.

1404

Semi-Automated Longitudinal Lesion Tracking In PACS Reveals High Proportion of Metastatic Lesions Showing Mixed Response To Radiosurgery

G Cassinelli Petersen[1], T Verma[2], K Bousabarah[3], L Jekel[1], S Merkaj[1], R Bahar[1], S Abi Fadel[4], I Ikuta[5], M Lin[6], A Omuro[1], M Aboian[4]

[1]Yale School of Medicine, New Haven, CT, [2]Yale School of Medicine, Ossining, NY, [3]Visage Imaging GmbH, Berlin, CT, [4]Yale University, Woodbridge, CT, [5]Yale University School of Medicine, New Haven, CT, [6]Yale University School of Medicine and Visage Imaging, Inc., New Haven, CT

Purpose

Brain metastases are the most common neoplasm of the brain. Gamma-Knife (GK) allows precise radiation of individual lesions. In contrast, classical methods of assessing treatment response use the overall sum of diameters, failing to convey how individual lesions

contribute differently to overall tumor burden. Demonstrate a PACS-integrated method of assessing multiple follow-up MR scans to characterize treatment response of individual metastatic lesions.
Materials and Methods
100 patients who underwent GK for brain metastases were randomly selected and scanned for exclusion criteria. Lesion tracking was performed using PACS-integrated Lesion Tracking Tool (LTT) (Visage Imaging) beginning with the GK-scan and followed for up to 7 scans, depending on availability. Lesions =>10mm longest diameter (LD) were classified as progressive, receding, or stable if LD increased >20% from nadir, decreased >30% from baseline, or neither, respectively. For lesions <10mm LD a minimum change of at least 3mm was needed to classify as changing. By comparing the different lesions within a patient, treatment response was classified as homogenous or as mixed at the last available follow-up study
Results
81 patients were eligible; 472 lesions were measured [mean follow-up: 376 days (Range: 71-1374)]. 71 patients had >1 lesion. At last date of follow-up, 81.7%, 12.7%, 1.4%, 4.2% of patients had a mixed; homogenously decreasing, stable, and increasing response to treatment, respectively. Proportion of patients with mixed response increased from 52.3% in patients with 2 lesions (n=19) to 96.2% in those with >4 (n=26). Follow-ups performed within 90 days post-intervention showed mixed response in 54.9% of patients (n=71 patients), while this proportion rose to 74.4% in patients that were followed for more than a year (n=39).
Conclusions
Assessing treatment response of metastatic lesions in the brain allows personalized treatment planning. Our study shows that metastatic lesions in a patient can differ in their response to the same treatment, arguing in favor of tracking individual lesions. We recommend incorporation of PACS-integrated lesion tracking in clinical practice to better characterize growth changes in patients with metastatic lesions.

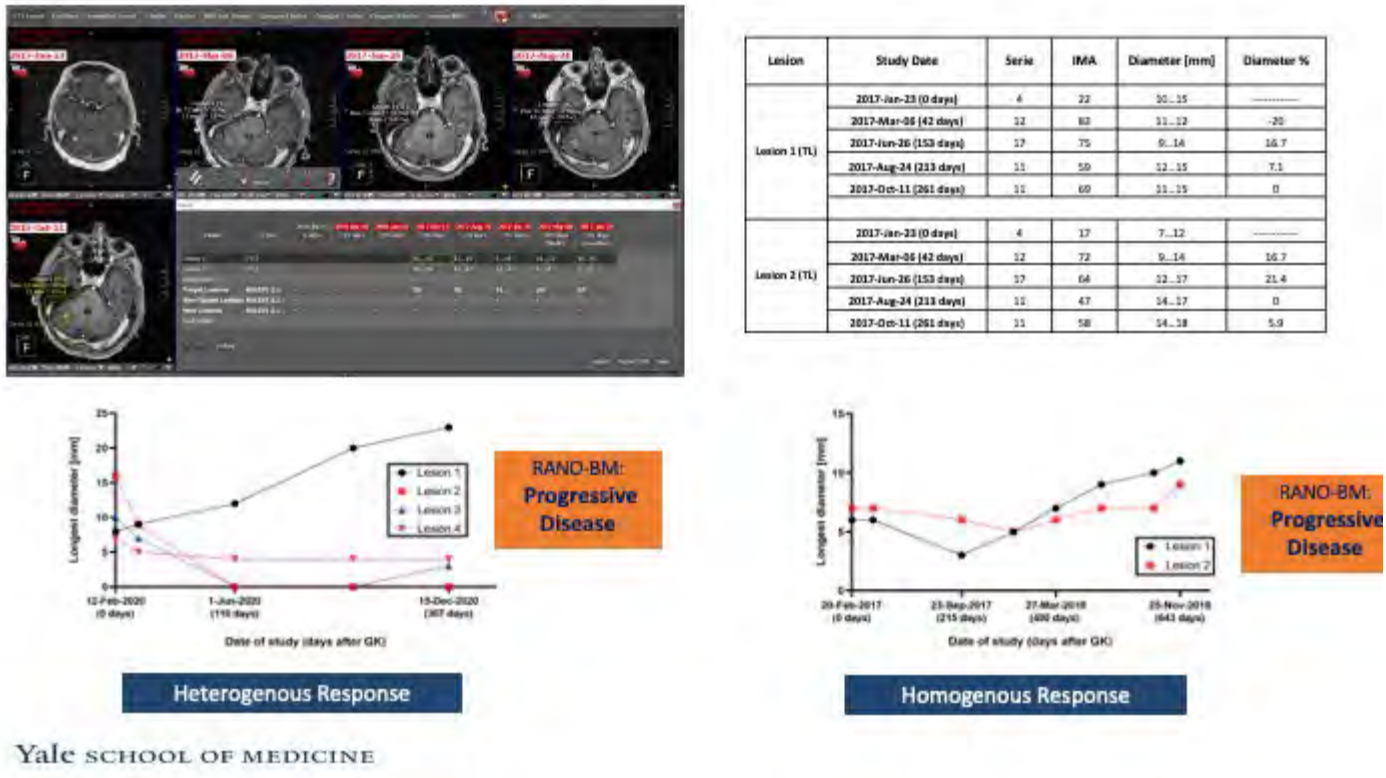

(Filename: TCT_1404_Figures_20211115.jpg)

263

Towards Artificial Intelligence-driven Neuro-oncology Workflows

S Chakrabarty[1], S Abidi[2], M Mousa[3], M Kelsey[3], P LaMontagne[3], M Hileman[3], A Sotiras[4], D Marcus[3]
[1]Washington University in St. Louis, Saint Louis, MO, [2]Mallinckrodt Institute of Radiology, St Louis, MO, [3]Washington University School of Medicine, St. Louis, MO, [4]Washington University in St. Louis, St. Louis, MO

Purpose
Modern neuro-oncology workflows involve large collections of high dimensional and heterogeneous magnetic resonance imaging (MRI) data obtained using varying acquisition protocols that need to be carefully curated and pre-processed prior to algorithmic use. Additionally, there is a growing need for quantitative measures for accurate tumor tracking, response assessment (e.g., Response assessment in neuro-oncology criteria [RANO]), and treatment planning. Currently, these processes require manual intervention and can be extremely time-intensive and tedious. To this end, we leverage artificial intelligence (AI) based approaches to devise an automated workflow for curation and preprocessing of neuro-oncology studies, with subsequent extraction of quantitative phenotypes.

Materials and Methods

Our AI-driven end-to-end workflow i) uses natural language processing [1] and convolutional neural network [2] to classify MRI scans into different anatomical and non-anatomical types; ii) preprocesses (co-registration to an anatomical atlas and skull-stripping) the data in a reproducible way; and iii) uses AI [3] to delineate tumor tissue subtypes, enabling extraction of volumetric information along with shape and texture-based radiomic features. Moreover, it is robust to missing modalities and adopts an expert-in-the-loop approach, where segmentation results may be manually refined by radiologists. This workflow was implemented as Docker Containers in a local XNAT [4] instance and applied on preoperative MRI scans from 100 patients with histopathologically confirmed gliomas (grade II-IV). Data were retrospectively collected from the Washington University School of Medicine. Segmentation results were refined by two neuroradiologists (R1 and R2), and performance was quantified by using Dice Similarity Coefficient (DSC) between predicted and expert-refined tumor masks.

Results

The scan-type classifier yielded a 98.99% accuracy and could identify appropriate multi-modal scans from all 100 sessions that can be given as input to the AI segmentation tool. 5 sessions were excluded due to failure in image registration. Compared to R1 and R2, the segmentation model achieved mean DSCs of 0.968 (0.084) and 0.959 (0.101), respectively.

Conclusions

The developed pipeline was able to automatically process and segment raw MRI data of patients with different grades of gliomas without expert supervision. This can enable an AI-driven diagnostic radiology workflow or assist in the curation of large-scale neuro-oncology datasets.

Table 1: Demographic and clinical information of patient data acquired from Washington University School of Medicine (WUSM)

	WUSM (n = 100)
Age	53 (34 - 65)
Sex	
female	37 (37.0%)
male	63 (63.0%)
WHO Grade	
G2	25 (25.0%)
G3	25 (25.0%)
G4	50 (50.0%)

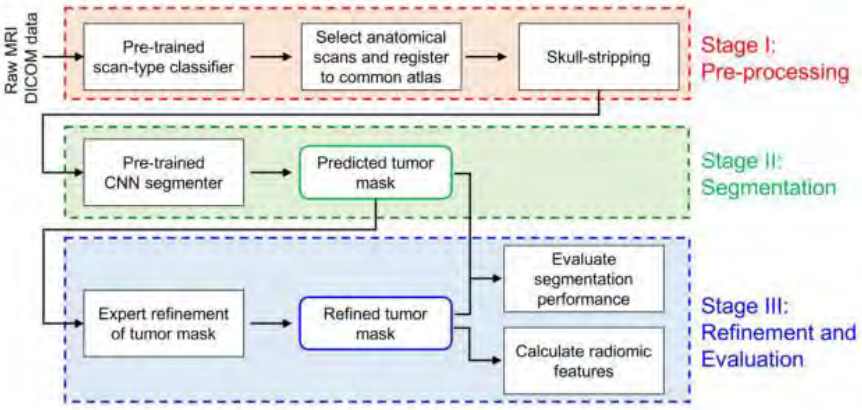

Figure 1: Overview of proposed end-to-end workflow.

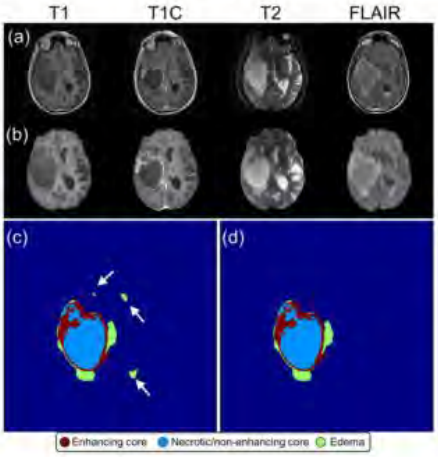

Figure 2: Figure shows (a) unprocessed pre- and post-contrast T1-weighted (T1, T1C), T2-weighted (T2), and Fluid Attenuated Inversion Recovery (FLAIR) sequences, (b) same sequences after registration to anatomical atlas and skull-stripping, (c) tumor segmentation predicted by AI, (d) tumor segmentation after refinement. White arrows in (c) signify the false-positives which were corrected in the refinement (d).

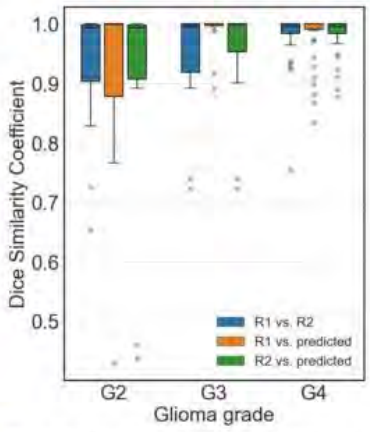

Figure 3: Figure shows the dispersion of Dice Similarity Coefficient (DSC) values, stratified by tumor grade, between the tumor segmentation masks of the two radiologists (R1 vs. R2), and between radiologists and the predicted segmentation (R1 vs. predicted, R2 vs. predicted)

(Filename: TCT_263_Figure300.jpg)

127

A Systematic Review of Recurrent Ischemic Stroke Outcomes

S Ferrone[1], A Boltyenkov[2], Z Lodato[1], J O'Hara[2], J Vialet[2], A Malhotra[3], J Katz[2], J Wang[4], C Feizullayeva[2], P Sanelli[2]
[1]Feinstein Institutes for Medical Research, Manhasset, NY, [2]Northwell Health, Manhasset, NY, [3]Yale University School of Medicine, New Canaan, CT, [4]Northwell Health, Manhassett, NY

Purpose
Recurrent stroke patients suffer significant morbidity and mortality, representing almost 30% of the stroke population. Our objective was to determine the clinical outcomes and costs of recurrent ischemic stroke (recurrent-IS) patients.
Materials and Methods
Our study protocol was registered with the International Prospective Register of Systematic Reviews (CRD42020192709). Following PRISMA guidelines, our medical librarian conducted a search in EMBASE, PubMed, Web-of-Science, Scopus, and CINAHL (last performed on August 25, 2020). Inclusion criteria: (1) Studies reporting clinical outcomes and/or costs of recurrent-IS; (2) Original research published in English in year 2010 or later; and (3) Study participants aged ≥18 years. Exclusion criteria: (1) Case reports/studies, abstracts/posters, Editorial letters/reviews; and (2) Studies analyzing interventions other than intravenous thrombolysis and thrombectomy. Studies were selected with review of titles/abstracts and full-text, and data extraction performed by four independent reviewers using Covidence software. Discrepancies were resolved by a senior independent arbitrator. Quality of studies and risk-of-bias was assessed using the Mixed Methods Appraisal Tool.
Results
The PRISMA flow diagram (Figure 1) displays the selection of studies. Initial search yielded 20,428 studies. After duplicates were removed, 9 studies were selected based on inclusion/exclusion criteria, consisting of 24,499 recurrent-IS patients. The characteristics of each study included in the data extraction is shown in Table 1. In 5 studies, recurrent-IS ranged from 4.4-56.8% of the ischemic stroke population with mean age 60-80 years, and female proportions 38.5-61.1% (Table 2). Clinical outcomes included mortality 11.6-25.9% (3 studies), mean length-of-stay 9.2–19.7 days (5 studies), and discharge-to-home 28.3-55.6% (2 studies). In one study from the U.S., the mean in-hospital costs per patient were $17,121(SD $53,693) and 1-year disability costs were $34,639(SD $76,586) (Table 3).
Conclusions
Our study highlights the paucity of data on the clinical outcomes and costs of recurrent-IS and identifies gaps in existing literature to direct future research. Importantly, there is a lack of demographic and socioeconomic data on recurrent-IS. Without a clear understanding of recurrent-IS patient characteristics, any disparities that may exist in clinical outcomes and costs cannot be addressed.

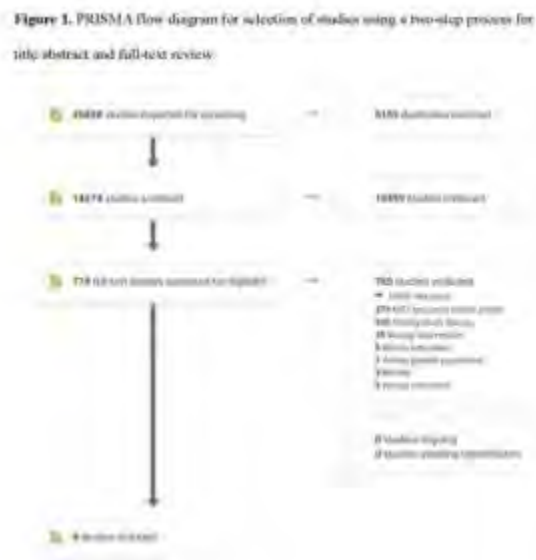

Table 1. Study Characteristics

First Author (Last name)	Publication Year	Country	Study Period (Years)	Data Source	Ischemic Stroke (N)	Recurrent Ischemic Stroke (N)	Recurrent Ischemic Stroke (%)	Follow-up Recurrence Period (Months)
Johnson[10]	2016	U.S.	2008-2013	Commercial Medicare	51,351	10,217	19.9%	3
Albright[11]	2018	U.S.	1999-2013	Medicare	128,789	10,450	8.1%	12
Shah[9]	2020	U.S.	2006-2015	Medicare	31,987	1,399	4.4%	3
Engel-Nitz[13]	2010	U.S.	2002-2003	D Innovus managed care plan	2,180	372	17.1%	12
Kwon[12]	2014	South Korea	2003-2009	Single center	1,986	391	19.7%	Not-defined
Rha[13]	2013	South Korea	2006	Multi-center (8 centers)	594	95	16.0%	Not-defined
Huang[14]	2013	Taiwan	2005-2007	Single center	982	558	56.8%	Not-defined
Ma[15]	2010	China	2008	Single center	557	64	11.5%	Not-defined
Meretoja[17]	2011	Finland	1999-2007	PERFECT Stroke database	8,204	953	11.6%	12

Table 3. Medical Care Costs of the Recurrent Ischemic Stroke Study Cohorts

First Author (Last name, Publication year)	Data Source	Recurrent Ischemic Stroke (N)	Currency and Year	In-hospital costs	In-hospital costs converted to 2021 USD	Disability costs and Follow-up period	Disability costs converted to 2021 USD
Johnson[10] 2016	Commercial Medicare	10,217	USD 2013	-	-	-	-
Albright[11] 2018	Medicare	10,450	-	-	-	-	-
Shah[9] 2020	Medicare	1,399	-	-	-	-	-
Engel-Nitz[13] 2010	D Innovus managed care plan	372	USD 2005	Mean: $17,121 (SD $53,693)	Mean: $23,145 (SD $72,585)	1-year follow-up Mean: $34,639 (SD $76,586)	1-year follow-up Mean: $46,826 (SD $103,532)
Kwon[12] 2014	Single center	391	USD 2003	Mean: $4,423 (SE $368)	Mean: $6,816 (SE $568)	-	-
Rha[13] 2013	Multi-center (8 centers)	95	Korean 2007	-	-	2-year follow-up KRW 4,668,993	2-year follow-up $7,719
Huang[14] 2013	Single center	558	USD 2012	Mean: $1,389 (SD $2,172)	Mean: $1,584 (SD $2,478)	-	-
Ma[15] 2010	Single center	64	-	-	-	-	-
Meretoja[17] 2011	PERFECT Stroke database	953	USD 2008	-	-	1-year follow-up Mean: $43,093	1-year follow-up Mean: $57,141

(Filename: TCT_127_Figure_Tables_ASNR_Abstract.jpg)

1192

Automated measurement of stroke reperfusion volume after endovascular thrombectomy using digital subtraction angiography

H Ullman[1], A Kansagra[1]
[1]*Washington University in St Louis, ST LOUIS, MO*

Purpose

The degree of reperfusion of hypoperfused brain tissue is an important biomarker for measuring the technical success and prognosis after endovascular thrombectomy (ET) in acute ischemic stroke. Currently, the most widely adopted scale in use for measuring the technical success of ET is the Expanded Treatment In Cerebral Infarction (eTICI) score. While easy to use for operators and not reliant on additional imaging, its use as a biomarker is limited by subjectivity and non-granularity. Here, we propose a fully automated and objective method for estimating the volume of reperfused brain following ET using digital subtraction angiography (DSA).

Materials and Methods

Standard anterior-posterior (AP) and lateral projections of internal carotid artery angiography were acquired at 2 frames per second and converted into a two-dimensional time series. Independent component analysis was applied to pre- and post-ET images to separate

three independent projected components corresponding to arterial, capillary, and venous phases. Corresponding phases from pre- and post-ET DSA were matched to each other by calculating a correlation matrix and identifying the pairings with greatest overlap. The pre-ET capillary phase was subtracted from the post-ET capillary phase to yield AP and lateral maps of increased perfusion after ET. These maps were thresholded and spheres were fitted to estimate the volume of reperfused brain parenchyma.

Results

The independent component analysis consistently separated three components that visually corresponded to the arterial, capillary, and venous phases (Figure 1a). The resulting reperfusion maps (Figure 1b) visually corresponded to the area of reperfusion on the post-ET angiogram and allowed estimation of the volume of reperfusion after ET (Figure 1c).

Conclusions

Our proposed method allows automated and objective estimation of the volume of reperfusion after ET using only DSA images that are routinely acquired during ET. The method has the potential for being used as a biomarker measuring the technical success of ET. Further studies are needed to evaluate clinical use of the biomarker.

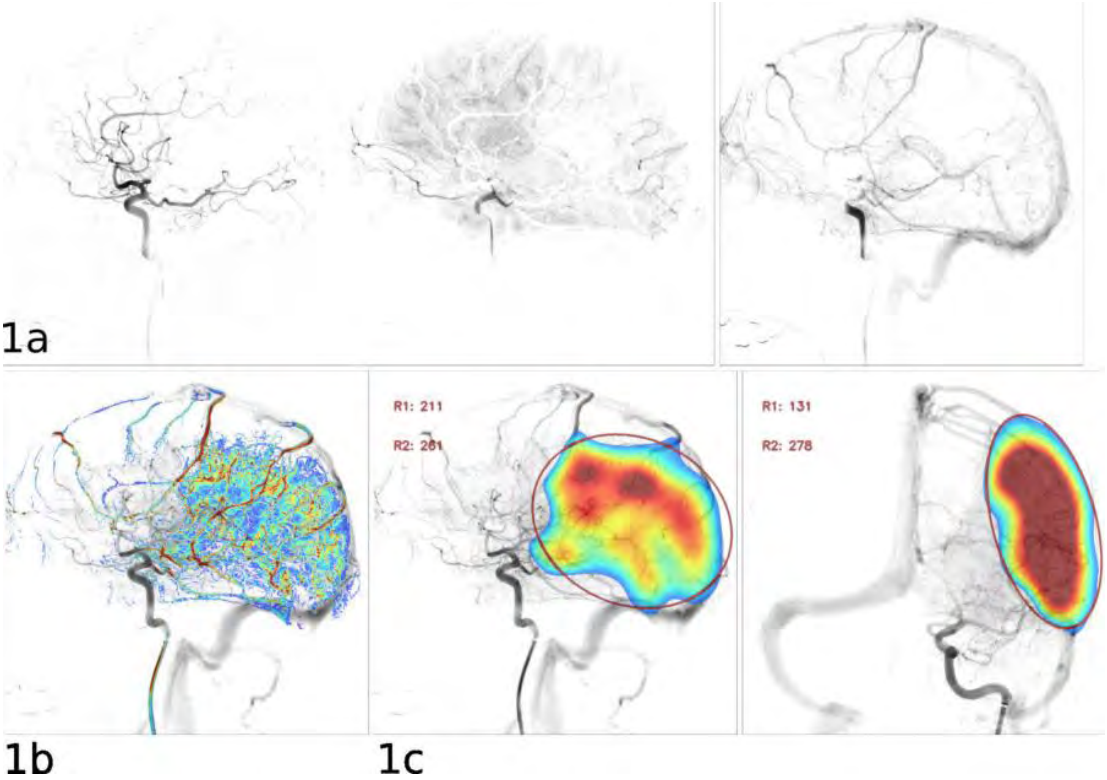

(Filename: TCT_1192_qqkWxo.jpg)

319

Benefit of Successful Reperfusion Achieved by Endovascular Thrombectomy for Patients with Ischemic Stroke and Moderate Pre-stroke disability (mRS 3): Results from the MR CLEAN Registry.

F Benali[1], M Kappelhof[2], J Ospel[3], A Ganesh[4], R McDonough[5], A Postma[6], R Goldhoorn[7], C Majoie[8], I van den Wijngaard[9], H Lingsma[10], W van Zwam[11], M GOYAL[12]

[1]Maastricht University Medical Center, Maastricht, Limburg, [2]Amsterdam UMC, University of Amsterdam, Amsterdam, Noord-Holland, [3]University Hospital Basel, Basel, Basel, [4]Departments of Clinical Neurosciences and Community Health Sciences and the Hotchkiss Brain Institut, Calgary, Alberta, [5]University of Calgary, Calgary, Alberta, [6]MUMC+, Maastricht, limburg, [7]Maastricht University Medical Center (MUMC+), Maastricht, Limburg, [8]Amsterdam University Medical Centers, Amsterdam, Noord-Holland, [9]Department of Neurology, Haaglanden Medical Center (HMC), The Hague, the Netherlands., The Hague, Zuid-Holland, [10]Department of Public Health, Erasmus MC University Medical Center, Rotterdam, the Netherlands., Rotterdam, Zuid-holland, [11]Maastricht UMC+, Maastricht, Maastricht, [12]University of Calgary, CALGARY, ALBERTA

Purpose

Most pre-stroke dependent patients (modified Rankin Scale score (mRS) ≥3) were excluded from clinical trials on endovascular treatment (EVT) for acute ischemic stroke (AIS) in the anterior circulation. As a result, there is little evidence for EVT in those patients, EVT decision-making is further complicated by the temporary or permanent cause of the dependence. We aim to investigate safety and efficacy of EVT in moderate pre-stroke disability patients (mRS 3) and explore the relationship between outcome and cause for dependence.

Materials and Methods

We used data from the Multicenter Randomized Clinical Trial of Endovascular Treatment for Acute Ischemic stroke in the Netherlands (MR CLEAN) Registry. All patients treated with EVT for AIS of the anterior circulation with pre-stroke mRS 3 were

included. We assessed the causes for their dependence and compared patients with successful reperfusion (defined as an expanded Thrombolysis in Cerebral Infarction scale (eTICI) score 2B-3) to patients without successful reperfusion. Our primary outcome was 90-day mRS 0-3 (functional improvement or return to baseline) and our secondary outcomes were occurrence of symptomatic intracranial hemorrhage (sICH) at 24 hours and 90-day mortality.

Results

A total of 204 patients were included, of whom 166 (81%) had a permanent disability, with various causes; 25% had a previous stroke. Patients with successful reperfusion were more likely to return to baseline or showed improvement (adjusted odds ratio [aOR] 4.73, 95%CI 1.68–13.33) compared to those with unsuccessful reperfusion. They were furthermore less likely to develop symptomatic intracranial hemorrhage (aOR 0.47, 95%CI 0.14–1.65) and had lower mortality rates (aOR 0.38 (95%CI 0.17–0.83)).

Conclusions

Although AIS patients with pre-stroke mRS 3 comprise a heterogenous group with respect to disability causes, we observed improved outcomes when patients achieved successful reperfusion after EVT, indicating possible treatment benefit.

331

Clinical Outcome of Patients with Mild Pre-Stroke Morbidity Following Endovascular Treatment – a HERMES Substudy

R McDonough[1], J Ospel[2], C Majoie[3], J Saver[4], P White[5], D Dippel[6], S Brown[7], A Demchuk[8], T Jovin[9], P Mitchell[10], S Bracard[11], B Campbell[12], K Muir[13], M Hill[14], F Guillemin[11], M GOYAL[15]

[1]University of Calgary, Calgary, Alberta, [2]University Hospital Basel, Basel, Basel, [3]Amsterdam University Medical Centers, Amsterdam, Noord-Holland, [4]UCLA, Los Angeles, CA, [5]Newcastle University, Newcastle, Tyne & Wear, [6]Erasmus Medical Center, Rotterdam, Zuid-Holland, [7]BRIGHT Research Partners, Mooresville, NC, [8]Cumming School of Medicine, University of Calgary, Calgary, Alberta, [9]University of Pittsburgh, Pittsburgh, PA, [10]Royal Melbourne Hospital, Melbourne, Melbourne, [11]Université de Lorraine, Nancy, na, [12]Royal Melbourne Hospital, University of Melbourne, Melbourne, Melbourne, [13]University of Glasgow, Glasgow, na, [14]Cumming School of Medicine, University of Calgary, Caglary, Alberta, [15]University of Calgary, CALGARY, ALBERTA

Purpose

Analyses of the effect of pre-stroke functional levels upon outcome of endovascular therapy (EVT) have focused upon the course of patients with moderate-substantial pre-stroke disability. The effect of complete freedom from pre-existing disability (modified Rankin Scale [mRS] 0) versus predominantly mild pre-existing disability/symptoms (mRS1-2) has not been well delineated.

Materials and Methods

The HERMES meta-analysis pooled data from 7 randomized trials that tested the efficacy of EVT. We tested for a multiplicative interaction effect of pre-stroke mRS on the relationship between treatment and outcomes. Ordinal regression was used to assess the association between EVT and 90-day mRS (primary outcome) in the subgroup of patients with pre-stroke mRS1-2. Multivariable regression modeling then tested the effect of mild pre-stroke disability/symptoms on the primary and secondary outcomes (delta-mRS, mRS0-2/5-6), compared to pre-stroke mRS=0 patients.

Results

We included 1764 patients, of whom 199 (11.3%) had a pre-stroke mRS1-2 (162 (81.4%) mRS=1, 37 (18.6%) mRS=2). No interaction effect of pre-stroke mRS on the relationship between treatment and outcome was observed. Patients with pre-stroke mRS1-2 had worse outcomes compared to those with pre-stroke mRS=0 (adjusted common odds ratio [acOR] 0.53 (95%CI:0.40-0.70). Nonetheless, a significant benefit of EVT was observed within the mRS1-2 subgroup (cOR:2.08 (95%CI:1.22-3.55, Figure). No differences were observed with regards to rates of reperfusion (aOR:1.04, 95%CI:0.58-1.86) and symptomatic intracerebral hemorrhage (sICH, OR:0.88, 95%CI:0.41-1.89) between patients who were asymptomatic prior to stroke and those with predominantly mild pre-stroke disability/symptoms.

Conclusions

Patients asymptomatic/without disability prior to onset have better outcomes following EVT than patients with mild disability/symptoms. Patients with pre-stroke mRS1-2, however, more often achieve good outcomes with EVT compared to conservative management, with similar rates of reperfusion and sICH. These findings indicate that mild pre-existing disability/symptoms influence patient prognosis after EVT but do not diminish EVT treatment effect.

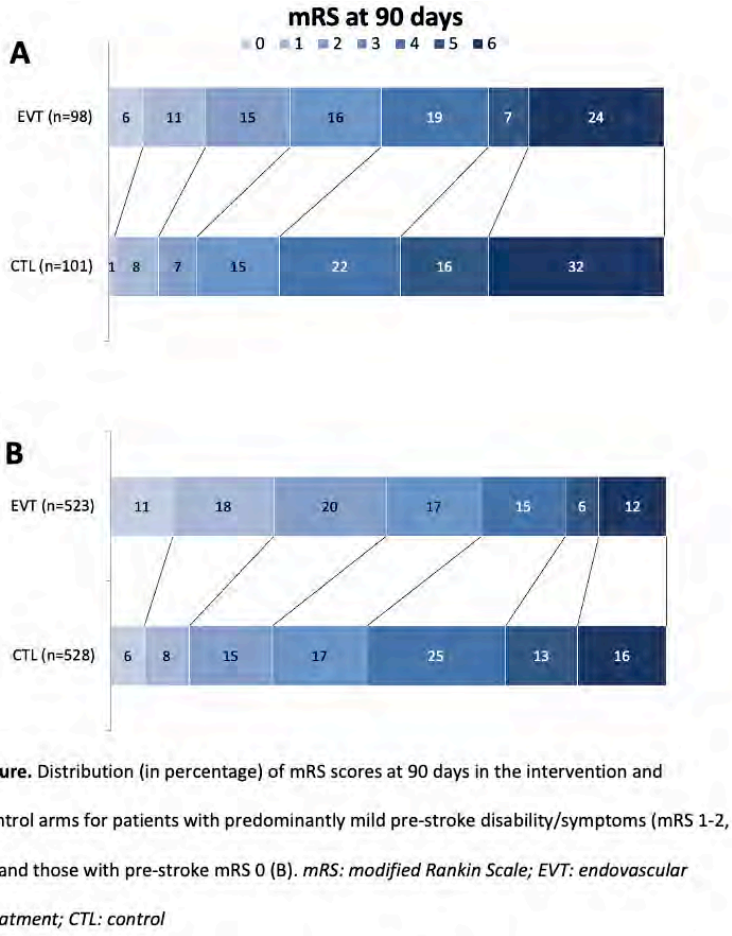

Figure. Distribution (in percentage) of mRS scores at 90 days in the intervention and control arms for patients with predominantly mild pre-stroke disability/symptoms (mRS 1-2, A) and those with pre-stroke mRS 0 (B). *mRS: modified Rankin Scale; EVT: endovascular treatment; CTL: control*

(Filename: TCT_331_mRS_fig.jpg)

1020

Delayed Effects of Intra-arterial Nimodipine on SAH-related Intracranial Vasospasm

M Schönfeld[1], C Zaeske[1], D Zopfs[1], K Laukamp[2], L Pennig[1], J Kottlors[1], L Goertz[1], N Abdullayev[1], C Kabbasch[1], M Schlamann[1]
[1]University Hospital Cologne, Cologne, NRW, [2]University Hospital Cologne, Cologne

Purpose
Intra-arterial administration of the calcium antagonist nimodipine has been shown to be an effective treatment for cerebral vasospasm after subarachnoid hemorrhage and can be performed as a rescue therapy if oral or intra-venous therapy fails.1 We evaluated the delayed effect of nimodipine as a salvage therapy for cerebral vasospasm after subarachnoid hemorrhage.
Materials and Methods
We retrospectively reviewed all cases of intra-arterial treatment for subarachnoid hemorrhage-related cerebral vasospasm in a single institution between January 2021 and September 2021. Patients were included if digital subtraction angiography runs were performed before and immediately after nimodipine administration, and a delayed run for the most affected vessel was performed at the end of the procedure. Nimodipine was infused at a rate of 0.10–0.13 mg/min for 5-20 min into the cervical segments of the internal carotid artery or vertebral artery as deemed necessary. Changes in vessel diameters (at the most spastic vessel and the vessel segment proximal to the spasm), nimodipine dose and timing of administered nimodipine were assessed.
Results
Delayed runs were performed in 18 cases (9 patients) with a median delay of 26 min (IQR 18-32 min) after nimodipine administration. A median of 4.5 mg (IQR 4-5.5) nimodipine was infused with 2 mg (IQR 1-2) per vessel. In all cases spastic and non-spastic vessel segments showed a progressive dilatation after local nimodipine administration that was independent of the dose of nimodipine administered to other vessels between the immediate controls and delayed runs. Dilatation of the most spastic vessel segments was more pronounced in the delayed runs compared to the immediate controls by 116% vs. 41% of the initial diameter (SD 99% vs. 30%; $p=0.002$). The difference in non-spastic vessel segments was less prominent with a dilatation in the delayed runs compared to the immediate controls by 31% vs. 19% of the initial diameter (SD 13% vs. 11%; $p<0.001$). In one case, the affected vessel was occluded before and immediately after nimodipine infusion but it was found reopened in a delayed run 37 min after nimodipine infusion.
Conclusions
Intra-arterially administered nimodipine seems to exert a delayed vasodilatory effect on spastic vessels more than on non-spastic vessels. This effect should be considered before judging vasodilatory therapy to be unsuccessful and expand treatment towards angioplasty.

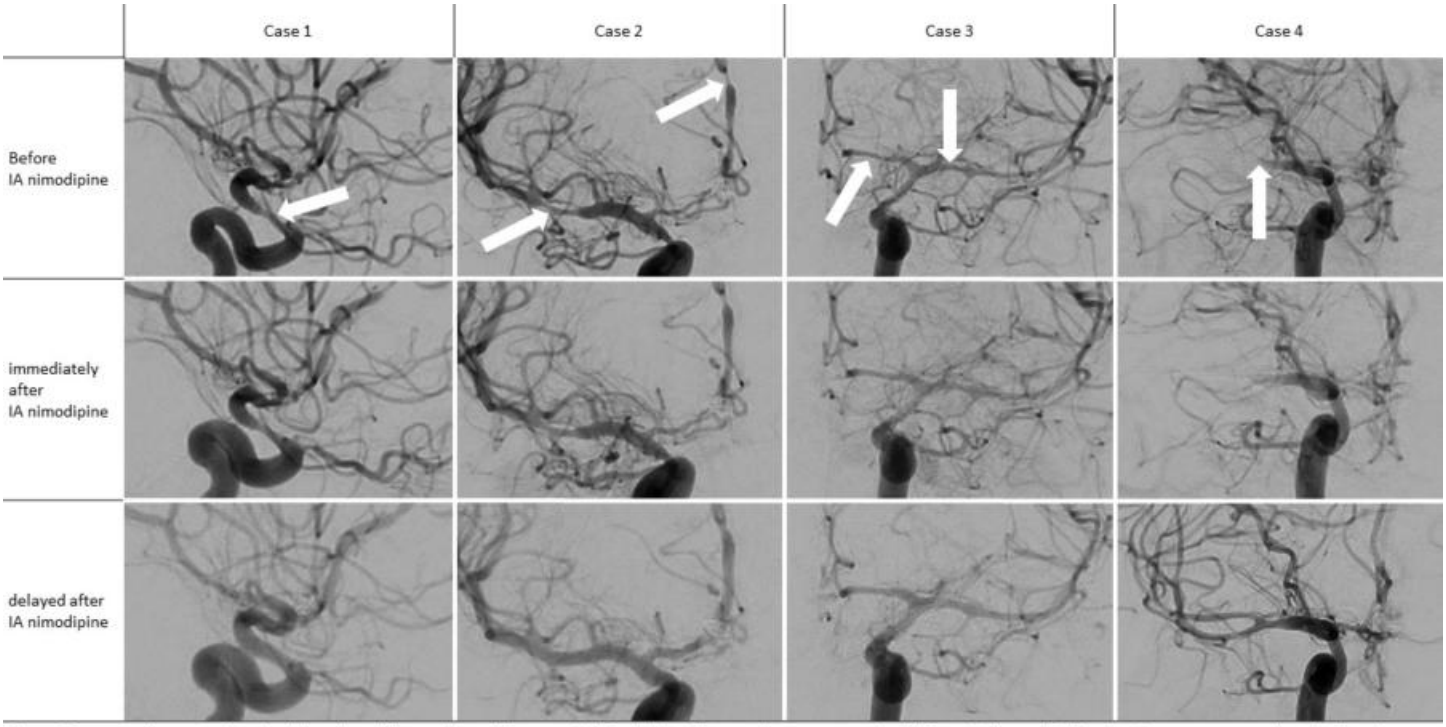

Figure: Four cases demonstrating the delayed vasodilatory effect of intra-arterial nimodipine. All cases show a progressive dilation of all vessels. This effect is most pronounced at the site of localized vasospasm (white arrows). While in cases 1, 2 and 4 intra-arterial Nimodipine was infused into other vessels between the immediate control run and the delayed run, in case 3 no additional nimodipine was infused. The occlusive vasospasm of the M1-Segment in case 3 was unchanged at the time of the immediate control run but was shown to be regressive in the delayed control run.

(Filename: TCT_1020_FigureASNR2022NimodipineVasospasmolysis.jpg)

948

Do effects of Nimodipine and Milrinone vary according to the involved segments of the circle of Willis in vasospasm following aneurysmal subarachnoid hemorrhage?

A Kotwal[1], A Ramalingaiah[1], K Kulanthaivelu[1]
[1]*NIMHANS, bengaluru, Karnataka*

Purpose

Vasospasm (VS) is one of the commonest causes of mortality and morbidity in patients with aneurysmal subarachnoid hemorrhage (aSAH). The role of intra-arterial Nimodipine (IAN) and intra-venous Milrinone (IVM) in the management of VS following aneurysmal subarachnoid hemorrhage was studied using Transcranial Doppler (TCD).

Materials and Methods

It was a prospective observational study done (between July 2020 and June 2021) at the National Institute of Mental Health and Neuro-Sciences (NIMHANS), Bangalore, India. Treatment-naive patients (age ≥19-yrs) of post-aSAH VS diagnosed on TCD who were (randomized) treated by either IAN or IVM were included. In IAM protocol, the 0.05mg/kg Nimodipine over 20 minutes was injected at 24 hrs intervals (for 5 days) in the involved cervical carotid or vertebral artery. In IVM protocol, 0.5 microgram/kg/min was infused for 5 days. Twelve hourly TCD analysis was done during the course of the therapy. Bilateral proximal Middle (MCA), anterior (ACA), and posterior (PCA) cerebral arteries were insonated on TCD. Pre-and post-treatment mean flow velocity (MFV), peak systolic velocity (PSV), and pulsatility index (PI) were evaluated at each of these segments of the circle of Willis. A mixed-effects regression model was used to analyze group-level trends in the data. P-value <0.05 was considered statistically significant.

Results

Thirty-four patients were included [13/34(38.2%) IVM, 21/34 (61.7%) IAN] in the study. Mixed effect analysis revealed a significantly greater beneficial effect of IAN compared to IVM on ACA and PCA vasospasm metrics [ACA PI(p=0.025), ACA PSV(p=0.043), PCA PI (p=0.005)] irrespective of different time points. Although MCA vasospasm [MCA MFV(p=0.000) and MCA PSV(p=0.000)] was responding significantly over time to either of the IAN or IVM protocols, the interaction effect of time and group was significant for the IAN group as compared to the IVM group, suggests increasing the beneficial effect of IAN on MCA vasospasm [MCA MFV (p= 0.000), MCA PSV(p=0.022)] as compared to IVM over time.

Conclusions

In this study, both IAN and IVM had comparable effects in MCA vasospasm, however, IAN proved better over time. Further, IAN had a favorable outcome on TCD metrics of ACA and PCA VS compared to IVM.

Parameters	Analyzed effect	Estimate	T value	P value
MCA_MFV	Main effect	93.04	13.11	0.000
	Time_Index	-1.96	-13.20	0.000
	Group Index	-5.10	-0.56	0.576
	Interaction Time_Index:Group Index	-0.87	-3.87	0.000
MCA_PI	Main effect	0.87	10.02	0.000
	Time_Index	0.07	10.55	0.000
	Group Index	-0.06	-0.50	0.621
	Interaction Time_Index:Group Index	0.01	0.95	0.341
MCA_PSV	Main effect	118.27	15.68	0.000
	Time_Index	-2.31	-9.69	0.000
	Group Index	-7.02	-0.73	0.470
	Interaction Time_Index:Group Index	-0.83	-2.30	0.022
ACA_MFV	Main effect	48.89	13.47	0.000
	Time_Index	-0.20	-1.58	0.114
	Group Index	12.96	2.80	0.008
	Interaction Time_Index:Group Index	-0.97	-5.11	0.000
ACA_PI	Main effect	1.38	13.95	0.000
	Time_Index	0.03	4.51	0.000
	Group Index	-0.30	-2.32	0.025
	Interaction Time_Index:Group Index	0.02	1.65	0.099
ACA_PSV	Main effect	71.98	15.27	0.000
	Time_Index	-0.21	-1.40	0.164
	Group Index	12.63	2.10	0.047
	Interaction Time_Index:Group Index	-1.02	-4.48	0.000
PCA_MFV	Main effect	39.23	17.68	0.000
	Time_Index	0.04	0.29	0.771
	Group Index	-2.48	-0.87	0.388
	Interaction Time_Index:Group Index	0.03	0.18	0.861
PCA_PI	Main effect	1.40	13.41	0.000
	Time_Index	0.03	3.21	0.001
	Group Index	0.39	2.93	0.003
	Interaction Time_Index:Group Index	-0.04	-3.02	0.003
PCA_PSV	Main effect	70.41	18.30	0.000
	Time_Index	-0.08	-0.44	0.662
	Group Index	0.20	0.04	0.967
	Interaction Time_Index:Group Index	-0.21	-0.76	0.448

(Filename: TCT_948_asnrvasospasm.JPG)

324

Endovascular Therapy Versus Medical Therapy Alone for Basilar Artery Stroke: A Semi-Automated Systemic Review and Meta-Analysis

G Adusumilli[1], J Pederson[2], N Hardy[3], K Kallmes[3], K Hutchison[3], H Kobeissi[4], D Heiferman[5], J Heit[1]
[1]Stanford University School of Medicine, Stanford, CA, [2]Superior Medical Experts,, St Paul, MN, [3]Nested Knowledge, Inc, St. Paul, MN, [4]Central Michigan University College of Medicine, Mt. Pleasant, MI, [5]Semmes-Murphey Clinic, Memphis, TN

Purpose
Endovascular thrombectomy (EVT) is an effective treatment for acute ischemic stroke (AIS) due to large vessel occlusion of the anterior circulation (AC-LVO). Randomized trials of posterior circulation large vessel occlusion (PC-LVO) patients have failed to

show a benefit of EVT over medical therapy (MEDT). We performed a systematic review and meta-analysis to understand better whether EVT is beneficial for PC-LVO.
Materials and Methods
Using the Nested Knowledge AutoLit living review platform, we identified randomized control trials and prospective studies that reported functional outcomes in patients with PC-LVO treated with EVT versus MEDT. The primary outcome variable was 90-day modified Rankin Scale (mRS) 0-3, and secondary outcome variables included 90-day mRS 0-2, 90-day mortality, and rate of symptomatic intracranial hemorrhage (sICH). A separate random effects model was fit for each outcome measure to calculate pooled odds ratios.
Results
Three studies with 1,248 patients, 860 in the EVT arm and 388 in the MEDT arm, were included in the meta-analysis. The favorable outcome rate (mRS 0-3) in EVT patients was 39.9% (95% CI: 30.6-50.1%) versus 24.5% in MEDT patients (95% CI: 9.6-49.8%). EVT patients had higher mRS 0-2 rates (31.8% [95% CI: 25.7-38.5%] versus 19.7% [95% CI: 7.4-42.7%]) and lower mortality (42.1% [95% CI: 35.9-48.6%] versus 52.8% [95% CI: 33.3-71.5%]) compared to MEDT patients, but neither result was statistically significant. EVT patients were more likely to develop sICH (OR=10.36; 95% CI: 3.92-27.40).
Conclusions
EVT treatment of PC-LVO trended toward superior functional outcomes and reduced mortality compared to MEDT despite a trend toward increased sICH in EVT patients. Existing randomized and prospective studies are insufficiently powered to demonstrate a benefit of EVT over MEDT in PC-LVO patients.

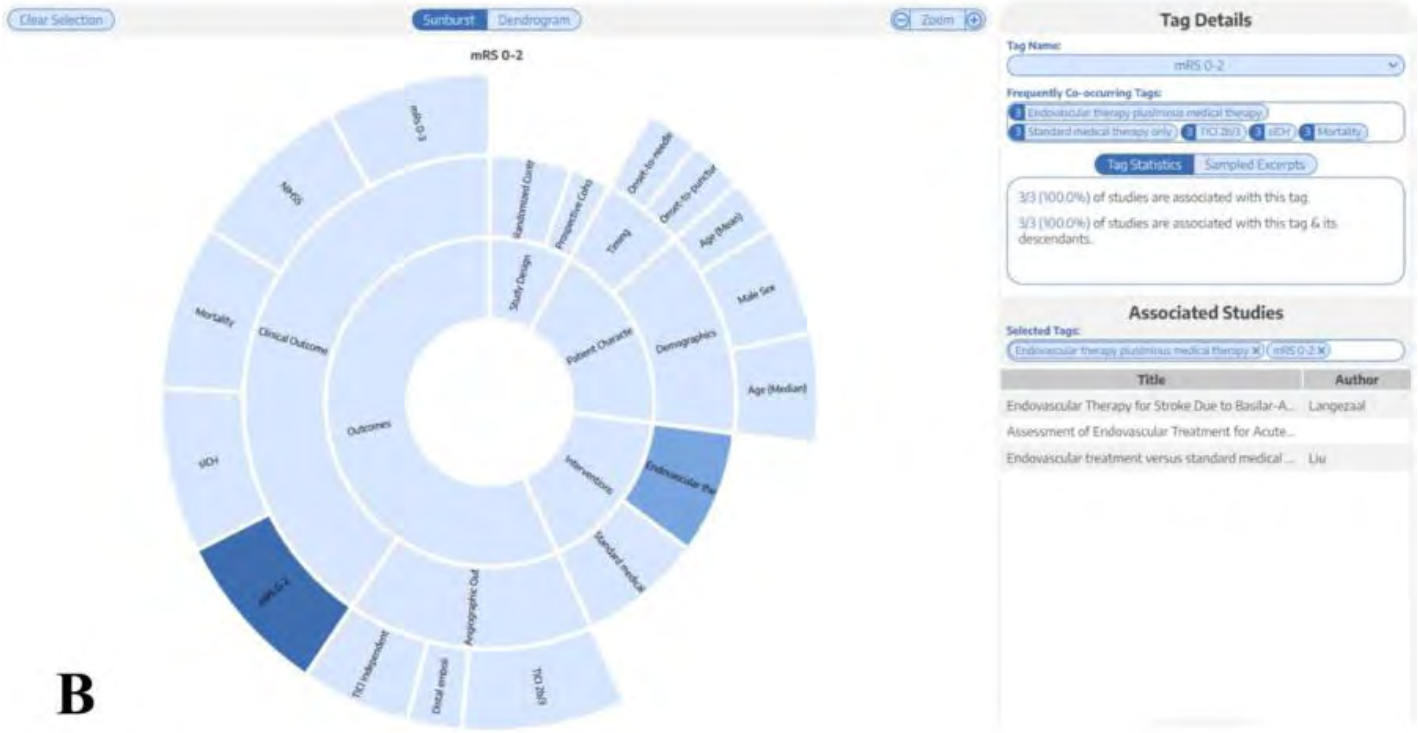

(Filename: TCT_324_NestedKnowledgeforBasilarEVTvsMEDT-SystematicReview.jpg)

836

How Far is Too Far in Stroke Thrombectomy ? From XL to XS Vessel Occlusions with Radially Adjustable Stent-retrievers - Tigertriever XL and Tigertriever 13

a guenego[1], M Wang[2], B Mine[3], T Bonnet[3], s elens[3], b lubicz[3]
[1]Erasme Hospital, Brussels, Belgium, [2]Erasme University Hospital, Brussels, Brussels, [3]erasme, brussels, brussels

Purpose
A New class of Radially adjustable Stent-retrievers, Tigertriever XL and Tigertriever 131, 2 (Rapid Medical, Yoqneam, Israel) are respectively CE-Marked for large, and distal, medium vessel occlusions (DMVO). Despite no randomized data support distal vessels recanalization yet, we report our initial experience with the Tigertriever 13 in DMVO3 and illustrate it with a case where Tigertriever XL and 13 were needed to obtain a complete recanalization.
Materials and Methods
We performed a retrospective analysis of all consecutive acute ischemic stroke (AIS) patients with primary or secondary DMVO who underwent mechanical thrombectomy with the Tigertriever 13. Patients' clinical, procedural and angiographic characteristics were reviewed.

Results

Between November 2019 and November 2021, 24 DMVO were included (46% female, median age 63 [51-65] years). The overall successful reperfusion rate (mTICI 2b-3) was 88% (21/24) for the dedicated vessel. Follow-up imaging showed a subarachnoid-hemorrhage in 29% of the cases and a parenchymal hematoma in 8% while symptomatic Intracranial hemorrhages did not occurred. At 3 months, 62% of the patients (15/24) had a favorable outcome (mRS 0-2). Figure : From XL to XS Vessel Occlusions with Radially Adjustable Stentretrievers- Tigertriever XL and Tigertriever 13 : The figure depicts the thrombectomy of a patient (consent obtained), who presented an acute AIS, baseline NIHSS of 16, baseline head CT showed a left carotid occlusion, IVtPa was not performed (under anticoagulation). Femoral puncture was performed 190min after symptom onset, under local anesthesia. After 1 pass of Tigertriever XL (the largest available stentriever) the carotid T was recanalized (A-B), as the patient was agitated we decided to go under general anesthesia. One more pass of Tigertriever XL (B-C-D) managed to recanalize the large vessel. We decided to catheterize the M4 segment thanks to an Headway Duo. A complete reperfusion (mTICI 3) was achieved after 1 pass of Tigertriever13 (F-G), 65min after femoral puncture. No SAH was seen, day 1 NIHSS was 3, with an mRS of 1 at discharge.

Conclusions

Mechanical thrombectomy for both primary or secondary DMVO seems feasible and as safe as for LVO. Our initial experience using the Tigertriever13 is of special interest as it shows we can potentially significantly expand AIS population that can benefit from mechanical thrombectomy treatment.

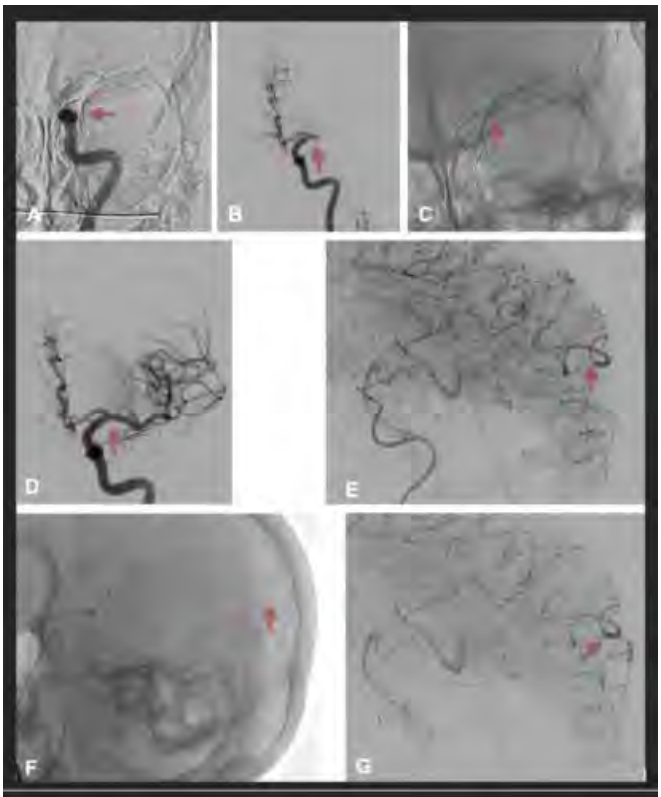

	All
Number of occlusions	24 (100%)
Age, years (median, IQR)	63 (51-65)
Female (%)	11 (46%)
Baseline NIHSS (median, IQR)	10 (6-19)
Intravenous tPA (%)	10 (42%)
Time Onset to Puncture in min (median, IQR)	233 (201-387)
Core volume (mL)	5 (4-22)
TMax >6sec (mL)	35 (25-62)
Side (left, %)	16 (67%)
Mechanical Thrombectomy	
General Anesthesia (%)	22 (92%)
Number of Tigertriever13 Passes (median, IQR)	1 (1-2)
Final TICI 2b/2c/3 (%)	21 (88%)
Final TICI 2c/3 (%)	17 (71%)
Procedural Complication (%)	5 (21%)
Time Puncture to Recanalization in min (median, IQR)	63 (42-81)
Time Onset to Recanalization in min (median, IQR)	308 (250-421)
Outcomes	
Day 1 NIHSS (median, IQR)	7 (3-9)
Day 1 Hemorrhagic Transformation (any type, %)	9 (38%)
ECASS PH-Type (%)	2 (8%)
ECASS SAH-Type (%)	7 (29%)
mRS (median, IQR)	2 (1-4)
Good outcome (mRS 0-2) (%)	15 (62%)
Excellent outcome (mRS 0-1) (%)	9 (38%)

(Filename: TCT_836_Image.jpg)

791

Immediate Cone-beam CT after endovascular thrombectomy for 24h-haemorragic transformation prediction: quantitative imaging analysis and proof-of-concept application of Machine Learning

V Da Ros[1], A Duggento[1], A Cavallo[1], L Bellini[1], F Pitocchi[1], N Toschi[1], A Mascolo[1], F Sallustio[1], F Di Giuliano[1], M Diomedi[1], R Floris[1], F Garaci[1], I Maestrini[1]

[1]*University of Rome Tor Vergata, Rome, Italy*

Purpose

Hemorrhagic transformation (HT) is an independent predictor of unfavorable outcome in acute ischemic stroke (AIS) patients undergoing endovascular thrombectomy (EVT). Its early identification could help tailoring acute patients' management. We

hypothesize that a quantitative imaging analysis with Machine Learning (ML) validation on Cone-Beam Computed Tomography (CB-CT) performed immediately after EVT helps predicting the risk of 24h-HT.
Materials and Methods
We prospectively enrolled AIS patients undergoing EVT, post-procedural CB-CT and 24h-non-contrast CT (NCCT). Three raters independently analyzed imaging at four anatomic levels in a qualitative and quantitative manner selecting region-of-Interest (ROI) <5 mm2. Each ROI was labelled as "hemorrhagic" or "non-hemorrhagic" depending on 24h-NCCT. For each level of CB-CT, Mean Hounsfield Unit (mHU), signal (SNR) and contrast to noise ratios (CNR) were calculated and the differential HU-ROIs value was compared between both hemispheres. We performed a ROC analysis for 24h-HT prediction and subsequently ML with best validation performance was selected.
Results
We extracted 172 ROIs from affected hemispheres of 43 patients, classifying: 92 unremarkable, 5 parenchymal contrast staining, 29 ischemia, 7 subarachnoid hemorrhages, 39 HT. mHU (best cut-off 96.5 HU, sensitivity=0.72; specificity=0.85; accuracy=0.83) and CNR (best cut-off 0.8, sensitivity=1; specificity=0.64; accuracy=0.72) were the most significant variables for HT prediction. The leave-p-out-iteration was the best ML classifier (sensitivity=1; specificity=0.75; accuracy=0.82), though precision was 0.60.
Conclusions
mHU and CNR are the most accurate parameters for quantitative prediction of HT on immediate post-EVT CB-CT. The ML lower precision in HT prediction unmasked the need to standardize CB-CT quantitative interpretation to overcome operator-dependent variability

395

Intravenous Alteplase Increases Edema Volume in Stroke Patients with Complete Endovascular Recanalization

G BROOCKS[1], L Meyer[2], M Bechstein[2], J Fiehler[2], U Hanning[2]
[1]University Hamburg, Hamburg, NA, [2]University Hamburg, Hamburg, Hamburg

Purpose
Intravenous thrombolytic therapy with alteplase (IVT) is standard of care in ischemic stroke, and its application before endovascular thrombectomy (EVT) is currently investigated compared to direct EVT. Yet, the effect of IVT on functional outcome and secondary injury volumes in patients with complete endovascular recanalization has not been analyzed. We hypothesized that IVT is associated with worse functional outcome and aggravated secondary injury volumes when administered to patients who subsequently attained complete reperfusion after EVT.
Materials and Methods
Anterior circulation ischemic stroke patients with complete reperfusion after thrombectomy defined as thrombolysis in cerebral infarctions (TICI3) after thrombectomy admitted between 01/2013-01/2021 were analyzed. Primary endpoints were the proportion of patients with functional independence defined as modified Rankin Scale (mRS) score 0-2 at day 90, and secondary injury volumes: Edema volume in follow-up imaging measured using quantitative net water uptake (NWU), and the rate of symptomatic intracerebral hemorrhage (sICH).
Results
219 patients were included. 128 (58%) patients received bridging IVT before thrombectomy. The proportion of patients with functional independence was 28% for patients with bridging IVT, and 34% for patients with direct thrombectomy (p=0.35). Edema volume was significantly higher in patients with bridging IVT compared to patients with direct thrombectomy (6 ml, IQR: 2-17, versus 4 ml, IQR:1-11; p=0.04). The rate of sICH was significantly higher after bridging IVT (20% versus 7.7%, p=0.01). Multivariable logistic and linear regression analysis confirmed the independent association of bridging IVT with sICH (aOR: 2.78, 95%CI: 1.02-7.56, p=0.046), and edema volume (aOR: 8.70, 95%CI: 2.57-14.85, p=0.006).
Conclusions
Bridging IVT was associated with significantly increased edema volume and risk for sICH as secondary injury volumes. The results of this study encourage direct EVT approaches, particularly in patients with higher likelihood of successful EVT.

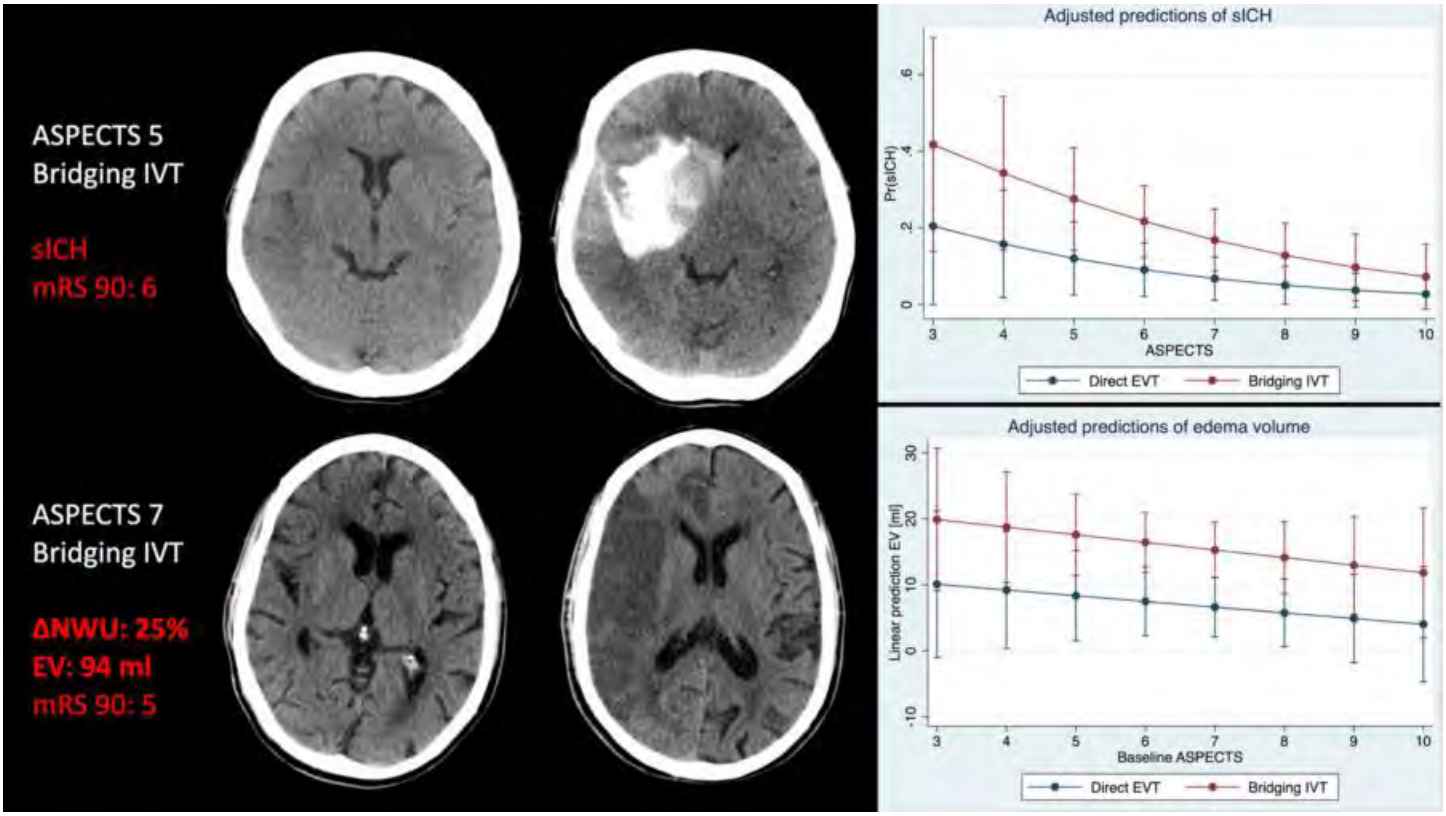

(Filename: TCT_395_ASNR_TICI3_FIG.jpg)

359

Outcomes with Endovascular Treatment of M2-Middle Cerebral Artery Occlusions in The Late Time Window- Results from Pooled Multinational Studies

F Bala[1], B Kim[2], I Casetta[3], S Nannoni[4], P Michel[5], J Thornton[6], M GOYAL[7], E Fainardi[8], D Herlihy[9], P Sarah[9], V Saia[10], G Pracucci[11], A Demchuk[12], S Mangiafico[13], K Boyle[14], M Hill[15], D Toni[16], S Murphy[17], A Ademola[18], B Menon[19], M Almekhlafi[19]
[1]University of Calgary, calgary, Alberta, [2]Department of Neurology, Seoul, Republic of Korea, Seoul, seoul, [3]Clinica Neurologica, University of Ferrara, Italy, Ferrara, Ferrara, [4]Stroke Center, Neurology Service, Lausanne University Hospital and University of Lausanne, Lausanne,, Lausanne, Lausanne, [5]Stroke Center, Lausanne,, lausanne, lausanne, [6]Neuroradiology Department, Dublin, Ireland, Dublin, Dublin, [7]University of Calgary, CALGARY, ALBERTA, [8]Neuroradiology Unit, University of Florence, Italy, Florence, Florence, [9]Neuroradiology Department, Beaumont Hospital, Dublin, Ireland, Dublin, Dublin, [10]Stroke Unit, Santa Corona Hospital, Pietra Ligure (SV), Italy, Florence, Florence, [11]Stroke Unit, Careggi University Hospital, Florence, Florence, Florence, [12]Cumming School of Medicine, University of Calgary, Calgary, Alberta, [13]Interventional Neuroradiology Unit, IRCCS Neuromed , Pozzilli (IS), Italy, Pozzilli , Pozzilli, [14]Department of Geriatric and Stroke Medicine, Beaumont Hospital, Dublin, Ireland, Dublin, Dublin, [15]Cumming School of Medicine, University of Calgary and Foothills Medical Centre, Caglary, Alberta, [16]Emergency Department, Stroke Unit, Sapienza University Hospital, Rome, Italy, Rome, Rome, [17]Department of Geriatric and Stroke Medicine, University College Dublin, Dublin, Ireland, Dublin, Dublin, [18]Department of Community Health Sciences, University of Calgary, Calgary, Alberta, Canada., Calgary, Calgary, [19]University of Calgary, Calgary, Alberta

Purpose
Two randomized trials in the late window (6-24 hours from onset) have demonstrated the efficacy and safety of endovascular treatment (EVT) in patients with large vessel occlusion. Patients with M2 segment middle cerebral artery (MCA) occlusions were excluded from these trials. Current literature suggests EVT safety and efficacy among M2 occlusion patients treated within six hours from symptoms onset. We compared outcomes with EVT in patients with M2 vs. M1 occlusions presenting between 6 and 24 hours after symptom onset.
Materials and Methods
Analyses were based on pooled data from 7 trials and registries enrolling stroke patients treated with EVT between 6 and 24 hours after symptom onset or last known well. Baseline characteristics, 90-day functional independence (modified Rankin Scale ≤ 2), mortality, symptomatic intracranial hemorrhage (sICH) and successful reperfusion (modified Thrombolysis in Cerebral Infarction 2b-3) were compared between patients with M2 and M1 occlusions. We further investigated the factors associated with 90-day functional independence when adjusted for age, sex, baseline NIHSS score, ASPECTS and occlusion location.
Results
Of 449 patients with MCA occlusions, 367 (81.7%) had M1 occlusion and 82 (18.3%) had M2 occlusion. Patients with M2 occlusion were older (median 75 years vs. 69 years) and had lower median baseline NIHSS (11 vs. 16, p<0.001). Puncture to reperfusion time

was longer in M2 patients (median 45 minutes vs. 30 minutes, p= 0.001). No statistically significant differences were noted in the proportion of successful reperfusion (81.7% vs. 81.1%, p>0.99), 90-day functional independence (57.1% vs. 45.0%, p=0.059) or mortality (13.0% vs.17.2%, p=0.50). sICH rate was lower in patients with M2 vs. M1 occlusions (2.5% vs.12.2%, p=0.007). In multivariable analysis, only age (OR 0.60, p<0.001) and NIHSS score (OR 0.89, p<0.001) were associated with 90-day functional independence.
Conclusions
Patients with M2 occlusions treated late with EVT achieved similar reperfusion and clinical outcome rates but lower sICH rates compared to patients with M1 occlusions. These results support the safety of EVT for M2 patients in the late window.

Tuesday, May 17, 2022
3:35-5:05 PM
ASHNR Programming: Essentials of Neuroradiology: Beyond Your Wildest Dreams: Imaging Techniques That Will Set You Free

1374

Diagnostic accuracy of artificial intelligence for abnormality detection in routine, clinical neuroimaging: a systematic review and meta-analysis

S Agarwal[1], D Wood[2], M Din[3], T Booth[4]
[1]King's College London School of Biomedical Engineering and Imaging Sciences, London, London, [2]King's College London, London, UK, [3]King's College London, London, London, UK, [4]Kings College London, London, London

Purpose
To examine the accuracy of fully automated algorithms for the detection of abnormalities in structural CT or MR brain imaging. In order to demonstrate generalisability to clinical workflows which contain all abnormalities, AI studies need to demonstrate their performance in a test set containing multiple abnormalities.
Materials and Methods
In accordance with the PRISMA-DTA statement, 42870 unique abstracts were identified from MEDLINE, Embase, Cochrane Library and Web of Science which were searched until September 2021. 4703 full texts were reviewed for final inclusion. Studies reporting test accuracy of fully automated algorithms that could classify a single MRI or CT brain study as normal or abnormal, tested on a dataset of normal and at least two categories of pathology were eligible for inclusion. Articles were assessed for quality using the Quality Assessment of Diagnostic Accuracy Studies-2 (QUADAS-2) tool. A bivariate model was created for meta-analysis of included studies. This study is registered on PROSPERO as CRD42021269563.
Results
Of the 14 studies that matched these criteria, all used deep learning, and 10 validated their findings in consecutive or randomised clinical datasets. Within this, 8 supervised CNN models were created for single pathology detection. 5 supervised CNN models and 1 unsupervised GAN model were identified for multiple pathology detection. Bivariate analysis of all studies performing abnormality detection at the examination level demonstrated a pooled sensitivity of 0.856 (95% CI 0.789 - 0.905) and specificity of 0.846 (0.767 - 0.902). A subset of studies investigating intracranial haemorrhage detection in CT scans demonstrated a pooled sensitivity of 0.879 (0.788 - 0.934) and specificity of 0.879 (0.802 - 0.929), and a subset investigating multiple pathology detection had a pooled sensitivity of 0.785 (0.727 - 0.833) and specificity of 0.688 (0.429 - 0.866).
Conclusions
In the studies included, while the diagnostic accuracies reported do not match neuroradiologist interpretation, they represent the state-of-the-art for detecting abnormalities at the examination level in clinical datasets. The use of these models in a clinical pipeline is minimally explored - only 3 studies go on to further study their use in worklist triage. It is worth noting that the accuracy of ICH detection models constrained to clinically applicable datasets are lower than others in the literature without such robust validation.

600

Evaluation of a new, deep-learning-enabled head and neck CTA bone subtraction algorithm

G Bathla[1], S Priya[2], M Schoebinger[3], Z XU[3], M Schwier[3], A Halaweish[4], C Derdeyn[5]
[1]University of Iowa Hospitals and Clinics, Iowa City, IA, [2]University of Iowa hospitals and Clinics, IOWA CITY, IA, [3]Siemens Healthcare GmbH, Erlangen, AK, [4]Siemens Healthineers, Malvern, PA, [5]University of Iowa Hospitals & Clinics, Iowa City, IA

Purpose
We sought to evaluate the visual quality of bone subtracted head and neck CT angiography scans (CTA) when employing a new deep learning enabled bone subtraction algorithm.
Materials and Methods
A prototype AI algorithm was developed to remove the bones from thin-slice CTA scans in the head and neck region. The algorithm

was trained on a collection of 1014 manually annotated CTA datasets, where bones and other high-intensity structures such as metal implants or cables were labeled as to be removed. The algorithm is based on an image-to-image deep learning technique, employing a convolutional encoder-decoder architecture combined with multi-level feature concatenation. When applying the algorithm, a segmentation mask is generated which is used to remove the bones from the original volume for unhindered vasculature visualization. In this study, we retrospectively evaluated the AI algorithm against a traditional head and neck bone removal algorithm on a separate cohort of 50 patients. Algorithm results were pre-generated and presented to two Radiologists (R1 and R2), blinded to the version of the algorithm. No editing was applied. The readers independently ranked the algorithm results on 5-point Likert scales (1: very bad, 2: bad, 3: acceptable, 4: good, 5: very good) with a focus on completeness of the removal of bones, and completeness and consistency of the remaining vessels. The ratings of traditional and AI algorithms were compared and tested for statistical significance employing a one-tailed Wilcoxon signed-rank test for paired data.

Results

With the AI algorithm, the average bone removal quality rating increased from 3.44 to 4.94 for the R1, and from 3.18 to 4.72 for R2. The bone removal quality was rated as 'good' or 'very good' in 100% of the cases by R1 and in 98% of the cases by R2, as opposed to 52% and 36% in the traditional algorithm. The average vessel display quality rating increased from 2.24 to 3.88 for R1, and from 1.84 to 3.04 for R2. In the AI algorithm, the vessel display quality was rated as 'good' or 'very good' in 78% of the cases by R1 and in 40% of the cases by R2, as opposed to 10% and 10% in the traditional algorithm. For both readers, the AI algorithm showed a statistically significant improvement ($p < 0.0001$).

Conclusions

Compared to the traditional algorithm, the AI algorithm showed significantly improved bone subtraction and vessel completeness. Removal of background noise and separation of arteries and veins would benefit from further algorithm improvements.

475

Exploring the associations of intracranial hypertension and brain herniations (Encephalocele) into arachnoid granulations in patients with pulsatile tinnitus

J Remer[1], E Smith[1], M Caton[1], A Baker[1], V SHAH[1], J Villanueva-Meyer[1], M Amans[2]
[1]UCSF, San Francisco, CA, [2]Ucsf, San Francisco, CA

Purpose

To explore if patients with pulsatile tinnitus, a debilitating condition where a "whooshing" sound is heard with each heart beat, with MR imaging findings of brain herniations through arachnoid granulations have an increased odds of having idiopathic intracranial hypertension (IIH) compared to patients with pulsatile tinnitus without imaging findings of brain herniations through arachnoid granulations

Materials and Methods

Retrospective review of a cohort of 262 patients from pulsatile tinnitus clinic was conducted. All patients underwent MRI on 1.5 and 3.0T scanners including MR venogram, pre- and post-contrast T1- and T2-weighted sequences. Examinations were reviewed by three experienced neuroradiologists blinded to clinical data to identify brain herniations. With respect to brain herniations we documented location, signal intensity, size, presence of arachnoid granulation, and dural sinus stenosis. Clinical records were reviewed for diagnosis of IIH, history of prior lumbar puncture, and opening pressure. Statistical analysis was performed using a Chi Square and Odds ratio test and significance was defined as $p < 0.05$

Results

Of the cohort of 262 patients with pulsatile tinnitus, 16 patients (6%) were found to have at least one herniation through an arachnoid granulation into a dural venous sinus. 11 patients had unilateral temporal or occipital lobe herniations in the transverse sinus or the transverse-sigmoid junction, 3 had unilateral cerebellar herniations and 2 had bilateral herniations. Of the 16 patients with MRI findings of brain herniations through arachnoid granulations, 9 had a clinical diagnosis of IIH with 7 confirmed by LP. Of those patients without MRI findings of brain herniations through arachnoid granulations 55 patients had a clinical diagnosis of IIH with 39 confirmed by LP. There was a significant increased odds (OR 4.2, CI 1.5- 12) of pulsatile tinnitus patients having IIH with brain herniations compared to pulsatile tinnitus patients having IIH without brain herniations.

Conclusions

Within a cohort of patients with pulsatile tinnitus, there was a significant association of brain herniations through arachnoid granulations with idiopathic intracranial hypertension. This study provides new evidence on the role of using brain herniations through arachnoid granulations as an MR imaging biomarker for diagnosis of idiopathic intracranial hypertension.

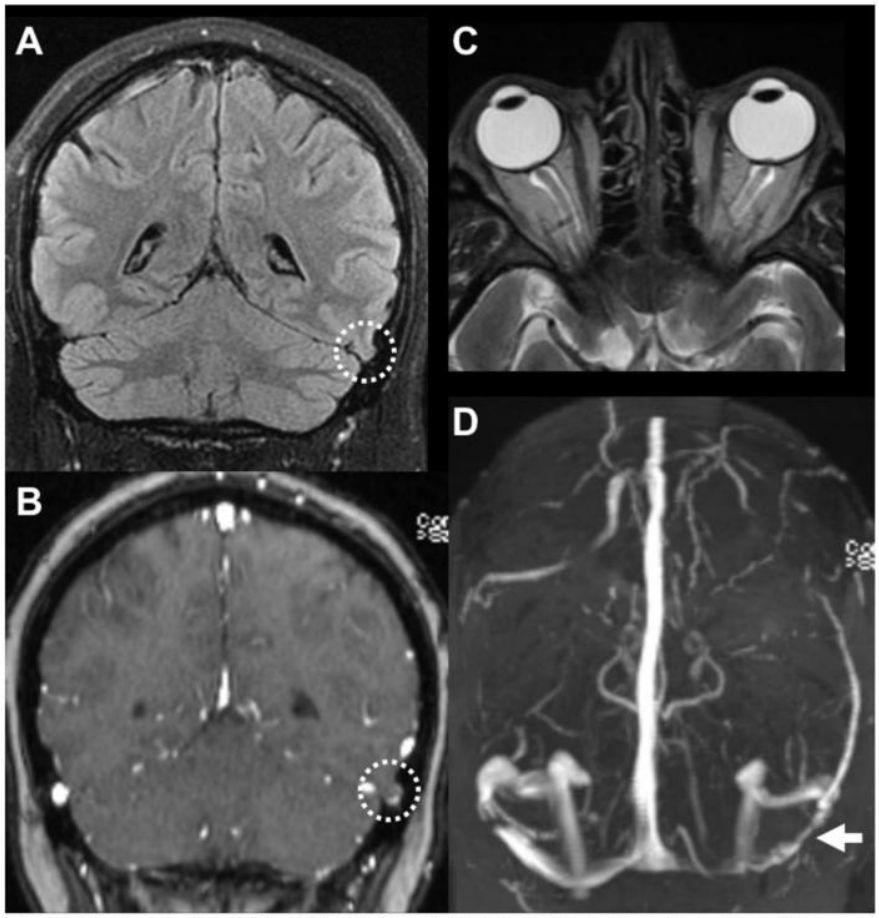

MR imaging example of idiopathic intracranial hypertension in the setting of a left transverse brain herniation from our pulsatile tinnitus cohort. (A, B) Coronal T2 FLAIR and T1 post-contrast MR images show a small herniation of the left occipital lobe into the transverse sinus (dashed circle). (C) Axial T2 MR image shows flattening of the posterior globes and protrusion of the optic nerve heads as well as prominent optic nerve sheath subarachnoid space, findings suggestive of elevated intracranial pressure. (D) MR venogram shows bilateral, left greater than right, transverse sinus stenosis, most pronounced at site of herniation (white arrow).

(Filename: TCT_475_ASNR_FIGURE_EDITED.jpg)

Tuesday, May 17, 2022
3:35-5:05 PM
ASSR Programming: Spine Imaging: What Does the Future Hold?

1284

Quantitative assessment of antero-posterior dispersion of cauda nerve roots in spinal stenosis: a weight-bearing MRI study

R Levi[1], M Battaglia[2], F Garoli[3], G Savini[4], D Cannizzaro[5], A Ortolina[6], D Milani[7], M Fornari[8], L Politi[9], M Grimaldi[8]

[1]Humanitas University, Pieve Emanuele, Italy, [2]Humanitas University, Rozzano, Milano, [3]Humanitas University, Rozzano, Milano (Italy), [4]Humanitas research Hospital, Rozzano, Milano, [5]Humanitas University, Pieve Emanuele, Milan, [6]Humanitas Research Hospital, Rozzano, Italy, [7]Humanitas Research Hospital, Rozzano, Milano (Italy), [8]Humanitas Research Hospital, Rozzano, Milano, [9]Humanitas University, Pieve Emanuele, Milano

Purpose

To quantify variations of caudal nerve roots dispersion within the dural sac in patients with lumbar spinal stenosis between orthostasis and clinostasis using weight-bearing MRI.

Materials and Methods

Lumbar spinal stenosis is a pathologic condition that causes neurogenic symptoms mainly in elderly population. Dural sac cross section area is the current standard to assess the severity of the stenosis using axial MRI, but there is evidence that this measurement doesn't correlate significantly with clinical symptoms. Schizas et Al. proposed a classification based on the morphology of dural sac in

correspondence of the lumbar stenosis. However, there is still no quantitative evaluation of the dispersion of nerve roots at a level adjacent the lumbar stenosis. Therefore, we propose an automated quantitative assessment of nerve root dispersion in lumbar weight-bearing MRI that can acquire orthostasis and clinostasis imaging of the spine. This automated technique could be helpful in better correlate clinical symptoms and improve pre-surgical planning. Six patients with lumbar stenosis underwent a lumbar MRI with a weight-bearing magnet (G-scan, ESAOTE). 3D HYCE sequences (T2-weighted) were acquire in both supine and standing positions. Initially, we extracted the axial MR image perpendicular to lumbar lordosis at three levels: maximum spinal canal stenosis level, center of vertebral body cranial to the stenosis, and center of vertebral body caudal to the stenosis level. Then, we computed the anteroposterior diameter dural sac and the dispersion of the nerve roots using radiomics approach at each of the 3 levels. Eventually, we compared the measurements with clinostasis and orthostasis position.

Results

From clinostasis to orthostasis position, nerve root dispersion was found to be decreased cranially to the stenosis (modification of -2.07 mm ± 2.97 mm), and increased caudally to the stenosis (modification of 2.58 mm ± 3.42 mm). Moreover, we found a significant correlation between nerve dispersion at stenosis level and the variation at inferior vertebral level (0.66, R correlation, $p<0.05$).

Conclusions

The proposed automated quantitative evaluation of nerve root dispersion could represent a novel approach to assess clinical significance of spinal canal stenosis using weight-bearing MRI.

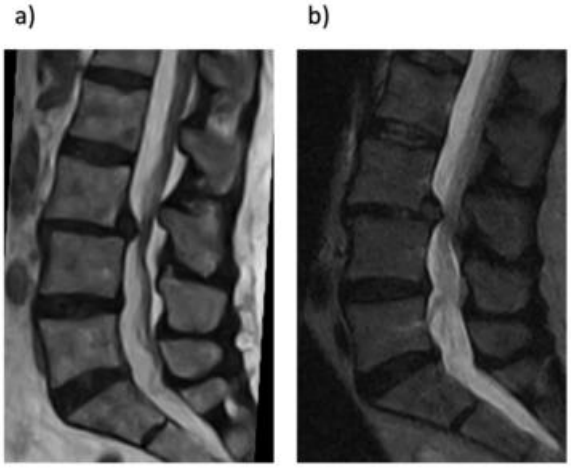

Figure 1: Sagittal MRI in clinostasis (a) and orthostasis (b) position in patient with spinal stenosis.

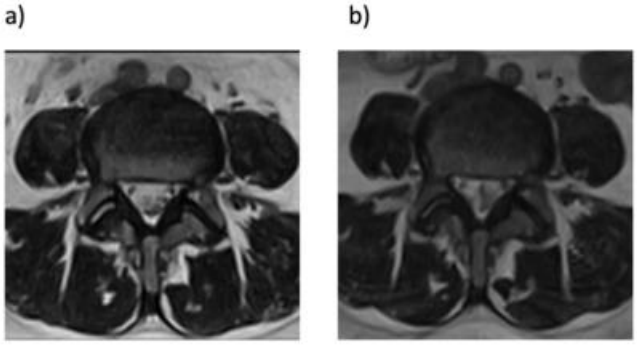

Figure 2: Axial MRI in clinostasis (a) and orthostasis (b) position in patient with spinal stenosis below the spinal stenosis.

(Filename: TCT_1284_ASNR_2022_cauda_dispertion.jpg)

655

A Retrospective Review of Isolated Prevertebral Edema in the Emergency Department at a Level 1 Trauma Center

A Ye[1], J Talbott[2]

[1]University of California San Francisco, San Francisco, CA, [2]UCSF and ZSFG, San Francisco, CA

Purpose

Prevertebral edema is an under appreciated and often difficult to interpret finding on imaging of the cervical spine and neck. There is little literature in interpretation for isolated prevertebral edema in the absence of associated traumatic or infectious pathology. This study looks to help characterize isolated prevertebral edema in the absence of clear causes as seen on CT and further understand the importance of prevertebral edema in the emergent setting.

Materials and Methods

A retrospective search was performed including all MRI scans ordered from the ED from 2020 to the present which included a CT comparison and had "prevertebral edema" within the body of the report excluding the phrase "no prevertebral edema". 81 studies were identified with 19 scans excluded for either lack of appropriate recent CT comparison or involved either the thoracic or lumbar spine leaving 62 studies that were reviewed by 2 trainees and by a neuroradiology attending specialist with a measurement of maximal prevertebral edema thickness performed on an axial soft-tissue CT. 19 of the 62 studies had a clear reason for prevertebral edema on CT (commonly traumatic or infectious) and were also excluded from further analysis.

Results

The remaining 43 studies were further split into 4 categories, with 4 negative CTs with a ligamentous or osseous injury on subsequent MRI (false negative), 19 positive CT with additional findings on MRI in addition to prevertebral edema (true positive), and 11 isolated prevertebral edema seen on CT with a subsequent MRI which only showed prevertebral edema (false positive). 7 studies were also performed with a prior CT without visible prevertebral edema and isolated trace prevertebral edema on MRI. Therefore, the specificity of isolated prevertebral edema for ligamentous or osseous injury on CT is 82.6% with a positive predictive value of 63.3%.

Conclusions

This study attempts to better quantify the utility of isolated prevertebral edema on CT in the emergent setting to give clinicians a better understanding of the significance of this finding. From preliminary results, it appears that prevertebral edema is has good specificity with regards to additional ligamentous or osseous injury but limited positive predictive value. Further work will be done to increase the number of cases, quantify the utility of prevertebral edema thickness, and to include the number of true negatives to fully establish sensitivity and negative predictive value.

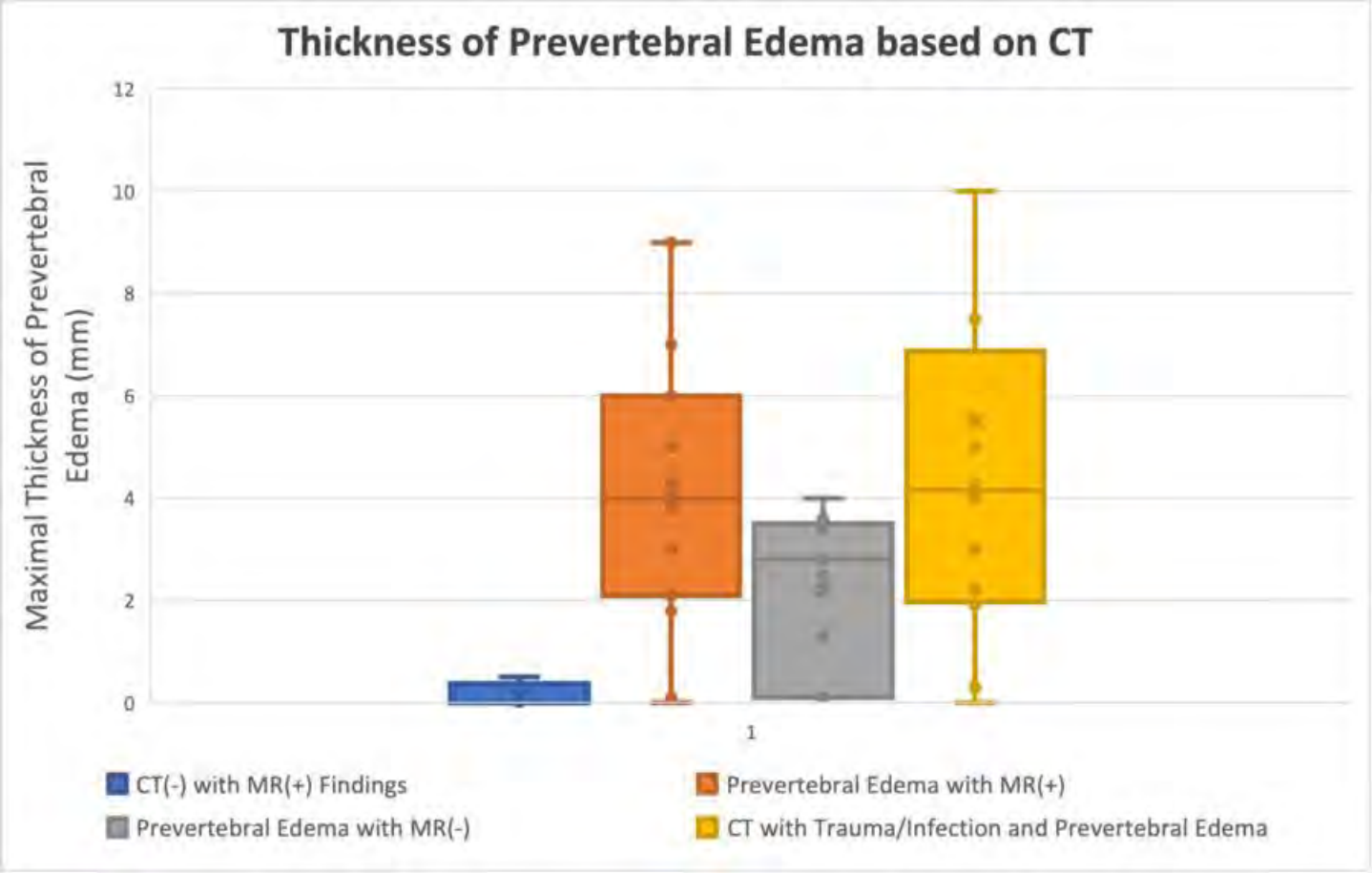

(Filename: TCT_655_ChartofPVEThickness.jpg)

715

Assessment of Treatment Response to Dendritic Cell Vaccine Immunotherapy in Patients with Recurrent Glioblastoma Using Multiparametric MRI Based Prediction Model

L de Godoy[1], S Wang[1], M Nasrallah[2], S Brem[3], A Desai[4], L Loevner[1], S Chawla[1], S MOHAN[1]
[1]Department of Radiology, Perelman School of Medicine at the University of Pennsylvania, Philadelphia, PA, [2]Department of Pathology, Perelman School of Medicine at the University of Pennsylvania, Philadelphia, PA, [3]Department of Neurosurgery, Perelman School of Medicine at the University of Pennsylvania, Philadelphia, PA, [4]Department of Medicine, Perelman School of Medicine at the University of Pennsylvania, Philadelphia, PA

Purpose

Immunotherapy, such as Dendritic Cell (DC) vaccine, is an alternative treatment for recurrent glioblastoma (GBM), inducing inflammation at the tumor bed, referred to as pseudoprogression (PsP), which limits standard MRI assessment.1 The purpose of this study was to investigate our established multiparametric MRI based predictive model2 in evaluating response in GBM patients treated with DC vaccine.

Materials and Methods

Seventeen patients with recurrent GBM treated with DC Vaccine were included. When tumor specimen was available from repeat surgery, histopathologic findings were used to identify true progression (TP) (>25% malignant features; n=12) or PsP (<25%malignant features; n=1).3 In the case of non-availability, >2 consecutive MRIs using mRANO criteria4 were assessed to determine TP (n=2) or PsP (n=2). The multiparametric model consists of DTI derived fractional anisotropy, linear anisotropy, and DSC derived maximum rCBV from contrast-enhancing regions in differentiating TP/mixed response from PsP (accuracy of 90%).2 In this study, we used this model2 to compute the progression probabilities (PP) at the time point when tumor progression was suspected on follow-up MRIs. The most recent multiparametric MRI preceding re-resection was used to calculate PP values and correlate with pathology. Lesions were considered TP if PP was ≥ 50% and PsP if PP was ≤ 50%.5 Based upon the PP values, the cases correctly classified as TP/PsP were determined. Pearson's test was performed to correlate our model with pathology and mRANO criteria. Fisher exact x2 tests were performed to estimate the frequency of MGMT methylation in TP and PsP, and Kaplan Meier was applied to determine overall survival using Ki-67, MGMT, and EGFRvIII status as independent variables.

Results

While characterizing each lesion as TP or PsP, our predictive model correctly predicted TP in 64% of cases (9/14) and PsP in 100% (3/3), reflecting a significant correlation between PP and histopathology/mRANO criteria (r = 0.49; p = 0.04). The frequency of MGMT methylated patients was significantly higher in PsP cases by pathology and mRANO criteria (p=0.01), as well when assessing PP values (p=0.03). The overall survival (mean 20.4 months) was significantly higher (p=0.02) in patients with Ki-67 below the median (median = 27.5%) and showed trends of longer survivals in MGMT methylated and EGFRvIII negative patients (p>0.05).

Conclusions

Our findings indicate that multiparametric MRI help assesses response to DC vaccine in recurrent GBM patients.

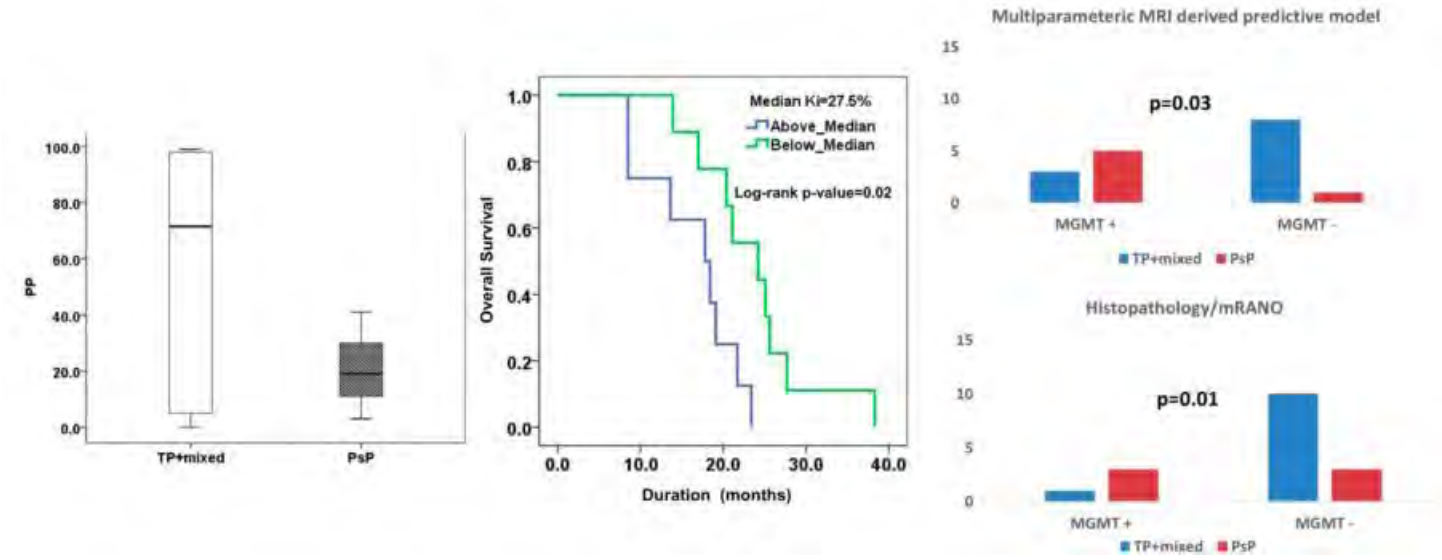

(Filename: TCT_715_FigureASNR.jpg)

1236

Beyond T2 FLAIR mismatch sign in IDH mutant 1p19q non-codeleted astrocytoma

J Jen[1], M Patel[1], U Pohl[1], V Sawlani[1]

[1]*Queen Elizabeth Hospital, University Hospitals Birmingham, Birmingham, West Midlands, United Kingdom*

Purpose

T2-FLAIR mismatch is a validated radiological correlate for the diagnosis of IDH mutant 1p19q non-codeleted astrocytoma. Central FLAIR suppression may be inhomogeneous, corresponding to regions of intra-tumoural heterogeneity, the true nature of which remains uncertain. We aimed to use multiparametric MRI to further interrogate these tumours.

Materials and Methods

128 IDH mutant diffuse gliomas were included for retrospective analysis (2014-2019) by two primary readers blinded to the molecular status. T2-FLAIR mismatch sign was strictly applied. Multiparametric MRI data, including single voxel spectroscopy (SVS), 2D chemical shift imaging (CSI), dynamic susceptibility contrast (DSC) perfusion, and ADC maps, were correlated with histology and molecular biomarkers.

Results

9 showed true T2-FLAIR mismatch, all astrocytomas, 55% grade 2 (5/9) and 45% grade 3 (4/9), median follow-up 7.1 ± 3.3 years. 6/9 had multiparametric MRI. 3/6 showed a normal choline/creatine ratio (Cho/Cr), the other half showed mildly raised Cho/Cr 1.37 - 1.56 on SVS. However, 2/6 showed significantly raised Cho/Cr 2.14 - 2.33 on CSI. Areas with the highest Cho/Cr corresponded to more solid areas within the tumour, seen as ADC/T2 hypointensity and FLAIR hyperintensity. None enhanced or showed hyperperfusion (defined as relative cerebral blood volume, rCBV >2.0). Accurate rim ADC measurement was impaired by partial voluming from displaced white matter tracts.

Conclusions

T2-FLAIR mismatch is infrequently seen in astrocytomas, but 100% specific when present. Correlating structural MRI with intra-tumoural choline mapping on spectroscopy best characterised regions of intra-tumoural heterogeneity, suggesting the greatest volume of cellularity/activity in specific areas of the core. Tumours with the highest Cho/Cr grew on follow-up. Core areas were targeted for biopsy, and also corresponded to areas of recurrence if not completely debulked. The FLAIR hyperintense rim is radiologically a tumoural border zone bound by displaced white matter. Spectroscopy is a useful adjunct to interrogating non-enhancing mismatch tumours.

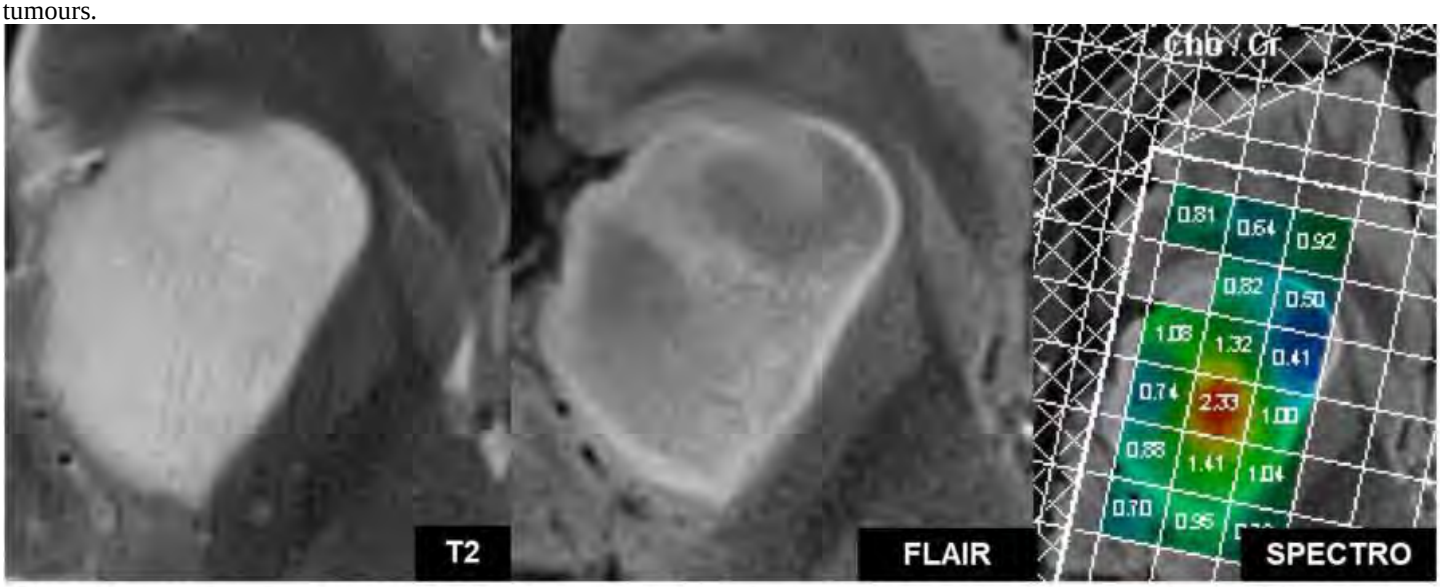

Fig 1. Panel showing classical T2-FLAIR mismatch tumour, confirmed IDH mutant 1p19q non codeleted ATRX mutant astrocytoma. Fairly homogeneous central T2 is shown with variable internal FLAIR suppression. Areas of greatest FLAIR suppression corresponded to lowest choline/creatine (Cho/Cr); areas of non FLAIR suppression corresponded to low ADC (not shown) and highest Cho/Cr, suggesting the greatest amount of cellularity/activity in certain areas of the core.

(Filename: TCT_1236_ASNR2022final.jpg)

1294

Can multiparametric MRI and T2-FLAIR mismatch help provide an integrated diagnosis for IDH mutant 1p19q non-codeleted astrocytoma?

V Sawlani[1], J Jen[1], M Patel[1], U Pohl[1]

[1]*Queen Elizabeth Hospital, University Hospitals Birmingham, Birmingham, West Midlands, United Kingdom*

Purpose
The new 2021 WHO classification amalgamates histological and molecular biomarkers for the diagnosis of diffuse glioma. We investigate whether T2-FLAIR mismatch, T2* DSC-perfusion, ADC and MR spectroscopy findings can provide an integrated approach towards the WHO 2021 glioma classification.
Materials and Methods
Imaging of 101 IDH-mutant diffuse glioma cases (2019-2021) were retrospectively analysed by two neuroradiologists blinded to molecular diagnosis. Degree of T2-FLAIR mismatch and pre-biopsy multiparametric MRI were assessed for grading purposes. Cutoff values were pre-determined for high grade lesions; ADC<1000, rCBV>2, Cho/Cr>1.8 (TE=135ms).
Results
16/101 cases showed T2-FLAIR mismatch, confirmed as IDH-mutant 1p19q non-codeleted astrocytomas; 50% were grade 2 (8/16) and 50% grade 3 (8/16). 12/16 of T2-FLAIR mismatch tumours had multiparametric MRI for correlation. A combination of Cho/Cr >1.8 and rCBV >2 accurately predicted histology grading of grade 3 and above in 82% of cases. There was mismatch between histology and radiological grading in two cases showing high Cho/Cr ratio, and one of these transformed to grade 4 at follow-up.
Conclusions
IDH mutant 1p19q astrocytomas are dynamic tumours and can show a spectrum of T2-FLAIR mismatch. The combination of multiparametric MRI information in this cohort has helped for a non-invasive integrated approach to diagnosis and grading tumours in this molecular subtype. Based on this experience, the future direction for imaging should involve a similar integrated approach using morphological assessment, enhanced use of multiparametric MRI and artificial intelligence.

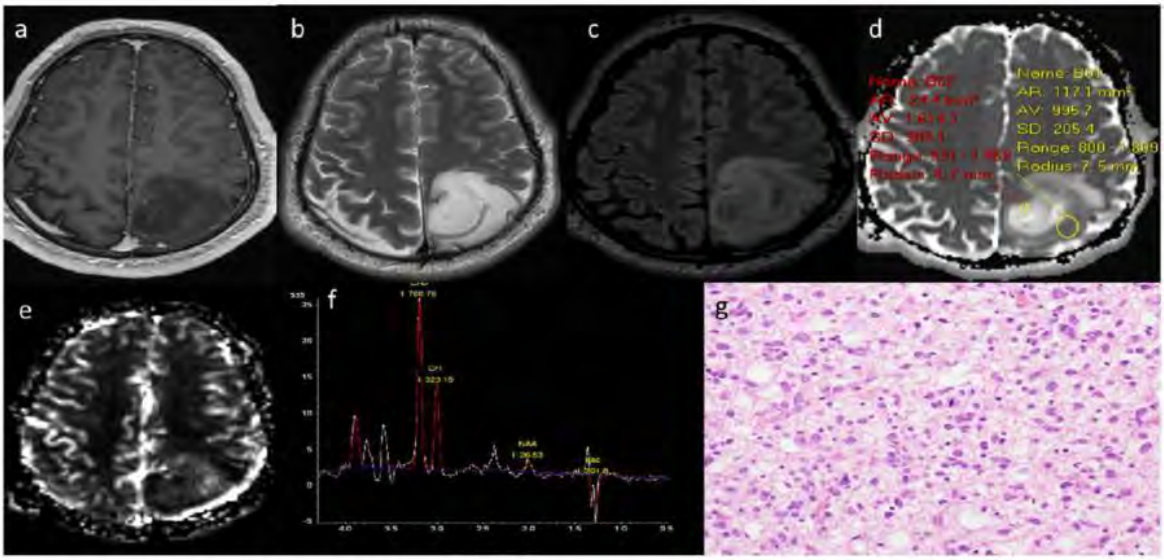

Multiparametric MRI of T2-FLAIR mismatch tumour. (a) CE-T1WI shows non-enhancing tumour in the left parietal lobe, with (b) fairly homogenous T2 signal, and (c) areas of internal FLAIR suppression. (d) Low ADC values (<1000); (e) high perfusion (rCBV>2); (f) raised Cho/Cr ratio (>1.8). Proposed integrated imaging diagnosis: IDH mutated, 1p19q non-codeleted diffuse glioma likely grade 3 astrocytoma. (g) Pathology slide confirming grade 3 astrocytoma and molecular subtype was 1p19q non-codeleted.

(Filename: TCT_1294_ASNR2022VS.jpg)

1489

Combined diagnostic accuracy of Diffusion and Perfusion MR Imaging to differentiate radiation-induced necrosis from recurrence in Glioblastoma

A JAJODIA[1], D Pinto[2]
[1]MCMASTER UNIVERSITY, Hamilton, Ontario, [2]Jackson Memorial Hospital, Miller school of medicine, Miami, FL

Purpose
We aimed to use quantitative values derived from perfusion and diffusion-weighted MR imaging (PWI & DWI) to differentiate radiation-induced necrosis (RIN) from tumor recurrence in Glioblastoma (GBM) and investigate the best parameters for improved diagnostic accuracy and clinical decision making.
Materials and Methods
A retrospective analysis of follow-up MRI with new enhancing observations was done in histopathologically confirmed subjects of post-treated GBM, who underwent re-surgical exploration. Quantitative estimation of rCBV (relative Cerebral blood volume) from PWI and three methods of Apparent diffusion coefficient (ADC) estimation were done namely ADC R1 (whole cross-sectional area of tumor), ADC R2 (only solid enhancing lesion), and ADC R3 (central necrosis). ROC curve and logistic regression analysis was done.

Confusion matrix table created using excel provided the best combination parameters to ameliorate false-positive and false-negative results.
Results
Forty-four subjects with mean age 46 years (range, 19–70 years) underwent re-surgical exploration with RIN in 28 (67%) and recurrent tumor in 16 (33%) on histopathology. rCBV threshold of >3.4 had best diagnostic accuracy (AUC = 0.93, 81% sensitivity and 89% specificity). Multiple logistic regression model showed significant contribution from rCBV (p <0.001) and ADC R3 (p = 0.001). After analysis of confusion matrix ADC R3 > 2032 x 10-6 mm2 achieved 100% specificity with gain in sensitivity (94 % vs. 56 %).
Conclusions
Combination of parameters had better diagnostic performance and stepwise combination of rCBV and ADC R3 obviated unnecessary biopsies in 10 % (3/ 28) leading to improve clinical decision-making.

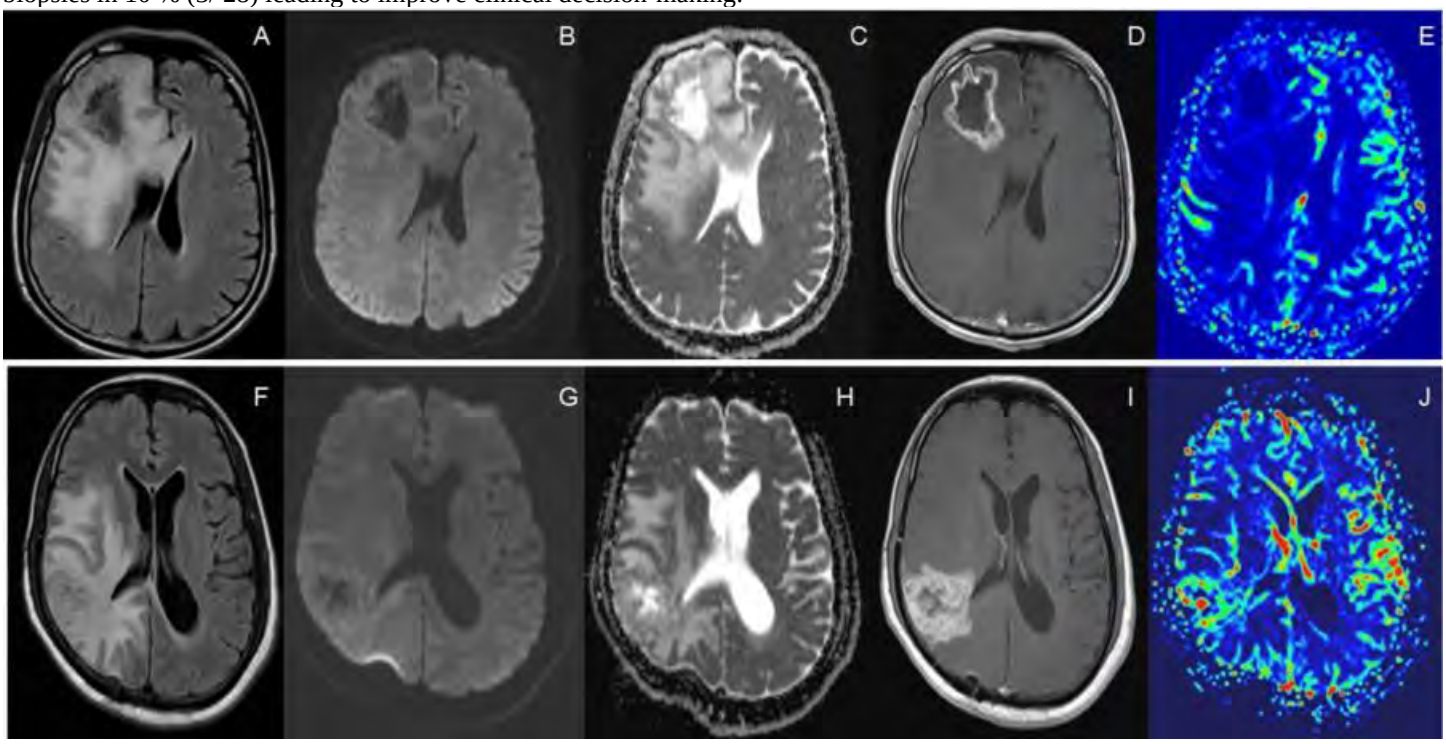

(Filename: TCT_1489_FINALIMAGE1.JPG)

1383
Correlation of in vivo MR spectroscopy and ex vivo 2-hydroxyglutarate concentration for prediction of isocitrate dehydrogenase mutation status in diffuse glioma
B van Dijken[1]
[1]*University Medical Center Groningen, Groningen, Groningen*

Purpose
Introduction: Isocitrate dehydrogenase (IDH) mutation status is one of the most important biomarkers in glioma to define the subtype and corresponding prognosis and treatment. Noninvasive determination of IDH mutation status is of particular interest. This study proposes a straightforward method for 2-hydroxyglutarate (2-HG) quantification by MR spectroscopy for IDH mutation status detection and directly compares in vivo 2-HG MR spectroscopy with ex vivo 2-HG concentration measured in resected tumor tissue in patients with diffuse glioma.
Materials and Methods
Methods: Adult patients with suspected lower grade glioma were prospectively included. Preoperatively 3T point resolved spectroscopy (PRESS) was acquired. The 2-HG peak was measured as the percentage elevation of Glx3 (the sum of 2-HG and Glx) compared to Glx4. During surgery, tissue specimens were collected. IDH mutation status was assessed by immunochemistry or direct sequencing. The ex vivo 2-HG concentration was determined using gas chromatography mass spectrometry. Pearson correlation was used for assessment of correlation between in vivo MR spectroscopy and ex vivo 2-HG concentration.
Results
Results: Eleven consecutive patients (ten IDH1; one IDHwt), were included. MR spectroscopy was positive for 2-HG in eight patients, all of whom had IDH1 tumors. A strong correlation (r=0.80, p=0.003) between 2-HG MR spectroscopy and the ex vivo 2-HG concentration was found.
Conclusions
Conclusion: This study demonstrates a strong correlation between in vivo 2-HG MR spectroscopy and ex vivo 2-HG concentration in

patients with lower grade glioma. Our results add to a growing body of evidence that 2-HG MR spectroscopy is promising for noninvasively determining IDH status in glioma.

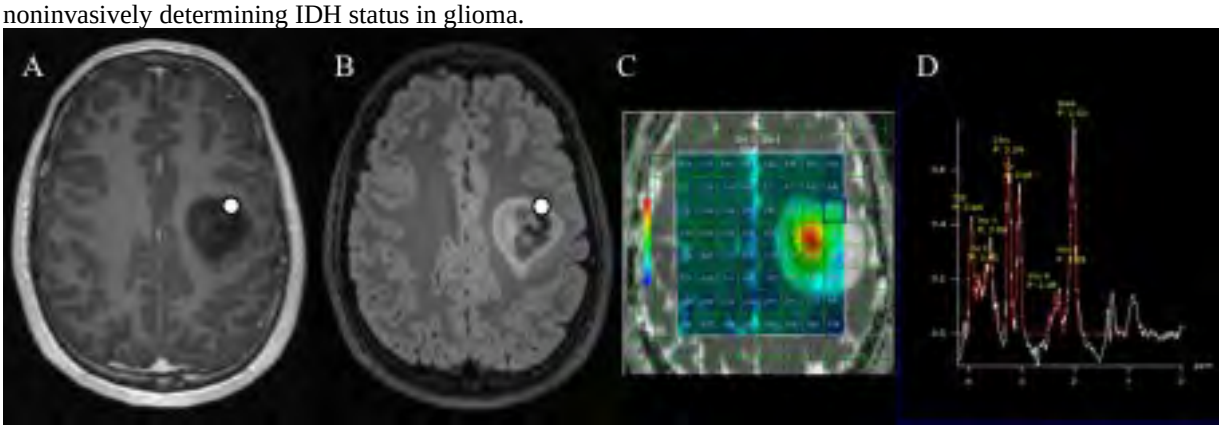

(Filename: TCT_1383_Figure3_2HG.jpg)

720

Differentiating Radiation Necrosis from Recurrent Glioblastoma Using Apparent Diffusion Coefficient Values

A Kamali[1], L Nunez-Rubiano[2], R Riascos[2]

[1]University of Texas Health Science Center Houston, Houston, TX, [2]The University of Texas Health Science Center at Houston, Houston, TX

Purpose

Radiation necrosis is one of the complications of treatment with radiation therapy in glioblastoma patients. The appearance of recurrent glioblastoma and radiation necrosis maybe confusing since both may show enhancement and diffusion restriction on conventional imaging. Biopsy is the gold standard for diagnosis; however, it is costly, invasive, and susceptible to sampling bias. We set out to investigate if the Apparent Diffusion Coefficient (ADC) values can differentiate these two pathologies from one another, noninvasively.

Materials and Methods

In this IRB approved retrospective study, the list of all glioblastoma patients who underwent radiation, surgery and chemotherapy from 2016-2020 was recorded. Subjects with history of treatment with Avastin and steroid were excluded from the study. A total of 100 patients between the age of 50-80 years were analyzed, including 50 patients with biopsy proven radiation necrosis, and 50 age-and-sex-matched patients with biopsy proven recurrent glioblastoma. The MRI scans were investigated and the ADC values of the areas of diffusion restrictions and normal appearing white matter (NAWM) from the contralateral hemispheres were measured by two neuroradiologist.

Results

Among the group with pathology proven radiation necrosis, the mean ADC value for the lesion (n=50) was 479.0 ± 105.2 mm2/s, and the mean ADC value for the normal appearing white matter (NAWM) was 730.0 ± 70.8. Among the group with pathology proven recurrent glioblastoma (n=50), the mean ADC value for the lesion was 0.789 ± 0.105 mm2/s, and the mean ADC value for NAWM was 723.3 ± 64.0. There is significant difference in ADC values of radiation necrosis and recurrent glioblastoma (p value <0.001). The mean ADC values of the NAWM was comparable between the two groups (p value = 0.41).

Conclusions

This study shows that ADC values may be used as a noninvasive diagnostic imaging marker for differentiating radiation necrosis from recurrent glioblastoma in MRI scans of the treated glioblastoma patients.

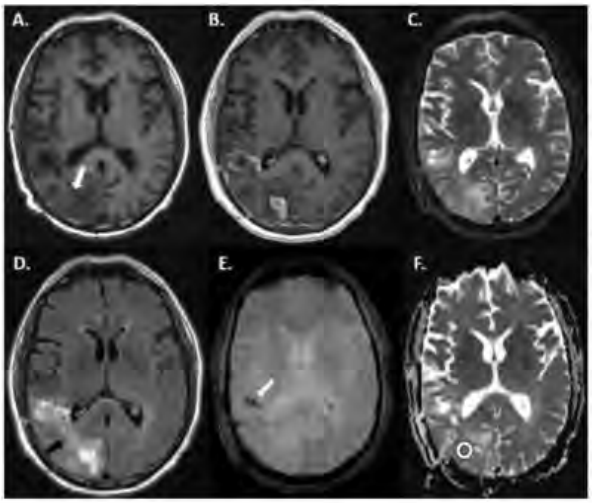

Figure 1. A patient with tumor progression. Axial MR imaging of the brain including T1WI (A), post-contrast T1W1 (B), T2WI (C), FLAIR (D), GRE (E), and ADC map (F). The area with greatest hypo intensity on the ADC map is selected for ROI placement (F). Please note that the ROI corresponds to a non-contrast enhancing portion of the tumor (B) with dirty FLAIR appearance (black arrow in D). Additional information extracted from different sequences including areas of necrosis, hemorrhage (white arrow on E), contrast enhancement, and dirty T2/FLAIR hyperintensities (black arrow on D). This information was used for accurate ROI placement on the darkest ADC signal in the solid component of the lesion (circle on F).

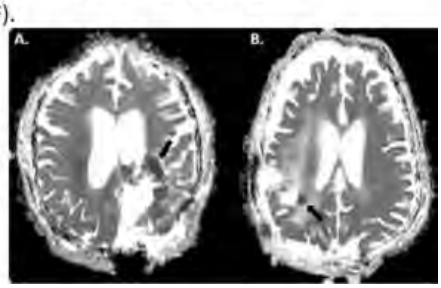

Figure 2 . Apparent diffusion coefficient maps of a patient with radiation necrosis (A), and tumor recurrence (B). Regions of interest (white arrows) were placed in the areas of greatest ADC hypo intensity on the solid tissue.

(Filename: TCT_720_Figures.jpg)

673

Early Volumetric and Perfusion Changes Predict IDH Inhibitor Treatment Response in IDH1-Mutant Gliomas

N Cho[1], A Hagiwara[1], B Eldred[1], C Raymond[1], C WANG[1], F Sanvito[1], A Lai[1], P Nghiemphu[1], N Salamon[1], I Hassan[2], L Steelman[2], T Cloughesy[1], B Ellingson[1]

[1]University of California, Los Angeles, Los Angeles, CA, [2]Servier Pharmaceuticals, Boston, MA

Purpose

Although IDH-mutant gliomas are associated with better prognosis than IDH-wild type gliomas,1 there remains no standard of care for IDH-mutant gliomas. Inhibition of the IDH-mutant enzyme is a novel and only recently explored therapeutic target in IDH-mutant gliomas,2 so early biomarkers of treatment efficacy in these tumors following IDH inhibition are largely unknown. In the current study we explored the value of early volumetric and perfusion MRI-derived normalized relative cerebral blood volume (nrCBV) changes on progression-free survival (PFS) in IDH mutant gliomas during treatment with IDH inhibitors.

Materials and Methods

Twenty-nine IDH1-mutant glioma patients who 1) received AG-120 or AG-881 IDH inhibitor and 2) obtained dynamic susceptibility contrast (DSC) perfusion MRI and structural MRI before treatment 3) and at 3-6 weeks (n=23) and/or 2-4 months (n=13) after treatment initiation were studied. A region of interest (ROI) was placed on the entire T2/FLAIR hyperintense lesion, and nrCBV (normalized to the rCBV value of the centrum semiovale contralateral to the tumor) and FLAIR hyperintensity volumes were obtained. Patients who underwent craniotomy within 6 months after IDH inhibitor start date were excluded from survival analyses. Wilcoxon Signed-Rank tests were conducted to assess percent changes in MRI metrics, and log-rank tests were conducted by looping through quantitative values to find optimal thresholds for associations between MRI metrics and PFS.

Results

After 3-6 weeks of treatment, patients exhibited an overall increase in nrCBV (P=0.02; mean % change=23% (95% CI: 6-41%)). Increasing FLAIR volume at 3-6 weeks was associated with shorter PFS (P=0.01; HR=9.38 using a threshold of 14 cm3). While most patients exhibited a transient increase in nrCBV after therapy, high post-treatment nrCBV only trended to shorter PFS at this timepoint (P=0.08; HR=4.46 using a threshold of 1.55). By 2-4 months from start of treatment there was no significant change in nrCBV compared to baseline when examining all patients (P=0.95), but an increase in nrCBV>10% (P=0.02; HR=10.09) and post-treatment nrCBV>1.55 (P=0.04; HR=4.35) was associated with shorter PFS.

Conclusions

Changes in FLAIR volume, but not nrCBV, 3-6 weeks after IDH inhibitor treatment were predictive of PFS benefit. Changes in nrCBV 2-4 months after treatment were predictive of PFS. After 2-4 months of treatment, nrCBV may be useful for assessing IDH inhibitor treatment response.

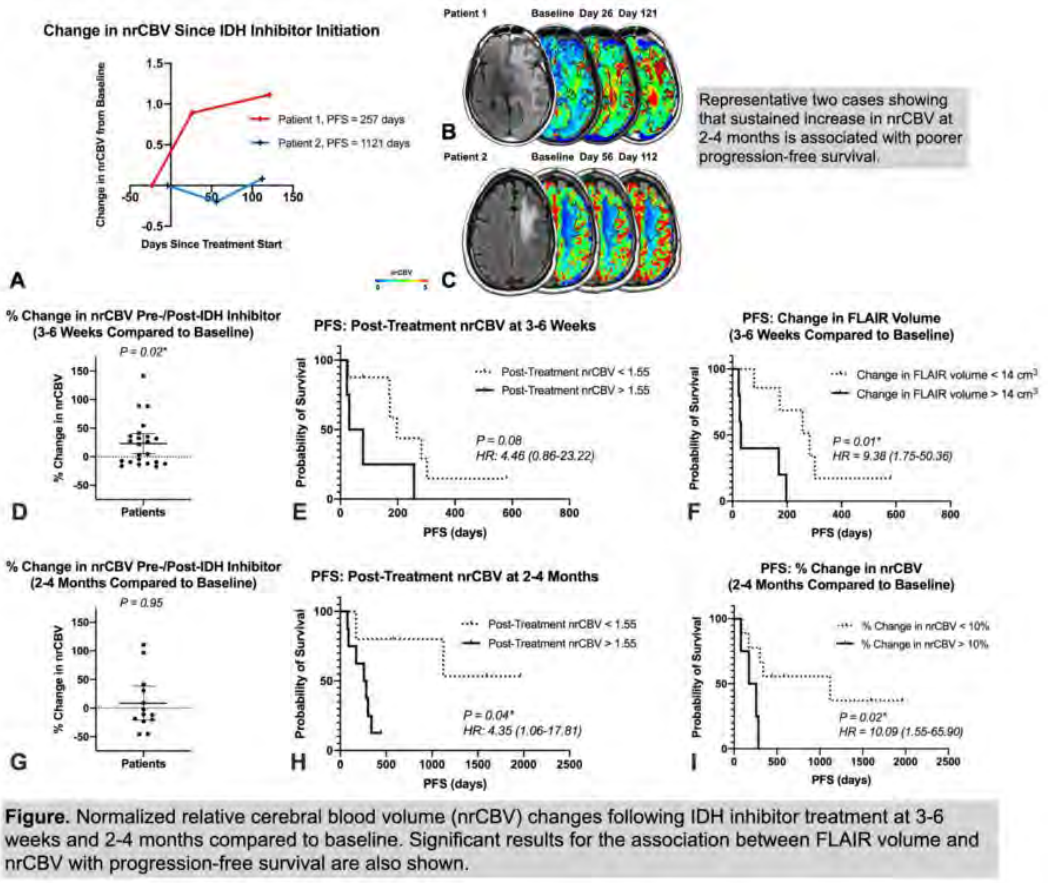

Figure. Normalized relative cerebral blood volume (nrCBV) changes following IDH inhibitor treatment at 3-6 weeks and 2-4 months compared to baseline. Significant results for the association between FLAIR volume and nrCBV with progression-free survival are also shown.

(Filename: TCT_673_Figure_ASNR2022_PerfusionIDHinhibition.jpg)

1362

Glioblastoma survival duration is associated with increased tumor outside of radiological annotations at autopsy

S Bobholz[1], A Lowman[1], M Brehler[1], S Duenweg[1], F Kyereme[1], E Cochran[1], D Coss[1], J Connelly[1], M Agarwal[1], A Banerjee[1], P LaViolette[1]

[1]*Medical College of Wisconsin, Milwaukee, WI*

Purpose

This study tested the hypothesis that glioblastoma (GBM) patients with longer overall survival have more tumor presence beyond what is visible on MRI at autopsy.

Materials and Methods

This study included 9 pathologically confirmed GBM patients with MRI collected within 1 month of death (M(SD) = 18.8 (7.0) days). Each patient's last clinical MRI scans were annotated by a board-certified radiologist (MA) for areas of suspected tumor using all available acquisitions. A total of 24 large tissue samples were collected across patients at autopsy from areas near suspected tumor, including tissue beyond the contrast enhancing margin. These samples were then processed, stained for hematoxylin and eosin (HE), and digitized using a sliding stage microscope at 40X magnification (0.2 microns/pixel). The digitized scans were then annotated for pathological tumor presence and segmented to compute local cell density using a color deconvolution algorithm. Tissue data was aligned to each patient's FLAIR image using a non-linear control-point-based registration software, developed in-house (1-2). The proportion of annotated pathological tumor (TProp) and median cell density (CD) falling outside of radiologist annotations was then computed for each patient to assess the extent of tumor beyond current imaging signatures. Pearson correlations were then used to compute the association between tumor beyond the imaging defined margin and overall survival (in months).

Results

Tumor outside of radiological annotation was found in every patient, with TProp ranging from 0.003 to 1 across the sampled tissue regions (M(SD) = 0.54(0.32)). Median CD outside radiologist annotation was positively associated with overall survival (R=0.79, p=0.01). A trending positive association was also observed for TProp outside of radiologist annotation (R=0.66, p=0.054).

Conclusions

These results suggest that GBM patients that survive longer tend to have more tumor outside of traditional imaging signatures at autopsy. Different treatments such as radiation and bevacizumab are known to influence tumor appearance on MRI, so patients with longer treatment histories could see more non-identifiable tumor at autopsy. GBMs also tend to show substantial pathological heterogeneity, such that tumors that have been given more time to progress will have more complicated radio-pathomic relationships.

Future studies should address the effects of specific treatments and specific pathological features to assess their influence on how GBMs present on MR imaging.

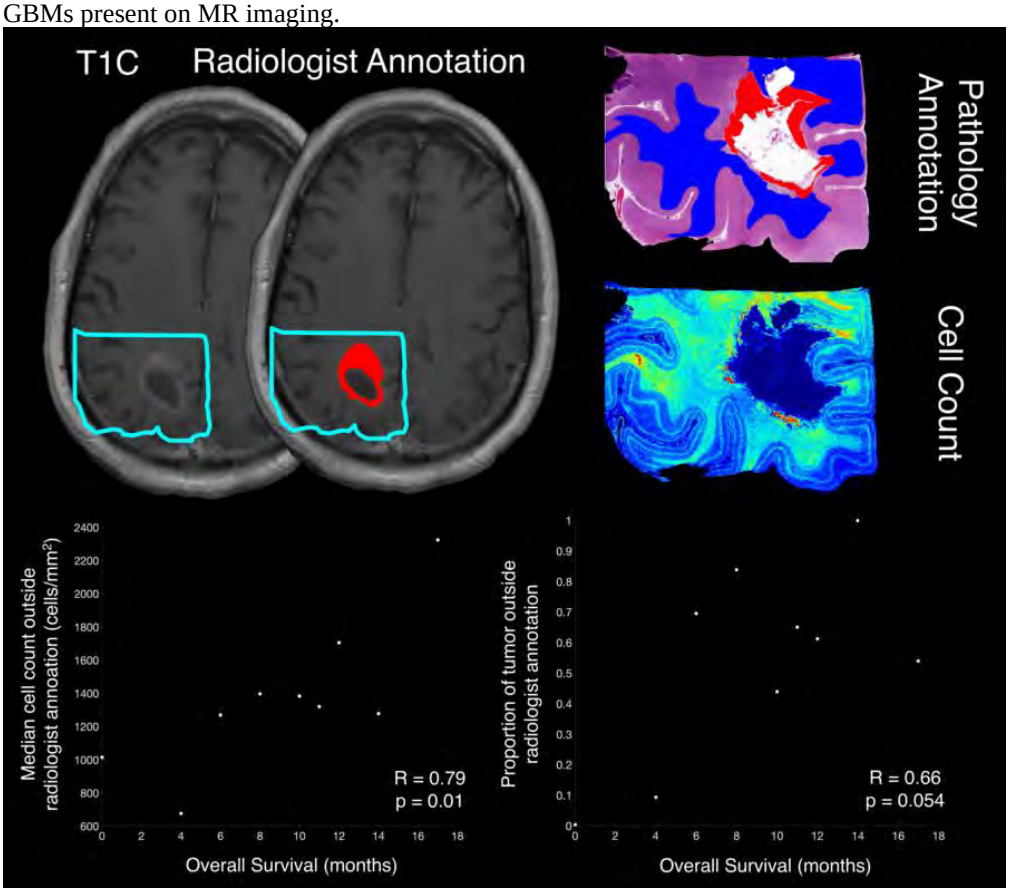

(Filename: TCT_1362_ASNR22_AB1_Fig.jpg)

1149

Longitudinal Tumor Habitat Analysis for Differentiation of Radiation Necrosis from Tumor Progression Using Physiologic MRI

D Lee[1], J Park[1], H Kim[1]
[1]*Asan Medical Center, Seoul, Korea, Republic of*

Purpose
Differentiating between tumor progression (TP) and radiation necrosis (RN) in brain metastasis after stereotactic radiosurgery (SRS) is still challenging but crucial for treatment. Our study aimed to longitudinally analyze tumor habitats in the structural and physiologic magnetic resonance imaging (MRI) for distinguishing two entities.
Materials and Methods
Total 83 brain metastasis patients with 103 growing enhancing lesions after SRS underwent longitudinal multi-parametric MRIs including contrast-enhanced T1 (T1ce)- and T2-weighted MRI, apparent diffusion coefficient (ADC), and cerebral blood volume (CBV). The reference standard was based on pathological results and response assessment in neuro-oncology brain metastases (RANO-BM). K-means voxel-wise clustering identified three structural MRI habitats (enhancing, solid low-enhancing, and nonviable) and three physiologic MRI habitats (hypervascular cellular, hypovascular cellular, and nonviable). As the single time-point parameters were assessed to predict RN and TP using univariable logistic regression, associations of longitudinal parameters for time-to-progression (TTP) were investigated using Cox proportional hazard modeling.
Results
The mean time interval between two multi-parametric follow-up MRIs was 99 days (standard deviation, 51). At single time-points, large solid low-enhancing habitat (low T2 and less-T1ce enhancing) were most predictable for TP (odds ratio=1.54~1.95, largest P=.04, respectively). In longitudinal analysis, TP group exhibited a significant increase of hypovascular cellular habitat (low ADC and low CBV value) while RN group did not (P =.004). In addition, an increase of hypovascular cellular habitat (hazard ratio=2.68, P =.001) was the most significant predictor for shorter TTP.
Conclusions
Structural MRI-based habitats are helpful to diagnose radiation necrosis from tumor progression at a single time point, while the longitudinal change of physiologic MRI-based habitats may be helpful predictors of clinical outcome in patients with SRS treated brain metastases. A prospective observational study is warranted for further evidence.

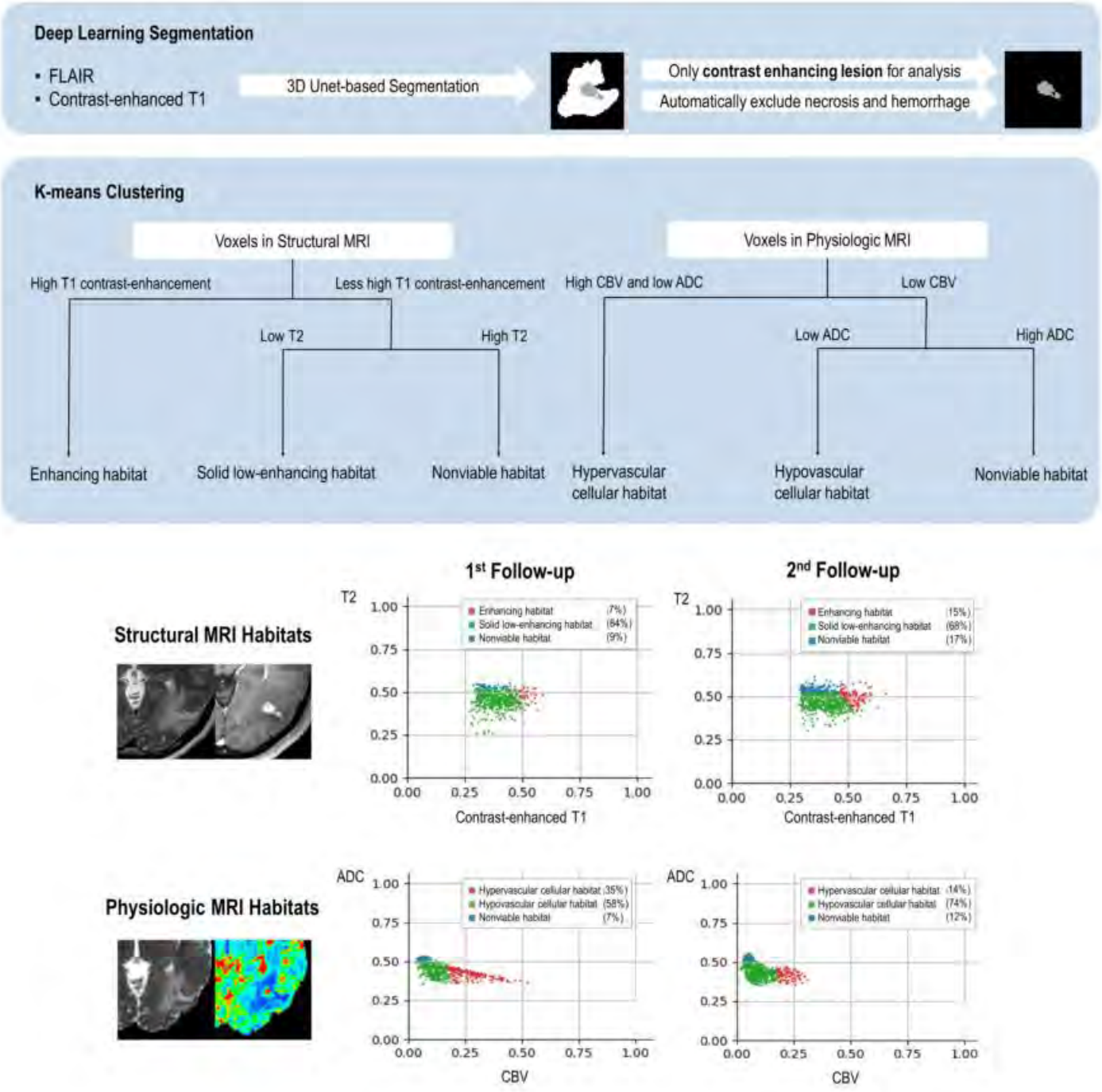

(Filename: TCT_1149_EDA_SRS_Long.jpg)

485

Pre-treatment ADC Histogram Analysis as a Prognostic Imaging Biomarker for Patients with Recurrent Glioblastoma Treated with Bevacizumab: A Systematic Review and Meta-analysis

R Kurokawa[1], M Kurokawa[1], A Baba[1], A Capizzano[1], Y Ota[1], J Kim[1], T Moritani[1], A Srinivasan[1]
[1]*University of Michigan, Ann Arbor, MI*

Purpose

The mean ADC value of the lower Gaussian curve (ADCL) derived from the bi-Gaussian curve fitting histogram analysis has been reported as a predictive/prognostic imaging biomarker in patients with recurrent glioblastoma treated with bevacizumab; however, its systematic summary has been lacking. We applied a systematic review and meta-analysis to investigate the predictive/prognostic performance of ADCL in patients with recurrent glioblastoma treated with bevacizumab.

Materials and Methods
We performed a literature search using PubMed, Scopus, and Embase on August 24, 2021, without date limits. A total of 1344 abstracts were screened, of which 83 articles were considered potentially relevant. Data were finally extracted from six studies including 578 patients. Forest plots were generated to illustrate the hazard ratios (HRs) of overall survival (OS) and progression-free survival (PFS). The heterogeneity across the studies was assessed using Cochrane's Q test and I2 values.
Results
The pooled HRs for OS and PFS in patients with ADCL lower than the cutoff values were 1.89 (95% CIs: 1.53–2.31) and 1.98 (95% CIs: 1.54–2.55) with low heterogeneity among the studies. Subgroup analysis of the bevacizumab-free cohort showed a pooled HR for OS of 1.20 (95% CIs: 1.08–1.34) with low heterogeneity.
Conclusions
This systematic review with meta-analysis confirmed the prognostic value of ADCL in patients with recurrent glioblastoma treated with bevacizumab with low ADCL demonstrating decreased OS and PFS. On the other hand, the predictive role of ADCL for bevacizumab treatment was not confirmed.

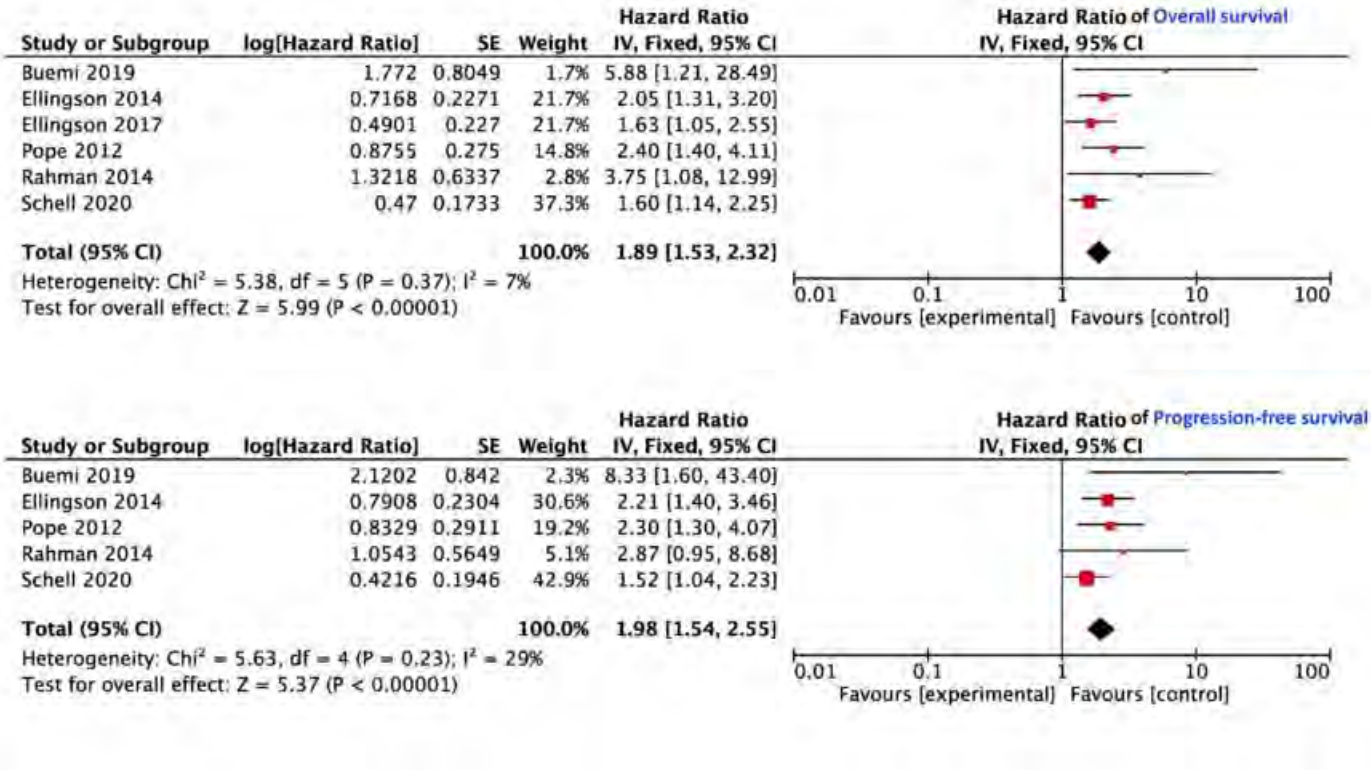

(Filename: TCT_485_ADCL_Figure.jpg)

1402

Spine Oncology Imaging Score Macro and Imaging Referral Pipeline

R MATTAY[1], C FREEMAN[1], L Loevner[2], V Patel[3], a hassankhani[4]
[1]HOSPITAL OF THE UNIVERSITY OF PENNSYLVANIA, PHILADELPHIA, PA, [2]Hospital of the University of Pennsylvania, Philadelphia, PA, [3]University of Pennsylvania, Philadelphia, PA, [4]N/A, N/A

Purpose
The Spine Instability Neoplastic Score (SINS) and the Epidural Spinal Cord Compression (ESCC) scale integrate imaging and clinical characteristics to grade tumor-related instability of the vertebral column and spinal cord compression and can be used to guide surgical and radiation treatment plans. We have developed a new spine oncology imaging score (SOIS) macro incorporating the MRI findings from SINS with an additional metric regarding cord compression. Use of this macro in a report automatically triggers an email to a multidisciplinary subspecialty group of spine neurosurgeons, radiation oncologists, and radiologists at our health system's tertiary care center for immediate review. Patients who require urgent consultation are contacted in an expedited fashion, and others with a sufficiently high SOIS are discussed at the next weekly multidisciplinary conference. Here we describe our preliminary experience with this new imaging referral pipeline.
Materials and Methods
The SOIS breakdown is shown in Table 1, which is an adaptation of the MRI features from SINS and ESCC. We retrospectively reviewed all cases utilizing the SOIS macro since its inception and collected patient demographics, primary neoplasm, and imaging scores.

Results

Figure 1 shows an example of an MRI spine with neoplastic involvement with appropriate scoring breakdown. 278 studies associated with 125 patients (55 male, 70 female, mean age 62 years +/- SD 12.6 years) contained the SOIS macro. 24 sets of reports were from emergency room visits, 54 from inpatient admissions, and 63 from outpatient visits. Mean SOIS across all patients was 8 and mean compression score was 1.4. The multidisciplinary team received email notifications for all patients.

Conclusions

Preliminary data from the use of this new macro show that our new imaging referral pipeline is both technically successful and practical for automating referrals to a multidisciplinary oncology team. By generating an email immediately after the finalized radiology report is available, the time to placement of a consultation to neurosurgery and radiation oncology is essentially immediate, allowing us to expedite patient care. Moreover, we have developed a simple spine imaging oncology score that integrates aspects of two separate scoring systems, SINS and ESCC, and addresses two important aspects of evaluating cancer in the spine: instability and cord compression.

Site of Maximum Spine Oncology Imaging Score	
Description	**Points**
Location	
Rigid spine (S2-S5)	0
Semi-rigid spine (T3-T10)	1
Mobile spine (C3-C6, L2-L4)	2
Junctional spine (Occiput-C2, C7-T2, T11-L1, L5-S1)	3
Alignment	
Normal	0
Deformity (kyphosis/scoliosis)	2
Subluxation	4
Collapse	
None	0
Mild (No collapse with > 50% vertebral body involvement)	1
Moderate (<50% height loss)	2
Severe (>50% height loss)	3
Posterior Elements	
None	0
Unilateral	1
Bilateral	3
Total SOIS Score Range:	**0-13**

Site of Greatest Spinal Compression	
Description	**Grade**
Osseous disease only	0
Epidural involvement without thecal sac deformity	1a
Thecal sac deformity without cord contact	1b
Thecal sac deformity with cord contact	1c
Cord compression with preservation of some CSF	2
Cord compression with complete effacement of CSF	3
Intramedullary/cord or drop metastasis	4
Intradural and extradural	5

Table 1: Spine Oncology Imaging and Spinal Compression Score Breakdown

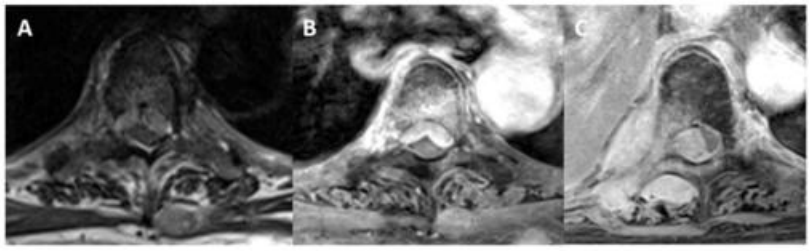

Figure 1: A and B) T2 axial and Post-contrast T1 axial imaging at T4 showing spinal compression with some preservation of CSF (Grade 2). C) Post-contrast T1 axial imaging at T10 showing spinal compression with complete effacement of CSF (Grade 3) and a SOIS of 4 (1 point for location in the semirigid spine at T10 and 3 points for bilateral involvement of the posterior elements).

(Filename: TCT_1402_SOIN22Mattayfig.jpg)

1407

T2 Relaxivity in the Prediction of Progression-Free Survival in Patients with Primary Glioblastoma: Whole Brain Measurements and Deep Learning

A Rulseh[1], J Vymazal[1]

[1]Na Homolce Hospital, Prague, Czech Republic

Purpose

Glioblastoma (GBM) is the most common and aggressive primary brain tumour. We aimed to evaluate T2 relaxation times in the follow up of these patients.

Materials and Methods

In this partially retrospective study, 50 patients with non-recurrent GBM followed at our department after surgery and combined chemo-radiotherapy were included (>180 days progression-free survival [PFS] as determined by RANO1, ≥3 MRI examinations in the PFS interval [same scanner & protocol]). All data used were prior to progression; standard imaging included a dual echo fast spin echo sequence. T2 relaxation rates (1/T2) were calculated voxel-wise assuming mono-exponential decay; preliminary comparison with CPMG showed high correlation. Brain extraction was performed on T2-weighted images and masks applied to 1/T2 volumes. Whole-brain (WB) values were extracted including skewness, kurtosis, mean, median, 15 and 85 percentile histogram values and variance. We additionally segmented the 1/T2 volumes using a 5 compartment Gaussian mixture model (Python v.3.8.2; Fig.A), producing mean, variance and percentage of voxels for each component. To evaluate predictive potential with respect to PFS, we used a deep long short-term memory (LSTM) model (Fig.B) in Tensorflow v2.3.1 (4 timesteps). Twenty subjects were included in the predictive model, as inclusion criteria differed (progression, ≤120 days between all MRIs [mean 43.6 days], ≥4 PFS MRIs). Two models were

tested: a regression model (days to progression) and a classification model (±18 months PFS; models differed in output layer). Both models were run 10 times; mean results are presented.

Results

We found WB median 1/T2f correlated with PFS, as values decreased prior to progression (Fig.C). WB median 1/T2 linear regression slopes also differed in progression vs. pseudo-progression (Fig.D). The deep LSTM regression model achieved an R2 of 97%. The deep LSTM classification model achieved a mean macro precision of 86%, recall 85% and F1 accuracy of 85% in classifying progression/no progression within 18 months.

Conclusions

We found very intriguing results with WB median 1/T2 measurements in distinguishing progression from pseudo-progression, and in suggesting progression despite otherwise unremarkable imaging. A more complex predictive model, using a fully-automated segmentation method followed by deep learning, showed very promising results. The present results may find utility in the monitoring of GBM patients and may be advantageous to include in multimodal predictive models.

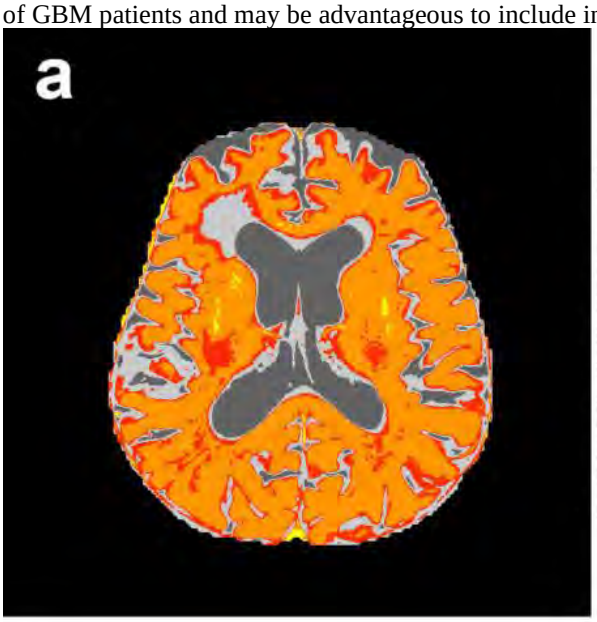

b

Layer (type)	Output Shape	Param #
lstm_8 (LSTM)	(None, 4, 138)	91080
lstm_9 (LSTM)	(None, 69)	57408
dropout_8 (Dropout)	(None, 69)	0
dense_8 (Dense)	(None, 512)	35840
dropout_9 (Dropout)	(None, 512)	0
dense_9 (Dense)	(None, 128)	65664
dense_10 (Dense)	(None, 1)	129

Total params: 250,121
Trainable params: 250,121
Non-trainable params: 0

None

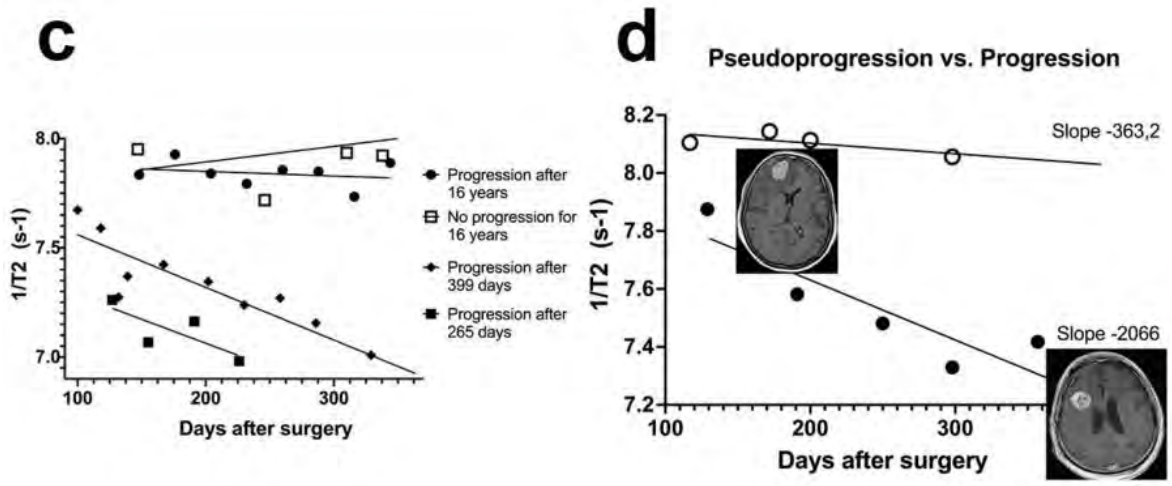

(Filename: TCT_1407_fig.jpg)

1216

Anterior chamber enhancement predicts optic nerve infiltration in retinoblastoma - Stasis of the orbital glymphatic system?

K Deike-Hofmann[1], P von Lampe[2], M Eerikaeinen[2], D Paech[3]
[1]Universityclinic Bonn, Bonn, DE, [2]Universityclinic Essen, Essen, Nordrhein-Westfalen, [3]Universityclinic Bonn, Bonn, Nordrhein-Westfalen

Purpose

Recently, brain clearance imaging revealed regular penetration of intravenously injected gadolinium-based contrast agent (CA) into the eye bulb via the anterior eye chamber (AC) [1,2] as well as perivascular drainage from the posterior globe to the postlaminar optic nerve (ON) [2,3], which was termed the orbital glymphatic system. As a previous study suggested a correlation between AC enhancement and presence of ON infiltration in a small cohort of retinoblastoma (RB) patients (n = 16) [4], we aimed to review the supposed correlation in a large data set from a major national RB center. Results were interpreted in consideration of recent knowledge on ocular fluid dynamics.

Materials and Methods

Our local ethics committee approved this retrospective single-center study, which encompassed 539 orbital MRIs performed between 2010 and 2019. MRI was performed with an orbital coil and with the children in a state of general anesthesia. Differences of signal intensity ratios of the AC to the lens (ΔSIRs) were determined between native and GCA-enhanced T1-weighted images. Subsequently, ΔSIRs of RB eyes were compared to healthy eyes and correlated with histopathologic tumor features derived from enucleation such as infiltration of the ON, choroid, ciliary body, sclera and AC.

Results

ΔSIRs were significantly higher in RB eyes compared to healthy eyes ($p < 0.001$). ΔSIR of the RB eye was an independent, significant predictor for ON invasion in multivariate analysis with adjustment for tumor size ($p < 0.05$) and increased with infiltration level. ΔSIR was not predictive for any other assessed histopathologic tumor feature.

Conclusions

CA enhancement of the AC predicts ON infiltration. We hypothesize that this is caused by dysfunction of the recently described orbital glymphatic system, which is supposed to serve retinal homeostasis and clearance of toxic metabolites and is mediated by perivascular fluid transport from the retina to the postlaminar ON. In RB with ON infiltration this posterior efflux path is likely to be impeded with consecutively disturbed retinal homeostasis, which leads to release of vascular endothelial growth factor followed by iris neovascularisation. Iris neovascularisation is known to increase penetration of CA into the AC.

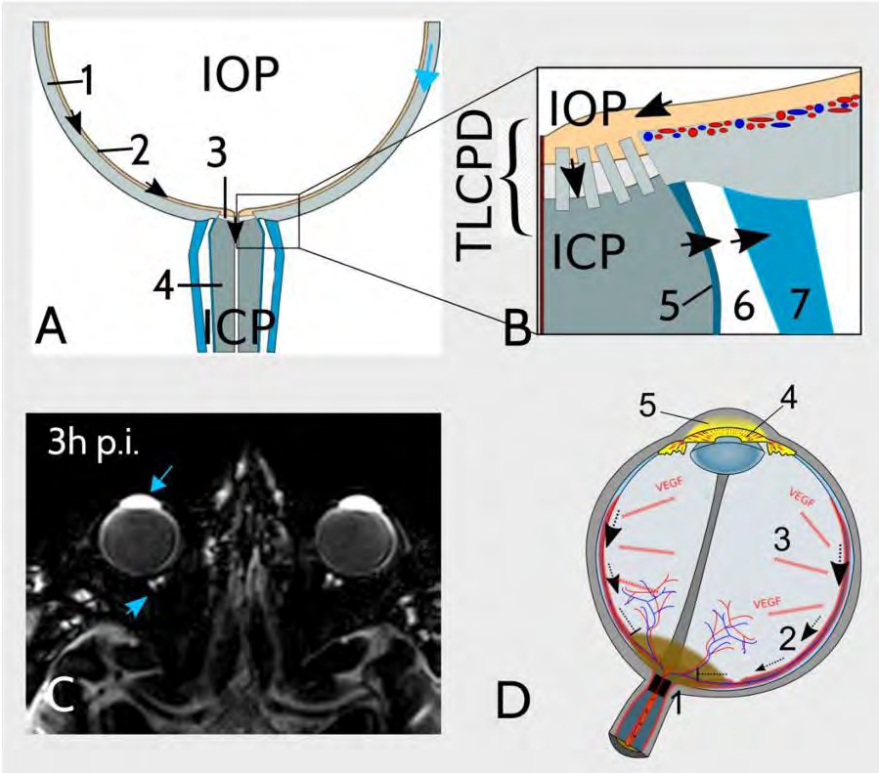

(Filename: TCT_1216_Abb_ASNR2.JPG)

657

Cost-Effectiveness of Endovascular Thrombectomy in Childhood Stroke: An Analysis of the Save ChildS Study

W KUNZ[1]

[1]*LMU Munich, Munich, Bavaria*

Purpose

The Save ChildS Study demonstrated that endovascular thrombectomy (EVT) is a safe treatment option for pediatric stroke patients with large vessel occlusions with high recanalization rates. Our aim was to determine the long-term cost, health consequences and cost-effectiveness of EVT in this patient population.

Materials and Methods

In this retrospective study, a decision-analytic Markov model estimated lifetime costs and quality-adjusted life years (QALY). Early outcome parameters were based on the entire Save ChildS Study to model the EVT group. As no randomized data exist, the Save ChildS patient subgroup with unsuccessful recanalization was used to model the standard of care group. For modeling of lifetime estimates, pediatric and adult input parameters were obtained from the current literature. The analysis was conducted in a United States setting applying healthcare and societal perspectives. Probabilistic sensitivity analyses were performed. The willingness-to-pay (WTP) threshold was set to $100,000 per QALY.

Results

The model results yielded EVT as the dominant (cost-effective as well as cost-saving) strategy for pediatric stroke patients. The incremental effectiveness for the average age of 11.3 years at first stroke in the Save ChildS Study was determined as an additional 4.02 lifetime QALYs, with lifetime cost-savings that amounted to $169,982 from a healthcare perspective and $254,110 when applying a societal perspective. Acceptability rates for EVT were 96.60% and 96.66% for the healthcare and societal perspectives.

Conclusions

EVT for pediatric stroke patients with large vessel occlusions resulted in added QALY and reduced lifetime costs. Based on the available data in the Save ChildS Study, EVT is very likely to be a cost-effective treatment strategy for childhood stroke.

Table 1. Base-Case Values and Source of Input Parameters

Model Input	Base-Case Value*	Distribution	Source
Initial Probabilities			
For each health state mRS 0-6 of EVT-treated patients	Discharge mRS distribution for mTICI 0-3 recanalization	Dirichlet	Save ChildS Study Sporns et al. (Figure 2)
For each health state mRS 0-6 of SC-treated patients	Discharge mRS distribution for mTICI 0-2a recanalization	Dirichlet	Save ChildS Study Sporns et al. (Figure 2)
Treatment with IVT	0.219	β	Save ChildS Study Sporns et al.
Transition Probabilities			
Pediatric recurrent stroke rate	0.066 (over first 5 yrs)	β	Sträter et al.
Adult recurrent stroke rate	Based on cycle age and time since index stroke	β	Pennlert et al.
Annual death rate	0.000103 (for 11 y/o)	β	US Life Table 2017
Annual death hazard rates for survivors mRS 0 / 1 / 2 / 3 / 4 / 5	1.53 / 1.52 / 2.17 / 3.18 / 4.55 / 6.55	Log normal	Hung et al.
After recurrent pediatric stroke	Discharge mRS distribution for mTICI 0-2a recanalization	Dirichlet	Save ChildS Study Sporns et al.
After recurrent adult stroke	90-day mRS control arm	Dirichlet	HERMES Goyal et al.
Health Care Costs			
Costs within first 90 days after stroke for mRS 0 / 1 / 2 / 3 / 4 / 5 / 6 (excluding IVT and EVT)	$8,778 / $12,117 / $19,091 / $23,536 / $31,537 / $37,674 / $8,856	γ	Davison et al.
Additional cost of IVT treatment	$7,641	γ	NIS 2018
Additional cost of EVT treatment	$15,977	γ	Shireman et al.
Long-term annual costs after stroke for mRS 0 / 1 / 2 / 3 / 4 / 5	$12,344 / $12,711 / $14,704 / $25,258 / $51,104 / $75,131	γ	Shireman et al.
Recurrent stroke hospitalization	$25,288	γ	Chambers et al.
Utilities			
mRS 0 / 1 / 2 / 3 / 4 / 5 / 6	1.00 / 0.91 / 0.76 / 0.65 / 0.33 / 0.00 / 0.00	β	Chaisinanunkul et al.
Societal Costs			
Paid Workforce Productivity			
Average annual earnings of employed population	$13,441 (for 18 to 24 y/o)	γ	US Census Bureau 2018
Population employment rate	0.400 (for 18 to 19 y/o)	β	US Bureau of Labor Statistics 2020
Relative earnings of stroke survivors	0.825	β	Vyas et al.
Return-to-work after stroke mRS 0 / 1 / 2 / 3 / 4 / 5	0.63 / 0.72 / 0.49 / 0.19 / 0.14 / 0.00	β	Tanaka et al.
Unpaid Domestic Productivity			
Informal annual caregiving costs	mRS 0-1: $1,650 mRS 2-5: $8,259	γ	Hickenbottom et al.

Figure 1. Model Structure

Figure 2. Outcome Data from the Save-ChildS Study

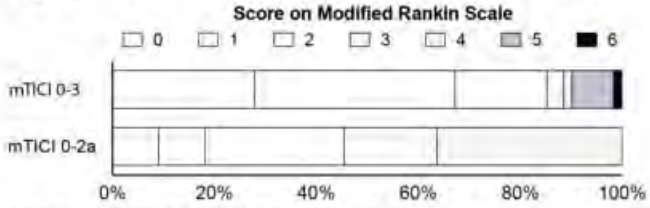

mTICI 0-3 represents the entire Save ChildS study.
mTICI 0-2a represents unsuccessful recanalzation.
Outcomes are measured on the modified Rankin Scale (mRS) 90 days after stroke.
mRS 0 = no symptoms, mRS 2 = living independent, mRS 5 = patient bed-ridden requiring long-term nursing care, mRS 6 = death.

Figure 3. Cost-Effectiveness Plane

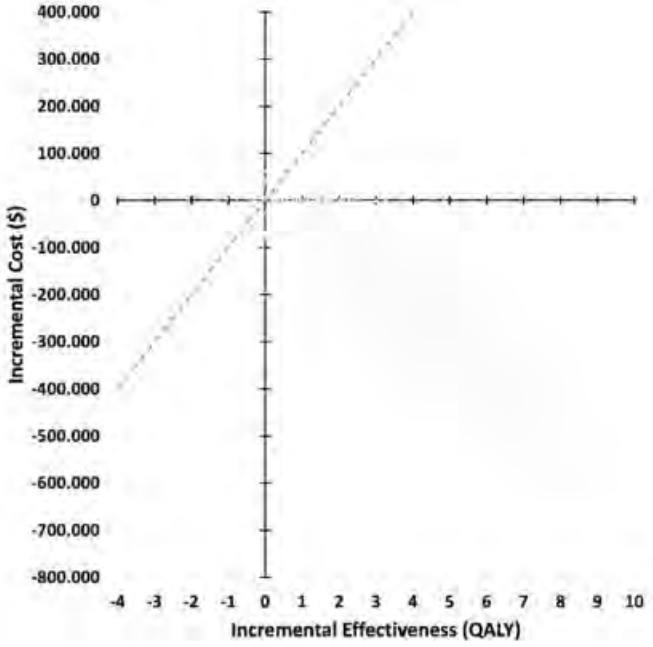

(Filename: TCT_657_211108ABSTRACTCost-EffectivenessofEndovascularThrombectomyinChildhoodStroke.jpg)

187

Differentiation of Medulloblastoma Molecular Subtypes with Multiparametric MRI Findings Including MRI Based Texture Analysis

B Aslan[1]
[1]*Marmara University School of Medicine, Istanbul, Turkey*

Purpose
The aim of our study was to differentiate medulloblastoma molecular subtypes with multiparametric MRI findings including magnetic resonance imaging-based texture analysis.
Materials and Methods
Fifty-eight patients with preoperative MRI and histopathological diagnosis of medulloblastoma after surgery were included in our study. The patients were divided into two groups as SHH pathway active and group 3/group 4 medulloblastoma. Morphological findings in brain MRI, ADC measurements and texture analysis features of the lesions in both groups were compared.
Results
Thirty-two (55.2%) of 58 medulloblastoma patients included in the study were SHH pathway, while the others were group 3-4 molecular subtype. Among the morphological findings, being out of midline or in the cerebellar hemisphere ($p<0.001$), peri-tumoral edema ($p=0.041$), macrocyst ($p=0.001$) and nodular involvement/lobulation ($p=0.002$), as well as heterogeneous contrast enhancement ($p=0.002$) 0.011) were statistically more common in SHH active tumors. The ratio of the solid part of the tumor to the thalamus in

ADC measurements was statistically significantly lower in SHH tumors (p<0.001). When the threshold value for this ratio was determined as 0.855, the sensitivity was 82.1% and the specificity was 92.3%. As for texture analysis parameters, kurtosis (p=0.023), SumOfSqs (p=0.022) and 01-10-50-90% percentile (respectively p=0.011; p=0.001; p=0.006; p=0.013) values obtained from ADC images and kurtosis (p=0.041), SumOfSqs (p=0.005), SumVarnc (p=0.014), SumEntrp (p=0.032) values obtained from T1W images were statistically significant in differentiating SHH and group 3/ group 4 medulloblastoma.
Conclusions
The use of morphological MRI findings, ADC measurement, and texture analysis parameters provide useful diagnostic information in identifying medulloblastoma molecular subtypes.

238

Enhanced Arterial Spin Labeling with Multiple Delays Can Detect Vasculopathy in Children

M Zhao[1], K Yeom[2], E Tong[3], R Duarte Armindo[1], M Moseley[1], G Zaharchuk[1]
[1]Stanford University, Stanford, CA, [2]Stanford University, Palo Alto, CA, [3]Stanford University School of Medicine, Stanford, CA

Purpose
Arterial spin labeling (ASL) is a non-invasive and quantitative MRI technique for measuring cerebral blood flow (CBF). ASL with a single delay has been recommended as the standard clinical application for CBF mapping [1]. However, it is limited by the variations in arterial transit time and macrovascular artifact, both of which are more profound in pediatric patients due to a higher blood flow than adults. ASL with multiple delays (multi-delay ASL) and combined with bipolar flow suppression gradients can alleviate these issues for a more accurate CBF and transit time measurement. The strength of multiple-delay over single-delay ASL has been demonstrated in adults stroke patients and validated using the gold standard 15O-water PET imaging technique [2,3]. Here, we apply multi-delay ASL to investigate the hemodynamic of children with arteriovenous malformation.
Materials and Methods
ASL data with a single-delay (post-labeling delay = 1.524s, labeling duration = 1.45s, scanning time = 4:49min) and 7 delays (post-labeling delays = 0.7s, 1.4s, 2.1s, 2.8s, 3.5s, 4.2s, 4.9s; labeling duration = 0.55s, scanning time = 4:23min) were collected from 5 children with AVM using a 3T GE SIGNA Premier MRI 3. The other acquisition parameters were identical to our previous work that investigated the vascular hemodynamics of adult stroke patients [3]. CBF and transit time were computed by fitting the ASL data to a general kinetic model using the FSL tool BASIL.
Results
The figure shows the hemodynamic maps of a 12-year-old boy with left thalamic arteriovenous malformation. CBF of both single and multiple delays ASL captured signal enhancement near the left transverse sinus, indicating blood flow bypassing capillaries to fully perfuse. Additionally, the ATT of multi-delay ASL showed a signal reduction, implying the presence of congenital vasculature that prevented the inflowing blood to perfuse to surrounding tissues. These hemodynamic markers were confirmed by findings on T2 FLAIR image.
Conclusions
We demonstrated the strength of ASL with multiple delays in pediatric neuroimaging. Multi-delay ASL enabled the mapping of both CBF and transit time using the same scanning time as the single delay ASL in less than 5 minutes. The hemodynamic maps of multi-delay ASL revealed both tissue perfusion and blood circulation characteristics, which can be potentially applied to pediatric cerebrovascular diseases.

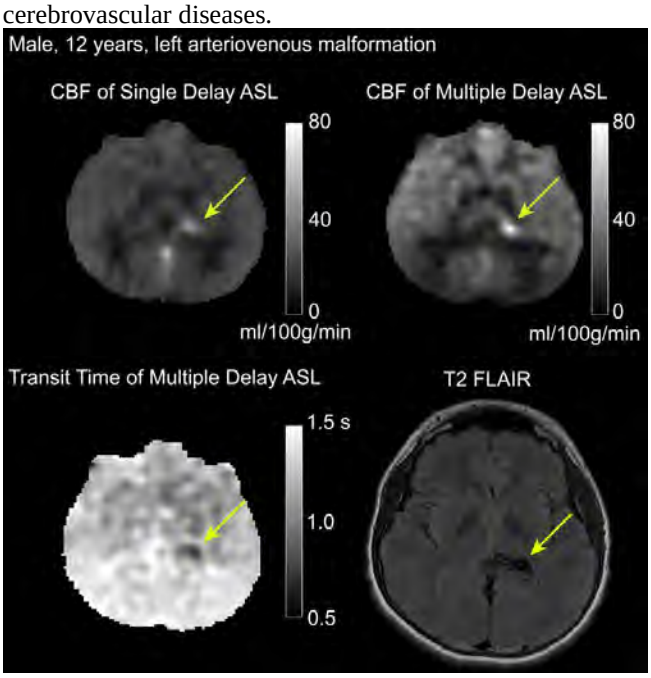

(Filename: TCT_238_Figure.jpg)

963

Imaging Subtypes of pLGG Patients Determined by Multi-parametric MRI and Radiomics are Associated with Gene Expression Profiles

D Haldar[1], A Fathi Kazerooni[2], S Arif[2], R Madhogarhia[2], H Anderson[3], S Bagheri[2], J Ware[2], A Familiar[4], A Vossough[1], P Storm[4], A Resnick[4], A Nabavizadeh[2]

[1]University of Pennsylvania, Children's Hospital of Philadelphia, Philadelphia, PA, [2]University of Pennsylvania, Philadelphia, PA, [3]Hospital of the University of Pennsylvania, Philadelphia, PA, [4]Children's Hospital of Philadelphia, Philadelphia, PA

Purpose

To identify distinct radiomic profiles of pediatric low grade gliomas (pLGGs) that correspond to clinical features and underlying molecular markers.

Materials and Methods

A total of 96 pediatric patients with low grade glioma (WHO Grade 1 and 2) from a single institution, with available pre-surgical and pre-treatment multi-parametric MRI (mpMRI) scans, including pre- and post-contrast T1-weighted, T2-weighted, T2-FLAIR, and diffusion-weighted imaging, were included in this study. Quantitative radiomic features (n=1096) including measures of morphology, intensity, histogram and texture were computed from mpMRI. Principal component analysis (PCA) was carried out to reduce dimensionality of radiomic features. Unsupervised clustering to obtain imaging subtypes was performed using K-Means with n = 10,000 iterations. Whole genome and RNA sequencing for the patients were obtained from PedCBioportal. Differences in genomic mutations among the imaging subtypes were assessed using chi-squared analysis, and in expression profiles using Student's t-test with Benjamini-Hochberg correction for multiple comparisonswith q-values reported. Molecular data was obtained through the PedCBioportal(1,2).

Results

PCA analysis yielded 30 components that explained 95% of the variance in the data, followed by K-means clustering revealing four distinct imaging subtypes . Significant differences were found in mutations in 56 genes ($p < .01$, $q < .05$) and expression levels in 11 genes ($p < 0.001$, $q < 0.05$). Also, Kruskal-Wallis test showed that the clusters differed in age ($p = 1.996e\text{-}3$, $q = 0.0180$) with the oldest subgroup having a median age of 9.5 years and the youngest subgroup having a median age of 7months. Furthermore, tumor location was significantly different between the clusters ($p = 0.0115$, $q = 0.0412$).

Conclusions

In this study, we utilized advanced multivariate imaging analysis methods on mpMRI scans of pLGG patients and identified four distinct imaging subtypes that are associated with differential characteristics in patients' age, anatomical location, and molecular composition. These subtypes can provide noninvasive and in vivo biomarkers of the underlying tumor biology and guide personalized therapies.

855

Lower-Order Texture Radiomic Analysis of Pediatric Pontine Neoplasms: Utility in Imaging Differential Diagnosis and Overall Survival Prediction

F Goncalves[1], A Zandifar[2], J Kim[2], L Tierradentro-García[2], A Vossough[2]

[1]Children's Hospital of Philadelphia, Philafelphia, PA, [2]Children's Hospital of Philadelphia, Philadelphia, PA

Purpose

Pediatric brainstem tumors (PBST) can present diagnostic, treatment, and prognostic challenges. Diffuse midline glioma, H3K27M-altered (DMG) are highly malignant with poor prognosis. At times, other tumors may mimic DMG on imaging and clinically. This study aimed to assess the application of radiomic texture analysis of T2 and DWI signals pre-operatively to differentiate PBST and assess their association with overall survival.

Materials and Methods

We evaluated 48 consecutive pathology-proven PBST from 2016-21. There were 29 DMG cases and a variety of other entities. PBSTs were manually segmented and T2 signal and ADC histogram metrics were calculated on a pixel-by-pixel basis. Analysis was performed both on raw data and after ratio normalization to the thalamus, to decrease differences related to image acquisition. 17 lower-order histogram radiomic metrics were calculated and compared. Lower-order radiomic features were evaluated as they have generally shown higher reproducibility than higher-order features. Mann–Whitney U test was used to evaluate differences between the largest groups. Relationship of the various radiomic features at initial MRI and overall survival for the DMG group was analyzed by Kaplan-Meier analysis with log-rank comparisons.

Results

There was no significant differences in any radiomic features between DMG, and PAs. AA, ETMR, LGG, PXA, and PMA were not compared due to low frequency, but had overlapping values. ETMR and HGG-wt were the only entities with reduced diffusion relative to the thalamus. The only T2-based metric associated with better survival was T2ratio kurtosis (430±122 vs 260±52 days,p=.03). Multiple ADCabsolute derived features were associated with better survival, for example: minimum ADC>875, (204±45 vs 545±148 days,p=.004); 10th percentile>1100 (242±52 vs 507±153 days,p=.02); median ADC>1350, (226±52 vs 499±141 days,p=.046), total energy>3x1010, (230±48 vs 549±164 days,p=.02), kurtosis<4 (492±172 vs 277±53 days,p=.048). Several normalized ADCratio related parameters were associated with better survival, for example: minimum ADC>1.5, (225±45 vs 525±153 days,p=.002); 10th percentile>1.75 (209±45 vs 573±159 days,p=.007); mean >1.8 (217±46 vs 533±151 days,p=.008).

Conclusions
Brainstem DMG and PAs were indistinguishable based on T2-based radiomic features. No DMGs had true reduced diffusivity, which was only seen in ETMR and HGGwt. T2ratio kurtosis and multiple lower order diffusivity metrics can predict overall survival in DMGs based on initial MRI.

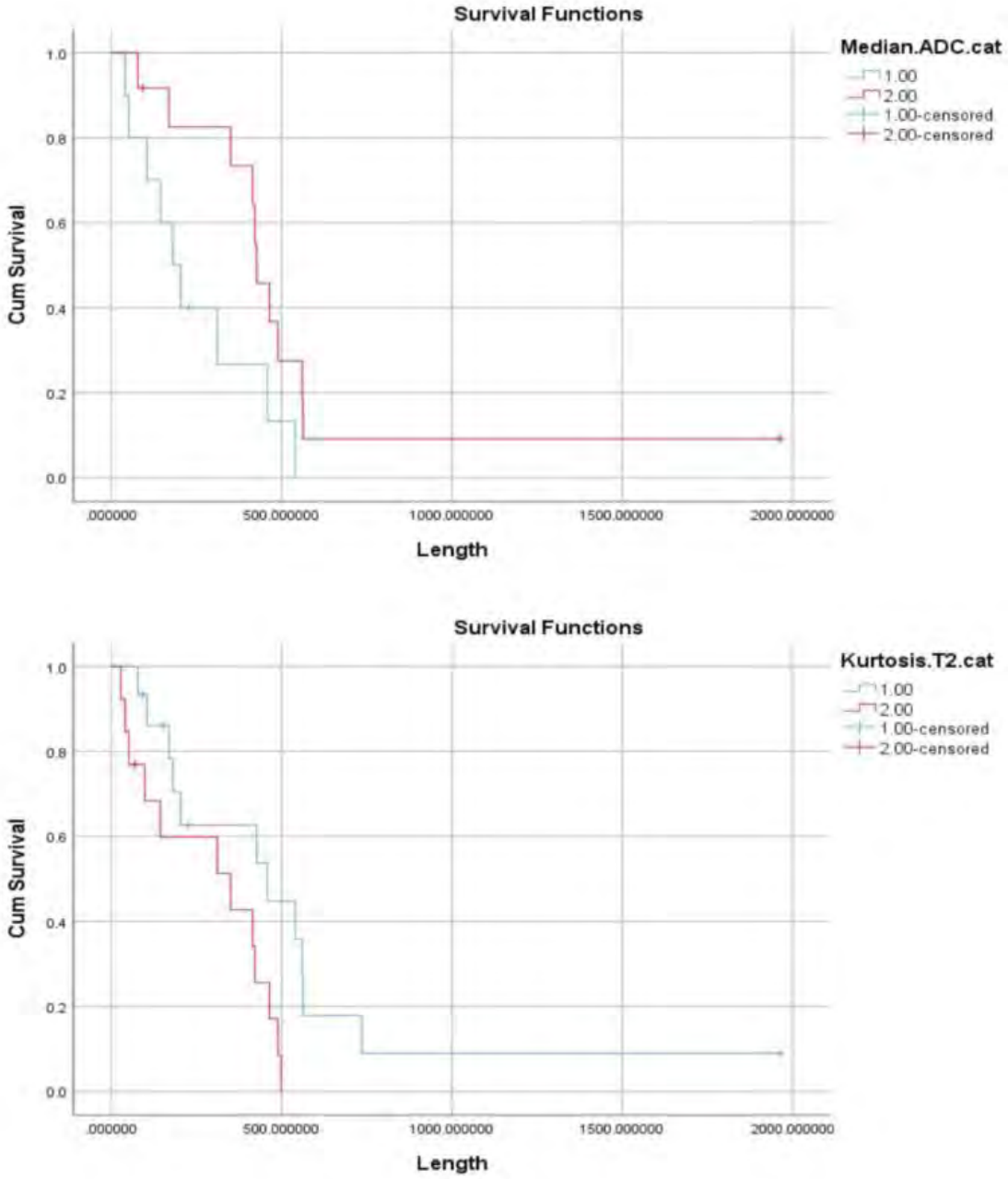

(Filename: TCT_855_FIGURE.jpg)

343

Microstructural Changes of the Cerebral and Cerebellar White Matter in Langerhans cell Histiocytosis

S Kralik[1], N Desai[2], T Huisman[3], A Meoded[1], C Allen[1], O Eckstein[4], K McClain[5]
[1]Texas Children's Hospital, Houston, TX, [2]Texas Children's Hospital, Sugar Land, TX, [3]Texas Children's Hospital and Baylor College of Medicine, Houston, TX, [4]Teas Children's Hospital, Houston, TX, [5]Texas Children's Hospital and Baylor College of Medicine, Houston, TX

Purpose
The purpose of this research was to evaluate the microstructure of the brain in LCH patients with and without neurodegeneration.
Materials and Methods
A retrospective study from 2009-2019 was performed on patients with pathology proven LCH. Conventional MRI sequences were reviewed to confirm presence of CNS LCH neurodegenerative disease (LCH-ND). Diffusion tensor imaging (DTI) with a minimum of

16 diffusion sampling directions were acquired in all patients at 1.5T or 3T with b-value of 1,000 second/mm2, in-plane resolution of 2 mm, and slice thickness of 2 mm. Algorithms in the TORTOISE software package were used to correct DTI raw data for motion artifacts and distortion by eddy currents and to calculate the tensor and DTI metrics maps. Voxelwise statistical analysis of the fractional anisotropy, mean diffusivity, radial diffusivity, and axial diffusivity data DTI of LCH-controls and LCH-ND was carried out using TBSS (Tract-Based Spatial Statistics), part of FSL The Randomize tool in FSL (5000 permutations), which conducts permutation-based inference on t-statistic maps, was used to identify clusters of voxels that differed between LCH controls and the LCH-ND group, using the Threshold-Free Cluster Enhancement with the threshold for significance of $P < 0.05$ with corrections for multiple comparisons across space (Family wise Error Rate, FWE). Each subject's raw DTI data were registered to standard space (MNI 152 2 × 2 × 2 mm) using FLIRT (FMRIB's Linear Image Registration Tool).

Results

A total of 75 patients with mean age 4.7 years were included. 19 patients (25%) had LCH-ND, most commonly identified in the dentate nuclei (84%) and brainstem (58%). There was no statistical difference between LCH-controls and LCH-ND for age at diagnosis, age at time of DTI, or presence of CNS risk disease. Compared to LCH-control patients, LCH-ND patients decreased FA throughout the cerebellar white matter, central and posterior pons, thalami, corpus callosum, left external capsule, occipital periventricular white matter (left>right), and multifocal subcortical white matter including the anteromedial left temporal lobe, bilateral sensorimotor cortex, bilateral inferior parietal lobes, bilateral posterior cingulate gyri, and right middle and inferior frontal gyri.

Conclusions

LCH-ND patients demonstrate widespread alterations in the white matter microstructure compared to LCH-control patients. DTI may represent an imaging biomarker for assessment of the global brain injury caused by LCH-ND.

698

Neuroimaging in Patients with Juvenile Xanthogranulomas of the Central Nervous System

B Serrallach[1], S Kralik[1], H Tran[1], T Huisman[1], C Allen[1], K McClain[1], N Gulati[1], C Dillard[1], N Desai[1]

[1]Texas Children's Hospital and Baylor College of Medicine, Houston, TX

Purpose

Juvenile xanthogranuloma (JXG) is a rare disease belonging to the group of non-Langerhans cell histiocytoses.1,2 Typically, JXG is a benign disorder of infancy/early adulthood often presenting as a solitary red-brown or yellow skin papule/nodule.3 A small subset present with systemic JXG, which may be associated with significant morbidity and mortality.2 Extracutaneous involvement may include the central nervous system (CNS).4 Involvement of the CNS is only seen in up to 2.3% of cases.5 To date, there is only scarce literature dealing with neuroradiologic manifestations of JXG in the CNS.1,4 The goal of this study is to evaluate and categorize neuroimaging findings in a relatively large cohort of pediatric patients with CNS JXG.

Materials and Methods

Inclusion criteria for this retrospective review were: (1) children/adolescents with pathology-proven CNS JXG, and (2) brain and/or spine MRI data using standard pulse sequences. MRI studies were reviewed and categorized by a board-certified neuroradiologist.

Results

14 patients (8 females, 6 males, mean age 84 months) fulfilled the inclusion criteria. Five were categorized as unifocal CNS JXG, eight with multifocal CNS JXG and one with multifocal CNS JXG with intracranial and spinal leptomeningeal disease. On T1W images (12 available), XGs were isointense compared to cortical gray matter in seven patients (7/12), hyperintense in four subjects (4/12) and hypo- to isointense in one patient (1/12). On T2W images (13 available), XGs were isointense in five patients (5/13), hyperintense in four subjects (4/13), iso- to hyperintense in three patients (3/13) and hypo- to isointense in one child (1/13), respectively. In 13 patients with available T2W images, perlesional edema was evident in 11 cases (11/13). Necrosis was seen in six patients (6/14). XGs of 13 patients (13/14) showed homogeneous contrast enhancement of solid components on T1W+C images. Seven patients with available DWI showed restricted diffusion (7/11).

Conclusions

In this cohort of patients with pathology-proven JXG, supra- and infratentorial CNS involvement is categorized into three primary neuroradiologic patterns: unifocal, multifocal and multifocal leptomeningeal. In the majority of cases, XGs were typified by small to large masses with isointense signal on T1W, iso- or hyperintense signal on T2W images, had restricted diffusion and perilesional edema. In almost all cases, XGs showed a homogeneous contrast enhancement of solid components.

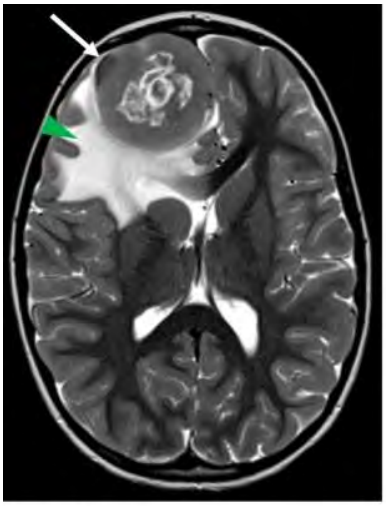

Figure 1

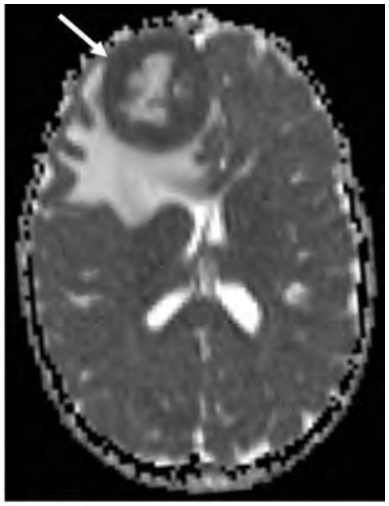

Figure 2

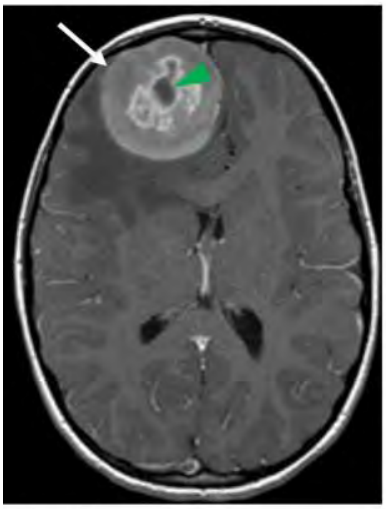

Figure 3

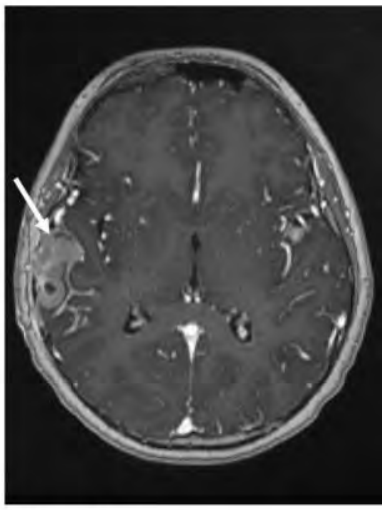

Figure 4

(Filename: TCT_698_cns-jxg_figure1_4_300dpi.jpg)

1059

Pharmacokinetics, safety and efficacy of a new gadolinium-based contrast agent, gadopiclenol, in pediatric patients (2 to 17 years) undergoing MRI

I Makedonska[1], J HAO[2]

[1]Municipal non-profit enterprise city children's clinical hospital #5 of Dnipro City Council, Dnipro, Dnipropetrovska oblast, [2]Guerbet, Paris, France

Purpose

To evaluate the pharmacokinetic (PK) profile, safety and efficacy of gadopiclenol, a new high-relaxivity gadolinium-based contrast agent 1, in children aged 2 to 17 years.

Materials and Methods

Children scheduled to undergo contrast-enhanced MRI of the Central Nervous System (CNS cohort) or other organs (Body cohort) were included into 3 age groups (12 17, 7 11 and 2 6 years) and four blood samples were collected after gadopiclenol administration (0.05 mmol/kg). A population PK modeling was used with the CNS cohort and adult subjects from a previous study. Adverse events (AEs) were recorded, and efficacy was assessed for all children.

Results

Eighty children were included (male: 51.3%): 60 in the CNS cohort and 20 in the Body cohort. The two-compartment model with linear elimination from the central compartment developed in adults was also suitable for children. PK parameters were very similar between adults and children. Terminal half-life was 1.82 h for adults and 1.29 to 1.77 h for age classes 12-17 to 2 6 years. Median clearance ranged from 0.08 L/h/kg in adults and 12-17 years to 0.12 L/h/kg in 2-6 years. Median central and peripheral volume of distribution were 0.11-0.12 L/kg and 0.06 L/kg, respectively, for both adults and children. Simulations of plasma concentrations showed minor differences and median area under the curve was 590 mg.h/L for adults and 403 to 582 mg.h/L for children. Two

patients (2.5%) experienced AEs considered related to gadopiclenol (none serious): a mild QT interval prolongation and a moderate maculopapular rash. As for diagnostic efficacy in this population, there was no difference among the pediatric age groups.
Conclusions
Gadopiclenol PK in children aged 2 to17 years seems similar to that observed in adults. Thus, there is no indication for dose adaptation based on age, and comparable plasma gadopiclenol concentrations are predicted to be achieved with body weight-based dosing. Gadopiclenol had a good safety profile in these patients and positive efficacy results were obtained.

1300

Quantitative Volumetric and Regional Analysis of Neonatal Hypoxic Ischemic Injury in a Large Prospective Cohort from the HEAL Trial

E Calabrese[1], S Gillon[1], J Wisnowski[2], A Mathur[3], R McKinstry[4], S Juul[5], Y Wu[1], Y LI[6]
[1]University of California San Francisco, San Francisco, CA, [2]University of Southern California, Los Angeles, CA, [3]Saint Louis University, St. Louis, MO, [4]Washington University in St. Louis, St. Louis, MO, [5]University of Washington, Seattle, WA, [6]UCSF, San Francisco, CA

Purpose
Hypoxic ischemic encephalopathy (HIE) affects approximately 1.5 out of every 1000 live births and is an important cause of cerebral palsy, epilepsy, and cognitive impairment in children. Neonatal diffusion weighted MRI (DWI) performed before day 10 of age can identify the presence of acute injury and stratify children at highest risk for major disability; however, there is a need for robust, quantitative tools capable of predicting outcomes for the individual patient. We propose an automated DWI processing pipeline that allows quantitative assessment of ischemic injury volume and location. We evaluate this new method on infants enrolled in the High-dose Erythropoietin for Asphyxia and Encephalopathy (HEAL) trial.
Materials and Methods
500 infants were enrolled in HEAL (NCT02811263) based on the presence of moderate to severe encephalopathy by Sarnat examination. All diffusion MRI data was acquired as 30-direction DTI in the axial plane at b = 1000 s/mm2. DTI data were processed using an automated pipeline implemented in Python 3.8. Processing steps included eddy current correction, DTI processing yielding several parametric maps including the apparent diffusion coefficient (ADC), and diffeomorphic registration of derived data to the University of North Carolina (UNC) neonatal brain atlas. Average whole-brain ADC values and average and percentage volume of acute whole brain injury (defined as voxels with ADC < 800 x 10-6 mm2/s, based on previously published studies) were calculated. Regional average ADC values and volume of acute injury was also evaluated for the deep gray nuclei, white matter, and cortex.
Results
We present preliminary data on 256 infants who were imaged at a median age 5.0 (IQR 4.5-5.8) days. The median volume of acute injury with ADC < 800 x 10-6 mm2/s in the whole brain was 522 uL (IQR 25-5545, range 0-242965). The median percentage of the brain with acute injury was 0.2% (IQR 0.009%-2%, range 0%-90%). The median value for mean ADC of the whole brain was 1219 x10-6 mm2/s (IQR 1180 x 10-6 mm2/s -1253 x 10-6 mm2/s). Analysis of the deep gray nuclei, white matter, and cortical injury is shown in the Table.
Conclusions
Automated quantitative ADC analysis of DTI data in neonates with HIE allows for objective quantification of injury in individual patients and determination of areas of highest injury across a large cohort. Future work including the full cohort of 500 infants will determine the correlation between quantitative measures of injury and neurodevelopmental outcomes.

Table

	Median	IQR	Range
Whole brain acute injury (uL)	522	25-5545	0-242965
Whole brain percentage acute injury (%)	0.2	0.009-2	0-90
Whole brain mean ADC (x 10^{-6} mm^2/s)	1219	1180-1253	206-1344
Deep gray acute injury (uL)	0	0-13	0-17100
Deep gray percentage acute injury (%)	0	0-0.07	0-97
Deep gray mean ADC	1116	617-1258	513-1393
White matter acute injury (uL)	106	2-1679	0-128817
White matter percentage acute injury (%)	0.08	0-1.3	0-99
White matter mean ADC	1235	1199-1269	230-1361
Cortex acute injury (uL)	348	16-3300	0-138890
Cortex percentage acute injury (%)	0.2	0.01-2.3	0-0.98
Cortex mean ADC	1216	1177-1250	189-1347

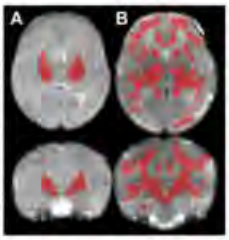

Figure 1. Quantitative maps of tissue with ADC < 800 x 10^{-6} mm^2/s in two different patients allowing for automated calculation of volume of acute brain injury (depicted in red) and illustrating different patterns of injury in the setting of HIE: Patient (A) demonstrates a basal ganglia/thalamic pattern and patient (B) demonstrates a combined basal ganglia/thalamic and watershed pattern.

Figure 2. Volume rendered color map encoding frequency of tissue injury throughout the brain with hot colors indicating regions that are commonly injured and cool colors indicating regions that are less commonly injured. Scale represents the number of cases in the cohort.

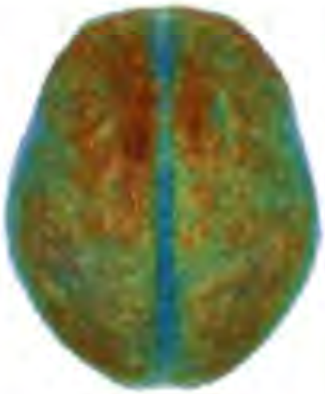

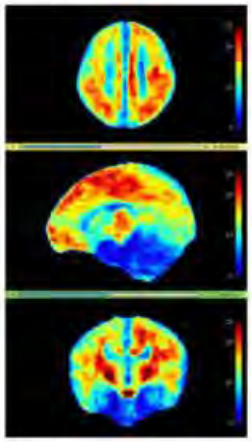

(Filename: TCT_1300_fig.jpg)

626

Role of MRI in differentiating pediatric low-grade cerebral tumors according to BRAF and NF1 status

S Shrot[1], J Belenky[1], A Kerpel[1], M Yalon[1], M Lurye[1], C Hoffmann[1]
[1]*Sheba Medical Center, Ramat-Gan, Israel*

Purpose
BRAF and NF1 status are distinctive features in pediatric low-grade brain tumors with prognostic and therapeutic implications. This retrospective study aimed to analyze the imaging features of BRAF V600E-mutant, BRAF-KIAA fusion, and wild-type BRAF versus NF1-associated pediatric low-grade brain tumors.
Materials and Methods
We retrospectively evaluated 40 pediatric patients with histologically proven pilocytic astrocytoma (PA, n=32), ganglioglioma (GG, n=4), pleomorphic xanthoastrocytoma (PXA, n=3), and diffuse astrocytoma grade 2 (n=1). Ten NF1 patients underwent conventional MRI with a diagnosis of a low-grade tumor without a biopsy. BRAF molecular analysis was performed for non-NF1 patients. Eleven patients presented BRAF V600E-mutant, twenty patients had BRAF-KIAA fusion, and nine BRAF wild-type tumors. Imaging studies were reviewed for dominant site, margin definition, hemorrhage, calcifications, cystic components, and contrast enhancement. Histogram analysis of tumoral diffusivity was performed.
Results
There were significant differences between evaluated low-grade tumors in their margins and cystic component ($p=0.04$ and $p<0.001$). Well-defined margins were characteristic for BRAF-KIAA or wild-type BRAF rather than BRAF V600E-mutant or NF1 tumors. None of the NF1 tumors showed a cystic component. Diffusion histogram metrics (mean, median, 10 and 90 percentiles), but not kurtosis or skewness, were different between tumors ($p<0.005$). Diffusivity was lowest in BRAF V600E-mutant and highest in BRAF-KIAA fusion tumors (10th percentile reached AUC of 0.9 on ROC analysis).
Conclusions
Imaging features of pediatric low-grade brain tumors, including quantitative diffusion metrics, may assist in predicting BRAF and NF1 status, suggesting radio-genomic correlation and might enable rapid molecular characterization.

569

Validation of Radiogenomics of Pediatric Pontine Diffuse Midline Glioma Using Multiparametric MRI and Molecular Genetics

V Rameh[1], S Vajapeyam[1], A Ziaei[1], P Kao[1], W London[1], J Lucas[2], C Tinkle[3], Z PATAY[2], K Wright[4], T Poussaint[1]

[1]Boston Children's Hospital, Boston, MA, [2]St. Jude Children's Research Hospital, Memphis, TN, [3]St. Jude Children's Research Hospital, Memphis, TN, [4]Dana Farber Cancer Institute, Boston, MA

Purpose

The new fifth edition of the World Health Organization Classification of Tumors of the Central Nervous System (WHO CNS5) emphasizes the role of molecular profiling as the key feature in the "integrated diagnosis" of CNS tumors. We aimed to validate previously identified prognostic MR features of pontine diffuse midline glioma to identify mutational histone H3 and wild type profiles.1

Materials and Methods

Baseline MRIs from subjects with pontine diffuse midline glioma were analyzed retrospectively prior to initiation of treatment. MR imaging studies included standard pre- and post-contrast sequences and diffusion imaging; imaging analysis included median, mean, mode, skewness, and kurtosis of apparent diffusion coefficient (ADC) of the tumor volume based on FLAIR, as well as enhancement at baseline. Histone H3 mutations were identified through immunohistochemistry and/or next-generation sequencing. Overall survival (OS) was presented at 1-year ± standard error. The log rank test was used to identify imaging factors prognostic of survival. Wilcoxon rank-sum and Fisher's exact tests were used to compare imaging measures between groups.

Results

Eighty-three patients met eligibility. Median age was 6 years (range: 0.7-17), 52% were male, and 28% were non-white. Fifty patients (60%) had tumors harboring a histone H3 mutation in HIST3F3A, 11 (13%) in HIST1H3B/C, 7 (8%) with H3 mutant NOS, and 15 (18%) H3 wild type. The 1-year OS was 37±5.5%, with median follow-up time of 10.3 months (range: 2.3-76.2) in surviving patients. OS was statistically significantly higher in HIST1H3B/C compared to H3F3A tumors (p=0.003), and in wild type profiles compared to any histone mutation (p=0.001). Poorer OS was observed in the presence of ADC enhancement (p=0.02) for lower mean ADC-enhancement (p=0.03). Mean ADC FLAIR (p=0.98), median ADC FLAIR (p=0.9), mode ADC FLAIR (p=0.9), median ADC-enhancement (p=0.06), and mode ADC-enhancement (p=0.07) were not associated with OS. HIST1H3B/C altered tumors showed higher mean, median, and mode ADC FLAIR (all p<0.0003), and higher mean (p=0.004), median (p=0.003), and mode (p=0.002) ADC-enhancement, as well as lower ADC FLAIR skewness (p<0.003) and kurtosis (p<0.002) relative to H3F3A-altered tumors.

Conclusions

MR imaging features including enhancement and ADC histogram parameters are differentially correlated with H3K27-altered and H3-wild type pediatric pontine diffuse midline glioma.

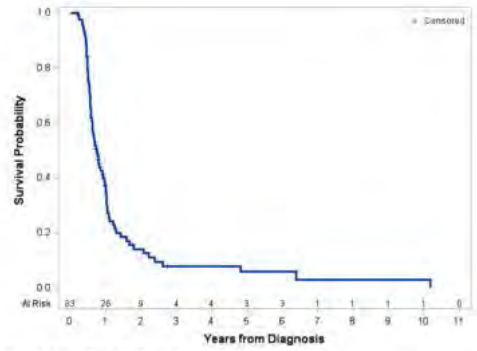

Figure 1. Kaplan-Meier plot of overall survival (n=83)

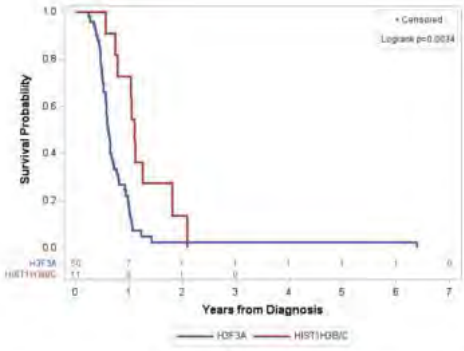

Figure 2. Kaplan-Meier curves of OS for histone H3 status subgroups: H3F3A (n=50) versus HIST1H3B/C (n=11)

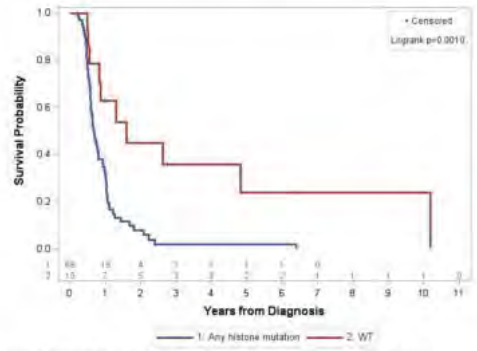

Figure 3. Kaplan-Meier curves of OS for any histone mutation (n=68) versus wild type (n=15)

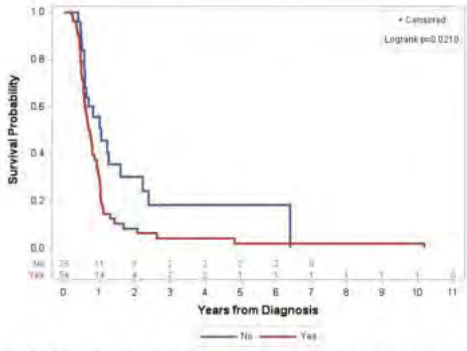

Figure 4. Kaplan-Meier curves of OS for ADC enhancement (n=54) versus no ADC enhancement (n=25)

(Filename: TCT_569_ASNR2022figures.jpg)

1230

Assessment of Extracranial Carotid Artery Stenosis in Acute Ischemic Stroke Using Relaxation-Enhanced Angiography without Contrast and Triggering (REACT)

L Pennig[1], C Hoyer[2], S Lennartz[1], N Abdullayev[1], L Goertz[1], K Laukamp[3], C Kabbasch[1], J Borggrefe[4], K Weiss[5]
[1]University Hospital Cologne, Cologne, NRW, [2]University Hospital Cologne, 50937, NRW, [3]UKK, Cologne, NRW, [4]Johannes Wesling University Hospital, Minden, GA, [5]Philips GmbH, Cologne, NRW

Purpose

Atherosclerotic disease of the carotid arteries, e.g., internal carotid artery (ICA) stenosis or occlusion resulting from atherosclerotic plaques, represents a major cause of acute ischemic stroke (AIS) [1]. The purpose of this study was to compare the detection of proximal ICA stenosis and plaques as well as the image quality of extracranial carotid arteries between a novel Relaxation-Enhanced Angiography without Contrast and Triggering (REACT) sequence [2] and contrast-enhanced magnetic resonance angiography (CE-MRA) in AIS.

Materials and Methods

This was a retrospective, single-center study of 105 consecutive AIS patients (65.3±18.7 years, 42 females) who received a stroke protocol at 3T in clinical routine that included Compressed SENSE (CS) accelerated (factor 4) flow-independent 3D isotropic REACT (scan time: 02:46 min) and CS accelerated (factor 6) 3D CE-MRA. Three radiologists assessed scans for the presence of proximal ICA stenosis and plaques (including hyper-/hypointense signal) with concomitant diagnostic confidence (DC) using 3-point scales (3=excellent). Vessel quality, artifacts, and image noise of extracranial carotid arteries were rated on 5-point scales (5=excellent/none).

Results

REACT achieved a sensitivity of 89.8% and specificity of 95.2% for any and of 93.5%/95.8% for clinically relevant (≥50%) ICA stenosis while yielding a to CE-MRA comparable DC (mean 2.76±0.45 vs. 2.72±0.49, P=.0305). REACT showed an almost perfect intersequence agreement with CE-MRA regarding the assessment of the disease grade (Cohen's Kappa of 0.90; Figure 1). Using REACT, readers detected more plaques overall (n=57.3 vs. 47.7, P=.0001) and plaques of hyperintense signal (n=12.3 vs. 5.7, P=.024) with higher DC (2.77±0.47 vs. 2.57±0.66; P <.0001) compared to CE-MRA. Vessel quality of all segments combined (4.61±0.66 vs. 4.58±0.68, P=.0299) and artifacts (4.51±0.70 vs. 4.44±0.73, P>.05) were comparable between the sequences with REACT yielding a lower image noise (4.43±0.67 vs. 4.25±0.71, P<.0001).

Conclusions

In AIS, REACT provides a high sensitivity and specificity for detection of ICA stenosis and a potentially improved depiction of plaques while yielding an equal vessel quality compared to CE-MRA.

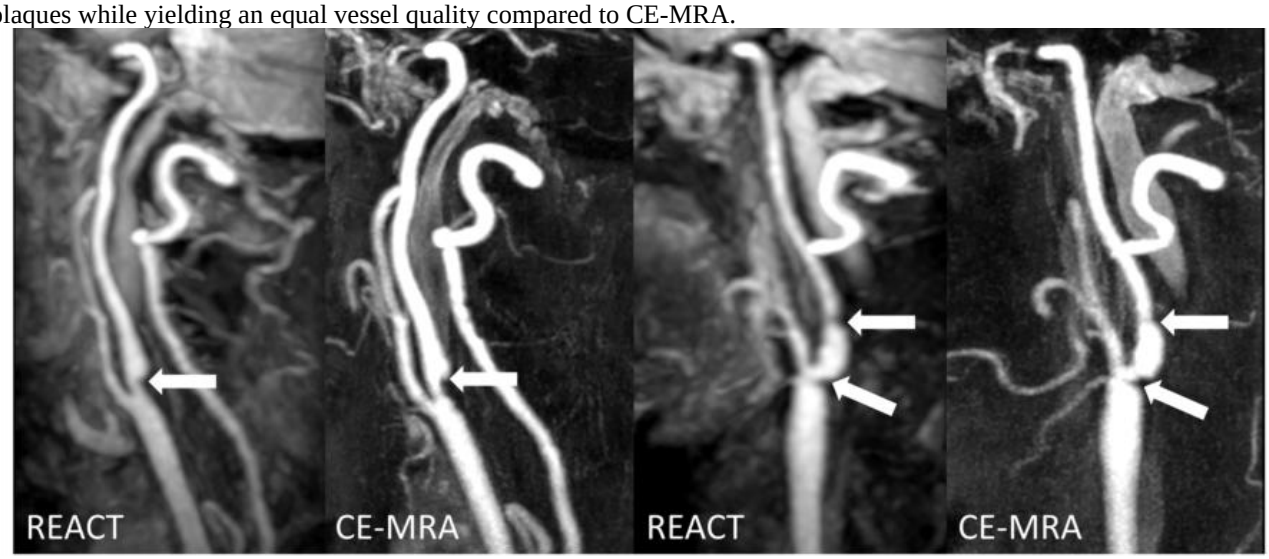

Figure 1: MIPs with angulation to the left carotid bifurcation (slice thickness: 20 mm) in two different patients with AIS showing ICA stenoses (wide arrows) with good agreement between REACT and CE-MRA.

(Filename: TCT_1230_REACTSIII20.jpg)

865

Changes in T1 and FLAIR Image Intensities Inform Tau Pathology in Patients with Autosomal Dominant Alzheimer Disease

F Rahmani[1], M Brier[2], S Keefe[1], N McKay[1], C Chen[3], T Benzinger[1]

[1]Washington University in St.louis, Saint Louis, MO, [2]Washington University School of Medicine in Saint Louis, Saint Louis, MO, [3]Washington University in St. Louis, St. Louis, MO

Purpose

Autosomal Dominant Alzheimer Disease (ADAD) has a predictable age of symptom onset that provides an opportunity to investigate the clinical applicability of novel imaging biomarkers. We have developed a new technique to measure image intensity information similar to quantitative relaxometry using clinical T1 and FLAIR images. If successful, this approach could provide an easy-to-use assessment of AD pathophysiology.

Materials and Methods

We included 1200 MR sessions from 523 participants (age: 37.4±10.2, 318 mutation carriers, 227 men) enrolled in the Dominantly Inherited Alzheimer Network (DIAN) cohort to examine the applicability of a new method to normalize image intensities and quantify grey matter (GM) abnormalities. Bivariate image intensity histograms representing T1-weighted and FLAIR voxel intensities were normalized to reference intensity histogram of age- and sex-matched controls. Normalized signal intensity mean (μ) and standard deviation (σ) were examined over 7 ADAD-specific FreeSurfer-defined cortical regions on T1 and FLAIR images separately (1). The estimated years from symptom onset (EYO) was calculated by subtracting a participant's age from their mutation/parental age of symptom onset.

Results

Cortical regions with significant amounts of atrophy demonstrated a striking increase in signal variability in both images (T1σ and FLAIRσ), along with an increase in average cortical grey matter signal on T1 (T1μ) and decrease in average signal on FLAIR images (FLAIRμ) beginning at symptom onset in mutation carriers (ANOVA P<0.01) (Fig1). EYO was associated with a significant increase in T1σ and decrease in FLAIR μ in the left cingulate isthmus and precuneus, as well as right inferior and superior parietal, lateral occipital and precuneal cortices in symptomatic mutation carriers. All associations survived after controlling for the effect of atrophy measured through cortical GM volume. Given the late-onset of image intensity changes we investigated a potential association with regional tau burden. In a subgroup of 58 participants with tau PET imaging, regional cortical tau burden was significantly associated with increased signal variability (σ) in T1 and FLAIR images, an effect that was more prominent in symptomatic mutation carriers (P<0.01 in all models).

Conclusions

Changes in the variability and average cortical signal intensity in standard MR clinical sequences are informative of late stage Alzheimer disease pathology and may represent a novel MRI signature of cortical tau deposition.

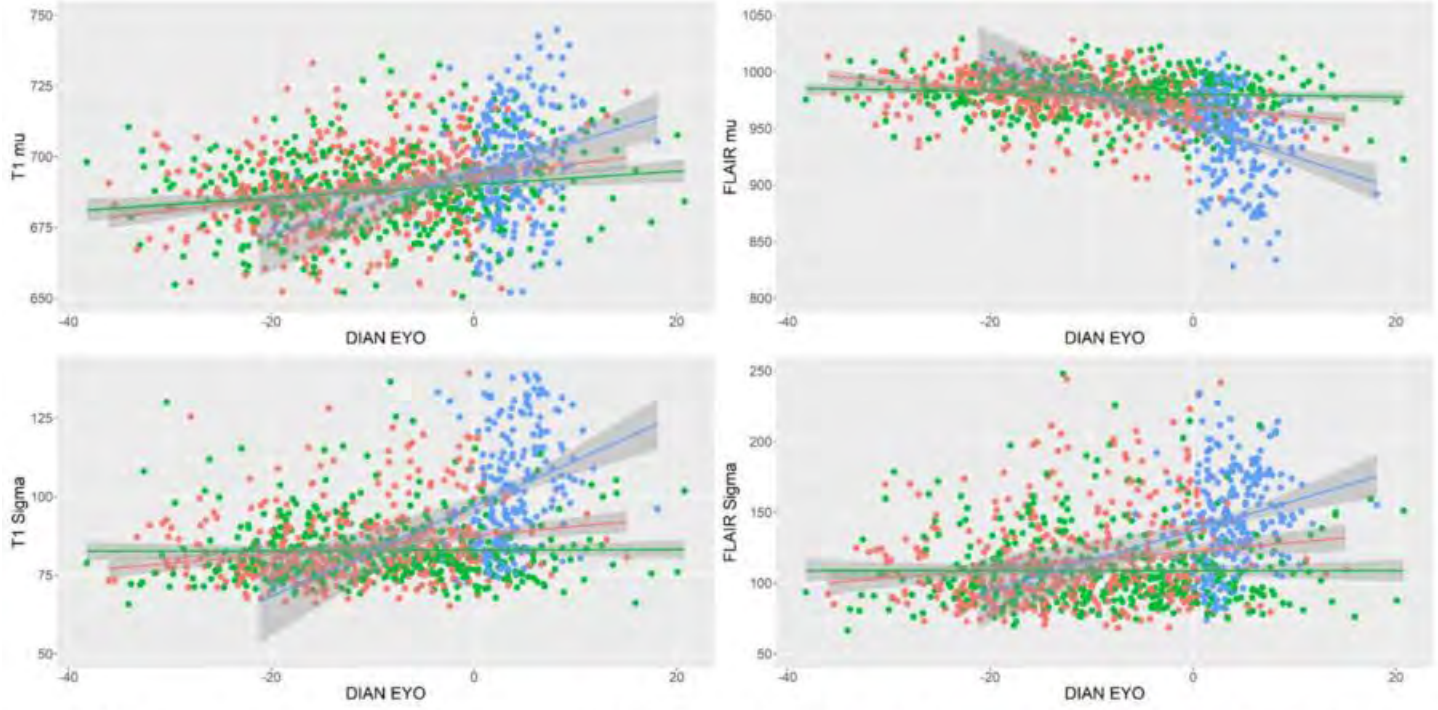

Fig 1. Changes in image intensity metrics across the EYO span in the early-onset AD cortical signature regions (right inferior parietal cortex). Note the later onset of changes in intensity metrics in mutation carriers typically after the symptom onset i.e. divergence of the blue fit line after EYO=0.

(Filename: TCT_865_Fig1_mat.jpg)

1472

Comparison of Three Automated Computed Tomography Perfusion Software Packages

L Pisani[1], M Bouslama[2]

[1]St Vincent Hospital, Worcester, MA, [2]New York University, New York City, NY

Purpose

Computed tomography perfusion (CTP) has played an important role on patient selection for mechanical thrombectomy (MT) in acute ischemic stroke. We aimed to compare the perfusion parametric maps of three software packages – the commonly used RAPID (IschemaView) with two novel packages - Viz CTP (Viz.ai) and e-CTP (Brainomix).

Materials and Methods

We retrospectively reviewed a prospectively maintained MT database during September 2018 to November 2019. Patients with an anterior circulation large vessel occlusion (LVO) involving the internal carotid artery or proximal middle cerebral artery (MCA-M1 segment) with near-complete or complete reperfusion (eTICI2c–3) were included. Between-group testing was performed for the categorical and continuous variables; CTP parameters and FIV were correlated with Spearman's p correlation coefficient.

Results

In this preliminary analysis of 242 ischemic stroke patients, a strong correlation for CBF<30% between RAPID and Viz CTP [rs=0.844, p<.001] as well as RAPID and e-CTP [rs=0.833, p<.001] was found. Similarly, a strong correlation was seen for Tmax>6s between RAPID and Viz CTP [rs=0.892, p<0.001] and RAPID and e-CTP [rs=0.752, p<.001]. The accuracy for FIV prediction was moderate in all three packages [rs=0.637, p<.001; rs=0.601, p<.001; rs=0.605, p<.001, RAPID, Viz CTP and e-CTP respectively].

Conclusions

CTP parameters strongly correlate across RAPID, Viz CTP and e-CTP software packages. CTP has only moderate accuracy in predicting final infarct volume in fully reperfused patients and should not be used as a solo deciding tool to exclude patients from endovascular reperfusion in the early time window. Further statistical interpretation, including Bland-Altman analysis will be incorporated to this presentation.

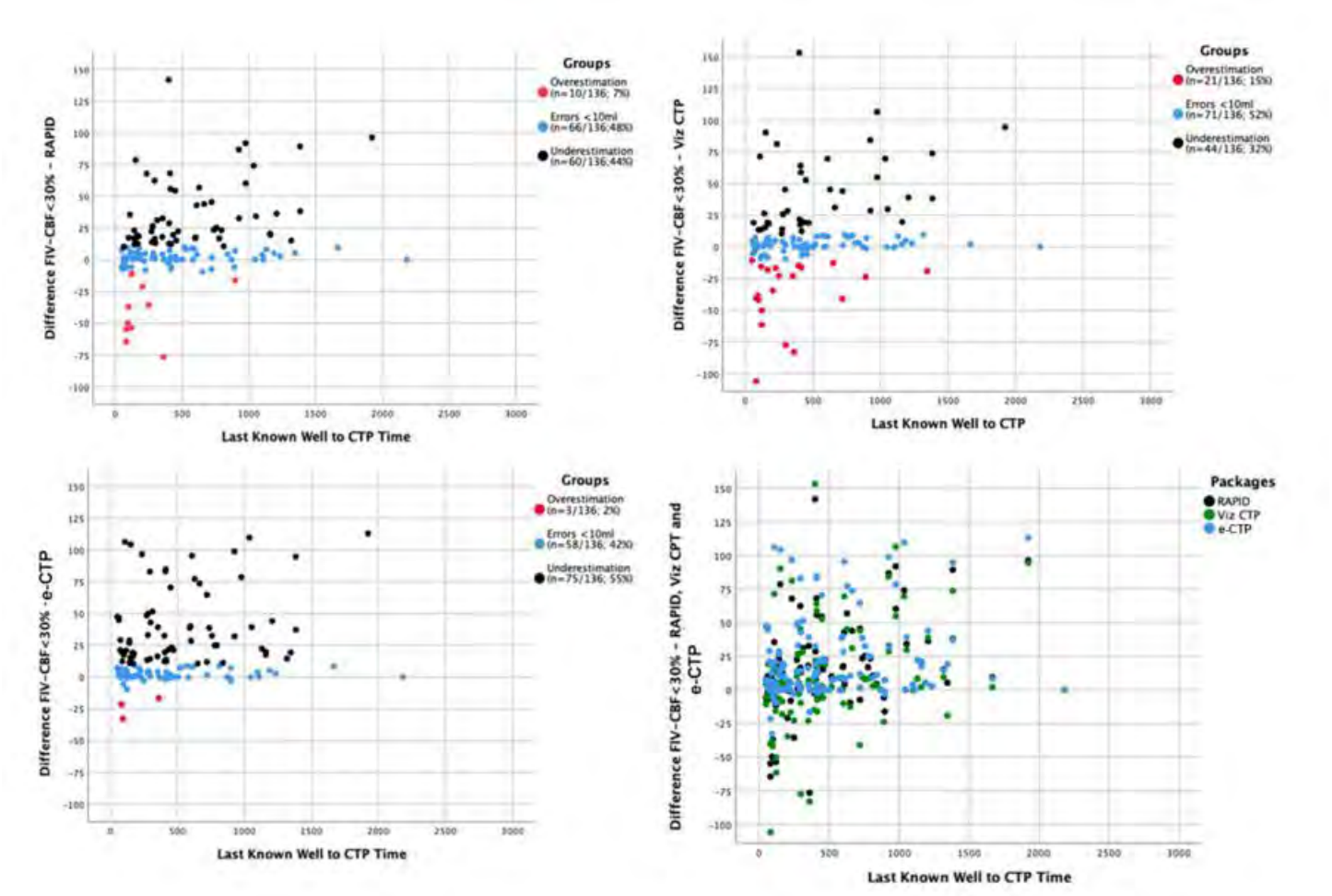

(Filename: TCT_1472_fig1.jpg)

161

Deep Learning Classification of Large Vessel Occlusion with Multiphase CTA Subtraction Maps

K Nelson[1], I Padilha[1], E Zarour[1], L Letourneau-Guillon[1], F Guilbert[1]
[1]Centre Hospitalier de l'Université de Montréal, Montreal, QC

Purpose
Stroke is a leading cause of morbidity worldwide. Automatic detection of large vessel occlusion (LVO) could decrease delays in diagnosis and improve clinical outcomes. However, automated LVO detection remains available mainly through commercial software. This study aims to develop a 3D convolutional neural network based on multiphase CTA subtraction maps to detect treatable LVOs with an end-to-end processing pipeline based on widely available open-source tools.
Materials and Methods
Consecutive patients with multiphase CTA presenting for acute management of ischemic stroke from 2018 to 2020 were included (total patients = 1004). After co-registration, exams were post-processed to create gray-scale subtraction maps between the arterial and delayed phases. Exams were positive for acute LVO if the carotid terminus, M1, proximal M2, or the vertebrobasilar axis were occluded. Ground truth annotation was retrospective by a single neuroradiology fellow. An inter-observer reliability study was performed on a subgroup of 50 patients. A subset of 374 consecutive patients was used for initial model development. Image pre-processing included downsampling, skull stripping, and contrast stretching (window/level). Models were developed in Keras with Tensorflow and were based on shallow 3D versions of Densenet-121. The data was split into training, validation, and test sets following a standard 70:15:15 distribution with standard data augmentation during training. Two models were evaluated on the test set of 58 patients: a single input model using subtraction maps and a dual input model which also included the delayed phase MIPs.
Results
Inter-observer variability analysis revealed a kappa of 0.90 (95%CI 0.75-1.00) between two neuroradiology fellows. Prevalence of LVO was 0.31 overall, 0.28 in the training set, 0.36 in the validation set, and 0.36 in the test set. The best single input model achieved sensitivity of 0.86 (95%CI 0.64-0.97), specificity of 0.95 (95%CI 0.82-0.99), PPV of 0.90 (95%CI 0.68-0.99), NPV of 0.92 (95%CI 0.79-0.98), and an AUC of 0.88 (95%CI 0.76-0.98). The best dual input model achieved sensitivity of 0.95 (95%CI 0.76-1.00), specificity of 0.86 (95%CI 0.71-0.95), PPV of 0.80 (95%CI 0.59-0.93), NPV of 0.97 (95%CI 0.84-1.00) and an AUC of 0.94 (95%CI 0.88-0.99).
Conclusions
Both the single and dual input models accurately detected LVO within the test set. While there were small differences in diagnostic performance between the models, these differences were not statistically significant.

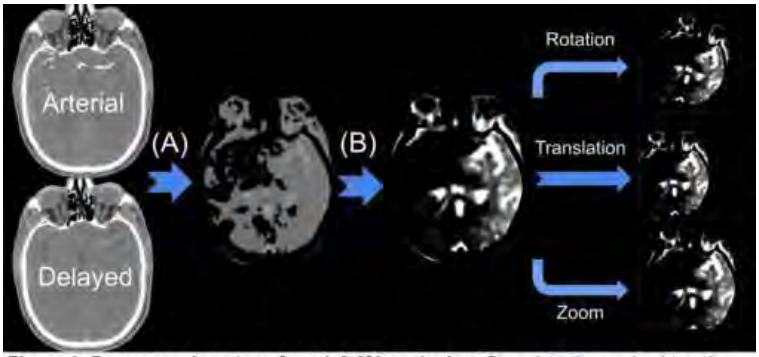

Figure 1: Preprocessing steps for a left M1 occlusion. Coregistration and subtraction followed by smoothing, thresholding, and skull stripping (A) to create gray scale subtraction maps (note the delayed signal in the left MCA territory) followed by contrast stretching (B). Standard data augmentation was used during training including random rotation, translation, flipping, and zooming of the images.

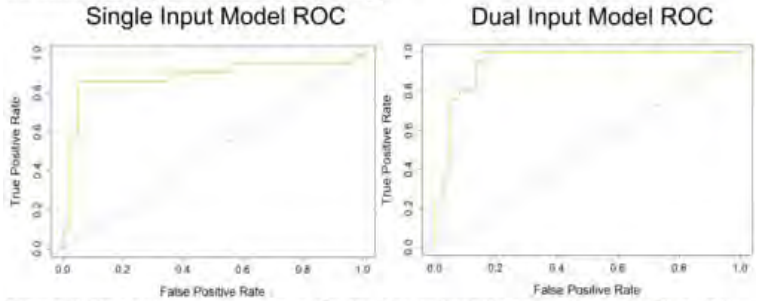

Figure 2: Receiver operator curves for the single (right) and dual input (left) models. The AUC for the single and dual input models were 0.86 and 0.94 respectively.

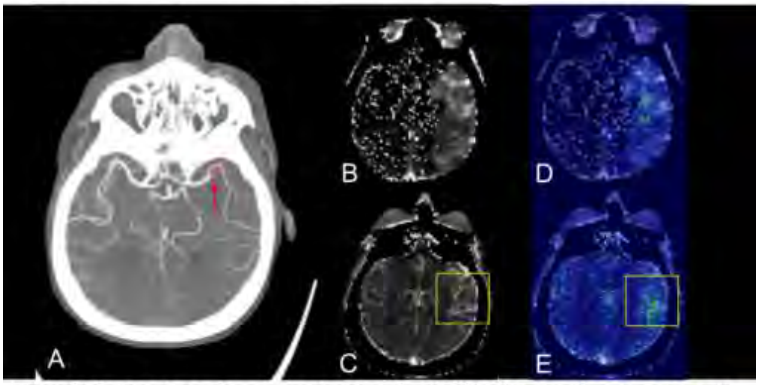

Figure 3: Saliency map for a correctly classified LVO by the dual input model. Axial MIP image (A) demonstrates a left M1 occlusion (red arrow). Select axial images of the gray scale subtraction map (B) and delayed phase MIP (C) inputs for the dual input model. Overlaid saliency maps (D and E) reflect the individual pixels which are most important for the correct classification (red > blue). Note the delayed enhancement in the left MCA territory which is critical for the models correct classification (yellow boxes).

(Filename: TCT_161_ASNRFigureFinal.jpg)

1405

Dual-Energy Computed Tomography in Stroke Imaging: Value of a new Image Acquisition Technique (TwinSpiral) for Ischemia Detection after Mechanical Thrombectomy

R Grkovski[1], L Acu[2], D Nakhostin[3], P Thurner[4], L Wacht[5], Z Kulcsar[6], H Alkadhi[6], S Winklhofer[6]
[1]University Medical Center Maribor, Maribor, Slovenia, [2]Kantonsspital Aarau, Aarau, Switzerland, [3]University Hospital of Zurich, Zuerich, Switzerland, [4]University Hospital Zurich, Zurich, Canton of Zurich, [5]Stadtspital Zürich Triemli, Zürich, Switzerland, [6]University Hospital Zurich, Zurich, Zurich

Purpose

Purpose of the study was to assess whether TwinSpiral dual energy CT (DECT), a new dual spiral DECT technology, which consecutively acquires datasets at two different energy levels for spectral separation, allows for an improved visualization of ischemic brain tissue after mechanical thrombectomy in acute stroke patients.

Materials and Methods

Twin-Spiral DECT head scans (tube voltages 80 and 150Sn kVp) of a total of 41 patients (18 women (44%), 23 men (56%), mean age 73±11.2 years, range 50-93 years) in the acute setting after endovascular thrombectomy due to acute M1 occlusion ischemic stroke were retrospectively evaluated. Standard (mixed) images and virtual non-contrast (VNC) images were reconstructed. Infarct visibility

and image noise were assessed qualitatively by two readers using a 4-point Likert scale. Quantitative Hounsfield units (HU) were used to assess density differences of ischemic brain tissue versus healthy tissue on the non-affected contralateral hemisphere.

Results

Infarct visibility was significantly better in VNC images compared to mixed images for both readers R1 (VNC: medium 1 (range 1-3); mixed: 2 (range 1-4), $p < 0.05$) and R2 (VNC: medium 1.5 (range 1-3); mixed: 2 (range 1-4), $p < 0.05$). Image noise was significantly higher in VNC images compared to mixed images for both readers R1 (VNC: medium 3 (range 2-3); mixed: 2 (range 2-3), $p < 0.05$) and R2 (VNC: medium 2 (range 1-3); mixed: 1 (range 1-3), $p < 0.05$). Mean HU were significantly different between the infarcted tissue and the reference healthy brain tissue on the contralateral hemisphere in VNC (infarct 23.6 ± 3.3, reference 31.2 ± 1.9 ¬¬) and mixed images (infarct 33.4 ± 4.7, reference 38.3 ± 3.4 ¬¬) ($p < 0.05$, each). The mean HU difference between VNC ischemia and VNC reference (mean 7.7 ± 3.4) ¬was significantly higher ($p < 0.05$) compared to the mean HU difference in mixed images in ischemia and reference tissue (mean 4.9 ± 3.9).

Conclusions

TwinSpiral as a new DECT technique allows for an improved objective and subjective visualization of ischemic brain tissue. Our study indicates that TwinSpiral DECT might be a valuable tool for imaging of ischemic stroke patients after endovascular treatment.

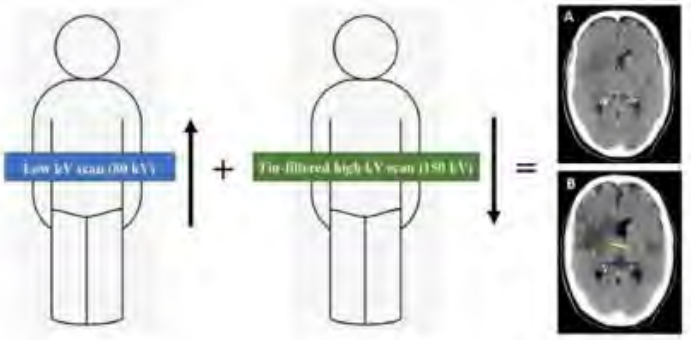

Fig 1 Schematic presentation of single-source TwinSpiral dual-energy CT. Two consecutive scans at different energies (low and a high kV scan) are performed directly one after the other. Conventional mixed CT images (A), as well as dedicated reconstructions, such as virtual non-contrast (VNC) images (B) are postprocessed. Yellow arrow depicts better contrast of infarcted area.

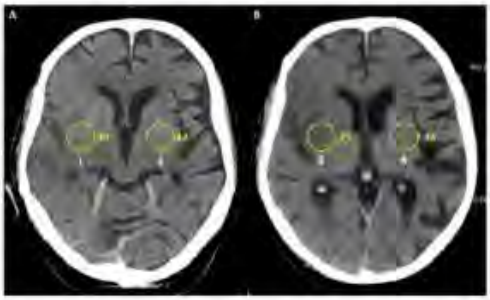

Fig 2 Right sylvian artery stroke. HU measurements on right (affected) and contralateral left (unaffected) side, with yellow circles representing HU measurements. There is a higher difference in VNC images (B; factor of 8) compared to standard mixed images (A; factor of 3).

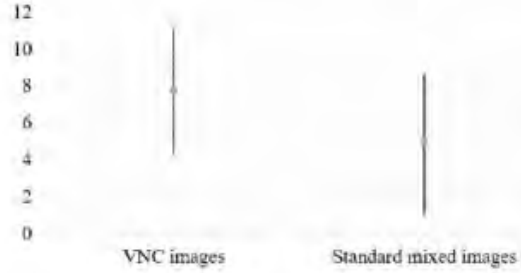

($p < 0.05$)

Fig 3 Mean HU difference between ischemia and contralateral healthy reference tissue.

(Filename: TCT_1405_FIGURES_sw-page0001.jpg)

634

Hypoperfusion lesion and target mismatch prediction from baseline diffusion imaging using a 3D convolutional neural network

Y Yu[1], S Christensen[2], F Scalzo[3], D Liebeskind[3], G Zaharchuk[1]

[1]Stanford University, Stanford, CA, [2]GrayNumber Analytics, Lomma, Sweden, [3]UCLA Stroke Center, Los Angeles, CA

Purpose

Perfusion imaging is important in target mismatch assessment but requires contrast agents and post-processing software, which can delay care. Clinical-diffusion mismatch was reported to miss candidates that meet target mismatch criteria and could benefit from thrombectomy. We explored whether a neural network can predict the critical hypoperfusion lesion and identify target mismatch patients from diffusion-weighted imaging (DWI) and clinical information alone.

Materials and Methods

Acute anterior circulation ischemic stroke cases with baseline MR perfusion and DWI were included from two multi-center trials and one single-center registry for model development, and tested in a separate randomized trial DEFUSE 3 for external validation. MR perfusion images were post-processed by RAPID software, which automatically segments hypoperfusion lesion (Tmax ≥ 6s) and the ischemic core lesion (apparent diffusion coefficient [ADC]≤ 620 ×10−6 mm2/s). A 3D U-Net was trained using baseline DWI, ADC, NIH stroke scale and side of stroke as input, with the union of critical hypoperfusion and ischemic core segmentation serving as the ground truth. 5-fold cross-validation was performed for model development cohort. Model performance was evaluated by Dice score coefficient (DSC) and volume difference. Sensitivity and specificity of target mismatch from model and clinical-DWI mismatch using the DAWN criteria were compared, using the DEFUSE 3 target mismatch as ground truth.

Results

Of 524 patients available from 3 studies, 413 patients were included in the analysis. 46 out of the 49 MRI cases in the DEFUSE 3 were included in the external validation cohort. In model development and external validation cohort, the model achieved median DSC of 0.61 (interquartile range [IQR] 0.45, 0.71) and 0.62 (IQR 0.53, 0.72); and volume difference of 3 ml (IQR -37, 41) and 7 ml (IQR -24, 32), respectively (Figure1). Compared to the clinical-DWI mismatch approach, the 3D U-Net model identifies target mismatch patients with a sensitivity of 89.5% vs 49.3%, a specificity of 77.5% vs 89.2% in the model development cohort, and a sensitivity of 95.6% vs 41.3 % in external validation cohort.

Conclusions

A 3D U-Net can predict hypoperfusion lesions from baseline DWI, ADC, and clinical information, with more sensitive identification of target mismatch patients compared to a clinical-DWI mismatch.

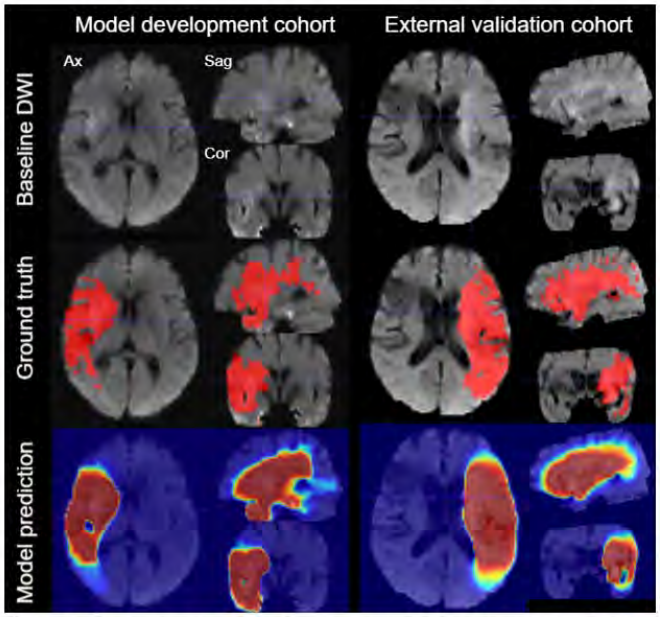

Figure 1. Two test case examples from model development and external validation cohort. (Left) 60 year old female presenting with NIHSS of 2 and right MCA M1 occlusion. RAPID segmented hypoperfusion lesion of 146 ml and core of 32 ml. The model predicted 201 ml for the hypoperfusion lesion as showed in the third row, with accurate spatial location and DSC of 0.71. (Right) 64 year old female presenting with NIHSS of 27 and left MCA M1 occlusion. RAPID segmented hypoperfusion lesion of 190 ml and core of 37 ml. The model predicted 213 ml for the hypoperfusion lesion, with accurate spatial location and DSC of 0.80. DSC: Dice score coefficient, Ax: Axial view, Sag: Sagittal view, Cor: Coronal view.

(Filename: TCT_634_Picture2.jpg)

392

Improving Treatment Selection in Ischemic Stroke with Extensive Baseline Infarction Using a Novel Rating Tool - Results from the I-LAST Study

G BROOCKS[1], T Faizy[2], S Elsayed[2], L Meyer[2], J Fiehler[2], A Kemmling[3]

[1]University Hamburg, Hamburg, NA, [2]University Hamburg, Hamburg, Hamburg, [3]University Marburg, Marburg, Hessen

Purpose

The effect of mechanical thrombectomy (MT) on functional outcome in acute ischemic stroke patients with low Alberta Stroke Program Early CT Score (ASPECTS) is still uncertain. We hypothesized that 1) quantitative lesion water uptake as imaging biomarker in admission-CT stratifies low ASPECTS patients and mediates the effect of thrombectomy on functional outcome, and 2) an edema-adjusted ASPECTS is a better predictor of outcome than ASPECTS alone and may indicate futile MT.

Materials and Methods

Improving Low ASPECTS Stroke Thrombectomy (I-LAST) is an academic, independent, prospective, multicenter, observational registry study (Clinical trial registration: NCT04862507). The aim of this study is to investigate the role of advanced imaging biomarkers in patients with large early infarct. For this analysis, ischemic stroke patients with large vessel occlusion and ASPECTS≤5 admitted between 03/2015-03/2020 were consecutively analyzed. Net water uptake (NWU) was assessed as quantitative imaging biomarker in admission-CT and was used to calculate an edema-corrected ASPECTS (ecASPECTS). Functional outcome was assessed using the modified Rankin Scale (mRS) score at day 90. The optimal cut-off value of ecASPECTS distinguishing outcome was calculated and further validated in a prospective validation cohort.

Results

254 patients admitted between 03/2015-03/2020 were included. The derivation cohort consisted of 179 patients from two stroke centers, of which 83 patients (46%) underwent MT. In receiver operating characteristic (ROC) curve analysis, ecASPECTS yielded the highest diagnostic accuracy to classify outcome (AUC: 0.92, 95%CI: 0.87-0.95, sensitivity/specificity: 83.3%/87.3%, cut-off: >5.5) and was more accurate than ASPECTS (AUC: 0.81), or NWU (AUC: 0.84) alone (DeLong'p<0.001). Multivariable logistic regression analysis confirmed that ecASPECTS is a significant and independent predictor of outcome besides recanalization status and age. In patients with ecASPECTS<5.5, successful recanalization was not associated with better clinical outcome. Applying this cut-off to the validation cohort from two further stroke centers (n=75), sensitivity and specificity to classify outcome were 81.8%/79.4%, respectively.

Conclusions

ecASPECTS was a superior predictor of outcome compared to ASPECTS, or NWU independent of treatment, and was an indicator of futile MT in low ASPECTS patients. ecASPECTS could be tested as tool to select low ASPECTS patients for MT.

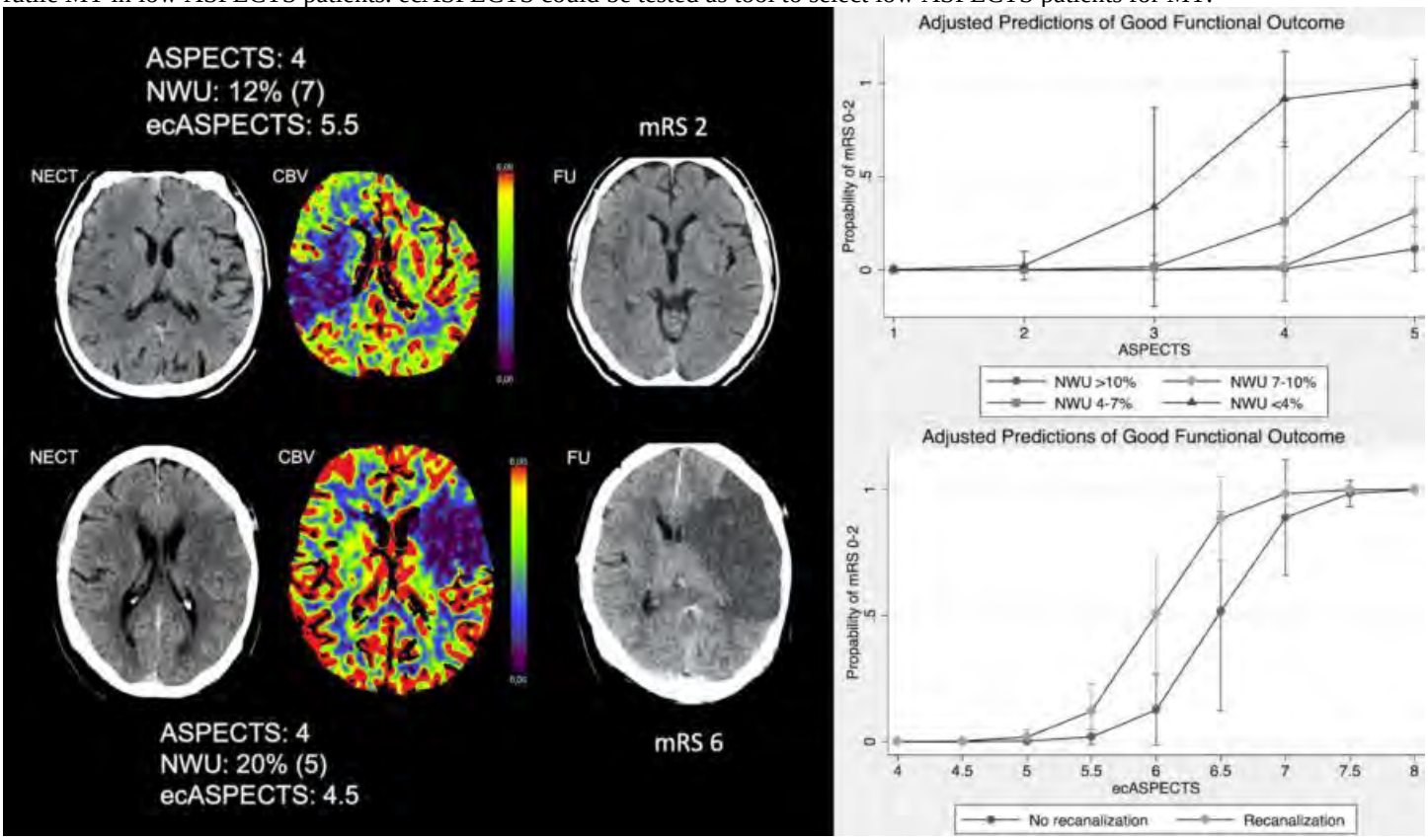

(Filename: TCT_392_ASNR_LA2_FIG.jpg)

258

Increased Relative Risk of Delayed Hemorrhage in Patients Taking Anticoagulant/Antiplatelet Medications with Concurrent Aspirin Therapy: Implications for Clinical Practice Based on Four Year Retrospective Analysis in a Large Health System

W CHANG[1], D Yin[1], C LI[1], P Annigeri[1], M Spearman[1], M Kulzer[2], T Tragon[1], A Sohn[1], B Weston[1], L Eisenmenger[3], M Goldberg[1]
[1]Allegheny Health Network, Pittsburgh, PA, [2]Allegheny Health Network, PITTSBURGH, PA, [3]University of Wisconsin - Madison, Middleton, WI

Purpose

Intracranial hemorrhage (ICH) is a major source of morbidity and mortality. The risk of delayed ICH (DH) in patients on anticoagulant (AC) and antiplatelet (AP) medications is not well established, with studies estimating between 1-10% risk of DH and 0-3% mortality. Determining the true risk of DH in patients taking AC/AP medications, especially with concurrent aspirin therapy, is critical given the high mortality and morbidity associated with ICH. We present our four year retrospective analysis of patients with head trauma taking AC/AP medications including patients taking concurrent aspirin.

Materials and Methods

1312 patients taking AC/AP medications who suffered head trauma who received repeat CT to evaluate for DH were included. Average follow-up time to repeat CT was 21 hours and 99% were within 3 days. Positive studies were reviewed by two board certified neuroradiologists. Patients were excluded if ICH was retrospectively identified on the initial examination. Cases were reclassified as negative if ICH on the follow-up examination was thought to be not present or artifactual. Cases were considered positive if the initial examination was negative and the follow-up examination demonstrated new ICH.

Results

Overall, there was 1.68% rate (22 patients) of DH and 0.3% overall mortality (4 patients). The rate of DH in patients taking AC/AP with aspirin (15/449 patients, 3.3%) was significantly higher (RR 4.1, p<0.002) than those taking AC or AP alone (7/865 patients, 0.8%). Incidence of DH in patients taking DOACs with aspirin was higher than patients taking DOACs alone (2.1% vs 0.2%, RR 10.8, p<0.03). The group of patients taking warfarin or AP agents had higher rate of DH (3.1% compared to 0.8%, RR 3.9) and higher mortality (0.9% compared to 0.0%) compared to the DOAC group (p<0.01).

Conclusions

The risk of DH was markedly increased in patients taking both aspirin and AC/AP medications, especially in patients taking DOACs. Repeat imaging should be obtained for patients with head trauma on both AC/AP agents and aspirin. The risk of DH was higher in patients taking warfarin/AP agents compared to patients taking DOACs, with or without aspirin therapy. Repeat examination should be strongly considered on patients taking warfarin or AP agents even without aspirin given relatively higher risk of DH. Given the relatively low risk of DH in patients taking DOACs without aspirin (1 /526, <0.2%), repeat imaging is unnecessary unless there are external signs of trauma or a dangerous mechanism of injury.

Medication	Total Patients	Negative	Positive	% Positive	Deaths	% Death	Aspirin	Positive w/ aspirin
Apixiban (Eliquis)	475	475	0	0	0	0	135	0
Warfarin (Coumadin)	354	343	11	3.11%	2	0.6%	99	6
Rivaroxaban (Xarelto)	211	206	5	2.37%	0	0	54	4
Clopidogrel (Plavix)	199	193	6	3.02%	2	1.0%	121	5
Other	73	73	0	0	0	0	40	0
Total	1312	1290	22	1.68%		0.3%	449	15

All Patients	DH	No DH
Aspirin	15 (3.3%)	434
No Aspirin	7 (0.8%)	858
p < 0.002, RR = 4.13		

DOACs	DH	No DH
Aspirin	4 (2.1%)	185
No Aspirin	1 (0.2%)	525
p < 0.03, RR = 10.8		

Warfarin + AP	DH	No DH
Aspirin	11 (5.0%)	209
No Aspirin	6 (1.8%)	327
p < 0.03, RR = 2.78		

Figure 1: a:(top left) Table with incidence of delayed hemorrhage for each anticoagulant and antiplatelet agent, with number of patients also taking aspirin. **b:(bottom left)** Incidence of delayed hemorrhage broken out by patients in each group. **c:(right)** Proposed recommendations for repeat imaging in patients taking anticoagulant/antiplatelet therapy.

(Filename: TCT_258_figureasnrdh.jpg)

405

Individual Small Vessel Disease Markers on MRI Have Distinct Sets of Risk Factors: Results of the APRISE Study

L Wang[1], B Williamson[1], H Sucharew[2], A Mahammedi[1], R Cornelius[1], M Gaskill-Shipley[1], T Tomsick[1], D Wang[3], V Khandwala[1], S Gangatirkar[1], T Maloney[1], J Carrozzella[1], K Alwell[1], M Haverbusch[1], P Horn[2], B Kissela[1], P Khatri[1], A Vagal[1]
[1]University of Cincinnati, Cincinnati, OH, [2]Cincinnati Children's Hospital Medical Center, Cincinnati, OH, [3]I-MED Radiology, Melbourne, Australia

Purpose

Imaging markers of chronic small vessel disease (SVD) include white matter hyperintensity (WMH), lacunes, perivascular spaces (PVS), and microbleeds. It is, however, rather intriguing that most patients do not have all of these imaging findings and some have a predominant SVD marker. Our objective was to identify clinical and demographics risk factors associated with individual SVD imaging markers.

Materials and Methods

All stroke and TIA patients were ascertained and characterized in a metropolitan population of 1.3 million served by 15 different inpatient hospitals for the calendar year of 2015, as part of the NIH-funded Greater Cincinnati/Northern Kentucky Stroke Study. We then collected and characterized all associated MR brain imaging through the ancillary NIH-funded Assessing Population-based Radiological brain health in Stroke Epidemiology (APRISE) study. MRIs were evaluated by trained, central neuroradiologists using STRIVE criteria for small vessel disease, including WMH, PVS, microbleeds and lacunes. Multivariable logistic regression models for each SVD imaging parameter were performed. Logistic regression models with LASSO selection were then used to identify important covariates.

Results

Of the 3788 adult hospital-ascertained events, including TIAs, ischemic stroke and ICH/SAH in the population during 2015, the current analysis represents partial cohort (~70%) of 1287 patients (1336 events) with ischemic stroke who underwent MRI (mean age 69, 25% black, 52% female) (Figure). Important covariates of individual SVD imaging findings, including odds ratios (OR), p-values and 95% confidence intervals (CI), are shown in the Figure. History of prior strokes are associated with all 4 SVD markers (OR 1.55-2.27). Age is associated with WMH, lacunes, and PVS. WMH is associated with prior stroke and black race, and inversely associated with high cholesterol. Lacunes are associated with prior stroke and hypertension. Microbleeds are associated with prior stroke. PVS are associated with prior stroke. Results of the full patient cohort and full multivariable models will be presented.

Conclusions

Within the spectrum of small vessel disease, each individual imaging parameter has distinct risk factors in our large-scale cohort, whereas history of prior stroke is associated with all SVD markers.

Figure 1: Association between individual risk factors and small vessel disease imaging markers

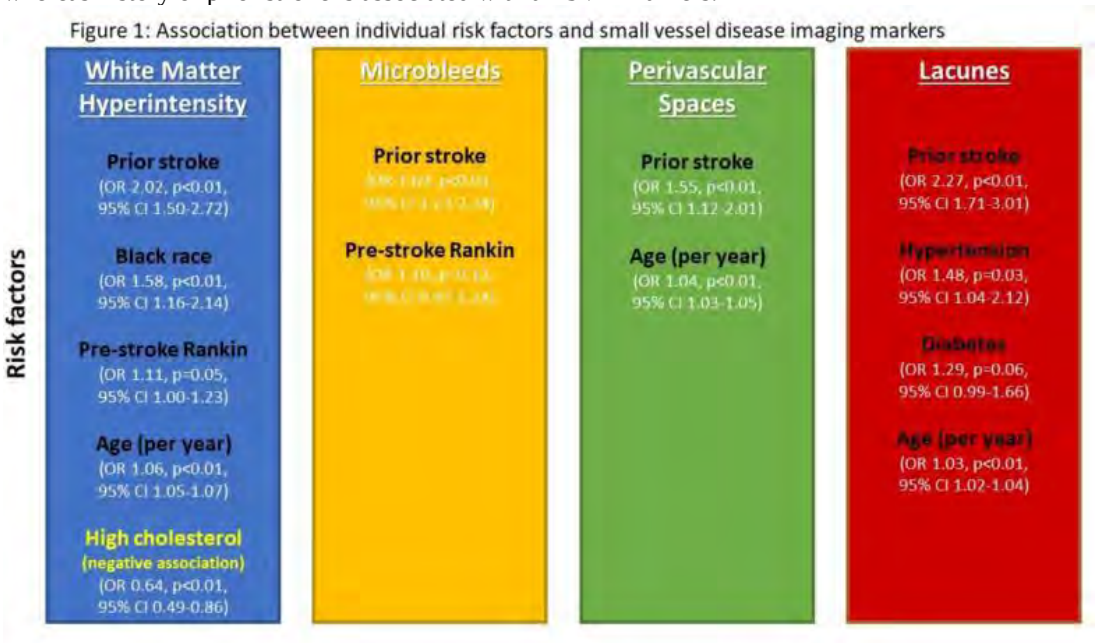

Table 1: Demographics, clinical, and imaging characteristics

	Cohort (N=1287) N (%), mean (SD) or median (IQR)
Age, mean (SD)	69 (14)
Black	317 (25%)
Female	675 (52%)
Risk factors – history of	
Hypertension	1067 (83%)
Diabetes	491 (38%)
High cholesterol	777 (60%)
Atrial fibrillation	233 (18%)
Heart failure	218 (17%)
Coronary artery disease	416 (32%)
Peripheral vascular disease	98 (8%)
Deep venous thrombosis	49 (4%)
Prior stroke	313 (24%)
Dementia	122 (9%)
Current smoker	341 (27%)
Heavy alcohol	66 (5%)
Pre-stroke Rankin, median (IQR)	2 (0 to 3)
Imaging characteristics:	
Lacunar infarct	543 (42%)
Microbleed	255 (20%)
PVS basal ganglia >=11	442 (34%)
WMH (deep >=2 or Periventricular = 3)	494 (38%)

(Filename: TCT_405_ASNRfigure.JPG)

336

Inter-Rater Agreement and Detection Accuracy for Medium Vessel Occlusions Using Single-Phase and Multi-Phase CT Angiography

J Ospel[1], F Bala[2], R McDonough[3], O Volny[3], N Kashani[4], W Qiu[3], B Menon[3], M GOYAL[5]

[1]University Hospital Basel, Basel, Basel, [2]King's College Hospital NHS Foundation Trust, London, Greater London, [3]University of Calgary, Calgary, Alberta, [4]Foothills Medical Centre, University of Calgary, Calgary, Alberta, [5]University of Calgary, CALGARY, ALBERTA

Purpose

Accurate and reliable detection of medium vessel occlusions (MeVO) is important to establish the diagnosis of acute ischemic stroke and initiate appropriate treatment with intravenous thrombolysis or endovascular thrombectomy. However, MeVOs are often challenging to detect, especially for inexperienced readers. We aimed to evaluate accuracy and inter-rater agreement of MeVO detection using single-phase and multi-phase CT angiography.

Materials and Methods

Single-phase and multiphase CT angiography (mCTA) of 120 acute ischemic stroke patients (20 with no occlusion, 44 with large vessel occlusion and 56 with medium vessel occlusion in the anterior and posterior circulation) were assessed by 3 readers with varying levels of experience (session 1: single-phase CTA, session 2: mCTA). Inter-rater agreement for occlusion type (large vessel occlusion [LVO] vs. MeVO vs. no occlusion) and for detailed occlusion site was calculated using Fleiss' kappa with 95% confidence intervals. Accuracy for MeVO detection was calculated for each reader using classification tables.

Results

Inter-rater agreement for occlusion type was moderate for single-phase CTA (K=0.58, 95%CI: 0.56-0.62) and almost perfect for mCTA (K=0.81, 95%CI: 0.78-0.83). Inter-rater agreement for detailed occlusion sites was moderate for single-phase CTA (K=0.55, 95%CI: 0.53-0.56) and substantial for mCTA (K=0.71, 95%CI: 0.67-0.74). On single-phase CTA, readers 1, 2 and 3 classified 33/56 (59%), 34/56 (61%) and 32/56 (57%) correctly as MeVOs. On multiphase CTA, 48/56 (86%), 50/56 (89%) and 50/56 (89%) MeVOs were classified correctly (Figure).

Conclusions

Inter-rater agreement for MeVOs is moderate when using single-phase CTA and almost perfect with mCTA. Detection accuracy is substantially higher with mCTA compared to single-phase CTA, suggesting that mCTA might be a valuable tool for assessment of MeVO stroke.

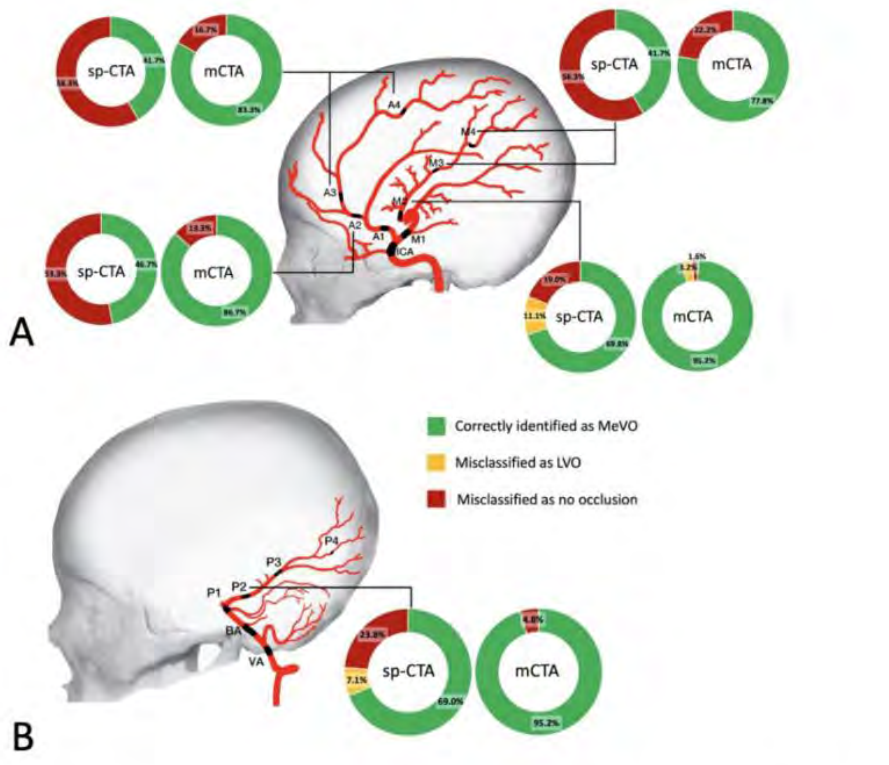

Proportion of MeVOs that were correctly classified as MeVOs (green), misclassified as LVOs (yellow) and misclassified as no occlusion (red) on single-phase and multi-phase CTA, stratified per occlusion site. A) shows proportions for M2, M3/4, A2 and A3/4 MeVOs. B) shows proportions for P2 MeVOs.

(Filename: TCT_336_mevo_interrater_fig.jpg)

1021

Midline Shift from Chronic Subdural Hematoma – Inter-Rater Reliability of Measuring Methods and Implications for Standardized Rating in Embolization Trials

M Bechstein[1], J Fiehler[2], S Gellissen[3]

[1]University Medical Center Hamburg-Eppendorf, Hamburg, Hamburg, [2]University Hospital Hamburg-Eppendorf, Hamburg, Hamburg, [3]University Medical Hospital Hamburg-Eppendorf, Hamburg, Hamburg

Purpose

Trials evaluating the efficacy of middle meningeal artery embolization in chronic subdural hematoma (cSDH) largely rely on radiologic outcome parameters, such as midline shift (MLS), as marker of space occupying effects (References). In clinical practice, evaluation of cSDH treatment success also relies on radiologic measures, in particular hematoma volume, width and MLS. Nevertheless, there are no validated standards for MLS measurement in cSDH. We hypothesized that magnitude of MLS in cSDH differs among readers depending on the measurement location and technique. The aim of this study was to identify the most reliable measurement location and technique for MLS.

Materials and Methods

Admission CT scans of 57 patients with unilateral cSDH were retrospectively analyzed. Axial slices (thickness 4-5mm) were evaluated by four raters with MLS measurement in 4 locations (Foramina Monro [FM], thalamus [Th], mid septum pellucidum [SP], maximum overall MLS [max]) with 2 different techniques: displacement perpendicular to ideal midline (MLS-M), and displacement relative to the tabula interna in relation to the width of the intracranial space (MLS-T) (Figure A). Intraclass correlation coefficients (ICC) were calculated to assess inter-rater reliability and agreement of MLS-M and MLS-T measurement techniques. Measurements of cSDH volume and width were conducted for further data alignment.

Results

ICCs between readers were excellent (>0.9) for all MLS-M locations and for MLS-T_Th and ML-T_FM. The ICC was higher for MLS-M than for MLS-T in all locations. MLS-M_max showed the highest correlation coefficient of 0.78 with cSDH volume (Figure A). Variance of MLS-M_max was explained in 64% of cases (adj. R2) by cSDH volume based on a simple linear regression model. An increase of 10 ml cSDH volume resulted in an average increase of 0.8mm MLS-M_max (Figure B).

Conclusions

Measurements of MLS-M and MLS-T show excellent agreement for all tested anatomical locations. However, the MLS-M method seems to be superior when it comes to inter-rater reliability. Since MLS-M is less prone to artefacts secondary to misaligned CT examinations or skull anomalies after surgery, it can be regarded as superior to MLS-T for standardized MLS assessment. MLS measurement in cSDH patients should be standardized, and due to its high inter-rater reliability, the MLS-M technique should be used.

A.

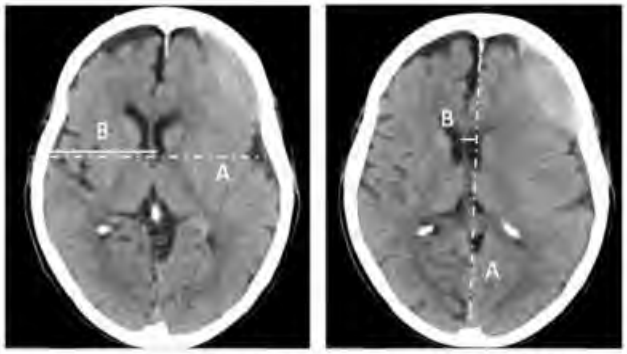

Midline-shift transverse (MLS-T) = A/2-B *Midline-shift midline (MLS-M)*

	ICC (95% CI)	
	MLS-T	**MLS-M**
Foramina Monro	0.901 (0.863-0.931)	0.946 (0.926 – 0.963)
Thalamus	0.905 (0.868-0.934)	0.940 (0.914-0.959)
Septum Pellucidum	0.886 (0.833-0.924)	0.941 (0.950-0.976)
Maximum	0.879 (0.833-0.916)	0.954 (0.920-0.972)

Intraclass-Correlation-Coefficient (ICC) for agreement of raters for midline-shift midline (MLS-M) and midline-shift transverse (MLS-T)

B.

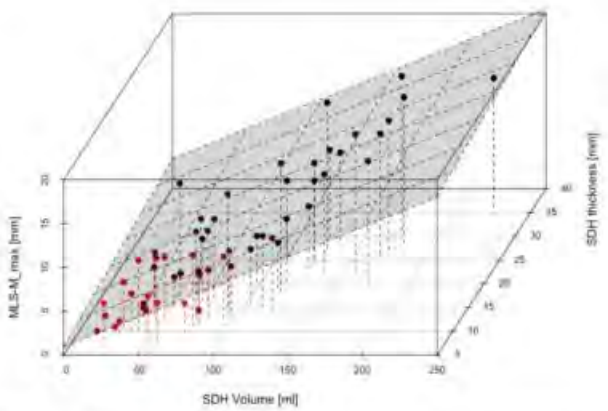

Regression plane including cSDH thickness and cSDH volume as predictors for MLS-M_max.

(Filename: TCT_1021_Fig_ASNR2.jpg)

333

Multiphase CTA-Derived Tissue Maps Aid in Detection of Medium Vessel Occlusions

R McDonough[1], W Qiu[1], J Ospel[2], B Menon[1], P Cimflova[1], M GOYAL[3]

[1]University of Calgary, Calgary, Alberta, [2]University Hospital Basel, Basel, Basel, [3]University of Calgary, CALGARY, ALBERTA

Purpose

Medium vessel occlusions (MeVOs) can be challenging to detect on imaging. Multiphase computed-tomography angiography (mCTA) has been shown to improve large vessel occlusion (LVO) detection and endovascular treatment (EVT) selection. The aims of this study were to determine if mCTA-derived tissue maps can 1) accurately detect MeVOs; and 2) predict infarction on 24h follow-up imaging with comparable accuracy to CT perfusion (CTP).

Materials and Methods

Two readers assessed mCTA tissue maps of 116 ischemic stroke patients (58 MeVO, 58 non-MeVO and determined by consensus: 1) MeVO (yes/no) and 2) occlusion site, blinded to clinical or imaging data. Sensitivity, specificity, and area under the curve (AUC) for MeVO detection were estimated in comparison to reference standards of 1) expert readings of baseline mCTA and 2) CTP maps. Volumetric and spatial agreement between mCTA and CTP-predicted infarcts was assessed using concordance/intraclass correlation and Dice coefficients. Interrater agreement for MeVO detection on mCTA tissue maps was estimated with Cohen's Kappa.

Results

MeVO detection from mCTA-derived tissue maps had a sensitivity of 91% (95%CI:80-97), specificity of 82% (95%CI:70-90), and AUC of 0.87 (95%CI:0.80-0.93) compared to expert reads of baseline mCTA. Interrater reliability was good (0.72, 95%CI:0.60-0.85). Compared to CTP maps, sensitivity was 87% (95%CI:75-95), specificity was 78% (95%CI:65-88), and AUC was 0.83 (95%CI:0.76-0.90) (Figure). The mean difference between mCTA and CTP-predicted final infarct volume was 4.8 mL (limits-of-agreement:–58.5 to 68.1) with a Dice coefficient of 33.5%.

Conclusions

mCTA tissue maps can be used to reliably detect MeVO stroke and predict tissue fate.

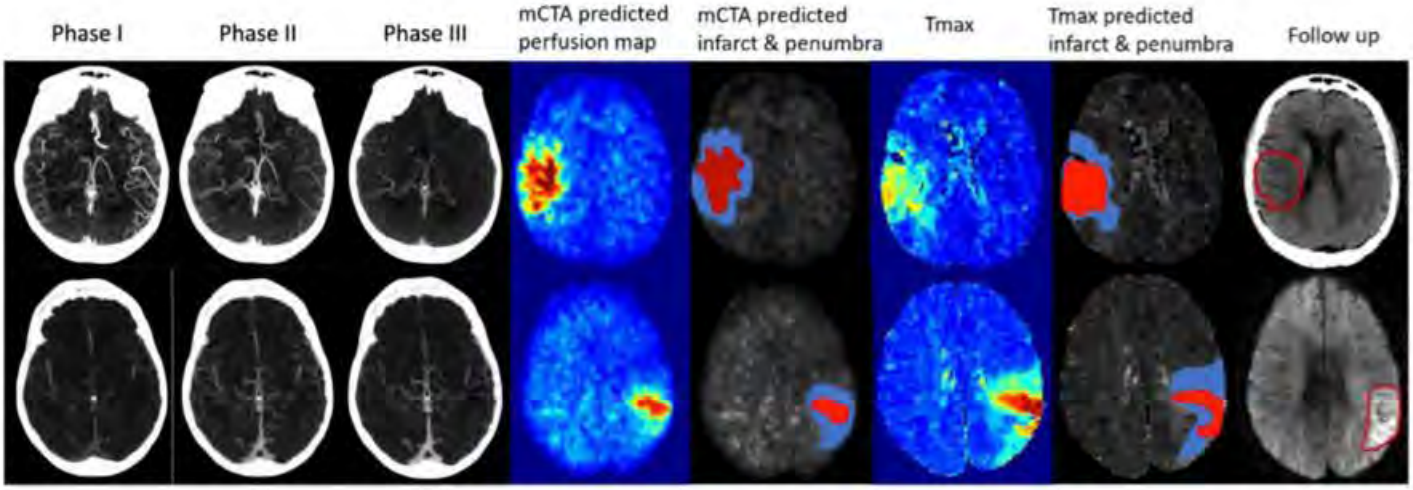

Figure. mCTA and CTP time dependent Tmax thresholded maps of predicted infarct and penumbra, compared to follow-up infarct. Rows: two separate patients, each with a MeVO. Columns (left to right): mCTA phases I-III, predicted perfusion maps, mCTA predicted core (red) and penumbra (blue) overlaid on the mCTA predicted perfusion map, CTP Tmax maps, CTP time dependent Tmax threshold predicted infarct (red) and penumbra (blue), infarct contoured on follow-up imaging. mCTA: multiphase computed tomography angiography (mCTA); CTP: CT perfusion; Tmax: time to maximum; MeVO: medium vessel occlusion

(Filename: TCT_333_mCTA_fig.jpg)

Tuesday, May 17, 2022
5:15-6:15 PM
Scientific Podium Presentations: Interventional

990

Clinical And Procedural Comparative Evaluation Of MRgFUS Vim Ablation In Essential Tremor And Parkinson's Disease

E Tommasino[1], F Bruno[2], A Splendiani[3]
[1]University of L'Aquila, L'aquila, Italy, [2]University of L'Aquila, L'Aquila, Abruzzo, [3]University of L'Aquila, L'AQUILA, l'aquila

Purpose
MRgFUS thalamotomy is a novel minimally invasive procedure for symptomatic tremor treatment. Initially approved for patients with ET, it has becoming increasingly used also in PD tremor. Our purpose is to evaluate the procedural and clinical outcome differences in patients with ET and PD treated by unilateral MRgFUS Vim ablation.
Materials and Methods
We evaluated 101 patients (46 ET, 55 PD). Clinical scores (CRST for tremor, QUEST for quality of life, MOCA for cognitive assessment) were recorded before treatment and with follow-up at 1 day and 1, 6, and 12 months. Technical parameters were recorded in all procedures. A comparison of all variables was made between the two groups.
Results
In ET patients CRST scores improved by 63.1%, immediately after treatment. The improvement remained substantially stable at the following 1-month, 6-months, and 1-year follow-up, with mild recurrence of tremor in 4 patients. In PD patients, CRST scores improved by 64% at 1 day, 56% at 1 month, and 59.2% at 1 year, with mild recurrence of tremor in 4 patients. Tremor reappearance occurred in 7 patients, between the 3- and 6-months follow-up. QUEST and MOCA score changes were not statistically significant between the two groups. Thalamotomy-related complications occurred in 6 ET patients and 6 PD patients. No statistically significant differences were found between the two groups in terms of technical procedural parameters, except for a higher number of sonications in the PD group.
Conclusions
MRgFUS is an effective treatment for both ET and PD patients, with milder deterioration of tremor and QoL scores improvement in the PD group during the follow-up.

983

Comparing Rates of Growth of Established Versus De Novo Brain Arteriovenous Malformations

A Ye[1], K Mueller[2], H Kim[1], S Weinsheimer[1], P Jolivalt[1], D COOKE[3]
[1]University of California San Francisco, San Francisco, CA, [2]Siemens Medical Solutions Inc., Malvern, PA, [3]UCSF, San Francisco, CA

Purpose
Arteriovenous malformations (AVM) are typically considered a congenital lesion; however, a growing body of research has demonstrated de novo growth of AVMs after a previously negative imaging study. While there is heterogeneity in the clinical presentation of those with de novo growth of an AVM, the variable growth of established AVMs has also come under question and may be a key factor in understanding the risk of hemorrhage and natural history of these vascular lesions. This abstract investigates the rates of growth for both de novo AVMs as reported in the literature and compares these findings to untreated AVMs in our medical system.
Materials and Methods
A review of all AVMs within our institution with multiple imaging time points without any interventions (including surgery, embolization, or radiotherapy) was performed and resulted in 60 patients. Patients were excluded from analysis if the imaging time points was less than 12 months apart resulting in a total of 19 patients. In comparison, the 58 de novo AVM cases were identified in the literature also reviewed and only references which described the maximal dimension of the AVM nidus and time interval between initial negative scan and follow-up were tabulated and resulted in 22 total cases. It is of note that the de novo AVMs all had a baseline abnormality or initial symptom in order to initiate neuroimaging which did not demonstrate any AVMs.
Results
On a per annum basis, the de novo AVMs demonstrated more growth changing 6.6 mm/year as compared to the established AVMs changing 0.7 mm/year. The standard deviation was also greatly increased for de novo AVMs versus established AVMs calculated at 7.2 mm/year and 1.9 mm/year, respectively.
Conclusions
Hypothesized causes of de novo AVMs center on a "two-hit" hypothesis in which a genetic predisposition is coupled with a cerebral insult including neoplasms, infarcts, trauma, seizures, or inflammatory conditions. This study highlights the temporal differences between AVMs in an environment after the "second hit" ripe for AVM growth versus those established AVMs that have significantly less growth potential. As expected, de novo AVMs demonstrated significantly increased growth which may relate to the proximity to a "second hit". These findings likely underestimate the prevalence of de novo AVMs as many of these patients would not have initial imaging to establish a clean baseline and highlight the complexity of understanding AVM development and growth.

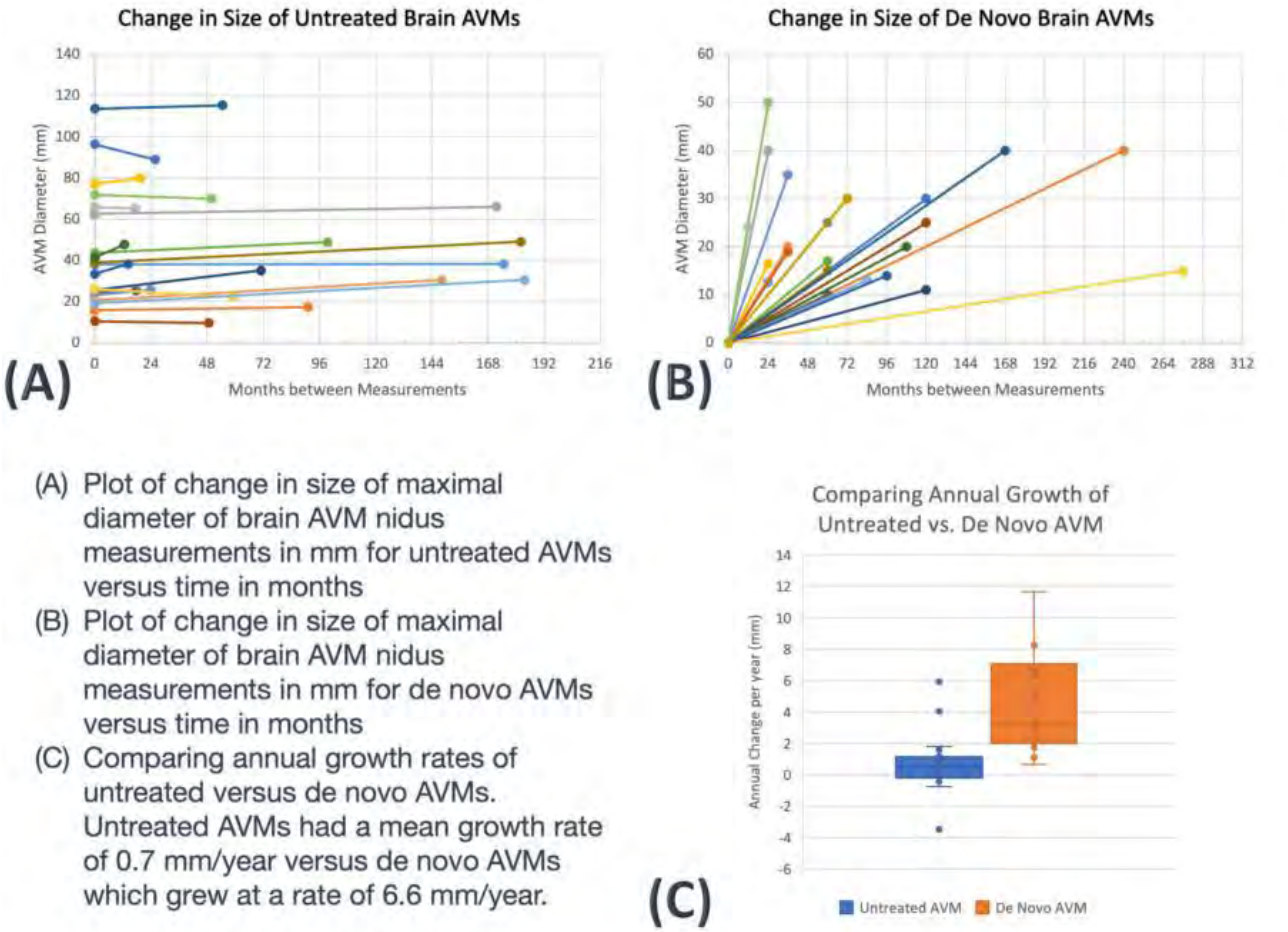

(Filename: TCT_983_Figure.jpg)

1305

Early Intervention with Multiple CT-guided Pudendal Nerve Blocks Offers Hope for Controlling Pudendal Neuralgia

A Rahman, MD; DO[1], D Phan[2], A Choe[3]

[1]University of Rochester Medical Center, Rochester, NY, [2]University of Rochester Scool of Medicine and Dentistry, Rochester, NY, [3]University of Rochester School of Medicien and Dentistry, Rochester, NY

Purpose

This study aimed to evaluate the benefit of multiple regularly spaced computed tomography (CT) guided nerve blocks (>3) with a combination of anesthetics and steroids for the treatment of pudendal neuralgia. The accuracy of localization of the pudendal nerve during blockade, demographics, and social factors were analyzed to determine the influence on CT-guided pudendal nerve blocks.

Materials and Methods

217 patients diagnosed with pudendal neuralgia per the NANTES criteria underwent CT-guided pudendal nerve block and were assessed for outcome and response rate. The patients' demographics, inciting events, initial pain criteria, treatment data, and follow-up data were collected. Non-responders to treatment were compared to responders using unpaired t-test for continuous variables, Fisher's exact test for binary variables and chi squared test for categorical variables. Univariate logistic regression was used to examine prediction of response to the nerve block. A p value <0.05 was indicative of a significant difference.

Results

The most common chief complaint was pain during sitting or squatting and most common areas of pain involved the vulva, labia, perineum, and vagina (44.2%). Treatment response rates increased with the number of blocks with a maximum response rate of 92.2% after the 4th dose. Responders underwent more nerve blocks in the first year when compared to treatment non-responders (3.1±1.5 vs. 2.6±1.6, p=0.026). For the first 2 blocks, accuracy of needle placement was significantly improved in treatment responders for left-sided blocks (90.9% vs 53.8% for block 1, p=0.009; 91.7% vs 50.0% for block 2, p=0.023). Accuracy of needle placement for right-sided blocks and for blocks 3 and 4 were not significantly different between responders and non-responders. 29.4% of treatment non-responders were on disability compared to 9.7% of responders (p=0.043). History of preadolescent sexual abuse was present in 41.7% of non-responders versus 15.7% in responders (p=0.046), and was a significant predictor of response to treatment (odds ratio = 0.27, p=0.04).

Conclusions

CT guided pudendal nerve block improves pain in patients meeting NANTES criteria. Significant predictors of response included the

number of blocks administered within the first year and accuracy of needle placement for the first 2 blocks. Other predictors included history of preadolescent sexual abuse and being on disability at the time of treatment.

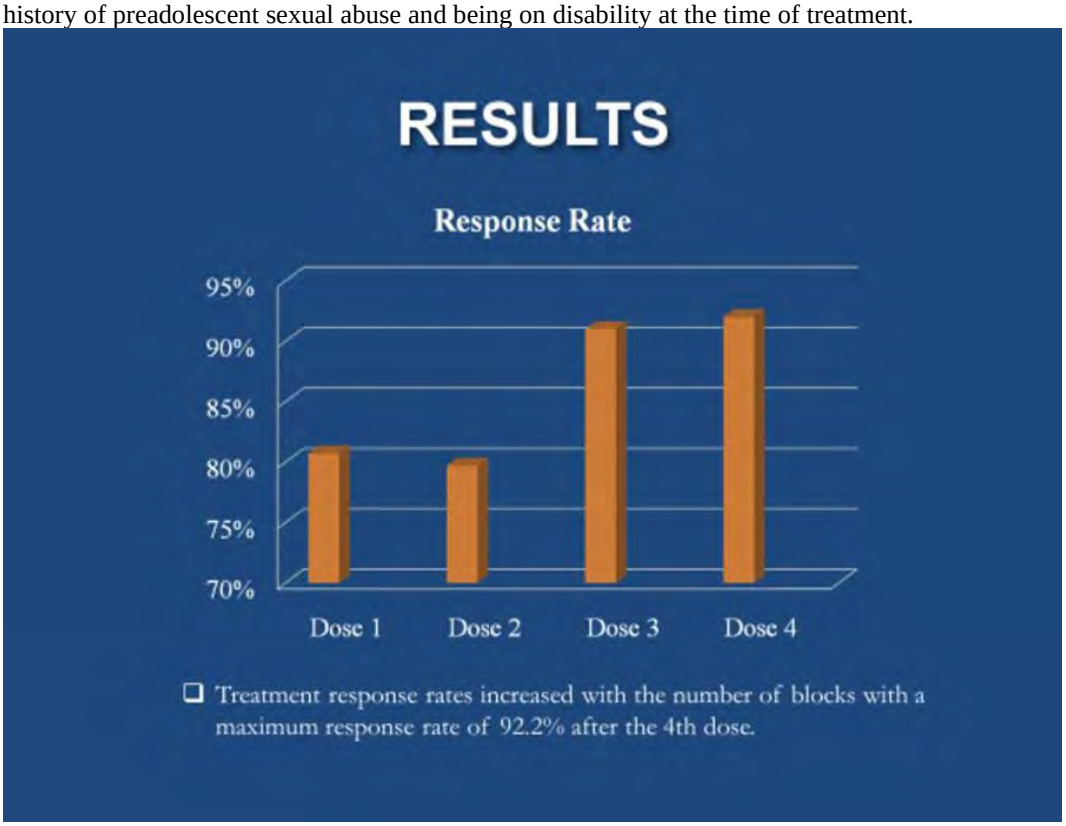

(Filename: TCT_1305_pudendal1.jpg)

1185

Four Tract Tractography for Treating Essential Tremor with MRgHIFU. Preliminary Results.

F Feltrin[1], M Elkurd[2], R El-Nazer[3], L Lanford[2], R Chopra[2], B Shah[4]

[1]UTSouthwestern Texas University, Dallas, TX, [2]UT Southwestern Medical Center, Dallas, TX, [3]UT Southerstern Medical Center, Dallas, TX, [4]UT Southwestern, Dallas, TX

Purpose

Compare the safety profile of four tract tractography for treating Essential Tremor with MRgHIFU with the available literature for indirect based targeting.

Materials and Methods

Ten consecutive Essential Tremor (ET) patients with at least a 3-month follow-up were treated with MRgHIFU guided by a novel method, 4 tract tractography. Using a 3T, 32 direction DTI sequence the corticospinal tract (CST), medial lemniscus (ML), non-decussating dentatorubrothalamic tract (ndDRTT), and decussating dentatorubrothalamic tract (dDRTT) were identified. Final targeting was guided with tractography and planned in BrainLab guided by the following principles: i) the final target had a 2 mm safety margin to the CST and ML; ii) the final target was centered at the overlap of the ndDRTT and dDRTT. Neurological side effects during and after the treatment were reviewed by neurological exams performed at 1 month, and 3 months after the procedure. Archimedes Spirals represent an excellent surrogate measure of total tremor score. Spirals on all patients before and after treatment were graded by two blinded movement disorder neurologists. Interestingly voice tremor and axial tremor resolved after treatment and remained absent at 3 months (n=5).

Results

The 4 tract- tractography based target was more anterior, medial and superior (on average at AC-PC distance A =7.4mm M=13.4mm S=2.2mm) than the indirect target (on average at AC-PC distance A: 6.97mm M14mm S=0mm). During the first day after treatment 2 patients complained of imbalance which resolved by 1 month. At 1 month, no patients exhibited side effects. The average Archimedes spiral score changed from 3.16 (range 2.5-4) to 1 (range 0.5-1.5) at 1 months and lasted for at least 3 months. There was 75% improvement in the average tremor score based on spirals without any persistent neurological side effects.

Conclusions

In comparison to prior studies performed with indirect targeting, tractography based targeting reduces adverse effects while maintaining adequate tremor response. These preliminary results suggest that our tractography based targeting method for MRgHIFU is safe and effective when evaluated at 3 months.

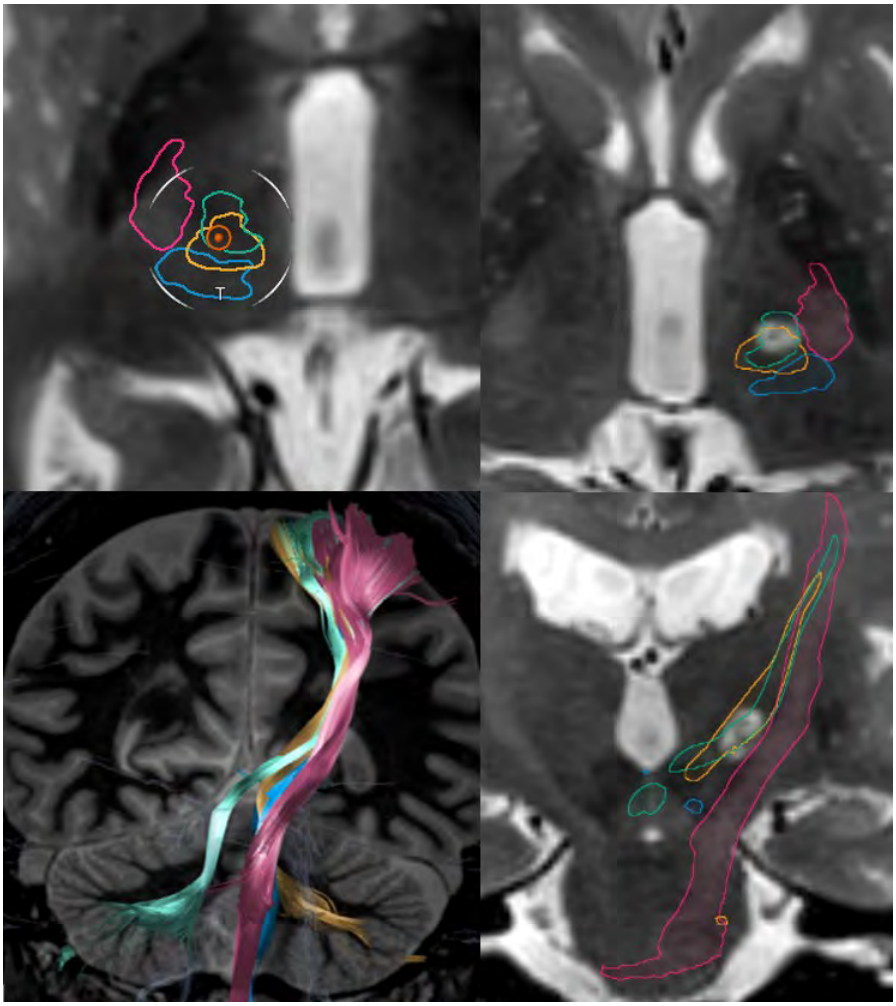
(Filename: TCT_1185_ASNR.jpg)

635

REBOUND CSF HYPERTENSION EXPERIENCE IN A COMMUNITY HOSPITAL-BASED SPINAL CSF LEAK TREATMENT SERVICE (SPONTANEOUS INTRACRANIAL HYPOTENSION SYNDROME AND IATROGENIC SPINAL CSF LEAKS)

F Mihlon[1], K Renner[2]

[1]EASTERN VIRGINIA MEDICAL SCHOOL AND HAMPTON ROADS RADIOLOGY ASSOCIATES, VIRGINIA BEACH, VA, [2]UNC Chapel Hill, Franktown, VA

Purpose

Spinal CSF leak diagnosis and repair is a nuanced process and the minor complication of rebound CSF hypertension following epidural patching can be alarmingly painful for the patient in the days following a successful patch. The paper I am preparing is a presentation of sixteen consecutive spinal CSF leak patients who had leak repairs using epidural blood (autologous) and tisseel or only blood (autologous) and their experiences with rebound CSF hypertension. This information will be useful to others who treat spontaneous intracranial hypotension syndrome and iatrogenic spinal CSF leaks.1

Materials and Methods

This is a retrospective (chart and phone call) review of 16 consecutive spinal CSF leak patients who were treated during 2020. The data collected was presence of rebound CSF hypertension symptoms (new nonpositional bifrontal headache +/- nausea that developed within less than a week of epidural blood or blood/tisseel patching), whether the patient took diamox or diamox and zofran to treat the symptoms, the nature of the CSF leak (SIH, incidental durotomy, post LP, spinal cord stimulator placement, etc), duration of CSF leak symptoms prior to patching, level and location patched, and other details.

Results

8 of 16 patients developed a CSF hypertension like syndrome followed epidural patching, 6 did not, and the data on two are still being collected. 7 of the 8 patients with rebound hypertension symptoms took diamox. 1 of the 8 patients required a lumbar puncture due to severe intractable headache and blurred vision (pseudotumor "crisis"). 1 of the 8 patients required admission the same day as the procedure for intractable nausea and vomiting but did not require LP. 1 of the other 8 rebound hypertension patients developed nausea at home and took zofran to alleviate the symptoms. The patients who developed rebound CSF hypertension had longer duration of spinal CSF leak symptoms prior to patching than those who did not develop rebound CSF hypertension syndrome.

Conclusions

Rebound CSF hypertension syndrome developed in at least half of the patients in this retrospective case series of 16 consecutive patients who underwent percutaneous patching of spinal CSF leaks. Clinicians who treat spinal CSF leaks may do well for their patients to routinely prescribe prn diamox to alleviate those cases of rebound CSF hypertension that develop, especially in those patients who present with longstanding symptoms of intracranial hypotension.

PATIENT	Rebound CSF HTN	Zofran	Diamox	LP	Admit	topamax	location	level	blood patch	tisseel	DX	SIH Brain MRI	Sex	age	Lesion	csfleak sympt
1	yes	no	yes?	no	no	300 mg daily	dorsal	thoracolumbar	18ml		sih	pos	F	47	not characterized	31 years
2	no	no	no	no	no	no	dorsal	thoracolumbar	30ml@1, 25ml@2		sih	pos	M	74	not characterized	14 months
3	no	no	no	no	no	no	left interlaminar	L3-4	30ml		sih	neg	M	53	nc	3months
4	no	no	no	no	no	no	dorsal	L1-2	26ml		sih	pos	F	40	nc	18 years
5	yes	no	yes 3 days	no	no	no	dorsal	thoracolumbar	28ml		sih		F	43	calcified disc protrusion	6months
6	call	at	night	no	no		left ventral	t8-9	9ml@2, 10ml@2	patch#2: 4ml	sih	neg	F	53	non calcified disc protrusion	9 months
7	no	no	no	no	no	no	right lat	L4-5	15ml@1, 9ml@2	patch#2: 6ml	iatrogenic		M	62	incidental durotomy	7 days
8	yes	yes?	13 days	no	no	no	right dorsal @ 1, left dorsal @ 2, left dorsal @3	L5-S1@1@2, L3-4@3	6ml@1, 15ml@2, 10ml@3	patch 1: 4ml, #2: 6ml, #3: 8ml	iatrogenic	neg	F	30	incidental durotomy	1.5 months
9	yes	no	2 days	yes	no	no	billat posterolateral transforaminal ventral	T5-6	4ml	4ml	sih	pos	F	39	calcified disc protrusion	3 months
10	yes	no	yes	no	no	no	left neural foramen at axilla of nerve root sleeve	T9-10	8ml	4ml	sih	pos	F	51	csf vein fistula	6months
11	call at night						dorsal	L2-3	25ml		sih	neg	F	38	nc	15 months
12	yes		4 weeks	no	no		left lateral transforaminal ventral	T7-8, T6-7	15ml, 10ml	2ml, 2ml	sih	pos	M	51	nc	8 weeks
13	yes	no	no	no	no	yes	dorsal	L2-3	18ml		iatrogenic		M	38	LP	11 days
14	no	no	no	no	no	no	laminectomy defect	L3-4	17ml	2ml	iatrogenic		M	50	incidental durotomy	11 days
15	yes		3 days	no	yes		dorsal	thoracolumbar	30 ml, both patches		sih	pos	M	67	nc	21 months
16	no	no	no	no	no	no	rt neural foramen	S2	30ml		sih	pos	F	62	perineural cyst	3 years

(Filename: TCT_635_REBOUNDCSFHTNPAPER.jpg)

1000

Single-center Experience with Pipeline Shield for Treatment of Cerebral Aneurysms

A Kuhn[1], J Singh[2], V Naragum[2], F Massari[3], S Puri[4]

[1]N/A, N/A, [2]University of Massachusetts Medical Center, Worcester, MA, [3]UMass, Southborough, MA, [4]Currently at Univ. of Massachusetts Medical Center., Worcester, MA

Purpose

To describe the first US single-center experience with the Pipeline Shield flow diverter.

Materials and Methods

We retrospectively reviewed our prospectively maintained neurointerventional database from June 2021 to November 2021 and identified all patients who underwent Placement of a Pipeline Shield flow diverter for treatment of an intracranial aneurysm. Patient demographics, procedural data, imaging follow up results and clinical outcome information was collected.

Results

35 cases were identified in the 6-month since the device approval in the US (April 2021). Twenty-four patients were female. Mean age was 60 yrs (range 21-80 yrs). Seventeen patients harbored multiple intracranial aneurysms and 11 had a positive family history. Most aneurysms were unruptured and located along the intracranial ICA (n=28). All aneurysms were wide-necked and mostly saccular in morphology. Ten aneurysms had a branch arising from the aneurysm sac or neck. Most aneurysms were not previously treated. One aneurysm was previously coiled, another was previously treated with a PED but remained unchanged and another aneurysm was treated with a combination of coils and a PED but didn't occlude as anticipated on follow-up. Mean aneurysm diameter 4.3mm. All elective patients were started in dual antiplatelet therapy at least 5 days prior to the procedure. The patient with the ruptured aneurysm was started on an IV antiplatelet medication drip (Cangrelor) during the procedure and transitioned to oral dual antiplatelet medication postop. Platelet function testing (Verify Now) was performed in most patients and antiplatelet medications adjusted as needed. All procedures were performed under general anesthesia with 29 via transfemoral and 6 via transradial access. One single device was placed in all cases. Angioplasty was performed in 7 patients to optimize device-to-vessel wall apposition. Incomplete neck coverage was seen in 1 case but did not require additional treatment. No acute in-device platelet aggregation or thromboembolic complications occurred. There was no change from baseline neurological status in all elective cases. Mortality or permanent morbidity was 0%.

Conclusions

Use of the new PED Shield flow diverter for intracranial aneurysm treatment is technically feasible with no procedure related mortality or permanent morbidity. Preliminary findings suggest the PED Shield is safe and effective with a performance comparable to the FLEX generation of the device. Long-term data will be needed to confirm our findings.

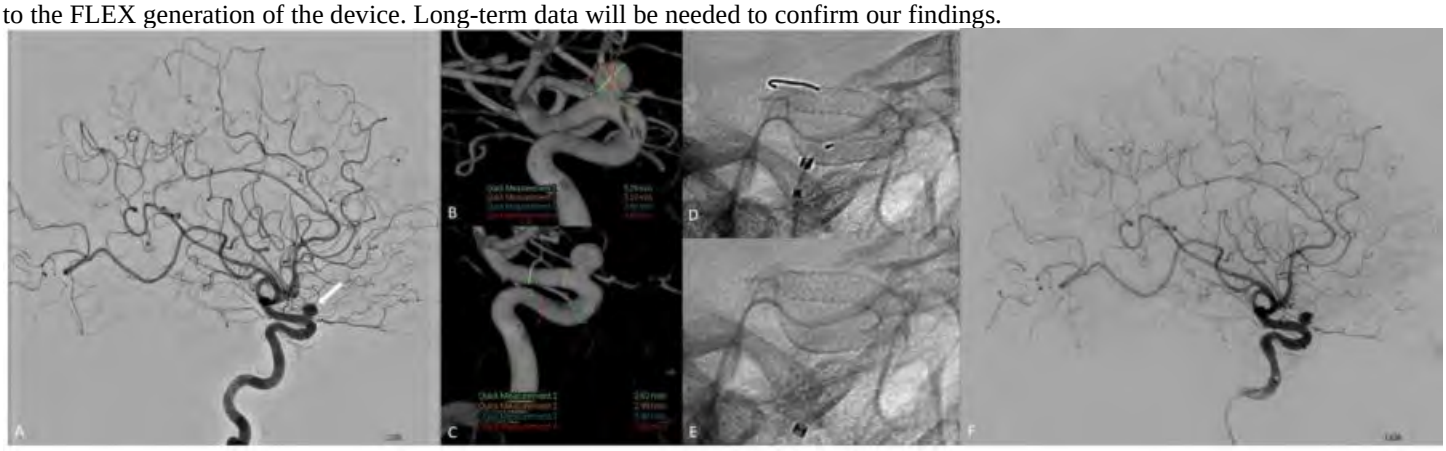

(Filename: TCT_1000_Fig7.jpg)

1254

Stent-assisted embolization with the Woven EndoBridge: angiographic characteristics, complications and clinical outcome

L Goertz[1], T Liebig[2], L Pennig[1], M Schönfeld[3], K Laukamp[4], J Kottlors[1], C Zaeske[1], D Zopfs[1], N Abdullayev[1], M Schlamann[1], C Kabbasch[1]

[1]University Hospital Cologne, Cologne, NRW, [2]LMU KLinikum,, 81377 München, Bavaria, [3]University Hospital Cologne, Köln, NRW, [4]UKK, Cologne, NRW

Purpose

The Woven Endobridge (WEB) is an intrasaccular flow-disruptor for endovascular treatment of intracranial aneurysms, in particular for wide-necked and bifurcation aneurysms. Due to its spherical shape, stent assistance is not routinely required. However, in some cases, additional stent implantation may be necessary to counteract WEB protrusion into the parent vessel and to optimize intraaneurysmal WEB positioning. The objective was to analyse cases that required additional stent-implantation in terms of aneurysm characteristics, complications and angiographic outcome.

Materials and Methods

All WEB procedures for aneurysms < 11 mm between 2011 and 2020 were retrospectively reviewed. Aneurysm characteristics (ruptured status, location, size, neck width, various size indices, morphology), procedural specifics (WEB type, additional coiling/stent implantation), adverse events (hemorrhagic and thromboembolic events) and angiographic results were determined and compared between aneurysms treated by WEB only and by WEB + stent using univariate and multivariate statistics.

Results

A total of 178 patients (mean age: 58 ± 12 years, 71% female) were identified. Among 178 aneurysms treated with the WEB (means size: 7.0 ± 2.4 mm, mean neck width: 4.3 ± 1.6 mm, 30% ruptured), additional stent implantation was performed in 15 cases (8.4%). Baseline patient and aneurysm characteristics were comparable between both groups. In the stent-assisted group, the rate of overall (symptomatic and asymptomatic) thromboembolic complications was higher than in the WEB only group (33.3% vs. 8.0%, p=0.002), while ischemic stroke rates were comparable between the groups (0% vs. 1.8%, p=1.0). There were no significant differences regarding hemorrhagic complications and procedural morbidity (each p> 0.05). Six-month complete and near-complete occlusion was attained in 73.4% and 92.7% in the WEB only group, respectively, and in 66.7% and 83.3% in the WEB + stent group, respectively (p=0.538).

Conclusions

Stent-assisted WEB embolization showed comparable safety and efficacy to aneurysms treatment by WEB only. Of note, the use of intracranial stent requires long-term anti-platelet medication, which annihilates the advantages of the WEB as a purely intrasaccular device. To this point, stent-assisted WEB implantation can serve as a rescue treatment after failed WEB only treatment or for complex aneurysms, as an alternative treatment option to stent-assisted coiling.

Tuesday, May 17, 2022
5:15-6:15 PM
Scientific Podium Presentations: Spine

120

Cervical MRI Assessment of Traumatic Anterior Atlanto-Occipital Membrane Complex Injuries with Evaluation of Ancillary Findings

P Fiester[1], G Rahmathulla[2], M Jenson[2], J Patel[3], E Soule[3]
[1]UF Health Jacksonville, Jacksonville, FL, [2]University of Florida College of Medicine Jacksonville, Jacksonville, FL, [3]University of Florida College of Medicine - Jacksonville, Jacksonville, FL

Purpose
The purpose of this study was to identify and classify the different types of anterior atlanto-occipital membrane complex injuries on MRI and evaluate for the presence and location of a prevertebral effusion.
Materials and Methods
Patients who suffered an anterior atlanto-occipital membrane complex injury were identified retrospectively using Nuance mPower software. The cervical CT and MRI exams for these patients were reviewed for the presence and location of a prevertebral effusion. Age matched positive and negative control groups were obtained.
Results
Fifty patients were identified with an acute anterior atlanto-occipital membrane complex injury. Three distinct patterns of anterior atlanto-occipital membrane complex injury were observed: 1) increased STIR signal and disruption of the anterior atlanto-occipital membrane (19 patients); 2) increased STIR signal and disruption of the anterior atlantoaxial membrane (10 patients); 3) increased STIR signal and disruption of both the anterior atlanto-occipital membrane and anterior atlantoaxial membrane (21 patients). Ninety four percent of patients with an anterior atlanto-occipital membrane complex injury presented with a prevertebral effusion at the craniocervical junction with an average anteroposterior dimension of 8 mm. Zero out of 50 age matched control patients with fractures of C1/C2 demonstrated a craniocervical prevertebral effusion. Six out of 50 age matched control patients with a subaxial tear of the anterior longitudinal ligament demonstrated a prevertebral effusion extending to the level of the craniocervical junction. Statistical analysis revealed a statistically significant association between anterior atlanto-occipital membrane complex injury and a craniocervical prevertebral effusion.
Conclusions
A craniocervical prevertebral effusion was observed in 94% of patients with an anterior atlanto-occipital membrane complex tear. Based on our findings, the presence of a craniocervical prevertebral effusion is 94% sensitive and 94% specific for an anterior atlanto-occipital membrane complex injury in high velocity trauma victims.

117

Diagnostic Utility of Anterior Atlantodens Interval Widening on Cervical Spine CT for Assessing Transverse Atlantal Ligament Injury

P Fiester[1], D Rao[2], E Soule[3], G Rahmathulla[2], P Orallo[3]
[1]UF Health Jacksonville, Jacksonville, FL, [2]University of Florida College of Medicine Jacksonville, Jacksonville, FL, [3]University of Florida College of Medicine - Jacksonville, Jacksonville, FL

Purpose
Post-traumatic atlanto-axial instability is classically associated with tears of the transverse atlantal ligament at C1-C2 and is indirectly evaluated on plain film and cervical spine CT. The purpose of our study was to determine which method is most sensitive in predicting transverse atlantal ligament injury.
Materials and Methods
Adult and pediatric trauma patients who suffered a transverse atlantal ligament tear on cervical MRI were identified retrospectively using Nuance mPower software. The cervical CT and MRI exams for these patients were reviewed by two neuroradiologists for the following: anterior and lateral atlanto-dens interval widening, lateral C1 mass offset, C1-C2 rotatory subluxation, and transverse atlantal ligament injuries on cervical MRI.
Results
Twenty seven trauma patients were identified with a tear of the transverse atlantal ligament on cervical MRI. Eleven percent of these patients demonstrated an anterior dens interval measuring greater than 2 mm, 26% of patients demonstrated lateral mass offset of C1 on C2, 18% of patients demonstrated an asymmetry greater than 1 mm between the left and right lateral atlantodens interval, and one patient demonstrated atlanto-axial rotation measuring greater than 20%.
Conclusions
An anterior atlantodens interval measuring greater than 2 mm is an unreliable methodology to screen trauma patients for transverse altantal ligament injuries and atlanto-axial instability. Moreover, C1 lateral mass offset, lateral atlantodens asymmetry, and atlanto-axial rotation were all poor predictors of transverse atlantal ligament tears. Our findings underscore the importance of cervical MRI in the diagnostic workup and management of patients with acute, high-velocity cervical spine trauma and suggest that anterior atlantodens interval widening on cervical CT is an unreliable screening method for atlanto-axial instability.

1461

Effect of level of experience in grading upper cervical spine injuries on CT according to the AO spine classification

Y Cai[1], S Khanpara[2], J McCarty[3], N Doyle[4], L Nunez[1], A Aein[1], R Patel[5], R Riascos[5]

[1]University of Texas Health Science Center at Houston, Houston, TX, [2]University of Texas MD Anderson Cancer Center, Houston, TX, [3]UTHealth Houston, Houston, TX, [4]University of Texas Health Science Center Houston, Houston, TX, [5]The University of Texas Health Science Center at Houston, Houston, TX

Purpose

The AO spine Society recently published a new classification system attempting at a universal system for grading the upper cervical spine[1]. The level (occipital bone, C1 and C2) and type of injury (A, B and C) are evaluated as the grade criterion. The AO spine classification includes assessment of tension band injuries which are not easily apparent on CT and may rely on indirect imaging signs, detection of which may depend on the radiologist's experience. In this study, we investigate the effect of level of experience of a radiologist in assessing the accuracy of grading the upper cervical spine injuries on CT according to the AO spine classification.

Materials and Methods

Retrospective analysis of patients (>18 years) with upper cervical spine injury in the year 2019-2020 was performed. Both CT and MRI of the spine were performed at the time of admission. The level and type of injury were noted down on a CT by a senior resident (R3), and neuroradiology attending at different time points. Both of them were blind to MRI results, which were reviewed by the third radiologist and were used as the gold reference. The accuracy rate was recorded in both level and type of injuries. Chi-Square test was used to check if there is a statistical difference between the readers.

Results

Total 38 patients were included with mean age 50 years old and M:F 1.78:1. Total 74 level-type injury were detected on the MRI. Since some level injuries read by these two radiologist were not matched with the MRI results, the MRI results were paired with the radiologist's CT reading for comparison based on the level injury. The attending radiologist had 78 level-type injuries pairs for comparison: level injury accuracy was 71/78(91%) and type injury accuracy was 44/78 (56.4%). The resident radiologist had 79 comparison pairs: 69/79 (87.3%) and 41/79 (51.9%) accuracy respectively, p=0.46 and p=0.57 for level and type injuries respectively. For both readers, the level accuracy was significantly higher than the type accuracy (both of p<0.0001). Figure 1 shows that from CT images only, both radiologist cannot identify the findings of C0:B and C1:B which were identified in MRI images.

Conclusions

We conclude that the level of experience provided similar precision in grading AO spine injuries on CT. However, both readers had poor accuracy when compared to MRI, validating higher sensitivity of MRI in detection of type B and C injuries.

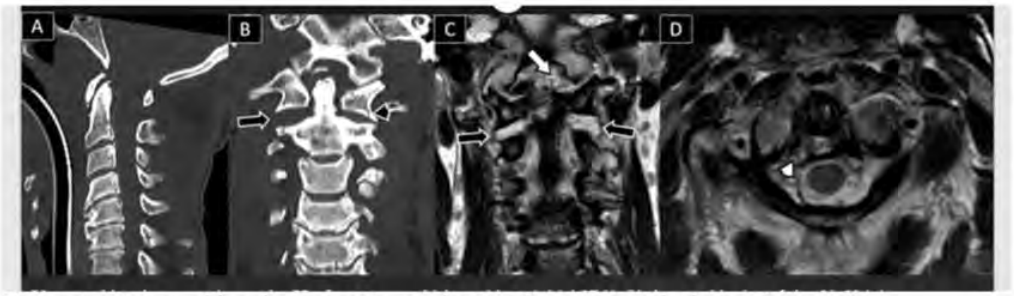

Figure 1: 59-year-old male presenting to the ED after motor vehicle accident. Both radiologists identify the widening of the C1-C2 joint space on the right side (black arrow) with nondisplaced fracture of lateral mass of C1 on the left side (black arrowhead), consistent with a C1:C injury, C1:A injury. MR of the craniocervical junction (C, D) done later the same day corroborated the C1:C injury (black arrows), which now looks more prominent on the left side compared to the CT. However, complete rupture of the left alar ligament (white arrow, C0:B) and the right attachment of transverse atlantal ligament (white arrowhead C1:B) identified in MRI cannot be detected by both radiologists in CT image only.

(Filename: TCT_1461_picture2.jpg)

686

Improved Workflow and Efficiency Utilizing Artificial Intelligence-Based Reconstruction for MR Spinal Surveys

M Chen[1], H Sharma[1], P Belani[1], A Doshi[1]

[1]Mount Sinai Hospital, New York, NY

Purpose

Long MR acquisition times contribute to patient discomfort and increased costs. This study evaluates a particular use case for AI accelerated MR, which leverages shorter acquisition times to obtain more comprehensive spine imaging with increased efficiency.

Materials and Methods
Previously at our institution, a radiologist would view inpatient sagittal MR spinal survey images immediately after acquisition to determine the need for selected axial coverage ("conventional" protocol). After October 2020, both sagittal and axial images of the entire spine were obtained without intermediate clinician review using a DICOM-based AI reconstruction algorithm ("AI accelerated" protocol) (1). 200 consecutive adult inpatient MR spinal surveys were reviewed. Metrics were compared between conventional (n = 100, average age = 62.2 ± 14.7 y) and AI accelerated (n = 100, average age = 63.5 ± 16.1 y) studies, including 1) early exam termination (excluded from further review), 2) exam duration (obtained from exam scheduling records), 3) scanner time (obtained from DICOM data), and 4) recall rate (repeat spinal MR imaging within 24 hours).
Results
The AI accelerated protocol was significantly shorter for both exam duration (conventional = 1:11:01 ± 30:25, AI accelerated = 1:02:29 ± 24:40; $p < 0.05$, n = 168) and scanner time (40:26 ± 20:16 for conventional, 31:04 ± 14:07 for AI accelerated; $p < 0.001$, n = 174). Recall rate was significantly less with the AI accelerated protocol (9.3% for conventional, 2.3% for AI accelerated; $p < 0.05$, n = 174).
Conclusions
With AI accelerated MR acquisition, complete sagittal and axial images of the spine can be obtained in less time and with fewer clinician interruptions compared to conventional imaging. Furthermore, the additional information provided by complete axial images may reduce the utilization of short-term follow-up imaging.

1343
Multimodal advanced MRI imaging of nerve roots in lumbar radiculopaty using DWI, DTI and T2 mapping sequences: clinical and neurophisiological correlations
F Bruno[1], E Tommasino[2], A Splendiani[3]
[1]University of L'Aquila, L'Aquila, Abruzzo, [2]University of L'Aquila, L'aquila, Italy, [3]University of L'Aquila, L'AQUILA, l'aquila

Purpose
To assess lumbar nerve root DWI, DTI and T2 mapping MRI metrics in patients with lumbar disc herniation sciatica, and evaluate their correlations with clinical and neurophisiological findings
Materials and Methods
We prospectively evaluated 45 patients suffering from unilateral lumbar radiculopathy due to L5-S1 discoradicular conflict. All patients were submitted to MRI examinations using a standard spine protocol and additional DWI, DTI, and T2 mapping sequences. Relative metrics of ADC, FA, and T2 relaxation times were recorded placing ROIs at the preforaminal, intraforaminal, and post-foraminal level, either at the affected side and the contralateral side, used as control. All patients were also submitted to EMG testing, recording the spontaneous activity, voluntary activity, F wave amplitude and latency, motor evoked potentials (MEP) amplitude and latency, either at the level of the tibialis anterior and the gastrocnemius muscles. Clinical features (diseases duration, pain, sensitivity, strength, osteotendinous reflexes) were also recorded.
Results
Among clinical features, we found positive correlation of pain intensity with ADC values of the lumbar nerve roots. The presence of spontaneous activity correlated with lower ADC values of the affected lumbar nerve root. F wave and MEP latency correlated with decreased FA values at the foraminal level and increased values at the post-foraminal level. The same neurophysiological measures correlated positively with pre-foraminal T2 mapping values and negatively with post-foraminal T2 mapping values. Increased T2 mapping values at the foraminal level correlated with disease duration.
Conclusions
Evaluation of lumbar nerve roots using advanced MRI sequences may provide useful clinical information in patients with lumbar radiculopathy, potentially indicating active inflammation/myelinic damage (DTI, T2 mapping) and axonal damage/cronicity (DWI).

1533
Reliability of the new AO spine classification for grading of upper cervical spine injuries on CT
S Khanpara[1], N Doyle[2], J McCarty[3], A Aein[4], Y Cai[4], R Patel[5], R Riascos[5]
[1]University of Texas MD Anderson Cancer Center, Houston, TX, [2]University of Texas Health Science Center Houston, Houston, TX, [3]UTHealth Houston, Houston, TX, [4]University of Texas Health Science Center at Houston, Houston, TX, [5]The University of Texas Health Science Center at Houston, Houston, TX

Purpose
The upper cervical spine comprising of the occipital bone, the Atlas and the Axis, is a unique and a complicated anatomical and functional unit. Hence a separate classification system for injury to the upper cervical spine is imperative. The AO spine Society recently published a new classification system attempting at a universal system for grading these injuries[1]. One of the components of an ideal classification system is its applicability in routine practice with a consistent reproducibility. In this study, we evaluate the interrater variability of the new AO spine classification for grading the upper cervical spine on CT among reader with varying experience, since CT is the first modality used for evaluation of traumatic injury.
Materials and Methods
Retrospective analysis of 50 patients (>18 years) with upper cervical spine injury was performed at a level I trauma center presenting

during a course of 1 year. All of these 50 patients were randomly selected from a list generated from the institutional database for trauma for the year 2019-2020 and had CT of the spine performed at the time of admission. 12 patients were excluded during the selection process due to following reasons: no upper cervical spine injury, no acute injuries and presence of motion artifact limiting evaluation. The level (occipital bone, C1 and C2) and type of injury (A, B and C) were noted down on a CT by a senior resident, Neuroradiology fellow and Neuroradiology attending at different time points. The interrater variability for the level and type of injury was calculated using the Fleiss' kappa score.

Results

Mean age of the study group was 50 years with a male to female ratio of 1.78:1. Etiology of the injury in these cases were as follows: motor vehicle accident (n = 31), fall ≤ 8 feet (n = 13), fall > 8 feet (n = 4) and sports related injuries (n = 2). Substantial agreement was noted among the 3 readers for the level of injury (Fleiss' K = 0.82, CI = 0.7-0.93) with only fair agreement for the type of injury (Fleiss'K = 0.29, CI = 0.17-0.41).

Conclusions

We conclude that CT provides good reproducibility for identifying the level of but only poor reproducibility for the type of injury. This contrasts with what has been reported recently by Maeda et al[2]. The major reason for poor agreement in the type of injury is believed to be due the inability of CT to resolve soft tissue injuries (type B and C injuries). Level of experience is another determining factor.

Table 1: Fleiss' kappa estimates based on the data of three readers on 50 subjects:

	Fleiss' kappa estimate	95% CI
Level of injury	0.82	0.70 – 0.93
Type of injury	0.29	0.17 – 0.41

κ	Interpretation
< 0	Poor agreement
0.01 – 0.20	Slight agreement
0.21 – 0.40	Fair agreement
0.41 – 0.60	Moderate agreement
0.61 – 0.80	Substantial agreement
0.81 – 1.00	Almost perfect agreement

(Filename: TCT_1533_picture3.jpg)

1357

Remote Changes in Spinal Cord Interstitial Space-Subarachnoid Space Communication 24 Hours after Acute Mild Traumatic Spinal Cord Injury in a Miniature Spine Model: A Case for Early Wallerian Degeneration?

R Bert[1], M Negahdar[1]
[1]*University of Louisville, Louisville, KY*

Purpose

While spinal cord edema adjacent to a traumatic spinal cord injury (TSCI) has been studied using T2-weighted imaging, little is known about remote edematous effects of TSCI, as spinal cord T2-weighted imaging is relatively insensitive. We have used MRI myelography to study acute remote spinal cord interstitial space changes ~24 hours after mild TSCI in a standardized miniature swine model, testing the hypothesis that acute TSCI results in interstitial changes remote to the site of injury.

Materials and Methods

IACUC approval was obtained before investigation. Yucatan miniature swine underwent focal contusion of the thoracic spinal cord using a standardized weight drop (50g weight dropped 10 cm) onto an exposed thecal sac at the T10 level. Structural imaging was performed ~48 hours before surgery and ~24 hours after injury. During both occasions, images were obtained before and after intrathecal administration of gadolinium-based myelographic contrast at L5-S1 under general anesthesia using T1 Fat Saturated images. The swine were then recovered for physiologic testing. Imaging ROI were drawn at distinct regions of the spinal cord (central gray matter and white matter: anterior columns, dorsal columns and lateral columns) using standard research software. ROI means, areas and standard deviations were entered into standardized spreadsheet software and graphed after normalization for signal strength and contrast concentration by two independent analysts.

Results

Results are shown in the accompanying figure. Graphs top to bottom are spinal cord levels. Blue bars are normalized signal before myelography, brown bars are normalized signal post myelography. The left and right columns of graphs are pre and post injury data.

After intrathecal contrast injection, all cord ROI increased in both the pre and post injured pig, indicating communication between the subarachnoid space and the spinal cord interstitial fluid. However, the post contrast increase in the ROI values was consistently higher in the pig BEFORE injury than AFTER injury.

Conclusions

We attribute the decrease in cord enhancement post injury to edema within the cord within the intracellular compartment, reducing spinal cord interstitial space communication with the CSF. This remote phenomenon would be consistent with white matter swelling secondary to early Wallerian degeneration occurring within 24 hours after injury. This finding may explain absence of behavioral improvement to therapeutic myelotomies conducted at 48 hours after injury.

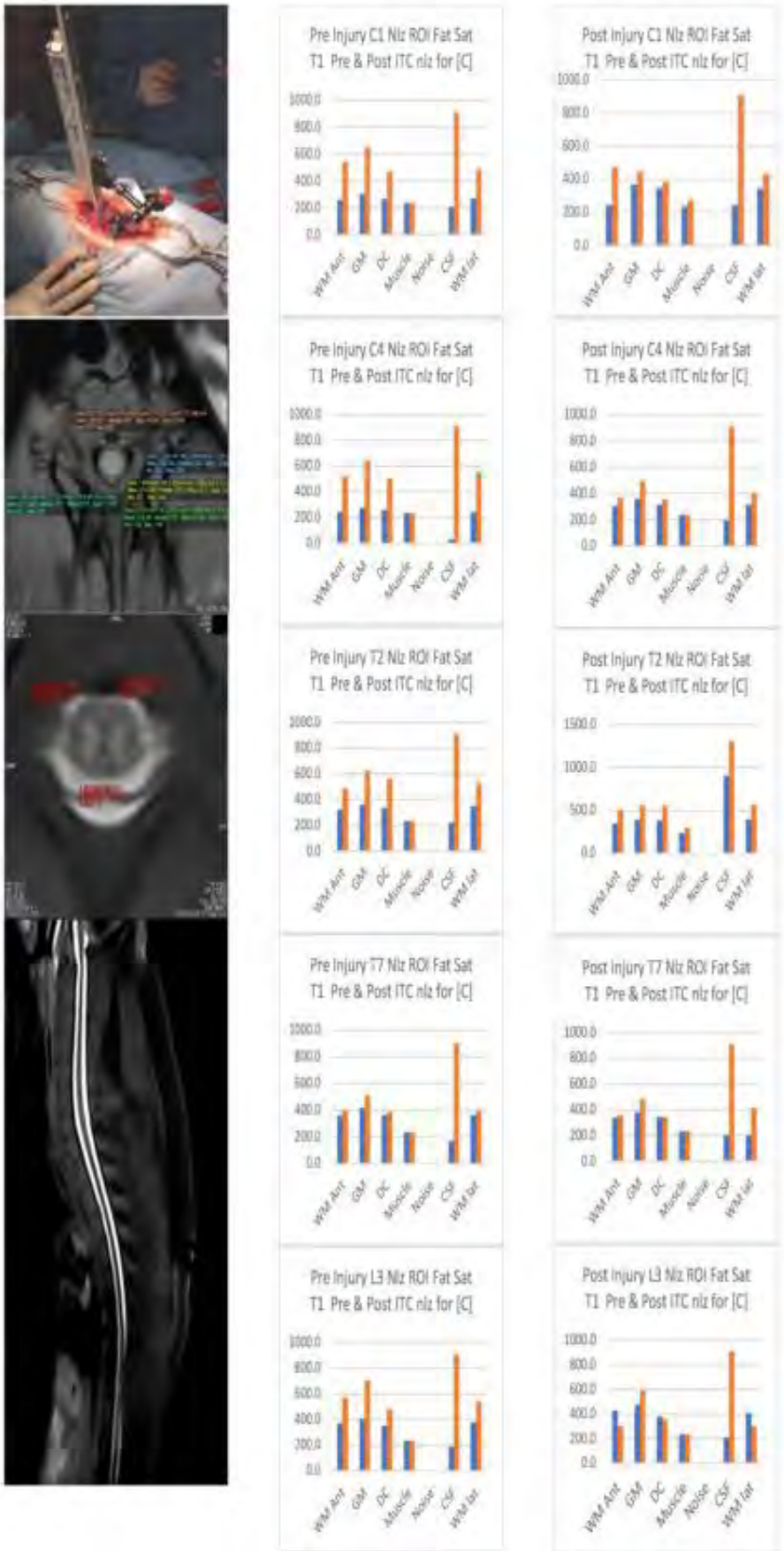

(Filename: TCT_1357_TSCI_Myelography_Figure.jpg)

Wednesday, May 18, 2022
10:45 AM-12:15 PM
Scientific Podium Presentations: Functional

714

Assessing the microstructure of Sensory Processing Disorder with and without ADHD using Neurite Orientation Dispersion and Density Imaging

I Mark[1], J Wren-Jarvis[1], M Lazerwitz[2], S Parekh[1], I Bourla[1], E Marco[2], P Mukherjee[1]
[1]UCSF, San Francisco, CA, [2]Cortica Healthcare, San Rafael, CA

Purpose
"Sensory processing disorder" (SPD) refers to a clinical deficit in the ability to modulate, discriminate, or create an organized motoric response to sensory information. It affects up to 16% of children and contributes to impairment of learning and development at school and in the community.(1) Approximately 50% of SPD patients will also meet research criteria for ADHD.(2) Our study is the first ADHD dimensional study of SPD to examine the neural architecture of SPD with ADHD (SPD+ADHD) and SPD without ADHD (SPD-ADHD) using Diffusion Tensor Imaging (DTI) and Neurite Orientation and Dispersion Density Imaging (NODDI), a multi-compartment biophysical model of brain microstructure.
Materials and Methods
We prospectively enrolled 57 subjects, ages 8-12 years, with neurodevelopmental concerns and evaluated for SPD and ADHD. Whole brain 3T multi-shell diffusion MRI (b=0, 1000, and 2500 s/mm2) was performed. Tract Based Spatial Statistics (TBSS) were used to extract standard DTI and NODDI metrics and mapped to 46 designated tracts from the Johns Hopkins University White-Matter Tractography Atlas for direct cohort comparison.
Results
Compared to the SPD-ADHD cohort (29 subjects), the SPD+ADHD cohort (28 subjects) had lower Fractional Anisotropy (FA) values in the left anterior corona radiata (p=.03), left posterior corona radiata (p=.01), right posterior corona radiata (p=.02), and left posterior limb of the internal capsule (p=.04) as well as a trend towards lower Axial Diffusivity (AD) values in the left superior corona radiata (p=.05). Modeling the cellular microstructure using NODDI, the SPD+ADHD had significantly higher neurite Orientation Dispersion Index (ODI) values in the body of the corpus callosum (p=.04), left anterior corona radiata (p=.004), left posterior corona radiata (p=.02), and left superior corona radiata (p=.003).
Conclusions
The SPD+ADHD cohort had lower FA or AD throughout the corona radiata and the posterior limb of the limb of the corona radiata, especially within the left cerebral hemisphere. The posterior predominance of the affected tracts is consistent with a meta-analysis of DTI TBSS studies of ADHD.(3) Involvement of posterior and superior corona radiata agrees with correlates of cognitive and visuomotor control in SPD.(4) The differences in FA or AD were attributed to higher ODI, which reflects less collimated axonal fibers, providing new insight into the biological basis of ADHD in the setting of sensory processing dysfunction.

731

Brain Cortical Complexity Alteration in Amyotrophic Lateral Sclerosis: A Preliminary Fractal Dimensionality Study

L Cai[1], H Chen[2]
[1]Fujian Medical University Union Hospital, Fuzhou, China, [2]Fujian Medical University Union Hospital, Fuzhou, Fujian

Purpose
Fractal dimensionality (FD) analysis provides a quantitative description of brain structural complexity;[1-3] The application of FD analysis has provided evidence of amyotrophic lateral sclerosis- (ALS-) related white matter degeneration[4]. This study is aimed at evaluating, for the first time, FD alterations in a gray matter in ALS and determining its association with clinical parameters.
Materials and Methods
This study included 22 patients diagnosed with ALS and 20 healthy subjects who underwent high-resolution T1-weighted imaging scanning. Disease severity was assessed using the revised ALS Functional Rating Scale (ALSFRS-R). The duration of symptoms and rate of disease progression were also assessed. The regional FD value was calculated by a computational anatomy toolbox and compared among groups. The relationship between cortical FD values and clinical parameters was evaluated by Spearman correlation analysis.
Results
ALS patients showed decreased FD values in the left precentral gyrus and central sulcus, left circular sulcus of insula (superior segment), left cingulate gyrus and sulcus (middle-posterior part), right precentral gyrus, and right postcentral gyrus. The FD values in the right precentral gyrus were positively correlated to ALSFRS-R scores (r = 0:44 and P = 0:023), whereas negatively correlated to the rate of disease progression (r = −0:41 and P = 0:039). Meanwhile, the FD value in the left circular sulcus of the insula (superior segment) was negatively correlated to disease duration (r = −0:51 and P = 0:010).
Conclusions
The observed FD reduction suggests a decrease in GM structural complexity in ALS, which involves motor-, sensory-, and cognition-

related areas. This finding further supports the notion that ALS is a multisystem disease. FD analysis may shed more light on the pathophysiology of ALS.

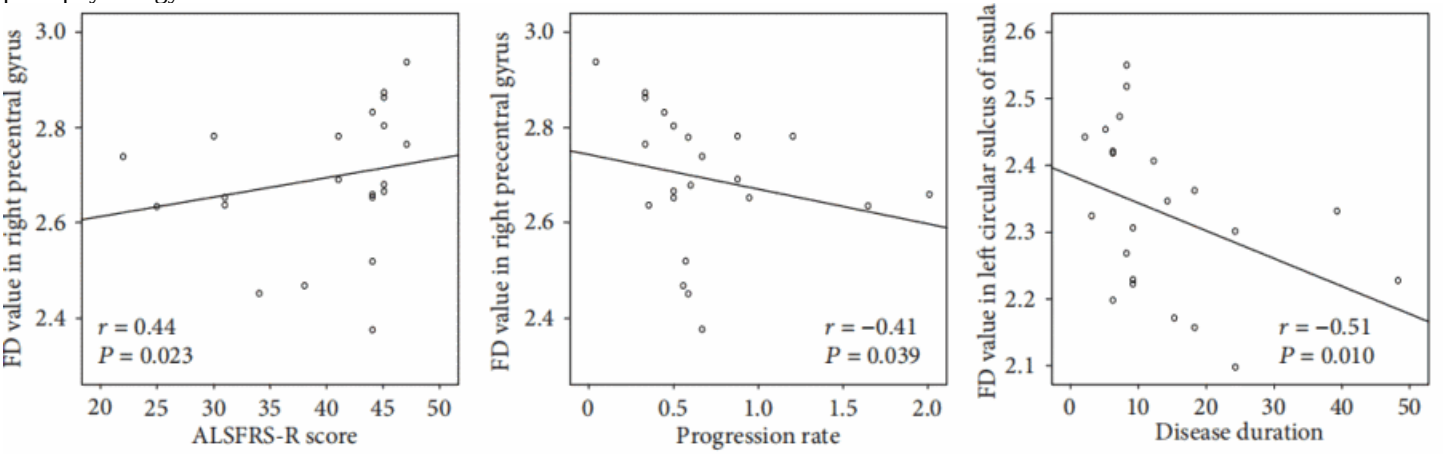

FIGURE 1: The correlations between FD measurement and ALS patients' clinical parameters.

(Filename: TCT_731_Figure1.gif)

1480

Changes in Connectivity Between Insula and Right Parietal Cortex After a Season of High School Football

W Flood[1], C Sheridan[2], J Urban[2], J Stitzel[2], E Davenport[3], J Maldjian[4], C Whitlow[2]

[1]Wake Forest University, Winston-Salem, NC, [2]Wake Forest School of Medicine, Winston-Salem, NC, [3]University of Texas Southwestern, Dallas, TX, [4]University of Texas Southwestern Medical Center, Dallas, TX

Purpose

Head-trauma-related effects on language function remain understudied. Connections between insular and parietal regions are known to be important in language function (Oh et al. 2014). The current study examined resting-state functional connectivity between the insula and parietal language regions in head-impact-exposed athletes and non-contact controls. We hypothesized that impact-exposed athletes would exhibit hyperconnectivity between insula and parietal language regions compared to non-contact controls.

Materials and Methods

In this IRB approved study, we computed whole-brain seed-to-voxel connectivity from BOLD rsfMRI acquisitions at pre- and post-season timepoints in male high-school football players (n=22;mean age 16.3 ± 1.01 years) and age-matched non-contact controls (n=17;mean age 15 ± 2.4 years). Football players who suffered a concussion during the season (n=8) were separated from those who did not (n=14). Twelve insula seed regions were selected from the Brainnetome Atlas (voxel threshold uncorrected p<.001, two-sided; cluster threshold FDR-corrected p<.05). ANOVA followed by Tukey's HSD was used to assess differences in connectivity (Fisher's Z) across group and time.

Results

Both the left and right hypergranular insula independently demonstrated significant differences in connectivity with overlapping clusters containing the right angular and right supramarginal gyri [left insular seed F([2 33]) =16.01, p<.001; right insular seed F(2 33) = 29.01, p<.001].. With respect to left insula-right parietal connectivity, concussed athletes (mean=0.138, SD= 0.219) differed significantly from controls (mean=-0.167, SD= 0.132; p<.001), but not from sub-concussed athletes (mean=0.0738, SD= 0.152; p=.64); sub-concussed athletes differed significantly from controls (p<.001). With respect to right insula-right parietal connectivity, concussed athletes (mean= 0.175, SD=0.155) differed significantly from controls (mean= -0.174, SD= 0.121; p<.001), but not from sub-concussed athletes (mean = .0457, SD = 0.129; p=.09); sub-concussed athletes differed significantly from controls (p<.001).

Conclusions

Athletes exposed to repetitive head trauma demonstrated hyperconnectivity between the posterior insula and language associated parietal clusters compared to controls. These results suggest that concussed and sub-concussed athletes may require higher connectivity between these regions to produce control-level higher-order language performance.

788

Characterizing sensorimotor-related area abnormalities in amyotrophic lateral sclerosis: An intravoxel incoherent motion magnetic resonance imaging study

L Cai[1], H Chen[2]

[1]Fujian Medical University Union Hospital, Fuzhou, China, [2]Fujian Medical University Union Hospital, Fuzhou, Fujian

Purpose

To investigate the microperfusion and water molecule diffusion alterations in sensorimotor-related areas in amyotrophic lateral sclerosis (ALS) using intravoxel incoherent motion (IVIM) magnetic resonance imaging[1].

Materials and Methods

IVIM data were obtained from 43 ALS patients and 31 controls. This study employed the revised ALS Functional Rating Scale (ALSFRS-R) in evaluating disease severity. IVIM-derived metrics were calculated, including diffusion coefficient (D), pseudo-diffusion coefficient (D*), and perfusion fraction (f). Conventional apparent diffusion coefficient was also computed. Atlas-based analysis was conducted to detect between-group difference in these metrics in sensorimotor-related gray/white matter areas. Spearman correlation analysis was employed to establish correlation between various metrics and ALSFRS-R.

Results

ALS patients had f (×10-3) reduction in the left presupplementary motor area (preSMA) (60.72 ± 16.15 vs. 71.15 ± 12.98, P = 0.016), right preSMA (61.35 ± 17.02 vs. 72.18 ± 14.22, P = 0.016), left supplementary motor area (SMA) (55.73 ± 12.29 vs. 64.12 ± 9.17, P = 0.015), and right SMA (56.53 ± 11.93 vs. 63.67 ± 10.03, P = 0.020). Patients showed D (×10-6 mm2/s) increase in a white matter tract projecting to the right ventral premotor cortex (PMv) (714.20 ± 39.75 vs. 691.01 ± 24.53, P = 0.034). A negative correlation between D of right PMv tract and ALSFRS-R score was observed (r = -0.316, P = 0.039).

Conclusions

These findings suggest aberrant microperfusion and water molecule diffusion in the sensorimotor-related areas in ALS patients, which are associated with motor impairment in ALS.

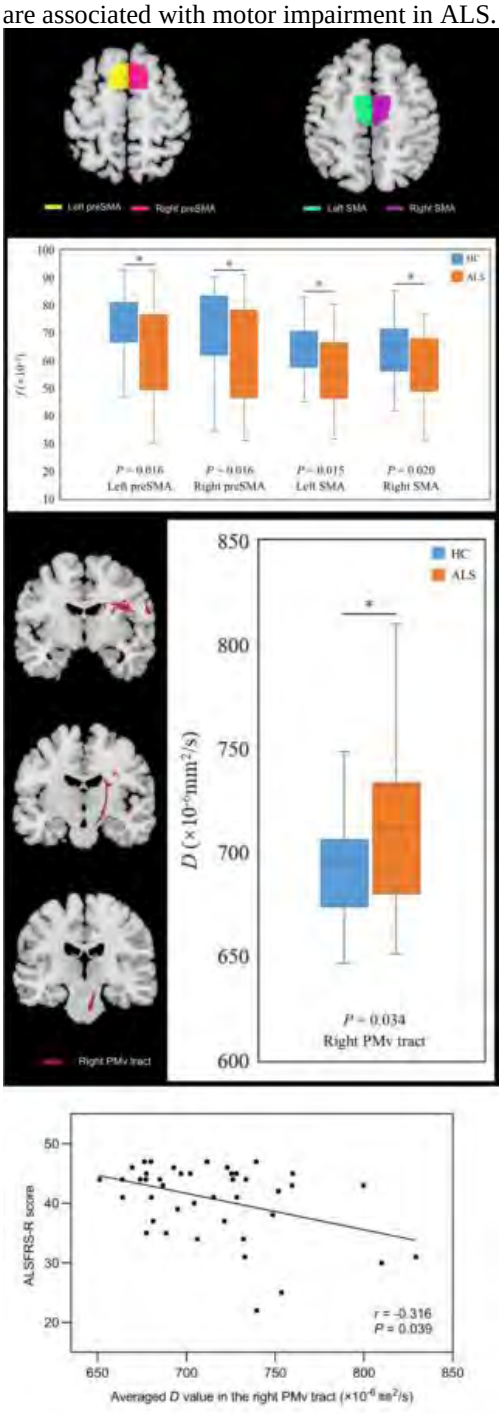

(Filename: TCT_788_Figure1-3.jpg)

542

Dynamic Changes in Functional Network Connectivity Involving Amyotrophic Lateral Sclerosis and Its Correlation to Disease Severity

J Shi[1], H Chen[1]
[1]*Fujian Medical University Union Hospital, Fuzhou, Fujian*

Purpose

Aberrant static functional connectivity (FC) has been well demonstrated in amyotrophic lateral sclerosis (ALS). To better characterize the time-varying properties within and among brain networks in resting-state fMRI studies, novel analytical methods such as dynamic FC (dFC) and dynamic FNC (dFNC) have been proposed[1; 2]. However, ALS-related alterations in FC dynamic properties remain unclear, although dynamic FC analyses contribute to uncover mechanisms underlying neurodegenerative disorders. Thus the aim of this study was to investigate dynamic FNC properties in ALS patients and their relationship to disease severity.

Materials and Methods

Subjects: 32 ALS patients and 45 healthy controls. Field Strength/Sequence: Multiband resting-state functional images using gradient echo echo-planar imaging and T1-weighted images were acquired at 3.0 T. Assessment: Disease severity was evaluated with the revised ALS Functional Rating Scale (ALSFRS-R) and patients were stratified according to diagnostic category. Independent component analysis was conducted to identify the components of seven intrinsic brain networks (i.e. visual/ sensorimotor(SMN)/auditory/cognitive-control(CCN)/default-mode(DMN)/subcortical/cerebellar networks). A sliding window correlation approach was used to compute dFNC. FNC states were determined by k-mean clustering method, and then state-specific FNC and dynamic indices (fraction time/mean dwell time/transition number) were calculated. Statistical Tests : Two-sample t-test used for comparisons on state-specific FNC and dynamic indices and Spearman's correlation analysis used to investigate relationship between dynamic indices and ALSFRS-R.

Results

ALS patients showed increased FNC between DMN-SMN in State-1 and between CCN-SMN in State-4. Patients remained in State-2 (showing the weakest FNC) for a significantly longer time (mean dwell time: 49.8 ± 40.1 vs 93.6 ± 126.3; $P < 0.05$) and remained in State-1 (showing a relatively strong FNC) for a shorter time (fraction time: 0.27 ± 0.25 vs 0.13 ± 0.20; $P < 0.05$). ALS patients exhibited less temporal variability in their FNC (transition number: 10.2 ± 4.4 vs 7.8 ± 3.8; $P < 0.05$). A significant correlation was observed between ALSFRS-R and mean dwell time in State-2 ($r = -0.414$, $P < 0.05$) /transition number ($r = 0.452$, $P < 0.05$). No significant between-subgroup difference in FNC dynamic properties was found.

Conclusions

Our findings suggest aberrant dFNC properties in ALS, which is associated with disease severity.

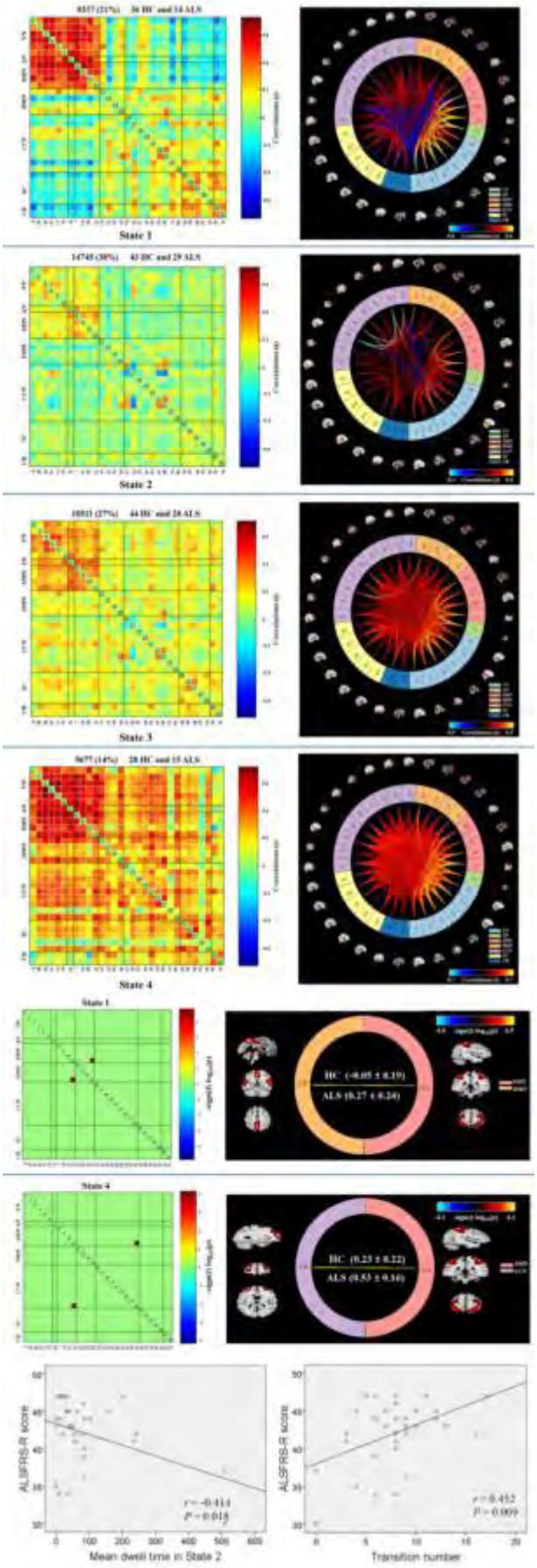

(Filename: TCT_542_IMG282.jpg)

694

Dynamic Changes in Functional Network Connectivity Involving Amyotrophic Lateral Sclerosis and Its Correlation With Disease Severity.

L Cai[1], H Chen[2]

[1]Fujian Medical University Union Hospital, Fuzhou, China, [2]Fujian Medical University Union Hospital, Fuzhou, Fujian

Purpose

Aberrant static functional connectivity (FC) has been well demonstrated in amyotrophic lateral sclerosis (ALS)[1,2]; however, ALS-related alterations in FC dynamic properties remain unclear, although dynamic FC analyses contribute to uncover mechanisms underlying neurodegenerative disorders.We aimed to explore dynamic functional network connectivity (dFNC) in amyotrophic lateral sclerosis(ALS) and its correlation with disease severity.

Materials and Methods

Subjects: Thirty-two ALS patients and 45 healthy controls. Field Strength/Sequence: Multiband resting-state functional images using gradient echo echo-planar imaging and T1 weighted images were acquired at 3.0 T. Assessment: Disease severity was evaluated with the revised ALS Functional Rating Scale (ALSFRS-R) and patients were stratified according to diagnostic category. Independent component analysis was conducted to identify the components of seven intrinsic brain networks (ie, visual/sensorimotor (SMN)/auditory/cognitive-control (CCN)/default-mode (DMN)/subcortical/cerebellar networks). A sliding-window correlation approach was used to compute dFNC. FNC states were determined by k-mean clustering, and state-specific FNC and dynamic indices (fraction time/mean dwell time/transition number) were calculated. Statistical Tests: Two-sample t test used for comparisons on dynamic measures and Spearman's correlation analysis.

Results

ALS patients showed increased FNC between DMN-SMN in state 1 and between CCN-SMN in state 4. Patients remained in state 2 (showing the weakest FNC) for a significantly longer time (mean dwell time: 49.8 ± 40.1 vs. 93.6 ± 126.3; $P < 0.05$) and remained in state 1 (showing a relatively strong FNC) for a shorter time (fraction time: 0.27 ± 0.25 vs. 0.13 ± 0.20; $P < 0.05$). ALS patients exhibited less temporal variability in their FNC (transition number: 10.2 ± 4.4 vs. 7.8 ± 3.8; $P < 0.05$). A significant correlation was observed between ALSFRS-R and mean dwell time in state 2 ($r = -0.414$, $P < 0.05$) and transition number ($r = 0.452$, $P < 0.05$). No significant between-subgroup difference in dFNC properties was found (all $P > 0.05$).

Conclusions

Our findings suggest aberrant dFNC properties in ALS, which represent an additional characteristic of ALS and may underlie the neuropathological mechanisms of motor dysfunction. The dFNC analysis could provide the alternative biomarker for assessing disease severity of ALS.

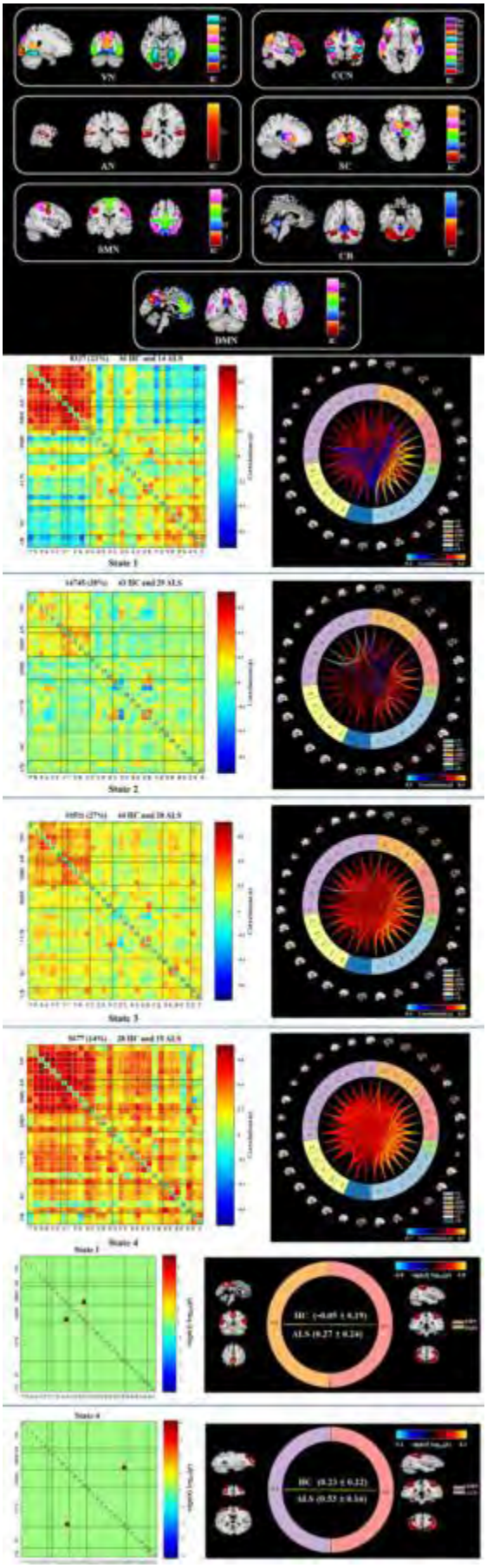

(Filename: TCT_694_Figure1-3.jpg)

487

Evaluating the minimal number of gradient directions for Constrained Spherical Deconvolution

P Nicholas[1], H Taylor[1], L Crawford[1], I Young[1], O Tanglay[1], M Sughrue[1], S Doyen[1]
[1]*Omniscient Neurotechnology, Sydney, New South Wales*

Purpose
Constrained spherical deconvolution (CSD) has become a leading model for resolving magnetic resonance imaging tractography, however the minimum requirements for data acquisition in terms of the number of gradient directions and their spatial distribution are yet to be investigated. As CSD becomes more widely utilized in clinical settings and approaches, identifying the minimum requirements for accurate tractography is integral to ensure quality process and optimize resource expenditure. Herein, we simulated various acquisition parameters and observed their impact for generating CSD tractography against quality thresholds.
Materials and Methods
We obtained 30 normal subject diffusion weighted imaging (DWI) scans performed on a 3T Siemens Trio scanner. Images were processed using the prescribed processing steps from the diffusion imaging in python (DIPY) package available in the Python language. From the original 64 gradient directions collected in each series, test cases with subset gradient directions were built for each subject to simulate if the images were collected at: 12,16,20,24,28 and 32 gradient directions. Fiber response functions were estimated for each subset, and the diffusion tensors were calculated using CSD at four different maximal spherical harmonic degrees. Deterministic tractography was performed with random seeding. In addition to visually inspecting the quality of tracts generated, metrics representing the number and average length of streamlines were collected to assess the quality of CSD output.
Results
Increasing the number of gradient directions collected in DWI improved the quality of tractography generated using CSD. Retaining a uniform distribution of included gradient directions significantly improved the minimum requirements to generate accurate CSD Tractography. The number of spherical harmonic degrees used during CSD was positively related to the number of gradient directions required to generate accurate tractography.
Conclusions
A minimum of 28 non-b0 slices constitutes the lower threshold requirement for generating credible CSD tractography that passes the test of the expert eye at 6 spherical harmonics. In general, increasing the number of spherical harmonics in CSD tractography generation increased the requisite gradient directions. Additionally, having a uniform distribution of gradient directions was key to generating accurate tractography, and the threshold requirement was lowered when the distribution of included gradient directions was uniform.

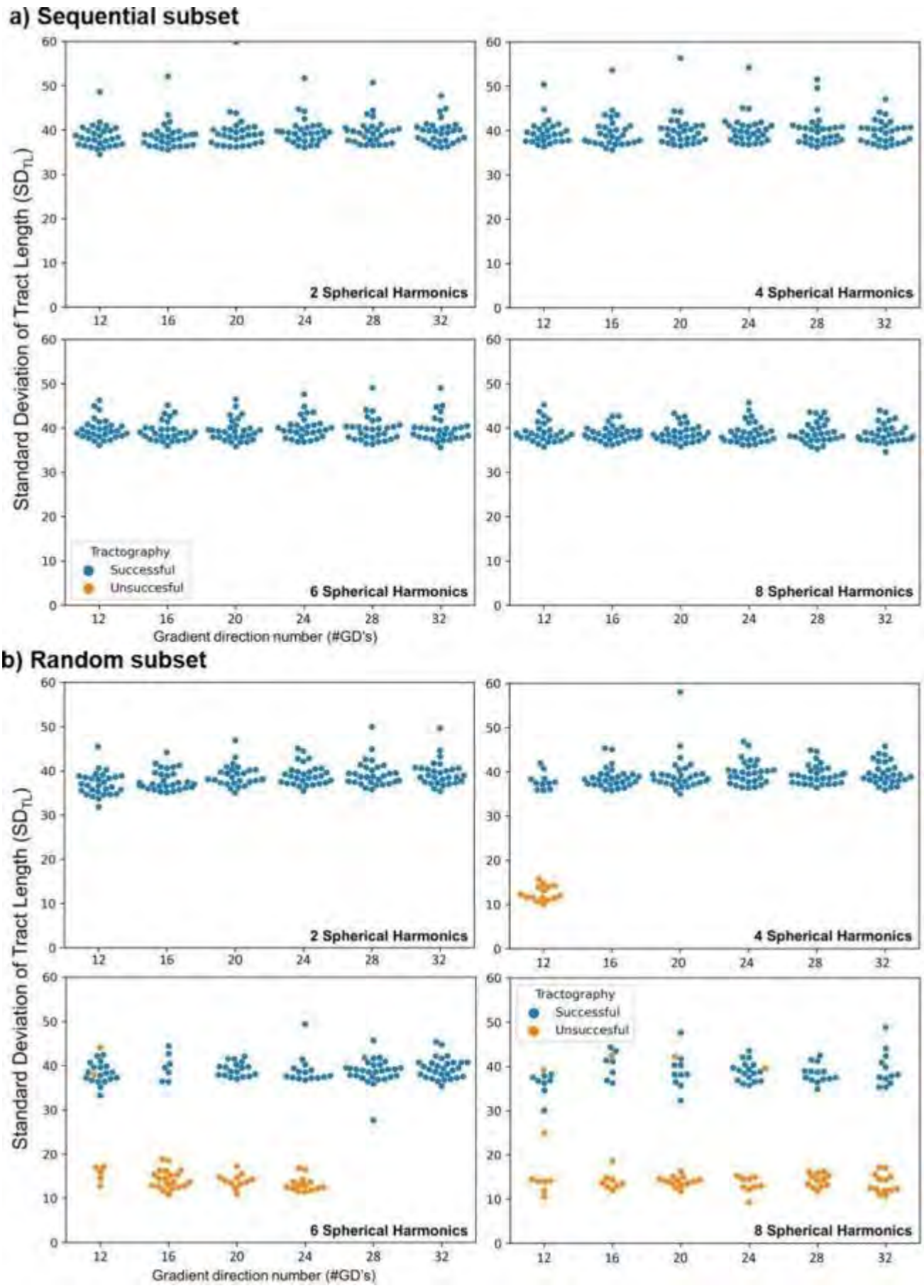

(Filename: TCT_487_Picture1.jpg)

193

Pretreatment Neuroimaging for Personalized Antidepressant Response Prediction

F Ali[1], R Parsey[1], C DeLorenzo[2]

[1]Stony Brook University, Stony Brook, NY, [2]Stony Brook University, Stony Brook, NY

Purpose

Pretreatment neuroimaging data can provide information for identifying neural markers to predict depression remission [1,2], but no image-based markers have been advanced to clinic [3], and identification of these markers has been inconsistent [4]. The purpose of this abstract is to develop a machine learning model for predicting antidepressant efficacy using brain structural and connectivity information from pretreatment neuroimaging data.

Materials and Methods

This study used pretreatment noninvasive magnetic resonance imaging (MRI) including structural MRI (sMRI) and diffusion MRI (Diffusion Tensor Imaging, DTI) performed in the same scanner in a recently completed multicenter antidepressant, placebo-controlled trial (n=167; Train/Cross-validation/Test split: 60/20/20). The brain structural measures include number of vertices (unitless), surface area (mm^2), gray matter volume (mm^3), average thickness (mm), thickness standard deviation (mm), integrated rectified mean curvature (mm^-1), integrated rectified Gaussian curvature (mm^-2), folding index (unitless), and intrinsic curvature index (unitless). The DTI measures include fractional anisotropy (FA) of cerebral white matter. The depression severity of subjects was quantified by expert raters. The imaging features, along with age, sex, treatment status, handedness (measured using Edinburgh Handedness Inventory (EHI) 20-item questionnaire) and scan site information, were entered into the widely used machine learning classifier, extreme gradient boosting (XGBoost) [5] to predict antidepressant efficacy after eight weeks of treatment. The model hyperparameters were optimized to control for overfitting, a major limitation of XGBoost.

Results

Our predictive model showed 75% specificity with 64.71% overall accuracy for predicting antidepressant response. The XGBoost classifier selected following 5 neuroimaging features as the most predictive of antidepressant efficacy: mean curvature of the right pericallosal sulcus (mm^-1), folding index of the left superior frontal gyrus (unitless), intrinsic curvature index of the left anterior transverse collateral sulcus (unitless), average cortical thickness of the right frontal pole (mm), and standard deviation of cortical thickness of the left orbital gyrus (mm).

Conclusions

Our predictive model using neuroimaging features hold the potential to be clinically useful for predicting antidepressant response. Our future research will focus on improving sensitivity (50%) of this model through hyperparameter tuning.

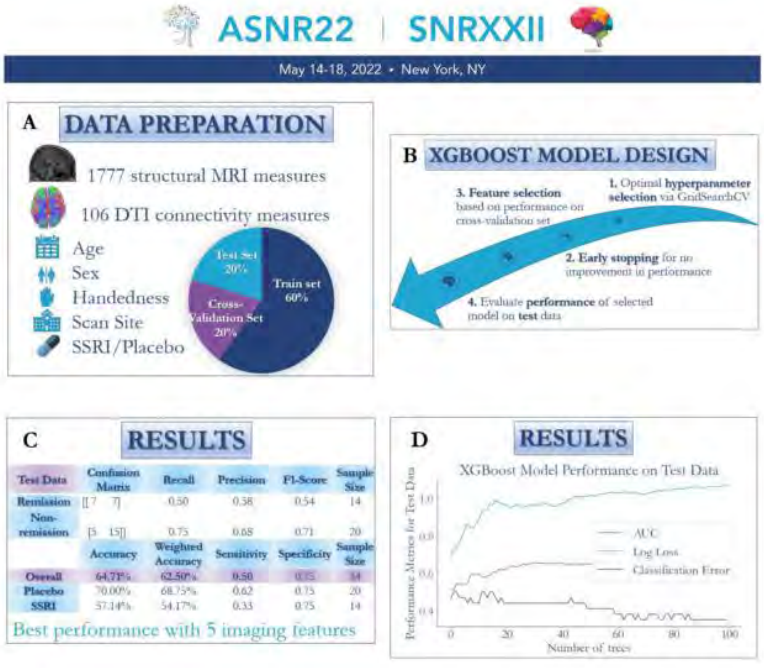

Fig 1.

(*A*) Data preparation with 1,777 structural MRI and 106 DTI connectivity measures from the brain of individual subjects, along with information on age, sex, handedness, scan site, and treatment status (selective serotonin reuptake inhibitor or SSRI/placebo). The data set was split into 60% train set, 20% cross-validation set and 20% test set. (*B*) The model was optimized with hyperparameter selection with GridSearchCV, early stopping for subsequent iterations that showed no improvement in performance, and model selection based on cross-validation performance. (*C-D*) Performance metrics for model evaluation on unseen test data.

AUC: Area under the receiver operating characteristic (ROC) Curve.

(Filename: TCT_193_asnr_graphic.jpg)

549

Quantitative Cellular and Molecular Neuroimaging using Magnetic Resonance Phenotyping

A Singh[1], V Jain[1], J Yu[1]

[1]*University of Wisconsin School of Medicine and Public Health, Madison, WI*

Purpose

Multi-compartment diffusion weighted (MC-DWI) MRI provides quantitative non-invasive imaging of brain microstructure. Previous studies have demonstrated MC-DWI MRI as a highly sensitive but non-specific tool for neuroimaging (1,2,3). Radiomics analyses have recently been used to generate possible biomarkers from large databases of human radiological images, however these studies suffer from poor standardization and weak biological interpretability (4,5). This project introduces and presents a novel bottom-up technique for neuroimaging biomarker development we term Magnetic Resonance Phenotyping (MRP). MRP is a standardized neuroimaging technique and quantitative data analysis pipeline that combines the biological sensitivity of MC-DWI with the specificity of radiomic image analyses to detect neuropathological changes that correspond to cellular and molecular biology.

Materials and Methods

Ex-vivo MC-DWI MRI, neurite orientation dispersion and density imaging (NODDI) modeling, and automatic region of interest (ROI) segmentation were used to examine the microstructural differences in the genetic rodent models of neurodevelopmental illness (Nrxn1 -/- (n=4), Disc1 -/- (n=6)) and Alzheimer's disease (5XFAD (n=6)) against control animals. Texture features were extracted with a fix bin width of 0.1 using Pyradiomics, resulting in 88 untransformed radiomic features per ROI analyzed. Statistically significant differences in texture features between control and experimental animals for a given ROI were identified using Student's t-tests followed by multiple testing correction (FDR $p<0.05$) with Python SciPy, NumPy, and Pandas libraries.

Results

32 radiomic features were identified as significantly different (FDR $p<0.05$) in NODDI ODI images of the left hippocampus of 5XFAD animals, consistent with early deposition of histologically confirmed amyloid beta, demonstrating the higher sensitivity of MRP over conventional neuroimaging analyses. In the functionally related Nrxn1 and Disc1 animal models, high similarity (Jaccard Index of 0.62) of right hippocampus radiomic features for NODDI parameters of ODI was discovered, indicating that MRP detects similar signatures in these models of disrupted synaptic function.

Conclusions

MRP is an innovative and novel imaging technique and data analysis method that demonstrates exquisite sensitivity to neuropathology and an expanded parameter space capable of specifically capturing the complexity of underpinning cellular and molecular changes.

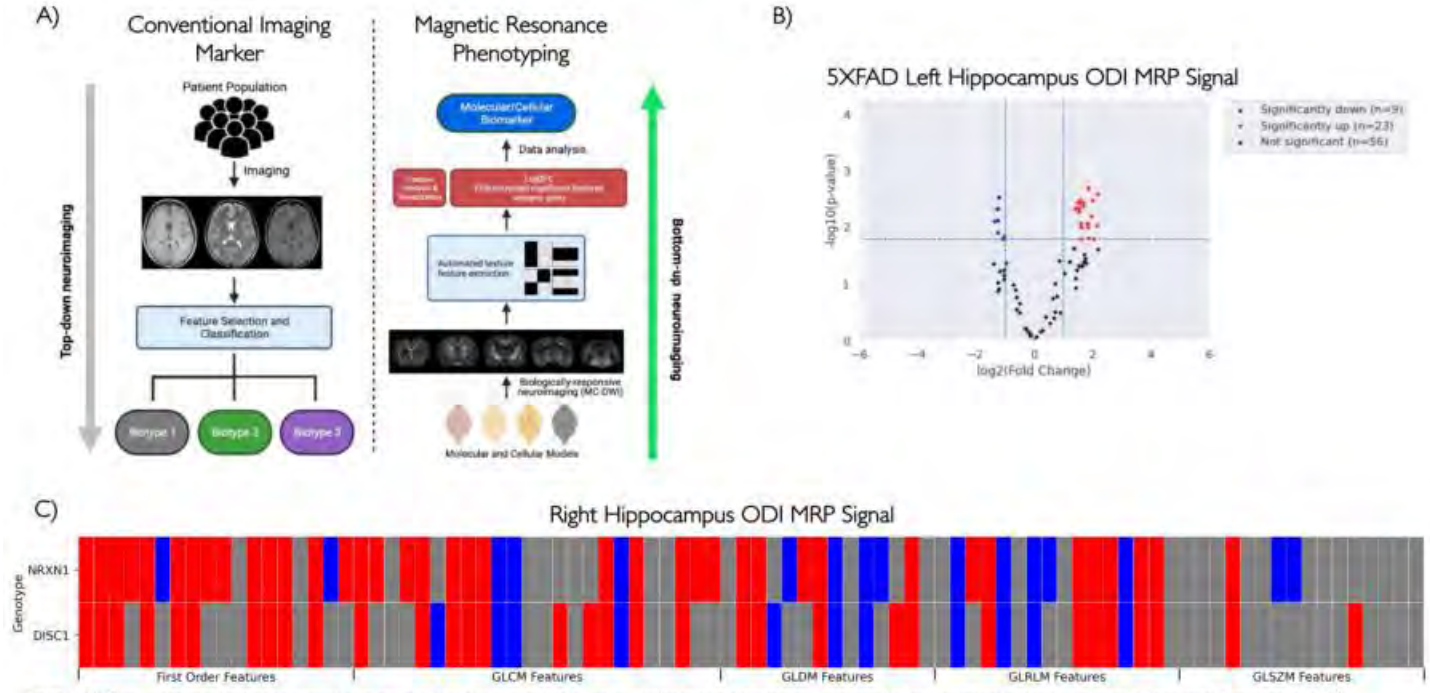

Figure 1: A) Diagrams demonstrating the current, conventional, top-down approach to neuroimaging marker development compared to our proposed bottom-up Magnetic Resonance Phenotyping (MRP) method for neuroimaging marker development. B) Volcano plot of the MRP signal produced from the ODI parameter of the NODDI signal in the left hippocampus of the 5XFAD model of Alzheimer's dementia. C) MRP signal produced from the ODI parameter of the NODDI signal in the right hippocampus of the Nrxn1 and Disc1 knockout models of synaptic dysfunction (Jaccard Similarity Index of 0.629). Red signifies significant increase in the signal. Blue signifies a significant decrease in signal. Gray indicates no difference in signal from control animals.

(Filename: TCT_549_abstract_figure.jpg)

1454

Reinforcement learning can accurately classify Autism and Neurotypical resting state fMRI for very small training sets

J Stember[1], H Shalu[2]

[1]Memorial Sloan Kettering Cancer Center, New York, NY, [2]Indian Institute of Technology Madras, Madras, Madras

Purpose

Functional MRI (fMRI) data, is generally sparse and difficult to collect in large, labeled data sets. As such, an artificial intelligence (AI) method that can train effectively on small fMRI data sets would be useful in a wide variety of research applications. In recent work, Li et al. [1] developed and applied Graph Neural Networks (GNNs) to train fMRI graphs using Supervised Deep Learning (SDL) to classify autism spectrum disorder (ASD) versus control neurotypical patients. Reinforcement learning (RL) has emerged as an effective way to train on sometimes very small data sets [2]. In this work, we set out to combine GNNs with RL. We sought to show as proof-of-princple that RL + GNNs can effectively classify fMRI graphs even when trained on a very small number of such graphs. We hypothesized that RL can learn in a generalized manner on the small data set, whereas the SDL would overfit and the training set and not generalize well to a separate testing set.

Materials and Methods

We employed RL using Deep Q Networks whose architecture is essentially identical to GNNs. We studied a small subset of the full public ABIDE database [3], examining 100 training images with both SDL and RL. We tested both types of trained networks on a separate testing set of 50 patients.

Results

RL achieved markedly better testing set accuracy at 74%, compared to 46% from SDL. This result is displayed in Figure 1.

Conclusions

We have shown proof-of-principle application of RL using Graph Neural Networks to a small training set of 100 fMRI graphs. We have demonstrated that RL is able to learn in a generalized manner even on this very small training set, whereas SDL cannot learn effectively on such a small training set. Future work will refine our initial RL approach to approach higher accuracy, and apply the approach to fMRI data sets at our institution.

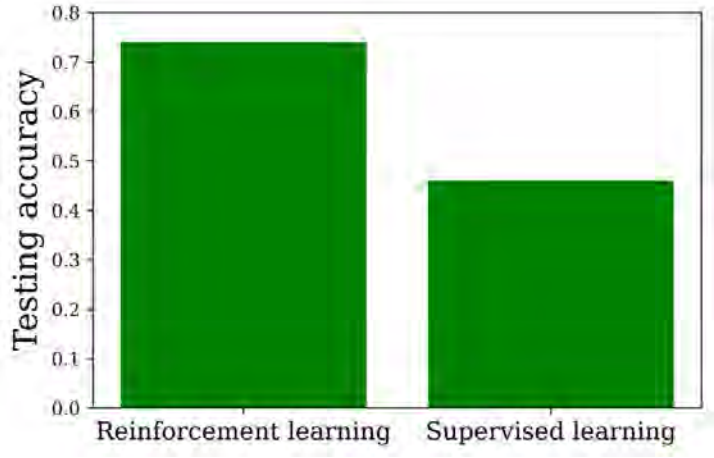

(Filename: TCT_1454_acc_comp_classification-2.jpg)

1158

Resting state fMRI for presurgical mapping: how much data is needed?

M Fakhri[1], J Shimony[2], R Eldaya[3]

[1]UCSF, SAN FRANCISCO, CA, [2]Washington University School of Medicine, St. Louis, MO, [3]Washington University, St Louis, MO

Purpose

Resting-state functional magnetic resonance imaging (RS-fMRI) is of particular value as a means of non-invasive presurgical mapping because it does not require patient compliance with task performance. In the current standard clinical practice, approximately 5-10 minutes of data is acquired, and image analysis is done with spatial independent component analysis (sICA) (1). However, results often generate highly inconsistent maps and low localization precision. The central hypothesis of this study is that by increasing the amount of acquired data (and thus signal-to-noise ratio), the precision of RS-fMRI localization can be significantly increased. The aim is to quantify the relationship between language cortex localization error (in millimeter) and the quantity of analyzed data (in minutes).

Materials and Methods

A total of 18 patients with a glial tumor near Broca's area, WHO grade 2-4, centered in the inferior frontal gyrus, were included. For each subject a total of 30 minutes functional fMRI data was available. Data was randomly resampled into increments of 1-minute, making examinations blocks spanning from 1 to 30 minutes. ICA was computed using FSL (Oxford University, UK, https://fsl.fmrib.ox.ac.uk/). The language component was selected by three neuroradiologists and inter-rater reliability was calculated. For each block of duration, the root mean square error (RMSE) in localization of the center of mass for each individual was calculated and plotted against the quantity of analyzed data.

Results
The mean age of the study participants was 44.7±11.2 years and 50% of the patients were female. Interclass correlation for the three readers was 0.534, p= 0.002. Our results show with increase in the analyzed data quantity, localization error measured in millimeter (center of the language mass to the mean center of the mass) will decrease (fitted curve r=0.88, p<001). However, this inverse relationship was saturated after 20 minutes. These findings are summarized in figure 1.
Conclusions
Longer acquisition times improve the precision of RS-fMRI language localization, but it ultimately asymptotes (Figure 1). This demonstration is essential to prove that more data is needed to improve current practice. It also assures that the optimum clinical scan times will still be achievable given the behavior of the time versus error function curve (plateau in <20 minutes). We also provided proof for the feasibility of measuring localization errors in millimeters as it matters the most to the neurosurgical team.

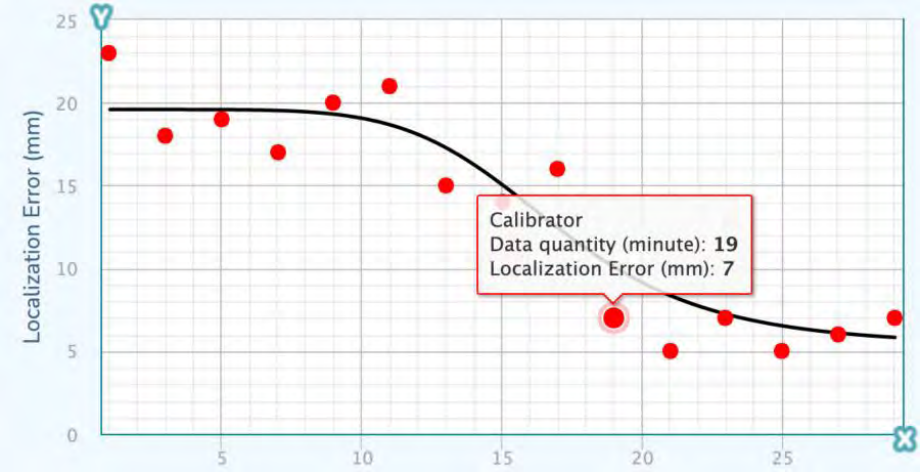

(Filename: TCT_1158_Figure1.jpg)

Wednesday, May 18, 2022
10:45 AM-12:15 PM
Scientific Podium Presentations: Vascular

587
Amplified Flow to Assess Wall Motion of Intracranial Aneurysms: A Comparative Analysis Between Unstable Vs. Stable Aneurysms
A Pionteck[1], J Abderezaei[2], Y Chuang[1], Y Sakai[3], P Belani[4], B Rigney[5], R De Leacy[6], J Fifi[7], A Chen[8], R Jahan[8], g duckwiler[9], J Sayre[8], J Mocco[5], M Kurt[10], K Nael[8]
[1]Stevens Institute of Technology, Hoboken, NJ, [2]stevens institue of technology, Hoboken, NJ, [3]N/A, N/A, [4]Mount Sinai Hospital, new york, NY, [5]Icahn School of Medicine at Mount Sinai, New York, NY, [6]Mount Sinai Health System, New York, NY, [7]Icahn School of medicine at Mount Sinai, New York, NY, [8]UCLA, Los Angeles, CA, [9]ucla, Los Angeles, CA, [10]stevens institue, Hoboken, NJ

Purpose
Intracranial aneurysm (IA) wall motion abnormalities have been associated IA growth and rupture 1,2. Detection and accurate assessment of wall motion however is challenging considering small size of IA. Recently, a new image processing algorithm called amplified Flow (aFlow) has been used to successfully track IA wall by combining the amplification of cine and 4D flow MRI 3. We sought to apply aFlow to assess wall motion as a potential marker of instability in paired-wise analysis of patients with unstable vs. stable aneurysms.
Materials and Methods
In this prospective study, patients with IA underwent MRI including MRA and 4D flow at baseline and were followed up to 5 years. After a cross sectional analysis at the end of 5th year from initial imaging, 10 patients were identified with growing IA. These were matched with a cohort of patients with similar size and location of IA, whose aneurysms remained stable in size. 4D flow imaging parameters: (3D phase-contrast peripherally-gated sequence, TR/TE: 5.5/2.8 ms; FOV: 160 x 112 mm, matrix: 224 x 224 mm2, 40 x 0.8 mm slices, 3D-velocity encoding value: 80 cm/s). The aFlow algorithm was applied to the 4D flow MRI data to visualize and quantify the 3D displacement of the IA wall at selected frequency ranges (main harmonics: 0-1.7Hz, higher frequencies: 1.7-10Hz). Histogram analysis was performed and 10th, 50th and 90th percentile values of wall motion in addition to standard deviation (SD) and interquartile range (IQR) of wall deformation were calculated. The associations of aFlow parameters with commonly used risk factors and morphometric features were assessed using a paired-wise univariate and multivariate analyses.

Results
There was no significant difference in basic demographic (age, sex, race), risk factors such as smoking, hypertension, alcohol consumption, PHASES scores, and morphometric features (size, aspect ratio) between the two group. 90th percentile values of IA wall displacement acquired from the aFlow was 68% higher in unstable IAs (P=0.03). Unstable IAs also showed higher variability of deformation across their geometry evident by dispersion variables including SD and IQR (Figure). ROC analysis also showed high predictive accuracy for differentiating stable from unstable IAs using 90th% wall displacement and dispersion variables (Figure).
Conclusions
aFlow MRI-derived wall motion variables including 90th percentile wall displacement and dispersion variables including SD and IQR at baseline may be able to identify unstable from stable IAs.

Variable	Stable (n 10)	Unstable (n 10)	P value	AUC, sensitivity, specificity
$10^{th\%}$	0.987 (0.381)	1.373 (0.438)	0.511	--
$50^{th\%}$	1.126 (0.402)	2.018 (0.441)	0.108	--
$90^{th\%}$	1.389 (0.584)	2.336 (0.721)	0.035	0.85, 100%, 70%
SD	0.259 (0.179)	0.655 (0.216)	0.008	0.91, 90%, 90%
IQR	0.388 (0.301)	1.024 (0.381)	0.010	0.90, 90%, 80%

(Filename: TCT_587_aFlowfigure.jpg)

189

Applying Deep Learning Convoluted Neural Networks to Identify Aneurysms on 3-D Time-Of-Flight MRA Sequences

S Culleton[1], C Vachet[2], E Quigley[3], J Roberts[2], M Alexander[1], A Sakata[4], J McNally[1]
[1]University of Utah, Salt Lake City, UT, [2]University of Utah, Salt Lake City , UT, [3]University of Utah, SLC, UT, [4]Kyoto University, Kyoto, N/A

Purpose
This study aimed to develop and test a deep learning workflow for the detection of intracranial aneurysms on 3-D TOF MRA.
Materials and Methods
In this IRB-approved retrospective study, 3-D TOF sequences acquired at 3T between 2015-21 were reviewed for the presence of aneurysms. Thrombosed and fully treated aneurysms were excluded. Positive cases were confirmed by two neuroradiologists using consensus and additional CTA and DSA imaging when available. Aneurysms were manually segmented using ITK-SNAP [1] to generate the ground truth dataset. A deep learning pipeline was developed with DeepMedic [1] applying 5-fold-cross-validation using the dataset divided into training (69%), validation (11%) and test (20%) cases. Image acquisitions were down-sampled, and intensity normalized to a zero-mean, unit-variant space. Output predictions from the model were post-processed, using a detection threshold of 5mm3 if multiple predictions occurred, and a maximum aneurysm count of 5. Segmentation accuracy was measured using the Dice similarity coefficient and Hausdorff distance. The overall sensitivity of aneurysm detection for all sizes was determined.
Results
The dataset consisted of 122 subjects with 135 aneurysms (Table) grouped by size into three categories: ≤3 mm was classified as small (n=40, 29.6%), >3 mm and ≤7 mm as medium (n=69, 51.1%), and >7 mm as large (n=26, 19.3%). Post-processing steps improved the Dice similarity coefficient from 0.38 (SD, 0.31) to 0.41 (SD, 0.34), and Hausdorff distance from 153.62 (SD, 40.53) to 79.23 (SD, 62.68). Additionally, the number of false positives decreased to 1.4 FP/case (SD, 1.37). The overall sensitivity of detection was 68.9% (95% CI [61.08%-76.70%]). Sensitivity was greatest for large aneurysms (96.2%, [88.76%-100%]), moderate for medium-sized aneurysms (78.3%, [68.53%-87.99%]), and poor for small aneurysms (35.0%, [20.22%-49.78%]).
Conclusions
Deep learning can be used with 3-D TOF MRA to detect aneurysms larger than 3 mm with moderate-to-high sensitivity. The sensitivity of this model for detecting small aneurysms may improve with further training and processing steps.

Ground Truth Dataset	
Subject Characteristics	**Subjects n=122**
Age, mean (SD)	61.27 (15.3)
Females, n (%)	87 (71.3)
No of aneurysms, n (%)	
- Single	111 (91.0)
- Multiple aneurysms	11 (9.0)
-2 aneurysms	9 (7.4)
-3 aneurysms	2 (1.6)
Aneurysm Characteristics	**Aneurysm n=135**
Location, n (%)	
Anterior circulation	113 (83.7)
- ICA	50 (37.0)
- ACA/ACOMM	33 (24.4)
- MCA	30 (22.2)
Posterior Circulation	22 (16.3)
- Basilar	9 (6.8)
- Vert	7 (5.2)
- PCOMM	6 (4.4)
Size, (mm)	
- Largest diameter, mean (SD)	5.6 (3.5)
- Small ≤3 mm, n (%), mean (SD)	40 (29.6), 2.6 (.6)
- Medium > 3 & ≤ 7mm, n (%), mean (SD)	69 (51.1), 5.2 (1.1)
- Large > 7 mm, n (%), mean (SD)	26 (19.3), 11.2 (3.7)
- Volume, mean (SD) mm^3	108.7 (283.6)
Shape, n (%)	
- Saccular	128 (94.8)
- Fusiform	7 (5.2)
Confirmatory imaging, n (%)	
- DSA or CTA	111 (90.9)

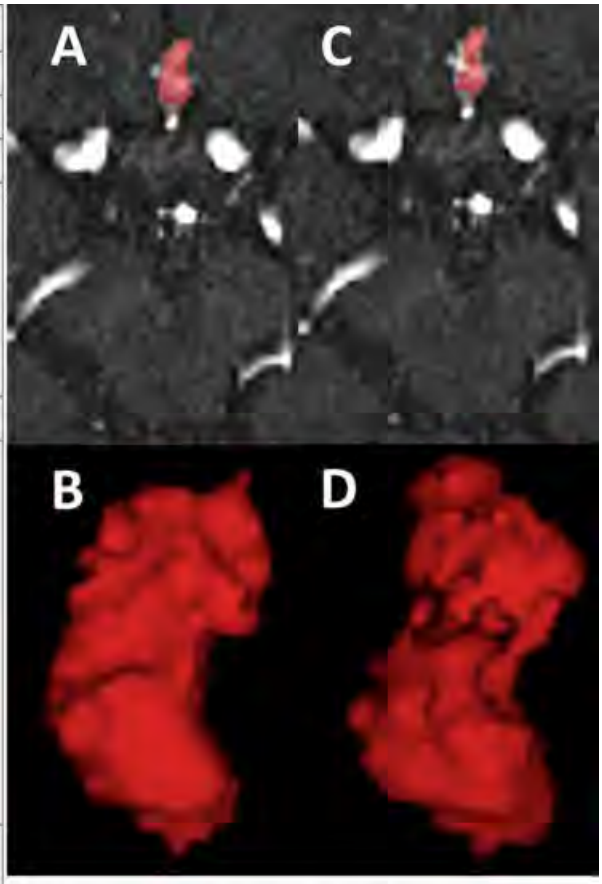

Table: displays the patient and aneurysm characteristics that formed the ground truth dataset for manual segmentation.

Images: A-B shows an anterior circulation, ACA aneurysm, which was manually segmented (A, red label) and the 3-D image generated with ITK-SNAP software (B).
Images C-D shows the model identifying the aneurysm with DeepMedic software (C, red label) and the associated predicted 3-D volume (D).

(Filename: TCT_189_Aneurysmcombinedimage.jpg)

1162

Assessment of hemodynamic biomarkers in severe middle cerebral artery ICAD patients using cerebrovascular dual-venc 4D Flow MRI

J Moore[1], M Aristova[1], R Abdalla[1], A Ragin[1], E Russell[1], F Caprio[1], S Schnell[2], M Markl[1], S Ansari[1]
[1]Northwestern University, Chicago, IL, [2]University of Greifswald, Greifswald, Germany

Purpose
Intracranial atherosclerotic disease (ICAD) results in narrowing of major intracranial arteries in the circle of Willis (CoW) and is associated with a risk of ischemic stroke [1,2]. Dual-venc 4D Flow MRI allows for comprehensive in-vivo assessment of cerebrovascular hemodynamics over the cardiac cycle with full volumetric coverage of the CoW. Our goal was to assess the impact of ICAD on changes in hemodynamic biomarkers in the CoW, including vessel flow normalized to total cerebral inflow (flow through the Internal Carotid Arteries (ICAs) and Basilar Artery (BA)), peak velocity, pulsatility index (PI), and resistive index (RI).
Materials and Methods
10 ICAD patients with severe middle cerebral artery (MCA) stenosis (69.0 +/- 14.6 years, 6 female) and 10 healthy controls (48.1 +/- 21.5 years, 4 female) with no cerebrovascular disease history were included in this retrospective IRB approved study. Two experienced neuroradiologists (S.A.A. and R.A.) used the WASID method to quantify and confirm >70% MCA stenoses [3]. 3T MRI (MAGNETOM Skyra, Siemens, Erlangen, Germany) ICAD protocol included dual-venc 4D Flow MRI [4] (TR = 6.1 ms, TE = 3.3

ms, flip angle=15 deg, low venc = 80 cm/s, high venc = 160 cm/s, voxel size = 1 mm isotropic, temporal resolution 86.8 ms, k-t PEAK-GRAPPA acceleration R = 5). 4D Flow MRI data analysis was conducted as previously described [5]. Hemodynamic data was extracted via analysis planes placed every 1 mm along segmented vessels of interest: BA, ICA, MCA, Anterior Cerebral Artery (ACA), and Posterior Cerebral Artery (PCA). Parameters were compared vessel-wise for patients vs healthy controls and for stenosis affected (Aff) vs unaffected (UA) hemispheres using the Wilcoxon rank sum test.

Results

Global hemodynamics were compared using patient Aff and UA vessels vs healthy controls (see Figure). PI and RI were significantly different for all CoW vessels, $p < 0.01$. UA MCA, ACA, and PCA showed evidence of flow redistribution, $p < 0.05$. Aff vs UA hemisphere analysis suggests a trend toward flow compensation in ICA and MCA. UA ICA and MCA vessels show a 16.3% and 13.2% increase in flow and a 12.9% and 8.63% increase in peak velocity, respectively.

Conclusions

Global hemodynamics are significantly altered in ICAD patients relative to controls. In a limited sample size, affected hemispheric hemodynamics show trends toward differences vs unaffected hemisphere – suggesting flow redistribution as a result of focal stenosis. There is a need for a larger cohort and age-matched controls.

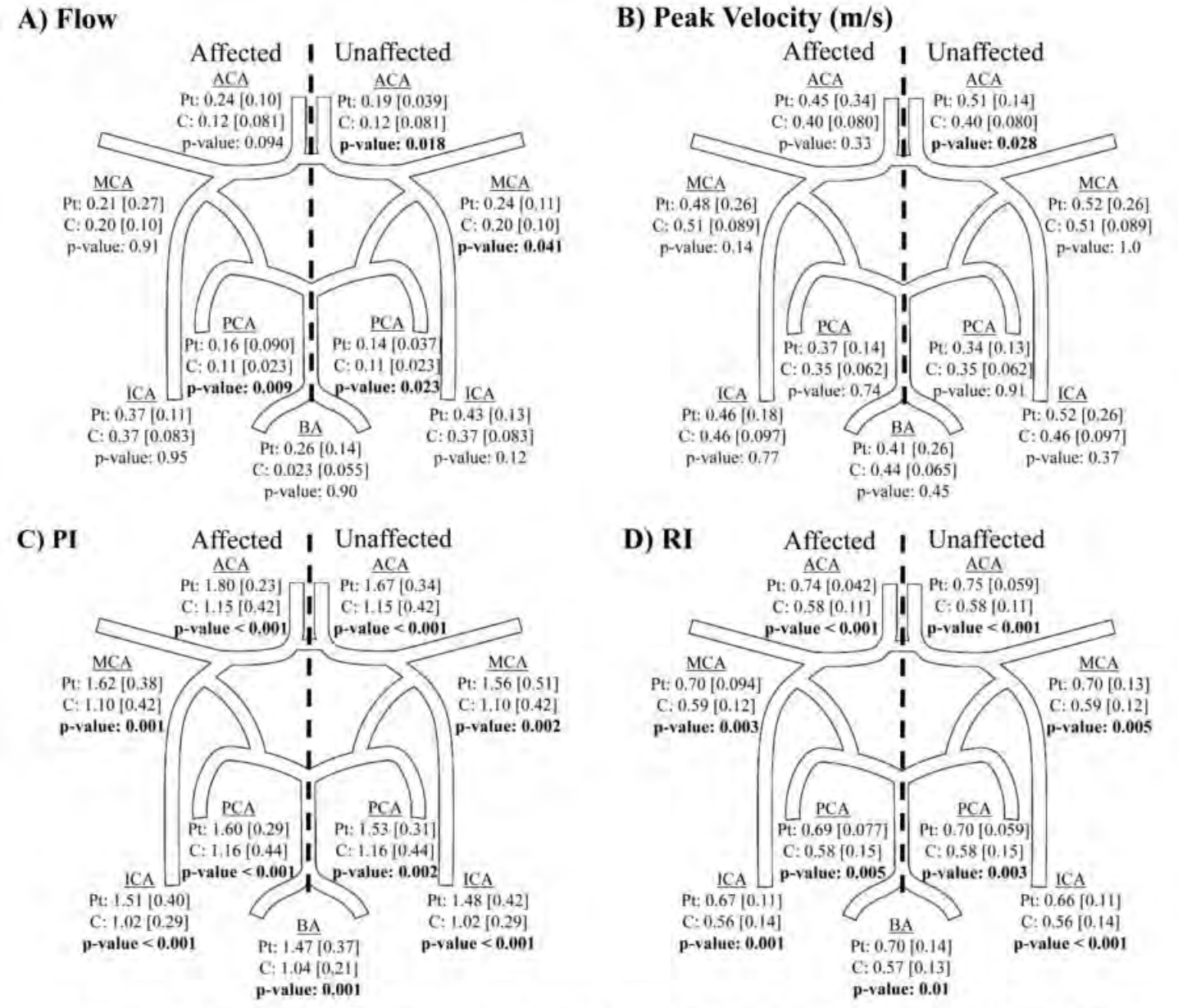

Figure 1: Circle of Willis (CoW) diagrams show the regional distribution of hemodynamic measures (flow, peak velocity, PI, RI, reported as median and interquartile range) across different CoW vessels. For each CoW segment, hemodynamic parameters for ICAD patients (grouped by affected and unaffected hemisphere) are directly compared to healthy controls. Significant differences ($p < 0.05$) are shown in bold.

(Filename: TCT_1162_ASNR_2022_Fig_BW.jpg)

675

Background Subtraction Angiography with Deep Learning using Multi-Frame Spatiotemporal Angiographic Input

D Cantrell[1], L Cho[1], C Zhou[1], A Shaibani[1], M Potts[2], B Jahromi[3], S Ansari[4]

[1]Northwestern University, Chicago, IL, [2]Northwestern University - Feinberg School of medicine, Chicago, IL, [3]N/A, N/A, [4]Northwestern University, CHICAGO, IL

Purpose

Catheter Digital Subtraction Angiography (DSA) is an essential imaging technique that allows physicians to visualize blood vessels, and perform minimally-invasive interventions that treat numerous pathologies, including stroke and myocardial infarction. However, DSA images are markedly degraded by all voluntary, respiratory, or cardiac motion artifact that occurs during the exam acquisition. Prior efforts directed toward enhancing DSA images with artificial intelligence have focused on extracting vessels from individual, isolated 2D angiographic frames utilizing a 2D U-Net generator [1,2].

Materials and Methods

Cerebral angiograms generated by Siemens Artis Q and Artis Zee systems were collected and processed on a Dell 7290 Precision workstation with an NVIDIA RTX 8000 GPU using TensorFlow 2.3. A total of 516 angiographic studies were collected from 404 unique patients between January 1, 2019 and December 31, 2019. From each of these angiographic series, we used a method based on OpenCV ORB to identify matching image features across all angiographic frames, and estimate the affine transformation from all frames of the series back onto the base frame. Angiograms were separated into two categories: "motionless" (2468 series in the training set and 713 in the test set), and "motion degraded" (2577 in the training set and 689 in the test set). Series of affine matrices measured from the "motion degraded" category were then applied to the "motionless" category to create a motion-augmented dataset suitable for training 2D and 3D UNet models to predict vascular intensities from raw angiographic input in the setting of motion.

Results

Inferences were made on a hold-out test set, and the resulting images were stretched to utilize the full dynamic range. When compared to 2D UNets with a single frame of raw angiographic input, 3D UNets utilizing 16 input frames achieve a reduced Mean Squared Error (723±418 vs 554±352, $p < 0.0001$; mean ± std dev), and an improved Multi-Scale Structural Similarity (0.86±0.08 vs 0.93±0.05, $p < 0.0001$) on motion-degraded angiographic exams.

Conclusions

Temporal information can boost the performance of Background Subtraction Deep Learning algorithms when applied to motion-degraded raw angiographic series.

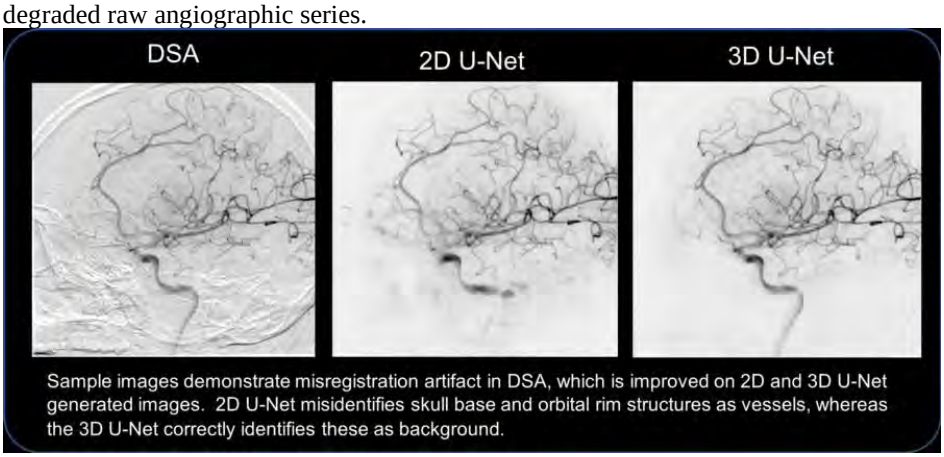

(Filename: TCT_675_Fig1JPG.jpg)

236

Interrelation between cardiac and brain small vesse disease: a quantitative PET-MRI study

B Mazini[1], M Dietz[1], B Marechal[2], R Corredor-Jerez[2], J Prior[1], V Dunet[1]

[1]Lausanne University Hospital, Lausanne, Vaud, [2]Siemens Healthineers, Lausanne, Vaud

Purpose

Beyond large vessel occlusions, small vessel disease (SVD) plays a crucial role in cardiac and brain ischemia. However, little is known about potential interrelation between both. We aimed at assessing the interrelation between cardiac and brain SVD by using quantitative Rb-82 cardiac PET/CT and brain MRI.

Materials and Methods

We retrospectively evaluated 186 patients without cardiac/brain large vessel disease, of whom 29 had pure cardiac SVD and 157 had no cardiac SVD as defined by cardiac perfusion PET/CT and coronarography. All underwent both a cardiac Rb-82 PET/CT and a brain 1.5T or 3T MRI (Siemens Healthcare, Erlangen, Germany). Left-ventricle myocardial blood flow (LV-MBF) and flow reserve (LV-MFR) were recorded from Rb-82 PET/CT, while Fazekas score, white matter lesion (WMab) volume, deep grey matter lesion (GMab) volume, and brain morphometry using the MorphoBox prototype software were derived from T1-/T2-weighted images.

Groups were compared with Kruskal-Wallis test, and the potential interrelation between heart and brain SVD markers was assessed using Spearman's correlation coefficient.
Results
Compared with healthy controls, patients with cardiac SVD had lower stress LV-MBF and MFR ($p<0.0019$) but similar Fazekas scores and WMab volumes ($p>0.45$). In patients with cardiac SVD, but not in controls, increased rest LV-MBF was associated with left-putamen Z-score reduction (rho=–0.62, p=0.033), right-thalamus (rho=0.64, p=0.026) and right-pallidum (rho=0.60, p=0.039) GMab volume increase. Decreased stress LV-MBF was associated with left-caudate Z-score reduction (rho=0.69, p=0.014) while decreased LV-MFR was associated with left- (rho=0.75, p=0.005) and right- (rho=0.59, p=0.045) putamen Z-score reduction and increased right-thalamus GMab volume (rho=–0.72, p=0.009).
Conclusions
This retrospective study data supports the hypothesis of an association between cardiac and brain SVD, especially regarding deep grey matter alterations.

106

Photorealistic depiction of intracranial arteriovenous malformations using cinematic rendering of volumetric MRI data for pre-surgical planning and patient education.

D Lakhani[1], A Al Halak[2], F Yuan[1], A Tarabishy[1], G Deib[1]
[1]West Virginia University, Morgantown, WV, [2]WVU Medicine, Morgantown, WV

Purpose
Cinematic Rendering (CR) algorithm incorporates a complex lightening technique that allows for the creation of photorealistic models from utilizing 3D reconstruction of isotropic imaging data. While the use of CR algorithms to depict computed tomography (CT) data is well described, its use to visualize MRI-based intracranial pathologies remains limited in the literature. The purpose of this study aimed to assess the utility of CR of MRI data in patients with arteriovenous malformations (AVM) for pre-surgical planning and patient education.
Materials and Methods
3D photorealistic reconstructed images of intracranial AVMs are provided. Isotropic, high-resolution volumetric T1-MPRAGE, 3T-MRI images of affected patients were derived from an institutional database. 3D Cinematic Rendering of these images was achieved using a customized post-processing software platform (Anatomy Education, Siemens, Munich, Germany). The appearance of cerebral structures of interest was accentuated by adjusting window, lighting direction and brightness settings of CR brain reconstructions derived from clinical MRI data.
Results
Consistent visualization of AVM components and critical adjacent structures, including the surrounding subarachnoid space, the vascular nidus, the feeding arteries, the draining veins, and adjacent cortex and white matter structures, was achieved. The 3D photorealistic brain-AVM models allowed for direct visualization of the intracranial pathology, including arterial feeders, the nidus, and venous outflow components. In addition, the model provided information regarding the AVM's spatial relationship to the native cortical surface anatomy, dural-based structures, and scalp landmarks for optimal presurgical planning. There are several advantages of using MRI-based in pre-surgical planning which includes: Ability to enlarge, rotate, and arbitrarily shift the model to provide additional viewing angles that cannot be achieved using conventional modalities; Complex, small structures can be displayed in photorealistic resolution; and better appreciation of the depth and architecture of the sulci.
Conclusions
MRI-based CR brain-AVM models could improve pre-surgical planning of patients with cerebral AVM by providing a simple-to-use imaging modality with a photorealistic resolution to help surgeons identify adjacent structures' relative proximity in all dimensions and degrees of freedom. Furthermore, CR provides a more intuitive understanding of AV shunt pathology in patient education and physician training.

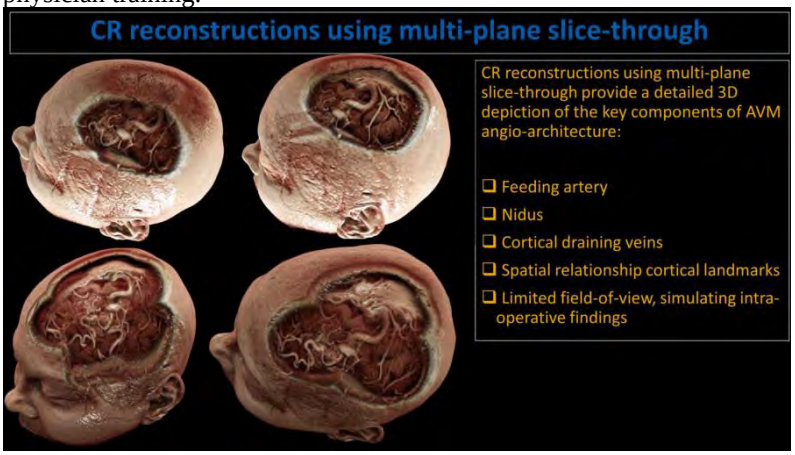

(Filename: TCT_106_ASNRFigure.jpg)

1371

Pictorial Essay of Central Variant of Acute Hypertensive Encephalopathy (Central PRES)

A Kamali[1], S JOSEPH[2], L Nunez-Rubiano[3], R Riascos[3]

[1]University of Texas Health Science Center Houston, Houston, TX, [2]UTH, Houston, TX, [3]The University of Texas Health Science Center at Houston, Houston, TX

Purpose

Posterior Reversible Encephalopathy Syndrome (PRES) is characterized by reversible vasogenic edema of the brain that presents with a wide range of clinical manifestations and is diagnosed via clinical findings and imaging. Pure central variant of this disease such as involvement of basal ganglia, brainstem, and cerebellum without cortical and sub-cortical edema is rare. Diffusion restriction and hemorrhages are uncommon manifestations of PRES. We provide a pictorial and educational review of various presentations of central variant of PRES to aid in neuroimaging interpretation and clinical management of the patients.

Materials and Methods

In this IRB approved retrospective study, we comprehensively reviewed the imaging findings of various presentations of central PRES in eight patients with confirmed diagnosis of central variant of PRES. The regions involved and the signal intensity of the affected areas on T1, T2, FLAIR and DW sequences were recorded by a neuroradiologist and a neuroradiology fellow. The location of the abnormal signal intensity as well as the presence or absence of atypical features such as diffusion restriction and hemorrhage were also recorded. Treatment response and follow up imaging were also reviewed.

Results

The imaging features and resolution time vary in each case. Basal ganglia, cerebellum, brainstem, and thalamus were involved. Hyperintense signals on T2 and FLAIR sequences were the most common findings. Few cases demonstrate restricted diffusion and hemorrhage. Imaging characters such as bilateral and multiple vascular territory involvement along with Clinical history and resolution of abnormality in follow up imaging were key in accurate diagnosis.

Conclusions

Only a rare number of individual cases of PRES have been described to show isolated involvement of the central areas of the brain. Due to the small number of reported cases of Central PRES, it is important that radiologists increase awareness of this variant of the syndrome and its presentation in order to accurately recognize and diagnose these patients in a timely manner to avoid unnecessary procedures such as biopsy.

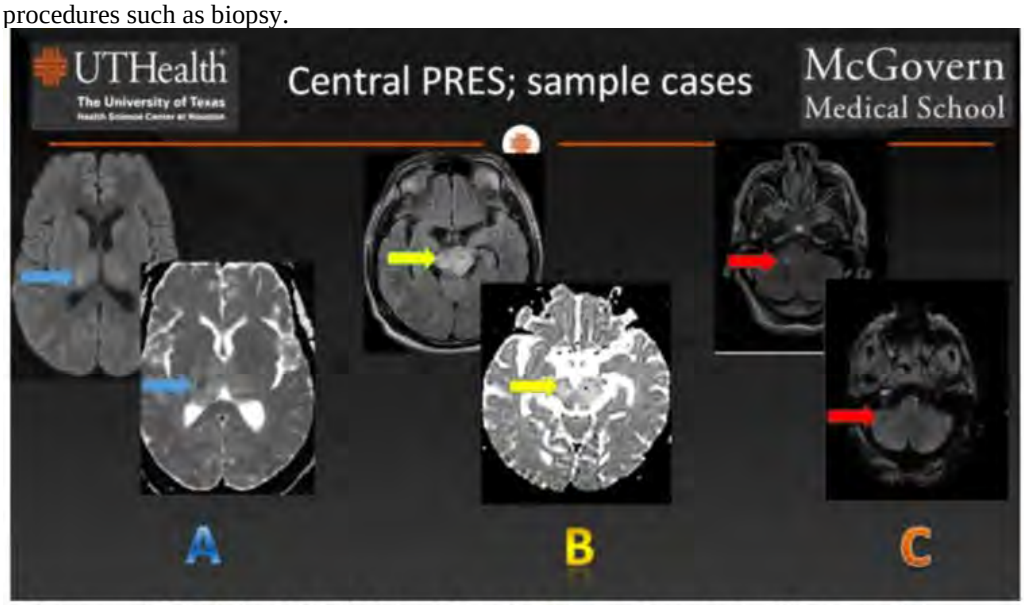

A), Increased T2/Flair signal in both thalami. The right thalamus demonstrates diffusion restriction.
B), Increased T2/Flair signal in the brainstem without diffusion restriction.
C), Increased T2/Flair signal in the cerebellum. The right cerebellum demonstrates micro-hemorrhages.

(Filename: TCT_1371_FIGURE.jpg)

327

Prevalence and Risk Stratification of Cerebral Microbleeds in Endocarditis

S Walia[1], C FREEMAN[1], V Patel[1], S MOHAN[1], a hassankhani[1]

[1]University of Pennsylvania, Philadelphia, PA

Purpose

Cerebral microbleeds (CMB) are a known complication of endocarditis affecting prognosis and timing of surgical intervention and may represent a metric of disease severity. The purpose of our study is to determine the prevalence and patterns of CMB in infective

endocarditis and non-bacterial thrombotic endocarditis (NBTE) with respect to variables that could increase risk of systemic embolization, including valve involvement and culture positivity.
Materials and Methods
A monocentric retrospective review was performed of all patients with suspected endocarditis undergoing MR brain imaging in a 3-year period from 2018-2020. Inclusion criteria were defined as patients with transesophageal echocardiography-confirmed endocarditis who underwent both CT and MR brain imaging within 1 week of the echocardiogram. Relevant imaging was independently reviewed by 2 neuroradiologists who were blinded to patient data, with discrepancies resolved by a 3rd neuroradiologist. The presence of microbleeds was determined by identifying foci of susceptibility on GRE.
Results
The study group included 91 patients with an average age of 59 years. Infective endocarditis was diagnosed in 84 patients and NBTE in 7. Valve involvement overall demonstrated left-sided predominance (75). Most common bacterial pathogens included Staphylococcus aureus (33) and group A streptococcus (21). Incidence of CMB in all patients was 67% (67% in IE and 71% in NBTE) with strong inter-rater concordance (k=0.9). Furthermore, 62% of cerebral microbleeds were occult on CT. Differential CMB laterality was noted with left heart involvement (70%) more common than right heart involvement (63%). No significant difference was noted in rate of CMB between S. Aureus (78%) and group A Streptococcus (76%). 45% of patients with infective endocarditis required cardiothoracic intervention for valve replacement within 7 days of admission.
Conclusions
There is a high incidence of cerebral microbleeds in patients with both infective endocarditis and NBTE that are occult on CT imaging. Increased incidence of CMBs was noted with left-sided (aortic and mitral) vegetations, but with no significant difference between bacterial pathogens. Additionally, a high proportion of patients with endocarditis-induced CMBs underwent early surgical intervention, possibly reflecting tolerable perioperative risk.

1273
Spectral detector CT derived virtual non contrast reconstructions improve differentiation between vascular structures and calcifications in stereotactic planning CT scans of cystic intracranial tumors
D Zopfs[1], C Nelles[1], C Zaeske[1], S Lennartz[1], N Große Hokamp[1], M Schönfeld[2], C Kabbasch[1], M Schlamann[1], K Laukamp[1]
[1]University Hospital Cologne, Cologne, NRW, [2]University Hospital Cologne, Köln, NRW

Purpose
Stereotactic biopsy of brain lesions is often preceded by contrast-enhanced CT of the head for intervention planning, in which differentiation between enhancement and calcified structures can be challenging. Besides craniopharyngioma, numerous other intracranial neoplasms may have cystic components possibly requiring stereotactic biopsy, such as glioblastoma or metastases (1,2). The aim of this study was to compare spectral detector dual-energy CT (SDCT) derived virtual unenhanced images (VNC) with conventional images (CI) for differentiating wall-associated contrast enhancement and calcifications of cystic intracranial tumors.
Materials and Methods
SDCT planning examinations prior to stereotactic biopsy of 48 patients with cystic brain tumors that had both wall-associated contrast uptake and calcifications were retrospectively included. Reference diagnoses were established by two radiologists using MRI. For each patient, two lesions were labeled in CI to be classified as contrast enhancement or calcification by two additional, independent radiologists. In a first reading CI were assessed, in a subsequent second reading session after eight weeks, CI and additional VNC were assessed. In addition to the diagnosis (enhancement vs. calcification), diagnostic confidence and image noise were assessed using 5-point Likert scales.
Results
Diagnostic accuracy increased from 64% to 83% with additional use of VNC compared to CI ($p<0.01$). Diagnostic confidence increased from 3(2-3) to 4(4-5), while image noise was rated lower in VNC (CI: (5(4-5) vs. VNC:4(3-5), $p<0.01$). While in CI the differences in contrast-to-noise ratios between brain white matter and marginal calcification or contrast enhancement were not significant (2.9 vs. 3.5, $p=0.07$), they differed significantly in VNC (2.6 vs. 1.3, $p<0.01$).
Conclusions
The additional usage of VNC resulted in significantly higher diagnostic accuracy and confidence compared to CI in the assessment of wall-associated contrast enhancement and calcifications of cystic brain lesions. In conclusion, VNC of SDCT facilitate an improved differentiation of wall-associated calcifications and contrast enhancements in stereotactic planning CT examinations in patients with cystic brain tumors.

1361
The Diagnostic Accuracy of Artificial Intelligence in the Detection of Cerebral Aneurysms: A Systematic Review and Meta Analysis
M Din[1], S Agarwal[1], D Wood[1], T Booth[2]
[1]King's College London School of Biomedical Engineering and Imaging Sciences, London, UK, [2]Kings College London, London, London

Purpose
Intracranial aneurysm rupture is a major cause of nontraumatic subarachnoid haemorrhage (1) and is associated with significant

morbidity and mortality. (2) Early identification with the help of automated systems may improve patient outcomes. The purpose of this study is to examine the diagnostic accuracy of fully automated algorithms for the detection of cerebral aneurysms in CTA,MRA, and DSA.

Materials and Methods

MEDLINE, Embase, Cochrane Library and Web of Science were searched, with no restrictions on language or publication date up until August 2021. Eligibility criteria included studies reporting fully automated algorithms that can detect cerebral aneurysms, with the input as a single MRI, CT or DSA study. The review was reported in accordance with PRISMA-DTA, and articles were assessed for quality using QUADAS-2. PROSPERO: CRD42021278454

Results

43 studies, of which 41 were retrospective, were included in the systematic review, from Oct 2004 to August 2021. 34 studies focused on the performance of an AI method as a standalone, whilst 9 studies assessed the AI assisting a reader. 20 used a conventional CAD tool (e.g., specialised filters or "classic" machine learning techniques), and 23 used deep learning methodology (e.g., convolutional neural networks). Only 13 studies used DSA as a reference standard. Studies prioritised a high sensitivity, which came at a cost of high false positive rates. The risk of bias assessment and concerns regarding applicability are summarised in figure 2. Forest plot for both groups are seen in figure 3. A scatter plot of false positive rates (1-specificity) and true positive rate (sensitivity) shown in figure 4 demonstrates individual ROC point estimates and a summary ROC (SROC) giving an AUC of 0.936 and 0.91 for AI alone and AI+reader respectively.

Conclusions

Majority of evidence is subject to limited interpretation due to a high risk of bias and applicability concerns. Two main issues are: lack of external test sets, and patient selection bias. Studies generally illustrate high sensitivity, suggesting that AI methods have potential in supporting clinicians in diagnosis of intracranial aneurysms. Few studies provide diagnostic accuracy metrics on the patient level, which limits clinical applicability. Further studies that investigate the position of AI in this clinical pipeline is required. Ideal studies would include AI tools that are trained on a diverse data set, and are evaluated on a large prospective cohort spanning multiple institutions.

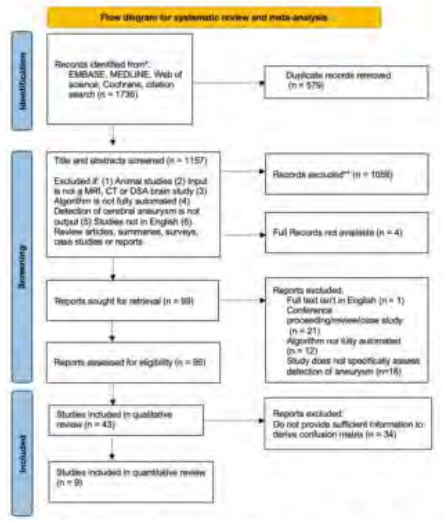

Figure 1: Flow diagram for systematic review search

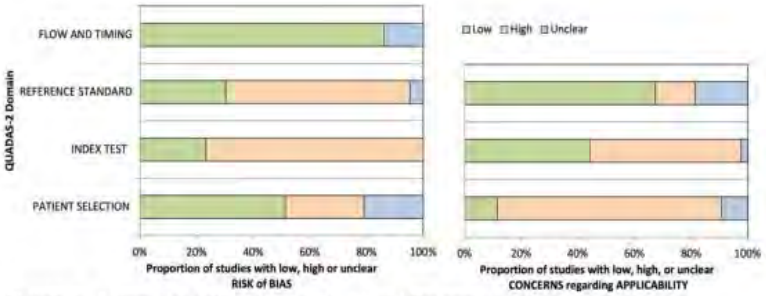

Figure 2: Summarised risk of bias and applicability concerns for all studies using QUADAS-2 domains

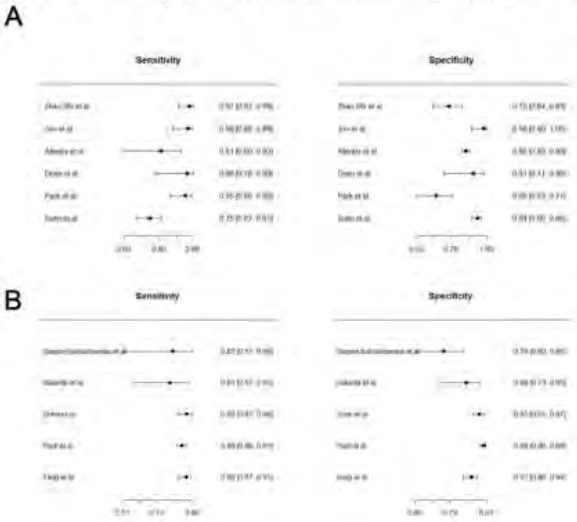

Figure 3: Forest plots of sensitivity and specificity (A) AI standalone subgroup (B) AI+Reader group

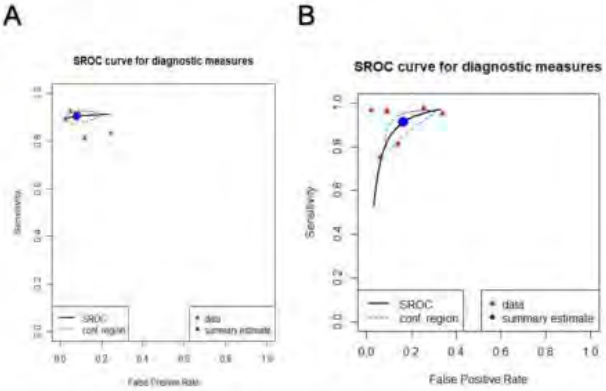

Figure 4: SROC curve (A) AI standalone subgroup (B) AI+Reader group

(Filename: TCT_1361_combined3.jpg)

1506

Utility of MR Vessel Wall Imaging in the Diagnosis of Ruptured Blister Intracranial Aneurysm

T Chaudhry[1], T Hijaz[2], R Abdalla[1], Y Moazeni[3], A Patel[3], A Shaibani[1], B Jahromi[1], D Cantrell[1], M Potts[1], S Ansari[1]

[1]Northwestern University- Feinberg School of Medicine, Chicago, IL, [2]Northwestern Memorial Hospital, Chicago, IL, [3]Northwestern University, Chicago, IL

Purpose

Blister aneurysms are small, broad-based outpouchings, typically involving non-branching or sidewall arteries. They remain a diagnostic challenge in patients presenting with subarachnoid hemorrhage given their small morphology and inconspicuous locations. Given the low prevalence, blister aneurysms may not be detected even after conventional cerebral angiography with high rerupture risk due to intracranial dissection pathology. There is limited literature describing the utility of MR vessel wall imaging (VWI) in the diagnosis of blister aneurysms or as an adjunctive imaging modality.

Materials and Methods

A double-blinded retrospective analysis was performed on a total of fifteen patients by two independent diagnostic neuroradiologists with expertise in neurovascular imaging. Seven patients had confirmed ruptured blister aneurysms and eight patients served as controls that presented with subarachnoid hemorrhage. CTA, MRA, DSA, and MR VWI modalities were independently reviewed and graded for the presence of a blister aneurysm. Subsequently, each patient's imaging was viewed serially with an additional binary score to assess if MR VWI provided value in a final diagnosis. General statistical analyses, sensitivities, specificities, positive predictive values, and negative predictive value were calculated for each modality.

Results

Average sensitivity, specificity, positive predictive value, and negative predictive values of MR VWI were 80%, 100%, 100%, and

87.5% among the two neuroradiologists for diagnosing blister aneurysms. There was good inter-and intra-observer agreement upon DSA diagnoses ranging from 94% to 100%. CTA was the least sensitive modality with a sensitivity of 43.8%, although highly specific of 93%. MRA had a sensitivity of 60% with a specificity of 50%. DSA was the most sensitive at 94%. Neuroradiologists graded MR VWI as a useful adjunct in diagnosing blister aneurysms in 75% of cases.
Conclusions
MR VWI is a promising adjunctive imaging modality in this diagnosis or exclusion of typically occult blister aneurysms in patients presenting with subarachnoid hemorrhage.

	VWA	CTA	MRA	DSA
Sensitivity	80.0%	43.8%	60.0%	93.8%
Specificity	100.0%	92.9%	50.0%	100.0%
PPV	100.0%	91.7%	45.0%	100.0%
NPV	87.5%	60.3%	66.1%	93.8%

(Filename: TCT_1506_tableblister.jpg)

Wednesday, May 18, 2022

10:45 AM-12:15 PM

SNIS Programming: Essentials of Neuroradiology: Evidence for Challenging NIR Situations

824
Head and Neck Endovascular Curative Repair of Vascular Malformations
W Yakes[1]
[1]The Yakes Vascular Malformation Center, Englewood, CO

Purpose
To determine the efficacy of ethanol embolotherapy of extracranial head and neck vascular malformations of all types, particularly after failure of other endovascular and surgical treatments.
Materials and Methods
One hundred and sixty-six patients (64 males, 102 females; mean age: 38 yrs) presented with extracranial arteriovenous malformations (AVMs) of the head and neck area. Over half of the patients had undergone previous failed therapies (Glue, Onyx, PVA, Coils). All patients underwent ethanol embolotherapy under general anesthesia. Forty-five patients had AVMs and 121 patients had venous malformations (VM).
Results
Of 45 AVM patients, 26 patients are cured (mean follow-up 2 ½ years); of 121 venous malformation patients, 65 are at end-therapy (mean follow-up 4 ½ years). The remaining patients are not at end-therapy and are being treated for their residual malformations. In AVM follow-up, arteriography is the main imaging modality to determine cure or residual AVM as MR is less sensitive in the evaluation of residual AVM. In VM follow-up, MR is the main imaging tool, particularly with T- 2 fat suppression and/or STIR imaging. All patients demonstrated improvement post-therapy. Complications were 4.5%, to include bleeding (self-limited), partial 7th nerve palsy (with recovery), skin injury (not requiring skin grafts), infection, and pain.
Conclusions
Ethanol has proven its consistent curative potential at long-term follow-up for high-flow AVMs and low-flow VM lesions at long-term follow-up as lesions in the periphery. Complication rates remain low. The procedures are tolerated well by the patients and done on an out-patient basis. Prior surgery and embolization procedures can cause difficulty in lesion access, but does not obviate further ethanol endovascular treatment.

822
Management of Tongue Venous and Lymphatic Malformations
W Yakes[1]
[1]The Yakes Vascular Malformation Center, Englewood, CO

Purpose
To determine the efficacy of ethanol embolization in management of tongue venous and lymphatic malformations.
Materials and Methods
48 patients (29 females, 19 males; mean age: 38 years) presented with tongue low-flow malformations. 47 patients had undergone 61 failed previous procedures (embo, laser, surgery, steroid injection, alpha-interpheron, radiation). All patients had baseline arteriograms and MRs. All patients underwent direct puncture ethanol endovascular therapy.

Results
Of 48 patients with venous and lymphatic malformations, 37 patients had dramatic reduction and 11 patients' therapy is on-going with concurrent reductions (mean f/up: 60 months). 1 patient with AVM required additional surgery and 1 patient with mixed veno-lymphatic malformation required surgical debulking of excess tissues. Minor complications such as tongue blisters (9 instances) healed spontaneously; 3 tongue focal areas of necrosis healed spontaneously; 3 infections responded to antibiotic treatment; 1 focal tongue hemi numbness resolved. 1 patient with dense VMs had a portion of the tongue slough and the tongue healed and remolded with no treatment required.
Conclusions
Ethanol embolotherapy is a primary and consistent form of therapy to eradicate low-flow vascular malformations of the tongue permanently at long-term follow-up. Rarely is concurrent surgery required. Ethanol sclerotherapy is a curative treatment in which recurrences do not occur and permanent ablations are the rule. Complications are minor and rare.

899

Periprocedural Aspects of Multimodal Endovascular Management of Carotid Cavernous Fistulas Using Different Techniques.

G Alatzides[1], M Opitz[1], Y Li[1], K Wrede[2], M Darkwah Oppong[2], i wanke[3], B Frank[4], C Deuschl[1]
[1]Department of Diagnostic and Interventional Radiology and Neuroradiology, University Hospital Essen, Essen, Germany, [2]Department of Neurosurgery, University Hospital Essen, Essen, Germany, [3]neuroradiologie Hirslaneden, zurich, zurich, [4]Department of Neurology, Universitiy Hospital Essen, Essen, Germany

Purpose
Treatment of Carotid-cavernous fistulas (CCF) can be a great challenge for neurointerventionalist. With the evolvement of neuroendovascular techniques high occlusion rates with good clinical and functional outcome are feasible but until now there is still little evidence available. Therefore, we conducted a single center retrospective study to assess different periprocedural aspects of the endovascular treatment of patients with CCF at our institution.
Materials and Methods
We retrospectively reviewed all patients undergoing endovascular embolization of CCF at our hospital and collected epidemiological, clinical and imaging data as well as interventional procedure reports and clinical efficacy.
Results
After screening for eligibility 59 patients were included with a mean age of 69.8 ± 16.2 years. In most cases there was a spontaneous etiology of the CCF (72.9%, 43/59) while 18.6% (11/59) developed a CCF posttraumatic and 8.5% (5/59) along with an intracranial aneurysm. 49.2% (29/59) patients presented with a Barrow type D fistula followed by Barrow type A fistulas with 42.4% (25/59). In the majority of cases endovascular therapy could be completed in one session (74.6%, 44/59) with a transvenous approach in 57.6% (34/59), transarterial in 33.9% (20/59) and combined in 8.5% (5/59). Coils were used solely in 45.8% (27/59) while a combination of Onyx and Coils was applied in 44.1% (26/59). An assist device (either stent or balloon) prior to insertion of the embolic material was implanted in 20.3% (12/59). Complete obliteration was achieved in 91.5% (54/59) with an overall procedure-related complication rate of 16.9% (10/59).
Conclusions
Endovascular treatment of CCF is an effective method to reach high occlusion rates. Although complication rates are low, further data and research are required to improve the periprocedural morbidity.

Table 2: procedural data & outcome/complication

	Entire Cohort n = 59
Procedural data	
Number of sessions	
One-stage	44 (74.6)
Two-stage	15 (25.4)
Approach	
Transarterial	20 (33.9)
Transvenous	34 (57.6)
Combined	5 (8.5)
Material used	
Onyx alone	4 (6.8)
Coils alone	27 (45.8)
Onyx + Coils	26 (44.1)
Stent	1 (1.7)
PVA particles	1 (1.7)
Onyx amount (ml)	0.7 (1.6)
Assist devices	
No	47 (79.7)
Stent assisted	2 (3.4)
Balloon assisted	10 (16.9)
Periinterventional heparinization	18 (30.5)
Outcome	
Angiographic	
Complete obliteration	54 (91.5)
Partial obliteration	5 (8.5)
Failed obliteration/Recanalization	0 (0)
Postinterventional cross sectional imaging	42 (71.2)
Complete obliteration	35 (83.3)
Partial obliteration	7 (16.7)
Failed obliteration/Recanalization	0 (0)
Clinical	46 (78.0)
Significantly improved	37 (80.4)
Stable, undulating	9 (19.6)
Worsened	0 (0)
Complications	
Overall procedure-related complications	10 (16.9)
Severity	
Clinically not significant	1 (10.0)
Clinically significant	9 (90.0)
Kind of complication	
Extravasation of embolic agent	2 (20.0)
Thrombosis, Infarct, spasm	5 (50.0)
Local, other	3 (30.0)

Values represent as count (percentage)
* Values represent median (IQR)

(Filename: TCT_899_Table.jpg)

Wednesday, May 18, 2022
1:30-3:00 PM
ASPNR Programming: Interesting Pediatric Neuroradiology Case Session

898

Accelerated Brain Aging in Congenital Heart Disease and Relation to Neurodevelopmental Outcome

R Lankalapalli[1], Y Ou[2]
[1]University of California, Berkeley, Berkeley, CA, [2]Boston Children's Hospital, Harvard Medical School, Boston, MA

Purpose
Recent studies of observed brain/behavior changes suggest accelerated brain aging in adolescent and young adult survivors (AYAs) of

congenital heart disease (CHD)[1–4]. We have conducted the first study to quantify the severity of accelerated aging in AYAs with CHD, including contributing factors, and the potential of accelerated aging to predict neurodevelopment outcome.

Materials and Methods

This IRB-approved study used a deep learning brain age estimator trained on T1-weighted brain MRIs from 16,705 healthy brain MRIs[5], and on 96 AYA survivors of CHD age 8-30 years in the 8-site Pediatric Cardiac Genomics Consortium (PCGC). We computed the severity of brain aging by deltaAge = (Artificial Intelligence (AI) estimate - chronological age) and compared AYA to normal controls using a t-test. A regression model assessed the association between deltaAge and contributing factors, including demographics (sex, age at MRI, Body Mass Index (BMI)), genetics (High Brain Expression, Chromatin-modifying, Neurodevelopmental disorder, probability of loss of function intolerance, and ApoE genes), and Socioeconomic Status (SES: parental education, income). A further regression model was used to assess the association between deltaAge and neurodevelopment scores (Wide Range Achievement Test-IV, Wechsler (version IV for adults and V for children), controlling for demographics, genetics and SES.

Results

AI-estimated deltaAge was 1.37 > 1.00 yrs ($p<0.01$) for AYAs with CHD (Fig 1), with 1.0115 years of brain aging for every year of chronological aging between 8 to 30 years age, after an initial brain aging of 1.18 yrs by age 8 years (Fig 2). ANOVA test showed that a higher BMI ($p=0.014$, Fig 3) and the e3/e4 alleles in the ApoE gene ($p=0.021$, Fig 4) were significantly associated with a greater deltaAGE. Among 22 neurodevelopmental scores, AI-estimated deltaAge was significantly positively associated with Matrix Reasoning ($p=0.021$), Vocabulary($p=0.026$), Verbal Comprehension Index ($p=0.050$), and Fluid Reasoning Index (0.035), controlling for demographics, genetics, and SES.

Conclusions

Survivors of CHD experience 1.37 yrs of accelerated aging between 8 and 30 years. Lower acceleration occurred with lower BMI and the absence of the ApoE gene. The severity of accelerated brain aging offers a new MRI metric to identify individuals at risk for some neurodevelopmental impairments. Next steps will be longitudinal studies in larger datasets.

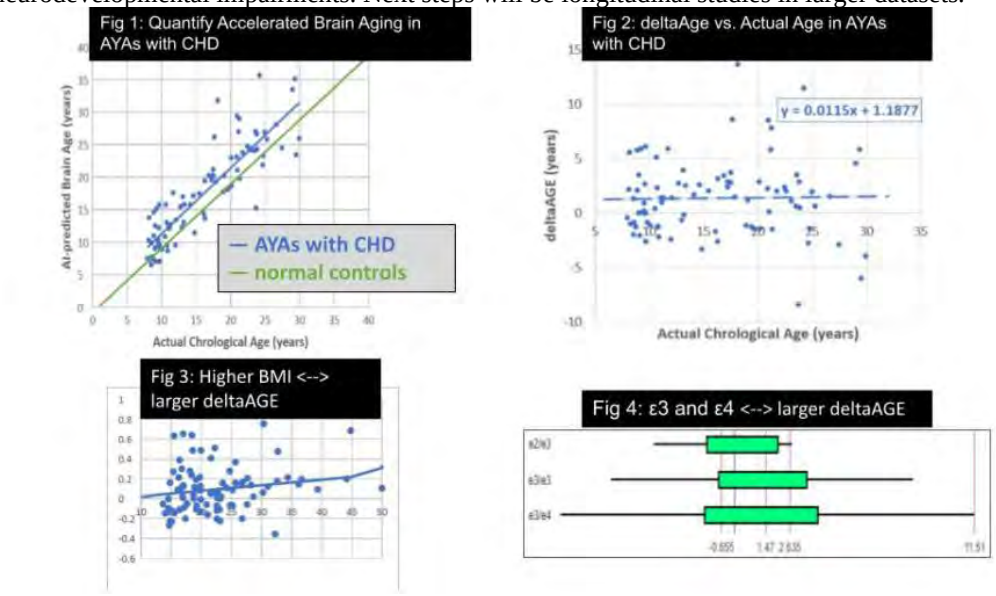

(Filename: TCT_898_FiguresCHDAbstract1.jpg)

583

Quantitative MRI Investigating the Development of the Human Fetal Ganglionic Eminence – Neuroradiological Insights into a Transient Brain Structure

M Stuempflen[1], E Schwartz[1], M Diogo[2], S Glatter[1], B Pfeiler[1], V Schmidbauer[1], C Mitter[3], D Prayer[3], G Kasprian[4]

[1]Medical University of Vienna, Vienna, Vienna, [2]Hospital Garcia de Orta, Hospital CUF Tejo, Vienna, Portugal, [3]Medical University Vienna, Vienna, Vienna, [4]MEDICAL UNIVERSITY OF VIENNA, VIENNA, TX

Purpose

Failure of fetal interneuron migration arising from the ganglionic eminence (GE) may lead to neuropsychiatric and neurodevelopmental disorders.(1,2) Early detection of anomalies within this transient brain structure at prenatal stages, may improve the MRI phenotyping of neurodevelopmental diseases. This atlas-based fetal MRI study aimed to quantitatively assess longitudinal development of the GE.

Materials and Methods

In this retrospective, IRB-approved single-center study, postprocessing was conducted based on semiautomated segmentation of super-resolution fetal brain 1.5T and 3T MR datasets. After assessment of data quality, a longitudinal, quantitative atlas-based analysis of the ganglionic eminence was conducted by several raters.

Results
A total of 112 patients (gestational age 19-39 weeks, mean 27.5 GW) without structural brain anomalies, cardiac defects, fetal growth restriction, and/or poor super-resolution image quality were included and analyzed. In the observed time interval, the volume of the ganglionic eminence ranged from 53.25mm3 to 1,100.25mm3 (mean 572.31mm3, SD 232.01) with average volumes continuously decreasing from 19 to 39 GW. For each gestational day, a volumetric reduction of 3.59mm3 (95% CI 2.45 – 4.73) within the GE was detected. Validation of this dataset was based on an additional, exemplary patient (two observations, 28+6 and 33+3 GW) with reportedly delayed development of the GE: Utilizing the same postprocessing techniques, abnormally increased GE volumes were detected confirming the proposed set of reference values.
Conclusions
Super-resolution based quantitative MR volumetry allowed to analyze the continuous reduction in size of the GE from 19GW onwards - initially documenting a physiological degenerative process in the developing human brain. The first set of reference values of this structure was provided, enabling radiologists to objectively quantify GE development using fetal MRI.

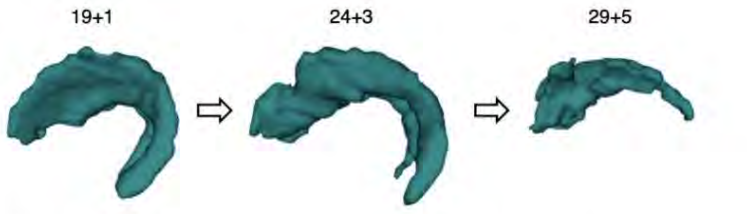

Figure 1:
Longitudinal volumetric development of the ganglionic eminence
Segmentation and 3D-reconstruction of the ganglionic eminence at 19+1, 24+3, and 29+5 gestational weeks.

(Filename: TCT_583_AbstractGEASNR-Figure1.jpg)

Wednesday, May 18, 2022
1:30-3:00 PM
ASSR Programming: Spectrum of Spine Intervention

1141
Safety and Efficacy of Atlantoaxial Joint Injection Under CT Guidance
R Frederick[1], W Gibbs[2]
[1]Mayo Clinic Arizona, Phoenix, AZ, [2]Mayo Clinic, Scottsdale, AZ

Purpose
Unilateral atlantoaxial joint osteoarthritis (AAOA) is an underrecognized and undertreated source of chronic neck pain. Injection of anesthetic and steroid into the joint can provide short term relief, which confirms the joint as the source of pain, indicating that C1-2 arthrodesis may provide a definitive solution. However, many practitioners express concern that this procedure is dangerous, given the trajectory of the needle near the vertebral artery, C2 nerve, thecal sac, and potential rare variant anatomy, such as a low-lying PICA. Prior reports of adverse events and complications of atlantoaxial joint injection all involved fluoroscopic guidance. The use of CT guidance during this procedure allows us to see the critical structures (or their radiographic landmarks) along the needle path so important structures can be avoided. In the case that we cannot definitely determine the course of the vertebral artery in diagnostic studies used for planning, an intraprocedural, limited CTA can provide this information to increase confidence and mitigate risk.
Materials and Methods
A retrospective chart review was conducted on 10 atlantoaxial joint injections performed by the study authors in 2021. The injections were performed with CT-fluoroscopic guidance in the prone position using a posterior approach. Intraarticular needle tip position was confirmed with a small amount of myelographic contrast, followed by slow injection of dexamethasone and bupivicaine into the joint. We collected reported information from the patient consultation, medical history, history of prior cervical treatment for their pain, procedural and post procedural adverse events, and short and long term outcomes.
Results
All patients had symptoms of unilateral occipital pain and pain with head rotation, and all had unilateral AAOA on imaging. No patient had a complication or adverse event during or after the procedure. All patients experienced greater than 50% pain relief within

one hour after the procedure. 9/10 patients had sustained pain relief at 2 days post procedure. 6/10 had 3 week follow up information, and 5/6 reported that they experienced >50% pain relief, while one patient's symptoms returned to baseline.

Conclusions

CT-guided atlantoaxial joint injection provides substantial short term pain relief for neck pain caused by atlantoaxial osteoarthritis. CT guidance allows for confident needle placement, which increases safety, efficacy, and diagnostic confidence, optimizing treatment selection and patient outcomes.

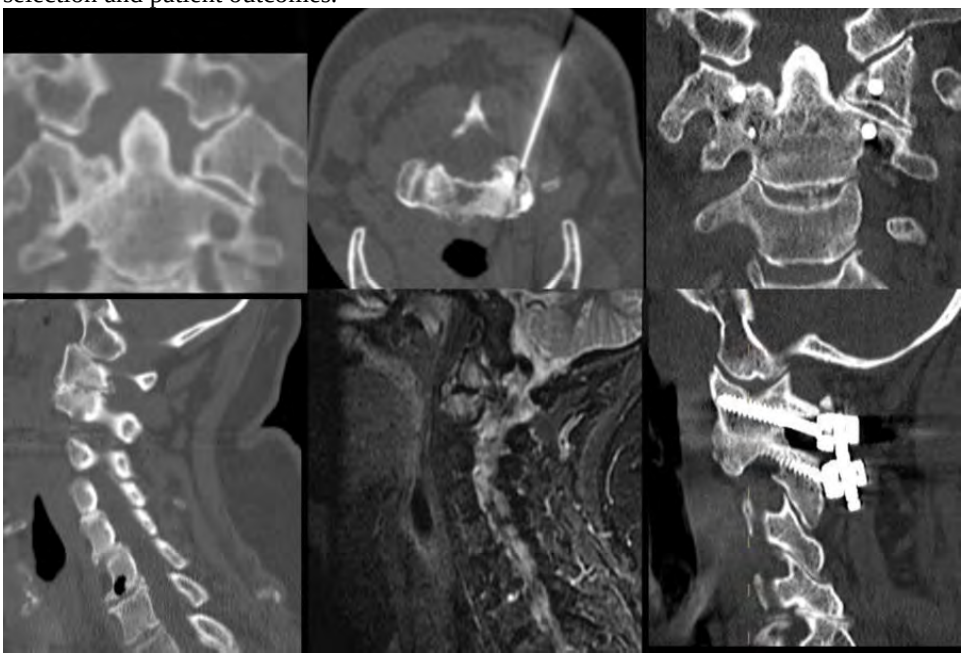

(Filename: TCT_1141_AAOA_ASNR.jpg)

1215

Predicting Bone Density from Spine CT and Demographic Data with a Multimodal Regression Network

J Lee[1], C Li[1], M Khan[1], M Repajic[1], A Rajamohan[2], V Patel[1]

[1]University of Southern California, Los Angeles, CA, [2]Kaiser Permanente - West Los Angeles Medical Center, Los Angeles, CA

Purpose

Osteoporosis is increasingly prevalent, placing over 50 million Americans at increased annual fracture risk. While DEXA remains the gold standard for diagnosis, CT reports often include a subjective evaluation of the trabecular bone density. There have been several studies aimed at predicting fracture risk with non-DEXA modalities including quantitative acoustics, radiography, CT, and MRI [1]. Previous studies using CT have focused on predicting fracture risk based on Hounsfield units [2] and using adaptive multivariable modeling [3]. In this work, we train a multimodal regression network on demographic characteristics and spinal CT data to predict DEXA t-scores as a surrogate for fracture risk.

Materials and Methods

We queried our PACS for patients with near-concurrent DEXA scans and CT studies of the lumbar spine or abdomen/pelvis. We cropped extra-spinal tissues, augmented each data point by introducing subtle variations in image rotation, age, and t-score, and divided the data into training:validation:testing sets in an 8:1:1 ratio. Using age, gender, and CT images as inputs, we trained a combined multi-layer perceptron (MLP) and convolutional neural network (CNN) to predict the DEXA t-score as shown in Figure 1. We measured our model's performance for the prediction of osteopenia and osteoporosis using standard metrics and established DEXA t-score thresholds.

Results

Table 1 shows the patient characteristics, including DEXA t-scores and demographics. The confusion matrix for the predictions of our trained model on the testing set is shown in Figure 2. The overall accuracy of our model was 57% (287/500). The sensitivity and specificity of the model were the highest (0.88 and 0.84, respectively) for identifying normal bone mineral density. The precision was the highest for classifying osteoporosis at 1.00; however, the sensitivity for detecting osteoporosis was only 0.33. Other metrics are summarized in Table 2.

Conclusions

We evaluated the performance of a combined MLP-CNN model at grading bone mineral density. With the increasing utilization of CT, this type of model may enable the earlier detection of bone demineralization, enabling earlier therapeutic interventions and lifestyle modifications. In addition, such a model may be used retrospectively to study the degree of age and gender bias in subjective reporting of osseous demineralization. Our upcoming work will target expanding the training set to improve the accuracy and generalizability of the model.

Figure 1: The multimodal regression network. CT data is processed by the CNN branch while the patient demographic information (sex, age) is processed by the MLP branch. The outputs from each branch are concatenated and processed through a final dense layer for prediction.

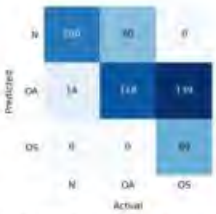

Figure 2: Confusion matrix for model predictions on the test dataset shows relative performance on normal mineralization (N), osteopenia (OA), and osteoporosis (OS) samples.

Table 1: Patient Characteristics in the Training, Validation, and Testing Sets

Group	Age (y)	Female (%)	DEXA t-score	Normal (%)	Osteopenia (%)	Osteoporosis (%)
Training	57.49 ± 13.00	60.8% (48/79)	-1.62 ± 1.42	32.4% (1278/3950)	37.3% (1474/3950)	30.3% (1198/3950)
Validation	60.49 ± 7.96	70.0% (7/10)	-1.80 ± 1.75	20.0% (100/500)	47.4% (237/500)	32.6% (163/500)
Testing	56.38 ± 11.25	80.0% (8/10)	-1.68 ± 1.30	22.8% (114/500)	35.4% (178/500)	41.6% (208/500)

Note: The mean ± standard deviation is shown for age and t-score.

Table 2: Model Performance in Bone Density Grading

Grading	Sensitivity	Specificity	Precision	Recall	F1-score
Normal	0.88	0.84	0.63	0.88	0.73
Osteopenia	0.88	0.52	0.44	0.88	0.53
Osteoporosis	0.33	0.88	1.00	0.33	0.50

(Filename: TCT_1215_DEXA-graphic-01.jpg)

648

Identification of skeletal fragility from trabecular bone structure on CT images: an artificial intelligence-based radiomics study

F Garoli[1], E Biamonte[1], R Levi[1], M Battaglia[1], D Rizzo[1], G Savini[2], D Milani[2], M Fornari[2], G Mazziotti[1], M Grimaldi[2], L Politi[1]
[1]Humanitas University, Pieve Emanuele, Milano, [2]Humanitas Research Hospital, Rozzano, Milano

Purpose

To identify radiomics features associated with skeletal frailty from lumbar CT scans

Materials and Methods

Osteoporosis is a metabolic bone disease characterized by the reduction in bone mass and deterioration in texture and architecture of the trabecular bone; it is one of the most common age-related diseases and one of the main risk factors for developing fractures. Current fracture risk scores rely on the estimation of bone mineral density through DEXA and in the evaluation of the FRAX score. However, both methods show a relatively low accuracy, with the FRAX score reaching only 45.7% of sensitivity in predicting vertebral fractures in 10 years. Radiomics is an emerging field of medical image analysis that could be able to quantitatively evaluate the trabecular structure from a CT scan. We manually annotated spherical regions-of-interest (ROIs, 9 mm of diameter) in the center of the vertebral body of each lumbar vertebrae (L1-L5) in 182 subjects undergoing lumbar CT for back pain and in 58 osteoporotic subjects with morphometric dorsal fractures, and we evaluated 93 radiomics features from each ROI. Subjects with a known history of cancer or traumatic vertebral fractures were excluded. We performed a machine learning classification model based on support vector machine to identify radiomics features able to distinguish textural alterations between the unfractured vertebrae of the two groups. To assess the reliability of the model, we split the complete dataset into train and test sets (75/25); we validated our final model on the test set using accuracy, sensitivity, specificity, and area under the ROC curve. Further, Pearson and Spearman's statistical tests were employed to assess correlations among radiomics features and FRAX score, DEXA, clinical and laboratory data

Results

Univariate analysis showed 20 significative radiomics features ($p<0.05$, Bonferroni correction) that differ between case and controls. Moreover, our support vector machine learning model reached 0.83 of ROC AUC and 64.3% sensitivity on the test set. Feature importance showed that Gray Level Size Zone Matrix features capture bone texture alterations in our dataset; furthermore, the first-order maximum reached a 0.69 R-correlation with lumbar DEXA t-score

Conclusions

Artificial intelligence-based radiomics analysis of lumbar CT images can identify skeletal fragility better than current clinical standard practice such as BMD and FRAX.

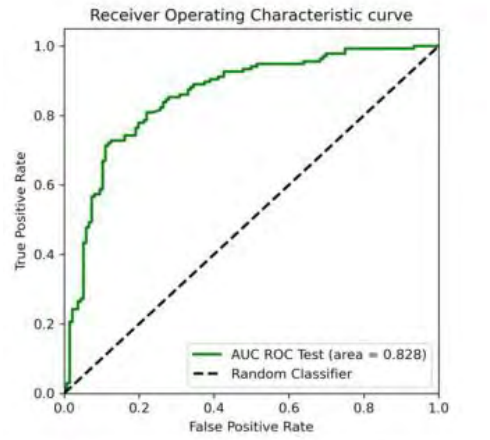

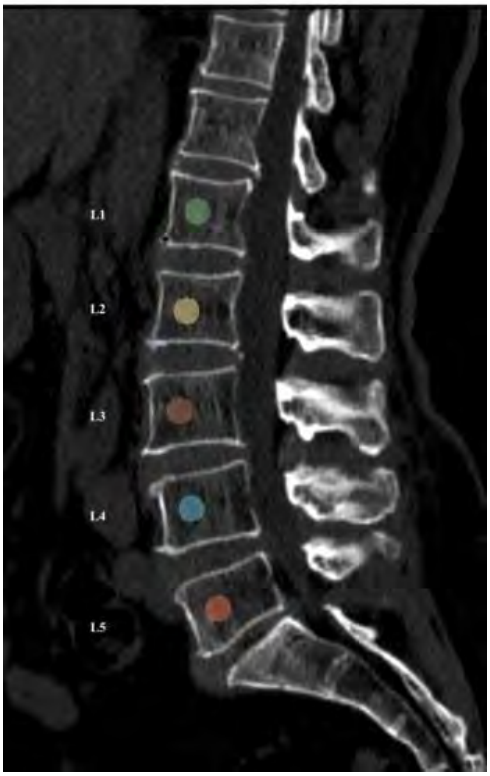

(Filename: TCT_648_imgonline-com-ua-twotoone-LqvAeU4EHhqzLi.jpg)

Wednesday, May 18, 2022
1:30-3:00 PM
Scientific Podium Presentations: Brain Tumors 2

1098

68Ga-DOTATATE PET/MRI in Meningioma: Correlation with Immunohistochemical Assessment of SSTR2 Expression

A Haghdel[1], M Roytman[1], S Kim[1], B Liechty[1], D Pisapia[1], N Smith[1], T Schwartz[1], S Pannullo[1], R Ramakrishna[1], R Magge[1], N Karakatsanis[1], J Knisely[1], E Lin[1], J Ivanidze[1]

[1]Weill Cornell Medicine, New York, NY

Purpose

Meningiomas are the most common primary intracranial tumors [1]. Gallium 68 ([68Ga])-DOTATATE is a PET radiotracer targeting somatostatin receptor 2 (SSTR2), a highly sensitive and specific pathologic biomarker for meningiomas [2]. [68Ga]DOTATATE PET/MRI has shown utility in meningioma diagnosis, differentiation of residual/recurrent tumor from post-treatment change, and

radiotherapy planning [3]. More accurate correlative histopathological analyses are needed to further validate DOTATATE PET/MRI as a diagnostic approach in newly diagnosed and recurrent meningiomas. We sought to correlate SSTR2 expression and DOTATATE PET SUV in meningioma.

Materials and Methods

We analyzed a subset of patients from our IRB approved prospective clinical trial evaluating DOTATATE PET/MR in meningioma in whom SSTR2 immunohistochemistry (IHC) staining was performed. For SSTR2 IHC, a tissue microarray approach was employed on resected meningioma specimen, graded independently by two neuropathologists on a semi-quantitative scale (1-5). DOTATATE PET SUV was recorded for each meningioma for which pathology correlative data was available. Spearman's Rank-Order correlation was performed to quantify this relationship and Mann-Whitney U test was used for non-parametric analysis.

Results

25 patients met inclusion criteria (mean age 57.6 years; 72% female; 20% WHO Grade I vs 75% WHO Grade II/III). Majority of patients (78%) had 68Ga-DOTATATE PET/MRI done postoperatively (average 571 days after resection), the rest were done preoperatively. We found a significant moderate positive correlation between absolute lesion SUV and SSTR2 expression ($r= 0.46$, $p=0.010$). Of note, both lesion SUV ($p=0.262$) and SSTR2 expression ($p=0.357$) were not significantly different between WHO-I and WHO-II/III meningiomas.

Conclusions

We found a strong correlation between histological SSTR2 expression and its molecular imaging substrate, DOTATATE PET SUV. Our data validates prior studies and lays a basis for future exploration of meningioma biology. Limitations include a relatively small sample size and heterogeneity of the cohort with regard to prior treatment which may affect SSTR2 expression, and probably accounts for a lack of even higher correlation between PET and IHC within our cohort. Future work will focus on correlation of DOTATATE PET and emerging molecular genetic biomarkers in meningiomas, and on wider clinical implementation of DOTATATE PET/MRI in meningioma diagnosis and treatment in clinical practice.

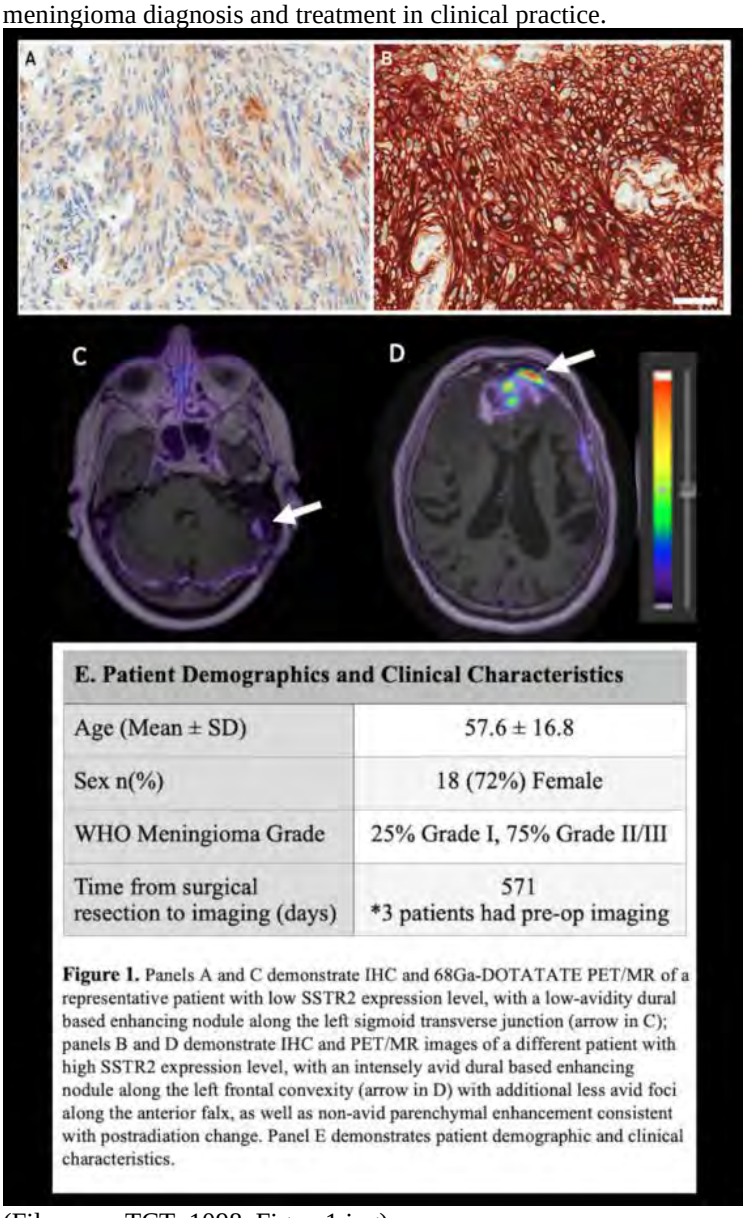

E. Patient Demographics and Clinical Characteristics

Age (Mean ± SD)	57.6 ± 16.8
Sex n(%)	18 (72%) Female
WHO Meningioma Grade	25% Grade I, 75% Grade II/III
Time from surgical resection to imaging (days)	571 *3 patients had pre-op imaging

Figure 1. Panels A and C demonstrate IHC and 68Ga-DOTATATE PET/MR of a representative patient with low SSTR2 expression level, with a low-avidity dural based enhancing nodule along the left sigmoid transverse junction (arrow in C); panels B and D demonstrate IHC and PET/MR images of a different patient with high SSTR2 expression level, with an intensely avid dural based enhancing nodule along the left frontal convexity (arrow in D) with additional less avid foci along the anterior falx, as well as non-avid parenchymal enhancement consistent with postradiation change. Panel E demonstrates patient demographic and clinical characteristics.

(Filename: TCT_1098_Figure1.jpg)

313

A Pictorial Essay of Non-hemorrhagic and Non-calcified Hyperdense Brain Tumors on CT Scan

A Kamali[1], C Yalniz[2], D Timaran-Montenegro[3], L Nunez-Rubiano[4], A Kamali[1]

[1]University of Texas Health Science Center Houston, Houston, TX, [2]UTH McGovern Medical School, Houston, TX, [3]McGovern Medical School at UT Health, Houston, TX, [4]The University of Texas Health Science Center at Houston, Houston, TX

Purpose

Hyper attenuation on non-contrast CT might be due to hemorrhage, calcification, hyper cellularity, high protein or melanin content. Specific MRI sequences might be helpful to differentiate between different causes of hyperdense CT appearances. The purpose of this study is to demonstrate a review of the non-hemorrhagic and non-calcified hyperdense brain tumors on CT and to elaborate on how to differentiate them apart using brain MRI sequences.

Materials and Methods

We illustrate.. - Hyperattenuating neoplasms on CT due to hyper cellularity: Lymphoma, Medulloblastoma, meningioma, choroid plexus carcinoma, germinoma, papillary tumor of pineal gland, hemangiopericytoma - Hyperattenuating neoplasms on CT due to high protein contents: metastatic mucinous adenocarcinoma to brain, pituitary macroadenoma, craniopharyngioma - Hyperattenuating neoplasms on CT due to high melanin contents: metastatic melanoma to brain

Results

Calcifications and hemorrhage demonstrate susceptibility artifacts on SWI images. High-protein-content tumors demonstrate T1 hyperintensity, T2 hypointensity and diffusion restriction. Melanin containing tumors demonstrate T1 hyperintense and T2 hypointense signal on MRI. Hypercellular tumors demonstrate diffusion restriction on DWI sequences. In this pictorial essay we illustrate hyperattenuating lesions on non-contrast CT mainly due to hyper cellularity, high protein or melanin content.

Conclusions

- A review of non-hemorrhagic and non-calcified hyperdense brain tumors on CT - We illustrate multiple hyperdense brain neoplasms due to hyper cellularity, high protein and melanin contents

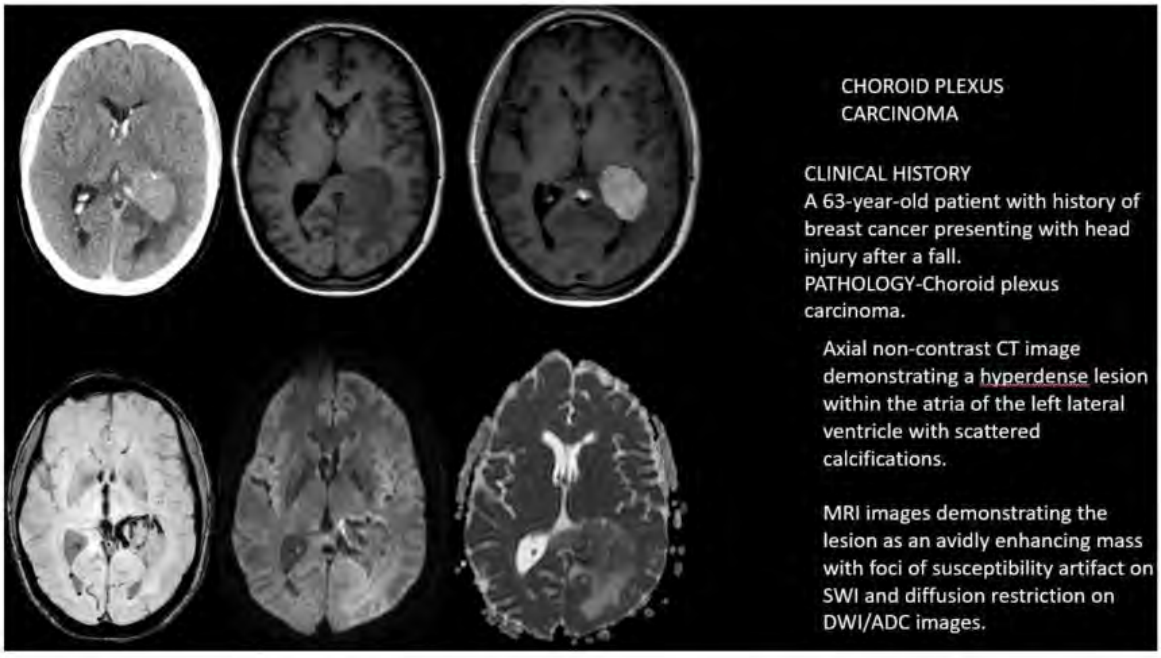

(Filename: TCT_313_Figure.jpg)

1318

Applying a Glioma-Trained Deep Learning Automatic 3D Segmentation Algorithm for Primary CNS Lymphoma Segmentation – Preliminary Results

G Cassinelli Petersen[1], S Merkaj[1], K Bousabarah[2], I Dixe de Oliveira Santo[3], L Jekel[1], S Abi Fadel[4], I Ikuta[5], A Huttner[1], A Omuro[1], M Lin[6], M Aboian[4]

[1]Yale School of Medicine, New Haven, CT, [2]Visage Imaging GmbH, Berlin, CT, [3]Yale New Haven Hospital, New Haven, CT, [4]Yale University, Woodbridge, CT, [5]Yale University School of Medicine, New Haven, CT, [6]Yale University School of Medicine and Visage Imaging, Inc., New Haven, CT

Purpose

With the advent of Machine Learning (ML)-based classification methods, automated segmentation of brain tumors is a necessity to quickly process large quantity of image volumes. Primary CNS Lymphomas (PCNSL) are rare intracranial tumors but often a differential diagnosis to gliomas. Due to the rarity of these tumors acquiring sufficiently large datasets for training a deep learning

(DL) network for automatic segmentationis a challenge. A potential solution is to apply DL algorithms trained on gliomas for PCNSL segmentation. The aim of this study is to evaluate the segmentation performance of a previously developed glioma segmentation algorithm on PCNSL images.

Materials and Methods

In this retrospective study a systematic search of pathology reports at our institution was performed to identify histologically confirmed PCNSL, with the intent of selecting 10 patients for this pilot study. A previously developed PACS-integrated U-Net-based segmentation algorithm trained on 1501 high- and low-grade gliomas (BraTS + own dataset) was deployed. The algorithm segmented "Whole Tumor" (tumoral + peritumoral hyperintensity in FLAIR), "Tumor Core" (enhancing tumor + necrosis on SPGR), and "central non-enhancement (NE)". Finally, the ML based segmentation was revised by a neuroradiologist with 4 years of experience. Dice scores (DSC) between the ML based and radiologist revised segmentations were calculated.

Results

The pathology report search yielded 80 patients with PCNSL. Ten were randomly selected for this pilot study. Nine lymphomas showed strong enhancement, one only faint. Three tumors exhibited small areas of NE, and one central large NE. Four lymphomas were monocentric.The algorithm segmented NE areas in every study. Mean (Median, Range) DSC for Whole Tumor, Tumor Core, and NE in PCNSL were 0.725 (0.815, 0-0.91), 0.645 (0.805, 0-0.94), 0.09 (0, 0-0.77), respectively. DSC were lower compared to the average on BraTS images (0.9, 0.87, 0.67). The algorithm achieved a DSC of 0 in the case of a very faintly enhancing tumor. Highest DSC for Tumor Core were achieved in homogenously enhancing tumors.

Conclusions

Repurposing a glioma-trained segmentation algorithm for PCNSL images is a solution for bypassing the challenge of acquiring large datasets. A first trial of segmentation without previous training resulted in moderate segmentation performance. Future training with PCNSL cases has the potential to significantly improve automatic segmentation of CNS lymphomas to develop clinically applicable tools.

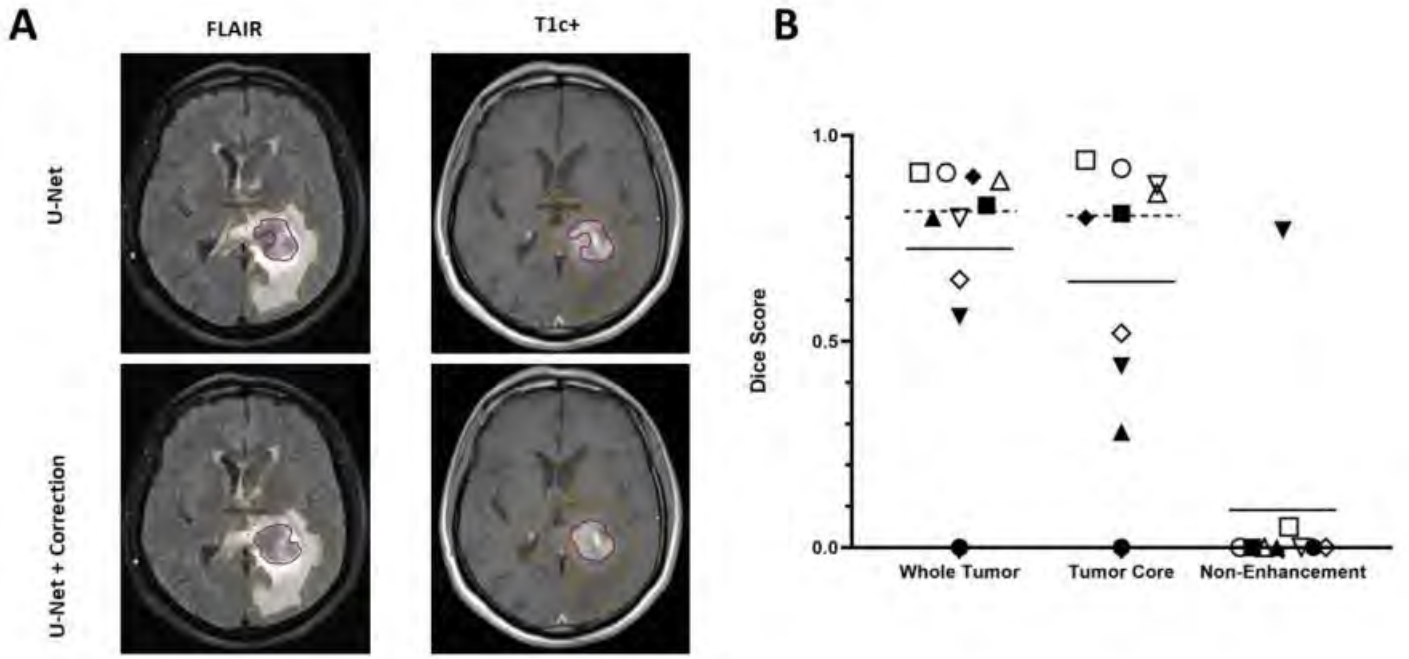

Panel A: Example of a fully automated PCNSL segmentation (first row) and after manual correction by the authors (second row). The Dice scores between both segmentations were 0.89 (Whole Tumor) and 0.86 (Tumor Core). **Panel B:** Distribution of Dice scores for 10 PCNSL patients (each a different symbol). The mean DSC is represented by the full line, and the median by the dashed line. The mean/median DSC for Whole Tumor was 0.725/0.815, for Tumor Core 0.645/0.805, and for central Non-Enhancement 0.09/0.

(Filename: TCT_1318_Slide1-2.JPG)

1008

ASL Perfusion for the Evaluation of Radiation Response in Meningiomas

P MANNING[1], S SRINIVAS[1], D Bolar[1], M Rajaratnam[1], D Piccioni[1], C McDonald[1], J Hattangadi-Gluth[1], N Farid[1]
[1]UC San Diego Health, La Jolla, CA

Purpose

Evaluation of post-radiation treatment response in meningiomas remains challenging. 3D pseudocontinuous arterial spin labeling (3D PCASL) may be beneficial for assessment of post-radiation change in meningiomas because this technique provides physiologic information about radiotherapy response, beyond the typical structural information provided by conventional contrast-enhanced MRI. The purpose of this study is to assess 3D PCASL for the evaluation of treatment response in patients with radiation-treated meningioma.

Materials and Methods
Twenty patients with meningioma who were treated with surgical resection followed by radiation or radiation alone were included in this retrospective, single-institution study. Patients were evaluated with 3D PCASL imaging before and after treatment (median follow up: 6.5 months), and ASL perfusion estimates of normalized cerebral blood flow (ASL-nCBF) within each meningioma were calculated. Additionally, size of each meningioma was measured by area of contrast-enhancement. Wilcoxon signed-rank tests were used to compare pre- and post-radiation ASL-nCBF values as well as pre- and post-radiation contrast-enhancing areas.
Results
Post-radiation ASL-nCBF significantly decreased compared to pre-radiation ASL-nCBF ($p < 0.001$), with all treated meningiomas demonstrating a decrease in ASL-nCBF after radiation. Contrast-enhanced meningioma size also decreased after radiation ($p = 0.008$) in nearly half of the patients (9), but the effect was smaller, and there was no change in meningioma size for half of the patients (10).
Conclusions
ASL perfusion provides a complementary quantitative and physiologic measure of treatment response in meningiomas after radiation therapy. This complementary information could aid clinical decision-making and provide an additional endpoint for clinical trials.

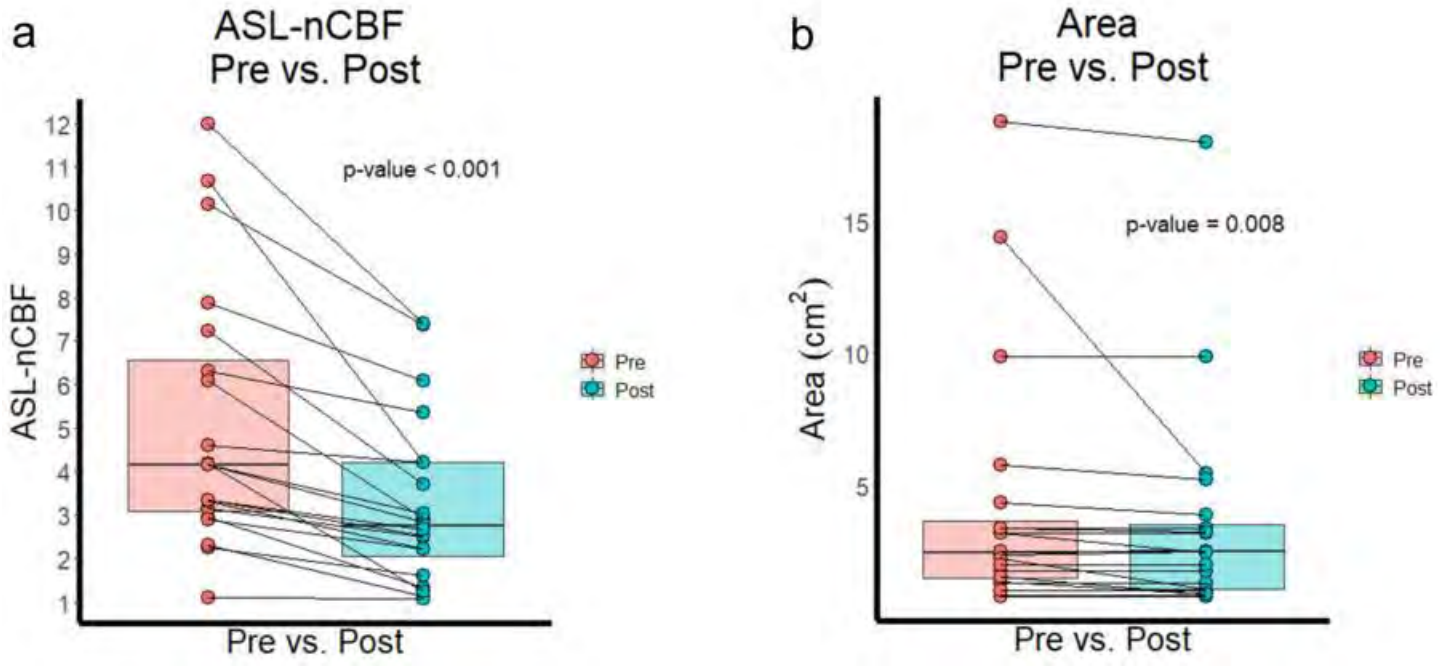

(Filename: TCT_1008_ASNR2022ASLMeningiomaFigure.jpg)

1094

Development of Novel PACS-based Deep Learning Brain Tumor Segmentation Algorithm for Clinical Implementation

S Merkaj[1], K Bousabarah[2], M Lin[3], A Pala[4], G Cassinelli Petersen[1], L Jekel[1], R Bahar[1], N Tillmanns[1], J Cui[5], A Malhotra[6], M Aboian[7]
[1]Yale School of Medicine, New Haven, CT, [2]Visage Imaging GmbH, Berlin, CT, [3]Yale University School of Medicine and Visage Imaging, Inc., New Haven, CT, [4]Ulm University, Ulm, Baden-Württemberg, [5]Yale University, New Haven, CT, [6]Yale University School of Medicine, New Canaan, CT, [7]Yale University, Woodbridge, CT

Purpose
Tumor segmentation is a laborious process, which impedes the progress of data production for development of classification/prediction algorithms. We present a novel PACS-based workflow for deep learning-based auto-segmentation of gliomas that allows generation of annotated images during clinical workflow. This approach allows for real-time building of large, labeled datasets by experts in the field.
Materials and Methods
We pretrained a deep learning algorithm (U-Net) on BraTS 2021 dataset and consequently retrained on YNHH (Yale New Haven Hospital) data to auto-segment whole, core, and necrotic tumor on Visage 7 (Visage Imaging, Inc., San Diego, CA). We established a segmentation workflow within PACS, which made it possible for us to automatically segment and manually correct the internal YNHH dataset in a timeframe of three months. PyRadiomics was natively embedded into PACS and once activated, feature extraction of the segmentations in all sequences was done automatically. We performed test-retest analysis for our feature extraction pipeline by extracting features in PACS (Pyradiomics) and outside of PACS (Python Script). The accuracy of the AI algorithm was measured based on Dice Scores (DSC) between the automatic segmentations and the manually modified segmentations.
Results
U-Net was trained on 1251 tumors from BraTS 2021 dataset, evaluated on 35 gliomas from YNHH, and retrained on 250 tumors from YNHH. Our test-retest analysis for our feature extraction pipeline initially resulted in <2% error, which was brought to zero after the versions of PyRadiomics were matched. U-Net trained on BraTS 2021 achieved DSC of approx. 0.82, which gradually improved to

approx. 0.84 throughout our retraining process. We noticed that signal intensity contrasts were less pronounced on segmentations generated after our retraining process, resulting in ground base segmentations that are closer to what a neuroradiologist would segment in daily clinical practice.

Conclusions

We demonstrate that clinical implementation of segmentation algorithms in neuroradiology practice is feasible through a PACS-integrated workflow and specific batch-based pretraining using hospital's data. This workflow allows real-time generation of large, annotated datasets of brain tumors.

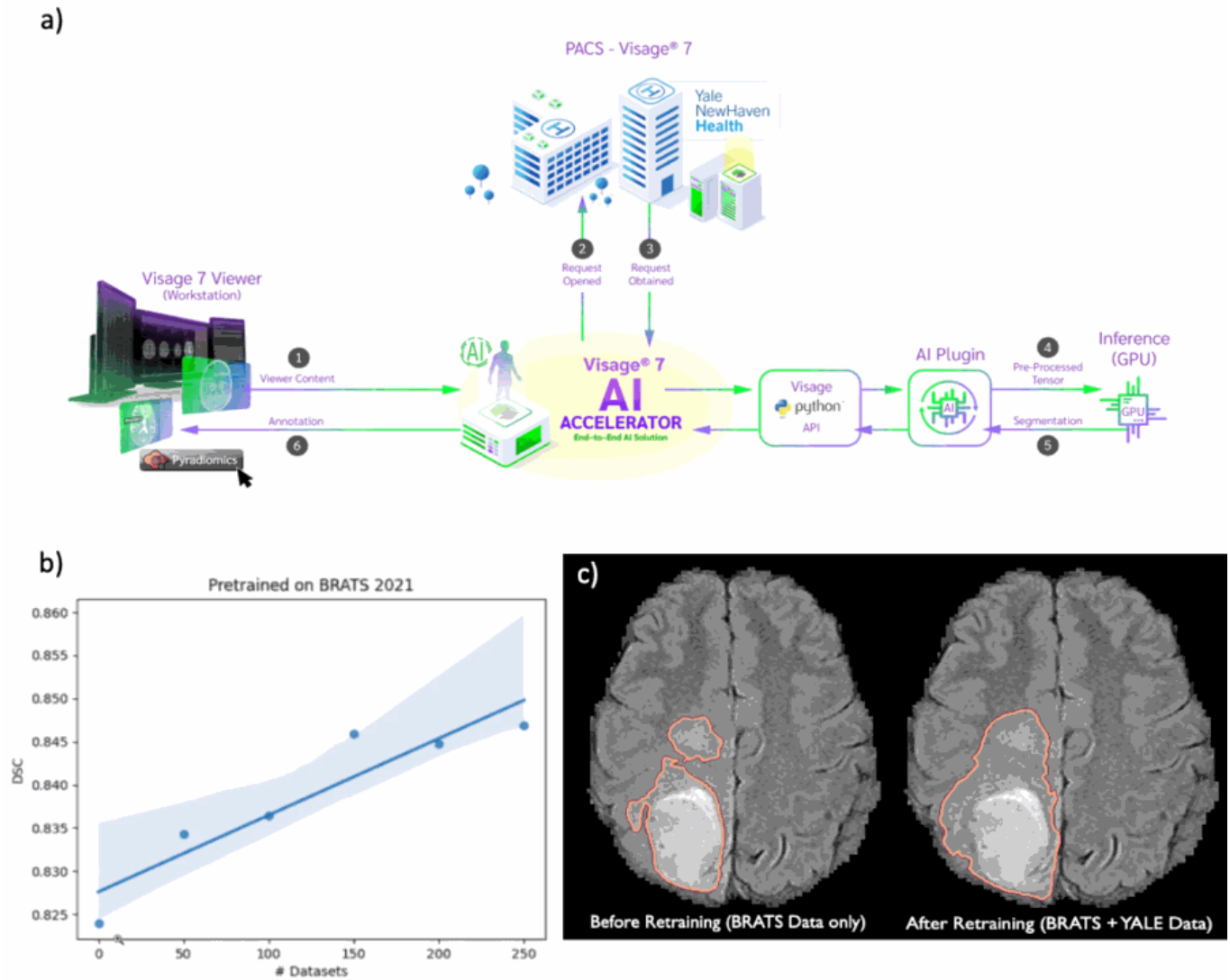

Figure 1: a) Schematic diagram of auto-segmentation and feature extraction tools incorporated into clinical PACS on Visage Imaging platform. b) Dice Scores (DSC) measured between the automatic segmentations and the manually modified segmentations for each step of the incremental training process. 0 = BrATS pretrained algorithm (baseline). 50-250 = batches of data used for step 1-5 of the gradual training process. c) Example of a high-grade glioma automatically segmented through using U-Net before retraining (left) and after retraining on YNHH data (right) on FLAIR MRI sequence.

(Filename: TCT_1094_Presentation4.gif)

1073

Development of PACS-based Autosegmentation Linked to Clinically Applicable Machine Learning Tool for Preoperative Glioma Grade Prediction

S Merkaj[1], T Zeevi[2], K Bousabarah[3], E Kazarian[4], M Lin[5], A Pala[6], L Staib[1], G Cassinelli Petersen[1], L Jekel[1], R Bahar[1], N Tillmanns[1], J Cui[7], I Ikuta[8], R Bronen[8], S Abi Fadel[9], M Aboian[9]

[1]Yale School of Medicine, New Haven, CT, [2]Yale, New Haven, CT, [3]Visage Imaging GmbH, Berlin, CT, [4]Yale University, Greenwich, CT, [5]Yale University School of Medicine and Visage Imaging, Inc., New Haven, CT, [6]Ulm University, Ulm, Baden-Württemberg, [7]Yale University, New Haven, CT, [8]Yale University School of Medicine, New Haven, CT, [9]Yale University, Woodbridge, CT

Purpose
The most common primary brain malignancy, gliomas, are graded according to the World Health Organization (WHO) criteria into grades 1/2 (low-grade gliomas (LGG)) and grades 3/4 (high-grade gliomas (HGG)). As prognosis and treatment vary between HGGs and LGGs, there's a need for preoperative glioma grading. The current gold standard for diagnosis, histopathology, is a lengthy and invasive procedure, which carries associated surgical risks. Machine learning (ML) models and radiomics present novel solutions to overcome these current obstacles. We developed a non-invasive, clinically integrated, preoperative glioma grade prediction tool, which can potentially assist clinicians in their daily clinical practice.
Materials and Methods
We pretrained a deep learning algorithm (U-Net) on 1251 tumors from the multi-institutional BraTS 2021 dataset and evaluated on our internal test dataset from Yale New Haven Health (YNHH). We consequently retrained the U-Net on YNHH data to auto-segment whole, core, and necrotic portions of glioma on Visage 7 (Visage Imaging, Inc., San Diego, CA). Segmentations were made available on FLAIR, T1, T1ce, T2, ADC and SWI MRI sequences. We extracted cumulative 1926 quantitative radiomics features using PyRadiomics. Subjects with more than 80% missing values across sequences and ROIs were excluded from our analysis. XGBoost was used to classify HGG versus LGG. Our model was internally validated using thirty repetitions of five-fold cross-validation method. For each patient, mean prediction across 30 repetitions were calculated and AUC-ROC and CI was reported sing DeLong et. al (1988).
Results
342 high- and low-grade gliomas were included in the HGG/LGG classification. A total of 1926 radiomic features derived from 3 ROIs and 6 sequences were identified and incorporated into XGBoost algorithm. We performed 13 total experiments using combinations of different sequences and ROIs. We achieved best mean AUC using FLAIR and PG sequences and Core, Whole and Necrotic ROIs. Mean AUC was 0.86 (CI = 0.81-0.90; n=314). Similar mean AUC were achieved for FLAIR, PG, SWI/GRE and ADC sequences. Additional experiments with PG alone, T2 alone, ADC alone and FLAIR alone also showed similar mean AUC results.
Conclusions
PACS based autosegmentation of clinically available images linked to XGBoost classification of HGG versus LGG potentially allows clinical translation of image-based glioma grade prediction into clinical practice.

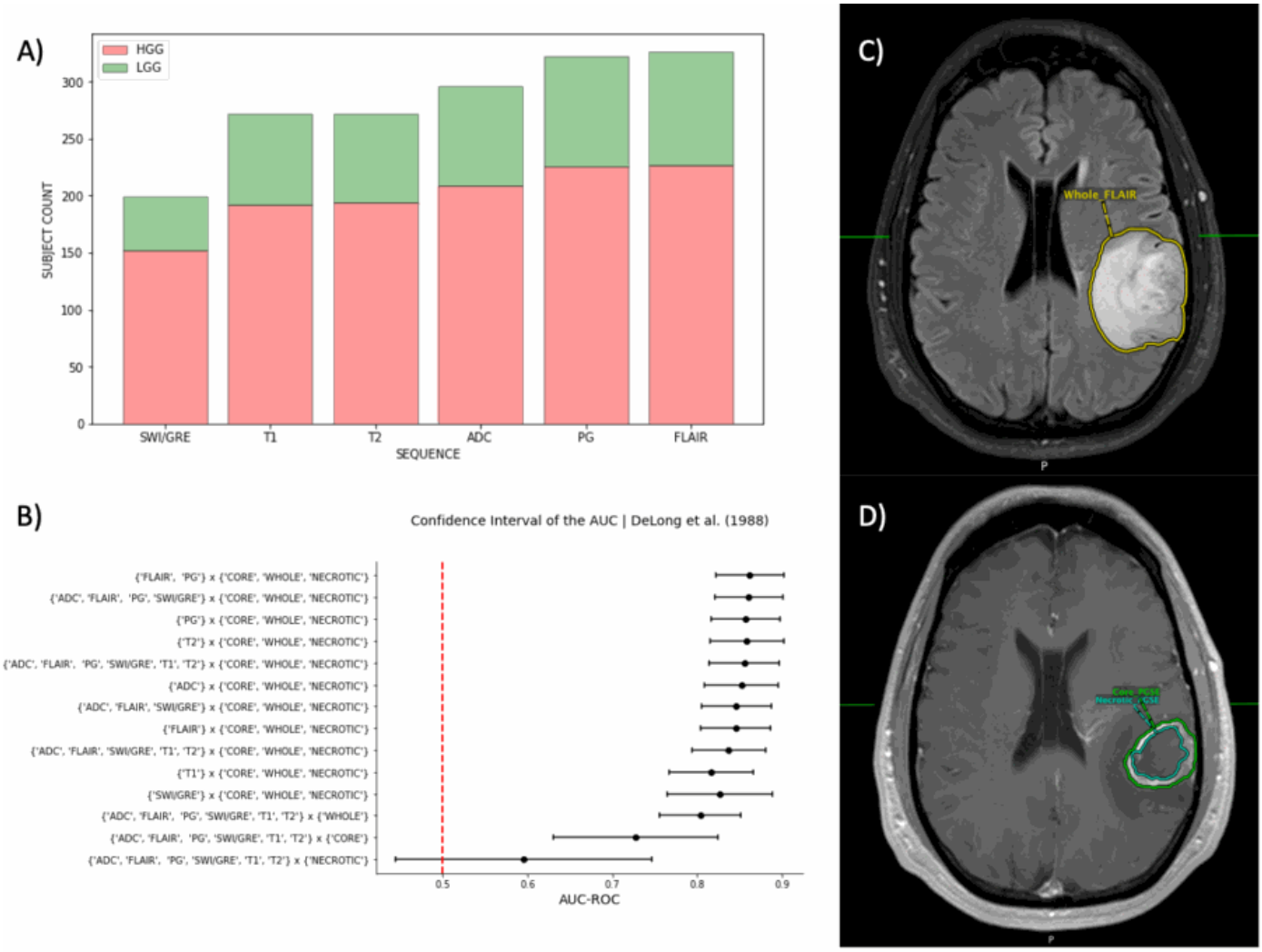

Figure 1: A) Number of subjects for each available sequence. HGG and LGG ratios are presented in pink and green colors (HGG=High-grade glioma; LGG= Low-grade glioma). B) AUC-ROC and Confidence Interval for different sequence and ROI combinations (ROI = Region of Interest). C) Example segmentation of whole tumor ROI on FLAIR sequence. D) Example segmentation of core and necrotic tumor ROIs on PGSE sequence.

(Filename: TCT_1073_Figure.gif)

754

EVALUATING COMPARTMENTAL WATER DISTRIBUTION/DIFFUSION USING NODDI (Neuritic orientation dispersion density imaging) IN ADULT INTRAAXIAL BRAIN TUMOURS

D Sharma[1], J Saini[2], K Kulanthaivelu[3]

[1]NIMHANS Bangalore, Nagpur, India, [2]NATIONAL INSTITUTE OF MENTAL HEALTH & NEURO SCIENCES, BANGALORE, India, [3]National Instituite of Mental Health and Neurosciences, Bangalore, Karnataka

Purpose

To identify role of NODDI indices in differentiating low grade from high grade gliomas. Evaluating diagnostic utility of these indices in differentiating IDH mutant from wild variants.

Materials and Methods

Prospective study of 45 cases with conventional imaging showing intra-axial lesion. Conventional MRI sequences were done along with multi-shell diffusion sequence for 7 minutes. All the cases were done on Phlips Ingenia 3T scanner

Results

Low grade (grade I & II) gliomas showed less intracellular volume fraction (ICVF) in tumoural and peritumoural region as compared to high grade gliomas. Low grade gliomas showed higher isotropic volume fraction in intratumoural and peritumoural regions. Significant increase in orientation dispersion indices in high (grade III & IV) grade lesions. NODDI indices showed no statistical difference in IDH wild and mutant type gliomas.

Conclusions

NODDI diffusion model gives three indices ICVF, ISO, ODI which appears to show significant variation in tumoural, peritumoural region according to tumour grade. ICVF appears to be most important parameter in differentiating low grade from high grade lesions

with consistently increased value in Intratumoural and peritumoural regions in high grade lesions. NODDI parameters were inconclusive in differentiating IDH wild from mutant lesions.

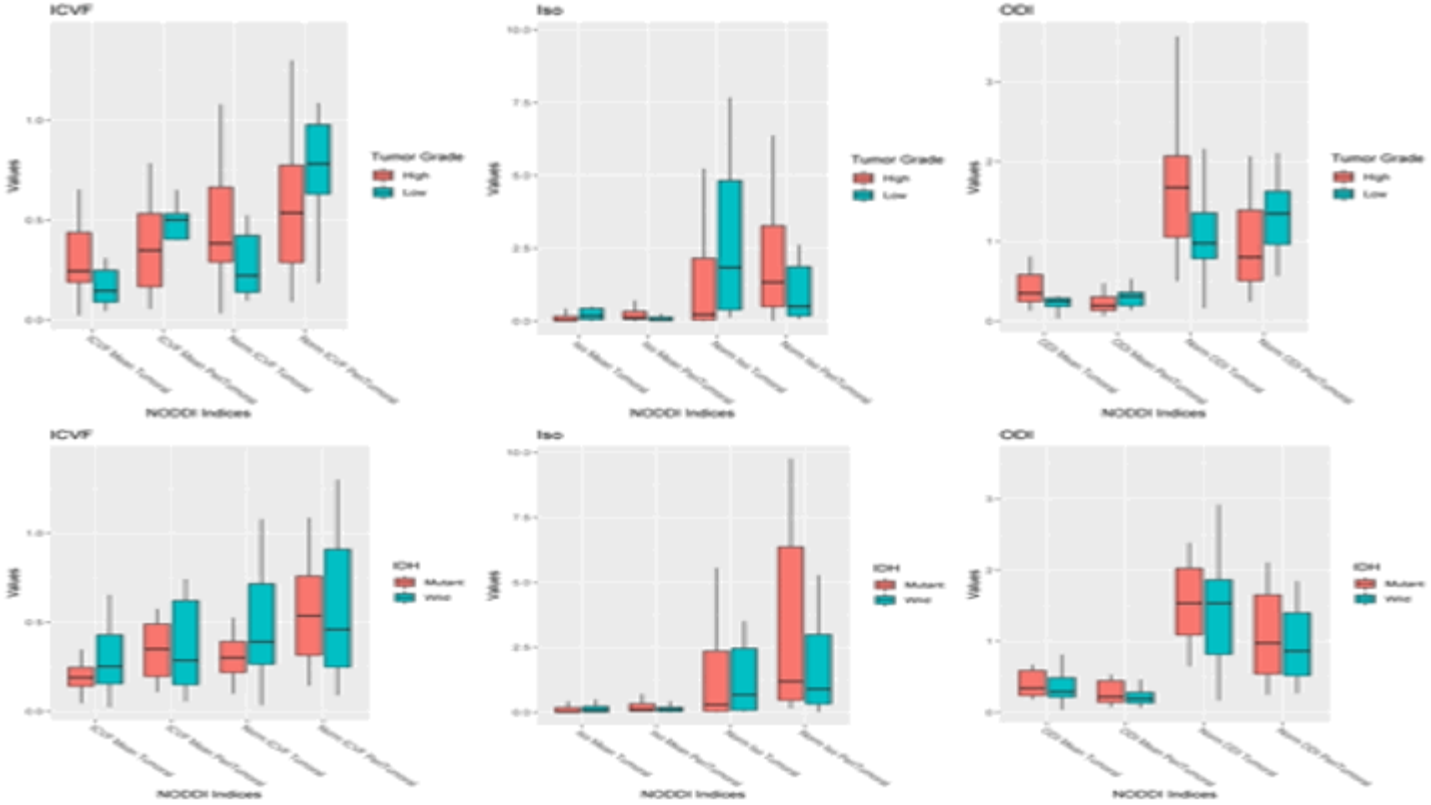

(Filename: TCT_754_asnrrn.gif)

814

MRI Radiogenomics Analysis Predicts KRAS, EGFR and MET Mutational Status in Non-Small Cell Lung Carcinoma Brain Metastasis

M Ak[1], P Mamindla[1], M Yilmaz[1], V Peddagangireddy[1], N Tahon[1], L Stabile[1], T Burns[1], R Colen[1]
[1]Hillman Cancer Center, University of Pittsburgh Medical Center, Pittsburgh, PA

Purpose

Non-small cell lung cancer (NSCLC) has the highest incidence of metastases to the brain.1 Targetable alterations are often present in brain metastasis not found in the primary tumor. A non-invasive strategy is needed to detect brain-specific alterations. This study was conducted to assess the potential of radiogenomics to predict KRAS, EGFR and MET mutation status in brain metastasis from NSCLC patients.

Materials and Methods

We retrospectively identified 159 NSCLC brain metastasis with both imaging and genomic annotation available. For each lesion, we segmented edema, contrast enhancement, and necrosis volume of interest (VOI) on both T2 FLAIR and T1 post-contrast sequences.2 Additionally, contralateral white matter (cWM) was also segmented for feature normalization. 10 histogram based first-order features and 195 second-order gray level co-occurrence matrix features were extracted from each VOI.3 After feature normalization, we divided the 195 second order features by the volumes of each VOI to produce another 195 volume-independent features per VOI for a total of 2,400 extracted features per lesions. We performed feature selection with Least Absolute Shrinkage and Selection Operator (LASSO). We split the cohort into 70% training and 30% testing sets for KRAS and EGFR and 80% training and 20% testing sets for MET models. We report the area under the curve (AUC) for classifying mutation status of each lesion and XGBoost (eXtreme Gradient Boosting) was used to generate radiomics model.

Results

Out of the 2,400 total features, LASSO identified 32 features for the EGFR mutant (mt) prediction model; of which the 20 most relevant were used for model building. The model achieved 78% accuracy, 77% sensitivity and 100% specificity. For the KRAS mt prediction model, LASSO defined 91 features and the model was generated with the top 30 features attaining 71% accuracy, 82% sensitivity and 60% specificity. Similarly, LASSO determined 90 features for MET mt prediction model, of which the top 15 features were used for the model demonstrating 77% accuracy, 76% sensitivity and 83% specificity.

Conclusions

This study demonstrates that radiomics-based signatures can predict brain-specific molecular alterations including KRAS, EGFR and MET mutations. While further validation is warranted in a larger cohort, the proposed predictive radiomics-based approach is cost-effective, non-invasive and will help identify NSCLC patients with brain metastasis that are likely to respond to targeted treatments.

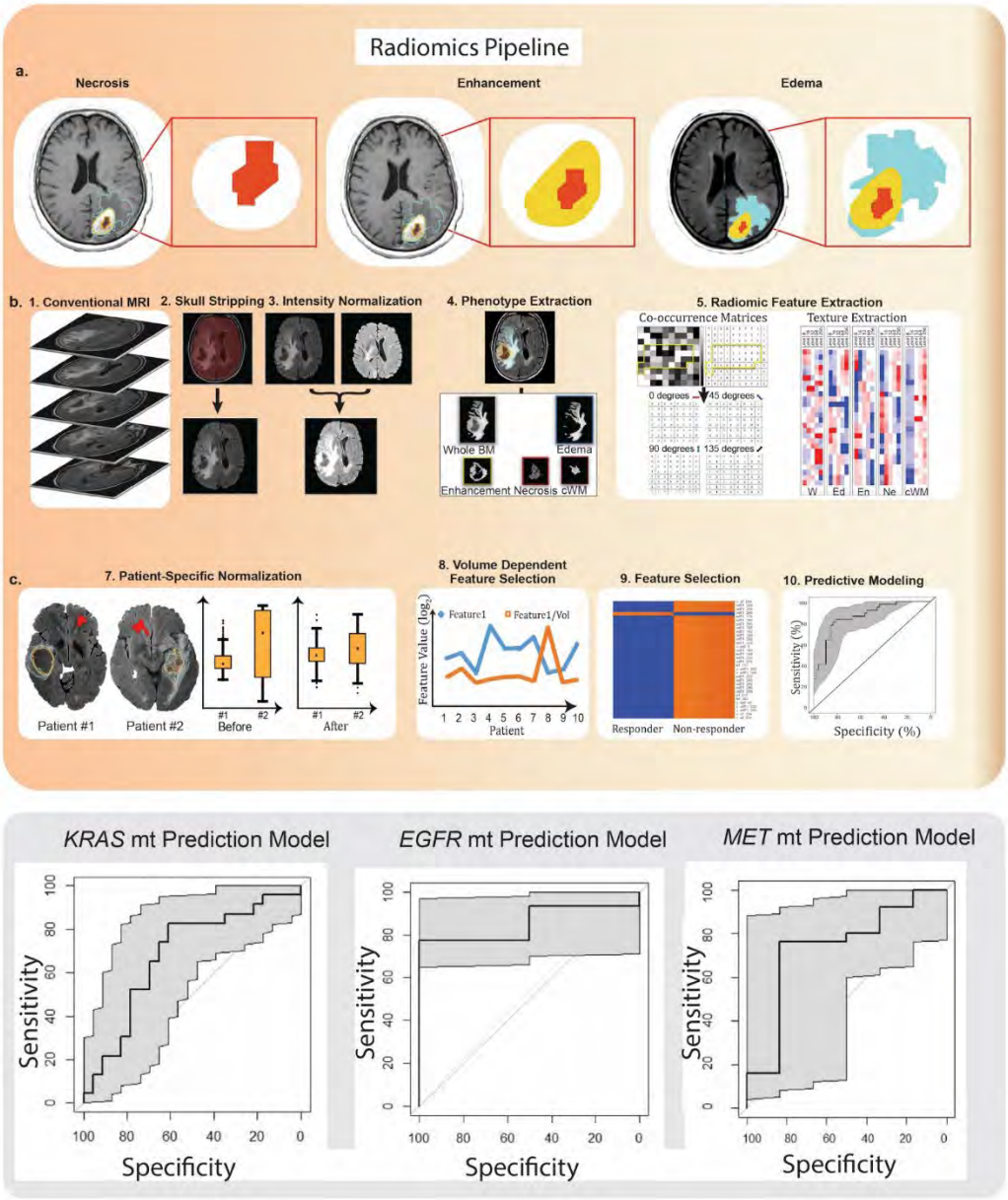

(Filename: TCT_814_BrainMetsFig-03.jpg)

470

Multi-site Benchmark Study for DSC-MRI Perfusion Imaging in Untreated Brain Metastases Using the Consensus Acquisition Protocol.

S Kohn[1], M Kong[2], D Phung[3], M Prah[4], J Urcuyo[5], J Ye[6], F Attenello[6], J Mendoza[7], M Shiroishi[8], L Hu[2], K Schmainda[4]

[1]Medical College of Wisconsin, Wauwatosa, WI, [2]Mayo Clinic, Arizona, Phoenix, AZ, [3]University of Southern California, Los Angeles, CA, [4]Medical College of Wisconsin, Milwaukee, WI, [5]Mayo Clinic, Phoenix, AZ, [6]Keck School of Medicine of USC, Los Angeles, CA, [7]Jesse W L Mendoza, Placentia, CA, [8]KECK SCHOOL OF MEDICINE, USC, Los Angeles, CA

Purpose

To determine standardized rCBV (sRCBV) in untreated brain metastases in comparison to glioblastoma and normal appearing brain, using the DSC-MRI national consensus acquisition protocol.

Materials and Methods

Patients from three sites (Medical College of Wisconsin, Mayo Clinic-Arizona, Keck School of Medicine of USC) with untreated enhancing brain metastases on MRI were considered for inclusion in this retrospective study. MRIs performed at 1.5T or 3T included post-contrast T1w(T1+C) images obtained after administration of GBCA (0.1 mmol/kg), which serves as a preload for the DSC-MRI data collection, consistent with the consensus recommendation(1,2). A 2nd GBCA dose (0.1 mmol/kg) was administered 40-60sec after the collection of baseline GRE-EPI images using recommended settings (FA=60o, TE/TR=30ms/1100-1250ms) for 120s. Data was post-processed with IB Rad Tech (Imaging Biometrics LLC, ElmGrove, WI) designed to generate dT1 maps(3), for delineation of

T1+C ROIs, and standardized (calibrated) rCBV (sRCBV)(4) that do not require normalization. Mean sRCBV for metastases, using dT1 or T1+C ROIs, and normal appearing white matter (NAWM) were determined and compared to untreated glioblastoma (GBM) from a previous study(5). Pairwise comparisons were performed using the Mann-Whitney nonparametric test with $p<0.05$ considered significant.

Results

N=47 patients with primary histologies of lung (n=23); breast (n=6); skin (melanoma and squamous cell carcinoma) (n=7); gastrointestinal (GI: n=3) and genitourinary (GU: n=8) cancers were included in comparison to GBM (n=31). Example images are shown (Fig. 1). The mean sRCBV of all metastases (1.83+/-1.09) were significantly lower (p=0.0013) than mean sRCBV for GBM (2.67+/-1.34) with both statistically greater ($p<0.0001$) than NAWM (0.71+/-0.16) (Fig. 2a). The sRCBV from histologically-distinct metastases are shown (Fig. 2b) with each being statistically greater than NAWM ($p<0.0001$).

Conclusions

This study describes initial results of a multi-site benchmark study using the consensus DSC-MRI acquisition protocol in untreated brain metastases. Similar to GBM, the sRCBV for untreated brain metastases are significantly higher than normal appearing brain. This confirms use of sRCBV to readily identify biologically active untreated brain metastases when using the consensus protocol.

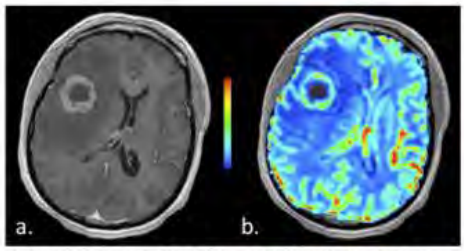

Figure 1. Example (a) T1+C and (b) sRCBV standardized rCBV for a patient with primary lung cancer.

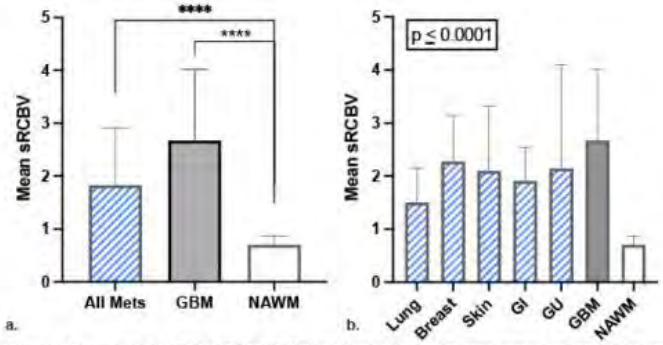

Figure 2. Mean standardized rCBV (sRCBV) for (a) untreated metastases and untreated glioblastoma (GBM) are statistically different from eachother ($p<0.0001$) and each significantly greawter than for normal-appearing white matter (NAWM) ($p<0.0001$). b. The sRCBV for individual brain metastases are also significantly higher than NAWM with $p<0.0001$.

(Filename: TCT_470_AJNR22_Kohn_BrainMetsSRCBV_Figures10241024_1.jpg)

1258

Objective assessment of glioblastoma (GBM) extent of resection (EOR) using quantitative delta T1 (dT1) maps.

B Laing[1], M Prah[2], K Schmainda[2]

[1]Medical College of Wisconsin, Wauwatosa, WI, [2]Medical College of Wisconsin, Milwaukee, WI

Purpose

To demonstrate in glioblastoma (GBM) the utility of a quantitative and objective method, delta T1 (dT1), to replace the current variable, imprecise and subjective approach (1) of assessing extent of brain tumor resection (EOR).

Materials and Methods

54 patients provided informed written consent to this IRB-approved and HIPAA-compliant study. Inclusion criteria consisted of IDH wild-type glioblastoma for whom complete image datasets of matched pre/post T1w imaging were obtained both before and within 0-14 days after initial tumor resection and prior to initiation of adjuvant therapy. Delta T1 (dT1) maps were generated from the difference between standardized (calibrated) post- and pre-contrast T1-weighted (T1w) images, providing quantitative difference maps (Imaging Biometrics LLC, Elm Grove, WI) (2) The dT1 are free of confounding pre-contrast T1 signal, such as from blood products, which can confuse the determination of the true contrast-enhancing lesion ROIs. A previously determined threshold (2) was applied to dT1 to generate consistent ROIs of enhancing tumor. Next, the extent of resection was quantified by determining the percent difference between the pre- and post-resection dT1 ROI volumes. Kaplan-Meier survival analysis was performed to determine if

overall survival (OS), measured from time of surgery, is influenced by the EOR. The EOR was categorized as EOR>90% (n=5), 50%<EOR<90% (n=16) and 10%<EOR<50% (n=6), which reflect previous designations of near-total, subtotal and partial resections. An additional analysis, motivated by a previous meta-analysis of elderly (>60y) patients with glioblastoma (3) was performed to assess age-dependent benefits of EOR.

Results

N=27 patients, ranging in age from 36-84y, satisfied the inclusion criteria. Example pre and post-resection T1w, T1w+C and dT1 maps are shown in Figure 1. No significant differences in OS based on EOR were determined for all patients combined (not shown). However, as shown in Figure 2, EOR may be more beneficial for younger (<60y) than older patients (>60y) for whom the trends seem to show worse outcomes with greater EOR.

Conclusions

The results suggest that maximizing EOR for IDH1-wildtype glioblastoma may be of greater importance for younger patients. However, the study sample size is small requiring a larger study for confirmation. Overall, this study demonstrates the utility of using the quantitative marker, dT1, to objectively define EOR and provide important information to assess the risks and benefits of maximizing EOR.

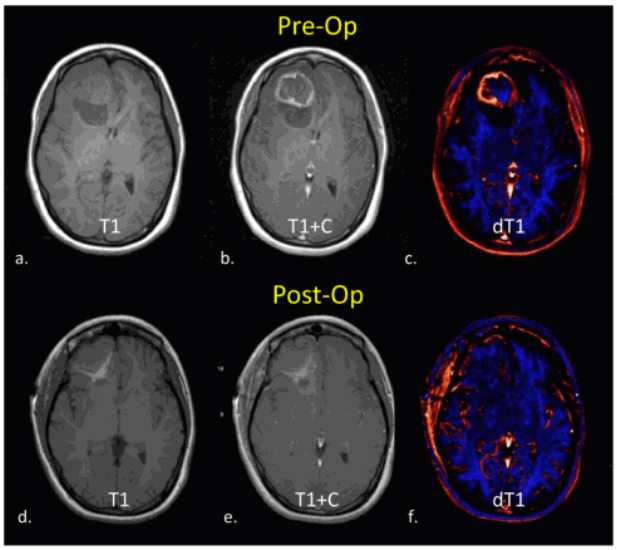

Figure 1. Example T1w, T1w+C and dT1 images, from 59 y female with IDH1-wild type glioblastoma, obtained 3 days before and 1 day after tumor resection (ie pre/post-op). Despite the bright signal on the post-resection pre-contrast T1w image (d) the post-resection dT1 clearly shows near-total resection with 82% removal of enhancing tumor for the entire tumor volume (all slices not shown).

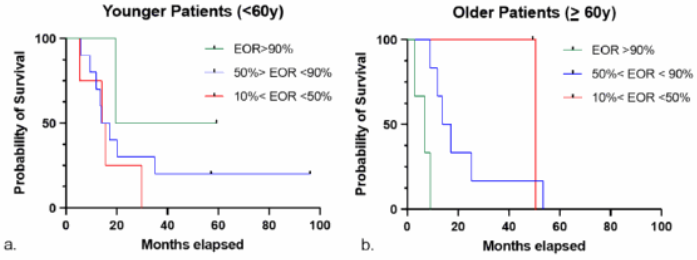

Figure 2. Kaplan-Meier survival curves based on extent of resection (EOR) for (a) younger patients <60 y (n=13) and (b) older patients > 60y (n=10) with glioblastoma. While not significant for this small sample size there is a trend towards improved survival with greater EOR for younger patients, and a reverse trend for older patients.

(Filename: TCT_1258_BLaing_ASNR2022_Figures.gif)

810

Treatment-induced tissue changes or viable tumor tissue? A prospective monocentric study in patients with brain tumor treated by chemo-radiotherapy, comparative analysis of DSC-MRI and contrast clearance TRAMs.

F Piccoli[1], G Savini[1], R Levi[2], L Bellu[1], E Clerici[1], A Franzini[1], S Olei[1], M Scorsetti[2], F Pessina[2], P Navarria[1], L Politi[2]
[1]Humanitas Research Hospital, Rozzano, Milano, Italy, [2]Humanitas University, Pieve Emanuele, Milano, Italy

Purpose

Radionecrosis following stereotactic radiotherapy of brain metastasis and pseudo-progression after radiotherapy with concomitant and

adjuvant chemotherapy in GBM may be misdiagnosed as true tumor progression.In these settings, contrast-enhanced MRI is frequently unable to differentiate tumor from treatment-induced tissue changes. For TRAM (treatment response assessment map) analysis,3D T1W sequences are acquired 5 and 90 minutes after contrast injection: in viable tumor tissue the rapid enhancement upon Gadolinium injection is followed by contrast clearance (CC) compared to normal-appearing white matter (NAWM); on the contrary, anomalous contrast accumulation (CA) occurs in radionecrotic tissue. The purpose of this prospective work is to compare the accuracy of TRAMs[1] and dynamic-susceptibility contrast (DSC)-MRI[2] in the differentiation of tumor progression and treatment-induced effects in patients with GBM and/or brain metastasis following standard-of-care treatment.

Materials and Methods

DSC-MRI and delayed-contrast MRI were acquired in 10 patients (3 GBM, 7 brain metastasis) with equivocal findings on a prior contrast-enhanced MRI. TRAMs resulted from the subtraction of T1W sequences acquired at 90 minutes after the injection of Gadolinium from those acquired at 5 minutes after contrast injection. Whole tumor and enhancing tumor volumes were segmented using a convolutional neuronal network[3]. Upon co-registration, we measured corrected relative cerebral blood volume (rCBV) normative values (90th percentile) in CA and CC volumes derived from TRAMs. We also measured the CC relative volume (rvCC) within the whole tumor volume. Eventually, the accuracy of DSC and TRAM-derived metrics was evaluated using clinical and radiological follow-up (available for at least 6 months in all subjects) as reference.

Results

We observed significantly increased rCBV values in CC volumes compared to CA and NAWM regions. Patients with progressive disease (PD) showed significantly greater rvCC than subjects with stable disease (SD) or partial response (PR). TRAMs metrics were in agreement with DSC results and both techniques identified PD and SD or PR with comparable accuracy [rvCC: 0.80; crCBV: 0.80].

Conclusions

These preliminary data suggest that CC regions within enhancing tumor volumes on high-resolution TRAMs correspond to viable tumor tissue according to crCBV values. TRAM and DSC-MRI metrics have comparable accuracy in discriminating true tumor progression from treatment-induced tissue changes.

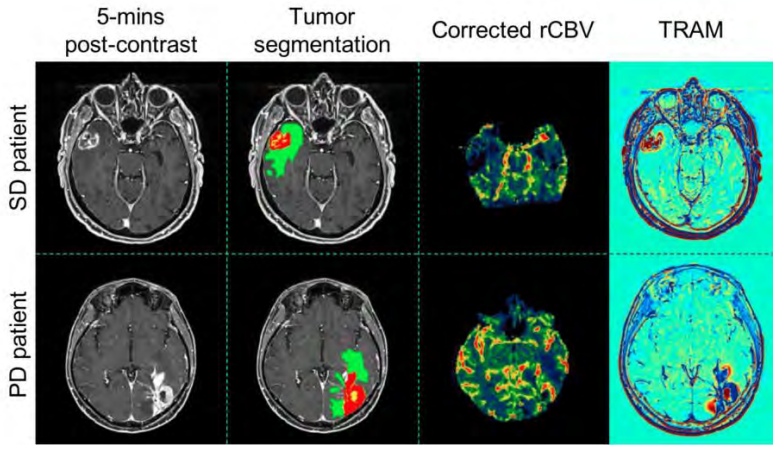

(Filename: TCT_810_tram.jpg)

Wednesday, May 18, 2022

3:40-5:10 PM

ASHNR Programming: Don't Be Spatially Confined: A Key Primer on Head and Neck Spatial Anatomy

419

Performance of NI-RADS to Predict Residual or Recurrent Head and Neck Squamous Cell Carcinoma

S Ali[1], D Kaht[1], J Lee[1], S Johnson[1], S Stock[1], J Bullen[1]
[1]*Cleveland Clinic, Cleveland, OH*

Purpose

The Head and Neck Imaging Reporting and Data System (NI-RADS) is a classification system that standardizes follow up reports for head and neck cancer cases. Level of suspicion for primary site and nodal recurrence is ranked on a scale of 1-4, from no recurrence to biopsy proven recurrence. Each NI-RADs category is associated with a specific management recommendation, including routine surveillance, direct visual inspection, short term (3 month) interval follow up, biopsy and clinical management in order from lowest to highest suspicion. The original results from this reporting system came from an institution that utilized dedicated head and neck Neuroradiologists. Since only a relative small number of institutions have dedicated head and neck Neuroradiologists, our purpose was to assess if general Neuroradiologists would have similar results.

Materials and Methods
Our study is a retrospective review of 608 NI-RADS reports (464 patients) from a group of 16 CAQ Neuroradiologists, including 2 who attend the weekly ENT tumor board. Patients with at least three months of follow up demonstrating no recurrence were considered true negatives, while patients with recurrence observed within one year were considered true positives. Receiver operating characteristic (ROC) methods for clustered data were used to assess accuracy.
Results
Recurrence rates for NIRADS 1, 2, 3 and 4 at the primary site were 5%, 29%, 80% and 100% and for lymph nodes were 3%, 10%, 80% and 100%, respectively. Overall, the area under the ROC curve (AUC) for NI-RADS was 0.765 (95% CI: 0.694, 0.836) at the primary site and 0.820 (95% CI: 0.733, 0.906) at the lymph node. ENT tumor board Neuroradiologists and general Neuroradiologists performed similarly in determining primary site recurrence (AUC of 0.765 and 0.762, respectively, 95% CI for difference: -0.13, 0.14; p = 0.966), though the former slightly outperformed the latter in determining nodal recurrence, but this was not significant (AUC of 0.872 and 0.779, respectively, 95% CI for difference: -0.07, 0.25; p = 0.249). Additionally, there were no statistically significant differences in AUC between first post-treatment scans (primary site: 0.903, lymph node: 0.778) and subsequent post-treatment scans (primary site: 0.756, lymph node: 0.825)(p = 0.149 and 0.743).
Conclusions
Our general neuroradiology practice demonstrated similar proficiency with NIRADs compared to dedicated head and neck Neuroradiologists, predicting recurrence with good distinction between the four categories.

908

Association of Conductive Hearing Loss with Isolated Tegmen Dehiscence with Ossicular Contact: A Retrospective Review and Evaluation of Prevalence on Temporal Bone CT

F Taghizadeh[1], B Hamilton[2]
[1]Oregon Health and Science University, Beaverton, OR, [2]Oregon Health & Science University, WEST LINN, OR

Purpose
The prevalence of isolated ossicular contact to a dehiscent tegmen and its relationship to conductive hearing loss (CHL) is unknown. This study aimed to determine the frequency of such findings on imaging, and to evaluate a link to CHL.
Materials and Methods
A retrospective review of all the temporal bone CT images obtained at our institution in 2020 to assess the prevalence of radiologic contact of the malleus to a dehiscent tegmen tympani. We performed a second search of our institutional database of radiology reports over the past 20 years to find cases of isolated ossicular contact to tegmen dehiscence presenting with CHL using the search terms "conductive hearing loss" and "tegmen dehiscence". We excluded any other radiologic causes for CHL, including overt meningoencephalocele. Electronic medical records were reviewed in positive cases to correlate with clinical findings.
Results
The consecutive temporal bone CT prevalence study identified only 1/318 (0.3%) patient having malleus contact of a contiguous segment of dehiscent tegmen during the one-year period. For the database search, we identified 278 patients. Following exclusions, 5 patients were found to have isolated malleus contact of a directly contiguous tegmen dehiscence as the only clearly identifiable source of their CHL.
Conclusions
Ossicular contact of a contiguous dehiscent tegmen in the absence of apparent meningoencephalocele is a rare isolated temporal bone abnormality associated with CHL. Future studies could evaluate the success of operative repair on CHL and allow assessment for the presence of occult meningocele.

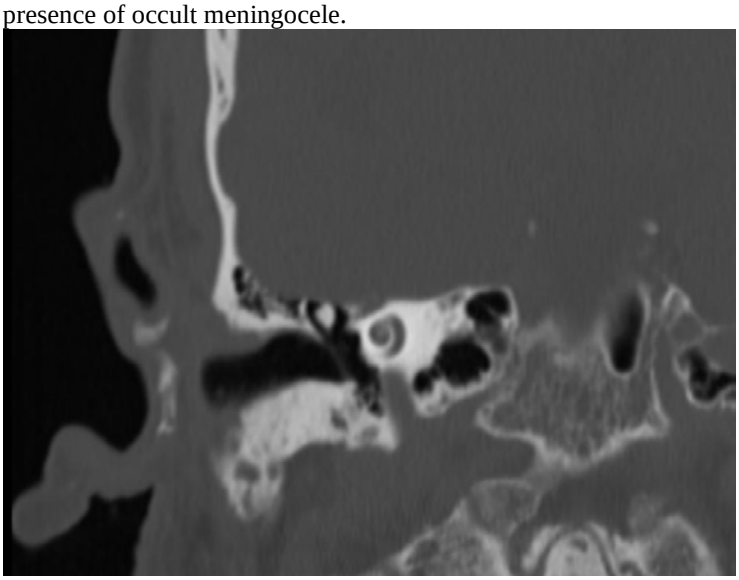

(Filename: TCT_908_tegmendehiscence.jpg)

374

Automated quantitative MRI distinguishes Alzheimer's disease from healthy controls in an academic and community health system

M Lim[1], S Dash[1], B Steach[2], J Pattee[1], P Pressman[1], B Bettcher[1], A Thaker[1], J Tanabe[1]
[1]University of Colorado Anschutz Medical Campus, Aurora, CO, [2]Icometrix, Boston, MA

Purpose
Dementia is a significant and growing public health care problem for which MRI remains the most widely used imaging tool. Qualitative determination of brain atrophy on MRI is unreliable and has prompted the use of automated quantitative software programs. Icobrain dm® automatically segments cortical and subcortical structures and has been shown to accurately quantify brain volumes with good diagnostic performance in differentiating patients with Alzheimer's disease (AD) from healthy controls [1,2]. However, validation in different clinical settings and diverse populations is still needed. We tested the hypothesis that patients with AD would demonstrate lower temporal, parietal, and hippocampal volumes compared to those with subjective complaints (SC) seen in an academic and community health care system.
Materials and Methods
IRB-approved retrospective review of the electronic medical record of the University of Colorado Health System was performed. Potential subjects were identified using the TriNetX database with filters for ICD-10 codes corresponding to diagnoses of AD (G30) and other specified cognitive deficit (R41.84). All subjects received the diagnosis after 2016 and had a volumetric brain MRI within one year of diagnosis. Inclusion for AD: clinical diagnosis of AD confirmed by a board-certified neurologist or APP in the neurology clinic. Inclusion for SC: age ≥35 years, subjective cognitive complaints. A diagnosis of MCI was not an exclusion for SC. MRIs were sent from PACS to Icobrain dm®(5.7.1) for analysis. After passing automatic QC, segmented volumes normalized to head size were extracted. Multiple linear regression of hippocampal and cortical lobar volumes was conducted and adjusted for age and sex.
Results
65 AD (32% male, mean age 76.7 years (SD 8.01)) and 40 SC (35% male, mean age 57.6 years (SD 13.1)) were eligible. Compared to SC, AD had significantly lower hippocampal ($p < 0.001$), temporal ($p = 0.004$), and occipital lobe cortical volumes ($p = 0.003$). There was no significant difference in parietal or frontal lobe cortical volumes.
Conclusions
Significantly lower hippocampal and temporal volumes in AD compared to SC are consistent with known patterns of atrophy in Alzheimer's disease. Our results suggest that Icobrain dm® applied to a diverse population in a health care system may offer a quantitative measure to the radiology report that could increase confidence in diagnosis. Larger samples and inclusion of other dementias are needed for further validation.

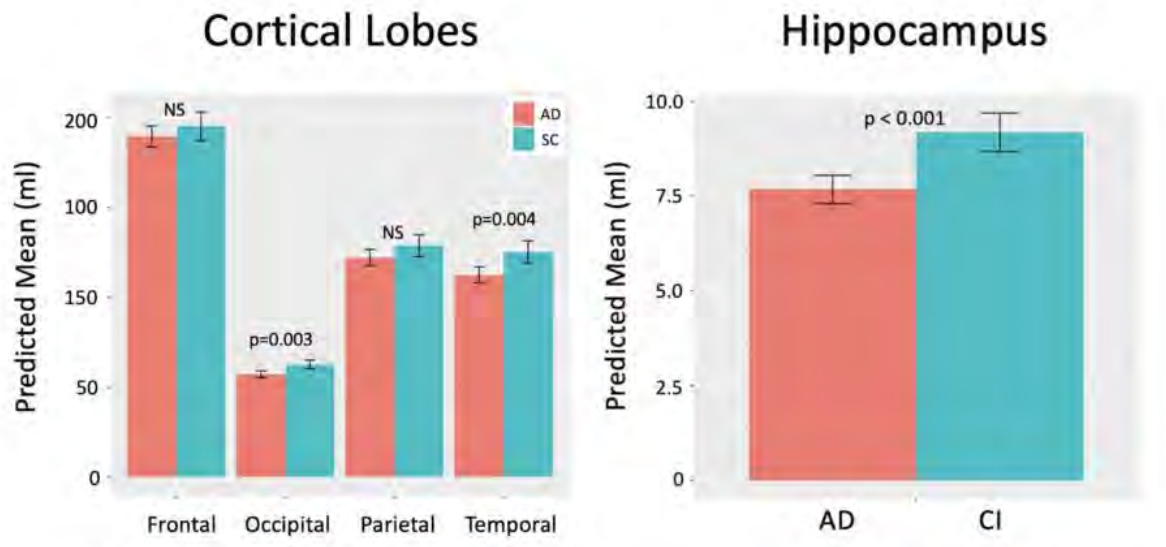

Figure. Mean brain region volumes. Volumes for the four cortical regions (left) and the one subcortical region (right) are stratified by group and adjusted for age and sex. Error bars represent the model-estimated 95% confidence interval.

(Filename: TCT_374_Figure.jpg)

477

Calibration of a Practical ARIA-E MRI Severity Scale Suitable for Clinical Practice

G Klein[1], L Bracoud[2], D Purcell[3], P Delmar[4], S Bullain[4], D Abi-Saab[4], J Barakos[3], M Baudler-Klein[4], P Fontoura[4], G Kerchner[4], R Doody[4]

[1]Roche Pharma Research and Early Development, Basel, Switzerland, [2]Bioclinica Inc., Lyon, France, [3]California Pacific Medical Center, San Francisco, CA, USA, [4]Roche/Genentech Product Development, Neuroscience, Basel, Switzerland

Purpose

Vasogenic edema and sulcal effusions detected with magnetic resonance imaging (MRI) are known and manageable possible side effects of many anti-amyloid immunotherapies. Periodic MRI scans and severity assessment of these imaging findings, known as amyloid-related imaging abnormalities – edema (ARIA-E) are currently mandated in clinical trials evaluating these therapies. Previous studies of gantenerumab have used a 60-point severity scale (the Barkhof Grand Total Scale [BGTS]),^1 which is effective for research purposes with good inter-rater reliability (intraclass correlation coefficient [ICC]=0.78, 95%CI [0.36-0.94]) between trained neuroradiologists. Other anti-amyloid studies have used a simpler 3-point severity scale, which has excellent inter-rater reliability (ICC=0.93, 95%CI [0.89-0.96])^2 and is likely to be of more practical use in clinical practice. This work compares the BGTS with the 3-point scale, and with a more refined, 5-point scale.^2

Materials and Methods

T2- Fluid-attenuated inversion recovery (FLAIR) and T2*- Gradient Echo (GRE) MRI scans (5 mm slices, no gap, 256x256 matrix) from 100 participants (87 with previously detected ARIA-E, 13 without ARIA from original BGTS assessment) in the Marguerite RoAD gantenerumab study (NCT02051608)^3 were selected. After excluding 3 scans due to missing data or unacceptable quality, all valid scans were re-read using all three severity scales by one neuroradiologist with extensive experience (>500 reads) on all three scales. The reader was presented with pairs of baseline/follow-up scans, blinded to prior read results. Assessment of ARIA-H was also completed. Scale descriptions are previously published.^1,2

Results

Median (inter-quartile range) BGTS scores for the 3-point scale were 0=0(0-0), 1=1(1-3), 2=8(5-14), and 3=20(20-20), and for the 5-point scale were 0=0(0-0), 1=1(1-3), 2=6(4-9), 3=NA, 4=15(10-20), and 5=20(20-20) (Figure 1). Spearman's rank correlation between BGTS and the 3-point scale was 0.85 and 0.91 for the 5-point scale. Regression analysis of ARIA-E severity scale to ARIA-H count showed moderate positive association with Pearson's r of 0.37 (3-point), 0.40 (5-point), and 0.50 (BGTS).

Conclusions

The simplified 3- and 5-point scales are well correlated to the 60-point BGTS ARIA-E severity scale; the 5-point scale had better correlation than the 3-point scale. Further study is warranted to assess reliability for reads performed by non-specialist radiologists in real-world applications.

Figure 1.
Comparison of BGTS to simpler 3- and 5-point ARIA-E severity scales

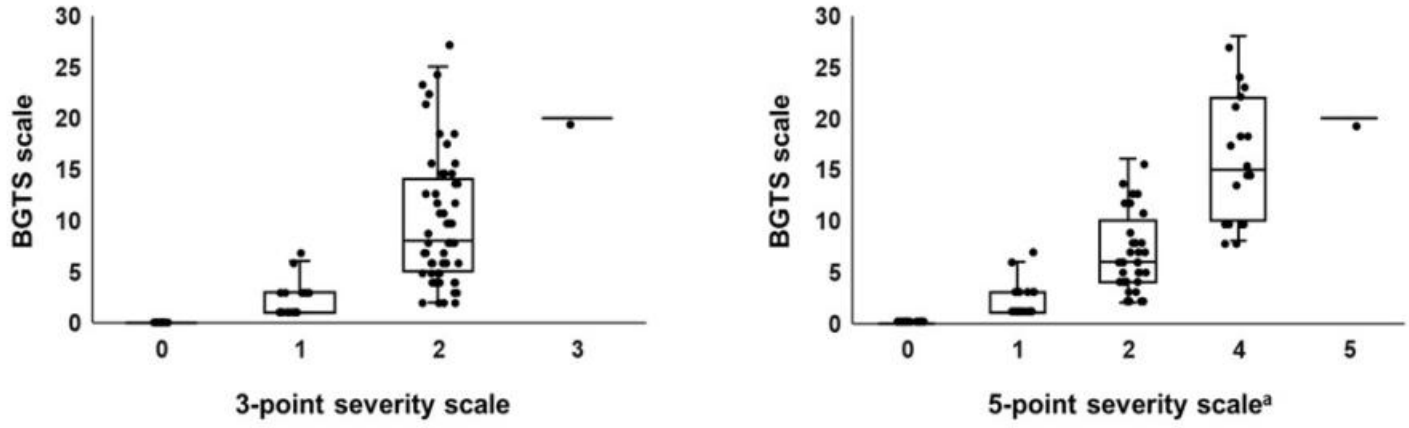

[a]No patients scored a "3" on the 5-point scale

(Filename: TCT_477_ASNR2022_ARIAscaleabstract_figure.jpg)

937

Hippocampal Subfield Volumes are Differentially Reduced in Diagnoses of Alzheimer and Mixed Dementia

I Kwak[1]

[1]*Washington University in St. Louis, Valhalla, NY*

Purpose

Hippocampal volume abnormalities are detailed in multiple neurocognitive disorders, but it remains unclear whether hippocampal substructure, comprised of separate hippocampal subfields, are affected in varying patterns across these diagnoses. Manual segmentation of the hippocampus remains the gold standard but is limited by time and inter-operator variability. We therefore utilized the automated segmentation tool, volBrain's HIPS pipeline, to analyze hippocampal subfield volumes in diagnoses of dementia and other neurocognitive disorders.

Materials and Methods

Brain MRI scans from 134 participants (Average age = 74.8, Age range = 56-94, Women:Men ratio = 1.83) were drawn from The Open Access Series of Imaging Studies (OASIS-4) (https://www.oasis-brains.org/) and delineated by clinical diagnosis: Alzheimer Dementia (AD, n = 50), AD/Vascular Dementia (AD/VD, n = 38), Frontotemporal Dementia (FTD, n = 20), Parkinson's Disease (PD, n = 10), and Vascular Cognitive Impairment (VCI, n = 16). Hippocampal subfield volumes were calculated using volBrain's HIPS pipeline, resulting in 5 subfield volumes: Cornu Ammonis (CA) 1, CA2-CA3, CA4-Dentate Gyrus (DG), Strata Radiatum/Lacunosum/Moleculare (SR-SL-SM), and Subiculum. Analysis of covariance (ANCOVA) were used to compare hippocampal subfield volumes between diagnostic groups when controlling for age, sex, and intracranial volume (ICV). Results were corrected for multiple comparisons ($p < 0.005$).

Results

Hippocampal subfields CA1, SR-SL-SM and Subiculum were specifically affected in AD ($p < 0.05$) while CA2-CA3 was affected in AD/VD Mixed Dementia ($p < 0.05$) compared to other dementia diagnoses (FTD and VCI). CA4-DG was affected in both AD and AD/Vascular Mixed Dementia ($p < 0.01$) compared to FTD and VCI.

Conclusions

Hippocampal subfields are differentially affected across various dementias and other neurocognitive disorders. This work also contributes to further study to validate the use of hippocampal subfield segmentation and volumetric quantification as a contributing diagnostic tool for neurocognitive disorders.

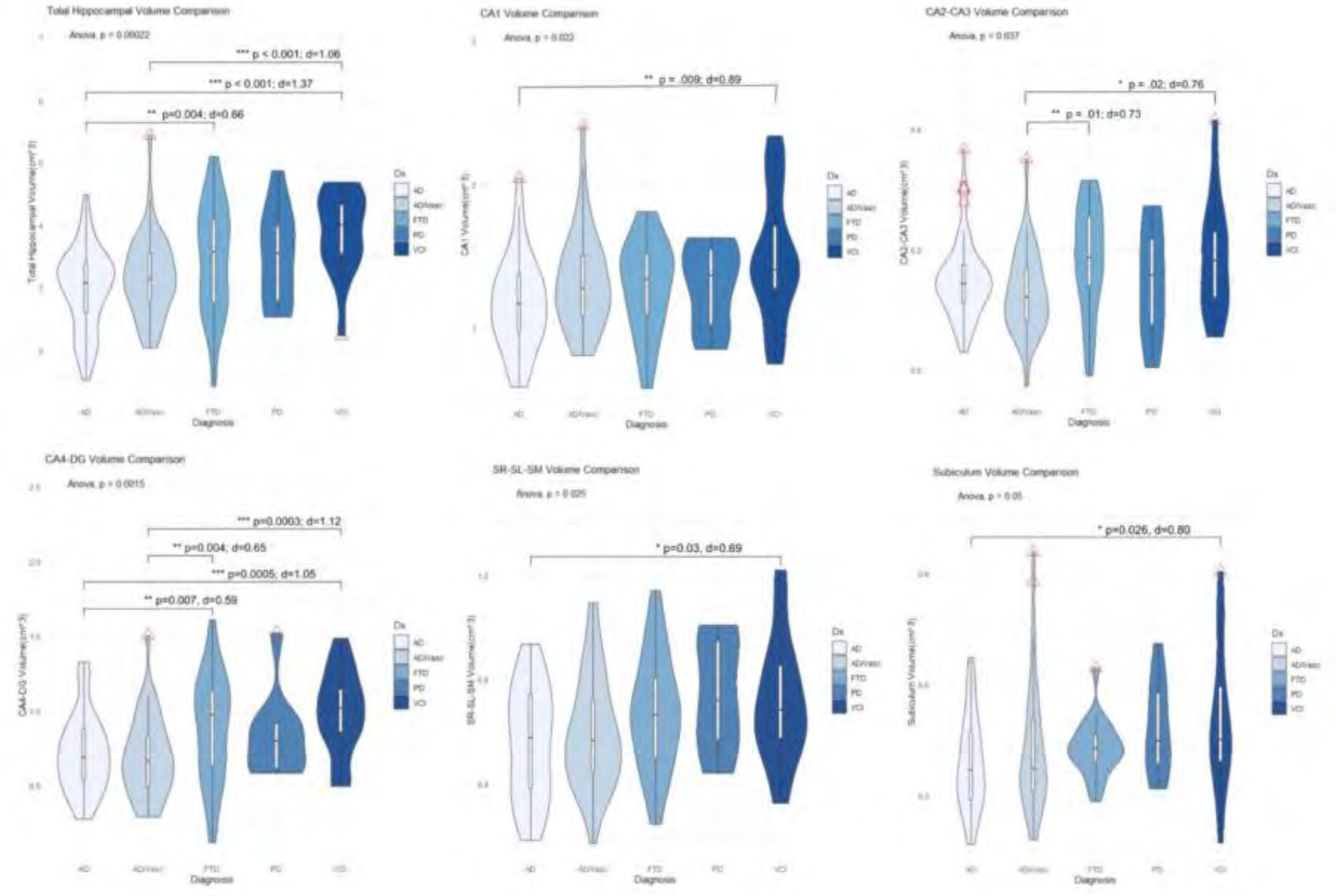

(Filename: TCT_937_IKwak_figure.jpg)

1240

Machine Learning on Top of Deep Learning-based Brain Morphometry to Support Objective Scoring and Diagnosis of Neurodegenerative Disorders

M MAROS[1], C Cho[2], L Hausner[3], A Förster[4], C Groden[4], H Wenz[2]

[1]Heidelberg University, Medical Faculty Mannheim, Mannheim, Baden-Wuerttemberg, [2]Medical Faculty Mannheim, Heidelberg University, Germany, Mannheim, Baden-Wuerttemberg, [3]Central Institute of Mental Health (ZI), Mannheim, Baden-Wuerttemberg, [4]Medical Faculty Mannheim, Heidelberg University, Mannheim, Baden-Wuerttemberg

Purpose

We investigated whether supervised machine learning (ML) algorithms can be effectively applied to segmentation results of an FDA-approved deep learning-based brain morphometry algorithm in order to aid objective empirical neuroradiological scoring and comprehensive dementia diagnosis [1].

Materials and Methods

275 patients (157F, 57.1%; age median: 68yrs, range: 17-95yrs) with suspected neurocognitive disorders was re-trieved from local RIS/PACS (01/2012-08/2020) and matched to clinical neuropsychiatric diagnoses (Fig. 1A). Brain volumetric segmentation (BVS) of 47 anatomical structures was performed using the proprietary AI-Rad Companion MR Brain (Siemens Healthineers) software based on 3T isotropic (1mm) sagittal T1-MPRAGE images (Fig. 1B). Three neuroradiologists generat-ed consensus values of well-established empirical scoring systems including global cortical atrophy (GCA), medial temporal lobe atrophy (MTA), Koedam- for parietal atrophy and Fazekas scales for white matter lesions and NPH (overall 12 features; Fig. 1B). Supervised ML algorithms such as dense neural networks (DNN), tree-based algorithms were trained on BVS values within 5x-fold nested cross validation setup [2] to suggest these empirical scores and clinical diagnoses, respectively (Fig. 1C).

Results

Clinical diagnoses were highly heterogeneous, ~50% comprised of mild cognitive impairment (n=78,28.4%), Alz-heimer's disease (n=53,19.3%) and vascular dementia (n=11,4.0%) while the rest was a mixture of neuropsychiatric disorders including depression (n=29,11%) or schizophrenia (n=13,4.7%). Segmented volumes (rsp=0.68, $p<0.001$) showed a higher association with age than consensus empirical scores of experts (rsp=0.4, $p<0.001$). DNNs achieved the highest top 3 classification accuracies (70-88%) for clinical diagnoses. Random forests could automatically match the most relevant BVS features for each empirical scores without manual pairing.

Conclusions

Multilayer ML setup with supervised algorithms trained on top of deep learning-based volumetric morphometry can objectively aid radiological and clinical diagnosis of neurocognitive disorders while providing robust and reproducible measures for follow-up evaluation. Due to its anonymized nature, our study cohort could serve as benchmark data set for comparing algorithms of various vendors.

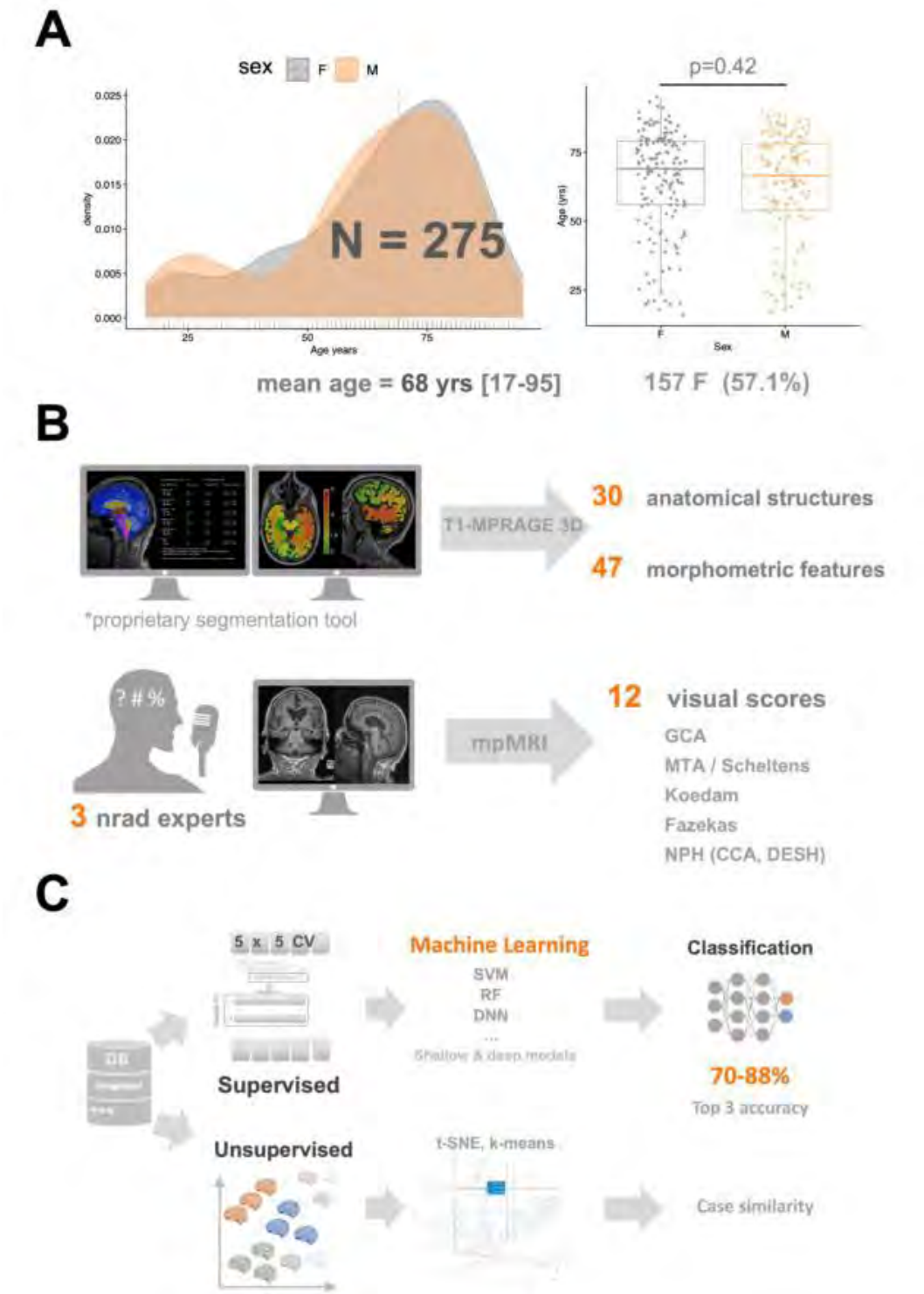

(Filename: TCT_1240_ASNR2022-MarosMEetal-Fig1A-C-UPLOADED.jpg)

1224

Multimodal Deep Neural Networks for Predictive Diagnosis and Prognosis of Alzheimer's Disease

R Hussein[1], K Poston[2], J Fairchild[1], E Mormino[1], G Zaharchuk[1]

[1]Stanford University, Stanford, CA, [2]Stanford University, Palo Alto, CA

Purpose

Worldwide, around 50 million people have dementia, and there are nearly 10 million new cases every year [1]. Alzheimer's disease (AD) is the most common cause of dementia among older adults. Mild cognitive impairment (MCI) is an intermediary condition between normal aging and the more serious cognitive decline of AD. Identifying MCI individuals at high risk of developing AD is crucial for developing treatments for this disease. We developed a multimodal deep neural network that integrates neuroimaging,

genetics, and clinical assessments to predict whether an MCI patient will remain stable, revert to normal cognition, or progress to Alzheimer's disease.

Materials and Methods

This study uses the Alzheimer's Disease Neuroimaging Initiative (ADNI) [2] database for the analyses. Our dataset of 312 participants includes 80 subjects with normal cognition (NC), 148 patients with MCI (78 MCI converter [MCIc] and 70 MCI stable [MCIs]), and 84 patients with AD. The multimodal algorithm, shown in Figure 1, performs information fusion from heterogeneous medical data modalities to further improve the MCI-to-AD conversion prediction. The data modalities include neuroimaging (MRI and FDG-PET), genetics (APOE status), cognitive assessments, and blood biomarkers. The proposed architecture incorporates a Gated Recurrent Unit (GRU) to extract the distinguishable features from the clinical timeseries data, and dilated 3D Convolutional Neural Networks (CNN) to capture wider contextual information from MRI and PET exams. The intermediate features generated from the GRU and dilated CNN are concatenated and passed to an additional multilayer perceptron network for feature integration. The model performance was evaluated with tenfold cross-validation.

Results

The results show that multimodal deep neural networks can efficiently extract relationships amongst features from different data modalities, thus improving the prediction of AD and adequately measure the progression of MCI. Compared with the previous imaging and non-imaging single-modality methods [3], the proposed multimodal algorithm yields better prediction performance, achieving an average classification accuracy of 0.90(±0.26) for the three-class classification problem of NC-MCI-AD and 0.84(±0.32) for the binary classification problem of separating MCI stable from MCI converters.

Conclusions

This study demonstrates that multimodal deep neural networks that integrate multiple medical data modalities can accurately predict the different stages of Alzheimer's disease.

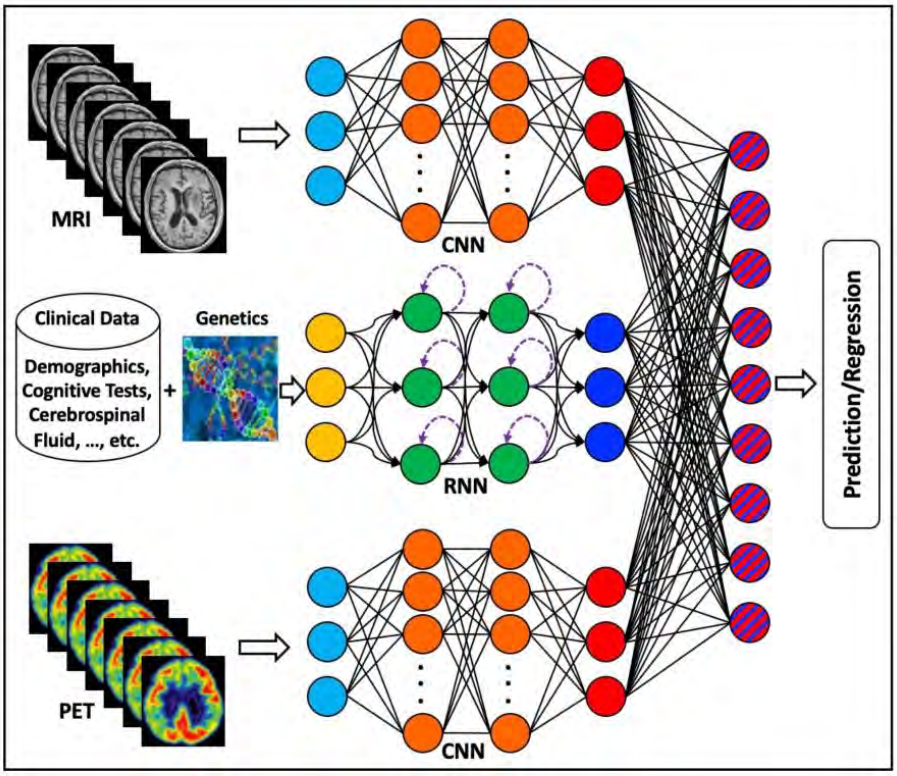

Figure 1. Our multimodal deep learning framework for MCI-to-AD conversion prediction

(Filename: TCT_1224_Figure1.jpg)

1427

Neuromelanin Sensitive MRI and Quantitative Susceptibility Mapping of the Substantia Nigra in Parkinson's-Linked Asian LRRK2 Carriers

L Chan[1], S Hartono[2], A Tan[1], W Lee[3], R CHEN[4], E Tan[5]

[1]Singapore General Hospital, Singapore, Singapore, [2]National Neuroscience Institute, Singapore, Singapore, [3]Singapore General Hospital, Singapore, N/A, [4]SINGHEALTH, SINGAPORE, SINGAPORE, [5]National Neuroscience Institute, Singapore, N/A

Purpose

Asian-specific leucine-rich repeat kinase 2 (LRRK2) gene risk variants are associated with increased risk of idiopathic Parkinson's disease (PD) and accelerated motor progression in disease. We examined the role of quantitative susceptibility mapping (QSM) and

neuromelanin-sensitive MRI (NMS) in quantifying iron deposition and dopaminergic denervation in the substantia nigra (SN) in (1) PD and healthy controls and (2) LRRK2 risk-carriers and non-carriers in PD.
Materials and Methods
Forty-seven PD patients and 32 healthy controls (HC) were included in this prospective study. All subjects underwent brain MRI scan on a 3T scanner including multi-echo SWI and NMS sequences. QSM images were reconstructed from the multi-echo SWI images. Visual and quantitative assessment (Figure 1) were performed.
Results
Visual assessment of the SN with NMS had a sensitivity of 71.88% and specificity of 93.62% to distinguish PD and HC. Visual assessment of the SN with SMWI had a sensitivity of 100% and specificity of 95.74% to distinguish PD and HC. SN size with high neuromelanin concentration in NMS was significantly reduced in PD (PD: 57.61 ± 51.28 mm2, HC: 163 ± 83.42 mm2; $p < 0.0001$). QSM susceptibility was significantly increased in PD (PD: 129.97 ± 32.15 ppb, HC: 91.26 ± 25.21 ppb, $p < 0.0001$). SN size with high iron deposition in SMWI was significantly increased in PD (PD: 67.39 ± 68.65 mm2, HC: 23.69 ± 35.96 mm2, $p = 0.0004$). QSM susceptibility and high-iron area in the SN were significantly increased in PD risk-carriers compared to non-carriers; NMS showed no difference between these two groups. Combined quantitative QSM models displayed good classification performance discriminating risk-carrier from non-carrier groups (68.4% sensitivity, 92.3% specificity, AUC 0.804) in PD.
Conclusions
NMS and QSM offered excellent classification of PD and HC through specific imaging of dopaminergic neurons and iron deposition, respectively. Furthermore, QSM had excellent diagnostic accuracy for identifying LRRK2-associated PD from idiopathic PD.

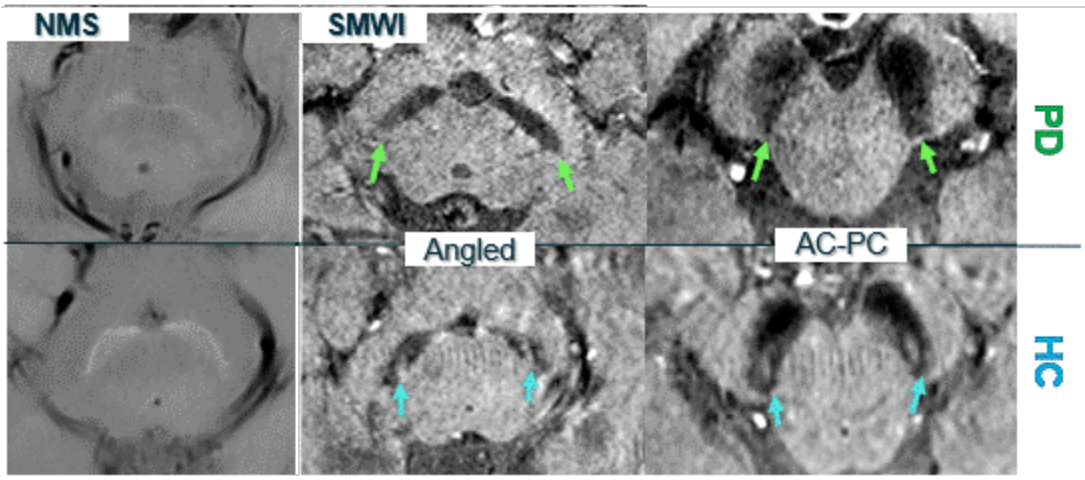

(Filename: TCT_1427_Fig1.gif)

879
Relationship of Cortical Microstructure Changes to Alzheimer's Disease Diagnosis and Plasma Amyloid and Tau Biomarkers
A Thaker[1], A Jensen[1], B Bettcher[1]
[1]*University of Colorado Anschutz Medical Campus, Aurora, CO*

Purpose
In vivo characterization of neurodegeneration associated with mild cognitive impairment (MCI) and Alzheimer's Disease (AD) has seen substantial advances. Recent techniques such as neurite orientation dispersion and density imaging (NODDI) has allowed complex and biologically relevant evaluation of diffusion signal, including within grey matter. Assessment of biomarker status in AD has also evolved, with plasma markers showing promise in replacing CSF and PET. In this study we applied NODDI to characterize microstructural changes within AD-vulnerable cortex and examine relationship with disease status and plasma biomarkers.
Materials and Methods
77 subjects enrolled in a longitudinal biomarker study with structural MRI, multi-shell DWI, and plasma biomarkers were included for analysis. All subjects underwent neurocognitive testing with 48 controls, 21 MCI, and 8 AD in the cohort. DWI was preprocessed followed by NODDI analysis in Matlab. T1 sequences were processed with Freesurfer for grey matter segmentation and applied to orientation dispersion index (ODI) and neurite density index (NDI) maps to extract means within defined regions-of-interest. Plasma biomarkers were assessed utilizing single molecular array (SiMoA) assays for assessment of Aβ42/Aβ40 ratio and phosphorylated-tau. Statistical analyses were performed utilizing R version 4.1. Linear regression models were used to evaluate whether ODI/NDI means were associated with clinical diagnosis while adjusting for demographics. A parallel analysis was used to assess whether an association existed between ODI/NDI and amyloid/tau plasma biomarkers.
Results
In MCI subjects, non-medial temporal cortex showed lower ODI (-0.007, $P = 0.016$) compared to controls. No significant ODI or NDI associations were identified in medial temporal, parietal, frontal, or cingulate cortex. In AD subjects, no significant ODI or NDI associations were identified in the examined regions. Trends were identified between Plasma tau and medial temporal ODI (0.010, P =

0.085), cingulate NDI (-0.011, P = 0.099), and parietal NDI (-0.012, P = 0.085). No significant association was identified between plasma amyloid and regional ODI or NDI across all participant diagnoses.
Conclusions
Microstructural changes in ODI are present in MCI in non-medial temporal cortex known to be involved in AD pathology. Though no AD associations were found, this preliminary analysis may be underpowered. Plasma tau biomarkers, but not amyloid, show a trend with NODDI microstructural measures.

596

Risk Estimation for Patients with Idiopathic Normal Pressure Hydrocephalus: Development and Validation of Deep Learning-based Nomogram

S Yun[1], C Suh[1], S Kim[1]
[1]*Asan Medical Center, Seoul, Seoul*

Purpose
Idiopathic normal pressure hydrocephalus (iNPH) is a potentially reversible disease which can be treated by CSF shunt surgery. However, there is a limitation in clinically diagnosing iNPH because a diagnostic method using non-invasive findings is not well established. The aim of this study was to develop and validate a nomogram based on brain MR imaging features to predict the probability for iNPH.
Materials and Methods
Patients who were clinically diagnosed as iNPH, Parkinson's disease (PD), Alzheimer's disease (AD), healthy control and who underwent MR imaging including 3D T1-weighted volumetric MR imaging were retrospectively identified. Clinical (age, sex) and imaging features (Sylvian fissure enlargement, high convexity tightness, Evans' index, callosal angle, adjusted ventricle volumes by ICV using DeepBrain) associated with iNPH were assessed. Japanese guideline served as the reference standard for iNPH. A prediction model was developed by using logistic regression and was then transformed into a nomogram. The performance of the nomogram was assessed with respect to both discrimination and calibration. The nomogram was internally validated using the bootstrap method.
Results
A total of 452 patients (mean age ± standard deviation, 70.0 ± 9.9; 200 men) were evaluated. Of these, 111 (25%, 74.5 ± 5.7; 73 men) patients were iNPH group and 341 (75%, 72.8 ± 6.7; 127 men) patients were non-iNPH group. A multivariable analysis, high convexity tightness (odds ratio [OR], 35.1; 95% CI: 4.5, 275.5), callosal angle < 90° (OR, 12.5; 95% CI: 3.1, 50.0), and adjusted lateral ventricle volume (OR, 4.2; 95% CI: 2.7, 6.7) were associated with iNPH. The matching nomogram using three variables displayed an area under the curve of 0.995 (95% CI: 0.991, 0.999) in the study sample and 0.994 (95% CI: 0.990, 0.998) in the internal validation sample. Calibration curve of probability of iNPH show good agreement between nomogram predictions and observed probability of iNPH.
Conclusions
A new nomogram that includes presence of high convexity tightness, callosal angle < 90° and adjusted lateral ventricle volume could help accurately estimate the probability for iNPH.

Table 1. Demographic and radiologic data of patients in the derivation cohort and results of univariable/multivariable analysis for identifying factors associated with normal pressure hydrocephalus

		Univariable		Multivariable	
factor		Odds ratio*	P value	Odds ratio*	P value
Age		1.04	0.019		
Sex	Male	3.2	<0.001		
Sylvian fissure enlargement	1	5.5	<0.001		
High convexity tightness	1	268.0	<0.001	35.1	0.001
Evans' index	>0.3	121.4	<0.001		
Callosal angle	<90	134.9	<0.001	12.5	<0.001
Adjusted 3rd ventricle volume	Per 0.1 unit	34.3	<0.001		
Adjusted 4th ventricle volume	Per 0.1 unit	7.7	<0.001		
Adjusted lateral ventricle volume	Per 1 unit	5.4	<0.001	4.2	<0.001

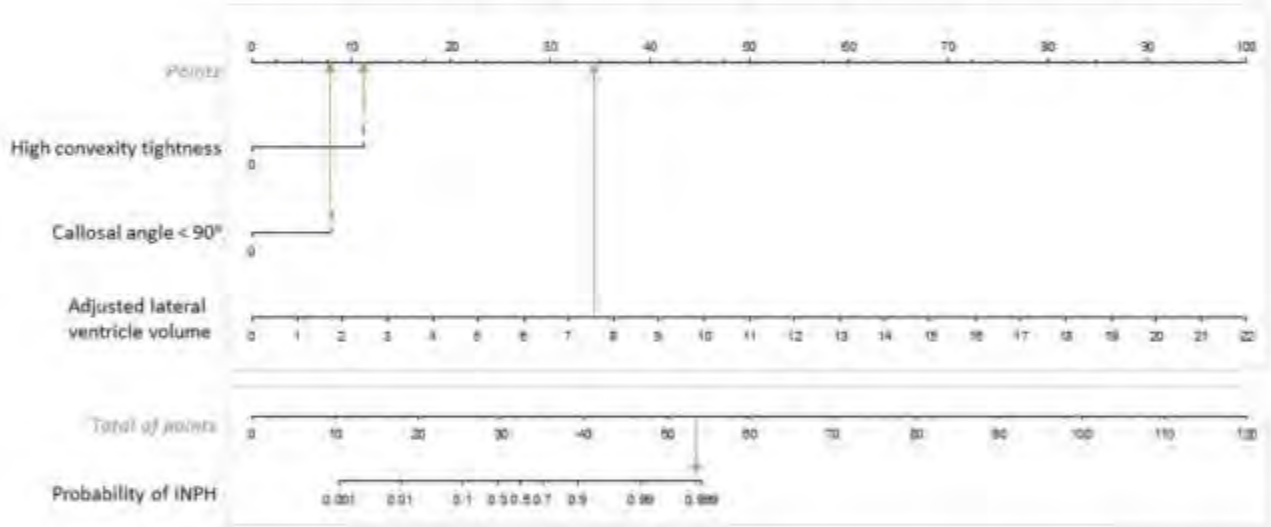

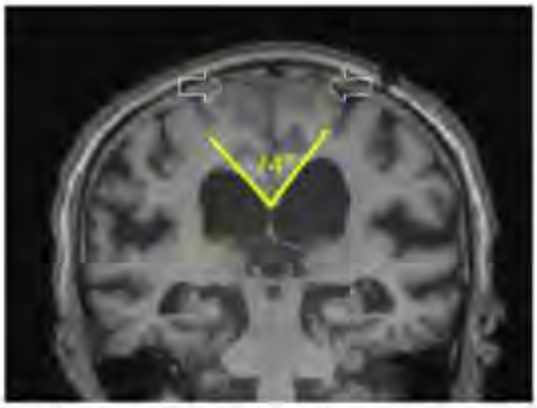

Lateral ventricle volume 105.542
Intracranial volume 1379.625

Adjusted lateral ventricle volume = 7.65

Figure 1. Examples of the nomogram in clinical practice. Figures illustrate the process of calculating the probability scores of iNPH. Coronal T1-weighted image in a 76-year-old man. MR imaging features were analyzed as follows: high convexity tightness = "yes" (arrows), callosal angle < 90° = "yes" (yellow lines, 74°), and adjusted total ventricle volume = 7.65. The total score is 53.93, which corresponds to a probability of iNPH greater than 0.99.

(Filename: TCT_596_asnr_figure.jpg)

244

The Impact of Carotid Intraplaque Hemorrhage on Cerebral Beta-Amyloid Deposition

S Culleton[1], H Baradaran[1], S Kim[1], D Parker[2], J Hoffman[3], K Duff[4], J McNally[1]

[1]University of Utah, Salt Lake City, UT, [2]University of Utah, Salt Lake City , UT, [3]University of Utah, Salt lake, UT, [4]Center for Alzheimer's Care, Imaging, & Research, Salt Lake, UT

Purpose

Carotid intraplaque hemorrhage (IPH) is a key feature of plaque vulnerability known to have downstream cerebral effects including stroke. The effect of IPH on brain amyloid accumulation, and the potential resultant cognitive implications, has yet to be fully elucidated. Consequently, this study aimed to determine the association between IPH and cerebral amyloid deposition.

Materials and Methods

After IRB approval, subjects considered for carotid intervention were recruited from neurovascular services. For inclusion, symptomatic subjects required ≥1 carotid plaque with ≥50% stenosis and ≥70% stenosis if asymptomatic. A 3T carotid MRI with MPRAGE was performed for IPH assessment and an 18F-Flutemetamol PET-CT evaluated cerebral amyloid deposition. SUVRs in 8 brain regions (pons as the reference standard), and z-scores were calculated [1]. Cognitive status was assessed using the Repeatable Battery for the Assessment of Neuropsychological Status (RBANS). Plaque features, cardiovascular risk factors, and medications were examined for confounding. A multivariable linear regression model was fitted to the outcome of amyloid deposition. The initial model included IPH and suspected confounders, p<.20. Backwards elimination to a p<.10 generated the final model. Univariable Pearson's correlation (r), multivariable linear regression coefficients (β) and two-tailed p-values were recorded.

Results

Forty-two subjects with a mean age of 70.5±7.6 years were included (Table). IPH was present in 17/42 (40.5%). The association between amyloid deposition and IPH was greatest in the occipital and sensorimotor regions. The final amyloid prediction model for occipital deposition included IPH (r=0.28, β=1.1, p=.03), max plaque thickness (r=-0.26, β=-0.5, p=.03), and smoking history (r=-0.31, β=-1.0, p=.06). For the sensorimotor region, the amyloid prediction model consisted of IPH (r=0.32, β=1.35, p=.004), max plaque thickness (r=-0.24, β=-0.47, p=.032), male (r=-0.28, β=-1.43, p=.023), and smoking history (r=-0.32, β=-0.87, p=.085). The RBANS delayed memory index (n=35) negatively correlated with amyloid deposition in occipital (r=-0.39, β=-4.01, p=.019) and sensorimotor regions (r=-0.43, β=-5.05, p=.011).

Conclusions

The association between IPH and amyloid deposition was greatest in the occipital and sensorimotor regions. Amyloid deposition in those areas negatively correlated with RBANS memory indices. Continued investigation would further delineate the contributions of IPH to brain amyloid deposition and memory decline.

Characteristics	Subjects n=42	
Age in years, mean (SD)	70.5 (7.6)	
Male, n (%)	36 (85.7)	
BMI in kg/m^2, mean (SD)	31.1 (7.3)	
Comorbidities		
Dyslipidemia, n (%)	35 (83.3)	
Hypertension, n (%)	33 (78.6)	
Smoking history, n (%)	32 (76.2)	
Diabetes, n (%)	21 (50.0)	
Stroke (within 2 months), n (%)	11 (26.2)	
Renal failure, n (%)	2 (4.8)	
Medications		
Statin, n (%)	38 (90.5)	
Antihypertensive, n (%)	30 (71.4)	
Antiplatelet, n (%)	30 (71.4)	
Anticoagulation, n (%)	6 (14.3)	
Carotid plaque features		
Ulceration, n (%)	29 (70.7)	
IPH, n (%)	17 (40.5)	
Maximum plaque thickness, mean (SD)	4.7 (1.0)	
Stenosis in mm, mean (SD)	2.5 (1.0)	
NASCET percent diameter stenosis, mean (SD)	49 (20.0)	
Intraluminal thrombus, n (%)	3 (7.1)	
Amyloid uptake ^{18}F-Flutemetamol (SUV relative to pontine uptake)		
Supratentorial ^{18}F-Flutemetamol radiotracer uptake	*SUVR*	*Z-Score*
- Composite, mean (SD)	0.46 (.26)	0.04 (2.52)
- Lateral prefrontal, mean (SD)	0.44 (.25)	-0.05 (2.35)
- Anterior cingulate, mean (SD)	0.45 (.39)	-0.06 (2.16)
- Precuneus and posterior cingulate, mean (SD)	0.53 (.14)	0.57 (2.44)
- Parietal, mean (SD)	0.44 (.31)	-0.10 (2.16)
- Lateral temporal, mean (SD)	0.49 (.25)	0.04 (2.35)
- Occipital, mean (SD)	0.53 (.12)	0.05 (1.68)
- Sensorimotor, mean (SD)	0.44 (.26)	-0.51 (1.60)
- Mesial temporal, mean (SD)	0.53 (.07)	0.21 (1.27)

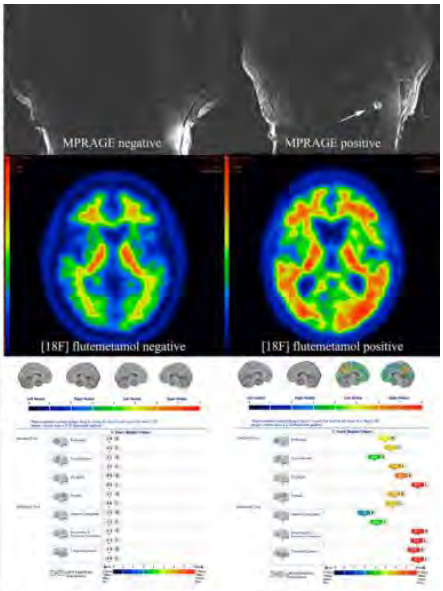

Table: shows the subject characteristics and carotid plaque imaging features. Amyloid uptake in the different brain regions is indicated by the Z-Scores and SUVR values. SUVR values are relative to pontine uptake.

Images: demonstrate MPRAGE and ^{18}F-Flutemetamol PET-CT images for two subjects, one positive (right) and negative (left) case. One subject is negative for IPH on the MPRAGE sequence and does not show abnormal ^{18}F-Flutemetamol brain uptake. The subject with IPH on MPRAGE shows abnormal radiotracer uptake, reflecting amyloid deposition.

(Filename: TCT_244_ImageAmyloidcombinedOct26JPEG.jpg)

ELECTRONIC POSTERS

1252

Accuracy of MR Perfusion without and with Gadolinium at 3T in the Diagnosis of Patients with Suspected Recurrent High Grade Gliomas

T Nguyen[1], S Velasco[2], A Guarnizo[3], G Cron[4], J Woulfe[5]
[1]The Ottwa Hospital, Ottawa, ON, [2]University of Ottawa, Ottawa, Ontario, [3]Fundación Santa Fe de Bogotá, Bogotá, Colombia, [4]Stanford University, Stanford, CA, [5]The Ottawa Hospital, Ottawa, Ontario

Purpose
Evaluate the diagnostic accuracy of ADC, DCE-MRI,DSC-MRI and ASL in differentiating recurrent tumor from radiation-induced brain injury in patients with high grade gliomas. For DCE-MRI, to assess reproducibility of parameters obtained from a standard T1 mapping technique and from a Look-Locker technique.
Materials and Methods
This is a prospective study which recruited consecutive patients with a biopsy proven high grade glioma and who developed a newly enhancing lesion following standard chemoradiation. Each patient underwent a conventional MRI sequences with additional research sequences. From DCE, plasma volume (Vp) and transfer coefficient (Ktrans) parameters were calculated using T1 maps from both MOLLI and SMART1Map sequences. Relative cerebral blood volume (rCBV) and leakage corrected cerebral blood volume (corrected rCBV) were obtained from DSC. ADC value was obtained from DWI. Lesion was classified as radiation necrosis or tumor recurrence based on histopathological analysis or from clinical/radiological follow-up.
Results
After excluding patient with small lesions (<1cm) and MR artifacts, there were 33 lesions included in the final analysis. From ASL, median CBF values were 24.5 ml/100mg/min (95% CI 15.6-43.1) for patients with radiation necrosis compared to 38 ml/100mg/min (95% CI 31.7-51.3) for those with tumor recurrence (p=0.024). From DSC, median rCBV ratio was 1.77 (95%CI 1.50-2.72) for radiation necrosis and 3.69 (95%CI 2.43-4.67) for tumor recurrence (p=0.049).There was no statistical difference in the corrected rCBV ratio, ADC and DCE-derived parameters between the two groups (p>0.05). The diagnostic accuracy for CBF was good (AUC=0.74, 95% CI 0.56-0.88) for the differentiation between the groups. Using the criterion of CBF>26.1 ml/100mg/min, sensitivity was 0.90 (95% CI 0.71-0.99) and specificity was 0.64 (95% CI 0.31-0.89). There was also a slightly lower diagnostic accuracy for rCBV ratio (AUC=0.68, 95%CI 0.50-.83). There was a good reproducibility between DCE parameters obtained from both T1 mapping techniques.
Conclusions
In patients with GBM who developed a newly enhancing lesion following standard chemoradiation treatment, CBF from ASL and rCBV ratio from DSC-MRI might be used clinically to differentiate between tumor recurrence from radiation necrosis.

679

Adherence to Follow-Up Imaging Recommendation for Incidental Renal Lesions Found on Lumbar Spine MRI and Their Outcome.

J Lee[1], A Somasundaram[2], X Wu[1], A Davarpanah[3]
[1]Division of Neuroradiology, Department of Radiology, Emory University School of Medicine, Atlanta, GA, [2]Department of Radiology, Emory University School of Medicine, Atlanta, GA, [3]Division of Abdominal Imaging, Department of Radiology, Emory University School of Medicine, Atlanta, GA

Purpose
Incidental renal lesions are common on non-contrast lumbar spine MRIs and up to one-third of the studies show renal lesions that are unrelated to the original indication and numerous subsequent follow-up imaging recommendations are made for further evaluation of these incidentally discovered renal lesions [1]. The purpose of this study is to explore the variability in practice of follow-up imaging recommendation made for renal lesions identified on non-contrast MRI exams of lumbar spine, the rate of adherence to these follow up recommendations, and the outcome from these imaging studies.
Materials and Methods
Radiology reports of non-contrast MRI of lumbar spine with incidental renal lesions mentioned in the Impression along with recommendation for follow-up imaging were identified. The reports were retrospectively reviewed, and the renal lesions were groups into 5 groups (generic/simple cyst, hemorrhagic cyst, complex cyst, generic/complex renal lesion, and renal mass) based on the descriptive terminology used in the reports. Adherence to follow-up imaging recommendation, results from subsequent recommended imaging studies, and if needed, surgical and pathology reports were reviewed to determine the final outcome of the renal lesions. If recommended imaging study was not performed for a patient, any subsequent relevant imaging studies were identified and reviewed in order to determine the outcome of the renal lesions.
Results
1057 studies with renal lesions mentioned in the impressions were identified, with 220 studies (21.8%) offering a definitive recommendation for follow-up imaging related to the renal lesions. Overall adherence rate for renal imaging recommendation is low at 25.5%, and adherence rates for each group are shown in Table 1. In terms of outcome, 100% of simple cysts and 92.9% of

hemorrhagic cysts showed benign etiology or stability for at least 2 years on subsequent imaging. Outcome of other renal lesion groups are detailed in Table 2.

Conclusions

In this cohort of non-contrast MRI lumbar spine reports with incidental renal findings, 21.8% offered definitive imaging follow-up recommendations. Overall adherence to follow-up recommendation is low, possibly related to confusion caused by recommendations made for simple and hemorrhagic cysts, which generally do not require follow-up as per Bosniak criteria [2].

Table 1: Adherence to follow-up imaging recommendation for incidental renal lesions.

Renal Lesion groups	No. of studies with follow-up imaging recommendation	Adherence to follow-up imaging recommendation
Generic/Simple cyst	95	8.4% (8/95)
Hemorrhagic cyst	32	28.1% (9/32)
Complex cyst	23	26.1% (6/23)
Generic/Complex Renal lesion	55	36.4% (20/55)
Renal mass	15	86.7% (13/15)
Overall	220	25.5% (56/220)

Table 2: Etiology of incidenally discovered renal lesions

Renal Lesion groups	No. of studies with follow-up imaging recommendation	No. of studies with relevant subsequent imaging*	Benign etiology	Stable or without suspicious features for at least 2 years	Suspicious features on subsequent imaging	Pathology proven RCC/Oncocytoma
Generic/Simple cyst	95	32/95	90.6% (29/32)	9.4% (3/32)	0% (0/32)	0% (0/32)
Hemorrhagic cyst	32	14/32	92.9% (13/14)	0% (0/14)	7.1% (1/14)	0% (0/14)
Complex cyst	23	12/23	75.0% (9/12)	8.3% (1/12)	16.7% (2/12)	0% (0/12)
Generic/Complex Renal lesion	55	31/55	77.4% (24/31)	9.7% (3/31)	12.9% (4/31)	9.7% (2 RCCs, 1 Oncocytoma)
Renal mass	15	14/15	14.2% (2/14)	7.1% (1/14)	78.6% (11/14)	78.6% (10 RCCs, 1 Oncocytoma)

*No. of studies with relevant subsequent imaging, including recommended follow up renal imaging studies and any other relevant imaging studies.

(Filename: TCT_679_TableJPG-300.jpg)

230

Amide proton transfer imaging for Differentiation of Glioblastoma from Brain metastasis

U Kaewumporn[1], D Wongsawaeng[1], S Piyapittayanan[1], C Ngamsombat[1], P Chaysiri[1], J Kittikornchaichan[1], K Ningunha[2], N Tisavipat[2], T Itthimathin[2], K Rayaruji[2], O Chawalparit[1]

[1]Department of Radiology, Faculty of Medicine Siriraj Hospital, Mahidol University, Bangkok, Thailand, [2]Bangkok International Hospital, BDMS, Bangkok, Thailand

Purpose

Until now, the differentiation between glioblastoma and brain metastasis still has some limitations and inconclusive findings. This study aimed to use amide proton transfer (APT)-weighted imaging to differentiate glioblastoma from brain metastasis.

Materials and Methods

A total of 14 patients (age range 46-76 years) including 10 patients with glioblastomas and 4 patients with brain metastases were enrolled and underwent preoperative brain 3T-MRI with APT-weighted sequence using the 3D spin-echo approach with TR/TE 6491/7.8 ms, voxel size 1.8x1.8 mm, matrix size 256x256, TSE factor of 174, EPI factor of 1, and scan time 4 mins. A pulse-train radiofrequency saturation (saturation power 2 μT, saturation time 2.0 sec.) was used. Multi-offset from 0 to ±6 was done. Each 10.03-mm ROI was placed in enhancing solid portion, peritumoral high FLAIR area, and contralateral normal appearing white matter (CNAWM). The magnetization transfer ratio asymmetry (MTRasym) and normalized magnetization transfer ratio asymmetry (nMTRasym) values; normalized by the CNAWM, were obtained, and compared for statistical analysis. Final diagnosis was validated by pathological results.

Results

Qualitative visual assessment (Fig 1, Fig 2) The APTw color map showed higher signal (most of them seen as yellow color) at the peritumoral high FLAIR area in glioblastomas than metastasis (all showed green color). All gd-enhancing solid portions, either glioblastoma or brain metastasis, had the same yellow color shading on APT color map which was difficult to differentiate them by visual assessment. The intratumoral necrotic areas showed red color which represented more higher APT signal than that enhancing solid portions. Quantitative assessment The quantitative evaluation was performed in every lesion in all studies. Totally there were 19 lesions of GBM group and 11 lesions of metastasis group. The MTRasym and nMTRasym values of the enhancing solid portion of GBM and peritumoral high FLAIR area were significantly higher than that of brain metastases. (Table 1)

Conclusions

APTw MR imaging could be used to distinguish glioblastomas from brain metastases by evaluating the enhancing solid portions and peritumoral high FLAIR areas. Moreover, the technique could be performed repeatedly for long term follow up with no concern of gadolinium deposition in the organ, especially in brain.

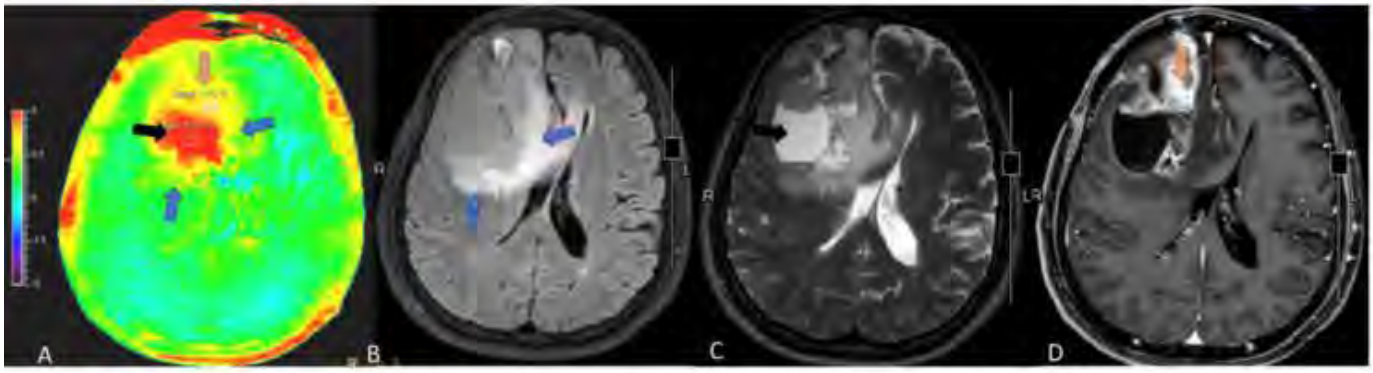

Figure1 APT-weighted and conventional MR images of a 62-year-old male with glioblastoma at right frontal lobe. APT color map (A) showed yellow color corresponding with the enhancing solid portion in Gd-enhanced T1W-image (D) (orange arrow). Necrotic portion (black arrow) showed red color on APT color map (A) with turbid fluid SI on FLAIR image (B) and high SI on T2W image (C). Two peritumoral hyperintense FLAIR regions showed yellow color on APT color map (A) (blue arrow) comparing to background green color of normal white matter.

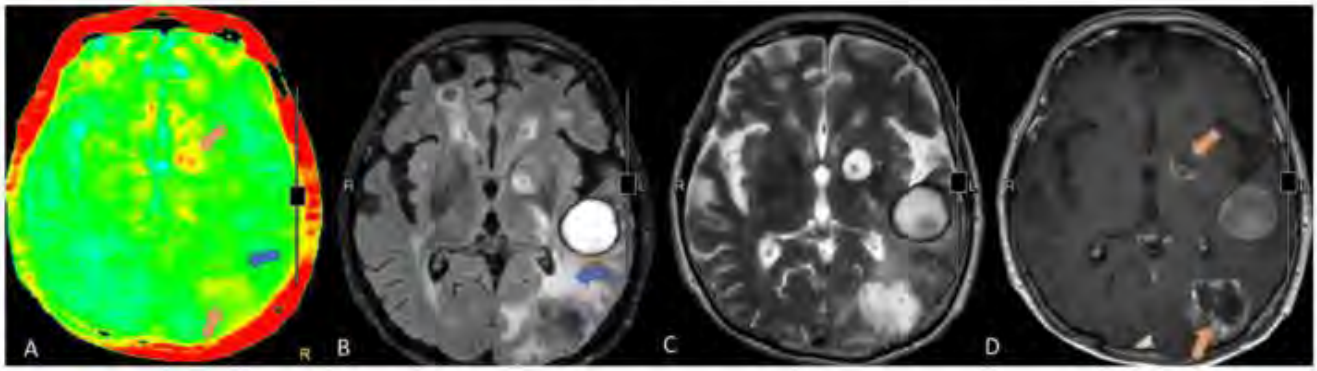

Figure2 APT-weighted and conventional MR images of a 68-year-old female with 2 rim-enhancing metastatic breast cancer lesions at left occipital and left basal ganglia. APT color map (A) showed yellow color corresponding with enhancing component of these 2 lesions on Gd-enhanced T1W-image (D) (orange arrow). The perilesional hyperintense on FLAIR (B) and T2W (C) at left temporo-occipital region show green color on APT color map (A) (blue arrow) which indistinguishable from the normal brain background.

Table1 APT results of glioblastomas and metastatic brain tumor

APT parameters	GBM (19 lesions)	Metastasis (11 lesions)	p value
MTRasym: (Mean±SD)			
Enhancing solid portion	2.90 ± 1.01	1.83 ± 0.95	0.008
Peritumoral high FLAIR area	1.92 ± 1.04	1.11 ± 0.45	0.021
nMTRasym: (Mean±SD)			
Enhancing solid portion	2.24 ± 1.14	1.36 ± 0.90	0.037
Peritumoral high FLAIR area	1.44 ± 1.17	0.65 ± 0.53	0.043

(Filename: TCT_230_Picture12.jpg)

279

Anterior Osteophyte Fractures of the Cervical Spine: Factors Affecting Management Decisions

J Godreau[1], M Hernandez[1], M Jenson[1], J Patel[1], P Fiester[1], D Rao[1]

[1]*Department of Diagnostic Radiology, University of Florida College of Medicine - Jacksonville, Jacksonville, FL*

Purpose

Review imaging of patients with reported anterior osteophyte fractures in the subaxial (C2-C7) cervical spine on unenhanced CT to determine true positive from false positive fractures. Analyze associations between types of fracture (false positive, stable, or unstable) and multiple variables including imaging findings of instability, Rigid Spine (AS or DISH), prevertebral soft tissue swelling (PVSTS), clinical symptoms and management including MRI utilization and treatment. Analyze clinical decision making with regard to questionable fractures and associated symptoms.

Materials and Methods

Retrospective chart review of patients aged 18-92 with unenhanced cervical spine CT scan at a level 1 trauma center (UF Health Jacksonville) with reported anterior osteophyte fractures of the cervical spine between June 1, 2015 & July 31, 2021. We recorded demographic details, symptoms, MRI utilization and findings, management utilizing a fracture classification system (false positive fracture, stable fracture, unstable fracture) (Table 1). 2 Neuroradiologists with CAQ independently reviewed CT scans, then classified each fracture as no fracture, stable fracture or unstable fracture. They identified whether these patients had prevertebral soft tissue swelling; evidence of subluxation, distraction or listhesis; & Rigid Spine (Table 1). Statistical analysis was performed with SPSS using a chi-square test for statistical significance and effect size was calculated Cramer's V, based on the degrees of freedoms of comparison (Table 2).

Results

Results are described in tables 1 & 2. The demographic data including age, sex, injury mechanism, and statistical variables are displayed in Table 1. Statistical Analysis is displayed in Table 2.

Conclusions

Patients with false positive fractures without CT findings of instability, PVSTS and were asymptomatic were unlikely to require evaluation with MRI, or require external bracing or surgery. Patients with stable fractures were largely managed with external bracing. Patients with unstable fractures were likely to undergo spinal stabilization surgery. Symptomatic patients were more likely to utilize MRI after CT than asymptomatic patients.

Table 1: Descriptive Data

Categorical Variables		#	Categorical Variables		#
Age (Yrs)	20-29	5	Presentation	MVC	72
	30-39	7		Fall	37
	40-49	26		ASM	4
	50-59	32		U. Neck Injury	7
	60-69	27		Others	9
	70-79	20	Follow-Up Imaging	No	75
	80-89	8		Yes	54
	90-100	4	Fracture Classification	False Positive	80
Sex	Male	93		Stable	33
	Female	36		Unstable	16
PVSTS	No	115	Management Decision	Nothing	69
	Yes	14		Hard Collar	40
Rigid Spine	No	99		Surgery	20
	Yes	30	Associated Symptoms	Asymptomatic	38
S/D/L	No	118		Neck Pain	68
	Yes	11		Neurological	23

PVSTS: Prevertebral Soft Tissue Swelling; Rigid Spine: Diffuse Idiopathic Skeletal Hyperostosis & Ankylosing Spondylitis; *S/D/L: Subluxation/Distraction/Listhesis; U Neck Injury: Unspecified Neck Injury; Hard Collar: Hard Collar/Miami-J Collar/HALO; Neurological: Myelopathic/Radicular Pain.*

Table 2: Statistical Analysis

Variable A	Variable B	$p \leq$	ϕ_c	df
Follow-up Imaging	Fracture Classification	0.001*	0.378†	2
	S/D/L	0.030*	0.191¥	1
	PVSTS	0.003*	0.260¥	1
	Rigid Spine	0.302	0.091†	1
	Associated Symptoms	0.001*	0.433‡	2
	Management Decision	0.001*	0.591†	2
Management Decision	Fracture Classification	0.001*	0.567†	4
	S/D/L	0.001*	0.497†	2
	PVSTS	0.001*	0.431‡	2
	Rigid Spine	0.006*	0.283‡	2
	Associated Symptoms	0.001*	0.342†	4
Fracture Classification	Rigid Spine	0.001*	0.383†	2
	Associated Symptoms	0.047*	0.193‡	4

**statistically significant at ≤ 0.05; Φc (Cramer's V) Effect Size: †Large; ‡ Medium; ¥ Small; PVSTS: Prevertebral Soft Tissue Swelling; S/D/L: Subluxation/Distraction/Listhesis; Rigid Spine:* Diffuse Idiopathic Skeletal Hyperostosis & Ankylosing Spondylitis.

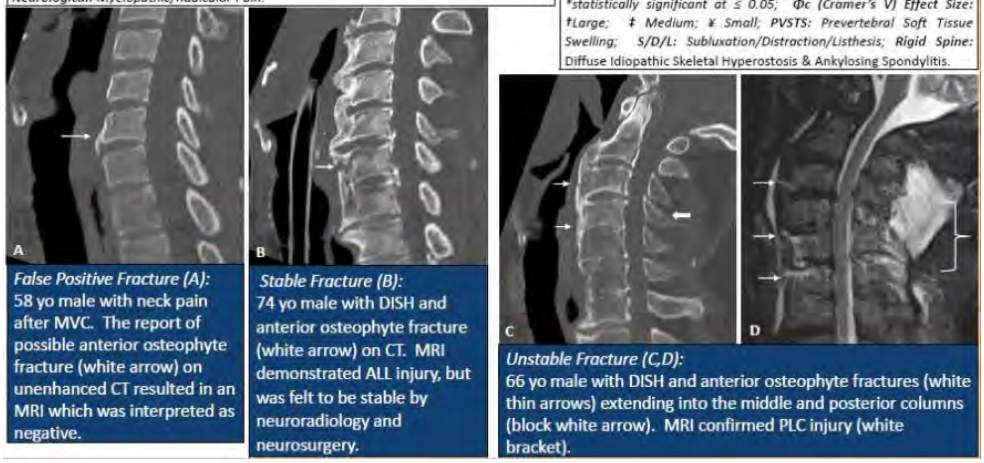

False Positive Fracture (A): 58 yo male with neck pain after MVC. The report of possible anterior osteophyte fracture (white arrow) on unenhanced CT resulted in an MRI which was interpreted as negative.

Stable Fracture (B): 74 yo male with DISH and anterior osteophyte fracture (white arrow) on CT. MRI demonstrated ALL injury, but was felt to be stable by neuroradiology and neurosurgery.

Unstable Fracture (C,D): 66 yo male with DISH and anterior osteophyte fractures (white thin arrows) extending into the middle and posterior columns (block white arrow). MRI confirmed PLC injury (white bracket).

(Filename: TCT_279_AOFPosterMRIImagesJPG102721.jpg)

465

Apparent Diffusion Coefficient for Differentiation between Benign Post-treatment Changes and Recurrence in Head and Neck Cancer: A Systematic Review and Meta-Analysis

A Baba[1], R Kurokawa[1], M Kurokawa[1], Y Ota[1], A Srinivasan[1]
[1]*University of Michigan, Ann Arbor, MI*

Purpose

Follow-up images after head and neck cancer treatment can be difficult to interpret and sometimes necessitate pathologic confirmation of their findings. Previous studies reported that the apparent diffusion coefficient (ADC) values of recurrent head and neck cancer lesions are lower than those of post-treatment changes, however, the utility of ADC to differentiate them has not been definitively summarized and established. The purpose of this study is to evaluate the diagnostic benefit of ADC calculated from diffusion-weighted MRI in differentiating recurrent lesions from posttreatment changes in head and neck cancer.

Materials and Methods

MEDLINE, via PubMed, Scopus, and Embase databases, were searched in July 2021 according to the Preferred Reporting Items for Systematic Review and Meta-analysis 2020 statement, for studies that compared the ADC values of both head and neck cancer recurrence and benign post-treatment changes. Forest plots and meta-analysis were used to assess the mean difference of ADC values. Heterogeneity among the studies was evaluated by using Cochrane's Q test and the I2 statistic.

Results

The review identified 10 studies with a total of 707 patients (742 lesions) that were eligible for the meta-analysis. There were 356 patients with recurrent lesions and 386 with benign post-treatment changes. Among included studies, the mean ADC values of recurrent lesions ranged from 0.77 to 1.21 with an overall mean of 1.03 x 10-3mm2/s, and the mean ADC of the benign post-treatment changes among all studies ranged from 1.17 to 1.69 with an overall mean of 1.51 x 10-3mm2/s. The ADC value of recurrence was significantly less than that of post-treatment changes in head and neck cancer (pooled MD [mean difference]: -0.47, 95% CI: -0.56–0.37, p < 0.0001). The threshold of ADC value between recurrent lesions and post-treatment changes was suggested to be 1.13 x 10-3mm2/s.

Conclusions

The ADC values in recurrent head and neck cancers are lower than those of post-treatment changes and the threshold of ADC value between them was suggested.

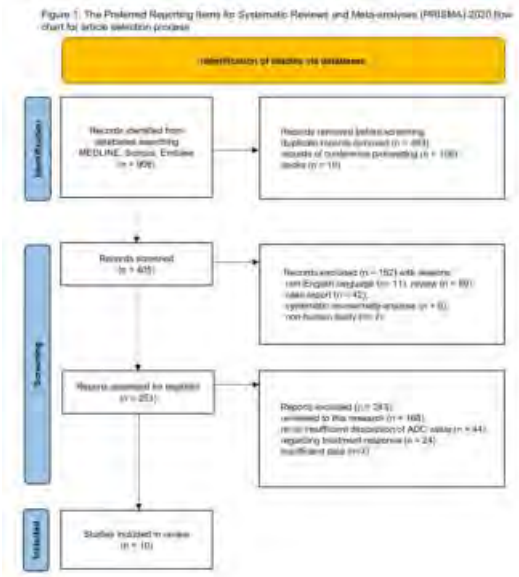

Figure 2. Forest plot (association of ADC value between recurrence and posttreatment change)

Study	Recurrence Total	Mean	SD	Post-treatment change Total	Mean	SD	MD	95%-CI	Weight (fixed)	Weight (random)
Tshering Vogel DW , 2013	18	1.13	0.5000	28	1.60	0.4700	-0.47	[-0.76; -0.18]	1.4%	5.9%
Hwang I et al , 2013	20	1.21	0.2440	13	1.65	0.3190	-0.44	[-0.65; -0.24]	2.8%	8.2%
Razek AAKA et al , 2015	26	0.94	0.1600	15	1.37	0.1200	-0.43	[-0.52; -0.34]	15.3%	11.8%
Razek AAKA et al., 2018	31	1.11	0.1000	16	1.49	0.1000	-0.38	[-0.44; -0.32]	31.5%	12.4%
Ailianou A et al., 2018	36	1.10	0.2950	64	1.66	0.4180	-0.56	[-0.70; -0.42]	5.8%	10.2%
Becker M et al., 2018	43	1.10	0.2400	62	1.59	0.4200	-0.49	[-0.62; -0.36]	7.1%	10.6%
Vaid S et al., 2017	44	0.93	0.1900	42	1.39	0.3200	-0.46	[-0.57; -0.35]	9.2%	11.1%
Wang C et al., 2018	61	0.77	0.4595	99	1.45	0.3260	-0.68	[-0.81; -0.55]	6.6%	10.5%
Jajodia A et al., 2019	50	1.01	0.2200	12	1.69	0.4000	-0.68	[-0.92; -0.45]	2.1%	7.3%
Huang W et al., 2019	27	0.98	0.1670	35	1.17	0.1450	-0.19	[-0.27; -0.11]	18.3%	12.0%
Random effects model							**-0.47**	**[-0.56; -0.37]**	–	**100.0%**

Heterogeneity: I^2 = 85%, τ^2 = 0.0182, p < 0.01

(Filename: TCT_465_asnrfigure.jpg)

1366

Application of Electric Properties Tomography to Ischemic Stroke: Comparison of Conductivity between Infarct and Contralateral Brain

I Park[1], B Baek[2]
[1]*Chonnam National University, Gwangju, Gwangju,* [2]*Chonnam National University Medical School, Gwangju, Korea, Republic of*

Purpose

Electrical Properties Tomography (EPT) is a new, noninvasive MRI technique that delivers information on tissue electrical properties and has been applied to cancer imaging [1]. The aim of this study was to measure the conductivity values in infarct lesions and compare them to the contralateral normal brain tissue from patients with ischemic stroke with a long-term goal to develop a new imaging contrast for stroke.

Materials and Methods

Twenty-seven patients (mean age, 75; range 54-90) who presented with acute ischemic stroke at a tertiary stroke center were included in this study. The EPT data were acquired using a balanced-Fast Field Echo (b-FFE) sequence (TR/TE = 3/1.62 ms, flip angle=30°, pixel size=1.15×1.15×2 mm) from a clinical 3T scanner (Philips, Netherlands, Amsterdam). The mean time from stroke onset to the EPT scan was 102 hours (range, 19 – 193 hr). The EPT data were reconstructed using the previously described method [2]. The conductivity (σ) map was quantified and compared between the lesion and the contralateral normal brain tissue in 4 regions depending on the location of infarct: basal ganglia & thalamus (BGT, n=10), cerebral hemisphere (CH, n=10), pons (PN, n=5) and cerebellum (CB, n=2).

Results

The ischemic lesion demonstrated a significantly higher mean conductivity value (0.93 ± 0.097 S/m) than the contralateral brain tissue (0.83 ± 0.095 S/m, p=0.00004). This pattern, however, was specific to the location of the infarct. Both BGT and CH demonstrated significantly higher levels of conductivity in the lesion compared to their corresponding contralateral normal tissues, while PN and CB exhibited comparable levels of conductivity between the ipsilateral and contralateral sides (Fig 1). In addition, there seemed to be region-specific differences in conductivity. BGT and CH had a significantly different level of conductivity in their lesions, while the contralateral tissue of supra-(BGT+CH) and infratentorial (PN+CB) brains had significantly different levels of conductivity (Fig 2). Figure 3 and 4 show examples of patients who had infarcts in CH and CB, respectively, showing the different levels of conductivity between the ipsilateral and contralateral brains.

Conclusions

We demonstrate the feasibility of obtaining conductivity using EPT MRI from patients with stroke. The results from this study suggest that this new technique may provide a potential, new imaging contrast for stroke and warrant further investigation of this method with the broader range of patients with stroke.

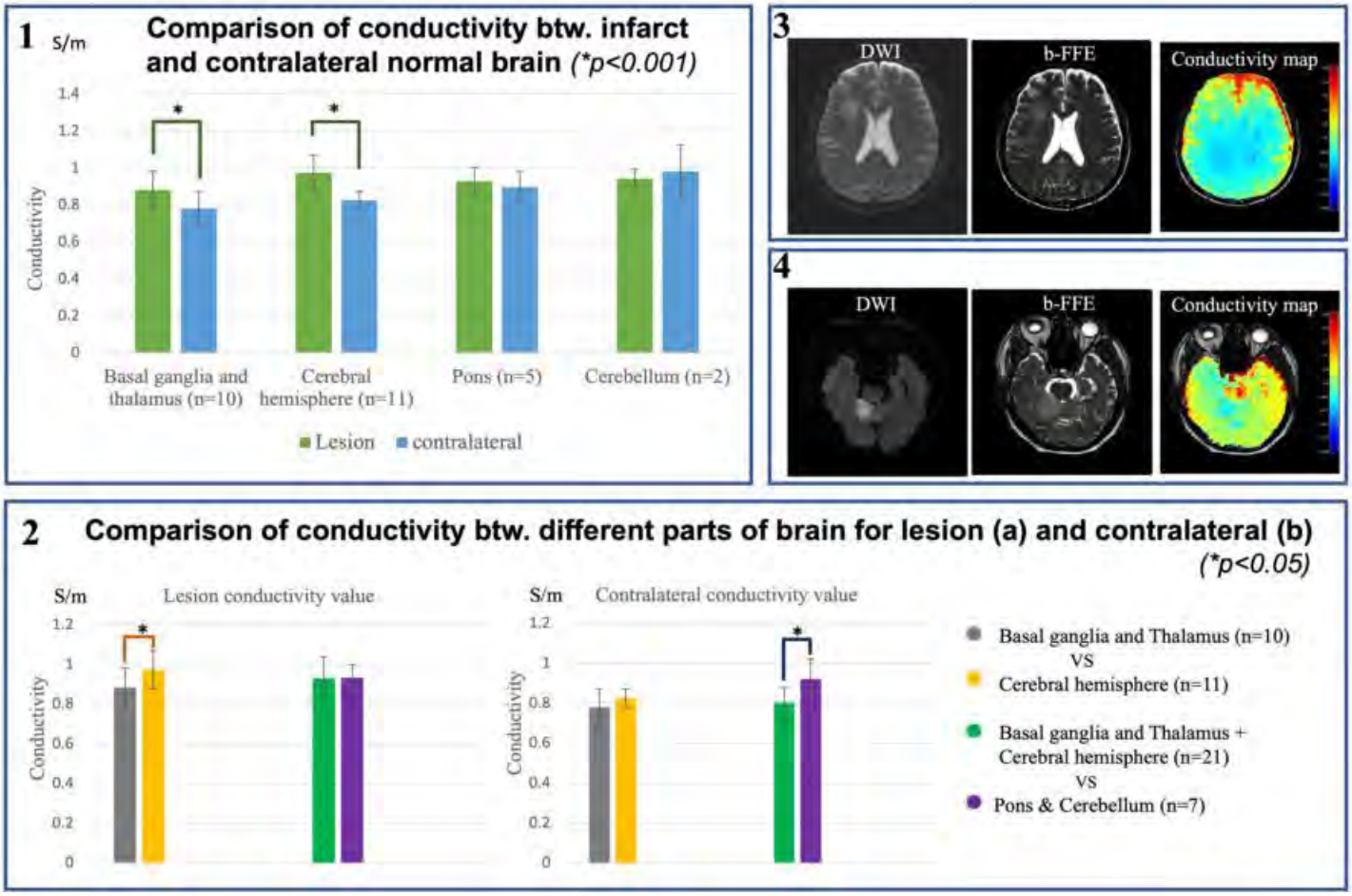

(Filename: TCT_1366_Fig.jpg)

1271

Association of MRI-based imaging parameters, including CAA, CMBs, and WMH, with cognitive decline

M Lee[1], J Byun[2]
[1]Yeouido ST. Mary's Hospital, Seoul, Korea, Republic of, [2]Yeouido St. Mary's Hospital, Seoul, Seoul

Purpose

To evaluate the association of cognition with MRI-based imaging parameters; presence of cerebral amyloid angiopathy (CAA) location of cerebral microbleeds (CMBs), and white matter hyperintensity (WMH).

Materials and Methods

Institutional review board approved this retrospective study. Written informed consent was obtained from all participants. Study population included those who underwent brain MRI and cognitive testing. Population was divided in to three groups including cognitive normal (CN), mild cognitive impairment (MCI), and Alzheimer's disease (AD). MRI scans were reviewed to evaluation the presence of CAA, location and number of CMB, and degree of WMH. The diagnostic performance was compared with imaging parameters using the area under the receiver operating characteristics curve (AUC).

Results

Of 138 patients analyses, 57 patients were CN, 50 patients were MCI, and 31 patients were AD. The prevalence of CMBs was 35.5% (mean count [range 1-100]). The presence of CAA and lobar distribution of CMBs showed higher prevalence in cognitive decline groups (MCI + AD) than that of CN group (P=0.009) and significantly improved the distinction of cognitive decline group from CN group (AUC 0.58 and 0.60, P=0.009 and P=0.021), whereas the deep location of CMBs was not helpful. The cognitive decline group showed higher degree of WMH (P=0.003), and the AUC for distinguishing the cognitive decline group from CN group was 0.63 (P<0.001). Adding degree of WMH to CAA or lobar distribution of CMBs parameters improves performance for diagnosing cognitive decline group from CN group (AUC 0.58 vs 0.67 or AUC 0.60 vs. 0.66, P<0.05).

Conclusions

In present study, we evaluated association between MRI-based imaging parameters and cognition. The presence of CAA, lobar location of CMBs, and higher degree of WMH showed significant association with cognitive decline than that of deep location of CMBs. The combination of the parameters of CMBs with degree of WMH can improve the diagnosis of cognitive decline group.

515

Automated ASPECTS Scoring Using AI-Based Histogram Differences.

A ERAN[1], T Eisenberg[2], F Wenzel[3], A Ewald[3], N Fläschner[4]
[1]RAMBAM HEALTH CARE CAMPUS, HAIFA, Israel, [2]Meir Medical Centre, Kefar Sava, N/A, [3]Philips GmbH Innovative Technologies, Hamburg, non us, [4]Philips GmbH Innovative Technologies, Hamburg, GA

Purpose

The ASPECTS scheme is a 10-point quantitative score on non-contrast CT scans used in patients with middle cerebral artery (MCA) occlusion with an impact on therapy options. Manual, visual assessment of the inferior and superior ASPECTS image has shown to suffer from high inter-rater variability. This study presents an approach for computer-aided ASPECTS scoring utilizing 3D-guided identification of ASPECT areas and AI-based estimation of the presence of lesions based on bi-lateral histogram differences.

Materials and Methods

A retrospective dataset of NCCTs head scans from two clinical sites with 3D region annotations (n=88) and information about the presence of a lesion per region, based on follow up NCCTs (n=115) served for training. First a shape-constrained deformable anatomical model for segmenting 10 bilateral ASPECTS areas was created. Next a convolutional neural network analyzing corresponding bilateral histogram differences was used for estimating the probability for the presence of an abnormality, which is presented to the user in terms of a color code per region, next to the contoured ASPECTS images. Trained algorithms have been used for quantifying the need for correction of segmented regions in n=35 scans (measured by DICE similarity coefficient), and for comparing inter-rater variability with respect to manual assessment (measured with Fleiss' kappa coefficient and three expert readers on n=41 scans).

Results

An average DICE similarity coefficient of 0.9994 could be obtained as average over all ASPECTS areas. The Fleiss' kappa coefficient increased from 0.661 (manual assessment, fair agreement) to 0.756 (computer-aided ASPECTS scoring, good agreement).

Conclusions

Computer-aided ASPECTS scoring, using AI-Based histogram differences, can enhance clinical workflow due to accurate segmentation of ASPECTS regions and slice extraction, leading to significantly reduced inter-rater variability and increased sensitivity with respect to lesion detection in these regions.

892

Can a Deep Neural Network Predict Final Ischemic Stroke Lesion Volume and Location from Baseline Diffusion Weighted Images Alone Without Perfusion Information?

S Nazari Farsani[1], Y Yu[2], R Duarte Armindo[2], C Levin[1], M Lansberg[3], G Albers[4], G Zaharchuk[2]
[1]Stanford University, Palo Alto, CA, [2]Stanford University, Stanford, CA, [3]Stanford, Stanford, CA, [4]Stanford University Medical Center, Palo Alto, CA

Purpose

The success of acute ischemic stroke reperfusion treatments highly depends on the time interval between stroke onset and treatment. Accordingly, stroke patients need to be triaged fast, for which accurate estimation of the final lesion volume is vital. Diffusion-perfusion mismatch measurement is a common practice for estimating final infarct volume. However, perfusion-weighted imaging (PWI) is time-consuming, expensive, and injection of the contrast agent could cause complications for some patients. We aimed to predict the final infarct volume from only baseline diffusion-weighted images (DWI) using a deep convolutional neural network (DCNN).

Materials and Methods

We collected 445 baseline DWI studies in acute ischemic stroke patients (including 93 from Imaging Collaterals in Acute Stroke [iCAS], 198 from Diffusion and Perfusion Imaging Evaluation for Understanding Stroke Evolution [DEFUSE, DEFUSE-2], and 154 from University of California, Los Angeles [UCLA] stroke registry) for training and validating an attention-gated (AG) U-shaped DCNN1. The input channels include DWI, apparent diffusion coefficient (ADC), and thresholded-ADC with values less than 620×10-6 mm2/s. The ground truth for the model was the binary mask of the final infarct lesions delineated by a neuroradiologist on follow-up DWI obtained 3-7 days after the stroke onset. The predicted lesion volumes were compared to the ground truth in terms of Dice similarity coefficient (DSC) and absolute volume error. Five-fold cross-validation was performed to evaluate the performance of the model in terms of area under the curve (AUC), sensitivity, and specificity.

Results

The model showed a median AUC of 0.91 (IQR: 0.84-0.96), median sensitivity of 0.59 (IQR: 016-0.84), and median specificity of 0.97 (IQR: 0.93-0.99). The median DSC and absolute volume error were 0.50 (IQR: 0.17-0.66) and 27 ml (IQR: 7-60) respectively. The predicted volumes by the model showed high correlation (correlation coefficient = 0.71, p-value < 0.0001) with the ground truth volumes.

Conclusions

An attention-gated U-net was able to predict the final infarct volumes with comparable performance to that of previously reported models where both DWI/PWI or CT perfusion images were used as input (DSC of 0.24 - 0.53 compared to 0.50 in our study) 1–4. We believe this is a valuable finding, since avoiding PWI to evaluate final lesion volume in stroke patients could be beneficial at many levels, particularly to speed up patient's triage time.

Table 1. Summary of the DCNN and ADC-thresholding model performance

Metrics Median (IQR)	AUC	Sensitivity	Specificity	DSC	Absolute volume error (ml)
DCNN Model	0.91 (0.84-0.96)	0.59 (0.16-0.84)	0.97 (0.93-0.99)	0.50 (0.17-0.66)	27 (7-60)
ADC-thresholding	0.62 (0.56-0.69)	0.26 (0.12-0.40)	0.98 (0.97-0.99)	0.18 (0.10-0.35)	64 (25-96)

AUC: Area under the curve
DSC: Dice similarity coefficient
IQR: Interguartile range

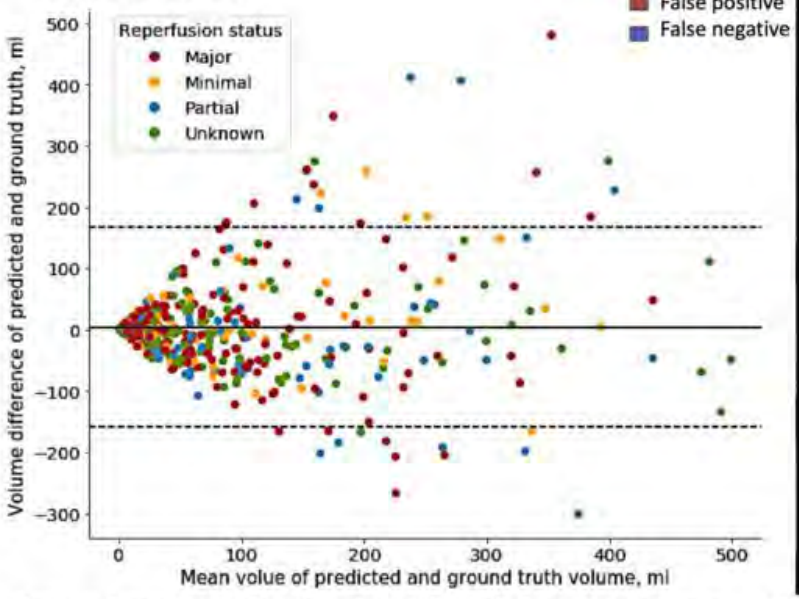

Figure 1: Bland-Altman plot comparing model prediction with true lesions. The solid line represents the mean, and the dashed lines represent the upper and lower limit of agreement.

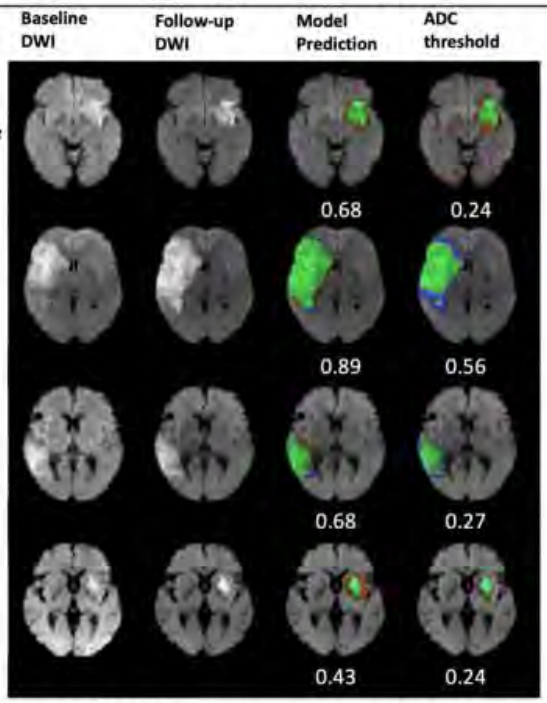

Figure 2: Model predictions compared with simple ADC-thresholding. Dice scores below the images are calculated by comparison of the outcomes with the ground truth in all slices.

(Filename: TCT_892_Abstractfigure_12112021_modified.jpg)

364

Can MRI differentiate between infectious and immune-related acute cerebellitis?

G Orman[1], S Kralik[1], N Desai[1], H Sangi-Haghpeykar[1], G Jallo[2], E Boltshauser[3], T Huisman[4]

[1]Texas Children's Hospital, Houston, TX, [2]Johns Hopkins All Children's, St. Petersburg, FL, [3]Department of Pediatric Neurology, University Children's Hospital of Zurich, Switzerland., Zurich, other, [4]Texas Children's Hospital and Baylor College of Medicine, Houston, TX

Purpose

Acute cerebellitis (AC) is an acute neurological condition that is attributable to a recent or concurrent infection, a recent vaccination or ingestion of medication, and in which there is MRI evidence of cerebellar edema. MRI can confirm anatomic abnormality and may allow for the radiologist to establish a differential diagnosis. The purpose of this research is to evaluate the MRI findings in children with AC due to 1) infectious versus 2) immune-related conditions, in particular if MRI findings allow differentiation.

Materials and Methods

Electronic medical records were reviewed between 2003 and 2020 in our quaternary children's hospital. Data included demographics, clinical records: presentation/symptoms, final diagnosis which includes 1) infectious AC and 2) immune-related AC, length of stay, treatment, condition at discharge and laboratory findings. Retrospective independent review of all brain MRI studies was performed.

Results

Forty-three patients (male/female: 28/15) were included in this study. Average age at presentation was 7.08 (range 0.05-17.52) years. Thirty-five had infectious and 8 children had immune-related AC. Significant differences in neuroimaging were 1) T2-FLAIR hyperintense signal in the brainstem (37.50% vs 2.85%), p=0.016; and 2) T2-FLAIR hyperintense signal in the supratentorial brain was higher in the immune-related (37.50% vs 0.00%), p=0.004; and 3) downward herniation was higher in the infectious AC groups (42.85% vs 0.00%), p=0.03.

Conclusions

AC is a rare condition and MRI is helpful in differential diagnosis. T2-FLAIR hyperintense signal in brainstem and supratentorial brain may be indicative of immune-related AC, and downward herniation may be indicative of infectious AC.

1304

Cerebellar tonsillar bleeds in Primary CNS vasculitis: prevalence and its significance

A Garg[1], S Agarwal[2], L Sebastian[3], V Goel[2], R Bhatia[2], V VY[2], A Srivastava[4], A Elavarsi[2], V Padma[2]

[1]All India Institute of Medical Sciences, New Delhi, India, [2]AIIMS, New Delhi, Delhi, [3]N/A, N/A, [4]All India Institute of Medical Sciences, NEW DELHI, Delhi

Purpose

The cerebellar tonsils are ovoid structures on the inferomedial surface of each cerebellar hemisphere. In our experience, we had seen multiple cases of tonsillar bleeds in patient with primary CNS vasculitis (PCNSV). In this retrospective study, we study the prevalence of tonsillar bleeds in cases of biopsy proven primary CNS angiitis and compare with prevalence of tonsillar microbleeds in patients with hypertensive angiopathy (HA).

Materials and Methods

We included 50 patients of biopsy-proven PCNSV and 64 cases of hypertensive arteriopathy who had susceptibility-weighted imaging (SWI) or T2* imaging. We reviewed the SWI and T2* images for presence of hemorrhages in region of cerebellar tonsils (CeT).

Results

The median age of the patient was 34 years (range, 18-69) in PCNSV group and 55.5 years (20-85) in HA groups, ($p<0.001$). There were 40 (80%) males in PCNSV group and 45 (70.3%) males in HA group; statistically not significant. All patients with PCNSV and HA had microhemorrhages in the brain. The CeT hemorrhages were present in 31 (62%) patients in PCNSV group and 19 (29.7%) patients in HA group, ($p<0.001$). The first case of PCNSV shows multiple microhemorrhares in SWI image (a) and multiple punctate enhancing foci (b) in CeT. The second case of PCNSV shows macrohemorrhages in SWI image (a) and T2-WI (d). Third row shows a case of HA with hemorrhages in CeT (e) and bilateral basal ganglia (f).

Conclusions

Cerebellar tonsillar bleeds are quite common in PCNSV. Presence of tonsillar bleeds in a young patients raise the possibility of PCNSV.

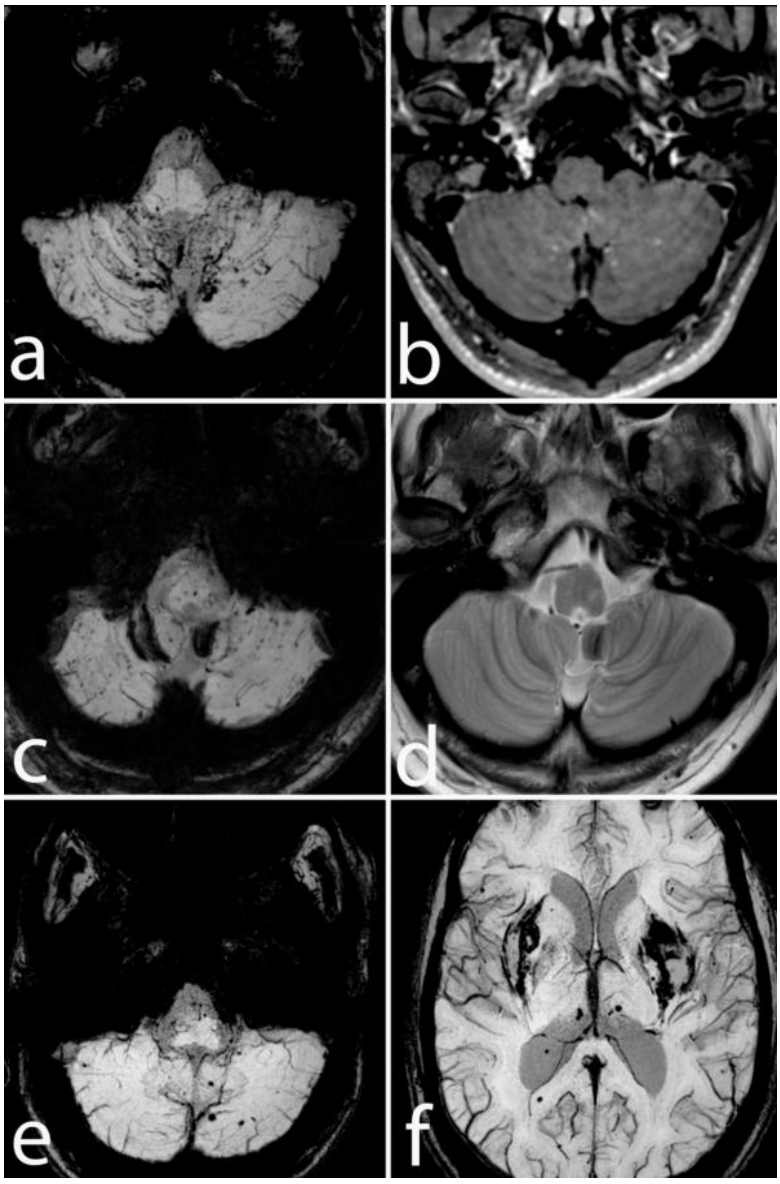

(Filename: TCT_1304_PCNSV.jpg)

567

Cerebrospinal Fluid Features in Patients With Coronavirus Disease 2019 and Neurological Manifestations: Correlation with Brain Magnetic Resonance Imaging Findings in 58 Patients

F LERSY[1], I Benotmane[2], S Kremer[3], S Fafi-Kremer[4]

[1]University hospitals of Strasbourg, Strasbourg, France, [2]Strasbourg University Hospital, Strasbourg, Bas-Rhin, [3]University hospitals of Strasbourg, STRASBOURG, FRANCE, [4]Strasbourg University Hospital, Strasbourg, France

Purpose

Neurological manifestations are common in patients with coronavirus disease 2019 (COVID-19), but little is known about pathophysiological mechanisms. In this single-center study, we examined neurological manifestations in 58 patients, including cerebrospinal fluid (CSF) analysis and neuroimaging findings.

Materials and Methods

The study included 58 patients with COVID-19 and neurological manifestations in whom severe acute respiratory syndrome coronavirus 2 (SARS-CoV-2) reverse-transcription polymerase chain reaction screening and on CSF analysis were performed. Clinical, laboratory, and brain magnetic resonance (MR) imaging data were retrospectively collected and analyzed

Results

Patients were mostly men (66%), with a median age of 62 years. Encephalopathy was frequent (81%), followed by pyramidal dysfunction (16%), seizures (10%), and headaches (5%). CSF protein and albumin levels were increased in 38% and 23%, respectively. A total of 40% of patients displayed an elevated albumin quotient, suggesting impaired blood-brain barrier integrity. CSF-specific immunoglobulin G oligoclonal band was found in 5 patients (11%), suggesting an intrathecal synthesis of immunoglobulin G, and 26 patients (55%) presented identical oligoclonal bands in serum and CSF. Four patients (7%) had a positive

CSF SARS-CoV-2 reverse-transcription polymerase chain reaction. Leptomeningeal enhancement was present on brain MR images in 20 patients (38%).
Conclusions
Brain MR imaging abnormalities, especially leptomeningeal enhancement, and increased inflammatory markers in CSF are frequent in patients with neurological manifestations related to COVID-19, whereas SARS-CoV-2 detection in CSF remained scanty.

174

Cervical Arteriovenous Fistulas: Single Center Retrospective Analysis of Classification, Presentation, Treatment, and Outcomes

M Isikbay[1], M Caton[1], K Narsinh[1], M Amans[1]
[1]*UCSF, San Francisco, CA*

Purpose
Arteriovenous fistulas (AVFs) are vascular anomalies that can occur throughout the central nervous system. While rare, AVFs of the spine benefit from prompt identification and treatment given their risk of debilitating deficits such as paralysis. While spinal AVFs in the thoracic and lumbar spine have previously been reported and classified, data regarding cervical AVFs is limited given their rarity. We present the largest cohort of cervical AVFs ever reported. We highlight key features including clinical presentation, treatment considerations, and single center outcomes. Notably we also propose a novel modified classification system specific to the cervical spine which is adapted and updated from the widely used Toronto classification for spinal AVFs.
Materials and Methods
Using our institution's mPower website, and Boolean search phrases, 32 cases of diagnosed cervical AVFs were identified in the past 20 years. Analysis of medical record for each patient was performed to collect relevant data. Lesions were classified into the following categories (based upon dominant venous drainage pathways): dural, epidural, paraspinal, and extraspinal cervical AV fistulas (Figure 1). Routine statistical analysis (calculations of ratios/percentages) was performed on both stratified and pooled patient data with respect to each studied clinical variable.
Results
All the results from this analysis are summarized in the attached table (Table 1) which includes AVF classification, demographics, clinical presentation, treatment, follow up, and outcomes data.
Conclusions
While rare, cervical AVFs are important vascular lesions to be aware of. We the largest cohort of cervical AV fistulas ever reported and apply an updated anatomical classification system. Notably our classification system introduces the category of "extraspinal" AV fistulas, specifically relevant to the cervical spine given draining vessels like the jugular vein which are not present in the thoracic or lumbar spine. Our analysis reveals most cases at our center presented either with neck pain or were completely asymptomatic at the time of diagnosis. Almost all cases were treated exclusively with endovascular therapy (91%), with endovascular coils as the most common embolic agent (used in 74% of treated cases). Of the patients who received follow up imaging, 87% demonstrated complete resolution of their fistula.

FIGURE 1

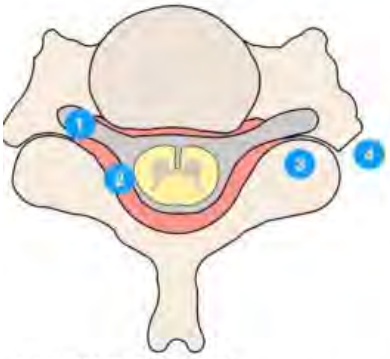

CLASSIFICATION SYSTEM

1.) Dural AV Fistula: dominant venous drainage is within the dural space (Ex. Perimedullary vein)

2.) Epidural AV Fistula: dominant venous drainage is within the epidural space (Ex. Epidural venous plexus)

3.) Paraspinal AV Fistula: dominant venous drainage involves the paraspinal venous structures (Ex. Paraspinal venous plexus)

4.) Extraspinal AV Fistula: dominant venous drainage includes veins outside the spine (Ex. External Jugular Vein)

TABLE 1

Classification	Age	Sex	Clinical Presentation	Treatment Type	Treatment Agent	Clinical Improvement?	Follow Up Angiogram Obtained?	Complete Cure?
Dural (n = 3, 10%)	**Adult (3, 100%)**	**Female (3, 100%)**	**Neck Pain (2, 67%), Extremity Weakness (2, 67%), Extremity Pain (2, 67%)**	Endovascular (1, 33%), **Surgical (2, 67%)**	Coils (1, 33%), **Surgical Clips (2, 66%)**	**Yes (2, 67%)**, No (1, 33%),	**Within 3 months (2, 67%)**, No (1, 33%)	Yes (1, 50%), No (1, 50%)
Epidural (n = 10, 31%)	**Adult (9, 90%)**, Pediatric (1, 10%)	Female (4, 40%), **Male (6, 60%)**	**Neck Pain (3, 30%)**, Asymptomatic (2, 20%), **Extremity Weakness (3, 30%), Pulsatile Tinnitis (3, 30%)**, Extremity Pain (2, 20%), Trauma (2, 20%), Headache (1, 10%)	**Endovascular (10, 100%)**	**Coils (8, 80%)**, Detachable Balloons (2, 20%), Glue (3, 30%),	**Yes (7, 70%)**, No (1, 20%), Asymptomatic/unchanged (2, 20%)	Within 3 months (1, 10%), After 3-6 months (2, 20%), After 6-12 months (1, 10%), After 5 years (1, 10%), **Pending Follow up (3, 30%)**, No (2, 20%)	**Yes (4, 80%)**, No (1, 20%)
Paraspinal (n = 11, 34%)	**Adult (9, 82%)**, Pediatric (2, 18%)	**Female (6, 55%)**, Male (5, 45%)	Neck Pain (2, 18%), **Asymptomatic (3, 27%)**, Extremity Weakness (1, 9%), Pulsatile Tinnitis (1, 9%), Extremity Pain (1, 9%), Trauma (2, 18%), **Palpable Thrill (3, 27%)**, Headache (1, 9%),	**Endovascular (10, 91%)**, None (1, 9%)	**Coils (7, 70%)**, Detachable Balloons (2, 20%), Ethanol (1, 10%)	Yes (4, 40%), No (1, 10%), **Asymptomatic/unchanged (5, 50%)**	After 6-12 months (1, 10%), **After 1-5 years (3, 30%)**, After 5 years (1, 10%), No (5, 50%)	**Yes (5, 100%)**
Extraspinal (n = 8, 25%)	**Adult (7, 87%)**, Pediatric (1, 13%)	**Female (6, 75%)**, Male (2, 25%)	**Asymptomatic (2, 25%), Pulsatile Tinnitis (2, 25%)**, Trauma (1, 13%), **Palpable Thrill (2, 25%)**, Headache (1, 13%),	**Endovascular (8, 100%)**	**Coils (7, 87%)**, Detachable Balloons (1, 13%),	**Yes (4, 50%)**, No (1, 13%), Asymptomatic/unchanged (3, 37%)	After 3-6 months (1, 13%), **After 6-12 months (2, 25%)**, No (5, 63%)	**Yes (3, 100%)**
Total (n= 32)	**Adult (28, 87%)**, Pediatric (4, 13%),	**Female (19, 59%)**, Male (13, 41%)	**Neck Pain (7, 22%), Asymptomatic (7, 22%)**, Extremity Weakness (6, 19%), Pulsatile Tinnitis (6, 19%), Extremity Pain (5, 16%), Trauma (5, 16%), Palpable Thrill (5, 16%), Headache (3, 9%),	**Endovascular (29, 91%)**, Surgical (2, 6%), None (1, 3%)	**Coils (23, 74%)**, Detachable Balloons (5, 16%), Glue (3, 10%), (Surgical Clips, 2, 6%), Ethanol (1, 3%)	**Yes (17, 55%)**, No (4, 13%), Asymptomatic/unchanged (10, 32%)	Within 3 months (3, 10%), After 3-6 months (3, 10%), **After 6-12 months (4, 13%)**, After 1-5 years (3, 10%), After 5 years (2, 7%), Pending Follow up (3, 10%), No (13, 40%)	**Yes (13, 87%)**, No (2, 13%)

(Filename: TCT_174_ASNRFigure.jpg)

300

Cervical MR Imaging Characteristics of Sagittal Line Types in Chiari and Control: Central Canal vs. Anterior Median Fissure?

T Tomsick[1], C Slack[1], R Scott[2], E Goldstein[1], L Wang[1]

[1]University of Cincinnati Hospital, Cincinnati, OH, [2]University Cincinnati, Cincinnati, OH

Purpose

Midline T2-hyperintense craniocaudad lines on sagittal cervical MRI (SL) and T2-hyperintense foci (HIF) less than 3 mm. wide in the anterior spinal cord are usually attributed to the central canal. Prior exploratory control and Chiari cervical MRI studies suggest the anterior median fissure (AMF) is also associated with HIF, appearing to connect with some HIF (AMF>HIF), and is responsible for some SL. We propose to confirm these HIF, AMF, and SL relationships, and to examine SL imaging characteristics in Chiari and control patients in order to correlate axial-image HIF, AMF, and AMF>HIF/pt. with SL characteristics and types.

Materials and Methods

We compared SL incidence, incidence and frequency of cervical-MR identified HIF/pt., AMF/pt. in 46 Chiari versus 356 control patients, in 28 Chiari SL and 89 control SL patients, and in 28 Chiari SL vs 18 no-SL patients. We identified specific predominant imaging characteristics and types of SL based on nature of SL T2 hyperintensity, SL length and continuity, and SL edge sharpness on T2 cervical MR in the 28 Chiari SL patients and in 46 age-matched non-Chiari control patients. We correlated axial image HIF, AMF, and AMF>HIF frequency to SL characteristic type in order to determine which SL features were associated with HIF, AMF, and AMF>HIF.

Results

SL incidence, HIF/pt. and AMF/pt. frequency, and AMF>HIF incidence were increased in 46 Chiari patients vs. 356 control. 28 Chiari SL patients demonstrated increased AMF/pt. (4.3 vs 3.7) and HIF/pt. (11.4 vs 7.1) ratios, and more observed-than-predicted AMF>HIF/pt. (2.8 vs. 2.2) compared to 18 no-SL Chiari patients. Three types of SL were identified based on predominant imaging features, with variable lengths (Fig.1-3). 13 Chiari Type 1 SL (CSF-hyperintense, continuous, sharply-circumscribed) showed increased HIF/pt. vs. 9 less-circumscribed Type 3 (discontinuous, dot-and-dash SL of CSF hyperintensity; Table, p=0.05). Type-3 Chiari SL had increased AMF/pt. (p=0.05), and more numerous AMF>HIF vs. Type-1. 33 Type-3 control SL exhibited more numerous AMF/pt. vs.12 control Type 2 SL (less hyperintense, of variable continuity, less-sharply circumscribed; p=0.08), with similar HIF/pt. Wide AMF may demonstrate broad hyperintense bands.

Conclusions

SL incidence and HIF and AMF/pt. are more numerous in Chiari patients. AMF are responsible for some axial HIF and some dot-and-dash, less hyperintense Type-3 SL in both Chiari and control patients. Type-1 SL represent the central canal in Chiari and control patients.

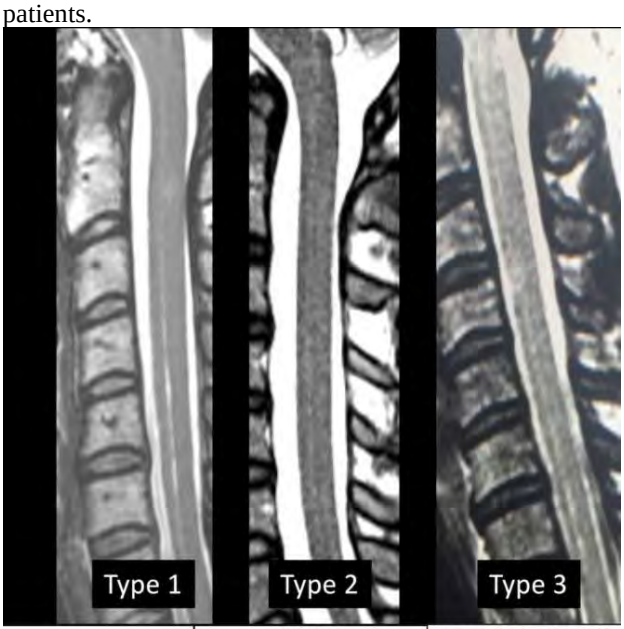

		Chiari SL (n=28)				Control Age-Match SL (n=46)	
Sagittal Line Type	n	HIF/pt	AMF/pt	AMF> HIF/pt*	n	HIF/pt	AMF/pt.
Type 1 CSF Intensity	13	14.2[a]	3.1[b]	1.7	1	22	2.0
Type 2 Partial Volume	6	12.7	2.0	0.6	12	6.8	1.5[c]
Type 3 Dot-dash	9	8.0[a]	8.4[b]	2.1	33	6.4	2.9[c]

[a]p=0.05 [b]p=0.05 [c]p=0.08

(Filename: TCT_300_Table1AbstractTypesFinal.jpg)

226

Characterizing Brain White Matter Alterations in Diabetes: A Cross-sectional UK Biobank Study of Neurite Orientation Dispersion and Density Imaging.

A Alotaibi[1]

[1]*King Saud bin Abdulaziz University for Health Sciences/University of Nottingham, Nottingham, United Kingdom*

Purpose

Type 2 diabetes mellitus is a metabolic disorder that is associated with white matter microstructural changes. Diffusion tensor imaging (DTI) has been widely used to characterize white matter microstructural abnormalities in patients with diabetes. Despite its sensitivity in detecting microstructural changes in white matter, DTI still lacks specificity. Neurite orientation dispersion and density imaging (NODDI) has been proposed to characterize white matter microstructures precisely. Although NODDI has not been applied in diabetes, this technique is promising in investigating the complexity of white matter pathology, as it is more specific than DTI. We aimed to investigate brain white matter alterations in patients with type 2 diabetes using NODDI; and to assess the association between white matter changes in diabetes and disease duration/glycated hemoglobin.

Materials and Methods

We examined 48 white matter tracts separately using diffusion measures derived from the UK Biobank in 3338 patients with type 2 diabetes (36.34% women, mean age 65.85 years) and 31471 healthy controls (53.92% women, mean age 63.71 years), with focus on previously reported white matter tracts. Participants underwent 3.0T multi-parametric brain imaging (T1 weighted imaging and diffusion imaging for DTI/NODDI). Tract of interest analysis of fractional anisotropy (FA), mean diffusivity (MD), orientation dispersion index (ODI), Intracellular volume fraction (ICVF) and isotropic water fraction (IsoVF) was conducted to assess white matter abnormalities. A general linear model was performed to evaluate intergroup white matter differences and their association with the metabolic profile.

Results

The preliminary result showed that patients with type 2 diabetes have subtle white matter microstructural deficits (including the previously reported white matter tracts in the literature). ICVF was significantly reduced, ODI was increased considerably, and IsoVF was increased/decreased in patients with type 2 diabetes ($P<0.05$). However, few tracts showed no significant differences. Weak to moderate correlations were found between disease duration, glycated hemoglobin and white matter differences.

Conclusions

Type 2 diabetes is evident to cause white matter microstructural abnormalities that have association with metabolic profile. NODDI is able to give biophysical information for understanding the diabetic impact on brain microstructure. It may lead to a better imaging biomarker for monitoring disease progression.

Figure 1 shows intergroup WM differences detected by NODDI and DTI that represent axonal loss or lower axonal density, associated neuroinflammation, and vasogenic edema in patient with type 2 diabetes.

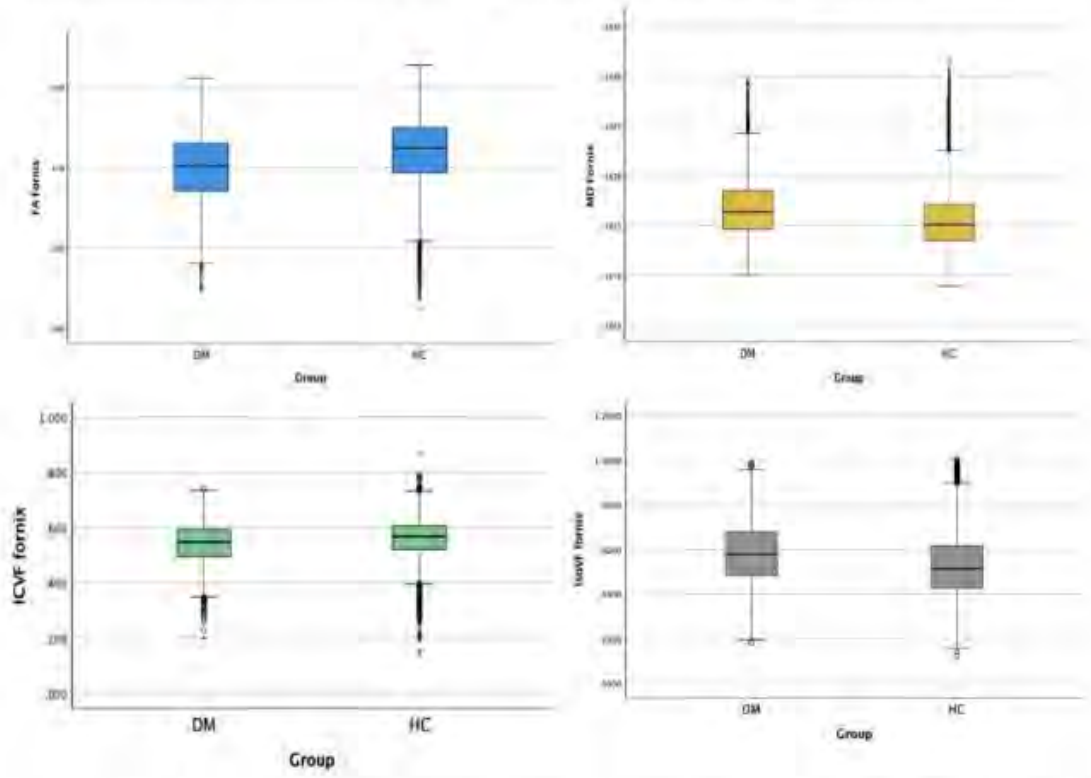

Clinical Information	(*N* = 3338) T2DM (mean ± SD)	(*N* = 31471) HC (mean ± SD)	χ2/T	Mean difference	95% CI	
					Lower	Upper
Gender **F (%)**	1213/36.34%	16969/53.92%	374.5	--	--	--
Age **(years)**	65.85 ± 7.23	63.71 ± 7.50	16.189	2.140	1.881	2.399
Systolic blood pressure (mmHg)	140.29 ± 17.33	136.08 ± 18.66	12.712	4.216	3.565	4.866
Diastolic blood pressure (mmHg)	83.59 ± 10.29	81.18 ± 10.43	12.378	2.416	2.033	2.799
Hb1AC (mmol/mol)	46.36 ± 11.68	34.3 ± 3.52	56.847	12.030	11.615	12.445
BMI (kg/m^2)	30.4 ± 5.27	26.3 ± 4.02	43.695	4.118	3.933	4.302
Disease duration (years)	11.52 ± 11.07	--	--	--	--	
Education level	**T2DM (%)**	**HC (%)**				
(A)	576 (19.1)	4420 (15.2)				
(B)	701 (23.6)	5970 (20.5)				
(C)	427 (14.4)	4109 (14.1)				
(D)	1262 (42.5)	14621(50.2)				

Table 1 shows the baseline characteristics of the included participants from the UKB database. * = dataset tested using Pearson's chi-square test; ± = mean and standard deviation; mmHg = millimeters of mercury; A = College or University degree; B = A levels/AS levels or equivalent; C = O levels/GCSEs or equivalent; D = CSEs or equivalent.

(Filename: TCT_226_NODDI-DM.jpg)

807

Characterizing Dementia using Cross-Sectional Biomarkers from Multicenter FLAIR MRI

O Crystal[1], J DiGregorio[1], A Gibicar[1], P Jabehdar Maralani[2], P Tyrrell[2], A Moody[3], H Khosravani[2], A Khademi[1], S Black[3]
[1]Ryerson University, Toronto, Ontario, [2]University of Toronto, Toronto, Ontario, [3]Sunnybrook Health Sciences Centre, Toronto, Ontario

Purpose

Fluid-attenuated inversion recovery (FLAIR) MRI is routinely used for the analysis of white matter lesions (WML). Despite this, many automated biomarker extraction algorithms are developed for T1-weighted or multi-modal inputs [1][2]. We present one of the

first studies that automatically extracts and analyzes cross-sectional total brain volume (TBV), cerebrospinal fluid (CSF), and WML using multicenter FLAIR-only data. This demonstrates the viability of FLAIR as a stand-alone imaging modality for biomarker analysis and establishes FLAIR-only benchmarks.

Materials and Methods

FLAIR MRI from ADNI (1051 subjects) and CCNA (254 subjects) were used in this analysis. See [3][4] for cohort details. Diagnostic labels for ADNI are CN, MCI, AD and for CCNA are SCI, MCI, vMCI, AD. Demographic data, including sex/age are available. To extract TBV, CSF and WML volumes, validated intensity standardization [5], ICV segmentation using MultiResUNet [3] and WML segmentation using a skip connection U-Net [4] (Fig.1) methods were used to segment objects. Same thresholds are applied to intensity standardized ICV images to find TBV and CSF (Fig.1). Cross-sectional biomarkers utilized baseline volumes from each patient. ANCOVA testing (controlling for age/sex) was used to find differences between cognitive groups.

Results

Cross-sectional biomarkers from CCNA, ADNI showed an increase in CSF/WML volumes, and TBV decreased for worse cognitive diagnosis (Fig.2). WML loads were highest for vMCI in CCNA (mean = 1.78%). ANCOVA showed significant differences ($p < 0.05$) in TBV/CSF/WML volumes across CN/AD and MCI/AD comparisons. ANCOVA on CCNA revealed significant differences ($p < 0.05$) between all disease groups for TBV/CSF, and vMCI/SCI, vMCI/MCI and vMCI/AD for WML.

Conclusions

This work measures biomarkers from a large multicenter FLAIR dataset of subjects with dementia. Results from cross-sectional analyses are in line with known trends associated with cognitive impairment and thus demonstrate FLAIR can suffice as a stand-alone imaging modality for biomarker analysis.

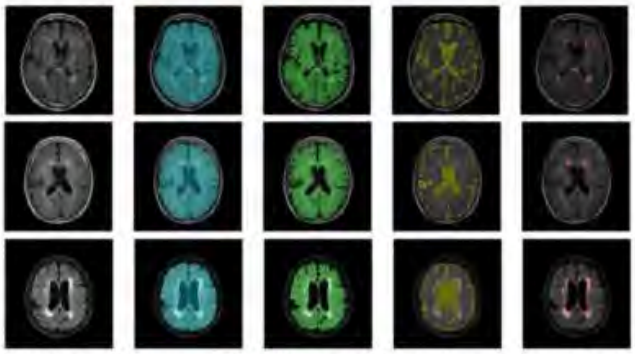

Figure 1: ICV (blue), TBV (green), CSF (yellow) and WML (red) segmentations for three subjects

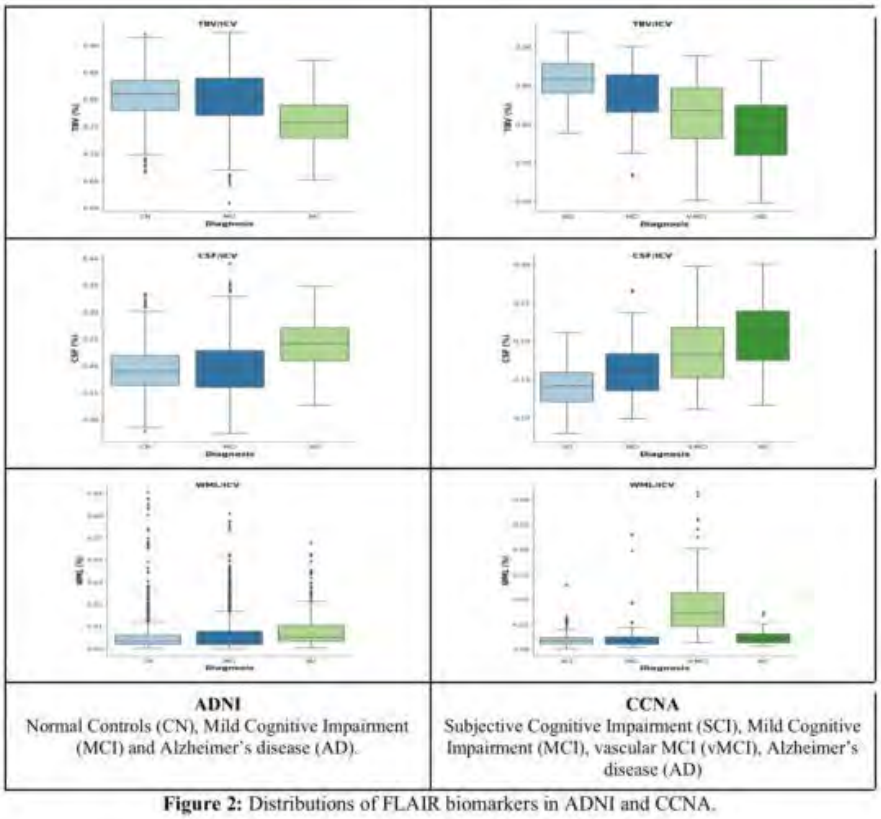

Figure 2: Distributions of FLAIR biomarkers in ADNI and CCNA.

(Filename: TCT_807_onepage_figs.jpg)

163

Clinical application of intravoxel incoherent motion (IVIM) imaging in patients with acute ischemic stroke

K Yamashita[1], R Kamei[1], K Furuya[1], S Harada[1], J Maehara[1], T Noguchi[1]
[1]National Hospital Organization Kyushu Medical Center, Fukuoka, Fukuoka

Purpose

Intravoxel incoherent motion (IVIM) MR imaging allows simultaneous extraction of perfusion and diffusion parameters. For this reason, IVIM imaging would be one of the best methods for assessing acute ischemic stroke (AIS). Theoretically, IVIM imaging provides less misregistration of lesions that appear hyperintense on diffusion-weighted imaging (DWI) than other functional imaging or imaging modalities. However, the inter-observer reliability of IVIM imaging and clinical characteristics of patients with decreased or non-decreased IVIM parameters have not been well explored. Therefore, this study was aim to evaluate inter-observer agreement and the clinical utility of IVIM MR imaging in patients with AIS.

Materials and Methods

We retrospectively studied 29 patients with AIS (M: F = 17:12; mean age ± SD = 75.2 ± 12.0 years old, median = 77 years old). Each patient underwent IVIM MR imaging with a 1.5-T MR scanner. Diffusion sensitizing gradients were applied sequentially in the x, y, and z directions with 6 different b-values (0, 50, 100, 150, 200, and 1000 s/mm2). From the IVIM MR imaging data, diffusion coefficient (D), perfusion fraction (f), and pseudo-diffusion coefficient (D*) maps were obtained using a two-step fitting algorithm based on the Levenberg-Marquardt method. The presence of decreases in IVIM f and D* values compared with the contralateral normal-appearing brain was graded on a two-point scale by two independent neuroradiologists. Inter-observer agreement on the rating scale was evaluated using kappa statistic. Clinical characteristics of patients with non-decreased IVIM f and/or D* as rated by the two observers were also assessed.

Results

Inter-observer agreement was shown for IVIM f ($\kappa = 0.854$) and D* ($\kappa = 0.789$) maps, which indicated almost perfect and substantial agreements, respectively. Patients with non-decreased IVIM f tended to show recanalization of occluded intracranial arteries than patients with decreased IVIM f. Patients with non-decreased IVIM f as rated by observers tended to show recanalization of occluded intracranial arteries more frequently than patients with decreased IVIM f.

Conclusions

IVIM MR imaging could be performed in less than 1 min in addition to routine diffusion-weighted imaging. IVIM parameters non-invasively provide feasible, qualitative perfusion-related information for assessing patients with AIS.

1011

Clinical diffusion kurtosis MRI using deep neural network

D Park[1], J Kim[1]
[1]University of Alabama at Birmingham, Birmingham, AL

Purpose

Demonstrate the clinical feasibility and utility of deep neural network (DNN)-based fast diffusion kurtosis imaging (DKI) in various disease conditions.

Materials and Methods

DNN model that encodes fast DKI signal intensities to target parameters (i.e. MK and MD) was implemented under the TensorFlow platform. The model comprised of 1D oversampling layer and 4 fully connected layers of feed forward neural network with ReLU and sigmoid activations. Adam gradient descent algorithm was used for training optimization of neural network. We generated a numerical phantom of synthetic diffusion signal as training data set that has scaled beta distribution with shape parameters simulating different tissue conditions (n = 700,000). The model training was performed on numerical training data set using a single GPU-equipped PC. We retrospectively analyzed clinical cases (n=49) of MRI obtained from 3T or 1.5T MR scanners, which included cerebral abscess, intraparenchymal hemorrhage, acute infarction, GBM, low-grade glioma, primary CNS lymphoma, meningioma, and intraoperative scan of laser interstitial thermal therapy. Diffusion-weighted imaging was acquired with b=0, 1000 and 2000 s/mm2 in 1, 4 and 4 diffusion-gradient orientations (1:47 min scan duration). MK and MD maps were predicted from trained model on clinical datasets through a pipeline processing incorporated within a fully automated streamline workflow. For comparison, conventional MK and MD maps were also generated using a linear fitting method available from the DIPY toolkit [2].

Results

Mean kurtosis (MK) maps derived from conventional linear model fitting (DIPY) method exhibited 4.82~18.1% "black hole" artifacts (mean±S.D.=9.17±2.96) in the entire brain volume in comparison to complete artifact-free maps from DNN method. In addition, DNN method was immune to the excessive motion related image degradation.

Conclusions

The "black hole" artifact arises from erroneous computation of negative MK, which is nonphysiological. As Gibbs-ringing is attributed to the major source of this intractable problem [3], previously local subvoxel-shift based correction method was proposed [4]. However, this method is unable to eliminate "black hole" artifact arising from other causes in DKI such as motion and CSF partial volume. Alternatively, image denoising methods such as non-local means filtering cause a significant image smoothing disadvantage [5]. In this work, we found clinical feasibility of fast DKI with superior quality MK maps using DNN method.

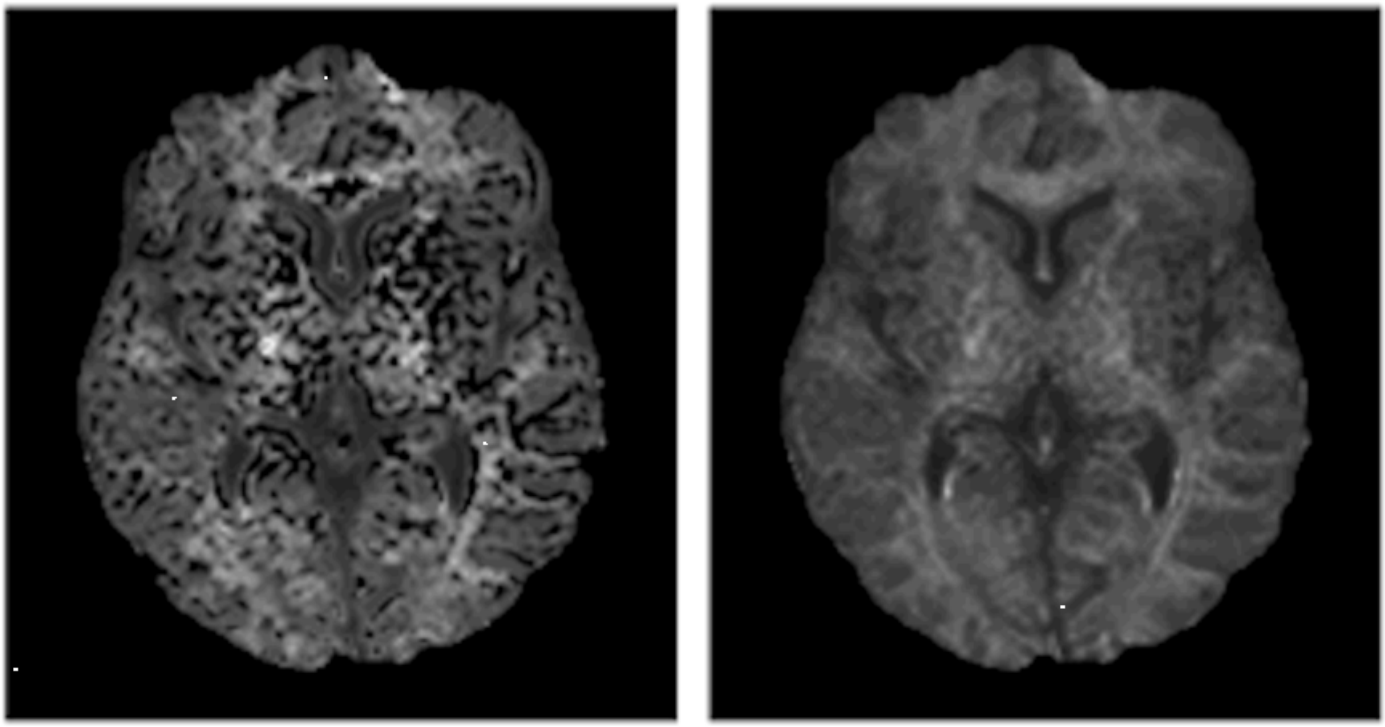

(Filename: TCT_1011_figure2.gif)

841

CNS lesions identified with F18-Fluciclovine PET/CT

J Wang[1], R Kuker[1], R Quencer[1], A Serafini[1], M Foley[1], G Saigal[1], S Falcone[1], A McKinney[1]
[1]*Jackson Memorial Hospital/University of Miami Health System, Miami, FL*

Purpose

Fluciclovine, also known as anti-1-amino-3-[18F]-fluorocyclobutane-1-carboxylic acid or Axumin, is a PET radiotracer utilized to assess suspected recurrent prostate cancer in patients with elevated PSA levels. It has been demonstrated that human astrocytic tumor and glioma cells utilize the amino acid transporter system for fluciclovine uptake. Therefore, it is plausible to evaluate CNS tumors via F18-Fluciclovine PET/CT. The purpose of this study is to determine the frequency of CNS lesions incidentally found on F18-Fluciclovine PET/CT for patients with history of prostate cancer.

Materials and Methods

Patients with history of prostate cancer and biochemical recurrence with increased PSA levels were evaluated with F18-Fluciclovine PET/CT from 05/2017 - 09/2021 (1146 males). For patients demonstrating incidental positive findings in CNS, further characterization of the lesions was performed utilizing MRI of the brain and or the spine.

Results

Six patients showed incidental F18-Fluciclovine positive lesions in the brain and the craniocervical junction. These included a meningioma (SUV 9.4), a pituitary adenoma (SUV 7.5), multiple spinal meningiomas (SUV 9.1), a cerebellopontine angle mass (SUV 6.5), prostatic cancer brain metastases (SUV 3.7) and radiation necrosis (SUV 3.3).

Conclusions

In addition to the evaluation of prostate cancer recurrence and or metastasis, F18-Fluciclovine PET/CT is able to detect CNS lesions in the brain and the spinal canal and could be used in the evaluation of such patients. While glioblastoma multiforme, glioma and anaplastic oligodendroglioma are known to demonstrate F18-Fluciclovine uptake, we extend this experience with the cases shown here including meningioma, pituitary adenoma, radiation necrosis, and prostatic cancer brain metastases. F-18 Fluciclovine-PET/CT may be a more sensitive marker for the evaluation of CNS tumor given its optimal contrast resolution and high lesion to background ratio than F-18 FDG-PET/CT.

Case	Age	Gender	Diagnosis	Location	SUV Lesion	SUV Brain Background
1	76	Male	Brain meningioma	R middle cranial fossa	9.4	0.5
2	69	Male	Pituitary adenoma	Pituitary gland	7.5	0.1
3	67	Male	Spinal meningioma	Cervical spinal canal	9.1	0.5
4	81	Male	MRI Pending	Cerebellopontine angle	6.5	0.3
5	64	Male	Prostatic cancer brain metastases	Left temporal lobe	3.7	0.7
6	80	Male	Radiation necrosis	Right temporal lobe	3.3	0.6

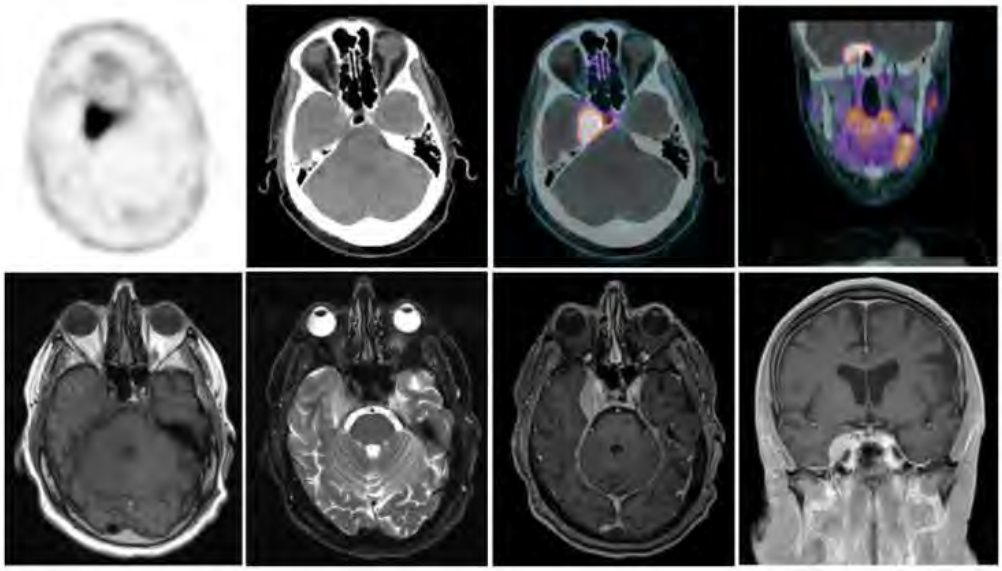

One 76-year-old male patient with a history of prostate cancer demonstrated F18-Fluciclovine avid lesion in the medial right temporal fossa, SUV 9.4, and on MRI it corresponded to a dural based enhancing mass along the medial right middle cranial fossa, suggestive of meningioma or metastatic disease in this patient given the known history of prostate cancer. The clinical follow-up and MRI studies have been stable over a 2 year period of time; this is consistent with the diagnosis of meningioma.

(Filename: TCT_841_Picture2.JPG)

494

Combination of 18F-FET PET/CT Dynamic and Texture Analysis in Prediction of Glioma Grade and IDH1 Status.

R Hajri[1], J Prior[1], V Dunet[1]

[1]*Lausanne University Hospital, Lausanne, Vaud*

Purpose

Gliomas are the most frequent malignant brain tumors and are heterogeneous in histology, genetics, and outcome. Mutation in isocitrate dehydrogenase (IDH) 1 has been described by several studies as an independent predictor of survival and represents a target of new molecular drugs. A longer survival is observed in glioma patients carrying an IDH1 mutation. We aimed at evaluating the respective value of O-(2-[18F]fluoroethyl)-L-tyrosine (18F-FET) PET/CT dynamic and texture analysis in patients with untreated glioma to assess grade and IDH1 mutation status.

Materials and Methods

Seventy-five patients were included (male: 49, median age: 47 [35-59]) and underwent a 18F-FET PET/CT for initial glioma evaluation. Thirty-five had a WHO grade 2 and forty a grade 3-4 glioma. IDH1 status was available in 62 patients. Time-activity-curve (TAC) type and 20 parameters (conventional, texture, shape and histogram derived) obtained from static analysis using the LIFEx software were recorded. Respective performance was assessed using receiver operating characteristic (ROC) curve analysis and stepwise multivariate regression analysis.

Results

TAC type was an independent predictor of glioma grade (AUC 0.84 [95%CI 0.76-0.93]; OR 21.3 [4.97-90.77], p<0.001). In low-

grade but not in high-grade glioma, gray-level co-occurrence matrix (GLCM) correlation and coarseness, and Shape_surface additionally demonstrated good performance for IDH1 status identification (AUC 0.78 [0.57-0.98], 0.82 [0.64-1.0] and 0.76 [0.54-0.98] respectively). On stepwise multivariate analysis, GLCM_correlation tended to be an independent predictor for IDH1 status in low-grade gliomas (OR 36.3 [0.95-1389], p=0.053), with higher value in IDH1 mutant.
Conclusions
Combining 18F-FET PET/CT dynamic and texture analysis may help predicting both glioma grade and IDH1 status, especially in low-grade tumors.

1352

Comparing Deep Learning and Classical Machine Learning Methods For Differentiating Primary CNS Lymphomas From Gliomas – A Systematic Review

G Cassinelli Petersen[1], J Shatalov[2], T Verma[3], W Brim[4], S Merkaj[1], R Bahar[1], H Subramanian[1], J Cui[4], M Johnson[4], A Malhotra[5], A Omuro[1], M Aboian[6]
[1]Yale School of Medicine, New Haven, CT, [2]University of Richmond, Richmond, VA, [3]Yale School of Medicine, Ossining, NY, [4]Yale University, New Haven, CT, [5]Yale University School of Medicine, New Canaan, CT, [6]Yale University, Woodbridge, CT

Purpose
To compare and synthesize the findings on the application of different Deep Learning (DL)- versus classical ML- (cML) based models in differentiating Primary CNS Lymphomas (PCNSL) from gliomas.
Materials and Methods
A systematic search of literature was performed in October 2020 and February 2021 on Ovid Embase, Ovid MEDLINE, Cochrane trials, and Web of Science – Core Collection. The search strategy included keywords and controlled vocabulary including the terms: gliomas, artificial intelligence, machine learning, deep learning, and related terms. Publications were reviewed and screened by four different reviewers in accordance with TRIPOD.
Results
The literature search yielded 11,727 studies and 1,141 underwent full-text review. Data was extracted from 23 publications. Nineteen studies used cML only, two DL only, and two both. The analyzed databases had an average size of 99 patients per study. 26.1% of publications reported external validation. The most tested ML and deep learning algorithms were Support Vector Machines (SVM) and Multilayer Perceptron Networks (MLP), respectively. For cML a Logistical Regression model achieved the highest AUC (0.961) in external validation, while an MLP achieved the highest for DL (0.947). Both were trained on conventional radiomic features from routine and DWI sequences. End-to-end classifiers like Convolutional Neural Networks (CNN) achieved lower AUC in external validation (0.49 and 0.89) compared to MLP.
Conclusions
AI-based methods for differentiating gliomas and PCNSL have been reported and show that ML models can achieve AUC > 0.94 in external validation. Classifiers using precalculated handcrafted features performed better than end-to-end deep classifiers. CNNs, when not regularized properly, are prone to overfitting and benefit from large datasets. With few studies using DL algorithms further research into novel DL-based approaches is recommended. Additionally, most studies lack large datasets and external validation, increasing the risk of overfitting.

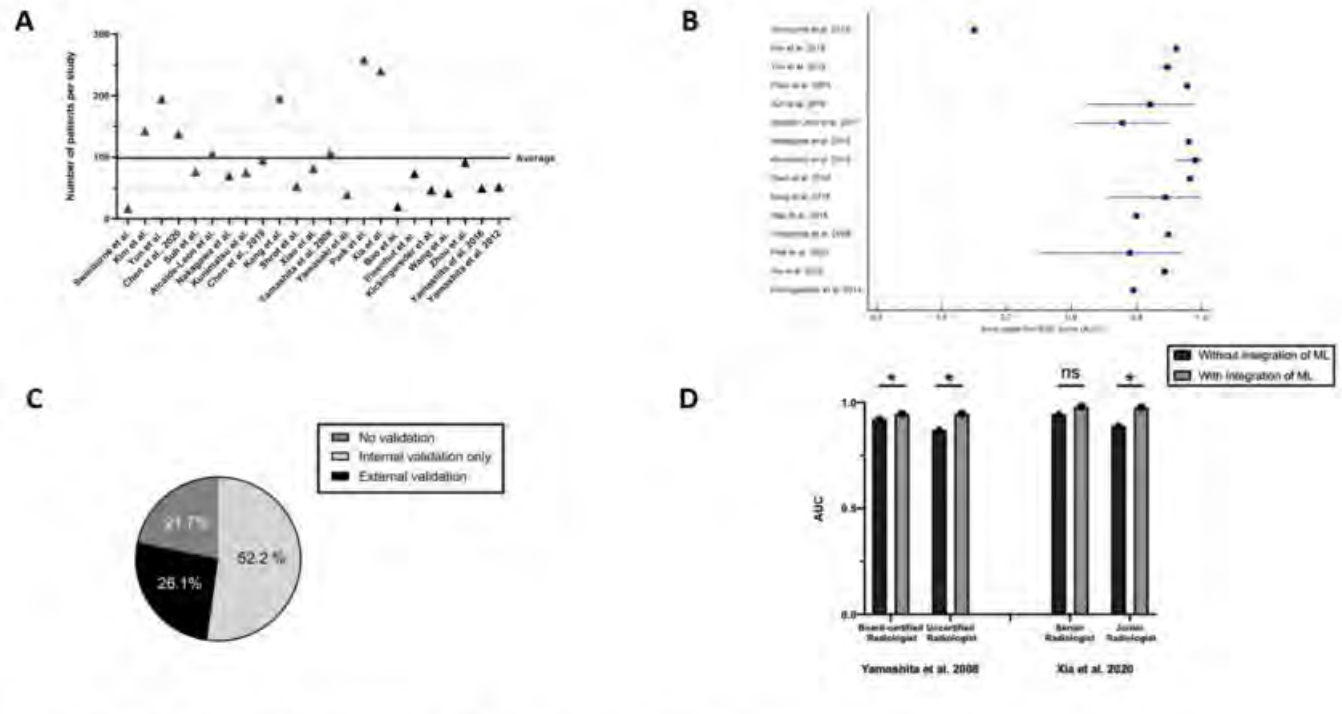

A) Scatterplot displaying the number of patients included in every study.
B) Forest plot showing the best achieved and reported AUC of a ML model in validation. AUC reported in testing but without any type of validation is not included in this graph.
C) Type of validation performed in the studies
D) Performance of radiologists before and after incorporation of ML pipeline in their decision process

(Filename: TCT_1352_VAMOMKTV-1083433-1-ANY.jpg)

709

Comparison of Efficacy and Safety Outcomes After Emergency Stenting in Patients with Intracranial Atherosclerotic Stenosis-related Large-vessel Occlusion Stroke with and without of Intravenous Infusion of Tirofiban.

R Garayzade[1], C Maurer[1], A Berlis[1], S Schiele[2], G Mueller[2]
[1]*University Klinik Augsburg, Germany,* [2]*Institute of Mathematics, Augsburg University, Germany*

Purpose
Intracranial rescue Stent Angioplasty is a bail-out strategy in case of unsuccessful stent-retriever thrombectomy due to underlying atherosclerotic stenosis. However, there is no consensus upon a preprocedural and intraprocedural antiplatelet regimen. This study aimed to compare the efficacy and safety outcomes after emergency stenting in patients with intracranial atherosclerotic stenosis-related large-vessel occlusion stroke with and without of intravenous infusion of tirofiban.
Materials and Methods
We performed a retrospective analysis of 78 patients who were treated with rescue stent angioplasty between 2010 and 2019 due to acute ischemic stroke.Patients were divided into 2 groups: those who received periinterventional a bolus of tirofiban (10 µg/kg) over 3 minutes and an subsequent infusion of tirofiban (0.15 µg/kg/min) (intravenous tirofiban group, n=37(47.4%)) and those who did not receive intravenous tirofiban (control group, n= 41(52,6 %)). The following treatment outcomes in the 2 groups were compared: symptomatic hemorrhage, and 90-day functional outcome and mortality.
Results
The rates of symptomatic hemorrhage, 90-day good outcome, and mortality were not significantly different between the 2 groups. The rate of symptomatic hemorrhage was not significantly more frequent in the intravenous tirofiban group than in the control group (16.2% versus 14.6%, p=0.847). A good outcome (90-day modified Rankin Scale score of 0–2) was not significantly more frequent in patients with infusion of tirofiban than in those without it (45.9% versus 34.1%, P=0.289). Mortality was not significantly more frequent in the intravenous tirofiban group than in the control group (21.6% versus 17.1 %, p=0.611)
Conclusions
The use of intravenous tirofiban was associated with no increased risk of hemorrhage in patients with intracranial atherosclerotic stenosis-related large-vessel occlusion stroke with rescue stenting.

349

Comparison of Machine Learning Approaches for Predicting Delayed Infant Brain Myelination from T1 & T2 MRIs

G Chaudhari[1], J Chen[1], Y LI[2], A Rauschecker[3]

[1]University of California, San Francisco, San Francisco, CA, [2]UCSF, San Francisco, CA, [3]UCSF Radiology, Mill Valley, CA

Purpose

Progression of infant brain myelination over the first two years of life follows an orderly, predictable pattern, with changes on T1- and T2-weighted MRI imaging based on gestationally corrected age (GCA) [1]. Delays in myelination are associated with infant developmental delay [2]. Determination of delayed myelination requires subjective visual inspection of the brain using reference milestones, allowing for improved standardization with artificial intelligence (AI). In this study, we compare end-to-end and hybrid Convolutional Neural Networks (CNNs) for predicting delayed myelination status in infants given T1 & T2 MRIs and GCAs.

Materials and Methods

Our institutional database was queried for patients aged 0-25 months with normal myelination from 1995-2019 (n=5838) and delayed myelination from 1995-2021 (n=426). For normal myelination MRIs, infants in the overrepresented 0-3 months bin were excluded (N=2659). MRIs without reports indicating normal brain myelination (N=1047), those missing gestational age (N=1352), and those without appropriate T1 and T2 imaging (N=309) were excluded. For delayed myelination MRIs, those missing gestational age (N=162) and without T1 and T2 imaging (N=107) were excluded (Figure 1). Myelination qualifiers of mildly and markedly delayed myelination were collected from reports, if present. The prototype AI method was an end-to-end CNN with input of paired T1 & T2 MRIs and GCA. The other two methods were extended from a CNN pre-trained to predict GCAs of normally myelinated brains: using an XGBoost classifier on the pre-trained model's post-convolution features to predict delayed myelination, and using a linear classifier on the true and CNN-predicted GCA to predict delayed myelination. Ten-fold cross-validation was used for all methods.

Results

600 infant brain MRIs with normal myelination and 157 with delayed myelination were included. The end-to-end CNN (AUC 0.835 ± 0.055) outperformed the other methods, including the XGBoost classifier trained on post-convolution features and true GCA (0.789 ± 0.025) and the linear classifier trained on pre-trained CNN outputs (0.640 ± 0.037; Fig 2). All three approaches show significantly increased prediction confidence for the "markedly delayed" cases than for "mildly delayed" cases (Fig 3).

Conclusions

End-to-end and hybrid deep learning approaches can predict delayed myelination status in infants given T1 & T2 MRIs and GCAs. Further research will be required to understand how such approaches can augment radiology workflows.

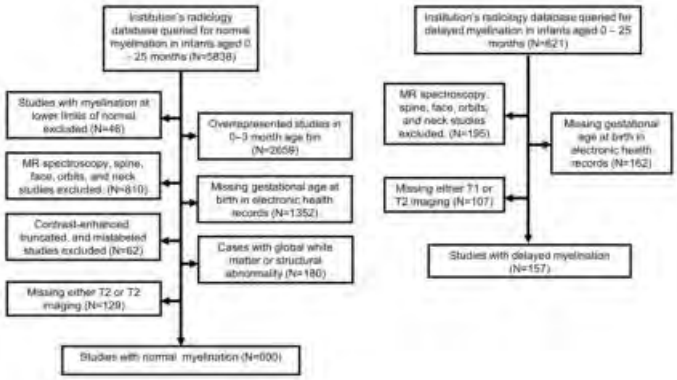

Figure 1: Flowcharts of data inclusion and exclusion criteria for cases with normal and delayed myelination.

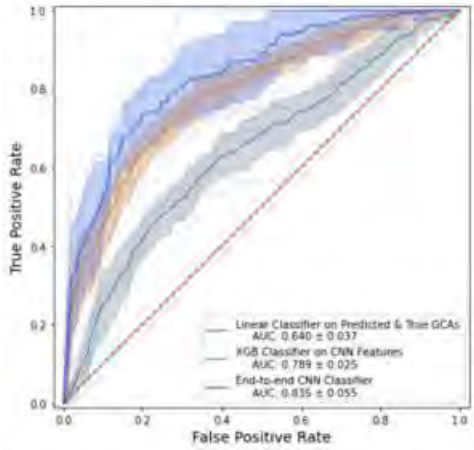

Figure 2: Average Receiver Operating Characteristic (ROC) curves showing performances of networks for detecting delayed myelination. Shaded regions represent mean +/- one standard deviation, and the individual run ROC curves are depicted in lighter colors.

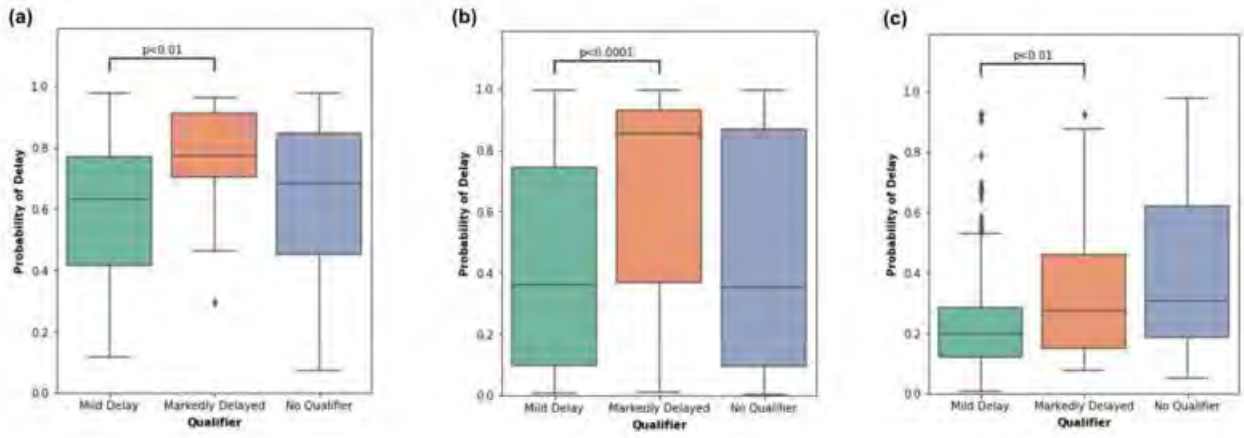

Figure 3: Boxplots of performances on qualifiers for (a) End-to-end CNN classifier, (b) XGBoost on CNN features, and (c) Linear classifier on predicted GCAs.

(Filename: TCT_349_ASNRAbstractFigures2022.jpg)

489

Comparison of pre-contrast T1-SPACE and MPRAGE for the identification of intrinsic T1 hyperintensity attributable to melanin

A Lasocki[1], S Stuckey[1], L Caspersz[1], G McArthur[1]
[1]*Peter MacCallum Cancer Centre, Melbourne, Victoria*

Purpose

Volumetric turbo spin echo (3D-TSE) T1-weighted imaging (T1WI) techniques are increasingly replacing volumetric magnetization prepared gradient recalled echo (3D-GRE) sequences for investigating intracranial metastases (IM), due to improved detection[1]. T1WI may also identify intrinsic T1 hyperintensity (T1H) pre-contrast, for example due to melanin or blood products, but the ability of pre-contrast 3D-TSE to appreciate T1H has not been assessed to our knowledge. This study compared 3D-TSE to 3D-GRE for the detection of T1H attributable to melanin.

Materials and Methods

Patients with metastatic melanoma and reported T1H were identified prospectively. MRIs were performed at 3T utilizing a standardized protocol including both 3D-GRE (MPRAGE, Magnetization-Prepared Rapid Acquisition with Gradient Echo) and 3D-TSE (T1-SPACE, Sampling Perfection with Application optimized Contrasts by using different flip angle Evolutions) pre-contrast, and Susceptibility-Weighting Imaging (SWI). Pre-contrast MPRAGE and T1-SPACE images were reviewed by a neuroradiologist, comparing the ability to identify T1H. SWI was also assessed to determine whether the T1H could be 1) entirely attributed to melanin,

2) potentially reflected a combination of melanin and blood products ('mixed'), or 3) could be solely due to blood products. Review by a second neuroradiologist is ongoing.
Results
146 lesions were identified in 20 patients (median 2 per patient, range 1-73) on single-reader assessment. 111 lesions had T1H attributable to melanin, 26 had T1H potentially attributable entirely to blood products, and 7 lesions were mixed. T1H was similarly conspicuous with both T1-SPACE and MPRAGE in 53 lesions, less conspicuous with T1-SPACE in 91 lesions, and more conspicuous in 2 lesions. Overall, 63% of lesions with T1H attributable to melanin were less conspicuous with T1-SPACE, as well as 73% of lesions with T1H attributable to blood products. Second MRI reader results will also be presented.
Conclusions
Pre-contrast 3D-GRE is better at detecting intracranial melanoma metastases than 3D-TSE, which is of particular value in patients with a contraindication to gadolinium, as well as potentially patients with intracranial metastases from an unknown primary.

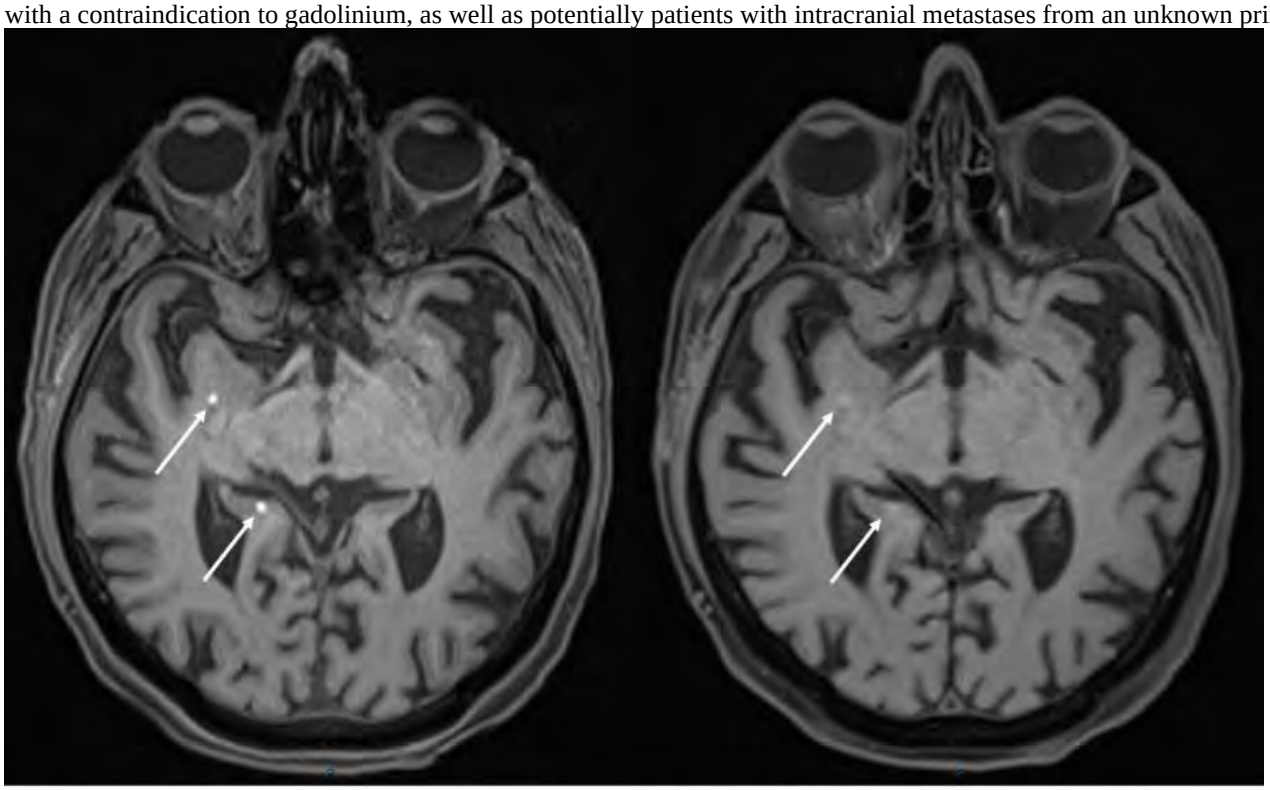

Pre-contrast MPRAGE (left) and T1-SPACE (right) images demonstrating two intracranial melanoma metastases (arrows) which are more conspicuous on MPRAGE than T1-SPACE.

(Filename: TCT_489_Lasocki-C-3D-GREvs3D-TSEinmelanoma-Figure1.jpg)

391

Comparison of the Evaluations by Radiologists, Machine Learning, and Synthetic MRI in Detecting T2-FLAIR Mismatch Sign

K Kikuchi[1], A Hiwatashi[1], O Togao[2], M Obara[3], K Ishigami[1]
[1]Kyushu University, Fukuoka, [2]Kyushu University, Fukuoka, Fukuoka, [3]Philips Japan, Tokyo

Purpose
This study aimed to compare the evaluations made by radiologists, machine learning (ML), and synthetic MRI (SyMRI) in detecting T2-FLAIR mismatch sign in diffuse astrocytoma, IDH-mutant.
Materials and Methods
Between May 2019 and May 2020, 13 patients (six males, seven females; 29–63 years of age; median age, 43 years), including seven patients with astrocytoma, IDH-mutant and six with oligodendroglioma, IDH-mutant and 1p/19q-codeleted, were retrospectively evaluated. The T2-FLAIR mismatch sign was assessed and compared by the following: qualitative evaluation by five radiologists; semi-quantitative evaluation using an ML model trained on seven other astrocytomas; quantitative evaluation by SyMRI. The Fleiss kappa coefficient, Mann–Whitney U test, and receiver operating characteristic (ROC) were used for statistical analyses.
Results
Sensitivity, specificity, and accuracy of radiologists were 57.1%, 83.3%, 69.2%, while those of ML were 85.7%, 50.0%, and 69.2%, respectively. SyMRI evaluation presented 100% of sensitivity, specificity, and accuracy. There was a significant difference in mean T2-values for astrocytoma vs. oligodendroglioma: 253.9 ± 124.4 ms vs. 108.7 ± 16.2 ms, P = 0.0012). The ROC showed that the T2-value had the best diagnostic performance (AUC, 1.00).

Conclusions
The T2-values, assessed using SyMRI, compared to those estimated by radiologists and ML, were found to be more effective for the diagnosis.

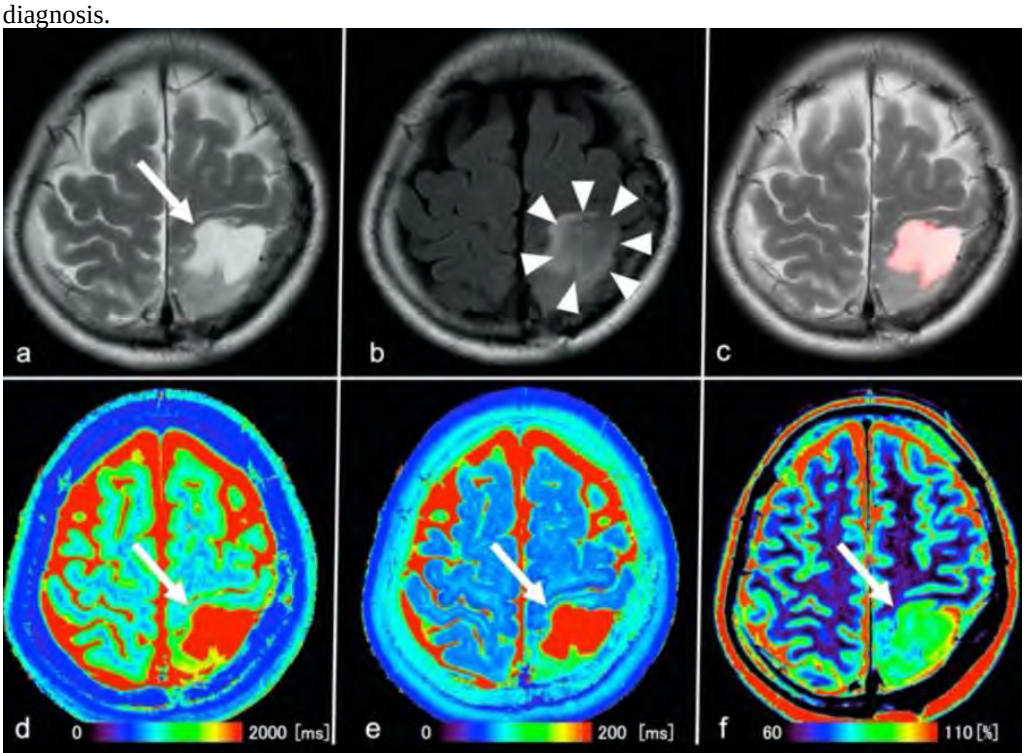

Images of diffuse astrocytoma, IDH-mutant in a 49-year-old woman. a, T2WI shows a heterogeneous T2-prolonged mass in the left parietal lobe (arrow). b, FLAIR shows partial signal suppression, indicating a T2-FLAIR mismatch sign (arrowheads). c, ML correctly detects a T2-FLAIR mismatch sign. d, e, and f, T1, T2, and PD maps derived using SyMRI show T1- (2436 ms*) and T2- (287 ms*) relaxation time prolongations, and increased PD (94.9%*) (arrows) in the tumor.
IDH, isocitrate dehydrogenase; ML, machine learning; PD, proton density; SyMRI, synthetic MRI, *Data is represented as mean.

(Filename: TCT_391_Figleg_ASNR2022_20211026_kk01.jpg)

232

Convolutional Neural Network Identification of Medtronic Strata Ventriculoperitoneal Shunt Valve Settings with Skull Radiographs

C Sabottke[1], M Greenhill[1], R Mushtaq[1], J Becker[1]
[1]*University of Arizona, Tucson, AZ*

Purpose
Several programmable ventriculoperitoneal (VP) shunts with variable valve settings are clinically used to regulate intracranial pressure [1]. Radiologists are often tasked to identify and interpret the valve settings which relies on comparing radiographs to different diagrams with valve setting positionings. This task can be time consuming and error prone; therefore, we sought to develop convolutional neural networks (CNNs) to identify VP shunt valve settings on shunt series radiographs with specific attention to the performance level (P/L) settings of Medtronic Strata devices.
Materials and Methods
We are currently engaged in ongoing data collection of shunt series radiographs with Medtronic Strata valves and identifiable P/L settings. With a preliminary dataset of 127 skull radiographs, we have used a DenseNet121 architecture convolutional neural network (CNN) to identify the five possible Strata P/L settings of 0.5, 1.0, 1.5, 2.0, and 2.5. Given the small initial size of our preliminary dataset, we have performed image augmentation using randomly applied image flips, rotations, warping, zooming, brightness and contrast changes, and pixel jitter in order to improve performance. We have also utilized the mixup technique for regularization [2].
Results
For our preliminary training and validation dataset splits, we have achieved validation dataset accuracy of 91% with an upper bound for the standard error estimated as 15%.
Conclusions
Although our preliminary dataset is small, there is still demonstrable potential for CNNs to identify VP shunt valve settings in skull

series radiographs. Our ongoing work in this area will involve expanding the dataset size and increasing the complexity of our neural network so that it can identify a wider variety of VP shunt valve settings and types rather than being limited to a single type of valve.

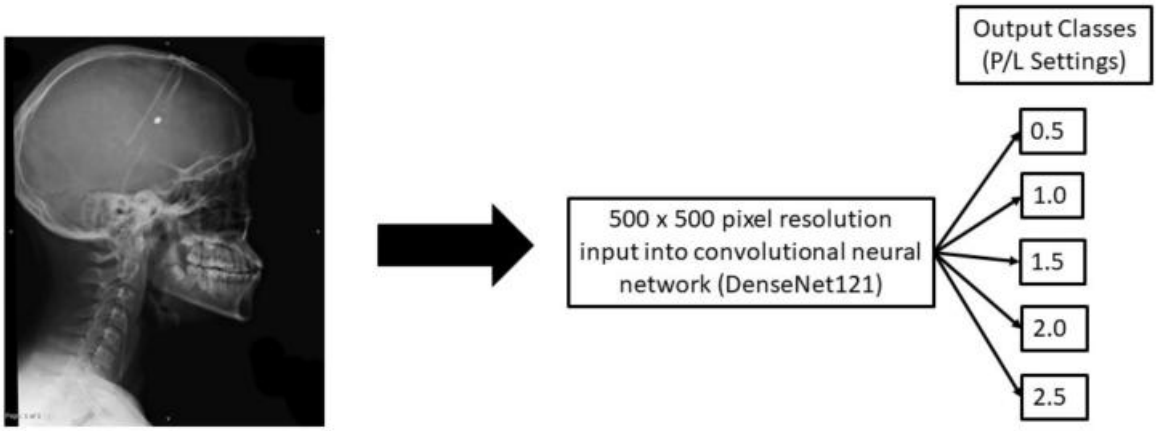

Basic outline of the neural network model pipeline with skull radiograph inputs and 5 possible output classes based on the P/L valve settings for a Medtronic Strata II valve. The example input has valve setting of 1.5 P/L.

(Filename: TCT_232_PosterAbstractFigurev1.jpg)

529

Critical illness-associated cerebral microbleeds for patients with severe COVID-19: etiologic hypotheses.

F LERSY[1], F Cotton[2], S Kremer[3]

[1]University hospitals of Strasbourg, STRASBOURG, France, [2]MRI center, Centre Hospitalier Lyon Sud, Hospices Civils de Lyon,, Lyon, FRANCE, [3]University hospitals of Strasbourg, STRASBOURG, FRANCE

Purpose

During the COVID-19 outbreak, the presence of extensive white matter microhemorrhages was detected by brain MRIs. The goal of this study was to investigate the origin of this atypical hemorrhagic complication.

Materials and Methods

Between March 17 and May 18, 2020, 80 patients with severe COVID-19 infections were admitted for acute respiratory distress syndrome to intensive care units at the University Hospitals of Strasbourg for whom a brain MRI for neurologic manifestations was performed. 19 patients (24%) with diffuse microhemorrhages were compared to 18 control patients with COVID-19 and normal brain MRI.

Results

The first hypothesis was hypoxemia. The latter seemed very likely since respiratory failure was longer and more pronounced in patients with microhemorrhages (prolonged endotracheal intubation (p=0.0002), higher FiO_2 (p=0.03), increased use of extracorporeal membrane oxygenation (p=0.04)). A relevant hypothesis, the role of microangiopathy, was also considered since patients with microhemorrhages presented a higher increase of the D-Dimers (p=0.01) and a tendency to more frequent thrombotic events (p=0.12). Another hypothesis tested was the role of kidney failure, which was more severe in the group with diffuse microhemorrhages (higher creatinine level [median of 293µmol/L versus 112µmol/L, p=0.04] and more dialysis were introduced in this group during ICU stay [12 versus 5 patients, p=0.04]).

Conclusions

Blood-brain barrier dysfunction secondary to hypoxemia and high concentration of uremic toxins seems to be the main mechanism leading to critical illness-associated cerebral microbleeds, and this complication remains to be frequently described in severe COVID-19 patients.

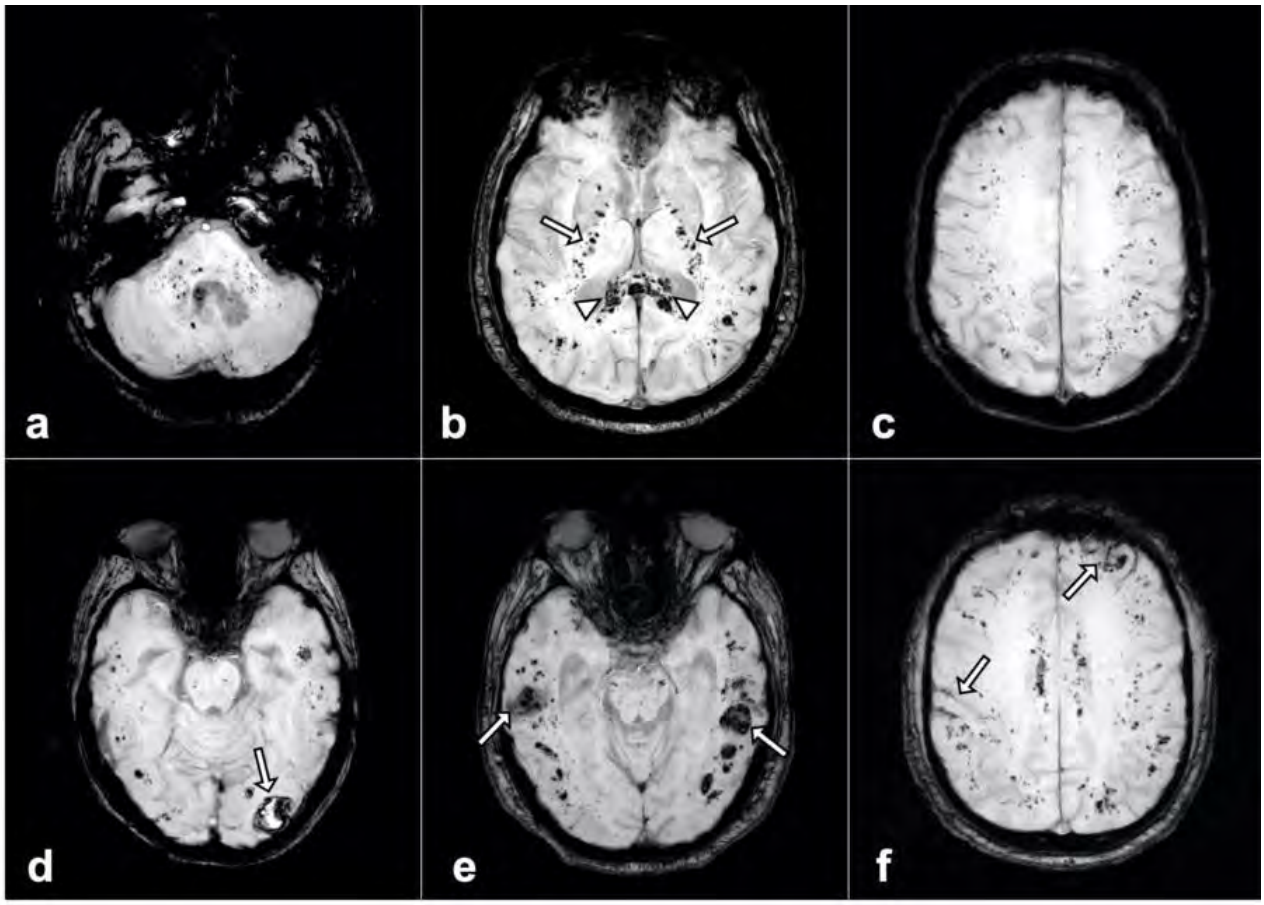

(Filename: TCT_529_Covid-19.jpg)

371

Defining Ischemic Core in Acute Ischemic Stroke using CT Perfusion: A Multi-center Validation Study

P Shahrouki[1], J Fifi[2], A Bauer[3], A Vagal[4], P Khatri[5], A Srinivasan[6], A Mitulescu[7], S Campana[8], B Bucciarelli[8], J Sayre[1], H Shoirah[9], J Mocco[2], K Nael[1]

[1]UCLA, Los Angeles, CA, [2]Icahn School of medicine at Mount Sinai, New York, NY, [3]Kaiser Permanente, Fontana, CA, [4]University Of Cincinnati Medical Centee, Cincinnati, OH, [5]University of Cincinnati, Cincinnati, OH, [6]University of Michigan, Ann Arbor, MI, [7]Olea Medical, La Ciotat, Bouches du Rhone, [8]Olea Medical, La Ciotat, France, [9]Mount Sinai, New York City, NY

Purpose

Estimation of infarction based on computed tomographic perfusion (CTP) remains challenging, mainly due to noise associated with CTP data and variability in reported thresholds ischemic core esstimation. Commercial software companies have attempted to establish CTP thresholds; for example, a relative cerebral blood flow (rCBF) of <30% for RAPID™ (iSchemaView). In this retrospective multi-center study, we sought to establish and validate CTP threshold values for estimation of ischemic core using Olea Sphere® software (Olea Medical Solutions).

Materials and Methods

Under an approved multi-institutional protocol, patients with acute ischemic stroke of the anterior circulation from three comprehensive stroke centers were included if they met the following criteria: baseline CTP, recanalization achieved (Thrombolysis in cerebral infarction scale ≥ IIb), and follow up MRI (DWI) performed. Perfusion maps were generated from the CTP data by the Bayesian probabilistic model and oscillation singular value decomposition (oSVD). CTP parameters, including time to peak (TTP), rCBF, time to max (Tmax), and Delay (equivalent of Tmax in Bayesian model) were generated. Brain was extracted from CTP and coregistered with the follow up MRI. An infarction mask and non-infarcted masks were drawn on MRI. We used a robust logistic regression to assess the binary outcome of our voxel-based analysis (infarcted vs non-infarcted) by adjusting for intra-subject correlations.

Results

Eighty-one patients (42 Male; mean age 67.4 ±17.3) were included. All CTP parameters for the Bayesian and oSVD methods showed significant differences between infarcted and non-infarcted areas ($p < 0.001$). In the Bayesian model, a combination of rCBF at threshold of <38% and delay at threshold of 0.80 sec provided diagnostic accuracy (AUC/sensitivity/specificity): 0.79/0.69/0.79; Figure 1). In the oSVD method, a combination of rCBF at threshold of <42% and Tmax at threshold of 4.00 sec provided diagnostic accuracy (AUC/sensitivity/specificity): 0.70/0.64/0.73; Figure 1).

Conclusions
Using heterogenous CTP data from three stroke centers, we established thresholds for estimation of ischemic core on Olea software that can be used for both Bayesian and oSVD postprocessing models.

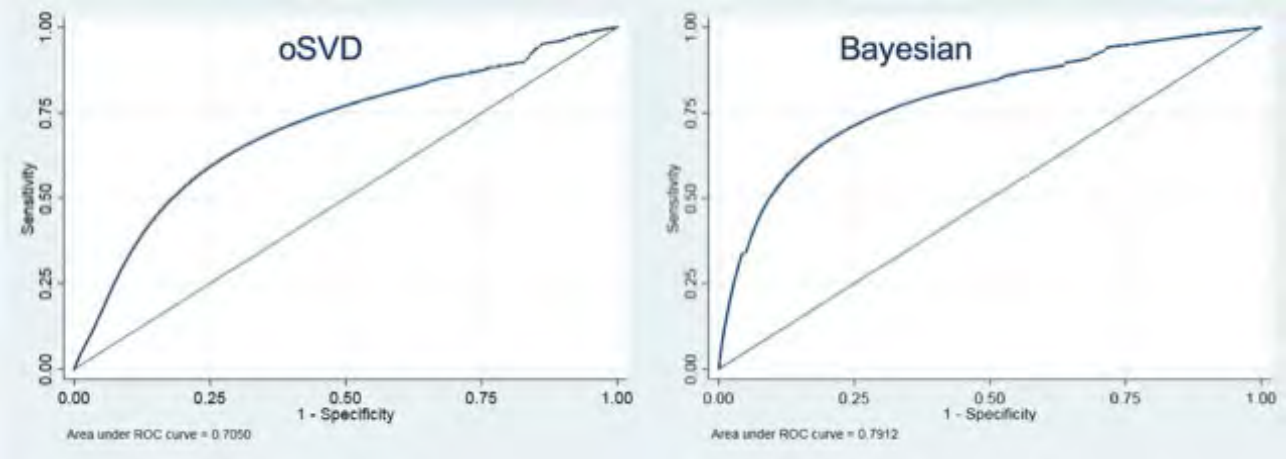

(Filename: TCT_371_Figure1.jpg)

669
Definitive DSM: A Fellow's Experience At A High Volume DSM Center
J Shafa[1]
[1]Cedars Sinai, West Hollywood, CA

Purpose
An analysis of the 150+ DSM I have performed through my initial 4 months of fellowship at Cedars Sinai in an attempt to elucidate any statistically significant patterns between patient demographics such as sex and age, study characteristics including laterality/location/opening pressure, and whether a leak was found or not. Also including follow up on each patient on whom a leak was found, the treatment they underwent, and their most recent status.
Materials and Methods
Analysis of my first 150 DSM cases throughout my first 4 months of fellowship. 113 of these were initial cases while 37 were contralateral cases on previously performed patients.
Results
Average patient age was 51. 73% of suspected CSF leak patients were female, and 27% male. Out of 150 DSMs, leaks were confirmed or highly suspected in 42 cases, for a positivity rate of 28%. The average age of the 42 leaks was also 51, not statistically different from our overall patient population, and was 2:1 female to male, not significantly different from our overall population There was no statistically significant correlation between opening pressure value and whether a leak was found or not. Of the positive cases, 3 underwent paraspinal vein embolization with Onyx, 5 underwent targeted fibrin glue injection, and 30 underwent operative repair Of the negative cases, 12 underwent a subsequent blood patch.
Conclusions
CSF leaks were suspected and seen in females more than males. Against conventional thinking, opening pressure had no statistical correlation to whether a CSF leak was found or not. Previous logic suggested that low opening pressures suggested a CSF leak somewhere along the spinal canal, but our 42 cases had an opening pressure range of 4 cm H20 to 28 cm H20, on opposite sides of the normal 10-25cm H20 range, with an average of 14 cm H20. As for treating CSF leaks, surgical repair, involving a combination laminectomy, foraminotomy, foraminal clipping for fistula ligation, and dural patch repair, tends to produce the best long-term results. Endovascular paraspinal vein Onyx embolization targeted at the levels of suspected CSF-to-venous fistula produce promising results, fibrin glue injection produces good short term results but often needs re-injection, and, when a non-targeted treatment is needed, epidural blood patch produces good short-term improvement as well.

651
Delayed gadolinium leakage into ocular structures on brain MRI
R Olatunji[1], T Lim[1], B Jones[2], A Lin[3], A Bharatha[1], S Suthiphosuwan[1]
[1]St. Michael's Hospital, University of Toronto, Toronto, Ontario, [2]St. Michael's Hospital, Toronto, Ontario, [3]St Michael's Hospital, Toronto, Ontario

Purpose
Gadolinium leakage into ocular structures (GLOS) was recently described as hyperintense signal in anterior and/or vitreous chamber of the globe on FLAIR sequence performed after delayed gadolinium-based contrast agent (GBCA) administration. This phenomenon has been reported in association with various pathologies including strokes, transient ischemic attack, small vessel ischemic disease, and transient global amnesia, However, the true pathomechanism of GLOS remains poorly understood. The aim of this study was to

describe the prevalence of GLOS on the routine brain MRI performed within 7 days after GBCA injection for the initial MRI studies; and to determine the factors that are associated with the presence of GLOS on the brain MRI.

Materials and Methods

We retrospectively reviewed brain MRI of patients who had documented GBCA administration for their initial MRI studies done within the 7 days prior. Relevant clinical, imaging and laboratory data were collected. Descriptive statistics and correlation analysis were performed.

Results

439 patients [242 (55.1%) females, median age: 55 years (range: 18-87 years)] were included for analysis. GLOS was present in 26 patients (5.9%) [14 females (53.8%), median age: 71.5 years (range: 27-84 years]. Among the patients with GLOS, 4 (15.4%) patients had normal brain MRI, 2 (7.7%) had infarctions, and 9 (34.6%) had brain tumors. GLOS was bilateral in 22/26 (84.6%). GLOS involved both anterior and vitreous chambers in 7 (26.9%) patients, only anterior chambers in 1 (3.8%) patient, and only vitreous chambers GLOS in 18 (69.2%) patients. GLOS was present in 3 (11.5%), 7 (26.9%), 7 (26.9%), and 9 (34.6%) patients, who performed brain MRI scan within 24 hours, 24-48 hours, 48-72 hours, and >72 hours after GBCA injection (median: 62 hours, range: 6-161 hours). The presence of GLOS was associated with age (r=0.161, p=0.001), serum creatinine (r=0.179, p <0.0001), time interval since GBCA injection (r=-0.140, p=0.003), and prior cataract surgery (r=0.141, p=0.003).

Conclusions

In our study, GLOS is a rare phenomenon present only in a minority of the patients who had gadolinium administration within 7 days prior. Our study found that GLOS is not limited to stroke as in previous reports and can be depicted in brain MRI that showed various CNS pathologies, including in normal MRI brain. GLOS is associated with older age, higher serum creatinine levels, prior cataract surgery, and shorter interval imaging.

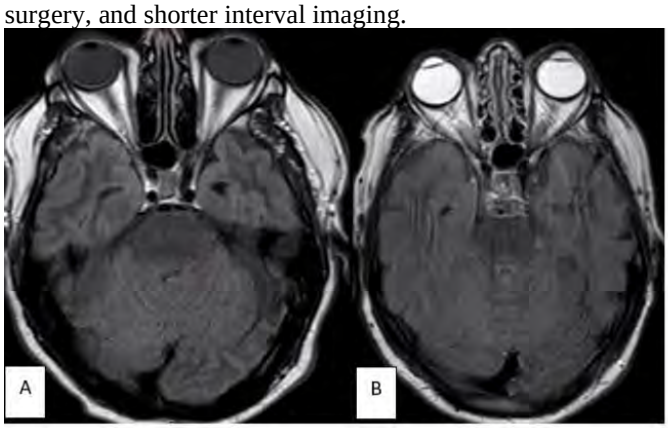

Figure: Positive (A) and strongly positive (B) GLOS on delayed axial FLAIR images acquired 36 hour and 27 hours after last GBCA administration for relapse of lymphoma (patient 1) and multiple myeloma (patient 94) respectively. No brain parenchymal or ocular abnormality was detected. The patient in B had evidence of prior bilateral cataract surgery.

(Filename: TCT_651_Figure.JPG)

1474

Delineating Resting State Brain Networks From Raw Data with Deep Learning

M Cekic[1], N Salamon[2]

[1]University of California, Los Angeles, Los Angeles, CA, [2]University of California Los Angeles, Los Angeles, CA

Purpose

Recent evidence suggests that neuronal connectivity underpinning the resting-state functional MRI signal (rs-fMRI) may extend beyond currently accepted resting state networks determined through functional connectivity (FC) analyses and may entail dynamic changes within existing networks as well as additional networks. We attempt to evaluate this idea with a purely data-driven analysis by applying deep learning algorithms directly to rs-fMRI data, thereby bypassing various assumptions inherent in standard FC analysis.

Materials and Methods

We describe a novel deep learning algorithm for the analysis of multivariate time-series that uses a combination of convolutional, recurrent, and generative methods with attention developed to analyze rs-fMRI signal across multiple spatial and temporal scales. We demonstrate that the network is able to extract information from the data by appropriately classifying a subset of subjects from the ABIDE dataset. We then apply this network to a homogeneous sample of subjects from the Human Connectome Project (HCP) database. After training the network and extracting a latent space, we reverse the process in order to recover the anatomical brain networks that map into the latent space, effectively generating an approximate inverse function.

Results

We are able to recover the major known resting state networks using our model, although with more overlap than expected using standard FC analysis. We also recover several additional networks that appear more diffuse and that may represent either dynamic

existing network interactions or novel areas of connectivity. We also observe some variability in the integrity of the known networks across different timescales, consistent with dynamic network structure.
Conclusions
We present a data-driven analysis of the resting-state fMRI signal using a novel deep learning algorithm that bypasses the assumptions of standard functional connectivity analysis. We show that the algorithm can perform as well as standard functional connectivity on a classification task and is able to recover known networks. We also demonstrate several novel patterns of connectivity that may represent dynamic network interactions or new resting state brain networks.

649

Detection of Calcification in Carotid Atherosclerotic Plaque Using Quantitative Susceptibility Mapping Compared with Conventional Vessel Wall Imaging Techniques

H Ishimaru[1], Y Ikebe[2], M Morikawa[3], R Ideguchi[4], M Uetani[1]
[1]Nagasaki University Hospital, Nagasaki, outside US, [2]Hokkaido University Hospital, Sapporo, Hokkaido, Please select an option below, [3]Nagasaki University Hospital, Nagasaki, Nagasaki, [4]Atomic Bomb Disease Institute, Nagasaki University, Nagasaki, outside US

Purpose
Assessment of the degree of carotid plaque calcification may be useful to predict which plaques will cause cerebrovascular ischemic events. Calcification is usually defined as a hypointense area on all contrast weightings (T1-, T2-, and proton density (PD)-weighted and TOF). However, the optimal MR imaging sequence for detecting calcification has not yet been investigated in detail. We aimed to compare quantitative susceptibility mapping (QSM) that provides a quantitative measure of tissue magnetic susceptibility using gradient-echo phase data and conventional vessel wall MR imaging techniques to determine the optimal sequence for detecting carotid artery calcification.
Materials and Methods
Twenty-two patients who underwent carotid vessel wall MR examination using a 3T system and neck CT were enrolled. Multiecho 3D FLASH was performed using the following parameters: number of TEs, 5; first TE, 4.38 ms; TE spacing, 2.26 ms; TR, 25 ms; flip angle, 11°; FOV, 15 × 15 cm2; acquisition matrix, 320 × 320; section thickness, 0.45 mm; and imaging time, 2 minutes 31 seconds. QSM was calculated from the phase images of the 3D FLASH using STI Suite version 2.2 (STI Suite; https://people.eecs.berkeley.edu/~chunlei.liu/software.html). Four slices of 6-mm sections from the bilateral internal carotid bifurcation were subdivided into 4 segments according to clock position (0-3, 3-6, 6-9, and 9-12) and assessed for calcification. Two blinded radiologists independently reviewed 704 segments and scored the likelihood of calcification using a 5-point scale on T1-, T2-, PD-weighted imaging, FLASH, and QSM. The observer performance for predicting calcification was evaluated by a multireader, multiple-case receiver operating characteristic study. Weighted κ statistics were calculated to assess interobserver agreement with respect to calcification scoring.
Results
QSM had a mean area under the receiver operating characteristic curve of 0.85, which was significantly higher than that of any other sequence ($p < 0.01$) and showed substantial interobserver agreement ($\kappa = 0.68$). When a segment with a score of 3-5 was defined as positive and a segment with a score of 1-2 was defined as negative, the sensitivity and specificity of QSM were 0.75 and 0.87, respectively.
Conclusions
QSM can be the standard sequence for the prediction of plaque calcification in patients without CT.

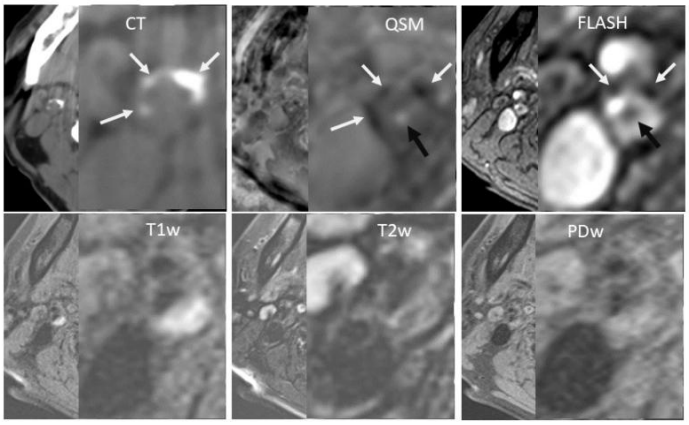

On CT, the 0-3, 6-9, and 9-12 clock segments of the arterial wall have calcification (white arrows). These segments show definite low signals on QSM and FLASH (white arrows). There is another low signal on FLASH that corresponds to the high signal on QSM (black arrow), which may reflect the T2 * shortening effect of some blood products, such as hemosiderin. On T1-, T2-, and PD-weighted imaging, it is difficult to discern a low signal indicating calcification.

(Filename: TCT_649_ASNR.jpg)

1455

Detection of misalignments between multi-contrast brain MR datasets using Deep Learning

Y Li[1], B Duffy[2], K Datta[1]

[1]Subtle Medical, Menlo Park, CA, [2]Subtle Medical Inc., menlo park, CA

Purpose

The quality control (QC) of medical image registration is essential for controlling the failure rates of many downstream clinical applications. To deal with contrast generalizability problem of QC registration, we propose an image synthesis pipeline that can generate perfectly aligned or misaligned image pairs of arbitrary contrast and shapes, for building a deep learning registration QC model with better generalizability.

Materials and Methods

A medical imaging synthesis pipeline was designed based on SynthMorph. This process consists of three parts: generating a label map, synthesizing gray-scale images, and performing deformations. Label maps are generated by random geometrics shapes from noise images. Gray-scale image is synthesized from a label map by drawing the intensities of the labels from a normal distribution. SVF deformation, as well as affine deformation, are included in the pipeline. We call this synthetic dataset "synthmed" dataset. To validate the generalizability and performance of the model on real MRI data, we also included the BRATS dataset for brain MRI in our study. The BRATs dataset contained 1251 T1 and T2 image pairs that were pre-registered with SimpleElastix and then deformed with affine transformation. A deep learning image net based on ResNet34 without pre-training is used in this study. The input of the model was image pairs with two channels, each channel containing an image of different contrast. And the models were trained to predict binary labels of whether movement exists in the input image pair. The proposed model was trained on "synthmed" and evaluated on its corresponding test set, as well as BRATs dataset as an external validation set. A model is also trained and tested on the BRATs dataset. In this work, 2D networks were used, but in real use cases, 3D image alignment is also often considered. So the models are evaluated slice-wise and image-wise, with F1 score, precision, recall, and confusion metrics respectively.

Results

The model results are presented in figure2, with each row to be the dataset that the model is trained on, and column to be the dataset that the model is validated on. Though both models can do very well in the corresponding validation dataset, "synthmed" model can better generalize to BRATs dataset, which indicates better generalizability and broader use cases for "synthmed" model.

Conclusions

In summary, we designed a synthetic image pipeline that enables better generalizability of the image registration QC task.

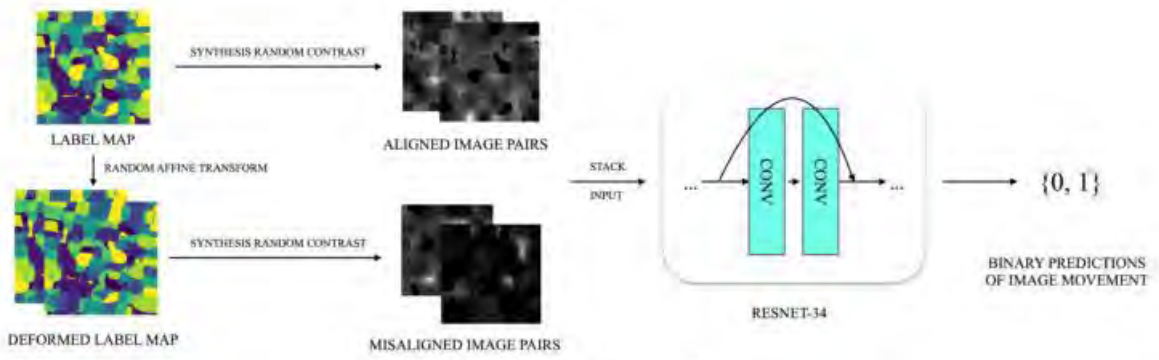

Figure 1. Illustration of model pipeline

Model	brats	synthmed
brats	0.9996	0.4916
synthmed	0.5266	1.0000

Table 1: F1 score of model validation results

Model	brats	synthmed
brats	0.9992	0.4489
synthmed	0.60526	1.000

Table 2: Precision of model validation results

Model	brats	synthmed
brats	1.0000	0.0733
synthmed	0.1533	1.0000

Table 3: Recall of model validation results

Model	brats	synthmed
brats	{TP: 20, TN: 20, FP: 0, FN: 0}	{TP: 19, TN: 0, FP: 20, FN: 1}
synthmed	{TP: 20, TN: 0, FP: 20, FN: 0}	{TP: 20, TN: 20, FP: 0, FN: 0}

Table 4: Confusion matrix of model validation results

Figure 2. Result tables of models. Each row represents a trained model, each column is the validation dataset

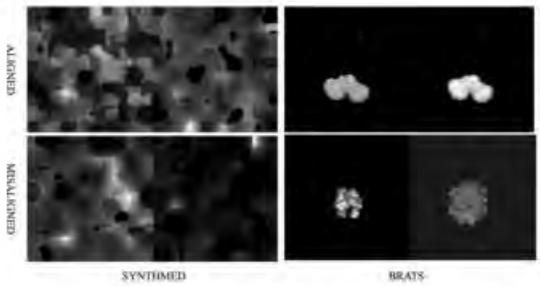

Figure 3. Example of correctly predicted aligned or misaligned image pairs by "synthmed" model in "sythmed" or BRATs dataset.

(Filename: TCT_1455_ASNR.jpg)

1042

Diagnostic Errors in Neuroradiology: Correlation of Attending Neuroradiologist Errors and Shift Volume at a Large Tertiary Academic Medical Center

A Paydar[1], L Hacein-Bey[2], R Assadsangabi[3], V Ivanovic[4]

[1]University of Califronia-Davis, Sacramento, CA, [2]UC Davis, Sacramento, CA, [3]University of California Davis, Sacramento, CA, [4]UC Davis Medical Center, Sacramento, CA

Purpose

Medical errors result in significant mortality and morbidity(1). The purpose of this study is to evaluate association of diagnostic errors in radiological interpretation with daily shift volume among attending neuroradiologists at a single tertiary academic center.

Materials and Methods

The Institution's Neuroradiology Quality Assurance Database of diagnostic errors was searched for attending radiologist misses from 2014 – 2020. We collected the data on the mean number of CT and MRI studies interpreted per shift during the study time-period, shift volume on the days when errors were made, error types (interpretive, perceptual), and their clinical significance (RADPEER 2b, 3b).

Results

During the study period, a total of 283,248 CT and MRI exams were interpreted by our Neuroradiology Section, with a mean volume of 35.24 interpreted studies per shift. A total of 654 studies contained an error, with a mean volume of 46.58 interpreted studies on shifts when error was documented, compared to a mean volume of 34.01 studies on shifts when no error was documented. The results suggest a highly significant difference, $p<0.00001$, with studies containing an error interpreted during higher volume shifts. 82% of errors were perceptual, and 91% clinically significant.

Conclusions

Our data shows that studies containing an error were interpreted during higher volume shifts and majority of errors were clinically significant.

525

Diagnostic Performance of a High-spatial-resolution Template of Neuromelanin-sensitive Imaging in Early-stage Idiopathic Parkinson's Disease

E Kim[1], Y Kim[1], M Seong[1]

[1]Samsung Medical Center, Seoul, Korea, Republic of

Purpose

It is desirable to test diagnostic performance for idiopathic Parkinson's disease (IPD) with neuromelanin-sensitive MRI (NM-MRI) by measuring contrast ratios (CRs) based on a high-spatial-resolution NM-MRI template instead of measuring volume or contrast ratios of the substantia nigra pars compacta (SNpc) by semiautomated segmentation or manual drawing of regions of interest because a voxel-wise analysis based on a template has higher reliability. However, such a study has yet to be reported. We aimed to assess the diagnostic performance of the CRs between early-stage IPD patients and healthy controls (HCs) using a high-spatial-resolution NM-MRI template.

Materials and Methods

We retrospectively enrolled early-stage IPD patients (n = 50) and HCs (n = 50) who underwent both 0.8-mm isovoxel NM-MRI and dopamine-transporter PET. The PET served as the reference of standard. A template-based voxel-wise analysis revealed two regions in nigrosomes 1 and 2 (N1 and N2, respectively), with significant differences in each SNpc between IPD and HCs. The mean CR values of N1, N2, volume-weighted mean of N1 and N2 (N1+N2), and whole SNpc on each side were compared between IPD and HC using the independent t-test or the Mann-Whitney U test. The diagnostic performance was compared in each region using receiver operating characteristic curves.

Results

The mean CR values in the right N1 (0.149459 vs 0.194505), left N1 (0.133328 vs 0.169160), right N2 (0.230245 vs 0.278181), left N2 (0.235784 vs 0.314169), right N1+N2 (0.155322 vs 0.278143), left N1+N2 (0.140991 vs 0.276755), right whole SNpc (0.131397 vs 0.141422), and left whole SNpc (0.127099 vs 0.137873) significantly differed between IPD patients and HCs (all $P < 0.0001$). The areas under the curve of the left N1+N2, right N1+N2, left N1, right N1, left N2, right N2, left whole SNpc, and right whole SNpc were 0.994 (sensitivity, 98.0%; specificity, 94.0%), 0.985, 0.804, 0.802, 0.777, 0.766, 0.632, and 0.606, respectively.

Conclusions

Our NM-MRI template-based CR measurements revealed significant differences between early-stage IPD patients and HCs. The CR values of the left N1+N2 demonstrated the highest diagnostic performance.

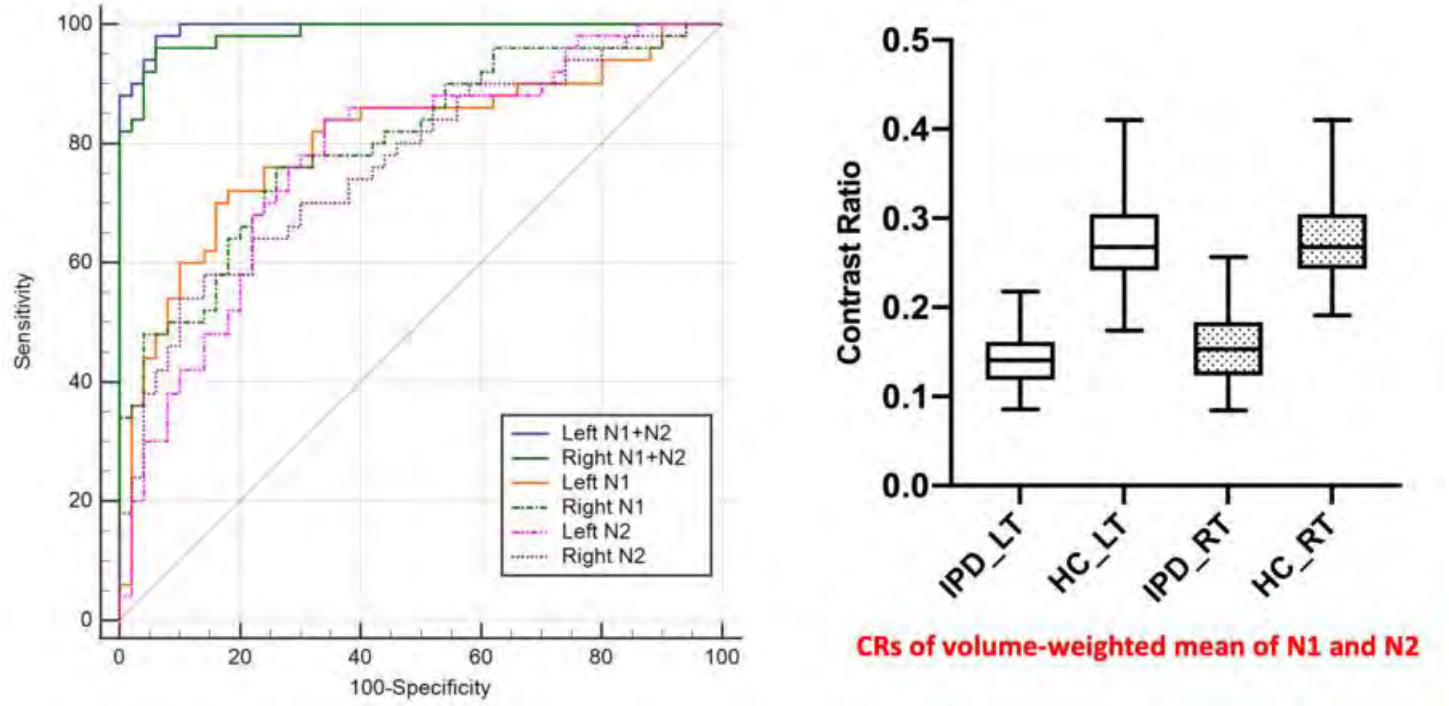

(Filename: TCT_525_Figure.jpg)

1523

Differences in Clinical Presentation and Imaging Findings of Spontaneous Intracranial Hypotension due to Spinal Dural Tears versus CSF-Venous Fistulas

S Teixeira[1], A Chang[1], V SHAH[2], W Dillon[1]

[1]University of California, San Francisco, San Francisco, CA, [2]UCSF, San Francisco, CA

Purpose

To differentiate between clinical presentation and imaging findings of spontaneous intracranial hypotension due to spinal dural tears versus CSF-venous fistulas (CVFs).

Materials and Methods

Retrospective review of CT myelogram-confirmed CSF-leaks due to dural tears vs CVFs (n=44) in patients of any age, between August 2011 and 2021, performed at the University of California, San Francisco.

Results

All CVFs were diagnosed in the thoracic spine, predominantly at T9-T12 (64.3%). Spinal dural tears occurred throughout the spine (p=0.007), but also more frequently in the lower thoracic spine (42.3%), followed by the upper thoracic spine (34.6%). CVFs occurred more frequently on the right (71.4%), while dural tears were ventral midline (33.3%) or paramedian (46.7%) in location. There was no statistically significant difference in CSF-opening pressures between the groups. Headache was the most common symptom among all patients (79.5%). In the dural tear group, they were predominantly positional (91%), while in the CVF group, there was a greater percentage of exertional headaches (50%) [p=0.016]. A variety of other neurological symptoms were present in both groups, including weakness (20%), confusion (15%), and vision changes (10%). In less than 10% of the cases, photo/phonophobia, tremors, numbness, gait impairment, tinnitus, and back pain were also reported. Aside from headache subtype, no other difference in clinical presentation was statistically significant. Brain MRI findings in both groups included distended dural venous sinuses (72%), dural enhancement (70.4%), enlarged pituitary gland (68%), tonsillar descent (61%), midbrain sag (59%), subdural collections (36%), calvarial hyperostosis (20%), and superficial siderosis (9%). Brain imaging findings difference were not statistically different. Spine MRI showed extradural collections in all cases of spinal dural tears, which were primarily ventral in location. By contradistinction, none of the cases of CVFs had spinal extradural collections on MRI (p=0.006).

Conclusions

Confirmed CVFs occurred more frequently on the right in the lower thoracic spine and were often associated with exertional headaches. Spinal dural tears occurred throughout the spine, in ventral locations, and associated with positional headaches. Most common brain MRI findings included distended dural venous sinuses, dural enhancement, and enlarged pituitary gland, although not statistically different. Spinal extradural collections were only seen in cases of dural tears.

	Dural Tear	CSF Venous Fistula	
	n=30 (68.2%)	n=14 (31.8%)	p-value
Age	46 ± 20	59 ± 9	0.004
Sex (% Female)	21 (70%)	7 (50%)	0.313
Opening pressure	9 (4-12)	9 (7-12)	0.511
Radiographic Findings			
Meningeal Enhancement	20 (66.7%)	11 (78.6%)	0.87
Midbrain Sag	17 (56.7%)	9 (64.3%)	0.444
Pituitary Prominence	19 (63.3%)	11 (78.6%)	0.257
Tonsilar Descent	17 (56.7%)	10 (71.4%)	0.275
Sinus Engorgement	21 (70%)	11 (78.6%)	0.417
Superficial Siderosis	3 (10%)	1 (7.1%)	0.621
Calvarial Hyperostosis	5 (16.7%)	4 (28.6%)	0.298
Subdural Collections	10 (33.3%)	6 (42.9%)	0.541
Extradural Collection w/o spur	14 (46.7%)	0 (0%)	0.006
Vertebral Body Level			0.007
Cervical	1 (3.8%)	0 (0%)	0.65
Upper Thoracic (T1-T4)	9 (34.6%)	0 (0%)	0.011
Mid Thoracic (T5-T8)	3 (11.5%)	5 (35.7%)	0.082
Lower Thoracic (T9-T12)	11 (42.3%)	9 (64.3%)	0.185
Lumbosacral	5 (19.2%)	0 (0%)	0.1
Laterality			0.001
Left	5 (16.7%)	4 (28.6%)	
Right	6 (20%)	10 (71.4%)	
Ventral	10 (33.3%)	0 (0%)	
Clinical Presentation			
Headache Type			0.016
None	3 (12%)	1 (7.1%)	
Positional	20 (80%)	6 (42.9%)	
Exertional	2 (8%)	6 (42.9%)	
Undifferentiated	0 (0%)	1 (7.1%)	
Gait	0 (0%)	3 (21.4%)	0.04
Confusion	3 (12%)	4 (28.6%)	0.194
Vertigo	1 (4%)	2 (14.3%)	0.289
Weakness	4 (16%)	5 (35.7%)	0.157
Tremor	1 (4%)	1 (7.1%)	0.595
Numbness	1 (4%)	1 (7.1%)	0.595
Backpain	1 (4%)	0 (0%)	0.641
Tinnitus	0 (0%)	1 (7.1%)	0.359
Vision changes	3 (12%)	1 (7.1%)	0.545
Photophobia/Phonophobia	3 (12%)	0 (0%)	0.252

(Filename: TCT_1523_Table_ASNR.jpg)

271

Differences in Diffusion Tensor Imaging White Matter Integrity Related to Verbal Fluency Between Young and Old Adults

B Yeske[1], J Hou[2], N Adluru[3], V Nair[3], V Prabhakaran[3]

[1]University of Wisconsin School of Medicine and Public Health, Madison, WI, [2]Center for Cross-Straits Cultural Development, Fujian Normal University, Fuzhou City, Fujian Province, China, [3]Department of Radiology, School of Medicine & Public Health, University of Wisconsin-Madison, Madison, WI

Purpose

Throughout adulthood the brain undergoes an array of structural and functional changes during the typical aging process (Caserta et al., 2009). These changes involve decreased brain volume, reduced synaptic density, and alterations in white matter structure (Resnick et al., 2003). While there have been some previous neuroimaging studies that have measured adult language production ability and its correlations to brain function (Pihlajamäki et al., 2000), structural gray matter volume (Zhang et al., 2013), and functional differences across young and old adults (Meinzer et al., 2009), the structural role of white matter in adult language production in individuals across the lifespan remains to be thoroughly elucidated.

Materials and Methods
The present study recruited 38 young adults and 35 old adults for diffusion tensor imaging (DTI) and to perform the Controlled Oral Word Association Test to assess verbal fluency (VF). Tract-Based Spatial Statistics were employed to evaluate voxel-based group differences of diffusion metrics for the values of fractional anisotropy (FA), mean diffusivity (MD), axial diffusivity (AD), radial diffusivity (RD) and Local Diffusion Homogeneity (LDH) in 12 white matter regions of interest associated with language production. To investigate group differences on each DTI metric an ANCOVA controlling for sex and education level was performed, and the statistical threshold was considered $p < 0.00083$ (0.05/60 labels) after Bonferroni correction for multiple comparisons. Significant DTI metrics identified in the ANCOVA were used to perform correlation analyses with VF scores.
Results
Compared to the old adults, the young adults had significantly: (1) increased FA values on the anterior corona radiata (ACR) bilaterally; (2) decreased MD values on the right ACR, but increased MD on the left uncinate fasciculus (UF); (3) decreased RD on the ACR bilaterally. There were no significant differences between groups for AD or LDH. Moreover, the old adults had only a significant correlation between the VF score and the MD on the left UF. There were no significant correlations between VF score and DTI metrics in young adults.
Conclusions
This study adds to the growing body of research that white matter areas involved in language production are sensitive to aging.

577

Differences in the Alzheimer Structural Connectome by Amyloid and Tau Imaging Biomarker Status

J Prescott[1], L Walden[1]
[1]*MetroHealth Medical Center / Case Western Reserve University, Cleveland, OH*

Purpose
The current work analyzes differences in the structural connectome between different amyloid/tau biomarker groups, using diffusion tensor MRI and PET imaging, respectively, with the intent of identifying further biomarkers of disease that may aid in earlier characterization of Alzheimer's disease.
Materials and Methods
Baseline data from the Alzheimer Disease Neuroimaging Initiative Phase 3 were used. T1 brain scans were segmented into 68 cortical regions of interest using FreeSurfer. DTI images were aligned to the T1 images and structural connectome matrices were calculated using DSI Studio. Connectivity metrics calculated included: degree, strength, clustering coefficient (binary and weighted), local efficiency (binary and weighted), betweenness centrality (binary and weighted), eigenvector centrality (binary and weighted), pagerank centrality (binary and weighted), and eccentricity (binary and weighted). Summary measures of amyloid and tau burden calculated from PET images and provided by ADNI were used to calculate amyloid status (positive or negative) and tau status (positive or negative). ANOVA was performed to analyze for differences in connectivity metrics between each combined amyloid/tau status group (e.g., A-/T-, A-/T+, A+/T-, A+/T+). This was an exploratory study and no adjustment for multiple comparisons was made.
Results
290 subjects from ADNI 3 were analyzed – 176 normal cognition (74 male, 102 female), 91 mild cognitive impairment (48 male, 43 female), 23 AD (13 male, 10 female). Pagerank centrality (both binary and weighted), a measure of the "importance" of a node base on the number of its connections to other "important" nodes, had the most significant differences between amyloid/tau status groups, particularly in the medial temporal lobes, with T+ subjects having a significant decrease in the metric compared to T- subjects regardless of amyloid status (Table 1, Image 1).
Conclusions
This exploratory study demonstrated that there were significant differences between amyloid/tau status groups along the AD spectrum, with the largest number of differences involving the medial temporal lobes. Further work is necessary to evaluate the utility of these differences in characterizing or predicting AD status in individual patients. In particular, further work involving more advanced statistical analysis, increased patient numbers, and longitudinal data is ongoing.

Metric	Cortical Region	p-value
Degree	Left: Entorhinal	0.005
Degree	Left: Parsorbitalis	0.05
Degree	Left: Transverse Temporal	0.09
Degree	Right: Entorhinal	0.01
Strength	Left: Entorhinal	0.03
Strength	Right: Lingual	0.05
Strength	Right: Isthmus Cingulate	0.05
Clustering Coefficient (Binary)	Left: Inferior Parietal	0.02
Clustering Coefficient (Binary)	Left: Paracentral	0.03
Clustering Coefficient (Binary)	Right: Parahippocampal	0.01
Clustering Coefficient (Weighted)	Left: Precuneus	0.01
Local Efficiency (Binary)	Left: Inferior Parietal	0.02
Local Efficiency (Binary)	Right: Parahippocampal	0.03
Local Efficiency (Weighted)	Left: Precuneus	0.005
Local Efficiency (Weighted)	Right: Bankssts	0.05
Local Efficiency (Weighted)	Right: Lingual	0.04
Local Efficiency (Weighted)	Right: Insula	0.03
Betweenness Centrality (Binary)	Left: Inferior Parietal	0.04
Betweenness Centrality (Weighted)	Left: Medial Orbitofrontal	0.03
Eigenvector (Binary)	Left: Entorhinal	0.006
Eigenvector (Binary)	Left: Parsorbitalis	0.005
Pagerank Centrality (Binary)	Left: Entorhinal	0.01
Pagerank Centrality (Binary)	Left: Lingual	0.05
Pagerank Centrality (Binary)	Left: Parsorbitalis	0.04
Pagerank Centrality (Binary)	Right: Entorhinal	0.03
Pagerank Centrality (Binary)	Right: Parahippocampal	0.02
Pagerank Centrality (Weighted)	Left: Entorhinal	0.03
Pagerank Centrality (Weighted)	Left: Isthmus Cingulate	0.02
Pagerank Centrality (Weighted)	Right: Inferior Parietal	0.04
Pagerank Centrality (Weighted)	Right: Isthmus Cingulate	0.009
Pagerank Centrality (Weighted)	Right: Parahippocampal	0.007
Eccentricity (Binary)	Left: Caudal Middle Frontal	0.04

Table 1. Results of ANOVA analysis of structural connectivity metric differences between amyloid/tau status groups. Only significant associations are shown ($p < 0.05$)

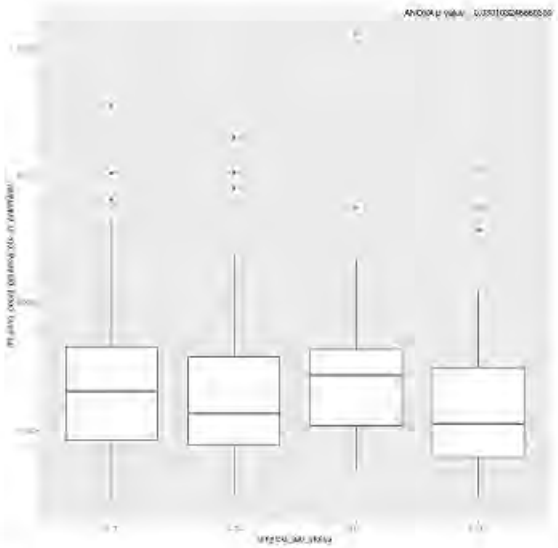

Figure 1. Boxplot of pagerank centrality in the left entorhinal cortex (p-value = 0.03). Note the means of the tau positive groups are less than that of the tau negative groups, in universe regardless of the amyloid status.

(Filename: TCT_577_tableandimage.jpg)

375

Differential Subsampling with Cartesian Ordering (DISCO)-MRA for Classifying Residual Treated Aneurysms – An Update

P Shahrouki[1], R Gupta[2], P Belani[3], A Chen[1], A Doshi[4], R De Leacy[5], J Fifi[6], J Mocco[6], K Nael[1]

[1]UCLA, Los Angeles, CA, [2]Icahn School of Medicine at the Mount Sinai Hospital, New York, NY, [3]Mount Sinai Hospital, new york, NY, [4]Mount Sinai Hospital, New York, NY, [5]Mount Sinai Health System, New York, NY, [6]Icahn School of medicine at Mount Sinai, New York, NY

Purpose

Using Differential Subsampling with Cartesian Ordering (DISCO), an ultrafast high-spatial resolution head MRA has been introduced. We aimed to determine the diagnostic performance of DISCO-MRA in grading residual aneurysm in comparison to TOF-MRA in patients with treated intracranial aneurysm (IA).

Materials and Methods
Patients with IA who were treated by endovascular treatment, and had DISCO-MRA, TOF-MRA and follow-up DSA were included for review. The voxel size and acquisition time were 0.75 x 0.75 x 1 mm3/6 seconds for DISCO-MRA and 0.6 x 0.6 x 1 mm3/6 minutes for TOF-MRA. Residual aneurysm was determined using the Modified Raymond–Roy Classification. TOF-MRA and DISCO-MRA were reviewed independently by two neuroradiologists for residual aneurysm grading, and compared against DSA as the reference of standard. Statistical analysis was performed using Kappa (k) statistic and the Chi-squared ($\chi 2$) test.
Results
Sixty-eight treated IAs were included. The intermodality agreement was k = 0.82, 95% CI 0.67 – 0.97 between DISCO and DSA and 0.44, 95% CI 0.28 – 0.61 between TOF and DSA. Modified Raymond-Roy Classification grading scores matched DSA scores in 60/68 cases (88%), $\chi 2 = 144.4$, $p < 0.001$, for DISCO and 46/68 cases (68%), $\chi 2 = 65.0$, $p < 0.001$, for TOF. The diagnostic accuracy for detection of aneurysm remnant was higher for DISCO (0.96, 95% CI 0.88 – 0.99; Table 1) than TOF (0.79, 95% CI 0.68 – 0.88; Table 1).
Conclusions
In patients with endovascularly treated IAs, DISCO-MRA provides superior diagnostic performance in comparison to TOF-MRA in delineating residual aneurysm, in a fraction of the time.

Modality	Sensitivity	Specificity	PPV	NPV	Accuracy
DISCO-MRA	0.94 (0.81-0.99)	0.97 (0.84-1.00)	0.97 (0.83-1.00)	0.94 (0.81-0.98)	0.96 (0.88-0.99)
TOF-MRA	0.63 (0.45-0.79)	0.97 (0.84-1.00)	0.96 (0.76-1.00)	0.71 (0.61-0.79)	0.79 (0.68-0.88)

(Filename: TCT_375_Table1.jpg)

1434
Differentiation Between PCNSL and Metastasis Presenting as Solid Enhancing Mass in the Cerebellum: Diagnostic Values of the Serrate Sign Using Contract Enhanced MRI
B Baek[1]
[1]*Chonnam National University Medical School, Gwangju, Korea, Republic of*

Purpose
Preoperative differentiation between primary central nervous system lymphoma (PCNSL) and metastasis may be difficult in patient with solid enhancing mass in the cerebellum. We hypothesized that unique anatomical architecture of the cerebellum characterized by compact foliation and soft, infiltrative nature of PCNSL might affect on morphologic feature of the 2 cerebellar tumors. This study aimed to investigate radiologic features for differentiating cerebellar PCNSL from metastasis by analyzing postcontrast MRI.
Materials and Methods
This retrospective study included pathologically proven 20 patients with PCNSL and 24 with metastasis in the cerebellum presenting with solid enhancing mass who underwent preoperative brain MRI. The following imaging features were assessed using contrast enhanced T1-weighted imaging: location, size, enhancement pattern, cerebellar surface involvement, and the serrate sign. The serrate sign was defined as the tumor demarcated by the gray-white matter interface with bracken-like branching pattern or outward spikes on any orthogonal planes. Diagnostic values of the serrate sign including sensitivity, specificity, positive predictive value, negative predictive value, and accuracy for predicting PCNSL were calculated.
Results
The serrate sign was identified only in the PCNSL group (75.0% vs. 0%, P<0.001). Homogenous enhancement was more frequently found in the PCNSL group than in the metastasis group (90% vs. 8%, P<0.001), whereas cerebellum surface involvement was more frequently seen in the metastasis group than in the PCNSL group (75% vs. 25%, P=0.001). In prediction of PCNSL, the serrate sign showed 75.0% sensitivity, 100% specificity, 100% positive predictive value, 82.8% negative predictive value, and 88.6% accuracy. Of the 20 patients with PCNSL, the serrate sign was more commonly observed on sagittal (73.7%, 14/19) than coronal (47.4%, 9/19) and axial (35%, 7/20) images.
Conclusions
We found that the serrate sign, homogenous enhancement, and no surface involvement were useful features for differentiating cerebellar PCNSL from solid enhancing metastasis. The serrate sign may have diagnostic implications for PCNSL in the cerebellum. In addition, thin section thickness and sagittal plane of post-Gd T1WI would be warranted for identification of the serrate sign.

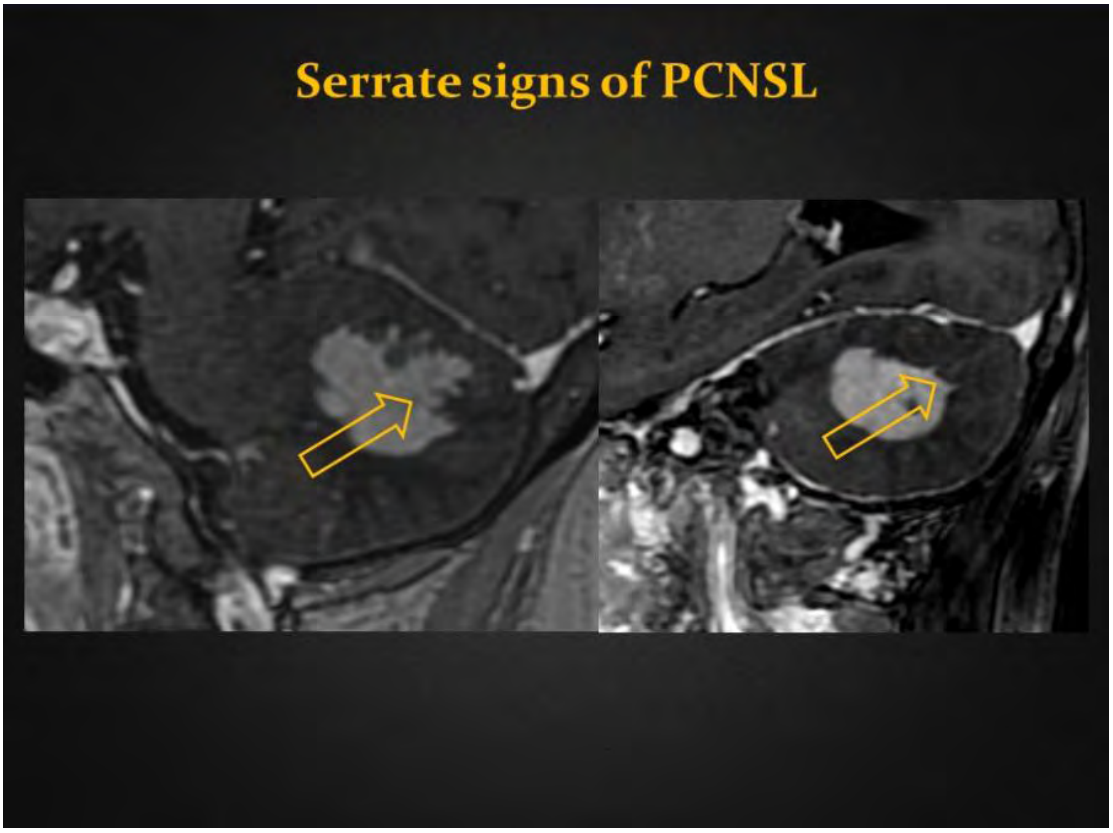

(Filename: TCT_1434_serratesign.jpg)

1180

DKI Provide Improved Sensitivity over DTI for Identification of Brain Microstructural alterations in HIV Clade-C Infection

S VYAS[1], T Salan[2], P Singh[1], V Govind[2]

[1]Postgraduate Institute of Medical Education and Research (PGIMER), Chandigarh, India, [2]University of Miami, Miami, FL

Purpose

While several studies have demonstrated that DTI metrics are reliable biomarkers of HIV-associated microstructural brain damage, few used DTI for assessing HIV clade-C [1,2]. Moreover, some have reported inconsistent DTI results in HIV infection [3]. So, the aim of this study is to investigate HIV clade-C associated abnormalities in the brain using DTI and diffusion kurtosis imaging (DKI) metrics.

Materials and Methods

Whole-brain MRI Data were collected on a 3T Siemens scanner from 107 cART-naïve HIV Clade-C subjects and 110 age-gender matched controls. MRI protocol included: T1 MPRAGE, DW-images (b = 1000/2000 s/mm2) with 30 directions per shell, and 2 b=0 images. Tensor fitting on the DW-images obtains DTI/DKI metrics: fractional anisotropy (FA), mean-, axial-, and radial-diffusivities (MD, AD, RD), kurtosis FA (kFA), mean-, axial-, and radial-kurtoses (MK, AK, RK). Metrics were evaluated at 14 HIV-relevant ROIs (Figure 1) to find significant between-group mean differences ($p<0.05$ Bonferroni corrected), effect size , and correlations with blood-based markers (CD4, HIV Viral Load).

Results

Our results indicate that MD and kFA are the strongest descriptors of HIV-related tissue damage in the brain. Significant between-group differences were observed in both white matter (WM) and grey matter (GM) structures, notably the basal ganglia. This study also demonstrates that DTI metrics alone, particularly FA as a measure of WM integrity, cannot always provide a full description of HIV-related microstructural abnormalities. While this may be due to the lower neurovirulence of HIV clade-C or to the variability in duration of infection, DKI metrics show relatively more sensitive measures for evaluating microstructural damages due to HIV.

Conclusions

Our results indicate that MD and kFA are the strongest descriptors of HIV-related tissue damage in the brain. Significant between-group differences were observed in both white matter (WM) and grey matter (GM) structures, notably the basal ganglia. This study also demonstrates that DTI metrics alone, particularly FA as a measure of WM integrity, cannot always provide a full description of HIV-related microstructural abnormalities. While this may be due to the lower neurovirulence of HIV clade-C or to the variability in duration of infection, DKI metrics show relatively more sensitive measures for evaluating microstructural damages due to HIV.

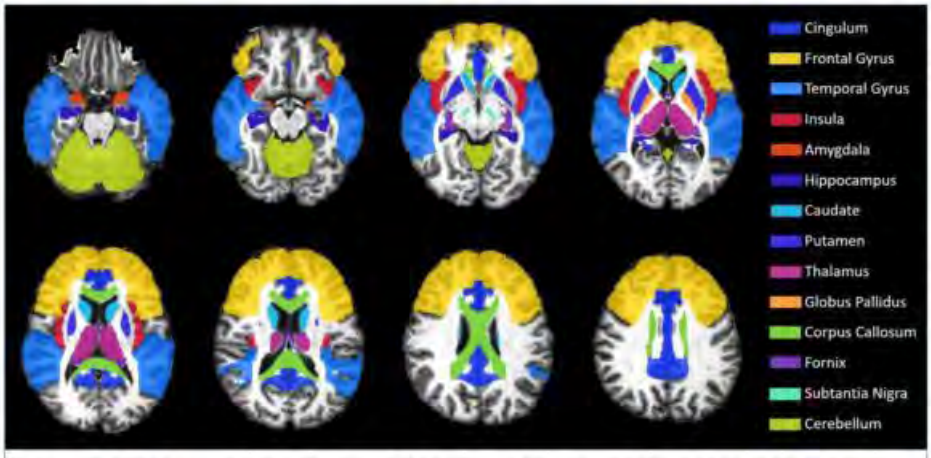

Figure 1: Axial T1 images show the location of 14 HIV relevant ROIs obtained from the JHU-MNI-SS-type2 atlas

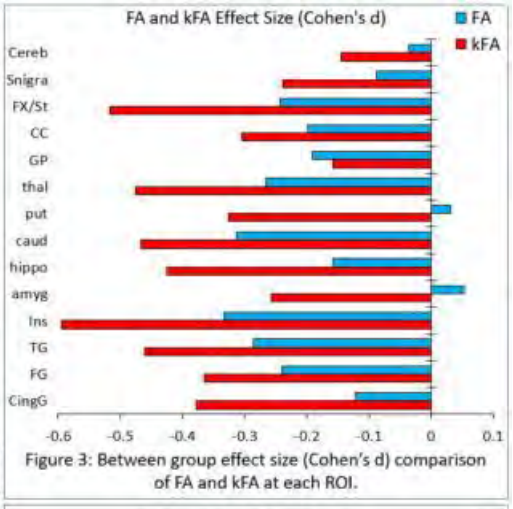

Figure 3: Between group effect size (Cohen's d) comparison of FA and kFA at each ROI.

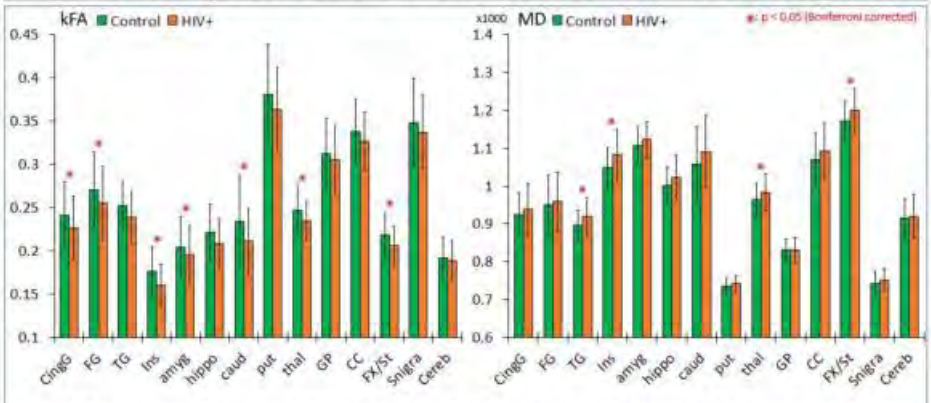

Figure 2: Bar plots comparing mean kFA, and MD values for the control and HIV groups at the 14 analyzed ROIs. Error bars represent the standard deviation. Red asterisks indicate regions with significant between-group differences.

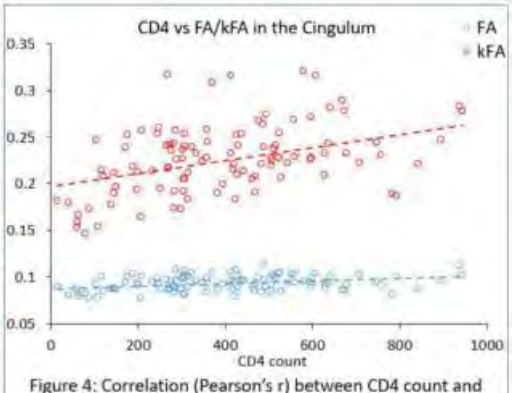

Figure 4: Correlation (Pearson's r) between CD4 count and FA/kFA measures. Moderate correlation is noted between kFA and CD4 (r = 0.441) while FA had no correlations.

(Filename: TCT_1180_DTI_DKI_Figure.jpg)

538

Duplication of the Pituitary Gland: CT, MRI and DTI Findings

B Serrallach[1], R Rauch[1], S Lyons[1], T Huisman[1]

[1]Texas Children's Hospital and Baylor College of Medicine, Houston, TX

Purpose

Duplication of the pituitary gland (DPG) is an extremely rare malformation (1-5). DPG is associated with a broad variety of midline and central nervous system malformations (DPG-plus syndrome), (1,2,5). The most frequently reported additional findings are hypertelorism, cleft palate, hypothalamic mass/(pseudo-)hamartoma, duplicated/broad sella, agenesis of the corpus callosum, cleft/fusion of vertebral bodies, cleft basisphenoid bone, duplication of the optic chiasm, oropharyngeal teratomas, duplication of the basilar artery and aberrant circle of Willis (5). The purpose is to present the imaging characteristics including an evaluation of the brainstem fiber architecture by DTI in a patient with DPG and a complex of associated midline malformations. The embryological pathogenesis is discussed.

Materials and Methods

N/A

Results

We present the CT, MRI and DTI findings (Figure 1-4) of a rare case of DPG with associated tuberomammillary fusion, oropharyngeal teratoma, cleft palate, hypertelorism, duplicated/broad sella, duplication/low bifurcation of the basilar artery, and craniovertebral midline anomalies. Qualitative DTI interpretation revealed normal white matter organization of the brain, in particular, there was a normal configuration of the major white matter bundles within the mesencephalon and brainstem. Traditional embryological studies postulated that the pituitary gland forms by a fusion of the craniopharyngeal evagination and the neuroectodermal evagination (1). There is however growing evidence that the pituitary gland develops as a single structure (1). It is believed that the close topographical relationship between the prechordal plate, the notochordal plate, the hypophyseal primordium and the oropharyngeal membrane during early embryogenesis gives rise to the development of the pituitary gland (1). The duplication of the prechordal plate and the rostral end of the notochordal plate is believed to lead to a duplication of the pituitary primordium and results in two morphologically normal glands (1). The time of induction of the teratogenic influence and the extent of the prechordal/notochordal plate abnormalities are thought to be the reason for the wide spectrum of associated midline abnormalities (1).

Conclusions
We report a rare case of DPG-plus syndrome. Qualitative DTI interpretation yielded normal white matter organization of the brain. Further research focused on advanced MR imaging findings could possibly give more insight in the understanding of this rare syndrome.

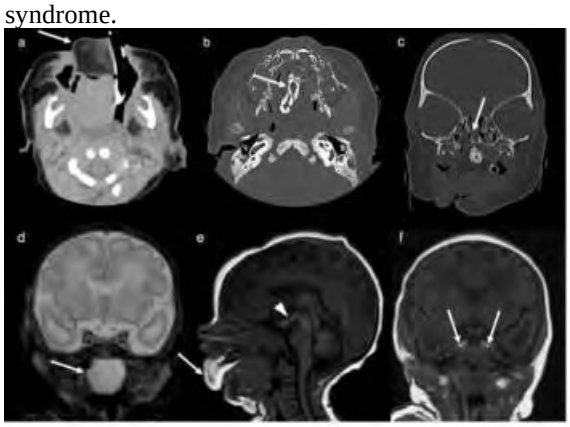

Figure 1

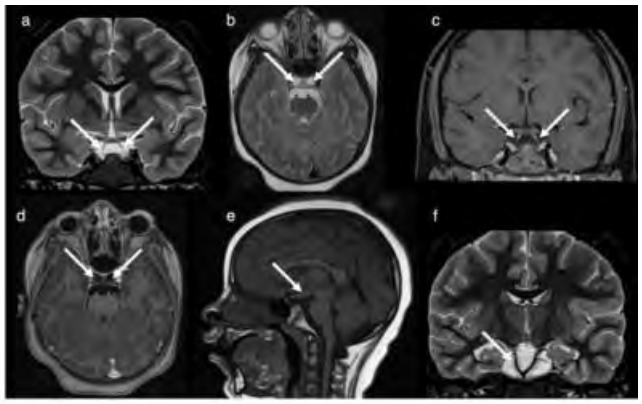

Figure 2

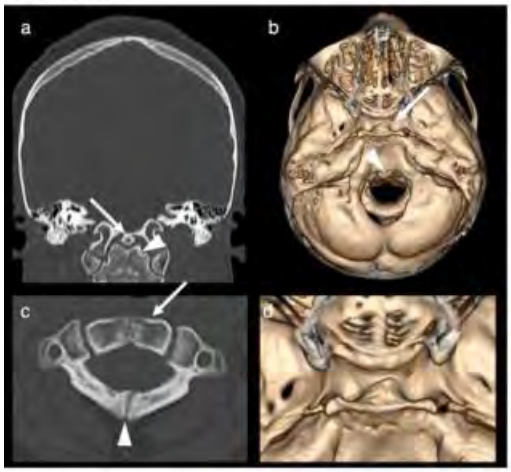

Figure 3

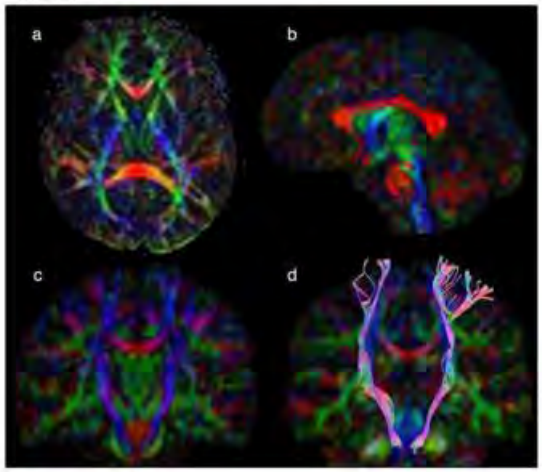

Figure 4

(Filename: TCT_538_abstract-dpg-asnr_300.jpg)

482

Duplication of the Vertebral Arteries. What is the Incidence and is it Clinically Significant?

C DesRoche[1], D Tampieri[2], B Kwan[1], I Silver[1], J Ortiz Jimenez[1], O Islam[1]
[1]Queen's University, Kingston, Ontario, [2]Queen's University KHSC, Kingston, Ontario

Purpose
Duplication of the vertebral artery (VA) is a rare vascular variant. Less than 50 cases have been reported in the literature1-3. VA duplication is usually detected as an incidental finding4. It is undetermined if VA duplication is associated with vascular pathologies such as VA dissection, intracranial aneurysm, and arteriovenous malformation (AVM)1,5. This study aims to determine the incidence of VA duplication at our center and discuss the radiological implications and clinical significance of this vascular variant.
Materials and Methods
The radiology reports of all CT head and neck imaging studies performed between 2015 and 2021 at a single tertiary academic medical center were retrospectively reviewed for VA duplication, using keyword search on radiology reports. Imaging was reviewed by neuroradiologists and only cases of confirmed VA duplication were included. VA duplication was defined as a condition in which the VA has dual origins and a variable level of fusion in the neck. Patient age, gender, clinical presentation, and imaging features were recorded.
Results
Of 62,570 CT Head and Neck imaging studies performed, VA duplication was identified in 14 patients (4 females, 10 males; age 25–88 years, with a mean age of 59 years) representing a prevalence of 0.02%. 10 patients had a right dual origin of the VA and 4 patients had a left dual origin of the VA (Table 1). In all 4 patients with a left dual origin, the limbs of the VA originated from the left subclavian artery and the aortic arch. In 9 patients with a right dual origin, both limbs of the VA originated from the right subclavian artery. In 1 patient with a right dual origin, one VA limb originated from the deep cervical artery. The level of fusion varied from C4-C6 for both right and left duplications, with fusion at C4 being the most common, observed in 5 patients. Additional vascular

anomalies were observed in 2 of the 14 patients (14.29%). These included an anterior communicating aneurysm and an AVM. The clinical presentation and imaging features of each patient are given in Table 1.
Conclusions
Duplication of the vertebral artery is a rare and normally incidental finding; however, it is likely underrepresented in the literature. Although significant vascular pathologies were observed in 14% of the cases, future studies are required to determine if there is an association between duplicated vertebral artery and the presence of additional vascular pathologies such as intracranial aneurysms or AVMs.

1242

Early Post-thrombectomy Contrast Extravasation on Dual-Energy CT Is Predictive of Stroke Outcomes and Complications: a Ten-Year Single-Centre Experience.

F Pinckaers[1], M Mentink[1], W van Zwam[1], H Boogaarts[2], R van Oostenbrugge[1], A Postma[1]
[1]Maastricht University Medical Center+, Maastricht, Netherlands, [2]Radboud University Medical Center, Nijmegen, Netherlands

Purpose
To determine the relevance of early post-thrombectomy contrast extravasation on dual-energy CT (DECT) in the prediction of stroke outcomes and complications.
Materials and Methods
630 patients underwent DECT within 3 hours post-thrombectomy between January 2010 and December 2019. 382 patients met our inclusion criteria after excluding 73 patients with postprocedural haemorrhage. Two readers scored hyperdense areas on DECT iodine overlay maps (IOM) in consensus according to the 10 regions of the ASPECTS, thus forming a contrast extravasation ASPECTS. Maximum parenchymal iodine concentration and maximum iodine concentration relative to the superior sagittal sinus were recorded. Follow-up imaging performed until discharge was reviewed for intracerebral haemorrhage (ICH) development. Clinical baseline and follow-up data were gathered from prospectively kept stroke records.
Results
Contrast extravasation was found in 303 patients (79%). 30/382 patients (8%) developed ICH on follow-up CT, of which 27 developed within regions of previous contrast extravasation. 16 ICHs were symptomatic. Stroke progression occurred in 60/382 patients (16%). Multivariate regression showed a statistically significant association between decreasing contrast extravasation ASPECTS and the NIHSS at 24-48 hours (adjusted (a)β: 0.60, 95% CI: 0.32 to 0.89), mRS at 90 days (acOR: 1.10, 95% CI: 1.02 to 1.12; Figure 1), mortality at 90 days (aOR: 1.15, 95% CI: 1.04 to 1.27), stroke progression (aOR: 1.15, 95% CI: 1.01 to 1.27), and ICH (aOR: 1.15, 95% CI: 1.01 to 1.35), but not with symptomatic ICH (aOR 1.19, 95% CI: 0.98 to 1.45). Iodine concentration was significantly associated with the NIHSS at 24-48 hours (aβ: 0.61, 95% CI: 0.22 to 1.01), mRS at 90 days (acOR: 1.19, 95% CI:1.07 to 1.33), mortality at 90 days (aOR: 1.18, 95% CI: 1.03 to 1.34), ICH (aOR: 1.46, 95% CI: 1.01 to 2.11), and symptomatic ICH (aOR: 1.23, 95% CI:1.05 to 1.43), but not with stroke progression (aOR 1.00, 95% CI: 0.87 to 1.16). Results of the analyses with iodine concentration relative to the sagittal sinus were similar to those of the absolute iodine concentration analyses, and did not seem to improve overall prediction.
Conclusions
Contrast extravasation ASPECTS and iodine concentration measures are both predictive of short- and long term neurological outcomes. Contrast extravasation ASPECTS is likely a better predictor for stroke progression than iodine concentration measures.

Figure 1: mRS distribution for contrast extravasation ASPECTS categories

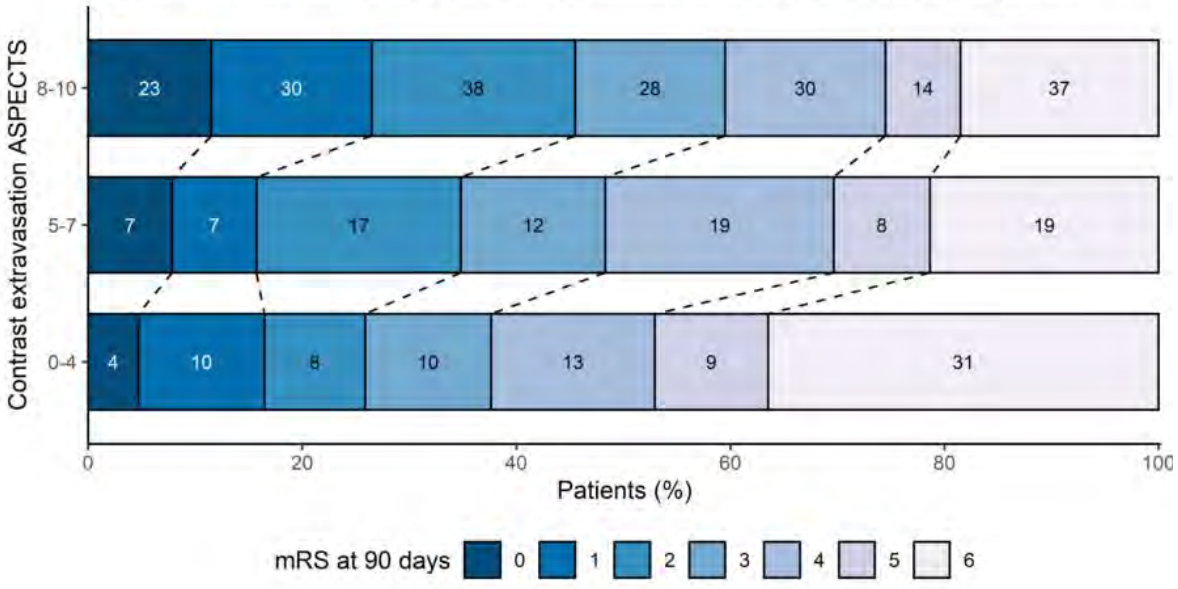

(Filename: TCT_1242_Figure1.jpg)

503

Effectiveness and Safety of EVT for LVO vs MeVO - A Single Center Experience

K Shek[1], S Alcock[1], J McEachern[1], A Trivedi[1], E Ghrooda[1], Z Kaderali[2], J Shankar[1]

[1]University of Manitoba, Winnipeg, Manitoba, [2]Health Sciences Centre Winnipeg, Winnipeg, MB

Purpose

There is growing evidence towards the utilization of endovascular thrombectomy (EVT) for medium vessel occlusions (MeVO) in the anterior intracranial circulation for patients with acute ischemic stroke. The purpose of this study was to compare outcomes of effectiveness and safety in patients undergoing EVT for large vessel occlusion (LVO) versus those with MeVO.

Materials and Methods

This retrospective cohort study, using an intention to treat design, compared 90-day mRS as the primary outcome between 43 patients with MeVO versus 199 with LVO who were treated with EVT. Secondary outcome measures included successful vessel recanalization, procedural complications, post EVT ICH, and infarct size. Logistic regression was also performed with 90d mRS as the dependent variable to determine predictors of poor outcome.

Results

The rate of good functional outcome (90-day mRS=0-2) was higher in patients with LVO vs those with MeVO (32.9% vs 27%), but this was not statistically significant (p=0.19). Rate of EVT procedural complication was also not significantly different between groups (p=0.10), nor was rate of ICH (p=0.30) and successful vessel recanalization (p=0.12). Multivariate analysis showed older age, not receiving recombinant tissue plasminogen activator (r-tPA), and larger infarct size were independent predictors of poor functional outcome at 90-days (mRS=3-6).

Conclusions

The primary outcome of 90-day mRS was not significantly different between the LVO and MeVO cohorts. Furthermore, there was no significant difference in rate of successful reperfusion or rate of peri-procedural complications. Older age, not receiving r-tPA, and larger infarct size were independent predictors of a poor outcome at 90 days.

Table 1: Comparison of demographic, clinical, imaging, and outcomes data between cohorts, as well as logistic regression analysis assessing for associations with good 90d mRS

	LVO (199)	MeVO (43)	P value: comparing cohorts	Univariate OR 90d mRS	P value 90d mRS	Multivariate OR 90d mRS	p value 90d mRS
Age (242)	71.3	76.1	0.25	1.81 (1.13-2.88)	0.01	2.45 (1.21-4.99)	**0.01**
Gender (242)	199	43	0.09	1.81 (0.98-3.35)	0.06	1.17 (0.50-2.76)	0.72
Male	98 (49.2%)	15 (34.8%)					
Female	101 (50.8%)	28 (65.1%)					
ASPECTS (232)	191	41	0.07	0.11 (0.023-0.50)	<0.01	0.16 (0.02-1.43)	0.10
7-10	161 (84.3%)	39 (95.1%)					
0-6	30 (15.7%)	2 (4.9%)					
EVT Performed (242)	166 (83.4%)	33 (76.7%)	0.31	0.72 (0.32-1.59)	0.42		
OTG (228)	187	41	0.43	1.64 (0.83-3.3)	0.15		
<6hr	126 (67.4%)	25 (61.0%)					
>6hr	61 (32.6%)	16 (39.0%)					
GTR (179)	149	30	0.39	1.03 (0.94-3.98)	0.07	1.81 (0.55-3.14)	0.54
<30min recanalization	90 (60.4%)	15 (50.0%)		1.61 (0.80-3.25)	0.18		
>30min recanalization	59 (39.6%)	15 (50.0%)					
r-tPA	198	43	0.52	0.25 (0.13-0.50)	<0.01	0.28 (0.11-0.69)	**0.01**
Yes	112 (56.6%)	22(51.2%)					
No	86 (43.4%)	21 (48.8%)					
TICI (240)	197	43	0.12	0.86 (0.68-1.09)	0.20		
Successful (2b-3)	143 (72.6%)	26 (60.5%)					
Unsuccessful (0-2a)	54 (27.4%)	17 (39.5%)					
Post EVT ICH (237)	89 (44.9%)	16 (37.2%)	0.30	0.30 (0.15-0.58)	<0.01		
Type of ICH (237)	194	43	0.39	2.98 (1.66-5.35)	<0.01	1.98 (0.97-4.05)	0.06
No ICH	105 (54.1%)	28 (65.1%)					
Non Severe	73 (37.6%)	13 (30.2%)					
Severe	16 (8.3%)	2 (4.7%)					
EVT Complication (242)	12 (6.1%)	0	0.10	0.80 (0.15-4.3)	0.79		
Infarct Size (237)	135	42	<0.01	2.00 (1.47-2.73)	<0.01	1.63 (1.08-2.48)	**0.02**
None	17 (8.7%)	3 (7.1%)					
<1/3	114 (58.4%)	25 (59.5%)					
>1/3 and <2/3	22 (11.2%)	12 (28.6%)					
>2/3	42 (21.5%)	2 (4.8%)					
90d mRS	158	37	0.19				
0-2	52 (32.9%)	10 (27.0%)					
3-5	52 (32.9%)	18 (48.7%)					
6	54 (34.2%)	9 (24.3%)					

(Filename: TCT_503_Table1_page-0001.jpg)

128

Effects of Artificial Gravity on Intracranial Anatomy and Physiology: A 3T MRI STUDY

L KRAMER[1], K Hasan[2], X Zhang[3], B Macias[4], K Marshall-Goebel[5], S Laurie[4], E Bershad[6]

[1]UTSHC-Houston, Houston, TX, [2]University of Texas Health Science Center, Houston, TX, [3]Univ. Of Texas Health Science Center, Houston, TX, [4]NASA, Houston, TX, [5]KBR, Houston, TX, [6]Baylor College of Medicine, Houston, TX

Purpose

Spaceflight associated neuro-ocular syndrome (SANS) is characterized by the development of optic disc edema, posterior globe flattening, choroidal/retinal folds and hyperopic refractive errors(1), hypothesized to be due to headward fluid shift that invariably occurs in microgravity. As a countermeasure, artificial gravity (AG) through centrifugation has been proposed to reduce this headward fluid shift. As an indicator of efficacy, the goal of this study was determine if AG can prevent or reduce known changes in brain volumetry, internal carotid artery (ICA) stroke volume and cerebral spinal fluid (CSF) flow velocity that occur during simulated chronic headward fluid shift using head down tilt bed rest (HDTBR) methodology(2).

Materials and Methods

24 volunteers (16 men, mean age = 33 years ± 9; mean BMI = 24.3 kg/m2 ± 2.0) were recruited for a prospective study using strict six-degree HDTBR for 60 days. Short-arm centrifugation was utilized to generate AG at 0.3g. Subjects were divided equally into three groups: No AG (control; n=8), daily intermittent AG (6 x 5 min iAG; n=8), and daily continuous 30 min cAG (n=8). Phase-contrast imaging was used to quantify ICA stroke volume and peak-to-peak CSF flow velocity in the mid cerebral aqueduct. 3D-SPGR was acquired for volumetric segmentation of the brain and CSF spaces. MRI studies were performed on a dedicated 3T scanner at baseline (BDC), 14 days into HDTBR (HDTBR14), 52 days into HDTBR (HDTBR52) and 3-5 days after HDTBR (recovery, R+3/5). The data were analyzed by the mixed model, which included intervention and time (BDC, HDTBR 14, HDTBR 52, R+3/5) as the fixed effects and included subject as the random effect.

Results

Strict six-degree HDTBR was characterized by progressive increases in combined brain and CSF volumes and progressive decreases in mean ICA stroke volume from baseline to 52 days post intervention (P<.01) (Figs. 1-2). Overall, mean CSF peak-to-peak flow velocity increased from baseline to 52 days post intervention (P<.01), reaching its maximum value at HDTBR14 (Fig. 3). Compared to baseline, only combined brain and CSF volumes did not return to baseline values in the recovery period (P<.01). Neither iAG nor cAG exerted any significant effects on the measured MRI brain parameters as compared to HDTBR alone (P=NS).

Conclusions

Thirty minute daily exposure to either iAG or cAG appears to be insufficient in preventing or reducing the intracranial effects of chronic HDTBR and thus may not be a suitable countermeasure as currently deployed.

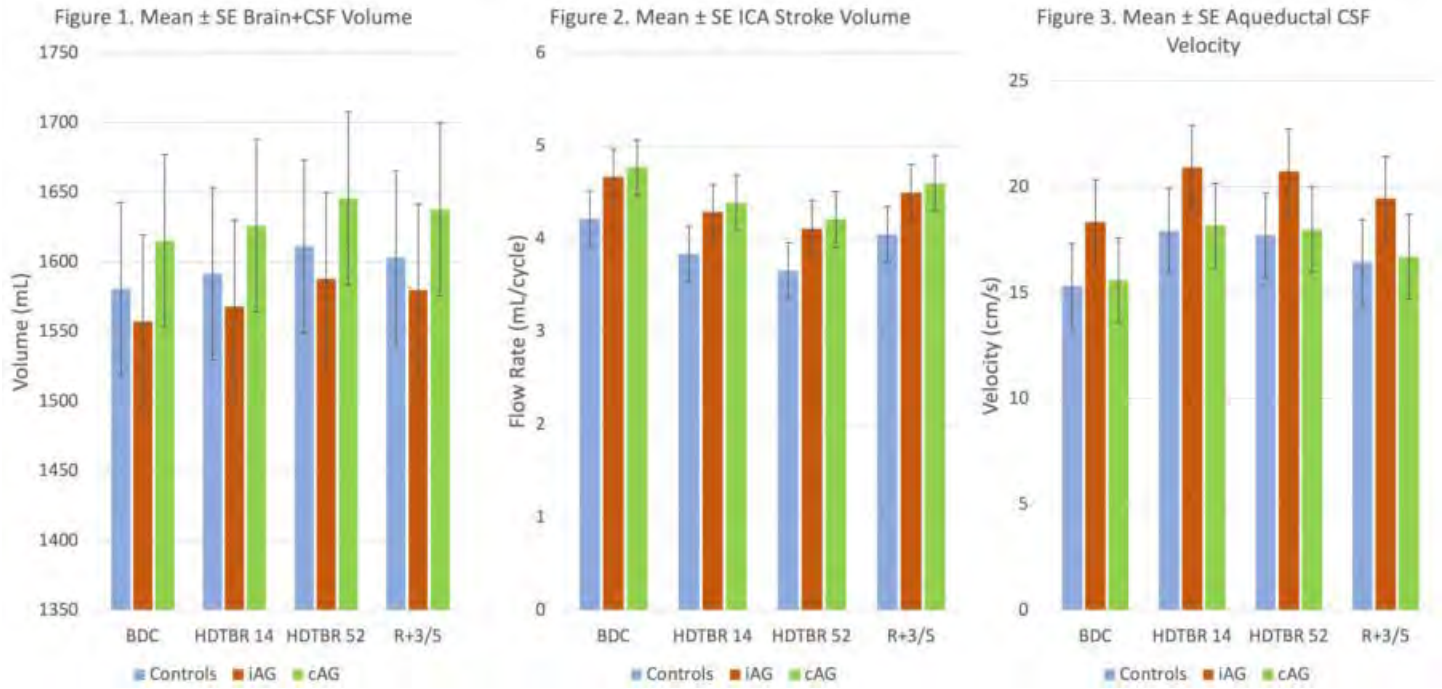

(Filename: TCT_128_GraphAGabstract.jpg)

1222

Efficacy of 4D Ultrashort-TE MR Angiography for Evaluation of Intracranial Aneurysms Treated with Stent-Assisted Coil Embolization

H Uetani[1], T Hirai[1]

[1]*Kumamoto University, Kumamoto, Japan*

Purpose

As a novel follow-up method for intracranial aneurysms treated with stent-assisted coil embolization (SACE), we applied 4D magnetic resonance angiography (MRA) with minimized acoustic noise utilizing ultrashort echo time (4D mUTE-MRA). We aimed to evaluate the efficacy of 4D mUTE-MRA for the follow-up of intracranial aneurysms treated with SACE.

Materials and Methods

This study included 31 consecutive patients with intracranial aneurysm treated with SACE who underwent 4D mUTE-MRA at 3T and digital subtraction angiography (DSA). Five dynamic 3D mUTE-MRA images with a spatial resolution of 0.5 × 0.5 × 0.5 mm3 were obtained every 200 msec. Two readers independently reviewed the mUTE and DSA images to visualize flow in the stent using a 4-point scale (from 1 [not visible] to 4 [excellent]) and to identify the aneurysm occlusion status (total occlusion, residual neck, and residual aneurysm). The interobserver and intermodality agreement was assessed using κ statistics.

Results

On DSA images, the lumen in the stents of all 31 patients treated with SACE had an excellent flow without stenosis. On 4D mUTE-MRA images, observers rated the flow in the stent as good or excellent for the patients. In terms of aneurysm occlusion status, the intermodality agreement between DSA and 4D mUTE-MRA was excellent (κ = 0.92) and the interobserver agreement was also excellent (κ = 0.96). 4D mUTE-MRA revealed protruding flow within the aneurysm in one case, but DSA did not.

Conclusions

4D mUTE-MRA is effective for the follow-up evaluation of intracranial aneurysms treated with SACE.

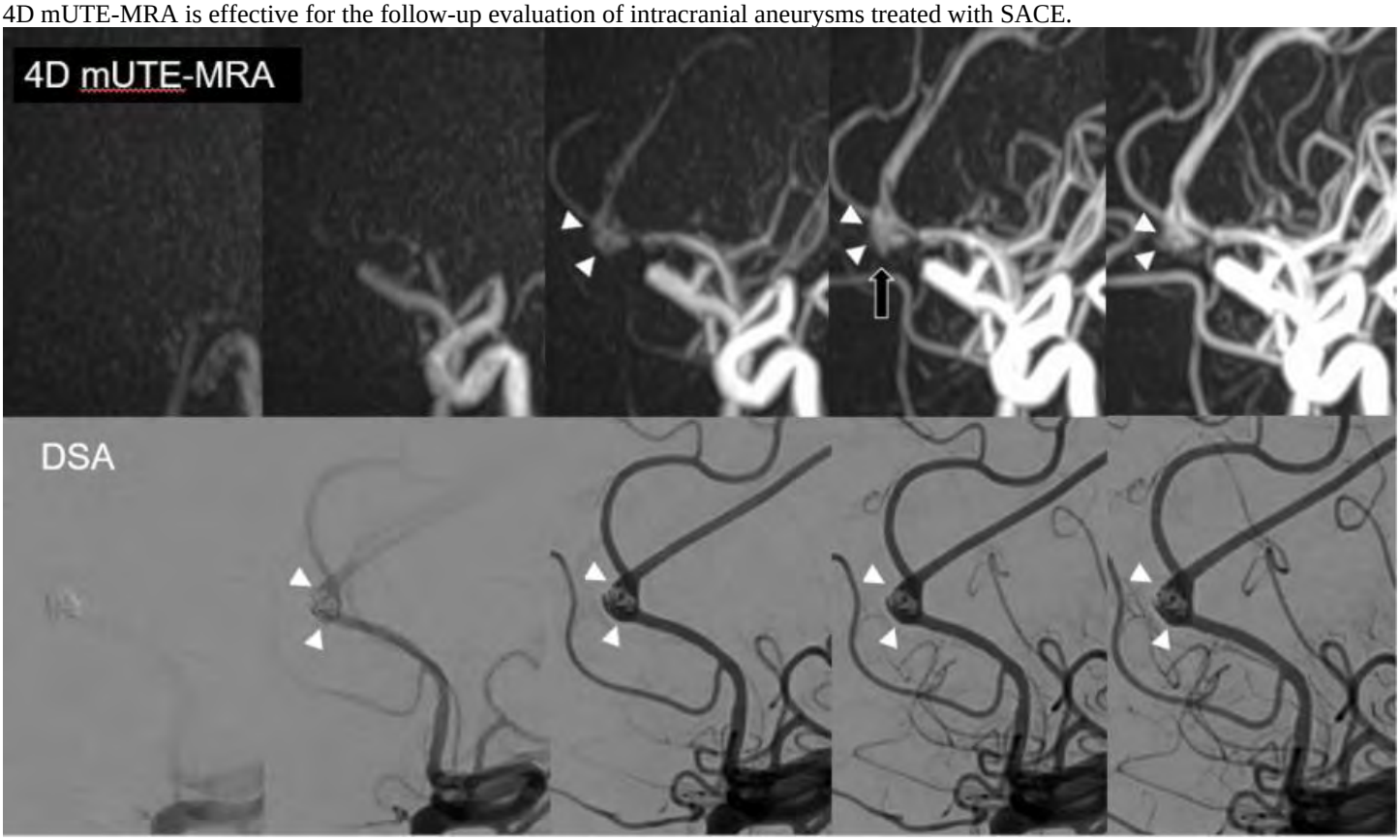

(Filename: TCT_1222_Figure.jpg)

197

Electron Density and Effective Atomic Number of Lumbar Intervertebral Disc Degeneration: A Preliminary Study

M Nakajo[1], K Kamimura[2], T Hasegawa[3], T NAKANO[4], Y Fukukura[5], K Takumi[6], H Nagano[7], M Bohara[8], T Yoshiura[1]

[1]Kagoshima University Graduate School of Medical and Dental Sciences, Kagoshima, Japan, [2]Kagoshima University Hospital, Kagoshima, Choose Any State/Province, [3]Kagoshima University graduate school of medical and dental sciences, Kagoshima, Kagoshima, [4]Kagoshima university, Kagoshima, Japan, [5]Kagoshima University Graduate School of Medical and Dental Sciences, Kagoshima, Kagoshima, [6]Kagoshima Univ Graduate School of Med & Dental Scs, Kagoshima, Japan, [7]Kagoshima University Graduate School of Medical and Dental Sciences,, Kagoshima, Select a State or Province, [8]N/A, N/A

Purpose

To preliminarily evaluate the usefulness of electron density (ED) and effective atomic number (Zeff) derived from dual energy CT (DECT) for detecting lumbar intervertebral disc degeneration (LIDD).

Materials and Methods

The study included 314 discs in 93 patients. All patients were evaluated using a dual-layer DECT, and images of conventional poly-energetic CT value (CTconv), ED, and Zeff were obtained. LIDD were classified using modified Pfirrmann grade (mPG) based on T2-weighetd MRI. Five ROIs were drawn in each disc, labeled as N1- N5 from anterior to posterior: N1 and N5 were in the annulus fibrosus, while N2-4 were in the nucleus pulposus. Mean CTconv, ED, and Zeff for each ROI were correlated with mPG using Spearman's rank correlation coefficient. The CTconv, ED, and Zeff values in N1-5 as well as their differences between N1and N3 (ΔN1-N3) and between N5 and N3 (ΔN5-N3) were compared between normal (mPG1 and 2) and degenerated discs (mPG3-7) using the Mann-Whitney U test. ROC curve analysis was used to assess the diagnostic abilities of CTconv, ED, and Zeff values.

Results

The mean CTconv was significantly positively correlated with mPG in N3 and N4 (ρ=0.294, 0.205, P<0.001), while it was significantly negatively correlated with mPG in N1 and N5 (ρ=-0.262, 0.162, P<0.001). The mean ED was significantly positively correlated with mPG in each of N2-4 (ρ=0.333 - 0.475, P<0.001), while it was significantly negatively correlated with mPG in N1, N5 (ρ=-0.337, -0.249, P<0.001). The mean Zeff was significantly negatively correlated with mPG in N2-4 (ρ=-0.237 - -0.349, P<0.001). The CTconv and ED of N2-4 in degenerated discs were significantly higher than those of normal discs (P<0.001-0.016). In addition, the CTconv and ED of N1 and N5 as well as their ΔN1-N3 and ΔN5-N3 were significantly lower than those of normal discs (P<0.001). The Zeff of N2-4 in degenerated discs were significantly lower than that in normal discs (P<0.001), while ΔN1-N3 and ΔN5-N3 of Zeff were significantly higher than those of normal discs (P<0.001). The AUC values for CTconv and ED of N1 to N5 ranged from 0.585 to 0.740, those for Zeff of N2 to N4 ranged from 0.625 to 0.679, those for ΔN1-N3 and ΔN5-N3 of CTconv, ED, and Zeff ranged from 0.625 to 0.901. The AUC value for ΔN1-N3 of ED performed best (AUC = 0.901) among those of all indices.

Conclusions

ED and Zeff derived from DECT may be useful parameters in detecting LIDD.

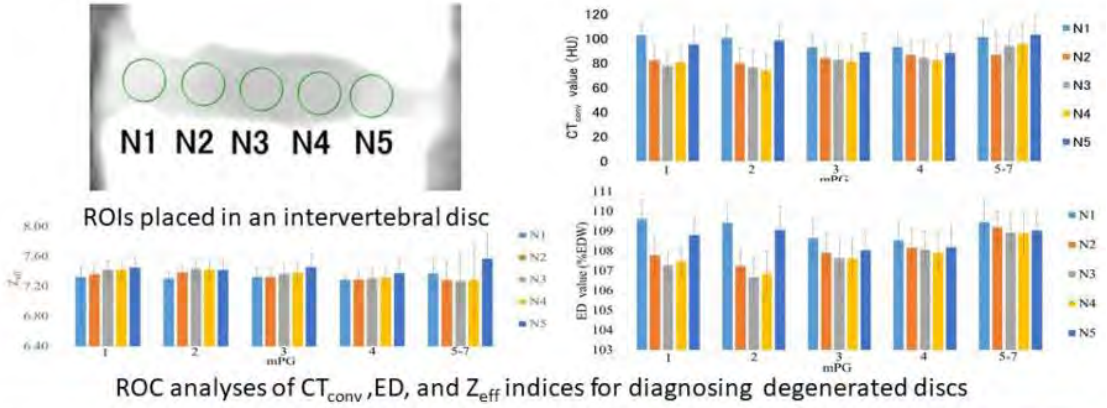

ROC analyses of CT_{conv}, ED, and Z_{eff} indices for diagnosing degenerated discs

		AUC	Cutoff	Sensitivity (%)	Specificity (%)	Accuracy (%)
CT_{conv}	N1	0.700 (0.646, 0.750)	≤ 99.2	69.54 (121/174)	61.43 (86/140)	65.92 (207/314)
	ΔN1-N3	0.775 (0.725, 0.820)	≤ 21.9	84.48 (147/174)	58.57 (82/140)	72.93 (229/314)
ED	N1	0.740 (0.688, 0.788)	≤ 108.9	63.22 (110/174)	75.00 (105/140)	68.47 (215/314)
	ΔN1-N3	0.901 (0.862, 0.931)	≤ 1.6	82.76 (144/174)	84.29 (118/140)	83.44 (262/314)
	ΔN5-N3	0.857 (0.813, 0.894)	≤ 0.6	67.82 (118/174)	86.43 (121/140)	76.11 (239/314)
Z_{eff}	N3	0.679 (0.624, 0.731)	≤ 7.34	55.17 (96/174)	74.29 (104/140)	63.69 (200/314)

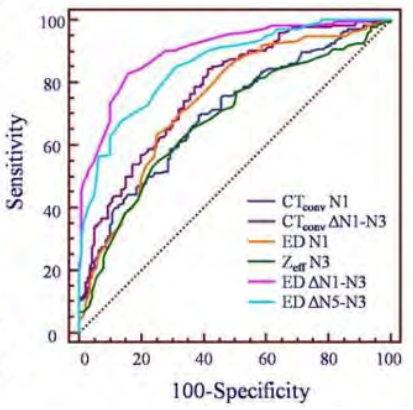

(Filename: TCT_197_ASNR2022.jpg)

527

Estimation of Multiphase Blood Flow Changes in Intracranial Arteries from Time-of-flight Signals by Machine Learning

A Wada[1], T Akatsu[2], Y Ikenouchi[2], T Akashi[3], S Fujita[3], K Sato[2], J Kikuta[3], K Kamagata[3], S Aoki[2]
[1]Juntendo Univeristy, Tokyo, Japan, [2]Juntendo University, Tokyo, Japan, [3]Juntendo University, Tokyo, Tokyo

Purpose
The purpose of this study is to extract the potential multiphase blood flow information from Time-of-flight (TOF) images using machine learning.
Materials and Methods
A training data set was constructed to convert the TOF image into an 8-phase blood flow image.The training data was generated on a dataset of 152 axial image of 3D TOF and 1216 ASL cases from 8 phases from a 3T MRI. For multi-temporal flow estimation, an LSTM network including a modified Unet was applied. The intra-arterial signal value for each phase was estimated as the normalized value of the maximum intra-arterial signal through all phases, with a value between 0 and 1. The difference between the estimated blood flow signal from TOF and ASL was evaluated by coefficients of determination R2 (R2), mean absolute error (MAE). And the temporal changes in the internal carotid artery, proximal and distal middle cerebral arteries were evaluated in one healthy subject and one case with unilateral internal carotid artery stenosis.
Results
The coefficients of determination R2 of the intra-arterial signal between estimation from TOF and ASL in 8 phases averaged 0.74 (0.66 to 0.88).The mean and standard deviations (SD) of the difference between the estimation signal and the ASL signal were 0.03 and 0.09. The 95% confidence interval (mean ± 1.96 SD) by Bland Altman analysis was -0.15 to 0.22.
Conclusions
Machine learning estimated the time-course change of multiple phases of intracranial arterial flow from TOF signals.

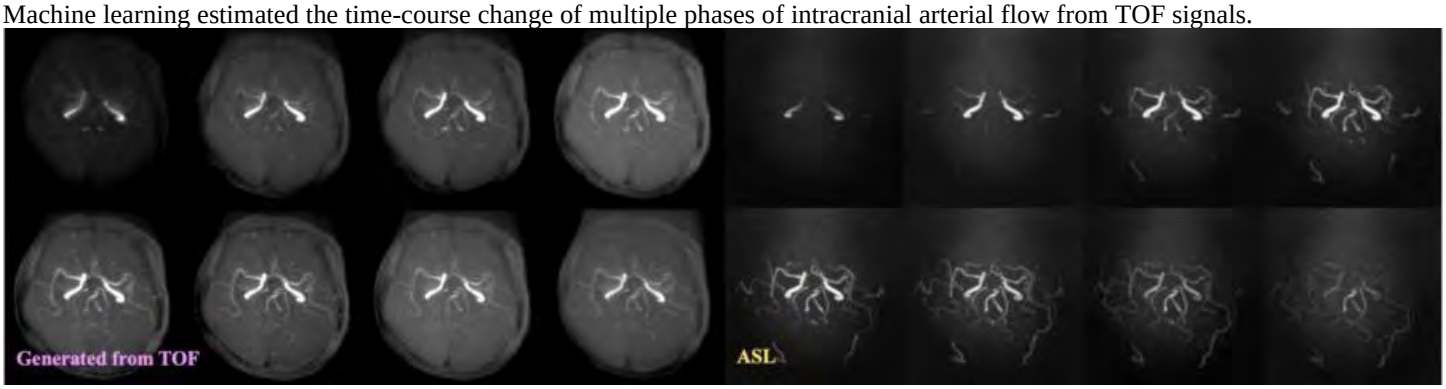

(Filename: TCT_527_for_ASNR2022.jpg)

762

Evaluating Diagnostic Accuracy and Determining Optimal Diagnostic Thresholds of Three Different Approaches to [68Ga]-DOTATATE PET/MRI Analysis in Patients with Meningioma

S Kim[1], M Roytman[2], R Magge[3], B Liechty[2], R Ramakrishna[2], T Schwartz[3], N Karakatsanis[1], E Lin[2], J Knisely[2], J Ivanidze[4]
[1]New York-Presbyterian Hospital/Weill Cornell Medicine, New York, NY, [2]Weill Cornell Medicine, New York, NY, [3]Weill Cornell Medicine/NewYork-Presbyterian Hospital, New York, NY, [4]Weill Cornell Medicine Radiology, New York, NY

Purpose
PET/MRI with [Ga68]-DOTATATE, a somatostatin analog PET radiotracer, has demonstrated clinical utility in evaluation of meningioma compared to contrast-enhanced MRI alone [1,2]. Multiple approaches to brain [68Ga]-DOTATATE PET analysis have been published, however have not been compared directly. Our purpose was to compare diagnostic performance of three approaches to quantitative brain [68Ga]-DOTATATE PET analysis in patients with suspected meningioma recurrence and to establish the optimal diagnostic threshold for each method.
Materials and Methods
Patients with suspected meningioma were imaged prospectively with [68Ga]-DOTATATE brain PET/MRI. Lesions were classified as meningiomas and post-treatment change (PTC), based on pathology findings and follow up MRI appearance. Lesion SUV was obtained along with SUV for the superior sagittal sinus (SSS) and pituitary gland in each patient. Lesions were reclassified using the following methods: absolute SUV threshold, SUV ratio (SUVR) to SSS (SUVRsss), and SUVR to the pituitary gland (SUVRpit). Diagnostic performance of the three methods were compared using contingency tables and McNemar's test. Previously published pre-determined thresholds were assessed where applicable [1,2]. Additionally, the optimal thresholds for each method were identified using Youden's J statistics.
Results
166 meningiomas and 41 PTC lesions were identified across 62 patients (Fig 1). SUV, SUVRsss, and SUVRpit of meningioma were significantly higher than those of PTC (P<0.0001). At the pre-determined thresholds, SUV demonstrated the highest sensitivity (98.2%) and the highest specificity was achieved with SUVRpit (87.8%). The optimal thresholds for SUV, SUVRsss, and SUVRpit were 4.65, 3.23, and 0.260, respectively (Table 1). At the optimal thresholds, SUV had the highest specificity (97.6%) and SUVRsss

had the highest sensitivity (86.1%). An ROC analysis of SUV, SUVRsss, and SUVRpit revealed AUC of 0.932, 0.910, and 0.915, respectively (P<0.0001) (Fig 2).

Conclusions

We compared different approaches to quantitative analysis of [68Ga]-DOTATATE PET/MRI in meningioma and found that the SUVRsss method may have the most robust combination of sensitivity and specificity, with the statistically determined optimal threshold of 3.23. Future studies validating our findings in different patient populations are needed to continue optimizing the diagnostic performance of [68Ga]-DOTATATE PET/MRI in meningioma, with the potential of improving treatment strategies and clinical outcomes.

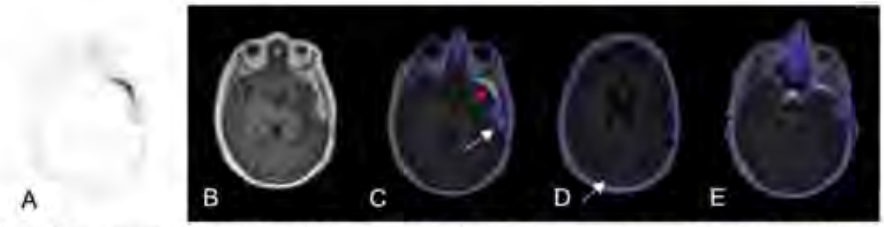

Fig 1 Axial images of [68Ga]-DOTATATE PET AC (A), 3D T1 post-gadolinium MR (B), fused PET/MR T1 (C, D, E) windowed SUV 0-15. This representative patient's fused PET/MR images demonstrate a lesion suspicious for a meningioma in the left anterior temporal pole with SUV of 13.6 (C, red arrow). The more posteriorly located enhancing lesion (C, white arrow) demonstrates SUV of 4.5 and was suspicious for post-treatment change, given that the SUV of the superior sagittal sinus was 2.3. The subsequent resection and biopsy of the two lesions a year later confirmed the suspected diagnosis of recurrent meningioma and radiation necrosis, respectively. The superior sagittal sinus (D, arrow) demonstrates SUV of 2.3 and the pituitary gland (E) demonstrates SUV of 12.4

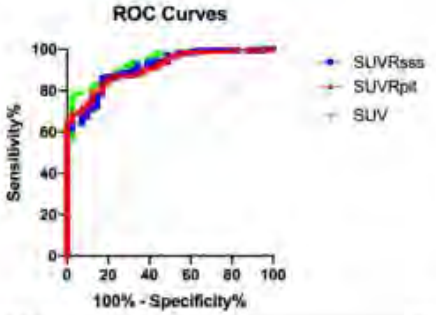

Fig 2 ROC Curves of the three methods: SUV, SUVRsss, and SUVRpit. ROC analysis revealed area under the curve of 0.932, 0.910, and 0.915 for SUV, SUVRsss, and SUVRpit, respectively (all P<0.0001)

Methods	J	Optimal Threshold	Sensitivity	Specificity
SUV	75.27	>4.65	77.7% (70.8-83.4)	97.6% (87.4-99.9)
SUVRsss	69.07	>3.227	86.1% (80.1-90.6)	82.9% (68.7-91.5)
SUVRpituitary	67.32	>0.260	79.5% (72.7-85.0)	87.8% (74.5-94.7)

Table 1 Optimal threshold of each method as determined by Youden's J Statistics with 95% confidence interval

	SUV vs SUVRpit	SUVRpit vs SUVRsss	SUV vs SUVRsss
Sensitivity	P=0.505	P=0.0098*	P=0.0012*
Specificity	P=0.1336	P=0.6171	P=0.0412*

Table 2 The McNemar's Test for sensitivity/specificity of the three methods at the optimal thresholds. *P value less than 0.05 was used to indicate statistical significance.

(Filename: TCT_762_Figures_ASNR.jpg)

380

Evaluating the Clinical Relevance of Age Prediction/Actual Age Discrepancy Utilizing a Convolutional Neural Network Paired with a Regression Algorithm Applied to T2 Weighted Fast Spin-echo and Fluid Attenuated Inversion Recovery Images of the Brain

M Conneely[1], B Swaminathan[1], P Vyas[1], A Bousquet[2], S Zelenberg[2], S Banerji[2], X Piao[1], A Fatima[1], P Patel[1], J Burke[1], B Golant[1], R Nolcheff[1]

[1]Chicago Medical School/Rosalind Franklin University, North Chicago, IL, [2]Lake Forest College, Lake Forest, IL

Purpose

1. To produce a deep learning model capable of estimating the patient's age from brain MRI images. 2. To examine the difference between the model's estimated patient age and actual patient age, the brain age index (BAI), as a potential biomarker with predictive value with respect to the presence of chronic disease state (hypertension (HTN), diabetes mellitus (DM) , traumatic brain injury (TBI), alcohol abuse (AA), and polysubstance abuse (PA).

Materials and Methods

Axial T2 weighted FSE and FLAIR images from 1104 patients ranging in age between 20 and 80 years were used to train a multi-layer CNN model comprised of convolutions, max pooling, flattenings, batch normalization, and dropout. The outputs were then combined using regression to produce a single age prediction. Both linear and quadratic regression were investigated (r^2=0.8 and r^2=0.84, respectively), and the BAI was calculated. A retrospective chart review was performed for all 1104 patients for ICD codes related to HTN, DM, TBI, AA, and PA and correlated with the BAI.

Results

Of the 1104 patients, 430 had ICD codes related to HTN, 184 to DM, 95 to TBI, 138 to AA, and 95 to PA. ANOVA testing of BAI, HTN, and PA illustrated a statistically significant difference of means (p=0.000) No such finding existed between the BAI and other ICD codes. HTN was inversely correlated with BAI (P=0.000). The presence of ICD codes related to HTN was inversely correlated with BAI. We collapsed HTN and DM into a one-dimensional score of 4 states (0=None, 1=HTN, 2=DM, 3=Both). Within the 2-D space of BAI and HTN/DM, we plotted patients with at least one ICD code of TBI, AA, or PA. A kNN model with (k=20) split the two-dimensional space where patients with AA or PA dominated regions corresponding to higher predicted age. This relationship disappears when patients with no such ICD codes are included, possibly indicating missing codes or other factors.

Conclusions

BAI appears to be a potentially useful biomarker for AA and PA. The model could therefore be used to add clinical value to MRI studies, potentially identifying patients who could benefit from additional screening/counseling for substance abuse. Further study, potentially in the form of a prospective study capturing the severity of disease rather than the presence/absence of ICD codes, could further elucidate the potential utility of BAI in identifying patients with chronic disease states and estimating clinical outcomes.

185

FMISO PET/MRI Hypoxic Burden As a Metric Glioblastoma Immunotherapy Response

R Barajas Jr.[1], N Mallak[1], A Brown[1], B Thurston[1], A Raslan[2], B Murphy[3], R Woltjer[4], L Muldoon[5], W Rooney[6], R Fu[7], S Holland[8], E Neuwelt[8], P Ambady[8]

[1]Department of Radiology, Oregon Health & Science University, Portland, OR, [2]Department of Neurological Surgery, Oregon Health & Science University, Portland, OR, [3]Department of Radiation Medicine, Oregon Health & Science University, Portland, OR, [4]Department of Pathology, Oregon Health & Science University, Portland, OR, [5]Oregon Health & Science University, Portland, OR, [6]Advanced Imaging Research Center, Oregon Health & Science University, Portland, OR, [7]School of Public Health, Oregon Health & Science University, Portland, OR, [8]Department of Neurology, Oregon Health & Science University, Portland, OR

Purpose

Hypoxia in patients with glioblastoma directly contributes to poor clinical outcomes by reducing chemoradiotherapy efficacy and portends poorer overall survival1. 18F-fluoromisonidazole (FMISO) positron emission tomography (PET) defines regions of hypoxia1-3. The use of checkpoint inhibition is actively being investigated in brain tumors. Response assessment criteria remain to be adjudicated. Our hypothesis is that the presence of hypoxic burden as defined by FMISO PET/MRI is capable of defining glioblastoma therapeutic failure.

Materials and Methods

Eight patients with newly diagnosed glioblastoma were recruited into our clinical trial (NCT03649880). All patients underwent maximal safe resection followed by Stupp protocol4 temozolomide based chemoradiotherapy augmented with concurrent pembrolizumab immunotherapy (NCT03347617). FMISO PET & MRI was performed at the time of first presumed disease progression as defined by iRANO criteria. 3.7 MBq/kg (0.1 mCi/kg; up to 10 mCi) of FMISO was administered intravenously 90 minutes prior to emission PET imaging of the brain1. The hypoxic volume (HV) was defined as 1.2x of mean cerebellar uptake1. Gadolinium enhancing volume was defined by a semi-automated approach from T1-weighted imaging. Relative standard uptake values (rSUV) were defined as the ratio of T2 hyperintense lesion and right cerebellum values. The hypoxic burden (HB) was the ratio of the hypoxic volume (HV) to enhancing volume. Clinical diagnosis was confirmed through surgical biopsy or follow-up MRI.

Results

At the time of presumed progression the 4 patients eventually diagnosed with recurrent glioblastoma demonstrated elevated rSUV of 1.2 ± 0.2, HV of 4.44 ± 5.65 ml, and HB of 1.4 ± 0.69. FMISO uptake was heterogenous with the rSUVmax of 1.56 ± 0.48 within the

most hypoxic regions. The 4 patients with neuroinflammatory pseudoprogression as an etiology for the growing enhancing volume by MRI was found to have a rSUV of 1.05 ± 0.09, HV of 0.73 ± 0.83 ml, and HB of 0.09 ± 0.11. The most hypoxic neuroinflammatory regions demonstrated a rSUVmax of 1.26 ± 0.39. HB was found to be significantly elevated in patients with recurrent disease (P= 0.03; Figure 1).

Conclusions

This small case series demonstrates preliminary evidence that the newly defined hypoxic burden FMISO PET/MRI metric may better assess glioblastoma therapeutic efficacy at the time of presumed disease progression. We continue our clinical trial enrollment to further refine these observations.

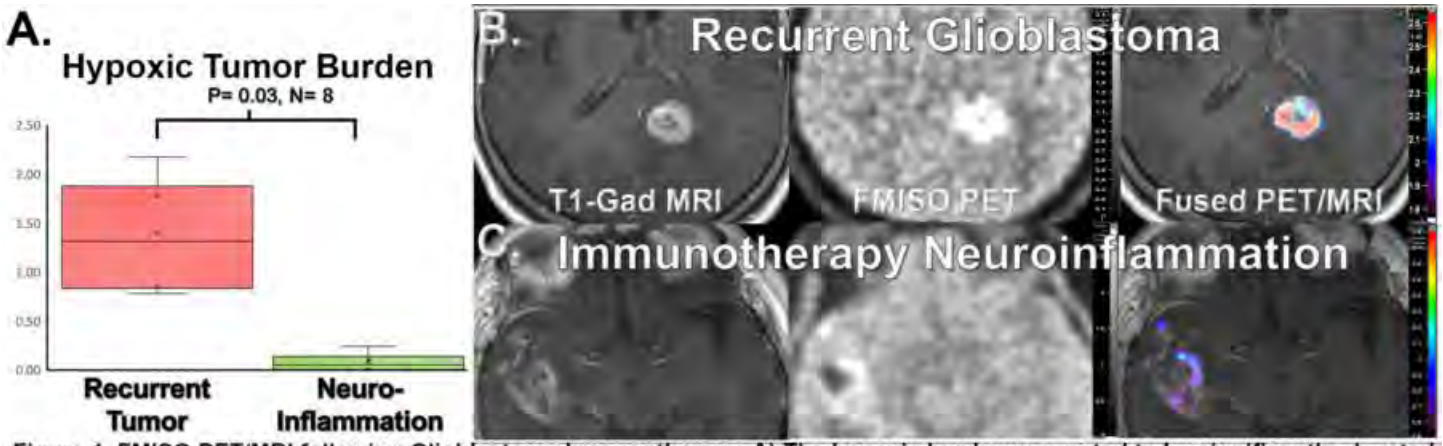

Figure 1. FMISO PET/MRI following Glioblastoma Immunotherapy. A) The hypoxic burden was noted to be significantly elevated within patients with therapeutic failure at the time of presumed disease progression. B) Recurrent disease was manifested by progressive contrast enhancement (left) comprised of diffuse hypoxia (middle, FMISO PET). This is best characterized by the hypoxic burden (right, fused FMISO PET with T1 Gad enhanced MRI). C) Conversely, patients with checkpoint immunotherapy mediated pseudoprogression demonstrated similar appearing mass like enhancement with minimal levels of hypoxia.

(Filename: TCT_185_Figure1copyfinalcopy.jpg)

1289

Fully Automatic CNN-based Segmentation of MRI FLAIR Sequences In patients with Intracerebral Hemorrhage

i TRIMECHE[1], D Cassereau[1], J Martini[1], L PUYBASSET[2], D Galanaud[2], V Perlbarg[1]

[1]BRAINTALE, Strasbourg, France, [2]APHP Hospital, Paris, France

Purpose

Intracerebral hemorrhage (ICH) is the most devastating subtype of stroke with high mortality and consciousness disorders. Multimodal brain imaging is extensively used to monitor hematomas and edemas volumes and localization known to be reliable outcome predictors. Automatic segmentation is then key feature of ICH patients management.

Materials and Methods

To segment hematomas and edemas in MRI-FLAIR images, we propose a fully convolutional neural network architecture revisiting U-Net architecture by replacing the original convolution blocks by the feature extractor from the InceptionResNetV2 network [1] and in adding a fire-squeeze block to the central stage of the U-Net [2]. The training and testing have been achieved in selected labeled FLAIR MRI acquisitions from the multi-centric MRI-COMA trial (NCT00577954). To increase the amount of training data and simulate various ICH localizations, we implemented data augmentation methods [3]. The segmentation performance was evaluated with the DICE score.

Results

We selected 217 raw images acquired from 7 patients for the training set, 48 images were selected as the validation set. The Figure 2 shows the segmentation results. Input image (left), reference mask (middle) and the predicted mask (right). Our model can extract precisely and automatically hematomas and edemas in MRI-FLAIR images, offering a good level of robustness against ICH variability in terms of size, location, orientation, along with contrast and noise variability due to the different MRI modalities used in this study. For the quantitative evaluation, we selected 10 sequences as a testing set and we evaluated the segmentation performance of our CNN model in terms of DSC, BF1-score, precision and recall, compared to the manual segmentation. Table 3 shows the quantitative evaluation results. Results showed very good performance in comparing automatic to manual segmentation in terms of DSC, BF1-score, precision and recall. Our method reaches accuracy better than recent published algorithm [4].

Conclusions

We proposed a new CNN architecture and training strategy accounting for the size, shape and location variability of hematomas and edemas in the brain, to achieve a completely automatic segmentation of these structures in MRI FLAIR images. These preliminary results shows performance that meets medical requirements in terms of reproducibility and precision but need to be confirm on larger datasets.

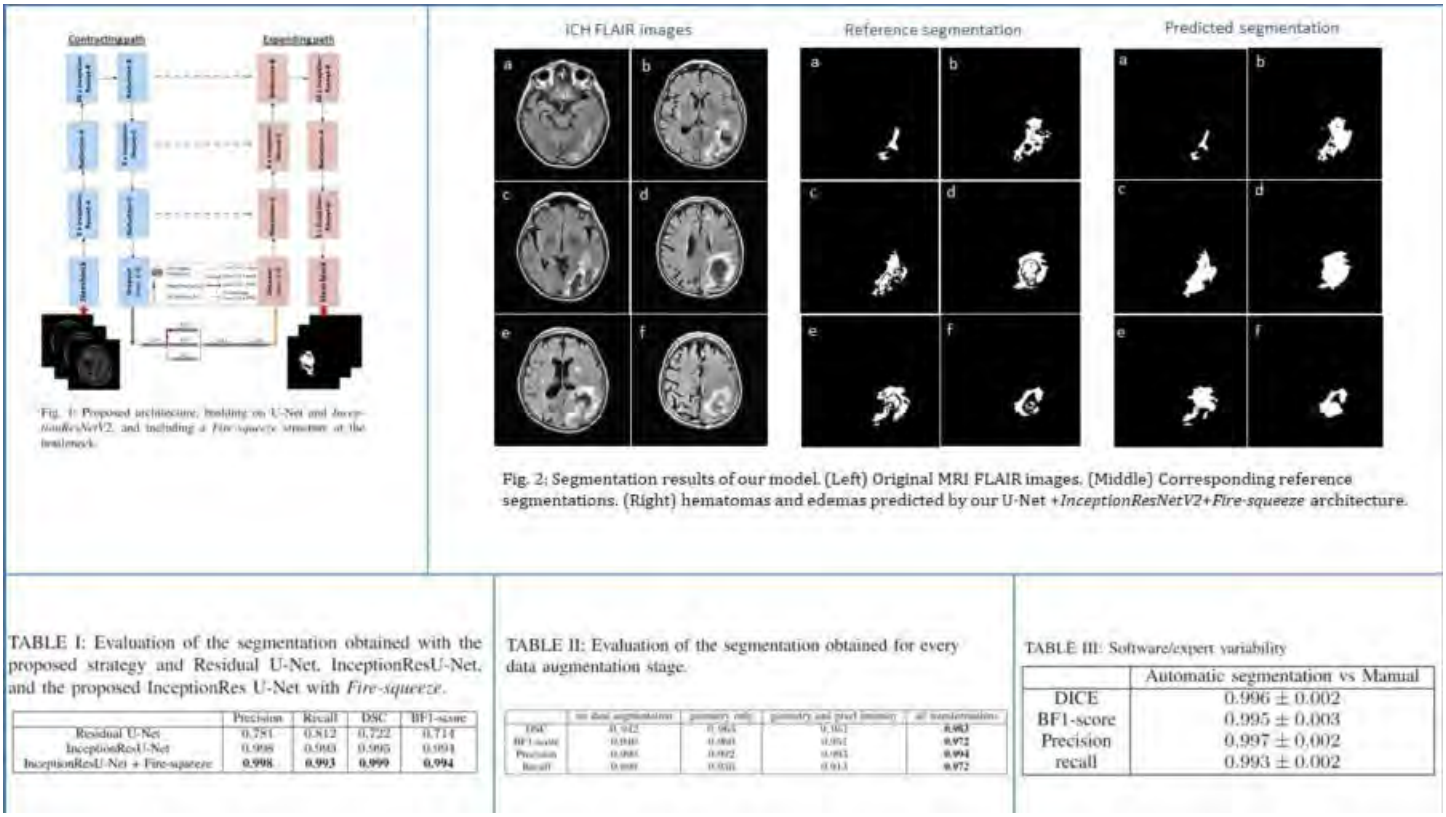

(Filename: TCT_1289_Abstract_ASNR22_jpeg_file.jpg)

352

Generalized Q-sampling Imaging to Characterize White Matter Degeneration in Parkinson's Disease

S Hartono[1], T Ong[2], P Seow[3], T Welton[1], Y Shih[4], W Lee[3], Z Kuek[3], C Chen[1], E Tan[1], L Chan[3]

[1]National Neuroscience Institute, Singapore, Singapore, [2]Nanyang Technological University, Singapore, Singapore, [3]Singapore General Hospital, Singapore, Singapore, [4]Yuan Ze University, Taoyuan, Taiwan

Purpose

We aim to investigate the utility of generalized q-sampling imaging (GQI) to characterize white matter degeneration in Parkinson's disease.

Materials and Methods

The study is approved by the local ethics board. Fifty-four healthy controls (HC) & 54 PD patients formed the study population (Table 1). Patients were diagnosed by movement disorder neurologist based on prevailing clinical criteria. All participants underwent motor & cognitive assessments & brain MRI on a 3T scanner using standardized protocol. Diffusion MRI was acquired with following parameters: SMS slice factor 3, TR/TE=4100/110ms, in-plane resolution=2×2×2 mm3, number of slices=81, 128 diffusion samplings with b-values up to 3000 s/mm2, scan duration=9 min 17 sec. Diffusion parameter maps were reconstructed from diffusion data using GQI model in DSI studio (Fiber Tractography Lab, University of Pittsburgh, Pennsylvania, USA).1,2 Cerebral white matter FA skeleton was generated using TBSS in FSL to investigate statistical group differences between PD patients & HC.3 Other diffusion values were extracted using FA skeleton. Statistical analysis was performed with significance defined at $p<0.05$.

Results

Mean cerebral white matter DSI metrics of the study cohort were tabulated in Table 1. No significant difference between PD patients & HC was found in conventional DTI parameters (FA, MD, AD, RD). Significant difference was found in cerebral white matter quantitative anisotropy (QA), ISO (isotropic component), RDI (restricted diffusion index) and NRDI (non-restricted diffusion index) between PD patients & HC. QA describes the number of anisotropic spins that diffuse along the fiber orientation in a specific direction while ISO describes the number of isotropic spins. RDI represents the density of intra-cellular diffusing spins and describes the local axonal diffusivity restricted by myelinated sheath & reflects axonal density while NRDI represents the extra-cellular compartment of diffusing spins.

Conclusions

DTI can characterize gross fiber orientation & is sensitive to changes in microstructure of human brains.4 However, it has limited specificity to differentiate & characterise complex processes occurring in white matter microstructure. High-order diffusion MRI techniques like GQI provide more comprehensive microscale diffusion information on varied tissue orientations. Each parameter is defined for each resolved fiber population & less susceptible to the partial volume effects of crossing fibers, free water & non-diffusive materials.

	Controls	PD patients	p-value
Number	54	54	
Age	66.23 ± 7.49	64.50 ± 10.15	0.796
Gender (M/F)	29/25	39/15	0.265
Disease duration (years)	-	6.44 ± 5.38	
Motor			
UPDRS-III	5.00 ± 5.63	28.31 ± 13.93	< 0.0001
H&Y	0.04 ± 0.27	1.93 ± 0.58	< 0.0001
Cognition			
MoCA	25.83 ± 2.87	24.37 ± 3.76	0.030
MMSE	27.24 ± 2.15	26.19 ± 2.77	0.027
DTI model			
FA	0.473 ± 0.017	0.470 ± 0.017	0.225
MD	0.552 ± 0.024	0.556 ± 0.026	0.383
AD	0.858 ± 0.024	0.859 ± 0.026	0.919
RD	0.399 ± 0.025	0.404 ± 0.026	0.252
GQI model			
QA	0.810 ± 0.127	0.740 ± 0.103	0.001
ISO	1.919 ± 0.275	1.770 ± 0.229	0.001
RDI	1.289 ± 0.192	1.185 ± 0.156	0.002
NRDI	0.430 ± 0.056	0.399 ± 0.049	0.001

(Filename: TCT_352_Table1.jpg)

141

High Resolution SWI as adjunctive imaging tool in The Evaluation Of Treatment Response Of Brain Metastasis Following Stereotactic Radiosurgery

A Nada[1], E Mahdi[1], H Ahsan[1], E Mahmoud[2], C LEIVA-SALINAS[1], J Cousins[1]
[1]University of Missouri Healthcare, Columbia, MO, [2]National Cancer Institute, Cairo University, Cairo, Cairo

Purpose
To evaluate the impact of longitudinal change in intratumoral susceptibility signal (ITSS) on high-resolution SWI to determine the treatment response along with the standard of care post contrast 3D T1 MPRAGE following stereotactic radiosurgery for the treatment of brain metastasis
Materials and Methods
An IRB approved restrospective study included 63 brain metastatic lesions within 49 patients (33females and 16 males) who have undergone stereotactic radiosurgery with at least one follow-up MRI and available clinicaldata. The average age was 63.17 years (±1.48, ranged from 34-83 years). The average age of male was 67 years while theaverage age of female was 60.82 years. The qualitative imaging pattern of intratumoral susceptibility was correlated intoenhancement pattern at the baseline and follow-up MRIs. Chi-square test was used to compare differences in categoricalvariables ITSS and enhancement pattern at baseline and follow-up MRIs. The accuracy measures were calculated.
Results
Our results demonstrated The longitudinal change in ITSS and enhancement pattern of BM lesions had also statistically significant difference (Wilcoxon Signed Ranks Test ($p < .001$, and $p = .003$, respectively). The longitudinal change in ITSS and enhancement pattern was compared to treatment response which had statistical significance (Mann Whitney U test, Exact significance (1-tailed) $p = 0.037$, and $p = 0.007$, respectively). There was no statistical significance in longitudinal change ITSS and enhancement pattern on follow up MRIs between men and women ($\chi2 = 0.446$, p-value = 0.8, $\chi2 = 5.064$, p-value = 0.079, respectively), nor different age groups (p-value = 0.963, p-value = 0. 374, respectively).
Conclusions
Qualitative assessment of different imaging patterns on SWI can be an adjunctive imaging tool and contribute supplementary information for monitoring treatment response of the brain metastases following stereotactic radiosurgery.

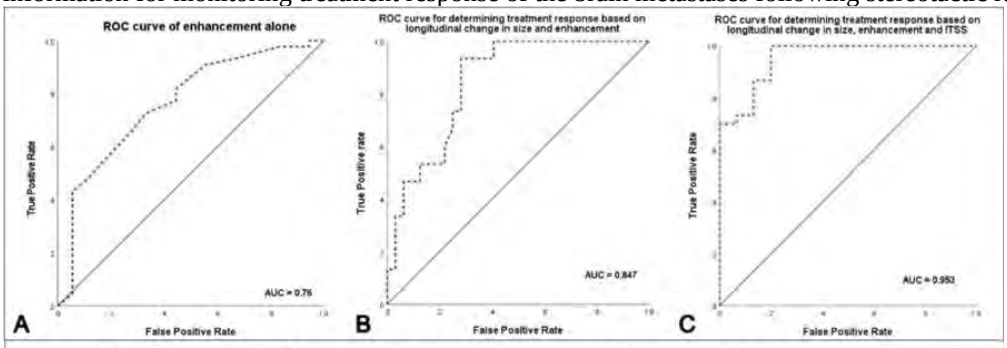

Figure. 2: ROC curves with AUC for predicting the tumor according to the longitudinal change in enhancement (A), longitudinal change in enhancement and size (B), longitudinal change in enhancement, size and ITSS.

(Filename: TCT_141_HighresolutionSWI.jpg)

176

Hypoperfusion on CTP in "Stroke Alert": Seizure Versus Acute Infarct: Clues in the Mediation List.

C Sidani[1], K Abrams[2], D Pinto[3]

[1]RASF, Miami, FL, [2]RASF. Baptist Health South florida, Miami, FL, [3]Jackson Memorial Hospital, Miller school of medicine, Miami, FL

Purpose

Stroke is a major cause of morbidity and mortality in the United States and worldwide. On average, every 40 seconds someone in the US suffers a stroke. Advancements in neuroimaging have made stroke diagnosis rapid, reliable, and cost-effective. The combination of non contrast enhanced CT of the brain (NECT), CT angiography (CTA) and CT perfusion (CTP) has become the preferred imaging studies at most stroke centers. The studies allow the exclusion of hemorrhage, diagnosis of several stroke mimics, exclusion of large vessel occlusion as well as identification of core infarct and salvageable tissue or penumbra. Of the many stroke mimics, seizure represents a major challenge. Clinically, nonconvulsive seizures, nonconvulsive status epilepticus, and postictal paralysis present similarly to acute stroke. On CTP however, majority of cases exhibit opposing perfusion patterns with infarct demonstrating hypoperfusion and seizure demonstrating hyperperfusion allowing for confident differentiation. However, when seizure cases present with a hypoperfusion pattern differentiating it from stroke becomes more challenging. We present Six clinically and/or by electroencephalogram (EEG) proven seizure cases that presented as "stroke alert" and demonstrated hypoperfusion on CTP. A review of the patients' charts revealed they had all received Propofol during or with in 2 hours from CTP. A review of the literature regarding possible effects of Propofol are discussed. Knowledge of the medication administered before CTP can help differentiate the etiology of a hypoperfusion on CTP

Materials and Methods

6 "stroke alert" cases with hypoperfusion pattern on CTP. All clinically and /EEG proven Seizure. All patients had received Propofol during or with in 2 hours from CTP

Results

Hypoperfusion on CTP is commonly caused by acute infarct. In the cases presented, seizure patients who received Propofol during or with in 2 hours from CTP had a similar CTP pattern. Knowledge of mediation administered can add confidence to making the diagnosis. Other differentiating characteristics include involvement of the temporal lobe in middle and posterior cerebral artery distributions, absence of occlusion on CTA, and follow up MRI without restricted diffusion matching the CTP hypoperfusion, all of which support the diagnosis of seizure

Conclusions

N/A

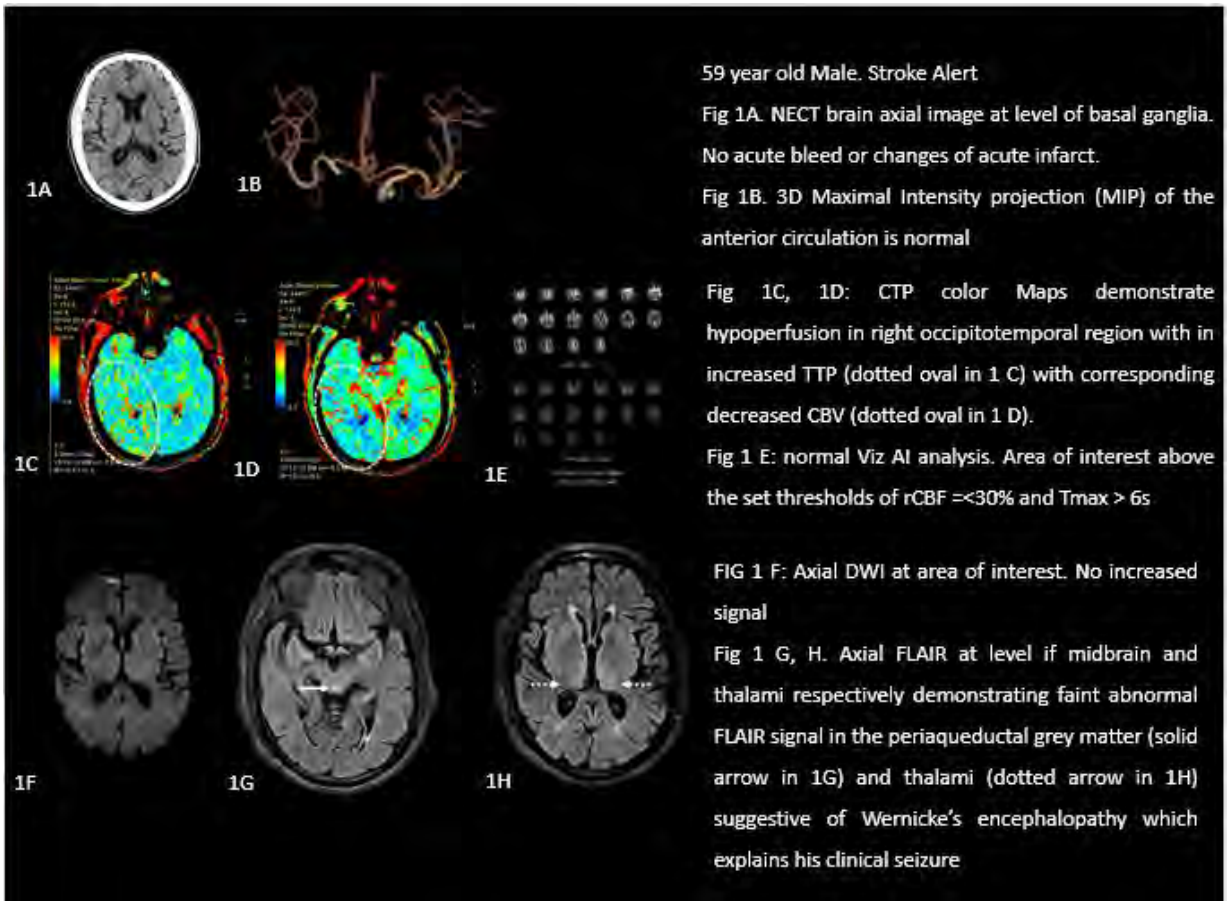

(Filename: TCT_176_CaASNRsubmission.JPG)

1463

Imaging Characteristics of Adult H3 K27M-Altered Diffuse Midline Gliomas.

M Kushdilian[1], K Salzman[1], T Richards[1], J Mendez[1], L Shah[2]
[1]University of Utah, Salt Lake City, UT, [2]University of Utah, Salt Lake Cty, UT

Purpose

Diffuse midline gliomas (DMG) with a K27M mutation of histone 3 (H3 K27M) is a distinct grade 4 tumor entity termed "H3 K27M-altered" in the latest consensus statement published by the World Health Organization in 2021. This glioma subset portends a poor prognosis in children, but outcomes in adults are less clear. Imaging characteristics of this tumor entity have been reported in the radiology literature mostly in pediatric patients but only scarcely described in adults. Therefore the aim of this study is to describe the MR imaging characteristics in adult H3 K27M-altered DMGs.

Materials and Methods

The MR imaging features of H3 K27M-altered DMG in adults were evaluated on the basis of location, signal characteristics, enhancement pattern, diffusivity, and leptomeningeal spread in this retrospective case series.

Results

Eight adult (>18 years) patients with pathologically-proven H3 K27M-altered DMGs were identified. The average age at presentation was 35 years (range 19-70 years) with a mean overall survival of 13 months (range 2-31 months). Tumors were located in or near midline structures including the midbrain/pons; 50% (n=4), thalamus; 38% (n=3), and thoracic spinal cord; 13% (n=1). Enhancement was heterogeneous or peripheral; 63% (n=5), or faint to no none; 38% (n=3). All tumors were hyperintense on T2-weighted sequences with variable patterns of surrounding T2/FLAIR hyperintensity. The majority; 75% (n=6) of these tumors were isointense or hyperintense relative to normal gray matter on ADC sequences with a mean value of 961 x 10−6 mm2/s (range 834-1200 x 10−6 mm2/s). Cystic or necrotic changes were relatively common; 75% (n=6). Leptomeningeal dissemination at the time of diagnosis and subsequent follow-up was relatively common compared to H3-wildtype gliomas; 38% (n=3).

Conclusions

In our series of adult H3 K27M-altered DMGs there is a wide range of MR imaging features. These include a relatively high prevalence of leptomeningeal dissemination and cystic/necrotic changes and relatively lower prevalence of tumor enhancement, findings comparable to those reported in pediatric patients. Neuroradiologists should become familiar with the spectrum of appearance of this tumor entity in adults to aid in diagnosis and serial follow-up imaging.

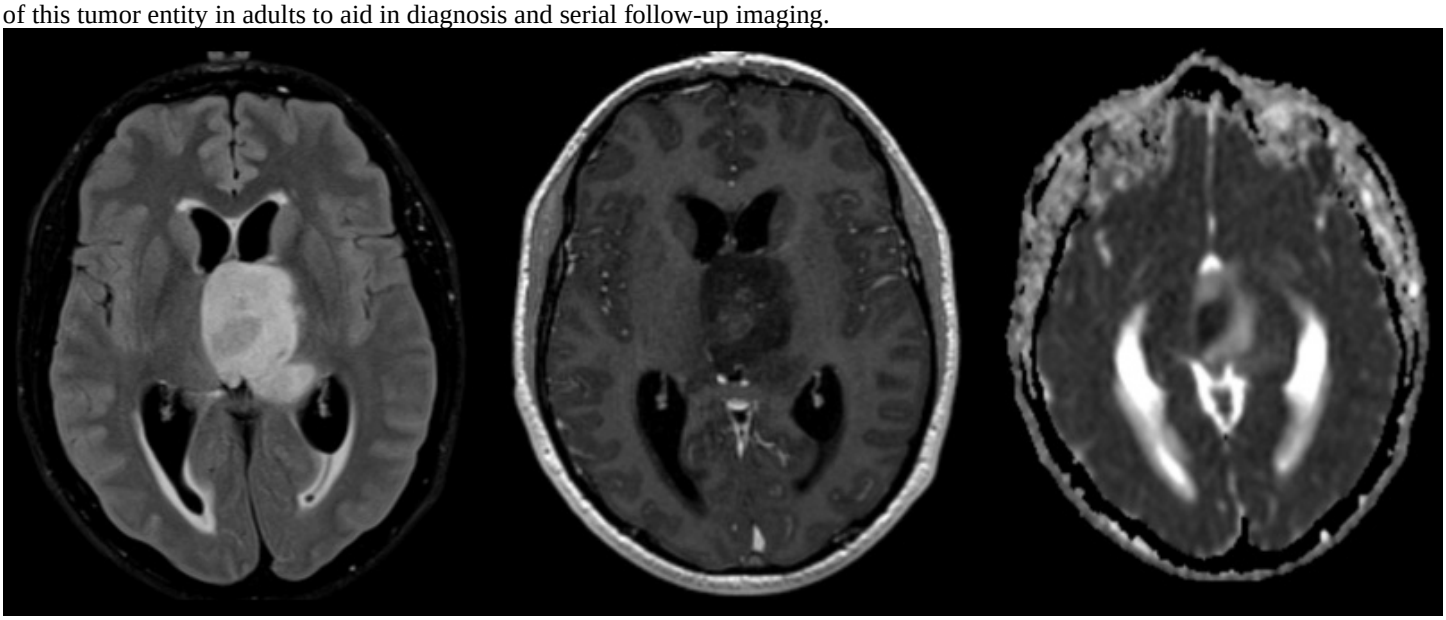

(Filename: TCT_1463_H3K27M---2.jpg)

842

Imaging grading system to predict HPV status in Head and Neck Squamous cell carcinoma

V Andreu Arasa[1], O Sakai[2]
[1]Boston Medical Center, Boston, MA, [2]Boston Medical Center, Boston University School of Medicine, Boston, MA

Purpose

Human papillomavirus (HPV) infection is a known risk factor for head and neck squamous cell carcinoma (HNSCC). HPV-positive oropharyngeal SCC (HPV+OPSCC) has been recognized as a clinically and biologically distinct entity from HPV-negative OPSCC (HPV-OPSCC), associated with younger age and higher response rates after induction chemotherapy or chemoradiation. The diagnostic approach for HPV+SCC includes tissue sampling followed by p16 immunohistochemistry testing through high-cost invasive procedures, leaving imaging just as a staging tool. Texture analysis has shown the potential to differentiate HPV+SCC from HPV-SCC. However, there is no systemic image-based method to determine HPV status in HNSCC, although some imaging findings

suggest HPV+OPSCC regarding the primary lesion and lymph nodes. Recently, plasma circulating tumor HPV DNA has been proven to be a sensitive and specific biomarker in HPV+SCC

Materials and Methods

Two ABR-certified radiologists with 20 and 5 years of experience in head and neck imaging reviewed the staging imaging studies of 133 patients with biopsy-proven HNSCC. Readers were blinded to the age or gender of the patient, location of the tumor, and HPV status. Imaging characteristics were evaluated qualitatively in both the primary tumor and suspected nodal metastasis. For the primary tumor, the following features were analyzed: Location, size, homogeneity, necrosis, margins, and adjacent muscular involvement. The size, margins, cystic/necrotic changes, suspected extracapsular extension, conglomerate appearance, and nodal metastasis/primary tumor size ratio were also evaluated on the suspicious lymph nodes. Qualitative imaging characteristic were graded and the readers decided on a cutoff value. Interobserver disagreements were resolved by discussion.

Results

The staging imaging studies (130 neck CTs and 3 MRIs) of 133 biopsy-proven HNSCC patients (66 HPV+ and 67 HPV-) were reviewed. Based on the proposed grading system, 52 out of 67 HPV+SCC and 57 out of 67 HPV-SCC resulted in true positive and true negative, respectively. Sensitivity and specificity were 78% and 85%, respectively. The positive predictive value was 83%, and the negative predictive value was 80%.

Conclusions

Certain imaging findings may suggest HPV+ in HNSCC. We propose a grading system with high specificity and positive predictive value that may permit clinicians, with additional clinical information such as plasma circulating HPV DNA, decide adequate management.

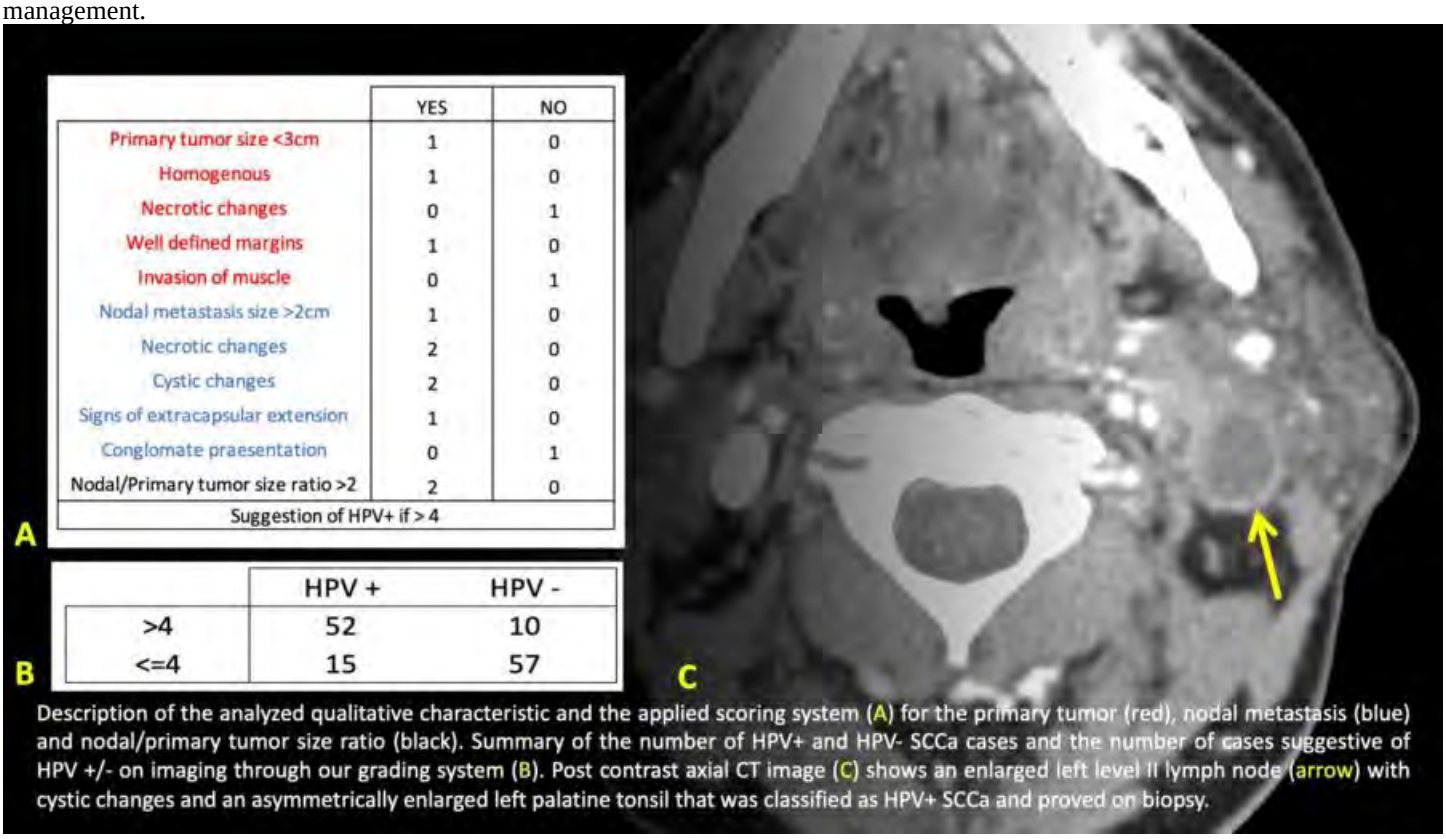

	YES	NO
Primary tumor size <3cm	1	0
Homogenous	1	0
Necrotic changes	0	1
Well defined margins	1	0
Invasion of muscle	0	1
Nodal metastasis size >2cm	1	0
Necrotic changes	2	0
Cystic changes	2	0
Signs of extracapsular extension	1	0
Conglomate praesentation	0	1
Nodal/Primary tumor size ratio >2	2	0
Suggestion of HPV+ if > 4		

	HPV +	HPV -
>4	52	10
<=4	15	57

Description of the analyzed qualitative characteristic and the applied scoring system (A) for the primary tumor (red), nodal metastasis (blue) and nodal/primary tumor size ratio (black). Summary of the number of HPV+ and HPV- SCCa cases and the number of cases suggestive of HPV +/- on imaging through our grading system (B). Post contrast axial CT image (C) shows an enlarged left level II lymph node (arrow) with cystic changes and an asymmetrically enlarged left palatine tonsil that was classified as HPV+ SCCa and proved on biopsy.

(Filename: TCT_842_ASNR22_ca.jpg)

616

Impact of the Woven EndoBridge (intrasaccular flow disruptor) device placement on the occlusion rates

S Ghozy[1], A Al-Abdulghani[2], Y DING[3], D Dai[1], J Arturo Larco[1], L Savastano[1], W Brinjikji[1], D Kallmes[1], R Kadirvel[1]

[1]Mayo Clinic, Rochester, MN, [2]Michigan State University Clinical Center, East Lansing, MI, East Lansing, MI, [3]MAYO CLINIC - ROCHESTER, ROCHESTER, MN

Purpose

To assess the role of an intrasaccular flow disruption device placement in relation to parent artery in the aneurysm occlusion rates.

Materials and Methods

Elastase-induced aneurysms were created in New Zealand white rabbits and treated with appropriately sized intrasaccular flow disruptor (Woven EndoBridge device. Microvention, CA). Aneurysm creation procedures were performed as previously described [1]. Aneurysms were treated at least three weeks after aneurysm creation [2]. Two investigators independently and retrospectively examined angiographic images to grade the device placement either placed high or low in the aneurysm relative to the parent artery,

and angiographic aneurysm occlusion (Figure 1). Angiographic occlusion was graded as complete aneurysm occlusion, complete occlusion with recess filling, aneurysm neck remnants, and aneurysm remnants [3].
Results
Device and aneurysm characteristics A total of 107 aneurysms were treated, with average aneurysm dimensions of 9.3±2.1 mm, 4.2±1.2 mm, and 3.8±1.1 mm for height, width, and neck, respectively. With a mean follow-up duration of 173.3±141.9 days, 35 devices were placed high and the other 72 were low-placed. There were no differenced in aneyrysm dimensions in the high-placed vs. low-plcaed groups, including the height (9.2±2.4 vs. 9.3±1.9; p= 0.8012), width (4.4±1.7 vs. 4.1±0.9; p= 0.266) and neck (3.9±1.1 vs. 3.8±1.1; p= 0.583) measurements. Occlusion rates The complete occlusion rate was higher in the low-placed intrasaccular flow disruptors (n= 29) when compared to the highly placed ones (n= 5) (40.3% vs. 14.3%; p= 0.013). On further investigation of different predictors for the complete occlusion (using Cox regression analyses), low-placed intrasaccular flow disruptors had three-times higher odds of subsequent occlusion as compared to the high placed ones (HR= 3.34; 95% CI= 1.29-8.64; p= 0.013), which was even more evident in the multivariable model (HR= 8.19; 95% CI= 2.64-25.43; p< 0.001).
Conclusions
The low placement of the intrasaccular flow disruptors is a potential predictor for higher long-term occlusion rates. To a lesser extent, device width and type may play a role and should be explored further. Until healing mechanisms are fully characterized and understood, progress will be substantially impeded. The uncertainty of the exact mechanism(s) associated with flow diverters has myriad consequences, including but not limited to hindering the development of next-generation devices from improving aneurysm healing.

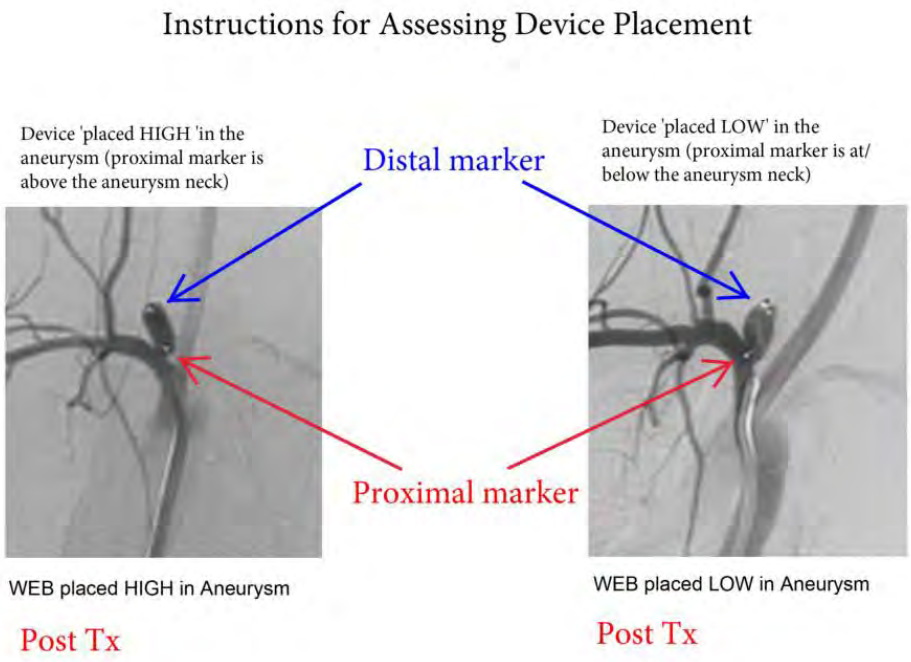

(Filename: TCT_616_Figure1.jpg)

1109
Improved heavily T2 weighted 3D-FLAIR MRI of the inner ear with deep learning-based reconstruction
H Lee[1], Y KANG[1], J Lee[2], S Banerjee[3]
[1]Inje University Haeundae Paik Hospital, Busan, Korea, Republic of, [2]GE Healthcare, Seoul, Korea, Republic of, [3]GE Healthcare, Menlo Park, CA

Purpose
Heavily T2-weighted volumetric fluid attenuated inversion recovery magnetic resonance imaging (hT2-w 3D-FLAIR MRI) is being used for evaluation of hearing loss, endolympahatic hydrops, or the glymphatic system. For hearing loss, this technique, has been shown to be more sensitive than regular contrast FLAIR (1), and has been shown to have prognostic value (2). However, this acquisition due to it's heavily T2-weighting and long TE. and high resolution required by small dimensions of the targeted structures, has high noise levels. In this study, we compared signal to noise levels between hT2-w 3D-FLAIR MRI reconstructed with conventional pipeline with and without image filter, and a recently introduced deep learning based method (DLRecon).
Materials and Methods
39 cases who underwent inner ear MRI protocol for evaluation of sensorineural hearing loss in which DLRecon for the post-contrast hT2-w 3D-FLAIR MRI was available, were included. Scans were acquired using a 3T MRI (SIGNA™ Architect, GE Healthcare, Waukesha, USA), with a 48-channel head coil, 7 minutes after a single intravenous dose of gadobutrol (Gadobrix, Taejoon Pharm, Seoul, Korea). The typical image parameters were similar to those propsed by Nahmani et al. (3) and the scan time was about 8

minutes. Three sets of images were generated: one with conventional reconstruction without any filters (original), one with image filter (G: noise reduction; filtered), and the other with a 2D based DLRecon algorithm with denoising and sharpening properties, that was retrained for 3D reconstruction (4) (DLR). Noise maps for each image sets were generated based on a hybrid Discrete Wavelet Transform (DWT) and edge information removal based algorithm described elsewhere (5). A neuroradiologist with 7 years of experience drew ROIs at brainstem, subcutaneous fat, and background air at the mid-modiolar level, and cochlea at area of highest perceived signal. Signal or contrast to noise levels were calculated by the dividing the mean signal of the fat or cochlear ROI or difference of brainstem and cochlea signal, by the standard deviation of the air ROI (SNR_f, SNR_c, CNR) or the mean value measured from the brainstem ROI on the noise map (SNR_f_nm, SNR_c_nm, CNR_nm), respectively.

Results

The values for the DLR set were significantly higher than the original and filtered images sets (P <.001; Table 1; Figure 1).

Conclusions

Use of DLRecon can significantly improve signal and contrast to noise levels for inner ear MRI using hT2-w 3D-FLAIR.

Figure 1. Contrast enhanced heavily T2-weighted FLAIR images of a 35-year-old patient with right side sensorineural hearing loss. The image with DLR (C) shows decreased noise as compared to original (A) and filtered (B) images. The high signal of the right side cochlea is visualized (arrows).

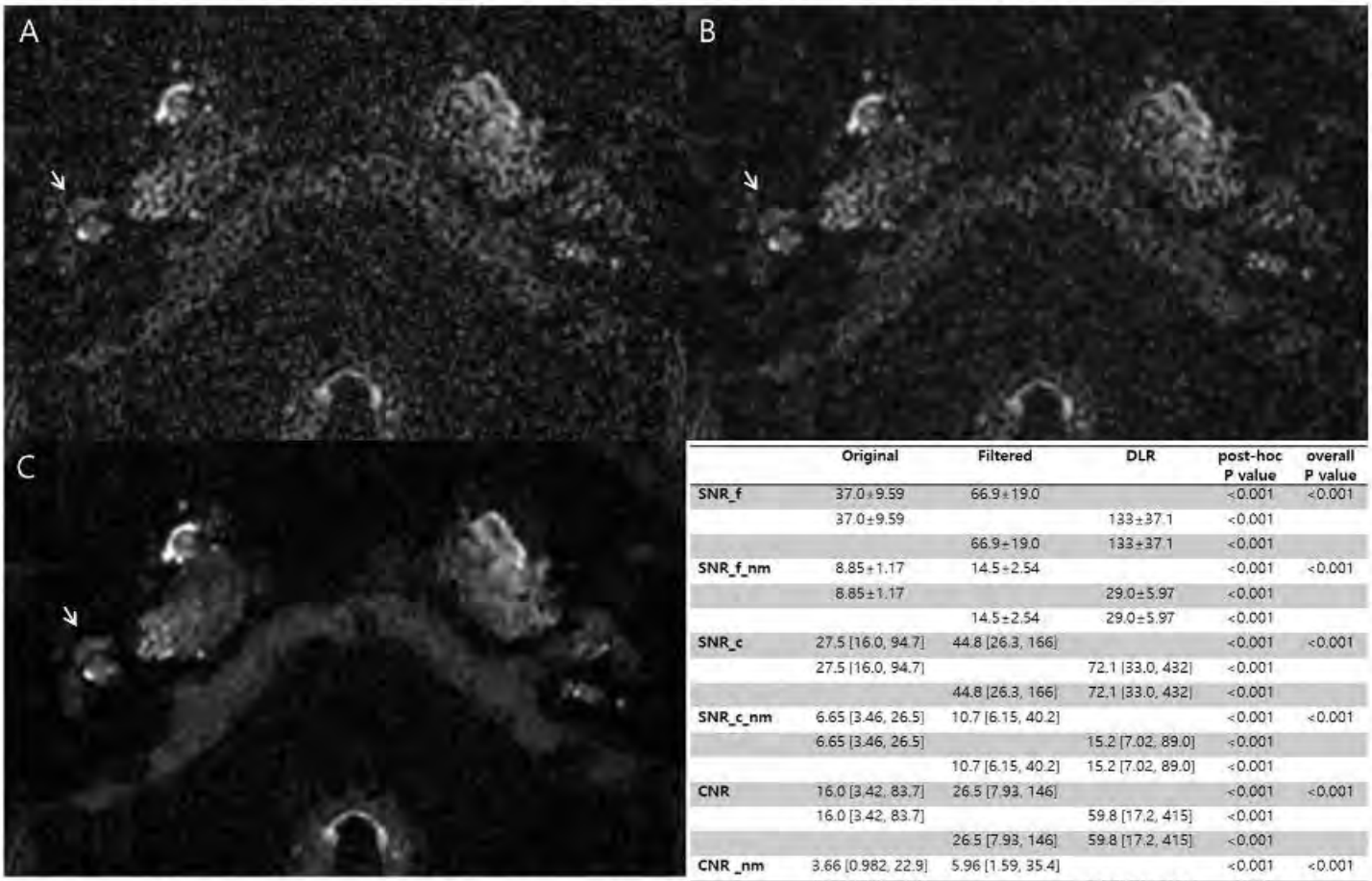

Table 1. Comparison of signal and contrast to noise levels for the three image sets

	Original	Filtered	DLR	post-hoc P value	overall P value
SNR_f	37.0±9.59	66.9±19.0		<0.001	<0.001
	37.0±9.59		133±37.1	<0.001	
		66.9±19.0	133±37.1	<0.001	
SNR_f_nm	8.85±1.17	14.5±2.54		<0.001	<0.001
	8.85±1.17		29.0±5.97	<0.001	
		14.5±2.54	29.0±5.97	<0.001	
SNR_c	27.5 [16.0, 94.7]	44.8 [26.3, 166]		<0.001	<0.001
	27.5 [16.0, 94.7]		72.1 [33.0, 432]	<0.001	
		44.8 [26.3, 166]	72.1 [33.0, 432]	<0.001	
SNR_c_nm	6.65 [3.46, 26.5]	10.7 [6.15, 40.2]		<0.001	<0.001
	6.65 [3.46, 26.5]		15.2 [7.02, 89.0]	<0.001	
		10.7 [6.15, 40.2]	15.2 [7.02, 89.0]	<0.001	
CNR	16.0 [3.42, 83.7]	26.5 [7.93, 146]		<0.001	<0.001
	16.0 [3.42, 83.7]		59.8 [17.2, 415]	<0.001	
		26.5 [7.93, 146]	59.8 [17.2, 415]	<0.001	
CNR _nm	3.66 [0.982, 22.9]	5.96 [1.59, 35.4]		<0.001	<0.001
	3.66 [0.982, 22.9]		12.4 [2.77, 63.4]	<0.001	
		5.96 [1.59, 35.4]	12.4 [2.77, 63.4]	<0.001	

Repeated measures ANOVA was used for normal data | Friedman test was used for non-normal data | Bonferroni correction for post-hoc analysis | mean±SD ; median [min, max]

(Filename: TCT_1109_figure_table_2.jpg)

1451

Incidence of Semantic Dementia, Especially Right-Sided Variance, in the Setting of Frontotemporal Dementia and Other Dementia Disorders

N Nagornaya[1], D Lehmkuhl[2], T Dhawan[2], A McKinney[3]

[1]Jackson Memorial Hospital/University of Miami, Miami, FL, [2]Jackson Memorial Hospital, Miami, FL, [3]University of Miami & Jackson Memorial Hospital, Miami, FL

Purpose

The semantic dementia (SD) variant of frontotemporal dementia (FTD) may present with progressive primary aphasia (PPA), similar

to the lopogenic and non-fluent agrammatic (NFA) variants. While the anterior temporal lobes (ATL's) typically affect the left side, there are anecdotal reports of the right; the degree of side asymmetry is much more profound in SD variant-FTD as compared to other dementia disorders. The aim of this study is to estimate the relative incidence of ATL atrophy in patients with the SD subtype of FTD, and the frequency of right versus left-sided ATL.

Materials and Methods

Using imaging report search software for the terms "semantic dementia", "frontotemporal dementia", and temporal atrophy", patients were identified for consensus review by two neuroradiologists, with corroboration with clinical notes from neurologists. The retrospective MRI review evaluated 6 regions on each side: the anterior and posterior temporal lobes (ATL, PTL), amygdala, hippocampi, frontal lobes and insula; notably, the degree of "side asymmetry" was also noted.

Results

Of 60 dementia patients with "temporal atrophy" from the report search, 13 SD patients were identified (mean age of 71 years, 69.2% female), 84.6 % of whom had asymmetric ATL atrophy (46.1 % on the right, and 23.1 % with "profound" asymmetry). Of note, 69.2% of SD patients also had insular atrophy. Regarding the other subtypes of FTD having "temporal atrophy", there were 6 with either lopogenic-type PPA or NFA-type FTD (66.6 % having asymmetric ATL atrophy). Other dementias with asymmetric "temporal atrophy" were: Alzheimer's (n=22, 36.6 % with ATL atrophy), vascular dementia (n=7, with 42.8 % with ATL atrophy, mild cognitive impairment (n=8, with 12.5% with ATL atrophy. None of the patients with Lewy Body Disease (n=2) or Parkinson's (n=2) demonstrated asymmetric anterior temporal lobe atrophy. Hence, SD patients made up 40.7% of the study's total patients with ATL atrophy, and 73.3 % of the FTD patients, where the degree of ATL atrophy was more profound than other dementia disorders.

Conclusions

Asymmetric right-sided ATL atrophy may be more common than previously described, being present in at least half of 46.1 % SD cases. While other forms of FTD and other dementia disorders may have ATL atrophy, the degree and "side asymmetry" of ATL atrophy in SD-type of FTD is more profound. Ergo, profound asymmetric ATL atrophy in the setting of dementia should prompt a suspicion of SD.

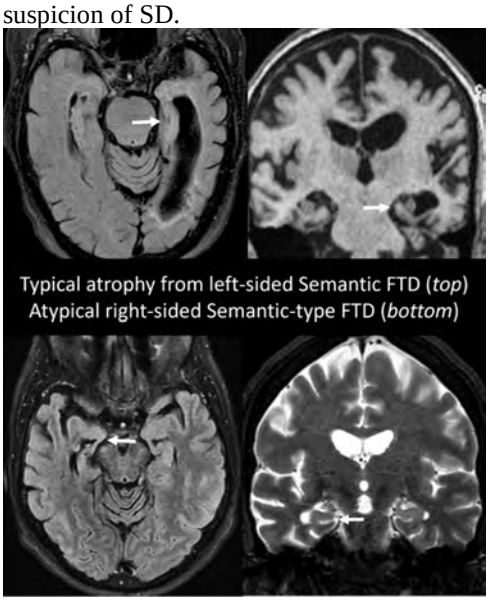

(Filename: TCT_1451_Capture3.GIF)

732

Initial Clinical Experience with Bedside, Point Of Care Non-contrast Brain MRIs

B Yep[1], E Kuoy[2], D Chow[3]

[1]UC Irvine Medical Center, Orange, CA, [2]UC Irvine, Orange, CA, [3]UNIVERSITY OF CALIFORNIA, IRVINE, IRVINE, CA

Purpose

We sought to evaluate the clinical and operational impact of deploying POC-MRI in emergency department (ED) and intensive care unit (ICU) patient settings for bedside neuroimaging.

Materials and Methods

All patients in the ED and ICU at a single academic medical center who received a non-contrast brain MRI between January 1-June 1, 2021 were retrospectively studied. Acquired POC-MRI sequences included axial DWI/ADC, axial T2-weighted FSE, axial T2/FLAIR, and axial T1-weighted FSE. Turnaround time (TAT), study limitations, relevant findings, and potential subsequent fixed MRI findings were recorded for patients who received POC-MRI. The TAT was compared between POC and fixed MRI units during the same time period.

Results

During the study period, POC-MRI represented 36 studies in 35 patients, 36% in the ED and 64% in the ICU. There were 12 POC-MRI studies interpreted as normal/negative, 14 with significant imaging findings, and 10 nondiagnostic for reasons including missing protocols and patient motion. Of 7 POC-MRI exams with subsequent fixed MRI exams, 2 of the fixed MR exams demonstrated

missed versus interval punctate infarctions measuring up to 6 mm not seen on the prior POC-MRI exam. The median TAT of POC-MRI versus fixed MRI studies were 3.4 versus 3.7 hours in the ED, respectively (p = 0.28), and 5.3 versus 11.7 hours in the ICU, respectively (p = 0.04).
Conclusions
Point-of-care MRI can be performed rapidly in the ED and ICU setting. Further studies are needed to determine the sensitivity of POC-MRI in detecting subtle neuropathologies to guide appropriateness of such devices.

1183

Initial investigation of MR Fingerprinting in patients with normal pressure hydrocephalus for prediction of neurosurgical outcomes

T Ejikeme[1], A White[2], J Lin[3], D Ma[4], K Nakamura[5], S Nagel[6], S Jones[6]
[1]Case Western Reserve University School of Medicine, Cleveland, OH, [2]Cleveland Clinic Lerner College of Medicine, Cleveland, OH, [3]Imaging Institute, Cleveland Clinic, Cleveland, OH, [4]Case Western Reserve University, Cleveland, OH, [5]Imaging Institute, Clevelad Clinic, Cleveland, OH, [6]Cleveland Clinic, Cleveland, OH

Purpose
Normal pressure hydrocephalus (NPH) is highly treatable with a shunt catheter in many patients. There remains no reliable non-invasive method to predict clinical response, and current neurosurgical practice is a test large volume CSF drain with inpatient observation1. While CSF flow measurements show potential, these are technically challenging for high clinical reliability and have not been widely adopted. Thus there remains an unmet need for a reliable non-invasive prediction of treatment response in NPH patients. We propose to use magnetic resonance fingerprinting (MRF) to provide whole brain quantified T1 & T2 maps. We hypothesize that treatable vs non-treatable NPH manifests as subtle differences of whole brain water concentration, without focal abnormality, for which MRF is well suited to detect. We aim to correlate clinical outcome of standard NPH treatment with pre- & post-procedure MRF, and thereby develop a novel radiographic measure to predict treatment success.
Materials and Methods
Ten NPH patients scheduled for CSF drain test were scanned with pre- & post- MRF. Standard clinical assessments including 10m walking test were obtained. MRF was a 20 slice 2D WIP, and a volumetric T1w was also obtained. MRF and volumetric maps were linearly coregistered. Brain and ventricular volumes were obtained from FreeSurfer. Custom software using IDL computed T1 & T2 histograms in white matter and grey matter. Coregistered maps assessed subtle changes pre- and post-treatment. Standard NPH metrics such as Evan's ratio, Callosal angle, and DESH were obtained. The EMR provided clinical presentation, response, and comorbidities.
Results
Patients less responsive to large volume CSF drain showed larger regions of white matter with abnormally increased T1 & T2 times, shown by sample white matter map from one patient (Fig A) and T1 histograms of all ten patients (Fig B). Abnormal mean T1 & T2 times in white matter2 also correlated to impaired clinical measurements as measured by improved walking tests and long term clinical response (Fig C). Ventricle volumes reduced by 3.0% pre- vs post- shunt, while brain volumes, T1 & T2 distributions showed insignificant change.
Conclusions
Mean tissue T1 and T2 values using MRF in patients with NPH show a correlation with clinical metrics and offers promise as a non-invasive technique to predict neurosurgical success of large volume drains and subsequent catheters.

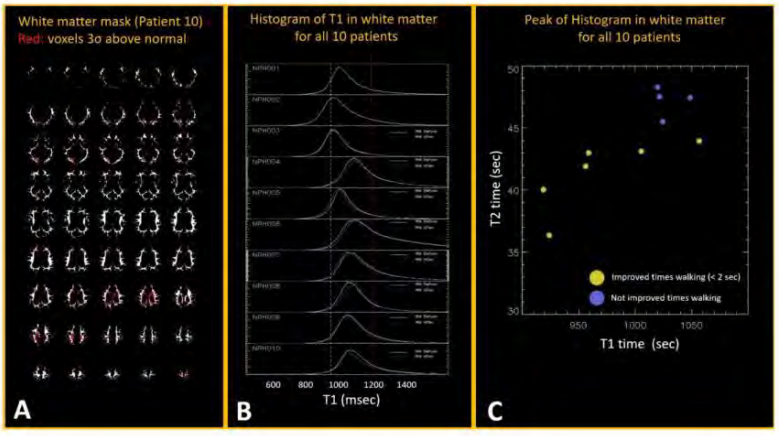

Figure. A: Overlay red shows voxels with T1 time above 3σ above mean in normal individuals4. B: Histograms of T1 times in WM for all 10 pts. Vertical white line is mean T1 and red is 3σ above mean from normal. C: Scatter plot for all patients of peak T1 and T2, with color indicating clinical response (reduced walking time of >2 seconds)

(Filename: TCT_1183_ASNRFigure_Final.jpg)

858

Intermethod validation of brain volumetry estimation : reliability of volume and normative percentile of clinically available brain volumetry softwares

S Jo[1], S Lee[2], E Khil[3], H Song[4]

[1]Hallym university Dongtan sacred hospital, Hwaseong-si, South Korea, [2]Dongtan Sacred Heart Hospital, Hallym University Medical Center, Hwaseong-si, South Korea, [3]Hallym University Dongtan Sacred Heart Hospital, Hwaseong-si, Gyeonggi-do, [4]Seoul National University Hospital, Seoul, Korea, Republic of

Purpose

To compare two clinically available MR volumetry software, NeuroQuant® (NQ) and Deep brain® (DB), using freesurfer as a reference standard and examine the inter-method reliabilities and differences between them.

Materials and Methods

This study included 145 subjects (age range, 51–88 years; mean age, 69.8 years), comprising 48 normal healthy subjects, 50 patients with mild cognitive impairment, and 47 patients with Alzheimer's disease. Magnetic resonance imaging scans were analyzed with DB, NQ and Freesurfer. Mean differences of regional volume and normative percentile values were compared with the paired t test. Inter-method reliability was evaluated with Pearson's correlation coefficients and intraclass correlation coefficients (ICCs). Effect sizes were also computed to document the standardized mean differences.

Results

The paired t test revealed significant volume differences in most of brain regions including cortical gray matter, hippocampus, and cerebral white matter between the DB and NQ. Nonetheless, inter-method measurements between DB and NQ showed good to excellent reliability ($0.71 < r < 0.99$, $0.83 < ICC < 0.99$) except for the pallidum, which showed moderate to substantial reliability (left: ICC = 0.56; right: ICC = 0.69). For the measurements of effect size, volume differences were large in most regions ($0.19 < r < 4.92$). The effect size was the largest in the pallidum and smallest in the thalamus. In terms of normative percentile measurement of two softwares, the paired t test showed significant normative percentile difference in most of brain regions except for caudate nucleus and putamen between the two softwares. In addition, inter-method measurements of normative percentile between DB and NQ showed wide variability ($0.12 < r < 0.67$, $0.21 < ICC < 0.80$)

Conclusions

Comparisons between DB and NQ showed significantly different volume measurements and normative percentile. Athough they showed good to excellent inter-method reliability in volumetric measurements for most of brain regions, there were poor to moderate reliability in normative percentile measurements for lots of brain regions. These differences should be taken into account when clinicians apply the values obtained from these two softwares to clinical practice.

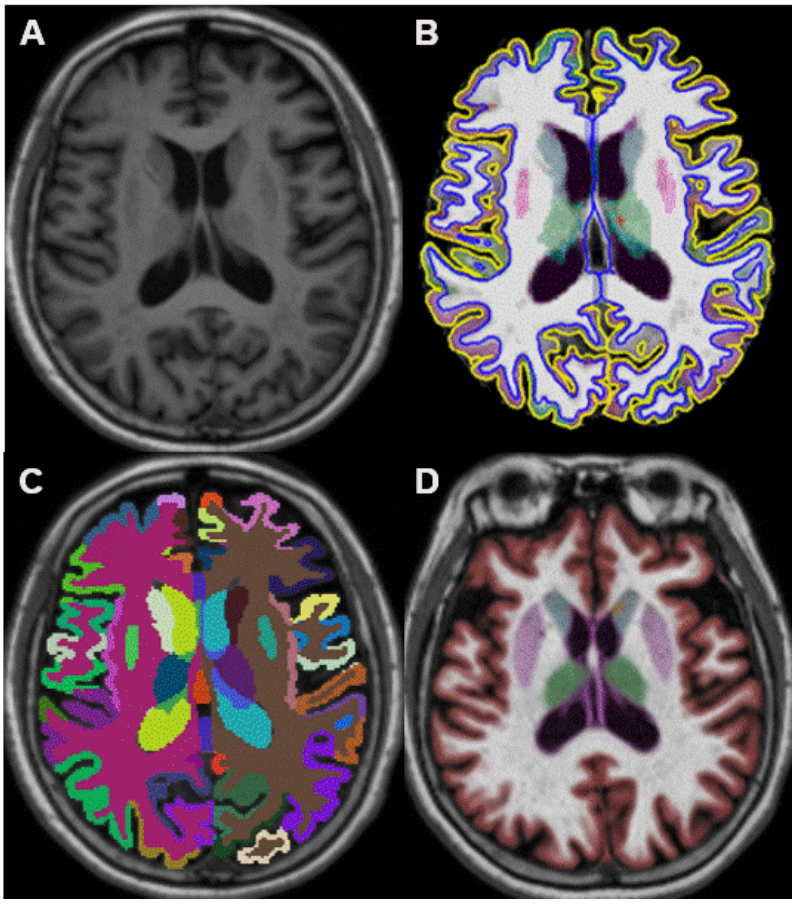

(Filename: TCT_858_Fig1axial4images.gif)

245

Investigation on the effectiveness of artificial intelligence(AI)-aided diagnostic systems as a second reader to assist different experience radiologists in the prediction of hematoma expansion (HE)

D Chen[1], W Wei[1], n dong[2], J Gu[3], Y Li[2]

[1]Dalian Municipal Central Hospital Affiliated to Dalian Medical University, Dalian, Liaoning, [2]Biomind Research Center Affiliated to Tiantan hospital, Beijing, Beijing, [3]Biomind Research Center Affiliated to Tiantan hospital, xi'an, shaanxi

Purpose

To evaluate the effect of AI as a second-reader on radiologists with different experiences in predicting hematoma expansion (HE).

Materials and Methods

Thirty-five non-contrast CT (NCCT) images of Intracranial Hemorrhage (ICH) patients were retrospectively collected from October/01/2020 to September/30/2021. Each participant performed a follow-up NCCT scan within 24 hours after the initial scan. Hematoma expansion was preliminarily determined if the hematoma size increase was more than 6 ml or 33%, and an experienced neuroradiologist reviewed the result to confirm the final ground truth of hematoma expansion. The initial CT scan images were evaluated by a ten-year-experienced senior radiologist and a three-year-experienced junior radiologist independently. Both radiologists interpreted images with the assistance of a commercial AI software (BioMind 3.0.0) as a second reader after a wash-out period of 14 days, respectively. The corresponding sensitivity for hematoma expansion predictions was calculated.

Results

Among thirty-five ICH patients, six patients had hematoma expansion and twenty-nine patients had no hematoma expansion. There were significant differences between the diagnostic sensitivity of junior radiologist and the junior radiologist assisted by AI (p=0.012, sensitivity: 16.7% vs 83.3%), and between the diagnostic sensitivity of senior radiologist and the senior radiologist assisted by AI (p=0.034, sensitivity: 66.7% vs 100%). Both the senior and junior radiologists dramatically improve hematoma expansion prediction sensitivity with the assistance of AI as a second reader compared with independent reading.

Conclusions

Radiologists assisted by AI as a second reader could tremendously improve the prediction sensitivity of hematoma expansion, the improved diagnosis may potentially spot more hematoma expansions for subsequent treatment and improved patient outcomes.

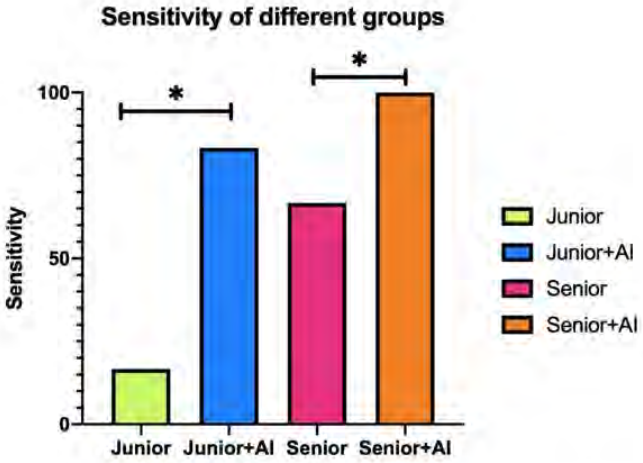

Figure 1 The prediction sensitivity of hematoma expansion for each of the four groups (Junior radiologist, Junior radiologist assisted by AI, Senior radiologist, Senior radiologist assisted by AI) is displayed as a bar chart. McNemar test was used and there were significant differences between the diagnostic sensitivity of junior radiologist and the junior radiologsit assisted by AI, and between the diagnostic sensitivity of senior radiologist and the senior radiologsit assisted by AI, *p <0.05.

(Filename: TCT_245_Figure1.jpg)

1205

Is Conservative Treatment Possible in Thoracolumbar Injury Classification and Severity (TLICS) Score 4 or 5?: Analysis of Initial Radiological Findings and Clinical Risk Factors For Treatment Failure

E Khil[1], S Lee[1], I Choi[1], K Lee[1], S Jo[1]

[1]Hallym University Dongtan Sacred Heart Hospital, Hwaseong-si, Gyeonggi-do

Purpose

To evaluate the outcome of conservative treatment in patients with thoracolumbar injury classification and severity (TLICS) score 4 and 5, and to analyze initial radiological findings and clinical risk factors of treatment failure.

Materials and Methods

This retrospective study evaluated patients with thoracolumbar fractures with a TLICS score of 4, 5 measured on MRI, from January

2017 to December 2020. Of them, patients with conservative treatment were divided into group 1 (treatment success) and 2 (treatment failure), based on their initial and 6-month follow-up outcomes; Treatment failure was defined as conversion to a surgical procedure or an increase of over 10 degrees in the 6-month Cobb angle (CA). For group 1 and 2, we compared clinical data, initial radiological findings included three kyphosis measurements (CA, Gardner angle, Sagittal index [SI]), anterior and posterior wall height, and central canal compromise (CC). Interobserver agreement between two reviewers was analyzed using intra-class correlation coefficient. The risk factors for treatment failure such as age, sex, and osteoporosis were analyzed by logistic regression.
Results
A total of 84 patients was included in the conservative treatment group (mean age, 60.25±15.53; range 22-85; 41 men), 57 group 1 and 27 group 2. More women, older age, and lower bone mass density were included in group 2 (p= 0.001-0.004). For the initial radiological findings, CA, SI, and CC were higher (p=0.001-0.042 or <0.001; these cut-off values: 18.33, 12.96, 8.0%, respectively), and anterior wall height was lower (p=0.001) in group 2 with good to excellent interobserver agreement values (0.72-0.99, p<0.001). Additionally, osteoporosis was found to be a significant risk factor (Odd ratio=5.19, p=0.007).
Conclusions
In patients with a TLICS score of 4 and 5, the conservative treatment failure group showed poor initial radiological findings, more women, older age, and osteoporosis. In addition, osteoporosis was a significant risk factor for treatment failure. A TLICS score of 4 or 5, is an important criterion to determine surgery, but it would be helpful to consider initial radiological findings and clinical risk factors in deciding conservative treatment.

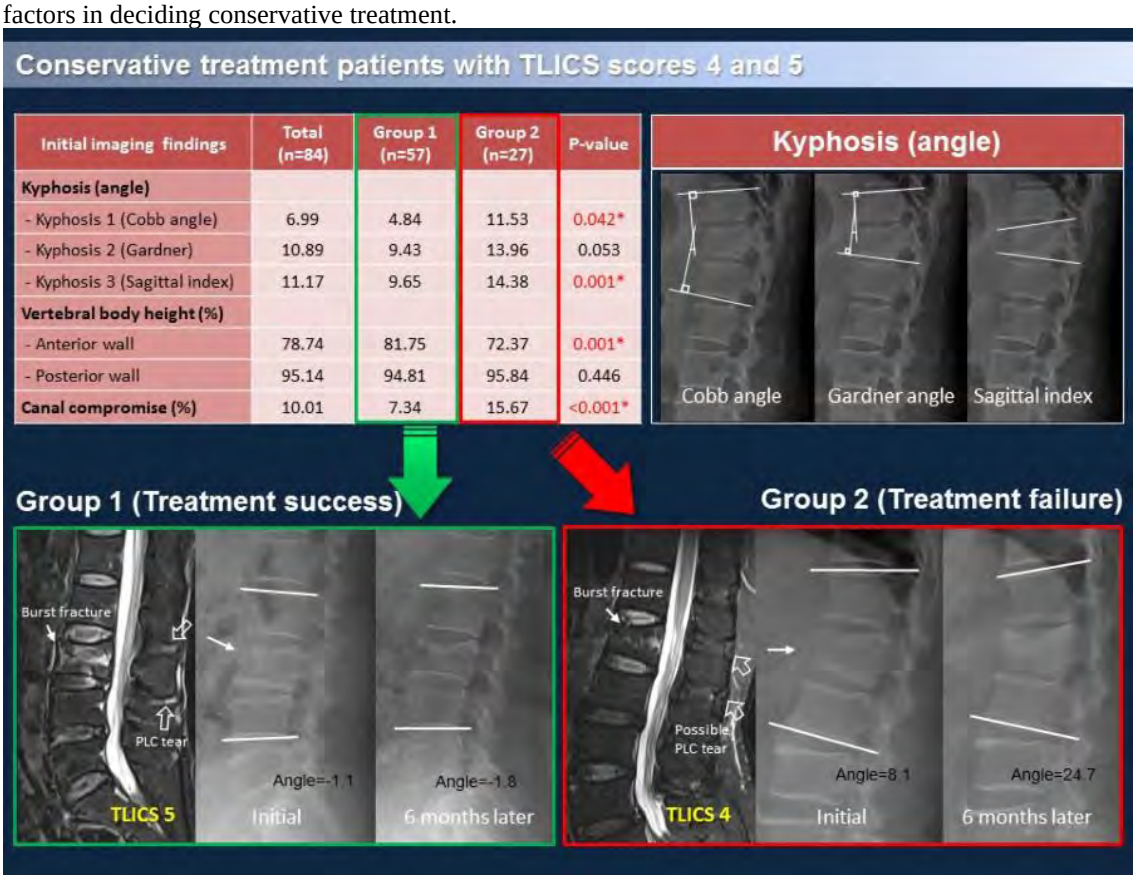

(Filename: TCT_1205_ASNR2022TLICSFigures.jpg)

1488
Is Normal Cerebral Perfusion Symmetric between Both Cerebral Hemispheres? : Effects of Carotid Artery Configuration and Heart Function
H Seo[1]
[1]*Eulji Medical Center, Uijeongbu-si, Gyeonggi-do*

Purpose
Brain perfusion MRI has been interpreted with the assumption that normal perfusion parameters are symmetric in both cerebral hemispheres. However, significant perfusion asymmetry throughout bilateral cerebral hemispheres has been reported on SPECT or PET in healthy humans. The purpose of this study is to identify the asymmetric cerebral perfusion in normal persons and the contributing factors to hemodynamic asymmetry on dynamic susceptibility contrast (DSC)-MRI.
Materials and Methods
This retrospective study included total 171 patients (82 males; mean age=59.59±13.49 years) who have neither carotid artery stenosis nor abnormality related to the pathologic perfusion. Cerebral DSC-MRI and neck MR angiography were acquired at 3T. TTP (time-to-peak), Tmax (time-to-maximum), CBF (cerebral blood flow), and CBV (cerebral blood volume)-were measured on DSC-MRI with

NordicICE. The difference values (Δ) of them between the right and left hemispheres were obtained at 5 pairs of region of interests. ΔCommon and internal carotid artery (CCA+ICA) length, diameter and tortuosity were measured on MR angiography. Cardiac functions were measured on echocardiography within 6 months from MR scan. Paired t-test and univariable and stepwise multivariable regression analysis models were used to assess interhemispheric perfusion asymmetry and its correlation with the variables of carotid artery configurations and cardiac function after adjusting for demographic factors.

Results

All perfusion parameters showed statistically interhemispheric asymmetry ($p<0.01$, respectively) (Table). TTP and Tmax were delayed, and CBF and CBV were decreased in right cerebral hemisphere. Independent predictors of ΔTTP were age, hypertension, ΔCCA+ICA length, ΔCCA diameter, and tissue Doppler imaging peak early diastolic velocity ($p<0.05$, respectively). Early diastolic velocity on tissue doppler was associated with ΔTmax ($p<0.01$). ΔCBF ratio and ΔCBV ratio did not have an associated covariate ($p>0.05$, respectively).

Conclusions

Interhemispheric asymmetry can be found in perfusion parameters on DSC-MRI without carotid artery stenosis. The asymmetry of TTP and Tmax tend to be related with carotid artery configuration, cardiac function, old age or hypertension.

Table. Measured variables and perfusion parameter

	Variables	Right	Left	Δ (Right - left)	*p*-value
Carotid artery configuration	CCA length (mm)	137.52±14.19[a]	125.78±12.04	11.74±9.60	<.01[b]
	CCA tortuosity	1.16±0.12	1.07±0.07	0.09±0.09	<.01[b]
	CCA diameter (mm)	6.23±0.90	6.22±1.00	0.01±0.79	0.93
	ICA length (mm)	150.67±13.56	149.11±13.69	1.56±7.73	<.01[b]
	ICA tortuosity	1.39±0.12	1.39±0.12	0.00±0.07	0.45
	ICA diameter (mm)	3.56±0.64	3.67±0.63	-0.1±0.67	0.03*
	CCA+ICA length (mm)	288.19±17.53	274.89±17.68	13.30±10.46	<.01[b]
	CCA+ICA tortuosity	1.27±0.09	1.22±0.07	0.05±0.05	<.01[b]
	Carotid output	1.16±0.17	1.17±0.18	-0.01±0.20	<.01[b]
	ICA-CCA angle (°)	25.33±13.36	31.08±14.23	-5.75±14.49	<.01[b]
Cardiac function	LVEF (%)	62.06±5.90			
	TDI Sa (cm/s)	7.44±1.64			
	TDI Ea (cm/s)	7.03±2.58			
Perfusion parameter	TTP (sec)	19.83±3.18	19.67±3.27	0.16±0.27 (0.12, 0.20)[c]	<.01[b]
	Tmax (sec)	0.23±0.36	0.15±0.26	0.08±0.17 (0.56, 0.11)[c]	<.01[b]
	rCBF (relative units)	19.54±29.21	20.25±30.00	-0.71±2.92 (-1.15, -0.27)[c]	<.01[b]
	rCBV (relative units)	293.94±79.24	308.99±81.08	-15.04±29.57 (-19.51, -10.58)[c]	<.01[b]

[a] Data are mean ± standard deviation.

[b] Statistically significant when $p<0.05$.

[c] 95% confidence interval of the difference.

Abbreviations: LVEF = Left ventricular ejection fraction; TDI = tissue Doppler imaging; Sa = peak systolic velocity; Ea = peak early diastolic velocity.

(Filename: TCT_1488_Table.JPG)

682

Limited Utility of Adding 3T Cervical Spinal Cord MRI to Monitor Disease Activity in Multiple Sclerosis

T Lim[1], S Palasamudram[1], S Suthiphosuwan[1], A Espiritu[1], A Jones[1], A Lin[1], J Oh[1], A Bharatha[1]

[1]*University of Toronto and St. Michael's Hospital, Toronto, Ontario*

Purpose

While the value of spinal cord magnetic resonance imaging (MRI) in multiple sclerosis (MS) diagnosis has been clearly established, its routine use for monitoring disease-modifying treatment (DMT) effectiveness and disease activity has been controversial1. This study aims to measure the frequency of new cervical spinal cord lesions (CSLs) detected on MRI in clinically stable MS patients, particularly asymptomatic CSLs not associated with new brain lesions (BLs), and to determine factors associated with development of new CSLs.

Materials and Methods

We identified clinically stable MS patients who underwent follow up 3T MRI of the brain and cervical spinal cord over a 9-month period at our academic MS center which follows over 7,000 people with MS (pwMS) annually. MRIs were reviewed by a neuroradiologist for the presence of new BLs and CSLs compared to prior scans. Clinical data were obtained from the clinic database. Multiple logistic regression analyses were conducted to determine factors associated with the development of new CSLs.

Results

The study included 1,613 pwMS, of which 292(18.1%) had a clinical relapse between scans, while 1,321(81.9%) were clinically stable. In those with stable disease (mean follow up interval of 16.4 mo.), 879(66.5%) showed no new lesions, 367(27.8%) had new BLs only, 50(3.8%) had new BLs and new CSLs, while 24(1.8%) had new CSLs only. Among all pwMS, development of new CSLs was significantly associated with ≥3 prior relapses (OR 1.47, 95%CI 1.04-2.09, p=0.027), no DMT use (OR, 0.71, 95%CI 0.50-0.99, p=0.044), younger age (OR 0.96, 95%CI 0.95-0.98, p<0.001), ≥3 new BLs (OR 5.57, 95%CI 3.94-7.88, p<0.001) and new clinical relapse (OR 6.14, 95%CI 4.33-8.71, p=0.001). After adjusting for age, sex, number of prior relapses and DMT use, new clinical relapse (OR 4.8 95% CI 3.2-7.2, p<0.001) and number of new BLs (OR 1.1, 95% CI 1.1-7.18, p<0.001) were independently associated with new CSLs. Among clinically stable pwMS, no DMT use (OR 0.62, 95%CI 0.38-0.99, p=0.047) and ≥3 new BLs (OR 7.17 95%CI 4.41-11.64, p<0.001) were associated with new CSLs. Number of new BLs (OR 1.19 95% CI 1.13-1.25, p<0.001) remained independently associated with new CSLs after adjusting for other variables.

Conclusions

In clinically stable pwMS, isolated asymptomatic CSLs developed in <2% of patients and were associated with concomitant new BLs. These findings suggest that routine cervical spinal cord MRI is unlikely to be of high yield in most pwMS to monitor for clinically-silent disease activity.

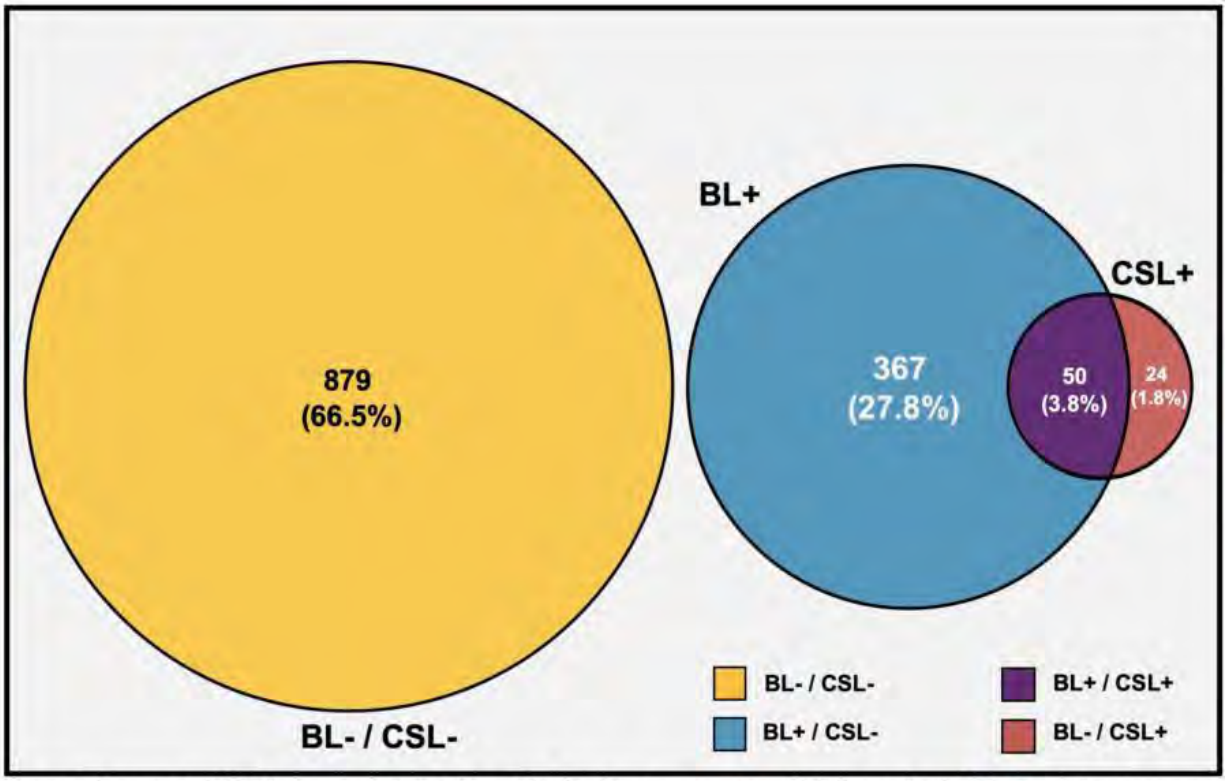

Figure 1. Frequency of MRI lesions in clinical stable pwMS. BL-: No new asymptomatic lesion on brain MRI. BL+: At least one new asymptomatic lesion on brain MRI. CSL-: No new asymptomatic lesion on cervical spinal cord MRI. CSL+: At least one new asymptomatic lesion on cervical spinal cord MRI.

(Filename: TCT_682_Figure1.jpg)

881

M1 Trunk vs. M2 Trunk Occlusions: Anatomic vs. Functional Considerations in Middle Cerebral Artery Occlusion

C Slack[1], A Ali[1], S Voleti[2], A Grossman[2], S Peyman[2], C Prestigiacomo[2], P Khatri[2], A Vagal[2], T Tomsick[2]

[1]University of Cincinnati College of Medicine, Cincinnati, OH, [2]University of Cincinnati Medical Center, Cincinnati, OH

Purpose

The M2 trunk (M2T) represents a continuation of the M1 segment beyond one or more M2 insular branch origins, proximal to M2 division origins. M2T occlusion beyond patent posterior temporal (PT), holotemporal (HoT), and/or orbito-operculofrontal branches (OOF) has been proposed as a relevant anatomic and clinical variant in endovascular therapy (EVT) of MCA occlusion. M2T occlusion designation may improve classification consistency and more uniform patient selection, and may narrow the range of imaging and clinical outcomes in EVT clinical trials compared to M1 occlusion without M2 branch filling.

Materials and Methods

Retrospective DSA registry review of 124 M1 and 69 M2 occlusions classified by operator was performed to identify M2 branch patency of orbito-operculofrontal (OOF), posterior temporal (PT), holotemporal (HoT) branches, with or without distal temporoparietal (TP) or temporo-occipital (TO) branch perfusion, indicating M2T occlusion. DSA occlusive lesion and mTICI were recorded. Head CT, DWI and SWAN were reviewed for baseline and 24-hr. ASPECTS and intracerebral hemorrhage (ICH). M2T were further classified according to presence of OOF, HoT-only, PT, TP, and TO branches for outcome comparisons. 3-month mRS was compared between M1 occlusion (M1T) and M2T occlusion groups.

Results

29/124 (23.4%) original M1 occlusions were adjudicated to have M2 branch patency proximal to occlusion, and 14/69 (20.3%) M2 occlusions were designated M2T occlusions, resulting in 95 M1T and 43 M2T occlusions for comparison. Post-EVT ASPECTS were higher in M2T compared to M1T occlusion (5.4 and 4.3, $p<0.05$). Post-EVT ICH was significantly lower in M2T than M1T (33.3% and 65.7%, $p<0.05$). A greater percentage of M1T patients were classified as ECASS PH1 or PH2 (parenchymal hematoma) compared to M2T (22.6% and 6.3%, $p<0.05$). 90-day mRS ≤ 3 was greater in M2T vs. M1T (58.9% and 43.2%, $p=0.052$). Mortality was numerically lower in M2T vs. M1T (12.8% and 22.7%, $p=0.08$). TP+PT (n=11) had a lower average mRS compared to HoT alone (n=6), OOF (n=10), and TO (n=11) branches in the M2T group (2.0, 3.7, 3.9 and 3.8, respectively; $p<0.05$).

Conclusions

Higher post-EVT ASPECTS, lower PH%, and greater % mRS 0-3 for M2T vs. M1T occlusions suggest a protective effect of patent M2 branches and validate clinical relevance of the M2 trunk. Addressing the M2T when defining MCA occlusion in EVT clinical trials may enhance precision by reducing baseline differences in robustness of collateral circulation proximal to the occlusion.

Figure 1. Composite diagram of M1-M2 trunk anatomy based on IMS-III post hoc analysis.

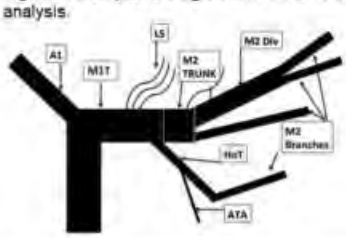

The M2 trunk is a continuation of the distal M1 trunk, beyond HoT artery. The M2 trunk divides into M2 Div

M1T= M1 trunk proximal to the lenticulostriate arteries (LS)
ATA= anterior temporal artery
HoT= Holotemporal M2 branch
M2 Div= M2 divisions

Table 1. Baseline Clinical Characteristics of M1T and M2T groups

	M1T	M2T	P-value
Age (mean)	67.29	68.67	0.29
Diabetes (%)	27.37	34.88	0.19
Hypertension (%)	72.63	81.40	0.12
NIHSS at admission (mean)	17.63	17.19	0.38
Window time (minutes) (mean)	428.09	387.36	0.26
# Thrombectomy passes (mean)	2.21	2.09	0.35
Contrast amount (mL) (mean)	133.58	126.62	0.27
Capillary index Score (mean)	1.98	2.04	0.37
Pre-EVT ASPECTS (mean)	6.68	7.22	0.14

Table 2. Clinical outcomes of M1T vs. M2T analysis.

	M1T	M2T	P-value
90d-mRS 0-3 (%)	43.18	58.97	**0.052**
90d-mRS 4-6 (%)	56.82	41.03	**0.052**
Post-EVT ASPECTS (mean)	4.27	5.40	**0.024**
Intracerebral hemorrhage (%)	65.75	33.33	**0.002**
Petechial hemorrhagic infract (%)	77.42	93.75	**0.027**
Parenchymal hematoma (%)	22.58	6.25	**0.027**
Contrast Extravasation (%)	57.69	39.13	0.072

Figure 2. 90-day modified Rankin Scale (mRS) for M1T and M2T.

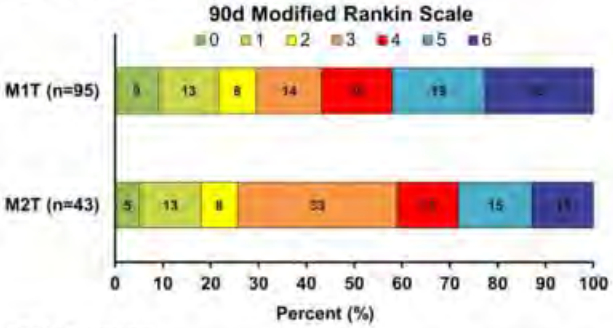

mRS 0= No symptoms
mRS 1= No significant disability, despite symptoms; able to perform all usual duties and activities
mRS 2= Slight disability; unable to perform all previous activities but able to look after own affairs without assistance
mRS 3= Moderate disability; requires some help, but able to walk without assistance
mRS 4= Moderately severe disability; unable to walk without assistance and unable to attend own bodily needs without assistance
mRS 5= Severe disability; bedridden, incontinent, and requires constant nursing care and attention
mRS 6= Death

(Filename: TCT_881_M1TM2T2021.jpg)

1055

Machine Learning (ML) for Enhanced Radiological Diagnosis of Cerebral Tuberculosis

K Aftab[1], S Fatima[2], N Aziz[1], E Baig[1], F Mubarak[3], M Khurram[2], S Enam[1]
[1]Aga Khan University, Karachi, Sindh, [2]NED University of Engineering and Technology, Karachi, Sindh, [3]Aga Khan University, Karachi, HI

Purpose
Cerebral tuberculosis (TB) is responsible for devastating sequelae and mortality, particularly in the developing world. It is a challenging diagnosis as it mimics other infectious and neoplastic pathologies of the brain. There is a need for a rapid and accurate diagnostic approach to prevent the dismal outcomes arising as a result of delayed or incorrect diagnosis.
Materials and Methods
72 cases of cerebral TB and 146 cases of non-TB (including meningiomas, gliomas, brain metastasis, fungal and bacterial brain infection) presenting to Aga Khan University Hospital, Karachi, Pakistan, were included and divided into training and test datasets. Features were selected using correlation, and besides age and gender, included radiological features recorded from MRI brain i.e., ring enhancement, homogenous enhancement, basal meningeal enhancement, meningeal enhancement (not basal), homogeneous diffusion restriction, remote Infarcts, hydrocephalus, bilateral multi focal lesions, unilateral multi focal lesions and multiple lesions within the same lobe. After the application of Synthetic Minority Over-sampling Technique (SMOTE), SMOTE-Tomek Links, Edited Nearest Neighbor (ENN) SMOTE-ENN, and Adaptive Synthetic (ADASYN) techniques for balancing the datasets, classifier accuracy was tested using two machine learning models.
Results
Highest accuracy (90.9%) for Tb vs non-TB was achieved using Logistic Regression along with SMOTE+TOMEK with an Area Under the Curve (AUC) of 95.4% Further analysis showed 96% accuracy for TB vs Tumor classification using Guassian Based Naive Bayes combined with Smote+TOMEK and 94.7% accuracy for Tumor Vs Infection using Support Vector Machine

Conclusions
Machine learning shows promising role in clinical decision support systems for quickly and non-invasively diagnosing cerebral tuberculosis. These classifiers can form basis for mobile apps to be used in clinical setups. Sampling techniques should be employed to boost the performance of classifiers.

1218

Machine learning-based feature importance for differential diagnosis of follicular thyroid lesions

E Ha[1]
[1]*Ajou University Medical Center, Suwon, Korea, Republic of*

Purpose
Differential diagnosis of various follicular thyroid lesions is crucial importance for management of thyroid nodules. This study aimed to evaluate the relative importance of sonographic features for differential diagnosis of follicular thyroid lesions using a machine learning.
Materials and Methods
From June to September 2015, 5,708 thyroid nodules (≥ 1.0 cm) in 5,081 consecutive patients who underwent thyroid US from 26 institutions were evaluated (THINK registry). Among them, 4787 nodules with a final diagnosis of nodular hyperplasia (NH, n=4461), follicular adenoma (FA, n=136), follicular carcinoma (FC, n=62), and follicular-variant papillary thyroid carcinoma (FVPTC, n=128) were included. US features of the thyroid nodules were retrospectively reviewed and compared among the groups using univariable and multivariable logistic regression analyses. LASSO was utilized to determine optimal clinical variables and leave-one-out cross-validation method was adopted for prediction model building. A random forest model was used to investigate the relative importance of variables.
Results
Follicular-patterned tumor (FA, FC, and FVPTC) showed differences from NH in tumor diameter ($P < 0.001$), composition ($P < 0.001$), echogenicity ($P = 0.003$), halo ($P = 0.022$), and TIRADS category ($P = 0.004$). On the other hand, follicular-patterned malignancy (FC and FVPTC) showed differences from FA in presence of macrocalcifications ($P=0.011$) and rim calcifications ($P=0.011$). The most important features for differential diagnosis of FC from FA were rim calcification and TIRADS category, and those of FVPTC from FA were echotexture, margin and macrocalcifications.
Conclusions
Although differential diagnosis of follicular thyroid lesion is difficult on US, the relative feature importance obtained from machine learning in a large clinical cohort provide additional information on important priorities.

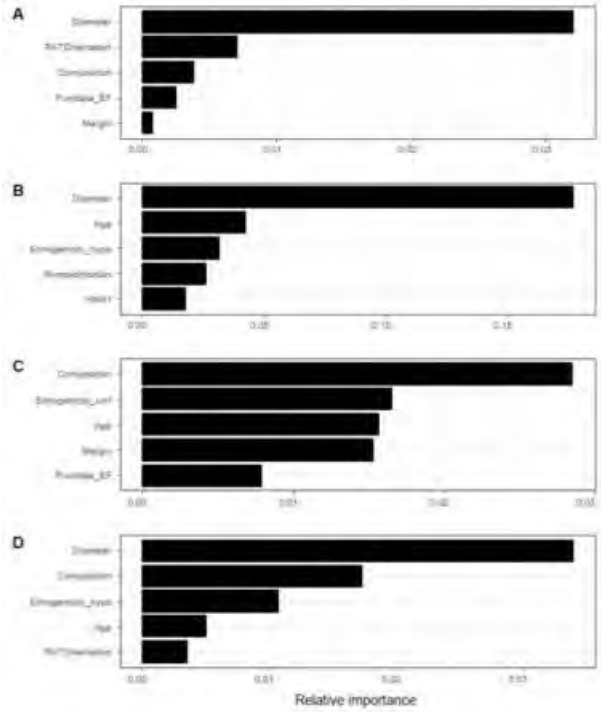

Follicular-patterned tumor (A: FA, B: FC, C: FVPTC, D: all) vs. NH

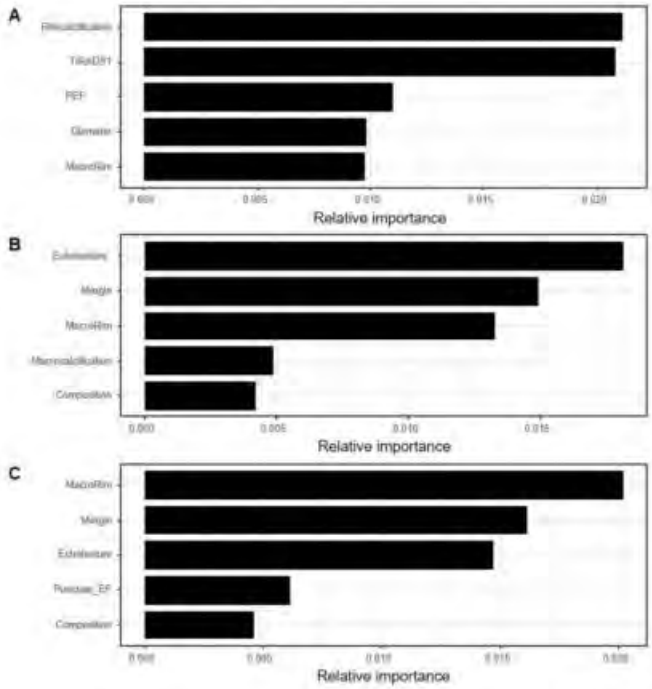

Follicular-patterned malignancy (A: FC, B: FVPTC, C: all) vs. FA

(Filename: TCT_1218_ASNR.jpg)

132

Malformations of Cortical Development in Hereditary Hemorrhagic Telangiectasia

S Forseen[1], J Gaines[1], J Gossage[1], W Parker[1], B Gilbert[1]
[1]*Medical College of Georgia at Augusta University, Augusta, GA*

Purpose

Hereditary hemorrhagic telangiectasia (HHT) is an autosomal dominant disorder that results in the abnormal formation of blood vessels. This manifests as relatively benign symptoms, such as nosebleeds and mucocutaneus telangiectasias, as well as serious complications including stroke, brain abscess, and brain AVM. Few studies thus far have focused on the neuroradiological findings related to abnormal cortical development in adult HHT patients. The purpose of this study was to identify the prevalence of malformations of cortical development in a group of adult HHT patients.

Materials and Methods

A total of 141 patients 18 years of age or older who were referred to the Augusta University HHT clinic and underwent a brain MRI between 1/19/2018 and 12/3/2020 were identified. All MRI examinations were performed at 3T and included pre- and post-contrast 3D T1-weighted spoiled gradient sequences. MRI examinations were reviewed retrospectively by two Board certified radiologists who hold Certificates of Added Qualification in Neuroradiology (B.C.G. and S.E.F.) with 7 and 10 years of experience, respectively. The presence of MCDs and AVMs were confirmed by consensus.

Results

The prevalence of patients with HHT and coexistent malformations of cortical development was 3.5% (5/141). Of the 5 HHT patients with malformations of cortical development, all 5 had polymicrogyria. Two of the five patients with polymicrogyria also had CSF-containing clefts (schizencephaly) lined with polymicrogyria, both of which were of the closed lip variety. The incidence of spatially coincident polymicrogyria and bAVMs in this sample was 40% (2/5 cases). Four of the five HHT patients with polymicrogyria had documented endoglin mutations (with the fifth being untested). Summary data from patients with HHT and polymicrogyria are seen in Table 2. Other data related to demographics, genetics, and anatomical defects can be seen in Table 1.

Conclusions

We are the first group to report two HHT patients with coexistent schizencephaly and porencephaly. The presence of schizencephaly and porencephaly in patients with HHT adds support to the hypothesis of in utero cerebral hypoxia as the etiology of MCDs in HHT.

Table 1: Summary of 141 patients

Demographic	Summary
Sex	
Male	36.9%
Female	63.1%
Age	45.3 yrs
MCD	
Yes	5
No	136
HHT mutation	
Endoglin	35.5%
ALK 1	27.0%
SMAD4	2.8%
RASA1	.7%
Negative x 5	14.9%
Unknown	19.1%
Curacao category	
Definite HHT	79.4%
Possible or suspected HHT	12.1%
Probable	4.3%
Unlikely	4.3%

Table 2. Description of 5 patients with MCD

Patient	Age	Sex	Curacao	Mutation	bAVM	pAVM	MCD	Symptoms
1	20	M	4	Not Tested	No	No	right frontoparietal closed lip schizencephaly; right frontotemporal parietal polymicrogyria	Migraine headaches
2	80	M	4	ENG	Yes	Possible	left perirolandic polymicrogyria; nodular heterotopia about a left perirolandic porencephalic cavity; left superior temporal gyrus AVM	None
3	26	F	4	ENG	No	Yes	right parietal occipital polymicrogyria and closed lip schizencephaly	Migraine headaches
4	18	M	4	ENG	Yes	Probable	right parietal polymicrogyria; right parietal AVM	Migraine headaches; right hand weakness

(Filename: TCT_132_Table1and2ASNRsubmission112.jpg)

1208

Mapping Brain Metabolite Differences between HIV Clade-C Infected Individuals and Healthy Subjects Using a Whole-Brain MRSI

S VYAS[1], T Salan[2], S Sheriff[3], V Govind[2], P Singh[1]

[1]Postgraduate Institute of Medical Education and Research (PGIMER), Chandigarh, India, [2]University of Miami, Miami, FL, [3]Uni, Miami, FL

Purpose

Studies using magnetic resonance spectroscopic imaging (MRSI) for identification of brain metabolite alterations in HIV infected individuals acquired MR spectra from single voxels to best encompass HIV relevant regions of interest (ROI) [1]. To our best knowledge, none have attempted to map these changes at the whole-brain level. This study aims at quantitating whole-brain metabolite concentrations in HIV clade-C infected subjects.

Materials and Methods

MRI Data were collected on a 3T scanner from 108 cART-naïve HIV Clade-C subjects and 108 age-matched controls. Protocol included: T1-weighted MPRAGE, and whole-brain MRSI using a 3-dimensional EPSI spin-echo sequence. MRSI data were processed using the Metabolite Imaging and Data Analysis System (MIDAS) [2] for finding metabolite levels at 38 unique ROIs covering the entire brain (Figure 1). T-tests and Cohen's d effect sizes were calculated for each metabolite/ROI to find significant group differences ($p < 0.05$ FDR-corrected). Metabolites analyzed were Creatine (Cr), N-acetylaspartate (NAA), choline (Cr), myo-inositol (m-Ins), and glutamate/glutamine (Glx) with their respective ratios over Cr.

Results

All metabolites except NAA were elevated in HIV subjects with significant increases for Cr, Cho, m-Ins, and Glx in 30, 20, 36, and 28 ROIs, respectively (Figure 2). NAA decreased in white matter (WM) ROIs but not significantly. Ratios of m-Ins/Cr and Glx/Cr also showed elevated values in the HIV group, while NAA/Cr had significant decreases concentrated in WM. Cho/Cr did not show any change since both Cr and Cho were increasing (Figure 3). The most regionally widespread and significant alterations were m-Ins, with individual ROI mean values (Figure 4), highlighting it as potentially the most relevant biomarker of HIV infection.

Conclusions

Widespread alterations in metabolite levels provide an insight into the mechanism by which HIV Clade-C infection damages the brain. Biggest reductions in NAA/Cr for HIV subjects are concentrated in WM. Reduced NAA is generally seen as an indicator of neuronal integrity, viability, and dysfunctions due to HIV infection. This is mirrored by the increase in Cho in WM ROIs and frontal and occipital lobes of HIV group reflecting cell membrane disruption, active demyelination, microglial proliferation, reactive astrogliosis and inflammation. Alterations in m-Ins are the most significant indicating gliosis and inflammation. Increased Glx also indicates compromised synaptic transmission and neurotoxicity in the brain [3].

Figure 1: Axial slices of an MNI space T1 template overlaid with the 38 ROI used for analysis.

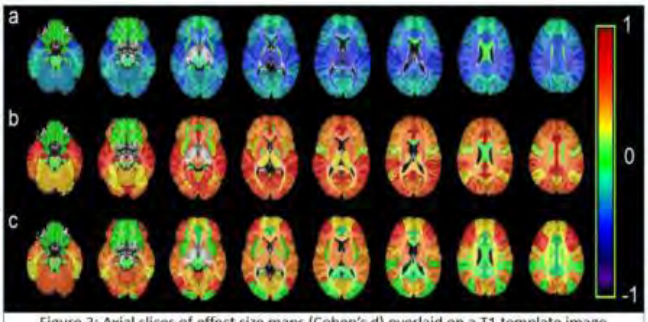

Figure 3: Axial slices of effect size maps (Cohen's d) overlaid on a T1 template image reflecting the ROI-based changes in metabolite ratios (a) NAA/Cr, (b) m-Ins/Cr, and (e) Glx/Cr.

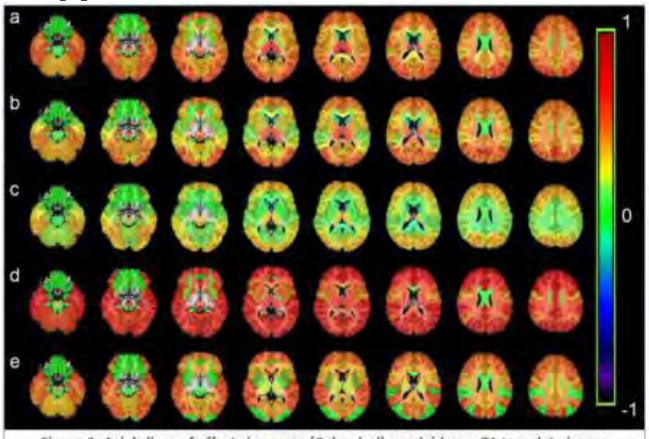

Figure 2: Axial slices of effect size maps (Cohen's d) overlaid on a T1 template image reflecting the ROI-based changes in metabolite level between the control and HIV+ groups. Negative effect size values indicate a decrease in the HIV+ group and positive values indicate an increase. Displayed maps are (a) Cr, (b) Cho, (c) NAA, (d) m-Ins, and (e) Glx.

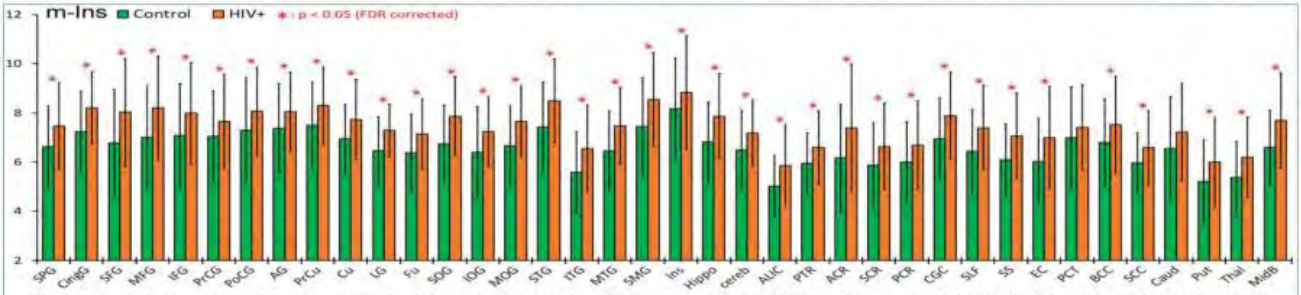

Figure 3: Bar plots comparing m-Ins concentration levels between the control and HIV+ groups at the 38 ROIs. Error bars represent the standard deviation. Red asterisks indicate regions with significant between-group differences ($p < 0.05$ Bonferroni corrected).

(Filename: TCT_1208_MRSI_Figures.jpg)

382

MR Diffusion Characteristics of Molecularly-Defined Posterior Fossa Ependymomas

S Pisani Petrucci[1], Y LI[2], S Cha[1]

[1]University of California San Francisco, San Francisco, CA, [2]UCSF, San Francisco, CA

Purpose

The 2021 WHO Classification of CNS tumors restructures the ependymoma family by anatomic site and molecular profile. For posterior fossa tumors, two groups are classified based on H3 K27 trimethylation status: PFA and PFB. Additionally, trisomy 1q is a genetic alteration found in some ependymomas associated with a poor prognosis. The PFA and PFB groups differ greatly in clinico-pathologic attributes, including affected populations and prognoses. However, the MRI features of each group are incompletely characterized, and no molecular-specific diffusion properties have been described. As diffusion characteristics correlate with molecular type and prognosis in many brain tumors, we sought to examine the diffusion properties of PFA and PFB ependymomas.

Materials and Methods

Pre-operative MRIs from 11 PFA patients and 9 PFB patients as well as MRIs from 4 patients with recurrent ependymomas (1 PFA, 3 PFB) and molecular profiling were included for analysis. ADC maps were viewed on PACS software and areas of low ADC identified within the tumor. A 2D, 3-ROI method adapted from prior studies was used to obtain mean minimum tumor ADC and mean white matter ADC, and ADCtumor: ADCwhite matter ratios were calculated. ADC maps were co-registered to anatomical and susceptibility-weighted sequences to avoid sampling areas of necrosis, hemorrhage, calcification, or edema. ADC ratios were compared using the Mann Whitney U-test, and subgroup analysis performed on the presence of trisomy 1q.

Results

Normalized ADCtumor:ADCwhite matter ratios were significantly lower ($p < 0.001$) in PFA ependymomas as compared to PFB ependymomas (Fig 1). Subgroup analysis demonstrated no significant difference in ADC ratios according to trisomy 1q, although analysis was limited due to a small sample size of tumors with known 1q status. Overall, normalized 2D ROI ADC ratios correlate well with reported whole-tumor volumetric ADC measurements for posterior fossa ependymomas not stratified by molecular subtype.

Conclusions

Our quantitative ADC results suggest a cellular imaging phenotype for the aggressive biologic behavior and poor prognosis seen among PFA tumors. These results align well with a large body of work demonstrating correlations between brain tumor diffusion characteristics, histological grade, and clinical outcomes. Ongoing investigations by our research group, including characterization of conventional MR imaging features and volumetric ADC analyses, aim to further define the radiogenomic profile of posterior fossa ependymomas.

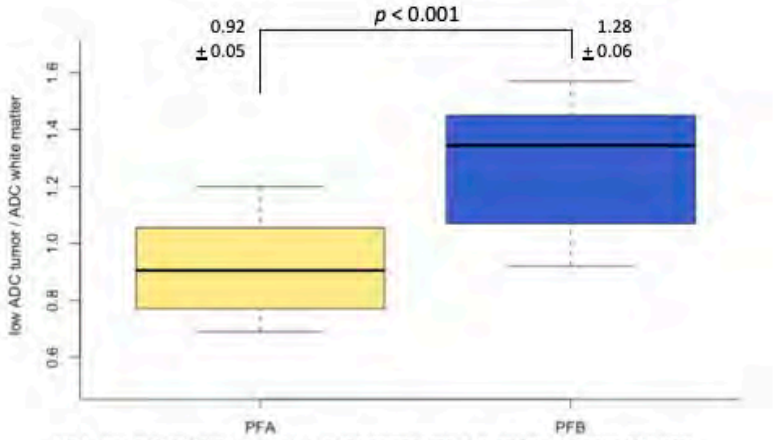

Fig 1. Box-and-whisker plots comparing normalized ADC values of Group PFA and Group PFB ependymomas. Group PFA tumors had significantly lower $ADC_{tumor}/ADC_{white\ matter}$ ratios than Group PFB tumors using a 2D, three-ROI method.

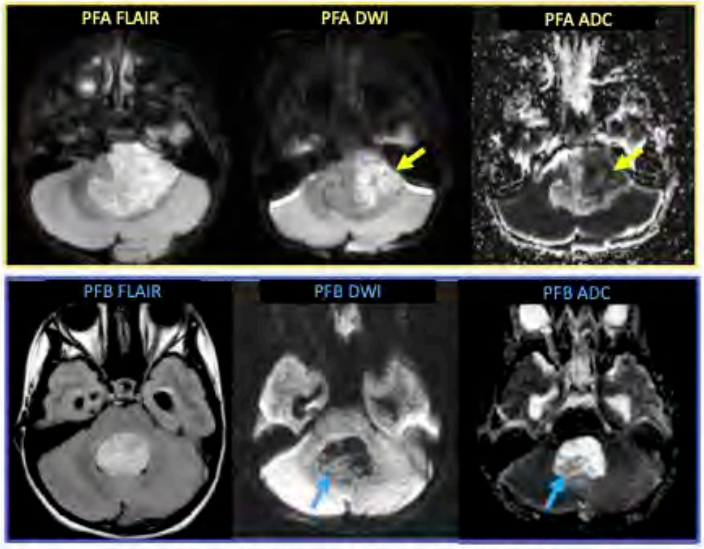

Fig 2. Representative MR images from Group PFA (top) and Group PFB (bottom) ependymomas. Note reduced diffusion and relatively low ADC signal in PFA tumor (yellow arrows) vs. intermediate diffusion and ADC signal in solid portion of PFB tumor (blue arrows).

(Filename: TCT_382_ASNR2022abstractfig.jpg)

366

Neuroimaging offers low-yield in SARS-CoV-2 positive children

G Orman[1], N Desai[1], S Kralik[1], S Victor[1], T Huisman[2]

[1]Texas Children's Hospital, Houston, TX, [2]Texas Children's Hospital and Baylor College of Medicine, Houston, TX

Purpose

Coronavirus disease 2019 (COVID-19) pandemic caused by Severe Acute Respiratory Syndrome coronavirus 2 (SARS CoV-2) most commonly presents with respiratory disease, but neurologic complications are being reported. Common neurological manifestations include fatigue, headache, and smell and taste disorders. We aim to investigate the prevalence of positive neuroimaging findings in SARS-CoV-2 positive children referred for neuroimaging between March 18-September 30, 2020.

Materials and Methods

A master database of all patients who tested positive for SARS-CoV-2 was assembled by the Texas Children's Hospital COVID-19 Imaging Taskforce. All imaging studies were extracted from the master database, and the neuroimaging studies were identified for this retrospective study. Data on demographics, new onset neurological symptoms, clinical features and laboratory findings were reviewed. New onset neurological symptoms that were primary indications for neuroimaging within one month of SARS-CoV-2 positive testing were classified as: 1. COVID-19 attributable indications and 2. Other indications. The neuroimaging studies were re-evaluated for the study.

Results

Forty-three neuroimaging studies of 20 children (male/female: 12/8) were included. All children had at least one neuroimaging study. The average age at neuroimaging was 8.8 (range, 0.6-17.8) years. 55% of patients had no previous medical conditions. In the remaining patients the following pre-existent conditions were recognized: epilepsy, sickle cell disease, obesity, overweight,

hemophilia C, Sturge Weber Syndrome and autism. Neurological symptoms at the time of neuroimaging included impaired consciousness (n=7), seizures (n=4), status epilepticus (n=2), headache (n=2), focal neurological findings on examination (n=2), fever with meningeal signs on examination (n=1), transient episode of aphasia (n=1) and fever with headache (n=1). Only 2 patients (10%) had acute findings on their initial MRI studies: subarachnoid hemorrhage (SAH) combined with posterior reversible encephalopathy syndrome (PRES) in one patient and a right sided hippocampal T2-hyper-intense signal alteration in the other patient, possibly secondary to seizure activity.

Conclusions

Our results showed that only 10% of patients with neurological manifestations demonstrate acute findings on their initial neuroimaging studies. In summary, neuroimaging in children may imply a low-yield in COVID-19 diagnosis and consequently requests for acute imaging should involve a careful risk-benefit analysis.

1157

Olfactory bulb height on MRI correlates with normal aging: Korean population study

M Lee[1], J Lee[2]

[1]Yeouido ST. Mary's Hospital, Seoul, Korea, Republic of, [2]Asan Medical Center, Seoul, Seoul

Purpose

To evaluate the olfactory bulb height in a large population without subjective olfactory dysfunction using age, gender difference, and patients' medical history as covariates.

Materials and Methods

Institutional review board approved this retrospective study. Written informed consent was obtained from all participants. Study population included those who underwent high-resolution MRI of the brain and had no subjective olfactory dysfunction. Coronal 3D T2-weighted imaging (T2WI) and proton density-weighted imaging (PD) were subject to analysis of the olfactory nerves. Population was divided into 6 age groups including 20-29 years, 30-39 years, 40-49 years, 50-59 years, 60-69 years, and equal to or older than 70 years. One-way ANOVA with post-hoc Bonferroni-correction were performed for comparison of olfactory bulb height among six age groups.

Results

Among 587 patients who underwent brain MRI without subjective olfactory dysfunction, 557 (Male:Female = 270:287; mean age, 52.2 years; range, 20-88 years) were finally enrolled after exclusion of 30 population who had history of head trauma, head and neck surgery, or radiation treatment for head and neck tumor. In all population, the olfactory bulb height showed significant correlation with age, gender, and presence of diabetes ($P<.0001$ and $P=0.023$). Mean olfactory bulb height in all population was 1.68 ± 0.34 mm. Mean olfactory bulb height was smaller with female gender at the same age group as well as with aging in both genders. Pairwise comparison of age groups after Bonferroni correction revealed significant difference in olfactory bulb height before and after the age of 50 years in female group as well as all population ($P < .001$).

Conclusions

In present study, we evaluated age-related change of olfactory bulb height on MRI. The olfactory bulb height was significantly decreased by aging and showed significant difference between before and after the age of 50 years in adult population. These results can be a good reference of detecting olfactory dysfunction in general population.

625

Optic Nerve Sheath Diameter Is Not A Predictor of ICH Outcomes

V Vagal[1], Y Aziz[2], M Gusler[3], P Sekar[2], T Behymer[2], D Woo[2]

[1]Stony Brook University Renaissance School of Medicine, Stony Brook, NY, [2]University of Cincinnati Medical Center, Cincinnati, OH, [3]University of Virginia, Charlottesville, VA

Purpose

Intracerebral hemorrhage (ICH) accounts for only a small percentage of all strokes (10-15%) yet carries the highest mortality rate (40%) of any other subtype. Increased intracranial pressure (ICP) resulting from ICH can be associated with neurologic decline. Widening of optic nerve sheath diameter (ONSD) may serve as an early marker of increasing ICP, with several studies reporting an association between ONSD and patient outcomes. The objective of our study was to investigate if changes in ONSD can predict functional outcomes. We hypothesized that enlarging ONSD in ICH patients would predict worse 90-day modified Rankin Scores (mRS).

Materials and Methods

We utilized the patient population from ERICH (Ethnic/Racial Variations of Intracerebral Hemorrhage), a prospective, multi-center, case-control study of 3000 subjects. Our inclusion criteria were ICH patients with a baseline CT, a follow-up CT between 5-7 hours with available demographic and outcome data. We measured ONSD bilaterally 2-4 mm behind the globe for baseline and follow-up CT. We determined a significant change in ONSD between baseline and follow-up CT to be greater than 5 percent. Poor outcome was defined as an mRS score of 3-6. We compared those with good outcome with those with poor outcome on demographics as well as presence/absence of significant change in ONSD. Furthermore, we did an analysis of variance to see if there were differences in ONSD among race/gender groups.

Results

We randomly selected a subset of 104 patients that fit our inclusion criteria. Among these ICH patients, the mean age was 63.5 (SD +/- 14.3) with 38.5% females. Forty-nine patients (47.1%) had significant ONSD change between baseline and follow-up CT. A total of 47 patients (45.2%) had poor outcomes and 57 (54.8%) had good outcomes. In the univariate analysis, age, ICH volume, GCS score, and presence of IVH were significantly associated with poor outcomes. However, change in ONSD was not a predictor of outcomes (Table 1). We found no significant difference by race/ethnicity or sex in ONSD change suggesting that these differences were not related to study design.

Conclusions

In this large, multi-center, multi-ethnic, prospective study of ICH cases, we found that change in ONSD between baseline and follow-up CT was not predictive of functional outcomes in ICH patients after controlling for traditional variables such as volume of ICH and presence of IVH.

Variables	Good Outcome (N=57)	Poor Outcome (N=47)	p-Value
Mean Age (SD)	60.9 (12.7)	66.7 (15.6)	0.0381
Females	20 (35.1)	20 (42.6)	0.4361
Race			
Black	16 (28.1)	12 (25.5)	
Hispanic	20 (35.1)	13 (27.7)	
White	21 (36.8)	22 (46.8)	0.5688
Hypertension	50 (87.7)	37 (78.7)	0.2169
Diabetes	15 (26.3)	17 (36.2)	0.2785
Smoking			
Current	10 (17.5)	12 (26.7)	
Former	20 (35.1)	9 (20.0)	
Never	27 (47.4)	24 (53.3)	0.2057
ONSD Change Left Globe			
Significant (>/= 5%)	18 (31.6)	11 (23.4)	
Not Significant (<5%)	39 (68.4)	36 (76.6)	0.3549
Presence of IVH	16 (28.1)	25 (53.2)	0.0091
Glasgow Coma Scale			
Mild (13-15)	47 (82.5)	29 (61.7)	
Moderate (9-12)	5 (8.8)	10 (21.3)	
Severe (3-8)	5 (8.8)	8 (17.0)	0.0575
ICH Location n (%)			
Deep	38 (66.7)	26 (55.3)	
Lobar	12 (21.0)	14 (29.8)	
Infratentorial	7 (12.3)	7 (14.9)	0.4829
ICH Volume (Median IQR)	5.8 (2.7, 15.5)	23.1 (7.6, 51.7)	0.0002

(Filename: TCT_625_Table_1.jpg)

229

Optimizing Dual-Energy CT Contrast Timing and Virtual Monochromatic Energy to Maximize Brain Metastasis Conspicuity

B Nan[1], A Rashiwala[1], A Krayyem[1], E Wang[1], H Pokhylevych[1], A Amer[2], H Alhasan[2], D Schellingerhout[1], S Ferguson[1], J Li[1], R Layman[1], J Johnson[2]

[1]MD Anderson Cancer Center, Houston, TX, [2]The University of Texas MD Anderson Cancer Center, Houston, TX

Purpose

Brain metastases (BM) have been reported to occur in up to 40% of patients with cancer. At present, gadolinium-enhanced MRI is considered to be the imaging technique of choice in patients suspected of BM; however, CT is cheaper, more widely available, and does not suffer from geometric distortion as seen with MR imaging. Prior studies have shown superior conspicuity of brain malignancy with delayed imaging times. We sought to optimize CT parameters for BM conspicuity in a prospective trial.

Materials and Methods

Twenty-three patients with 4.4±2.5 BM were scanned on a DECT scanner at 90 seconds, 5 minutes, 10 minutes, and 20 minutes following the injection of 123±8.0 ml of iohexol. Circular ROI was drawn on axial QC images where the largest BM had the largest cross-sectional diameter. BM with necrosis also had an ROI placed to cover the area of maximal enhancement. A ROI was also placed in the contralateral normal-appearing brain (NAB and in the air ("noise" measurement). A ROI was obtained at each imaging time point. A single-tail Students T-test was used for comparative statistics. DE virtual monochromatic reconstructed (VMR) images were created using Syngo. ROI were placed as above in both lesion and NAB. The HU were recorded for each energy between 40 and 190 keV. VMR lesion and NAB data were used to calculate SNR and CNR at each energy.

Results

At 90 sec, the mean BM HU was 85.3±12.0, SNR 27.0±10.0, CNR 12.8±4.7. At 5 min, the mean BM HU was 80.4±13.3, SNR 25.3±10.5, CNR 11.9±5.9. At 10 min, the mean BM HU was 77.2±12.0, SNR 22.5±6.7, CNR 10.0±3.5. At 20 min, the mean BM HU was 74.0±9.8, SNR 23.4±7.1, CNR 10.4±3.7. CNR was greatest at 90 sec, and this difference was statistically significant ($P < 0.05$) compared to 10 and 20 min. CNR at 5 min was also statistically significantly greater than later time points ($P < 0.05$). A negative linear relationship was observed between SNR/CNR and Kev with lower VMR energies resulting in the highest SNR and CNR and higher VMR showing the lowest SNR and CNR.

Conclusions

Despite prior reports demonstrating greater conspicuity for brain malignancy using later time points, our results show that earlier time points show objectively greater conspicuity. Although lower energies result in higher VMR noise, the increased iodine conspicuity at lower energies resulted in the highest SNR/CNR at lower VMR. Additional work remains to verify that earlier times and lower VMR energies lead to a difference in radiologist detection rate and confidence.

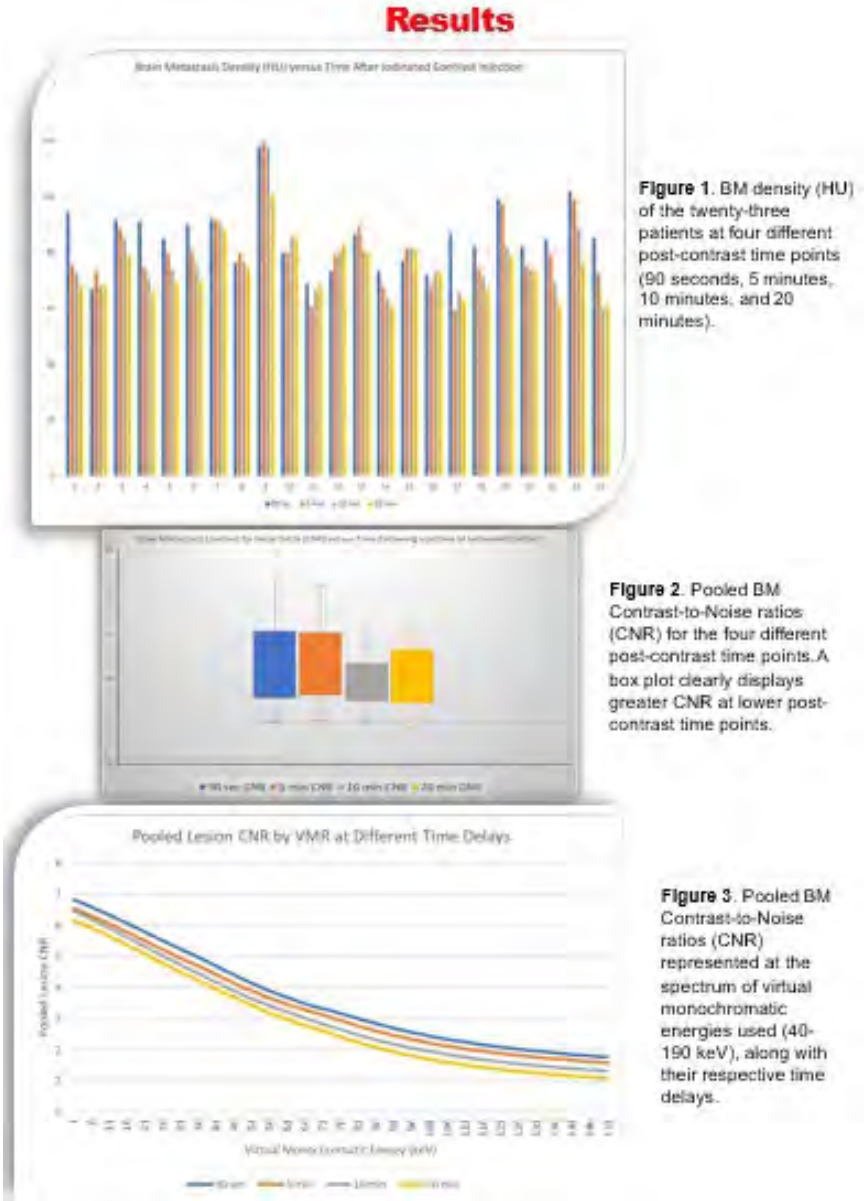

Figure 1. BM density (HU) of the twenty-three patients at four different post-contrast time points (90 seconds, 5 minutes, 10 minutes, and 20 minutes).

Figure 2. Pooled BM Contrast-to-Noise ratios (CNR) for the four different post-contrast time points. A box plot clearly displays greater CNR at lower post-contrast time points.

Figure 3. Pooled BM Contrast-to-Noise ratios (CNR) represented at the spectrum of virtual monochromatic energies used (40-190 keV), along with their respective time delays.

(Filename: TCT_229_ResultsImages.jpg)

1400

Our Experience In Complications Of Percutaneous Spine Procedure

a biagelli[1], r pantaleoni[2], l bellantonio[3], A Fiacca[4]

[1]azienda ospedaliera di perugia, perugia, italia, [2]azienda ospedaliera Perugia, perugia, italy, [3]azienda oospedaliera perugia, perugia, Italy, [4]azienda ospedaliera perugia, perugia, italy

Purpose

The purpose of this poster is to show our experience, correlated with a picture gallery, in spine percutaneous procedure complications performed in our institution: vertebroplasty, placement of interspinous spacer, TC guided laser discolysis and chemonucleolysis with discogel.

Materials and Methods

Between 2018 and 2020 we performed 673 procedures: 442 vertebroplasty; 39 placement of interspinous spacer; 177 tc guided laser discolysis and 15 chemonucleolysis with discogel. In our experience we had 11 (1,65%) compications: 2 (0,45%) after vertebroplasty; 5 (13%) after interspinous spacer placement; 3 (1,69%) after TC guided laser discolysis and 1 (6,67%) after chemonucleolysis with discogel .

Results

All type of procedures share risk of bleeding and infectious of the disc, vertebral soma, and site of access which are surgery intrinsic complications. Possible complications after interspinous spacer placement are: dislocation and/or malposition of the device, instability, leakage of cerebrospinal fluid and fractures, in particular spinous process fractures. In our experience we had 1 case of spontaneous dislocation of the device, 1 case of rupture and dislocation of the device after trauma, 2 cases of spinous process fracture and 1 case of spinous process fracture after prophylactic spinoplastica. Possible complications after discolysis are: intracranial hypotension, linked or not to liquor fistula, and arachnoiditis. In our experience, after TC guided laser discolysis, we had 2 cases of persistent intracranial hypotension, one of those required "epidural blood patch" treatment. After chemonucleolysis with discogel we had 1 case of acute myelopathy. Possible complications after vertebroplasty are: pulmonary cement embolism; cement leakage and rib or pedicles fracture. Fracture of adjacent vertebral soma are not considered true complications. We want to highlight 1 case of tumoral seeding from clear cell renal carcinoma vertebral metastasis to soft tissue and peridural space through the course of the needle.

Conclusions

Percutaneous spine procedures are safe procedures with infrequent, mostly of minor gravity and easily treatable, complications. Rarely we con have major, unexpected complications.

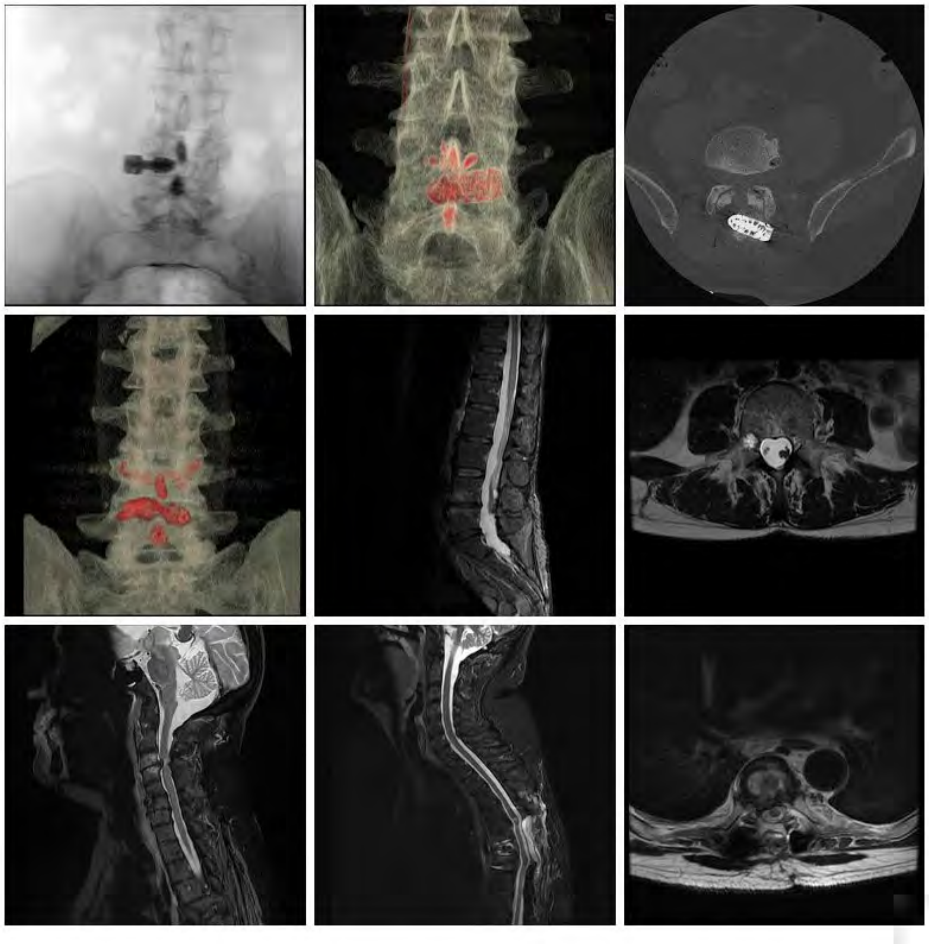

(Filename: TCT_1400_IM0-COLLAGE.jpg)

1420

Pattern based approach of spinal cord T2 high signal and characteristic enhancement for the diagnosis of myelopathy.

P Pokharel[1], A Swarnkar[2], R Mangla[3]

[1]SUNY upstate medical university, Syracuse, NY, [2]SUNY UpstateMedical University Hospital, Jamesville, NY, [3]Upstate Medical University, Syracuse, NY

Purpose

To distinguish whether various patterns of T2 hyperintensity and characteristic contrast enhancement can assist in diagnosis.

Materials and Methods

We reviewed our neuroimaging database along with T2 high signal and characteristic enhancement patterns consistent with the final diagnosis .We also collected additional information from the journal articles as well.

Results

Based upon our observations, we categorize these groups under T2 high signal intensity pattern such as inverted V sign in subacute combined degeneration (SACD) , owl's eyes sign in spinal cord infarct and characteristic enhancement pattern like pancake like enhancement of spondylotic myelopathy , ring like enhancement of NMOSD, missing piece sign in sDAVF, trident sign in Neurosarcoidosis and ring and flame sign in intramedullary metastasis .

Conclusions

On the basis of this study, we show that these patterns can be reliably distinguished and can assist in the diagnosis of myelopathy. Our pattern-based approach that combines pattern of T2 signal abnormality and characteristic enhancement provides a framework for radiologists to help narrow their differential diagnosis.

1370

Percutaneous CT Guided Biopsy of Deep-seated Head and Neck Lesions, Inaccessible with Ultrasound.

M Mangla[1], R Mangla[1], M Hussain[2], A Swarnkar[3]

[1]Upstate Medical University, Syracuse, NY, [2]SUNY Upstate Medical University, Syracuse, NY, [3]SUNY UpstateMedical University Hospital, Syracuse, NY

Purpose

The percutaneous sampling of the deep lesions can be performed with Fine needle aspiration cytology (FNA) and core biopsy. In this retrospective study we have evaluated the yield, technical consideration and safety in these deep-seated head and neck lesions which are inaccessible with Ultrasound.

Materials and Methods

In this IRB approved study, a retrospective data analyses of contiguous patients from January 2015 through September 2021, all the head and neck percutaneous core biopsy and Fine needle aspiration cytology cases were included. Clinical details including indication, prior surgery, patient demographics, location and size of lesion, biopsy or aspiration needle type, technical approach, dose-length product, use of moderate sedation and iodinated contrast, complications and diagnostic yield were recorded for all the patients.

Results

A total of 72 patients (30 Female) with age range 10 months-82 years were included in the study. In 44 cases FNA was performed and in 34 cases, core biopsy was performed (in 3 cases both FNA and biopsy was performed). The yield was 39/44 (88 %) for FNA and 32/34 (94%) for core biopsy. Out of 5 cases of nondiagnostic FNA, biopsy was performed in 3 cases in which 2 cases remain non-diagnostic and 1 case revealed the diagnosis. No complication was noted with either biopsy or FNA.

Conclusions

Percutaneous FNA and core biopsy of deep-seated head and neck lesions are safe and effective. Although core biopsy had better yield but in the difficult cases, FNA can also be performed with good yield.

224

Performance of Machine Learning Classifiers on MRI Based Radiomic Features to Differentiate BRAF-mutated and BRAF-fused Pediatric Low Grade Gliomas

M WAGNER[1], K Namdar[1], A Alqabbani[2], N Hainc[3], L Figueiredo[1], M Sheng[4], M Shroff[5], E Bouffet[1], U Tabori[1], C Hawkins[1], M Zhang[6], K Yeom[7], F Khalvati[1], B Ertl-Wagner[8]

[1]The Hospital for Sick Children, Toronto, Ontario, [2]University of Toronto, Toronto, Ontario, [3]University Hospital Zurich, Zürich, Canton of Zürich, [4]The Hospital for Sick Children, Toronto, IN, [5]Hospital for Sick Children University of Toronto, Toronto, Ontario, [6]Lucile Packard Children's Hospital Stanford, Palo Alto, CA, [7]Stanford University, Palo Alto, CA, [8]The Hospital for Sick Children, University of Toronto, Toronto, Ontario

Purpose

To assess the performance of five ML models to predict BRAF fusion or BRAF V600E mutation with step-wise increase of training data and to validate the results on an independent data set.

Materials and Methods

In this bi-institutional retrospective study, 251 pLGG FLAIR MRI datasets from 2 children's hospitals acquired between January 2000 and December 2018 were included and analyzed. Radiomics features were extracted from tumor segmentations and five models

(Random Forest, XGBoost, Neural Network (NN) 1 (100:20:2), NN2 (50:10:2), NN3 (50:20:10:2)) were tested to classify them. To keep the training and validation datasets independent, classifiers were cross-validated on the data from institution 1 and validated on the cohort from institution 2. Starting with 10% of the training data, models were cross-validated using a 4-fold approach at every step with an additional 2.25% increase in sample size. At each step, experiments were repeated 10 times using randomized versions of the respective percentage of the training data, resulting in 10 classifiers per step per model. At each step, these 10 classifiers were validated on the independent data set. Mean area under the curve (AUC) and 95% confidence intervals (CI) were calculated for every step for both training and independent data sets and the process was repeated for all five models.

Results

220 patients with pLGG (mean age 8.53 ± 4.94 years, 114 males, 67% BRAF fusion) were included in the training dataset, and 31 patients with pLGG (mean age 7.97±6.20 years, 18 males, 77% BRAF fusion) in the independent test dataset. NN1 (100:20:2) yielded the highest AUC. It predicted BRAF status with a mean AUC of 0.85, 95% CI [0.83, 0.87] using 60% of the training data and with mean AUC of 0.83, 95% CI [0.82, 0.84] on the independent validation data set.

Conclusions

Neural networks have the highest mean AUC and lowest standard deviations to predict BRAF status compared to Random Forest and XGBoost. Using 60% of the training set, the highest AUC for training and independent data and most stable outcomes in terms of variance were reached.

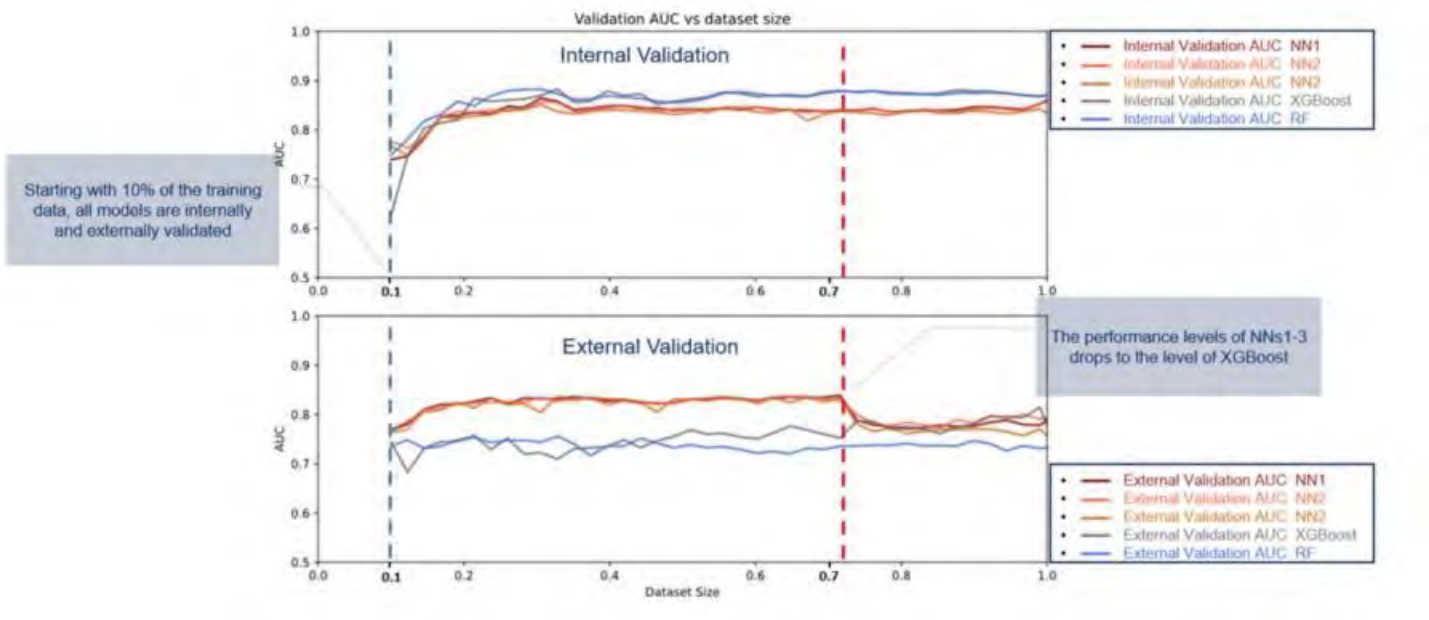

(Filename: TCT_224_ASNREPoster.jpg)

417

Perfusion Collateral Index vs. Hypoperfusion Intensity Ratio in Assessment of Angiographic Collateral Scores in Patients with Acute Ischemic Stroke

B Tsui[1], I Chen[1], J Qiao[2], M Nour[1], L Sharma[1], S Tateshima[1], M Bahr-Hosseini[1], G Colby[1], N Salamon[3], C Arnold[1], J Saver[1], R Jahan[1], g duckwiler[4], D Liebeskind[5], K Nael[1]

[1]UCLA, Los Angeles, CA, [2]UCLA, Los Angeles, CA, David Geffen School of Medicine at UCLA, Los Angeles, CA, Los Ageles, CA, [3]University of California Los Angeles, Los Angeles, CA, [4]ucla, Los Angeles, CA, [5]UCLA Stroke Center, Los Angeles, CA

Purpose

In acute ischemic stroke (AIS), perfusion imaging, while not directly visualizing collateral vessels, can provide important insight into collateral robustness, indexed by perfusion lesion volume and by perfusion lesion heterogeneity. Two proposed perfusion lesion heterogeneity measures indexing collateral status are the Perfusion Collateral Index (PCI) (1) and Hypoperfusion Intensity Ratio (HIR) (2). We aimed to compare the performance of PCI and HIR in collateral assessment in comparison to DSA and in determination of functional independence.

Materials and Methods

Consecutive AIS patients with anterior circulation large vessel occlusion who underwent pre-endovascular thrombectomy MRI perfusion imaging were included. MRI measures analyzed were: P1) Perfusion Collateral Index (PCI) - the volume of moderately hypoperfused tissue (arterial tissue delay time between 2 and 6 seconds: ATD 2-6sec) multiplied by its corresponding relative cerebral blood volume using Olea software; 2) Hypoperfusion Intensity Ratio (HIR) 2 ratio of moderate TMax >6 s lesion volume versus severe Tmax >10 s lesion volume with the RAPID software program. DSA collateral scores were evaluated by ASITN grading and dichotomized to inadequate (ASTIN <2) vs. adequate (ASTIN equal to or greater than 3). Functional outcome was determine by 90-day mRS.

Results
Among 126 patients meeting entry criteria, age (mean ± SD) was 71 (± 17.2), 58% female, and NIHSS (median, IQR) was 15 (10-19). For HIR, there was no significant difference in score values in patients with adequate vs inadequate collaterals: 0.42 ± 0.20 vs 0.46 ± 0.44, p=0.46. ROC analysis using previously described cut-off of 0.4 (2) resulted in an AUC of 0.56 and sensitivity/specificity of 52% / 60%. For PCI, score values were significantly higher in patients with adequate vs inadequate collaterals, 106 ± 55 vs. 64 ± 45, p=<0.001. ROC analysis using previously described cut-off of 62 (1) resulted in an AUC of 0.78 and sensitivity/specificity of 82% / 74%. In addition, 74% of patients with good functional outcome (mRS<2) had PCI > 62 (P=0.003) while only 34% of patents with good functional outcome had HIR <0.4 (p=0.52).
Conclusions
MRI-PCI outperforms HIR in assessment of collateral status and determination of good functional outcome and may be a promising imaging biomarker in patients with AIS.

486

Perivascular Spaces, Stroke and Small Vessel Disease: Insights from the APRISE Study

T Thompson[1], K Alwell[1], J Carrozzella[1], R Cornelius[1], S Gangatirkar[1], M Gaskill-Shipley[1], M Haverbusch[1], P Horn[2], V Khandwala[1], P Khatri[1], B Kissela[1], A Mahammedi[1], T Maloney[1], H Sucharew[2], T Tomsick[1], D Wang[3], L Wang[1], B Williamson[1], A Vagal[1]
[1]University of Cincinnati, Cincinnati, OH, [2]Cincinnati Children's Hospital Medical Center, Cincinnati, OH, [3]I-MED Radiology, Melbourne, Australia

Purpose
Perivascular spaces (PVS) are commonly identified on clinical magnetic resonance (MR) imaging of the brain, but their etiology and potential relationship to other small vessel disease markers remains unclear. Our objective was to evaluate the association between PVS and other imaging markers of cerebral small vessel disease (CSVD) in a large-scale population-based cohort of patients with stroke or transient ischemic attack (TIA). We hypothesized that the presence and frequency of PVS would be associated with white matter hyperintensities, lacunes and cerebral microbleeds.
Materials and Methods
All stroke and TIA patients were ascertained and characterized in a metropolitan population of 1.3 million for the calendar year of 2015 as part of the NIH-funded Greater Cincinnati/Northern Kentucky Stroke Study. All associated MR brain imaging was then characterized by STRIVE criteria for small vessel disease through the ancillary NIH-funded Assessing Population-based Radiological brain health in Stroke Epidemiology (APRISE) study. Perivascular spaces were evaluated at the level of the centrum semiovale (CS) and basal ganglia (BG) and assigned a score of between 0 and 4 utilizing the following scale: 0 = not present, 1 = 1-10 PVS, 2 = 11-20 PVS, 3 = 21-40 PVS, and 4 ≥ 40 PVS. White matter hyperintensities (WMH) were graded according to the Fazekas scale. Cerebral microbleeds and lacunes were categorized as absent or present. Univariate and multivariable regression analyses were performed to determine the relationship between PVS and other imaging features of small vessel disease after adjusting for potential clinical confounders. For patients with more than one stroke or TIA event in the study year, only the first event was used in the analysis.
Results
We currently report results from 1756 stroke/TIA patients with associated MRIs (72% of projected total MRIs from the study population) with a mean age of 68 ± 15 years of whom 53% are women. Total PVS count (CS+BG) is associated with WMH severity and lacunes but not with microbleeds while controlling for relevant clinical variables. When considered separately, CS-PVS is only associated with lacunes while BG-PVS is associated with all three markers of CSVD including WMH, lacunes, and microbleeds (Table 1). Full results will be provided at the time of the final presentation.
Conclusions
PVS are common in the stroke/TIA population and are associated with other imaging markers of CSVD including WMH and lacunes but not with cerebral microbleeds.

Table 1: Linear regression and logistic models for PVS in the combined centrum semiovale and basal ganglia (CS+BG), centrum semiovale only (CS) and basal ganglia only (BG) regions

	CS+BG (Score 0-8)		CS Only (Score 0-1 vs 2-4)		BG Only (Score 0-1 vs 2-4)	
Study Variable	Coefficient (95% CI)	p-value	OR (95% CI)	p-value	OR (95% CI)	p-value
WMH (Fazekas scale)	**0.16 (0.11 to 0.21)**	**<0.01**	1.06 (0.99 to 1.13)	0.10	**1.33 (1.24 to 1.43)**	**<0.01**
Lacunes (Present)	**0.38 (0.21 to 0.55)**	**<0.01**	**1.36 (1.10 to 1.68)**	**<0.01**	**1.83 (1.46 to 2.30)**	**<0.01**
Microbleeds (Present)	0.15 (-0.05 to 0.36)	0.15	1.09 (0.84 to 1.41)	0.52	**1.35 (1.03 to 1.77)**	**0.03**

(Filename: TCT_486_Table1.jpg)

377

Pre-Clinical Magnetic Resonance Imaging Model of Glioblastoma Immunotherapy Mediated Neuroinflammation Replicates the Human Clinical Paradigm of Pseudoprogression

R Barajas Jr.[1], S Holland[2], P Ambady[3], L Muldoon[3], E Neuwelt[3]
[1]OHSU, Portland, OR, [2]Oregon Health & Science Univer, Portland, OR, [3]Oregon Health & Science University, Portland, OR

Purpose
Progressive enhancement on gadolinium enhanced magnetic resonance imaging (Gd-MRI) may be a manifestation of

neuroinflammatory mediated therapeutic response (pseudoprogression; Psp)1. Despite entirely different cellular compositions; Psp cannot be reliable differentiated from growing tumor by Gd-MRI. Innate immunity plays a biological role in Psp, and can be augmented by Amphotericin B2 (Amp B). The purpose of our study was to define the Gd-MRI characteristics and efficacy of AmpB based GBM therapy.

Materials and Methods

Adult Long Evans rats underwent intracerebral syngeneic xenograft implantation using RG2 GBM cells. Ten days later pre-therapeutic T2, T2* and T1-Gd-MRI (Gadodiamide, 70 mg/kg) confirmed tumor growth. Three treatment groups were studied; 1) untreated control (N= 18), 2) CRT only (irradiation [5 Gy] and temozolomide [20 mg/kg, PO x1] (N=16), or 3) CRT with AmpB (0.2 mg/kg, IP QD x 3-7 days) (N=15). Macrophages depletion with Clodronate liposomes provided a positive control (50mg/kg IP on day 7 & day 14 with AmpB). Post-therapeutic Gd-MRI was performed for symptoms requiring euthanasia or at day 40 following implantation. Rats without tumor Gd-MRI enhancement were censored for Kaplan-Meier Survival analysis. Semi-automated volumetric MRI segmentation was performed with Horos software. Significance was evaluated using Students T-test with unequal variances.

Results

Innate immune mediated neuroinflammation by CRT with AmpB showed prolonged survival (19.9 ± 6.8 days) compared to untreated controls (16.5 ± 3.8 days; P< 0.001) (Figure 1A) but not with Clodronate (18.6 ± 8.2 days; P= 0.08). CRT alone also extended survival (20.8 ± 8.5 days; P< 0.01). Similar to the clinical context, Gd-MRI volumes in the CRT group (88.7 ± 117 mm3) were not significantly different from the neuroinflammatory CRT with AmpB group (70.5 ± 65.5 mm3; P= 0.64; Figure 1B). But, was less than untreated controls (145 ± 71.5 mm3; P< 0.01). Histological assessment demonstrated reduced tumor burden within the CRT with AmpB group (P= 0.03), but not the CRT alone group (P= 0.14), compared to untreated controls (Figure 1C).

Conclusions

We report our initial experience with an immune competent GBM model of Psp. This is critically needed to ascertain mechanistic insights into specific aspects of neuroinflammation. Preliminary results suggest that AmpB augmented innate immune based neuroinflammation provides a significant survival benefit and replicates the nonspecific Gd-MRI clinical paradigm of Psp.

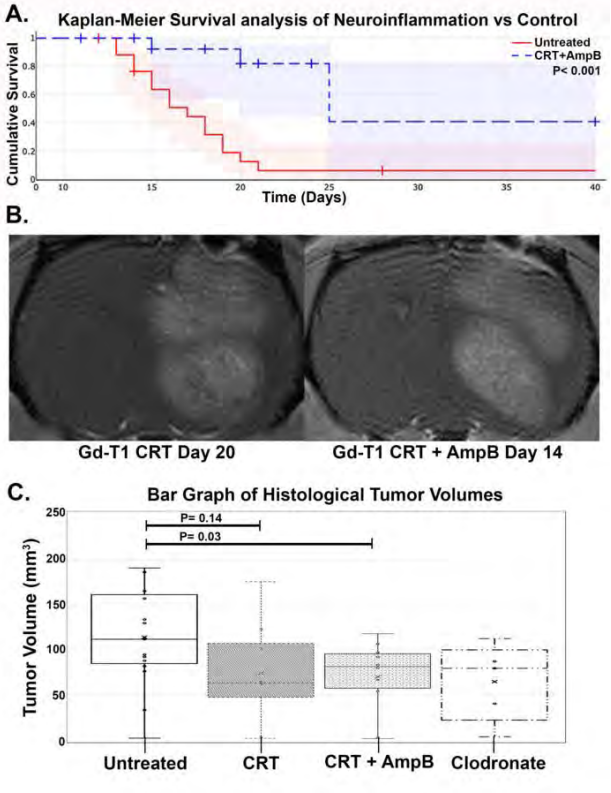

(Filename: TCT_377_Figurecopy.jpg)

1156

Prediction of amyloid β positivity in amyloid PET-CT: machine learning application to investigate amyloid β-related MRI markers

J LEE[1]

[1]*HANYANG UNIVERSITY HOSPITAL, SEOUL, Korea, Republic of*

Purpose

This study hypothesized that the integration of white matter hyperintensities (WMH), cerebral microbleeds (CMB), and regional volume could predict Aβ-positivity using multi-MR parameters and machine learning. Our study aimed to investigate the difference in

WMH, prevalence of CMB, and regional volume between Aβ-positive and Aβ-negative groups and to predict Aβ-positivity using a machine learning method.
Materials and Methods
This retrospective and cross-sectional study included 139 patients with MCI and AD who underwent both amyloid PET-CT and brain MRI from January 2017 to March 2020. Subjects were divided into Aβ-positive (n=84) and Aβ-negative (n=55) groups. Visual analysis was performed to evaluate the Fazekas scale of white matter hyperintensity (WMH) and cerebral microbleeds (CMB) scores. Quantitative measurements were used to assess the WMH and regional brain volume. Multivariable logistic regression analysis and machine learning methods were used to identify the best MRI predictors of Aβ-positivity. We adopted support vector machine (SVM) and logistic regression, which are frequently used in many classification studies, and evaluated binary classification performance between the Aβ-positive and the Aβ-negative groups.
Results
Aβ-positivity was observed in 60.4% of patients. Regarding clinical assessment, there was a significant difference between the groups in terms of MMSE, CDR, and CDRSB scores. In the visual analysis, the Aβ-positive group showed significantly higher Fazekas scale for WMH and CMB scores (p=0.02, and 0.04, respectively). Multiple regional volumes, including the hippocampus, entorhinal cortex, left parahippocampal gyrus, precuneus, and left parietal lobe, were significantly smaller in the Aβ-positive group ($p<0.05$). The volume of the third ventricle and inferior lateral ventricle were significantly larger in the Aβ-positive group (p=0.002, and p=0.003, respectively). The machine learning technique showed good accuracy (81.1%) with the mini-mental state examination (MMSE) and brain regional volumes. The SEN, SPE, PPV, NPV, and AUC for the logistic regression classifier were 91.6%, 65.5%, 80.4%, 85.3%, and 79.0% respectively.
Conclusions
In conclusion, the Aβ-positive group showed lower MMSE scores, higher volumes of WMH, more frequent CMBs, and regional brain volume changes. The machine learning method exhibited good accuracy in predicting Aβ-positivity with the MMSE score and regional volume, including the third ventricle, hippocampus, entorhinal cortex, and precuneus.

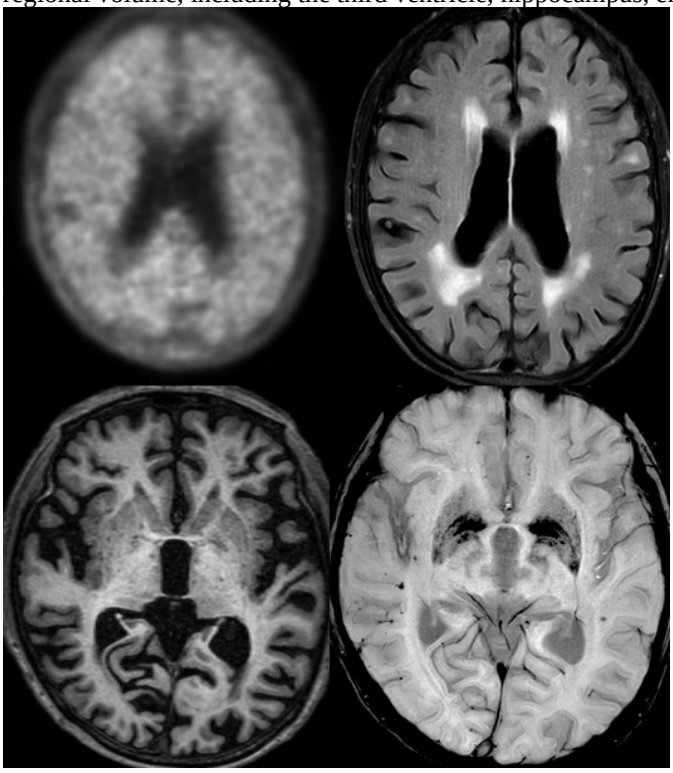
(Filename: TCT_1156_1.jpg)

856

Prediction of Hemorrhagic Complications After Ultrasound-Guided Biopsy of the Thyroid and Neck

J Lee[1], J Kim[1], H Chung[2], S Nam[2], R Yoo[1], I Hwang[1]
[1]Seoul National University Hospital, Seoul, Seoul, [2]Seoul National Unversity Hospital, Seoul, Seoul

Purpose
Hemorrhage occasionally occurs after ultrasound (US)-guided biopsy of the thyroid and neck and sometimes leads to serious complications. We aimed to identify predictors of hemorrhagic complications after US-guided biopsy of the thyroid and neck.
Materials and Methods
In this retrospective study, we analyzed consecutive patients who underwent US-guided biopsy from April to November 2020. Procedure characteristics, US features, and peri- and post-procedural patient symptoms and signs were compared between patients

with and without post-biopsy hemorrhage. Associations between clinical and imaging variables and post-biopsy hemorrhage were analyzed using univariate and multivariate regression analyses.
Results
A total of 305 patients who underwent US-guided biopsy of the thyroid and neck were included (219 women, 86 men; age range, 20-89 years). Seventeen (5.7%) cases of post-biopsy hemorrhage were detected 30 min after biopsy and manual compression. Among them, 10 developed hemorrhage at 30 min without immediate hemorrhage. In the multivariate analysis, a high tenderness score on the visual analog scale (VAS) at 30 min after biopsy (odds ratio [OR] 5.05, P < .001) was identified as an independent predictor of post-biopsy hemorrhage. In patients with hemorrhage at 30 min, tenderness scores significantly increased over 30 minutes of observation.
Conclusions
High tenderness scores at 30 min after biopsy and manual compression were independent predictors of hemorrhage after US-guided biopsy of the thyroid and neck. The tenderness score could serve as a valuable marker to triage patients who require further observation and management after a US-guided biopsy of the thyroid and neck.

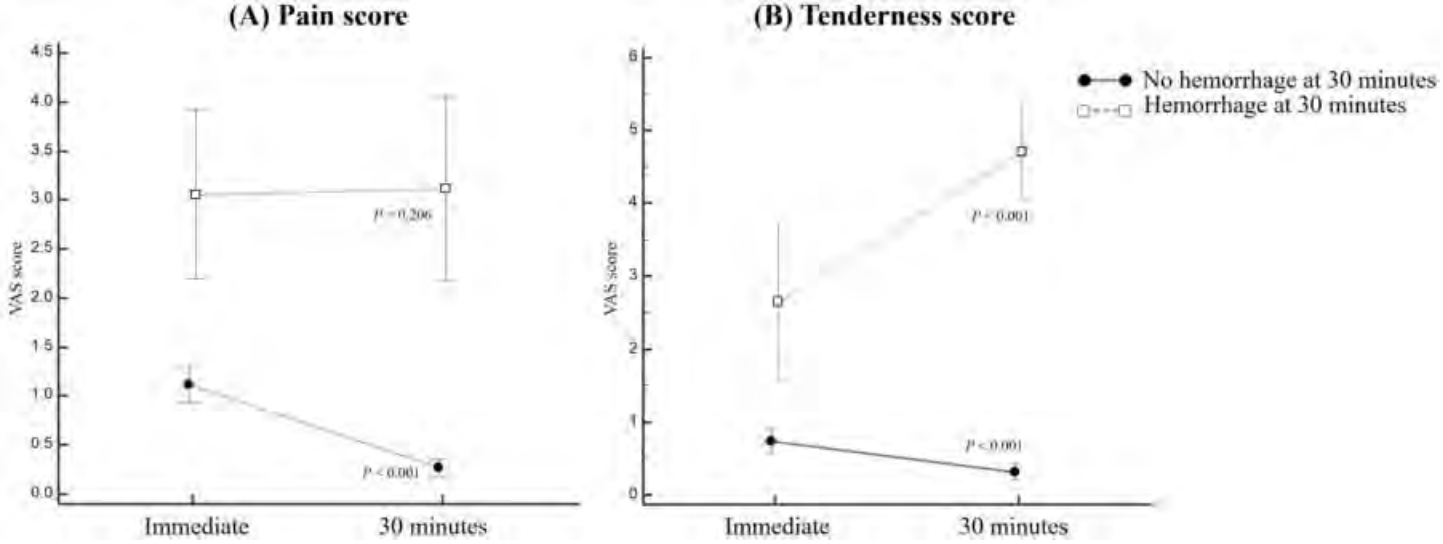

(Filename: TCT_856_Fig2.jpg)

1022
Prediction of MGMT promoter methylation status in glioblastomas using an ensemble neural network framework.
G Singh[1], M Bhattacharya[2], T Kainth[2], A Lignelli[3], V Spektor[3], P Prasanna[2]
[1]Newark Beth Israel Medical Center, Newark, NJ, [2]Stony Brook University, Stony Brook, NY, [3]Columbia University Irving Medical Center, New York, NY

Purpose
Glioblastoma Multiforme (GBM) is a highly aggressive neoplasm and accounts for over 45% of all primary malignant tumors in the brain. Surgery followed by Temozolomide and radiation is standard of care for GBM. The efficacy of Temozolomide may be affected by the methylation status of O6-methylguanine methyltransferase (MGMT) at promoter and enhancer regions. High activity of MGMT in cancer cells blunts therapeutic effects of alkylating agents. Methylation of MGMT regulatory regions silences the protein, increasing the efficacy of Temozolomide. Surgical sampling with or without resection is the gold standard to detect these genetic alterations. However, depending on patient comorbidities or location of neoplasm-for example in brain stem or eloquent area, an in vivo MGMT imaging marker is desired. Furthermore, due to tumor heterogeneity surgical sampling is inherently biased and potentially incomplete. Semantic imaging features on conventional MRI have been suggested to predict MGMT methylation, without expert consensus. In this study, we explore the efficacy of an ensemble neural network framework in predicting MGMT methylation status on treatment-naive multiparametric MRI.
Materials and Methods
Our dataset consists of 669 cases from the RSNA Radiogenomics challenge. The available imaging sequences include FLAIR, T1w, T2w, and T1wCE protocols. An ensemble of different DenseNet backbone architectures is proposed to predict MGMT methylation status. A cascaded ensemble of 3 different types of DenseNet backbones is introduced where individual backbones are connected in parallel. The features from these three backbones are extracted from all MR sequences. 500, 82, and 87 cases are used for training, validating, and testing. The extracted features are subjected to a Global Average Pooling layer followed by a series of dense layers with a Rectified Linear Unit-activation and dropout. The output from the previous layers is provided to the final classification dense layer with a softmax activation that outputs a probability value for the presence of MGMT promoter methylation. Finally, this ensemble architecture is trained with a Categorical Cross-entropy Loss.
Results
The proposed method achieves a final testing Area-under-Curve (AUC) value of 91.38% with a training loss of 0.0013.

Conclusions

Our deep learning model demonstrates high AUC in predicting MGMT methylation status in treatment-naive GBM. This may potentially enhance MR imaging capabilities to predict appropriate treatment and prognosis in GBM.

1498

Prediction of pTERT mutation in IDHwt-Glioblastoma Using Random Forest Algorithm to Analyze Preoperative MR Imaging features.

Y Cai[1], O Arevalo[2], S Shams[3], R Patel[4], C Sitton[5], R Samant[6], B Chen[1], D Timaran-Montenegro[7], S Khanpara[8], L Nunez[1], L De Alba[9], J Zhu[4], R Riascos[4]

[1]University of Texas Health Science Center at Houston, Houston, TX, [2]LSU Health Shreveport, Shreveport, LA, [3]San José State University, San Jose, CA, [4]The University of Texas Health Science Center at Houston, Houston, TX, [5]UT Health, Houston, TX, [6]UT Health, McGovern School of Medicine, Texas Medical Center, Houston, TX, [7]McGovern Medical School at UT Health, Houston, TX, [8]University of Texas MD Anderson Cancer Center, Houston, TX, [9]LSU SHREVEPORT, SHREVEPORT, LA

Purpose

Studies shows that promoter Telomerase Reverse Transcriptase (pTERT) mutation in glioblastoma(GBM) has worse prognosis[1]. Noninvasive preoperative prediction of pTERT can help to predict prognosis. Machine learning algorithms are more suitable for prediction than statistical methods. In our study, we deployed a random forest (RF) algorithm to predict pTERT status in GBM.

Materials and Methods

Preoperative MR scans of 155 IDHwt patients with known pTERT status were retrospectively analyzed (93 pTERTmut, 62 pTERTwt, 58.9±13.4 years). Age and BRAF mutation status were also included. MR features were evaluated using Visually AcceSAble Rembrandt Images (VASARI), and semiautomatic segmentation was performed (volumetric measurement of enhancement, FLAIR hyperintensity, and necrosis). A sklearn based code ran on the Google Colab platform to analyze a total of 28 features. A 5-fold cross validations were used. Statistical method was used to infer the association between pTERT status and these 28 features. Chi-Square and t-test were used to compare categorical and continuous variables respectively to obtain p values.

Results

Table 1 lists prediction accuracy, top 7 significant features and their feature importance (corresponding weight) RF algorithm calculated. Table 2 shows the statistical analysis of these top 7 features. Table 3 summarizes the sensitivity, specificity, positive predict value (PPV), negative predict value (NPV) and area under curve(AUC) when using 5-fold cross-validation.

Conclusions

Using 5-fold cross-validation, RF algorithm's prediction accuracy can reach 87%, higher than 74% of support vector machine (SVM) in previous work[2]. Our work also confirmed previous work[2] findings showing that the proportion of necrosis volume and age were significantly greater in pTERTmut GBM than in pTERTwt GBM. Although our study didn't show any statistical difference in the necrosis volume, proportion of nCET and proportion of enhancing, RF algorithm still ranks them as the top 7 important features, indicating that the RF is more stable than statistical methods in selection of important features since the univariate filters, such as a t-test do not account for interactions between variables and collinearity while RF as a multivariate predictive model is able to capture these interactions. Our study shows the sensitivity of RF algorithm can reach 94%, making it a great tool for screening of pTERT mutation. Incorporation of more features may strengthen our model's prediction accuracy further.

Table 1: prediction accuracy, top 7 features Random Forest Algorithm selects.

Prediction accuracy±Std in 5 fold corss validation	0.87±0.08	
Top 7 features / its weighting factor	Age	0.10583
	Tumor volume	0.103077
	F5 - Proportion of Enhancing	0.097838
	F6 - Proportion nCET	0.094228
	F7 - Proportion of Necrosis	0.087818
	Necrosis Volume	0.064843
	F14 - Proportion of edema	0.050905

Table 2: Statistically analysis of top 7 features RF model selects

Features	pTERT mutation		wild type	p value
Age	61.6±11.5	vs	55.0±15.0	0.004
Tumor volume	133.53±77.2	vs	159.8±90.3	0.031
Proportion of Enhancing	16.76%±8.09%	vs	17.94±10.4%	0.227
Proportion of nCET	77% ±10.4%	vs	75.73%±12.53%	0.246
Proportion of Necrosis	16.8%± 8.06%	vs	6.3%±6.6%	<0.0001
Necrosis volume	9.26%±10.34%	vs	9.92%±11.36%	0.357
Proportion of edema	3.6% ±0.91%	vs	4.08% ±0.85%	0.006

Table 3: Sensitivity, specificity, PPV, NPV and AUC in 5-fold cross-validation.

Sensitivity	94%
Specificity	69%
PPV	80%
NPV	82%
AUC	0.95

(Filename: TCT_1498_picture.jpg)

275

Prognostic Relevance of Adding Radiomics to the 2021 WHO Updates for IDH-Wildtype Histological Lower-Grade Gliomas with Known EGFR Amplification and TERT Promoter Mutation Status

Y Park[1], C Park[2], S Ahn[3], S Lee[4]

[1]Yonsei University College of Medicine, Seoul, Korea, Republic of, [2]Yongin Severance hospital, Gyeonggi-do, Gyeonggi-do, [3]Yonsei University College of Medicine, Seoul, Seoul, [4]Severance hospital, Seoul, Korea

Purpose

Epidermal growth factor receptor (EGFR) amplification and telomerase reverse transcriptase promoter (TERTp) mutation are key molecular markers based on the 2021 World Health Organization classification that predict a poor prognosis in IDH-wildtype (IDHwt) histological lower-grade gliomas (LGGs).The purpose of this study was to assess whether radiomic features could improve the accuracy of survival predictions of IDHwt histological LGGs over clinicopathological features.

Materials and Methods

Preoperative MRI data of 61 patients with IDHwt histological LGGs were included as the institutional training set. The test set consisted of 32 patients from The Cancer Genome Atlas. Radiomic features (n = 186) were extracted using conventional MRIs. The radiomics risk score (RRS) for overall survival was derived from the elastic net. Multivariable Cox regression analyses with clinicopathological features (including EGFR amplification and TERTp mutation status) and the RRS were performed. The integrated area under the receiver operating curves (iAUCs) from the models with and without the RRS were compared. The prognostic value of the RRS was evaluated using the external validation set.

Results

The RRS independently predicted overall survival (hazard ratio = 48.08; P = 0.001). Compared with the clinicopathological model alone (iAUC = 0.775), adding the RRS had a better overall survival prediction performance (iAUC = 0.910), which was internally validated, and a similar trend was found on external validation. The prognostic significance of the RRS was confirmed using the external validation set (P = 0.001).

Conclusions

Integrating radiomics with clinicopathological features (including EGFR amplification and TERTp mutation status) can improve overall survival predictions in patients with IDHwt LGGs.

Figure 1. Radiomics pipeline

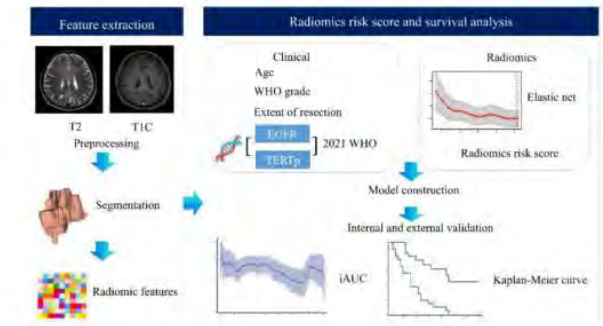

Figure 2. Time-dependent receiver operating characteristic curves for the models with and without the RRS.

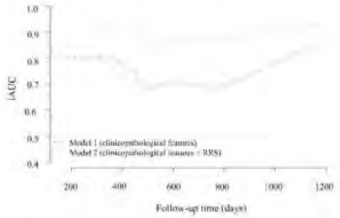

Figure 3. Kaplan-Meier curves for the (a) institutional training set and the (b) external validation set.

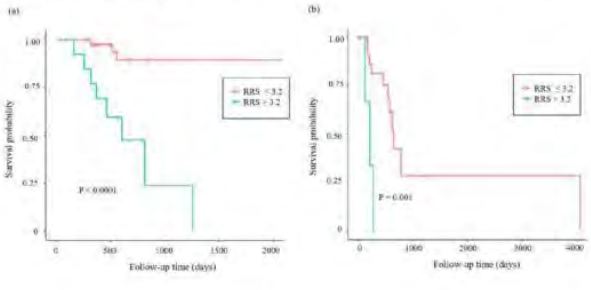

(Filename: TCT_275_Figure.jpg)

1061

Quantifying cerebrospinal fluid movements via the interventricular foramina: An original in-vivo study by phase contrast MRI on healthy subjects

N hamdan[1], E Pomero[2], L Thines[3]

[1]CHRU JEAN MINJOZ, BESANCON, France, [2]Besancon University Hospital, Besancon, France, [3]CHRU JEAN MINJOZ, BESANCON, Doubs

Purpose

Cerebrospinal fluid (CSF) macro-movements, recently studied by in-vivo MRI techniques, are found to be pulsatile and influenced by many intrinsic and extrinsic factors. Using phase contrast MRI technique (PC-MRI), quantitative parameters allowed intra individual (over time) and inter individual (healthy v/s pathological) comparison.

Materials and Methods

Healthy volunteers underwent two MRI scans (separated by at least 48 hours) with PC-MRI sequences on the same 3T MRI machine, for quantitative measurements of four CSF flow parameters (mean peak flow velocity, mean stroke volume, mean surface of Region of Interest (ROI) and net mean flow). Anatomically studied areas were the two interventricular foramina and the cerebral aqueduct. Two observers blindly delineated the ROI, allowing a software to extract all parameters values from raw images. Concordance correlation coefficients (CCC) were then calculated for each parameter to study intra-individual reproducibility and Intraclass correlation coefficients (ICC) to study inter-observer consistency.

Results

27 healthy volunteers (12 males and 15 females) with a mean age of 27.1 years (range 22-38) were included for analysis. Mean exam time was respectively 35 minutes and 26 minutes. Mean time interval between the two exams was 14.7 days (range 5-47). CCC for the IVF was considered fairly good for two parameters: mean stroke volume (0.82 CI95% 0.63-0.93) and mean peak flow velocity (0.86 CI 0.70-0.93). Inter-observer ICC for the IVF was either good or excellent for all the studied parameters (range 0.71-0.99).

Conclusions

This study demonstrates intra-individual reproducibility of an MRI sequence measuring quantitatively and for the first time two CSF flow parameters applied to the interventricular foramina. Further research will study evolution of these parameters through time and in pathological conditions (i.e. chronic hydrocephalus) before and after shunt surgery. Ultimately, a direct reliable personalized sequence of shunt dysfunction could be developed.

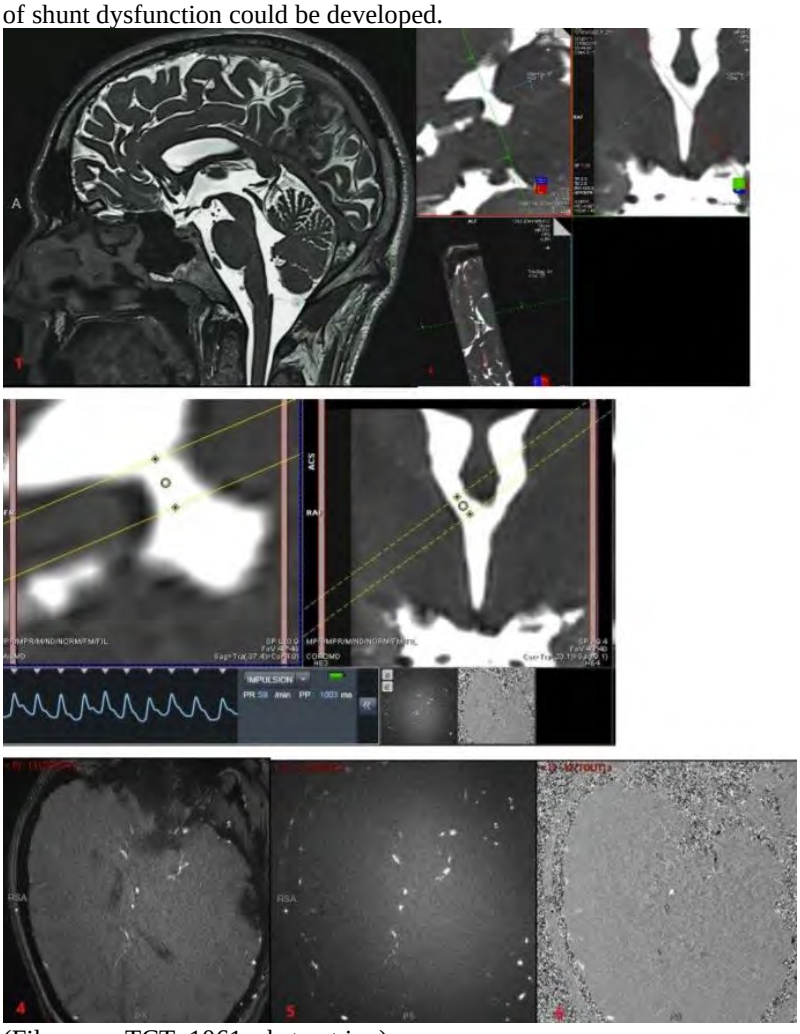

(Filename: TCT_1061_abstract.jpg)

1050

Quantitative Susceptibility Mapping of Deep Gray Matter Using Deep Neural Network at Ultra-High Magnetic Field Strength

C Otgonbaatar[1], G Jo[2], S Han[3], H Song[4], J Lee[2], I Hwang[2], R Yoo[2], K Kang[2], T YUN[2], S Choi[2], J Kim[2], C Sohn[2]

[1]Seoul National University, College of Medicine, Seoul, Korea, Republic of, [2]Seoul National University Hospital, Department of Radiology, Seoul, Korea, Republic of, [3]Institute for Basic Science (IBS), Suwon, Korea, Republic of, [4]Seoul National University Hospital, Biomedical Research Institute, Seoul, Korea, Republic of

Purpose

Increased iron deposition in the deep gray matter has been reported in patients with multiple sclerosis. Quantitative susceptibility mapping (QSM) is a recently introduced MRI technique that uses phase data to provide quantification of tissue iron. QSMnet+ uses a deep neural network to solve the ill-conditioned deconvolution issues and perform high-quality susceptibility map without long-acquisition-time and patient discomfort. Therefore, we aimed to assess the susceptibility of the deep gray matter with QSMnet+ and improved-sparse-linear-equation-and-least-squares (iLSQR) approaches at Ultra-High Field 7.0T MRI.

Materials and Methods

Thirty healthy controls (mean age 26±4 years; 15 males) were scanned with MAGNETOM Terra 7.0-T-MRI to analyze the magnetic susceptibility. QSM images were reconstructed using the deep neural network-based QSMnet+ and iLSQR algorithms. For ROI analysis, susceptibility values were analyzed from caudate nucleus (CN), globus pallidus (GP), putamen (PUT), red nucleus (RN), amygdala (AMG), substantia nigra (SN) and thalamic subnuclei (VPL, ventral posterolateral; VPM, ventral posteromedial; Pul, pulvinar; MD, medial dorsal; VL, ventral lateral; VA, ventral anterior; LD, lateral dorsal; LP, lateral posterior; An, anterior) bilaterally.

Results

QSMnet+ demonstrated significantly higher susceptibility in the AMG, CN left, lateral GP, medial GP left, Putamen right, RN, VPL, VPM, MD left, VL, An, LD right, and LP right than iLSQR ($p<0.03$). Table 1 illustrates the mean values of susceptibility in the deep gray matter among males and females in both algorithms. The mean of the standard deviations of susceptibility from all deep gray matter was significantly lower in the QSMnet+ than iLSQR approach ($p<0.001$). QSMnet+ showed significant difference in the susceptibility in the AMG right, CN left, Lateral GP left, medial GP, SN left, VPM right, Pul left, VL right, VA right between males and females ($p<0.04$). Fig. 1 demonstrates the comparison of the visualization of the deep gray matter on QSM images. QSMnet+ provides a better visualization of the anatomical boundaries of the deep gray matter.

Conclusions

The recently proposed QSMnet+ algorithm improved the susceptibility measurement in the deep gray matter at ultra-high-field 7.0-T MRI compared with iLSQR.

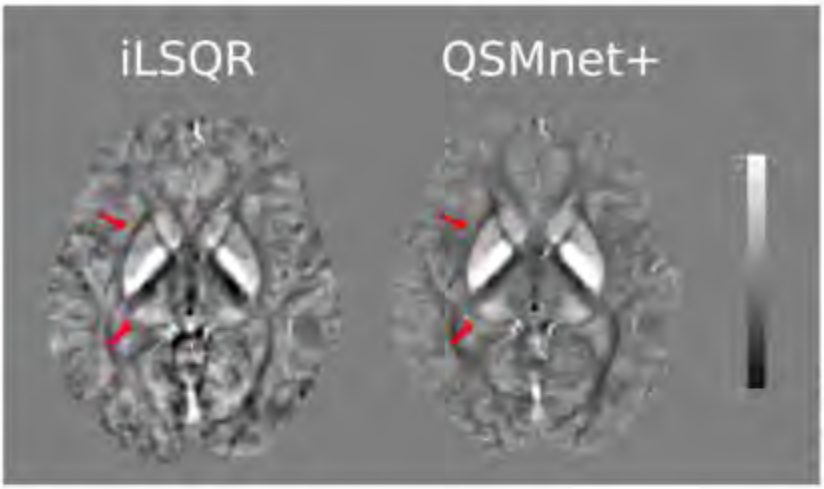

Fig. 1. The visualization of the deep gray matter on quantitative susceptibility mapping (QSM) between QSMnet+ and iLSQR algorithms at 7T MRI. QSM acquired by QMSnet+ demonstrated a more accurate and detailed visualization of the deep gray matter and its anatomical border (red arrow).

Table 1. The ROI analysis of susceptibility estimated for deep gray matter

Susceptibility	QSMnet+ (mean ppm value ± SD)					iLSQR (mean ppm value ± SD)					QSMnet+ vs iLSQR
	Female (n=15)	Male (n=15)	P value (Male vs Female)	P value (Right vs Left)	Total (n=30)	Female (n=15)	Male (n=15)	P value (Male vs Female)	P value (Right vs Left)	Total (n=30)	
VPL Left	-0.019±0.009	-0.014±0.011	0.161	0.181	-0.017±0.010	-0.028±0.009	-0.0a22±0.009	0.367	0.057	-0.024±0.009	0.002
VPL Right	-0.017±0.010	-0.009±0.010	0.051		-0.013±0.011	-0.031±0.009	-0.024±0.012	0.065		-0.028±0.011	0.003
VPM Left	0.002±0.007	0.006±0.006	0.098	0.001	0.004±0.007	-0.003±0.009	0.002±0.007	0.083	0.534	-0.003±0.008	0.028
VPM Right	0.007±0.005	0.012±0.004	0.012		0.010±0.005	-0.005±0.011	-0.001±0.012	0.398		-0.002±0.011	0.091
Pulvina Left	0.013±0.005	0.010±0.003	0.024	0.129	0.011±0.003	0.011±0.006	0.010±0.006	0.692	0.498	0.010±0.006	0.260
Pulvina Right	0.011±0.004	0.009±0.003	0.054		0.010±0.004	0.011±0.006	0.010±0.007	0.578		0.011±0.006	0.582
MD Left	0.005±0.004	0.007±0.005	0.180	0.734	0.006±0.004	0.003±0.006	0.002±0.010	0.868	0.769	0.002±0.009	0.031
MD Right	0.006±0.003	0.005±0.005	0.557		0.005±0.004	0.007±0.005	-0.001±0.006	0.001		0.003±0.007	0.098
VL Left	-0.013±0.004	-0.010±0.006	0.179	0.950	-0.012±0.005	-0.022±0.010	-0.014±0.005	0.002	0.002	-0.019±0.008	0.001
VL Right	-0.01e±0.009	-0.008±0.006	0.610		-0.013±0.009	-0.029±0.007	-0.019±0.007	0.001		-0.023±0.009	0.001
VA Left	-0.020±0.006	-0.016±0.007	0.133	0.681	-0.018±0.006	-0.029±0.011	-0.016±0.012	0.008	0.028	-0.022±0.013	0.125
VA Right	-0.029±0.009	-0.023±0.007	0.045		-0.026±0.009	-0.037±0.009	-0.019±0.013	0.001		-0.028±0.014	0.518
An Left	-0.005±0.004	-0.005±0.007	0.419	0.522	-0.004±0.006	-0.020±0.010	-0.021±0.013	0.956	0.366	-0.021±0.012	0.001
An Right	-0.004±0.005	-0.006±0.007	0.615		-0.005±0.006	-0.016±0.009	-0.021±0.012	0.211		-0.018±0.017	0.001
LP Left	-0.001±0.007	0.002±0.006	0.209	0.084	0.0002±0.006	-0.004±0.009	-0.001±0.009	0.310	0.369	-0.002±0.009	0.152
LP Right	0.0004±0.009	0.006±0.008	0.086		0.002±0.009	-0.009±0.011	0.0003±0.010	0.026		-0.004±0.011	0.082
LD Left	-0.001±0.008	-0.005±0.005	0.111	0.091	-0.003±0.007	-0.012±0.012	-0.007±0.021	0.416	0.940	-0.009±0.017	0.067
LD Right	0.003±0.009	-0.002±0.008	0.063		0.007±0.009	-0.003±0.013	-0.015±0.015	0.024		-0.009±0.015	0.001
AMG Left	-0.012±0.003	-0.010±0.003	0.079	0.001	-0.011±0.003	-0.005±0.010	-0.007±0.008	0.624	0.001	-0.006±0.009	0.002
AMG Right	-0.010±0.004	-0.006±0.004	0.022		-0.008±0.005	-0.005±0.009	0.003±0.010	0.262		0.003±0.010	0.001
CN Left	0.025±0.006	0.021±0.004	0.033	0.352	0.024±0.006	0.020±0.007	0.017±0.006	0.191	0.001	0.019±0.007	0.001
CN Right	0.024±0.005	0.021±0.004	0.063		0.023±0.004	0.025±0.008	0.024±0.009	0.827		0.024±0.008	0.507
Lateral GP Left	0.079±0.018	0.066±0.010	0.027	0.001	0.073±0.015	0.064±0.010	0.062±0.010	0.607	0.001	0.063±0.010	0.001
Lateral GP Right	0.068±0.013	0.051±0.011	0.105		0.065±0.012	0.056±0.012	0.058±0.012	0.711		0.057±0.012	0.001
Medial GP Left	0.084±0.025	0.058±0.017	0.001	0.685	0.071±0.025	0.060±0.025	0.057±0.014	0.233	0.084	0.062±0.020	0.032
Medial GP Right	0.080±0.024	0.062±0.019	0.035		0.071±0.023	0.067±0.019	0.067±0.015	0.969		0.067±0.017	0.339
PUT Left	0.022±0.009	0.020±0.007	0.559	0.001	0.021±0.008	0.019±0.004	0.020±0.007	0.783	0.001	0.019±0.006	0.070
PUT Right	0.017±0.006	0.015±0.006	0.537		0.016±0.006	0.011±0.007	0.012±0.008	0.630		0.011±0.007	0.001
RN Left	0.032±0.015	0.030±0.016	0.727	0.710	0.031±0.015	0.024±0.019	0.014±0.019	0.189	0.771	0.019±0.019	0.001
RN Right	0.034±0.017	0.030±0.016	0.489		0.032±0.017	0.022±0.013	0.017±0.022	0.495		0.020±0.018	0.001
SN Left	0.061±0.021	0.048±0.018	0.046	0.001	0.054±0.019	0.039±0.017	0.042±0.019	0.018	0.012	0.051±0.020	0.289
SN Right	0.047±0.020	0.034±0.017	0.055		0.040±0.020	0.042±0.023	0.038±0.021	0.644		0.040±0.021	0.946

Note: caudate nucleus, CN; globus pallidus, GP; putamen, PUT; red nucleus, RN; amygdala, AMG; substantia nigra, ventral posterolateral nucleus, VPL; ventral posteromedial nucleus, VPM; medial dorsal nucleus, MD; ventral lateral nucleus, VL; ventral anterior nucleus, VA; anterior nucleus, An; lateral posterior nucleus, LP; lateral dorsal nucleus, LD; standard deviation, SD; parts per million, ppm.

(Filename: TCT_1050_ajnrfigure.jpg)

992

Radiology Resident Retirement: Boom or Bust?

M Shahriari[1], B Franck[2], D Yousem[3]

[1]Christiana care Health system, Newark, DE, [2]Christiana Care Hospital, Newark, DE, [3]Johns Hopkins Medical Institution, Evergreen, CO

Purpose

Personal financial education is a necessity for radiology residents in the early stages of their training. The level of financial literacy among residents is low. Appropriate retirement planning is critical to secure financial stability but is rarely discussed during radiology residency. We sought to determine the prevalence of retirement plans offered to radiology residents, the choices available, and the degree of participation by trainees.

Materials and Methods

A survey was created with the assistance of a faculty member from our University's School of Business. The survey was administered through the Association of Program Directors in Radiology (APDR) and Association of Program Coordinators in Radiology (APCR) to distribute among radiology residents. The survey assessed demographic data, retirement plans offered by institutions, degree of participation, amount of debt and assets, and willingness to participate in formal didactic education on these topics.

Results

Ninety five residents (68% male, and 32% female) completed the survey. In all, 74.7% (71/95) of institutions offer a retirement program with 70.4% (50/71) offering 403(b), Roth 403(b), 19.7% (14/71) offering 401(k), Roth 401(k), and 2.8% (2/71) offering 457(b). At these institutions, 84.5% (60/71) of residents participate in the program. 56.8% (54/95) residents started investing in a retirement program in their first or second year of residency. 86.3% (82/95) of residents have a non employer sponsored retirement account, predominantly (72% -59/82) invested in stocks. Rates of educational debt among residents were high, with 97% (92/95) of respondents reporting educational debt, of which 64.1% had greater than $200,000 in educational debt and 71% of those had debts more than assets. 81% (77/95) of residents saved money for emergencies. Most respondents (89%) derive their financial knowledge from personal research. At work, 60% (57/95) of residents have no didactic lectures on investing, personal finance, or retirement. The majority (99%) of respondents felt that including additional financial training in residency education is a critical need.

Conclusions

Resident financial attitudes and practices are variable, ranging from highly engaged residents actively managing their financial wellness to unengaged residents who have low concern. This study suggests a role for formal financial education in the radiology curriculum to prepare residents for retirement and improve financial literacy.

1234

Radiomics-based neural network predicts recurrence patterns in glioblastoma using dynamic susceptibility contrast-enhanced MRI

K Choi[1], I Hwang[1], S Choi[1]

[1]Seoul National University Hospital, Seoul, Seoul

Purpose

The purpose of our study was to determine whether radiomics features from dynamic susceptibility contrast (DSC) MRI can predict recurrence patterns and prognosis of glioblastoma by using neural network models.

Materials and Methods

In this retrospective study, 192 histopathologically confirmed glioblastoma patients (115 male; mean age, 56.5 years old) who underwent standard therapy with identified recurrence pattern were enrolled from a single institution: patients with the recurrence (n=125) were classified into the local recurrence (LR) (n=93) and distant recurrence (DR) (n=76). We extracted 1,702 radiomics features from CBV maps, based on contrast enhancing regions and non-contrast enhancing T2 high signal intensity areas. Two prediction models were built for the 1) LR vs non-LR; and 2) DR vs non-DR. The radiomic features were subjected to recursive feature elimination with support vector machine (SVM-RFE) to select 32 important features for predicting each recurrence pattern. Next, neural network-based classifiers were developed and validated using the 32 selected features as input features in the 5-fold cross-validation. Using Shapley additive explanations (SHAP), top 10 important features with largest feature importance values are listed among each of 32 features. Using Cox regression with least absolute shrinkage and selection operator (Cox-LASSO), three important features were selected among the combined 64 selected features to build the "radiomic risk score", which was developed to predict progression free survival (PFS).

Results

The mean area under the curve (AUC) of the prediction model was 1) 0.82±0.09 for LR vs non-LR; and 2) 0.86±0.05 for DR vs non-DR, respectively. In the result of SHAP, perfusional intratumoral heterogeneity of contrast enhancing area were the most important features for both recurrence patterns. The radiomic risk score was developed as a linear combination of the three important features. In the cox regression for the PFS (C-index, 0.66), radiomic risk score showed increased risk of recurrence (hazard ratio (HR)=1.61; p=0.03), independent to clinical variables including age, sex, IDH mutation, and MGMT methylation status (HR=0.36; p<0.0001).

Conclusions

We found that the intratumoral heterogeneity of the CBV maps based on contrast enhancing area were crucial for the prediction of the both recurrence patterns and the PFS.

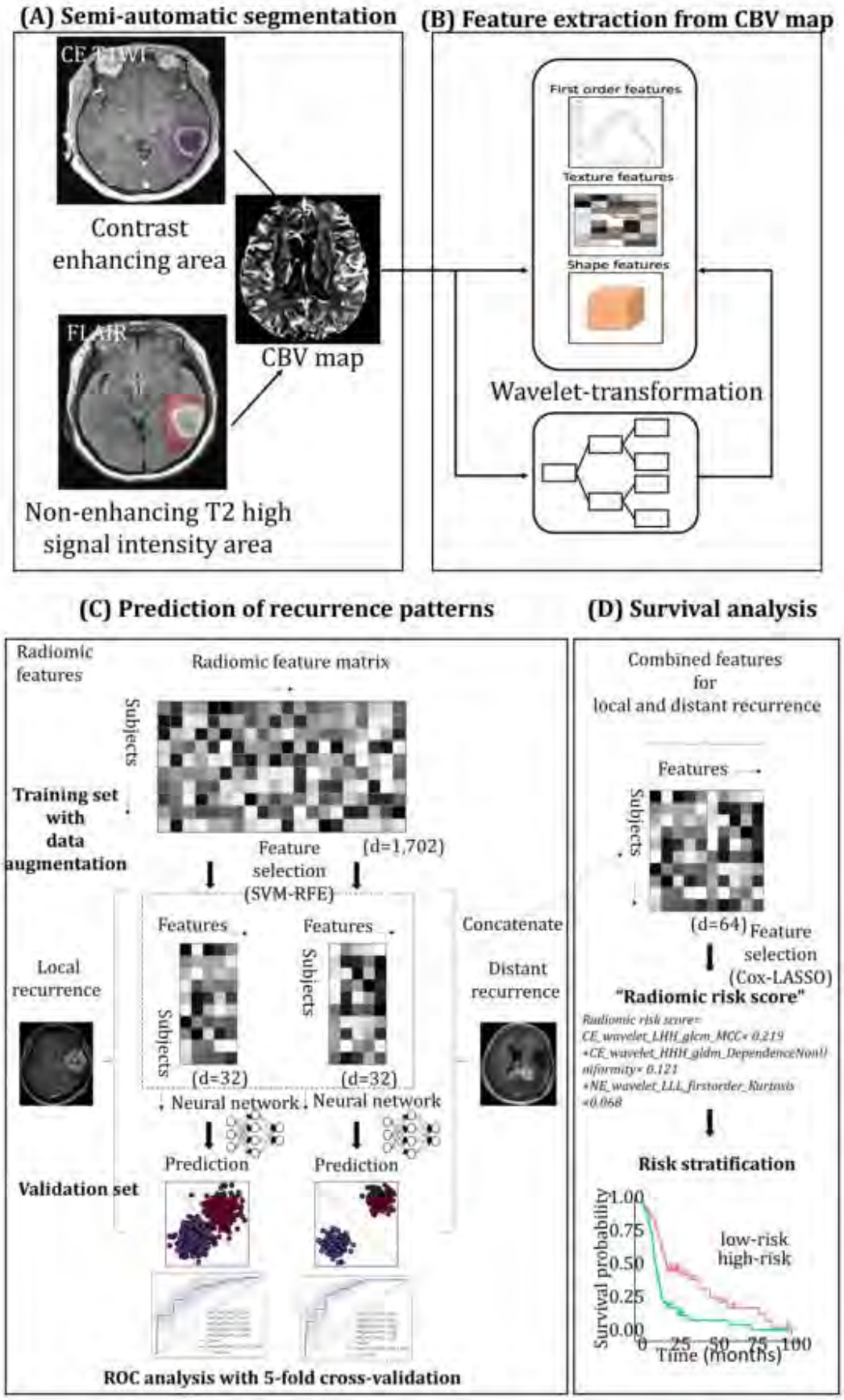

(Filename: TCT_1234_Fig_ASNR.jpg)

1063

Relative Metabolite Ratio to Improve Diagnostic Accuracy with Proton Magnetic Resonance Spectroscopy in Differentiating Recurrent Gliomas from Post-treatment Radiation Effects

M Kobayashi[1], M Hori[2], H Terada[3], K Maravilla[4]

[1]Toho University Omori Medical Center, Tokyo, Tokyo, [2]Toho University Omori Medical Center, Tokyo, N/A, [3]Toho University Sakura Medical Center, Sakura, Chiba, [4]Univ. of Washington, Seattle, WA

Purpose

Early detection of tumor progression is essential to guide therapy for post-treatment patients with glioma. However, differentiating recurrent tumor (RT) from post-treatment radiation effects (PTRE) by MRI remains challenging (1). Proton magnetic resonance spectroscopy (1H-MRS) has shown potential to improve the accuracy of diagnosing tumor progression in this setting (2). The purpose of this retrospective study was to assess the usefulness of quantitative relative metabolite ratio to improve diagnostic accuracy of 1H-MRS in distinguishing RT from PTRE.

Materials and Methods

All patients at our institution with previously treated gliomas who underwent 3-T MRI that included 1H-MRS between September 2007 and December 2019 for clinical evaluation of suspected RT were identified. ROIs were placed within both tumor and contralateral normal-appearing white matter (NAWM). Metabolite ratios of Cho/Cr and Cho/NAA were calculated along with relative metabolite ratios, rCho/Cr (relative Cho/Cr) and rCho/NAA (relative Cho/NAA) by dividing each metabolite ratio within the tumor by that within the contralateral NAWM. The categorization of cases for either RT or PTRE was confirmed by pathological diagnosis or combined clinical and imaging follow up. A quantitative 1H-MRS threshold to differentiate RT from PTRE for each metabolite ratio was identified using a ROC analysis. Diagnostic accuracy was compared between conventional quantitative 1H-MRS using Cho/Cr, Cho/NAA and relative 1H-MRS using rCho/Cr, rCho/NAA.

Results

We identified 86 patients (49 ± 12 years, 47 men) in total, with 51 RT cases. The optimal thresholds defined with ROC analysis for RT were as follows: Cho/Cr > 1.30 (sensitivity 92%, specificity 87%), rCho/Cr > 1.36 (sensitivity 98%, specificity 94%), Cho/NAA > 1.06 (sensitivity 77%, specificity 89%), rCho/NAA > 2.15 (sensitivity 69%, specificity 94%). Diagnostic accuracy of rCho/Cr was significantly higher than that of Cho/Cr (97% vs 91%, $p<0.05$).

Conclusions

Quantitative 1H-MRS using rCho/Cr has the potential to improve diagnostic accuracy in distinguishing recurrent tumor from post-treatment radiation effects.

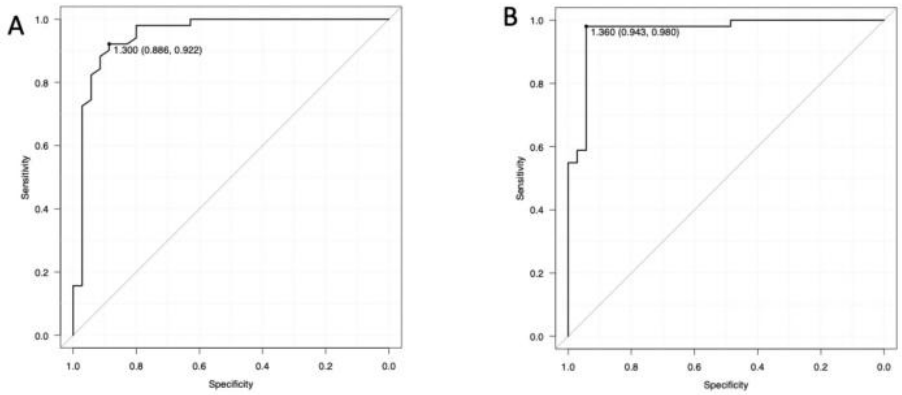

Figure 1. ROC analysis for Cho/Cr (A) and relative Cho/Cr (B) to differentiate recurrent tumor from post-treatment radiation effects.
AUC was 0.951 (95% CI: 0.898-1) for Cho/Cr and 0.966 (95% CI: 0.928-1) for relative Cho/Cr.

Table 1. Diagnostic performance of each parameter of differentiating RT from PTRE

	Threshold	Sensitivity	Specificity	PPV	NPV	Accuracy (95% CI)
tumor Cho/Cr	1.30	0.922	0.886	0.922	0.886	0.907 (0.825-0.959)
relative Cho/Cr	1.36	0.98	0.943	0.962	0.971	0.965 (0.901-0.993)
tumor Cho/NAA	1.06	0.765	0.886	0.907	0.721	0.814 (0.716-0.890)
relative Cho/NAA	2.15	0.686	0.943	0.946	0.673	0.791 (0.690-0.871)

(Filename: TCT_1063_ASNR2022Figure2.jpg)

724

Reveling the Posterior Human Limbic Network

A Kamali[1], G Hedayati[2], E Park[3], a Ali[4], M Hosseini[5]

[1]University of Texas Health Science Center Houston, Houston, TX, [2]University of Southern California, Los Angeles, CA, [3]University of Texas Houston, Houston, TX, [4]university of texas houston, Houston, TX, [5]University of Technology Sydney, Sydney, NSW

Purpose

Multiple new pathways have been recently introduced connecting the limbic structures to the parieto-occipital lobes and cerebellar hemispheres in the human brain. Some of these pathways include: the parieto-occipito-hypothalamic tract, cerebello-ponto-hypothalamic tract, occipito-septal and occipito-BNST tracts. The new pathways create multiple additional limbic circuits to the posterior human limbic network. The purpose of this study is to delineate and distinguish the posterior circuits of the human limbic network.

Materials and Methods

Fifteen healthy men (age range 24-37 years) were studied and written informed consent was obtained from all subjects. Conventional and DT-MRI Acquisition: Data were acquired using a Philips 3.0 T Intera system using a SENSE receive head coil. Diffusion-weighted image (DWI) data were acquired axially using single-shot multi-slice 2-D spin-echo diffusion with the balanced Icosa21 tensor encoding scheme. The b-factor = 500 sec mm-2, TR/TE = 14460/60 msec, FOV = 256 mm x 256 mm and slice thickness / gap/ #slices = 1 mm / 0 mm / 120. The EPI phase encoding used a SENSE k-space under sampling factor of two, with an effective k-space matrix of 112x112 and an image matrix after zero-filling of 256x256. Fiber Tracking: We used the FACT algorithm (DTIStudio) to reconstruct limbic structure fiber tracts with a fractional anisotropy (FA) threshold of 0.22 and angle threshold of 60 degrees.

Results

The cerebello-hypothalamic tract, parieto-occipito-hypothalamic, occipito-septal and occipito-BNST tracts create multiple posterior limbic connectivity including new loops and circuits which adds to the complexity of the posterior limbic network of the human brain.

Conclusions

The cerebellum along with the parietal and occipital cortices are tightly connected with the major limbic gray matter nuclei including the hypothalamus, BNST and septal nuclei. This connectivity creates multiple limbic loops and circuits which could be affected in many neurologic or psychiatrics diseases.

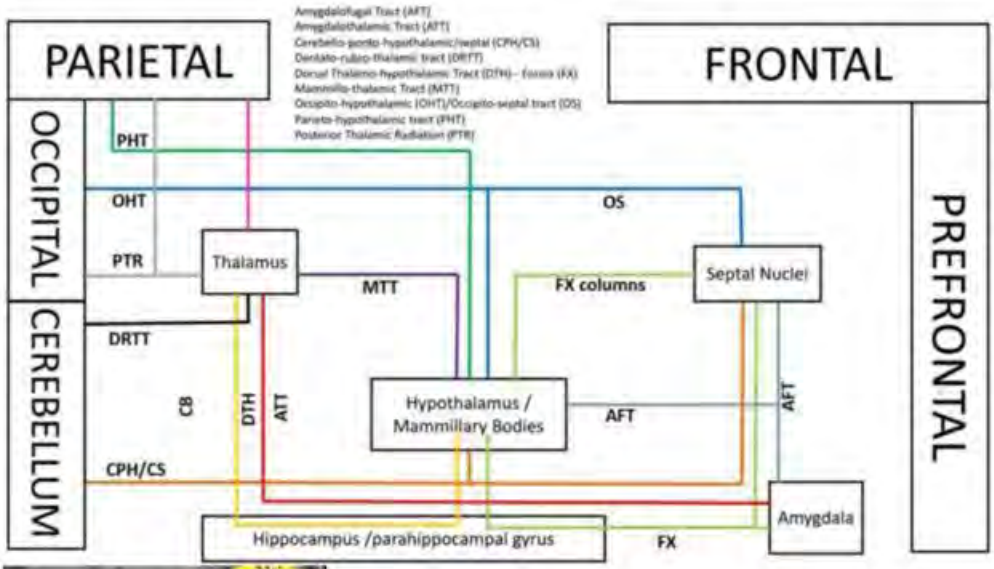

Fig. 1. Schematic view of the posterior cortico-limbic circuits including the posterior thalamic radiations (PTR), parieto-occipito-hypothalamic tract (POHT), occipito-hypothalamic(OHT), occipito-septal (OS) (shown by blue line), cerebello-ponto-hypothalamic (CPH), cerebello-septal (CS), mammillothalamic tract (MTT), fornix (FX), dorsal thalamo-hypothalamic tract (DTH), fornix (FX), amygdalofugal tract (AFT) and the amygdalothalamic tract (ATT).

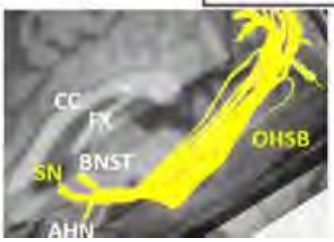

Fig. 2 illustrates the three branches arising from the occipito-hypothalamic/septal/BNST (OHSB) inserting at the BNST, septal nuclei (SN) and anterior hypothalamic nuclei (AHN).

(Filename: TCT_724_Fig1.jpg)

745

Role of Delayed Contrast & Subtracted Imaging to Differentiate Tumoral and Non-Tumoral Tissue in CNS tumors – An MR/PET Study with Various PET Tracers.

S M[1], P G V N[2], A Kotwal[3], J Saini[4], V K S[2]

[1]National Institute of Mental Health and Neurosciences (NIMHANS), Bengaluru, India, Bengaluru, Karnataka, [2]NATIONAL INSTITUTE OF MENTAL HEALTH AND NEUROSCIENCES, BANGALORE, KARNATAKA, [3]NIMHANS, bengaluru, Karnataka, [4]NATIONAL INSTITUTE OF MENTAL HEALTH & NEURO SCIENCES, BANGALORE, India

Purpose

The aim of this study to assess the role of Delayed Contrast and Subtracted Imaging to differentiate tumoral and non tumoral tissue in CNS tumors by comparing with the PET images.

Materials and Methods

We included 19 PET MRI cases in the study. Out of which, 10 were C11-Methionine PET cases, 2 were F18-FET PET cases, 4 were 18FDG-PET cases & 3 were F18-DOPA PET cases. In all cases immediate post contrast and 75 min delayed post contrast images were acquired. Subtracted images were obtained by using immediate and delayed post contrast images & color coding was applied similar to PET images(warm metal) for ease of comparison. Subtracted color coded images were correlated with PET color coded images. 75 min delayed post contrast images with gray scale inversion were correlated with PET-AC gray scale images & DWI images with gray scale inversion. On Immediate post contrast images both tumoral and non tumoral tissues show enhancement. But on delayed images the tumor washes out and radiation necrosis shows contrast pooling. Hence in subtracted images, the areas which are hyperintense are the areas of tumor tissue. If motion artifact is noted, we used delayed contrast images to make an inference directly.

Results

Out of 19 cases of PET, 3 had motion artefacts hence subtracted images could not be generated and 2 were non enhancing tumors. When PET was correlated with subtracted contrast images all cases had good correlation (14 out of 14 cases). When PET was correlated with DWI images there was good correlation with 11 out of 19 cases. Delayed Contrast Imaging has potential to be a good biomarker similar to PET. The volume and margins of tumor were similar when compared PET with subtracted images and immediate contrast images underestimated the tumor volume. Hence true tumor volumes are generated better with delayed contrast images.

Conclusions

Delayed Contrast & Subtracted Contrast Imaging along with routine MRI sequences can be done in peripheral centres where PET is not available to differentiate recurrence/ residual lesion from radiation necrosis. This technique has pitfall esp. in low grade & non enhancing tumors.

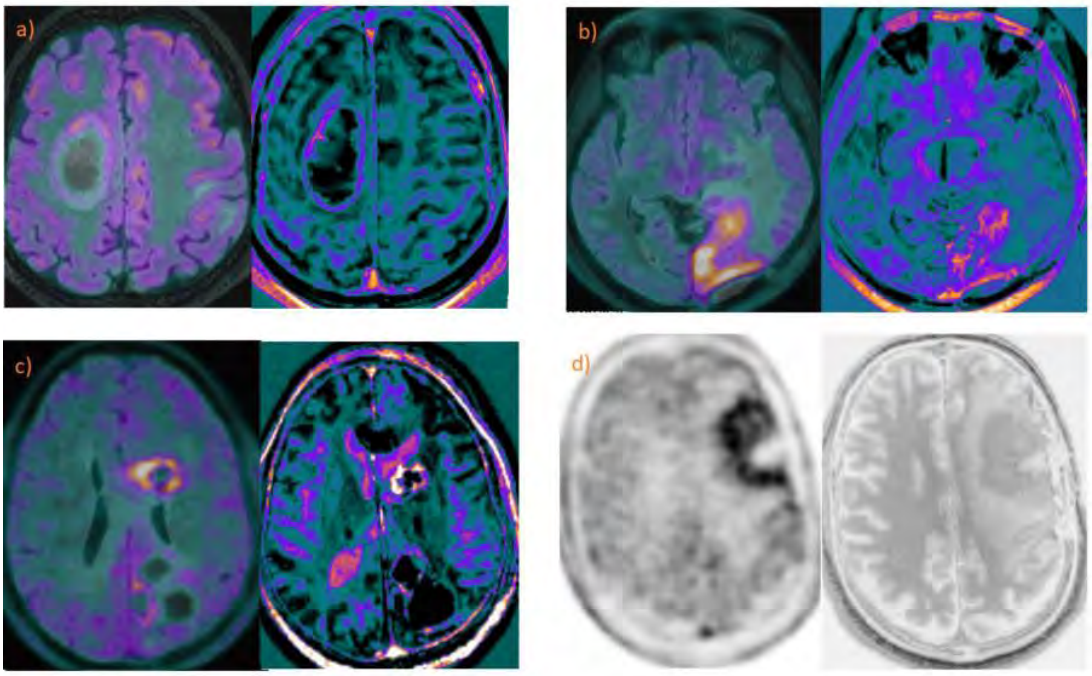

Figure a) shows FDG PET (left) metabolic uptake matched with Subtracted contrast (right) image in case of Adenocarcinoma lung with cerebral metastasis. Figure b) shows F18 DOPA PET (left) metabolic uptake matched with Subtracted contrast (right) image in a case of IDH wild type of Glioblastoma with recurrence in left parieto-occipital lobe. Figure c) shows C11 Methionine PET (left) metabolic uptake matched with Subtracted contrast (right) image in a case of IDH wild type of Glioblastoma with recurrence in pericallosal region. Figure d) shows F18 FET PET AC image (left) metabolic uptake matched with wash out in Delayed contrast (right) image in a case of IDH wild type of Glioblastoma with Residual/ Recurrence in left frontal region.

(Filename: TCT_745_Researchworkimage.jpg)

402

Rule-based Natural Language Processing for Automation of Stroke Data Extraction: A Validation Study

D Gunter[1], P Puac Polanco[2], O Miguel[2], R Thornhill[2], R Aviv[3]

[1]Ottawa Hospital Research Institute, Ottawa, Ontario, [2]University of Ottawa, Ottawa, Ontario, [3]The Ottawa Hospital, Ottawa, Ontario

Purpose

Data extraction from radiology free-text reports is time-consuming when performed manually. Recently, more automated extraction methods using natural language processing (NLP) are proposed. A previously developed rule-based NLP algorithm showed promise in its ability to extract stroke-related data from radiology reports accurately. We aimed to externally validate the accuracy of CHARTextract, a rule-based NLP algorithm, to extract stroke related data from free-text radiology reports.

Materials and Methods

Free-text reports of CT angiography (CTA) and CT perfusion (CTP) scans of consecutive patients with acute ischemic stroke were analyzed from January 2015 to January 2021. Stroke-related variables were manually extracted (reference standard) from the reports, including proximal and distal anterior circulation occlusion, posterior circulation occlusion, presence of ischemia, hemorrhage, Alberta stroke program early CT score (ASPECTS), and collateral status. These variables were simultaneously extracted using a rule-based NLP algorithm. The NLP algorithm's accuracy, specificity, sensitivity, positive predictive value (PPV), and negative predictive value (NPV) were assessed.

Results

The NLP algorithm's accuracy was >90% for identifying distal anterior occlusion, posterior circulation occlusion, hemorrhage presence, and ASPECTS. Accuracy was 85%, 74%, and 79% for proximal anterior circulation occlusion, presence of ischemia, and collateral status respectively. The algorithm had high negative predictive value for the absence of variable reporting and an accuracy of 87-100% when variables were not reported.

Conclusions

Rule-based NLP has a moderate to good performance for stroke-related data extraction from free-text imaging reports. The algorithm's accuracy was affected by inconsistent report styles and lexicon among reporting radiologists.

Table 1. Performance of the NLP algorithm for identification of stroke-related outcomes in free-text reports.

Stroke Variable	True Prevalence, n (%)	Sensitivity (%)	Specificity (%)	PPV[a] (%)	NPV[b] (%)	Overall Accuracy (%)
Anterior Proximal Occlusion	593 (77)	83 (80, 86)	91 (86, 95)	97 (95, 98)	62 (56, 68)	85
Anterior Distal Occlusion	101 (13)	82 (73, 89)	95 (93, 97)	72 (63, 80)	97 (96, 98)	94
Basilar Occlusion	63 (8)	81 (69, 90)	100 (99,100)	98 (90,100)	98 (97, 99)	98
Presence of Established Ischemia	517 (67)	69 (65, 73)	84 (79, 88)	90 (86, 93)	58 (52, 63)	74
Presence of Hemorrhage	8 (1)	100 (63, 100)	92 (90, 94)	12 (5, 22)	100 (99, 100)	92

Note: data are percentages with 95% confidence intervals in parentheses

[a]PPV = Positive Predictive Value

[b]NPV = Negative Predictive Value

Table 2. Performance of the NLP algorithm for identification of ASPECTS and collateral status in free-text reports.

Stroke Variable	True Prevalence, n (%)	Sensitivity (%)	Specificity (%)	PPV[a] (%)	NPV[b] (%)	Overall Accuracy (%)
ASPECTS						
Not Reported	655 (85)	100 (97, 100)	100 (99, 100)	98 (94, 100)	100 (99, 100)	100
<5	3 (<1)	100 (29, 100)	98 (94, 100)	60 (15, 95)	100 (97, 100)	98
≥5	115 (14)	98 (94, 100)	100 (29, 100)	100 (97, 100)	60 (15, 95)	98
Collateral Status						
Not reported	310 (40)	79 (75, 83)	99 (98, 100)	99 (98, 100)	76 (72, 80)	87
Poor	65 (8)	58 (46, 71)	82 (78, 86)	35 (26, 44)	92 (89, 95)	79
Intermediate	100 (13)	65 (55, 74)	83 (78, 86)	81 (42, 60)	90 (86, 93)	79
Good	298 (39)	88 (83, 91)	63 (55, 70)	81 (76, 85)	74 (66, 81)	79

Note: data are percentages with 95% confidence intervals in parentheses

[a]PPV = Positive Predictive Value

[b]NPV = Negative Predictive Value

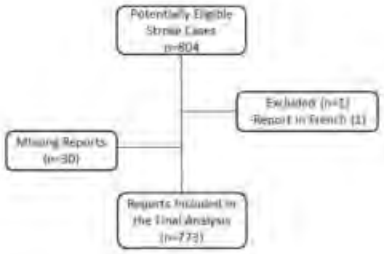

Figure 1. Population selection flowchart

(Filename: TCT_402_ASNR2022TablesandFigures.jpg)

623

Significance of Low Signal in Intracranical Vertebral Artery Wall Observed on Susceptibility Weighted Angiography (SWAN)

H Ishimaru[1], M Morikawa[2], R Ideguchi[3], M Uetani[1], Y Ikebe[4]

[1]Nagasaki University Hospital, Nagasaki, outside US, [2]N/A, N/A, [3]Atomic Bomb Disease Institute, Nagasaki University, Nagasaki, outside US, [4]Hokkaido University Hospital, Sapporo, Hokkaido, Please select an option below

Purpose

Susceptibility-weighted MR sequences have been applied in the field of cerebrovascular diseases for detecting intracranial hemorrhage, hemorrhagic transformation, and the oxygenation status of venous blood and thrombus. Recent studies reported that SWI, developed by Siemens, delineated intramural hematoma as an eccentric or concentric low signal in vertebral artery dissection (1) and vertebral artery calcifications (2). To date, however, no extensive studies have been conducted on the efficacy of susceptibility-weighted MR sequences in intracranial vessel wall estimation. We aimed to clarify the efficacy of susceptibility-weighted angiography for characterization of the intracranial vertebral artery wall.

Materials and Methods

We retrospectively reviewed susceptibility-weighted angiographies from 200 consecutive patients with acute ischemic stroke in the posterior circulation territory. SWAN acquisition was performed using a 3D multiecho gradient echo sequence (FOV=27.8×20 cm, acquired matrix=320×224, slice thickness=2.4 mm, TR=31 ms, center of 5 TEs = 23 ms, flip angle =15°). The presence of eccentric or concentric low signals in the vertebral artery wall was examined and evaluated. The etiology of the low signal was also investigated as much as possible by referring to CT and T1WI. We also compared its frequency in each stroke subtype.

Results

A low signal was observed in 128/200 patients (64%). The low signals (58%) corresponded to vessel wall calcification in 74 of 128 patients and to vessel wall thickening showing intermediate to low (n = 8) or high (n = 16) signal on T1WI in 24 (19%) patients. The low signal did not have vessel wall thickening or calcification in one patient, and the cause of low signal could not be verified in 29 patients. According to stroke subtypes, a low signal was observed in 14/14 (100%) vertebral artery dissections, all of which corresponded to intramural hematoma. A low signal was observed in 51/65 (78%) atherothromboses, which were significantly more frequent than cardioembolism (34/66; 52%) and small-artery disease (18/39; 46%) ($P < 0.01$). In atherothrombosis, calcification was the most common cause of low signal (n=32; 63%).

Conclusions

Low signals on susceptibility-weighted angiography were frequently observed in vertebral artery dissection and atherothrombosis, reflecting intramural hematoma in all of the former and predominantly calcification in the latter.

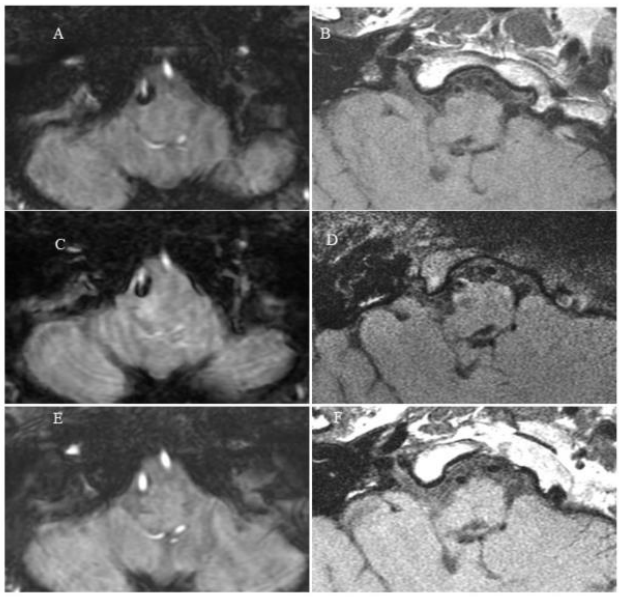

A 57-year-old woman with the right vertebral artery dissection. SWAN (A) and oblique axial T1WI (B) obtained at Day 1. SWAN (A) demonstrates an eccentric low signal around the right vertebral artery, but T1WI (B) shows no apparent high signal in the wall. SWAN (C) and oblique axial T1WI (D) obtained at Day 6. Intramural hematoma in the right vertebral artery is demonstrated as a low signal on SWAN (C) and as a high signal on T1WI (D). SWAN (E) and T1WI (F) obtained at one year demonstrate no vessel wall abnormality, which indicates regression of the intramural hematoma.

(Filename: TCT_623_ASNR.jpg)

582

Slow Thalamocortical Coherence Predicts Persistent Post-Concussive Symptoms

Y Li[1], C CHEN[2]

[1]Taipei Medical University, Taipei, Taiwan, [2]TAIPEI MEDICAL UNIVERSITY HOSPITAL, TAIPEI, Taiwan

Purpose

Thalamocortical coherence is crucial to cognitive functioning, and its disruptions can cause neuropsychiatric symptoms (R. R. Llinás et al., 1999). Because the onset and subsequent progression of thalamocortical disturbances is always unclear, it has been difficult to investigate the mechanism that sets off such chain of events that consequently lead to multiple neuropsychiatric symptoms.

Materials and Methods

We longitudinally tracked 70 mild traumatic brain injury (mTBI) patients and 48 healthy controls (HCs) for 2 years and followed up on their imaging, symptoms, and cognitive functioning. We also replicated the longitudinal rodent model with close-head injuries (CHI) within 24-hr to 7-week follow-ups. The mechanism of coherent thalamocortical rhythmicity was investigated using fMRI-based functional connectomic matrix to test whether the severity of thalamocortical disturbances can explain the prolongation of post-concussive symptoms.

Results

Our connectomic results showed that concussion predisposes patients to varying degrees of thalamocortical disturbance, which led to different increment levels of low-frequency temporal coherence, both within–thalami and thalamocortical, and ultimately determined the severity of post-concussive symptoms. Significant differences between mTBI and HCs in neurological dysfunctions could still be observed 2 years later, indicating that the symptoms had not improved significantly after 2 years. Crucially, patients with resolved vs prolonged symptoms exhibited distinct patterns of baseline connectomic biomarkers, which are closely related to the degree of long-term symptoms. The patterns of pathologically elevated slow thalamocortical coherence was able to differentiate patients with prolonged vs resolved symptoms, suggesting that the connectomic biomarkers not only can serve as predictive biomarker, but also diagnostic biomarker for thalamocortical disturbance.

Conclusions

This is the first study to use fMRI-based functional connectomic matrix to directly monitor the progression of thalamocortical disturbance. We demonstrate that mTBI can induce strong slow rhythmicity that disrupts thalamocortical coherence, and its severity can be quantified via connectomic biomarkers that are predictive of the degrees of long-term symptoms. These results strengthen our understanding of the origin and progression of slow thalamocortical coherence and its relationship with the prolongation of clinical symptoms.

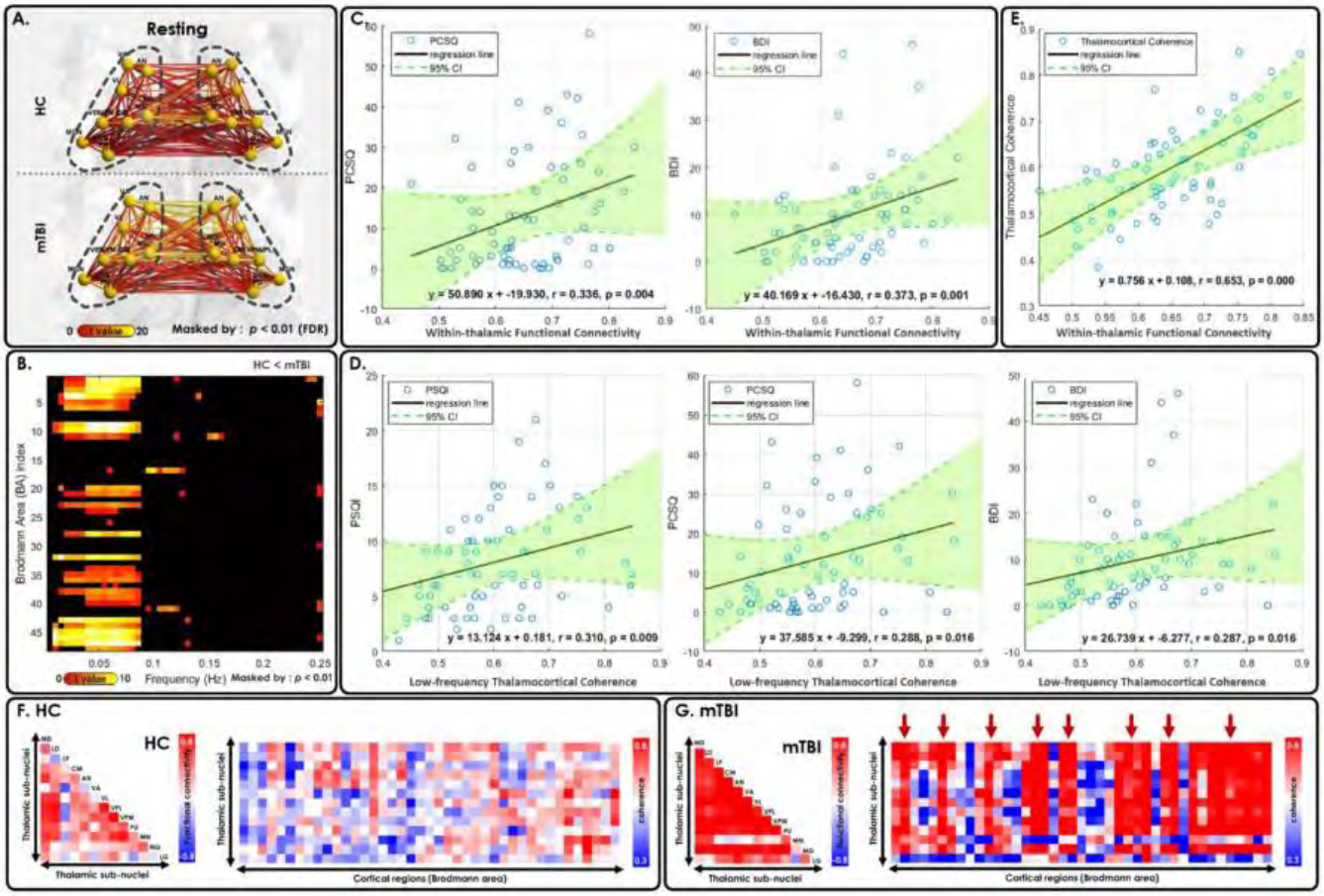

(Filename: TCT_582_Fig02.jpg)

285

Spectrum of Neuroimaging Findings in COVID-19 Induced Encephalitis

H Sotoudeh[1], S Gaddamanugu[2], M Tanwar[1]

[1]University of Alabama at Birmingham, Birmingham, AL, [2]Veterans Affairs Medical Center, Birmingham, AL

Purpose

Encephalitis is a common complication of the COVID-19 infection. However, diagnosing COVID-19 induced encephalitis is challenging because of the different spectrum of neuro-imaging findings. Therefore, this study has been conducted to evaluate the spectrum of the neuro-imaging manifestations of COVID-19 induced encephalitis.

Materials and Methods

After searching the electronic medical records during the COVID-19 pandemic from January 2020 to September 2021, all patients with the clinical diagnosis of the COVID-19 induced encephalitis and with pathologic findings on brain MRI were included. The brain MR images from these patients were collected and then reviewed by two neuro-radiologist regarding abnormal findings on the brain MRIs.

Results

53 patients with the clinical diagnosis of encephalitis were included in this study, including 24 men and 29 women with a mean age of 61.1 years, maximum age of 84, and minimum age of 28. Cerebral microhemorrhages were the most common neuroimaging manifestation in these patients and was detected in 20 patients. Abnormal FLAIR hyper signal intensities were noted in the insular cortex in 15 patients (28%). Abnormal FLAIR hyper signal intensities in medial temporal lobes were noted in 12 patients (22%). Abnormal FLAIR hyper signal intensities in the brain stem were detected in 9 patients (17%). Abnormal cortical-based FLAIR hypersignal intensities was noted in 7 patients (13%). Abnormal FLAIR signal was noted in thalami in 7 patients (13%). Abnormal T2-FLAIR hyper signal intensities were noted in the cerebellum in 4 patients (7%). Abnormal FLAIR hyper signal intensities were noted in basal ganglia in 4 patients (7%). Diffuse white matter abnormal signal intensity/ leukoencephalopathy was noted in 3 patients (5%). The abnormal intensity of splenium in three patients (5%) and abnormal intensity around the third ventricle was noted in one patient (1.8%).

Conclusions

The most common manifestation of COVID-19 encephalitis is scattered diffuse or focal microhemorrhages following by abnormal signal intensity in the insular cortex, medial temporal lobes, brain stem, abnormal cortical signal intensity, and abnormal signal intensity within thalami and basal ganglia. Diffuse leukoencephalopathy, the abnormal signal intensity of splenium of the corpus callosum, and periventricular white matter signal changes around the third ventricle are the other less common manifestations of COVID 19-induced encephalitis.

484

Spinal arachnoid webs in adults: clinical and imaging features. A multi-center experience.

S Elkadi[1], A Kraus[1], A Sayah[2]

[1]Georgetown University School of Medicine, Washington, DC, [2]Medstar Georgetown University Hospital, McLean, VA

Purpose

Spinal arachnoid web is thought to be a rare condition that can present with myelopathy. The purpose of this study is to analyze a large group of patients with this entity to assess clinical and imaging trends to aid in earlier and more accurate diagnosis of this condition.

Materials and Methods

An IRB retrospective 5.5-year review of spinal arachnoid web cases between 2016 – 2021 within a metropolitan, multi-hospital network. We searched the network wide PACS for imaging reads that included the term 'arachnoid web'. Of 71 hits, 60 patients had imaging or pathologically proven arachnoid webs. The demographic and clinical data of these 60 patients were collected, including treatment and prognosis. Additionally, the imaging data were also analyzed, including location of the web, association with the level of maximum thoracic kyphosis, and cord edema/syrinx.

Results

Of the 60 patients reviewed, arachnoid web was diagnosed in 35 as the etiology of primary symptomatology; with presenting symptoms shown in Table 1. Webs were found incidentally in the other 25 patients. Demographically, 28 were male and 32 were female with average of 58.8 and median of 58.5 (range 29 – 91). Majority (92%) of the webs were located between T2 and T6 spinal levels (55/60). The level at which the web was located was on average 2.35 0.37 vertebrae (95% CI) from the level of maximal thoracic kyphosis. 15 of the 60 patients had findings of edema/syrinx.

Conclusions

Over 5 years, our metropolitan multi-hospital system has diagnosed 60 patients with spinal arachnoid web. This study illustrates that this phenomenon is not as rare as initially anticipated. These patients present with symptoms similar to other causes of cord compression, and imaging should be performed and evaluated for the presence of such pathology.

Table 1. Presenting Symptoms of Patients with Primary Subarachnoid Webs from 2016-2021.

Symptom	Percent of Patients with Presenting Symptom (n=41)
Weakness	41.4%
Numbness	46.3%
Pain	75.6%
Incontinence	26.8%
Myelopathy	39.0%

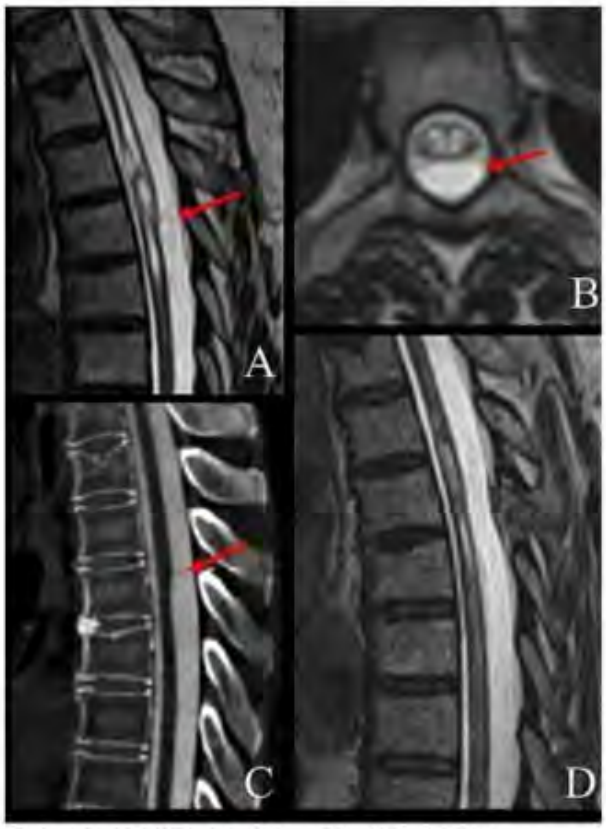

Subarachnoid Web Imaging. T2 sag (A) and T2 axial (B) shows a subarachnoid web (red arrow) with associated cord syrinx above and below the web. CT myelogram (C) depicting the web. Post web resection T2 sag (D) with resolution of the web and improvement in syrinx.

(Filename: TCT_484_ASNRImage.jpg)

808

Structural Connectome Analysis in Antibody-Mediated Demyelinating Diseases

D Fragoso[1], M Boaventura[1], B Pastorello[2], M Penteado Nucci[2], S Pereira[1], C Leite[1], C Rimkus[1]
[1]University of São Paulo, São Paulo, São Paulo, [2]Instituto de Radiologia, Hospital das Clínicas, São Paulo, São Paulo

Purpose

To analyze structural brain connectivity of neuromyelitis optica spectrum disorder (NMOSD) and myelin oligodendrocyte-associated disease (MOGAD) patients and to investigate differences among these antibody-mediated demyelinating diseases with healthy controls.

Materials and Methods

All individuals were over 18 years old. Only healthy adults without prior neurological or psychiatric illness were included in the HC group. Patients with NMOSD were selected according to the 2015 Wingerchuck criteria, with a positive result for anti-aquaporin-4 antibody by the CBA method. The combination of neurological changes attributed to disorders related to anti-MOG and the positivity to this antibody were the criteria to select MOGAD patients. Finally, only patients and healthy individuals with normal brain MR through conventional sequences analysis were selected. Exclusion criteria: Low quality images, artifacts, post-process error. MR data

were acquired on a 3T scanner using a 32-channel head coil. A neuropsychologist evaluated all patients during the same period as the MRI. The exams were processed using FreeSurfer (for parcellation) and MRtrix3 (structural connectome). At the end, we compare the whole-brain connectome of which group with HC.
Results
Twenty-four patients were prospectively recruited, seventeen (16 female; 23-59 years) of whom had NMOSD and seven (5 female; 27-57 years) had MOGAD. Fifteen HC (9 female; 21-55 years) were also recruited. The connectivity of the right frontal lobe demonstrated a positive correlation with both cerebral hemispheres, notably among the right frontal-orbital region with the nucleocapsular and thalamic regions and with the homolateral precentral and middle occipital gyrus and with the contralateral temporal pole, supramarginal and fusiform gyrus, between the HC and the MOGAD group. The connectivity of the left inferior parietal lobe showed a positive correlation with the contralateral hemisphere, especially the motor area, the inferior frontal operculum, and the temporal pole, between HC and the NMOSD group.
Conclusions
We showed brain connectivity correlation between HC and antibody-mediated demyelinating diseases without structural signal changes by conventional MR. The groups' correlations were different, which may reflect the combination, in variable degrees, of the distinct pathophysiological mechanism and the capacity for CNS adaptation. Multicenter prospective studies with a larger sample and using different equipment may confirm our findings.

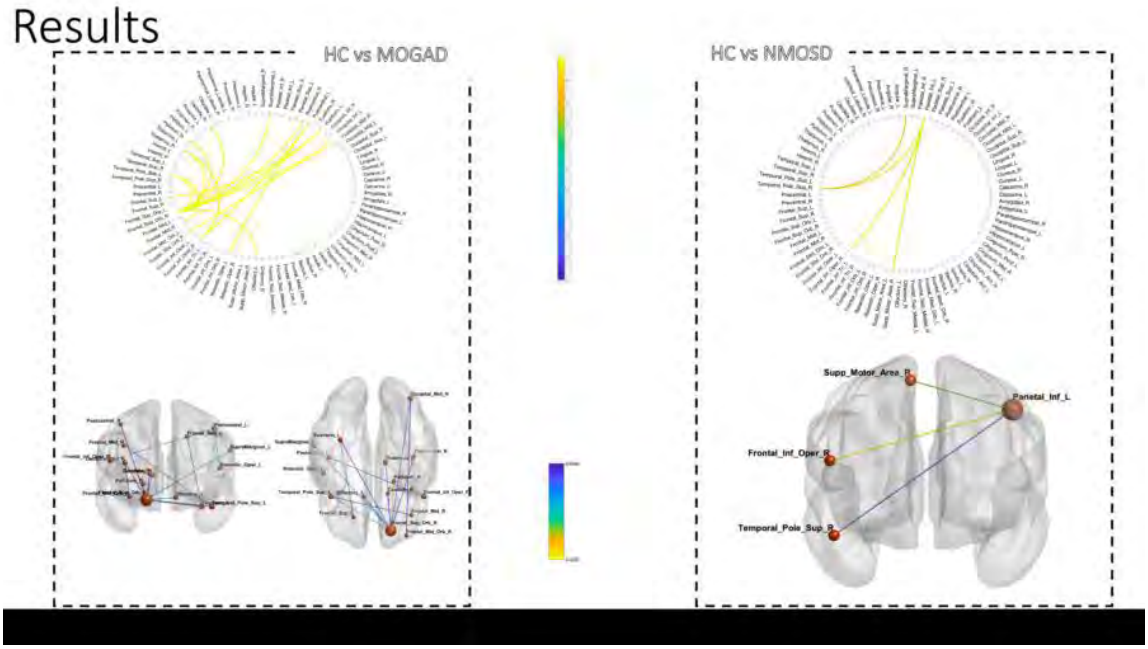

(Filename: TCT_808_4.jpg)

1207
T2 mapping of the lateral pterygoid muscle in patients with temporomandibular joint disorder: Relationship between T2 relaxation time of the lateral pterygoid muscle and disc displacement
S Lee[1], E Khil[2], S Jo[3]
[1]Dongtan Sacred Heart Hospital, Hallym University Medical Center, Hwaseong-si, South Korea, [2]Hallym University Dongtan Sacred Heart Hospital, Hwaseong-si, Gyeonggi-do, [3]Hallym university Dongtan sacred hospital, Hwaseong-si, South Korea

Purpose
The purpose of this study was to measure T2 relaxation time of lateral pterygoid muscle (LPM) related to different status of articular disc in temporomandibular (TM) joint of TM disorder patients.
Materials and Methods
Thirty-nine TMJs (19 of right and 20 of left joints) of twenty patients with TMD were performed with magnetic resonance imaging (MRI) on a 3.0T MR scanner. T2 value was measured from the sagittal slice where mid portion of the muscle belly was observed. The regions of interest were placed over the superior and inferior heads of LPM. Each TMJ was divided into three groups according to the disc displacement: normal disc position (ND), anterior displacement with reduction (DDWR), and anterior displacement without reduction (DDWOR). There were 13 joints in the ND group, 12 joints in the DDWR group, and 14 joints in the DDWOR group. Linear mixed effects models were used to assess the correlation between T2 relaxation times and disc displacement. Intercorrelation coefficient (ICC2,1) were applied to determine interrater reliability.
Results
The mean T2 values of the SHLPM were 54.99, 68.15, and 69.63 ms for ND, DDWR, and DDWOR, respectively. The mean T2

values of the SHLPM on the ND group were significantly lower than those on the DDWR and DDWOR ($p < 0.05$). There was no significant difference in the mean T2 values of SHLPM between the DDWR and DDWOR groups. The mean T2 values of the IHLPM were 53.95, 57.96, and 65.80 ms for ND, DDWR, and DDWOR, respectively. Also, the mean T2 values of the IHLPM on the ND groups were significant lower than those on the DDWR and DDWOR ($p < 0.05$) and there was no significant difference between the DDWR and DDWOR. Intraobserver agreements were good to excellent for both SHLPM and IHLPM, as determined by ICC(2,1) of 0.810 (SHLPM, $p < 0.001$) and 0.723 (IHLPM, $p < 0.001$).

Conclusions

The mean T2 value of LPM is correlated with the degree of disc displacement, both of SHLPM and IHLPM.

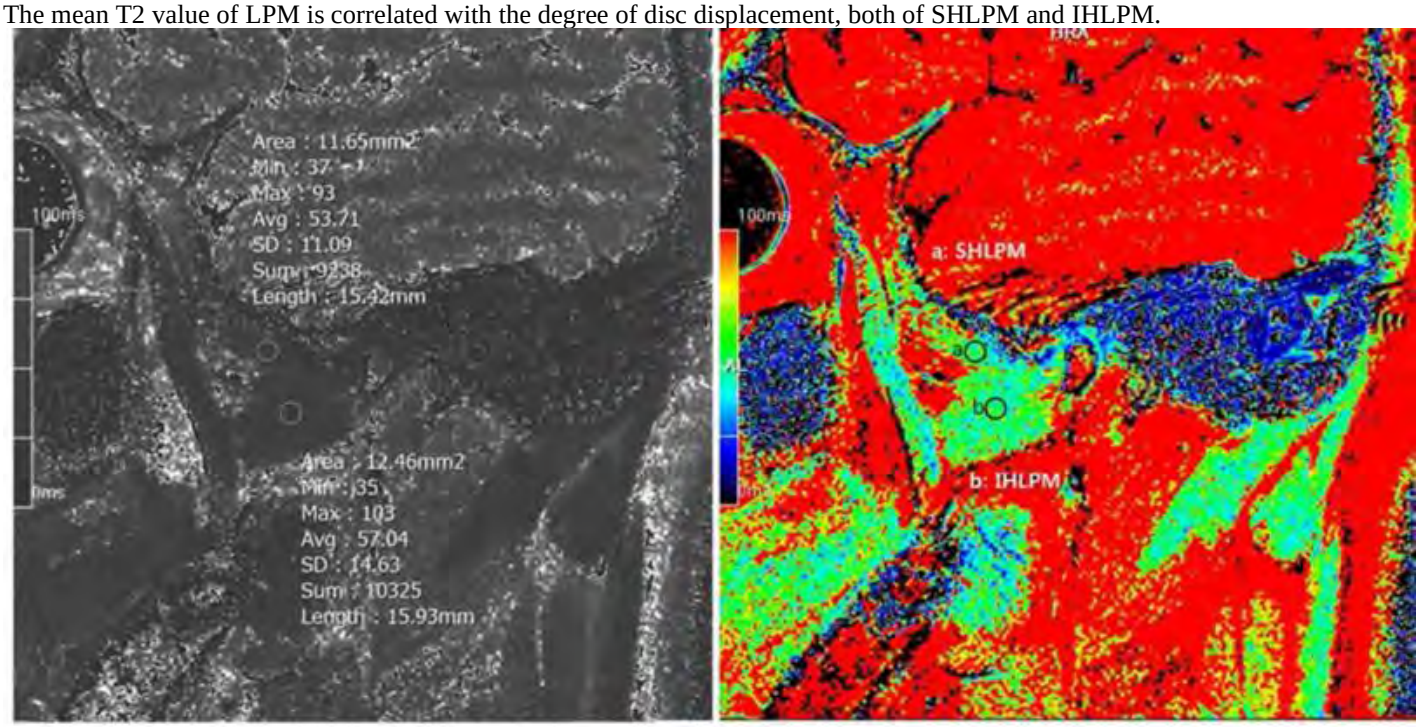

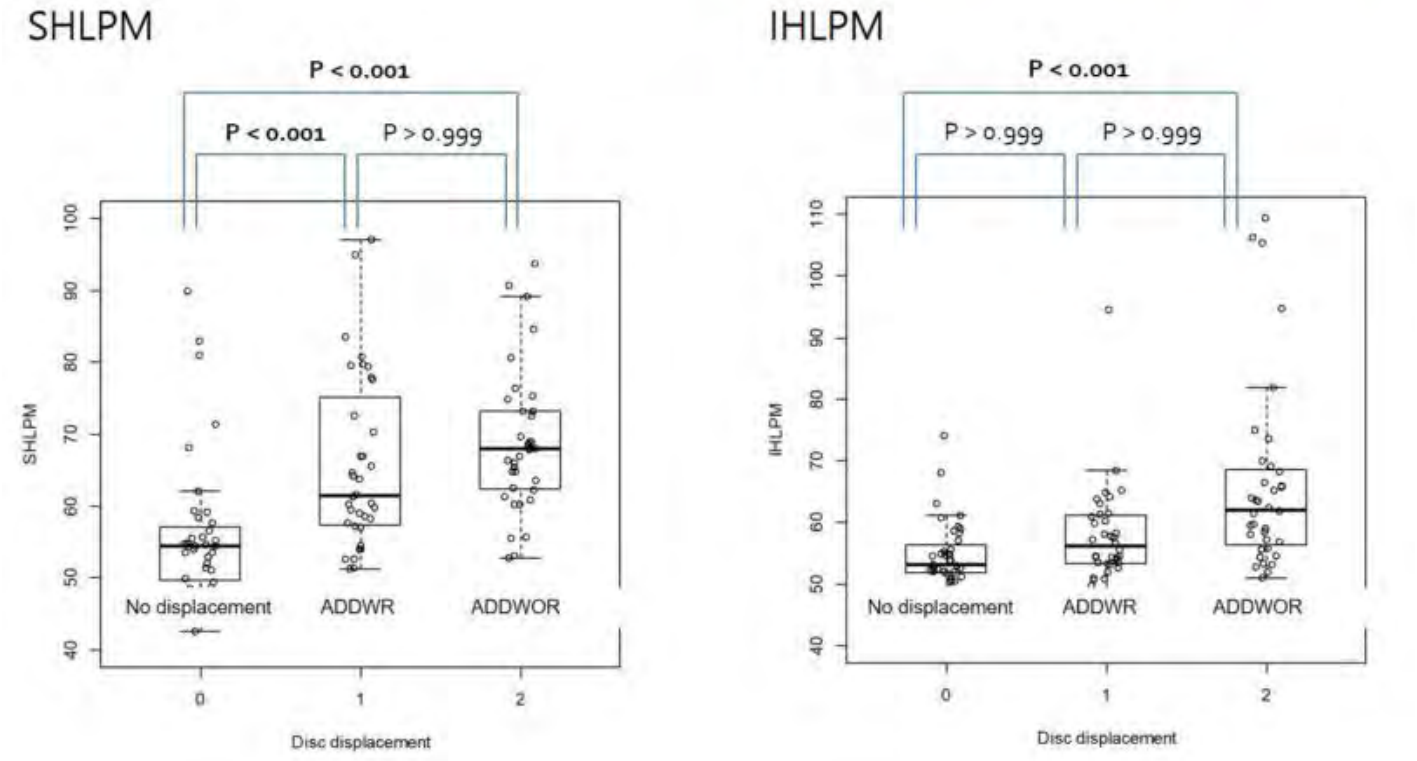

(Filename: TCT_1207_figureTMJfinal.jpg)

1521

T2 signal intensity as a imaging characteristic to differentiate dysembryoplastic neuroepithelial tumor from astrocytoma

K Yu[1]

[1]*Taipei Veterans General Hospital, Taipei, Taiwan*

Purpose

Dysembryoplastic neuroepithelial tumors (DNET) are benign slow growing glioneuronal tumors arising from either cortical or deep grey matter. Typically the tumor is diagnosed in children or young adults, and often associated with drag-resistant epilepsy. The seizure could be under well control after surgically removal of the tumor, while seizures caused by astrocytoma did not responded well to surgery. We aimed to discriminate DNET and astrocytoma based on T2 weighted imaging characteristic as another clue to aid clinicians making more accurate diagnosis before treatment.

Materials and Methods

Total 20 patients with pathology-proved DNET and 30 patients with pathology-proved low grade astrocytoma were included. Images were retrospectively evaluated including bubble appearance, bright rim appearance of the lesion, satellite nodules around the lesion, ADC value, contrast enhancement, and measured T2-weighted signal intensity ratio of the lesion. T2-weighted signal intensity ratio was measured by dividing T2-weighted signal intensity on lesion area by that in controlled area. The range of interest was circled manually about 1x1cm3, and the controlled area was circled in the counterpart of cerebral white matter. Three neuroradiologists reviewed the images respectively and were blinded to the pathological diagnosis. The association between image characteristics were analyzed by Chi-square test and univariate logistic regression.

Results

The average T2 signal intensity ratio of DNET is 3.36, and the average of low grade astrocytoma is 2.49. In univariate logistic regression analysis, higher T2-weighted signal intensity ratio (odds ratio [95% confidence interval] = 0.07 [0.01–0.36], P < 0.001) was associated with more accurate diagnosis of DNET, along with ADC value (odds ratio [95% confidence interval] = 0.99 [0.98–0.99], P < 0.001), bright rim FLAIR sign (odds ratio [95% confidence interval] = 9.75 [2.38–39.9], P = 0.002) and satellite lesions (odds ratio [95% confidence interval] = 19.68 [3.65-106.18], P < 0.001) . The interobserver correlation is adequate with kappa value = 0.75.

Conclusions

Higher T2-weighted signal intensity ratio may be another clue to differentiate DNET and low grade astrocytoma in addition to other pre-existing imaging characteristics.

Table 1: Patient demographics

Characteristic	DNET (n=17)	Low grade astrocytoma (n=29)	P value
Age at op, mean(SD)	19.1(10.0)	23.0(8.8)	0.186
Age at onset, mean(SD)	12.3(7.6)	13.5(9.2)	0.374
Male, n(%)	8(47.1)	14(48.3)	0.598
Epilepsy at presentation, n(%)	15(88.2)	21(72.4)	0.282
Epilepsy type, n(%)			
GTCS	10(66.7)	8(38.1)	0.142
CPS	4(26.7)	12(57.1)	0.285
SPS	1(6.7)	1(4.7)	0.511
Size, median(IQR[a])	3.6(3.4-4.2)	3.1(2.0-4.8)	0.585
Regular shape, n(%)	8(47.1)	9(31.0)	0.349
Well-defined surface, n(%)	11(64.7)	6(20.7)	0.003
Low T1 signal intensity, n(%)	17(100)	17(58.6)	0.002
High T2 signal intensity, n(%)	17(100)	17(58.6)	0.002
Contrast enhancement, n(%)	3(17.6)	7(24.1)	0.242
GTR, n(%)	13(76.4)	18(62.0)	0.135
Engel class I, n(%)	13(86.7)	14(66.7)	0.421

Abbreviations: GTCS: generalized tonic-clonic seizure, CP: complex partial seizure, SP: simple partial seizure, GTR: grossly total removal, IQR: interquartile range

[a]IQR denotes 25% to 75% quartiles

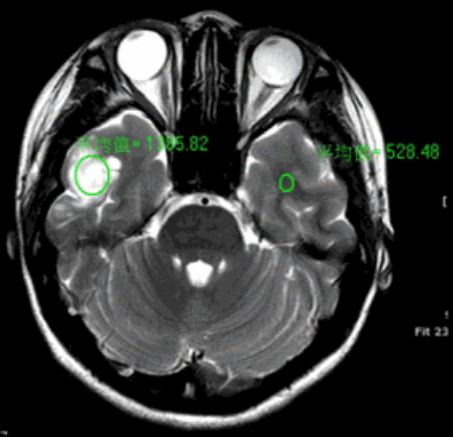

Table 2. Univariate logistic regression analysis of different imaging markers associated with DNET

	OR	95% CI	p value
ADC value	0.99	0.98-0.99	0.001
Bubble appearance	19.6	2.1-179.78	0.009
Bright rim	9.75	2.38-39.9	0.002
Satellite lesion	19.68	3.65-106.18	0.001
T2 signal intensity ratio	0.07	0.01-0.36	0.001

Abbreviations: OR: odds ratio, CI:confidence interval, ADC: apparent diffusion coefficient

(Filename: TCT_1521_Fig1Table1Table2.gif)

813

Texture Biomarkers of the Normal Appearing Brain Matter in FLAIR are Related to Cognition

K Chan[1], S Mitha[1], A Ghazvanchahi[1], H Khosravani[2], S Black[3], P Tyrrell[2], P Jabehdar Maralani[2], A Moody[3], A Khademi[1]
[1]Ryerson University, Toronto, Ontario, [2]University of Toronto, Toronto, Ontario, [3]Sunnybrook Health Sciences Centre, Toronto, Ontario

Purpose

More research into causes of dementia is needed to identify early precursors of cognitive decline and monitor disease progression. White matter lesions (WML) are established biomarkers which predict cognitive decline. Fluid Attenuation Inversion Recovery (FLAIR) MRI is primarily used for WML analysis, but studies have demonstrated other measurements from FLAIR MRI could be valuable additions to biomarker pipelines [1]. The aim of this study is to develop texture biomarkers from the normal-appearing brain matter (NABM) in FLAIR MRI and to investigate whether texture differences are associated with cognition.

Materials and Methods

Three cross-sectional FLAIR MRI neuroimaging archives (CAIN, ADNI, CCNA) are used with 1485 subjects from 87 imaging centres [2]. Images are intensity normalized [3], brain extracted [4] and spatially normalized. NABM is found by removing WML and CSF from standardized images [3]. NABM texture biomarkers called microstructural integrity (MII) and macrostructural damage (MAD) are extracted by computing local binary patterns and spatial correlation [5] that measure intensity changes in small regions. In subjects with homogeneous patterns, the MII feature will be high. For regions with small changes in intensities, the MAD feature will be low. To investigate biomarker properties, they are correlated to mean diffusivity (MD) in 98 DTI volumes in CAIN and CCNA. Using ANCOVA, the relationship between FLAIR texture biomarkers and cognition are examined across MoCA scores.

Results

FLAIR features were strongly correlated to MD ($p<0.01$) for MII ($r = -0.85$ CAIN, -0.66 CCNA) and MAD ($r = 0.86$ CAIN, 0.34 CCNA) demonstrating microstructural characteristics are effectively modeled with FLAIR texture features. Worse overall cognitive scores were associated with decreased MII and increased MAD. ANCOVA analysis showed significant differences between Normal vs. MCI ($p<0.01$) and MCI vs. AD ($p<0.01$) for MII and MAD, suggesting FLAIR NABM texture biomarkers are related to cognition (Fig. 2).

Conclusions

This study demonstrates clinical utility of texture biomarkers from FLAIR MRI as they were correlated with global cognition in a large cohort. FLAIR texture features were shown to quantify microstructural changes related to tissue structure and damage. As FLAIR is routinely used for neurological examinations, FLAIR texture biomarkers could supplement workflows for monitoring disease progression, determining optimal treatment points, or stratifying patients into disease subgroups for clinical trials.

Fig. 1. Biomarker extraction: Original slice, NABM segmentation, texture maps, statistical analysis.

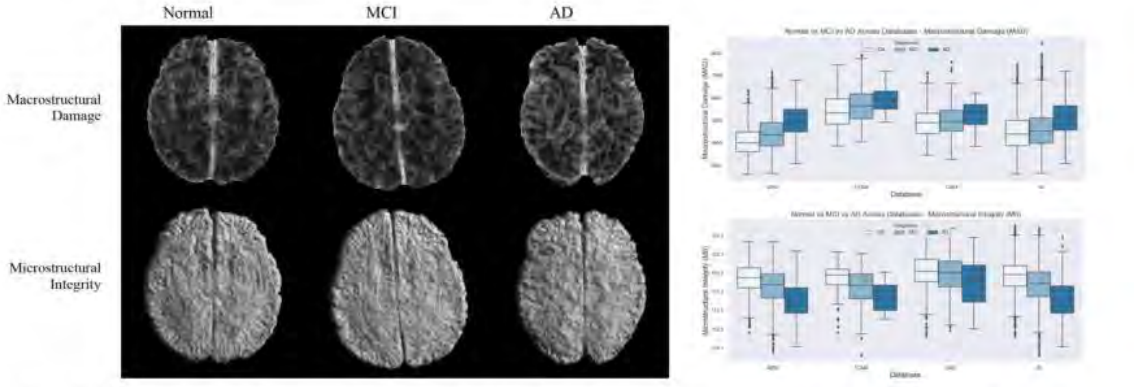

Fig. 2. Left: Texture features from the NABM for three MoCA groups. Right: Boxplots for each texture feature by MoCA group and cohort.

(Filename: TCT_813_TextureBiomarkers_ASNR_Figures_KChan.jpg)

1227

The Clinical Significance of Indeterminate Lymph Node Enlargement at Central Compartment in Patients with Thyroid Cancer and Concomitant Ultrasonographic Thyroiditis

J Rhim[1], J Lee[2], J Kim[3]

[1]SMG–SNU BORAMAE MEDICAL CENTER, Seoul, Korea, Republic of, [2]Seoul National University Hospital, Seoul, Seoul, [3]Seoul National University Hospital, Seoul, Other

Purpose

Indeterminate lymph node (LN) enlargement on ultrasonography has been reported to be frequent in patients with thyroiditis. We aimed to evaluate the clinical significance of indeterminate LN enlargement at central compartment in thyroid cancer patients with concomitant sonographic thyroiditis.

Materials and Methods

This study included 351 thyroid cancer patients prospectively enrolled from 7 institutions. According to the sonographic findings, patients were categorized into sonographic thyroiditis (ST) or non-thyroiditis (non-ST) groups and their central compartments were classified into suspicious, indeterminate and probably benign categories with regard to LN status. For indeterminate category, in which there were only indeterminate LNs that showed neither echogenic hilum nor hilar vascularity in the absence of any suspicious finding, irrespective of presence of probably benign LNs, the malignant rates were calculated and compared using Fisher's exact test between ST and non-ST groups and among the 3 categories within the same groups.

Results

A total of 531 central compartments were removed from 349 thyroid cancer patients (M:F=78:271, mean age 47.1±12.3 years (range, 15-78yrs)). Central LN dissection was performed more commonly in ST group than in non-ST group (p = 0.024), but the malignant rate was smaller in ST group (44/128 (34.4) than in non-ST group (175/403 (43.4)), p = 0.08) with marginal significance (Table 2). The malignant rate of indeterminate category in ST group was significantly lower than that in non-ST group (5/14 (35.7%) vs.23/32 (71.9%), P=0.047). Within ST group, malignant rate of indeterminate category was not significantly different from probably benign category (5/14 (35.7%) vs. 30/103 (29.1%), P=0.76) but lower than that of suspicious category (5/14 (35.7%) vs. 9/11(81.8%), P= 0.042). On the contrary, within non-ST group, malignant rate of indeterminate category was significantly higher than that of benign category (23/32 (71.9%) vs. 122/338 (36.1%), P=0.0001) and lower than that of suspicious group category (23/32 (71.9%) vs. 30/33 (90.9%), P=0.06) with marginal significance.

Conclusions

Sonographic indeterminate LNs at central compartment encountered in patients with thyroid cancer and concomitant ultrasonographic thyroiditis presumed not to increase malignant rate of corresponding LN level.

Table 1. Clinicopathological characteristics of the Study Population

No. of patients	ST group (n=77)	Non-ST group (n=272)	P-value
Age	45.7±12.1	47.4±12.3	0.29
Gender			**0.001**
Male	7 (9.1)	71 (26.1)	
female	70 (90.9)	201 (73.9)	
Tumor size	12.0±9.02	10.7±7.95	0.12
Multiplicity of tumor			**0.02**
single	39 (50.6)	177 (65.1)	
multiple	38 (49.4)	95 (34.9)	
Extra-thyroidal extension			0.24
macroscopic	4 (5.2)	26 (9.6)	
microscopic	37 (48.0)	141 (51.8)	
none	36 (46.8)	105 (38.6)	
No. of patient with central LN metastasis	31 (40.3)	140 (51.5)	**0.09**
No. of patient with lateral LN metastasis	17 (22.1)	50/70 (18.4)	0.51
Malignant rate of dissected LNs			
all	86/192(44.8)	292/602 (48.5)	0.41
central	44/128 (34.4)	175/403 (43.4)	**0.08**
lateral	42/64 (65.6)	117/199 (58.8)	0.38

ST group=sonographic thyroiditis group, non-ST group=sonographic non-thyroiditis group, ETE=extrathyroidal extension

[a]Data are shown as mean±standard deviation.

[b]Data in parentheses are percentages.

Table 2. Malignant rate of dissected central LN levels according to Sonographic Features

Category	Parameter	Total (349 pts/ 531 level)[a]	ST group (77 pts/ 128 level)[a]	non-ST group (272 pts/ 403 level)[a]	P-value
All category	Frequency of LN dissection per central compartment	531/698 (76.1)	128/154 (83.1)	403/544 (74.1)	**0.024**
	Malignant rate[b,c]	219/531 (41.2)	44/128 (34.4)	175/403 (43.4)	**0.080**
Suspicious category	Incidence	44/531 (8.29)	11/128 (8.59)	33/403 (8.19)	0.855
	Malignant rate[b,c]	39/44 (88.6)	9/11 (81.8)	30/33(90.9)	0.586
Indeterminate category	Incidence	46/531 (8.66)	14/128 (10.94)	32/403 (7.94)	0.284
	Malignant rate[b,c]	28/46 (60.9)	5/14 (35.7)	23/32(71.9)	**0.047**
Probably benign category	Incidence	441/531 (83.05)	103/128 (80.47)	338/403 (83.87)	0.417
	Malignant rate[b,c]	152/441 (34.5)	30/103 (29.1)	122/338 (36.1)	0.236

Pts=patients, LN=lymph node, ST group=sonographic thyroiditis group, non-ST group=sonographic non-thyroiditis group

[a] Data are shown as number of patients/number of dissected central compartment levels

[b] Malignant rates are calculated as numbers of LN levels with pathologically proven metastatic LN divided by numbers of dissected central LN levels

[c] Data in parentheses are percentages.

(Filename: TCT_1227_ASNRtable.jpg)

1219

The efficacy of "SpineJack®" device in AO A2, A3 and A4 traumatic ”burst” vertebral compression fractures: results in 52 patients.

M Bellini[1], C Zini[2], M Formisano[3], E Piane[4], P Galluzzi[5], L Monti[6]

[1]Unit of Neuroimaging, University Hospital Santa Maria Alle Scotte, Siena, Toscany, [2]Uniti of Radiology, Hospital Santa Maria Annunziata,USL Centro, Firenze, FI, [3]Institute of Radiology, Siena, Toscany, [4]Division of Diagnostic Imaging, Siena, Siena, [5]Unit of Diagnostic and Functional Neuroimaging, Siena, Tuscany, [6]NEUROIMAGING UNIT AOUS, SIENA, ITALY, siena, siena

Purpose

To retrospective evaluate the safety and the efficacy of titanium expandable devices to achieve anatomical restoration of traumatic burst vertebral compression fractures (BVCFs) of thoracolumbar spine.

Materials and Methods

52 patients (28 males, 24 females, mean age 23-79/60,3 ±14.9 years old) with traumatic BVCFs of the thoracic (N=25) and the lumbar (N=44) spine treated with SpineJack® device (Stryker Corp, Kalamazoo, MI). Exclusion criteria were spontaneous/osteoporotic and neoplastic vertebral fractures, as well as posterior wall involvement of more than 1/3 than of the spinal canal diameter. Visual analog scale (VAS) score has been administered before and 1 week and 6 months after procedure. Technical success was defined as correct deployment of the implant.

Results

A total of 69 vertebrae (A2.2 (N=32), A2.3 (N=21) ,A3.1 (N=12) and A4 (N=4)according to AO classification with 100% of technical success; in 17 patients, the procedure was performed at 2 levels during the same procedure. No major complications according to CIRSE guidelines occurred. 34 asymptomatic cement leakages along the fractures lines have been registered; no cement leakage into the spinal canal has been reported. All cases showed relevant improvement of symptoms with notable post-operative VAS scale reduction: pain measured decreased from median 8 preoperatively to 2 within 1 week and at 6-month drop to 1.

Conclusions

This percutaneous placement of SpineJack has been demonstrated to be safe and effective in patients with traumatic BVCFs, leading to immediate and lasting relief of pain. Further studies are needed to confirm those promising results on larger cohorts with long-term follow-up.

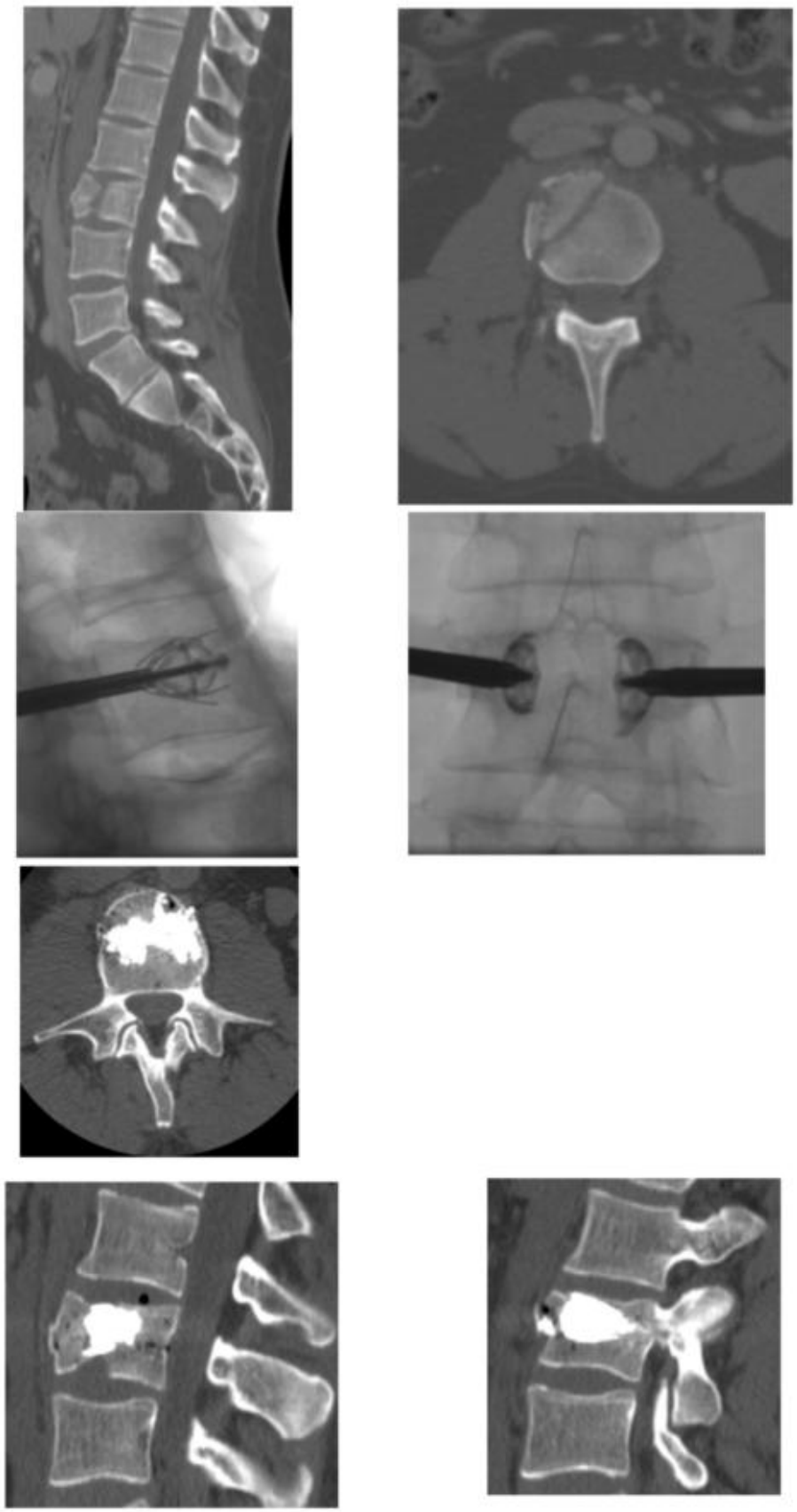

(Filename: TCT_1219_MB.jpg)

1203

The Korean ultra-high field young adult brain template with isotropic submillimeter resolution

H Song[1], I Hwang[1], S Han[2], S Lee[1], Y Kwon[1], C Oh[3], C Sohn[4]

[1]Seoul National University Hospital, Seoul, Seoul, [2]Center for Neuroscience Imaging Research, Institute for Basic Science (IBS), Seoul, Seoul, [3]Korea University, Sejong, Sejong, [4]Department of Radiology, Seoul National University College of Medicine, Seoul, Seoul

Purpose

The MNI152 template is most popular standard brain template for brain MRI study. However, the MNI152 template was developed with Caucasian population, 1.5T and 3T mixed brain MRI data. In addition, human brains show high variability in within group and phenotypic groups such as age and race. Therefore, this study aimed to develop high quality brain template of Korean young adult using isotropic submillimeter resolution using 7T scanner.

Materials and Methods

Sixty healthy participants aged 20 to 37 were recruited from the community. Anatomical data were acquired with MP2RAGE using SIEMENS 7T. Skull-stripping was applied for brain extraction using the BET2 of FSL1. N4 bias field correction was applied to correct low- frequency intensity non-uniformity in brain images. Bias corrected images were denoised with Rician filter using DenoiseImage Tool of ANTs. A template construction pipeline was performed to create template with preprocessed data using ANTs2. Symmetric image normalization (SyN) method was applied for inter-subject registration. The USCBrain atlas was registered to created template for an atlas template construction using the BrainSuite21a3 (Figure 2). The created Korean template was analyzed for differences to MNI152 and other brain templates (OASIS, NKI, Kerby, and IXI) with length, width, and height. Tissue probability maps for gray matter, white matter, and CSF (Figure 3) were created using DARTEL algorithm4.

Results

We constructed a brain template with high quality brain MRI data from 60 young adult participants using 7T. The created Korean template showed differences size in length, height, and width compared with MNI152 and other templates (Table 1). The Korean template is smaller than MNI152 template in length, width, and height and shorter than OASIS, NKI, and Kerby templates. The width and height show similar size between the Korean template and other templates (OASIS, NKI and Kerby). However, the Korean template is wider and higher than IXI template (Figure 1).

Conclusions

This study targeted to construct high quality a Korean young adult brain template to contribute a standard for a human brain mapping and morphometry study. The constructed Korean template might be useful to minimize a variability and bias in an age and race specific research.

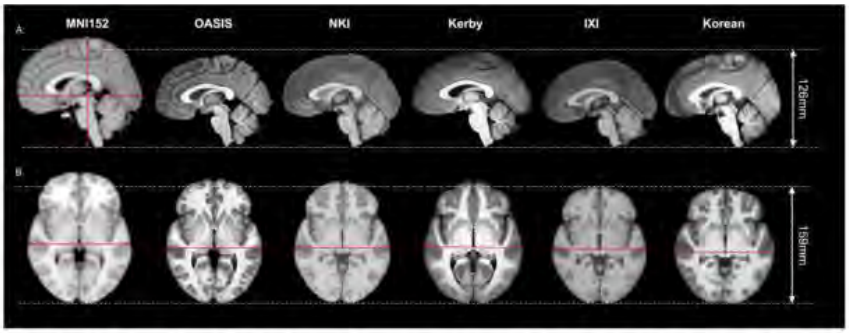

Fig 1. The length of brain template was measured from the anterior pole to the posterior pole through the AC-PC line as of the center of posterior commissure(A,B). The width was measured from the left pole to the right pole of the template through the center of posterior commissure on axial plane(B). The height was measured from the brain stem pole to superior pole as of a vertical line through the center of posterior commissure.

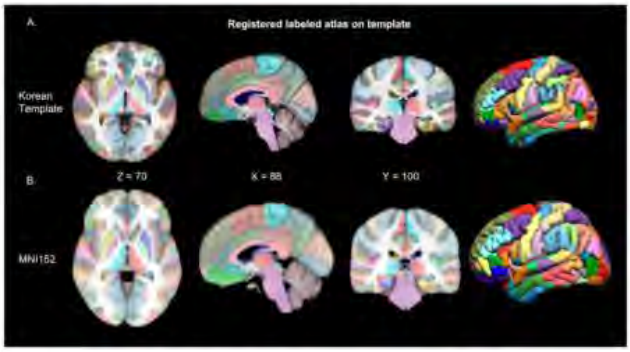

Fig 2. The USCBrain atlas was registered to the Korean template (A) and MNI152 template (B). A total of 130 cortical and 29 non-cortical brain region were registered and labeled to the Korean template.

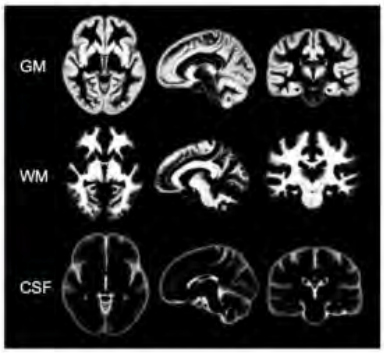

Fig 3. The DARTEL processing generated tissue probability maps of gray matter(top), white matter (middle), and CSF from young adult group.

Table 1. Comparison of the Korean Young Adult template to the MNI and other standard templates.

	MNI152	OASIS	NKI	Kerby	IXI	Korean
Length(mm)	175	167	164	163	159	159
Width(mm)	143	130	130	132	128	134
Height(mm)	148	123	125	128	118	126

(Filename: TCT_1203_Figure_table.jpg)

145

The Role of Artificial Intelligence in Assessing Acute Stroke

J Nguyen[1], V Prabhakaran[2]

[1]University of Wisconsin School of Medicine and Public Health, Madison, WI, [2]Univ. Of Wisconsin Hospitals and Clinics, Madison, WI

Purpose

The Alberta Stroke Program Early Computed Tomography Score (ASPECTS) is a qualitative grading tool used to assess the degree and distribution of early ischemic changes on non-contrast CT (NCCT) within the middle cerebral artery (MCA) territory. The overall objective is to compare ASPECTS assessed by iSchemaView's RAPIDTM and neuroradiologists in the setting of acute stroke.

Materials and Methods

ASPECTS was computed by neuroradiologists and iSchemaView's RAPIDTM from NCCT of patients that presented to UW Health's Emergency Department with concerns of acute stroke between January 1, 2020, and December 21, 2021. Cerebrovascular blood flow (CBF) was computed by iSchemaView's perfusion analysis software using CCT. Cohen's kappa statistics and the Pearson correlation coefficient (r) were used to compare ASPECTS.

Results

NCCT from 771 patients (359 male [mean age, 66 +/- 14] and 412 female [mean age, 66 +/- 18]) were evaluated. ASPECTS between neuroradiologists and iSchemaView's RAPIDTM demonstrated poor agreement for cases of concordant (ICC=0.32, n=758) and

discordant (ICC=-0.22, n=13) hemispheric agreement. ASPECTS between neuroradiologists and iSchemaView's RAPIDTM for patients that were evaluated within 6 hours of stroke onset (n=452) demonstrated poor agreement (ICC=0.31) in cases of concordant hemispheric agreement. ASPECTS between neuroradiologists and iSchemaView's RAPIDTM for patients that were diagnosed with MCA territory infarct (n=87) demonstrated good agreement (ICC=0.75) in cases of concordant hemispheric agreement. ASPECTS from iSchemaView's RAPIDTM and neuroradiologists demonstrated negative low (r=-0.34) and high (r=-0.62) correlation respectively.

Conclusions

ASPECTS between neuroradiologists and iSchemaView's demonstrated poor agreement overall, except for patients diagnosed with MCA territory infarct. However, ASPECTS from neuroradiologists more accurately predicted the degree of stroke burden, using CBF<30% as a marker for the extent of stroke. In addition, iSchemaView's RAPIDTM misdiagnosed the hemisphere of infarct for 13 cases of stroke. While this data brings into question the role of artificial intelligence in diagnosing acute stroke using NCCT, good agreement of ASPECTS between neuroradiologists and iSchemaView's RAPIDTM in MCA territory infarcts reinforces the initial intentions and limitations of the iSchemaView's RAPIDTM ASPECTS calculation tool.

133

The Role of Deep Convolutional Generative Adversarial Networks in Expanding Small Imaging Datasets for Improved Classification of Intracranial Hemorrhage

J Mayfield[1], S Decker[2], A Borkowski[3], K Bailey[4], N Viswanadhan[4]

[1]USF Health Department of Radiology, Tampa, FL, [2]USF Health Morsani College of Medicine, Tampa, FL, [3]USF Health Department of Pathology and Cell Biology, James A. Haley Veteran's Hospital, Tampa, FL, [4]James A. Haley Veterans' Hospital Department of Radiology, Tampa, FL

Purpose

Medical imaging inherently has a sparsity of annotated data available for machine learning models, a significant barrier to creating accurate classification and prediction algorithms[1,2]. We propose the use of a novel, proprietary Deep Convolutional Generative Adversarial Network (DCGAN) to expand a small (n=70) data set of non-contrast Computed Tomographies (NCCTs) demonstrating three patterns of intracranial hemorrhage (ICH). By bolstering the existing sparse dataset, we aim to improve performance in a proprietary Convolutional Neural Network (CNN) for classification of ICH.

Materials and Methods

One hundred and ten deidentified patients' NCCTs were selected from an anonymized ICH teaching database at the James A. Haley V.A. Medical Center. Images with postoperative changes were excluded resulting in seventy NCCTs for analysis containing three categories of ICH: intraparenchymal, intraventricular, and subdural. The DCGAN produced an additional seventy synthetic images, duplicating each of the ICH types. Normalized mean square error was calculated and synthetic images were assessed for artifact exaggeration. A proprietary CNN was used to classify ICH in (i) real images only, and (ii) real with synthetic images added. An RTT (ratio of training to testing) of 0.9 over 250 epochs was implemented. Classification accuracy and model loss were calculated.

Results

The GAN provided both qualitatively similar and unique representations of the ICH types to supplement the real images (Fig. 1a). The real image classification model demonstrated overfitting with increasing testing loss and decreasing accuracy, resulting in a testing accuracy of 40.0% and a categorical loss of 11.883. Addition of synthetic images significantly decreased overfitting, model loss, and increased classification accuracy of ICH type over the same number of iterations, resulting in a testing accuracy of 80.8% and a categorical loss of 1.338 (Fig. 1b).

Conclusions

The implementation of GAN synthetic images can provide significant improvements in CNN optimization and accuracy for classification of ICH in NCCTs given small data sets. Utilization of this method may serve remote healthcare imaging centers who wish to train categorical models on local populations in contrast to global models which may not represent their locoregional demographic.

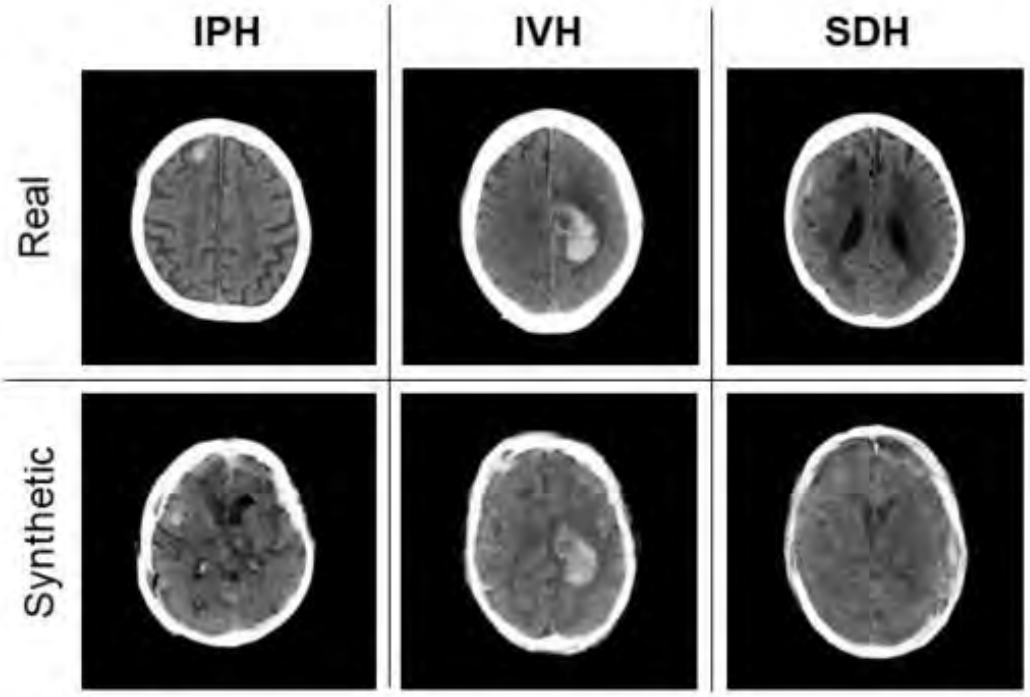

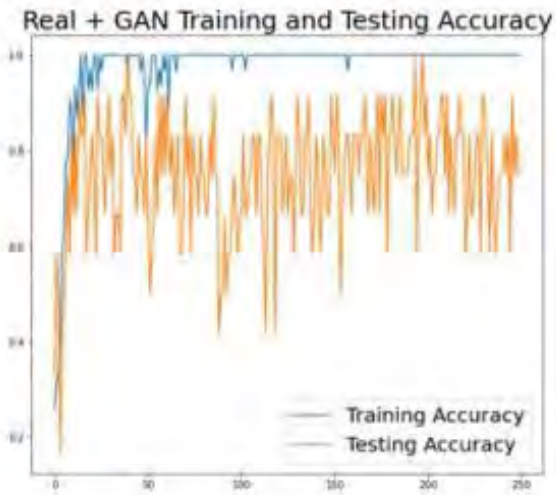

(Filename: TCT_133_Figure_1AB.jpg)

67

The Role of Machine Learning and Radiomics for Treatment Response Prediction in Idiopathic Normal Pressure Hydrocephalus

H Sotoudeh[1], Z Saadatpour[1], E Sotoudeh[2], O Shafaat[3], A Rezaei[1], A Singhal[1], M Tanwar[1]

[1]University of Alabama at Birmingham, Birmingham, AL, [2]Iranian Hospital in Dubai, Dubai, Dubai, [3]The Russell H. Morgan Department of Radiology and Radiological Science, Johns Hopkins University, Baltimore, USA

Purpose

Ventricular shunting remains the standard of care for patients with idiopathic normal pressure hydrocephalus (iNPH); however, not all patients benefit from the shunting. Prediction of response in advance can result in improved patient selection for ventricular shunting. This study aims to develop a machine learning predictive model for treatment response after shunt placement using the clinical and radiomics features.

Materials and Methods

In this retrospective pilot study, the medical records of iNPH patients who underwent ventricular shunting were evaluated. In each patient, the "idiopathic normal pressure hydrocephalus grading scale" (iNPHGS) and a "Modified Rankin Scale" were calculated before and after surgery. The subsequent treatment response was calculated as the difference between the iNPHGS scores before and after surgery. iNPHGS score reduction of two or more than two were considered as treatment response. The presurgical MRI scans were evaluated by radiologists, the ventricular systems were segmented on the T2-weighted images, and the Radiomics features were extracted from the segmented ventricular system. Using Orange datamining open-source platform, different machine learning models were then developed based on the presurgical clinical features and the selected radiomics features to predict treatment response after shunt placement.

Results

After the implementation of the inclusion criteria, 78 patients were included in this study. One hundred twenty radiomics features were extracted, and the 12 best predictive radiomics features were selected. Using only clinical data (iNPHGS and Modified Rankin Scale), the random forest model achieved the best performance in treatment prediction with an AUC of 0.71. Adding the Radiomics analysis to the clinical data improved the prediction performance, with the support vector machine achieving the highest rank in treatment prediction with an AUC of 0.8. Adding age and sex to the analysis did not improve the prediction.

Conclusions

Using machine learning models for treatment response prediction in patients with iNPH is feasible with acceptable accuracy. Adding the Radiomics analysis to the clinical features can further improve the predictive performance. SVM is likely the best model for this task.

857

The Underlying Causes of Internal Carotid Artery Occlusion in Acute Ischemic Stroke

W Chen[1]

[1]Division of neuroradiology, Department of radiology, Taichung Veterans General Hospital, Taichung, Taiwan

Purpose

Sometimes internal carotid artery occlusion (ICAO) can be noted in patients with symptom of acute ischemic stroke. In our experience, there are several causes of ICAO including terminal ICA thrombosis, acute long segmental ICA thrombosis, severe atherosclerotic stenosis with acute ICAO, chronic ICAO and ICA dissection. Appropriate method of endovascular thrombectomy (EVT) is mandatory for different causes of ICAO. So, accurate diagnosis of different causes of ICAO before EVT is important. We will find out image findings of CT angiography (CTA) for these underlying causes of ICAO.

Materials and Methods

We reviewed all patients of acute ischemic stroke who underwent EVT in our institute from 2015 to 2021 and found out the patients with ICAO. All patient received CTA before EVT. The final diagnosis of underlying causes of ICAO were confirmed by digital subtraction angiography (DSA). We compared CTA and digital subtraction angiography (DSA) for patients with ICAO and found out the CTA findings of different causes of ICAO.

Results

Total 250 patients with acute ischemic stroke who underwent EVT were reviewed. Twenty-five patients (10%) of ICAO were found. 14 of 25 (56%) were terminal ICA thrombosis, 6/25 (24%) were ICA dissection, 3/25 (12%) were severe atherosclerotic stenosis with acute ICAO. 1 of 25 (4%) was chronic ICA occlusion. 1 of 25 (4%) was long segmental ICA thrombosis. In cases of terminal ICA thrombosis, contrast filling at dependent part of proximal ICA with fluid-fluid level appearance in CTA was found. In cases of ICA dissection, smooth tapering of cervical ICA was noted and sometimes partial contrast filling in cervical ICA near skull base or petrous segment was noted. In cases of severe atherosclerotic stenosis with acute ICAO, CTA showed severe atherosclerotic plaques at carotid bifurcation or proximal ICA. In case of chronic ICA occlusion, blunting of ICA stump can be noted in CTA and DSA. In case of acute long segmental ICA thrombosis, filling defect in middle cervical ICA is noted by CTA and DSA.

Conclusions

Appropriate method of EVT is mandatory for different causes of ICAO. Before EVT, CTA image findings help differentiate different causes of ICAO.

1517

The Utility of Virtual Biopsies For Training Classification Models to Detect Tumor Infiltration in Peritumoral FLAIR-Hyperintense Regions

R Wujek[1], M Prah[1], M Al-Gizawiy[1], K Schmainda[1]
[1]*Medical College of Wisconsin, Milwaukee, WI*

Purpose

Delineation of invasive tumor within peritumoral FLAIR-hyperintense, non-enhancing lesion (NEL) remains a major obstacle to image-guided glioma treatment [1,2]. In prior studies, we have used tumor and non-tumor biopsies extracted from NEL, paired with colocalized MRI, to train classification models for this distinction [3-5] (Figure 1). To account for class imbalance in the data (Figure 2), additional non-tumor samples were sampled from NEL of non-invasive tumors. While histological confirmation is the preferred method for labeling, these "virtual biopsies" are assumed sufficient to benefit model performance, the hypothesis addressed by this study.

Materials and Methods

Dataset: Subjects with NEL biopsies, preoperative MRI (T1, T1+C, T2, FLAIR, DWI & DSC) were selected from a brain tumor database (n=52), with all standard images bias-corrected and normalized to white matter. ADC maps (b=0,1000) were extracted from DWI and leakage-corrected rCBV and rCBF maps derived from DSC-MRI and normalized to white matter. ROIs corresponding to biopsy extraction sites were manually drawn, linking histology to precise MRI regions. 116 tumor samples (WHO grades I-IV glial) and 20 non-tumor samples were obtained for a total of 136 true biopsies. An additional 96 ROIs were drawn within NEL of the subjects with non-invasive tumors for virtual biopsies. Model & Training: A 3D neural network with 4 convolution layers and 2 dense layers was used. To assess the value of virtual biopsies, training was repeated with the following conditions: 1) no data modifications, 2) standard augmentations (flips, rotations), 3) inclusion of virtual biopsies, & 4) inclusion of both augmentation and virtual biopsies. Data was split 70:30 for training and testing stages. Softmax cross entropy with L2 regularization was used for the loss & RMSProp for the optimizer. Training was done on an Nvidia Tesla K40 GPU.

Results

Accuracy, precision, sensitivity and specificity for different training conditions are given in Figure 3. Training without modification predicted nearly all samples to be tumor with slight improvements using standard augmentations. While virtual biopsies improved metrics, use of both dataset modifications proved best.

Conclusions

As expected, training without dataset modification yields poor results. Using virtual biopsies benefits training more than standard augmentations, specifically reducing the number of false positives by exposing the model to more non-tumor samples.

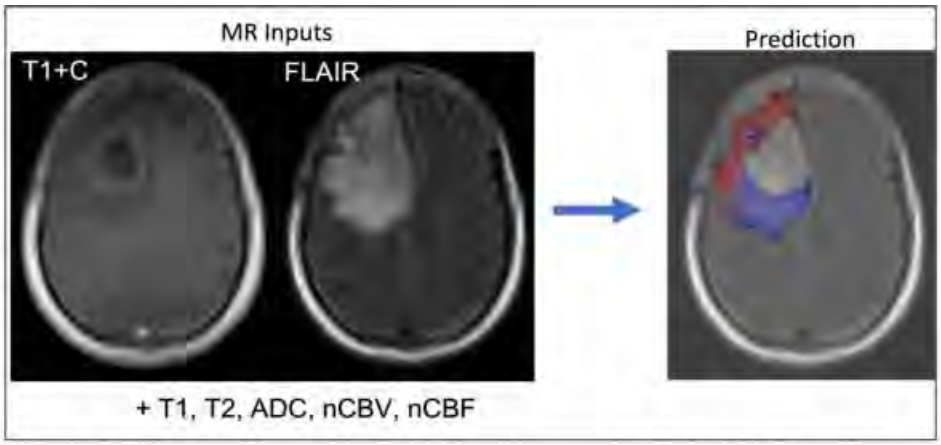

Figure 1: Predictive map of tumor infiltration into NEL with corresponding T1+C and FLAIR maps. Tumor infiltration maps (on the right) are generated by applying the trained model to each voxel within the NEL region, using all inputs as predictive features. Red indicates regions of predicted tumor infiltration. Blue indicates regions of predicted non-tumor.

Training Conditions	Training Data		Testing Data	
	Tumor Samples	Non-Tumor Samples	Tumor Samples	Non-Tumor Samples
1) no augmentation	81	14	35	6
2) standard augmentation	648	112	35	6
3) inclusion of virtual biopsies	81	81	35	35
4) both (2) & (3)	648	648	35	35

Figure 2: Number of samples for each training condition. Note that virtual biopsies alter the number non-tumor samples available overall, adding to training and testing data whereas augmentation only applies to training data.

Training Conditions	Accuracy	Precision	Sensitivity	Specificity
1) no augmentation	0.85	0.85	1.00	0.00
2) standard augmentation	0.73	0.85	0.83	0.17
3) inclusion of virtual biopsies	0.63	0.62	0.69	0.57
4) both (2) & (3)	0.94	0.94	0.94	0.94

Figure 3: Performance metrics for each training condition. The low specificity values for training conditions (1) and (2) result from a high number of false positives at testing. This problem is significantly reduced for conditions (3) and (4) as noted by the more balanced distribution of high values.

(Filename: TCT_1517_ASNR2022_figure.jpg)

249

Uncovering the Thalamo-hypothalamic connections of the Human Limbic System

A Kamali[1], G Hedayati[2], M Hosseini[3], a Ali[4], E Park[5]

[1]University of Texas Health Science Center Houston, Houston, TX, [2]University of Southern California, Los Angeles, CA, [3]University of Technology Sydney, Sydney, NSW, [4]university of texas houston, Houston, TX, [5]University of Texas Houston, Houston, TX

Purpose

The limbic system is involved in emotions, memory formation and storage. The thalamus receives and directs sensory information to various parts of the brain including the limbic system. The hypothalamus modulates the autonomic nervous system (i.e. vital signs, circadian rhythms, hunger) and instinctive behaviors (fear, learning, sociosexual activities) and is in direct connectivity with the thalamus and the rest of the limbic system. The mammillothalamic tract and the dorsal thalamo-hypothalamic tract are the two major known direct connectivity routes between the thalamus and hypothalamus in primates. The purpose of this study is to illustrate these pathways using high angular and high spatial diffusion weighted imaging technique.

Materials and Methods

30 healthy adults were scanned at 3T connectome project Philips Intera scanner with a dual quasar gradient system with a maximum gradient amplitude of 80 mT/m, maximum slew rate 200 mT/ms/m, and an eight-channel SENSE-compatible head coil. The conventional MRI (cMRI) protocol included axially prescribed 3-D spoiled gradient (repetition time (TR) = 58 ms; echo time (TE) = 54 ms; and flip angle = TR/TE/flip angle = 8 ms/4 ms/6), 3-D proton density-weighted (TR/TE/flip angle = 10,000 ms/10 ms/90, and 3-D T2-weighted (TR/TE/flip angle = 10,000 ms/60 ms/90 degree), with a square field-of-view (FOV) = 256 mm x 256 mm and a matrix of 256 x 256 pixels. The slice thickness for the MRI sequences was 1.0 mm with 120 contiguous axial slices covering the entire brain. DWI data were acquired using an EPI sequences. DTI studio used for tensor decoding, diagonalization, eigenvalue and scalar map estimations and tractography. Two experienced raters constructed tracts on all subjects using 2 ROIs.

Results
The dorsal thalamo-hypothalamic (DTH) pathway, originates from the dorsal and medial thalamic nuclei and projects to the anterior hypothalamic nuclei. Unlike the DTH which connects the dorsal thalamus to the anterior hypothalamus, the mammillothalamic tract (MTT) is a much smaller tract that connects the posterior hypothalamus to the ventral thalamus.
Conclusions
Using a high angular and high spatial resolution diffusion weighted tractography technique, we were able to show trajectories of the two most important thalamo-hypothalamic connectivity in the human brain. These pathways maybe involved in memory formation and storage as well as integration of sensory information into the autonomic nervous system response.

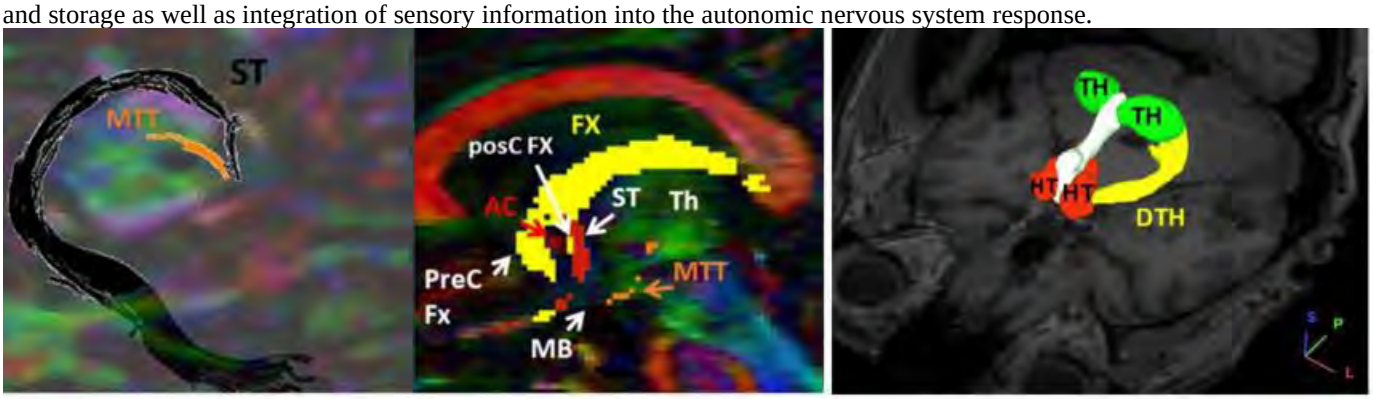

The small orange fiber tract is the mammillothalamic tract (MTT) connecting the mammillary bodies (MB) of the hypothalamus to the ventral thalamic nuclei (Th). The yellow fibers of the fornix (FX) and black (left image) and red fibers (right image) of the stria terminalis (ST) are also shown for comparison in size of the fiber tracts. AC: anterior commissure, PreC and PosC: precommissural and post commissural fibers of the fornix.

The yellow fiber tract is the dorsal thalamo-hypothalamic tract (DTH) connecting the dorso-medial thalamus (Th in green color) to the anterior hypothalamus (HT in red color). The white structure in the middle is the third ventricle.

(Filename: TCT_249_Figure1.jpg)

1155
Usefulness of Synthetic MRI for the Diagnosis of Cerebellar Subtype of Multiple System Atrophy
M Azuma[1], H Uetani[2], T Hirai[2]
[1]University of Miyazaki, Miyazaki, Japan, [2]Kumamoto University, Kumamoto, Japan

Purpose
Synthetic magnetic resonance imaging (sMRI) has not been used for evaluating the cerebellar subtype of multiple system atrophy (MSA-C). We aimed to clarify the diagnostic performance of sMRI sequences for MSA-C.
Materials and Methods
Our study included 10 healthy volunteers and 6 MSA-C patients who underwent two-dimensional sMRI studies at 3T. Two radiologists independently evaluated the visualization of the pons on 9 sMRI sequences [T1-weighted images (sT1WI), T2-weighted images (sT2WI), proton density-weighted images (sPDWI), fluid-attenuated inversion-recovery (sFLAIR) images, double inversion recovery (sDIR) images, T1 (sT1) maps, T2 (sT2) maps, proton density (sPD) maps, and myelin (sMyelin) maps] using a 5-point grading system. Kappa (κ) statistics, Man-Whitney test and receiver operating characteristic (ROC) analysis were used for statistical analysis. Pair-wise comparison of the ROC curves was performed using the area under the ROC curve (AUC).
Results
Interobserver agreement for sMRI sequences was very good to excellent ($\kappa = 0.83$-1.00). On sFLAIR image, sPDWI, sDIR image, sT1 map, sPD map, and sMyelin map, the mean pons visualization grade was significantly higher for MSA-C patients than volunteers ($P < 0.05$). sPDWI and sPD map had the highest diagnostic performance (AUC=1) and were significantly better than sT1WI, sT2WI, sFLAIR image, sT1 map, and sT2 map ($P < 0.05$) although no significant difference was observed with sDIR image and sMyelin map.
Conclusions
Among the sMRI sequences, sPDWI and sPD map yielded the best diagnostic performance for MSA-C.

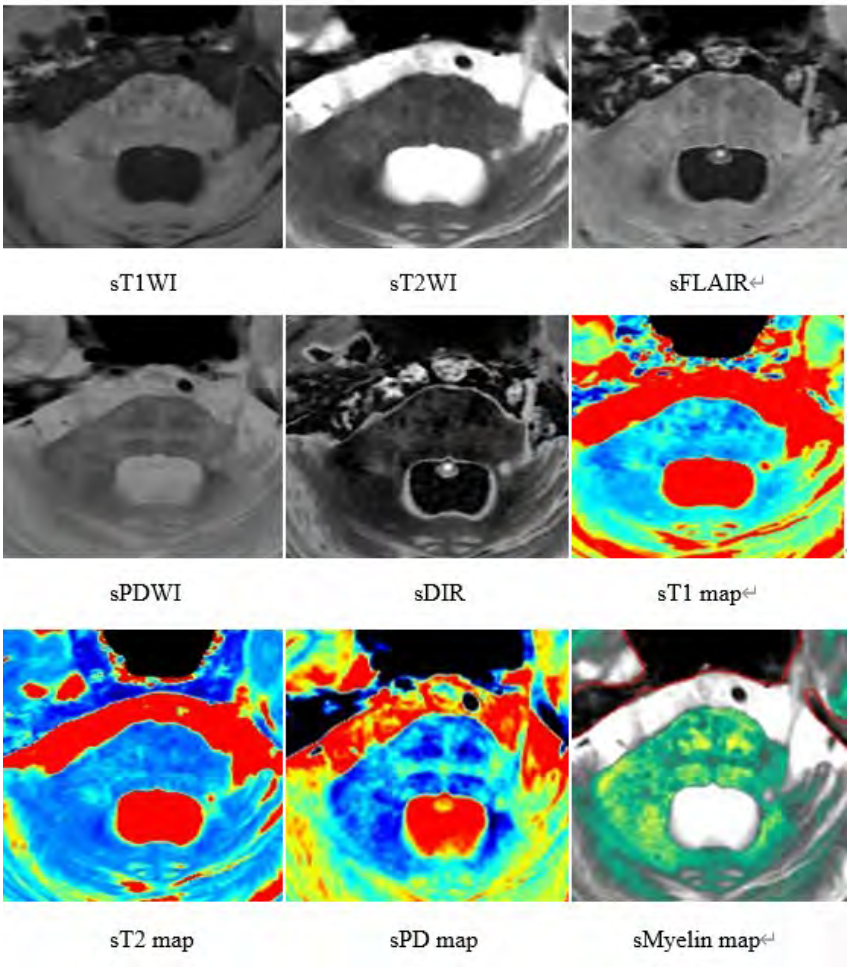

(Filename: TCT_1155_Figure.jpg)

526

Vanishing acute basal ganglion infarction on DWI: beware of the "T2 gray-out effect"

L Tsao[1], C Chiang[1], C Liu[1], D Chen[1]

[1]Taipei Medical University - Shuang Ho Hospital, New Taipei City, Taiwan

Purpose

Identification of basal ganglion involvement in acute infarction settings often bodes a worse patient outcome. DWI is highly sensitive in detecting acute infarction with its conspicuous hyperintense signal; therefore, it is not uncommon to review it in isolation without particular attention to ADC map. However, increased iron deposition in basal ganglia could lead to "T2 gray-out effect" and overlook of acute infarction on DWI. We aimed to assess the interpretation error in detecting acute basal ganglion infarct on DWI.

Materials and Methods

The retrospective study included 150 consecutive patients who received MRI for the evaluation of endovascular treatment in anterior circulation stroke. Two radiologists independently reviewed the DWI images solely to identify acute infarction in basal ganglion. The standard reference for acute infarction was an ADC value < 620 mm2/s. After consensus reading, the diagnostic performance in identifying acute basal ganglion infarction was evaluated. Furthermore, the signal intensities of the basal ganglion regarding the missed cases (false negative) were analyzed and compared to those within the non-infarcted and correctly identified cases.

Results

For the 400 slices at the level of basal ganglion, sensitivity, specificity and accuracy in detecting basal ganglion infarction on DWI were 88.66%, 98.6% and 93.8%. Twenty-two out of 192 slices (8.85%) that have basal ganglion infarction were misinterpreted as normal. In the by-case subgroup analysis of patients with concomitant basal ganglion and cortical infarction, 4 in 49 (8.16%) patients were diagnosed as cortical infarction only. Two in 30 (6.67%) cases with solely basal ganglion involvement were diagnosed as not infarcted. Illustrated cases were shown in Figure A. The ambiguity of DWI lesions in the missed cases was related to the lower signal intensity of basal ganglion on the DWI images at b=0 (p=0.013), resulting from T2 shortening effect (Figure B).

Conclusions

Among patients with acute infarction of anterior circulation, it is likely that basal ganglion infarction can be obscured under the background of T2 gray-out effect due to iron deposition when solely reviewing DWI; especially of those without cortical infarction, patient might be diagnosed as normal, impacting clinical decision and outcomes. Therefore, reviewing ADC maps ought to be performed routinely to avoid misinterpretation.

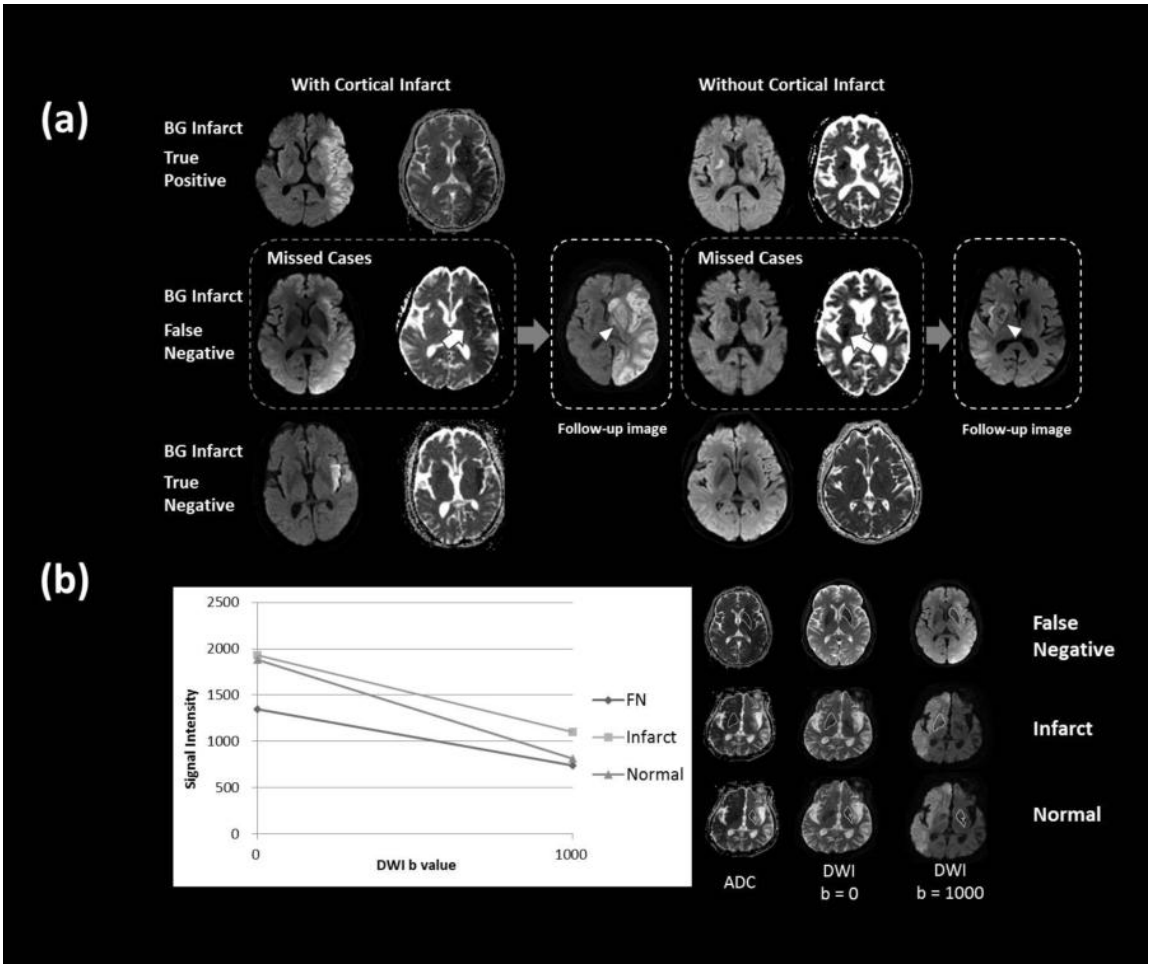

(Filename: TCT_526_figureforASNR2022.jpg)

692

Virtual neuroradiology-A New approach to CNS imaging

R Glikstein[1], A Guarnizo[2], S Chakraborty[3], C Torres[3], J Sutherland[3], D La Russa[3], B Schwarz[4]

[1]The Ottawa Hospital, University of Ottawa, Ottawa, ON, [2]Fundación Santa Fe de Bogotá, Bogotá, Colombia, [3]The Ottawa Hospital, U. of Ottawa, Ottawa, ON, [4]the ottawa hospital, ottawa, ON

Purpose

To evaluate virtual reality (VR) applied to brain tumors. Pilot study

Materials and Methods

Three neuroradiologists and one advanced neuroradiology fellow used VR to view MRIs of six patients with confirmed brain tumors. The radiologists underwent two to three hours of training prior to evaluating the brain MRIs in VR. Each tumor was segmented in VR and displayed with volume rendering and 2D cross-sections. The segmented model could be viewed with imaging data from any perspective, thereby providing optimal views of the tumour and surrounding anatomical structures. Imaging were analyzed, measured and recorded in VR and with conventional methods.

Results

The VR system enabled identification of tumors with exquisite separation from surrounding anatomical structures in a three-dimensional visual environment. The level of confidence and other personal evaluations demonstrated 63% improvement on reading cases when using VR

Conclusions

VR is an excellent tool that would help on diagnosis and treatment planning of brain tumors

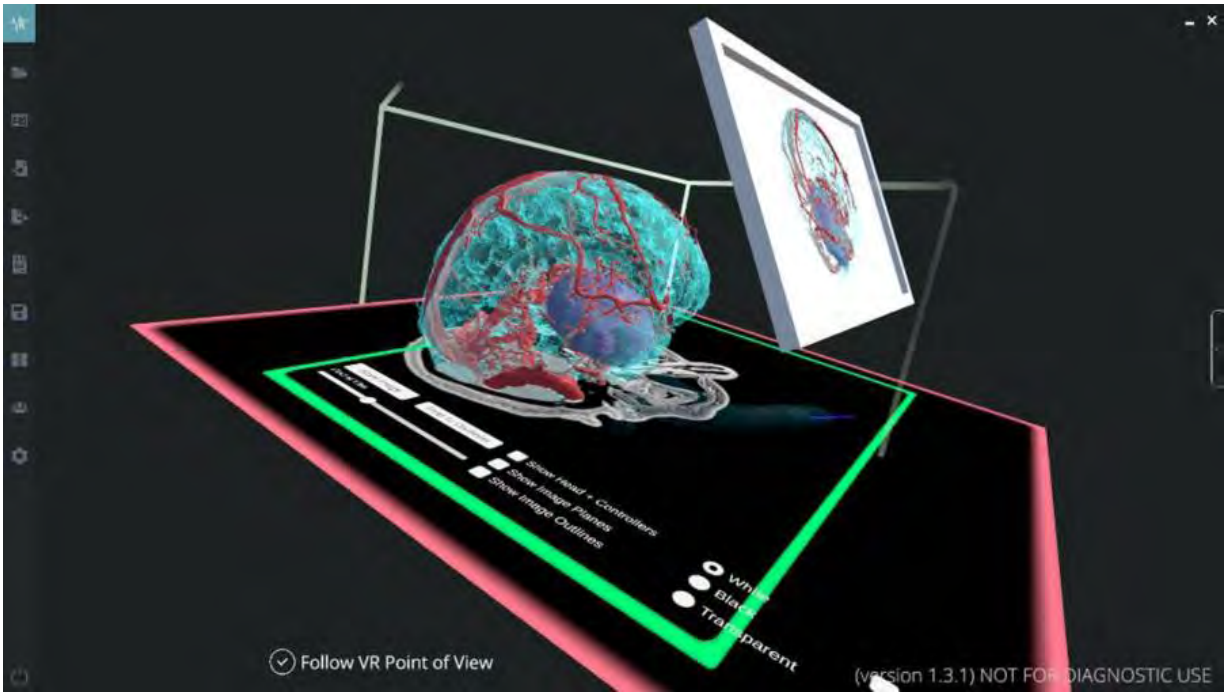

(Filename: TCT_692_Picture3.jpg)

1161

Volumetric Analysis of Multiparametric MRI to Predict Disease Progression in Patients with Minimal Cognitive Impairment in Alzheimer's Disease

T Kainth[1], X Xu[1], G Singh[2], P Prasanna[1]

[1]Stony Brook University, Stony Brook, NY, [2]Newark Beth Israel Medical Center, Newark, NJ

Purpose

Progression of Alzheimer's disease (AD) occurs in a continuum divided into three phases: a) preclinical AD, where patients are cognitively normal (CN), b) mild cognitive impairment (MCI), where patients have mild symptoms that do not affect activities of daily living (ADLs), and c) dementia, where symptoms affect most ADLs. MCI is a key area of interest because treatment/preventative recommendations at this stage may delay progression to dementia. Researchers have extensively studied differences between cognitively normal, MCI, and dementia stages of AD disease using volumetric and morphometric analysis of MRI. However, very few studies have elicited structural differences specifically within MCI phases. In this study, we perform a comparative volumetric analysis of multiparametric structural MRI data. Our goal is to identify structures related to AD progression in patients diagnosed with MCI.

Materials and Methods

Our dataset comprises 65 cases from the Alzheimer's Disease Neuroimaging Initiative (ADNI) database. We selected 3D T1w sagittal MRI sequences of patients in MCI group within ADNI 1, ADNI 2, and ADNI GO projects. We divided the patients into two groups based on Clinical Dementia Rating (CDR): 1) converters, whose baseline CDR of 0.5 changed to 1 at the latest diagnoses, and 2) non-converters, whose baseline CDR of 0.5 remained 0.5 at the latest diagnoses. We used FreeSurfer software to extract cortical and subcortical volumes and performed lobe mapping to get frontal, temporal, parietal, occipital, and cingulate lobes volumes. We selected 61 subcortical features and 10 cortical level features for comparison via Student's t-test.

Results

We performed a comparative analysis of 71 total features between the converter and non-converter groups. Volumes of only 5 subcortical features showed a statistically significant difference ($p<0.05$): the temporal horn of right lateral ventricle, left hippocampus, right hippocampus, left amygdala, and right nucleus accumbens.

Conclusions

Our results are consistent with the related literature that shows decrease in volumes of hippocampus and subcortical structures as one of the early structural changes seen on MRI in AD. However, after multiple comparison correction, our results are inconclusive and do not detect significant difference between the two groups. As our next step, we will use machine learning tools to extract radiomic descriptors and analyze the subvisual differences beyond volumetric features.

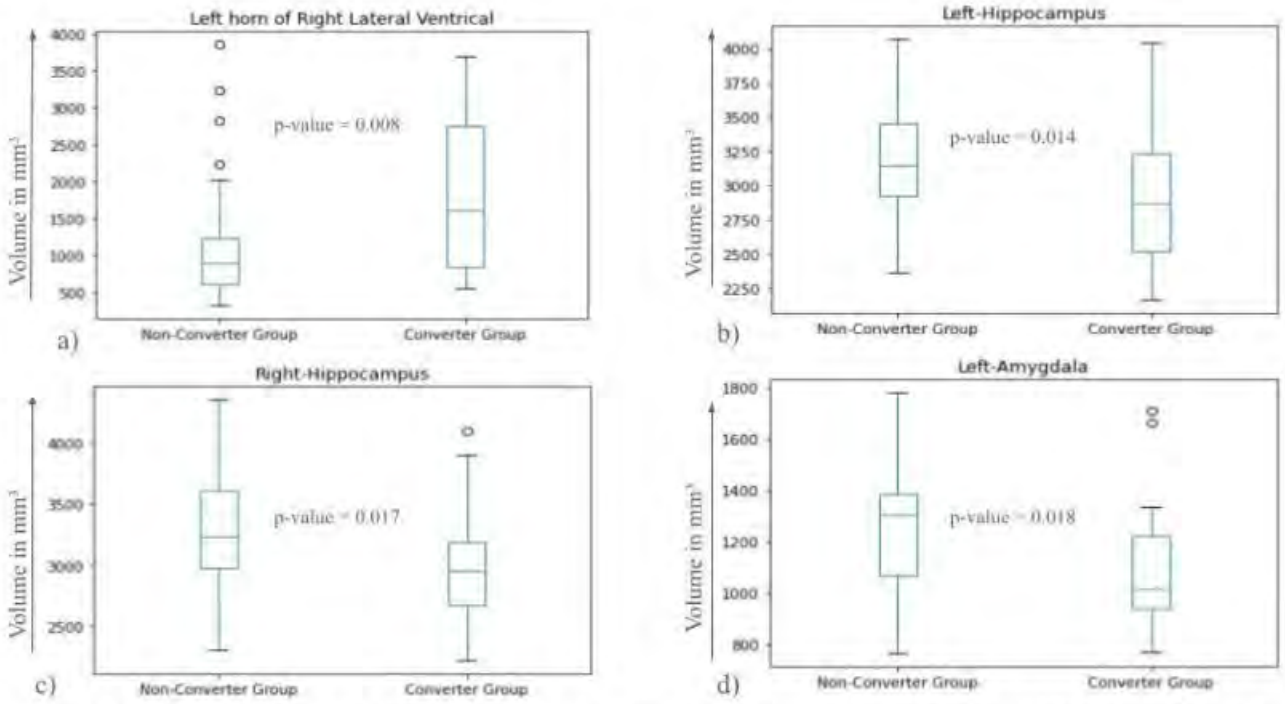

Box plots comparing volumes of subcortical structures in converters and non-converters: a) Left horn of Right Lateral Ventricle, b) Left-Hippocampus, c) Right-Hippocampus, and d) Left-Amygdala

(Filename: TCT_1161_AD-ASNR-2022.jpg)

147

Within-Subjects Comparison of Super-Resolution Single-Shot T2-Weighted Fetal Brain Imaging at 1.5T vs 3.0T

N Rubert[1], P Cornejo[1], S Anderson[2], L Goncalves[1]

[1]Phoenix Children's Hospital, Phoenix, AZ, [2]Arizona State University, Scottsdale, AZ

Purpose

The purpose of this study was to examine the image quality and reliability of three-dimensional fetal brain imaging created with super-resolution techniques at 1.5T and 3.0T.

Materials and Methods

Patients were recruited who were scheduled for a routine fetal MRI at our institution. Patients received two sets of fetal brain MRI's within minutes of each other: one on a 1.5 T Philips Achieva and one set on a 3.0T Philips Ingenia Elition scanner. At 1.5T nine acquisitions were obtained with a T2-weighted single-shot fast spin echo (SSFSE) sequence with an acquisition voxel size of 1.5 x 1.5 x 4.0 mm and a slice spacing of 4.4 mm. Six SSFSE acquisitions were obtained at 3.0T with a voxel size of 1.0 x1.0x3.0 mm and a slice spacing of 3 mm. SENSE was utilized at 3.0T to reduce acquisition time, yielding near equal acquisition times per slice and total acquisition times. All stacks from each scanner were used to reconstruct a super-resolution volume with a voxel size of 0.5 mm. Super-resolution volumes for each scanner were registered to a common template space and were presented to two radiologists in a blinded side-by-side view using Philips Intellispace Portal. Radiologists graded overall 3D image quality and the appearance of individual anatomy within the brain on a five-point scale. SNR was measured in the periventricular white matter and image gradient was measured throughout the brain volume for reconstructions free from artifact.

Results

12 Patients were recruited. The average gradient was 14% higher at 3.0T than at 1.5T, and the SNR at 1.5T was 22% higher than at 3.0T on average. Both these results indicate higher effective spatial resolution for the 3D reconstructions created using thinner slices and greater in-plane spatial resolution at 3.0T. Greater consistency in image quality was observed at 1.5T. The overall radiologist score was 3.4 ± 0.8 for scans at 1.5T and 2.4 ± 1.5 at 3.0T. Three 3D reconstructions failed at 3.0T because 2D acquisitions suffered signal loss due to B1 inhomogeneity. Only one reconstruction failed at 1.5T due to insufficient spatial resolution (brain volume < 60 ml).

Conclusions

Scanning at 3.0T more often yielded images with artifacts due to B1 inhomogeneity. Scanning at 1.5T yielded a diagnostic 3D volume more consistently. However, when artifacts are not a problem the higher SNR of 3T scanning may be used to produce a higher resolution volume with only a modest increase in noise than when scanning at 1.5T.

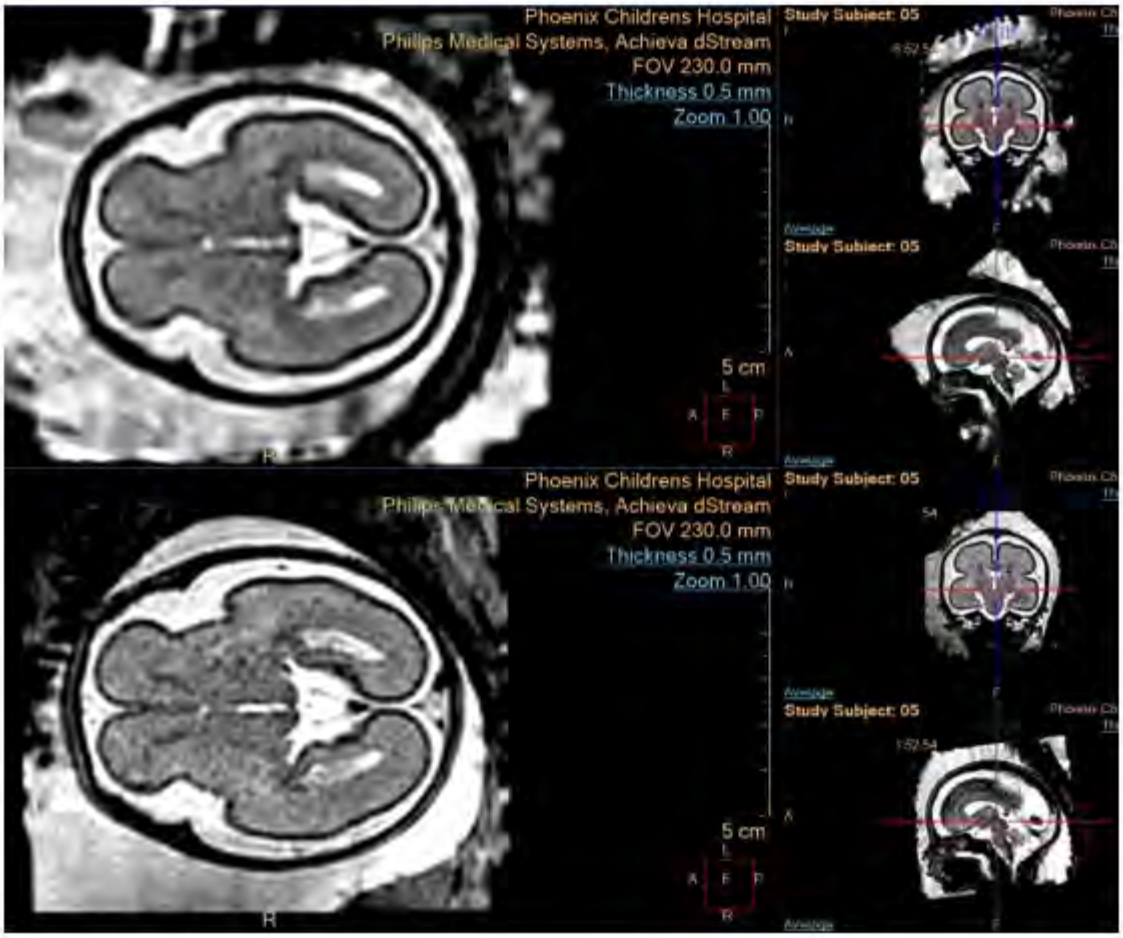

Figure 1. Side-by-side comparison view for a patient where radiologists rated overall image quality similarly at 1.5T (top) and 3.0T (bottom).

	Overall Score	Cerebellar Vermis	Cerebral Aqueduct	Corpus Callosum	Cavum of the Septum Pellucidum	Sylvian Fissure	Optic Nerves
1.5 T	3.4 ± 0.7	3.4 ± 0.7	3.3 ± 0.7	3.4 ± 0.6	3.6 ± 0.5	3.5 ± 0.5	3.4 ± 0.8
3.0 T	2.4 ± 1.5	2.5 ± 1.5	2.7 ± 1.6	2.5 ± 1.5	2.7 ± 1.6	2.8 ± 1.5	2.4 ± 1.5

Table 1. Average scores across patients and radiologists, ± one standard deviation across patients in each category.

(Filename: TCT_147_ASNR_supportingFigure.jpg)

252

A Case of Central Pontine Myelinolysis Following Guillain-Barre' Syndrome

A Kamali[1], L Nunez-Rubiano[2], Y Cai[3], A Kamali[1]

[1]University of Texas Health Science Center Houston, Houston, TX, [2]The University of Texas Health Science Center at Houston, Houston, TX, [3]University of Texas Health Science Center at Houston, Houston, TX

Purpose

We present an interesting case of central pontine myelinolysis following Guillain-Barre' syndrome (GBS) in a patient with systemic lupus erythematosus (SLE).

Materials and Methods

A 22-year-old man with PMH of SLE on immunosuppression and previously treated for Acute inflammatory demyelinating polyneuropathy (AIDP) by IVIG, presented to our institution with fever, recurrent lower back pain, hypotension, and progressive lower extremity weakness. The patient then underwent additional rounds of IVIG and steroid therapy for GBS treatment and was discharged to an inpatient rehabilitation facility. The CSF analysis showed increased protein, glucose with normal cell count. Further test showed positive ANA titer with positive GQ1b IgG antibody titer.

Results

Sagittal and axial post-contrast T1-weigthed images showied enhancement of the ventral cauda equina nerve roots. The Axial and coronal T2-Weighted and T2/FLAIR images demonstrated hyperintense signal changes localized to the pons. The post-contrast T1-weighted images showed no enhancement and no diffusion restriction on DWI in the pons. Follow up Spine and Brain MRIs revealed marked improvement in ventral cauda equina nerve root enhancement and near complete resolution of the T2 hyperintense signal in the pons.

Conclusions

Differential Diagnosis: - Acute disseminated encephalomyelitis (ADEM) following GBS - Bickerstaff brainstem encephalitis (BBE) following GBS - Viral myelopathy - Chronic inflammatory demyelinating polyneuropathy (CIDP) - Osmotic demyelination syndrome (Central pontine demyelination) GBS is described as a group of immune-mediated polyradiculopathy. This condition usually reported 1-3 weeks following the upper and/or lower respiratory infections. The SLE is the other predisposing factor for GBS. GBS subtypes ranged from acute inflammatory demyelinating polyradiculoneuropathy (AIDP) (most common) to acute sensory and/or motor axonal neuropathy [1,2]. BBE is a rare, self-limiting, and good prognosis immune-mediated condition and often included in the spectrum of GBS. This condition's mechanism is related to anti-GQ1b IgG. Anti-GQ1b IgG has also been detected as an autoantibody for GBS [3,4]. Teaching points: - Association of the GBS with SLE and Bickerstaff brainstem encephalitis (BBE) - Association of the central pontine myelinolysis with acute inflammatory demyelinating polyneuropathy (AIDP) - Central pontine demyelination eventually resolved few weeks later in the follow up MRI exam along with clinical improvement of the patient.

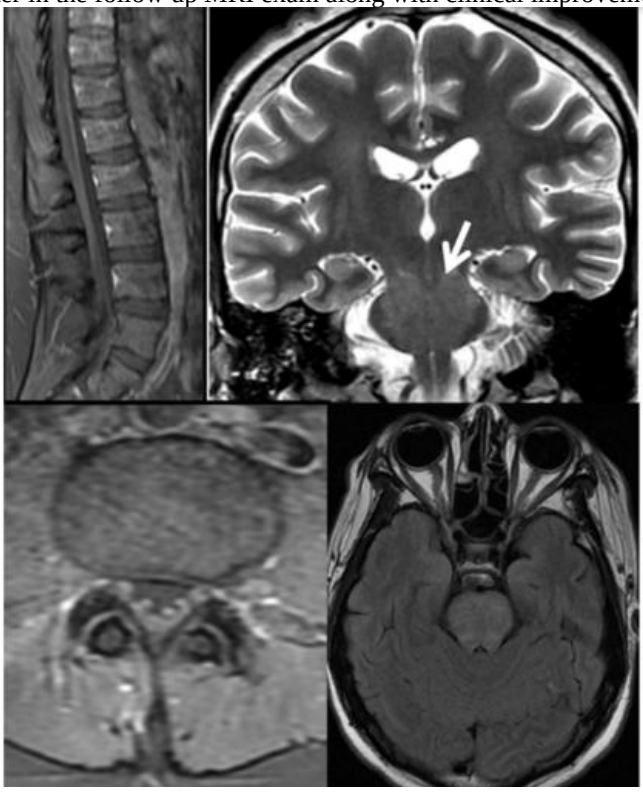

Sagittal and axial T1 post contrast views of the spine demonstrate the enhancing ventral nerve roots typical for GBS. The coronal T2 sequence Shows central pontine demyelination (white arrow) which eventually resolved few weeks later in the follow up exam (axial FLAIR)

(Filename: TCT_252_Figure1.jpg)

906

A Case of Neuromyelitis Optica Spectrum Disorder (NMOSD) Presenting as Isolated Baló's Concentric Sclerosis.

J Lee[1]

[1]*Montefiore Medical Center, Bronx, NY*

Purpose

A previously healthy 50-year-old man presented with transient palpitations, confusion, headache, right sided weakness and right homonymous hemianopia. Imaging show white matter lesions within the bilateral parieto-occipital lobes with involvement of the corpus callosum splenium, with alternating T2 hypo- and hyperintensities. MRI of the spine and the orbits were unremarkable. Biopsy of the left parietal lobe demonstrated a primary demyelinating process and negative for neoplastic cells. Laboratory workup revealed AQP4-IgG positive in serum and CSF. Negative workup for infectious etiologies. Patient was diagnosed with NMOSD and treated with IV steroids. Follow-up assessment 5 months later showed improved visual field defect and improved FLAIR hyperintensity and trace enhancement. Treatment of eculizumab was initiated to reduce the risk of recurrence.

Materials and Methods

Fig. 1: A. Axial FLAIR, signal abnormality involving the corpus callosum splenium with extension to the bilateral periventricular and juxtacortical white matter in the parietal-occipital lobes, greater on the left. B. Coronal T2 demonstrates alternating T2 hyperintense and hypointense signal abnormalities in the parietal-occipital periventricular white matter, left greater than right. C. Axial DWI, trace foci of restricted diffusion are present at the peripheral margins of the white matter signal abnormality. D. Axial T1 post contrast. Faint trace curvilinear enhancement is present at the peripheral and periventricular margins of white matter abnormality. No increased perfusion (not shown). MR spectroscopy demonstrates elevated choline peak with decreased NAA peak, and a peak at 2.3 ppm likely representing glutamate/glutamine (not shown). The latter has been reported in tumefactive demyelinating lesions (1).

Results

Balo's concentric sclerosis (BCS) has traditionally been regarded as a rare variant of multiple sclerosis (MS). However, both BCS and tumefactive demyelinating lesion can evolve into MS or NMOSD, and BCS can be seen in both MS and NMOSD (2,3). This case demonstrates that BCS can be associated with NMOSD, and may even present as an isolated finding without optic pathway or spinal involvement. Hence, differential diagnosis of an isolated mass-like demyelinating lesion should include NMOSD.

Conclusions

Balo's concentric sclerosis can present as an isolated finding in NMOSD. Differential diagnosis of a mass-like demyelinating lesion should include NMOSD.

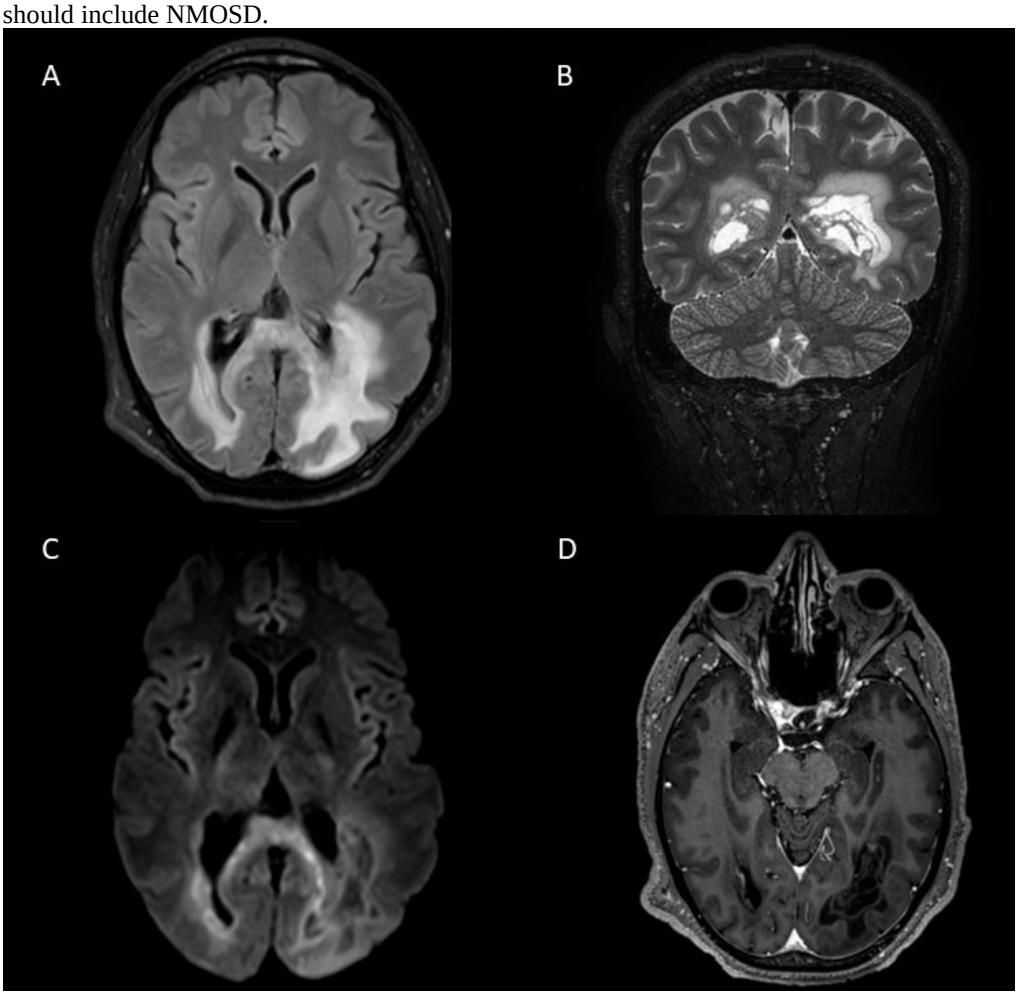

(Filename: TCT_906_Figure1.jpg)

499
A case of primary CNS HLH
A Reis[1], J Bello[2], K Shifteh[3]
[1]Montefiore, The Bronx, NY, [2]Montefiore Radiology, New York, NY, [3]Montefiore Hospital, Brooklyn, NY

Purpose
15 year old male with no past medical history presented with complaints of ataxia which had progressed over several months. The patient was found to have multiple hemorrhagic brain lesions of unknown etiology and required a prolonged course in the PICU. Blood cultures, CSF cultures, coagulation workup, NMDA receptors and autoimmune encephalitis panel returned negative. The patient was started on etoposide and decadron for primary CNS HLH confirmed by genetic testing with improvement in his symptoms.
Materials and Methods
Widespread T2/ FLAIR signal abnormality with subcortical enhancement. Multifocal enhancing hemorrhagic lesions in cerebellar white matter, brainstem, and cerebellum.
Results
HLH is a rare disorder that is characterized by infiltration of multiple organs by lymphocytes and histiocytes which may involve the CNS. Though reports have described imaging findings of CNS HLH including diffuse white matter infiltration, parenchymal atrophy, hemorrhage and calcifications, the findings are non-specific and not currently well characterized. (1- 4)
Conclusions
We aim to review the case and imaging findings of a rare disease with CNS involvement.

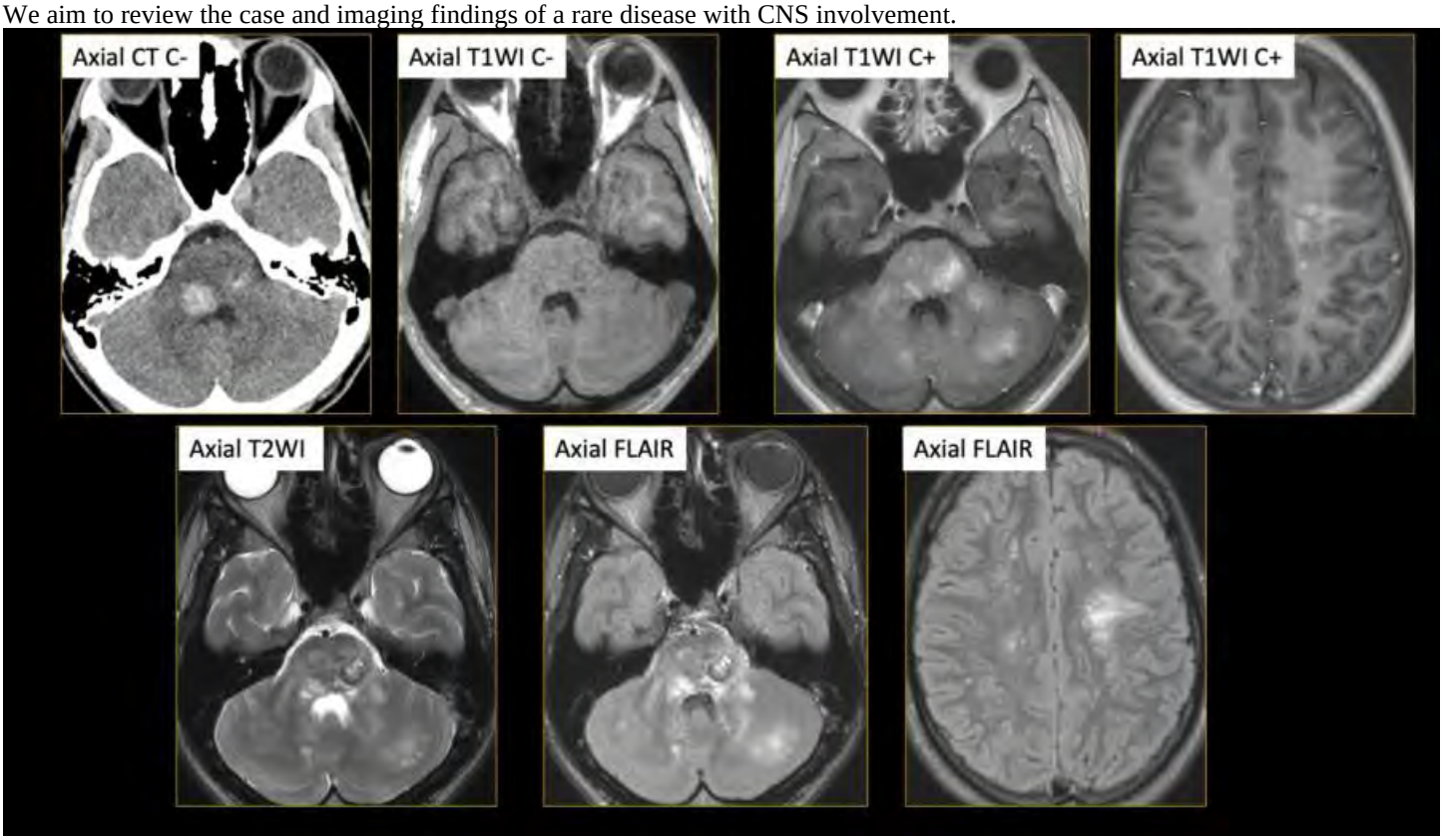

(Filename: TCT_499_HLHASNRcase.jpg)

1133
A Pediatric Patient with CNS Predominant Familial Hemophagocytic Lymphohistiocytosis, Type 2.
J Burns-Benggon[1], J Webster[1], P Kim[1]
[1]Loma Linda University Medical Center, Loma Linda, CA

Purpose
A 16 year old male with history of intellectual disability presents with three weeks of bilateral dysmetria, headache and slurred speech. The patient was admitted and an extensive multidisciplinary work-up was initiated. Initial MR Brain findings yielded a differential diagnosis including CLIPPERS, intravascular lymphoma, demyelination disease, vasculitis or disseminated infection. Lumbar puncture demonstrated mild lymphocytosis. An extensive work up for autoimmune, infectious and neoplastic etiologies was negative. Brain biopsy was performed with pathology demonstrating a perivascular pattern of lymphohistiocytic inflammation which was characterized as severe perivascular lymphohistiocytic encephalitis. The patients clinical condition and mentation deteriorated despite steroid therapy, however noticeably improved after initiation of plasmapheresis and IVIG; the patient was subsequently discharged

with follow-up. Trio WES genomic testing revealed a pathogenic homozygous variant in PRF1, associated with Familial Hemophagocytic Lymphohistiocytosis, Type 2.

Materials and Methods

Figures 1 demonstrates wide spread predominantly perivascular and leptomeningeal enhancing foci in the bilateral cerebral hemispheric white matter, deep gray nuclei, brainstem, cerebellum, and upper cervical cord (not shown). Corresponding T2 lengthening was noted. Multiple diffusion restricting lesions at the left frontal, parietal and occipital lobes and centrum semiovale were additionally seen (not shown).

Results

CNS predominant HLH is an uncommon entity and the HLF type II subtype is caused by an inherited, autosomal recessive defect in the PRF1 gene. The typical imaging findings of CNS HLH/FHL correlate with histopathologic findings and include diffuse leptomeningeal and perivascular enhancement and corresponding T2 lengthening with or without diffusion restricting lesions (1), all of which were seen in with this patient. CLIPPERS can share similar features such as perivascular enhancement and was a differential consideration in this patient. A recent study described patients with CLIPPERS and CLIPPERS-like syndromes having been found to have HLH gene mutations (2) which may suggest a a potential explanation for the overlapping and potentially misleading imaging presentation.

Conclusions

An understanding of the typical CNS imaging findings of HLH/FHL is essential for the radiologist to help facilitate prompt diagnosis and treatment in patients with this uncommon but life threatening entity.

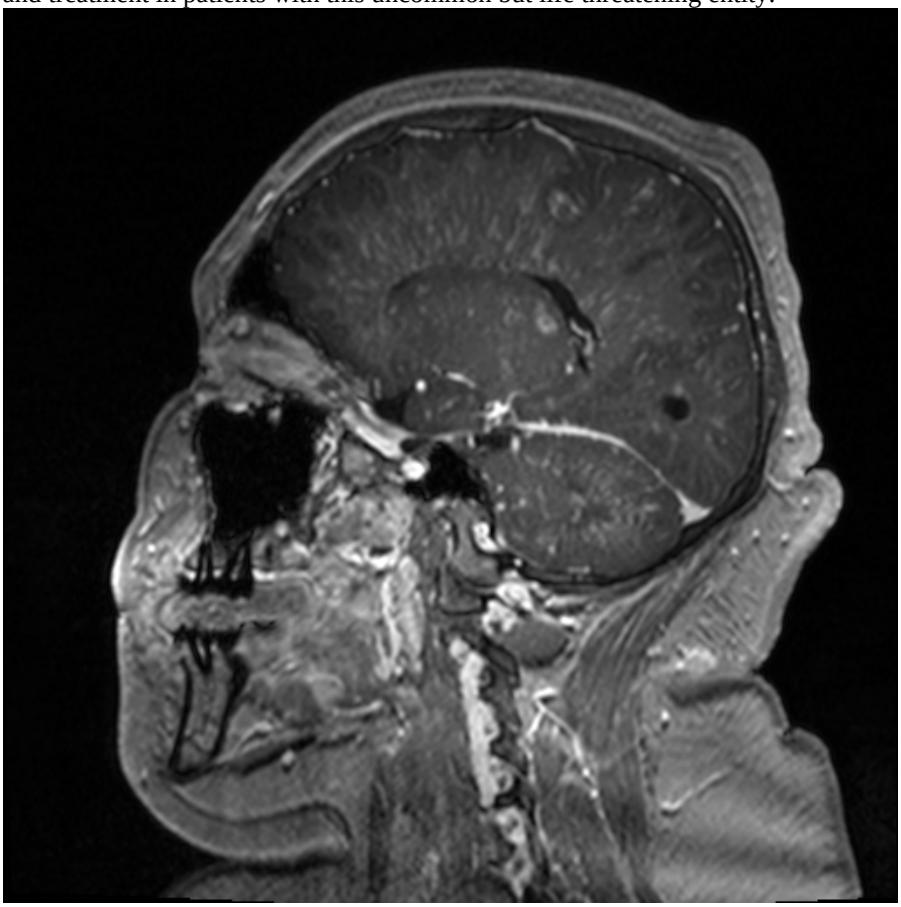

(Filename: TCT_1133_Figure2.jpg)

611

A Primary Cerebellopontine Angle Neuroendocrine Tumor.

A Reis[1], S Mizrachi[2], J Burns[3], J Bello[4], K Shifteh[5]

[1]Montefiore, The Bronx, NY, [2]Montefiore Medical Center, Bronx, NY, [3]Montefiore Medical Center, Bergenfield, NJ, [4]Montefiore Radiologu, Brooklyn, NY, [5]Montefiore Hospital, New York, NY

Purpose

32 year old female who presented with right sided facial weakness, progressive right sided hearing loss and vertigo. The patient was found to have a mass in the right cerebellopontine cistern and internal auditory canal. The patient underwent right suboccipital craniotomy. Pathology returned an unusual diagnosis of well differentiated neuroendocrine tumor. Additional imaging did not reveal any evidence of metastatic disease.

Materials and Methods
Large homogeneously enhancing soft tissue mass in the right cerebellopontine cistern and internal auditory canal isointense to gray matter on T2 and slightly hyperintense on T1.
Results
Neuroendocrine tumors infrequently metastasize to the brain with an incidence of up to 5%.(1-2) Our patient has no evidence of a primary tumor arising from another location, and it is likely that the brain is the primary source of this tumor. There are very limited reports of this phenomenon in the literature, with only case reports of possible CNS primary neuroendocrine tumors. (2) To our knowledge, this is the first described case of a neuroendocrine tumor involving the CP angle.
Conclusions
We aim to review the case, differential diagnosis and imaging findings of neuroendocrine tumor involving the CP angle.

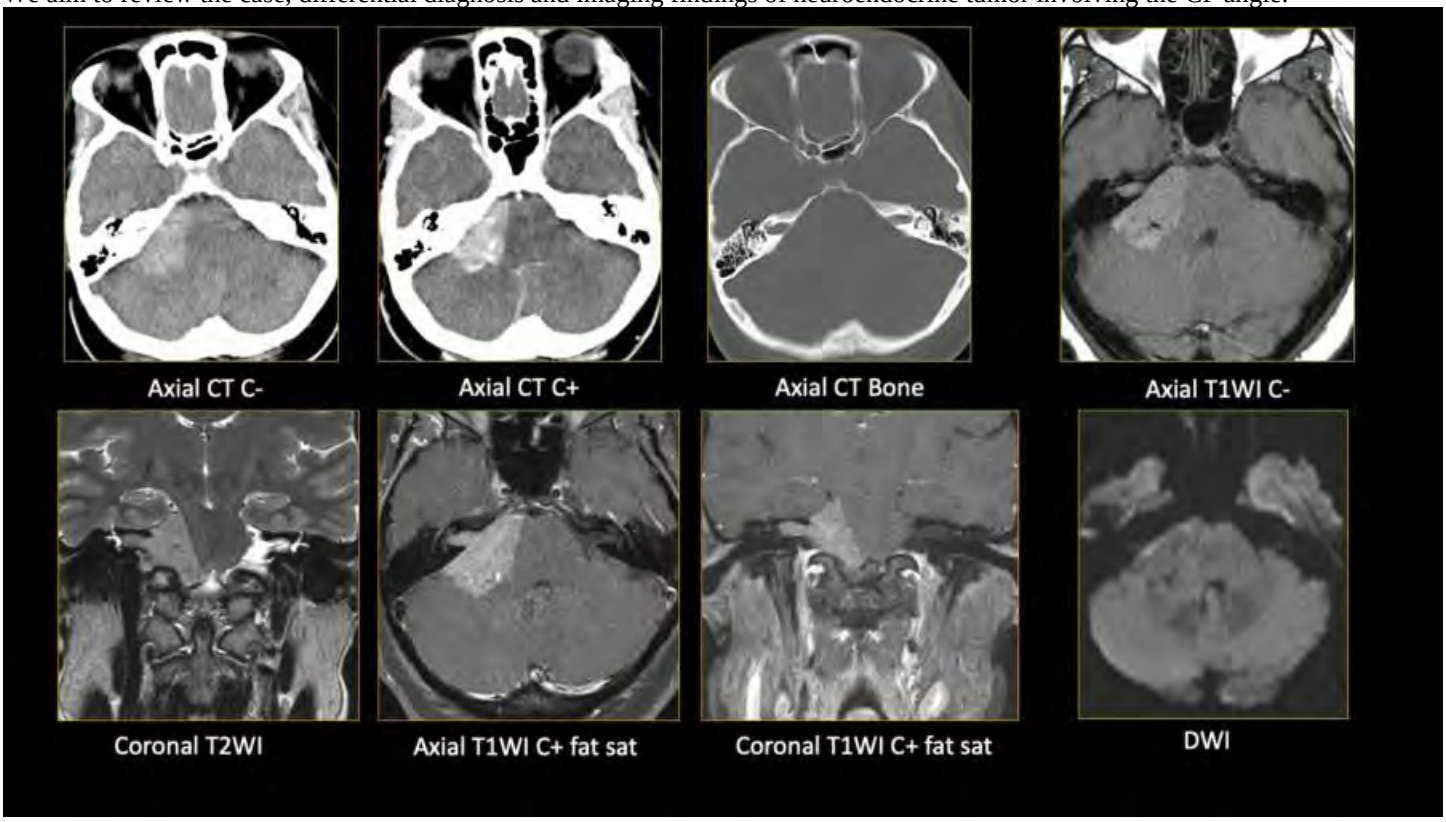

(Filename: TCT_611_CPANeuroendocrinemass.jpg)

844

A Rare Case of Autoimmune Glial Fibrillary Acidic Protein Astrocytopathy

A Dearden[1], J Doty[1], A Krishnan[1], J Fellows[1]
[1]*William Beaumont Hospital, Royal Oak, MI*

Purpose
This is a 69-year-old male who presented with cognitive decline, hypophonia, dyspraxia, course tremor, myoclonic jerks, and gait dysfunction, all developing over 3-4 weeks. Initial head CT and MRI brain without contrast were negative. EEG demonstrated diffuse slowing. CSF analysis revealed elevated protein and elevated white blood cells (lymphocyte predominant). Given neurological worsening, MRI brain and cervical spine with contrast were performed and unique findings were identified, detailed below. The CSF autoimmune panel returned positive for Glial Fibrillary Acidic Protein (GFAP). The patient was started on steroids with rapid clinical improvement.
Materials and Methods
MRI brain with contrast 2 weeks after initial imaging demonstrated extensive, predominantly periventricular curvilinear enhancement in a perivascular distribution. MRI cervical spine demonstrated symmetric posterolateral pathological enhancement within the cord. Given these findings and the CSF results, a diagnosis of autoimmune GFAP astrocytopathy was established, and the patient was started on steroid therapy. Repeat MRI brain with contrast 2 weeks later demonstrated marked interval decrease in the perivascular enhancement, with mild residual periventricular enhancement. Follow-up MRI brain with contrast 5 weeks after beginning steroid therapy demonstrated complete resolution of abnormal perivascular enhancement.
Results
First described in 2016, autoimmune GFAP astryocytopathy is a rare autoimmune inflammatory central nervous system (CNS) disorder. Typical symptoms include subacute progressive encephalopathy, involuntary movements, autonomic dysfunction, and fever. Key imaging findings include curvilinear periventricular enhancement in a perivascular distribution, which can also be seen in the

infratentorium and spinal cord. Cases generally feature elevated CSF protein and CSF pleocytosis. The vast majority of cases have been in parainfectious and paraneoplastic settings. Treatment regimens are not yet well-established, but patients who are treated with early immunotherapy generally show marked resolution of symptoms over a period of weeks.
Conclusions
Autoimmune GFAP astrocytopathy is a rare, novel immunotherapy-responsive inflammatory CNS disorder with key imaging findings including curvilinear periventricular enhancement in a perivascular distribution, with similar abnormal perivascular enhancement in the infratentorium, and spinal cord involvement. The findings share similarity to CLIPPERS syndrome, though more extensive.

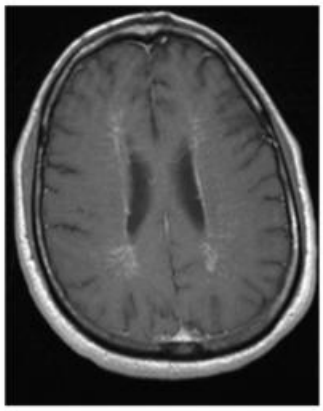

Figure 1. T1-weighted MRI brain with contrast demonstrates curvilinear periventricular enhancement in a perivascular distribution.

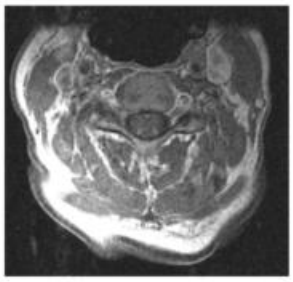

Figure 2. T1-weighted MRI cervical spine with contrast demonstrates symmetric posterolateral pathological enhancmenet within the cord.

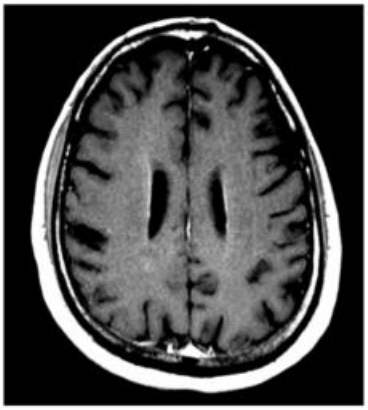

Figure 3. Two week follow up T1-weighted MRI brain with contrast demonstrates marked decrease in periventricular curvilinear enhancement with mild residual enhancement.

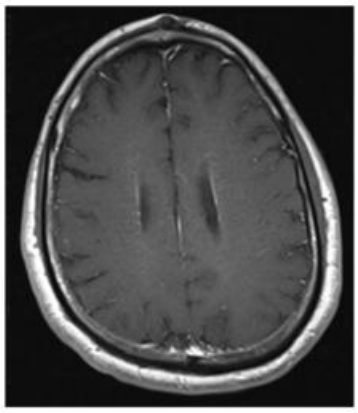

Figure 4. Five week follow up T1-weighted MRI brain with contrast demonstrates near-complete resolution of periventricular curvilinear enhancement.

(Filename: TCT_844_ImagesGFAP.jpg)

1509

A Rare Case of Diffuse Midline Glioma of the Cervicothoracic Spine

J Jones[1], K Salzman[2]
[1]University of Utah, Sandy, UT, [2]University of Utah, Salt Lake City, UT

Purpose
19-year-old previously healthy male initially presented with bilateral foot numbness and weakness that rapidly progressed up the lower extremities into the chest. Patient also complained of perfuse night sweats but no weight loss. The spinal cord lesion was thought to be inflammatory given his young age and positive ACE levels in the serum and CSF. At presentation, steroids were initiated. However, the lesion progressed on steroids and biopsy eventually confirmed a diffuse midline glioma, H3 K27-altered.
Materials and Methods
Spinal MR demonstrate a long segment expansile intramedullary cord lesion in the central aspect of cervicothoracic spinal cord that is T2/STIR hyperintense with heterogenous enhancement.
Results
Diffuse midline glioma, histone H3 K27M mutant was added to the World Health Organization Classification of Tumors in 2016 as a specific mutation of the previously classified diffuse astrocytoma. The K27M mutation appears specific for diffuse gliomas arising in midline structures. Specific gene mutation was the most important predictive factor of overall survival. No specific imaging features have been described in the literature for spinal cord lesions, but contrast enhancement and expansile increased T2/STIR signal was commonly seen. The presence of enhancement on MRI was not a predictive factor of patient outcome.
Conclusions
Diffuse midline gliomas can be found throughout midline structures of the central nervous system including the thalamus, brainstem, and spinal cord. Tumors in the thalamus and posterior fossa tend to be solid or infiltrative with infrequent necrosis. There are limited studies on spinal cord diffuse midline gliomas, however case studies report distant and early metastasis to the leptomeninges. Early detection could help facilitate timely treatment and possibly prevent metastatic disease in certain patients.

MRI of the cervicothoracic spine: Sagittal T2 weighted MRI of the cervical spine (A), T1 weighted post-contrast of the cervical spine(B), STIR of the thoracic spine (C), and T1 weighted post contrast of the thoracic spine (D) show an expansile long segment intramedullary lesion that is T2/STIR hyperintense and heterogeneously enhancing.

(Filename: TCT_1509_JJMidlineGlioma.jpg)

1535

A Rare Case of Laryngeal Amyloidosis

M Leung[1], K Nael[1], N Pham[1]
[1]UCLA, Los Angeles, CA

Purpose

A 67 year-old male without a significant medical history presented with progressive hoarseness over the last five years. He underwent laryngoscopy, revealing vocal cord nodules which were biopsied and revealed amyloidosis. An extensive workup included a normal echocardiogram, bone marrow biopsy, and PET/CT. Thus, we herein present a rare case of localized amyloid light-chain (AL) amyloidosis.

Materials and Methods

CT neck without contrast demonstrated asymmetric soft tissue thickening of the left true and false vocal fold.

Results

Amyloidosis is a disease characterized by excessive protein deposition in tissues and organs, which results in end-organ dysfunction. All forms of amyloidosis are identified by Congo red stain and a green birefringence pattern under polarized light. Fibril deposits isolated to a single organ system is defined as localized amyloidosis. Laryngeal amyloidosis is rare, with the vocal cords most commonly affected.

Conclusions

Most cases of localized laryngeal amyloidosis involves light chains. It is thought that amyloid deposits can occur from local overproduction by plasma cells or alternatively, circulating light chains can deposit in an area of inflammation.

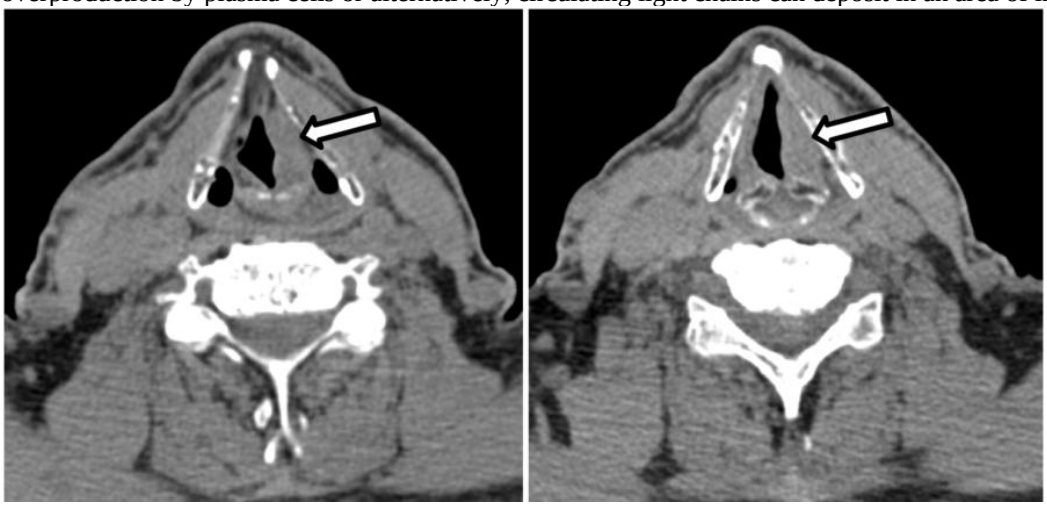

(Filename: TCT_1535_figure.jpg)

1137

A Rare Case of Metastatic Glioblastoma to Spine

A Kamali[1]

[1]University of Texas Health Science Center Houston, Houston, TX

Purpose

A 59-year-old man with a history of glioblastoma status post second resection and chemoradiation presents with progressive low back pain.

Materials and Methods

Baseline imaging of the brain demonstrated a rim-enhancing, centrally necrotic infiltrating mass in the right temporal lobe with extensive surrounding vasogenic edema on post-contrast axial T1-weighted image. Sagittal CT of the abdomen and pelvis demonstrated a pathologic fracture of L2 with a mixed sclerotic and lucent lesion and mild bulging of the posterior cortex. T2-weighted image showed heterogeneous hyperintensity and post-contrast axial T1-weighted image showed heterogeneous enhancement involving the L2 vertebral body. Histopathologic examination was consistent with Glioblastoma.

Results

While glioblastoma has a high tendency for local invasion, the incidence of its extra neural dissemination is less than 2%, with osseous involvement even being less common. Additionally, the most frequent location of osseous metastasis would be the vertebrae. Furthermore, literature has shown that the supratentorial glioblastoma tend to be less disseminative through cerebrospinal fluid compared to the infratentorial glioblastoma. To the best of our knowledge, isolated glioblastoma vertebral metastasis is rare and only a few cases have been described in the literature.

Conclusions

Although extra cranial spread of glioblastoma may not drastically shorten glioblastoma patient's survival time, physicians should be aware of its existence. Metastatic glioblastoma may present and progress quite rapidly. Early diagnosis of metastatic disease spread can help expedite alleviation of patient's discomfort.

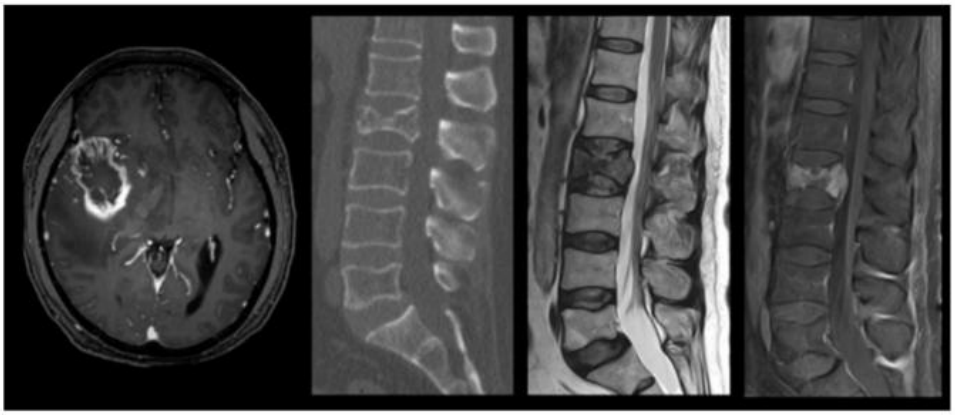

Figure 1. Baseline imaging of the brain demonstrated a rim-enhancing, centrally necrotic infiltrating mass in the right temporal lobe with extensive surrounding vasogenic edema on post-contrast axial T1-weighted image. Sagittal CT of the abdomen and pelvis demonstrated a pathologic fracture of L2 with a mixed lytic and sclerotic lesion and mild bulging of the posterior cortex. T2-weighted image showed heterogeneous hyperintensity and post-contrast axial T1-weighted image showed heterogeneous enhancement and pathologic compression fracture of the L2 vertebral body.

(Filename: TCT_1137_Figure1.jpg)

933

A Rare Case of Orbital Lymphoma

S Hegde[1]

[1]KVG Medical College and Hospital, Chicago, IL

Purpose

A 78-year-old female with history of Non-Hodgkin's lymphoma (NHL) presented with left-sided diplopia and gradually progressive vision loss. Patient refused treatment or further investigations. She returned 11 months later with total loss of vision and palpable painless mass. Lesion was biopsied post-imaging and found to be secondary NHL and she is currently undergoing chemotherapy.

Materials and Methods

On initial axial computed-tomography (CT) scan (Fig. A), an ill-defined, hyperdense homogenous mass mainly involving the medial extra-conal space of the left orbit and invading the medial rectus muscle, molding to the globe without bony involvement, is seen. CT

scan repeated on the second visit (Fig. B) showed an increase in size of the tumor with resultant proptosis and complete involvement of the left optic nerve. No optic canal, orbital fissures or intracranial involvement.
Results
Secondary NHLs are usually bilateral and orbital lymphomas are mostly unilateral. They originate in a single quadrant initially and extend to encase the eye (all 4 quadrants). Extra-conal and superior-lateral quadrant involvement is most common. The differential diagnosis for masses involving the intra- and extra-conal compartment include inflammatory/metabolic/infectious disease (orbital inflammatory pseudotumour, thyroid orbitopathy, sarcoidosis) and neoplasm (lacrimal tumours, cavernous hemangioma, benign and malignant lymphoproliferative lesions, orbital rhabdomyosarcoma, and metastasis) and Sjögren's. On a T1-weighted MRI scan, the orbital mass appears isointense or hypointense compared to the extraocular muscles, and it appears isointense to hyperintense on a T2-weighted scan.
Conclusions
Hyper-dense mass on CT and predisposition to mold to adjacent orbital structures points towards orbital lymphoma as an etiology for these symptoms.

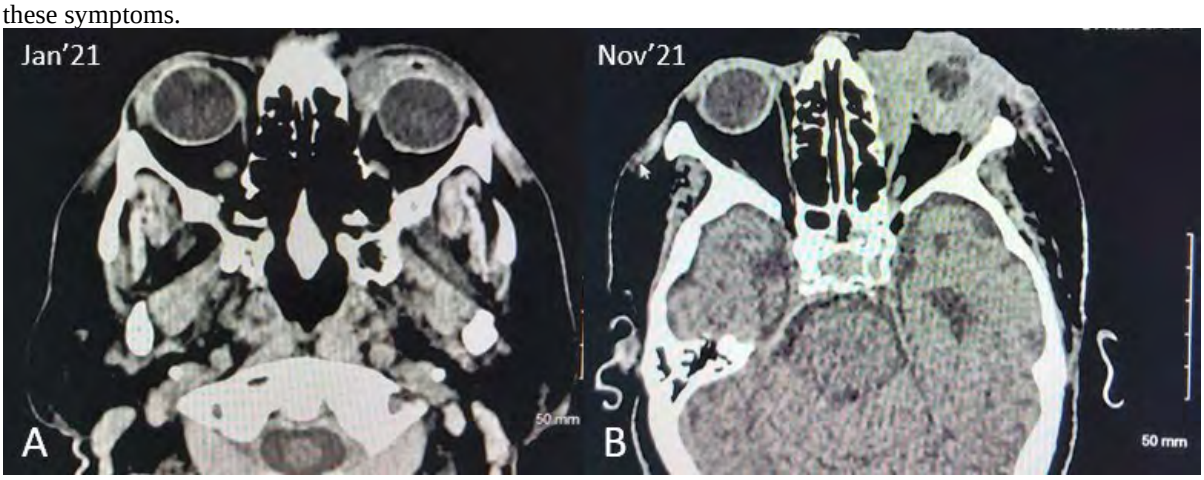

(Filename: TCT_933_Fig1.jpg)

297
A Rare Case of Paraneoplastic Cerebellar Degeneration
S Saith[1], O Raslan[1], R Assadsangabi[1], M Bobinski[1], L Hacein-Bey[1], A Ozturk[1]
[1]UC Davis Medical Center, Sacramento, CA

Purpose
A 63-year-old female with hypothyroidism presented with two months of progressive cerebellar dysfunction, including ataxia, nystagmus, dysarthria, and dysmetria.
Materials and Methods
Initial MRI of the brain showed abnormal FLAIR signal of the cerebellum and inferior vermis, with diffuse leptomeningeal enhancement with concern of acute cerebellitis (Figure 1).
Results
Initial CSF and serologic studies suggested autoimmune etiology and follow-up Mayo autoimmune encephalitis panel documented an unclassified autoantibody associated with paraneoplastic cerebellar degeneration (PCD). Subsequent malignancy work-up revealed multiple TR-4 thyroid nodules consistent with pathologically proven papillary thyroid carcinoma.
Conclusions
PCD is a rare cause of cerebellar dysfunction/abnormality. In the acute phase of PCD, differential considerations should include infectious or inflammatory cerebellitis. Diagnosis of PCD often requires exclusion of these more common pathologies, and a timely diagnosis is critical to clinical management.

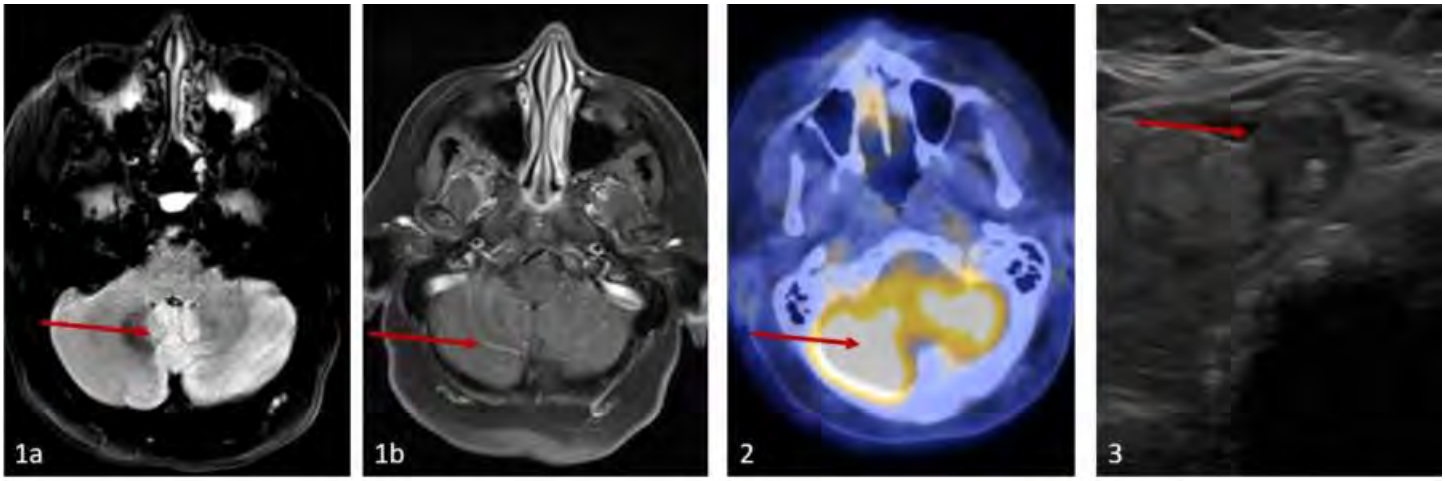

Figure 1. Axial FLAIR image of brain demonstrates signal abnormality involving the cerebellum and vermis (1a) with diffuse leptomeningeal enhancement on post Gad axial T1-W image(1b).

Figure 2. PET scan illustrates increased uptake in the posterior fossa concerning for cerebellitis.

Figure 3. Thyroid ultrasound revealed multiple TR-4 nodules ultimately found to represent papillary thyroid carcinoma.

(Filename: TCT_297_PCDimages.jpg)

873

A Rare Case of Segmental Spinal Dysgenesis with Repaired Open Spinal Dysraphism

D Lizarazo[1], Ó Torres[1], S Bermúdez[1], A Guarnizo[1]
[1]*Fundación Santa Fe de Bogotá, Bogotá, Colombia*

Purpose

A two-year-old male patient with history of imperforate anus repair and patent ductus arteriosus closure, came for imaging follow-up for correction of thoracolumbar myelomeningocele. On physical exam the patient was paraplegic.

Materials and Methods

In a whole spine tomography study, seven cervical vertebral bodies, twelve thoracic vertebrae, several lumbar spinal segments absent and two malformed vertebrae at the thoracolumbar junction with hyperkyphosis at this level were identified. Segmentation anomalies were also observed due to fusion defects in C2, spina bifida occulta in T11 and butterfly vertebra in T12. Posterior elements were absent in the malformed vertebrae. Sacral or coccyx agenesis was not observed. At the level of the thoracolumbar junction, severe spinal canal stenosis was observed with evidence of focal dilation of the ependymal canal at the level of T9-T10 seen on complementary magnetic resonance. Additionally, a decrease in the caliber of the cord was identified and the roots of the cauda equina were not observed. The spinal cord ended at myelomeningocele repaired site.

Results

Segmental spinal dysgenesis is a rare, congenital, closed spinal dysraphism that meets the criteria according to Chellathurai et al. There are two types of segmental spinal dysgenesis. The difference lies in the degree of kyphoscoliosis and the severity of spinal canal stenosis. In type 2 there is severe kyphoscoliosis and severe spinal canal stenosis (obliteration of the subarachnoid space >50%). Its etiology is explained by an abnormal somitogenesis generating vertebral segmentation anomalies that cause cord dysplasia due to mechanical compression. Mutations in the Notch signaling pathway are considered to be one etiological fact. It is important to determine the type of dysgenesis since type 2 unlike type 1 requires surgical management to prevent progression of neurological deterioration.

Conclusions

- Segmental spinal dysgenesis is a rare, congenital, closed spinal dysraphism which requires for its diagnosis tomography and magnetic resonance studies to characterize the abnormalities of vertebral segmentation and to identify absent or malformed segment of the spinal cord and underlying nerve roots. - There are two types of segmental spinal dysgenesis. The difference lies in the degree of kyphoscoliosis and the severity of spinal canal stenosis. - Type 2 segmental spinal dysgenesis requires surgical management to prevent progression of neurological deterioration.

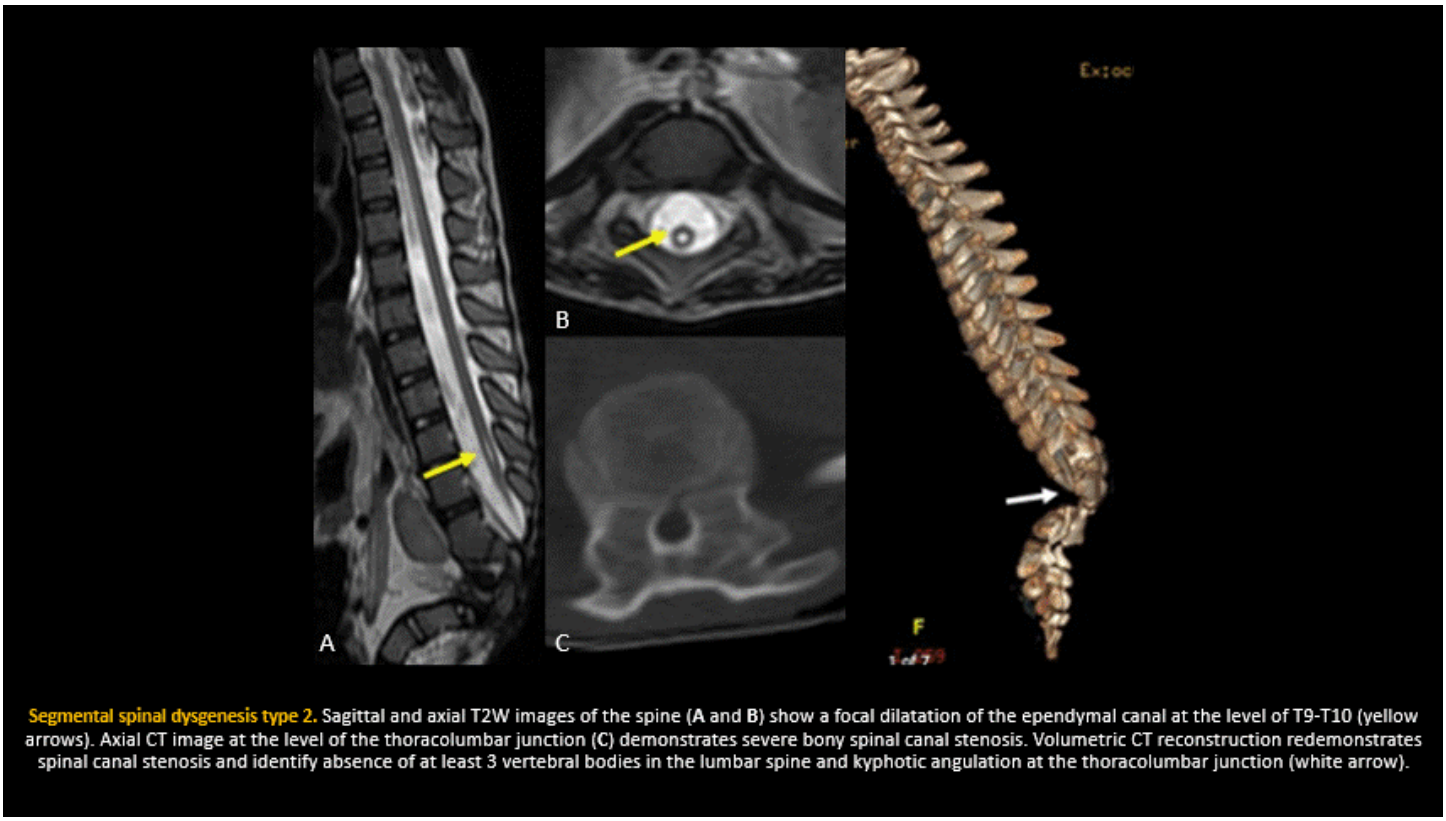

Segmental spinal dysgenesis type 2. Sagittal and axial T2W images of the spine (**A** and **B**) show a focal dilatation of the ependymal canal at the level of T9-T10 (yellow arrows). Axial CT image at the level of the thoracolumbar junction (**C**) demonstrates severe bony spinal canal stenosis. Volumetric CT reconstruction redemonstrates spinal canal stenosis and identify absence of at least 3 vertebral bodies in the lumbar spine and kyphotic angulation at the thoracolumbar junction (white arrow).

(Filename: TCT_873_Segmentalspinaldysgenesistype2.gif)

1049

A Rare Cause of Acute Blindness.

J Mutambuze[1], K Riley[1]
[1]*Indiana University School of Medicine, Indianapolis, IN*

Purpose

A 31-year-old male presented with acute onset blindness and confusion. This was preceded by a week of headaches and nasal congestion. The patient's clinical workup included CSF studies concerning for a bacterial meningitis. Subsequent MRI and maxillofacial CT demonstrated extensive pansinusitis with intracranial extension of infection resulting in pituitary abscess as well as a suprasellar abscess centered within the optic chiasm. The patient later underwent functional endoscopic sinus surgery and transsphenoidal drainage of the suprasellar abscess.

Materials and Methods

Axial noncontrast sinus CT (A) shows complete opacification of the sphenoid sinuses with areas of osseous thinning and possible dehiscence of the sphenoid septum (white arrow). Coronal T2 (B) and Coronal T1 post-contrast (C) MRI show peripherally enhancing fluid collections centered within the optic chiasm (red arrows) consistent with abscesses. Coronal diffusion-weighted imaging (D) shows expected central reduced diffusivity within the abscesses.

Results

Intracranial complications of bacterial sinusitis are uncommon but do occur in more fulminant cases. When present, these advanced sequelae usually include meningitis or cerebritis. Abscess within the substance of the optic chiasm and nerves is extremely rare, having only been reported in a few cases. Knowledge of this rare potential complication may allow the radiologist to make a difficult diagnosis in patients with advanced sinus disease presenting with acute blindness. CT and MRI imaging play complementary roles in making this diagnosis.

Conclusions

Optic chiasm abscess is a rare potential complication of bacterial sinusitis and should be considered in these patients presenting with acute vision loss.

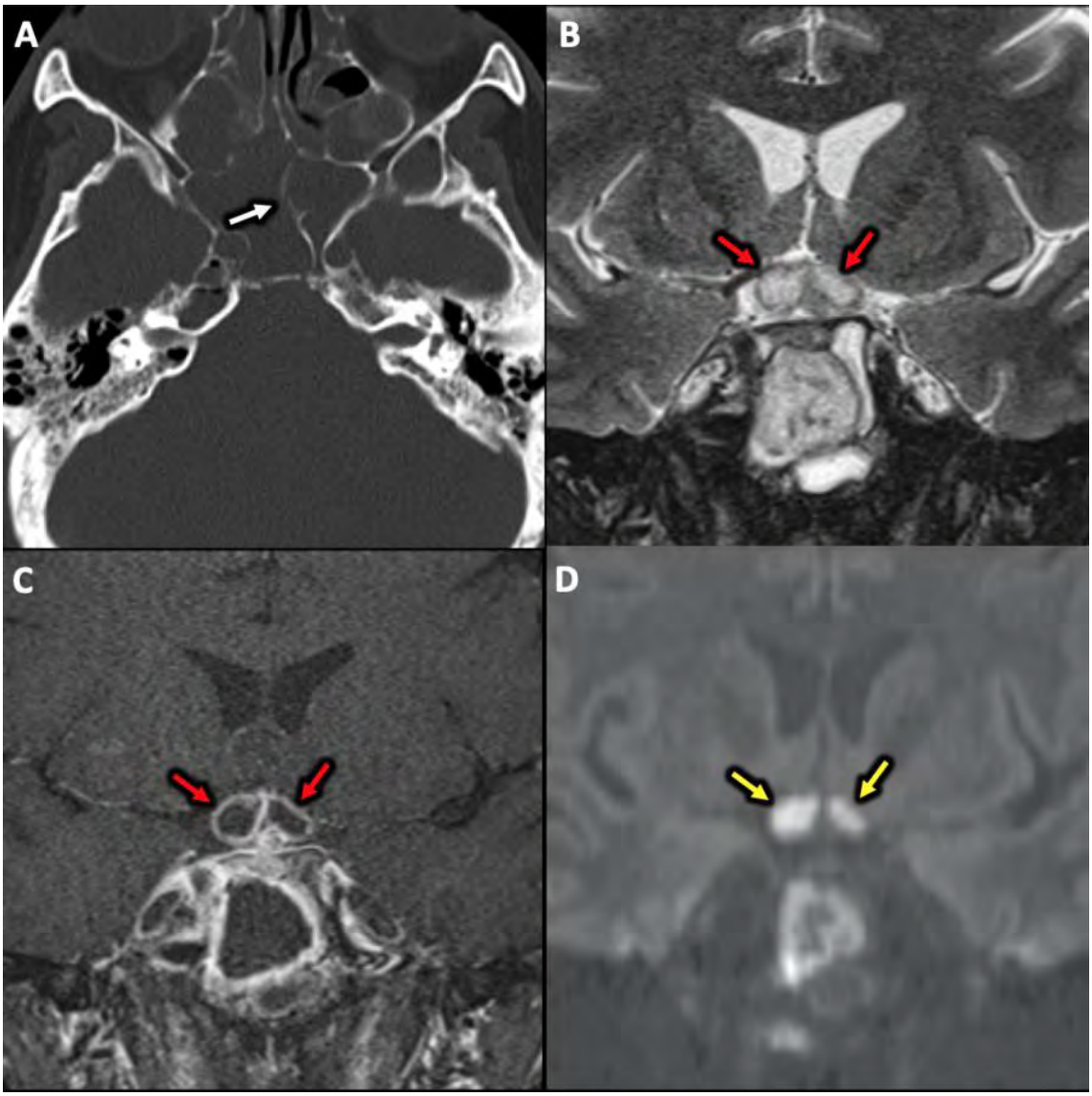

(Filename: TCT_1049_ASNRImagejpg.jpg)

1360

Acute necrotizing encephalopathy of childhood caused by Human Herpes Virus 6

A Degueure[1], C Soto[2], R Gilbow[3], O Arevalo[3]

[1]LSU Health Shreveport, Richmond, LA, [2]National University of Colombia, Bogota, TX, [3]LSU Health Shreveport, Shreveport, LA

Purpose

7-month-old male with past medical history relevant only for prematurity, presented for fever and vomiting. Patient was also noted to have a bulging fontanelle and abnormal movements. CSF sampling confirmed CNS infection by HHV-6.

Materials and Methods

Initial CT showed hypodensities in the bilateral insular regions and medial thalamus concerning for acute infarcts. MRI showed areas of hemorrhagic necrosis identified at the bilateral thalami and dorsal brainstem, associated with symmetrical necrosis of the subinsular white matter. Extensive areas of gyriform enhancement and restricted diffusion of the cerebral cortex bilaterally noted indicative of generalized cytotoxic edema. These findings are described in association with an acute necrotizing encephalopathy of the childhood.

Results

The acute necrotizing encephalopathy (ANE) of childhood is a rare type of encephalopathy manifesting as bilateral and fairly symmetrical lesions involving the thalami, basal ganglia, internal and external capsules, tegmentum and cerebellar white matter. Although most cases are sporadic, some have been associated to viral infections (1). Human Herpes Virus 6 (HHV-6) is classically known for roseola infantum of childhood. Uncommon cases of CNS infections by HHV-6 are usually seen in either infants or immunocompromised adults. ANE is an uncommon presentation of HHV-6 encephalitis affecting mainly immunocompetent children, characterized by symmetric involvement of bilateral thalami. The clinical presentation is similar to Herpes Simplex Encephalitis (HSE) with symptoms of temporal lobe seizures, fever, and mental status changes. Although some studies on radiological differences between the two suggest that HHV-6 is often limited to the mesial temporal lobes, in contrast to HSE seen in extratemporal areas (2),

larger series describe an extensive involvement of the deep gray matter structures with necrosis and cavitation (3). Furthermore, early distinction between HSE and HHV-6 via CSF PCR analysis is crucial for proper treatment due to HHV-6 resistance to acyclovir.
Conclusions
The acute necrotizing encephalopathy (ANE) of childhood is a rare type of encephalopathy that may be caused by HHV-6

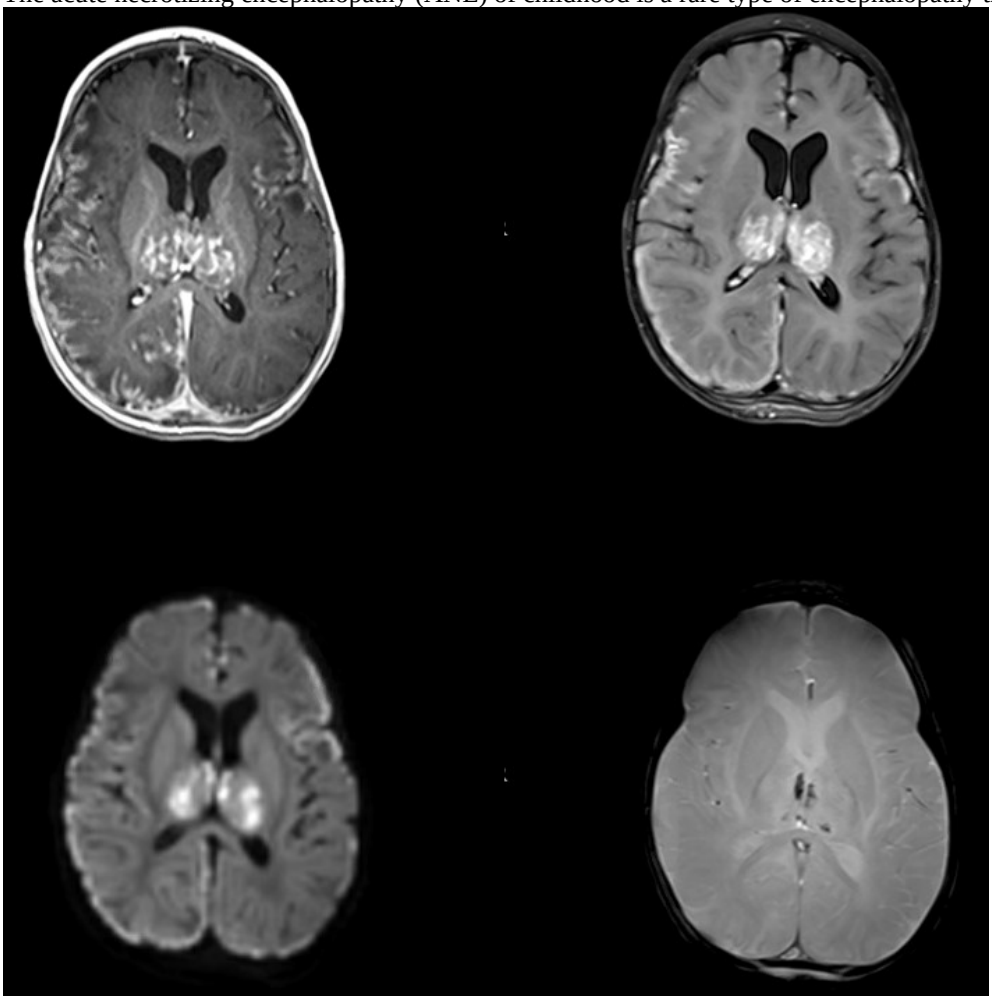

(Filename: TCT_1360_ANEpng.jpg)

1247

Adult onset neuronal intranuclear inclusion disease (NIID) presenting as acute encephalopathy

S Daghighi[1], J Vera[2], M Estrella[2], V Goodwill[2], N Farid[3]
[1]SUNY upstate medical University, Syracuse, NY, [2]UC San Diego, La jolla, CA, [3]UC San Diego, San Diego, CA

Purpose
We present a case of a 59 y/o female with medical history of systemic sclerosis and right MCA infarct in 2018 with subsequent seizures, well controlled with Keppra, who presented with acute altered metal status and aphasia. Stroke work up including CT angiography, and MRI brain was negative. EEG demonstrated diffuse slowing without epileptiform discharges. Five days later, the patient developed new right face and arm weakness. MRI was repeated and although it was negative for infarct, it had findings which were most suggestive of acute encephalitis with differential considerations including infectious, autoimmune, and paraneoplastic etiologies. Although inflammatory markers were positive (ESR of 80 mm/hr), an extensive work-up of both CSF and serum was negative for infectious, autoimmune, and paraneoplastic processes. Biopsy of the left parietal lobe was performed which demonstrated eosinophilic intranuclear inclusions characteristic of NIID.
Materials and Methods
MRI demonstrated diffuse cortical swelling with associated T2/FLAIR hyperintensity throughout the left posterior frontal, parietal, temporal, and occipital lobes. Postcontrast images showed associated diffuse cortical enhancement throughout the regions of cortical swelling and abnormal signal, as well as pial/leptomeningeal enhancement. ASL perfusion demonstrated marked hyperperfusion throughout this region.
Results
Adult-onset NIID may present with variable neurological manifestations. One of the less common manifestations is acute encephalopathy-like episodes. The imaging findings during these acute encephalopathy-like episodes have only recently been described in the literature (3) and bear a striking resemblance to the imaging findings in our case. Although this is an uncommon

manifestation of a relatively uncommon disease, it is important to be familiar with the imaging findings and to consider adult-onset NIID in the setting of acute cortical swelling and enhancement with associated hyperperfusion after ruling out infectious, autoimmune, and paraneoplastic etiologies as well as acute seizure activity.

Conclusions

N/A

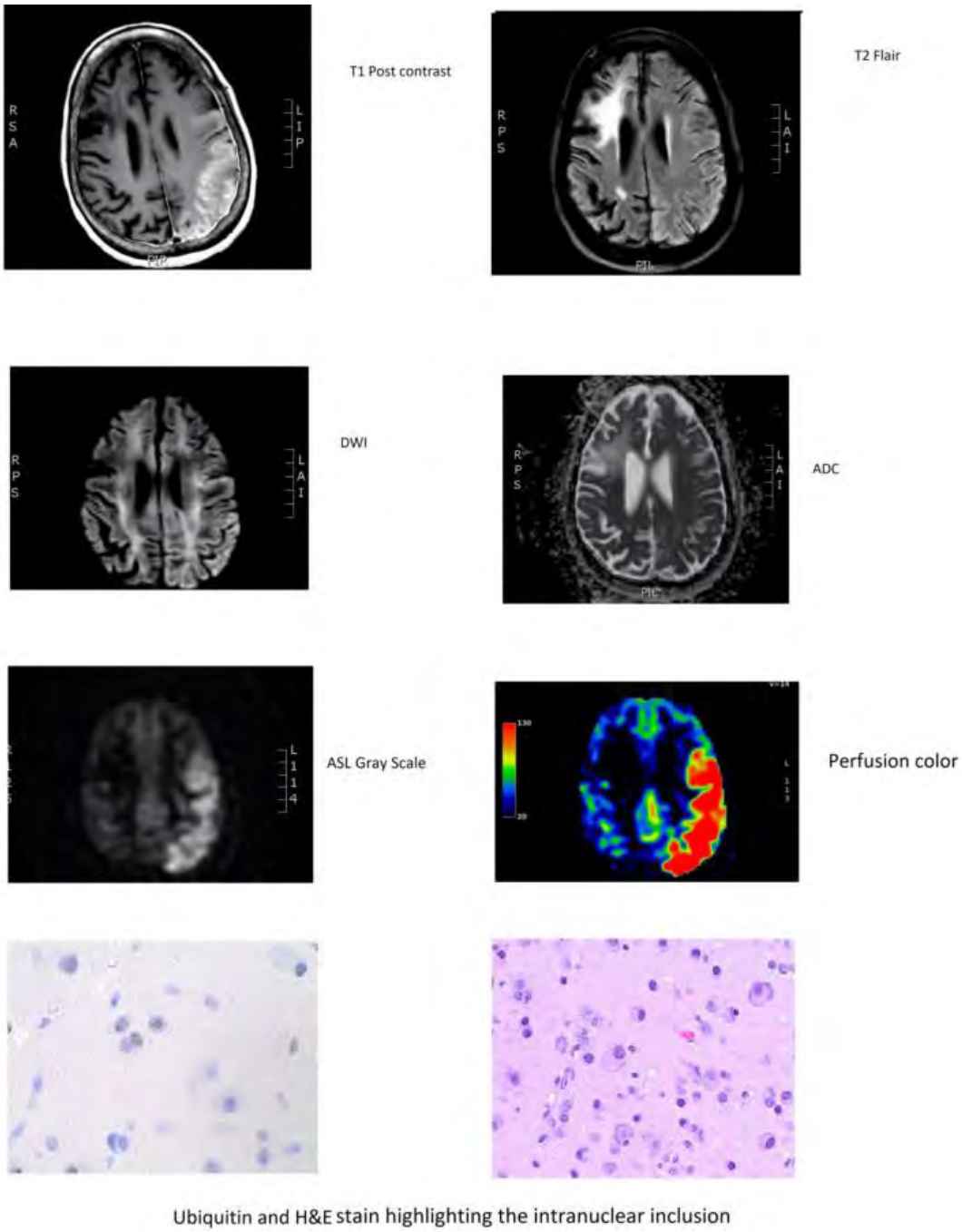

Ubiquitin and H&E stain highlighting the intranuclear inclusion

(Filename: TCT_1247_ImagesASNR.jpg)

513

Aggressive Nature of Acute Invasive Fungal Sinusitis

A Lad[1], S Ceglar[1]

[1]*Harbor UCLA, Torrance, CA*

Purpose

A 57-year-old female presented with right facial swelling and left-sided weakness. Imaging showed a right MCA territory infarct and signs of right-sided invasive fungal sinusitis. Biopsy revealed Mucormycosis. Progression of infection led to a mycotic aneurysm, intracranial hemorrhage, and death.

Materials and Methods
A. CT head: Subtle periantral fat stranding and nasal septal ulceration. B. MRI: Right MCA territory infarct. C. CTA: Right cavernous ICA occlusion (not shown) with normal distal ICA caliber. D. Follow-up CTA in 4 days: aneurysmal dilatation of the carotid terminus.
Results
This case highlights the importance of early diagnosis, as invasive fungal sinusitis was not initially suspected, and also demonstrates many complications associated with this aggressive disease process.
Conclusions
Invasive fungal sinusitis can lead to early intracranial infarct due to angioinvasion even in the absence of frank intracranial extension, thus necessitating a high degree of suspicion in cases with this constellation of findings.

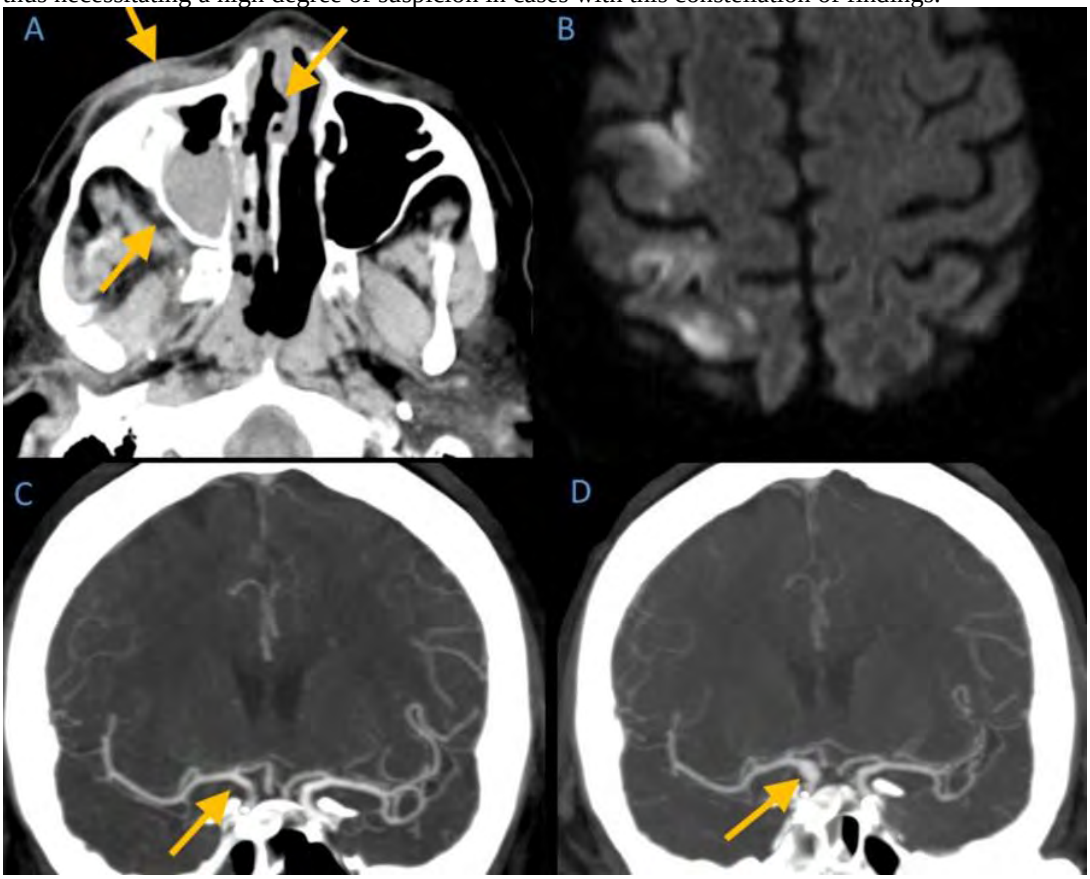

(Filename: TCT_513_mucorimages1.jpg)

1177
An Infected Pseudoaneurysm Of The Vertebral Artery Following Cervical Osteomyelitis
S Ramasamy[1], S Ahmed[2], S Aktan[1], A Mallik[3], J Rosenblum[1]
[1]Loyola University Medical Center, Maywood, IL, [2]Midwestern University Chicago College of Osteopathic Medicine, Downers Grove, IL, [3]Loyola University Medical Center - Strich School of Medicine, Maywood, IL

Purpose
A 67-year-old man with a history of COPD, atrial fibrillation, prostate, and penile cancer requiring radiation therapy presented with scalene muscle fluid collections.
Materials and Methods
CT and MRI of the cervical spine demonstrate C5-C6 discitis/osteomyelitis with a small epidural abscess and associated phlegmon. CTA demonstrates two complex left vertebral pseudoaneurysms near C5-C6, with intervening contour irregularity. The pseudoaneurysms are near the disc space and a nearby transverse foramen.
Results
Adjacent artery mycotic aneurysms are a rare but important complication of osteomyelitis. Abdominal or intracranial pseudoaneurysms are more commonly reported, often at bifurcations, but there are fewer reports of mycotic vertebral artery pseudoaneurysms. This case illustrates useful signs that can aid in the identification of a vertebral mycotic pseudoaneurysm.
Conclusions
Vertebral artery mycotic pseudoaneurysms can develop as a result of osteomyelitis.

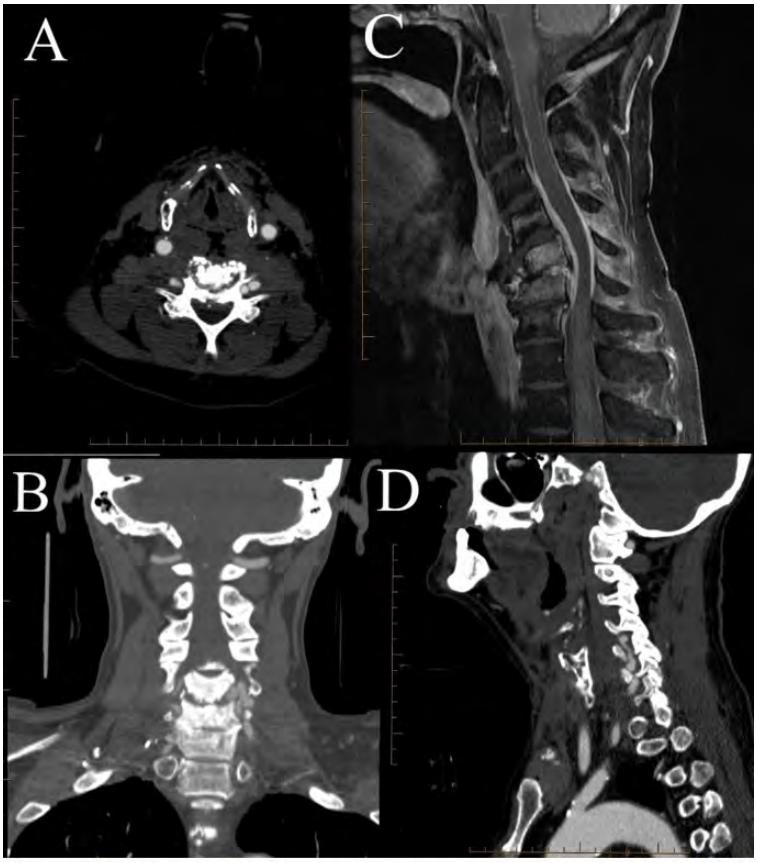

Figure: (A) CT Neck Angiography – Axial view at C5-C6 level (B) CT Neck Angiography – Coronal view (C) Sagittal T1 post contrast (D) CT Neck Angiography – Sagittal view demonstrating pseudoaneurysms of the left vertebral vessels

(Filename: TCT_1177_Finalimage.jpg)

1145

An Unusual Stroke Mimic: Inadvertent Intra-Arterial Contrast Administration on CT Angiography of the Head and Neck

M Czaplicki[1], A Mahajan[2]

[1]Yale, New Haven, CT, [2]Yale University, New Haven, CT

Purpose

A patient presented to the emergency department with a suspected stroke.

Materials and Methods

CT angiography of the head and neck was performed, with an inadvertent intra-arterial contrast injection in the patient's right arm. No contrast is seen in the aortic arch. Dense contrast bolus is seen in the right subclavian artery, the brachiocephalic artery, the right vertebral and bilateral common carotid arteries. The contrast density measured by Hounsfield units, decreases sequentially from the right vertebral, to the right common carotid, to the left common carotid, and there is minimal contrast in the left vertebral artery. There is more parenchymal opacification in the brain than would be typically expected for a CT angiogram, and there is a sharply demarcated area of the left posterior fossa which lacks parenchymal enhancement, corresponding with the lack of contrast opacification in the left vertebral artery. A delayed phase image obtained 65 seconds following the original contrast bolus shows patent left vertebral artery and evidence of posterior fossa infarction.

Results

This patient was transferred to our facility from an outside hospital for endovascular intervention due to concern that the left vertebral artery was acutely occluded, with an acute infarction in the left posterior fossa. When the patient arrived, the outside images were reviewed and it was determined that in fact, there was an inadvertent intra-arterial injection of contrast, therefore the initial bolus was non-diagnostic for evaluation of the left vertebral artery. The delayed images demonstrated normal patency of the left vertebral artery and no posterior fossa infarction. This entity is important for radiologists who are interpreting CT angiograms and stroke clinicians to be aware of, to avoid this pitfall. Additionally, radiologic technologists performing CT angiography studies should be aware of this entity, as is this case performing a delayed acquisition confirmed the diagnosis. Lastly, the radiologist should consider alerting the clinical team caring for the patient to be aware of the inadvertent arterial puncture and monitor the patient for development of an arterial pseudoaneurysm.

Conclusions

Radiologists, stroke clinicians, CT technologists need to be aware of the imaging findings of intra-arterial contrast injection on CT angiography, to avoid misdiagnosis and additional unnecessary procedures.

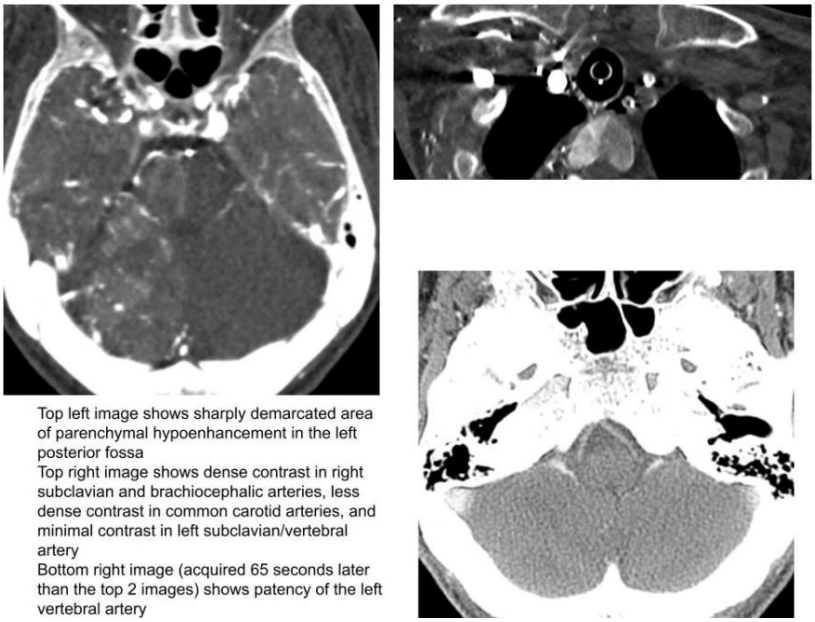

Top left image shows sharply demarcated area of parenchymal hypoenhancement in the left posterior fossa
Top right image shows dense contrast in right subclavian and brachiocephalic arteries, less dense contrast in common carotid arteries, and minimal contrast in left subclavian/vertebral artery
Bottom right image (acquired 65 seconds later than the top 2 images) shows patency of the left vertebral artery

(Filename: TCT_1145_annotatedimages.jpg)

520

Anti-Voltage-Gated Calcium Channel Autoimmune Cerebellitis

A Karandikar[1], D Wang[1], B Griffith[1], S Patel[1]
[1]*Henry Ford Hospital, Detroit, MI*

Purpose

We present the case of a 23-year-old female with a history of cirrhosis secondary to autoimmune hepatitis who had progressively altered mental status for 3 weeks. Her symptoms included nausea/vomiting, headache, confusion/agitation, and new onset ataxia. Lab testing was positive for N-type calcium channel binding antibody, indicating a diagnosis of autoimmune cerebellitis.

Materials and Methods

MR imaging of the brain demonstrated T2-FLAIR hyperintensity (A, B) within the bilateral cerebellar hemispheres with mild restricted diffusion (C), but without pathologic enhancement (D).

Results

Autoimmune encephalitis is an antibody-mediated CNS disorder, either paraneoplastic or non-paraneoplastic, which results in inflammation of the brain. While typically involving the limbic system, all parts of the brain, including the brainstem and cerebellum, can be involved.

Conclusions

Autoimmune encephalitis is a rare, but treatable cause of encephalitis. Radiologists must keep this diagnosis in mind in patients presenting with altered mental status of unclear etiology.

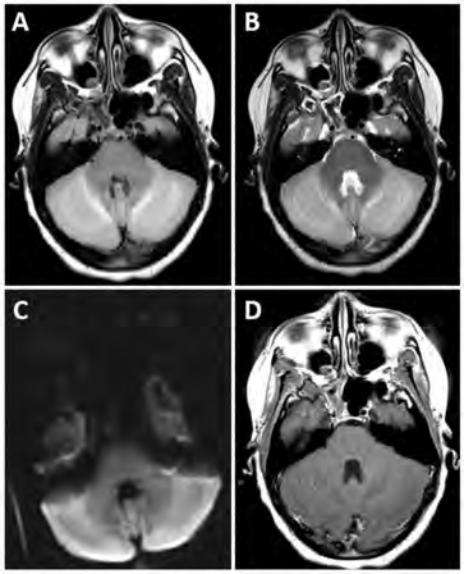

(Filename: TCT_520_cerebellitis.jpg)

1516

Approach to a Solitary Bubbly Appearance Brain Mass in a Young Patient

H Maya-García[1], M Mercado Flores[1]
[1]Hospital Universitario José Eleuterio González, Monterrey, Nuevo León

Purpose

25-yo-male with previous diagnosis of testicular cancer, treated with orchiectomy and radiotherapy, and a disease relapse treated with chemotherapy. 4 months later, he came with occipital oppressive headache, nausea, and retroocular pain. Negative tumor markers.

Materials and Methods

Supratentorial, intraaxial, multicystic appearance mass one the left occipital lobe, showing SWAN hypointensities related to blood products and heterogenous septa enhancement; the lesion was compressing the left lateral ventricle, causing subfalcine and uncal herniation, as well as supratentorial hydrocephalus. Pathology reported metastatic lesion from a mixed germinal tumor.

Results

The negative tumor markers made us consider the diagnosis of a metachronic primary tumor like astroblastoma and dysembryoplastic neuroepithelial tumor.

Conclusions

Even when there is a unique lesion in a young patient, the history of a previously known malignancy wouldn't make a metastatic process less probable.

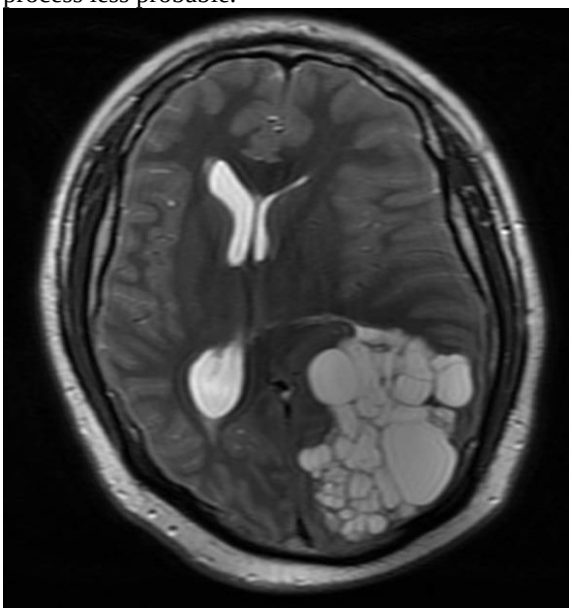

(Filename: TCT_1516_Screenshot_20211115_230136.jpg)

1306

Arachnoid Cyst Rupture with Subdural Hygroma

T Mujtaba[1], J Collins[1], S Ali[1]
[1]University of Chicago, Chicago, IL

Purpose

1st Case: Clinical History: 3 years-old male, presented with fall and vomiting. 2nd Case: Clinical History: 32 years-old female, 34 week gestation with anomaly seen on fetal sonogram, concerning for right-sided porencephaly. 3rd Case: Clinical History: 75 years-old male presenting with altered mental status.

Materials and Methods

1st Case: CT head demonstrated a large left middle cranial fossa cystic fluid collection compatible with an arachnoid cyst. One month later, patient presented with headache and subsequent CT head demonstrated ruptured arachnoid cyst and left subdural hygroma. Follow-up MRI one month later, demonstrated stable left subdural hygroma. 2nd Case: Fetal MRI brain demonstrated right occipital cystic structure with imaging findings consistent with arachnoid cyst, and mild mass effect on the subjacent brain parenchyma. MRI brain demonstrated rupture of right middle cranial process arachnoid cyst with right subdural fluid collection with CSF signal intensity, consistent with a subdural hygroma. 3rd Case: CT head demonstrated recent left frontal lobe infarct. Incidental right middle cranial fossa arachnoid cyst. Patient had status post trauma with follow up CT head demonstrating subarachnoid hemorrhage and CSF attenuating right subdural collection consistent with ruptured arachnoid cyst with hygroma.

Results

We would like to present 3 cases of ruptured arachnoid cysts with subdural hygromas. We will present clinical history, imaging correlation, and risk factors that increase the likelihood of arachnoid cysts to rupture. Arachnoid cysts are benign developmental

variants, and are incidental findings on brain imaging. In a few rare instances arachnoid cysts may rupture, and result in subdural hygromas which needs further imaging surveillance.
Conclusions
Patients with arachnoid cysts necessitate imaging evaluation with worsening CNS symptoms, and or even minor head trauma, to evaluate for rupture of the arachnoid cyst. Most commonly arachnoid cysts with subdural hygromas are treated conservatively, with follow-up imaging and resounding concept of reabsorption of the subdural hygroma.

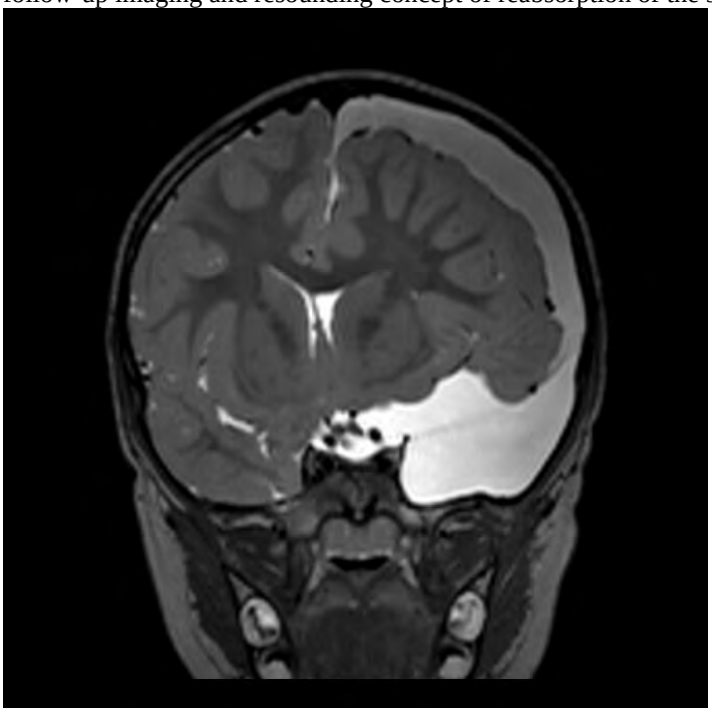

(Filename: TCT_1306_sample20image.jpg)

1095

Arterial Spin Labeling Perfusion in Acute Wernicke Encephalopathy: A Case Series Presentation

P Ann[1], M Chen[2], T Naidich[3], P Belani[4], K Nael[5]
[1]University of California Los Angeles, Los Angeles, CA, [2]Icahn School of Medicine at Mount Sinai, New York, NY, [3]N/A, N/A, [4]Mount Sinai Hospital, new york, NY, [5]UCLA, Los Angeles, CA

Purpose
A 70-year-old female presents with confusion, weakness, and urinary incontinence. She was started on antibiotics for sepsis secondary to vancomycin-resistant enterococcus urinary tract infection. However, she exhibited worsening delirium and lethargy with tachypnea and lactic acidosis; thus a Brain MRI was performed.
Materials and Methods
Brain MRI showed reduced diffusion (top row) and T2 hyperintensity (middle row) of the mamillary bodies, mammillothalamic tracts, midbrain (tectal plate and periaqueductal gray), with corresponding increase in cerebral blood flow on ASL images (bottom row).
Results
Wernicke's encephalopathy (WE) is a life-threatening neurologic disorder resulting from thiamine (vitamin B1) deficiency that can be secondary to chronic alcohol abuse, gastrointestinal surgery, systemic infectious and non-infectious diseases, and chemotherapy [1]. It is classically characterized on MRI by reduced diffusion and T2 prolongation along the mammillothalamic tracts mammillary bodies, periaqueductal grey and tectal plate [1, 2]. We present two patients with acute WE who had baseline arterial spin labeling (ASL) perfusion at the time of presentation, demonstrating increase in cerebral blood flow within the involved region (thalami, mammillary bodies, periaqueductal grey and tectal plate). Both patients were successfully treated with intravenous thiamine infusion. Follow up MRI after treatment demonstrated improvement of imaging findings of reduced diffusion and elevation of CBF within the involved structures with no complication. Our findings suggest that arterial hyper-perfusion may play a role in the pathophysiology of acute WE and are corroborated by histopathological assessment of acute WE lesions, in which luminal dilatation of arteries and arterioles with prominent undulation has been shown [3]. The root of this pathophysiologic process may trace back to thiamine's biochemical role in maintaining osmotic gradients and glucose metabolism, with failure to do so leading to arterial hyper-perfusion possibly as a compensatory or protective mechanism of central brain structures.
Conclusions
In summary, in patients with acute WE, increased perfusion in involved central structures (thalami, mammillary bodies, periaqueductal grey and tectal plate) offers insight into the pathophysiology and likely reflects the compensatory mechanism by which

increased metabolic demand is met. It plausible that patients with acute WE who have associated increased in CBF may be well within the window of treatment.

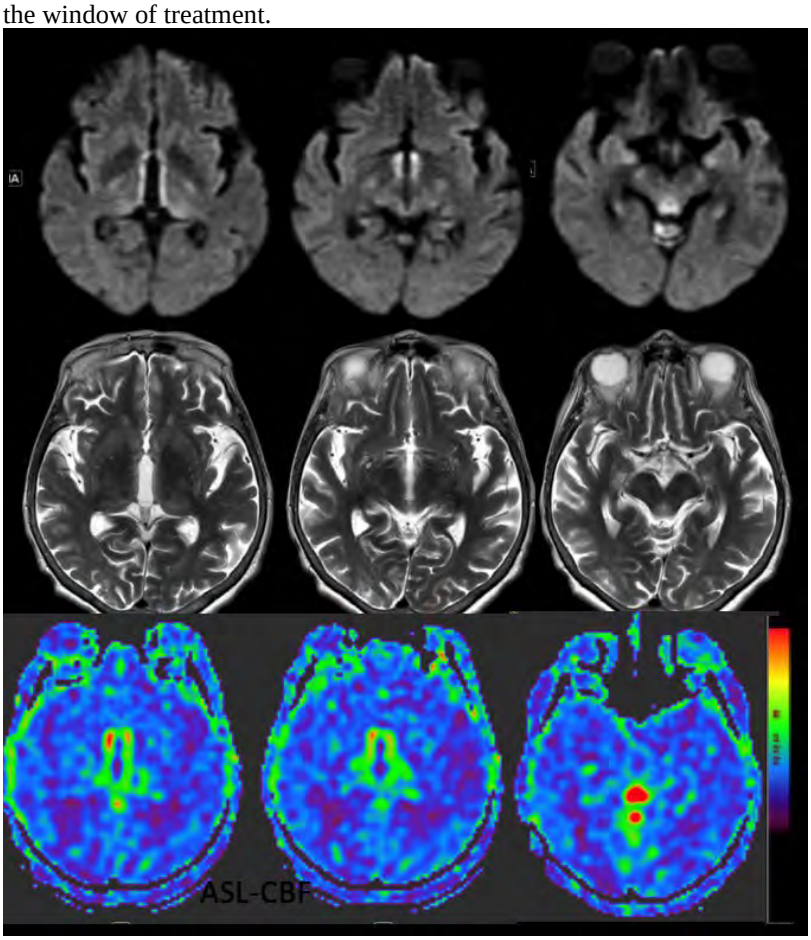

(Filename: TCT_1095_asl_WE.jpg)

151

Atretic Parietal Cephalocele and Associated Structural Neurovascular Anomalies

H Ahmad[1], S Ahmad[2], M Ahmad[2]

[1]New York University, Dix Hills, NY, [2]Touro COM Harlem, New York City, NY

Purpose

22 hour old female infant presented to the NICU with a midline scalp mass. Five months prior to birth, a Chiari malformation was noted on ultrasound, later seen to regress. Fetal MRI and non contrast CT revealed a T2 enhancing mass along the parietal scalp, vertically oriented straight sinus, and superior beaking of the tentorium diagnosed as Atretic Parietal Cephalocele (APC). No surgery was planned, patient was to be discharged when tolerating full feeds and stable temperature in an open crib. Neurosurgery followed to monitor the cephalocele and ventricular size.

Materials and Methods

Atretic Parietal Cephalocele MRI W/WO contrast: Sagital FLAIR demonstrated a vertically oriented straight sinus and draining CSF tract with a connecting fibrous stalk (Figure 1) Coronal FLAIR demonstrated a cystic appearing structure within the parietal scalp (Figure 2) Sinus Pericranii (SP) companion case imaging for comparison MRI W/WO contrast: Sagital T1 Post contrast demonstrated an enhancing mass in the parietal region with a vascular connection (Figure 3)

Results

A midline scalp mass may lead to the differential of SP, a scalp fistula of sorts. Unlike APC, CT imaging of SP shows thinning rather than a complete defect of the calvarial inner table. In addition, the venous content of SP causes it to enhance vividly with T1 weighted MR imaging while APC does not (Figure 1, 2, 3). Both can occur together and are believed to be associated (3). The fibrous stalk of an APC may provide a timeline for the initial insult and a potential causal association between APC and SP (4). During fetal weeks 11 and 12, the straight sinus can be observed in its vertical orientation. After week 19 the enlarging transverse sinus and the increasing volume of the telencephalon pull the meninges back into the developing hindbrain, descending the straight sinus into its horizontal orientation (5). The "Tether model" proposes that the fibrous stalk of an APC connects to and holds the meninges, resisting its decent, keeping the straight sinus vertical and causing a beaking appearance of the tentorium (Figure 4). Interference of a physical tether may also cause dural sinus-to-emissary vein fistulas, leading to SP.

Conclusions

The "Tether Model" proposes that the fibrous APC stalk physically limits descent of the straight sinus between fetal weeks 11 and 19,

causing characteristic radiographic dural venous anomalies. Interference of a physical tether may also cause dural sinus-to-emissary vein fistulas, leading to APC's association with SP.

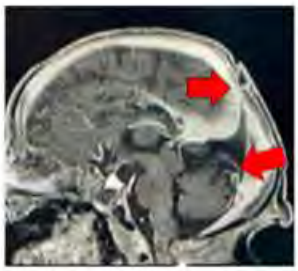

Figure 1: APC Sag FLAIR with Contrast revealing a vertically oriented straight sinus and draining CSF tract

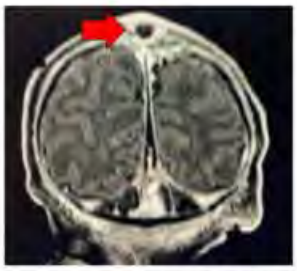

Figure 2: APC Coronal FLAIR with Contrast demonstrating a cystic-appearing structure within the parietal scalp

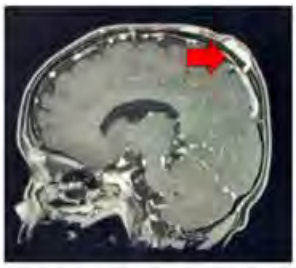

Figure 3: SP Sag T1 Post revealing an enhancing mass

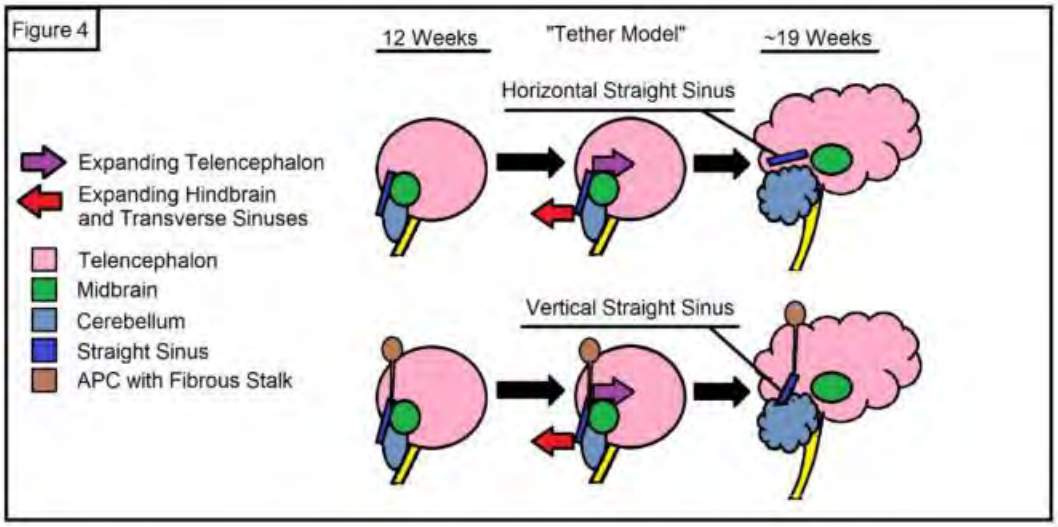

(Filename: TCT_151_APCposter2.jpg)

384

Atypical Aggressive Appearance of a Rare Benign Entity: CAlcifying PseudoNeoplasm Of Neuraxis (CAPNON)

A Hanafy[1], A Singh[1], A Gilbert[1], J Lally[1]
[1]*University of Texas Health San Antonio, San Antonio, TX*

Purpose

43 y/o Female patient with longstanding neck pain for 20 years, getting worse over last 2 years. Presented to outside hospital with dizziness and vertigo. Outside Imaging showed large mass at skull base, and patient was referred to our institution for further workup. We performed CT and MRI WOW. On physical exam, patient has no motor or sensory deficit. No hearing loss or vision changes.

Materials and Methods

•CT Head: large osseous expansile mass of the skull base and upper cervical spine with prominent granular calcifications and diffuse osseous sclerosis. •MRI Brain wow: • large infiltrative heterogenous enhancing mass at skull base extending into the medullary cistern, CP angle, R jugular foramen, hypoglossal canal, prevertebral and paraspinal soft tissue. • Mass-effect on brainstem and cerebellum with resultant hydrocephalus. • Involvement of the R sigmoid sinus and R IJV. • Encasement of the R vertebral artery V3 and V4 segments. • Parenchymal edema, and involvement not entirely excluded.

Results

Image findings represent large extraaxial osseous expansile and sclerotic mass with infiltrative pattern at the skull base. Intense heterogenous enhancement and prominent granular calcifications also noted. Primary consideration was osteosarcoma. DDx included metastasis, osteoblastoma, and intraosseous meningioma. However, sharp osseous margin at the clivus and posterior foramen magnum

is atypical and represent and chronic remodeling rather than aggressive infiltrative pattern. ϖ Intraoperative frozen pathology was also concerning for osteosarcoma.
Conclusions
• Final pathology report, however, was different; and rather consistent with CAPNON! • CAPNON is a very rare neoplasm – less than 100 case in literature. it is non-neoplastic non-inflammatory lesion with unknown etiology. Typically, it is an intraaxial lesion that is heavily calcified, showing very low T1 and T2 signals without enhancement (1, 2), hence the name 'brain stone' . • The radiologic presentation of our case is very atypical, much more concerning for an aggressive lesion, although the sharp margin at clivus& opisthion-tumor interface is not expected with aggressive tumors and rather suggests a chronic remodeling process.

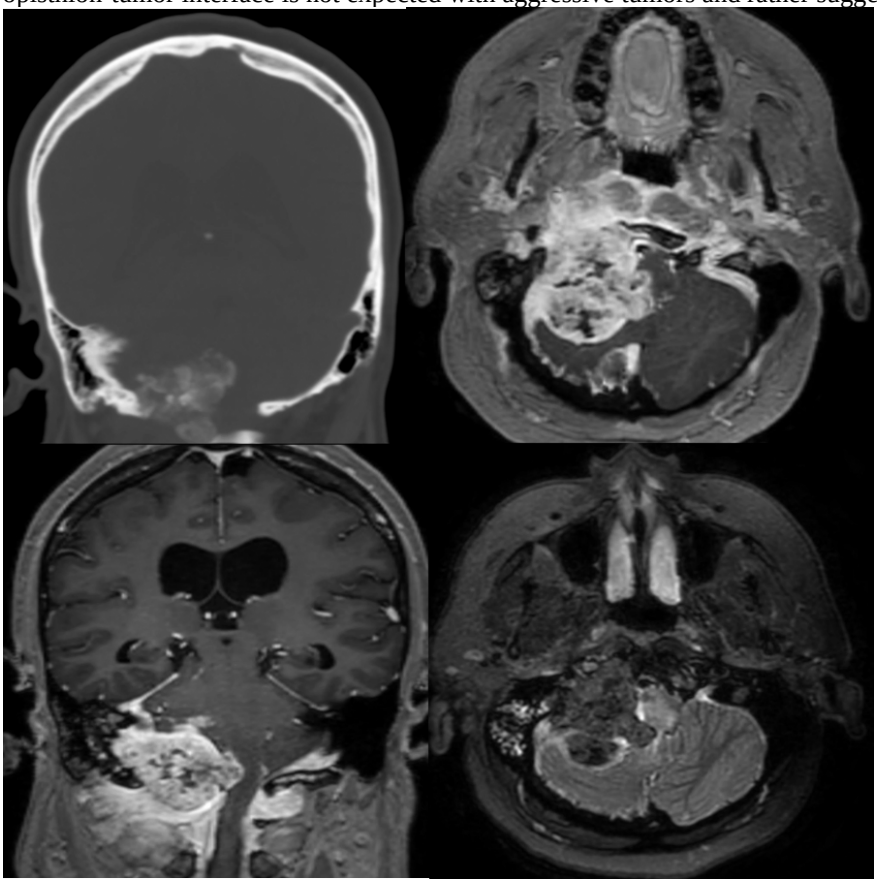

(Filename: TCT_384_Picture2.gif)

1184
Atypical Cervical Paraganglioma in a 5 year old Male
S Ahmed[1], S Ramasamy[2], K Lebioda[3], A Mallik[2]
[1]Midwestern University Chicago College of Osteopathic Medicine, Downers Grove, IL, [2]Loyola University Medical Center, Maywood, IL, [3]Rutgers, The State University Of New Jersey, Newark, NJ

Purpose
A 5-year-old male presented with progressively worsening right neck pain, difficulty eating, and right arm weakness. Physical exam revealed decreased range of motion with right neck rotation without neurologic symptoms.
Materials and Methods
MRI demonstrates a T2/STIR hyperintense, T1 hypointense avidly enhancing lesion involving the right paravertebral space and right anterolateral epidural space, extending from the foramen magnum to C6. CT shows lucent osseous changes but preservation of bony margins.
Results
The differential diagnosis for this lesion included nerve sheath tumors and metastases. Most paragangliomas in the head and neck are carotid body tumors, or glomus vagale, jugulare or tympanicum. However, they can occur anywhere along the sympathetic chain.
Conclusions
The cervical paraspinal region is an uncommon location for a pediatric paraganglioma, usually not suspected at the time of presentation.

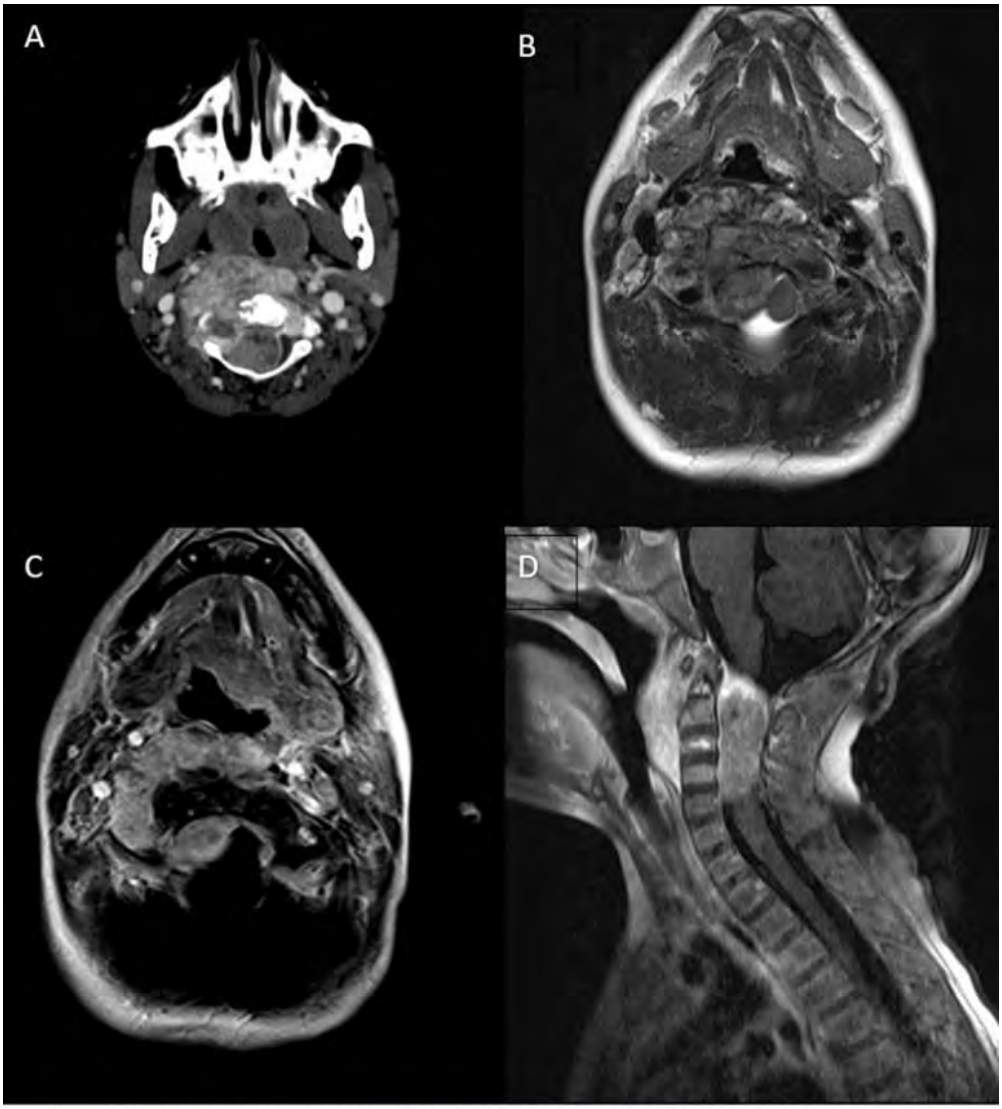

Figure: (A) CT Neck with IV Contrast – Axial view (B) Cervical MRI Axial T2 (C) Cervical MRI T1 Axial Post Contrast (D) Cervical MRI Sagittal T1 Post Contrast

(Filename: TCT_1184_Figure1Final.jpg)

138

Atypical Imaging Findings of a Common Diagnosis: Primary CNS Lymphoma (PCNSL)

S Mendonca[1], B Cohen[2], R Patel[3]

[1]Atlantic Health Systems, Morristown, NJ, [2]Atlantic Health Systems, South Orange, NJ, [3]Beth Israel Deaconess Medical Center, Boston, MA

Purpose

A 70 year old immunocompetent female presents with new seizures. She has a history of stage 1 breast cancer, in remission for 10 years. Dominant brain mass biopsy revealed diffuse large B-Cell PCNSL.

Materials and Methods

CT head showed right temporal vasogenic edema without a hyperdense mass. MRI demonstrated multiple ring enhancing lesions with intratumoral hemorrhage, favoring metastasis, given imaging findings and history of breast cancer.

Results

In immunocompetent patients, PCNSL typically presents as a solitary enhancing mass with multifocality and ring enhancement reported in 20-40% and 13% of cases, respectively, as opposed to 75% of cases in immunodeficient patients. Hemorrhage within PCNSL is a rare finding. This is a challenging case of multiple hemorrhagic ring enhancing lesions in an immunocompetent patient, mimicking metastases with overlapping findings of PCNSL in immunodeficient patients.

Conclusions

Hemorrhage within ring enhancing PCNSL is a rare finding and can mimic metastasis, in immunocompetent patients.

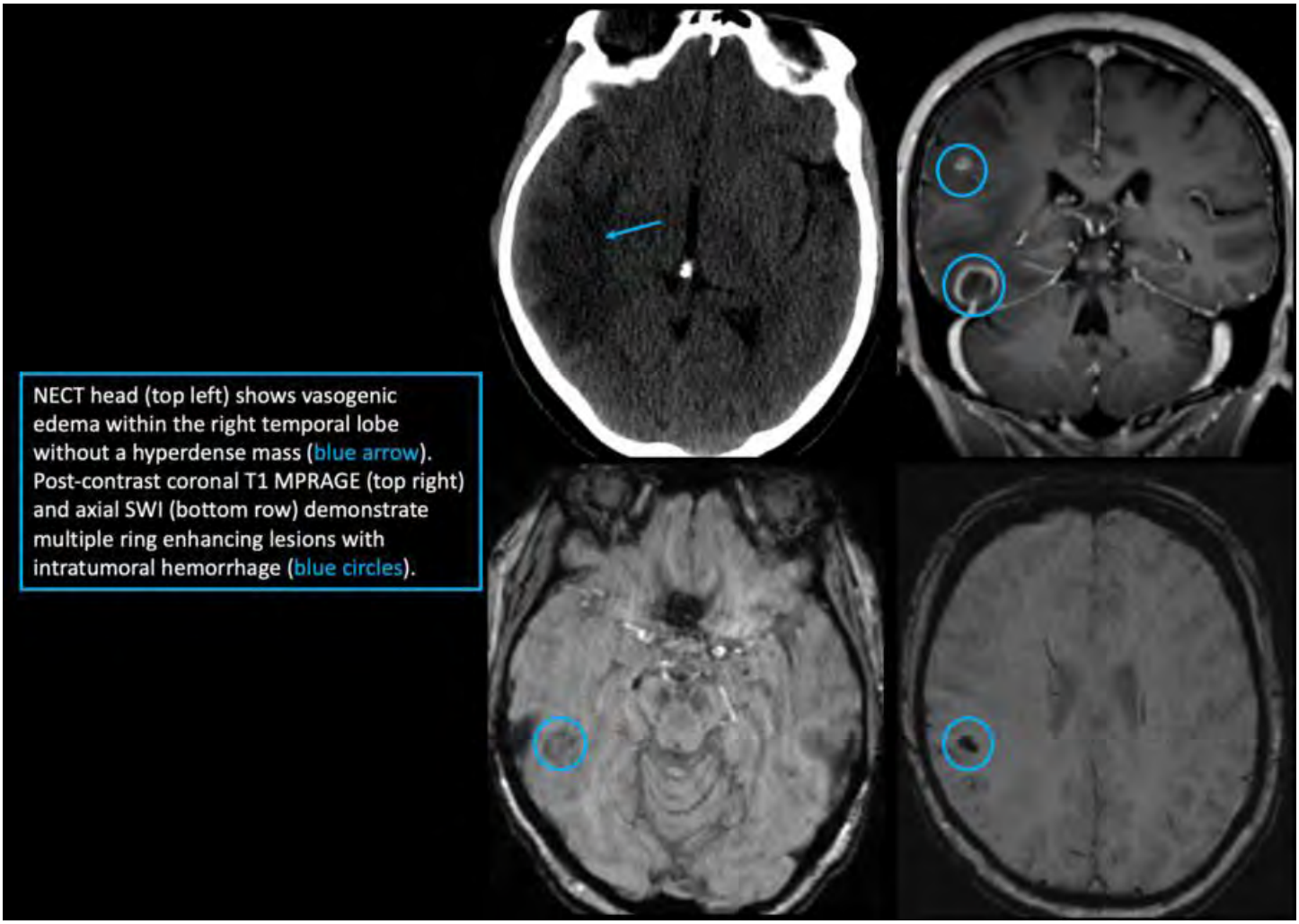

(Filename: TCT_138_annotatePCNSL.jpg)

580

Atypical Optic Neuritis and Perineuritis after COVID-19 Vaccination

M Corrigan[1], A Lee[2], S Fung[2]
[1]Houston Methodist, Houston, TX, [2]Houston Methodist Hospital, Houston, TX

Purpose

A 36 year-old African American man, previously healthy, presents with bilateral subacute painless and progressive blurred vision following second dose of COVID-19 vaccination.

Materials and Methods

Orbit MRI shows the optic chiasm and bilateral optic tracts symmetrically enlarged with increased T2 signal and mild enhancement. Optic nerves also demonstrate mildly increased T2 signal and mild enhancement but within normal limits in size. Optic perineuritis is observed with mild enhancement of perineural fat surrounding the optic nerves with indistinct fat margins. MRIs of the brain and spinal cord are normal.

Results

Working diagnosis is atypical optic neuritis and perineuritis, and temporal relationship with second dose of COVID-19 vaccination suggests this may be post-vaccination optic neuritis and perineuritis. Differential diagnosis includes neuromyelitis optica spectrum disorder (NMOSD), sarcoidosis, IgG4-related disease, systemic lupus erythematosus, Behcet's disease, granulomatosis with polyangiitis, syphilis, tuberculosis, herpes, and leukemia. Optic glioma cannot be excluded but considered unlikely given findings of perineuritis. Although serum tests were negative for AQP4 and MOG antibodies, seronegative NMOSD remains high on differential. Rheumatologic panel was negative. CSF from lumbar puncture showed normal protein and WBC, which argues against infectious and inflammatory etiology. During the hospital stay, patient completed methylprednisolone 1000 mg IV qd x 5 days and plasmaphoresis x 5 sessions with vision improving afterwards.

Conclusions

Optic perineuritis is a form of orbital inflammatory disease in which immune-mediated inflammation affects the optic nerve sheath with variable involvement of the optic nerve and is important to differentiate from demyelinating optic neuritis due to therapeutic and prognostic differences. Vaccines help develop immunity by imitating an infection by triggering a systemic immune response, although

vaccines can occasionally stimulate autoimmune reactions. Cases of NMOSD (NMO and MOG) have been described after COVID-19 infection and vaccination.

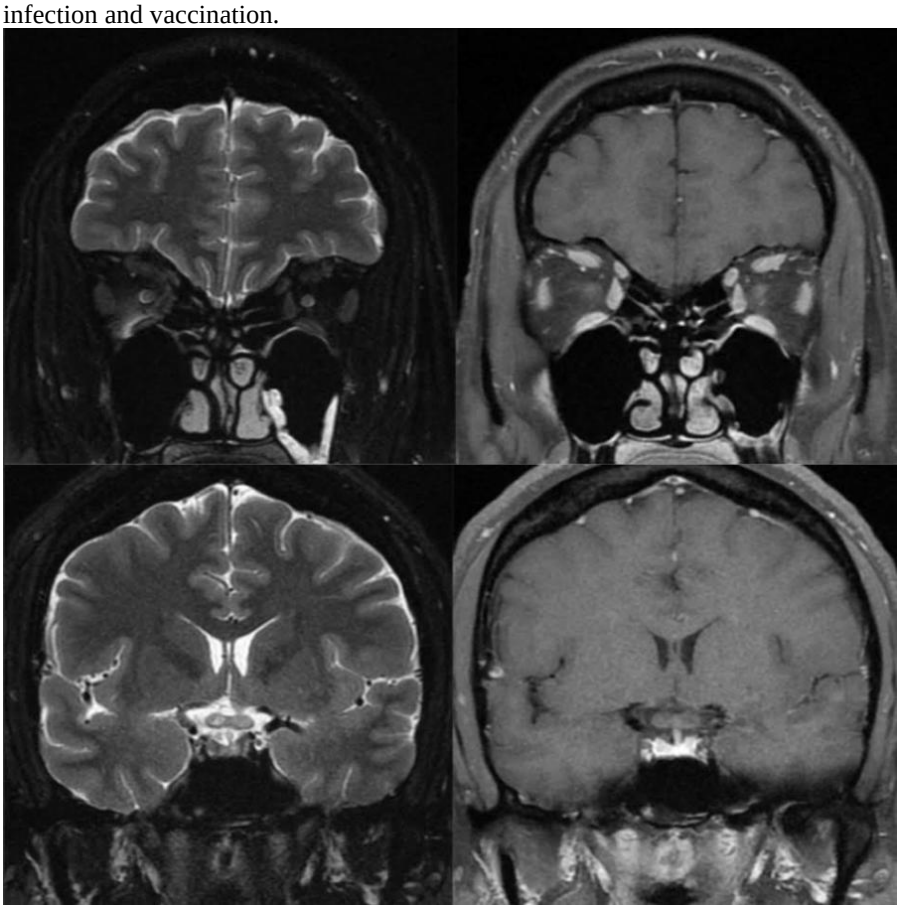

(Filename: TCT_580_opticnerveopticchiasm.jpg)

430

Autoimmune GFAP Astrocytopathy: Imaging Findings of an Emerging Novel Meningoencephalitis Diagnosis

E Shin[1], S Girn[1], J Soun[2]

[1]UC Irvine Medical Center, Orange, CA, [2]UCI Department of Radiological Sciences, Orange, CA

Purpose

Patient is a 35 year old female with no significant past medical history who presented with a 6 week history of paroxysmal transient confusion, memory loss and staring spells. Symptoms were accompanied by intermittent fevers, severe fatigue, and headache. Initial workup was concerning for viral encephalitis, neurosarcoidosis, TB meningitis, and MS. Patient additionally developed ophthalmoplegia and urinary retention. MRI brain and spine showed enhancing linear perivascular foci and subsequently enhancing periventricular lesions. Biopsy of a periventricular lesion showed lymphocytic infiltrates which were suspicious for anti-GFAP astrocytopathy, and CSF paraneoplastic immune panel showed evidence of anti-GFAP antibodies. Patient was initiated on several therapies including corticosteroids, plasma exchange, mycophenolate, and rituximab with improvement in symptoms.

Materials and Methods

Initial MRI brain demonstrated a periventricular perivascular distribution of T2/FLAIR hyperintensity, enhancement, and diffusion restriction, which has recently been described as a characteristic but insensitive feature of anti-GFAP astrocytopathy. One month later, repeat imaging showed improvement of perivascular enhancement. However, there was interval development of a new left parietal periventricular enhancing lesion as well as bilateral optic nerve enhancement. The periventricular enhancing lesion was biopsied and pathologic findings were suspicious but not specific for anti-GFAP astrocytopathy. Imaging of the cervical and thoracic spinal cord demonstrated linear long segment T2 hyperintensity.

Results

Anti-GFAP astrocytopathy is a newly described meningoencephalitis, first described in 2016 based on the presence of Anti-GFAP antibodies in serum or CSF, imaging findings, and clinical course. Investigators suspect that this is a similar or same disease process as the previously described chronic or suabcute corticosteroid responsive nonvasculitic autoimmune inflammatory meningoencephalitis. Characteristic MRI findings include perivascular periventricular lesions and leptomeningeal enhancement. This disease process is also associated with the presence of a neoplastic and/or autoimmune process. There currently exists no uniform diagnostic criteria for diagnosis. Treatment typically consists of steroids, plasma exchange, and other immunosuppressive therapies.

Conclusions

Anti-GFAP astrocytophathy is a novel description of an antibody-mediated meningoencephalitis with characteristic MRI findings.

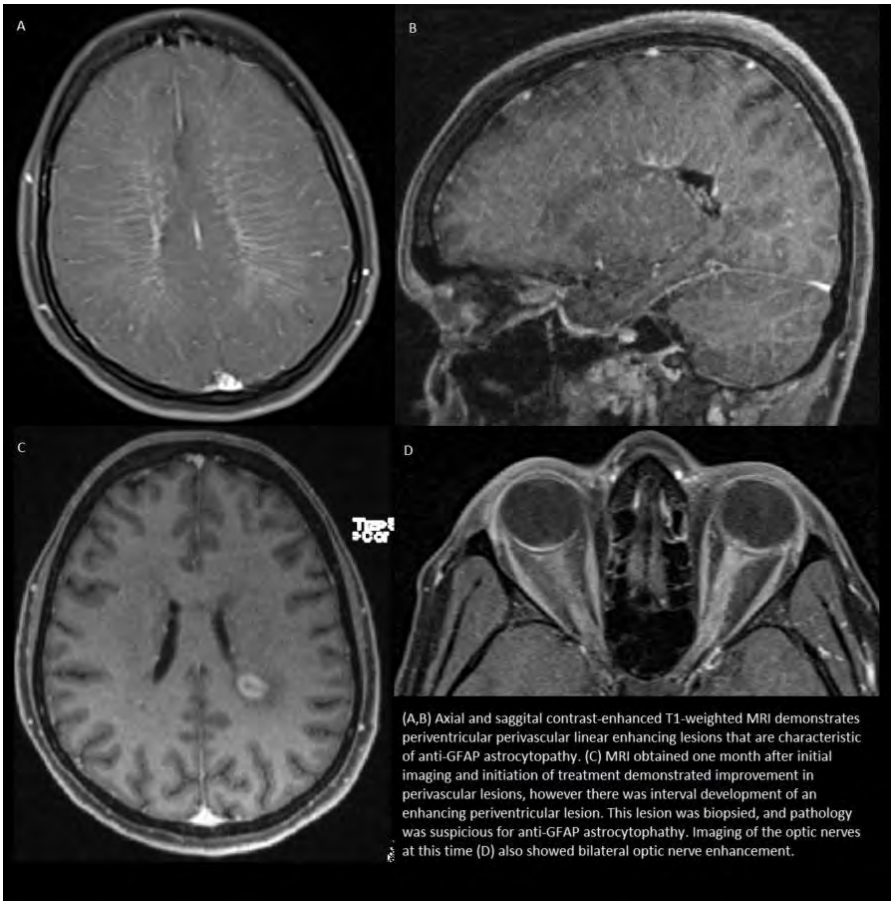

(Filename: TCT_430_Combinedimages2.jpg)

1229

Bilateral sialoectasia - Kussmaul vs Masseter

F Hierro[1], P Bem[1], I Prisco[1], R Garcia[1], P Moniz[1], A Reis[1]
[1]*Hospital Pedro Hispano, Matosinhos, Porto*

Purpose

A 60-year-old patient presents with recurrent episodes of edema of the parotid regions associated with chewing, but unrelated to specific foods, occasionally with associated pain. Bilateral masseteric hypertrophy was seen, interpreted as secondary to the patient's bruxism. This patient also complained of recurrent episodes of urticaria and angioedema, with dyspnea . No history of trauma, oral surgery, sialolithiasis, chronic parotitis or dry mouth. During the etiological study he performed successive analytical studies with sustained eosinophilia. The patient is on anti-allergy medication with modest improvement.

Materials and Methods

Parotid MRI with Sialo MRI showed bilateral ectasia of Stenson's ducts, with homogeneously hyperintense content on T2-weighted sequences and bilateral masseteric hypertrophy. Normal morphology and signal intensity of the parotid glands and surrounding tissues.

Results

Sialoectasia is the dilatation of the salivary ducts (1) which can occur secondarily to ductal obstruction. The obstruction may be due to sialolithiasis, stenosis or stricture, and there are cases of bilateral sialoectasia due to hypertrophy of the masseteric muscles (2). Another etiology for bilateral presentation is sialodochitis fibrinosa, or Kussmaul's disease. This is a rare disease of the salivary glands in which mucofibrinous plugs obstruct the salivary ducts causing recurrent swelling and pain of the salivary glands, described in patients with a history of allergy associated with eosinophilia (3).

Conclusions

A case of bilateral sialoectasia in a patient with masseteric hypertrophy and a heavy history of allergic manifestations, without identification of the triggering allergen, is described.

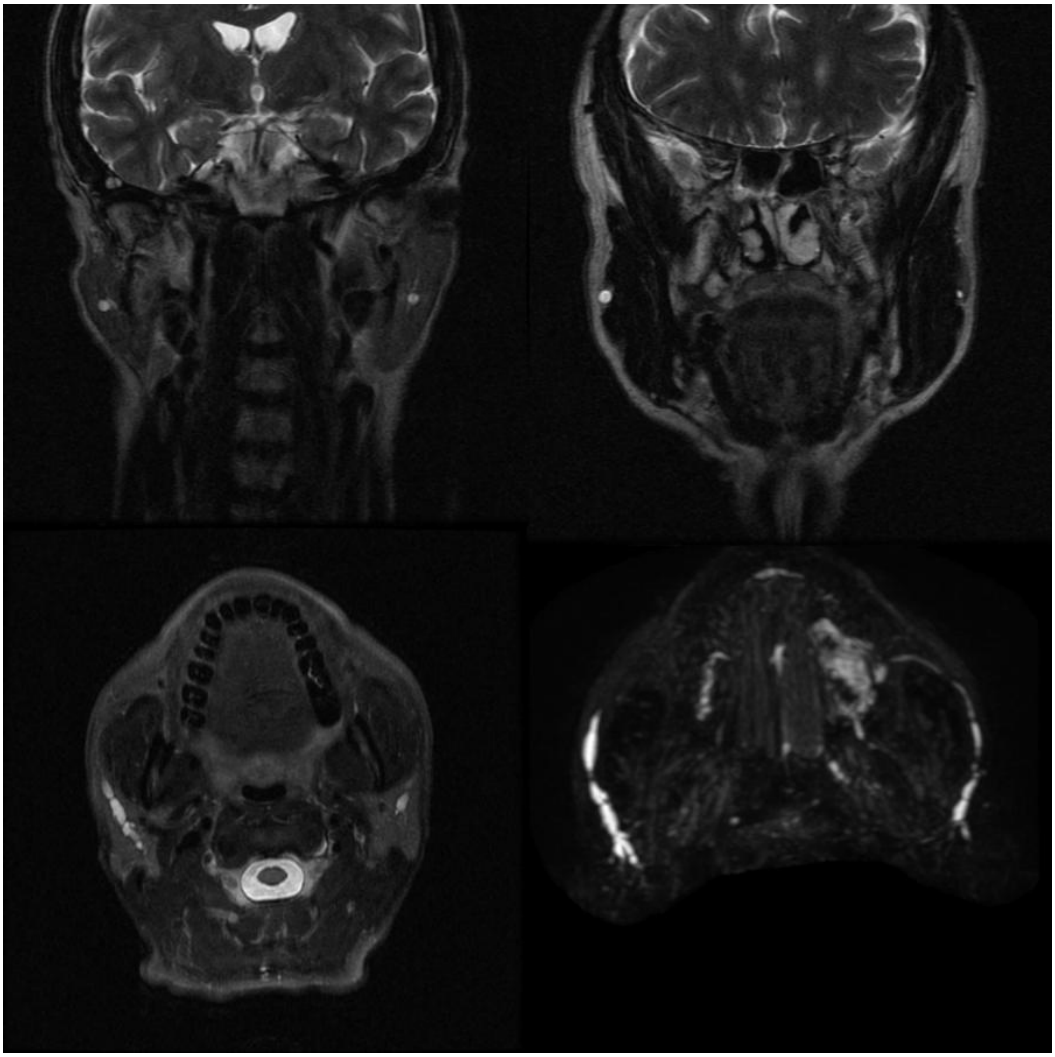
(Filename: TCT_1229_Images.jpg)

1051

Bing Neel syndrome with intracranial hemorrhage, A rare complication

Z Khan[1], S Saeed[1], S Nosheen[1]
[1]*Shifa International Hospital, Islamabad*

Purpose

67 years old male known case of Waldenström macroglobulinemia (WM) diagnosed by bone marrow biopsy (showing lymphoplasmacytic cells with IgM kappa monoclonality) presented with frontal headache and severe leg pains. He was earlier succesfully treated by immunosuppressive chemotherapy fludarabine 3 cycles. The hematologic laboratory values were normal. MRI brain with contrast was performed which confirmed diagnosis of Bing Neel syndrome and one month later he developed intracranial hemorrhage as its rare complication confirmed with CT scan and MRI brain.

Materials and Methods

On T1 axial post contrast MRI (Fig. 1a), 1 shows nodular meningeal enhancement involving the left parietal temporal lobe suggesting leptomeningeal spread of lymphoma, there was no intracranial hemorrhage or mass effect in brain parenchyma at that time. After one month non contrast CT was performed for decreasing GCS score (Fig. 2) shows hypodensity in the left temporal lobe with internal hemorrhage. MRI brain without contrast was performed next day because of raised creatinine level showed interval progression in CNS lymphoma with large abnormal T2W (Fig. 3 a) and FLAIR (Fig. 3 b) hyperintense mass like lesions in the left temporal lobe with mass effect causing enlargement of gyri having internal areas of hemorrhage on SWI sequence (Fig 3c).

Results

Bing-Neel syndrome (BNS) is a very rare complication of Waldenstrom's macroglobulinemia (WM) due to lymphoplasmacytoid infiltration in the CNS (1). Two different forms have been described: tumoral and diffuse infiltrative. MRI show subcortical mass-like lesion(s) with high signal on T2 and FLAIR, iso/hypointensity on T1 and contrast enhancement after gadolinium. In diffuse infiltrative form, leptomeningeal thickening with contrast enhancement are usually present. It was first described in 1936 by, two Danish physicians, working in Copenhagen, Jens Bing and Axel Valdemar Neel (1878-1952) (2).It is considered potentially treatable with cranial radiation therapy alone, or in combination with intrathecal chemotherapy (3).

Conclusions

Waldenstrom's macroglobulinemia is the most commonly reported subtype of lymphoplasmacytic lymphoma (LPL); it is characterised by IgM secretion. Bing-Neel syndrome should be suspected in patients with WM and neurologic symptoms. Neurological complications are common usually as a result of hyperviscosity. This is a unique case to our knowledge in which patient developed intracranial hemorrhage with ongoing Bing Neel syndrome.

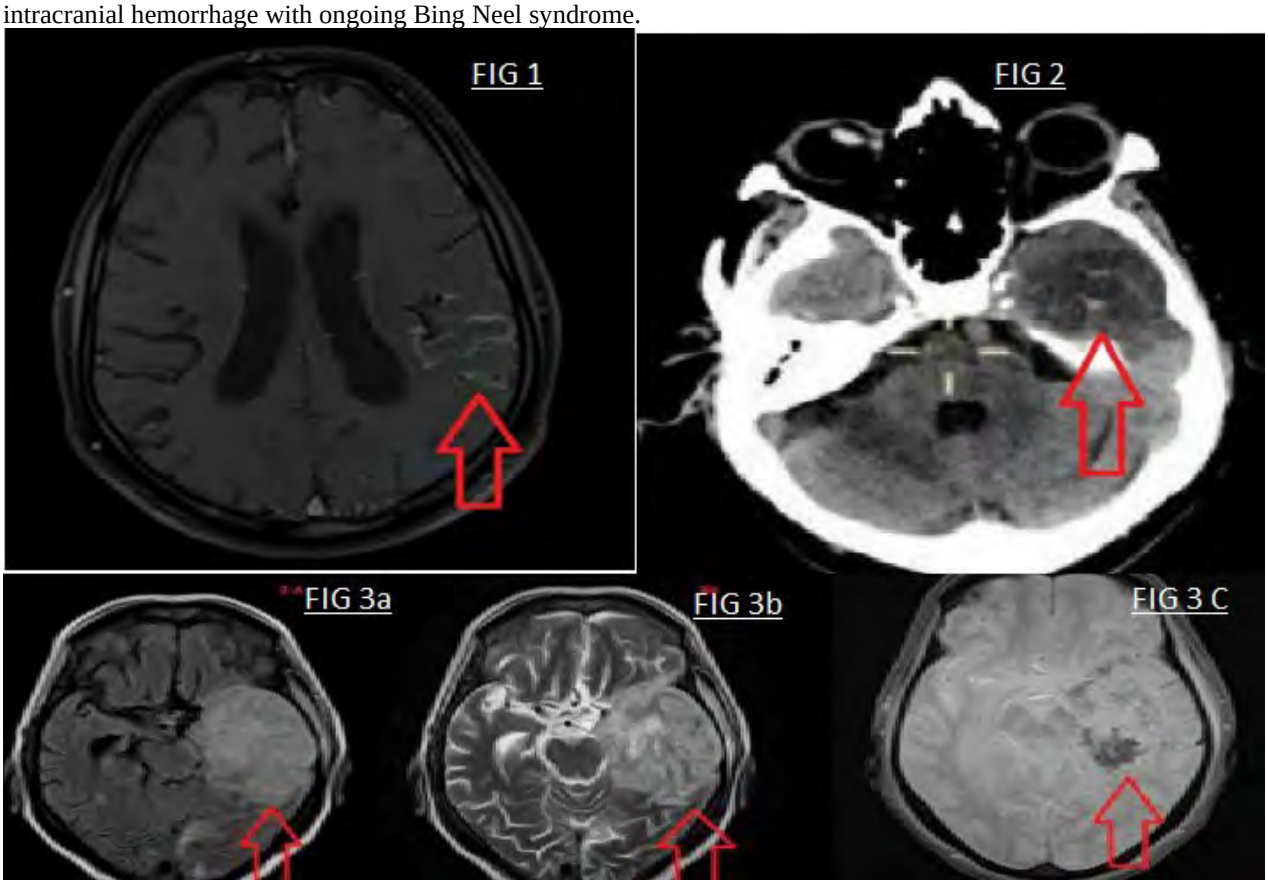

(Filename: TCT_1051_FIGURES.jpg)

381

Cementoosseous Dysplasia Complicated with Osteomyelitis

E Bonfante-Mejia[1], D Timaran-Montenegro[2]

[1]UTHealth, Houston, TX, [2]McGovern Medical School at UT Health, Houston, TX

Purpose

An 87-year-old- female with history of extraction of right mandibular molars with poor wound healing and infection treated with unsuccessful debridement. Patient complains of right mandible and gum pain. Physical examination reveals multiple missing teeth, right mandible fistula with pus secretion along the remaining molar #31.

Materials and Methods

Cementoosseous dysplasia is characterized by mixed lytic and sclerotic masses, often with a central area of calcification surrounded by a low-attenuation halo located at the periapical region (figure 2). Cementoosseous lesions are initially lytic and progress to a sclerotic appearance associated with a vital, non-restored tooth and intact periodontal ligament. Moreover, cementoosseous dysplasia may occur in the tooth-bearing jaw after dental extraction, and in multifocal disease (florid cementoosseous dysplasia [FCOD]), adjacent periapical lesions tend to coalesce involving the entire mandible. In cases of cementoosseous dysplasia with superimposed chronic osteomyelitis, lytic lesions are not confined to the tooth-bearing areas. Mottled, ill-defined lucency and sclerosis involve large segments of the mandible extending beyond the alveolar canal.

Results

FCOD is a strictly localized disorder that involves the tooth-bearing areas and not associated with any other skeletal disease. FCOD is associated to a reactive or dysplastic process that involves the replacement of bone by connective tissue matrix with varying degrees of mineralization. Patients with FCOD are usually asymptomatic and may present as an incidental radiologic finding. In other cases, infection may be associated secondary to hypercementosis and decreased bone vascularity. FCOD findings consists of multi quadrant sclerotic masses with radiolucent lesions centered above the alveolar canal. In our case, prominence of the cementum in the periapical regions of both maxillary and mandibular teeth was observed. FCOD patients complicated with chronic osteomyelitis, usually complain of recurrent pain episodes and soft tissue swelling associated with imaging findings that include ill-defined lesions that are not confined to tooth-bearing areas, as described in our case.

Conclusions

♣ Benign fibro-osseous lesions ♣ Normal bone replaced by highly cellular fibrous connective tissue and cementum ♣ Lucent and radioopaque bony changes surrounding the apices ♣ AA, Female predominnace 14/1 ♣ Symptomatic if superimposed osteomyelitis.

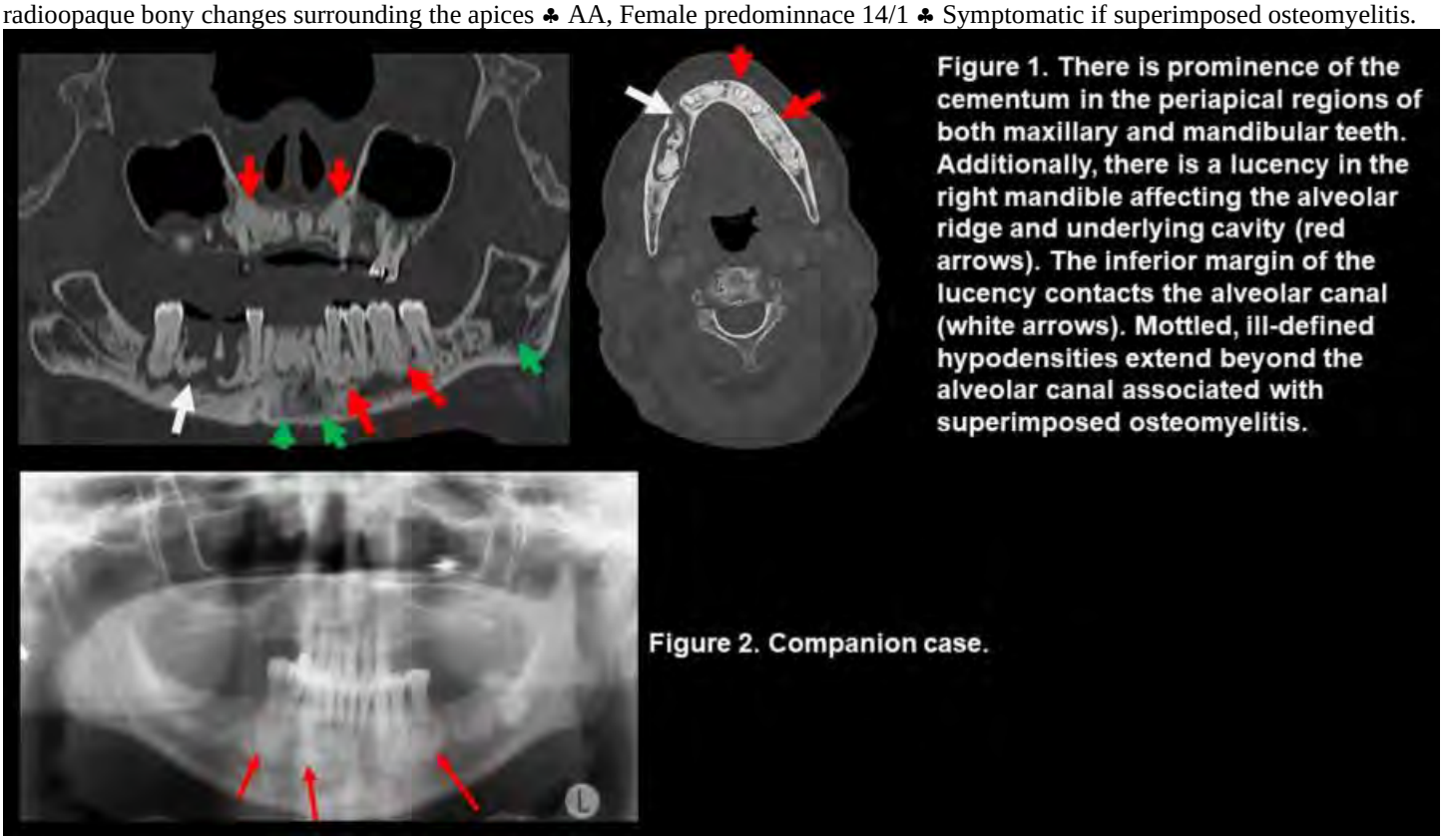

(Filename: TCT_381_Cemento-osseousdysplasiafinal.jpg)

1376

Cerebral Lipiodol Embolism after Thoracic Duct Embolization

S Hasan[1], D Pechersky[1]

[1]*McGaw Medical Center of Northwestern University, Chicago, IL*

Purpose

58 year-old patient with right lower lobe adenocarcinoma status post robotic right lower lobectomy which was complicated by persistent chylothorax postoperatively. Patient subsequently underwent coil and glue thoracic duct embolization. A day after embolization patient developed lethargy and altered mental status.

Materials and Methods

Non-contrast CT brain demonstrates heterogeneous areas of symmetric hyperdensity within the cerebral cortex and deep gray/white structures. However, on iodine-removed virtual non-contrast images the areas of hyperdensity are no longer visualized.

Results

Cerebral lipiodol embolism (CLE) is a rare complication seen after the use of lipiodol for lymphangiography and Hepatocellular carcinoma transarterial chemoembolization (TACE) procedures. The prevalence of CLE is not well documented but studies have shown a frequency of 1-2 per 1000 cases of TACE (1). The route by which lipiodol enters the cerebral circulation after a TACE has been widely discussed and various right-to-left shunt pathways have been elucidated including intracardiac shunts including a patent foramen ovale or septal defect, pulmonary arteriovenous malformations, and hepatopulmonary shunts. However, the route after lymphangiography is not as well understood but presumed to involve diffusion of lipiodol from the lymphatic network into the venous system and subsequent passage across the intrapulmonary capillary bed into the systemic circulation (2). The imaging findings of CLE can be mistaken for diffuse cerebral hemorrhage and can lead to inappropriate patient management and treatment. The advent of Dual-Energy CT can help problem-solve by differentiating between iodine and hemorrhage based on their high atomic numbers (3). Here, we present a case of cerebral lipiodol embolism as evidenced by the diffuse areas hyperdensity in the cerebral cortex and deep gray/white matter that is no longer present on virtual unenhanced images.

Conclusions

- Recognize imaging findings of cerebral lipiodol embolism as a rare complication of lymphangiogram and transarterial chemoembolization. - Understanding the use of Dual-energy CT to help differentiate between iodinated contrast and hemorrhage.

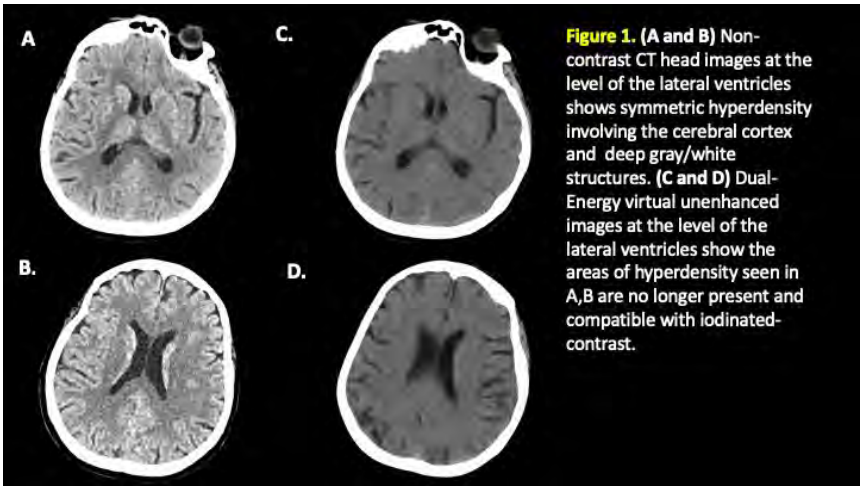

(Filename: TCT_1376_CLEfigure.jpg)

588

Cerebrospinal Fluid Leak With Multiple Meningoceles Secondary to Chronic Idiopathic Intracranial Hypertension

T Studer[1], M Oswood[2]
[1]University of Minnesota, Minneapolis, MN, [2]Hennepin Healthcare, Minneapolis, MN

Purpose

A 65-year-old woman with chronic headaches presents with clear rhinorrhea for 2 months. She has no history of prior sinus surgery or trauma. Nasal fluid was positive for beta-2 transferrin. CSF opening pressure was elevated at 25 cm.

Materials and Methods

Brain MR showed multiple areas of skull base dehiscence (arrows), including the right cribriform plate, bilateral middle cranial fossa into the sphenoid sinuses, and along the right hypoglossal canal. A CT-cisternogram revealed opacification of multiple meningoceles with active leak in the right nasal passage.

Results

Symptoms of idiopathic intracranial hypertension (IIH) typically include headaches and visual problems. On imaging, the most common features include posterior scleral flattening, optic nerve tortuosity, and intracranial venous stenosis. Less common features include meningoceles, and even more rarely, spontaneous cerebrospinal fluid (CSF) leak.

Conclusions

Cisternography is useful to localize CSF leak in chronic IIH complicated by multiple meningoceles.

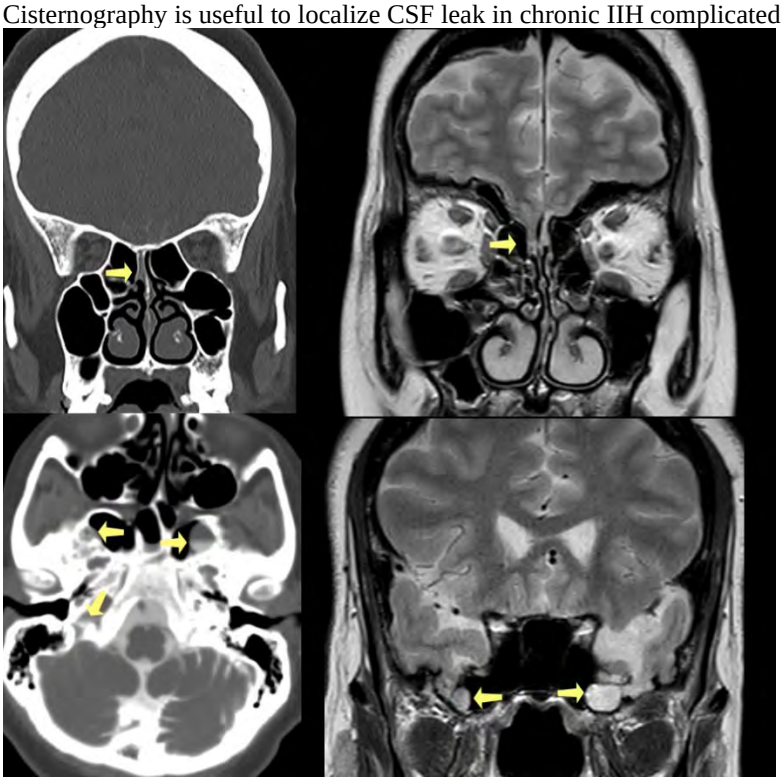
(Filename: TCT_588_asnr22.jpg)

677

CHANTER Syndrome (Cerebellar, Hippocampal, and Basal Nuclei Transient Edema with Restricted Diffusion)

K Mallikarjun[1], Z Nigogosyan[1], M Parsons[2], R Eldaya[3]

[1]Washington University in St. Louis School of Medicine, St. Louis, MO, [2]Mallinckrodt Institute of Radiology, St. Louis, MO, [3]Washington University, St Louis, MO

Purpose

Two patients presented to our emergency room similarly in an unresponsive state following fentanyl overdose. Both remained obtunded after opioid antagonist administration, and were found to have obstructive hydrocephalus on initial Computed Tomography (CT). Both patients were intubated on arrival and gradually improved after surgical treatment of their hydrocephalus and herniation. At discharge, both patients had mildly improved mental status with the ability to follow simple commands.

Materials and Methods

Initial CT demonstrated diffuse cerebellar swelling with obstructive hydrocephalus and herniation. MRI showed diffusion restriction involving the bilateral cerebellar cortex, hippocampi, and basal nuclei, with sparing of the cerebral cortex.

Results

These patients' imaging findings are consistent with a recently described diagnosis called cerebellar, hippocampal, and basal nuclei transient edema with restricted diffusion (CHANTER) syndrome. This syndrome is thought to be a result of opioid neurotoxicity, causing selective cytotoxic edema in the bilateral hippocampi and cerebellar cortices, which progresses to cause obstructive hydrocephalus. As in our patients, if this pattern is recognized early on imaging and quickly treated, the prognosis can be favorable. Without treatment, herniation can result and can be fatal.

Conclusions

This novel pattern of findings of CHANTER syndrome should be on the differential in patients who present to the hospital in an unresponsive state after recent opioid use in the context of the above imaging findings. Additional diagnoses on the differential with similar yet distinct imaging findings can include ischemic stroke, anoxic brain injury, toxic and metabolic insults, posterior reversible encephalopathy syndrome (PRES) and "chasing the dragon" leukoencephalopathy.

CHANTER syndrome 33 year old patient

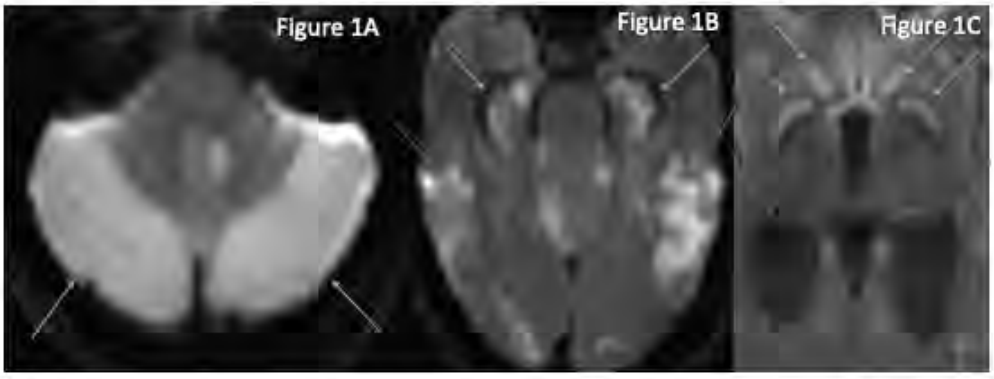

Figure 1. Magnetic Resonance Imaging (MRI). Diffusion Weighted Sequence (DWI). Figure 1A. MRI DWI sequence at the level of the cerebellum demonstrate diffuse cerebellar diffusion restriction (white arrows) (ADC map not shown). Figure 1B. DWI sequence demonstrate diffusion restriction of both hippocampi (white arrows) with additional cortical involvement (blue arrows). Figure 1C. DWI images demonstrate diffusion restriction involving both basal ganglia (white arrows) with obstructive hydrocephalus (blue arrows).

(Filename: TCT_677_CHANTERimageASNR.jpg)

819

Charcot Spine After Spinal Cord Lipoma Resection

C Yalniz[1], R Riascos[1], J McCarty[1]

[1]The University of Texas Health Science Center at Houston, Houston, TX

Purpose

45-year-old patient with history of spinal cord tumor resection and paraparesis presented with new onset back pain and MRI of thoracic and lumbar spine was ordered with indication of 'ruling out abscess'.

Materials and Methods

Sagittal T1-weighted, T2-weighted MRI images of the lumbar spine are demonstrating diffuse osseous destruction and disorganization

with accompanying debris at the lumbosacral junction, involving the posterior elements from L4 through S1 and extending to the anterior paraspinal soft tissues, adjacent psoas muscles and interspinous muscles. There is widening of the L5-S1 disc space with a large joint effusion as well as destruction of the L5 and S1 opposing endplates. Bony fusion of the L4 and L5 vertebrae is also seen. Sagittal CT and T2-weighted MRI images of the thoracic spine are demonstrating prior T2-T4 laminectomy, diffuse cord atrophy, and possible focal myelomalacia at T2-T3, consistent with patient's history of spinal cord lipoma removal. Spinal canal is severely narrowed between T6-T11 with short pedicles and facet hypertrophy resulting in cord compression. There is increased T2 signal, consistent with myelopathy at the level of the prior surgery and atrophy of the spinal cord from the upper thoracic spine to the level of T11. Findings are consistent with spinal neuroarthropathy at the lumbosacral junction with diffuse osseous destruction, disorganization with accompanying debris, disc space effusion and adjacent paraspinous muscle edema.
Results
Spinal neuroarthropathy (SNA), or Charcot spine is a progressive destructive arthropathy occurring after loss of neuroprotective sensation and proprioceptive reflexes, most commonly after a traumatic spinal cord injury. Repetitive microtrauma can lead to destruction of the intervertebral articulations, causing deformity and loss of function. The involvement of both anterior and posterior elements is the most important imaging finding for diagnosis of SNA. In addition, vacuum phenomenon within the disc, malalignment, fluid collections with osseos debris and paraspinal soft-tissue masses are other common findings. The treatment of SNA consists of surgical debridement, reduction, and fusion.
Conclusions
Imaging diagnosis can facilitate early intervention by distinguishing SNA from imaging mimics and prevent further neurologic damage.

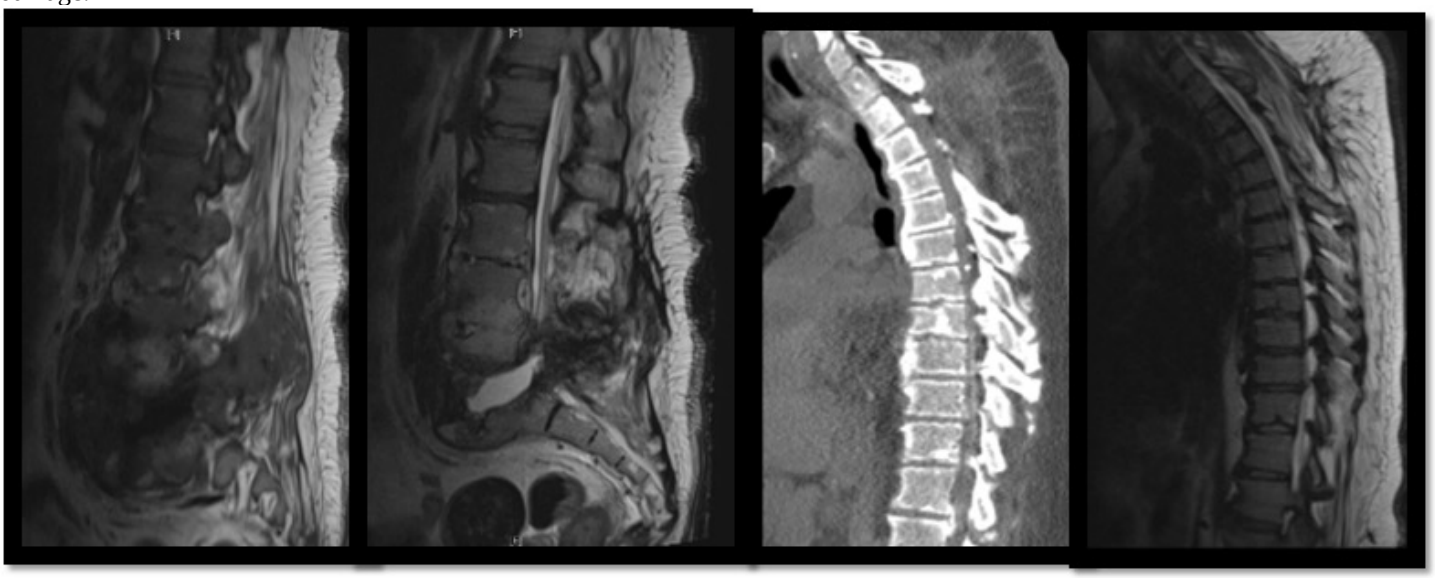

(Filename: TCT_819_Picture11.jpg)

914

Chemotherapy-Induced Myelopathy: An Uncommon Cause of Dorsal Cord Syndrome

D Cohen-Addad[1], S MOHAN[2], V Patel[1]
[1]University of Pennsylvania, Philadelphia, PA, [2]UNIVERSITY OF PENNSYLVANIA, PHILADELPHIA, PA

Purpose
54-year-old female with relapsed diffuse large B-cell lymphoma and bi-weekly intrathecal (IT) chemotherapy (methotrexate & cytarabine) presented 2-months later with worsening headaches, decreased per oral intake, and new onset loss of sensation
Materials and Methods
MRI shows symmetric holocord dorsal column signal abnormality, with sparing of the anterior and lateral columns, which was new from the pretreatment MRI two months prior. There was interval improvement in diffuse leptomeningeal enhancement
Results
Dorsal cord syndrome (DCS) is a debilitating condition with numerous etiologies. Clinical and laboratory workup did not identify a clear cause, with normal B12 levels, severe axonal sensory polyneuropathy on EMG, and elevated protein on CSF. Given interval development of symptoms and imaging findings after initiation of IT chemotherapy, treatment related myelopathy was the presumed etiology. Myelopathy has been reported with both methotrexate and cytarabine, hence the exact causative agent remains unclear, which we further explore in this Excerpta
Conclusions
DCS can be seen in association with IT chemotherapy, which is a rare but an important cause to recognize for optimal patient management

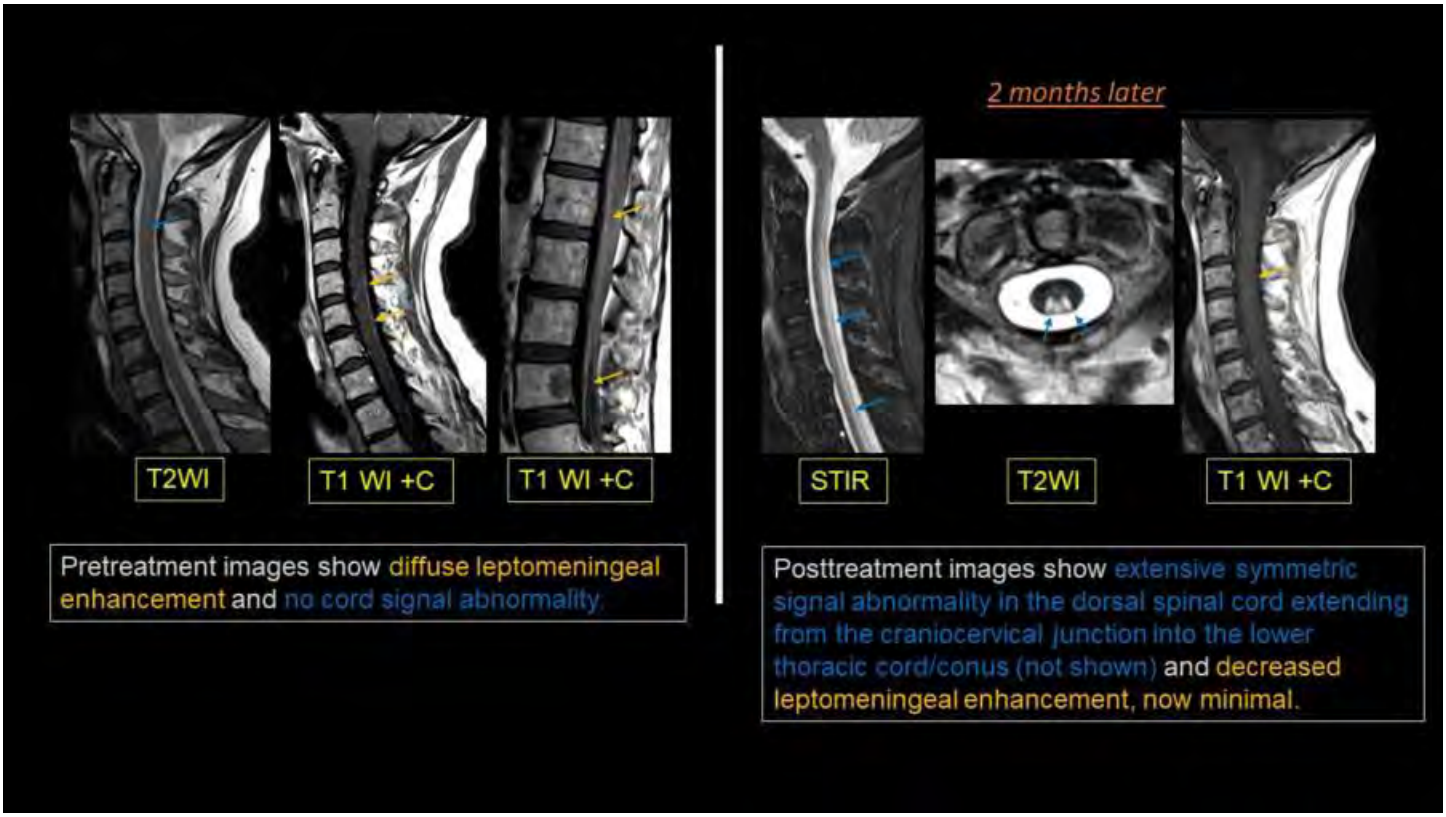

(Filename: TCT_914_AbstractfigureDCS.jpg)

693

Chronic non-granulomatous supraglottitis

A Silberzweig[1], M Starc[1], J Junn[1], M Mori[1]
[1]*Mount Sinai Health System, New York, NY*

Purpose

A 29-year-old woman presented with chronic progressive dyspnea with intermittent improvement with steroids. Laryngoscopy showed edematous supraglottic structures without change despite treatment. Biopsies were negative for tumor, vasculitis or granulomatous change. Serology was negative for rheumatologic and infectious markers.

Materials and Methods

CT and MRI of the neck in the sagittal and axial planes show diffuse enlargement of the epiglottis and aryepiglottic folds. MRI imaging one year later revealed no significant change.

Results

Chronic non-granulomatous supraglottitis is a rare cause of supraglottic edema. Diagnosis can be obtained only following a synthesis of laryngoscopy, imaging, and histologic findings showing chronic inflammatory changes in the absence of other etiology.

Conclusions

Chronic non-granulomatous supraglottitis is a diagnosis of exclusion. Patients present with long-standing dysphagia, dyspnea and dysphonia. On imaging, there is stable diffuse prominence of the supraglottic larynx.

2019

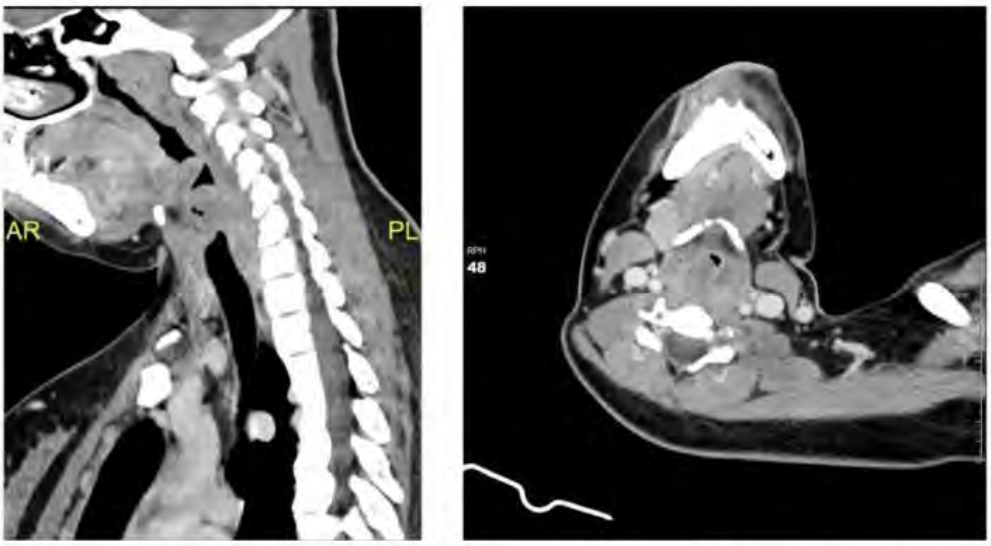

CT of the soft tissue neck with intravenous contrast in the sagittal (left) and axial (right) planes demonstrates diffuse prominence of the supraglottic larynx, causing severe airway narrowing.

2020

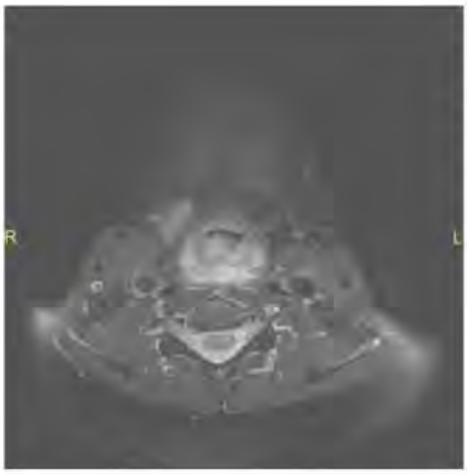

MRI of the soft tissue neck in axial STIR shows no change in supraglottic laryngeal prominence from the CT of the soft tissue neck performed one year earlier.

(Filename: TCT_693_ScreenShot2021-11-14at31754PM.jpg)

291

Cortical Venous Sinus Thrombosis as a Complication of CSF Leak as a Complication of Epidural Anesthesia in the Postpartum Setting: A Case Series

D Yin[1], M Goldberg[1], C LI[1], L Eisenmenger[2], W CHANG[1]
[1]Allegheny Health Network, Pittsburgh, PA, [2]University of Wisconsin - Madison, Middleton, WI

Purpose

Two cases of isolated cortical vein thrombosis (CVT) with intracranial hypotension (IH) after epidural anesthesia are described. Both patients were recently postpartum and presented to the ER with postural headaches and seizures.

Materials and Methods

Imaging showed tubular hyperdensities along the vertex on CT and susceptibility of the parasagittal high cortical veins on MRI, consistent with thrombosis. No dural sinus thrombosis was present. Both patients had findings of IH including cerebellar tonsillar ectopia and subdural collections. Both developed venous infarction in the territory of a thrombosed cortical vein.

Results

Inadvertent dural puncture during epidural anesthesia can result in serious complications. Imaging in both cases suggested IH with ICVT. It is thought that ICVT is the result of dilation and stasis of the cortical veins in the setting of IH.

Conclusions

ICVT in the setting of IH should be considered in recent postpartum patients who received epidural anesthesia presenting with seizures and postural headache.

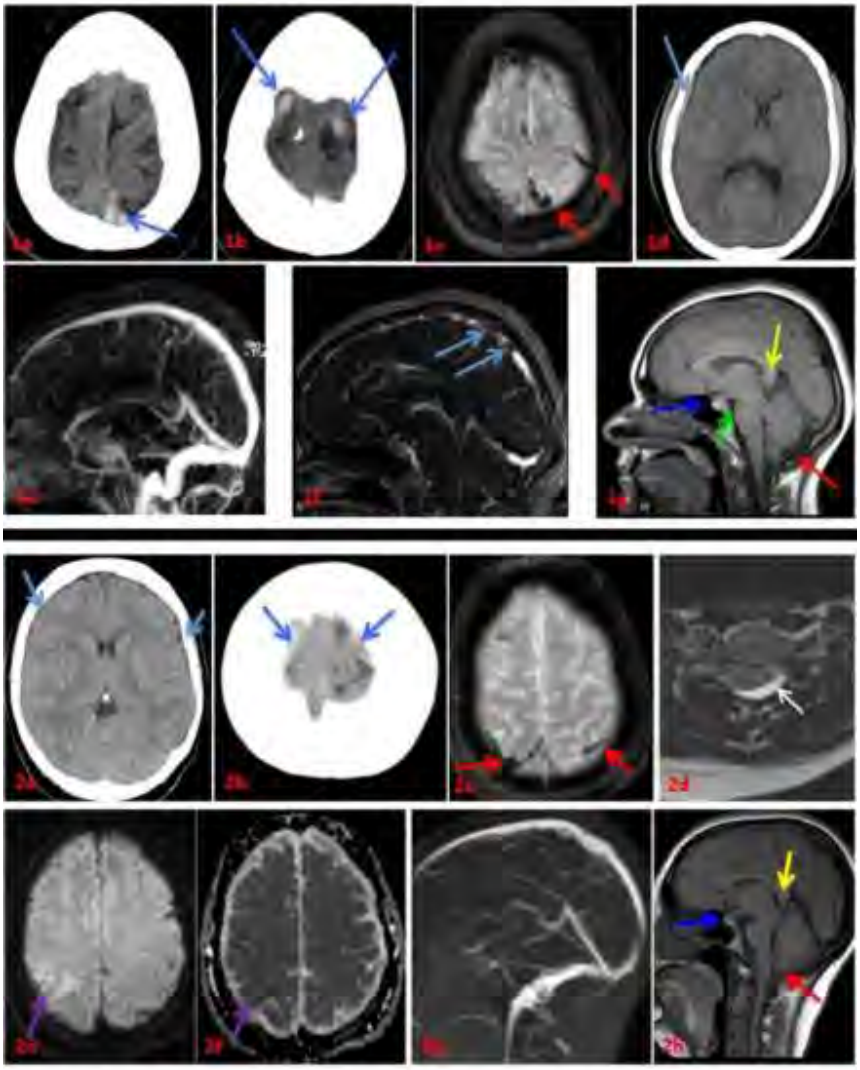

Figure 1 (from first postpartum patient): a-b: Small focal tubular hyperdensities (blue arrows) in the high parasagittal region likely represent thrombosed cortical veins. **c:** Increased susceptibility (red arrows) involving cortical veins in this region are also consistent with cortical venous thrombosis. **d:** Initial head CT demonstrated a right subdural collection of mixed density with acute subdural hematoma superficially and a low density collection deep likely reflecting a subdural hygroma (teal arrow) along the brain surface **e:** Reformatted MRV image demonstrates patency of dural venous sinuses. **f:** Parasagittal source image demonstrates thrombus in adjacent cortical veins (light blue arrows). **g:**T1 sagittal images demonstrate a relatively "closed" pons-midbrain angle (green arrow), splenium depressing the internal cerebral veins and vein of Galen junction (yellow arrow), and relative herniation of the cerebellar tonsils (red arrow), all of which are findings consistent with intracranial hypotension. Prominence of the pituitary (blue arrow) can be attributed to postpartum state and/or another finding of intracranial hypotension.

Figure 2 (from second postpartum patient: a: Initial head CT showed thin bilateral subdural collections (light blue arrows). **b:** Tubular hyperdensities (blue arrows) along the vertex bilaterally (blue arrows) and c: foci of increased susceptibility on gradient images (red arrows) involving cortical veins bilaterally, highly suspicious for thrombosed cortical veins. **d:** Small epidural collection along the dorsal epidural surface of the cervical spine (white arrow), shown here at the level of C6. **e-f:** Restricted diffusion in the right parietal lobe, near a thrombosed cortical vein, consistent with venous infarct. **g:** Reformatted MRV image demonstrates patency of dural venous sinuses. **h:** T1 sagittal images demonstrate splenium depressing the internal cerebral veins and vein of Galen junction (yellow arrow), relatively low-lying cerebellar tonsils (red arrow), and prominent pituitary (blue arrow).

(Filename: TCT_291_cvtasnr.jpg)

1102

CT "Bubble in Oil" Artifact Mimicking Pathology on Non-Contrast Head CT

N Naro[1], K Puthenpurayil[1]
[1]*University of Pittsburgh Medical Center, Pittsburgh, PA*

Purpose

A 36-year-old male patient with a remote history of COVID-19 infection presented with headaches and "fogginess". Initial workup included a head CT, which revealed patchy white matter abnormalities. The patient was admitted for further evaluation including a subsequent brain MRI.

Materials and Methods

Initial non-contrast head CT revealed patchy areas of white matter hypoattenuation affecting the periventricular and subcortical regions as well as the internal and external capsules with accentuation of the grey-white interface. Subsequent brain MRI was normal.

Results

This case is a representative example of a series of 45 cases of both suspected and confirmed artifactual white matter abnormalities obtained over a 3-week period at our institution. Upon discovery of the artifact and evaluation of the scanner, the service engineer found that air bubbles were introduced into the circulating oil that cools the X-ray generating tube, likely via a faulty gasket. Gas bubbles in the path of the beam occurred only when the gantry was tilted, typically only for head CT's. The gas bubbles altered the X-ray beam uniformity resulting in the patchy areas of hypoattenuation in the clinical images. Discovery of this artifact resulted in changes to our daily scanner quality control workflow.

Conclusions

Artifacts related to bubbles in the CT X-ray tube cooling apparatus can mimic pathology and lead to unnecessary treatment and imaging. Recognition of this artifact is important to ensure high quality of care and appropriate scanner quality control.

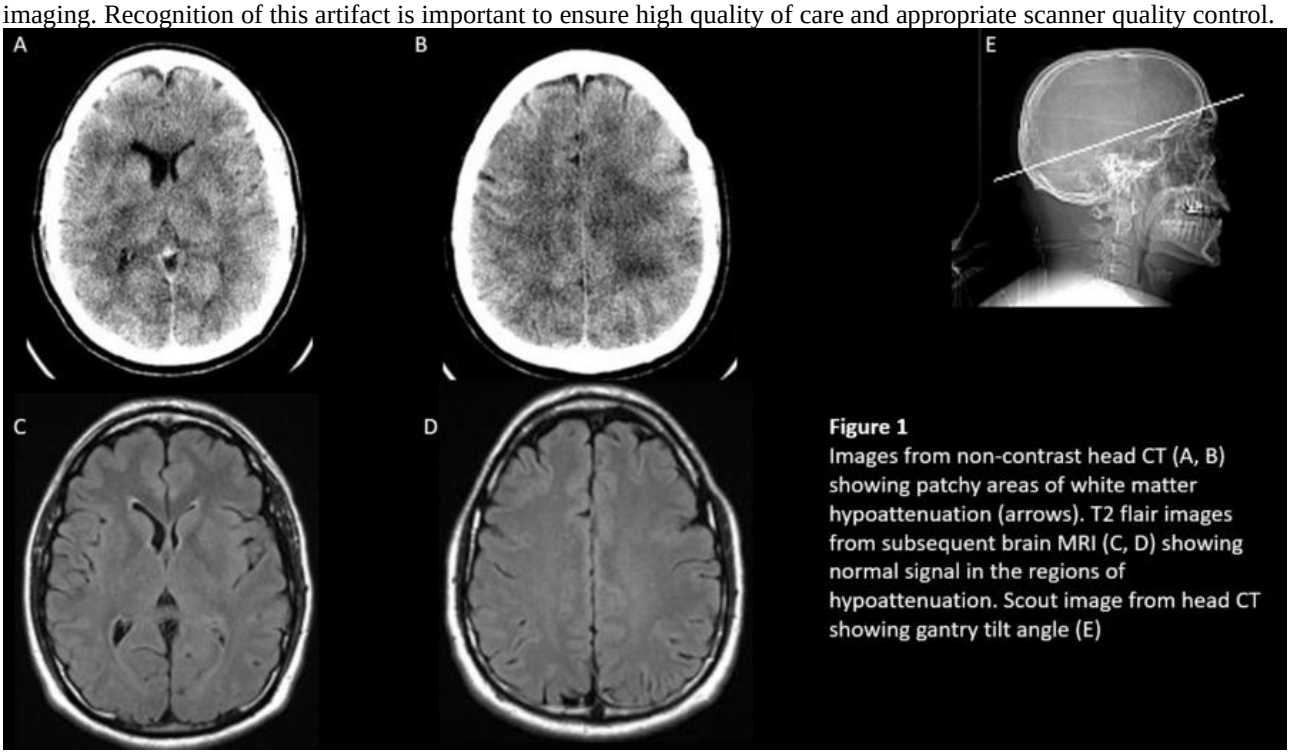

Figure 1
Images from non-contrast head CT (A, B) showing patchy areas of white matter hypoattenuation (arrows). T2 flair images from subsequent brain MRI (C, D) showing normal signal in the regions of hypoattenuation. Scout image from head CT showing gantry tilt angle (E)

(Filename: TCT_1102_Figure1.jpg)

1256

Dermoid Cyst Involving the Foramen Ovale: Characteristic Appearance in an Unusual Location

B Yost[1], E Weidman[2]
[1]*New York Presbyterian Hospital - Weill Cornell Medical Center, New York, NY,* [2]*Weill Cornell Medicine, New York, NY*

Purpose

10 year-old male presents with headache and diplopia for 6-8 weeks.

Materials and Methods

Contrast enhanced MRI demonstrates a well-defined extra-axial lesion centered in the right middle cranial fossa involving the right foramen ovale and lateral wall of the right cavernous sinus. The lesion is T2 hyperintense, T1 heterogenous, and diffusion restricting with areas of peripheral enhancement. CT demonstrates a low-density lesion with smooth expansion of the right foramen ovale.

Results

Given the imaging characteristics, the favored diagnosis was a dermoid or epidermoid cyst. Due to symptomatic 6th cranial nerve palsy the patient underwent surgical resection. Pathology was consistent with a dermoid cyst.

Conclusions

Dermoids/epidermoids most commonly occur in the midline due to persistent ectodermal tissue at sites of closure, such as osseous sutures or neural tube. Characteristic appearance is a diffusion restricting, non-enhancing, fat-containing lesion with indolent features. Dermoids involving the skull base and cavernous sinus have been rarely reported. Classic imaging appearance of these lesions helps troubleshoot in cases of unusual location.

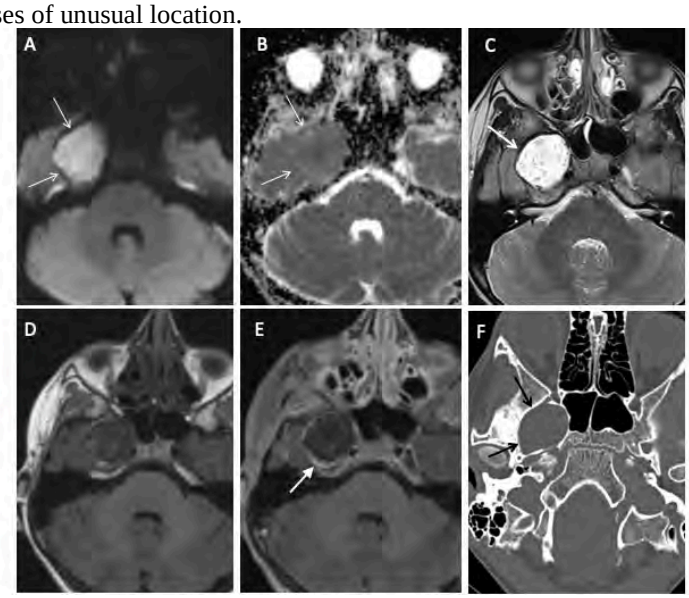

Figure 1: Axial DWI (A) and ADC (B) demonstrate diffusion restricting, well defined ovoid lesion centered in the right middle cranial fossa which is hyperintense on T2 (C) and T1 heterogenous (D). Areas of peripheral enhancement (E, *closed arrowhead*) with lack of internal enhancement. Non-contrast CT (F) demonstrates associated smooth expansion of the right foramen ovale.

(Filename: TCT_1256_ASNRDermoidFigure1Yost.jpg)

1499

Dialysis induced edema (DIE): a delicate interplay between neurons and nephrons

S Walia[1], H Nasser[1], a hassankhani[1], A Nabavizadeh[1], S MOHAN[1]

[1]*University of Pennsylvania, Philadelphia, PA*

Purpose

A 23-year-old male presented with metabolic acidosis in the setting of acute dehydration. A 35-year-old female with ESRD presented with malignant hypertension in the setting of acute transplant rejection. Both patients underwent emergent hemodialysis (HD) after which they suffered immediate neurological deterioration and loss of consciousness. Short-term follow up demonstrated resolution of clinical syndrome and imaging findings.

Materials and Methods

Initial head CT demonstrated bilateral sulcal and cisternal effacement and slit-like ventricles.

Results

Dialysis Disequilibrium Syndrome (DDE) is an uncommon and potentially fatal entity describing altered mental status and diffuse cerebral swelling in patients undergoing HD. We present two cases of clinical and neuroimaging findings strongly supporting a diagnosis of DDE.

Conclusions

While extremely uncommon, neuroradiologists should be familiar with this entity as the diagnosis of DDE can be strongly suggested in the setting of rapid neurologic deterioration after HD.

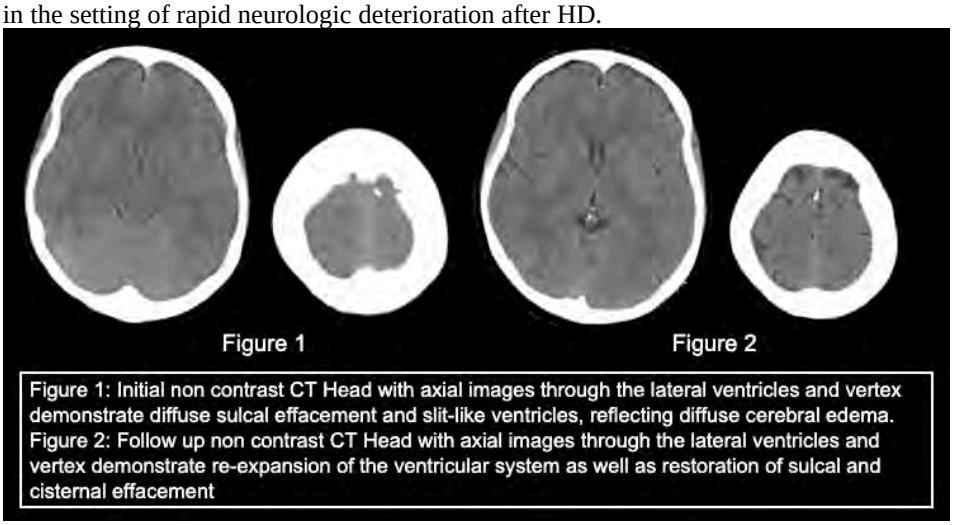

Figure 1: Initial non contrast CT Head with axial images through the lateral ventricles and vertex demonstrate diffuse sulcal effacement and slit-like ventricles, reflecting diffuse cerebral edema. Figure 2: Follow up non contrast CT Head with axial images through the lateral ventricles and vertex demonstrate re-expansion of the ventricular system as well as restoration of sulcal and cisternal effacement

(Filename: TCT_1499_FigureDDE.jpg)

764

DiGeorge syndrome: Malformations of the Middle and Inner Ear

F Hebroni[1], N Pham[2]
[1]UCLA, los angeles, CA, [2]UCLA, Los Angeles, CA

Purpose

We present a 9 year old female with history of 22q11.2 deletion syndrome and bilateral conductive hearing loss, with hearing aids. She also suffers from recurrent otitis media.

Materials and Methods

Right ear: Inner Ear Structures: Aplastic lateral semicircular canal with large common cavity with the vestibule. The cochlea and vestibular aqueduct are normal. Left ear: Inner Ear Structures: Dysplastic appearance of the lateral semicircular canal. Enlarged vestibule. The cochlea and vestibular aqueduct are normal.

Results

Otolaryngologic complications are often seen in 22q11 deletion syndrome and include cleft palate, recurrent otitis media, and hearing loss (most often conductive). Malformations of the middle and inner ear commonly seen in these patients are those of the lateral semicircular canal (including a single cavity with the vestibule), incomplete partition of the cochlea, and dense malleus or stapes. Many of these patients also suffer from recurrent otitis media.

Conclusions

Identifying the middle and inner ear malformations in patients with 22q11 deletion syndrome is important because they often require surgical intervention. We present a case of bilateral lateral semicircular canal (LSSC) malformation, which can complicate the identification of the facial nerve during surgery. LSSC malformations have been reported with both sensorineural and conductive hearing loss. Our patient also had a middle ear anomaly of the ossicular chain; bilateral dense stapes. This is a finding of unknown clinical significance and it is unclear if it is a congenital anomaly or the sequalae of chronic otitis media (tympanosclerosis).

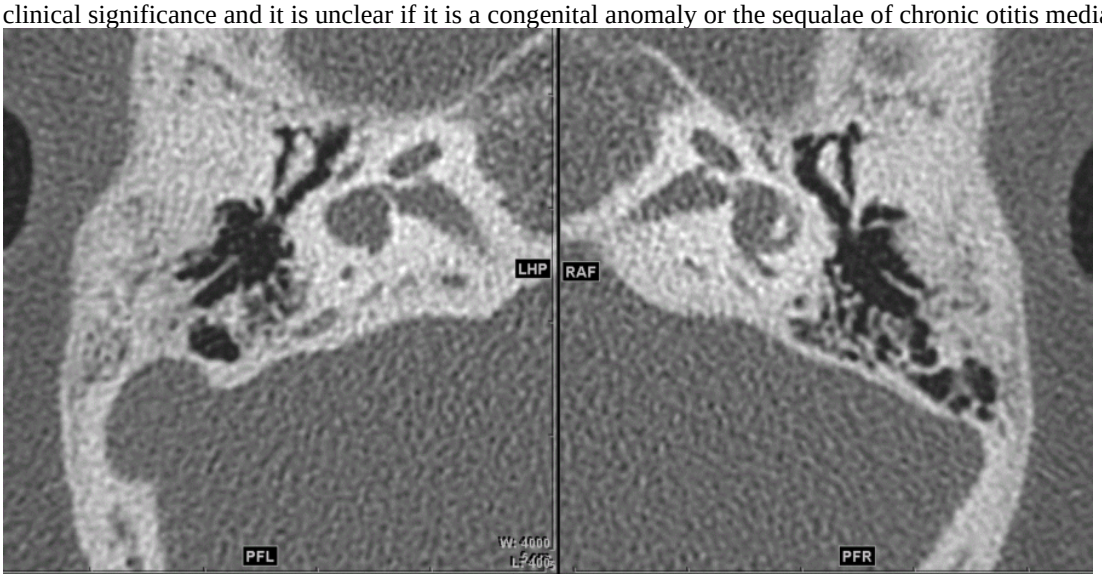

(Filename: TCT_764_DiGeorge.GIF)

989

Ectopic Parathyroid Adenoma within the Pyriform Sinus

W Tjong[1], N Pham[2]
[1]University of California, Los Angeles, Los Angeles, CA, [2]UCLA, Los Angeles, CA

Purpose

68 year old female with a history of papillary thyroid cancer and renal calculi presenting with back pain.

Materials and Methods

Noncontrast and contrast-enhanced CT images display a well-circumscribed avidly enhancing lesion within the left pyriform sinus. On FDG-PET, the lesion is not hypermetabolic. Tc99m-sestamibi scan displays increased radiotracer uptake.

Results

Parathyroid adenomas have typical imaging characteristics on multiple imaging modalities that help to confirm the diagnosis. During development, the upper parathyroid glands, thyroid gland and apex of the pyriform sinus arise from the fourth branchial pouch, providing an embryologic explanation for the positioning in this case.

Conclusions

Ectopic parathyroid adenomas can occur in a number of different locations, including the pyriform sinus. Knowledge of common and uncommon locations will help to improve diagnostic certainty and prevent misdiagnosis.

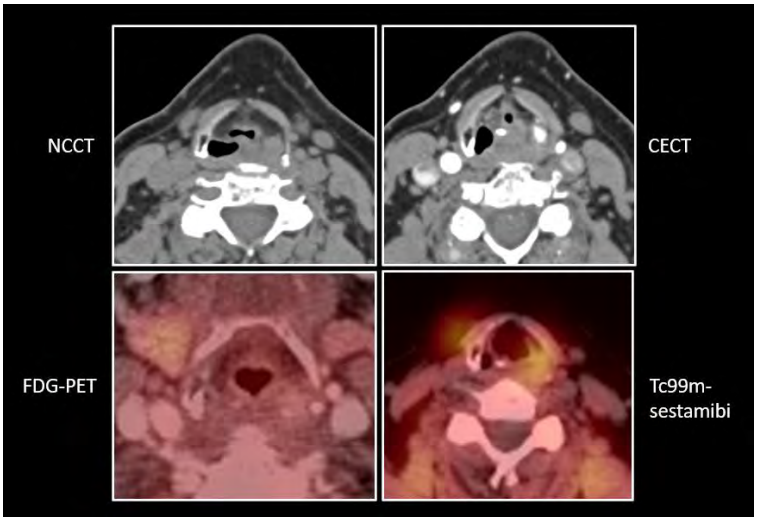

(Filename: TCT_989_EctopicParathyroid.JPG)

1036

Emphysematous osteomyelitis of the spine with epidural involvement

P Shahrouki[1], D Kim[1], J Villablanca[1], N Salamon[2], B Salehi[3]

[1]UCLA, Los Angeles, CA, [2]University of California Los Angeles, Los Angeles, CA, [3]UCLA, Los angeles, CA

Purpose

A 74-year-old male with history of uncontrolled diabetes mellitus type 2 presented to the emergency room with lower abdominal pain and diarrhea. He was found to have fever, leukocytosis, urinary tract infection, and acute renal failure. Initial CT of the abdomen and pelvis revealed findings concerning for pyelonephritis and emphysematous osteomyelitis of the spine at L4 and L5, including direct epidural extension. Urine and blood cultures grew extended spectrum beta-lactamase (ESBL) Escherichia coli. The symptoms and lab abnormalities improved gradually over three weeks of intravenous broad-spectrum antibiotic treatment.

Materials and Methods

Initial CT demonstrated mottled intraosseous air in the L4 and L5 vertebral bodies without cortical destruction. There were additional foci of air within the adjacent disc spaces, also additional extension into the epidural space and minimally to the left iliopsoas muscle. Non-contrast MRI confirmed presence of epidural collection and edema in the paraspinal soft tissues. No significant marrow edema was evident.

Results

Given the rarity of emphysematous osteomyelitis and its potentially rapidly disabling or fatal complications, awareness its imaging characteristics on CT and MRI can lead to early detection and appropriate management. Diagnosis of emphysematous osteomyelitis can be challenging on both CT and MRI, particularly in the spine. Presence of air in the disc space and vertebra is most commonly associated with degenerative changes of the spine, and its presence may lead to misdiagnosis of other entities associated with air in the spine, such as infection. Air-related signal loss on MRI may mask the infection related changes and make the diagnosis difficult on MRI in the early stages. In emphysematous osteomyelitis, cortical destruction is often absent, and instead, a mottled pattern of intraosseous air can be seen, also known as the "pumice stone" sign. The few cases of emphysematous osteomyelitis reported in the literature have more often been seen in patients with DM.

Conclusions

Emphysematous osteomyelitis of the spine is a rare, and potentially fatal, condition more commonly seen in patients with diabetes. It is often characterized by mottled intraosseous air and absence of cortical destruction.

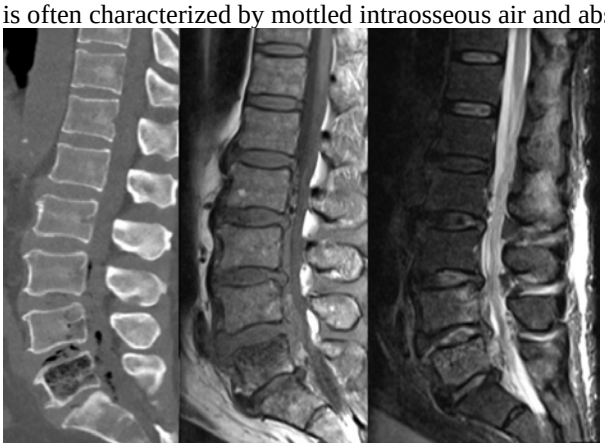
(Filename: TCT_1036_Figure1.jpg)

461

Encapsulated Unilateral Right Maxillary Sinus Polypoid Mass

D Lee[1], N Pham[1]
[1]UCLA, Los Angeles, CA

Purpose

A 33-y.o. male presents with a 2-mo. history of progressive, refractory nasal congestion. A right maxillary sinus mass was evaluated with CT/MRI. Pathological analysis of the mass showed an inverted papilloma, encapsulated by fungal elements.

Materials and Methods

CT showed complete opacification of right maxillary sinus with bony erosion of posterior wall. Postcontrast MRI demonstrated an enhancing mass with a stalk in lateral wall of right maxillary sinus measuring 3cm in diameter surrounded by a capsule of non-enhancing fluid.

Results

Inverted papillomas commonly demonstrate a characteristic striated/cerebriform pattern on MRI. Here, we showcase an atypical case of frond-like enhancement extending from right lateral maxillary sinus, completely encapsulated by non-enhancing fungal elements1.

Conclusions

Chronic rhinosinusitis can be exacerbated by a sinonasal mass. Here, an inverting papilloma concomitant with fungal elements led to an unusual appearance of a frond-like mass surrounded by a capsule of fungal containing fluid.

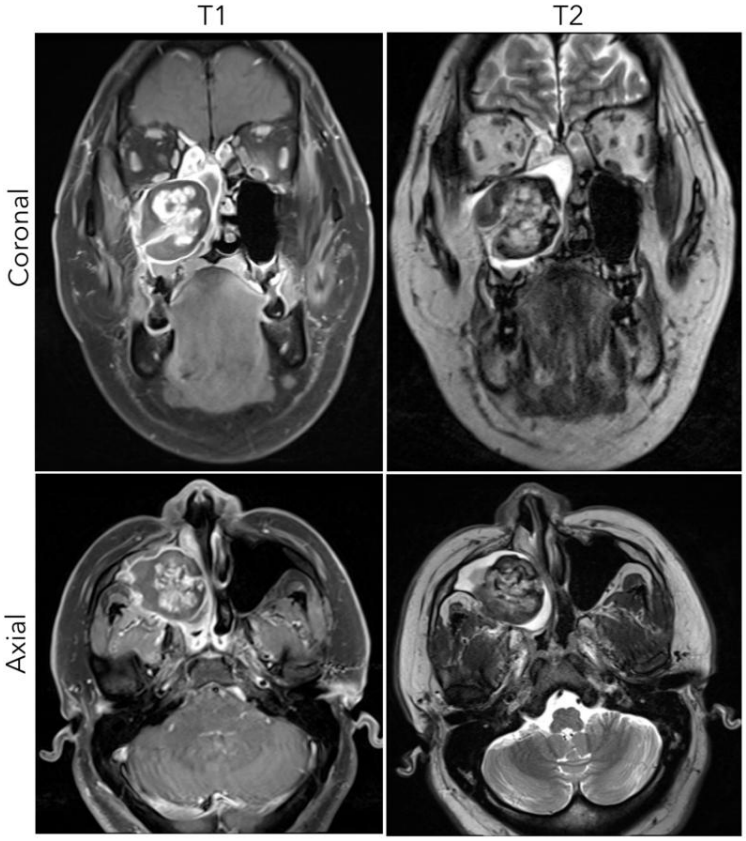

(Filename: TCT_461_ScreenShot2021-10-27at50939PMcopy.jpg)

772

Encephalocraniocutaneous Lipomatosis Presenting Without CNS Lipoma

J Schoen[1], S Edelman[2], K McCullagh[3], S Hung[4], M Castillo[5]
[1]University of North Carolina, Durham, NC, [2]University of North Carolina, Chapel Hill, NC, [3]Stanford University, Stanford, CA, [4]University of North Carlina, Chapel Hill, NC, [5]Radiology, Chapel Hill, NC

Purpose

4-month-old girl with seizures.

Materials and Methods

Head CT and MRI showed right cerebral dysplasia, a temporal arachnoid cyst, and cortical-subcortical calcifications. Contrast-enhanced MRI showed diffuse right hemispheric leptomeningeal (LM) enhancement. There were no CNS lipomas, but a fatty scalp lesion with overlying alopecia was present.

Results

Hemispheric asymmetry, cortico-subcortical calcifications and LM enhancement are considered hallmarks of Sturge-Weber syndrome

(SWS). In this case, SWS was initially suggested as the most likely diagnosis. Later, the diagnosis was revised to encephalocraniocutaneous lipomatosis (ECCL) due to scalp nevus psiloliparus and absence of port-wine stain. ECCL is a neurocutaneous disorder associated with nevus psiloliparus, eye choristoma, and CNS anomalies, of which CNS lipomas are most common (63.5%), followed by meningeal anomalies (arachnoid cyst (36.5%), LM angiomatosis (18.5%)), and hemispheric asymmetry (50%).

Conclusions

Besides SWS, in cases of unilateral cerebral abnormalities and LM angiomatosis, ECCL may be considered as it can present without usual CNS lipomas.

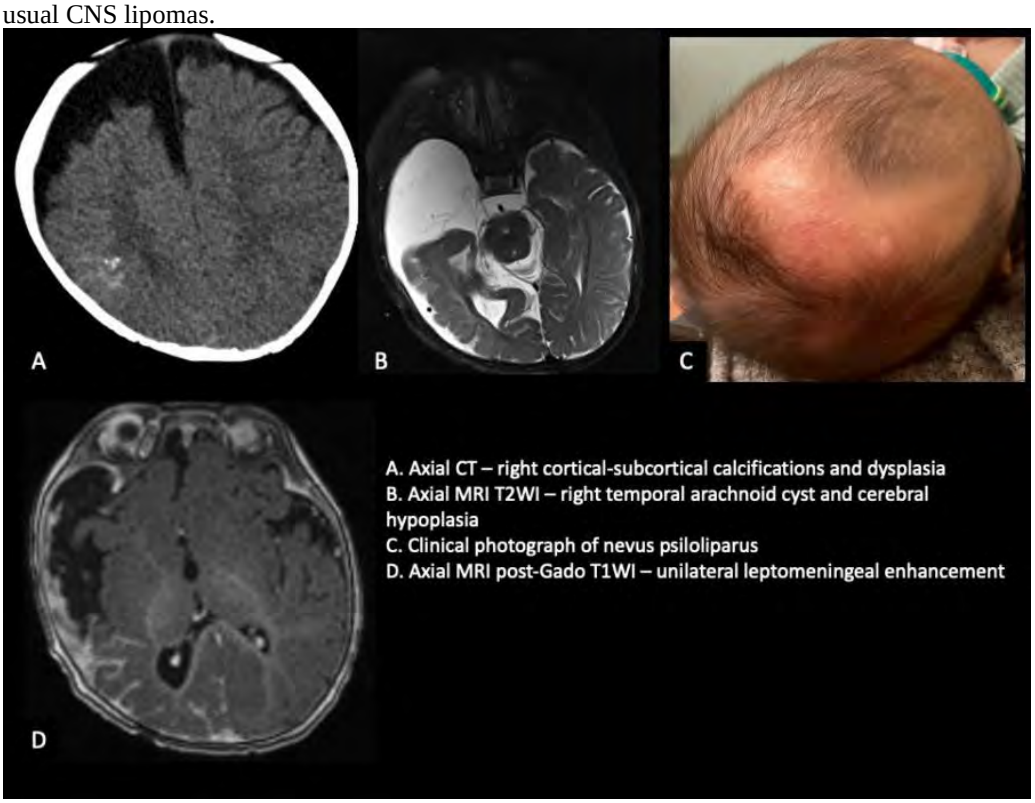

(Filename: TCT_772_Slide1.jpg)

660

Endogenous Endophthalmitis and Multifocal Septic Embolic Infarcts Secondary to Klebsiella Pneumoniae Pyogenic Liver Abscess

S Girn[1], E Shin[2], J Soun[3]

[1]UC Irvine Medical Center, Orange, CA, [2]UC Irvine Medical Center, Irvine, CA, [3]UCI Department of Radiological Sciences, Orange, CA

Purpose

A 59-year-old male with a history of diabetes presented with five days of fever and chills and was found to have numerous neurologic complications during his hospital course due to Klebsiella pneumoniae pyogenic liver abscess (KPPLA).

Materials and Methods

Imaging findings included seeding of the left orbit by Klebsiella causing thickening and enhancement of the margins of the globe and retrobulbar inflammatory changes concerning for post-septal cellulitis and endophthalmitis. Additionally, the patient developed numerous infarcts within the bilateral basal ganglia as well as left MCA territory suspicious for septic emboli.

Results

Endogenous endophthalmitis can develop as the result of KPPLA. Several recent reviews have stated that a large percentage of patients require evisceration with post-operative positive vitreous cultures for K. pneumoniae as in our patient.

Conclusions

K. pneumoniae endophthalmitis is a rare but devastating ocular infection. Physicians should be aware of this as a possibility in a diabetic older male patient with new visual deficits and ongoing systemic infectious symptoms.

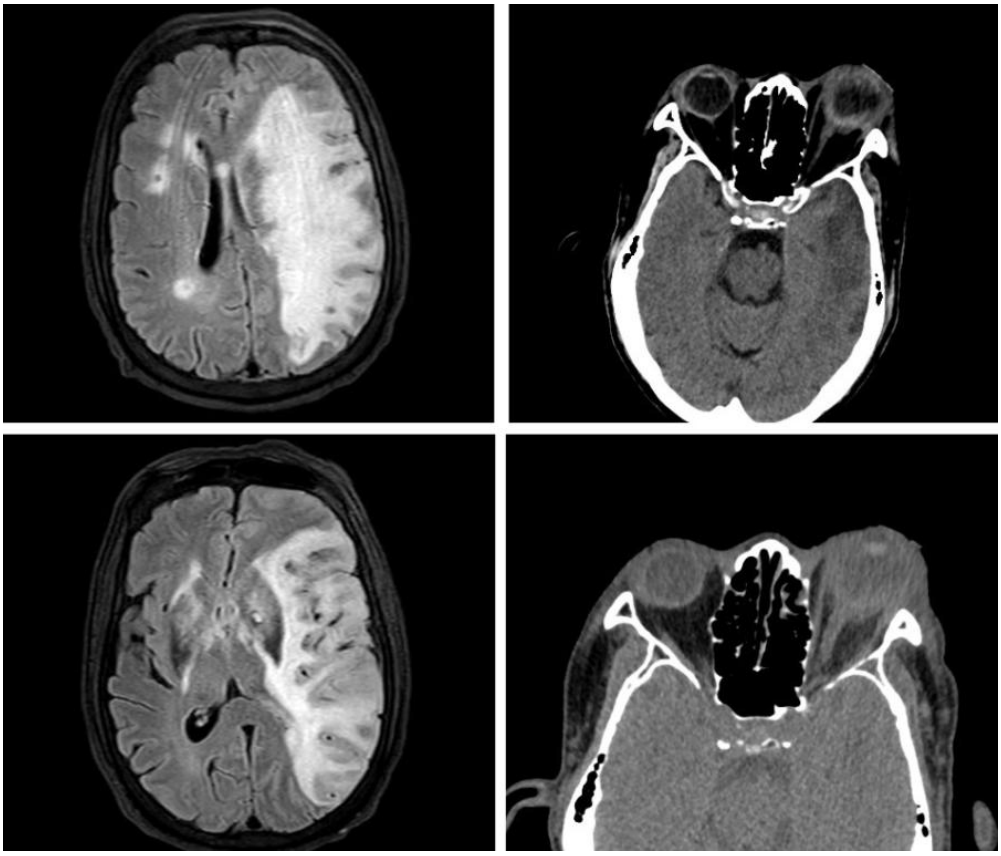
(Filename: TCT_660_KlebsiellaCaseImages.jpg)

915

Enlargement of the Anterior Median Spinal Vein in Craniospinal Hypotension Mimicking Dural Arteriovenous Fistula

D Cohen-Addad[1], V Patel[1]
[1]*University of Pennsylvania, Philadelphia, PA*

Purpose
65-year-old male with 2-year history of progressive ataxia and myelopathy. Outside institution MRI showed superficial siderosis and reported prominent anterior spinal "artery", raising possibility for dural AVF (dAVF)
Materials and Methods
MRI shows an epidural spinal CSF collection, epidural venous plexus engorgement, and enlargement of intradural spinal veins, most notably the anterior median spinal vein (not artery). There was no evidence of dAVF on angiography. CT myelogram shows a T8-9 calcified disc extrusion as the suspected cause of the CSF leak, with subsequent surgery and resolution of spinal venous enlargement on follow-up imaging
Results
Enlargement of intradural spinal veins, especially the anterior median spinal vein, is a rare finding that is not as well recognized or reported as the other repository of findings seen with craniospinal hypotension, which can also be explained by the Monro-Kellie hypothesis. This is an important finding to not mistaken for dAVF when seen along with other imaging findings of craniospinal hypotension
Conclusions
Enlargement of intradural spinal veins in craniospinal hypotension is a rare but important finding to recognize as it can mimic dAVF

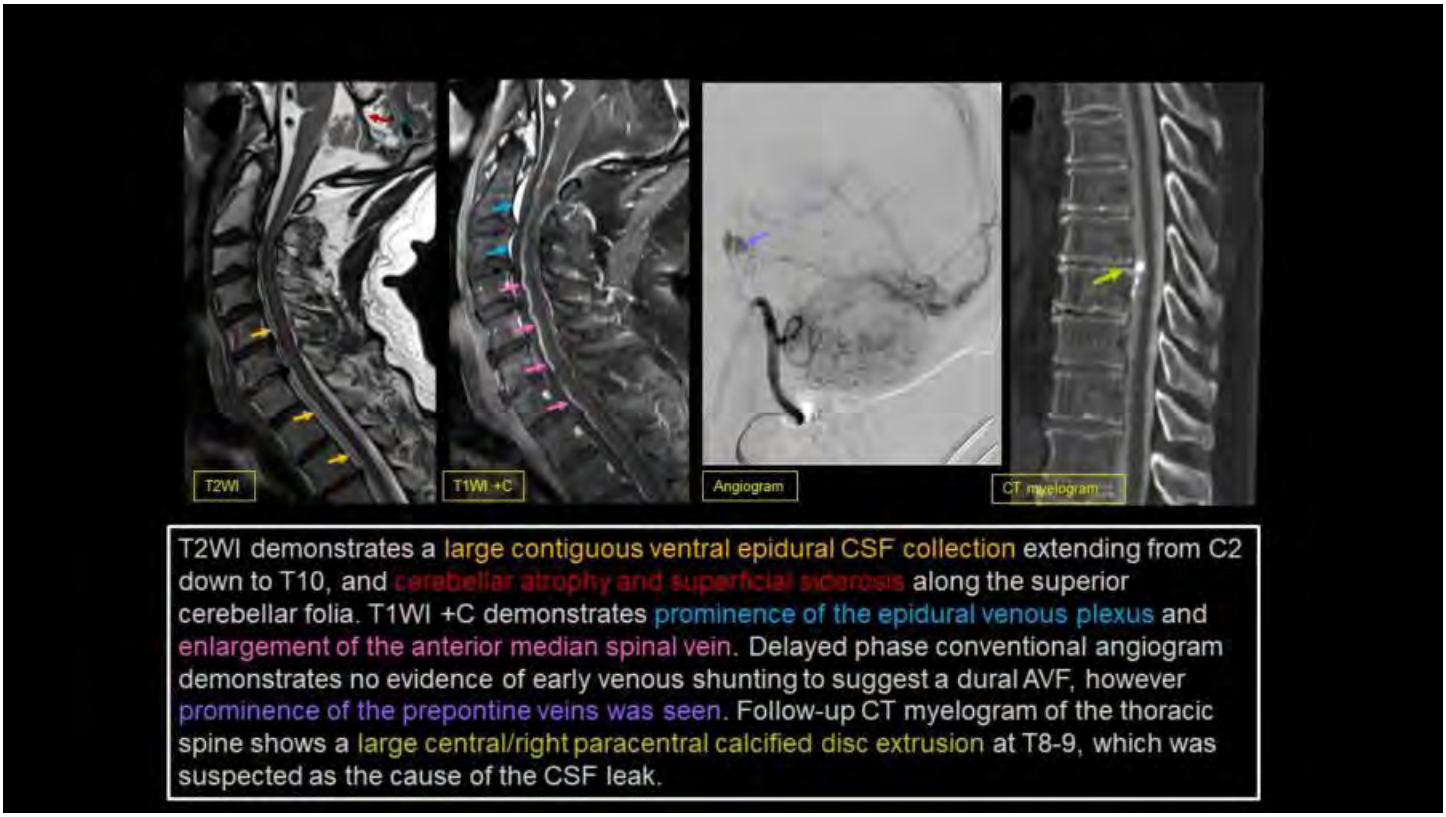

(Filename: TCT_915_Abstractfigure-Anteriormedularyvein.jpg)

1165

Giant Arachnoid Granulation With Associated Gyral Herniation

M Hurley[1], G Kilimnik[2], O Pasternak Wise[1]
[1]University of Chicago, Chicago, IL, [2]University of Chicago, Evanston, IL

Purpose

Asymptomatic 52yo male volunteer for research MR brain

Materials and Methods

Circumscribed, approx 1.5 cm rounded structures in the posterior superior sagittal sinus (SSS) and torcular herophili (TH), following CSF signal, consistent with giant arachnoid granulations (AGs) (arrows, arrowheads, Figure 1, A and B). The SSS AG contains a herniated precuneal gyrus with associated encephalomalcic gliosis (arrows, arrowheads, Figure 1, C and D).

Results

Brain herniation into arachnoid granulations (BHAG), has been recently well described with two large case series published in 2016. However, it remains a relatively unknown entity among neuroradiologists despite it often having an "Aunt Minnie" imaging appearance as in this case. Many cases described are more subtle and it is likely that tiny focal BHAGs may go unnoticed. Most occur along the transverse sinus where the AGs are most prominent and BHAG involving the Superior Sagittal Sinus is 5-10 times less common. In some cases, the AG itself can be small and not well visualized with apparent direct hernitation of brain into the sinus, however there is likely to be an unidentified AG in these cases. BHAG can be associated with headaches and pseudotumor cerebri. Not only does chronic intracranial hypertension cause AGs to enlarge but it may be a cause of the brain herniation. Most cases are otherwise asymptomatic although the associated brain injury can be a cause of seizures or focal neurological deficits. Whereas typical AGs follow CSF signal, giant AGs can have more variable signal due to traversing veins, septations and otherwise unidentifiable soft tissue. One should look carefully at the adjacent brain for cortical extrusion, deformity, atrophy and gliosis in the adjacent brain as evidence of BHAG.

Conclusions

Brain herniation into an arachnoid granulation is an often overlooked finding that can lead to misdiagnosis of brain injury

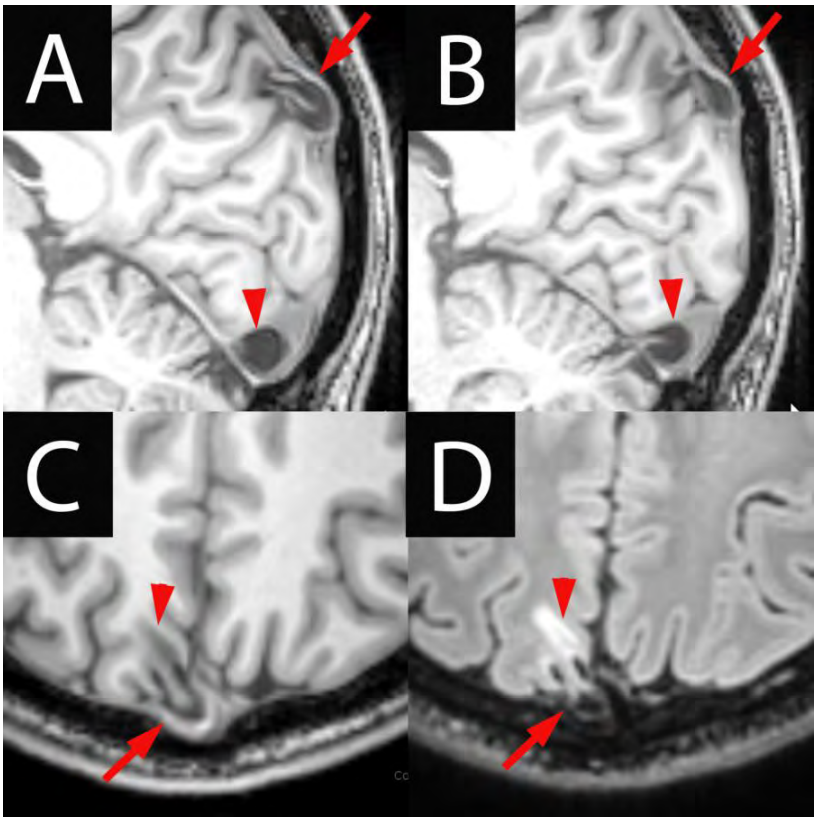

(Filename: TCT_1165_Figure1.jpg)

1245

Glioblastoma masquerading as an Intracerebral Hematoma : A Case Report.

S Kathpalia[1]

[1]ABVIMS and Dr. RML Hospital, Delhi, India, Delhi, Delhi

Purpose

A 60 year old female presented with insidious onset of headaches since 1 year followed by acute left sided hemiparesis and altered sensorium. Past medical history was unremarkable. Patient was intubated due to low GCS. The patient underwent right decompressive craniectomy on account of deteriorating GCS and significant midline shift.

Materials and Methods

Admission NCCT was done which revealed an ill defined intracranial hematoma in right lentiform nucleus and insular cortex with significant perilesional edema , causing midline shift of 11 mm. Decompressive craniectomy was done . Post operative NCCT revealed similar appearing lesion with a midline shift of 9 mm. MRI done 4 days later revealed a heterogenous signal intensity mass lesion involving right lentiform nucleus and insular cortex appearing hypointense with areas of peripheral hyperintensity on T1 weighted images. On T2 weighted and FLAIR images, few isointense and hyperintense regions are noted in the lesion with peripheral hypointense regions. . Post contrast images revealed thick, nodular peripheral enhancement with central necrosis. Spectroscopy revealed choline peak and increased choline creatine ratio in solid portion and lactate peak in central necrotic region.

Results

Glioblastomas or other intracranial neoplasms presenting as Intracranial hematoma (ICH) represent a diagnostic dilemma owing to the fact that recognition of the neoplastic lesion is not always possible with CT, which is the initial imaging modality to rule out an ICH. Intratumoral hemorrhage is an important entity that illustrates the concept of using MR to further characterize a CT documented hematoma which is very well illustrated in our case report. MR signal intensity patterns of hemorrhagic intracranial neoplasms are unalike from those of nonneoplastic intracranial hematomas. In malignant neoplasms, multiple concomitant stages of hematoma, presence of nonhemorrhagic tumor tissue, delayed evolution of blood breakdown products and persistent surrounding high signal intensity on T2/FLAIR images even in late stages which were all seen in our case.

Conclusions

A high index of suspicion on initial imaging has to be kept based on the patient demographics, atypical location and appearance. MRI is the basic workhorse, however advanced MRI imaging such as MRI spectroscopy can be particularly helpful in early diagnosis.

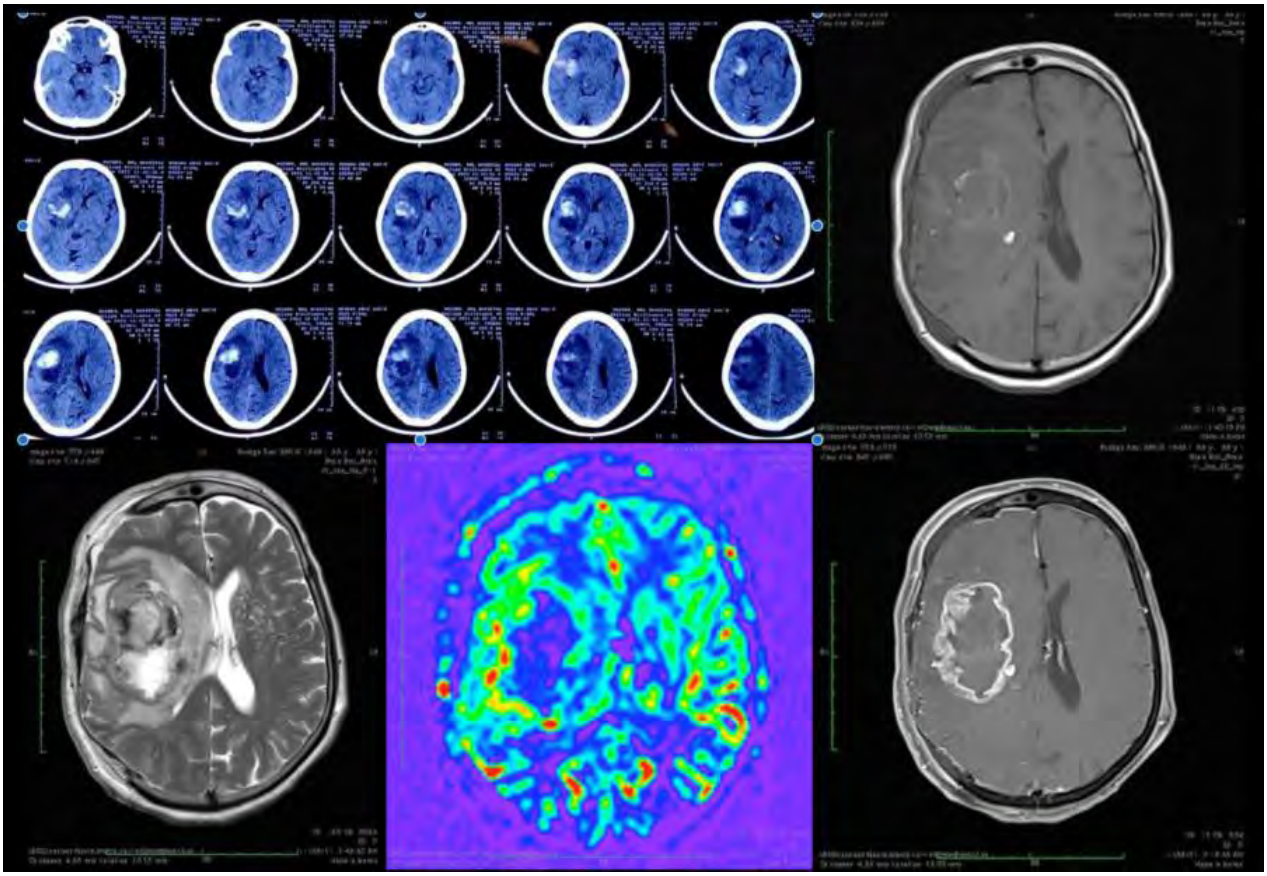
(Filename: TCT_1245_kathpalia.jpg)

1515

Hemibody Heaviness and Transient Aphasia

S Tamir[1], A Lignelli[2]

[1]Columbia NY Presbyterian, New York, NY, [2]Columbia University Irving Medical Center, New York, NY

Purpose

77 year old male with hypertension, hyperlipidemia, and past medical history of seizures and Rheumatoid arthritis (RA) presented with transient episodes expressive aphasia with right sided hemibody sensorimotor deficits. LP was notable for an inflammatory CSF profile. A similar episode 14 years prior responded to steroids.

Materials and Methods

Patient underwent contrast enhanced MRI of the brain which showed enhancing leptomeningeal disease in the left parietal lobe that restricted diffusion. Additionally, imaging showed scattered punctate foci of enhancement in bilateral white matter, some demonstrating restricted diffusion.

Results

Differential diagnosis included granulomatous inflammatory process such as neurosarcoid or rheumatoid arthritis, neoplasm such as lymphoma or metastasis, or infection. Patient subsequently underwent biopsy with final pathology demonstrating necrotizing granulomatous leptomeningitis consistent with rheumatoid leptomeningtitis. Definitive evidence for vasculitis was lacking however there was perivascular inflammation and gliosis. While intracranial manifestations of autoimmune diseases such as sarcoidosis and systemic lupus erythematosus (SLE) are well known and more common, the intracranial CNS manifestations of rheumatoid arthritis are rare. For example, neurosarcoid tends to show meningeal granulomatous inflammation/thickening and SLE can show white matter disease, infarcts and vasculitis. Rheumatoid arthritis indirectly involves the central nervous system (CNS). For example, atlantoaxial joint involvement eventually causes ligament laxity and craniocervical settling with mass effect on the craniocervical junction, and facet joint involvement can cause subluxation with mass effect on the spinal cord. Primary intracranial findings, however, are unusual. As Bathn JM et al explains in his paper, CNS pathology findings in rheumatoid arthritis patients include vasculitis, leptomeningeal disease, and nodules. This case restricted diffusion. While not common, RA should be considered in the differential diagnosis of focal leptomeningeal involvement, particularly if associated with restricted diffusion.

Conclusions

While not common, RA should be considered in the differential diagnosis of focal leptomeningeal involvement, particularly if associated with restricted diffusion.

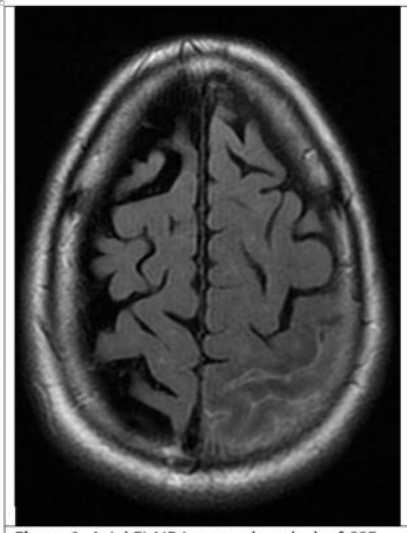

Figure 1. Axial FLAIR images show lack of CSF suppression in the left parietal lobe sulci.

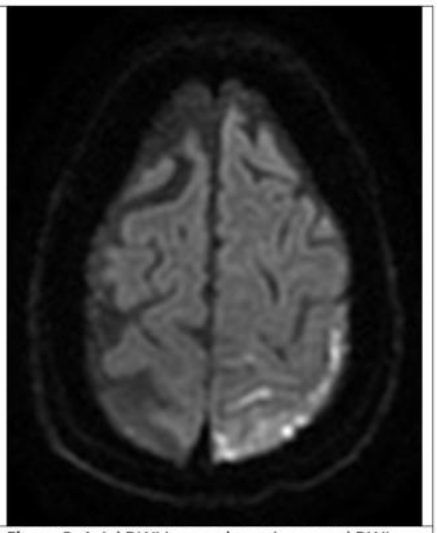

Figure 2. Axial DWI image shows increased DWI with corresponding decreased ADC (not shown) in the left parietal lobe sulci.

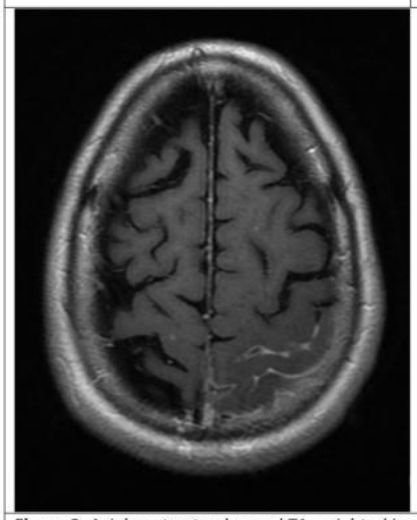

Figure 3. Axial contrast enhanced T1 weighted image shows leptomeningeal enhancement of the left parietal lobe.

(Filename: TCT_1515_Picture.JPG)

1281

Hyperperfusion Associated with a DVA: An Atypical Perfusion Pattern to Recognize

M PEARL[1], P Dave[2], J Murnick[3]

[1]Children's National Hospital, Washington, DC, [2]George Washington University School of Medicine, Atlanta, GA, [3]N/A, N/A

Purpose

18-year-old male with a history of ADHD, PTSD, and unexplained weight loss presents with persistent headaches.

Materials and Methods

A). Post contrast axial T1W image shows a mildly prominent left frontal vein and no distinct AVM nidus. B). Corresponding axial perfusion image shows elevated CBF in the parenchyma surrounding the prominent vein seen in A. C). Sagittal view from a left internal carotid (ICA) angiogram shows no AVM nidus and no evidence of arteriovenous shunting. D). Coronal 2D reconstruction from a left ICA 3D DSA shows the "caput medusa" appearance of a small left frontal DVA that corresponds to the area of hyperperfusion on MRI.

Results

DVAs are the most common cerebrovascular malformations, have a characteristic imaging appearance, and are frequently recognized on CT and MRI. They can be associated with other vascular anomalies including cavernous malformations and arteriovenous shunting lesions, in which case they are considered transitional malformations. Alterations in perfusion in and around the DVA can be present and these variations are important to recognize.

Conclusions
Variable perfusion patterns can be associated with DVAs in the presence or absence of arteriovenous shunting. Diagnostic cerebral angiography is helpful to make this determination.

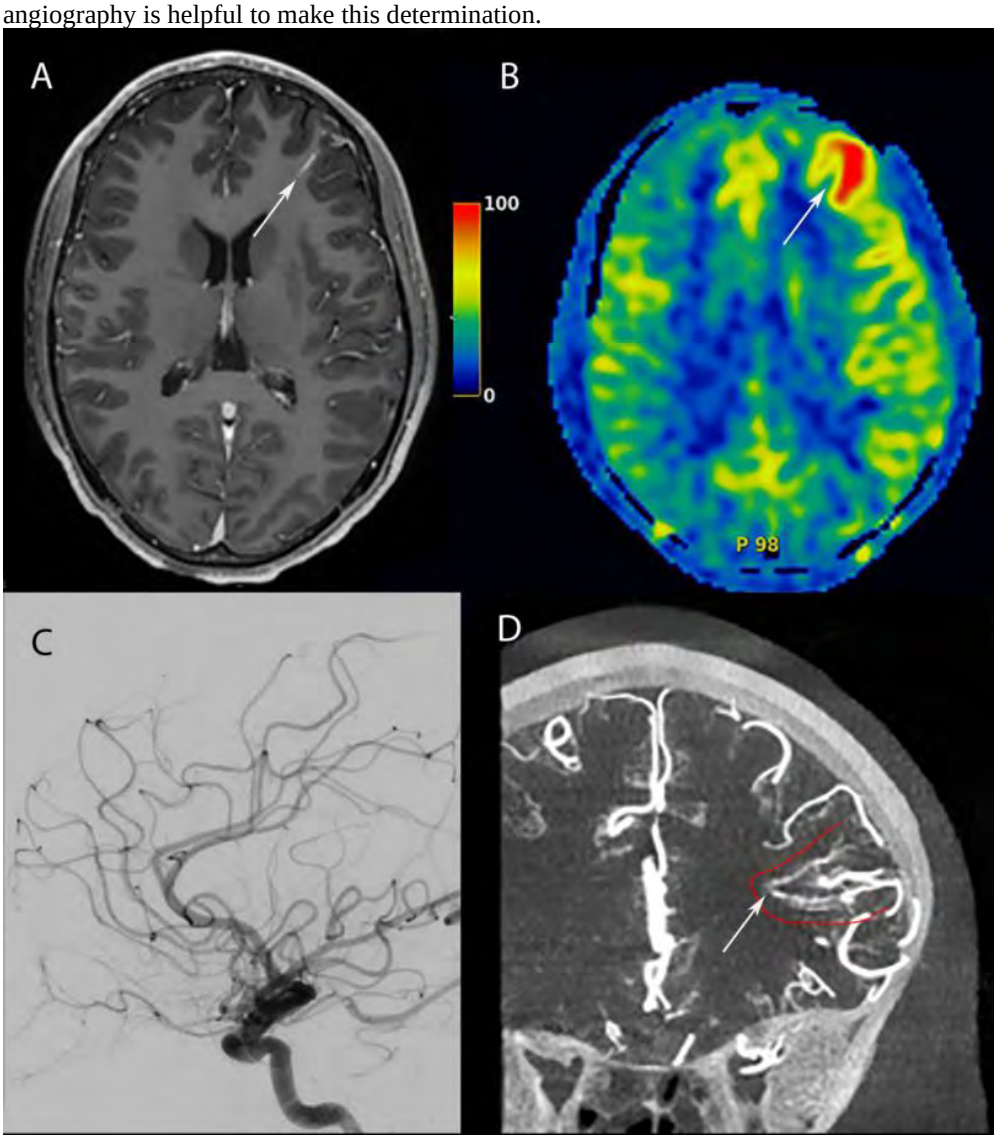

(Filename: TCT_1281_Figure.jpg)

838

Hypothalamic Mixed Glial Neuronal Tumor in an Adult Patient

C Yalniz[1], S Khanpara[1], R Riascos[1]
[1]*The University of Texas Health Science Center at Houston, Houston, TX*

Purpose
54-year-old male with history of thyroid cancer treated in 2010 presented on July 2020 after experiencing a generalized tonic-clonic seizure while swimming.
Materials and Methods
MRI images demonstrates a well-defined round lesion in the left thalamus, adjacent to the body of the left lateral ventricle and extending into the ventricle with a 'claw sign' on T2 sequence. It is predominantly hypointense on T1 and hyperintense on T2 with central curvilinear enhancing areas. On SWI images there are foci of susceptibility artifact within the lesion, consistent with calcification. There are no associated diffusion restriction, concerning for hypercellularity, increase in the cerebral blood flow on ASL or increased relative cerebral blood volume on DSC images. On spectroscopic evaluation, the lesion demonstrates prominent choline peak with inversion of the choline to NAA ratio which measures 2.6 and there is also mild prominence of the lipid peak at 1.3 ppm. The stereotactic biopsies of the mass showed a low-moderate cellularity with myxoid background, bland glial cells and dispersed larger neurons. There was no necrosis, microvascular hyperplasia or mitoses. The large neurons were highlighted with chromogranin, synaptohysin, phosphorylated neurofilament antibody. The findings were consistent with mixed glial and neuronal tumor, WHO grade 1.

Results

Neuronal and mixed glial tumors are uncommon tumors of the central nervous system with varying degrees of neural and glial elements, representing only 0.4-4% of all central nervous system tumors. They are usually seen in children or young adults and most of them are low grade except anaplastic ganglioglioma and other atypical variants. The most common location is temporal lobes, accounting for approximately 70% of the cases. Their imaging characteristic and enhancement can vary between a partially cystic mass with a mural nodule to a complete solid mass. On CT, they are isodense or hypodense, calcified in more than one third of the cases and enhancement can be seen in half of the cases. On MRI they are iso to hypointense on T1 and show T2 hyperintense solid component and variable signal in the cystic component depending on the protein and blood. Calcifications are seen as susceptibility artifact on T2* sequences.

Conclusions

Neuronal and mixed glial tumors are uncommon tumors of the central nervous system with varying degrees of neural and glial elements and they can present with atypical imaging findings and location.

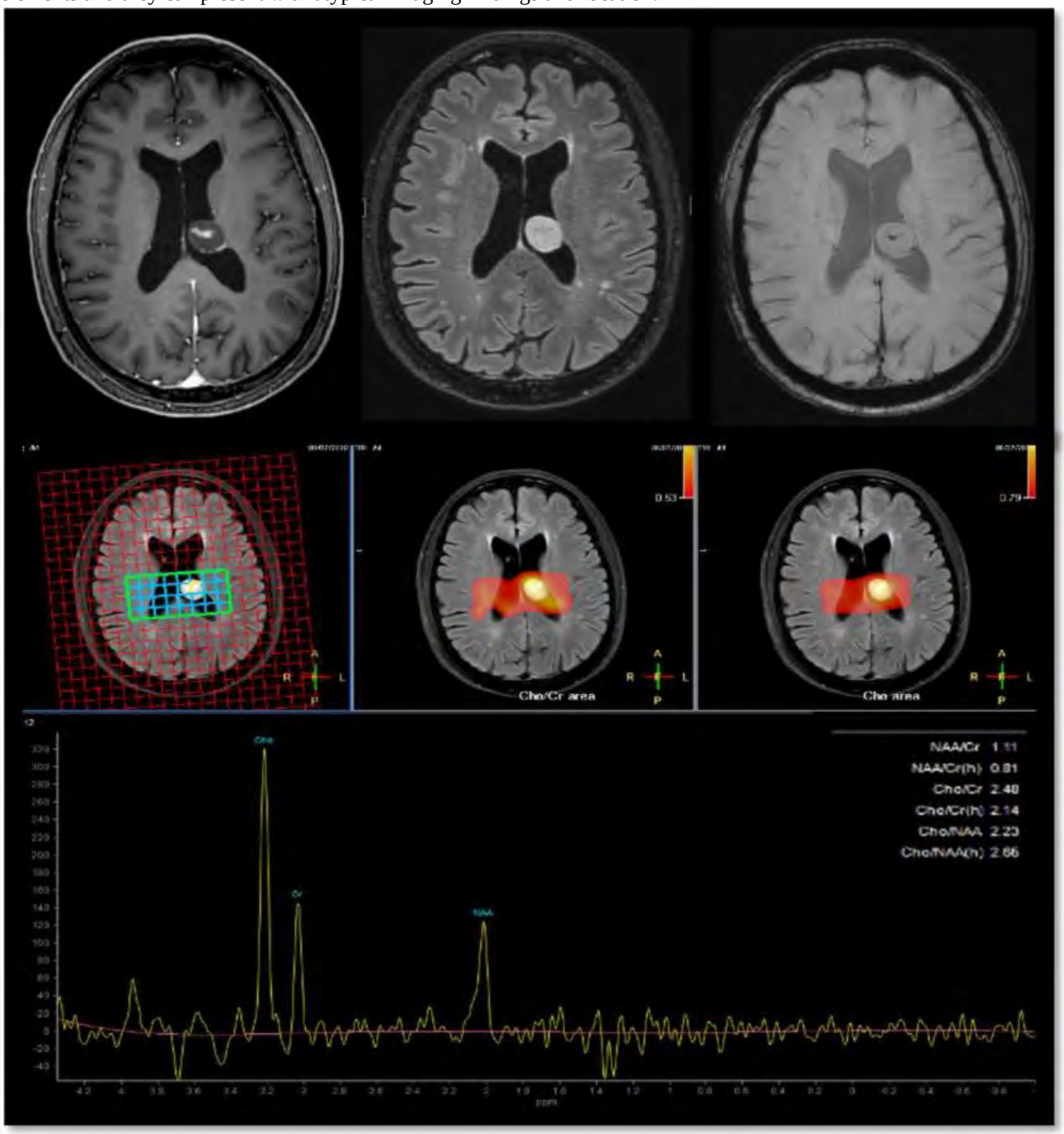

(Filename: TCT_838_Picture3new1.jpg)

1154

Imaging and Clinical Findings in Neuroinvasive West Nile Virus: A Timely Review

A Svec[1], M Shroads[2], D Ritchie[2], J Hughes[2]
[1]Creighton University - Arizona, Phoenix, AZ, [2]Barrow Neurological Institute, Phoenix, AZ

Purpose

In 2021, Arizona saw a rise in mosquito population and cases of West Nile Virus (WNV) after heavy seasonal rain. We describe three patients with severe cognitive, sensory, and motor deficits in whom WNV was confirmed by CSF analysis.

Materials and Methods

Case 1 exhibits classic findings of WNV encephalitis including symmetric thalamic and brainstem DWI and T2 FLAIR abnormality. Case 2 shows similar signal changes in the deep white and gray matter but with parenchymal and vessel wall enhancement in WNV-associated vasculitis. Case 3 demonstrates cauda equina nerve root enhancement in a patient with post-WNV GBS.

Results

On MRI, neuroinvasive WNV can follow the classic pattern or manifest as secondary sequelae of viral illness. Correlation with county rainfall and mosquito data suggests that the index of suspicion should be raised in regions with increased seasonal precipitation.

Conclusions

To review imaging findings in neuroinvasive WNV and to emphasize the role of local environmental factors in disease prevalence.

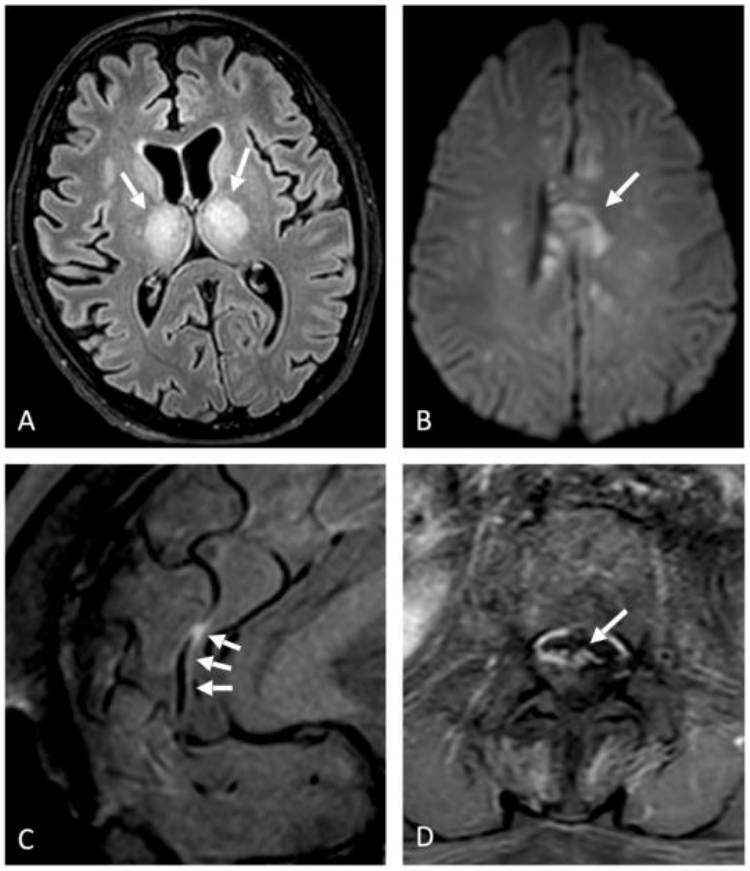

A: Axial T2 FLAIR image from case 1 demonstrates symmetric hyperintense signal abnormality involving both thalami (arrows).

B: Axial DWI image from case 2 shows patchy diffusion restriction in the deep periventricular and pericallosal white matter (arrow).

C: Sagittal post-contrast black blood vessel wall imaging sequence from case 2 demonstrates smooth circumferential wall enhancement of an ACA branch (arrows).

D: Axial post-contrast T1-weighted image from case 3 demonstrates enhancement of the ventral cauda equina nerve roots (arrow).

(Filename: TCT_1154_WNVImage.jpg)

785

Imaging Cerebrotendinous Xanthomatosis -- A Rare Treatable Genetic Disorder of Lipid Metabolism

J Martin[1], C Li[1], J Cline[1], M Ling[1], C Lee[1], J Acharya[1], V Patel[1], A Lerner[1]
[1]University of Southern California, Los Angeles, CA

Purpose

A 31 year old male presented with seizures rapidly progressing to gait disturbance, paraplegia, myopenia, dysarthria, and fecal/urinary incontinence. A sibling had similar symptoms. An Achilles tendon mass was noted. Laboratory tests confirmed cerebrotendinous xanthomatosis (CTX).

Materials and Methods

T2/FLAIR images showed global atrophy and symmetric hyperintensity in the corticospinal tracts and dentate nuclei.

Results
While similar corticospinal tract changes may be seen in amyotrophic or primary lateral sclerosis, the additional signal changes in the dentate nuclei and clinical features instead suggested CTX, a rare genetic disorder of lipid metabolism. Like the neuroimaging findings, tendon xanthomas are suggestive of the diagnosis, but not required. Early diagnosis enables the initiation of metabolite replacement therapy which can reverse symptoms.
Conclusions
Early diagnosis and treatment of CTX is essential to prevent permanent neurologic damage.

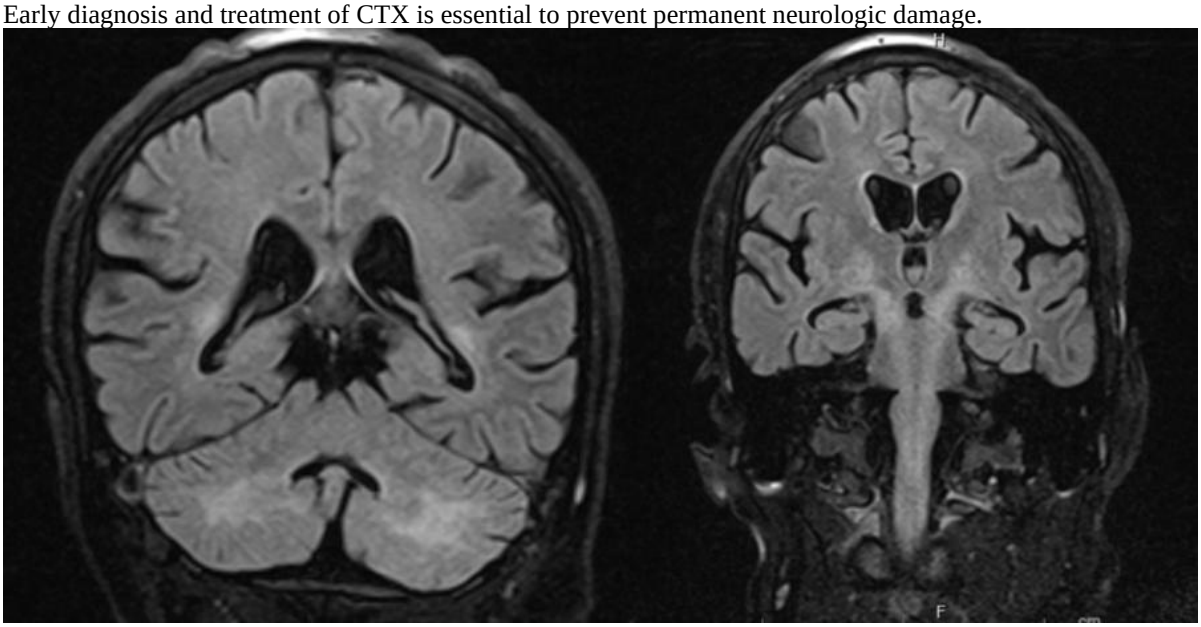

(Filename: TCT_785_CerebrotendinousXanthomatosis.jpg)

934

Imaging of CLIPPERS : Steroid Course not to be Clipped Short

S Bhuta[1], A Prabhu[2]
[1]Gold Coast University Hospital & Griffith University School of Medicine, Gold Coast, QLD, [2]Gold Coast University Hospital, Gold Coast, QLD

Purpose
A 57 year old man was referred for neurology review for vertigo, hearing loss, focal paraesthesia, urinary retention and ataxia for two years. He had no other co-morbid conditions and was not on any medications. On examination he was ataxic with a wide base of support and high stepping gait. He had bilateral lower limb incoordination with hyperreflexia and upgoing plantar reflexes. Upper limb examination was within normal limits. He had bilateral nystagmus, worse on left lateral gaze. He was diagnosed with CLIPPERS based on typical MRI findings. He was treated with IV methylprednisolone 1g for 5 days which showed an improvement in his symptoms. He was discharged on a weaning dose of oral prednisolone. When he was seen in clinic 2 months later, he showed a clinical and radiological response to steroids. His steroids were ceased at the 4 months, which resulted a clinical and radiological worsening of his condition. He had three episodes of inadequate response to steroids, and MRI brain showed overall worsening over 3 years. He was eventually started on 6 monthly Rituximab infusion and since patient had no recurrence of symptoms.
Materials and Methods
MRI brain is modality of choice as a baseline study and for follow up.Localized high signal on FLAIR and T2W images is seen in the inferior pons, middle cerebellar peduncle and sometimes cerebellum. Punctate and curvilinear gadolinium enhancement (peppering) the pons is a characteristic MRI feature of CLIPPERS. Imaging findings during relapses include pons or middle cerebellar peduncle swelling, closed ring enhancement, and normal initial MR imaging. Decrease in enhancement is seen on steroid or rituximab therapy.
Results
Chronic lymphocytic inflammation with pontine perivascular enhancement responsive to steroids (CLIPPERS) is a recently defined inflammatory central nervous system (CNS) disorder, prominently involving the brainstem and in particular the pons. The diagnosis is made with a combination of clinical, radiological and pathological findings. Our patient refused a biopsy and hence the diagnosis was made with clinical and radiological findings alone. Several case studies have reported improvement with steroids, however there are only 2 available case reports that examine the use of rituximab(1000mg) in this disease. Out patient responded to rituximab in 6 months and is symptom free (fig).
Conclusions
We illustrate how imaging dictates the management of Clippers disease and how it influences drug regime and dose modulation.

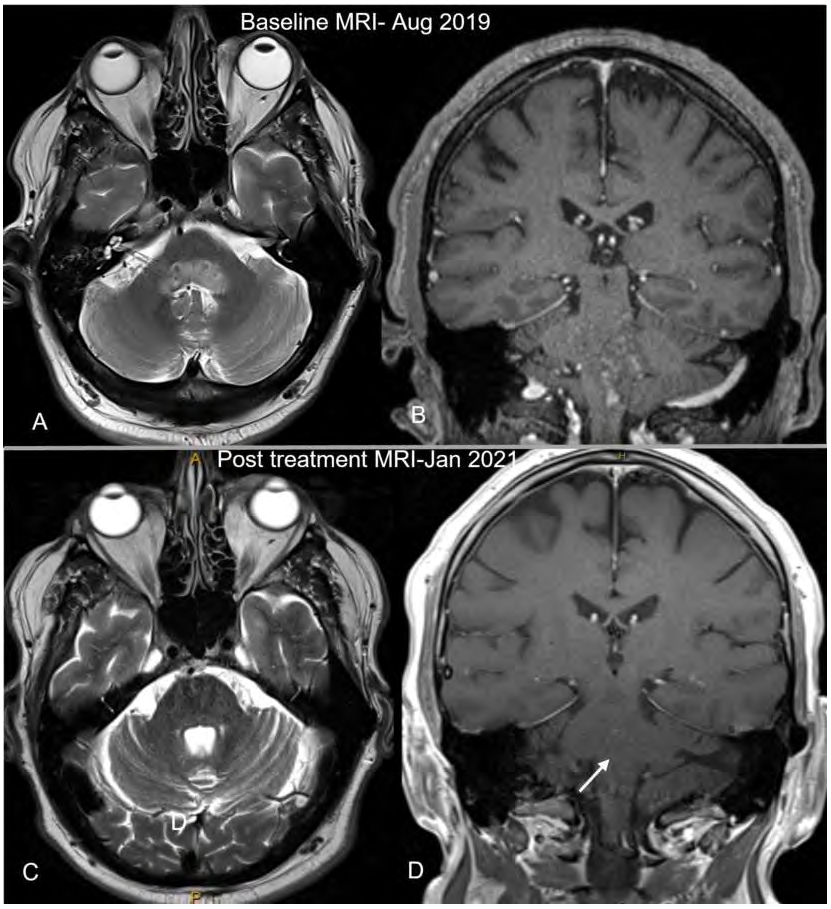

(Filename: TCT_934_Clippers.jpg)

298

Immune system gone wild: Hemophagocytic lymphohistiocytosis with CNS involvement in an Adult.

A Sosa[1], J Diestel[2], M Gracia[2], A TORRES MONARREZ[3], J Rubalcava Ortega[4], G Romero Sanchez[5]

[1]Instituto Nacional de Ciencias Medicas y Nutricion Salvador Zubiran, Ciudad de Mexico, Not Applicable, [2]Instituto Nacional de Ciencias Medicas y Nutricion Salvador Zubiran, Mexico, Not Applicable, [3]INSTITUTO NACIONAL DE CIENCIAS MEDICAS Y NUTRICIÓN SALVADOR ZUBIRAN, CIUDAD DE MEXICO, CIUDAD DE MEXICO, [4]Instituto Nacional de Ciencias Medicas y Nutricion Salvador Zubiran, Mexico City, Not Applicable, [5]Instituto Nacional de Ciencias Médicas y Nutrición Salvado Zubirán, Mexico City, Mexico

Purpose

47-yo male with primary immune thrombocytopenia. In 2021, he presented with fever, somnolence, and generalized weakness. The laboratory tests showed pancytopenia, hypertriglyceridemia and hypofibrinogenemia. Hemophagocytosis was documented in the bone marrow and CSF.

Materials and Methods

T2/FLAIR showed hyperintense rounded lesions with randomly distribution in gray and white matter. DWI Demonstrated lesions with restriction. T1+Gd showed multiple lesions with enhancement ranging from nodular, ring and patchy.

Results

HLH is a rare disease caused by a hyper-stimulated but useless immune response. The yearly incidence estimated of HLH in adults is 1/800 (1). The main predisposing factor in secondary HLH are hematological neoplasms (2), The patients should meet the HLH diagnosis criteria (3). In this case, the imaging findings, together with the previously described clinical characteristics, allowed the medical team to reach the final diagnosis.

Conclusions

HLH is an exaggerated inflammatory response with proliferation of histiocytes involving the CNS. The enhancement, restricted diffusion and localization of the lesions are the most important imaging findings, although non-specific, it helps to raise the suspicion of HLH under the appropriate clinical context.

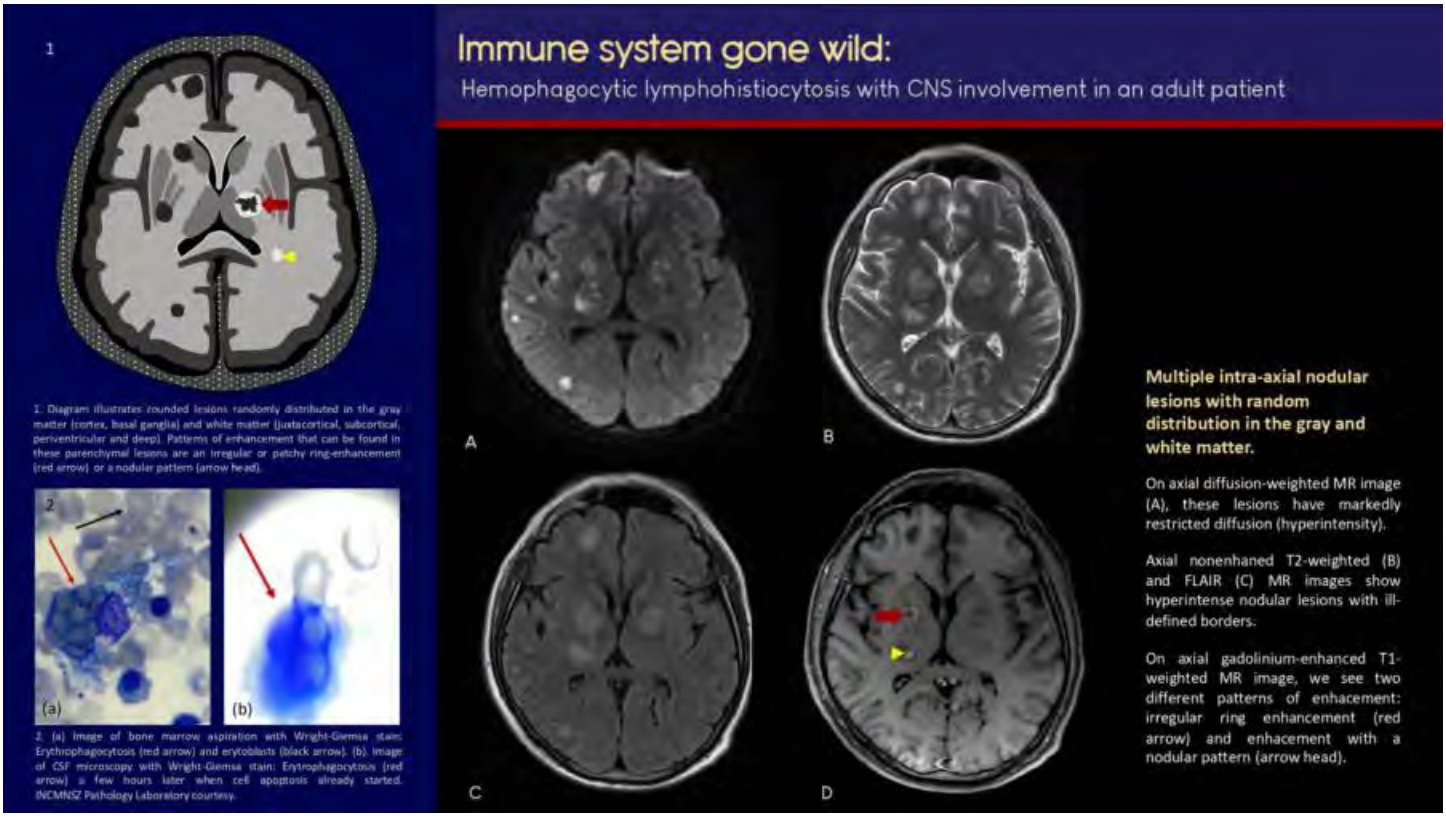

(Filename: TCT_298_HLH2_page-0001.jpg)

1347

Intracranial intravascular papillary endothelial hyperplasia of the cavernous sinus

A Degueure[1], C Soto[2], R Gilbow[3], H TAKEI[3], O Arevalo[3]

[1]LSU Health Shreveport, Richmond, LA, [2]National University of Colombia, Bogota, TX, [3]LSU Health Shreveport, Shreveport, LA

Purpose

23-year-old male with a 6-month history of worsening left-sided ptosis and diplopia. Further imaging workup demonstrated a left cavernous sinus mass.

Materials and Methods

MRI demonstrated a well-circumscribed and homogeneously enhancing mass arising from the anterior aspect of the left cavernous sinus presumed to be a meningioma. It is worth noting that the lesion had a high signal intensity on T2-weighted imaging and caused no narrowing of the internal carotid artery. Catheter angiography showed enlargement of infero-lateral trunk supplying the hyper-vascular mass. The patient received intravascular embolization followed by surgical resection. Intraoperatively, the lesion and the surgical bed bled profusely, and the patient developed a postoperative left hemispheric subdural hemorrhage requiring re-intervention. On the pathological examination, there is cellular proliferation of bland endothelial cells along with pericytes and fibroblasts with many capillaries present. Multiple organizing thrombi of varying sizes found to be intimately admixed with this vascular proliferative process. These findings are consistent with Intravascular papillary endothelial hyperplasia.

Results

Intravascular papillary endothelial hyperplasia (IPEH) is characterized by reactive endothelial cell proliferation in the setting of venous stasis and commonly associated with thrombosis. Most IPEH are extracranial in origin and often found in skin or subcutaneous regions of head and neck. Intracranial IPEH are extremely rare and based of imaging alone, very difficult to differentiate from other lesions such as meningioma, schwannoma, or angiosarcoma. Due to the lack of specific radiological features, diagnosis requires careful histological examination. In contrast to other vascular neoplasms, IPEH originates and is confined to the blood vessel lumen and thus total resection appears to be curative. Despite the rarity of intracranial IPEH it should be considered when evaluating differential diagnoses for hyper-vascularized skull base lesions.

Conclusions

Vascular lesions of the cavernous sinus may show similar appearance as meningiomas. High signal intensity on T2w images may suggest an alternate diagnosis.

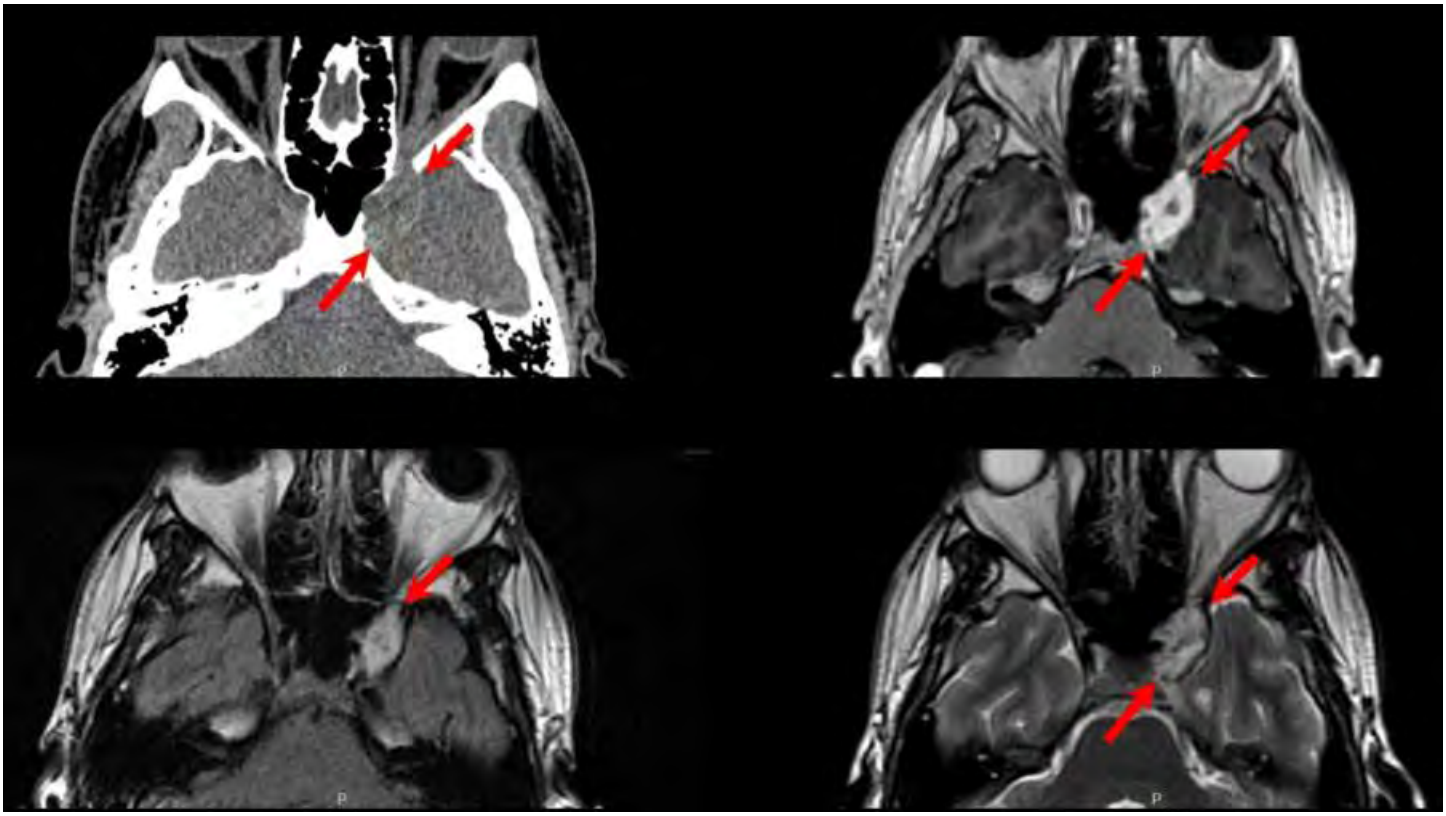
(Filename: TCT_1347_PEH.jpg)

771

Intramedullary Cystic Lesion Presenting as Weakness In Patient with Diastematomyelia

M Liu[1], N Nagirimadugu[1], P Harris[1], M Rosner[1], R Javan[1]
[1]*George Washington School of Medicine and Health Sciences, Washington, DC*

Purpose

63F with PMH diastematomyelia with prior thoracolumbar surgery presented with 1 week of progressive weakness, numbness, urinary and stool retention. She experienced mild improvement in her LLE after T8-T11 spinal cyst aspiration. Now status post T9-11 laminectomy and cyst removal (1B).

Materials and Methods

Cystic lesion, which does not fill with contrast on CT myelogram (1A), noted in the lower thoracic cord which appears intramedullary (1D) originating from the right-sided cord. It becomes exophytic, occupying the entirety of the spinal canal and causing significant mass effect and flattening of each spinal cord (1C). Syrinx is present in the right-sided cord and cyst does not demonstrate enhancing component.

Results

Diastematomyelia is a rare congenital abnormality characterized by splitting of the spinal cord. Associated spinal anomalies include scoliosis, meningocele, neurenteric cyst, dermoid cyst, spinal cord lipoma and hemangioma.

Conclusions

Diastematomyelia is a rare condition that can be associated with later development of intramedullary cysts leading to rapidly progressive neurological deficits.

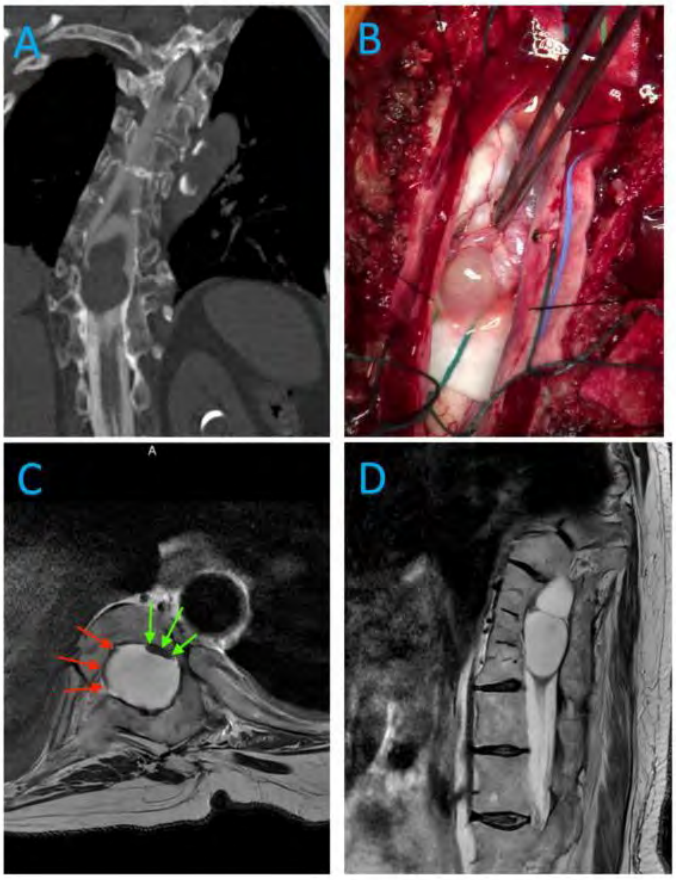

(Filename: TCT_771_ASNR2022Image.jpg)

1339

Intraventricular glioblastoma multiforme: a distinct imagiological presentation

A Canha Vedor Ferreira[1], A Almeida[1], S de Carvalho[1], R Silva[2], P Linhares[3], J Dias da Costa[1]

[1]Serviço de Neurorradiologia, Centro Hospitalar Universitário de São João, Porto, Portugal, [2]Serviço de Anatomia Patológica, Centro Hospitalar Universitário de São João, Porto, Portugal, [3]Serviço de Neurocirurgia, Centro Hospitalar Universitário de São João, Porto, Portugal

Purpose

A 61-year-old woman was admitted following complaints of progressive behavioral changes, associated with slurred speech and gait disturbances with subacute onset. Despite being previously autonomous and cognitively upright, the patient was disoriented, with no sensory or strength deficit on neurological examination. Head CT and brain MRI showed a well-circumscribed lesion on the left lateral ventricle extending to the third ventricle through the foramen of Monro, with avid heterogeneous contrast enhancement, defining a major cystic component. Perfusion study showed only a slight elevation on the relative cerebral blood volume (rCBV). These findings primarily suggested a subependymoma as the most likely diagnostic hypothesis. The patient underwent complete macroscopic resection of the lesion without significant intra-operative bleeding. Pathology showed a glial neoplasm with moderate cellular density, necrotic component, focal microvascular proliferation and low mitotic and proliferative (Ki67) index. Based on the pathological and molecular features of the lesion, the final diagnosis of glioblastoma multiforme (GBM), IDH "wild-type" was made.

Materials and Methods

N/A

Results

GBM is the most common primary cerebral tumor. Fast-growing and aggressive in nature, it is generally diagnosed in elderly people, typically located in the cerebral hemispheres, mainly in the frontotemporal region. Intraventricular location is extremely rare, with only few cases reported in the literature. Perfusion MRI is a promising additional tool in the CNS tumor diagnosis, with high rCBV supporting the diagnosis of high malignancy tumors (as vascular hyperplasia being reflected in rCBV values). The authors report an intraventricular GBM with only a slight increase in rCBV. Considering these unusual features, the macroscopic and pathological examination were essential to establish the final diagnosis. Therefore, we became aware that we were dealing with a poorly vascularized lesion, which can explain the perfusion study findings. A few studies bring up an association between low rCBV values in patients with histologically confirmed high-grade gliomas and a relatively favorable prognosis (in contrast with high-grade gliomas with high rCBV values).

Conclusions
It is important to recognize these unusual patterns, to establish a more adequate differential diagnosis between neoplastic lesions. More series of cases are needed to support the link between rCBV values and short-term outcome on high-grade gliomas.

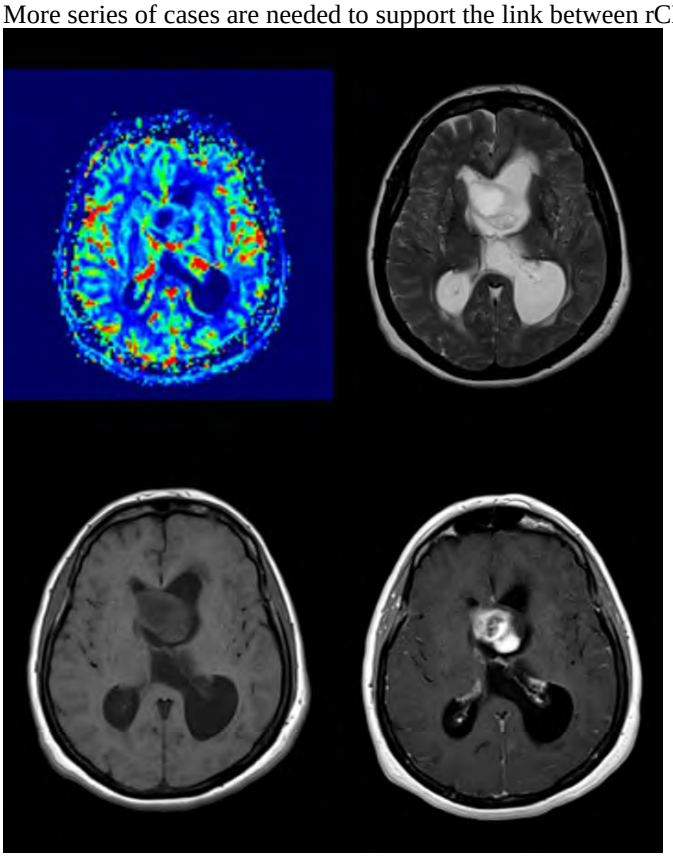

(Filename: TCT_1339_4Pictures_new.jpg)

643

Juvenile Xanthogranuloma mimicking Cephalohematoma; the Importance of Follow Up

E Goldstein[1], A Stephenson[2], V Rooks[1]
[1]Tripler Army Medical Center, Honolulu, HI, [2]Brian D Allgood Army Community Hospital, Camp Humphreys, APO AP

Purpose
An infant born via vacuum assisted delivery presented with a palpable parietal scalp mass. Although initial ultrasound suggested cephalohematoma, interval growth led to surgical resection yielding histopathologic diagnosis of juvenile xanthogranuloma.
Materials and Methods
Ultrasound demonstrated a well circumscribed 1.5 cm hypoechoic cystic lesion of the scalp. Follow up was recommended and demonstrated interval growth and internal color Doppler flow.
Results
Initial imaging features mimicked a cephalohematoma. Cephalohematoma, dermoid or epidermoid cyst, and pilomatricoma are common well circumscribed hypoechoic scalp lesions. Juvenile xanthogranuloma is commonly diagnosed clinically by its classic yellow-orange tint though this patient had no skin color change. Follow up imaging and excision were key to the diagnosis.
Conclusions
Clinical and imaging follow up for suspected cephalohematoma are important. Consider surgical excision for atypical or growing lesions.

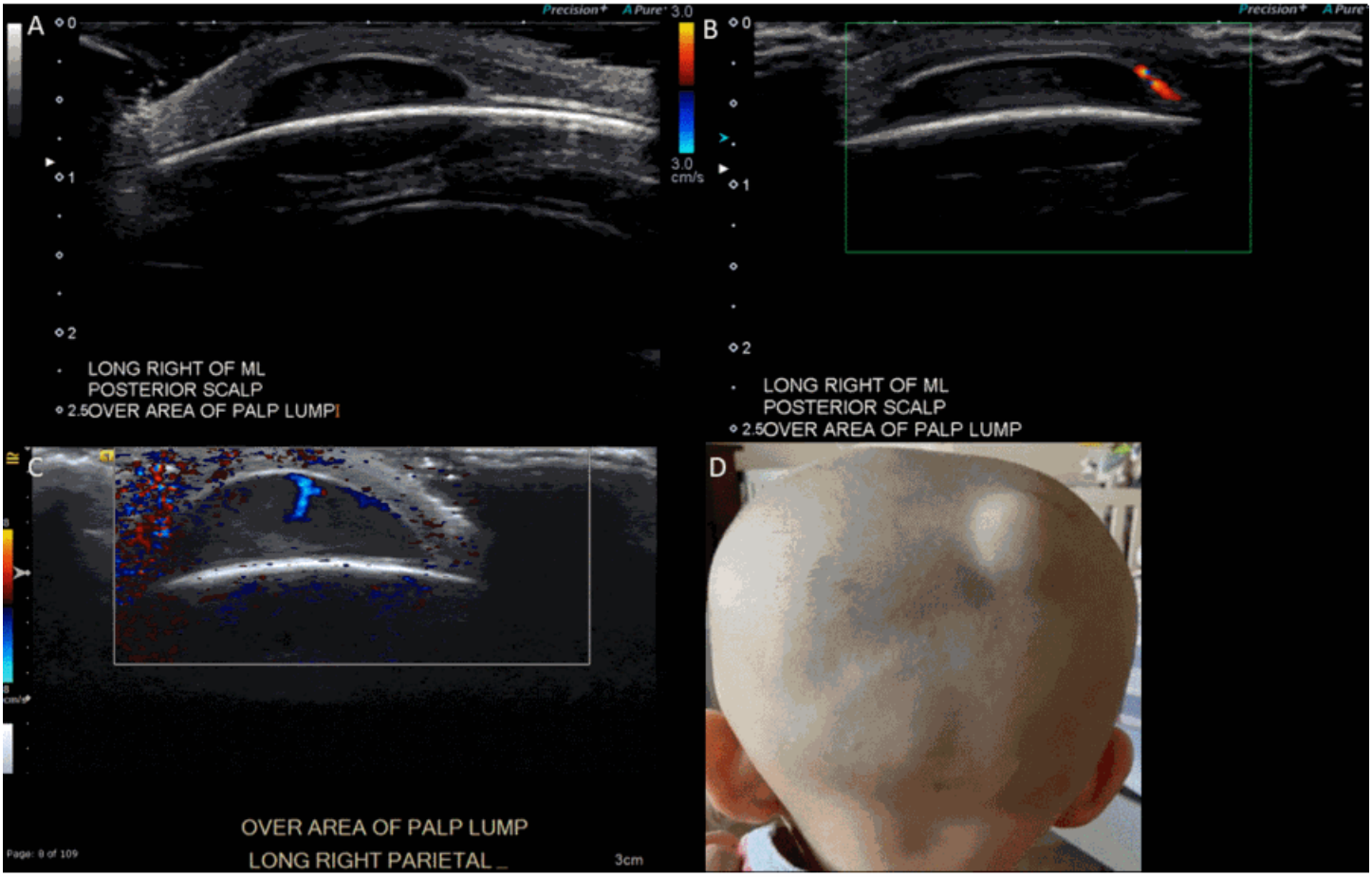

(Filename: TCT_643_Figure1-JXGcaseexcerpta.gif)

399

Magnetic Resonance Elastography in the localization of focal cortical dysplasia

Z Winchester[1], A Ong[2], N Salamon[2]

[1]UCLA, Los Angeles, CA, [2]University of California Los Angeles, Los Angeles, CA

Purpose

21-year-old female who presents with intractable epilepsy.

Materials and Methods

T2-weighted FLAIR sequence(left) demonstrates gray-white matter blurring in the left anterior temporal lobe. MRE image (right) shows increased parenchymal elasticity to the lesion.

Results

Achieving surgical cure for drug resistant epilepsy in children due to focal cortical dysplasia (FCD) is determined by identifying a spatially well-defined focus for resection.1 However, distinguishing the surgical borders of the lesion preoperatively with imaging and electrocorticography is often limited, and visually discerning normal from abnormal brain tissue intraoperatively can be challenging given the identical appearance.2,3 FCDs have been shown to be associated with increased brain stiffness.4 Magnetic Resonance Elastography(MRE) is a non-invasive, advanced imaging technique that can delineate tissue based on elasticity.5 Our preliminary data suggests that MRE offers the potential to identify FCDs with high sensitivity and can delineate the boundaries of the dysplastic cortex.

Conclusions

Magnetic Resonance Elastography (MRE) offers the potential to identify FCDs with high sensitivity and can delineate the boundaries of the dysplastic cortex due to the associated increased brain stiffness.

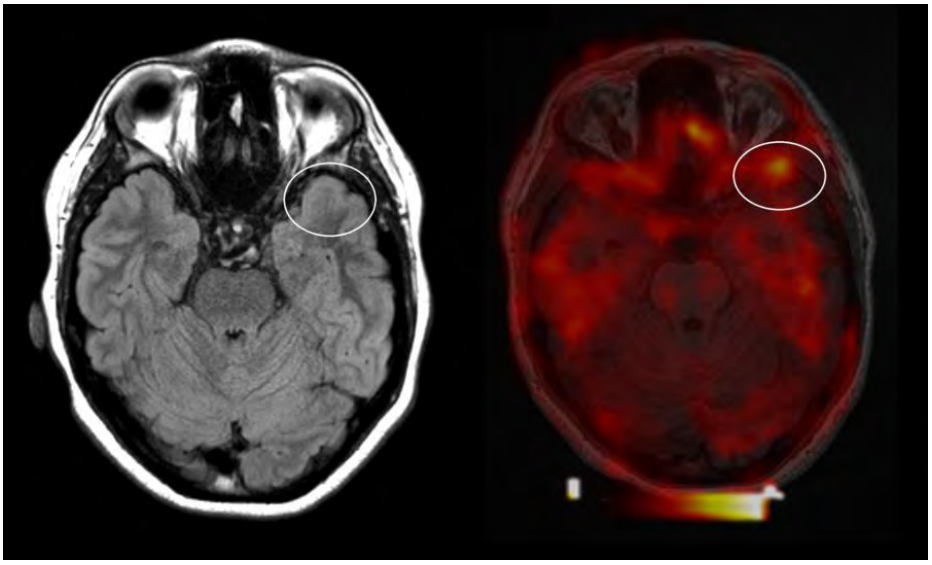

(Filename: TCT_399_MREFCD.jpg)

598

Meningeal Melanocytoma of the Cervicomedullary Junction

K Dammeyer[1], M Ali[1], B Griffith[1], J Corrigan[1], S Patel[1], J Duchak[2]

[1]Henry Ford Health System, Detroit, MI, [2]Henry Ford Hospital, Detroit, MI

Purpose

We present a 69-year-old female with progressive right-sided hemiparesis, difficulty ambulating, and multiple falls. Imaging demonstrated a mass centered at the cervicomedullary junction. At surgery, a pigmented lesion was found and pathology was consistent with a melanocytic neoplasm of the CNS most compatible with a meningeal melanocytoma.

Materials and Methods

MRI showed a mixed intra-/extramedullary T1 hyperintense, mixed T2 hypo/isointense, enhancing mass centered at the cervicomedullary junction with severe compression and edema.

Results

Meningeal melanocytomas are rare tumors arising from the normal melanocytic cells of the leptomeninges. These tumors most commonly occur in the posterior fossa, likely due to the increased concentration of melanocytes along the surface of the brainstem and upper cervical spinal cord.

Conclusions

Although rare, the presence of a mass with T1 hyperintense/T2 hypointense signal at the cervicomedullary junction should raise the possibility of a melanotic lesion such as a meningeal melanocytoma.

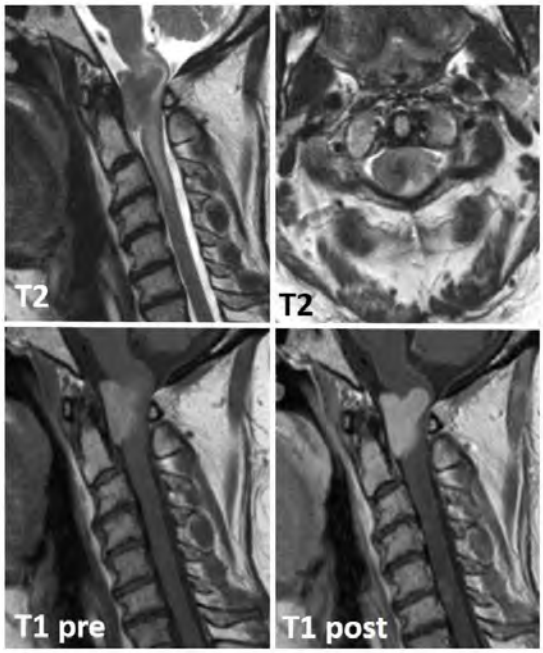

(Filename: TCT_598_mm.jpg)

303

Meningovascular Syphilis (MVS) Presenting as Multifocal Strokes- an Uncommon Diagnosis in a Post-antibiotic Era

T Chaudhry[1], M Kontzialis[1]

[1]Northwestern University Feinberg School of Medicine, Chicago, IL

Purpose

A 44-year-old male with history of HIV, syphilis, and chlamydia was admitted for headache, confusion, and right-sided weakness. CSF analysis demonstrated elevated WBCs of 390, elevated protein of 123, and positive VDRL (1:64). The patient also had a positive RPR (1:32).

Materials and Methods

MRI Brain with and without contrast demonstrated multiple areas of diffusion restriction, associated enhancement, and leptomeningeal enhancement.

Results

Meningovascular syphilis (MVS) is a neurovascular manifestation of tertiary syphilis characterized by endarteritis of the vessels supplying the leptomeninges and nervous system. This results in occlusion, stenosis, and aneurysm formation causing brain and spinal cord infarcts and hemorrhage. In the pos-tantibiotic era, MVS can be misdiagnosed for more common etiologies of stroke. In light of the patient's history and CSF analysis, MVS was favored the most accurate diagnosis.

Conclusions

A detailed history and workup in young patients who present with stroke is important to diagnose MVS as a cause of stroke.

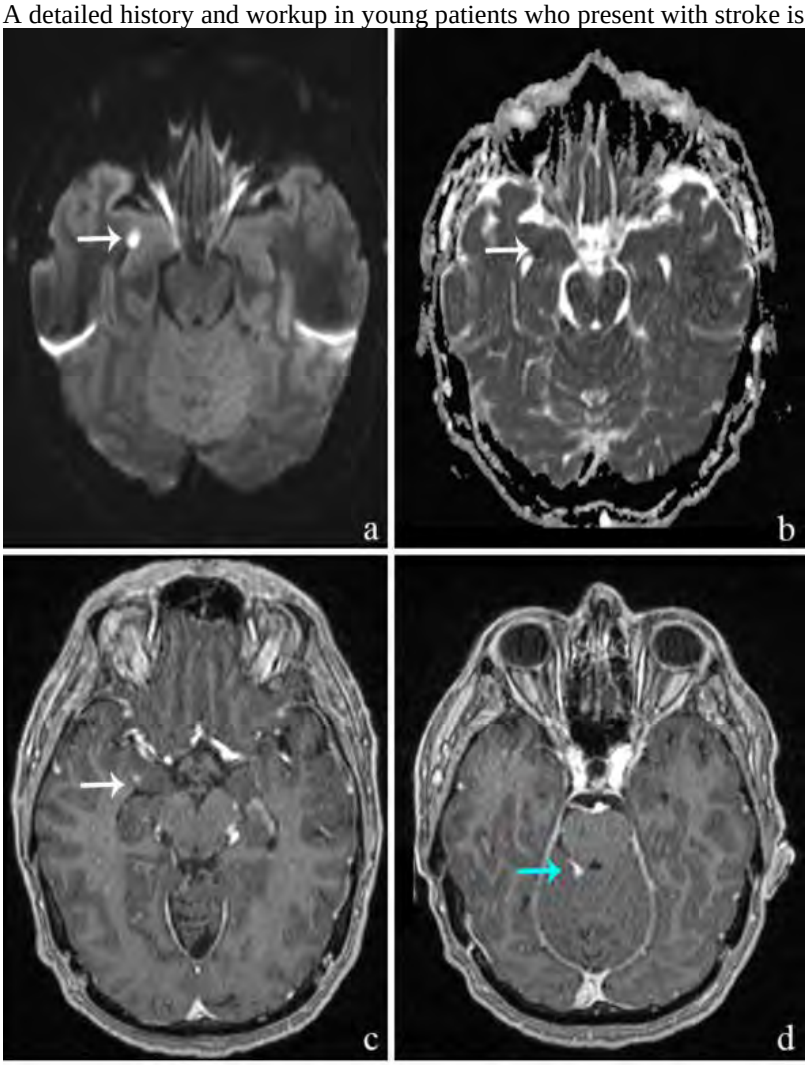

MRI at the level of the medial temporal lobes demonstrates a focus of hyperintensity on a) DWI with associated hypointensity on b) ADC map consistent with an acute infarct within the right medial temporal lobe. There is associated enhancement on the c) post-contrast MPRAGE image (white arrow). d) Post-contrast MPRAGE at the level of the superior vemis demonstrates leptomeningeal enhancement along the right superior cerebellar sulci (teal arrow).

(Filename: TCT_303_Figure1-new.jpg)

365

Midline High Flow Arteriovenous Lesions: Distinguishing a Dural Sinus Malformation from a Vein of Galen Malformation

M PEARL[1], P Dave[2]
[1]*Children's National Hospital, Washington, DC,* [2]*George Washington University School of Medicine, Atlanta, GA*

Purpose

A fetal MRI performed at 27 weeks gestation showed multiple flow voids, torcular dilation, and enlarged transverse sinuses. A maternal OB ultrasound showed midline posterior arteriovenous shunting and cardiac enlargement.

Materials and Methods

Axial T2 weighted images from a fetal MRI in a patient with a dural sinus malformation (DSM) (A, B) and an infant with a Vein of Galen malformation (VGAM) (C,D). Marked torcular enlargement (asterisk) is seen in the DSM, whereas the torcular and bilateral transverse sinuses are proportionately enlarged in the VGAM. The vein of Galen is aneurysmally dilated (D) in the VGAM, not seen in the DSM.

Results

DSMs and VGAMs are midline arteriovenous shunts that can be detected on prenatal imaging and may similarly present with cardiac failure and neurologic symptoms. DSMs typically affect the superior sagittal sinus (SSS), causing torcular dilation whereas the vein of Galen is focally dilated in a VGAM.

Conclusions

While VGAM is the most common arteriovenous lesion diagnosed prenatally, a DSM is an important consideration in the differential diagnosis, particularly when the torcular or SSS, and not the vein of Galen, is the site of disproportionate venous enlargement.

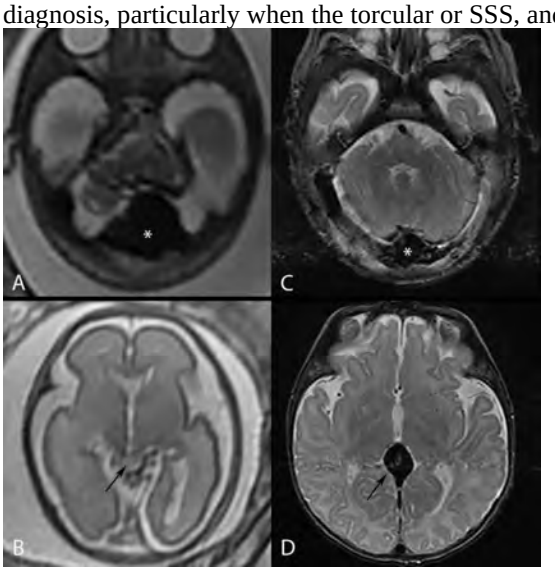

(Filename: TCT_365_Fig1combined.jpg)

373

MRI, DSA, and O-15 water PET evaluation of post-operative hemodynamics in a patient with Moyamoya disease

R Duarte Armindo[1], M Zhao[1], G Zaharchuk[1]
[1]*Stanford University, Stanford, CA*

Purpose

A 59-year-old male presented with right-hand weakness. After a diagnosis of Moyamoya disease was established, he received a left STA-M4 bypass without complications and has been asymptomatic since.

Materials and Methods

MRI showed subacute left-sided infarcts and supraclinoid ICA occlusion (Figure 1). A DSA study confirmed the Moyamoya pattern on the left. Imaging 6 months post surgery revealed a patent bypass, improvement in Moyamoya vessels, no apparent progression on the right, and no additional infarcts. 5-delay sequential ASL suggested poor cerebrovascular reserve (CVR) in the right (non-operated) hemisphere, despite this area being normal on oxygen-15 water PET and other ASL sequences (Table 1).

Results

Brain arterial flow patterns in MMD are complex. Contralateral hemodynamic changes after bypass have been reported with variable clinical outcomes1, 2 and undetermined causes (natural history vs post-operative changes)3. Multimodal evaluation (DSA, MR, and PET) and clinical correlation are warranted to guide management.

Conclusions

O-15 PET is the gold standard to evaluate regional CBF and CVR. In Moyamoya disease, ASL techniques are sensitive to arrival time issues and should be interpreted with caution.

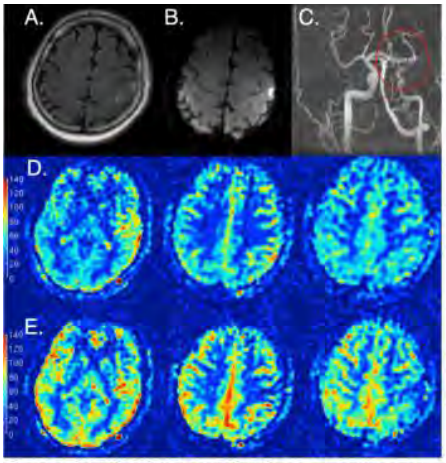

Figure 1. Axial T2 FLAIR (A) and DWI (B) images showing small subacute left frontoparietal cortical infarcts. TOF MRA 3D reconstruction (C) confirming occlusion of the left carotid terminus with numerous collateral vessels in the region. CBF maps before (D) and after (E) acetazolamide, with corresponding values of respectively of 51 and 71 mL/100g/min on the right (CVR 40%), 58 and 60 mL/100g/min on the left (CVR 3%), consistent with luxury perfusion and reduced augmentation in the infarcted regions.

		CBF pre-Diamox	CBF post-Diamox	CVR
PET	Left Hem	38.5 mL/100 g/min	42.8 mL/100 g/min	11%
	Right Hem	41.1 mL/100 g/min	47.5 mL/100 g/min	15%
Single-delay ASL	Left Hem	47.1 mL/100 g/min	63.5 mL/100 g/min	35%
	Right Hem	45.8 mL/100 g/min	60.3 mL/100 g/min	32%
3-delay Hadamard ASL	Left Hem	56.1 mL/100 g/min	73.6 mL/100 g/min	31%
	Right Hem	55.4 mL/100 g/min	74.5 mL/100 g/min	34%
5-delay sequential ASL	Left Hem	51.2 mL/100 g/min	54.8 mL/100 g/min	7%
	Right Hem	53.7 mL/100 g/min	46.9 mL/100 g/min	-13%

Table 1. Regional hemispheric CBF values determined by different perfusions techniques 6 months after revascularization surgery, with 5-delay sequential ASL suggesting poor cerebrovascular reserve (negative CVR) in the right hemisphere that the oxygen-15 water PET and other ASL sequences did not confirm.

(Filename: TCT_373_figureansdtable_rda.jpg)

1397

Multiple Intracranial Aneurysms related to Myxomatous Tumor Embolization

J Cline[1], C Li[1], M Ling[1], J Martin[1], V Patel[1], J Acharya[1], A Lerner[1], P Rajagopalan[1]
[1]*USC Keck School of Medicine, Los Angeles, CA*

Purpose

A 56-year-old female presents with headache. She reports recent history of subarachnoid hemorrhage (SAH) followed by coil embolization of a right internal carotid artery (ICA) aneurysm and remote resection of an atrial myxoma 10 years ago.

Materials and Methods

CTAngiogram reveals additional fusiform left cavernous ICA, saccular left supraclinoid ICA and left Posterior Communicating artery aneurysms; with sequela of prior SAH and Right ICA aneurysm coiling.

Results

Multifocal cerebral aneurysms in our patient are likely secondary to tumor embolization from atrial myxoma, especially in the absence of ongoing sepsis, polycystic kidney disease, autoimmune disorder and family history of aneurysms.

Conclusions

• Intracranial aneurysms are a rare complication of atrial myxoma • Aneurysmal formation is secondary to embolized myxomatous tumor that has invaded the intimal lining of the cerebral vessels • Aneurysms are often multiple, fusiform and peripheral in location, although saccular are also seen

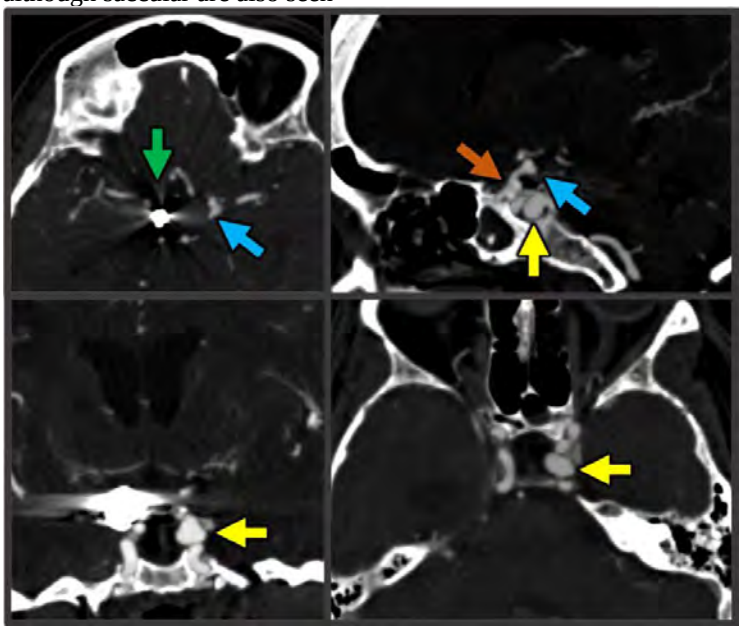

(Filename: TCT_1397_Aneurysm.jpg)

292

Multispatial Necrotizing Cellulitis of the Floor of Mouth (Ludwig's Angina). Imaging Findings and Pathophysiology.

K Sexton[1], M Kulzer[2], C LI[1], T Tragon[1], B Weston[1], P Annigeri[1], L Eisenmenger[3], M Goldberg[1], W CHANG[1]

[1]Allegheny Health Network, Pittsburgh, PA, [2]Allegheny Health Network, PITTSBURGH, PA, [3]University of Wisconsin - Madison, Middleton, WI

Purpose

Case 1: 27 yo M presented to the ED with 3 days of worsening left lower jaw pain. CT demonstrated multicompartmental abscess, likely of peritonsillar origin. The patient was subsequently intubated and transferred to OSH for surgery. Case #2 41 yo F was seen in the ED after tooth extraction with trismus. CT demonstrated multicompartmental abscess and odontogenic disease. She was taken for emergent surgery given concern for airway compromise.

Materials and Methods

CT scans demonstrated multicompartmental abscesses with associated peritonsilar abscess in Case 1 and odontogenic disease in Case 2.

Results

Ludwig's Angina is a diffuse, rapidly progressive and potentially life-threatening multispatial abscess/cellulitis involving the soft tissues of the neck which can arise from either odontogenic or peritonsillar origin.

Conclusions

Multispatial abscesses of the head and neck region are a surgical emergency due to the potential for airway compromise and can arise from either odontogenic or peritonsillar origin.

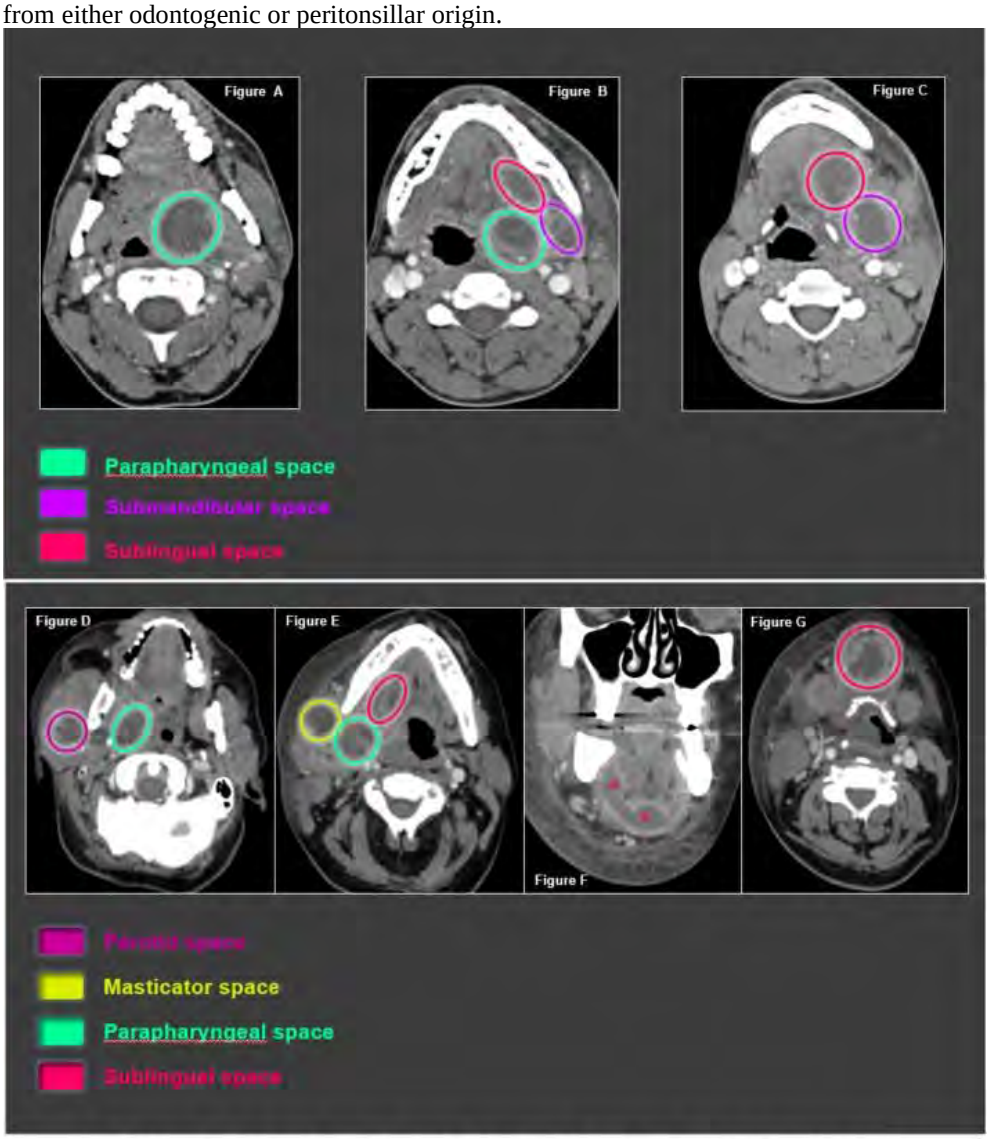

Figure 1: a-c) CT scan of a 28 year old male with history of sore throat and left neck pain with multicompartmental abscess extending from the left tonsillar pillar into the floor of mouth and involving the left submandibular and sublingual spaces. **d-f)** CT scan of a 41 year old female with history of recent right tooth extraction presenting with multicompartmental abscess involving the right parotid, masticator, submandibular, and sublingual spaces, likely of odontogenic origin.

(Filename: TCT_292_ludwigasnr.jpg)

551

Myoclonic Epilepsy with Ragged Red-Fibers- A Rare Cause of Pediatric Myoclonic Epilepsy

L Pelissier[1], A Foust[2]

[1]OSU Wexner Medical Center, columbus, OH, [2]University Hospitals Cleveland Medical Center, Cleveland, OH

Purpose

11-year-old boy presented with 2 months of increasing myoclonic jerks and unstable gait with frequent falls. Family history was significant for mitochondrial disorder and molecular studies revealed a mitochondrial 8334A>G tRNA Lys mutation with 97.8% heteroplasmy.

Materials and Methods

Brain MRI revealed mild cerebellar volume loss, T2/FLAIR hyperintensity and restricted diffusivity in the dorsal brainstem, particularly within the central tegmental tracts and superior cerebellar peduncles.

Results

Myoclonic epilepsy with ragged red fibers (MERRF) is caused by mitochondrial DNA mutations A8344G or A3243G. Patients present in adolescence with myoclonus, epilepsy, ataxia, and muscle weakness. Reported imaging findings include of cerebral and cerebellar atrophy, pallidal atrophy with calcifications, and T2 hyperintensity in cerebral white matter, striatum, dorsal brainstem and superior cerebellar peduncles.

Conclusions

Mitochondrial disorders are an important differential consideration for symmetric signal abnormality in the dorsal brainstem and, in the setting of myoclonic jerks, raises concern for MERRF.

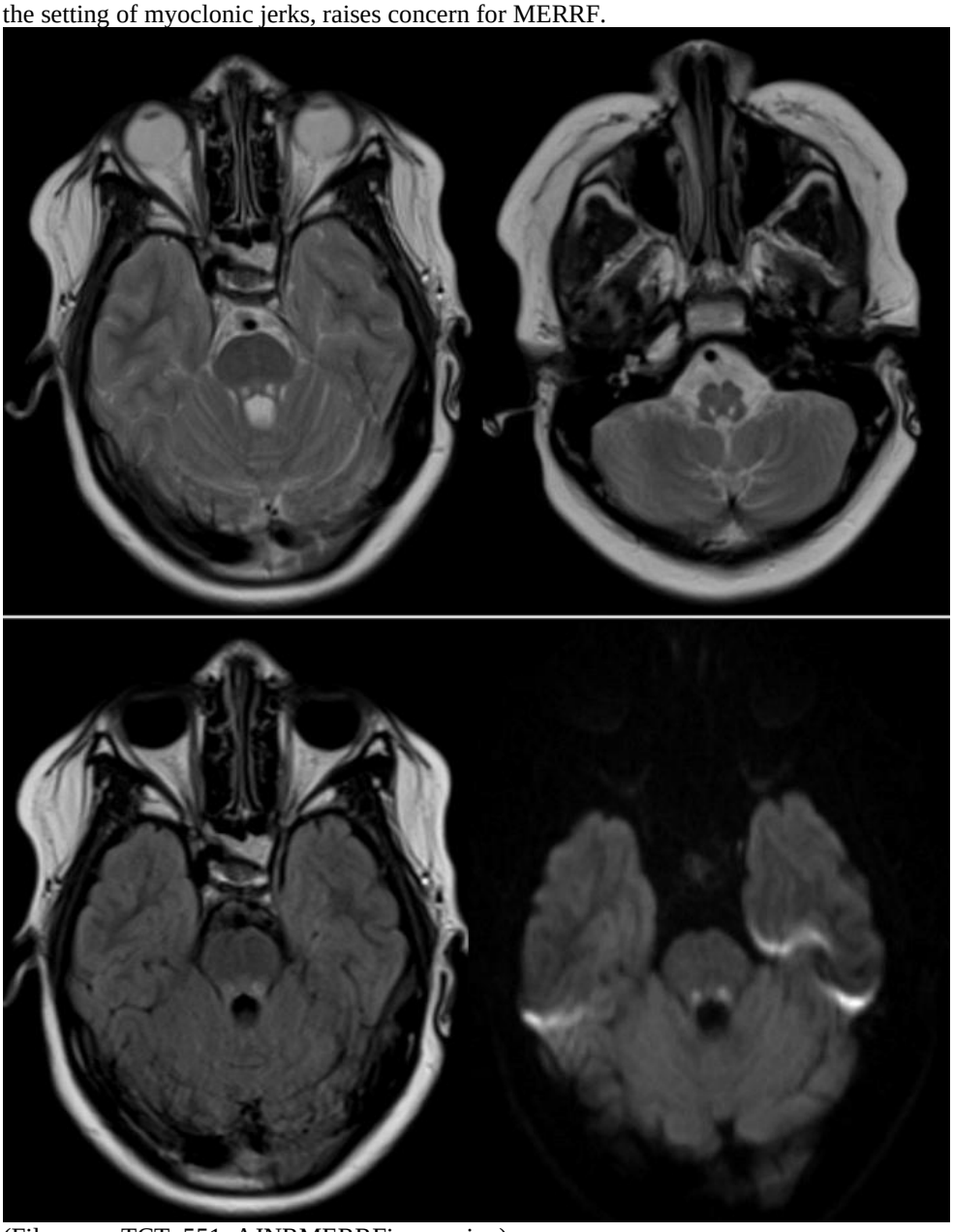

(Filename: TCT_551_AJNRMERRFimages.jpg)

1243

Neonatal Intracranial Teratoma: The Terrible Teratoma

L Rubio[1], S Li[2]
[1]Baystate Medical Center, Springfield, MA, [2]Baystate Medical Center_UMMS, Springfield, MA

Purpose

A 34-week preterm baby was born via cesarean section with macrocephaly. A fetal ultrasound showed a large mixed soft tissue and cystic echogenicity with multiple calcifications nearly replacing the entire brain parenchyma. A follow up MRI brain with and without contrast showed a large heterogeneous mass with multiple cystic and solid components. The mass replaced the midline structure of the supratentorial brain and protruded into the fourth ventricle causing brainstem compression and marked obstructive hydrocephalus. The patient was seen by neurology, neurosurgery, and pediatric oncology at Boston Children's Hospital who decided with the family to put the newborn patient on hospice care.

Materials and Methods

Figure 1: (Left) Axial T2-weighted MR image of the newborn head shows a 1.1 x 1.2 x 1.3 cm heterogeneous solid and cystic mass with multiple fluid bright cystic structures and massive obstructive hydrocephalus. (Right) Sagittal T1-weighted MR image of the newborn head.

Results

Congenital intracranial tumors are incredibly rare accounting for 0.5-1.5% of all pediatric brain tumors. Intracranial teratomas are the most common congenital intracranial tumors accounting for 33-50% of these tumors. They most commonly present supratentorial and midline within a cerebral hemisphere [1,2]. The hypothesized origin of teratomas is from misplaced pluripotential primordial germ cells that instead of reaching the urogenital ridge during the 6th week of development, become displaced along midline structures of the head, mediastinum, and the sacrococcygeal region. Despite well documented guidelines in the diagnosis of congenital intracranial teratomas using ultrasound, CT, and MR imaging, this diagnosis carries a 90% mortality rate [3]. A recent retrospective study single-cohort study by Ulm B, et al, demonstrates that MRI was the best modality for risk stratification of teratomas by detecting signs of immature or invasive tumor growth and allowing better planning of surgical resection [4]. Our objective is to present a case that demonstrates a massive intracranial teratoma discovered with ultrasound and follow up MRI.

Conclusions

Teratomas are often benign intracranial tumors but when they grow rapidly and replace normal brain tissue, they result in a very poor prognosis. Many high-risk intracranial lesions can be found with the use of ultrasound and follow up MRI to evaluate these high-risk lesions could lead to planning successful surgical interventions and a longer-term survival rate for patients.

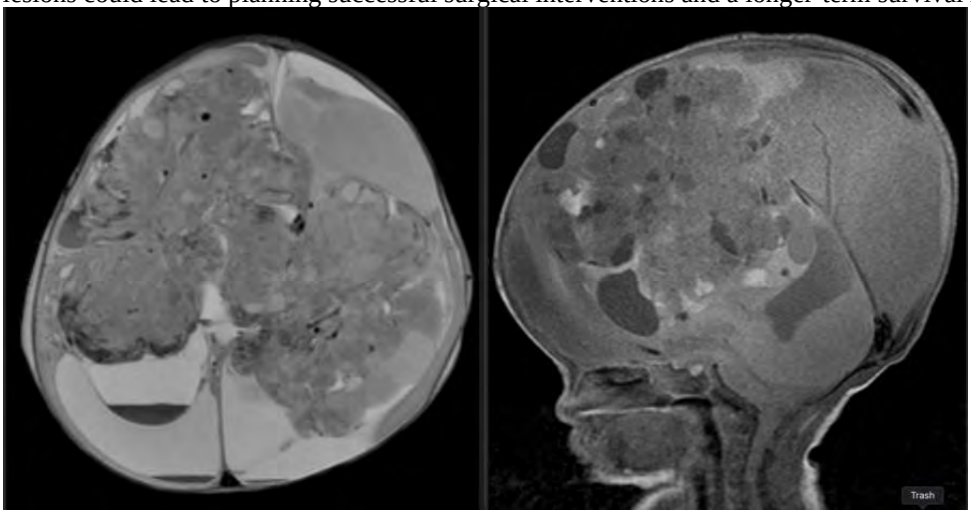

(Filename: TCT_1243_intracranial_teratoma_sagittal_T1_and_Axial_T2.jpg)

407

Neonatal Intraparenchymal Hemorrhage due to Severe Hypernatremia

M Kurdi[1], N Ali[1], R Lazarus[1]
[1]SUNY Downstate Medical Center, Brooklyn, NY

Purpose

A 9-day old male infant born to an HIV positive mother is brought to the ED after a seizure. In the emergency department, the patient was tachypneic and febrile. Reportedly, he was being fed 2-3 ounces of baby formula every 2 hours and had lost 10 percent of his weight over the past 2 days. Lab work was remarkable for signs of acute kidney injury and severe dehydration including sodium of 177 mEq/L. Urine analysis revealed moderate bacteriuria. He was admitted to the PICU for management of late-onset neonatal sepsis secondary to urinary tract infection. Lumbar puncture was performed due to concern for neonatal meningitis however subsequent CSF analysis was negative.

Materials and Methods
US head: Foci of increased echogenicity seen bilaterally, predominantly throughout the white matter and gangliocapsular regions. MRI Brain: Multiple foci of susceptibility throughout the cerebral hemispheres; predominantly in the gray-white junction and within the cerebellar hemispheres and to a lesser degree involving the basal ganglia. Many of these foci demonstrate loss of susceptibility and high signal on filtered phase images. NECT Head: Scattered ill-defined hyperdense foci, most notably within the right cerebellar hemisphere and dorsal vermis. Additional areas of hyperdensity are seen in the brain parenchyma, the left high parietal lobe and the gray-white junction bilaterally.
Results
Hypernatremia is defined as sodium level greater than 150 mEq/L [1]. The neurological consequences of neonatal hypernatremia include sinus thrombosis, seizures and intraparenchymal hemorrhage [2]. Neonates are at higher risk of developing severe hypernatremia due to immature renal and evaporative water losses [1]. Neonatal hypernatremia has multiple etiologies including improperly mixed feeding formula, diarrheal illness, elevated breast milk sodium and abuse [3]. These patients can present with feeding problems, irritability, lethargy and seizures [1]. In our case, the patient was brought in after a witnessed seizure. Initial laboratory studies showed severe hypernatremia. Given the maternal history of HIV, the US findings of echogenic foci suggested calcifications from possible TORCH versus intraparenchymal hemorrhage. After an equivocal MRI of the brain, radiology recommended obtaining a CT which confirmed subacute intraparenchymal hemorrhages due to hypernatremia.
Conclusions
What makes our case unique is that we corroborated imaging features of neonatal hypernatremia on US, CT and MRI.

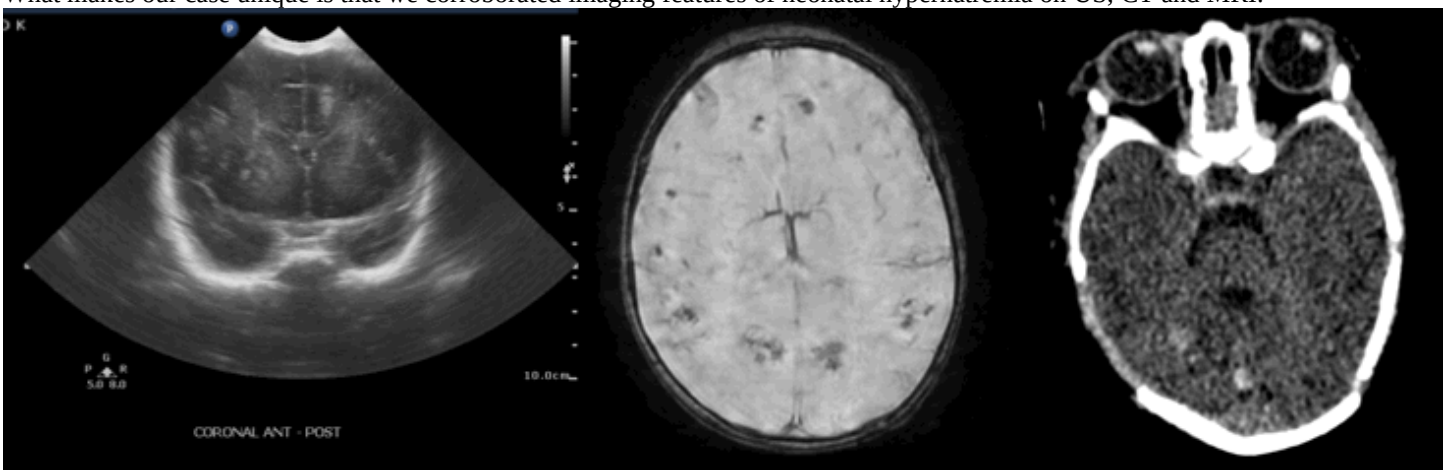

(Filename: TCT_407_ICH.gif)

325
Neuroimaging evaluation of Zellweger Syndrome
D Tribovane[1], S Matias[1]
[1]Hospital Beatriz Ângelo, Loures, Portugal

Purpose
We present two patients admitted to the neonatal intensive care unit for generalized hypotonia and poor feeding. Clinical examination revealed dysmorphic facial features. Laboratory results noted elevations in multiple very long chain fatty acids (VLCFA).
Materials and Methods
MRI in both patients revealed hypomyelination, bilateral incomplete opercularization and abnormal perisylvian polymicrogyria-like changes. Patient 2 had coexistent bilateral subependymal germinolytic cysts.
Results
ZS is a severe form of a spectrum of peroxisome biogenesis disorders that cause an accumulation of VLCFA, and present with distinctive facial stigmata, hypotonia, poor feeding, hepatic dysfunction, seizures and bone abnormalities. MRI findings are virtually pathognomonic, characterized by delayed myelination and extensive areas of polymicrogyria-like changes in the perisylvian regions. Subependymal germinolytic cysts along the frontal horns of the lateral ventricles and incomplete opercularization are also occasionally present.
Conclusions
N/A

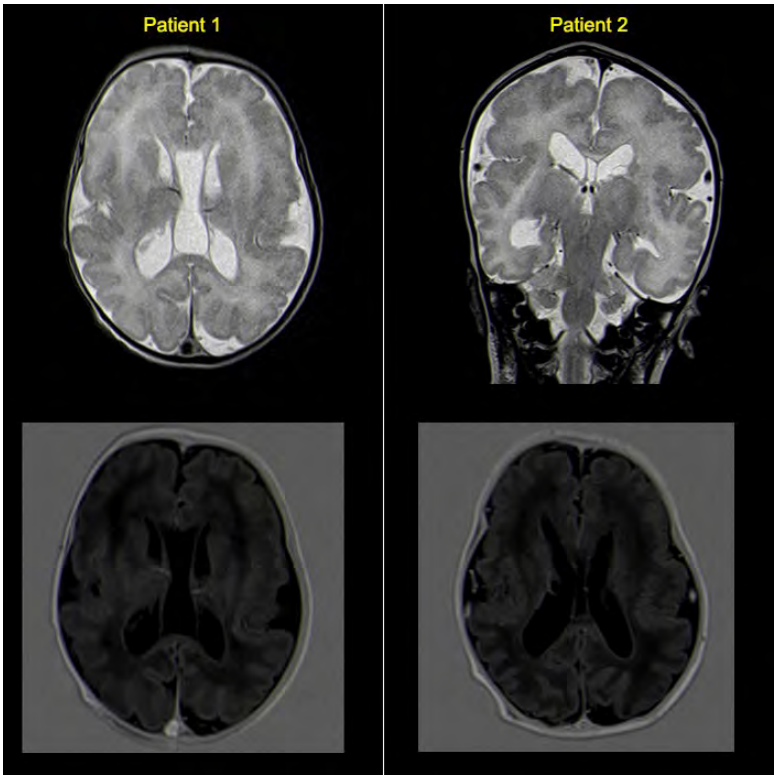

(Filename: TCT_325_Untitled-2.jpg)

234

Neuroimaging Findings of Adult-Onset Leukoencephalopathy with Axonal Spheroids and Pigmented Glia (ALSP)

B Haas[1], A Ozturk[1], A Paydar[1], V Ivanovic[1], R Assadsangabi[1], J CHANG[1], M Bobinski[1], L Hacein-Bey[1], A Dublin[1], W Benko[1], O Raslan[1]

[1]*UC Davis Medical Center, Sacramento, CA*

Purpose

Clinical History 46-year-old male with a 3-year history of gait changes, presenting with acute onset of left sided weakness. On examination, patient demonstrated Parkinsonian gait, pseudobulbar affect, and dysarthria.

Materials and Methods

Imaging Findings CT – Periventricular small foci calcifications adjacent to the posterior body of the lateral ventricles and hypoattenuating confluent white matter lesions (Fig 1A). MRI – Asymmetric, left more than right, periventricular confluent T2/FLAIR hyperintensities (Fig 1B) with pyramidal tract involvement extending to the brainstem (Fig1C). Multiple foci of reduced diffusion are seen within the centrum semiovale (Fig1D). Significant volume loss especially affecting the corpus callosum (figure not shown).

Results

Discussion Adult-onset leukoencephalopathy with axonal spheroids and pigmented glia (ALSP) is an autosomal dominant disease related to heterozygous mutations in the colony-stimulating factor 1 receptor (CSF1R) gene. The patients usually present in middle age with progressive cognitive impairment, parkinsonism, pyramidal signs, and epilepsy1,2. Neuroimaging findings of ALSP are illustrated in figure 1. In our patient, a genetics leukodystrophy panel identified a missense mutation in colony-stimulating factor 1 receptor (CSF1R) specifically c.2507G>A p.(Ser836Asn) that is a variant of unknown significance which is probably a novel causal variant of ALSP.

Conclusions

Teaching Point Early diagnosis of CSF1R-related leukoencephalopathy is critical because hematopoietic stem cell transplantation may be a promising therapy for patients and their relatives at risk. Asymmetric distribution of white matter lesions, persistent white matter reduced diffusion lesions and punctate calcifications[3] with corpus callosum volume loss on neuroimaging are highly suggestive of ALSP.

Figure 1 – Characteristic CT and MRI Findings in ALSP caused by CSF1R mutation

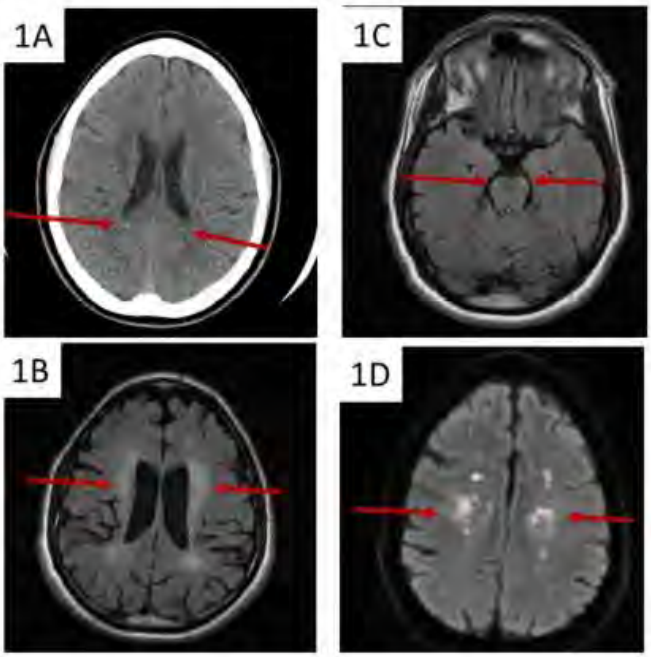

CT demonstrates periventricular punctate calcifications within the posterior periventricular white matter and confluent hypoattenuating white matter lesions (arrow, Fig 1A) . MRI also illustrates T2/FLAIR hyperintense asymmetric deep white matter, greater on the left (arrow, Fig 1B). Involvement of the pyramidal tracts in the brain stem (arrow, Fig1C) was also seen. DWI demonstrates persistent foci of reduced diffusion within the white matter which is a unique feature of ALSP (arrow, Fig 1D). Volume loss, especially involving the corpus callosum, is also a common finding of ALSP (figure not shown).

(Filename: TCT_234_ozturk_raslan_figure9.jpg)

882

Neuroimaging Findings of Cerebral Syphilitic Gumma. Case Report.

I ALONSO RAMON[1], A TORRES MONARREZ[2], R Hernández Ramírez[3], F FLORES GARCIA[4], M GUZMAN SOTO[5], Y TAPIA MORALES[5], G Romero Sanchez[6]

[1]INSTITUTO NACIONAL DE CIENCIAS MEDICAS Y DE NUTRICION SALVADOR ZUBIRAN, MEXICO, MEXICO, [2]INSTITUTO NACIONAL DE CIENCIAS MEDICAS Y NUTRICIÓN SALVADOR ZUBIRAN, CIUDAD DE MEXICO, CIUDAD DE MEXICO, [3]INSTITUTO NACIONAL DE CIENCIAS MEDICAS Y DE NUTRICION SALVADOR ZUBIRAN, Mexico, Ciudad de México, [4]INSTITUTO NACIONAL DE CIENCIAS MEDICAS Y NUTRICION SALVADOR ZUBIRAN, MEXICO, CIUDAD DE MEXICO, [5]INSTITUTO NACIONAL DE CIENCIAS MEDICAS Y DE NUTRICION SALVADOR ZUBIRAN, MEXICO, CIUDAD DE MEXICO, [6]Instituto Nacional de Ciencias Médicas y Nutrición Salvado Zubirán, Mexico City, Mexico

Purpose

58 yo immunocompetent male who started with seizures. Later, He presented oppressive headache, fever, and vomiting. CSF showed protein elevation, normal cells count and negative infectious panel. Stereotactic brain biopsy demonstrated a cerebral syphilitic gumma.

Materials and Methods

T2/FLAIR showed a hyperintense lesion at the left posterior insular and temporal regions. DWI demonstrated Foci of restricted diffusion. T1+Gd showed an ill-defined lesion with peripheral enhancement associated with a hypointense center. PWI showed a low rCBV. PET/MRI showed no increased uptake.

Results

Cerebral syphilitic gumma is a rare disease of the central nervous system that is an unusual type of tertiary syphilis (1). The radiological diagnosis of a cerebral syphilitic gumma is a challenge that could be easily misdiagnosed as different infectious or neoplastic brain lesions (2). MRI and PET/CT findings are very helpful in the diagnosis of this pathology.

Conclusions

MRI is an important diagnostic method for syphilitic gumma. The characteristic gadolinium enhancement on MRI combined with 18F-FDG PET/CT and laboratory examinations are helpful in distinguishing cerebral syphilitic gumma from brain tumors and infectious diseases.

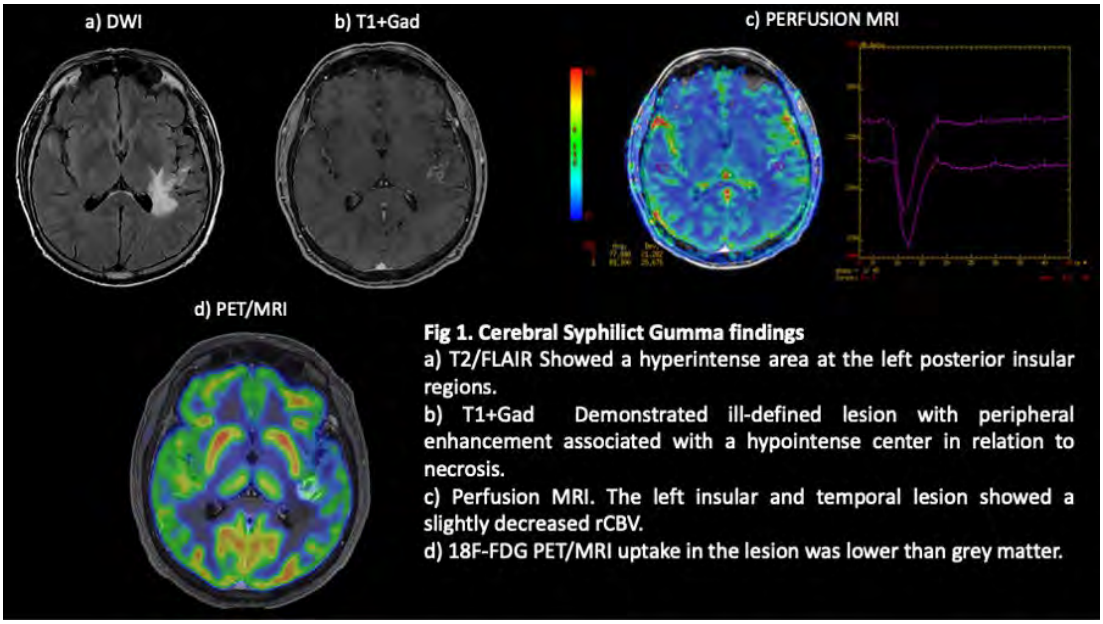

(Filename: TCT_882_GOMA.jpg)

782

Neuronal Intranuclear Hyaline Inclusion Disease (NIID): A Rare Disease with Characteristic MRI Findings

S Walia[1], S MOHAN[2], V Patel[1]
[1]University of Pennsylvania, Philadelphia, PA, [2]UNIVERSITY OF PENNSYLVANIA, PHILADELPHIA, PA

Purpose

24-year-old male presented with slowly progressive tremors, balance issues, irritability, and memory impairment.

Materials and Methods

DWI and FLAIR demonstrate characteristic symmetric band-like hyperintense signal at the corticomedullary junction as well as the splenium of the corpus callosum.

Results

NIID is a rare slowly progressive neurodegenerative disease with varied clinical manifestation and characterized by accumulation of eosinophilic intranuclear inclusions in the nervous system. Symmetric DWI hyperintensity at the corticomedullary junction is thought to be a strong indicator of NIID. Differential diagnoses include metabolic and genetic leukodystrophies, particularly FXTAS (fragile X-associated tremor/ataxia syndrome). Diagnosis can be confirmed with biopsy of the skin or peripheral nerves demonstrating intranuclear inclusions.

Conclusions

NIID is a rare disease that should be strongly considered in patients presenting with characteristic symmetric band-like DWI hyperintensity at the corticomedullary junction.

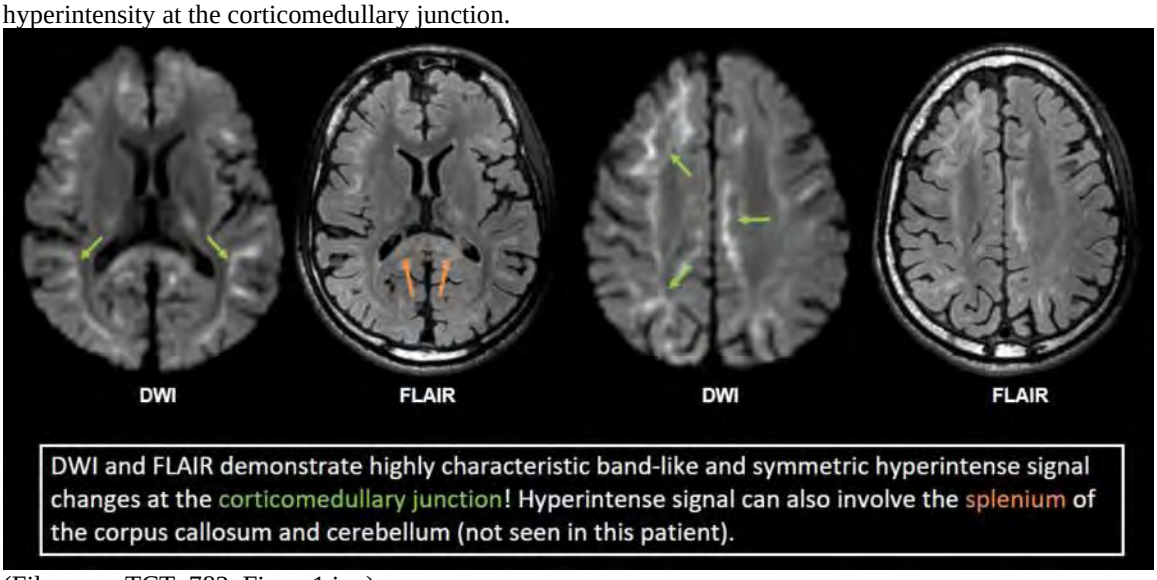

(Filename: TCT_782_Figure1.jpg)

451

Neuroradiologic Manifestations of PIGN Mutation, A Rare Cause of Pediatric Epilepsy

M Hornick[1], A Foust[2]
[1]University Hospitals Cleveland Medical Center, Cleveland, OH, [2]Boston Children's Hospital, Boston, MA

Purpose

Previously healthy term male presented with hypotonia, developmental delay, and seizures. Extensive clinical workup including serum and CSF testing were unrevealing. EEG demonstrated bihemispheric epileptogenicity. Whole exome sequencing revealed compound heterozygous mutation of the PIGN gene.

Materials and Methods

MRI showed bilateral symmetric diffusion restriction and T2 prolongation within the perirolandic corona radiata, optic radiations, posterior limb of the internal capsule (PLIC), and central tegmental tracts, prominent extra-axial spaces, and subtle frontal and cerebellar volume loss.

Results

Autosomal recessive mutations in PIGN are a rare cause of pediatric epilepsy with less than 30 reported cases. Described imaging findings include enlarged subarachnoid spaces, delayed myelination, cerebral and cerebellar atrophy. This is the first report of symmetric diffusion restriction involving the myelinating structures, particularly the PLIC and central tegmental tracts.

Conclusions

PIGN mutations may result in bilateral symmetric diffusion restriction in the PLIC and central tegmental tracts.

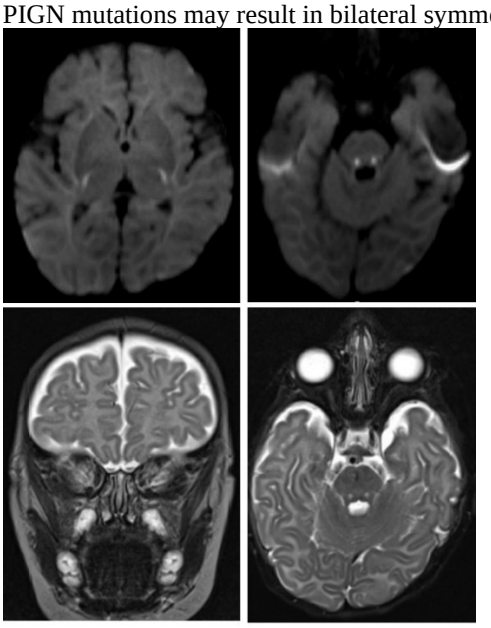

(Filename: TCT_451_PIGNfigure.jpg)

834

Non-functioning Pituitary Macroadenoma with Bilateral Internal Carotid Artery Aneurysms

C Yalniz[1], R Riascos[1], R Samant[1]
[1]The University of Texas Health Science Center at Houston, Houston, TX

Purpose

55-year-old female presented with persistent headache, nausea and vomiting. She had a fall three weeks ago and outside CT demonstrated a frontal bone fracture and a sellar mass which was biopsied the day before.

Materials and Methods

MRI demonstrated a T1 and T2 isointense, mildly enhancing destructive soft tissue mass centered in the sella surrounding bilateral internal carotid arteries (ICA). The right ICA was dilated so a CTA or MRA was recommended for further evaluation. CTA demonstrated bilateral tortuosity of the ICAs with areas of partial to complete encasement by the mass. Primary differential diagnosis was pituitary adenoma and other sellar masses such as craniopharyngioma were less likely. Pathology showed non-functioning pituitary adenoma.

Results

The association between intracranial tumors and asymptomatic aneurysms has been previously discussed in the literature. Pituitary adenomas and meningiomas are the most common tumors associated with aneurysms. Wakai et al. reported the incidence of co-existing aneurysm with pituitary adenoma as 7.4% and Jakubowski et al. observed aneurysms in 13.5% of growth hormone secreting adenomas and in 5.1% of non-functioning adenomas. Arteriosclerosis caused by prolonged elevated growth hormone has been proposed in patophysiology. Some authors speculated that the aneurysm formation might be induced by local circulatory products of tumors. Others stated that direct contact with vascular invasion or traction to the vessel wall might cause aneurysm. In our case, the

adenoma was non-functioning so the growth hormone levels were not elevated and there were multiple aneurysms, some of which had no mechanical contact with the mass.

Conclusions

Asymptomatic aneurysms co-existing with pituitary adenoma are rare and preoperative recognition can prevent catastrophic results and provide guidance for optimal surgical strategy.

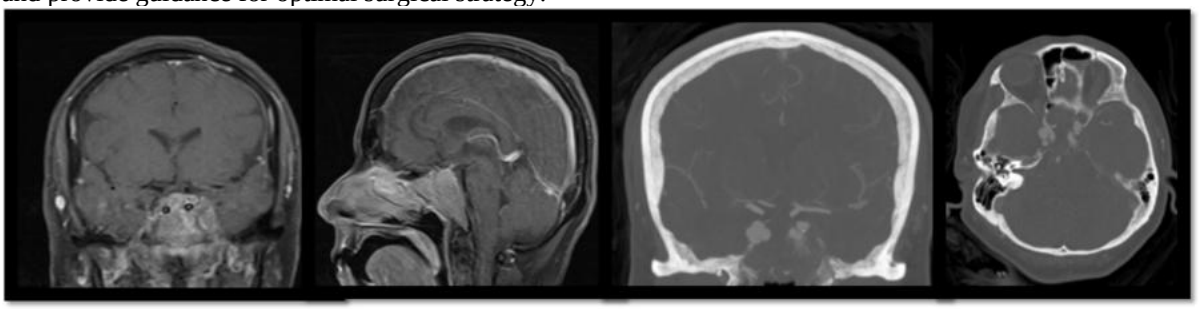

(Filename: TCT_834_Picture11.jpg)

1412

OPTIC NERVE PILOCYTIC ASTROCYTOMA

L Nunez[1], C Yalniz[2], R Riascos[3]

[1]University of Texas Health Science Center at Houston, Houston, TX, [2]UTH McGovern Medical School, Houston, TX, [3]The University of Texas Health Science Center at Houston, Houston, TX

Purpose

48-year-old African American woman with a 2-year history of progressive visual loss, now legally blind in the right eye. She also experienced progressive proptosis with downward and outward displacement of the right eye. There was no history or clinical findings suggestive of NF1.

Materials and Methods

Large cystic lesion causing enlargement of the right optic nerve, with enhancement of its solid component. No hemorrhagic or calcified component. Histopathologic examination demonstrated fragments of a Rosenthal fiber-rich and low cellularity neoplasm, with the characteristic biphasic architecture. The lesion was positive for GFAP and negative for BRAF (V600E) and P53.

Results

Pilocytic astrocytoma (PA) is a WHO grade 1 neoplasm that represents the most common primary brain tumor in the pediatric population. This tumor tends to arise in the cerebellum and optic nerve/chiasm, but can also occur in the brainstem, spinal cord and cerebral hemispheres. In the adult population, PAs represent only 1.5% of the brain tumors, and carry a worse prognosis compared to pediatric PAs. Around 70% of sporadic PAs are associated with the BRAF-KIAA fusion gene, resulting in the constitutive activation of the MAP kinase pathway. On the other hand, BRAF V600E point mutation, almost exclusively occurs in the pediatric population and is mutually exclusive with BRAF fusions. Hereby we intend to review the imaging manifestations and differential diagnosis of an adult optic nerve pilocytic astrocytoma.

Conclusions

PA is a tumor that rarely occurs in adulthood. When affecting this age group, optic pathway location is very uncommon. As it is usually related to NF1, adequate clinical and genetic evaluation is mandatory to rule out the presence of another primary neoplasm.

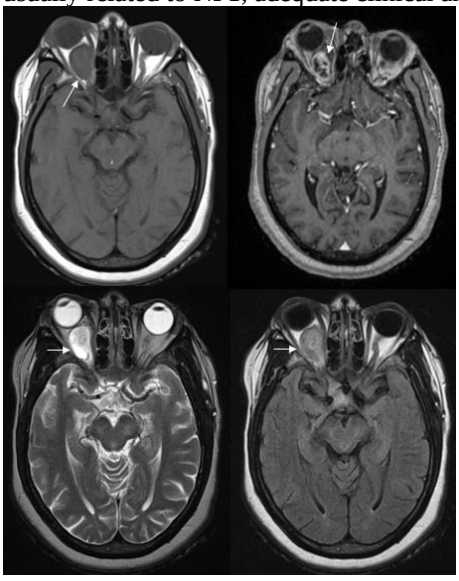

(Filename: TCT_1412_Figure1.JPG)

795

Orbital Canal 'Blind Spots', a Case of Fibrous Dysplasia Causing Bilateral Optic Nerve Compression.

A Khajuria[1], M Krishnakumar[1], S Gregson[2]
[1]Glan Clwyd Hospital, Rhyl, Denbighshire, [2]Royal Preston Hospital, Preston, Lancashire

Purpose

An 18 year old male, presented with blurred vision and papilloedema. Initially under neurology, imaging revealed radiological features of papillodema and a diagnosis of idiopathic intracranial hypertension was made. However, after further rapid decline in his visual acuity, repeat imaging was sought. Subsequent MRI of the orbits demonstrated bilateral optic nerve compression in stenotic optic canals. CT confirmed optic canal stenosis secondary to diffuse groundglass bone expansion, typical of craniofacial fibrous dysplasia (CFD). The patient was subsequently referred to occulo-plastics for consideration of decompression.

Materials and Methods

CT orbits and facial bones showed expansile groundglass bone architecture consistent with craniofacial fibrous dysplasia. Fibrous dysplasia was noted diffusely in the sphenoid bone including the anterior clinoids superiorly, the optic canals, the pterygoid plates inferiorly and the greater and lesser wings of sphenoid laterally. MRI brain showed bilateral optic nerve head cupping and optic canal stenosis with compression of the optic nerves, resulting in bilateral CSF distension of the optic nerve sheaths.

Results

Fibrous dysplasia is a congenital, non-cancerous bone disease. Characterised by replacement of normal bone and marrow, with fibrotic tissue, comprised of pre-osteoblastic cells. Common subtypes include: •Monostotic •Polystotic •Craniofacial CFD is typically seen before the age of 20, is more common in women than men and is usually unilateral. However in our case it is bilateral and affects both optic canals compressing the prechiasmatic optic nerves. On initial read of MRI brain, compression of the optic nerves was not appreciated. It was after progressive deterioration in visual acuity, that a neuroradiology opinion was sought and that the possibility of optic canal stenosis was considered. A CT of the orbits and facial bones was subsequently organised demonstrating the key features of CFD, delineating the degree of optic canal stenosis. A dedicated MRI of the orbits confirmed severe compression of the optic nerves in the optic canals. The patient was urgently referred to occulo-plastics for consideration of decompression.

Conclusions

The orbital apices and optic canals can be a 'blind spot' when reporting. We recommend making this a review area, looking for CSF distention or signal change in the optic nerves. Although rare, CFD can be a cause of optic nerve compression and should be considered as part of a differential.

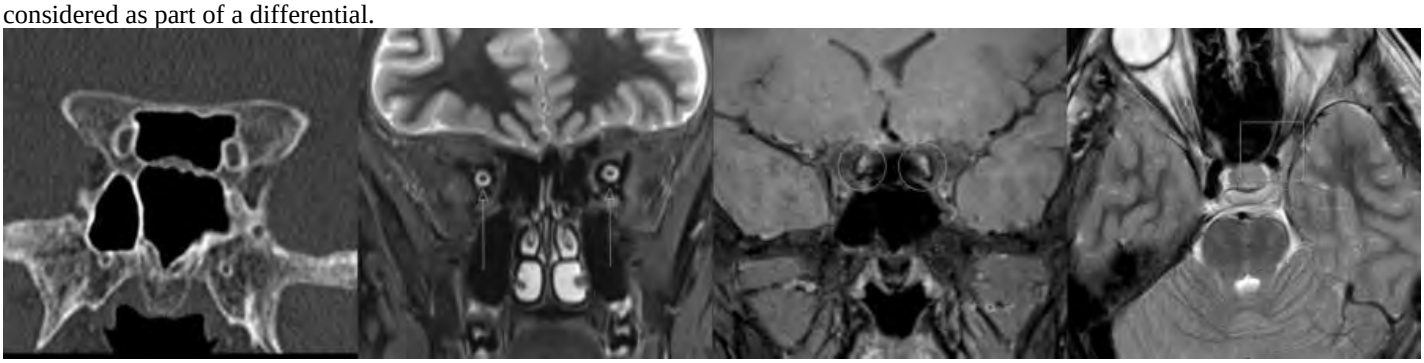

(Filename: TCT_795_ASNRfinal.jpg)

1146

Orbital Lipolysis in the Setting of Metastatic Pancreatic Adenocarcinoma

T Chaudhry[1], p aouad[1]
[1]Northwestern University Feinberg School of Medicine, Chicago, IL

Purpose

52-year-old male with history of metastatic pancreatic adenocarcinoma and failure to thrive presents with intermittent encephalopathy.

Materials and Methods

CT brain demonstrates interval decreased orbital fat content and enopthalamos compared to a prior scan three months prior. MRI brain demonstrates ill-defined enhancement of the retroorbital fat.

Results

Orbital lipolysis refers to the breakdown of fat within the orbit. This has been described in association with chronic catabolic states in cachexia and anorexia. Lipids and triglycerides stored in adipose tissue are broken down to release free fatty acids for energy. We present a case of a patient with new enopthalamos secondary to orbital lipolysis from a catabolic state induced by his metastatic cancer burden.

Conclusions

Orbital lipolysis can be seen in patients in chronic catabolic states such as anorexia, chronic illness, or cancer. This is a different mechanism from enopthalmos in metastatic scirrhous breast cancer described to be due to desmoplastic response.

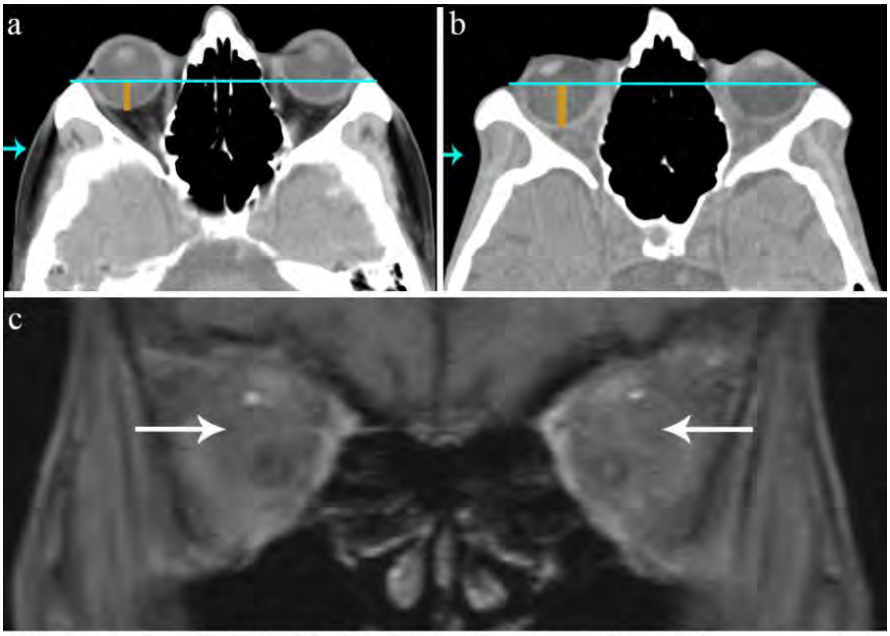

CT of the brain at the level of the lens demonstrates b) interval enopthalmos (orange line) compared to a prior a) CT four months prior in relation to the interzygomatic line (blue line) with loss of orbital fat. Note is also made of the interval severe cachectic state and subcutaneous fat loss (blue arrows). c) MRI Coronal T1 fat-saturated image at the level of the retroorbital fat demonstrates ill-defied enhancement of the retroorbital fat (white arrows).

(Filename: TCT_1146_figure.jpg)

1250

PANCREATIC ENCEPHALOPATHY- LEAST DESCRIBED COMPLICATION OF ACUTE PANCREATITIS

Z Khan[1], M Aslam[2], B Yawar Faiz[3]

[1]Shifa International Hospital, Islamabad, Punjab, [2]Shifa International Hospital, Islamabad, PAKISTAN, [3]Shifa International Hospital Islamabad, Islamabad, Islamabad

Purpose

A young male known diabetic, smoker and alcohol dependent with diagnosis of acute necrotizing pancreatitis and on conservative management for 15days presented to our hospital with falling GCS and involuntary jerky movements of all four limbs. Patient was intubated for ventricular fibrillation and revived after one round of CPR. All pertinent labs sent and despite correcting outright metabolic derangements, primary team could not retrieve this young patient's healthy condition. An EEG performed showed diffuse severe encephalopathy without any epileptic activity to support seizure disorder.Patient was further investigated with MRI brain which showed bilateral symmetrical areas of restricted diffusion in periventricular and centrum semiovale with subtle FLAIR hyperintensities signifying changes of acute encephalopathy. No territorial distribution or typical hypoxic ischemic insult pattern identified. Lack of clinical triad, absence of response to vitamin B1 trial and lack of relevant imaging findings excluded Wernicke encephalopathy in our patient. Though not recovered completely our patient is being managed conservatively for optimization of general physiological conditions and recurrent peripancreatic collections. Consequently, patient has shown improvement in GCS and is extubated.

Materials and Methods

Bilateral symmetrical restricted diffusion in centrum semiovale and periventricular white matter on axial MRI brain images.Correspondingly subtle FLAIR hyperintensities in bilateral centrum semiovale and periventricular white matter on axial MRI brain images.

Results

Fortunately, rare but one of the fatal complications of acute pancreatitis is pancreatic encephalopathy and therefore requires special consideration.The pathogenesis of pancreatic encephalopathy is incompletely understood. The objective of our case report is to consider an unusual but possible complication of acute pancreatitis. Furthermore, highlighting the importance of diagnostic brain imaging and its implication in excluding other likely possibilities of encephalopathy in such clinical setting, which always creates a state of perplexity among clinicians.

Conclusions

Pancreatic encephalopathy should only be considered after more likely possibilities like ischemia, uremia, hypoxemia, electrolyte abnormalities, thiamine deficiency, have been excluded. MRI brain shows restricted diffused with non-enhancing hyperintense lesions on T2 and hypointense lesions on T1.

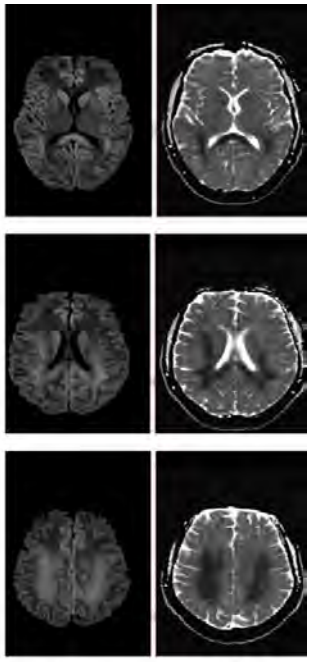

Bilateral symmetrical restricted diffusion in centrum semiovale and periventricular white matter on axial MRI brain images.

(Filename: TCT_1250_IMG_20211115_191451.jpg)

243

Papillary Thyroid Cancer in a Thyroglossal Duct Cyst – Multimodality Imaging Features

C Cave[1], M Ali[1], B Griffith[1], S Patel[1]
[1]Henry Ford Health System, Detroit, MI

Purpose

A 31-year-old female presents with increasing fullness under her chin for 8 months. On clinical exam a firm midline submental mass was found. Given concern for a neoplastic process, surgical excision was performed. Pathology showed a thyroglossal duct cyst (TDC) with associated papillary thyroid carcinoma invading the adjacent soft tissues and hyoid bone.

Materials and Methods

(A) CT demonstrates a cystic and solid submental mass with punctate calcifications. The mass abuts the hyoid bone. (B) US shows minimal vascularity within the solid component. (D) On MRI, the solid component shows avid enhancement.

Results

TDC's are relatively common, however, malignancy within a TDC is seen in less than 1% of patients and thought to arise from remnant thyroid tissue. Papillary thyroid cancer is most common. Concern for malignant degeneration should be raised in the setting of suspicious imaging features.

Conclusions

Malignancy should be excluded in a TDC that has imaging features of nodularity, enhancement, or calcifications.

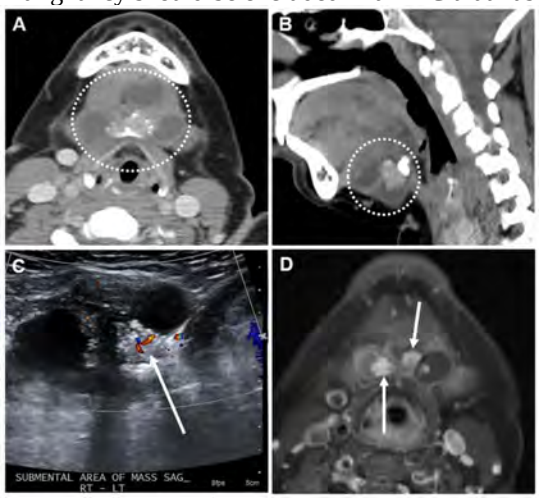

(Filename: TCT_243_TDC.jpg)

113

Pearls and Pitfalls of Primary Angiitis of Central Nervous System: Nailing An Evasive Diagnosis

D Montes[1], M Braileanu[1], A Singhal[1], M Martinez-Lage[1], B Sannananja[2], J Romero[1], R Peterson[3]
[1]Massachusetts General Hospital, Boston, MA, [2]Emory, Atlanta, GA, [3]EMORY UNIVERSITY SCHOOL OF MEDICINE, NORCROSS, GA

Purpose

A 55-year-old male patient with two prior strokes in the past month was admitted with new right-sided weakness. Physical examination was notable for right central facial paralysis, dense right hemiparesis, decreased light touch and pinprick sensation in the right hemi-body. Admission work-up laboratory tests were unremarkable. Initial imaging with CT angiography revealed a punctate focal hyper-density on the left middle cerebral artery and irregular opacification of left posterior cerebral artery. Brain MRI revealed widespread regions of acute and infarctions. The multi-vessel involvement, recurrent strokes, and rapid progression raised concerns for a vasculitic process. To further characterize, high-resolution vessel wall (VW) MRI and lumbar puncture (LP) were ordered. VW MRI showed concentric VW enhancement of the left P1 and M1 segments, while the LP was negative for infection or malignancy. Treatment with steroids and IV cyclophosphamide was implemented. One week after admission, the patient underwent brain biopsy and VW MRI follow-up. Despite a normal biopsy, a clinical diagnosis of PACNS was established based on the negative lab work-up, the elevated protein count on CSF analysis, and the marked improvement of symptoms and vessel wall enhancement.

Materials and Methods

Multifocal vessel narrowing with high-grade stenosis, multi-vessel acute and subacute strokes, multi-vessel vessel wall enhancement with response to treatment.

Results

•Symptoms include cognitive dysfunction, focal neurological deficit, headaches, or constitutional symptoms. •Intracranial vasculopathies share angiographic findings: intermittent vessel wall narrowing, fusiform dilations, or complete occlusion. •MRI findings include disseminated small acute infarcts, isolated white matter or leptomeningeal lesions, foci of restricted diffusion within white matter lesions, mass-like lesions, hemorrhage, concentric VW enhancement. •Brain biopsy may yield false-negative results due to the patchy distribution of PACNS.

Conclusions

•PACNS findings often overlaps with other more common neurological disorders. •Angiographic imaging techniques have low specificity. •Close to 100% of patients will have an abnormal MRI at the time of presentation. •Brain biopsy is valuable yet imperfect. •PACNS diagnosis is elusive; interdisciplinary communication between neuroradiologists, neurologists and neuropathologists is essential.

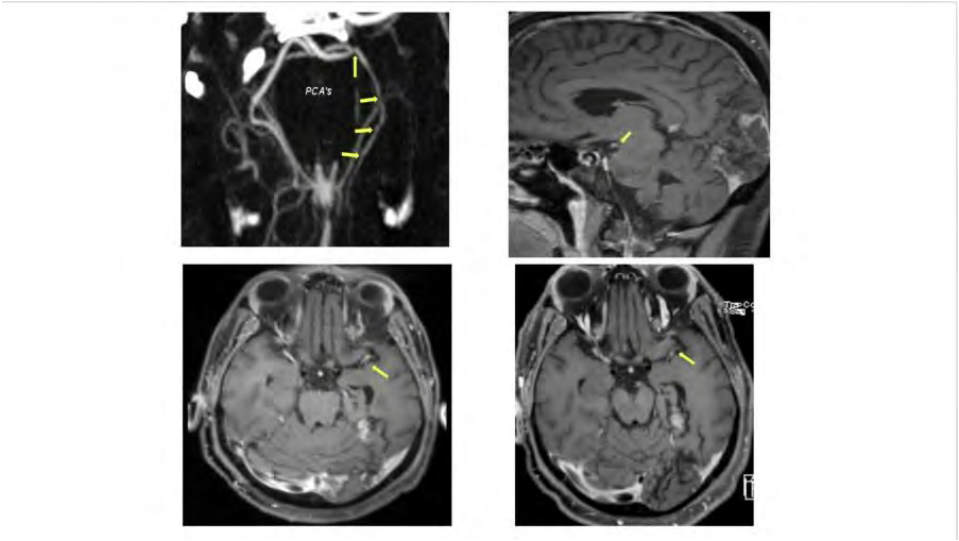

(Filename: TCT_113_ASNR4picsfinal.jpg)

1481

Pharyngo-Tympano-Stapedial Middle Meningeal Artery (PTS-MMA) Variant Supply to a Falcotentorial Dural Arteriovenous Fistula

A Baker[1], M Caton[1], K Raygor[1], K Narsinh[1], E Smith[1], C Dowd[1], D COOKE[1], R Higashida[2], M Amans[1], A Abla[1], S Hetts[3]
[1]UCSF, San Francisco, CA, [2]University of California, San Francisco, San Francisco, CA, [3]UCSF, San Fransico, CA

Purpose

A 58-year-old female with no prior medical history presented severe, daily headaches and gait imbalance.

Materials and Methods

MRI demonstrated arteriovenous shunting to a varix as well as precentral cerebellar and superior vermian veins in the falcotentorial region predominantly from an enlarged left MMA. Cerebral angiography confirmed a dAVF supplied by the left MMA, right PMA,

and Davidoff and Schechter arteries of the right PCA. The right ECA angiogram was notable for absence of a right MMA. Follow-up angiography three months status post transarterial Onyx embolization of the left MMA showed residual shunting predominantly from a hypertrophied right pharyngo-tympano-stapedial middle meningeal artery (PTS-MMA) variant.
Results
The PTS- MMA variant is extremely rare, and never described in the setting of arterial supply to a falcotentorial dAVF. Embryologically, this variant occurs when there is abnormal regression of the proximal stapedial artery 1-3. The PTS-MMA originates from the medial proximal cervical internal carotid artery to follow the course of the inferior and superior tympanic arteries to the posterior fossa2, and in this case, to the falcotentorial dAVF.
Conclusions
Middle meningeal artery variants, albeit rare, are important to understand for their contribution to intracranial vascular pathology and endovascular as well as surgical treatment.

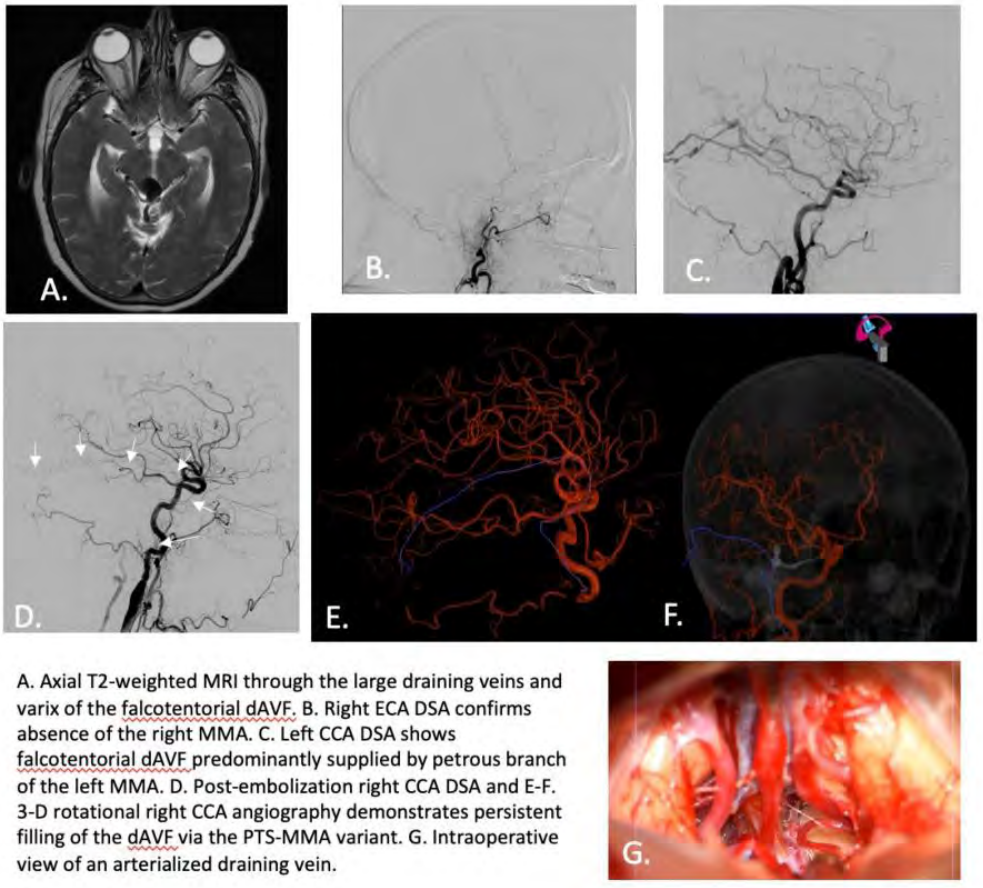

A. Axial T2-weighted MRI through the large draining veins and varix of the falcotentorial dAVF. B. Right ECA DSA confirms absence of the right MMA. C. Left CCA DSA shows falcotentorial dAVF predominantly supplied by petrous branch of the left MMA. D. Post-embolization right CCA DSA and E-F. 3-D rotational right CCA angiography demonstrates persistent filling of the dAVF via the PTS-MMA variant. G. Intraoperative view of an arterialized draining vein.

(Filename: TCT_1481_PTS_MMA_photocopy.jpg)

198

Phosphaturic Mesenchymal Tumor: A Multimodality Meningioma Mimic on MRI, In-111 Octreotide SPECT/CT, and Ga-68 DOTATATE PET/CT

B Burkett[1], S Broski[1], M Drake[1], A Folpe[1], C Hunt[2], D Johnson[2]
[1]Mayo Clinic, Rochester, MN, [2]Mayo Clinic, ROCHESTER, MN

Purpose
A 50-year-old man presented with presumptive osteomalacia, multiple insufficiency fractures, and hypophosphatemia. Fibroblast growth factor-23 was inappropriately normal.
Materials and Methods
Brain MRI showed an enhancing, dural-based lesion in the right inferior temporal fossa (Images A-B). In-111 Octreotide SPECT/CT (Image C), and more so, Ga-68 DOTATATE PET/CT (Image D) demonstrated avid uptake (SUVmax 75.1).
Results
In most cases, the differential for a lesion with these characteristics would include meningioma and solitary fibrous tumor. However, given the clinical suspicion of tumor-induced osteomalacia, a phosphaturic mesenchymal tumor (PMT) would also be considered. After resection of this mass, the patient experienced improvement in symptoms. Pathology confirmed the diagnosis of PMT. Often challenging to localize, PMTs can occur essentially anywhere in the bones or soft tissues and are usually small (3.4 cm mean

diameter) (1). Expression of the somatostatin 2A receptor is a consistent feature enabling localization with Ga-68 DOTATATE PET (2).
Conclusions
A PMT can perfectly mimic a meningioma on multiple imaging modalities. However, with high clinical suspicion, this rare entity is an important consideration and a treatable cause of osteomalacia.

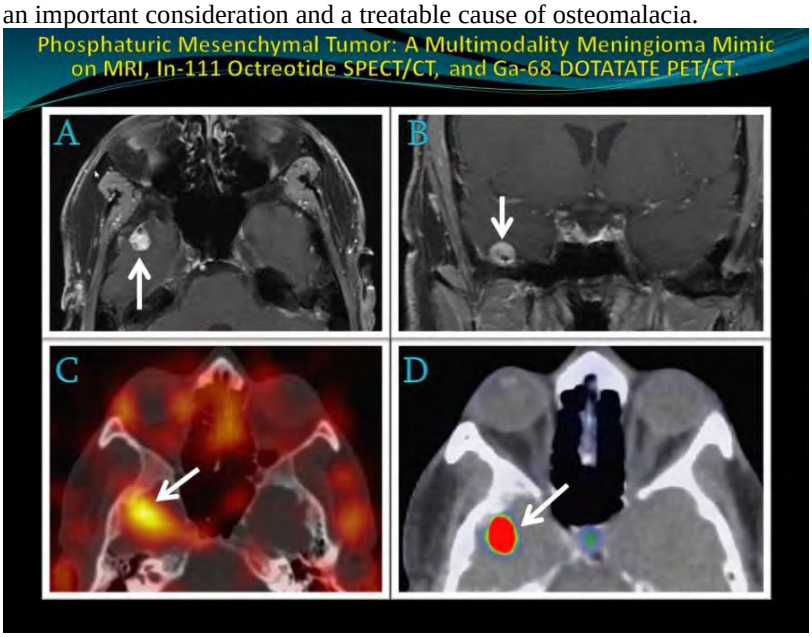

(Filename: TCT_198_PMT_excerpta_abstractfigure_final.jpg)

1107
Physiologic Enhancement of Scarpa's Ganglia Mimicking Bilateral Vestibular Schwannomas in Patient with Atypical Meningioma with NF2 Mutation
J Schmidgall[1], R Saucedo[1], P Dubey[1], D Baskin[1], B Teh[2], I Tremont-Lukats[1], S Fung[1]
[1]Houston Methodist Hospital, Houston, TX, [2]Houston Methodist, Houston, TX

Purpose
A 36 year-old man with remote history of treated medulloblastoma presents more recently with left temporal convexity dural-based mass that was resected. Pathology showed WHO grade 1 meningioma with high proliferation rate. The mass recurred 1.5 years later with invasion of the left temporalis muscle that was resected. Pathology this time showed WHO grade 2 atypical meningioma with NF2 mutation that prompted re-evaluation of small nodular enhancing foci in bilateral internal auditory canals (IACs), concerning for vestibular schwannomas.
Materials and Methods
Contrast-enhanced T1WI (top) shows symmetric 2 mm foci of enhancement in the fundi of bilateral IACs (yellow arrows), which have been stable over 10 years of serial imaging. CISS (bottom) shows normal smooth contours of fundal vestibular nerves without corresponding nodularity.
Results
Variable enhancement in the fundus of IACs is sometimes present without underlying pathology, presumably due to vascular enhancement in the region of Scarpa's ganglion. Presence of enhancement should be correlated with nodularity on CISS to support schwannoma. In our case, normal smooth contours of vestibular nerves on CISS and long-term stability support enhancement of Scarpa's ganglia more likely than schwannomas. Approximately 33-60% of patients with meningiomas have a somatic NF2 mutation, more prevalent in fibrous and transitional variants as well as in higher grade tumors and radiation-induced meningiomas. Our patient had genetic testing that was negative for NF2 mutation; therefore, the NF2 mutation noted on pathology represents somatic mutation within the meningioma tumor cell population.
Conclusions
Enhancement in the fundus of IACs due to physiologic enhancement of Scarpa's ganglion may result in false positive diagnosis of small intracanalicular vestibular schwannoma and should be correlated for nodularity on CISS. Additionally, one should be aware of the high rate of somatic NF2 mutation in meningiomas, especially atypical meningiomas, and not incorrectly assume this equates to germline NF2 mutation in the patient, which would greatly increase probability for bilateral vestibular schwannomas.

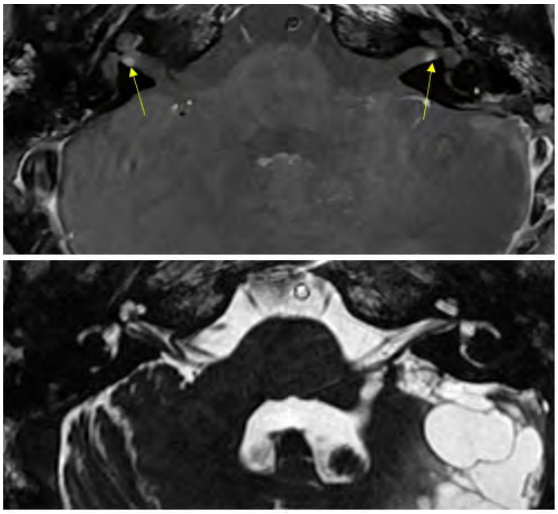

(Filename: TCT_1107_Figure3.jpg)

555

Pictures Worth a Thousand Words: The Importance of Using Multiple and Varied Imaging Modalities to Solve the Puzzle and Guide Treatment

K Bojicic[1], E Fedak Romanowski[1], H Garton[1], D Gomez-Hassan[1]
[1]*University of Michigan, Ann Arbor, MI*

Purpose

Our patient is 4 year old female with a history of infantile spasms beginning at 2 months of age and progressing to refractory epilepsy by 3 years of age. Patient presented to our institution for treatment after failure of medication to control her seizures and no source for her symptoms identified. During the course of her care, a total of 7 imaging studies were obtained with each contributing meaningful guidance towards identifying the etiology, directing treatment, and ultimately achieving a cure.

Materials and Methods

Epilepsy focused MRI demonstrated a broad area of gray-white matter blurring, cortical thickening and slight T2 FLAIR hyperintensity in the left parietal lobe suspicious for focal cortical dysplasia. SPECT imaging confirmed a corresponding area of hyperperfusion. A CT angiogram and an MR stealth were obtained for ROSA SEEG implantation. A grid focused MRI and CT head were obtained to localize the position of each electrode. Once seizures were localized and neurologic function was not affected, surgical resection was performed. Postoperative imaging confirmed complete resection of the lesion.

Results

Imaging tells a story in the management of patients with refractory epilepsy. Imaging was used to identify a focal cortical dysplasia, confirm the dysplasia as the source of symptoms, and guide the therapy performed to remove the dysplasia. The patient in our case initially presented with seizures occurring 4-5 times per day resulting in developmental delay. After treatment, the patient is off antiepileptic medication, seizure free, and making strides in learning and development. The treatment team guided by multiple and varied imaging studies was able to directly impact the patient's quality of life for the better.

Conclusions

Imaging provides essential diagnostic information and vital contribution to the management and treatment of epilepsy. Understanding the contribution each study makes to the workup will enhance our ability to guide treatment.

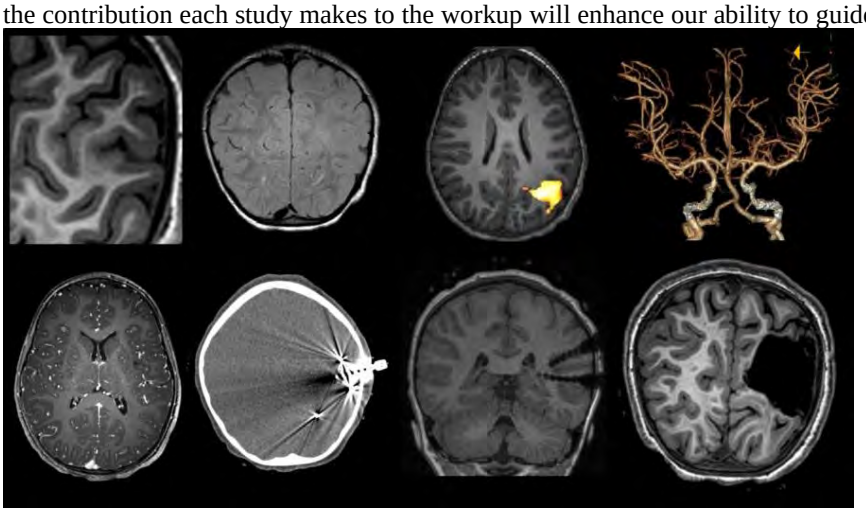

(Filename: TCT_555_ASNRExcerpta.jpg)

1490

Post-traumatic Intratumoral Hemorrhage in Craniopharyngioma Presenting with Cerebral Infarct

S Hegde[1], S Ansari[2]

[1]KVG Medical College and Hospital, Sullia, India, [2]Rush University Medical Center, Chicago, IL

Purpose

A 29-year-old male with a past medical history of biopsy-proven craniopharyngioma (adamantinomatous subtype), status post-subtotal resection, presented in January 2020 following a motor vehicle accident. On admission, E4V5M6 with right-sided paraparesis.

Materials and Methods

Non-contrast Computed Tomography (CT) of the brain revealed a heterogeneous mass in the sellar-suprasellar region with a hemorrhagic component. Right anterior temporal parenchymal hematoma and thin subdural hematoma along right cerebral convexity were significant findings. No calvarial fracture noted. Magnetic Resonance Imaging (MRI) brain with intravenous contrast obtained for further evaluation revealed a solid-cystic sellar-suprasellar mass, progressively increasing in size when compared to MRI from 2018 and 2019 (Figs. A, B and C). A new curvilinear hemorrhagic component was noted along the anterosuperior margin of the lesion (Fig. D) and a small hemorrhagic focus posteriorly. Interval increase in the mass effect on the left inferior frontal lobe and basal ganglia superiorly and on midbrain tegmentum inferiorly. Bilateral cavernous sinus and cavernous segment of internal carotid arteries were uninvolved. Acute infarct was noted involving the left corona radiata, caudate and lentiform nucleus (Fig. E). No large vessel occlusion or severe stenosis seen on Time of Flight MR Brain angiogram (Fig. F). A post-traumatic intratumoral hemorrhage causing an abrupt increase in lesion size with resultant compression of left lateral lenticulostriate arteries considered as possible etiology.

Results

Craniopharyngiomas (CPs) represent 3% of intracranial tumors with a bimodal age distribution (first and sixth decades). They represent Rathke pouch remnant. Two subtypes seen, adamantinomatous (most common) and papillary. Adamantinomatous CPs are mixed solid-cystic with a lobulated appearance, while papillary CPs are chiefly solid tumors. 60% are calcified. Cystic elements typically are hyperintense on T1-weighted images, secondary to high protein content, cholesterol, mild calcification or haemorrhage. Intratumoral hemorrhage is common in brain tumors (14.6%), however, very rare in craniopharyngioma. Only two articles report CP with intratumoral hemorrhage, out of which only one case was post-traumatic. No similar case of craniopharyngioma presenting with infarct reported in literature.

Conclusions

Abrupt intratumoral hemorrhage can lead to acute emergencies like infarct due to vascular involvement.

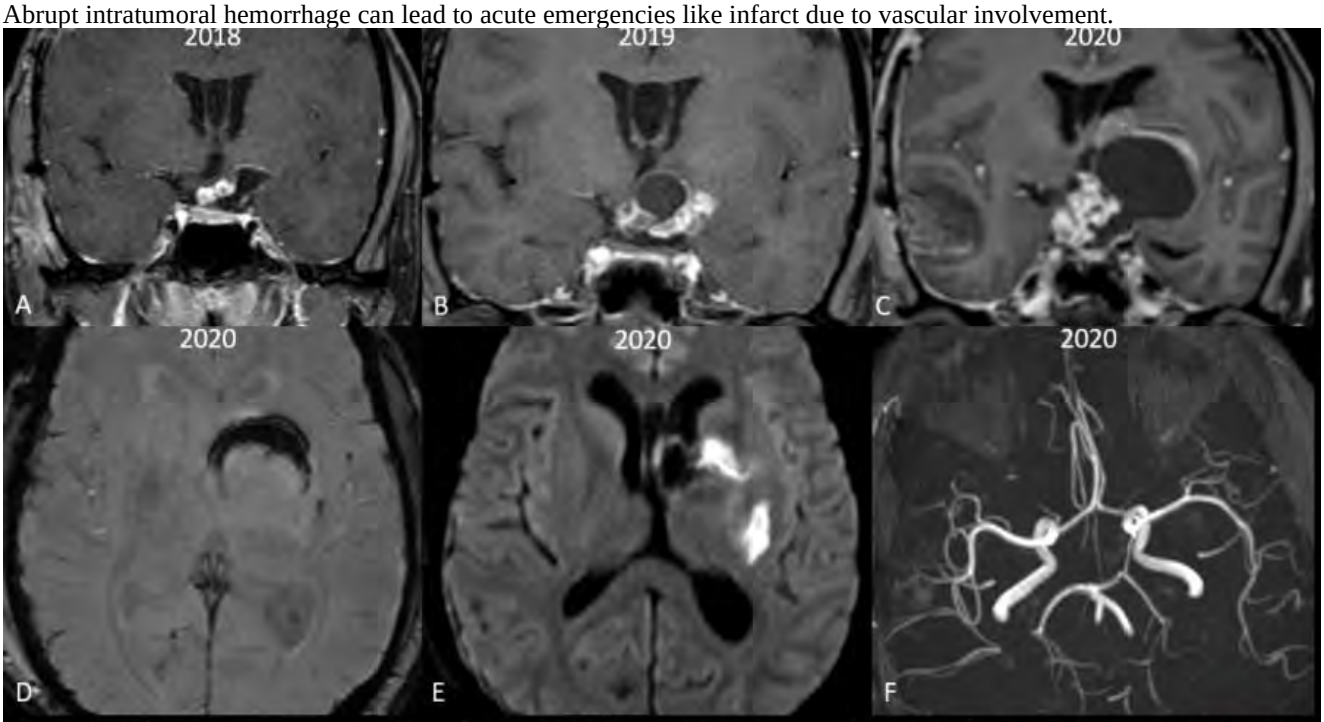

Figs. A, B and C: corresponding coronal sections of post contrast T1-weighted fat-suppressed images showing progressive increase in tumor size with associated mass effect. Fig. D: Susceptibility weighted imaging (SWI), axial section, showing curvilinear hemorrhage along the anterior margin of the lesion. Fig. E: Diffusion-weighted imaging (DWI), axial section, showing restricted diffusion involving left caudate and lentiform nucleus. Fig. F: TOF MRA 3D axial: No large vessel occlusion.

(Filename: TCT_1490_fig2.jpg)

1066

Postoperative Lumbar Fusion Paraspinal Desmoid Tumor Case Report

J Yan[1], J Chazen[2]

[1]New York Presbyterian Hospital Weill Cornell, New York, NY, [2]Hospital for Special Surgery, New York, NY

Purpose

A 76-year-old male with chronic back pain and lumbar spondylolisthesis underwent L3-L5 posterior spinal fusion in 2018. Postoperatively, patient experienced no complications and continued with regular interval follow ups.

Materials and Methods

Immediate postoperative imaging showed a normal appearance of paraspinal muscles (Figure 1A). Follow up MRI August 2021 showed a new T2 hypointense lesion in the right paraspinous soft tissues at the L1-L2 level, measuring 5 x 4 cm (Figure 1B). CT abdomen pelvis was performed at an outside institution on September 2021 (Figure 1C), which redemonstrated the mass. CT-guided biopsy was performed of the right L2 paraspinal muscle/soft tissue mass using a standard 18Ga 6 cm Bard biopsy needle (Figure 1D). Three core biopsies were taken and pathology results confirmed desmoid fibromatosis.

Results

Desmoid tumors, also called aggressive fibromatoses, are rare soft tissue tumors typically arising sporadically. Since 1961, only 7 cases of postoperative paraspinal desmoid tumors in adults have been reported. All cases have been female with four of seven cases involving posterior spinal instrumentation (1-2). This is the first reported postoperative desmoid tumor case in a male patient.

Conclusions

Although desmoid tumors are slow growing and benign, clinical course is variable. Thus, these lesions are important postoperative considerations.

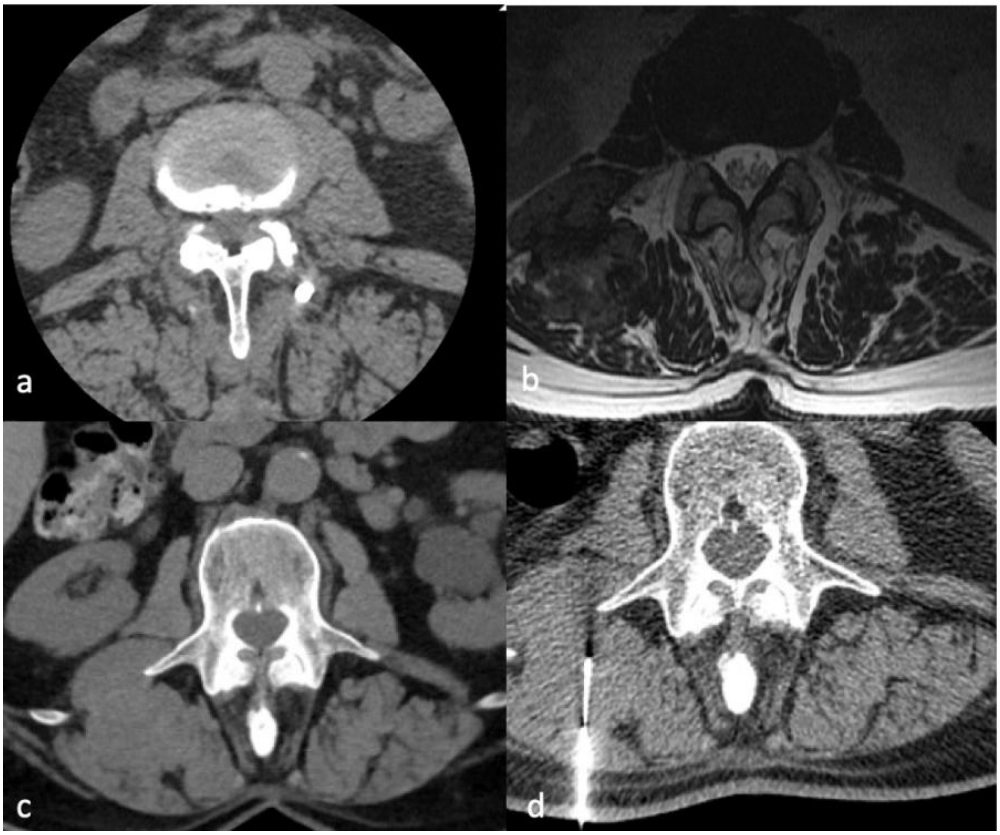

(Filename: TCT_1066_Figure1Desmoid.jpg)

346

Potential Role of ASL Perfusion Imaging in Stroke Mimics: Uremic Encephalopathy

B Patel[1], V Yedavalli[1]

[1]Johns Hopkins School of Medicine/Johns Hopkins Hospital, Baltimore, MD

Purpose

67 year old Korean female with ESRD, hypertension, diabetes mellitus, presented to the hospital with left facial droop, slurred speech, bilateral upper extremity weakness, for initial concern of acute stroke. Serum potassium was 7.5 mmol/L, creatinine was 11 mg/dL, and blood urea nitrogen was 93 mg/dL in the setting of missed dialysis session.

Materials and Methods
MRI shows increased FLAIR, abnormal DWI/ADC signal, elevated DSC CBF in the putamina with rim of surrounding T2 hyperintense edema. 3D pulsed ASL shows corresponding symmetric increased signal in the putamina, confirming UE.
Results
Uremic encephalopathy is a well-known complication which can occur in renal failure patients, presenting with acute confusion, visual deficits, movement disorders, and headaches. Imaging and clinical findings occur in 3 general patterns: cortical with PRES features, basal ganglia type usually in diabetics, and a white matter type. Accumulation of uremic metabolites can inhibit mitochondrial function. This, along with the vulnerability of the basal ganglia in diabetics due to microvascular damage and endothelial dysfunction, lead to both cytotoxic and vascular damage. This explains the FLAIR/DWI signal abnormalities and corresponding ASL findings. The symmetric elevated ASL signal in the putamina is due to increased blood pooling from edema and microscopic blood brain barrier disruption from uremic toxins and hyperkalemia. ASL confirms the cause of both the clinical presentation and DWI/ADC findings as toxic injury, rather than infarct. Stroke mimics can confound the optimization of candidate selection for thrombolysis. The most common mimics are partial epilepsy and psychiatric disorders followed by infectious, metabolic/toxic pathologies, tumors, cortical vein thrombosis, and demyelinating inflammatory disease. They can occur in up to 1-14.5% of patients treated with IV thrombolysis for suspected acute stroke. ASL, along with clinical history, can help to confirm or exclude nonvascular neurologic pathologies, and provide information for the differential diagnosis that reproduce the symptoms of stroke.
Conclusions
ASL signal patterns can complement MRI DWI/FLAIR findings in vascular and nonvascular causes. Symmetric signal changes point towards a toxic-metabolic pathology. ASL can aid in clinical management by alluding to another reversible cause or stroke mimic in the emergent setting. Since stroke and uremic encephalopathy can present acutely, ASL can be valuable in guiding appropriate management.

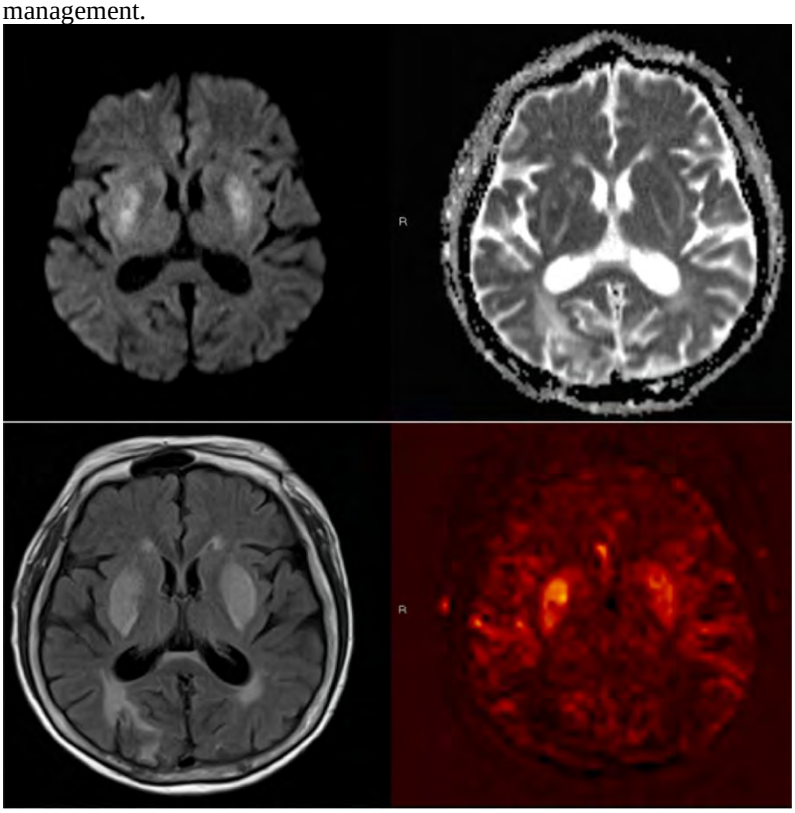

(Filename: TCT_346_ASNR2022.jpg)

1359
Pre-contrast Enhancement of Cerebral White Matter in X-ALD
A Swenson[1], D Nascene[1]
[1]University of Minnesota, Minneapolis, MN

Purpose
Six male pediatric patients with X-linked adrenoleukodystrophy (ALD) with varying degrees or genetic expression at presentation. Symptoms included behavioral changes, GI upset/vomiting, hearing changes, and asymptomatic screening due to first degree relatives with known ALD diagnosis.
Materials and Methods
Post hematopoietic stem cell transplant (HSCT) follow up imaging as well as imaging at presentation was reviewed. Brain MRI showed ALD related changes including symmetric post contrast rim enhancement and restricted diffusion surrounding the damaged

white matter. Areas of demyelination included the corpus callosum with sparing of the subcortical U-fibers. Presumed post contrast rim enhancement was also appreciated on some pre-contrast T1 images. Mineral like densities within the affected white matter were also visualized on some pre- and post-contrast images.
Results
Pre-contrast rim enhancement was observed in 3 of 6 reviewed cases. True post-contrast enhancement was seen in 1 case prior to (HSCT) and then resolved treatment. Mineral like deposition in the affected white matter was observed in 4 of 6 cases, more prominent in advanced disease. All 6 cases showed restricted diffusion at the peripheral edges of involved white matter.
Conclusions
Post-contrast rim enhancement is a key finding in the determination of active demyelination in ALD patients with progressing disease (Engelen et al). Just because something is bright on post-contrast T1 imaging does not mean it is truly enhancing. Careful review of pre-contrast T1 images is needed.

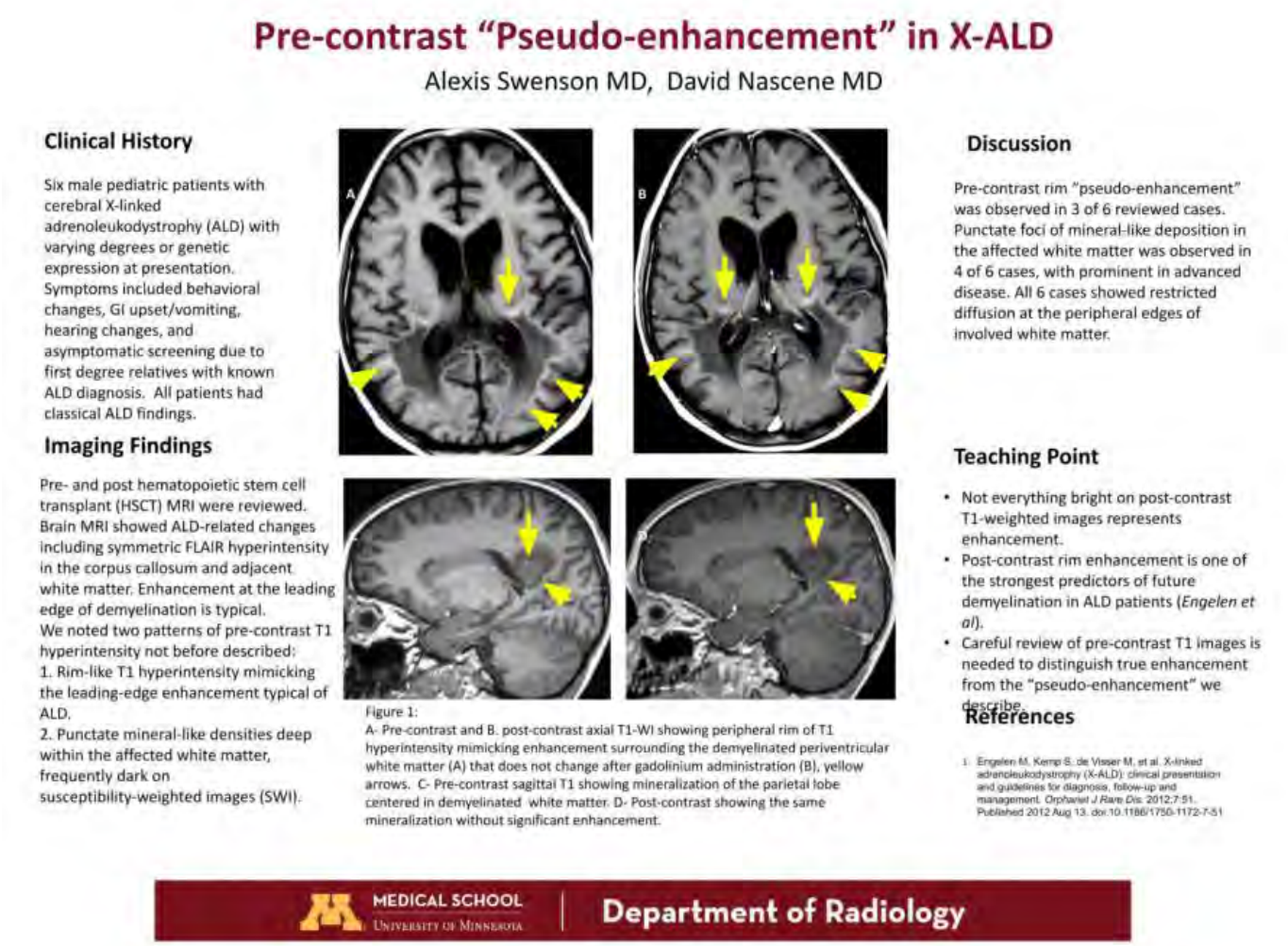

(Filename: TCT_1359_swenson.jpg)

825
Primary Central Nervous System Lymphoma with Parenchymal, Perivascular and Leptomeningeal Spread in an Immunocompetent Patient
C Yalniz[1], R Riascos[1], J McCarty[1]
[1]*The University of Texas Health Science Center at Houston, Houston, TX*

Purpose
64-year-old female with past medial history of migraines and depression presented with balance issues, manifesting as walking difficulty, left-sided upper and lower extremity weakness and headaches for past 2-3 days.
Materials and Methods
MRI images demonstrated an in intra-axial centrally cystic mass in the right parietal lobe with concentric enhancement pattern, more intense internal enhancement and more ill-defined less intense rim enhancement. There was restricted diffusion associated with the enhancing component but there was no hemorrhage or calcification. A similar appearing lesion was seen in the right pons. Additional more ill-defined scattered punctate parenchymal and linear perivascular enhancing lesions were noted in the splenium of corpus

callosum, right basal ganglia, right medial temporal lobe and a nodular focus was present along the dorsal cervicomedullary junction. Corresponding to the enhancing lesions, there were patchy areas of increased FLAIR signal. Findings were favored to represent an atypical infectious process such as tuberculosis, toxoplasmosis, fungal infections, inflammatory etiologies or central nervous system lymphoma. Demyelination was thought to be less likely, as were high-grade glioma or metastases. Pathology of the right parietal lobe lesion demonstrated diffuse large B-cell lymphoma, nongerminal center cell subtype, positive for CD20, BCL6, MUM1 and negative for CD10.

Results

Primary central nervous system lymphomas are relatively uncommon tumors, accounting for less than 3% of all brain tumors. It generally presents as a hyperdense enhancing mass on CT and T1 hypointense, T2 iso to hypointense avidly enhancing mass with diffusion restriction and relatively small vasogenic edema on MRI. They are usually supratentorial, in contact with ependymal surfaces and crossing corpus callosum. They can rarely demonstate T2 hyperintensity when there is associated central necrosis. In immuncomprised patients peripheral ring enhancement can be seen rather than homogenous enhancement.

Conclusions

Primary central nervous system lymphomas are relatively uncommon tumors. In immuncomprised patients they can demonstrate peripheral ring enhancement rather than homogenous enhancement and accompanying ill-defined parenchymal, perivascular and leptomeningeal enhancing lesions can be seen.

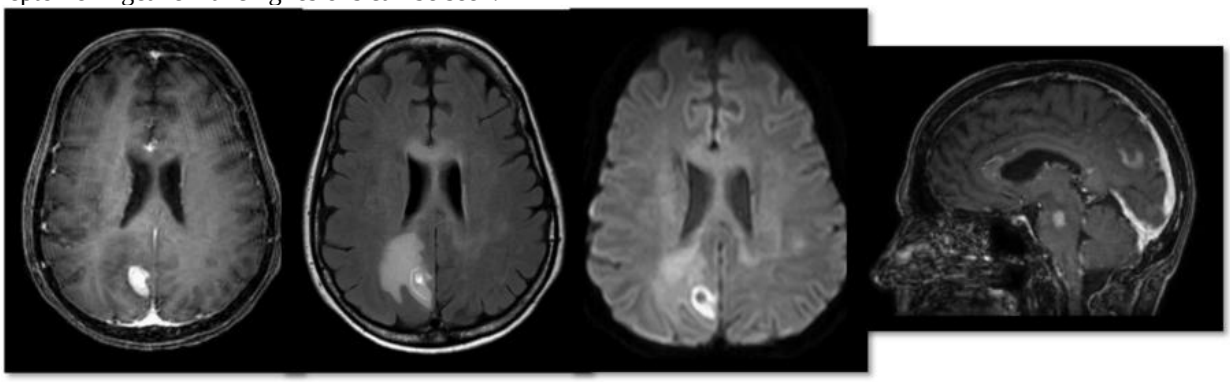

(Filename: TCT_825_Picture21.jpg)

1406

Pseudotumoral Hemicerebellitis in a Pediatric Patient

C Davis-Hayes[1], E Weidman[2]

[1]Cornell/ NYP, NEW YORK, NY, [2]Weill Cornell Medicine, New York, NY

Purpose

A previously healthy 8-year-old female presents with headaches for 10 days and vomiting for 1 day. 3 weeks prior, she was diagnosed with streptococcal pharyngitis and treated with oral antibiotics.

Materials and Methods

Contrast enhanced MRI demonstrates expansile T2 hyperintensity in the right cerebellum (Fig 1c) with facilitated diffusion (Fig 1a,b). Post-contrast T1 demonstrates pial enhancement (Fig 1d). Follow up MRI at 8 months with resolved enhancement and minimal gliosis (Fig 1e,f).

Results

Acute cerebellitis is a rare inflammatory disorder that occurs most frequently in children following infection. It is typically bilateral, but unilateral involvement can occur (hemicerebellitis or pseudotumoral cerebellitis). Differential diagnosis is broad, including ADEM, subacute infarction, Lhermitte Duclos, and medulloblastoma. Acute infectious rhomboencephalitis was excluded by CSF serologies.

Conclusions

Pseudotumoral hemicerebellitis is a rare manifestation of acute cerebellitis. Radiologists should be aware of this entity and its potential complications, including hydrocephalus and tonsillar herniation, and not mistake it for tumor.

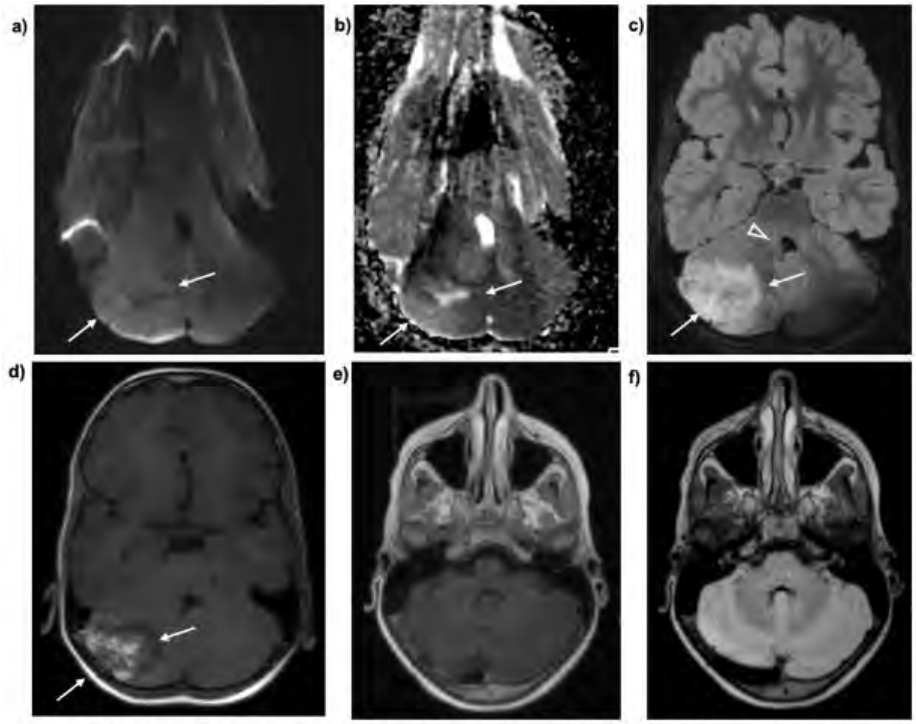

Figure 1: MRI Brain with and without IV contrast at time of presentation (**a-d**) and at 8 month follow up, after resolution of symptoms (**e, f**). **a, b,** axial DWI and ADC demonstrate facilitated diffusion *(arrows)*, **c,** axial T2 FLAIR with expansile heterogenous T2 hyperintense signal in the right cerebellum *(arrows)* causing mass effect on the 4th ventricle *(open arrow)*, **d**, axial T1 post-contrast demonstrates enhancement along the cerebellar folia *(arrows)*, **e, f,** axial T1 post-contrast and T2 FLAIR at 8 month follow up demonstrate resolution of signal abnormalities.

(Filename: TCT_1406_Figure.jpg)

736

Radiation Necrosis as a sequelae to Gamma Anterior Cingulotomy

D Sharma[1], J Saini[2]

[1]NIMHANS Bangalore, Nagpur, India, [2]NATIONAL INSTITUTE OF MENTAL HEALTH & NEURO SCIENCES, BANGALORE, India

Purpose

A fifty-four-year old housewife with polypharmacy-refractory depression for 28 years. She had multiple episodes with refractory condition, electroconvulsive therapy (ECT) was initiated frequency of sessions was increased to 2-3 per week with little improvement. After careful consideration, GKRS treatment was offered. A dose of 150 Cgy (GKRS) was delivered with an intent of bilateral anterior Cingulotomy. Her pre-GKRS Magnetic Resonance Imaging (MRI) was unremarkable.Nine-months post-procedure, she exhibited withdrawn behaviour and palilalia. Repeat MRI at this time point following gamma knife therapy showed nodular enhancing lesions involving bilateral anterior cingulate gyri with surrounding edema. The temporal sequence of imaging changes, their location conforming to the radiation site, the imaging characteristics, favoured a diagnosis of radiation necrosis. The imaging diagnosis was further substantiated by Perfusion MRI, which showed hypo perfusion in affected areas and Spectroscopy showing mild elevated choline, reduced NAA and elevated lactate peaks. She was managed with anti-edema measures and short course of systemic corticosteroid. Her symptoms improved and was discharged in stable condition. Follow up MRI after 3 months of treatment showed markedly reduced edema in the frontal lobe with reduction in the intensity and thickness of the enhancing margin.

Materials and Methods

The typical imaging features of radiation necrosis are T2 hypointense lesions in the area of the irradiated field which shows 'Swiss cheese pattern' or 'soap bubble' type of enhancement. On MR spectroscopy radiation necrosis shows increased lactate and lipid, reduced NAA and variable choline, commensurate with necrosis.

Results

Imaging differentials that were considered was a glioma, however, T2 isointense to hypointense nature of lesions, the symmetrical morphology and temporal resolution of signal changes favoured the diagnosis of radiation necrosis over glioma. Granulomatous lesions, although was a possibility was excluded in view of clinical history and typical location of the lesion.

Conclusions

To conclude, this report is the first to highlight novel imaging features of complication related to Radiation Necrosis in Gamma-knife Anterior Cingulotomy, "non-invasive stereotactic radiosurgery", challenging its "risk-free benign" connotation. Multimodal MRI, characteristic imaging timelines, the unique anatomical location, and response to steroids are key aspects in the diagnosis of this clinicoradiological entity.

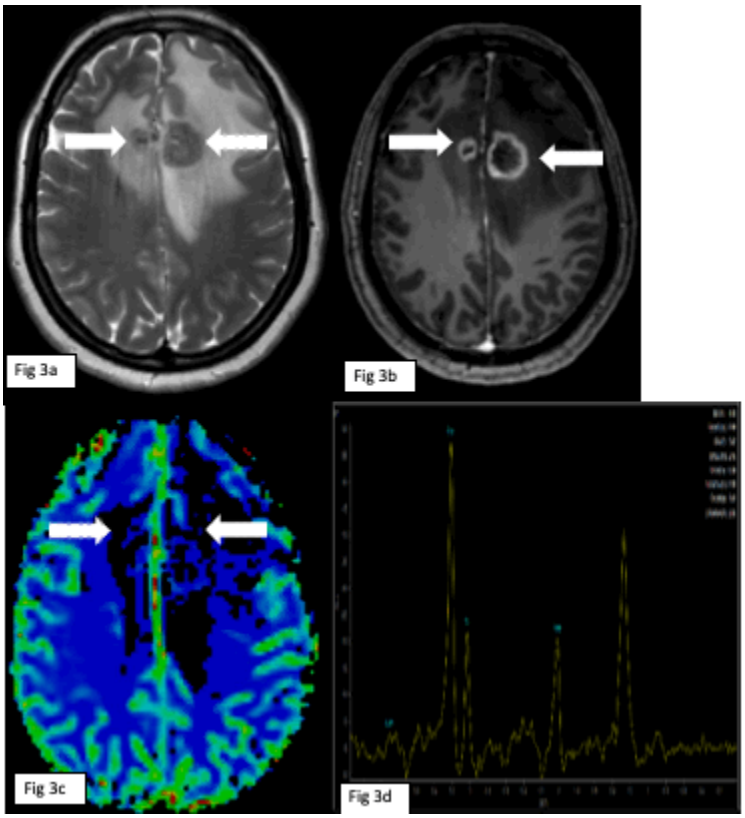

(Filename: TCT_736_figure3.gif)

1485

Radiological and Pathological Findings of Neonatal Salivary Gland Anlage Tumor: A Rare Case-Report.

J Gomez[1], K Malikayil[1], O Arevalo[1], A ASLAN[1], L De Alba[1]
[1]LSU Health Shreveport, Shreveport, LA

Purpose

A 17-days old male born at 38 weeks presented to an outside hospital with respiratory distress and hypoglycemia. Endoscopic evaluation by ENT showed a nasopharyngeal mass, and the patient was transferred to our facility for higher level of care. More detailed evaluation by our ENT revealed a multilobulated mass originating from the posterior base of the vomer and soft palate. MRI was recommended for further evaluation.

Materials and Methods

The MR study showed a lobulated enhancing mass centered in the nasopharynx measuring approximately 10 x 12 x 27 mm (AP, transverse, craniocaudal). The lesion was in close proximity to the basisphenoid, extending anteriorly obstructing both choanae, attached by a delicate pedicle, and extending inferiorly to the level of the soft palate partially obstructing the pharynx. The skull base was intact and there was no evidence of intracranial communication. Complete surgical resection was performed. On gross examination, the specimen measured 3.2 x 2.5 x 1.2 cm and weighed 2.06 g. Microscopic examination showed epithelial structures that blended with spindle-cells, nests of infiltrating highly pleomorphic basophilic neoplasm, high nucleus-to-cytoplasm ratio, and frequent mitoses with abrupt keratinization. Immunostaining showed the tumor cells are positive for pancytokeratin, p40, CD56, focal staining with CD 99, and synaptophysin.

Results

SGAT should remain a diagnostic consideration for neonatal respiratory distress. Other differential diagnosis for nasopharyngeal obstruction in a neonate may include a skull base cephalocele. CT and MR imaging are of paramount importance for a thorough evaluation of the extension of these lesions and most importantly for distinguishing from other entities that have intracranial extension or have more aggressive histological features.

Conclusions

Salivary gland anlage tumor (SGAT), also known as congenital pleomorphic adenoma, is a very rare benign tumor. Only few cases have been reported in the literature. This type of neonatal hamartoma usually arises as a polypoid lesion of the posterior nasopharynx leading to respiratory distress at birth or within the first few days or weeks of life. SGAT is a benign hamartomatous lesion involving the posterior nasopharynx occurring in newborns. Its clinical presentation and characteristic histologic features must be recognized because the differential diagnosis includes several malignant tumors and an erroneous diagnosis could lead to an inappropriate aggressive therapy.

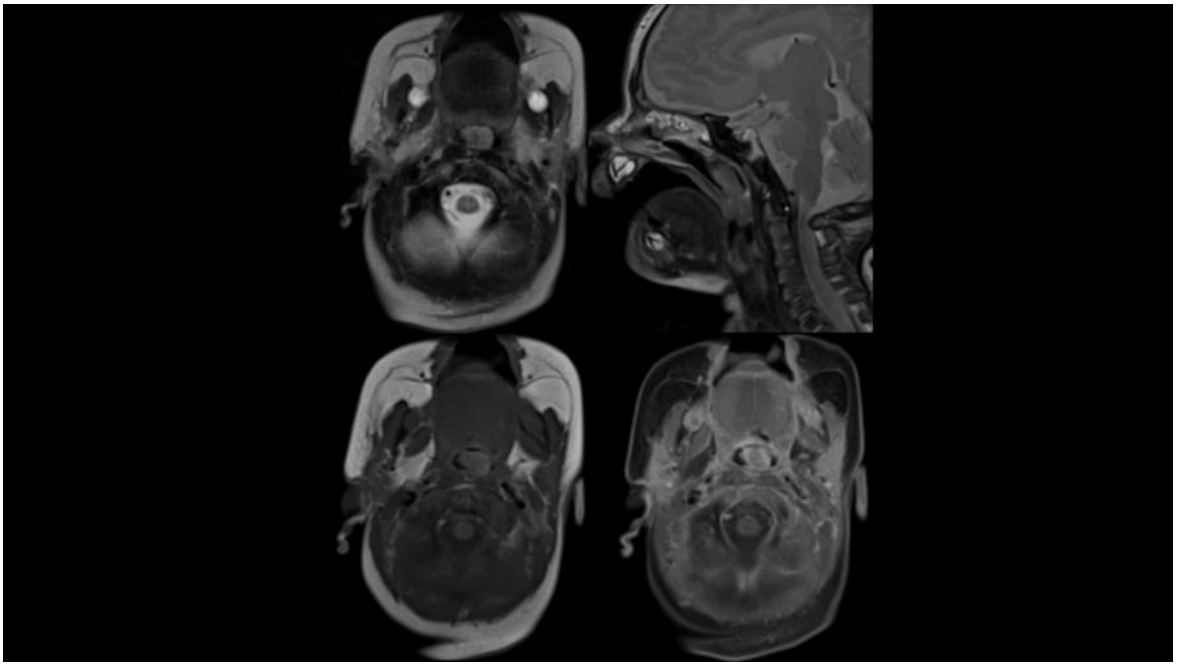

(Filename: TCT_1485_ASNREXCERPTADEALBA.jpg)

173

Radiosurgery-Induced Fibrinoid Vascular Necrosis Presenting as a Large Complex Cystic Mass

M Baggett[1], R Assadsangabi[2]

[1]University of California, Davis, Sacramento, CA, [2]University of California Davis, Sacramento, CA

Purpose

58-year-old female with history of mesial temporal sclerosis s/p gamma knife radiosurgery in 1990 presents with worsening daily seizures despite 3 AEDs.

Materials and Methods

Large cystic mass with an enhancing solid component centered in the left medial temporal lobe with areas of susceptibility and elevated perfusion parameters. Differential diagnosis included radiation-induced glial neoplasm, ganglioglioma, and pleomorphic xanthoastrocytoma.

Results

Patient underwent surgical cyst drainage and mass excision. Surgical pathology revealed organizing fibrin and hemorrhage with fibrosis and vascular canalization, as well as brain parenchyma with hyalinized vessels, gliosis, and hemosiderin, but no malignancy.

Conclusions

Gamma knife radiosurgery may induce fibrinoid vascular necrosis, which rarely can mimic malignancy with avid enhancement and elevated perfusion parameters. Delayed cyst formation may also occur, as in this unique case.

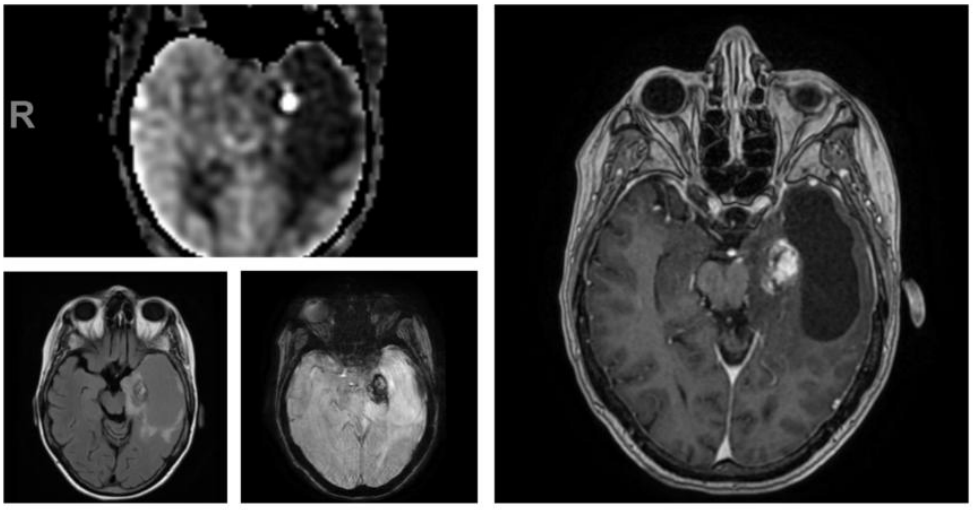

Top left: Axial perfusion CBF; Bottom left: Axial T2 FLAIR; Bottom middle: Axial SWAN; Right: Axial T1 FSPGR post.

(Filename: TCT_173_BaggettExcerptaImage.jpg)

1550

Rapidly evolving dural metastasis in a patient with colorectal adenocarcinoma

A Goncalves Filho[1], E Portela de Oliveira[1], R Glikstein[1]
[1]The Ottawa Hospital, University of Ottawa, Ottawa, ON

Purpose

67-year-old female experienced right leg drag and frequent falls. She had a known diagnosis of high-grade colonic adenocarcinoma with perineural invasion treated with right hemicolectomy and adjuvant chemotherapy. She was admitted in the emergency where a solitary metastasis was found in the left temporal lobe. She underwent gross total resection with no evidence of residual lesion. Subsequently completed SRT on the surgical cavity. After two months, the patient presented with nausea and painless vision loss in the left eye and right ocular palsy. There were new multiple dural-based lesions with extensive involvement along the anterior cranial fossa with encasement of several cranial nerves. The patient was admitted for palliative whole brain radiation. Unfortunately, patient continued to decline and died 13 days after her arrival.

Materials and Methods

(A) Axial T2 MRI showing a hypointense lesion in the left temporal lobe with surrounding edema and mass effect; (B, C and D) axial and coronal T1 Gd+ MRI showing florid multiple dural based lobulated enhancing lesions, predominantly at the floor of the anterior cranial fossa and along the left tentorium causing mass effect. The lesions extend into the olfactory grooves and encase the left optic nerve. It also extends to the right optic canal and orbital apex with encasement of the CN III.

Results

Metastasis involving the dura are most found from the breast, lung, melanoma, gastroenteric tract, and prostate. Rapidly evolving dural involvement appears to be particularly rare in comparison with metastasis generally found in the CNS of patients with colorectal cancer. Common sites of colorectal cancer metastases include the liver, lungs, and peritoneal cavity. Infratentorial metastases appear to predominate. Clinical presentation of these patients is frequently related to the mass effect resulting in focal neurological deficits. It is interesting to note that in our case, the main clinical signs were related to cranial nerve palsies. Prior surgical manipulation could have facilitated the meningeal dissemination. However, this rapidly evolving disease with florid manifestation was quite unexpected.

Conclusions

The dura mater is a very rare site of metastasis in patients affected by advanced colorectal cancer. This case is notable owing to the rapidly evolving dural metastasis and a clinical presentation dominated by cranial nerve palsies. A rapid diagnosis could enable starting an early specific treatment with radiotherapy or systemic.

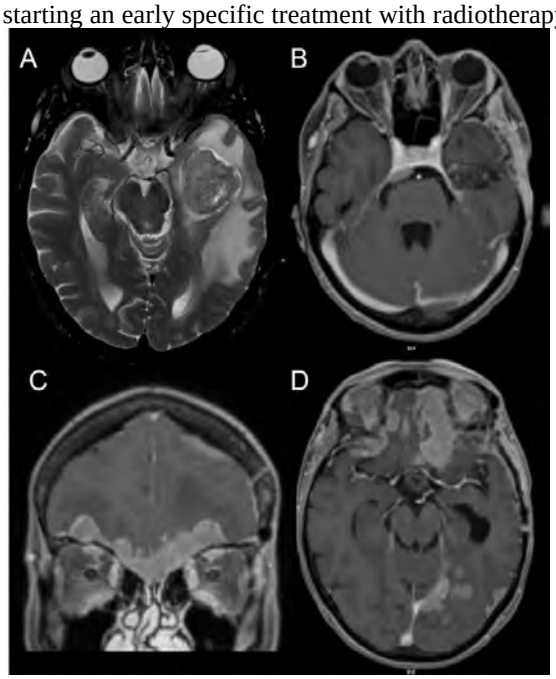

(Filename: TCT_1550_Picture1.jpg)

799

Rare Case of Malignant Atrophic Papulosis (Degos Disease)

D Milner[1], A Ginnaram[2]
[1]University of Alabama at Birmingham, Birmingham, AL, [2]Gandhi Medical College, Gachibowli, Hyderabad

Purpose

28 year-old male with history of treated right superior cerebellar artery aneurysm initially presented to an outside institution with bilateral lower extremity weakness, urinary incontinence, and paresthesias 1 week after an upper respiratory infection. The patient was initially diagnosed with transverse myelitis and treated accordingly. His weakness progressed over several weeks with eventual

involvement of the bilateral upper extremities and respiratory muscles. Acute inflammatory demyelinating polyneuropathy was suspected at the time of presentation to our institution, and he was then treated with plasma exchange therapy. He developed respiratory failure and progressive encephalopathy throughout his hospitalization.
Materials and Methods
Initial imaging findings demonstrated patchy dorsal column and lateral tract T2/STIR hyperintense signal on thoracic spine MRI. Brain MRI demonstrated ischemic strokes involving the posterior fossa, right cerebral hemispheric pachymeningeal, and right sided leptomeningeal enhancement. Patient also had a right cerebral convexity subdural hematoma
Results
Malignant Atrophic Papulosis (MAP) or Degos disease, is a rare cutaneous disorder characterized by obliterative vascular lesions of the skin, central nervous system (CNS) and gastrointestinal tract. MAP may also involve other organs such as the ocular, pulmonary, cardiovascular, and renal systems. In some individuals, the disease is limited to the skin (benign cutaneous Degos disease). Approximately 200 cases have been described in the literature. MAP tends to present between the second to fifth decade of life, with a slight female predilection (1:1.4). Familial patterns have also been seen, with first degree relatives showing autosomal dominant inheritance pattern. Neurological manifestations may present as follows: functional and sensory deficits, cranial nerve palsies, multiple disseminated infarctions, scattered hemorrhages, subdural collections, venous sinus thromboses, polyradiculoneuropathy, etc. Cognition and memory may also be affected. Involvement of the optic tract and eye in isolation has also been described. Neuroimaging findings include multifocal acute infarcts, subdural hematomas, and leptomeningeal enhancement. Vessel wall imaging may demonstrate vessel wall enhancement.
Conclusions
Recognize imaging manifestations of malignant atrophic papulosis in the central nervous system

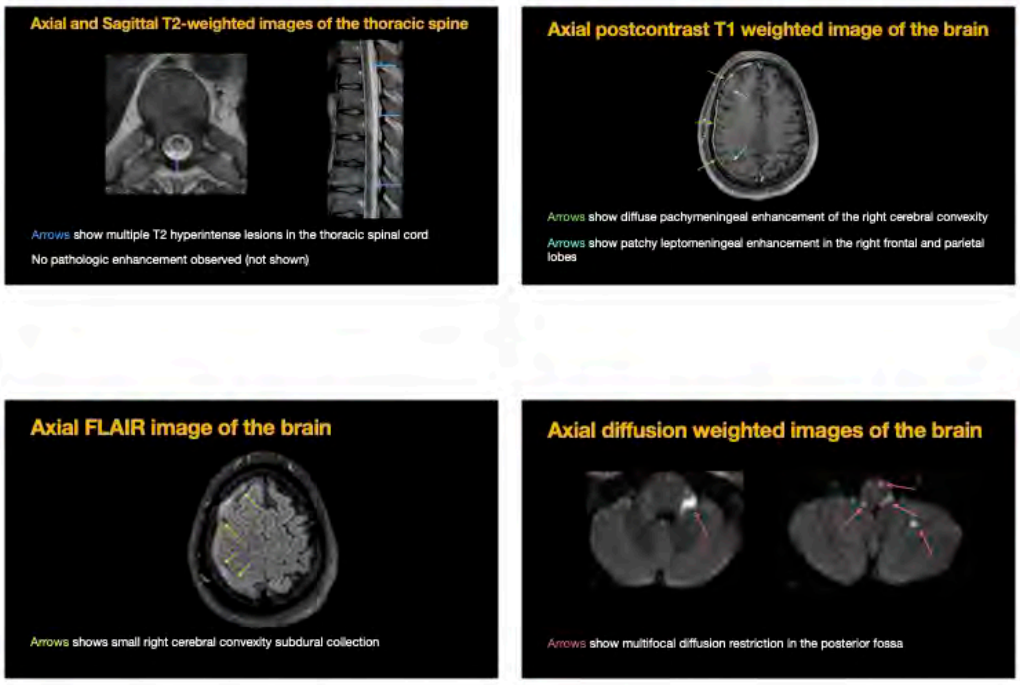

(Filename: TCT_799_Degos.jpg)

1385
Rare Extra-cranial Meningiomas Due to Seeding from Resected Intracranial Meningiomas
A Paydar[1], S Saith[2], B Haas[3], V Ivanovic[4]
[1]University of Califronia-Davis, Sacramento, CA, [2]UC Davis Medical Center, Redondo Beach, CA, [3]UC Davis, sacramento, CA, [4]UC Davis Medical Center, Sacramento, CA

Purpose
A 75-year-old female with history of a previously resected and irradiated right temporal meningioma presented with a right mandibular mass. Another 63-year-old female presented with recurrent left skull base atypical meningioma which showed a metastatic mass in left parotid gland, pathologically proven meningioma.
Materials and Methods
Figure 1a&b: Post-operative MRI shows progressive enlargement of temporal meningioma with significant edema of the temporal

lobe, extending to the site of previous craniotomy. There is a mandibular mass with adjacent osseous destruction and involvement of pterygoid musculature. Figure 2a&b: Partially visualized enhancing and enlarged left parotid gland, representing biopsy proven metastatic atypical meningioma

Results

Meningioma is a grade I tumor. Atypical (grade II) and anaplastic (grade III) Meningioma are rare and may show aggressive behaviour with extension or metastasis. Extra-cranial meningioma occurs following direct extension/ metastasis from intracranial lesions or as a true primary extra-cranial origin. Extra-cranial metastasis of meningioma accounts for 0.1% of cases (1). In this presentation, we present two examples of metastasis from intracranial meningiomas. The first is metastasis to the mandible and the second one is a metastasis to the parotid gland from an original base of skull lesion postoperatively. Seeding follow operation is a possible reason for metastasis. Both lesions showed an atypical grade II pattern on pathology.

Conclusions

Extra-cranial meningiomas occur rarely from extension or metastasis of intracranial higher-grade meningioma or primary ectopic arachnoid cells.

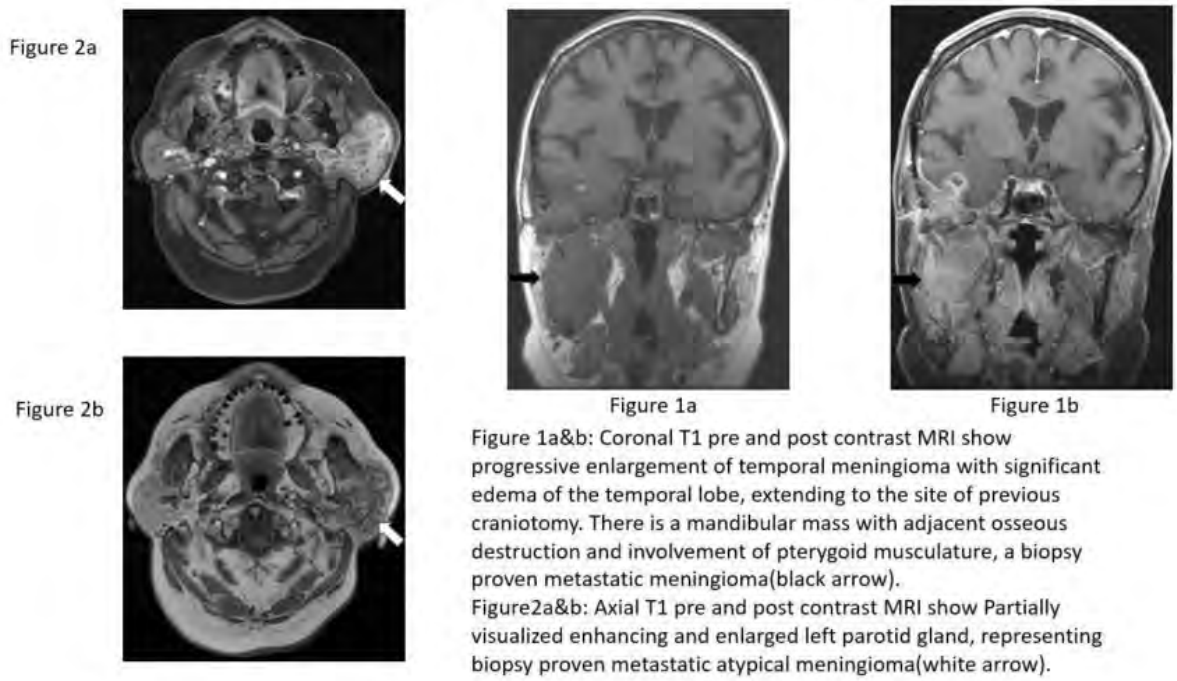

Figure 1a&b: Coronal T1 pre and post contrast MRI show progressive enlargement of temporal meningioma with significant edema of the temporal lobe, extending to the site of previous craniotomy. There is a mandibular mass with adjacent osseous destruction and involvement of pterygoid musculature, a biopsy proven metastatic meningioma(black arrow).
Figure2a&b: Axial T1 pre and post contrast MRI show Partially visualized enhancing and enlarged left parotid gland, representing biopsy proven metastatic atypical meningioma(white arrow).

(Filename: TCT_1385_Slide1.jpg)

1437

SMART Seizure Syndrome, Stroke-like migraine attacks after radiation therapy and seizures syndrome

S Mohammed[1], S Rogers[1], K Gupta[1], J Becker[1]
[1]*University of Arizona, Tucson, AZ*

Purpose

A 45-year-old male with migraines and a WHO grade III right frontal astrocytoma post resection and radiation therapy 10 years prior, presented to the ED with 5 days of migraine headache, slurred speech, and left upper extremity numbness, as well as more acutely with 1 day of left sided facial droop. After stroke work-up he was diagnosed with a right MCA infarct and discharged with an NIHSS score of 2. After 2 days he presented to the ED again after a seizure, followed by left-sided weakness, aphasia, and dysarthria that resolved with Versed and Keppra. The patient recovered to near baseline and continues anticonvulsant medications, with no new symptoms or recurrent seizures.

Materials and Methods

MRI demonstrates old right frontal craniotomy and resection cavity, with new right frontotemporal T2/FLAIR cortical hyperintensity and associated gyriform enhancement. Restricted diffusion at the right parietal lobe, but not in the frontotemporal regions of cortical edema and enhancement. Perfusion images show shunting of blood in the regions of enhancement, with increased rCBV and rCBF and decreased TTP. 7 month follow-up MRI for routine tumor surveillance showed resolution of the frontotemporal edema and enhancement, with gliosis at the previously seen right parietal DWI abnormality. There was no evidence of tumor recurrence.

Results

SMART syndrome is rare, presumed to be related to brain radiation, occurring months to years after radiotherapy. The diagnosis is difficult because of new brain enhancement in the setting of a treated brain tumor, variable diffusion restriction, and frequency of associated seizures. Main features include a history of brain radiation for cancer, prolonged reversible symptoms (migraine, seizures, hemiparesis or other neurological symptoms), characteristic reversible gyriform gadolinium enhancement in the radiation bed with

eventual complete or partial recovery, and no residual or recurrent tumor. Patients tend to improve after anticonvulsant therapy. Brain biopsy fails to demonstrate pathologic etiology, although radiation-induced vascular damage seizures likely the main pathophysiology.
Conclusions
SMART syndrome is a rare post radiation complication associated with seizures, with diagnosed based on exclusion and relative characteristic imaging findings. The radiologist plays a key role in the diagnosis and may be the first to suggest the importance of a seizure workup. Diagnosis aids in appropriate management and helps avoid unnecessary intervention such as brain biopsy.

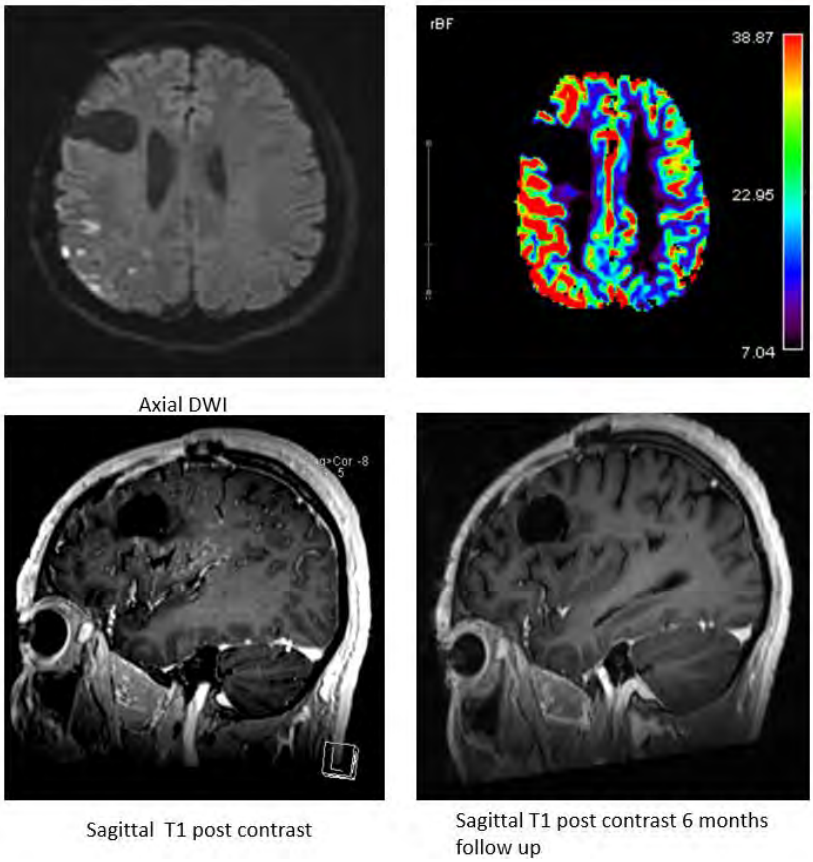

(Filename: TCT_1437_Final.JPG)

129

Solid Variant Aneurysmal Bone Cyst in the Skull Base of a Pediatric Patient

R Manos[1], N Patel[1], G Wrubel[1]
[1]*Hartford Hospital, Hartford, CT*

Purpose
A 13 year old male presented with right temporal scalp swelling. Ultrasound, MRI, and CT were performed, demonstrating a large transcalvarial mass centered within the right temporal bone. Surgical pathology was consistent with a solid variant aneurysmal bone cyst. A stereotactic guided right temporal craniotomy was performed for resection.
Materials and Methods
Ultrasound demonstrates a right temporal mass with heterogeneous echotexture deep to the subcutaneous tissues. Coronal T2 and Axial T1 post contrast images demonstrate a large and thinly encapsulated mass spanning the right temporal squamosa exhibiting intracranial and extracranial components that measured 5.6 x 4.5 x 4.2 cm. The lesion demonstrated mixed non enhancing cystic and avidly enhancing solid components, resulting in significant mass effect on the right temporal lobe without adjacent parenchymal edema. Axial CT scan of the head shows the aforementioned mass to be erosive and expansile. The mastoid air cells and lateral floor of the right middle cranial fossa were partly eroded. A spicule of ossification within the central aspect of the lesion most likely reflected partially resorbed calvarium. No definite lesional matrix.
Results
ABCs are benign and locally destructive lesions that occur more commonly among the pediatric population with a median age of 13 (4). While the metaphysis of long bones and the spine are the most frequent site of localization, ABC's are also known to affect the craniofacial structures in 3-6% of the cases, with a higher male predilection when temporal bones are involved (1, 2, 3). This case demonstrates a rare solid variant ABC involving the squamous portion of the temporal bone, the mastoid air cells, and the zygoma. The majority of previous case reports cited non-solid variant ABCs that were confined to the petrous bone (2, 4).
Conclusions
ABCs have a classic imaging appearance on various imaging modalities. On plain film and CT, they commonly present as a well

marginated lytic lesion with a sclerotic margin. MRI is the best imaging modality to demonstrate intra-lesional signal signal levels that vary in signal characteristics, typically surrounded by thin enhancing septations. Varying degrees of solid enhancing components can be seen in solid variant ABC and a lack of fluid fluid levels should not preclude from considering ABC in the differential diagnosis for otherwise similar lytic bone lesions.

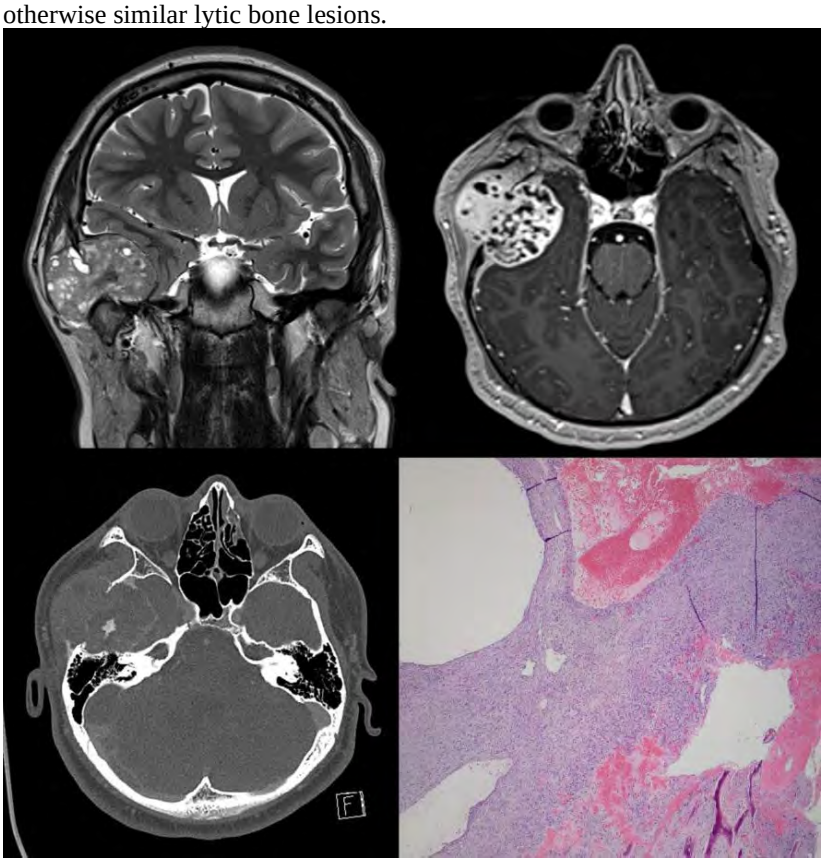

(Filename: TCT_129_ABC.jpg)

1085

Spontaneous Aneurysmal Subdural Hemorrhage: A Rare Entity

M Rizk[1], A Khan[1], J Ghannam[2], M Waheed[3]

[1]Beaumont Health, Royal Oak, MI, [2]William Beaumont Hospital, Royal Oak, MI, [3]Oakland University, Rochester, MI

Purpose

36-year-old female who presented to our emergency department for worsening headache and new onset left sided diplopia. Physical exam confirmed a left 3rd nerve palsy. A CT of the head was obtained which showed a subdural hemorrhage which ultimately resulted in coil embolization of a ruptured aneurysm. The patient tolerated the procedure well and was closely followed for vasospasm development with routine transcranial ultrasounds which were negative. Patient remained stable and reported resolution of her headache symptoms on discharge. However, she continued to have a left 3rd nerve palsy.

Materials and Methods

CT of the head was obtained which showed a subdural hemorrhage. Subsequent CTA of the head was positive for an 8 x 4 mm posterior communicating artery (PcomA) aneurysm. MRA and MRI of the head both demonstrated a posterior fossa subdural hemorrhage that was most predominant along the margins of the tentorium and cerebellum. The patient was diagnosed with aneurysmal subdural hemorrhage (AnSDH) and underwent endovascular embolization of the left PcomA aneurysm with multiple detachable platinum coils.

Results

Spontaneous aneurysmal subdural hemorrhage (AnSDH) without any subarachnoid hemorrhage, interventricular hemorrhage, or intracerebral hemorrhage is an extremely rare entity with only 30 cases reported in the literature(1). The most common location was ICA-PcomA aneurysms (15 cases) followed by MCA aneurysms (6 cases) (2). Although the pathogenesis of AnSDH remains a subject of controversy, the perianeurysmal environment, along with the variations of aneurysm location, may help further our understanding of AnSDH(5) Subdural hemorrhage without antecedent trauma or coagulopathy should raise suspicion for an intracranial aneurysm rupture. Protocols have been proposed for a suspected AnSDH(4). Patients with AnSDH have more profound deficits on presentation, recent evidence suggests they have better outcomes than those with non-AnSDH (5). Hematoma evacuation and aneurysm coiling or clipping are most common modalities of treatment, with better outcomes associated with early intervention. Our case highlights that an aneurysm rupture should be included in the differential for a patient who presents with an otherwise unexplainable subdural hemorrhage.

Conclusions
1. Present a case of a spontaneous aneurysmal subdural hemorrhage (AnSDH) without concomitant subarachnoid hemorrhage (SAH)
2. Discuss relevant anatomical considerations in patients with AnSDH 3. Discuss management and overall prognosis

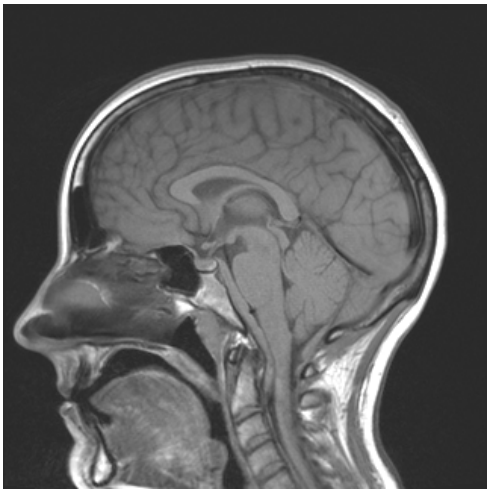

(Filename: TCT_1085_sagittalbrainmri.jpg)

853

Subacute Infarct Caused by Primary Angiitis of CNS Mimicking Neoplasm

M LEE[1], M Roubakha[2], B Salehi[3], N Salamon[4]
[1]UNIVERSITY OF CALIFORNIA LOS ANGELES, Los Angeles, CA, [2]UCLA, Los Angeles, CA, [3]UCLA, Los angeles, CA, [4]University of California Los Angeles, Los Angeles, CA

Purpose
36-year-old male presented to emergency room with 1 month of progressively worsening speech and cognitive changes. Upon further work up, he was found to have heterogeneously enhancing brain lesion. The brain biopsy revealed necrotic lesion with multifocal lymphohistiocytic angiitis and fibrinoid necrosis, most consistent with primary angiitis of the central nervous system.
Materials and Methods
Initial MRI demonstrated heterogeneously enhancing lesion in the posterior left cerebral hemisphere with extensive vasogenic edema. Follow-up MRI obtained 2 weeks later demonstrated cortical laminar necrosis and low cerebral blood volume on perfusion map.
Results
The initial MRI was confounding due to heterogeneous enhancement with extensive vasogenic edema, most concerning for neoplasm. It can be difficult to distinguish subacute infarct from neoplasm with such imaging findings and history of progressive worsening neurological deficits as in this patient.
Conclusions
Subacute infarct with significant vasogenic edema can mimic neoplasm, and follow-up MRI with advanced MR techniques such as MR perfusion can be helpful to reach accurate diagnosis in conjunction with pathology results.

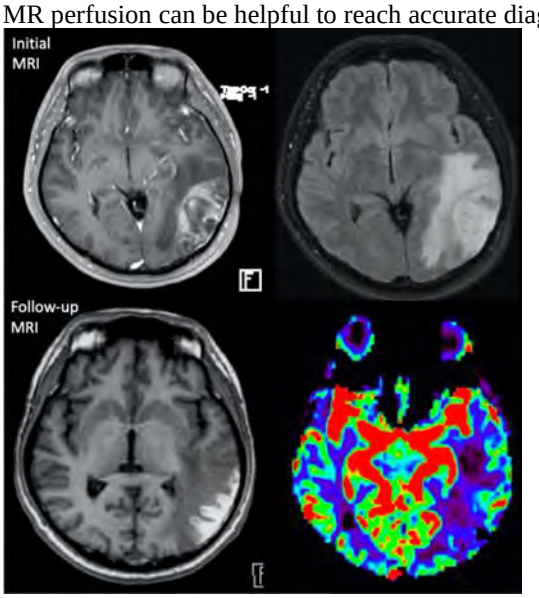

(Filename: TCT_853_CNSangiitis.jpg)

833

Superficial Temporal Artery Pseudoaneurysm in the Context of Endocarditis: a Case Report

K Massicotte-Tisluck[1], E Portela de Oliveira[2]

[1]CHUS (Centre Hospitalier Universitaire de Sherbrooke), Sherbrooke, Québec, [2]The Ottawa Hospital, Ottawa, Ontario

Purpose

A 30-year-olds woman without any medical history, presenting systemic infectious symptoms (myalgias, fever and arthralgia) with elevated white blood cells, positive hemocultures to Staphylococcus aureus and mitral valve vegetations on transthoracic echocardiogram. The source of infection was uncertain, possibly related to excoriated skin lesions. Few days after her admission, she developed headaches and mild visual changes likely representing amaurosis fugax.

Materials and Methods

CT head and CT angiogram demonstrated a large right frontal parenchymal hematoma with surrounding edema and mass effect. There was also minimal intraventricular hemorrhage. No aneurysm was identified on the CT angiogram. MRI was obtained the same day and showed in addition to the hematoma multifocal foci of restricted diffusion, with ring and nodular enhancement and blooming artifacts mostly in the gray-white matter junction that highly suggested septic emboli. The angiogram of the internal carotid arteries and vertebral arteries were unremarkable. While there was evidence of intracranial emboli, a pseudoaneurysm, likely "mycotic" was found involving a distal segment of the frontal branch of the right superficial temporal artery arising from the right ECA.

Results

In the context of bacterial endocarditis, mycotic aneurysms are well known but rare complication that may occur. When they happen in the intracranial arteries, they are more frequent in the distal MCA's branches and may cause intracranial bleed (hematoma or microbleeds), infarction or micro abscess. Aneurysms of the external carotid artery are rare. They can occur with atheromatosis. Pseudoaneurysm of the ECA can be related to trauma, neck neoplasm, iatrogenic (radiation, neck surgery or endovascular treatment of the carotid), or infectious process. Most of the reported cases in the literature involve the proximal ECA near the bifurcation or proximal branches and are related to neck infection. Even if intracranial bleeding in the context of endocarditis is not always related to infectious aneurysms, in our case the presence of the ECA aneurysm and septic embolisms reinforced the hypothesis of a ruptured infectious aneurysm to explain the parenchymal hematoma. The extracranial mycotic aneurysm was not considered the culprit for the intracranial hemorrhage.

Conclusions

To our knowledge, it is the first case reported of an infectious aneurysm of a small distal branch of the ECA in the context of proven endocarditis.

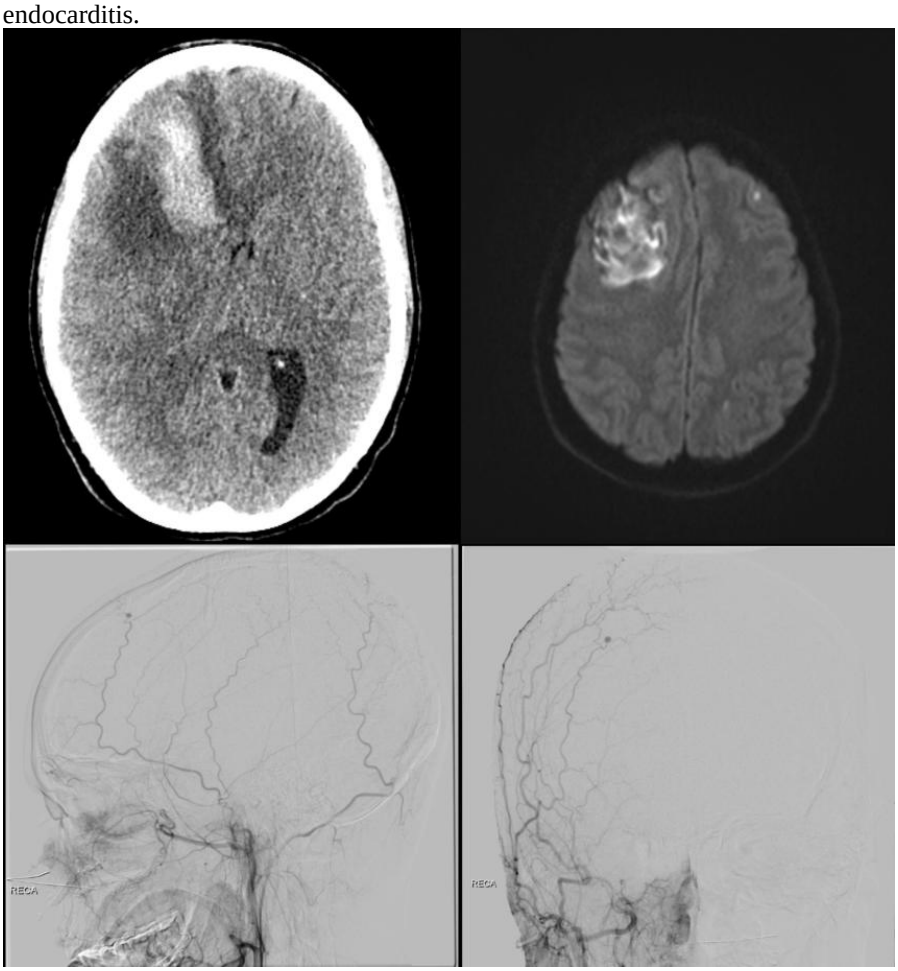

(Filename: TCT_833_ASNR2022.jpg)

1152

Teflon Granuloma: An Uncommon Etiology for Recurrent Symptomatology Following Microvascular Decompression

S Hasan[1], S Moum[2]

[1]McGaw Medical Center of Northwestern University, Chicago, IL, [2]Ann & Robert H. Lurie Children's Hospital of Chicago, Chicago, IL

Purpose

The patient is a 47-year-old female presenting with new episodic stabbing facial pain in the left V2 distribution. Initial MR brain imaging demonstrated impingement of the left trigeminal nerve. Given the clinical and imaging findings, a diagnosis of left V2 distribution trigeminal neuralgia was made. The patient underwent microvascular decompression, with return of her left-sided facial pain several weeks after surgery. Follow-up MR brain imaging was performed one year postoperatively.

Materials and Methods

Initial preoperative contrast-enhanced MR brain imaging demonstrates impingement of the left trigeminal nerve near the root entry zone by the left superior cerebellar artery as depicted on coronal high-resolution T2 imaging (Figure 1A). Postcontrast axial T1 fat saturated imaging from the same exam shows no abnormal enhancement in this location. One year after microvascular decompression, follow-up contrast-enhanced MR brain imaging demonstrates a surgically placed Teflon pledget at the left cerebellopontine angle along the margin of the cisternal segment of the left trigeminal nerve (Figure 1B). The pledget is in expected position. There is T2 hypointense signal within this focus as seen on axial high-resolution 3D T2 imaging (Figure 1B), with associated abnormal enhancement on axial postcontrast T1 imaging (Figure 1C). These findings are most consistent with Teflon granuloma formation in this patient with recurrent symptoms following microvascular decompression.

Results

Microvascular decompression is commonly employed for medically refractory trigeminal neuralgia and hemifacial spasm (1,2). Intraoperatively, a fragment of polytetraluoroethylene (i.e. Teflon pledget) is placed between the nerve and culprit vessel to limit nerve compression. Recurrent symptoms can uncommonly occur due to pledget dislocation, insufficient nerve decompression, or granuloma formation (1,2). Illustrated by this example, granuloma formation has been reported in approximately 1.1-7.3% of cases (1,2). As an enhancing cerebellopontine angle mass, a Teflon granuloma may be mistaken for other more common masses in this region, such as meningioma or schwannoma (3). While rare, this entity represents an important differential consideration for recurrent symptoms following microvascular decompression as resection may be curative (2).

Conclusions

Teflon granuloma represents a rare potentially treatable etiology for recurrent symptoms after microvascular decompression.

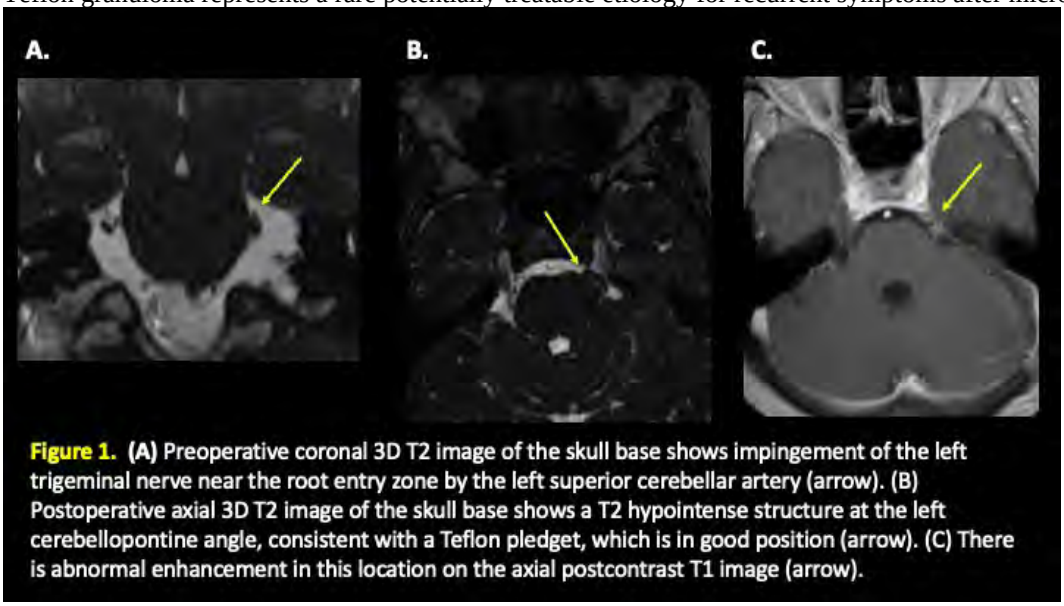

Figure 1. **(A)** Preoperative coronal 3D T2 image of the skull base shows impingement of the left trigeminal nerve near the root entry zone by the left superior cerebellar artery (arrow). (B) Postoperative axial 3D T2 image of the skull base shows a T2 hypointense structure at the left cerebellopontine angle, consistent with a Teflon pledget, which is in good position (arrow). (C) There is abnormal enhancement in this location on the axial postcontrast T1 image (arrow).

(Filename: TCT_1152_Teflon.jpg)

639

Terson's Syndrome in an Adult Patient with Acute Traumatic Head Injury

G Vilanilam[1], R Purushothaman[1], S Patro[2], S Vattoth[3], M Kumar[1], R Van Hemert[4], M Mian[1], S Sharma[1], R Ramakrishnaiah[5]

[1]University of Arkansas for Medical Sciences, Little Rock, AR, [2]N/A, N/A, [3]University of Arkansas for Medical Sciences, LITTLE ROCK, AR, [4]UAMS, Little Rock, AR, [5]Univ of Arkansas for Medical Sciences, Little Rock, AR

Purpose

20-year-old male presented following a gunshot injury to the head. On examination, there was a ballistic wound to the right temple with blood in the external auditory canal and right hemotympanum. He was hemodynamically unstable with a blood pressure of 68/50 mmHg and pulse rate of 172/min. He was intubated and with a Glasgow Coma Scale of 3. Detailed neurological examination could

not be performed due to his acute condition. He received 1 unit of packed red blood cells and 1 unit of platelets and was initiated on a titrating drip of norepinephrine. On repeat examination, he had no spontaneous movement or eye opening, no response to verbal stimuli or deep pressure. The pupils were fixed, dilated, and not responsive to light. The corneal, gag, cough, and oculocephalic reflexes were absent, clinically consistent with brain death. An 8-minute apnea test confirmed brain death.
Materials and Methods
Unenhanced computed tomography (CT) of the brain showed a penetrating injury to the right fronto-parietal bone with fracture fragments embedded in the right frontal lobe and a bullet embedded in the left frontal lobe (Fig 1A). There was also pneumocephalus with multiple areas of subarachnoid and subdural hemorrhages with diffuse cerebral edema and descending transtentorial and tonsillar herniation (Fig 1B, 1C). Bilateral layering vitreous hemorrhage was also seen (Fig 1D).
Results
Terson's syndrome (TS) has been described as intraocular hemorrhage in patients with subararchnoid hemorrhage (SAH), traumatic brain injury (TBI), or intracerebral hemorrhage (ICH). The pathophysiology of this condition stems from a sudden increase in intracerebral pressure, leading to rapid effusion of CSF into the orbit via the optic nerve sheath. Consequentially, the dilated retrobulbar portion of the optic nerve mechanically compresses the central retinal vein, resulting in venous hypertension, venous stasis and rupture of thin retinal vessels. While spontaneous regression of the intraocular hemorrhage may be seen in TS, vitrectomy may be necessary in about 50% of patients to prevent permanent visual deficits. Additionally, the presence of TS serves as a prognostic indicator (mortality of up to 90% and poor clinical outcome in 3 months).
Conclusions
Identification of the imaging features of TS presenting with SAH, ICH, or TBI is critical to prompt early fundoscopy and if required, vitrectomy to prevent devastating visual complications.

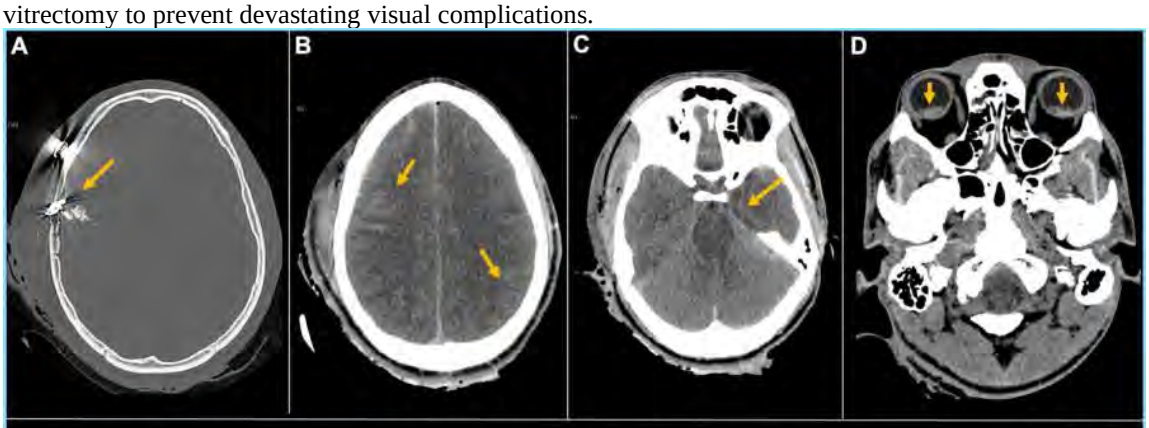

Fig A: Axial CT bone window showing a gun shot wound to the right frontal bone with comminuted right frontal **bone fracture and ballistic fragments** (arrow) in the brain parenchyma.
Fig B: Axial CT demonstrating **right frontal and left parietal subarachnoid hemorrhage** (arrows). Scattered areas of parenchymal contusions (not shown) were also present.
Fig C: Axial CT image at the level of suprasellar cistern and the brain stem shows **effacement of the suprasellar cistern and the pre-pontine cisterns** (arrow). There is effacement of the sulci denoting underlying diffuse cerebral edema. The patient also had tonsillar herniation.
Fig D: Axial CT image at the level of globe demonstrates dependent **vitreous hemorrhage** in both eyes (arrows).

(Filename: TCT_639_Tersonsyndrome.jpg)

183
Third Ventricle Xanthogranuloma Masquerading as an Epidermoid Cyst
P Noone[1], S Hung[2], M Castillo[3]
[1]University of North Carolina Medical Center, Chapel Hill, NC, [2]University of North Carolina School of Medicine, Chapel Hill, NC, [3]Radiology, Chapel Hill, NC

Purpose
A 35-year-old man presented with progressively worsening headache, visual changes, and a known third ventricular mass.
Materials and Methods
Initial brain MRI showed a T1 hypo, T2 hyperintense non-enhancing mass in the third ventricular floor with restricted diffusion. On follow-up MRI 5 years later, the mass had grown, compressed the optic chiasm and tracts, and appeared heterogeneous with mixed T1W and T2W signal, foci of nodular enhancement, intralesional hemorrhage, and restricted diffusion.
Results
Intracranial xanthogranuloma (XG) is a rare occurrence outside choroid plexuses but has been reported in the sellar-suprasellar locations presenting with T1W high and T2W iso- to high signals. We present a case of third ventricular XG which showed MRI features of an epidermoid cyst initially and later developed heterogeneous signal and focal enhancement.
Conclusions
Outside choroid plexuses, XG may present as a T1W hyperintense lesion in the sellar-suprasellar region. Rarely, XG can present as a

T1W hypointense lesion and mimic an epidermoid and other cysts. The MRI features of XG may change over time as shown in our patient.

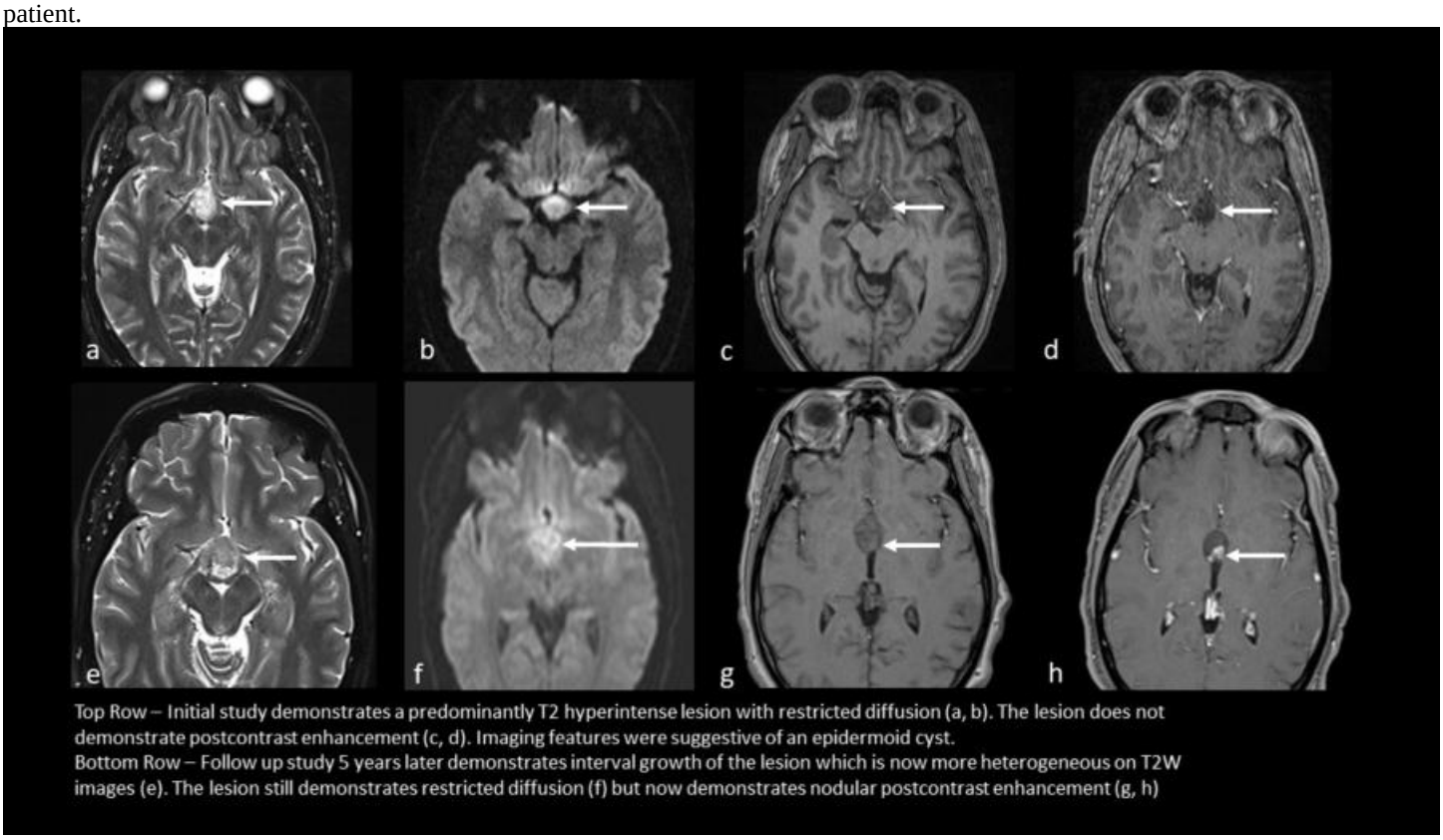

(Filename: TCT_183_xanthogranfigureupdatedv3.jpg)

501

Transforaminal Percutaneous Approaches to the Spine for Treatment of CSF Leak and Venous Fistula

A Thaker[1], D Bhaumik[1], V Timpone[1], A Callen[1]
[1]*University of Colorado Anschutz Medical Campus, Aurora, CO*

Purpose

Four patients with spontaneous intracranial hypotension (SIH) are presented, 3 with ventral dural tears resulting in CSF leak and 1 with CSF venous fistula. Each patient required unique transforaminal percutaneous approach to the spine for therapeutic intervention.

Materials and Methods

All patients had typical brain MRI findings suggestive of SIH, including mild pachymeningeal thickening, dural sinus engorgement, and changes in posterior fossa morphology. Three patients diagnosed with ventral dural CSF leak showed extradural contrast extravasation during prone dynamic CT myelography at C6-7, C7-T1, and T1-2. One patient diagnosed with CSF venous fistula showed enhancing paraspinal vein during decubitus dynamic CT myelography1 at T6-7. Utilizing intermittent CT fluoroscopic guidance, the following percutaneous transforaminal procedures were performed with therapeutic intent: C6-7 ventral tear: epidural blood patch via lateral neck retrovertebral approach with 22-gauge 3 inch spinal needle C7-T1 ventral tear: epidural fibrin patch via trans-deltoid approach with 20-gauge 8 inch spinal needle T1-2 ventral tear: epidural blood patch via post-scapular approach with 22-gauge 6 inch spinal needle T6-7 fistula: fibrin glue embolization via angled costovertebral approach with 22-gauge 3.5 inch spinal needle

Results

Two of three patients who underwent treatment for ventral dural tear had resolution of SIH symptoms without additional procedure. Patient with C7-T1 ventral dural tear ultimately required surgical repair of a large defect. Patient with CSF venous fistula had no change in symptoms following initial fibrin embolization.

Conclusions

Transforaminal percutaneous approaches for treatment of SIH due to ventral dural tear or CSF venous fistula, though technically challenging, may be safely performed with CT guidance and should be considered as a minimally invasive alternative to open surgery repair.

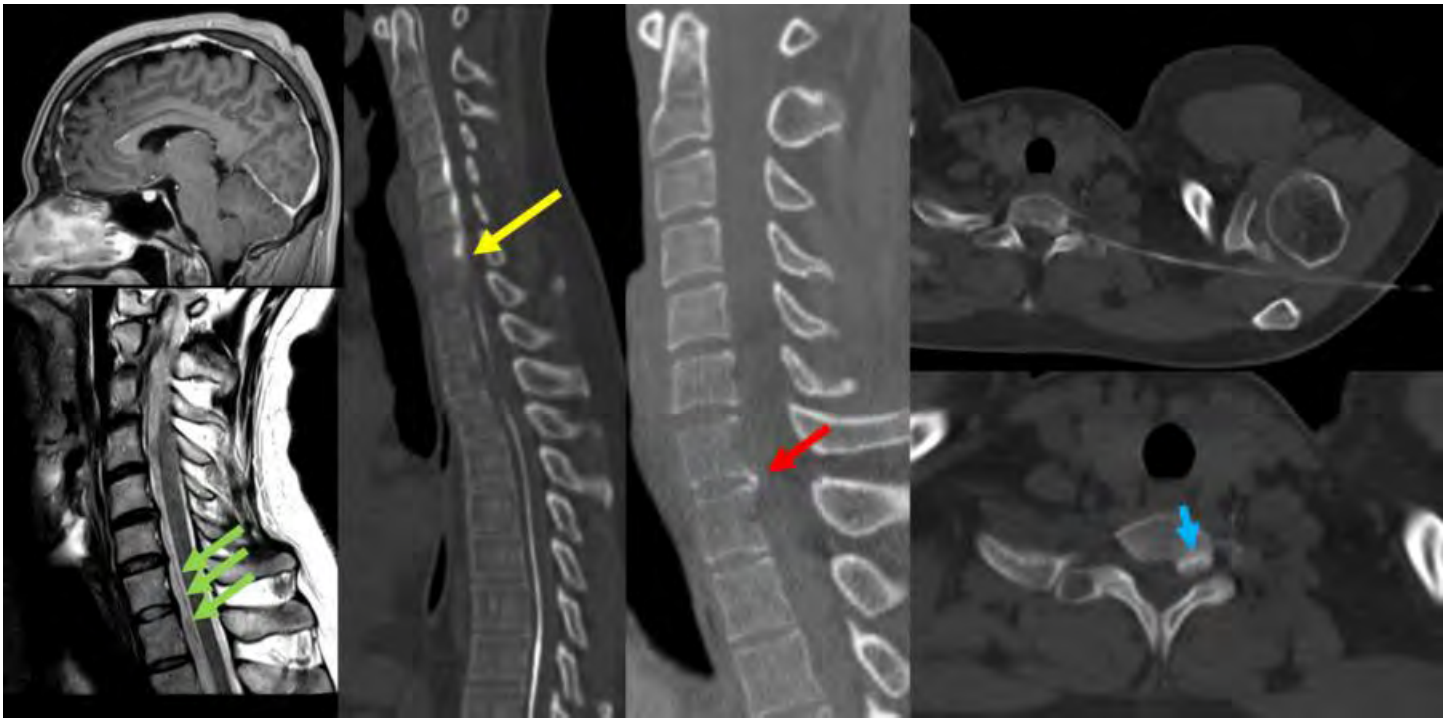
(Filename: TCT_501_ASNRexcerptafig.jpg)

974

Unusual presentation in of CLIPPERS after CAR-T cell therapy

S Velasco[1], C Torres[2]
[1]University of Ottawa, Ottawa, Ontario, [2]University of Ottawa, Ottawa, ON

Purpose

72-year-old female with relapsed refractory diffuse large B cell lymphoma, treated with autologous bone marrow transplant in September 2020. She relapsed in March 2021 and received CAR-T cell (FluCy Axi-cel) in April 26, 2021. She developed cytokine release syndrome (CRS) the day after and Immune effector cell-Associated Neurotoxicity Syndrome (ICANS) with mild confusion, expressive aphasia, tremor and gait difficulties three days after therapy. An initial course of dexamethasone was given. The neurological symptoms worsen at mid-May with severe sensory ataxia 4 limbs and athetosis. The patient received 4 days of high dose steroid treatment with improvement of the symptoms and imaging findings.

Materials and Methods

An MR of the brain and spine was done at presentation showing T2/FLAIR hyperintense signal involving the middle cerebellar peduncles, right cerebellum, and anterior aspect of the pons with associated patchy/perivascular enhancement. After 4 days of high-dose steroid treatment, in the follow-up MR an improvement in the enhancement was demonstrated. Of note, the MR of the spine was unremarkable.

Results

An MR of the brain and spine was done at presentation showing T2/FLAIR hyperintense signal involving the middle cerebellar peduncles, right cerebellum, and anterior aspect of the pons with associated patchy/perivascular enhancement. After 4 days of high-dose steroid treatment the patient demonstrated significant improvement of the sensory ataxia. Then, in the follow up MR an improvement in the enhancement was demonstrated. Of note, the MR of the spine was unremarkable.

Conclusions

In the setting of CAR-T cell therapy and Immune effector cell-Associated Neurotoxicity Syndrome (ICANS) CLIPPERS could be part of the imaging findings. In the current evidence other authors have described findings involving the thalami, brainstem, basal ganglia, hippocampus, splenium of the corpus callosum. Leptomeningeal enhancement has also been described. Similarly, other authors have described stroke and multifocal leukoencephalopathy.

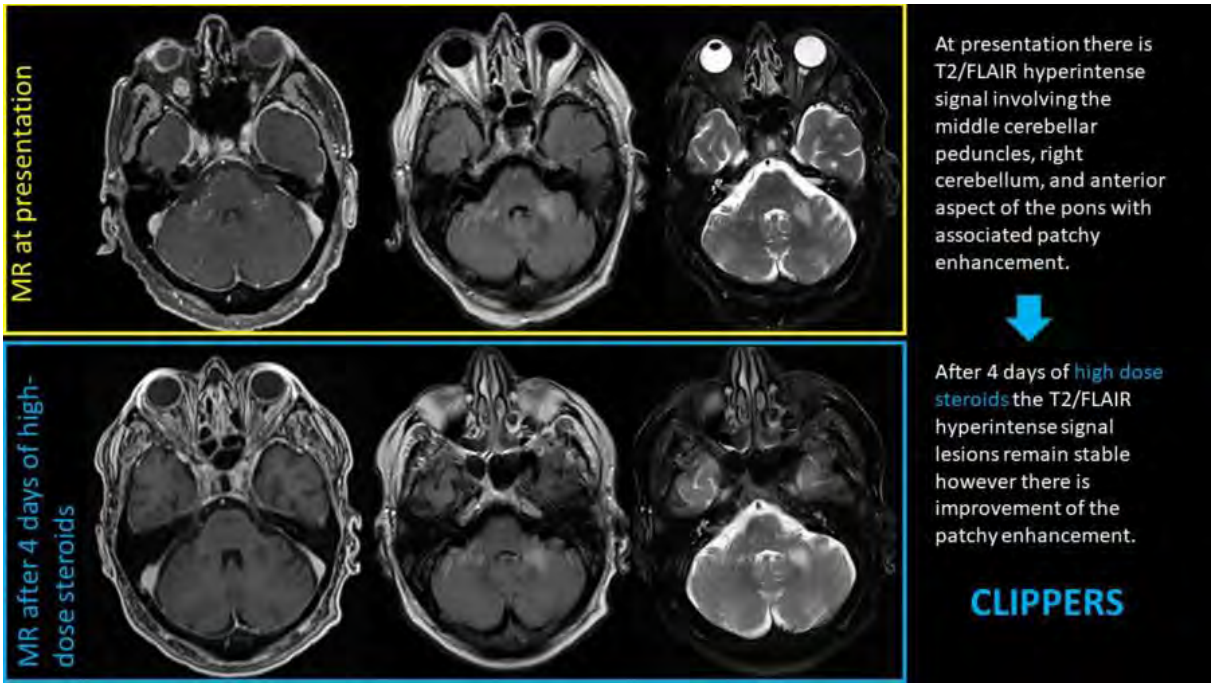

(Filename: TCT_974_FigCARTCELLSexcerpta.jpg)

425

Vessel Wall Imaging in Varicella-Zoster Virus Vasculopathy. Case Report.

A TORRES MONARREZ[1], A Sosa[2], M De los Santos Carmona[3], J Higuera-Calleja[3], G Romero Sanchez[1]

[1]Instituto Nacional de Ciencias Médicas y Nutrición Salvado Zubirán, Mexico City, Mexico, [2]Instituto Nacional de Ciencias Médicas y Nutrición Salvado Zubirán, Mexico City, Not Applicable, [3]Instituto Nacional de Ciencias Médicas y Nutrición Salvador Zubirán, Mexico City, Mexico City

Purpose

A 37-year-old male with HIV Infection clinically with AIDS.He started with headache, progressive visual loss in both eyes, distal paresthesia in the right lower extremities, bilateral amaurosis, papillary atrophy. CSF analysis revealed HSV-2 DNA, with viral load of 379 copies/mL

Materials and Methods

FLAIR and DWI showed hyperintense foci with restricted diffusion in the left lenticulostriate artery territory. 2D MIP and 3D TOF showed areas of multiple narrowing in the distal branches of the ACM arteries bilaterally. T1+Gd demonstrated meningeal thickening and enhancement. WVI-MRI presented concentric thickening and enhancement of multiple distal branches of the ACM arteries.

Results

Small/medium vasculopathy occurs more common in immunocompromised states. ln a retrospective U.K. cohort study, significant increase in cerebrovascular disease after zoster was found (1). Recent studies using VW-MRI, demonstrated, smooth, homogeneous, concentric arterial wall thickening and enhancement in patients with CNS vasculitis(2).

Conclusions

VW-MRI technique often demonstrates smooth, homogeneous, concentric arterial wall thickening and enhancement in patients with CNS vasculopathy.

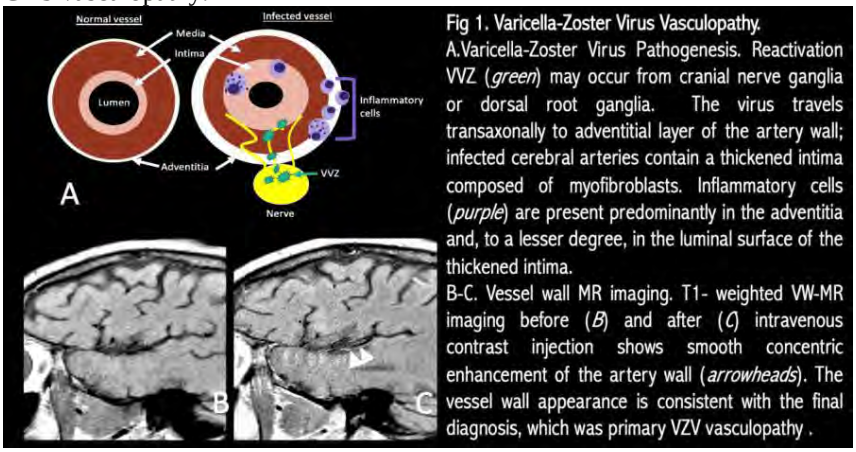

Fig 1. Varicella-Zoster Virus Vasculopathy.
A.Varicella-Zoster Virus Pathogenesis. Reactivation VVZ (*green*) may occur from cranial nerve ganglia or dorsal root ganglia. The virus travels transaxonally to adventitial layer of the artery wall; infected cerebral arteries contain a thickened intima composed of myofibroblasts. Inflammatory cells (*purple*) are present predominantly in the adventitia and, to a lesser degree, in the luminal surface of the thickened intima.
B-C. Vessel wall MR imaging. T1- weighted VW-MR imaging before (*B*) and after (*C*) intravenous contrast injection shows smooth concentric enhancement of the artery wall (*arrowheads*). The vessel wall appearance is consistent with the final diagnosis, which was primary VZV vasculopathy .

(Filename: TCT_425_VVZVASCULOPATHY.jpg)

432

Warthin's Tumor Infarction After Fine Needle Aspiration

P Rowley[1], A Kuner[2], G Hartig[1], L Eisenmenger[3]

[1]University of Wisconsin School of Medicine and Public Health, Madison, WI, [2]University of Wisconsin School of Medicine and Public Health, Middleton, WI, [3]University of Wisconsin - Madison, Middleton, WI

Purpose

A 65-year-old male initially presented with a slowly enlarging right-sided jaw mass, found to be a parotid lesion. Fine needle aspiration (FNA) was histologically consistent with a Warthin's tumor (WT); however, one month after FNA, the patient reported transiently increased pain followed by spontaneous resolution of the mass.

Materials and Methods

Baseline axial CT head and neck with IV contrast shows a solid, mildly heterogeneously enhancing 2.8 x 3.0 cm mass within the right parotid gland (Figure 1A). Follow-up six-month CT obtained for patient reported decreased mass size, confirmed decreased lesion size (2.5 x 1.5 cm), and interval development of cystic transformation with central hypoattenuation (Figure 1B).

Results

Parotid mass infarction is rare. It is known to occur spontaneously, but can also present as an extremely rare consequence of FNA (1). It occurs most often in WTs (adenolymphoma), potentially due to their high cellularity and poor vascular supply, with prior reports suggesting FNA may cause metaplastic changes and infarction within WTs (2).

Conclusions

It is important to be aware of and recognize the appearance of infarcted WTs. Misidentification may lead to unwarranted testing and procedural intervention.

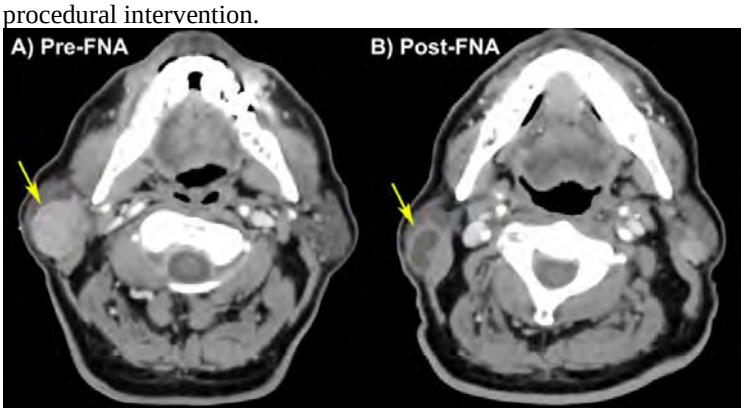

(Filename: TCT_432_parotidinfarctionv3.jpg)

1525

What lies beneath - mycotic aneurysm unveiled by thrombectomy

M Hurley[1], A Murphy[1]

[1]University of Chicago, Chicago, IL

Purpose

A 57yo right handed female presented initially as a typical large vessel embolic stroke emergency apart from a history over several months of arthralgia that was being worked up as a possible new onset of systemic lupus erythematosis. She underwent emergent thrombectomy of the right MCA M1 segment within the extended 24 hour window criteria with an NIHSS of 10, CTA showing a typical M1 occlusion and CTP with favorable perfusion parameters. After a successful first pass full recanalization of the M1 segment, a well defined 3mm fusiform aneurysm of a small pre-central branch of the right MCA superior division was revealed immediately downstream and was coiled with sacrifice of the small parent artery. The patient tolerated the procedure with an near complete resolution of symptoms. On review, the pseudoaneurysm, though subtle, was evident on the pre treatment CTA the possibility of mycotic embolism was raised. An echocardiogram showed sizeable vegetations on the aortic valve and after recovering from her stroke the patient underwent a valve replacement with anticoagulation.

Materials and Methods

Non contrast CT head (A) shows hyperdense blood product surrounded by vasogenic edema in the right frontal operculum. CTA head (B) shows fusiform dilatation of the right MCA prefrontal branch. DSA pre thrombectomy(C) shows right MCA M1 occlusion. Post thrombectomy DSA (D) shows fusiform aneurysm of the prefrontal branch.

Results

Endocarditis typically causes recurrent small embolic cerebral infarcts, microhemorrhages and occasionally angiographically visible aneurysms, most commonly distal and on the pial surface. Presentation with large vessel occlusion is rare but endocarditis should be considered if there is an unusual aneurysm (more distal, fusiform) associated with the occluded vessel. Recanalizing a large vessel occlusion upstream to a mycotic aneurysm has a risk of acute hemorrhage which should be weighed against the potential benefit of the thrombectomy.

Conclusions

An atypical intracranial aneurysm associated with a large vessel occlusion should raise suspicion for a mycotic embolism

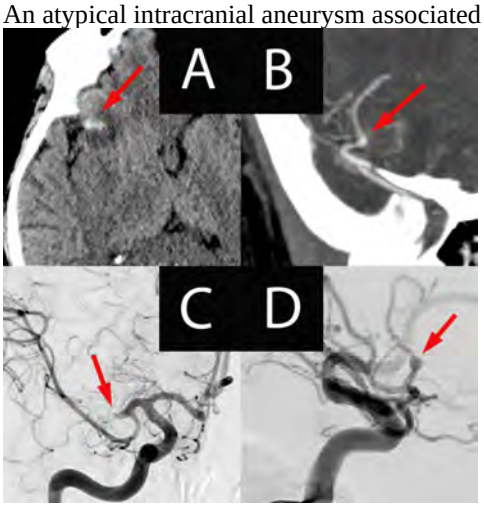

(Filename: TCT_1525_Figure1.jpg)

812

White Matter Hyperintensities - Where We've Been & Where We're Going - Taking It To the Extreme

B Varughese[1], D Dunaway[1], J Clark[1]

[1]Baylor College of Medicine, Houston, TX

Purpose

White matter hyperintensities (WMH) seen on brain MRI are a prevalent finding that have been identified on imaging since the late 1980s. We have come to understand that many diseases are associated with WMH. For example, microangiopathic changes and demyelinating disease commonly present as WMH in everyday practice. Other etiologies such as Alzheimer's dementia, traumatic brain injury, and normal pressure hydrocephalus are also frequently detected on imaging. Often, however, WMH still remain a diagnostic dilemma with a nonspecific differential diagnosis.

Materials and Methods

Hyperintensities on FLAIR and T2-weighted MRI sequences involving the subcortical, subinsular and/or periventricular white matter.

Results

Although we know much more about WMH than we did before, there is still much we do not know. This review discusses main theories for the pathogenesis behind WMH, examines the anatomy involved in WMH and addresses some of the lesser-known etiologies associated with WMH. Proposed mechanisms for WMH formation that are discussed include the following: microemboli formation, small vessel disease, pulse-wave encephalopathy and glymphatic dysfunction. Importantly, white matter lesions in individuals exposed to extreme environments, such as astronauts and U2 pilots, can be analyzed to draw wider conclusions that can be applied to more common clinical scenarios.

Conclusions

There are multiple proposed etiologies for the formation of WMH. Glymphatic dysfunction and pulse-wave encephalopathy are two etiologies which are suspected to cause the WMH in individuals exposed to extreme environments. As an increasing number of individuals are exposed to extreme environments due to recent advances in aviation and space travel, it will become more important to understand the nature of WMH and their pathogenesis.

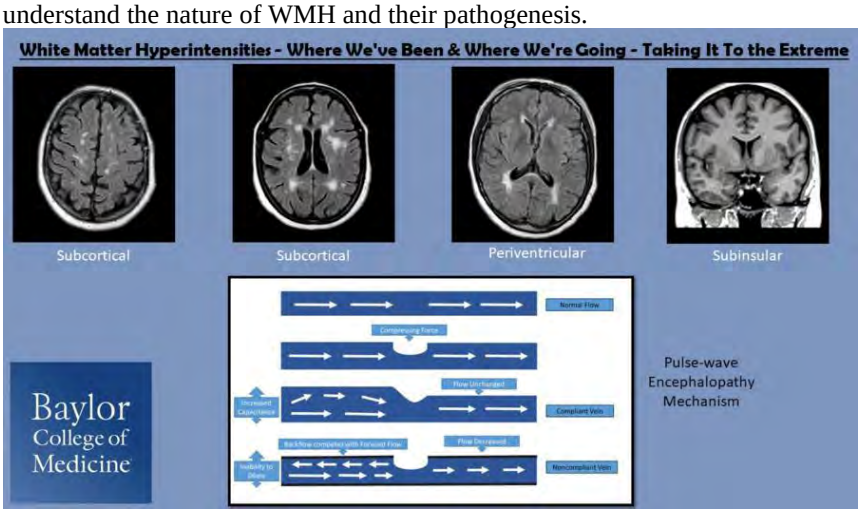

(Filename: TCT_812_Excerpta.JPG)

EDUCATIONAL EXHIBITS

290

2021 WHO Update and the Imaging Features of Molecular Glioblastoma

I Mark[1], S Cha[2]
[1]UCSF, San Francisco, CA, [2]University of California San Francisco, San Francisco, CA

Purpose

The World Health Organization (WHO) recently released the 2021 Classification of Tumors of the Central Nervous System. This update changes the paradigm of how glioblastomas are evaluated. The diagnosis of glioblastoma no longer requires the classic histopathologic characteristics and can be made by molecular markers: TERT promoter mutation, EGFR gene amplification, and Trisomy 7/Monosomy 10. -We will provide an overview of the new molecular genetic markers that are highlighted in the 2021 WHO update and are now essential in the diagnosis of glioblastoma. -We will provide a single center experience in performing molecular tumor testing that highlights the different imaging appearances of molecular glioblastoma (WHO grade IV). -We will provide imaging examples of tumors that do not meet the classic histopathological diagnosis of glioblastoma but are now classified as glioblastoma on the basis of molecular markers.

Materials and Methods

The purpose of this educational exhibit is to provide a comprehensive imaging overview and highlight characteristic imaging features of the molecular glioblastoma.

Results

Retrospective review of brain tumor imaging from a single institution in performing molecular genetic testing of brain tumors.

Conclusions

Molecular genetic testing of brain tumors is now at the epicenter of the diagnosis of glioblastoma following the 2021 WHO update. It is important for neuroradiologists to become familiar with these changes and their imaging appearance.

433

A Closer Look at Intraorbital Fat: An Educational Neuroimaging Review of a Wide Spectrum of Abnormalities

K Seifert[1], D Sivacharan Gaddam[1], S Tedla[1], B LANZMAN[2], M Wintermark[1], S Hashmi[1], T Massoud[1]
[1]Stanford University School of Medicine, Stanford, CA, [2]Stanford Hospital and Clinics, Stanford, CA

Purpose

The space between each globe, extraocular muscles, and vessels and nerves is filled with adipose tissue (the orbital adipose body). This intraorbital fat (IOF) is of interest owing to several distinctions from body fat by embryology, structure, and function. It is also of particular importance to neuroradiologists owing to a wide spectrum of abnormalities centered on IOF. We provide a focused pictorial and educational review of neuroimaging findings specific to the IOF.

Materials and Methods

We comprehensively review imaging findings of a wide spectrum of congenital and acquired abnormalities in the IOF, and classify these according to etiology and pathogenesis.

Results

The IOF consists of ~12 ml of white adipose tissue that differs from body fat by its smaller adipocytes and fat lobules, and denser stroma. We first review the cross-sectional imaging anatomy of IOF compartments. IOF may be seen on imaging to herniate through the lamina papyracea after trauma or complications of sinus surgery, after decompressive orbitotomies for thyroid eye disease (TED), as subconjunctival IOF prolapse through Tenon's capsule, and intracranially through the superior orbital fissure in TED. We demonstrate imaging findings of lipohypertrophy in TED, Cushing's disease, and obesity; and lipoatrophy in HIV, cancer cachexia, catabolic lipolysis, and anorexia. Notably, IOF is preserved in congenital and acquired generalized lipodystrophies. Imaging findings in orbital trauma include IOF hemorrhage and edema, e.g. in orbital compartment syndrome, and post-traumatic fat necrosis. Orbital infection also results in a "dirty fat" appearance and enhancement. Several orbital inflammatory conditions can generally or selectively involve the IOF. TED IOF findings also include an increase in fat to orbit ratio, and increase in signal intensity ratio on STIR MRI that positively correlates with that of extraocular muscles and with clinical activity scores. Other inflammatory conditions include idiopathic orbital inflammatory disease and IgG4-related ophthalmic disease. Tumors specific to the IOF include lipoma, lipoblastoma, and liposarcoma. Iatrogenic changes in IOF may be seen following fat grafting procedures for orbit volume loss, and after fat decompression procedures for TED.

Conclusions

Accurate neuroimaging differentiation of normal or pathological disorders centered on the IOF is important clinically. This presentation will aid in interpretation of focal and diffuse abnormalities of the IOF to improve patient management.

1212

A Functional MRI Paradigm Suitable for Autobiographical Memory Mapping in clinical practice.

A Camins-Simon[1], P Naval-Baudin[1], S Jacint[1], A Rosselló[1], E Cámara[2], I Rico[1], D Cucurell[2], I Martínez-Zalacaín[2], L Fuentemilla[2], M Falip[1], A Fernández-Coello[1]

[1]Bellvitge University Hospital, LHospitalet de Llobregat, Barcelona, [2]Universitat de Barcelona, LHospitalet de Llobregat, Barcelona

Purpose

To present the prognostic utility of functional MRI of autobiographical memory for epilepsy surgery planning. To review the concept of autobiographical memory and which anatomical structures are involved. To explain the paradigm that we use in our clinical practice to study autobiographical memory using functional MRI.

Materials and Methods

N/A

Results

Neuroimaging is crucial for the diagnosis and presurgical planning of patients with drug-resistant temporal lobe epilepsy. Anterior temporal lobectomy is a treatment option for these patients; however, it comes with a significant risk of memory deficits. Memory requires three basic processes: 1) encoding: the initial learning of information, 2) storing: the process of placing newly acquired information into memory, and 3) recall: the mental process of retrieval of information. We focused on the memory recall process through the study of voluntary autobiographical memory, which helps us to remember an event that happened at a specific time and location of our past. Functional MRI studies enable the identification of temporal structures and the extratemporal neural networks that are involved in this complex cognitive process. We describe in detail the specific paradigm that we use in our hospital to evaluate autobiographical memory. We present a series of functional MRI studies in healthy subjects and patients.

Conclusions

Functional MRI is useful to assess the location and lateralization of the structures involved in autobiographical memory.

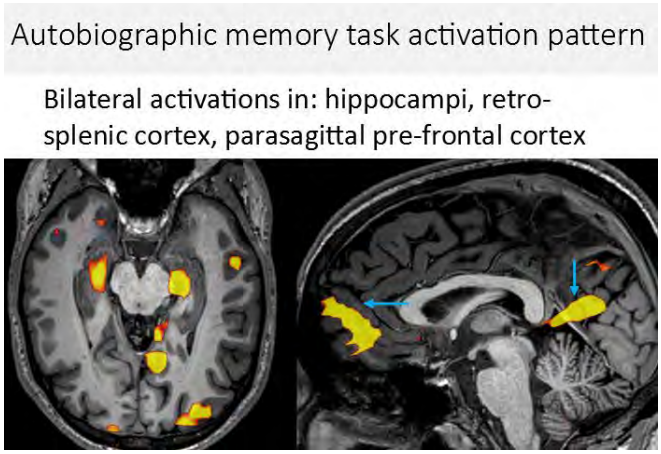

(Filename: TCT_1212_figure.jpg)

1546

A Pictorial Review of Jugular bulb variants causing Pulsatile Tinnitus

A Remunda[1], E Tang[1], S PATEL[2], S Ifthikharuddin[1], B Scott[1]

[1]Rochester Regional Health, Rochester, NY, [2]ROCHESTER GENERAL HOSPITAL, ROCHESTER, NY

Purpose

To discuss the most common causes of pulsatile tinnitus with particular attention to the jugular bulb. Characteristic imaging will be used to help distinguish each diagnosis. Specific cases discussed will include the high-riding jugular bulb, jugular bulb diverticulum, and jugular bulb dehiscence.

Materials and Methods

Tinnitus, known as ringing in the ear drum, can be described as pulsatile or continuous. Pulsatile tinnitus has a wide breadth of causes, from vascular to neoplastic in origin. Venous variants are the most common causes of pulsatile tinnitus. We will briefly discuss venous causes of pulsatile tinnitus, particularly jugular bulb variants. The anatomical variants that will be included are high-riding, diverticulum and dehiscence of the jugular bulb. We will review the common imaging features seen on bone algorithm computed tomographic (CT) studies, magnetic resonance (MR) images, and digital subtraction angiography (DSA).

Results

Pulsatile tinnitus originates from turbulent vascular blood flow within the inner ear which is synchronous to the patient's pulse. The Jugular bulb is unique in that it is a large volume area that can be a nidus for turbulent flow which can be acoustically transmitted by the temporal bone. The skull base and mastoids can only accentuate the synchronous heartbeat which transmits to the conductive auditory pathway and interfere with the cochlea.

Conclusions

High-riding jugular bulb is when the jugular bulb extends caudally into the petrous bone and is usually within 2 mm of the floor of the

internal auditory canal. Jugular bulb diverticulum is an oval-shaped outpouching at the superomedial aspect of the jugular bulb which embeds itself into the petrous bone. Jugular bulb dehiscence involves thinning of the jugular plate which is the floor of the hypotympanum and usually provides a barrier of the jugular bulb from the middle ear. Given that venous etiologies are the most common cause of pulsatile tinnitus they should be considered in an initial workup. The three jugular bulb variants are great early considerations. Pulsatile tinnitus rides on the principle of turbulent flow pulsation transmitting acoustically through the skull base to the which may occur in any of the venous structures such as the transverse or sigmoid sinuses.

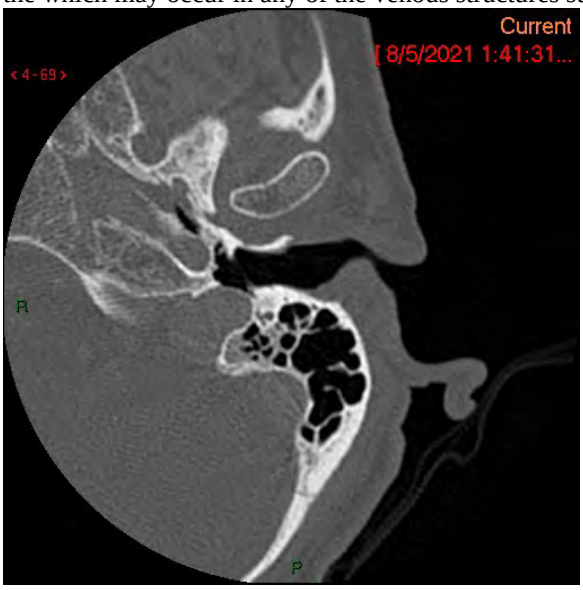

(Filename: TCT_1546_jugdihis.jpg)

735

A Pictorial Review: Understanding Autoimmune Diseases of the Spine

G Biddle[1], Z Jenner[1], V Ivanovic[1], R Assadsangabi[1], A Ozturk[1], J CHANG[1], M Bobinski[1], L Hacein-Bey[1], O Raslan[1]
[1]University of California Davis Medical Center, Sacramento, CA

Purpose

Autoimmune myelopathies are a heterogeneous group of disorders, with many recent updates on this broad spectrum of pathologies. Imaging plays a critical role in the early diagnosis of these cases which is pivotal in preventing permanent disability and improving patient outcome. Overlap of imaging features in many pathologies in this group makes diagnosis challenging. Our goal is to describe and highlight the imaging findings and diagnostic key points of autoimmune myelopathies of the spine

Materials and Methods

In this up-to-date comprehensive review, we aim to provide a practical diagnostic approach combining the clinical, laboratory and unique radiological findings of the immune-mediated diseases of the spinal cord to assist the radiologists in their understanding of these unique disorders and help them in making an accurate diagnosis or at the very least narrowing the differential diagnostic considerations, thus expediting patient care and avoid unnecessary investigations and interventions.

Results

We retrospectively searched all MRI studies from our PACS system with autoimmune diseases for this pictorial essay in order to provide a comprehensive review of the neuroimaging findings. The clinical and critical laboratory features of the most common autoimmune diseases affecting the spinal cord are also discussed in this review.

Conclusions

Major categories: • Demyelinating diseases (multiple sclerosis, neuromyelitis optica spectrum disorder (NMOSD), myelin oligodendrocyte glycoprotein IGG Associated disease (MOGAD), acute disseminated encephalomyelitis (ADEM), collapsin response mediator protein-5 autoantibody (CRMP-5), glial fibrillary acidic protein astrocytopathy (GFAP- IGG). • Systemic Autoimmune Disorders (Systemic Lupus Erythematous (SLE), Antiphospholipid Syndrome, Immunoglobulin G4–Related Disease, Sarcoidosis, Sjögren Syndrome, Behcet's Disease, Vogt-Koyanagi-Harada Disease. • Paraneoplastic Disorders including Stiff-Person Syndrome and Autoimmune/Paraneoplastic Motor Neuron Disorders. • Parainfectious Autoimmune Myelopathies (including coronavirus 2 (SARS-CoV-2) and hepatitis C virus. Conclusion: To highlight key imaging findings and helpful differential diagnostic clues aiding the radiologist at making the most accurate diagnosis.

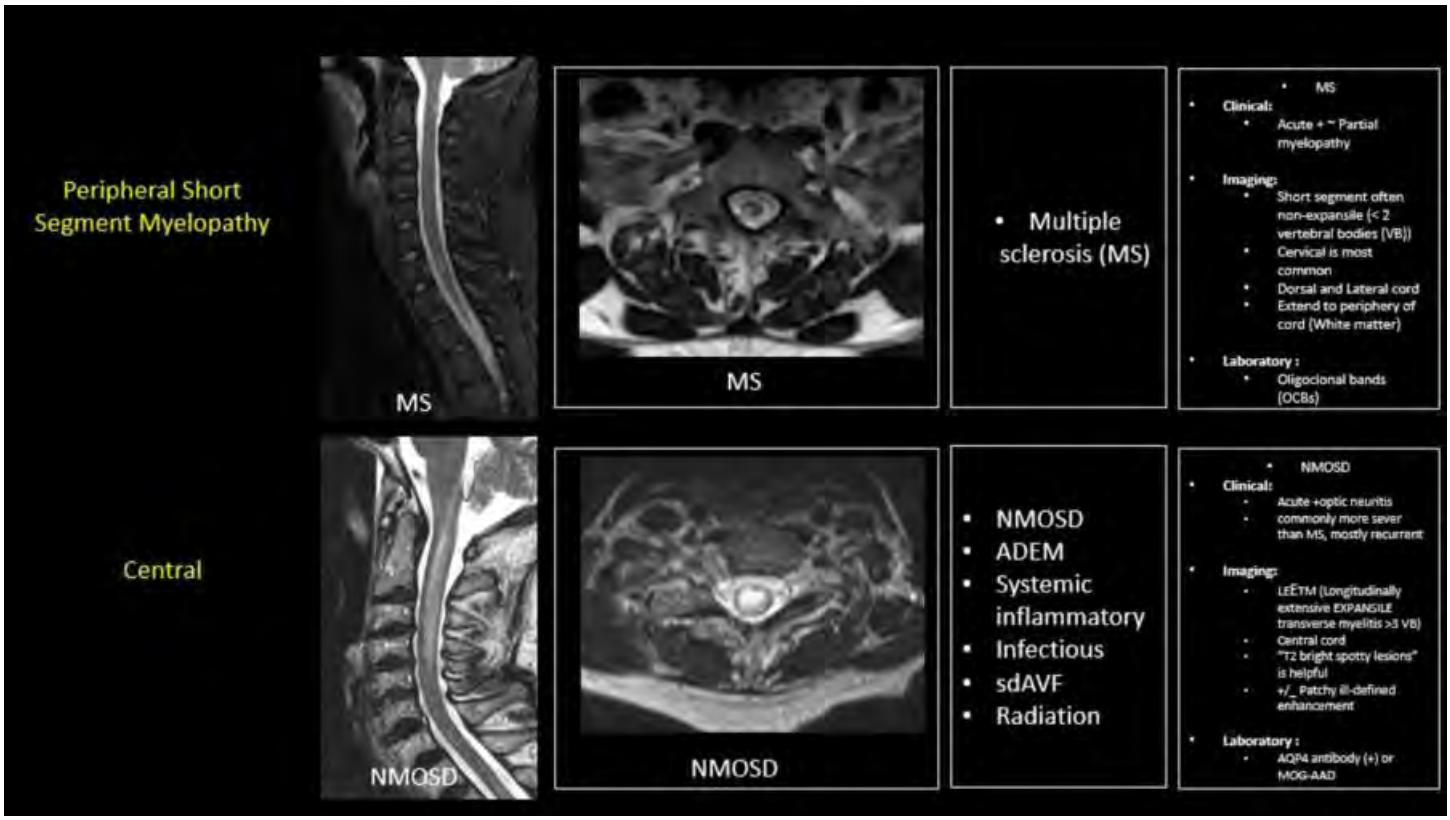

(Filename: TCT_735_FinalImagejpg.jpg)

1325

A Radiographic Review of Aggressive Pathology of the Paranasal Sinuses.

J Joshua[1], O Hassan[1], E Hoeffner[1]
[1]*University of Michigan, Ann Arbor, MI*

Purpose

To review the imaging findings of aggressive sinonasal pathology, including tumors and aggressive infectious and inflammatory processes, on CT and MRI. Optimal CT and MR imaging protocols for assessing aggressive sinonasal processes will be discussed. We will review imaging findings on CT concerning for a more aggressive sinonasal process, which often leads to the recommendation for an MRI. We will illustrate the importance of imaging in evaluating the patterns of spread, defining the full extent, staging and follow-up imaging in patients with sinonasal tumors. We will also delineate the complications of acute rhinosinusitis, fungal sinonasal infections and granulomatous infectious and inflammatory processes which present with aggressive imaging features.

Materials and Methods

We will review the following: • Normal paranasal sinus anatomy • Radiographic appearance of aggressive pathology of the paranasal sinuses - Evaluating the patterns of spread, defining full extent of disease, staging and follow-up imaging • Optimal CT and MR imaging protocols for assessing aggressive sinonasal processes.

Results

We will use cases of actual patients seen at the the University of Michigan Department of Radiology.

Conclusions

Familiarity with aggressive sinonasal pathology is important for the practicing radiologist. Our educational exhibit will help with audience develop a familiarity with the radiographic (CT/MRI) appearance of aggressive paranasal pathology, patterns of disease spread as well as protocol optimization and imaging follow-up.

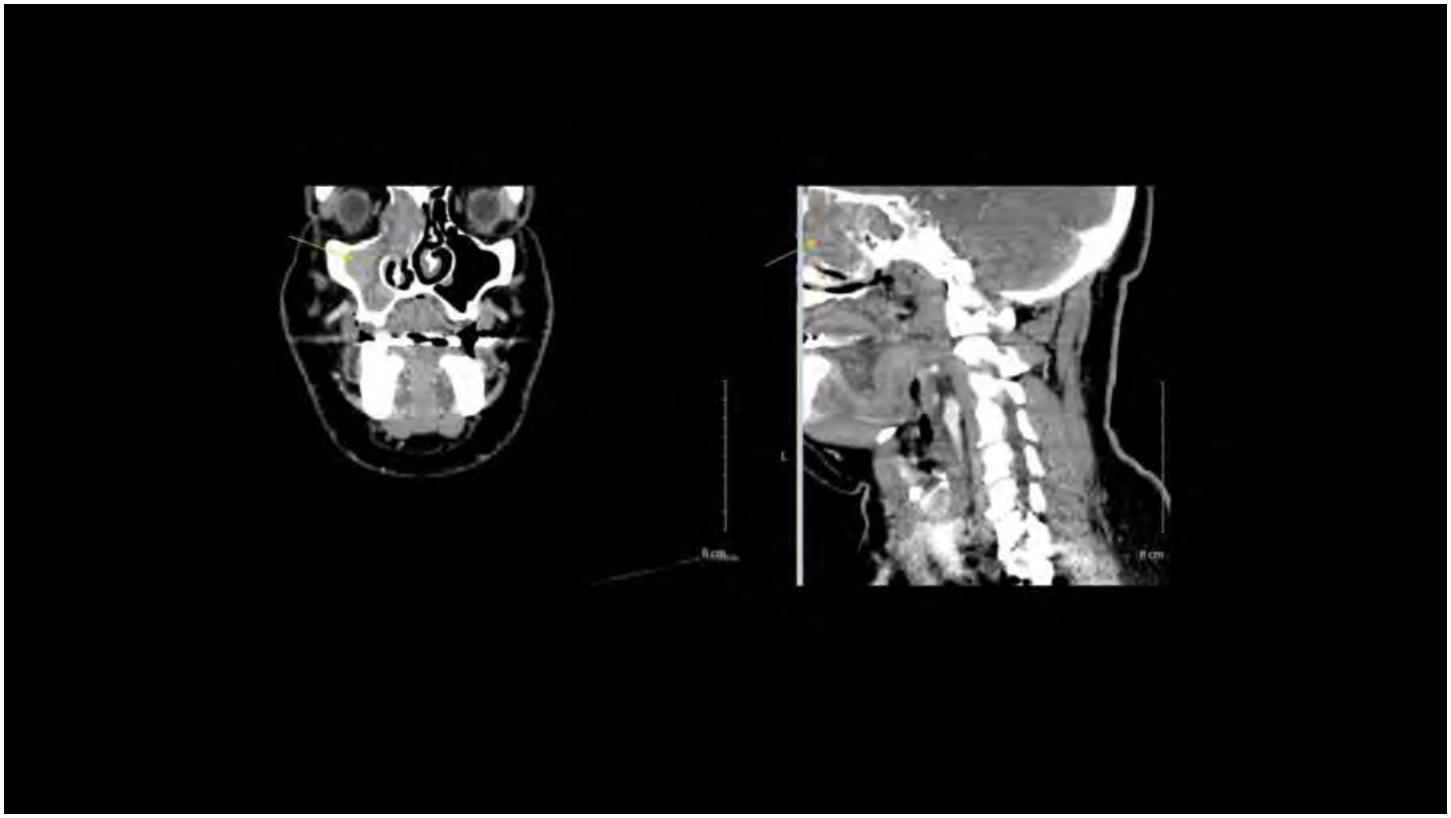

(Filename: TCT_1325_Paranasalsinustumor.jpg)

1387

A Review of Chronic Subdural (Intradural) Hematomas and Hygromas from a Glymphatic Perspective: Anatomy, Etiology, Pathophysiology and Imaging Findings

R Bert[1]

[1]*University of Louisville, Louisville, KY*

Purpose

The presentation will review epidemiology, pathophysiology and treatment of Chronic Subdural Hematomas (CSDH) with insights provided by the glymphatic hypothesis. Educational objectives will include: 1. Understand the ultrastructure of the dura. 2. Understand the interconversion of CSDH and Hygromas. 3. Understand simultaneous formation of SDH and more peripheral hygromas. 4. Understand bleeding sources of CSDH. 5. Learn to reliably differentiate widened subarachnoid spaces and CSDH.

Materials and Methods

To review the anatomic basis, epidemiology, pathophysiology and imaging features of chronic "subdural", hematomas (CSDH) and subdural hygromas (SH) with perspectives from the CNS Glymphatic hypothesis.

Results

literature dating from 1978 to present was gathered and reviewed. Supportive images and illustrations were selected from teaching files and licensed reprints.

Conclusions

Anatomy. The deep dural border layer consists of cells and connects to the arachnoid barrier layer. This dural border layer is a weak link in the meninges easily separated by fluid. Epidemiology. CSDH are typically a malady of the elderly; acute subdural hematomas (ASDH) are more typical in youth with serious head trauma. Pathophysiology. Classically, ASDH formed by tearing of dural "bridging veins", becoming CSDH after liquefaction and subsequent inner-outer membrane formation resulting in a dynamic equilibrium. Clot lysis factors emitted from the inner membrane liquified the clot, while eosinophiles in the outer membrane regulated blood resorption and new clot formation. The generality of this mechanism was challenged when many CSDHs were shown to originate from bleeding into SH. Pathologic studies established intradural arteries as additional bleeding sources, leading to treatment by meningeal artery embolization. SH, considered separate, supposedly originated from cerebrospinal fluid via rents in the arachnoid barrier layer, leaving SH forming peripheral to ASDH unexplained. Currently, the glymphatic hypothesis better fits these observations. Imaging findings. CT. CSDH can be isodense to gray matter or cerebral spinal fluid (CSF), making CSDHs, SH and widened subarachnoid spaces difficult to distinguish. When CSDHs contain membranes and septations, these are often hyperdense to CSF and enhance. MRI signal is heterogeneous in CSDH, vs. CSF intensity for SH. Both deep and superficial surfaces of CSDH often enhance. Veins extending from the cortex to the dural sinuses do not reliably exclude CSDH.

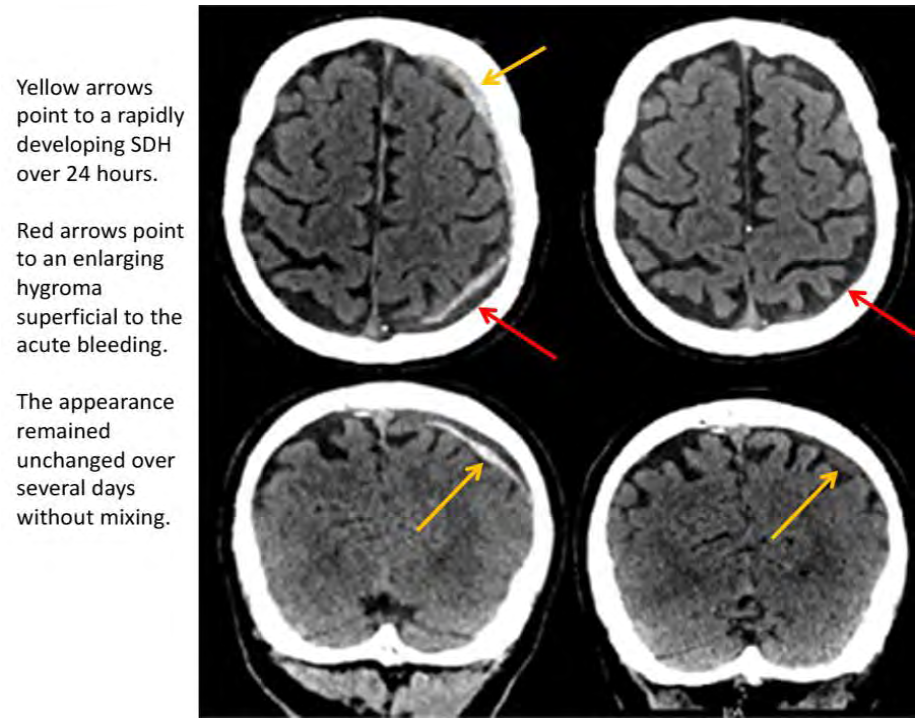

(Filename: TCT_1387_FinalFigureCSDH.jpg)

1501

A Single Tertiary Care Referral Center Experience of 270 C-11-PK11195 Brain Positron Emission Tomography Scans in 206 Pediatric and Adult Patients for Evaluation and Management of Neuroinflammation

A Kumar[1], O Muzik[2], H Chugani[3]

[1]Johns Hopkins University School of Medicine, Baltimore, MD, [2]Wayne State University, Detroit, MI, [3]New York University, New York, NY

Purpose

We will present our experience at Wayne State University Detroit Medical Center to demonstrate the safety, feasibility and usefulness of C-11-PK11195 Brain Positron Emission Tomography in the evaluation, treatment and prognostication of various neuroinflammatory conditions.

Materials and Methods

To present a single tertiary care referral center experience regarding the feasibility and usefulness of C-11-PK11195 Brain Positron Emission Tomography (PK PET) in the evaluation and management of various neuroinflammatory conditions.

Results

206 patients (33 adults (19 females; age: 37.4 ± 16.4 (18.3-72.7), 165 children (98 males; age: 9.7 ± 4.5 (1-18), 6 infants and 2 newborns) and 15 healthy adult volunteers (8 female; age 29 ± 8.5 years (20-49) underwent 270 dynamic brain PK PET from 2006 to 2019 with approval from Wayne State University IRB. PET scan was performed over 60 minutes after intravenous administration of 17 MBq/Kg of PK PET tracer. The volunteers also underwent whole body imaging. The data was analyzed by calculating binding potential, a measure of receptor-ligand binding, using reference tissue model. Reference brain area, to be used in lieu of arterial input, was identified using cluster analysis. Biodistribution and dosimetry analysis was also performed in 7 adult volunteers and 22 selected children.

Conclusions

We found that PK PET can be safely performed, including in children, and quantitative analysis can be performed without need for invasive arterial sampling. A wide variety of patients, such as those with a clinical diagnosis or suspicion of encephalopathy (n=12), Niemann Pick type-c (n=10), Infantile spasms (n=15), Tourette syndrome (n=14), pediatric autoimmune neuropsychiatric disorders (n=40), multiple sclerosis, (n=20), epilepsy (n=47), Rasmussen's encephalitis (n=8), etc. were evaluated using PK PET. Increased tracer binding was seen in various brain regions in most of the patients, and corresponded well to abnormalities detected clinically or on other tests (MRI/EEG). It sometimes changed the diagnosis or clinical suspicion, guided specific treatment, and was used to monitor the disease evolution. Our experience shows that PK PET is a safe and feasible procedure which can help in understanding the role of neuroinflammation in various neurological conditions. It can be potentially used as 'neuroinflammation imaging biomarker' to guide treatment, evaluate therapeutic response, and provide prognostic information across a wide age range and a variety of neurological conditions.

1012

Acute Traumatic Orbital Lesions: An Interactive Case-Based Review.

A Pulido[1], A Zalis[1], S Falcone[2], N Nagornaya[3], J Manov[4], G Saigal[3], D Pinto[5]

[1]University of Miami/Jackson Memorial Hospital, Miami, FL, [2]University of Miami, Coral Springs, FL, [3]Jackson Memorial Hospital/University of Miami, Miami, FL, [4]University of Miami, Miami Beach, FL, [5]Jackson Memorial Hospital, Miller school of medicine, Miami, FL

Purpose

Educational objectives: 1. To review the normal orbital and globe anatomy, including their normal appearance on both, Computed Tomography (CT) and Magnetic Resonance (MR) Imaging. 2. To recognize the indications, contraindications, advantages, and limitations of both modalities on the evaluation of acute orbital traumatic lesions. 3. To illustrate with an interactive case-based exhibition, the critical imaging findings of both, intraocular and extraocular acute orbital traumatic lesions. 4. To get familiar with the expected imaging appearance of different inorganic and organic intraorbital foreign bodies. 5. To discuss different mimics of acute traumatic lesions and intraorbital foreign bodies. Approximately 3% of all visits to the emergency department are due to primary acute ocular trauma. In the USA, there are nearly 2.5 million new eye injuries per year, and globally, the World Health Organization estimates that acute traumatic ocular lesions result in blindness in about 1.6 million people and unilateral blindness or decreased vision in approximately 19 million people, annually. Up to 16% of the patients who suffer major trauma, also present ocular and/or extraocular orbital lesions, often with coexistent facial fractures. Computed tomography (CT) is the modality of choice for the initial evaluation of orbital trauma, especially when there is suspicion of possible foreign bodies. However, the neuroradiologist must be familiar with the imaging findings of the acute orbital traumatic injuries on both, CT and Magnetic Resonance (MR) imaging, including the expected imaging appearance of inorganic and organic foreign bodies on both modalities. We have gathered several cases from a referral center for ophthalmologic pathologies, and from a Level I Trauma center located in Miami, Florida, to create a case-based interactive electronic educational exhibit, where the attendant will be able to recognize the different features of acute orbital injuries following an organized systematic approach.

Materials and Methods

N/A

Results

N/A

Conclusions

N/A

(Filename: TCT_1012_asnrcollage.jpg)

729

Adult Spinal Deformity: Pre-operative Imaging, Surgical Options, and Post-operative Outcomes.

J Hassan[1], L Bagley[2], A Ozturk[2]

[1]Hospital of University of Pennsylvania, Philadelphia, PA, [2]Hospital of University of Pennsylvania, Philadelphia , PA

Purpose

Adult spinal deformity is an important health concern for the aging population of the United States. Imaging plays a crucial role in evaluation of these patients. The objective of this exhibit is to familiarize a neuroradiologist with the pre-operative imaging, available surgical options, and post-operative outcomes.

Materials and Methods

Adult spinal deformity (ASD) is a cause of significant disability in the aging population of the United States. Although supportive measures have historically been the mainstay of therapy for patients with ASD, surgical correction procedures have been increasingly utilized. Correction of both coronal and sagittal malalignment is crucial for post-operative well-being of the patients. In addition, the spinopelvic alignment plays an important role in global balance and biomechanics of the spine. The purpose of this exhibit is to familiarize neuroradiologists with numerous radiographic parameters used in assessment of the extent of spinal deformity on pre-oprative imaging. This will include assessment of scoliosis, thoracic kyphosis, and lumbar lordosis, in addition to coronal pelvic decompensation (CPD), sagittal vertical alignment (SVA), pelvic obliquity, pelvic incidence (PI), pelvic tilt (PT), sacral slope (SS) and T1 pelvic angle. Additionally, the exhibit will illustrate various available surgical options such as posterior column osteotomy, pedicle subtraction osteotomy, and vertebral column resection. Lastly, it will illustrate desired post-operative imaging appearance as well as the wide range of peri-operative and delayed complications associated with spinal deformity correction procedures.

Results

We have collected cases of adult patients with thoracolumbar spinal deformity from our institution. We will elaborate on their pre-operative imaging, surgical procedures, and post-operative outcomes.

Conclusions

After completing this educational exhibit, the radiologist would be able to evaluate the extent of spinal deformity on pre-operative imaging, appreciate the available surgical options, and understand the desired post-operative outcomes in addition to recognizing the complications.

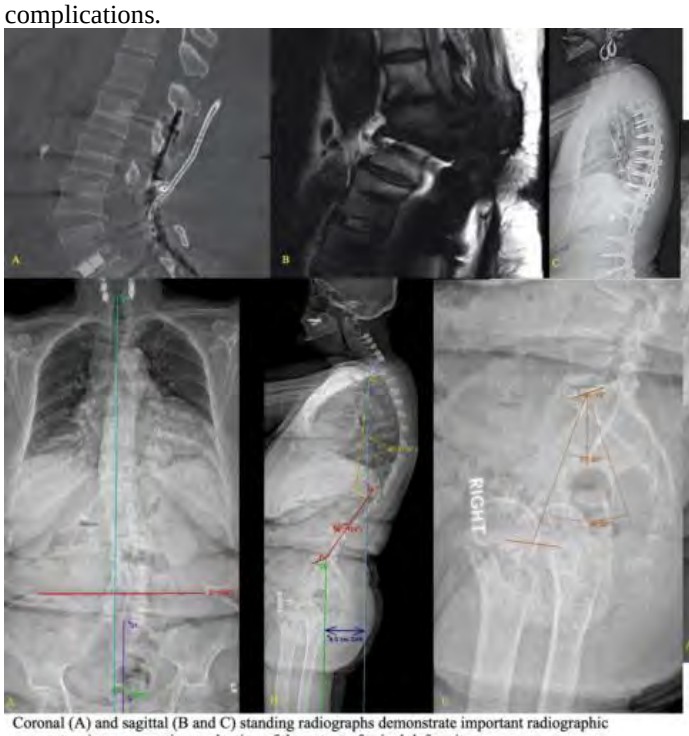

Coronal (A) and sagittal (B and C) standing radiographs demonstrate important radiographic parameters in pre-operative evaluation of the extent of spinal deformity.

74-year-old with L2-S1 fusion (A) complicated by proximal junctional kyphosis at L1-L2 (B). Patient underwent a vertebral column resection and cage insertion at L1-L2 and posterior instrumentation from T4-sacrum (C).

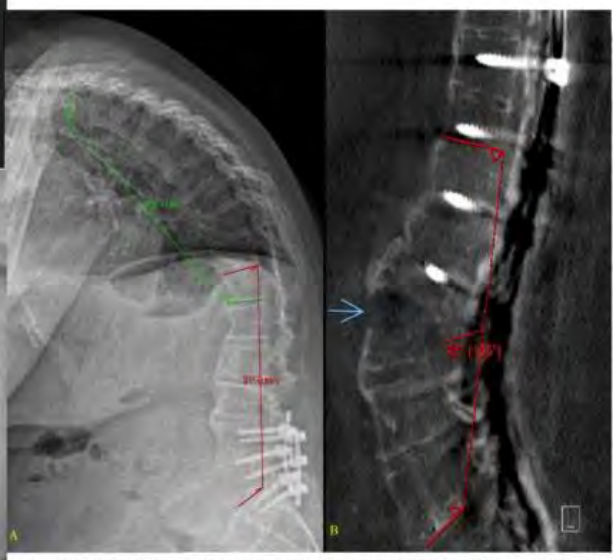

70-year-old with history of ankylosing spondylitis, marked thoracic kyphosis, and loss of lumbar lordosis underwent a PSO at L3 (arrow) with resultant increase in lumbar lordosis.

(Filename: TCT_729_ASNRfinal.jpg)

620

Advanced Imaging Features of Immunodeficiency-associated CNS Lymphoma

N Omid-Fard[1], P Puac Polanco[1], L Hamilton[1], C Torres[1], T Nguyen[1]

[1]University of Ottawa, The Ottawa Hospital, Ottawa, Ontario

Purpose

- Highlight the unique imaging findings in immunodeficiency-associated CNS lymphoma, a diagnosis that needs to be differentiated from other tumours with a similar appearance, such as metastasis or glioblastoma (GBM) given their different management. - Review different immunodeficiency scenarios in which CNS lymphomas can be seen, including cases where it might be unsuspected and

missed on the differential. - Review advanced imaging techniques in assessing CNS lymphoma, including MR spectroscopy, diffusion, and MR perfusion. - Highlight the differences in imaging presentation between immunocompetent versus immunodeficiency-associated CNS lymphoma, with histopathological correlation.
Materials and Methods
To review the spectrum of imaging findings in immunodeficiency-associated CNS lymphoma, including advanced imaging techniques, with emphasis on key MRI features that help differentiate it from CNS lymphoma in the immunocompetent patient.
Results
Retrospective chart review of CNS lymphomas seen at our institution over 20 years. Select cases will be chosen for the presentation.
Conclusions
In the immunocompromised setting, there are distinct radiologic findings of CNS lymphoma, including 1) multiplicity; 2) necrotic ring-enhancing lesions; 3) basal ganglia and callosal predominant involvement; and 4) increased propensity for intralesional hemorrhage. (1) In this clinical context, advanced imaging with MR perfusion, spectroscopy and diffusion-weighted imaging can be used to increase accuracy in the diagnosis of lymphoma over mimics such as GBM, metastases or infection. (2-3) This knowledge is particularly relevant to radiologists as the incidence of immune-deficiency related CNS lymphoma may be increasing. (4) Caption: Patient with history of systemic lupus erythematosus presenting with primary CNS lymphoma. Post-contrast T1 axial image (A) demonstrates a ring enhancing medial temporal lobe lesion. Diffusion restriction is seen in the solid peripheral component on the ADC map (B). Corrected DSC perfusion imaging demonstrates only mildly increased rCBV in the tumor periphery (C). Histopathology (D) shows coagulative-type necrosis (pink areas) within the tumor, a distinct feature of immunodeficiency associated CNS lymphoma (different patient).

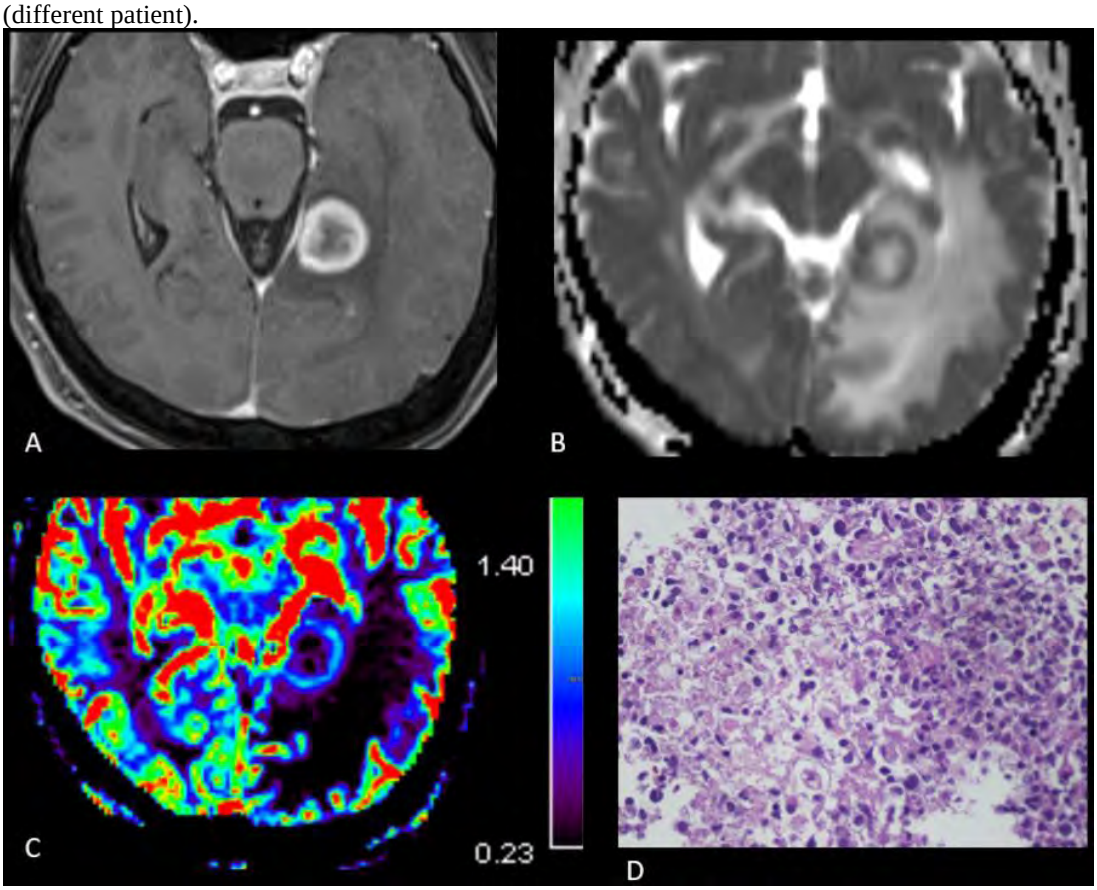

(Filename: TCT_620_ASNR2022AbstractGraphic.jpg)

846

An Eye for an Eye: Demystifying MRI Findings and Staging of Uveal Melanoma

A Carvalho[1], T Guarilha[2], B Pfluck[3], M Borri[4], A Wolosker[5], H Yamashita[6]
[1]Universidade Federal de Sao Paulo, Sao Paulo, Brazil, [2]UNIFESP, São Paulo, Indianópolis, [3]UNIVERSIDADE FEDERAL DE SÃO PAULO, São Paulo, São Paulo, [4]Federal University of Sao Paulo-Fleury Group-Hospital Sao Luiz-Rede d'Or, São Paulo, SP, [5]Federal University of Sao Paulo-Hospital Sao Luiz-Rede d'Or, sao paulo, -- SELECT --sao paulo, [6]UNIFESP, Sao Paulo, Brazil

Purpose
-To review basic ocular anatomy and classic diagnostic findings in uveal melanoma. -To elucidate the staging system used for uveal melanoma with MRI cases, discussing treatment planning implications for each circumstance.

Materials and Methods
To enable radiologists to understand and interpret common findings in uveal melanoma cases while providing additional knowledge about its specific staging system and its differential diagnosis.
Results
A retrospective study with a review of up-to-date literature will be performed. MRI illustrative cases of intraocular melanomas obtained from the participating institutions will be demonstrated and discussed, accompanied by annotated images.
Conclusions
Uveal melanoma is the most common primary intraocular neoplasm in adults. It can involve any part of the uveal tract, with most cases arising from the choroid and a small percentage involving the ciliary body and the iris. Clinical symptoms are related to the location and size of the lesion. It can range from asymptomatic to complete visual loss. The diagnosis is done with ophthalmoscopy, biomicroscopy, and ultrasonography. MRI has its role in the evaluation of the local extent of the lesion as well as its implication in the treatment planning and its follow-up. It is particularly helpful when there are opaque media in the eye making it difficult to clinically assess posterior segments.Uveal melanoma typically displays high signal on T1-weighted images and low signal intensity in T2 images but can vary depending on the degree of pigmentation and the presence of areas of necrosis or cavitation. The eye anatomy can be well assessed with T1 and T2 weighted images, defining the extent and the origin of the lesion, and identifying if there is ciliary body or scleral infiltration. MRI is also able to assess the extent of the lesion, nodal involvement and the presence of metastases, with accurate measurements performed using multiplanar reconstructions. Quantitative diffusion-weighted imaging (DWI) helps to distinguish tumors with high-cellularity and may also be useful in noninvasively detecting an early response of the lesion to radiotherapy. Dynamic contrast enhanced-MRI may also improve evaluation, due to the possibility of assessing the tumor's perfusion graphics. This increases diagnostic sensitivity while helping to differentiate melanoma from its differential diagnosis, such as adenoma of the retinal pigment epithelium.

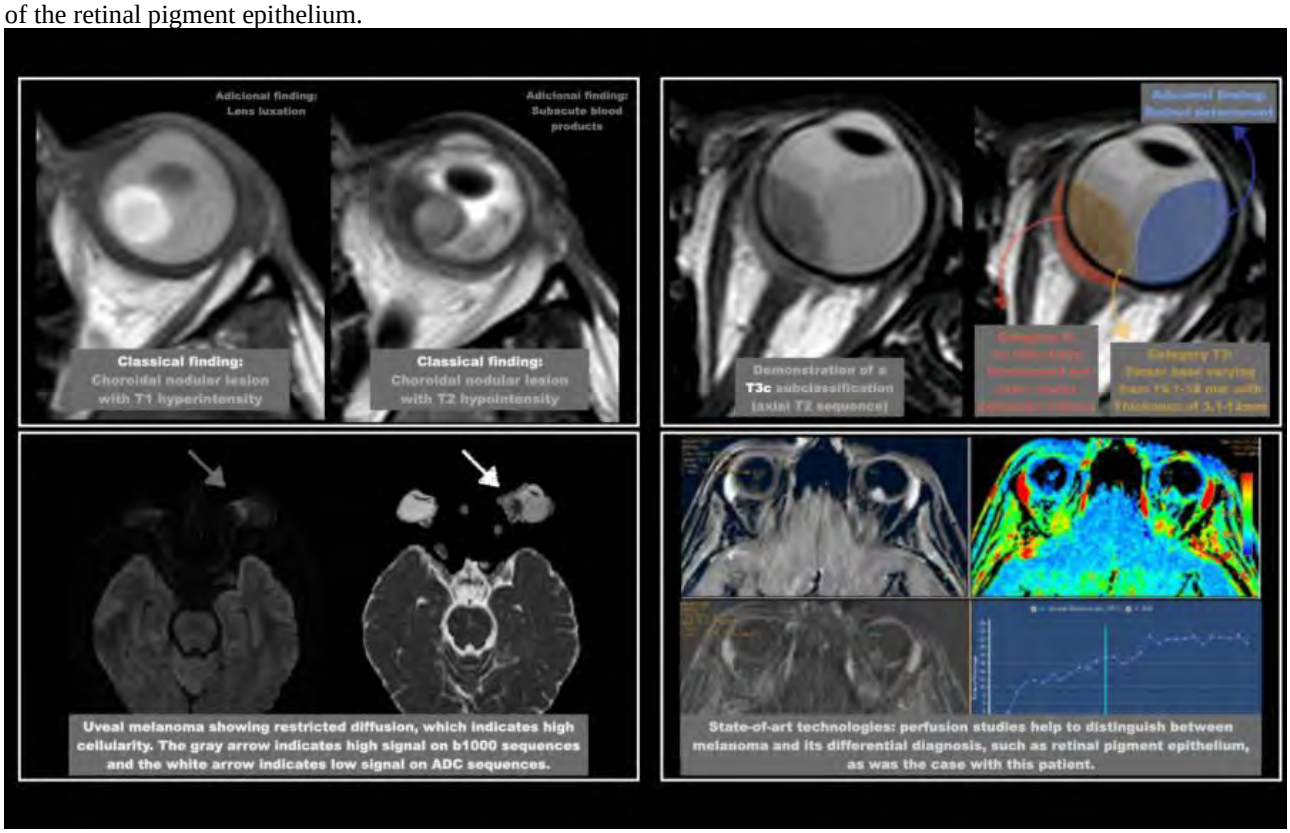

(Filename: TCT_846_ASNRmelanoma.jpg)

1317
An Overview of Imaging and Interpretation of Endolymphatic Hydrops.
N Shaheen[1], R Kuhnlein[1], J Chetta[2], H Rizk[3], M Spampinato[1]
[1]MUSC, Charleston, SC, [2]MUSC, Charleson, SC, [3]Medical University of South Carolina, Charleston, SC

Purpose
Review pathophysiology, imaging protocols and interpretation of endolymphatic hydrops.
Materials and Methods
Endolymphatic hydrops (EH), the pathological hallmark of Meniere's disease (MD), is characterized by increased hydraulic pressure in the endolymphatic system of the inner ear. EH can be further categorized into cochlear, vestibular or combined hydrops. Our goal is to review the use of delayed contrast-enhanced MRI for suspected MD.

Results
Our didactic exhibit will include: an overview of the pathophysiology of EH, a discussion of MRI protocols, a review of EH grading systems and imaging examples of EH from our institution as well as from the literature.
Conclusions
EH is characterized clinically by fluctuating hearing loss, episodic vertigo, tinnitus and aural fullness. To understand the pathophysiology, we must consider the perilymph and endolymph containing compartments separately. The cochlea contains three subcompartments: the perilymph-containing scala tympani, scala vestibuli and endolymph-containing scala media. The vestibule includes the endolymph-containing saccule and utricle which bath in the vestibular perilymph. As the endolymph hydraulic pressure increases, mass effect is placed on the surrounding perilymph-containing spaces. Two techniques have been developed to visualize these compartments relying on intratympanic (IT) and intravenous (IV) injection of gadolinium-based contrast agents (GBCA). IT injection provides better contrast but it is more invasive and requires imaging 24-hour post-injection. IV injection (used at our institution) is less invasive and requires only a 4-hour delay from injection to imaging. Delayed imaging allows for GBCA to admix with the perilymphatic space. 3D FLAIR is typically utilized to visualize delayed contrast-enhancement of the perilymphatic space. On delayed imaging of EH, the endolymph compartments (hypointense) enlarge to varying degrees obliterating the perilymph compartments (hyperintense). A commonly utilized grading system of EH was developed by Van Steekelenburg et al. (table 1). Delayed contrast-enhanced MRI has emerged as an imaging technique to evaluate and grade EH. Imaging detection of labyrinthine abnormalities can help support the diagnosis of MD; especially in complex and ambiguous cases. Further research is necessary to better understand the applications of this technique, including evaluation of treatment response.

	Grade	Imaging
Vestibular	1: Mild	Saccule equal in size or larger than utricle. Not confluent.
	2: Moderate	Saccule and utricle are confluent. Encompass >50% of the vestibule.
	3: Severe	Perilymphatic space in the vestibule is completely effaced.
Cochlear	1: Moderate	Scala media dilation partially obliterating scala vestibuli.
	2: Severe	Scala vestibuli is completely obliterated.

(Filename: TCT_1317_finalt1final.jpg)

1419

Anatomic and functional atlas of potential white matter degeneration and remote cortical atrophy due to infarcts in major vascular territories.

A Jeffries[1], A Wang[1], A Merkler[1], S Niogi[2]
[1]Weill Cornell Medicine, New York, NY, [2]New York Presbyterian Hospital - Weill Cornell, New York, NY

Purpose
The vast majority of stroke research and clinical focus is on management of the acute injury and the associated dominant functional deficit. However, animal modeling demonstrates additional behavioral deficits and cognitive decline may occur continuing through the chronic phases of injury. Utilizing quantitative diffusion imaging and tractography, we sought to create an atlas of white matter tracts and connected cortical areas susceptible to Wallerian degeneration and atrophy through simulated lesions in each vascular territory.
Materials and Methods
This anatomic atlas organized by vascular territory provides the framework for a functional atlas to aid clinicians and researchers to identify additional potential cognitive and behavioral deficits that may be amenable to rehabilitation and targets for future research.
Results
We utilized MR Imaging from a prototypical normal healthy adult chosen at random from the Human Connectome Project. Simulated infarctions were prescribed on a co-registered T2-weighted scan for each major vascular territory. Probabilistic tractography from the quantitative diffusion imaging was used to delineate the white matter pathways associated with the infract. T1-weighted, T2-weighted, and diffusion weighted imaging was utilized to properly identify the cortical areas connected to these white matter tracts. The anatomic accuracy of the tractograms and cortical areas were verified by a board-certified neuroradiologist. A literature review was performed to identify the potential functional and behavior deficits associated with these white and gray matter structures. A whole brain connectome was computed to better understand the impact to the structural connectivity for each simulated lesion. Twenty subjects with chronic infarcts and longitudinal imaging from the Alzheimer's Disease Neuroimaging Initiative database was used to demonstrate atrophy due to the infarction superimposed upon changes stemming from aging or dementia.
Conclusions
The resulting tractograms demonstrate numerous association pathways and short cortical U-fibers potentially disrupted. We provide a functional atlas to the processing deficits that can occur in each vascular territory. We further demonstrate differences in global

connectivity changes from infractions in each of the vascular zones. We hope that this atlas of potential injury will serve as an educational tool and aid clinicians to better understand, identify, and treat overlooked, but impact functional deficits subsequent to stroke.

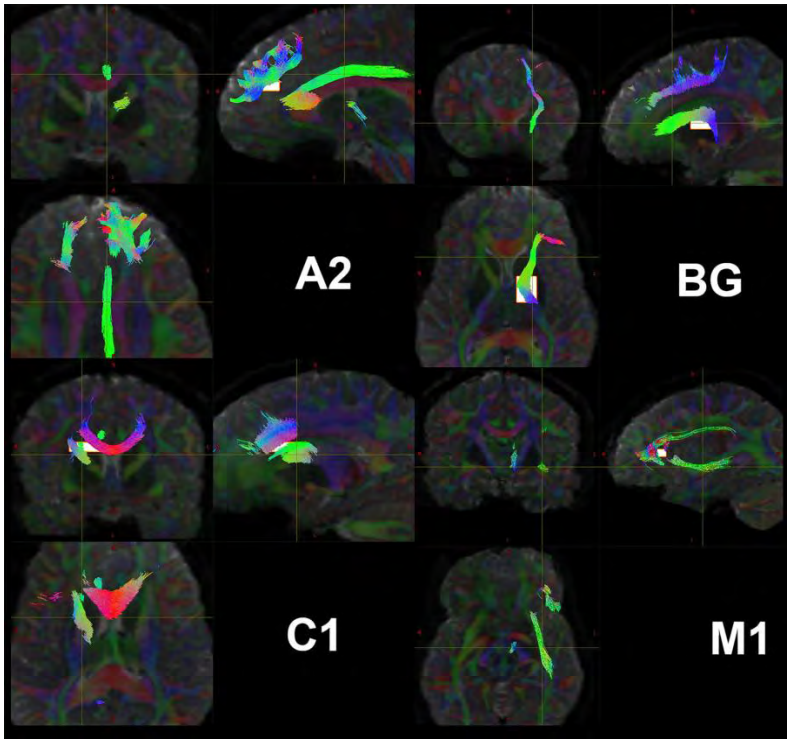

(Filename: TCT_1419_ASNR-fig1.jpg)

560

Anatomic and Pathologic Appearances of the Cranial Nerves on MRI: What to Look for and How to Look for it

D Shlensky[1], F Syed[1]
[1]*University of Michigan, Ann Arbor, MI*

Purpose

By the end of the exhibit, the viewer should be able to: 1. Understand the location and normal appearance of the cranial nerves and their branches on MRI. 2. Correlate MRI findings and anatomic cranial nerve conduits with CT findings of the skull base. 3. Diagnose example pathology associated with cranial nerves including aplasia/hypoplasia, perineural spread of malignancy, primary neoplasm, structural compression, and inflammatory processes. 4. Identify sequelae of cranial nerve pathology including "end organ" atrophy, and common clinical symptoms.

Materials and Methods

Cranial nerve (CN) and skull base evaluation on MRI can be challenging for Radiologists at all levels of training, in particular residents, and can be a blind spot for pathology. Typically, CN pathology presents with symptoms related to their unique function, such as facial weakness, reduced sensation, loss of special sensory input (i.e., smell), or pain, which can guide a Radiologist's search pattern. There are times, however, when CN disease is clinically occult. In these instances, radiological detection becomes even more important as missed pathology can result in suboptimal or incorrect treatment. For example, underdiagnosis of perineural spread of malignancy can result in too narrow of radiation fields, or too focal of surgical resection, leaving residual untreated cancer to propagate. A wide array of etiologies can underly CN pathology, some with subtle imaging features, and others which are more conspicuous. Example pathologies include primary neoplasm (schwannoma), secondary neoplasm (perineural spread of cancer), inflammation (pseudotumor, Bell's palsy), congenital (aplasia/hypoplasia), and structural (vascular compression). This presentation will demonstrate example pathology in a standardized framework with CT/MRI correlation to aid evaluation of cranial nerves, their skull base conduits, and their "end organs" to increase sensitivity for what can be subtle pathology. The end goal of which is to ensure diagnostic accuracy and help guide optimal clinical management.

Results

Example MRI and CT examinations with normal and abnormal cranial nerve and skull base structures will be systematically explored.

Conclusions

Using a standardized search pattern to evaluate the course and "end organs" of the cranial nerves can increase sensitivity for subtle pathology and facilitate more complete reporting of disease extent. Using knowledge of CT anatomy and specific symptoms of CN pathology can also aid in CN evaluation on MRI.

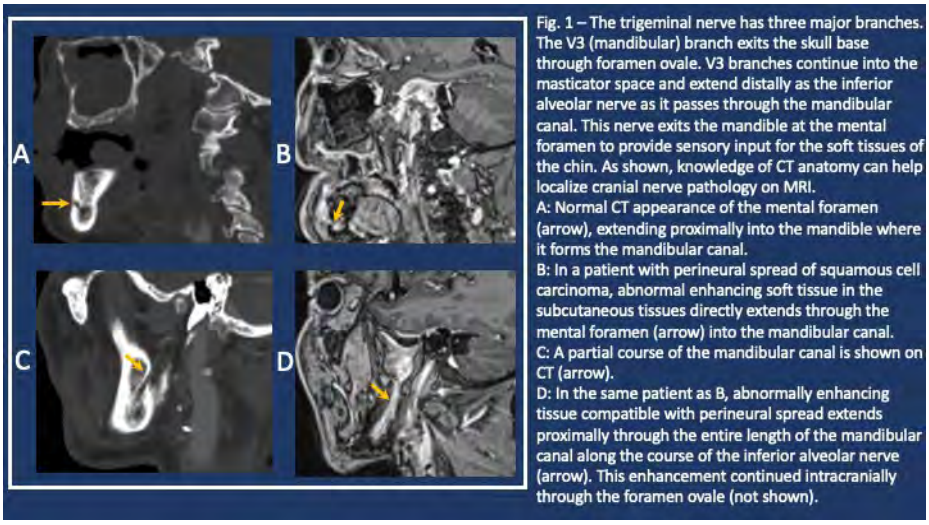

Fig. 1 – The trigeminal nerve has three major branches. The V3 (mandibular) branch exits the skull base through foramen ovale. V3 branches continue into the masticator space and extend distally as the inferior alveolar nerve as it passes through the mandibular canal. This nerve exits the mandible at the mental foramen to provide sensory input for the soft tissues of the chin. As shown, knowledge of CT anatomy can help localize cranial nerve pathology on MRI.
A: Normal CT appearance of the mental foramen (arrow), extending proximally into the mandible where it forms the mandibular canal.
B: In a patient with perineural spread of squamous cell carcinoma, abnormal enhancing soft tissue in the subcutaneous tissues directly extends through the mental foramen (arrow) into the mandibular canal.
C: A partial course of the mandibular canal is shown on CT (arrow).
D: In the same patient as B, abnormally enhancing tissue compatible with perineural spread extends proximally through the entire length of the mandibular canal along the course of the inferior alveolar nerve (arrow). This enhancement continued intracranially through the foramen ovale (not shown).

(Filename: TCT_560_Cranialnervepresentationfinal.jpg)

488

Anatomy and Pathology of the Larynx and the Hypopharynx: Do you Know What a Resident Needs to Know?

K Oh[1], A Aiken[1], K BAUGNON[1], X Wu[1]
[1]*Emory University, Atlanta, GA*

Purpose

Due to the complex regional anatomy, pathologies of the larynx and hypopharynx may seem especially daunting to radiology trainees. Moreover, both acute and indolent pathologies of the larynx and hypopharynx pose relatively poor prognoses if missed. Traumatic injuries and infections within this region can lead to immediate, life-threatening risks to airways. More occult tumors can lead to permanent damage to structures necessary for important functions such as speech or swallowing. A solid understanding of normal anatomy is crucial for identifying the subtle changes seen in the early stages of pathologies. Also important is understanding the normal boundaries and divisions of the larynx and hypopharynx, as management of many pathologies is dictated by the extent of disease. The goal of this educational exhibit is to review the anatomy of the larynx and hypopharynx as well as their relationship to other subsites of the head and neck. In addition, this exhibit will discuss the clinical presentation and imaging findings of basic pathologies affecting the larynx and hypopharynx, ranging from traumatic injuries to infectious and inflammatory pathologies and to neoplasms. To do so, the exhibit heavily utilizes labeled diagrams with a focus on how diseases affect or cross the boundaries and spaces between various structures in the neck. Following this educational exhibit, viewers can expect to identify normal anatomy of the larynx and hypopharynx on imaging as well as identify the changes seen in basic pathologies. Goals/Objectives - To review the anatomy of the larynx and hypopharynx as well as their relationship to other subsites of the head and neck - To discuss clinical presentations and imaging findings of common pathologies affecting the larynx and hypopharynx 1. Anatomy 1.1 Relationship of larynx and hypopharynx to the remainder of the neck 1.2 Larynx anatomy and laryngeal subdivisions - Supraglottic: pre-epiglottic space, paraglottic space - Glottic - Subglottic 1.3 Hypopharynx anatomy - Boundaries - Subdivisions - Pyriform sinus - Postcricoid region - Posterior pharyngeal wall 2. Pathology 2.1 Imaging modalities 2.2 Developmental and congenital pathologies - Thyroglossal duct cyst - Branchial cleft cysts - Laryngocele 2.3 Trauma 2.4 Vocal cord paralysis and dysfunction 2.5 Infection 2.6 Vascular 2.7 Neoplasms - Laryngeal SCCa - Hypopharyngeal SCCa - Laryngeal chondrosarcoma - Lymphoma

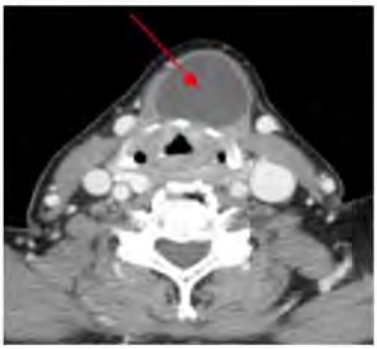

Fig. A: 85 year old female with cystic lesion in the infrahyoid strap muscles, anterior to the thyroid cartilage (arrow), compatible with thyroglossal duct cyst.

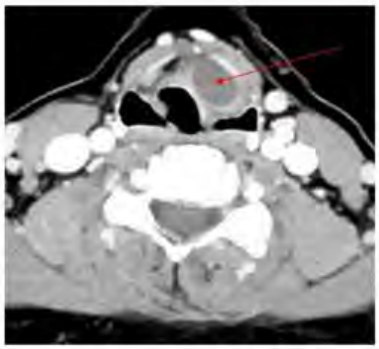

Fig. B: 67 year old female with fluid-filled, cystic lesion posterior to the thyroid cartilage within the paraglottic space (arrow), compatible with a laryngocele.

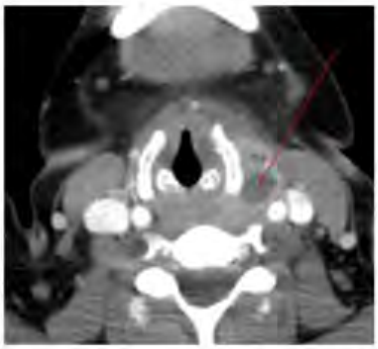

Fig. C: 34 year old female with cystic lesion in the left infrahyoid strap muscles lateral to the thyroid cartilage (arrow), compatible with a fourth branchial cleft cyst.

(Filename: TCT_488_exampleimageKO.jpg)

481

Anomalous Origins of the Vertebral Arteries; Pearls and Pitfalls

S Hasan[1]

[1]*McGaw Medical Center of Northwestern University, Chicago, IL*

Purpose

- Understand the embryological development of the vertebral arteries - Describe the different variants of the vertebral arteries - Understand the clinical implications caused by the different variants

Materials and Methods

Overall, anomalous origin of the vertebral artery is up to 7.41%, more common on the left compared to the right, and usually an incidental finding. However, variations in anatomy can predispose to vascular injuries either during surgical or angiographic procedures. Therefore, a better understanding and description of the anomalous origins of the vertebral arteries is needed for preoperative planning to avoid inadvertent vascular injury and in the diagnosis and management of acute strokes.

Results

Multi-detector computed tomography (MDCT) allows for evaluation of vertebral artery anatomy and normal variants.

Conclusions

- Patterns of regression in the embryological development of the aortic arch and brachiocephalic vessels have been proposed as the etiology of vertebral artery origin anomalies - Variant anatomy can predispose to symptomatology in tracheo-esophageal obstruction, vascular injuries during spinal fusion approaches, nerve blocks or during minimally invasive surgical and angiographic procedures - Anomalous origins may be associated with variances in origin or level of entry into the vertebral canal, duplication, as well as vessel tortuosity, vascular loops, and fenestration

Figure 1. A) CTA arch axial projection showing the dual origin of the right vertebral artery and aberrant origin of the left vertebral artery off the aortic arch. B) 3-D reconstruction demonstrating dual origin of right vertebral artery.

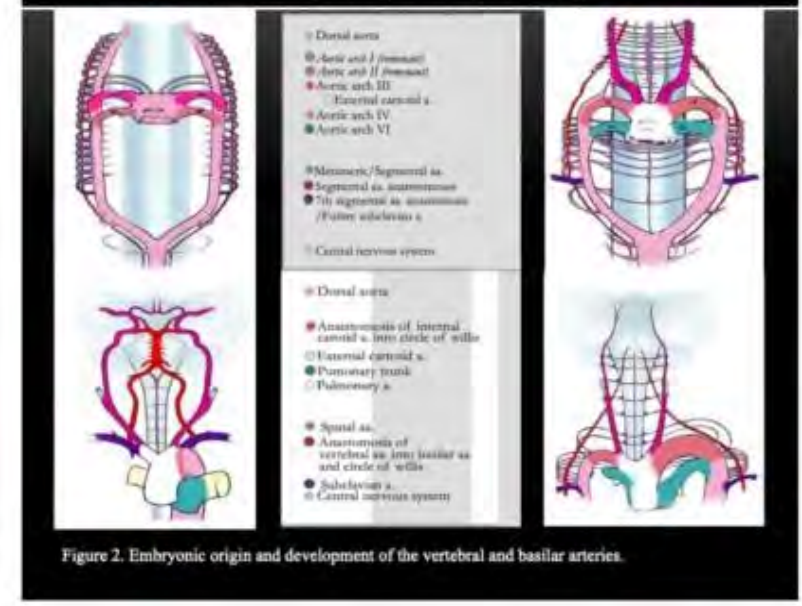

Figure 2. Embryonic origin and development of the vertebral and basilar arteries.

(Filename: TCT_481_Vertpics.jpg)

894

Another Brick in the Wall: Vessel Wall Imaging for Intracranial Aneurysms

A Peret[1], A Spahic[1], A Kuner[1], J Manunga[2], W Chang[3], J Junn[4], K Johnson[1], L Eisenmenger[1]

[1]University of Wisconsin-Madison, Madison, WI, [2]Minneapolis Heart Institute, Minneapolis, MN, [3]Allegheny Health Network, Pittsburgh, PA, [4]Mount Sinai Hospital Icahn School of Medicine, New York City, NY

Purpose

Review the most recent evidence on the value of vessel wall imaging in the assessment of intracranial aneurysms. Study aneurysmal wall enhancement as an imaging biomarker of aneurysmal instability, growth, and rupture. Outline the main limitations and challenges in magnetic resonance vessel wall imaging for intracranial aneurysms.

Materials and Methods

Unruptured intracranial aneurysms (UIA) are present in approximately 3-5% of the population. Most are asymptomatic and a large proportion will never rupture, with an estimated incidence of aneurysmal rupture of 0.4-10% per year. However, considering the high morbidity/mortality associated with aneurysmal rupture, preventive treatment or vigilant follow-up are recommended. Currently, decision making is guided by score systems based on aneurysmal size and morphology. These scores provide a limited guide and do not always correlate with histopathology. On the other hand, vessel wall imaging (VWI) has the potential to provide imaging biomarkers closer to the pathophysiology, showing encouraging results in predicting aneurysm instability and in risk stratifying patients with UIAs. Our primary aim is to explore the current evidence on the value of VWI to characterize UIAs, predict growth and risk of rupture, and potentially guide treatment decisions.

Results

This exhibit will be a literature-based discussion on the role of VWI in predicting UIA instability and in guiding clinical management of UIAs. It will also address the current limitations and challenges of VWI for UIAs.

Conclusions

The study of UIA using VWI consists primarily of the assessment of the aneurysmal wall enhancement (AWE) observed after intravenous gadolinium on high-resolution black blood T1-weighted MRI images. Despite a growing interest in VWI for UIA, the current literature consists of small retrospective studies, with only 2 meta-analyses. AWE is shown to be a strong predictor of aneurysm instability (OR = 20) and rupture (OR = 35), whereas the absence of enhancement indicates aneurysmal stability. The degree of AWE can be graded with regards to intensity, extent, and localization, offering differing profiles of instability. In conclusion, AWE is a promising biomarker of intracranial aneurysm instability, showing strong association with the risk of rupture or growth. Further prospective studies are needed to validate this biomarker for prospective risk stratification of patients with UIA and help guide clinicians in optimal decision making.

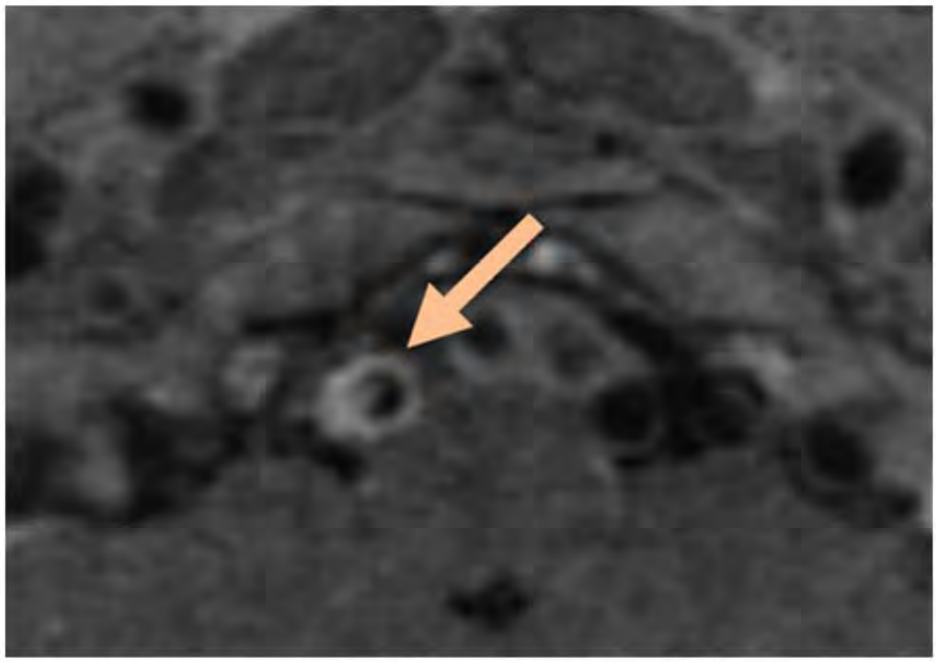

Figure 1 - Aneurysmal wall enhancement in a ruptured aneurysm. In this patient, post-contrast T1-weighted imaging shows wall enhancement (arrow) of a posterior inferior cerebellar artery (PICA) saccular aneurysm, in the context of a subarachnoid hemorrhage (SAH) diagnosed at computed tomography (not included). The PICA aneurysm enhancement is suggestive of instability and indicates that this aneurysm is likely responsible for the SAH in this patient.

(Filename: TCT_894_aneurysm_figure.jpg)

156

Applications of Cinematic Rendering to Cerebral MR Imaging

K Tsuchiya[1], S Hiraoka[1], H Tateishi[1], M Gomyo[2]

[1]JR Tokyo General Hospital, Shibuya-ku, Tokyo, Japan, [2]Kyorin University, Mitaka, Tokyo, Japan

Purpose

Cinematic rendering (CR) is a novel 3D reconstruction technique that can produce photorealistic 3D images from conventional CT and MRI data. In this exhibit, we present our experience of applying CR to cerebral MR imaging to visualize normal and pathological brain surface morphology and discuss its clinical value.

Materials and Methods

Teaching points of this educational presentation are the following: 1) to present basic concepts and technical aspects of CR in the field of clinical radiology; 2) to show how to generate brain surface MR images by CR; and 3) to show how they work in the diagnosis of cerebral lesions.

Results

Since the end of 2019, we have applied CR to cerebral MR imaging in more than 40 cases, which constitute the basis of this presentation. They were postprocessed on syngo.via system (Version VB50, Siemens Healthcare GmbH, Erlangen, Germany).

Conclusions

We could generate cerebral CR images in all these cases and, based on the experience, we present cases with discussion of clinical implications placing emphasis on demonstration of superficial tumors, developmental malformations, and degenerative diseases in conjunction with discussion including current limitations as well as future directions. We conclude that, as CR constantly creates realistic brain surface images, it provides images compelling to physicians, patients, and their family. It can also be valuable as preoperative guidance for neurosurgeons.

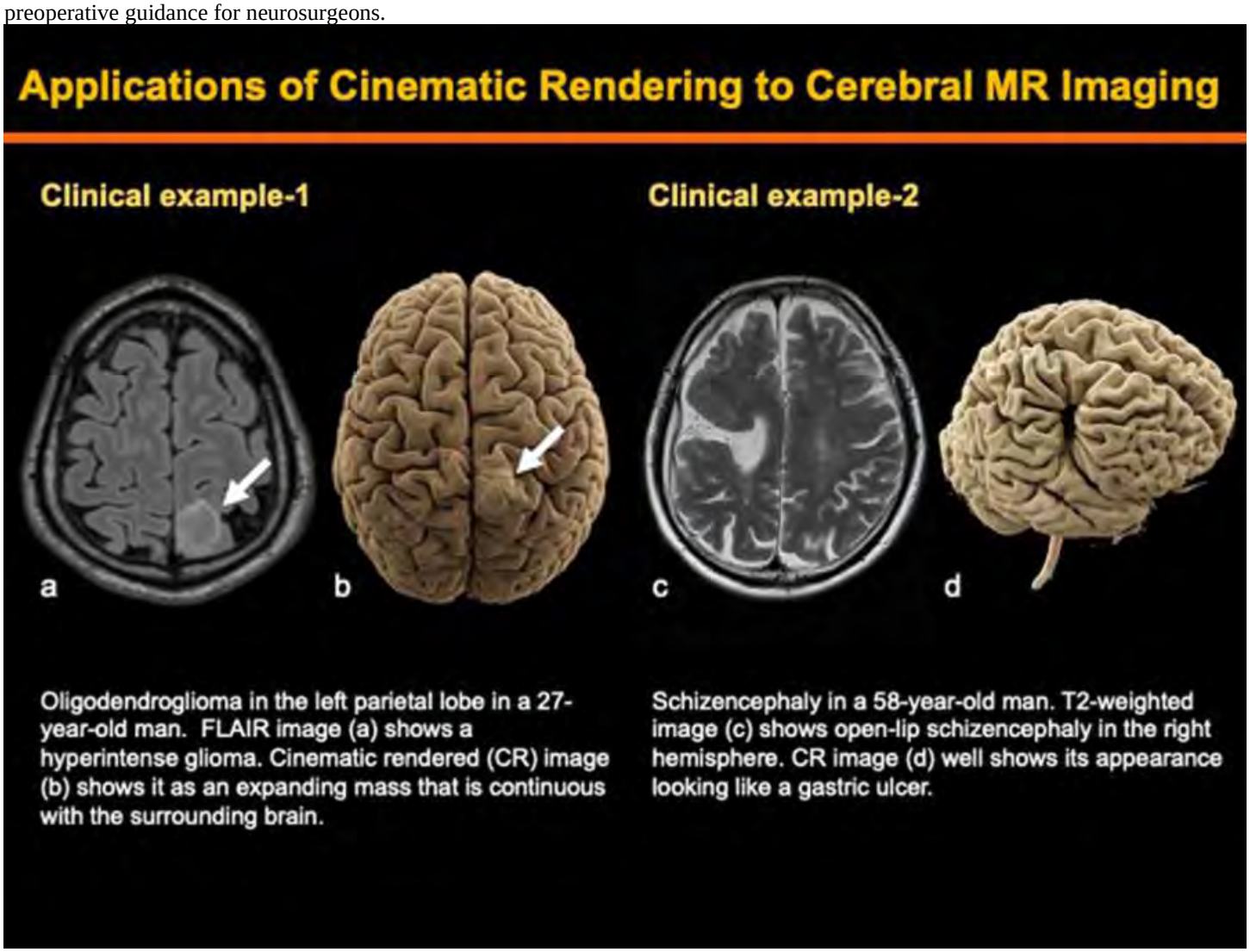

(Filename: TCT_156_2022_ASNR_SNR_EE_CVRT.jpg)

959

APT (amide proton transfer) - CEST (chemical exchange saturation transfer) imaging differentiates between growing and non-growing intracranial meningiomas

H Koike[1], M Morikawa[2], R Ideguchi[3], H Ishimaru[4], M Uetani[4]

[1]Nagasaki University Hospital, Nagasaki, Japan, [2]Nagasaki University Hospital, Nagasaki, Nagasaki, [3]Atomic Bomb Disease Institute, Nagasaki University, Nagasaki, outside US, [4]Nagasaki University Hospital, Nagasaki, outside US

Purpose

• Meningioma is the most frequently diagnosed primary brain tumor in adults. • Quantitative parameters using APT-CEST imaging can detect patients with growing intracranial meningiomas. • The MTR using APT-CEST imaging reflects proliferative ability in intracranial meningiomas and is useful to make a clearer distinction between growing and non-growing meningiomas.

Materials and Methods

Magnetization transfer ratio (MTR) values with amide proton transfer (APT) -chemical exchange saturation transfer (CEST) MRI are thought to reflect tumor proliferation. Meningioma is usually incidental; however, some growing meningiomas eventually require treatment. Therefore, the purpose of this study was to differentiate between growing and non-growing intracranial meningiomas using MTR values.

Results

We retrospectively evaluated 17 patients with suspected intracranial meningiomas who underwent APT-CEST MRI from November 2020 to April 2021. We evaluated MTR values on APT-CEST imaging as well as conventional MRI features. We compared these parameters in growing meningiomas vs non-growing meningiomas and compared the findings with previous MRIs. We also performed a ROC curve analysis to determine the diagnostic cutoffs for MTR.

Conclusions

Patients constituted 10 patients with growing meningiomas (2 male [20%], 8 female [80%]; mean age [standard deviation (SD)]: 59.9 years [16.0]) and 7 patients with non-growing meningiomas (7 female [100%]; mean age [SD]: 63.9 years [18.6]). We found significant differences in MTR values (0.0198 ± 0.0003 vs 0.0131 ± 0.0002; $p < 0.0001$) between the growing meningiomas and non-growing meningiomas groups, respectively. The ROC curve analysis showed that MTR values clearly differentiated between growing and non-growing meningiomas. At an AUC threshold of 0.0151, diagnostic sensitivity, specificity, positive predictive value, and negative predictive values for MTR were 100%, 85.7%, 90.9%, and 100%, respectively. Patients with growing meningiomas were well-discriminated from patients with non-growing meningiomas, using the MTR values on post-growth tumor APT- CEST imaging.

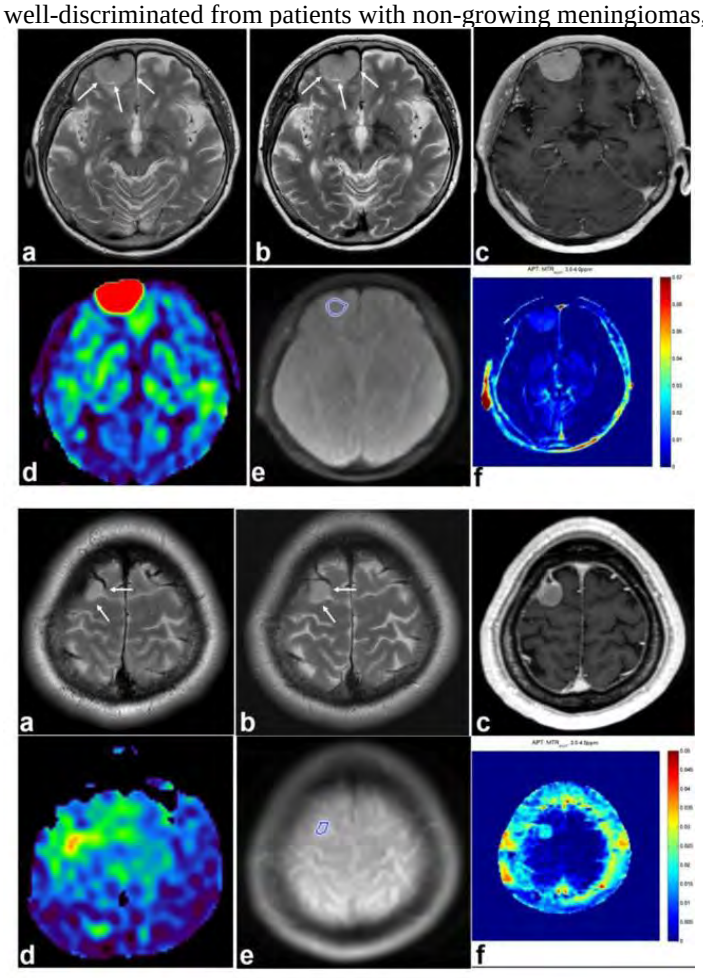

(Filename: TCT_959_Figure.jpg)

918

Arterial spin-labeled perfusion MRI of the brain: An Educational Guide to Implementation across Vendors and Field Strengths

A Verde[1], J Andre[2], S Dehkharghani[3], G Zaharchuk[1], T Massoud[4]

[1]Stanford University, Stanford, CA, [2]University of Washington, Seattle, WA, [3]NYU Langone Health, New York, NY, [4]Stanford University School of Medicine, Stanford, CA

Purpose

NA

Materials and Methods

Arterial spin labeling (ASL) is a noninvasive perfusion MRI technique for obtaining qualitative and quantitative parametric images of cerebral perfusion. It provides useful diagnostic information in many clinical neuroimaging applications, e.g., differentiating recurrent tumor from radiation necrosis, arteriovenous shunting, hypervascular tumors, epilepsy, and dementia. Avoiding IV contrast is also useful in patients with low renal function. Despite consensus recommendations available since 2014, and a clear need for greater dissemination of ASL imaging, there remain many logistical challenges to widespread clinical implementation. We provide a pictorial and educational best-practices guide on how to implement ASL clinically across the three main MRI vendors, sequence details relevant to different field strengths, and practical troubleshooting strategies for optimizing ASL image acquisition.

Results

We comprehensively review and present our own experiences, vendor-specific sequences, and literature consensus regarding clinical implementation of ASL imaging.

Conclusions

Each major MRI vendor offers clinical implementation of ASL at 1.5T or 3T. GE uses pseudocontinuous ASL (PCASL) with a 3D fast spin echo readout of stack-of-spirals acquisitions and background suppression. Siemens offers 2D pulsed ASL (PASL) with echo planar imaging (EPI) readout and motion correction, 3D PASL with background suppression and gradient and spin echo (GRASE) readout, and some newer scanners support 3D PCASL. Philips offers PASL with 2D EPI readout, and PCASL with 2D EPI or 3D GRASE readout. Hospital-specific challenges include which imaging settings can be altered for acquisition and postprocessing, institutional rules, and lack of funding to purchase the ASL options. We also provide a pictorial review of troubleshooting strategies to counter ASL artifacts and protocoling mistakes, including motion, field inhomogeneity, susceptibility, labeling failure, arterial transit artifacts, and performing scans after MRI contrast is given. When introducing ASL imaging in new clinical settings, it is important but challenging to ensure consistent image quality and implementation across MRI vendors and field strengths to deliver high-quality patient care. This presentation will outline useful strategies for best-practice implementation and optimization to enable the more widespread use of clinical ASL.

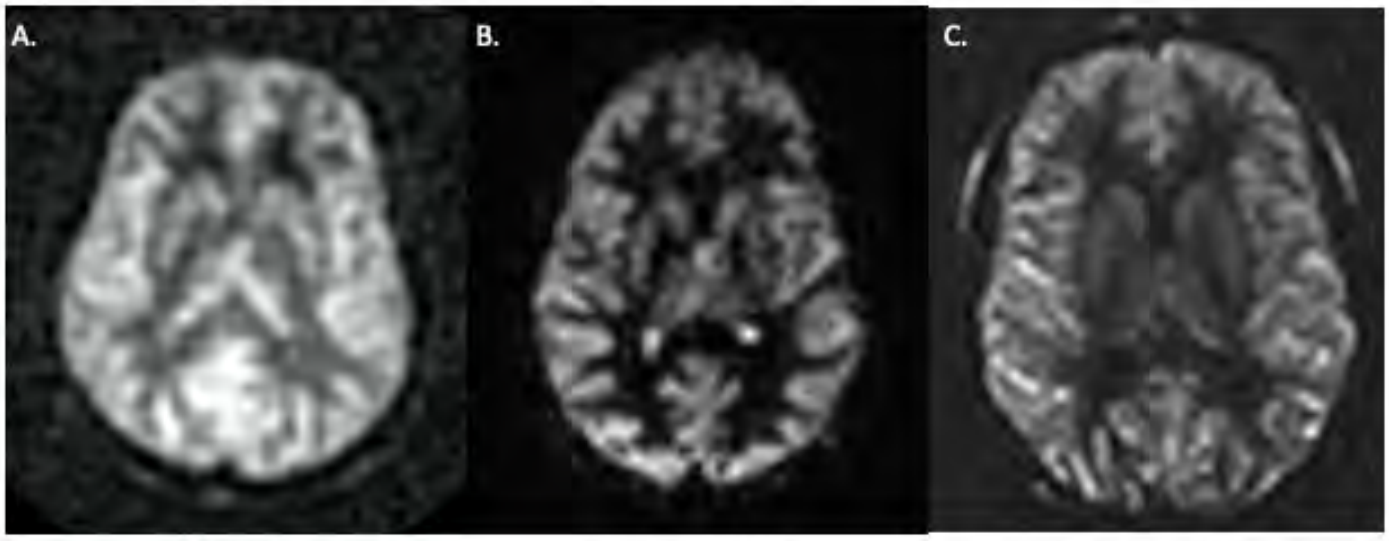

Figure 1. PCASL across vendors. A. GE PCASL, 3D FSE stack of spirals readout, background suppression, Discovery MR750 3T, PLD=2025 ms. **B**. Philips PCASL, 2D EPI readout, Ingenia 3T, LD=1800 ms, PLD=2000 ms. **C.** Siemens PASL, with 3D GRASE readout, Magnetom Prisma 3T, PLD=1990 ms.

(Filename: TCT_918_ASLFigure1_v3.jpg)

994

Assessment of the CNS manifestations of neurofibromatosis Type 2 (NF2): imaging and histological features and treatment effect assessment with emphasis on advanced imaging

Y Ota[1], A Capizzano[1], E Liao[1], A Baba[1], R Kurokawa[1], M Kurokawa[1], A Srinivasan[1]
[1]University of Michigan, Ann Arbor, MI

Purpose

Neurofibromatosis type 2 (NF2) is a tumor predisposition syndrome characterized by the development of distinctive nervous system lesions. NF2 is commonly associated with bilateral vestibular schwannomas, meningiomas, ependymomas, and other tumors. This exhibition reviews imaging and pathological characteristics and treatment effect assessment with emphasis on DWI, DSC-MRI, and DCE-MRI.

Materials and Methods

- Present imaging and pathological findings of each tumor - Present treatment effect assessment of schwannoma using DWI and DCE-MRI - Present future assessment of NF2 related schwannomas using DCE-MRI

Results

Imaging and pathological findings - Schwannomas - Meningioma - Ependymoma - Glioma Treatment effect assessment by DWI and DCE-MRI -Schwannomas Diagnostic assessment of NF2 related schwannomas using DWI and DCE-MRI

Conclusions

- NF2 is associated with different tumors such as schwannomas, meningiomas, ependymoma, and other tumors, and NF2 related schwannomas can show different findings compared to sporadic schwannoma on DWI and DCE-MRI. - DWI and DCE-MRI can help to assess treatment effect of anti-VEGF agents and distinguish NF2 related schwannomas from sporadic schwannomas.

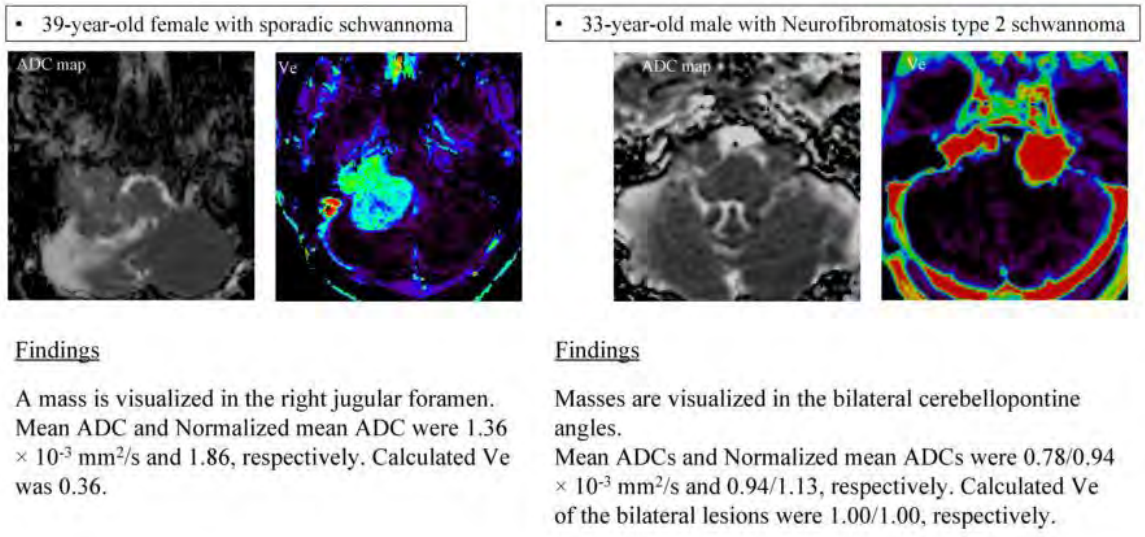

(Filename: TCT_994_NF2educational2.jpg)

210

Atypical Cerebellopontine Angle Masses

S Genet[1], S Kelly[2], D Zander[1], M Keiper[2], J Cramer[2]
[1]University of Colorado, Aurora, CO, [2]University of Nebraska Medical Center, Omaha, NE

Purpose

We present a series of cerebellopontine angle (CPA) lesions that pose a diagnostic challenge given their atypical imaging features and uncommon prevalence. The unique imaging characteristics and diagnostic considerations of these cases will be discussed with the goal of advancing our audience's understanding and diagnostic accuracy relating to uncommon pathologies in this region.

Materials and Methods

The purpose of this exhibit is to improve diagnostic accuracy of our audience about uncommon CPA masses through a case series-based educational comparative analysis and discussion.

Results

A series of atypical CPA cases will be presented, highlighting the unique imaging findings, differential diagnostic considerations, and key clinical historical information attributable to each case. Atypical cases will include WNT medulloblastoma, white epidermoid, glomus jugulare tumor, lipoma, choroid plexus papilloma, hemangioblastoma, cholesterol granuloma, lymphoma, ependymoma, endolymphatic sac tumor, and metastatic disease of the CPA. Comparison to characteristics of more common CPA lesions will be made and a systematic diagnostic categorical scheme will be provided.

Conclusions

Given the frequency of CPA masses, it is important to raise awareness of unique imaging findings seen with less often encountered

pathologies in this region. The CPA and surrounding regions are anatomically complex; thus, a broad range of pathologies may be encountered. Attention to unusual imaging findings and pertinent clinical history are key to appropriately narrowing differential diagnostic considerations. Neuroradiologists' familiarity with unusual CPA lesions can provide clinicians with valuable information which can alter treatment approaches specific to a unique pathology in this region, thereby improving patient outcomes.

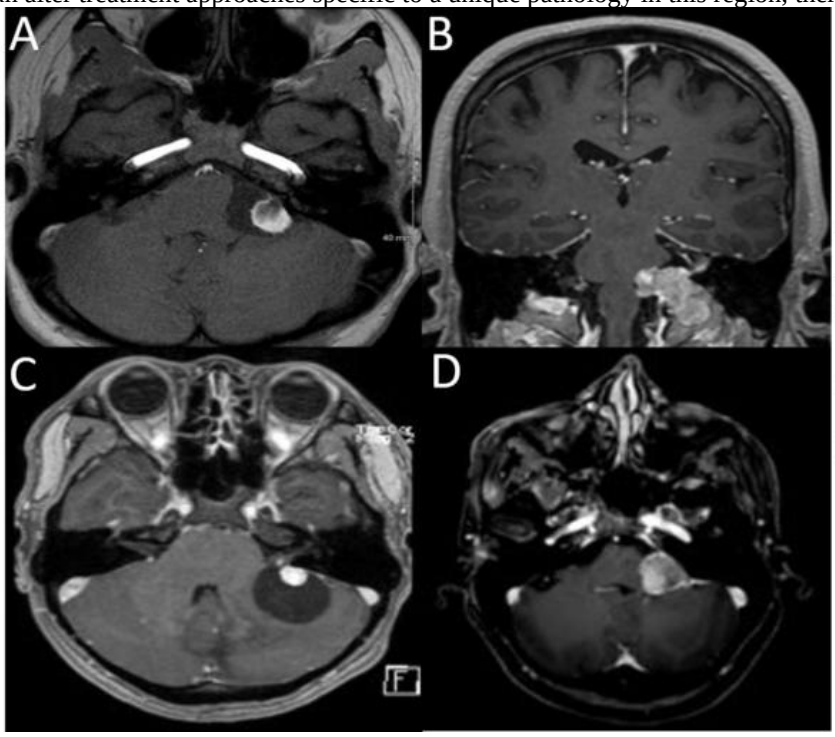

A. White Epidermoid

B. Glomus Jugulare Paraganglioma

C. Hemangioblastoma

D. Wingless Medulloblastoma

(Filename: TCT_210_ASNRabstractcases.jpg)

248

Autoimmune CNS Disease

C Norris[1], K Salzman[1]
[1]University of Utah, Salt Lake City, UT

Purpose

We aim to provide an image rich, HIPAA compliant review on the imaging manifestations of the major autoimmune disorders with neurologic findings. Pursuant to this, we will provide a brief overview and neuroimaging examples of the following disorders: Behcet's disease, Neurosarcoidosis, Granulomatosis with polyangiitis, Giant cell arteritis, Systemic Lupus Erythematosus, Sjögren's syndrome, IgG4 related inflammation, Chronic Lymphocytic Inflammation with Pontine Perivascular Enhancement Responsive to Steroids syndrome (CLIPPERS), Anti-GFAP IgG meningoencephalomyelitis, Anti-GQ1b IgG antibody syndromes including Miller-Fisher Syndrome, Bickerstaff encephalitis, and Guillain-Barré, autoimmune/postinfectious demyelinating disorders including Multiple Sclerosis, Acute Disseminated Encephalomyelitis (ADEM), and Neuromyelitis Optica Spectrum Disorder, drug induced/iatrogenic autoimmune disorders and paraneoplastic disorders.

Materials and Methods

In the past few decades, autoimmune disorders have become increasingly recognized as major causes of morbidity and disability. Due to the often non-specific, variable and/or incomplete modes of presentation, autoimmune neurologic disorders can be a source of consternation for providers. In addition to lumbar puncture with CSF analysis, imaging is a mainstay for the detection, surveillance, and diagnosis of many autoimmune neurologic disorders. While many autoimmune pathologies are uncommon, and many of the common autoimmune disorders are referred to tertiary subspecialty care hospitals, it is important for the general radiologist to be familiar with the common imaging appearances of these disorders, thus, prompt medical management may be initiated.

Results

N/A

Conclusions

N/A

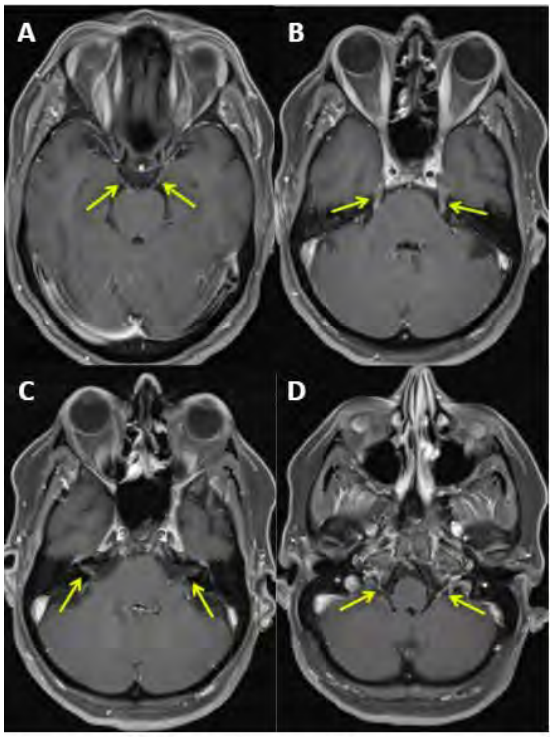

Figure 1. Acute Inflammatory Demyelinating Polyneuropathy (AIDP). Serial axial T1 postcontrast imaging through the brainstem demonstrates smooth enhancement of the A) oculomotor, B) trigeminal, C) vestibulocochlear and D) glossopharyngeal cranial nerves in a patient with Miller-Fisher variant AIDP.

(Filename: TCT_248_Capture.JPG)

107

Autoimmune Diseases of the Brain, Imaging and Clinical Review

G Shadmani[1], T Simkins[2], Z Jenner[1], R Assadsangabi[1], M Apperson[2], L Hacein-Bey[1], O Raslan[1], V Ivanovic[1]
[1]UC Davis, Medical Center, Radiology, Sacramento, CA, [2]UC Davis Medical center, Neurology, Sacramento, CA

Purpose

There is an extensive spectrum of autoimmune entities that can involve the central nervous system (CNS), which has expanded with the emergence of new imaging techniques and several clinicopathologic entities. Clinical presentation is usually nonspecific, and imaging has a critical role in the workup of these diseases. Immune-mediated diseases of the brain are not common in daily practice for radiologists and except for few of them (such as multiple sclerosis), radiologists are often faced with a difficult task of differentiating various entities based on the imaging findings. An understanding of unique imaging features of these disorders, along with clinical evaluation, may enable clinicians to decrease the need for tissue biopsy. In this presentation, we will provide imaging and clinical review and diagnostic approach in evaluating autoimmune diseases of the brain.

Materials and Methods

Our aim is to provide a practical diagnostic approach based on the unique and common radiological findings of the immune-mediated diseases involving the brain. We created four categories of the autoimmune diseases that might aid in the imaging approach and help narrow down differential diagnosis. These include: 1. Demyelinating diseases (Multiple Sclerosis, Acute Hemorrhagic Leukoencephalopathy, Neuromyelitis Optica Spectrum Disorders & Anti MOG associated Disease, Susac disease (not true demyelination); 2. Predominantly parenchymal non – demyelinating diseases (Autoimmune Encephalitis, Hemophagocytic Lymphohistiocytosis, Rasmussen's Encephalitis, Pituitary Hypophysitis, Hashimoto Meningoencephalitis, Systemic Lupus Erythematosus); 3. Predominantly meningeal-based Diseases (Sarcoidosis, Rheumatoid Arthritis, IgG4 related disease, Granulomatosis with Polyangiitis); 4. Brainstem and posterior fossa (CLIPPERS, Bickerstaff's Encephalitis, Paraneoplastic cerebellar degeneration, and Behçet disease), Each entities' unique imaging and clinical features will be discussed.

Results

All examples in our case collection had pathologically or clinically proven diagnoses and were selected from the Electronic Medical Record at the UC Davis Medical Center.

Conclusions

We hope our imaging review and suggested diagnostic approach will help radiologists expand their basic understanding of the discussed disease entities and narrow the differential diagnosis in specific clinical scenarios.

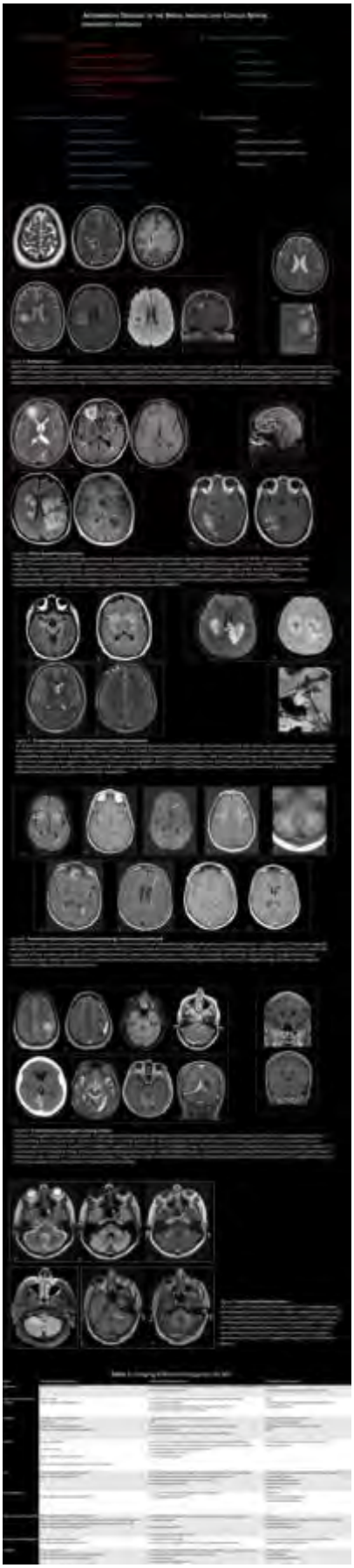

(Filename: TCT_107_Merged_document1.jpg)

1104

Back in the Saddle Again! Pituitary Adenomas and Beyond Neuroimaging Review

G Carpenter[1], S Aktan[2], J Kus[2], S Ramasamy[2], B Ploussard[2], A Germanwala[3], A Mallik[4]

[1]Loyola University Medical Center, Chicago, IL, [2]Loyola University Medical Center, Maywood, IL, [3]Loyola University Chicago Stritch School of Medicine, Maywood, IL, [4]Loyola University Medical Center, Oak Park, IL

Purpose

This image rich educational exhibit will review critical imaging points of MRI diagnosis of pituitary adenomas (PA) and assessment for surgical planning. Both trainees and practicing radiologists will benefit from embedded series, animations, and 3-D segmentation overlays. This exhibit will first review normal sellar and parasellar anatomy, followed by the breadth of PA imaging features. Approaches and pitfalls for PA microadenoma diagnosis will be presented. Learners will then compare MR assessment of cavernous sinus invasion including percent ICA encasement, modified Knosp criteria, and AI predictive models. Intraoperatively proven examples of each Knosp grade will also be provided. Additional directions of invasion to the suprasellar region, with displacement of the optic chiasm and pituitary infundibulum, skull base, and posterior fossa will be reviewed. The exhibit will conclude with case examples of pituitary adenoma mimics, including lymphocytic hypophysitis, variant craniopharyngiomas, and meningiomas, with discussion of strategies to distinguish these crucial imaging differentials.

Materials and Methods

Pituitary adenomas (PA) are common brain tumors and the most common sellar tumor in adults. These neuroendocrine tumors are generally slow growing, becoming clinically relevant if they secrete hormones or if they grow large enough to exert mass effect on surrounding structures such as the optic chiasm. Surgery via a minimally invasive transsphenoidal endoscopic approach is the preferred treatment that often results in total tumor resection. Some tumors can invade surrounding structures, making complete resection difficult and recurrence likely. MRI plays a key role in the diagnosis and grading of pituitary adenomas which can provide valuable information to surgeons about tumor size, invasion of surrounding structures, and resectability.

Results

N/A

Conclusions

After interacting with this exhibit, the learner will have reviewed the breadth of PA imaging features and be able to provide valuable insight to surgeons for planning.

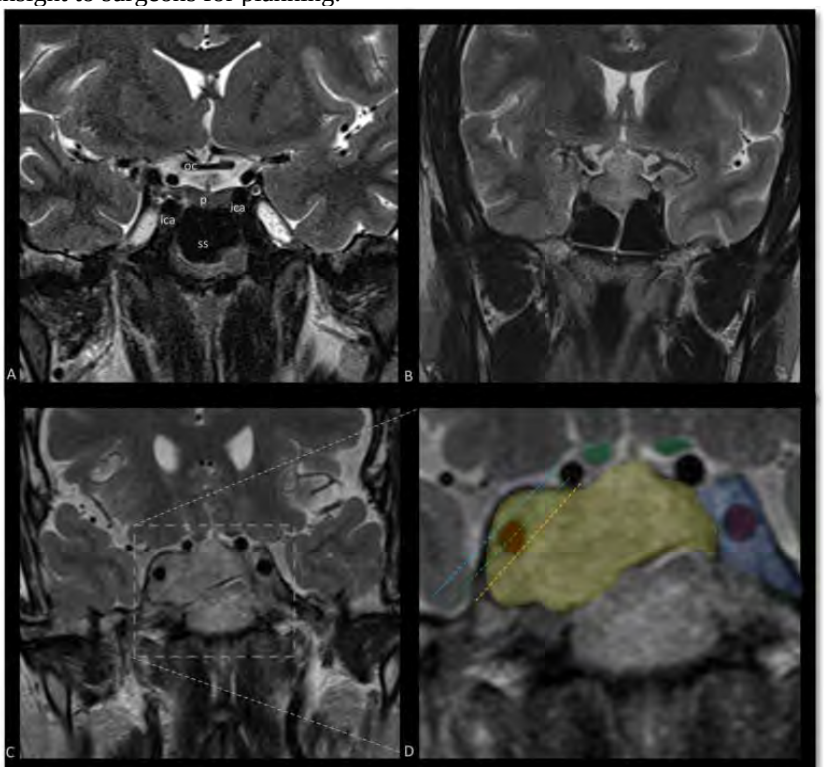

Coronal T2-weighted MRI images of the sella. **A)** Normal sella and parasellar structures. Labeled pituitary gland (p), optic chiasm (oc), cavernous internal carotid artery (ica), and sphenoid sinus (ss) **B)** Lymphocytic hypophysitis, a mimic of pituitary adenoma seen most commonly in women of childbearing age. **C)** Coronal image of a pituitary macroadenoma and **D)** zoomed in image with overlays detailing relevant anatomy. Yellow – pituitary gland with macroadenoma, Blue – Cavernous sinus, Red – Cavernous internal carotid artery, Green – Optic nerves. Medial tangent line (yellow), intercarotid line (green), and lateral tangent line (blue) used for macroadenoma grading according to modified Knosp classification. Depicted tumor is grade 4, extending beyond the lateral tangent line and encasing the cavernous internal carotid artery.

(Filename: TCT_1104_finalfinal.jpg)

1027

Back to the Basics: Stepwise Methodical Approach to Learning Brain Anatomy

E Agarwal[1], A KLEIN[2]

[1]Glenbrook North High School, Northbrook, IL, [2]Medical College of Wisconsin, Milwaukee, WI

Purpose

The knowledge of brain sulcal and gyral anatomy is essential to explain neurological deficits and is vital in localization of functional brain cortex in pre-surgical brain mapping. Identification of eloquent brain areas may be difficult but errors can be minimized if a methodical approach is used. The educational objectives of this exhibit are: 1. Identification of sulci of the brain will be reviewed using a methodical step-wise approach. 2. Relevant case examples will be shown to stress the importance of the knowledge of this anatomy

Materials and Methods

Knowledge of brain anatomy is essential for localization of functional areas of the brain. This understanding is essential to explain neurological deficits and for identification of eloquent cortices in pre-surgical brain mapping. The identification is however not always simple due to inter-subject variation in sulcal and gyral anatomy. For example, identification of the pre- and post-central gyri by neuroradiology trainees is commonly fraught with error if the method used is that of finding the 'hand knuckle' or the 'omega'; but can be greatly improved if they are trained to identify the superior frontal, pre-central, central and marginal sulci. In this exhibit, we will demonstrate a methodical approach to identify sulci of the brain to localize important gyri that subserve important brain function.

Results

Anatomical triplanar MRI images of the brain will be used to outline sulcal and gyral anatomy

Conclusions

Identification of brain sulci is important for localization of gyri that subserve important brain function. A methodical approach is necessary to minimize errors.

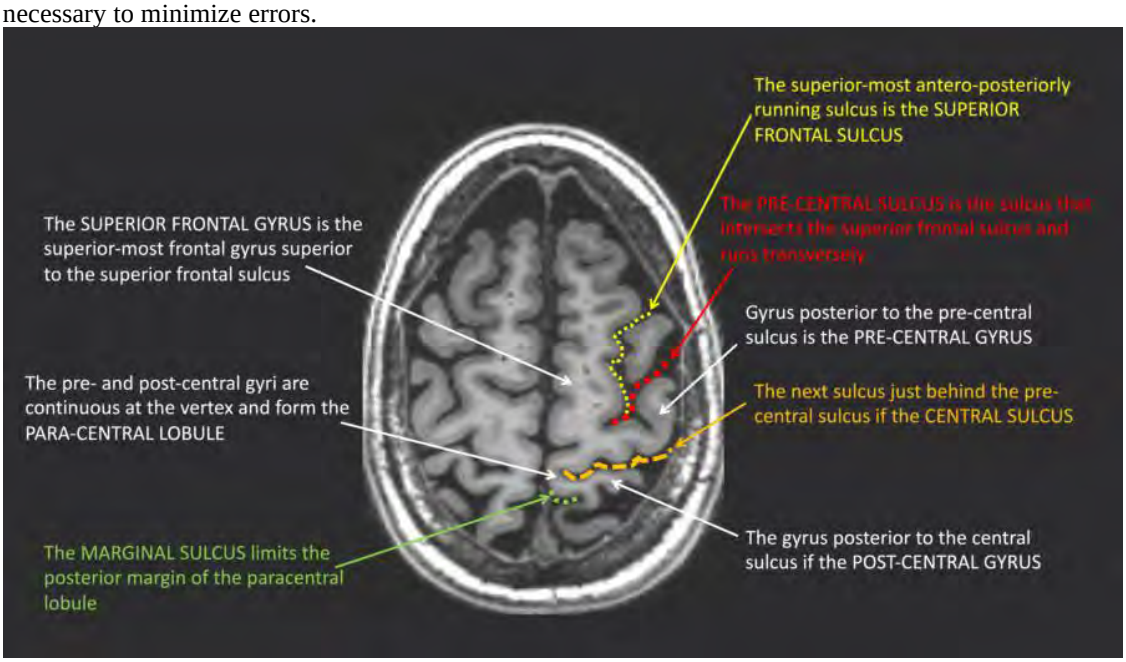

(Filename: TCT_1027_AnatomyASNR2022.jpg)

664

Bad to the Cartilage: An Educational Review of Sinonasal Chondrosarcoma

S Girn[1], J Soun[2], E Shin[3]

[1]UC Irvine Medical Center, Orange, CA, [2]UCI Department of Radiological Sciences, Orange, CA, [3]UC Irvine Medical Center, Irvine, CA

Purpose

Background information: Chondrosarcomas are the third most common malignant primary bone tumor following multiple myeloma and osteosarcoma, representing 11% of all primary malignant bone tumors. However, chondrosarcomas in the head and neck are rare compared to the rest of the skeletal system and have been observed in the sinonasal cavities, skull base, and larynx. There is a slight male predilection and peak incidence is from ages 30-60. Educational Objectives: -Learn the epidemiology of sinonasal chondrosarcoma -Understand the imaging patterns and why CT is initial modality of choice -Understand the concept of malignant degeneration and the lesions that typically degenerate into chondrosarcoma -Be able to list syndromes which are at higher risk for chondrosarcoma -Be able to list a differential for sinonasal chondrosarcoma and methods to differentiate this specific entity from mimics such as chondroblastic osteosarcoma and chondroid chordoma -Understand the histological grading system and differentiating high-grade from low-grade chondrosarcoma -Awareness of the different treatment strategies for sinonasal chondrosarcoma

Materials and Methods
The purpose of this educational exhibit is to review the presentation, epidemiology, imaging findings, associations, differential considerations, and treatments of sinonasal chondrosarcoma.
Results
A review of the literature on sinonasal chondrosarcoma will be performed. Case examples will be obtained from our institutional database to create this educational exhibit in a case-based review format.
Conclusions
Table of Contents: I. Epidemiology II. Typical imaging findings (see below) III. Associations a. Ollier disease b. Maffuci syndrome IV. Differential considerations a. Comparison to enchondroma b. Comparison to chondroid chondroma c. Comparison to chondroblastic osteosarcoma V. Grading a. Comparison of Grade I, II, III VI. Treatment strategies a. Surgical resection b. Adjuvant radiotherapy c. Radiotherapy alone Imaging Findings: -Top left and bottom left: Coronal and axial post-contrast T1 weighted MRI images illustrate heterogenous curvilinear enhancement and extension to the bilateral pterygopalatine fossae. -Top right and bottom right: Coronal and axial T2 weighted MRI images show significant T2 hyperintensity of the lesion due to the water content of cartilage. The areas of hypointensity correspond to the ring and arc calcifications typically seen on CT. Additionally, there is bilateral orbital involvement.

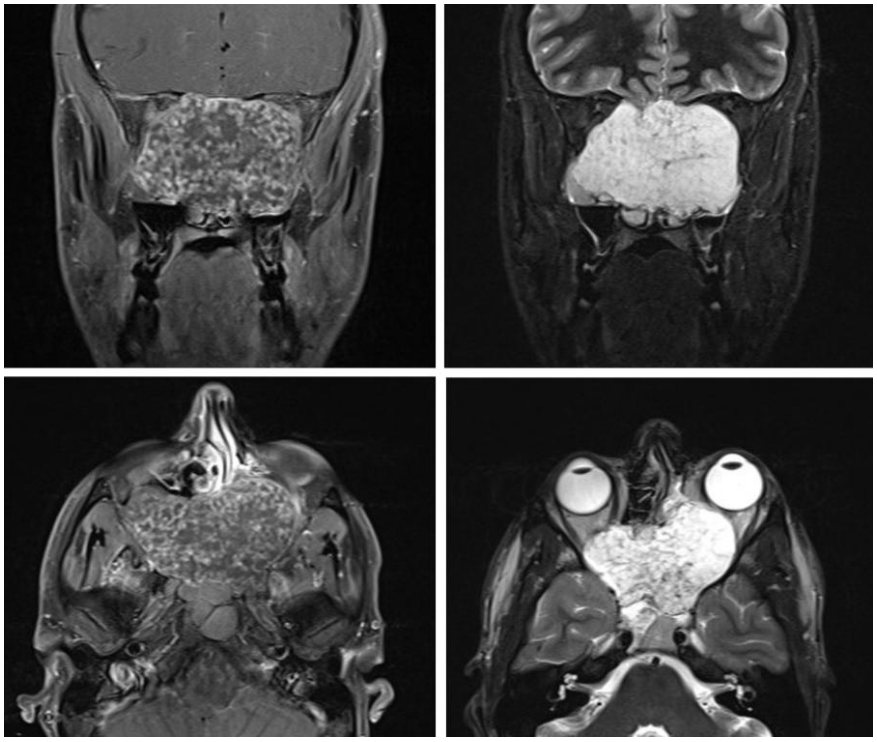

(Filename: TCT_664_sinonasalchondrosarcoma.jpg)

559

Benign and Malignant Cervical Lymphadenopathy: A Practical Imaging Approach to the Diagnosis of Common and Uncommon Conditions

A Dhaliwal[1], J Sharma[1], S Noujaim[1]
[1]Beaumont Hospital Royal Oak, Royal Oak, MI

Purpose
Generally, cervical lymphadenopathy is a benign, self-limited, and reactive process that is frequently encountered, especially in the pediatric population. However, when present in the setting of a neoplastic process, cervical lymphadenopathy is an important prognostic factor that can alter patient management. Determining the etiology of cervical lymphadenopathy is as essential as its detection. Etiologies include infection, granulomatous disease, malignancy, autoimmune disorders, iatrogenic causes, and miscellaneous or unusual conditions. Careful attention to clinical history and laboratory findings and the use of appropriate radiological imaging is crucial to obtaining the correct diagnosis. A variety of cases, including benign and malignant processes, will be presented along with explanations that emphasize the relevant features, imaging findings, and management (when appropriate) for each entity. Rare entities including but not limited to Rosai-Dorfman Disease, Kikuchi-Fujimoto Disease, Kimura Disease, and amyloidosis, as well as more common entities such as mononucleosis, sarcoidosis, leukemia/lymphoma, and metastatic pharyngeal mucosa and thyroid tumors will be presented in this exhibit.
Materials and Methods
- To highlight key imaging features of entities that can result in cervical lymphadenopathy. - To review the categories of conditions

that can lead to cervical lymphadenopathy. - To emphasize the relevant clinical history and ancillary imaging findings that may aid in making the correct diagnosis.
Results
N/A
Conclusions
N/A

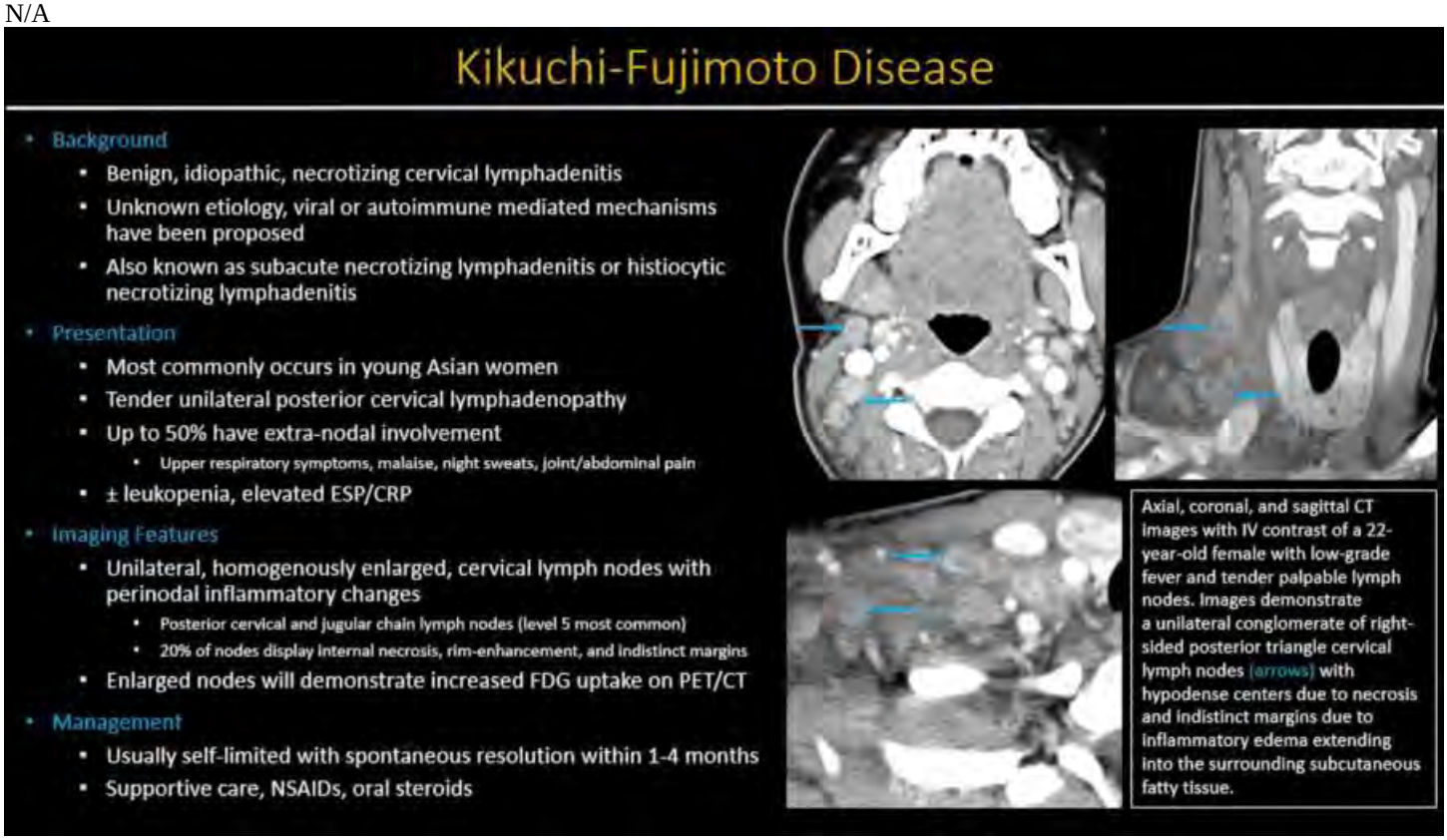

(Filename: TCT_559_ASNRSampleSlide.jpg)

1163
Beyond Meningioma: Review of Dural Lesions and the Role of Imaging in Diagnosis.
T KALELIOGLU[1], D Joyner[2]
[1]UVA, C/ville, VA, [2]University of Virginia, Charlottesville, VA

Purpose
This exhibit will provide viewers with an in-depth pictorial review of both common and uncommon pathologies affecting the dura and key characteristics that suggest uncommon diagnoses.
Materials and Methods
Dural lesions can be the result of a broad variety of pathologic processes including neoplastic, infectious and inflammatory disorders. This exhibit will familiarize viewers with common and uncommon entities directly involving the dura key imaging features and clues to uncommon diagnoses.
Results
Brain MRI cases with imaging findings of dural lesions were retrospectively collected from our institution.
Conclusions
Dural lesions share similar imaging characteristics; however, some have distinctive imaging findings that along with patient history and laboratory findings can guide the radiologist to the appropriate diagnosis. This pictorial review considers dural lesions including neurosarcoidosis (figure A), idiopathic (figure B) and IGG4 related pachymeningitis , dural lymphoma (primary and secondary) , solitary fibrous tumor, and dural metastases as well as the more common meningioma. Brief clinical vignettes including presenting symptoms, physical examination findings, and laboratory evaluations are provided for each case.

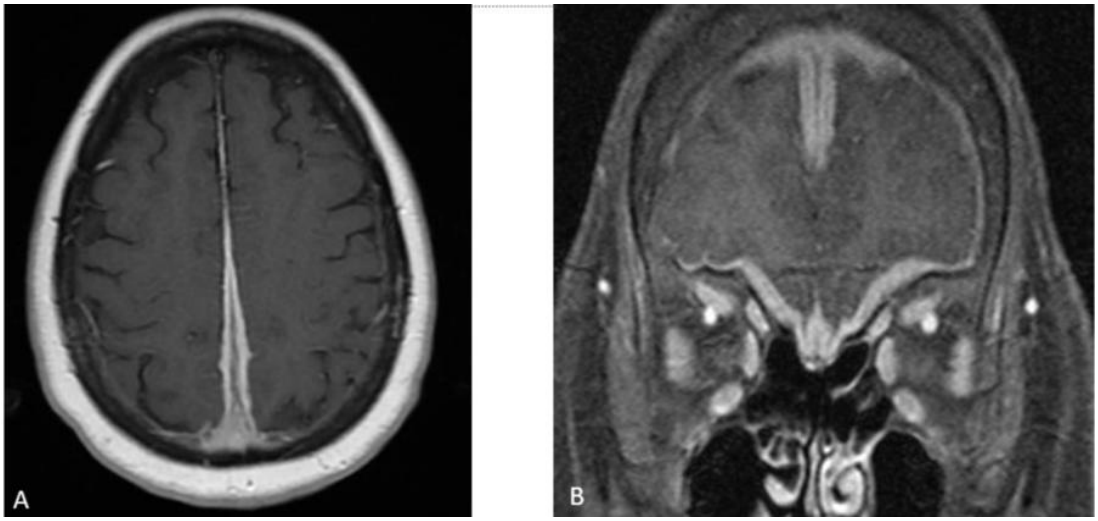

(Filename: TCT_1163_dura.jpg)

711

Beyond the Image: Head and Neck Cancer Genetics and Microbiology for the Imager

T Kong[1], N Pham[2], L Ledbetter[3]

[1]University of California Los Angeles, Los Angeles, CA, [2]UCLA, Los Angeles, CA, [3]David Geffen School of Medicine, Los Angeles, CA

Purpose

Characterization of head and neck tumors is traditionally based on histology and the anatomic extent of disease. However, in the genomics and radiomics era, tumors can be assessed at a finer, more precise scale. The objectives of this exhibit are to present: 1) Fundamental principles in head and neck cancer biology, 2) Emerging topics such as imaging and molecular biomarkers in the context of whole genome sequencing and machine learning, and 3) Novel therapeutics that have arisen from current understanding of cancer genetics and microbiology.

Materials and Methods

N/A

Results

A literature and case-based review was performed on the above topics.

Conclusions

Tumorigenesis pathways are diverse and can involve multiple processes such as cell cycle regulation, cell signaling, oxidative stress response, immune surveillance, and chromatin modification. The exhibit will present the biomarkers that have arisen from studying these pathways, which hold important implications for cancer imaging and intervention. For example, human papillomavirus (HPV), an established biomarker for squamous cell carcinoma (SCC), contains oncogenes that inhibit key gatekeepers of the cell cycle. Another biomarker, programmed death-ligand 1 (PD-L1) hampers the immune surveillance and portends poor prognosis. Although molecular changes occur on a sub-pixel scale, emergent imaging features have been associated with specific biomarkers, spurred by machine learning and radiomics. For example, HPV positivity, a good prognostic indicator for SCC, demonstrates distinct imaging features. The exhibit will present known associations between imaging features and molecular biomarkers, which have the potential to enhance diagnostic and prognostic capabilities beyond current TNM staging. Ultimately, these molecular and imaging are driving the development of precision cancer therapeutics. For example, pembrolizumab is specifically directed against PD-L1 to modify the immune milieu. Despite these promising advancements, there are many challenges, such as response negation by molecular feedback mechanisms and limitations in gene delivery technology, which also be discussed in this exhibit. Establishing a framework of the molecular biology of head and neck cancers will assist radiologists in assessing tumors in the context of new diagnostic and treatment methods.

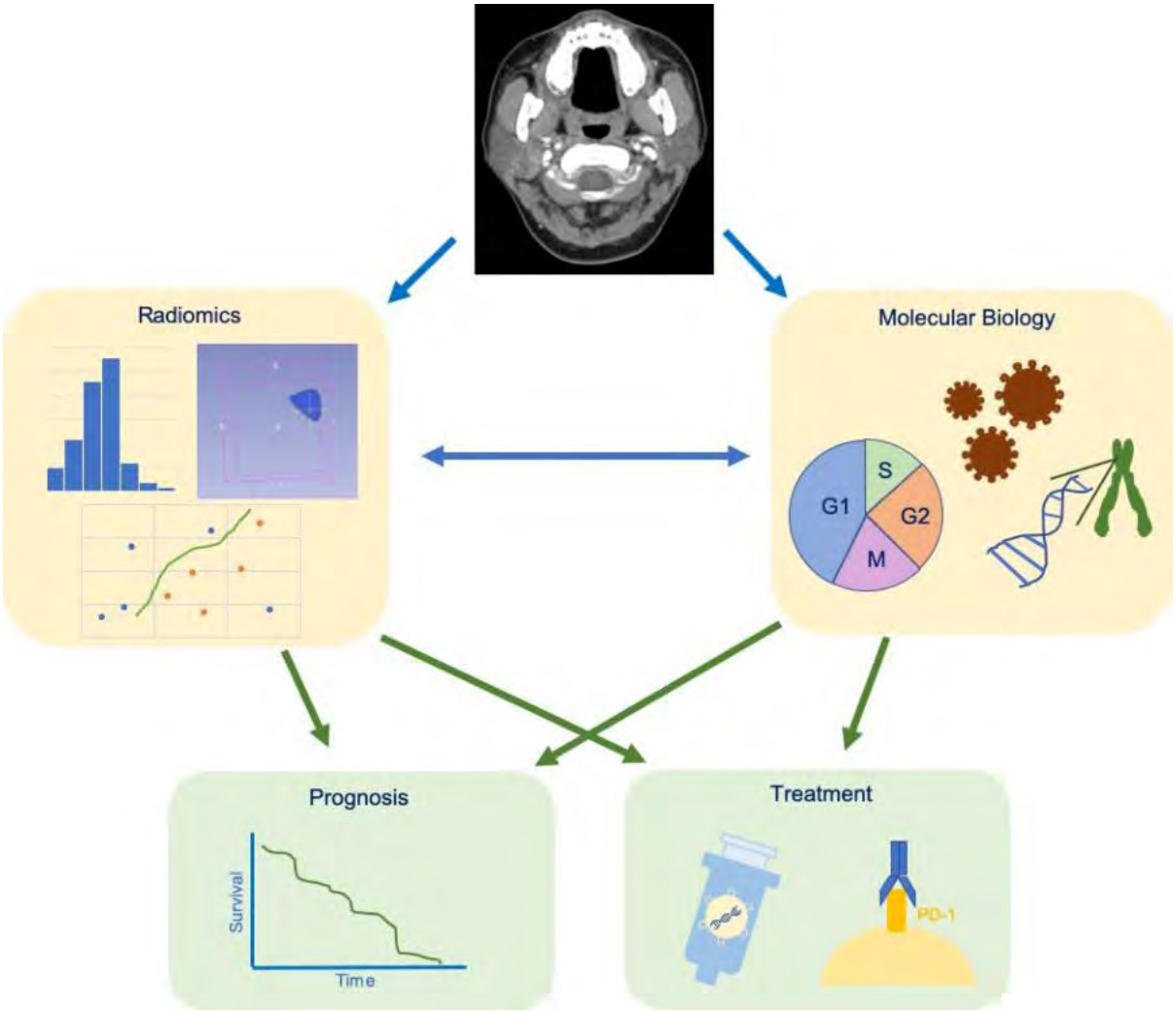

(Filename: TCT_711_ASNRfigure.jpg)

968

Beyond the Periapical Lucency: Review of the Most Common Jaw Lesions

N Jain[1], S Khanna[2]

[1]Temple University Hospital, Philadelphia, PA, [2]Jefferson Health, Philadelphia, PA

Purpose

Lesions in the mandible and maxilla are often encountered in daily practice. Although dental caries and periapical lucencies may be the most frequently seen lesions, there are several others that radiologists should be familiar with, particularly when it comes to entities that are potentially aggressive and may require early, more aggressive treatment. In this exhibit, examples of the most common odontogenic radiolucent, radio-opaque and mixed radio-opaque/radiolucent lesions will be discussed with pathologically proven imaging examples. Dental anatomy will first be discussed so there is familiarity with describing lesion location as well as discussion of both the Universal and the Federation Dentiare International systems of tooth counting. The following radiolucent lesions will be reviewed: radicular, residual and dentigerous cysts, as well as odontogenic keratocyst, and ameloblastoma. Key points that should be included in the radiology report of what the surgeon needs to know, particularly with respect to ameloblastoma will also be discussed. For odontogenic radio-opaque lesions, cemento-osseous dysplasia, cementoblastoma, condensing osteitis, odontomas, and idiopathic osteosclerosis will be discussed with some pathology proven imaging appearances. Some imaging examples of common non-odontogenic radio-opaque and radiolucent lesions will also be shown. Mixed radio-opaque and radiolucent lesions such as osteomyelitis, medication related osteonecrosis of the jaw, and osteoradionecrosis will be shown with discussions of both clinical and imaging criteria for these entities.

Materials and Methods

The purpose of this exhibit is to educate radiologists and trainees about dental anatomy and imaging appearances of several of the most common pathology proven odontogenic jaw lesions with emphasis on what the surgeon needs to know and clinical criteria for some entities.

Results

For educational purposes, a list of biopsied odontogenic lesions either within the mandible or maxilla were cross referenced with

PACS data in order to obtain CT and/or MRI images for multiple jaw lesion with definitive biopsy results. Those cases whose imaging was available were gathered together and used as a teaching lecture for radiology residents. This resident lecture was modified for this submission.
Conclusions
N/A

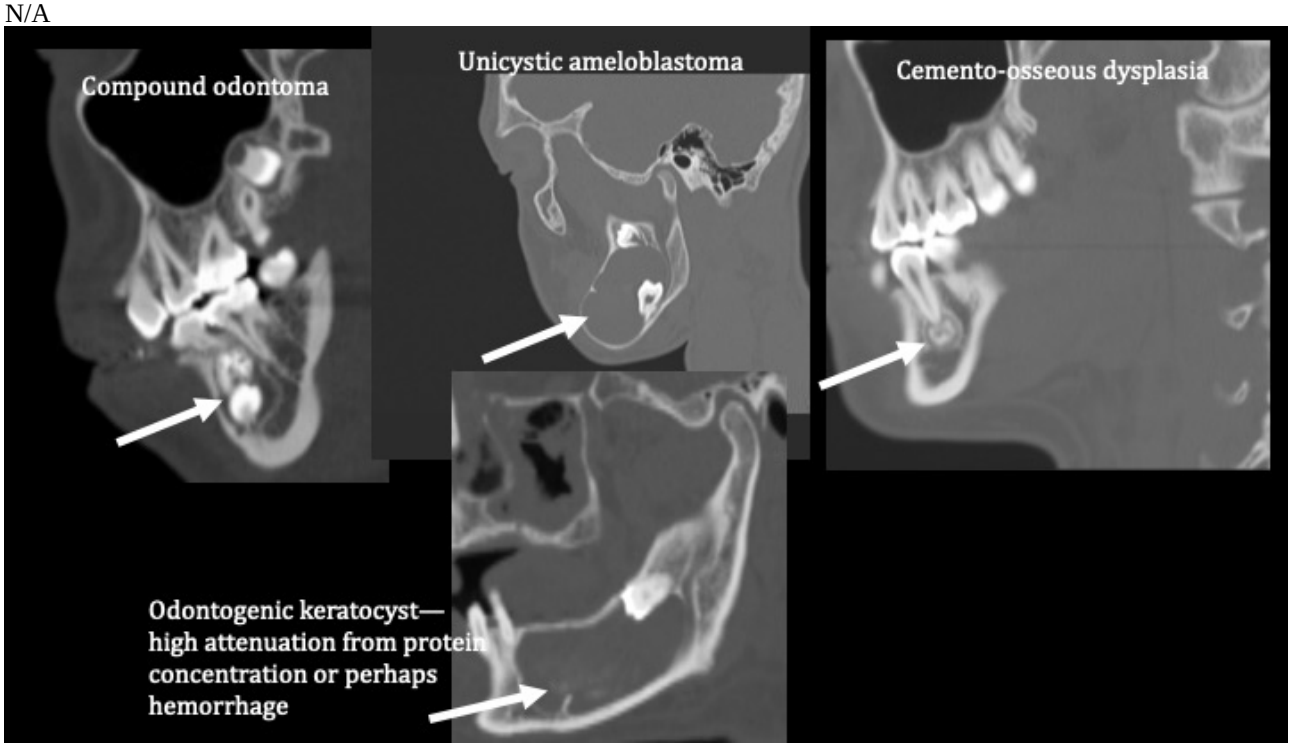

(Filename: TCT_968_jawlesionexamplesforasnrabstract.jpg)

689

Brainstem Lesions – Old and New Participants of MR T2/FLAIR/DWI Masquerade

Y AFANDIYEV[1], L KHALILOVA[2], L MUSAYEVA[3], A ISMAYILOV[4]
[1]Tusi memorial clinic, Baku, Azerbaijan, [2]Turk-American Medical Center, BAKU, Azerbaijan, [3]TUSI clinic, BAKU, Azerbaijan, [4]CCMSU Medical Imaging, TORONTO , ONTARIO

Purpose
The purpose of this educational presentation is to emphasize the role of clinical and laboratory findings in radiological differential diagnosis of brainstem lesions with MRI. These lesions include the diseases/conditions traditionally seen in MR imaging (i.e., old participants) as well as the ones that started showing up not too far ago due to advances of this modality (i.e., new participants).
Materials and Methods
We find it important to start with a brief review of the clinically relevant anatomy of the brainstem that includes midbrain, pons and medulla oblongata
Results
The brainstem lesions are classified based on etiology, pathogenesis and anatomical location. Examples/MR tomograms of each pathology are given in the presentation - Vascular Supply Pathology o Infarctions specific for Midbrain, Pons and Medulla Oblongata - Conditions Not Related to Vascular Supply o Tick–Borne Disease – Pontine Borreliosis (Lyme disease) o Infection – Tuberculosis o Brain Tumors – Pediatric Glioma o Monophasic acute inflammation and demiyelination – ADEM o Arteriovenous Malformations – Pontomedullary Cavernoma with Hemorrhage o Various metabolic diseases – Central Pontine Miyelinosis, Wilson's disease o Demyelinating Diseases – Pontine Plaque in Multiple Sclerosis o Neurodegenerative Mitochondrial Diseases – Leigh Syndrome The new participants of the brainstem T1/T2/DWI Masquerade include: o Behçet disease (Silk Road Disease) – autoimmune inflammation of the blood vessels o Pontine Focal Abnormal Focal Intensity (FASI) in Neurofibromatosis Type 1 – a condition with autosomal-dominant inheritance o Bickerstaff brainstem encephalitis – a self–limiting autoimmune neuropathy often seen after viral infections (varicella zoster and cytomegalovirus) o Vitamin B12 deficiency – myelosuppression (can also be seen with other metabolic disorders) o Various neurodegenerative diseases (e.g., multisystem atrophy, spinocerebellar ataxia, vasculitidis)
Conclusions
Message to Take Home - Most of the brainstem T2/FLAIR hyperintensities may be indistinguishable and not pathognomonic for a specific disease/condition/ - Clinical and family history, neurological manifestation/status along with laboratory findings is the key to the accurate and highly–specific radiological diagnosis when differentiating T2/FLAIR /DWI hyperintensities of the brainstem. The Powerpoint presentation contains MRI images from 21 clinical cases.

519

Carotid Diseases in the Neck – Beyond Atherosclerosis

O Intikhab[1], J Pulito[2], B Griffith[2], H Marin[2]
[1]Henry Ford Hospital, Detroit, MI, [2]Henry Ford Health System, Detroit, MI

Purpose

Although atherosclerosis is the most commonly encountered pathology involving the cervical internal carotid artery, with the increased use of CTA and MRA, radiologists will encounter an increasing number of less common disease processes, which are sometimes difficult to characterize appropriately. In this exhibit we will provide an overview of unusual presentations of cervical carotid pathology with an emphasis on the differentiating imaging features.

Materials and Methods

Beyond atherosclerosis, there is a wide spectrum of disease processes involving the cervical internal carotid artery including: Congenital, Inflammatory, Traumatic, and Neoplastic conditions. The purpose of this exhibit is to present a pictorial review of these many pathologies involving the carotid artery in the neck, including both unusual presentations of common etiologies, as well as more uncommon conditions.

Results

Using a case based approach we will review various pathologies affecting the cervical carotid artery. These include unusual presentations of atherosclerosis, dissection, aneurysm, congenital variants, and inflammation. Specific case examples include carotid web (Fig. 1), intraluminal thrombus in the setting of COVID-19 (Fig. 2), dissection (Fig. 3) and occlusion (Fig. 4). Various imaging modalities will be shown including MRA, CTA, ultrasound, and digital subtraction angiography (DSA).

Conclusions

Familiarity with unusual presentations of cervical carotid pathology and their normal variants will help neuroradiologists formulate the correct differential diagnosis and guide appropriate treatment. This exhibit will provide a pictorial review of uncommon pathologies affecting the carotid arteries in the neck.

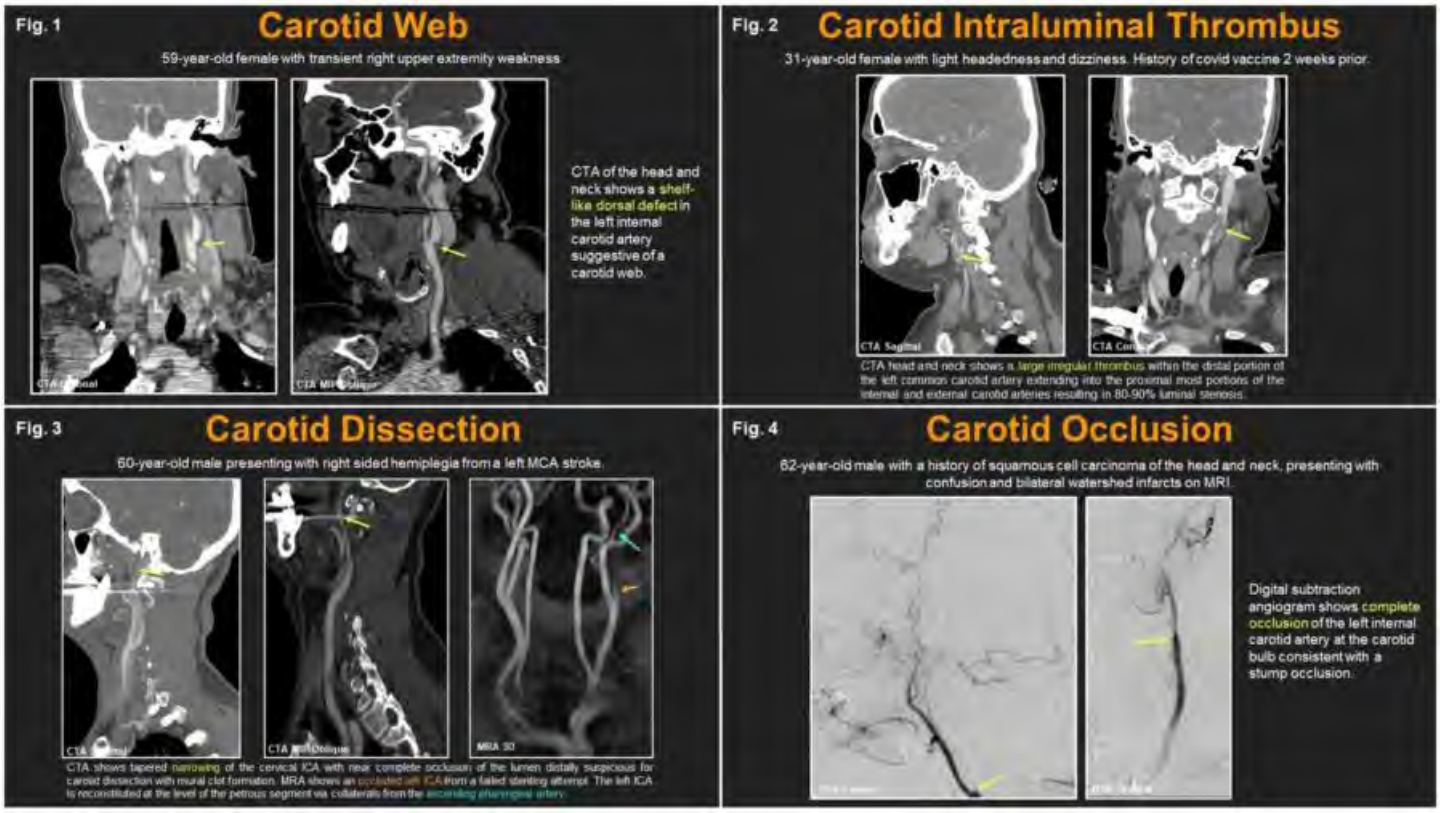

(Filename: TCT_519_Carotidabstractfigure.jpg)

443

Cerebral Calcifications, Epilepsy and Celiac Disease (CEC syndrome). A review.

G GIANNATEMPO[1]
[1]SCIENTIFIC INSTITUTE "CASA SOLLIEVO DELLA SOFFERENZA", SAN GIOVANNI ROTONDO, FG

Purpose

The association of cerebral calcifications, epilepsy and celiac disease (CEC) has been recognized as a distinct syndrome and it represents a rare and relatively little known neurological disorder.

Materials and Methods
To illustrate epidemiology, clinical and radiological findings of CEC and its differential diagnosis.
Results
Epilepsy mainly consists of occipital seizures, may be benign or drug-resistant and in some cases may evolve into severe epileptic encephalopathy. Celiac disease usually includes gastroenterological symptoms, but may also be olygosymptomatic or totally silent. Cerebral calcifications are typically occipital, cortical and subcortical, and bilateral, roughly symmetrical. They may also be parietal-occipital or associated with frontal or temporal calcifications. In rare cases unilateral occipital calcifications have been reported. They usually have a serpiginous shape, do not enhance after contrast administration and are not associated with cortical atrophy. Extent of calcifications is not related with the severity of the epilepsy. Patients may present large calcifications and benign clinical course or, conversely, small calcifications and intractable seizures. They usually do not change in follow-up studies, but in some cases may increase in size or develop in new cerebral areas.
Conclusions
CT scan is the technique of choice as MRI may fail to detect calcifications. Also in using sequences such as T2*-Gradient Echo (T2*-GE) or susceptibility weighted imaging (SWI), calcifications on CT may be more extensive than recognized on MRI. SWI has increased diagnostic sensitivity than T2*-GE. Differential diagnosis includes any disease associated with posterior cerebral calcium deposits. Clinical history easily rules out encephalitis, purulent meningitis, ossifying meningoencephalopathy, as well as treatment with methotrexate in leukemic children. Sturge-Weber syndrome (SWS) without facial nevus flammeus (absent in about 2%) must also be excluded. In these cases MRI with contrast is recommended as SWS is characterized by enhancement of pial angiomatosis as well as cortical atrophy and enlarged choroid plexus. MRI with contrast also consents to rule out meningioangiomatosis, a rare cortical/leptomeningeal malformation characterized by seizures, calcified cortex on CT and cortical enhancement on contrast MRI. In patients with seizures and calcifications on CT scan, CEC syndrome must be included in differential diagnosis, taking care that gastrointestinal symptoms may be subtle or absent.

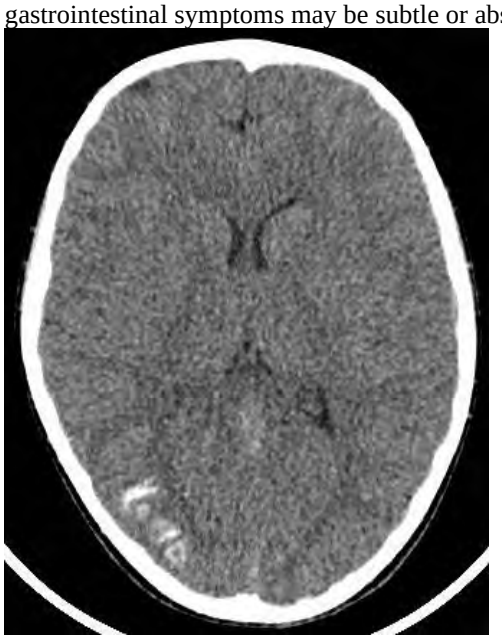

(Filename: TCT_443_CTCEC.jpg)

614

Characterizing Masses of the Fourth Ventricle

A Reis[1], S Mizrachi[2], R Tenney[3], K Shifteh[4], J Bello[5]
[1]Montefiore, The Bronx, NY, [2]Montefiore Medical Center, Bronx, NY, [3]Montefiore Medical Center, The bronx, NY, [4]Montefiore Hospital, Brooklyn, NY, [5]Montefiore Radiology, New York, NY

Purpose
To understand the normal anatomy of the fourth ventricle and the flow of CSF. To describe CT and MR features of masses involving the fourth ventricle. To classify fourth ventricle masses based on their features and age at which they typically occur.
Materials and Methods
In this educational exhibit we review characteristics and CT / MR imaging findings of patients with masses of the fourth ventricle. There is a diverse array of pathology that may affect the fourth ventricle. To understand how lesions affect the fourth ventricle it is essential to understand the normal anatomy and flow of CSF. Radiologists play an essential role in providing a differential diagnosis of fourth ventricle masses, describing the extent of disease, and detecting additional associated findings such as hydrocephalus.
Results
Multiple cases from our institution are used to illustrate CT and MR characteristics of masses involving the fourth ventricle.

Conclusions
Imaging Findings: Ependymoma – Contrast enhanced MR revealed a solid and cystic fourth ventricular mass causing widening and obstruction of the fourth ventricle. Choroid Plexus Papilloma – Contrast enhanced MR revealed an avidly enhancing mass in the fourth ventricle. Metastasis – Contrast enhanced MR reveals a T1 isointense mass within the fourth ventricle. Lymphoma – Contrast enhanced MR reveals multiple T1 intense masses, one of which is within the fourth ventricle, causing mass effect on the cerebellum and brainstem. Hemangioblastoma - MRI revealed a lesion along the inferior aspect of the fourth ventricle adjacent to the obex. ATRT – CT and contrast enhanced MRI reveal a calcified bilobed enhancing mass centered in the fourth ventricle and extending to the aqueduct of Sylvius. Medulloblastoma – Contrast enhanced MR reveals an enhancing mass within the inferior portion of the fourth ventricle causing hydrocephalus. Conclusions: There are key features including the age at which they occur and CT and MRI imaging characteristics which may help to differentiate between fourth ventricle masses. Understanding these features and how they affect the anatomy of the fourth ventricle may aid radiologists in providing an accurate diagnosis and extent of disease.

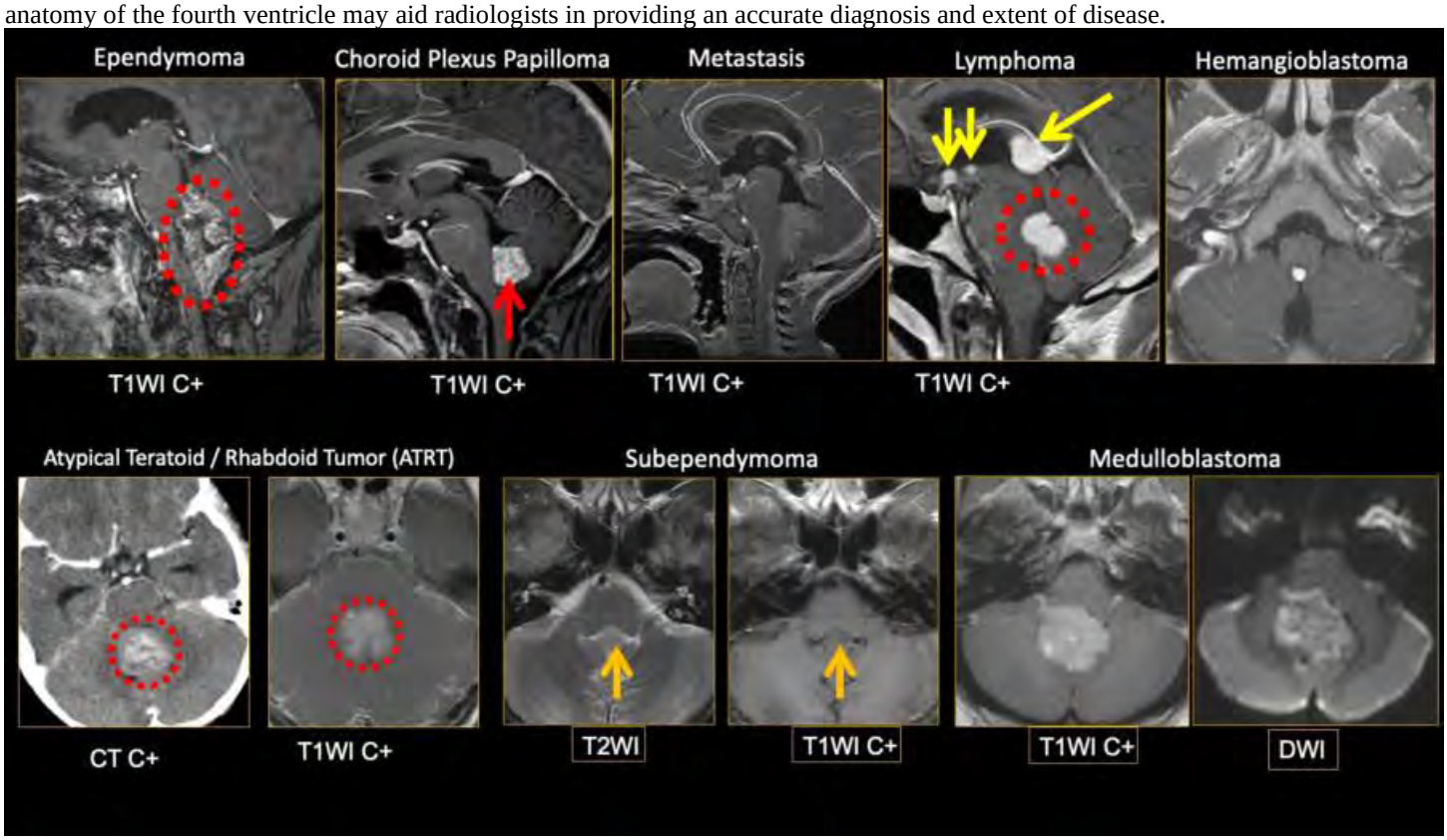

(Filename: TCT_614_4thVentricularmasses.jpg)

864
Children's Brain Tumor Network: Primer for Neuroradiologists to start research projects with CBTN
N Tillmanns[1], M von Reppert[2], S Abi Fadel[3], G Cassinelli Petersen[1], M Aboian[3]
[1]Yale School of Medicine, New Haven, CT, [2]Brain Tumor Research Group, Yale School of Medicine, New Haven, CT, [3]Yale University, Woodbridge, CT

Purpose
Nowadays patient data is more needed than ever. Especially if you want to train or test your machine learning approach for image processing, large, diverse and accurate data sets are needed. This information can be provided by the Children's Brain Tumor Network (CBTN) which contains rich imaging and genetic data.
Materials and Methods
We aim to equip neuroradiologists with a standard operating procedure to make better use of the many-faceted resources that can be found on CBTN.
Results
In the first step, we dealt with the CBTN website in small steps. We also had a discussion with the project coordinator Ryan Velasco. Then we also studied the introductory video of the website "Early career investigator session". In addition, our working group went through a project submission and approval process on the website and we worked with the data made available to us.
Conclusions
CBTN is the largest pediatric brain tumor biorepository available. It consists of more than 3,900 subjects paired with longitudinal clinical, genomic, imaging and histology data and is available for request by researchers across the world. The DICOM images that are stored on CBTN are accompanied by actual clinical radiology reports, which allows researchers to perform multifaceted studies that compare results of advanced imaging analysis to actual clinical information provided to patients and oncologists during clinical

practice. All MRI images and MRI reports are available for download from the Kids First DRC Portal or Cavatica. The CBTN collects MRIs at both pre-and-post-surgery, as well as at follow up appointments. This allows to perform projects on preoperative prediction of tumor subtypes and patient outcomes and allows detailed analysis of post treatment changes with chemo and radiotherapy. The MRI data will be provided via Flywheel (chop.flywheel.io) which you can access through your browser. You don't need to download the images and can open them directly in your browser within Flywheel. It's also possible to build AI analytic workflows for your project on Flywheel. To access the data, researchers need to follow a stepwise approach which includes filling out an online form, signed data agreement and scientific committee review. We provide a stepwise description of this approach in our exhibit. This exhibit describes a stepwise approach on how to start projects with CBTN, which is a rich data repository of pediatric brain tumors with imaging and genetic analysis from multiple institutions.

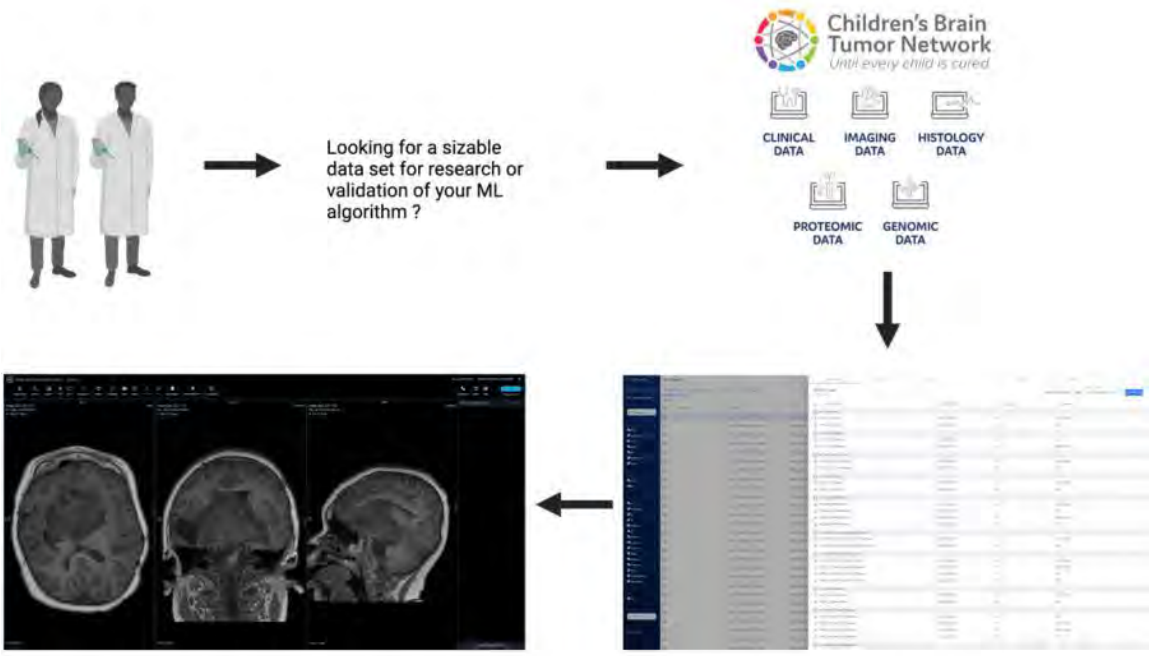

Figure: Flowchart of accessing imaging data via CBTN: Once your project is accredited you can access the data via Flywheel directly in your browser (Created with BioRender.com)
(Filename: TCT_864_ASNR_CBTN_figure.jpg)

1479
Clinical Decision Making in MRI Safety
M Antonucci[1], M Mercer[1]
[1]*Medical University of South Carolina, Charleston, SC*

Purpose
The presentation will consist of a series of multiple choice questions and answers designed to emphasize key principles of MR safety. The presentations simulate scenarios encountered in daily practice and promote awareness of the root causes of adverse events. The questions will address essential components of MRI safety with the following objectives: (1) Define MR safety personnel levels. (2) Understand MR safety zones. (3) Appreciate the risks of the MRI environment & techniques used to minimize these risks (including OSHA recommendations). (4) Determine MRI candidacy for patients with certain implanted devices. (5) Learn approaches for dealing with unexpected/emergency scenarios in the unique MR environment.
Materials and Methods
Facilitating MR safety is a critical non-interpretative component of neuroradiology and should comprise part of the training curriculum. Unfortunately, decisions on safe scanning practices may be delegated to one specified radiologist or non-physician personnel. For many, experience in MR safety consists solely of a brief internet search prior to imaging a patient with a particular device. Our radiology residency recently instituted a clinically-oriented MR safety curriculum, including a case-based quiz. The questions are designed to reinforce fundamental concepts in MRI safety. Our aim herein is to utilize a similar approach as an educational opportunity for the neuroradiology community.
Results
This educational curriculum is comprised of a series of multiple choice questions designed to emphasize key principles, including those contained in the American College of Radiology guidance documents. The presentations simulate scenarios encountered in daily practice and promote awareness of the root causes of adverse events.
Conclusions
The participant will answer questions that address essential components of MRI safety, including: -MR safety personnel -MR safety zones -Risks of the MR environment -Techniques used to mitigate risks -Occupational Safety and Health Administration

Recommendations -How advances in knowledge allow expansion of services to those with certain implanted devices (e.g. non-conditional pacemakers). -How to deal with unexpected/emergency scenarios in the unique MR environment. Conclusion: Utilizing clinical scenarios can reinforce the fundamentals of MR safety, enhance understanding of best practices, and optimize patient care.

546

CNS Complications of Local and Systemic Therapies

F Assunção[1], G Silva[1], N Calixto[1], L Martins[1], L Freitas[2], T Scoppetta[1]
[1]Hospital São Camilo/Grupo Fleury, São Paulo, SP, [2]Hospital São Camilo, São Paulo, SP

Purpose
Neurological complications associated with the use of the local and systemic therapies (vascular procedures, drugs, immunotherapy, radiotherapy, chemotherapy and surgery) have been recognized more and more frequently. The objective of this study is exhibit a series of cases demonstrating imaging features and patterns of CNS involvement of a wide range of treatment modalities available in our clinical practice and discuss the differential diagnosis for them.
Materials and Methods
The purpose of this exhibit is: To review the treatments modalities that may cause CNS complications To demonstrate the main CNS complications of local and systemic therapies To emphasize the key imaging features that help to differentiate them from other pathological conditions.
Results
We performed a retrospective and descriptive study of brain and spine MRI of patients with complications of local and systemic therapies in the central nervous system performed in our service.
Conclusions
We found several cases of CNS Complications of local and Systemic Therapies in our retrospective study. - Vascular procedures (granuloma, muslinoma...) - Chemotherapy (radionecrosis, necrotizing leukoencephalopathy, posterior reversible encephalopathy syndrome…) - Immunotherapy (induced autoimmune encephalitis, induced hypophysitis…) - Surgery (Sinking Skin Flap Syndrome...) - Drug Intoxication (anticonvulsivants...) - Others (Oxigenoterapy...) Imaging features and patterns of CNS involvement may be divided according to the type of focal and systemic treatment.

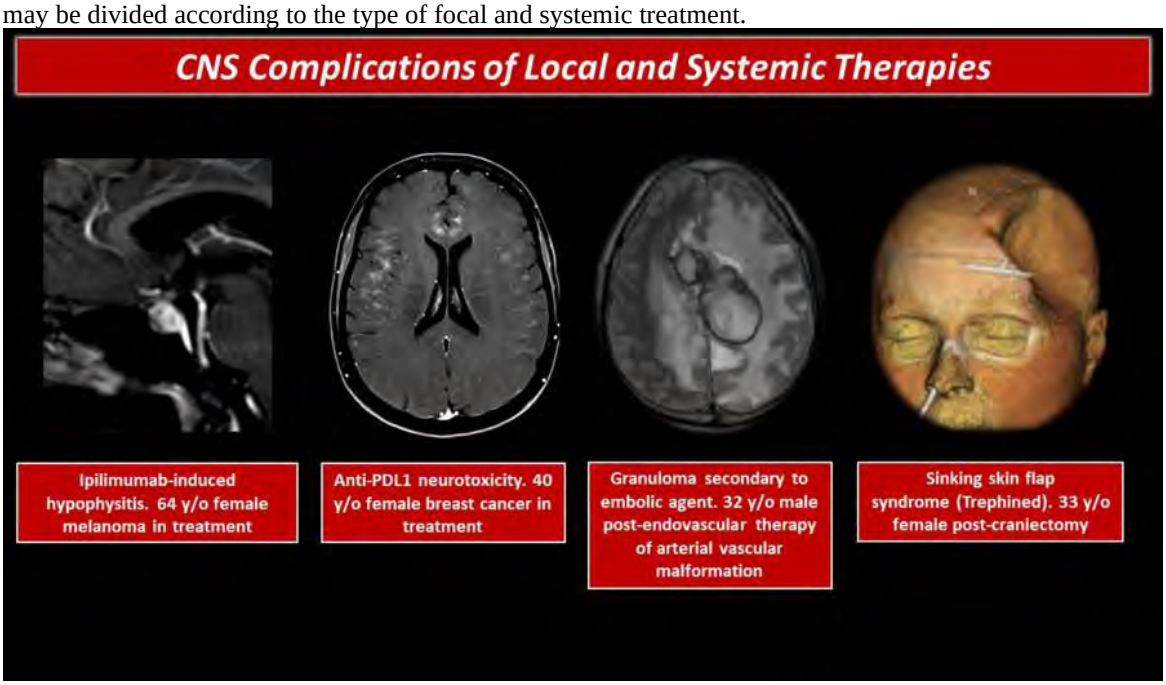

(Filename: TCT_546_Slide1.JPG)

545

CNS Fungal Infections: Clinical-Radiological Spectrum Findings

N Calixto[1], F Assunção[1], G Silva[1], L Martins[1], L Freitas[2], T Scoppetta[1]
[1]Hospital São Camilo/ Grupo Fleury, São Paulo, SP, [2]Hospital São Camilo, São Paulo, SP

Purpose
Fungal infections of the central nervous system (CNS) are rare, but potentially serious entities, especially in immunocompromised patients. The objective of this work is to review the clinical and epidemiological scenarios of the main fungal infections of the CNS and to carry out a pictorial review of their imaging findings.
Materials and Methods
The purpose of this exhibit is: Review the epidemiological and clinical scenarios of CNS fungal infections; Pictorial review of the

main CNS fungal infections involving CNS; To emphasize the key imaging features to narrow the differential diagnosis and prompt early aggressive treatment.
Results
We performed a retrospective and descriptive study of brain MRI of patients with CNS fungal infections performed in our service and evaluated the clinal-radiological spectrum findings.
Conclusions
- Fungal infections of the CNS represent a diagnostic challenge in clinical practice. - Through this poster, we were able to describe and characterize the main radiological findings of these infections - The radiologist must be familiar with the imaging patterns of the main fungal infections of the CNS and their differential diagnoses, allowing for the establishment of an adequate diagnosis and treatment for the patient.

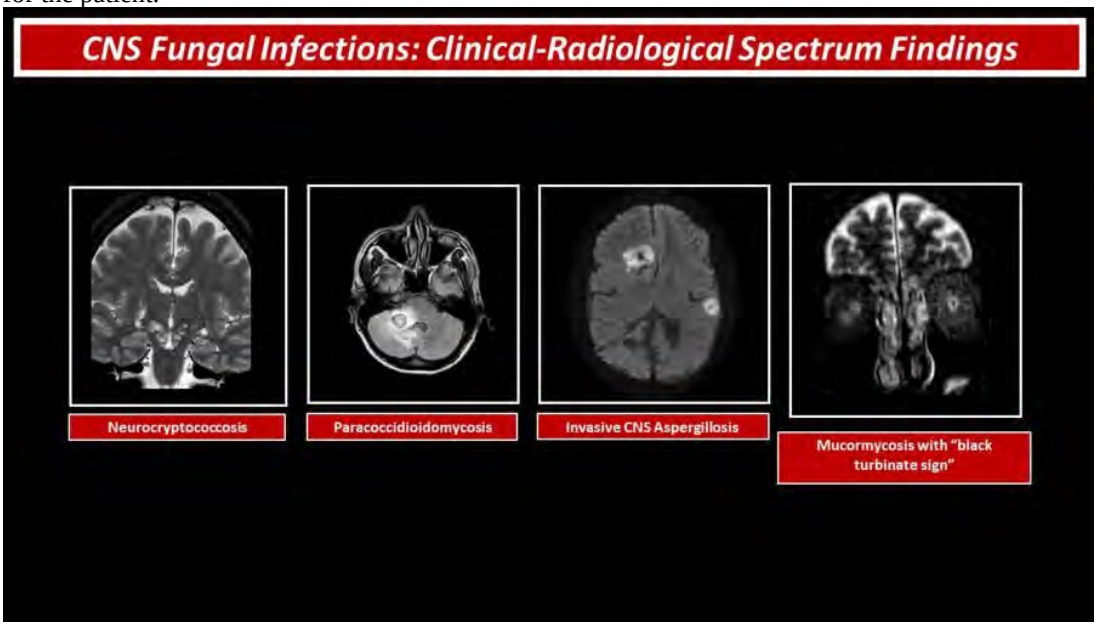

(Filename: TCT_545_Slide1.JPG)

1528
CNS Medication Toxicities: A Review
S Tamir[1], E Garcon[2]
[1]Columbia NY Presbyterian, New York, NY, [2]Columbia NYPH, New York, NY

Purpose
The imaging findings of drug induced neurotoxicity are ubiquitous and often overlooked in the evaluation of a routine MRI of the brain. We present an educational exhibit of our findings to illustrate the brain imaging findings of neurotoxicity. Some of the objectives include: 1. Approach to imaging findings and differential diagnosis. 2. Knowledge of particular patterns of brain imaging in neurotoxicity. 3. Reversibility of neurotoxicity imaging findings.
Materials and Methods
We present an educational exhibit of our findings to illustrate the brain imaging findings of neurotoxicity that any radiologist, especially those reading neuroimaging should be aware to increase their diagnosis accuracy.
Results
A search was performed through the dictation database at our institution for keywords "toxicity" and certain medications such as "phenytoin", "vigabatrin", "metronidazole", "methotrexate" and "tacrolimus" used in the treatment of patients with epilepsy, infection, neoplasm or organ transplant. Subsequently the medical record was correlated with the imaging findings to determine if a time dependent relationship existed between a medication administration and imaging findings. The particular pattern of brain imaging was then reviewed.
Conclusions
Our findings demonstrate that anti-epileptic medication such as Phenytoin (Dilantin) may cause a typical pattern of cerebellar atrophy and calvarial thickening. Other drugs such as Vigabatrin used to treat infantile spasms can cause a typical pattern of diffusion weighted signal abnormalities in the deep gray nuclei. Metronidazole which is widely used in the treatment of bacterial and protozoal infection may cause a typical pattern of high T2 and FLAIR signal abnormality in the cerebellum, corpus callosum and brainstem. Methotrexate, a drug used in the treatment of many cancers may show increased T2 FLAIR and DWI signal abnormality in the centrum semiovale. In conclusion, while involvement of the splenium and centrum semiovale may be nonspecific, other findings like involvement of the dentate nucleus may be more specific cluing a radiologist into the diagnosis of metronidazole toxicity. Most importantly, the clinical history of medication administration must be confirmed.

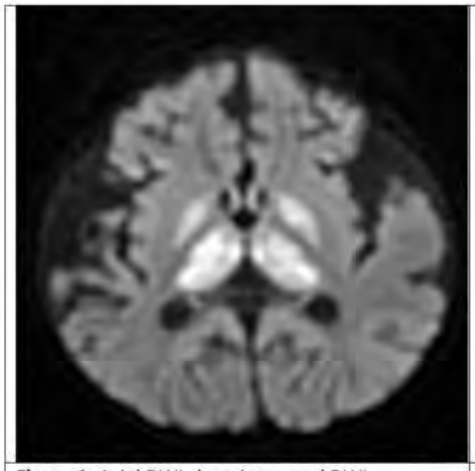

Figure 1. Axial DWI show increased DWI corresponding to decreased ADC (not shown) in the globi pallidi and thalami bilaterally.

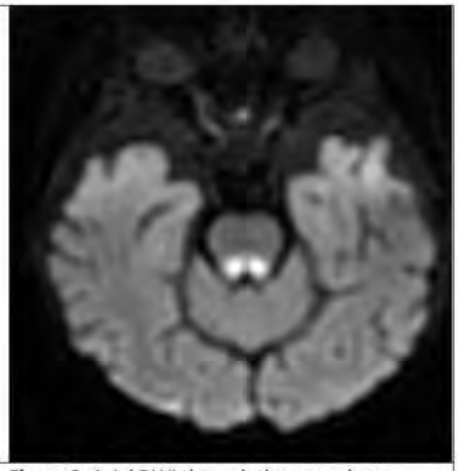

Figure 2. Axial DWI through the pons shows increased DWI corresponding to decreased ADC (not shown) in the posterior pons.

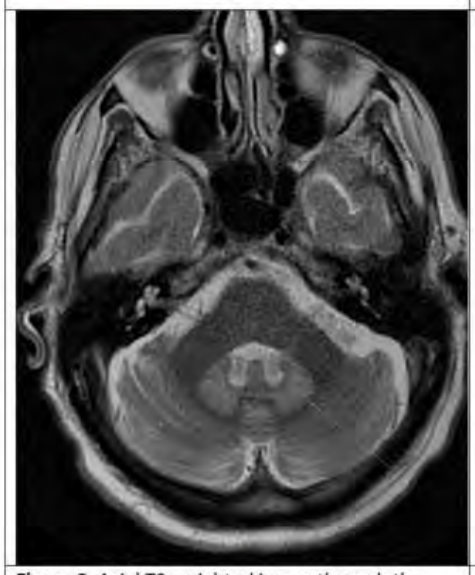

Figure 3. Axial T2 weighted image through the cerebellum in a patient with metronidazole toxicity shows hyperintensity of the dentate nuclei bilaterally.

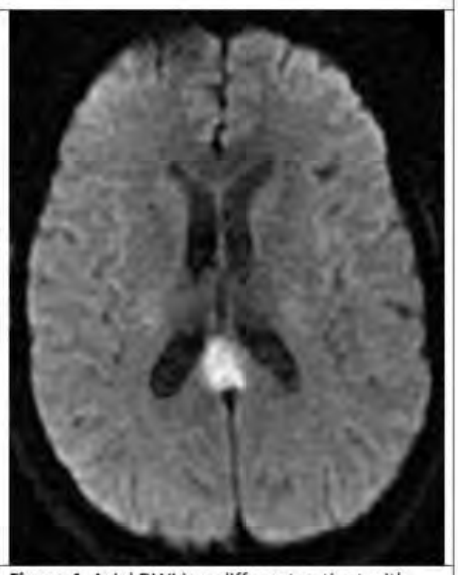

Figure 4. Axial DWI in a different patient with metronidazole toxicity shows increased DWI corresponding to decreased ADC (not shown) in the splenium and posterior body of the corpus callosum (not shown).

(Filename: TCT_1528_PictureExamples.JPG)

1076

Cochlear Implantation: Current and future roles of imaging before, during, and after implantation.

N Walker[1], N Pham[1], L Ledbetter[2]
[1]UCLA, Los Angeles, CA, [2]David Geffen School of Medicine, Los Angeles, CA

Purpose

Background: Sensorineural hearing loss (SNHL) is a widely prevalent disability resulting from the degeneration or absence of cochlear hair cells, which inhibits the conversion of acoustic energy into action potentials that are further processed. Since introduced in 1985, cochlear implants (CI) have revolutionized the treatment and rehabilitation of severe or profound SNHL. Cochlear implants are surgically implanted devices with an external microphone and sound processor that convert sounds into electrical signals. These signals are transmitted to the internal electrode, which directly stimulates the spiral ganglion of the cochlear nerve bypassing nonfunctional cochlear hair cells. Computed tomography (CT) and magnetic resonance imaging (MRI) play an essential role in the work up of CI candidates, intra-operative placement, and evaluation of post-operative complications and programming strategies.
Educational objectives: This exhibit will provide a literature and case-based overview of the indications, technology, and standard surgical technique for cochlear implantation. The viewer will become familiar with the CT and MRI findings that may preclude CI surgery or modify the surgical approach. Post-operative appearances with complications will be addressed.

Materials and Methods
N/A
Results
N/A
Conclusions
Key issues: Pre-operative imaging is central in the identification of inner ear variant anatomy or malformations such as cochlear aplasia, incomplete partition, or otosclerosis. Such findings may contraindicate CI or require extensive surgical planning with the use of varying internal electrode lengths, split electrodes, or custom-made device components. Intra-operative radiography or rotational C-arm fluoroscopy are routinely used to assess electrode positioning. Flat-beam CT or conventional CT are often utilized in complex cases where 3-D images are helpful in identifying landmarks. Post-operative imaging is generally obtained when there is suspicion for CI malfunction. Appropriate CI positioning is critical for programming accuracy and improved audibility. Electrode translocation, bending or folding are immediate complications that should be identified. Conclusion: As the radiologist plays a pivotal role in the process of cochlear implantation, it is important to understand the use and limitations of imaging studies. The ongoing refinement and expanding usage of CI technology presents opportunities for multidisciplinary innovation to improve patient outcomes.

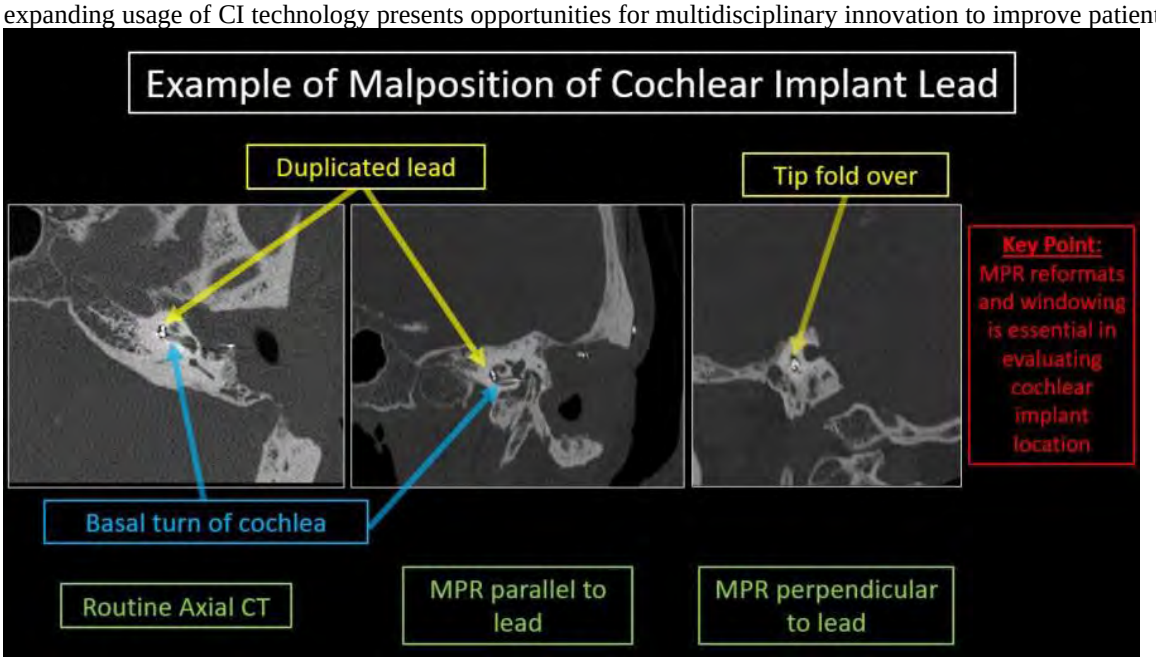

(Filename: TCT_1076_CIexample.JPG)

111
Cochlear implantation: surgical approach and a surgeon's perspective of the pre-operative CT
S Sharma[1], V Gautam[2]
[1]Mayo Clinic, Scottsdale, AZ, [2]Synergy Radiology Associates, Houston, TX

Purpose
Preoperative CT of the temporal bone is an integral part of surgical planning prior to cochlear implantation. In addition to ruling out the pathologies, an important role of pre-operative study is to evaluate the anatomy of the temporal bone and assess any variants along the surgical path. These variants may influence the level of the difficulty in accessing the round window or even necessitate an alternate approach to gain adequate exposure to the round window. A clear understanding of the surgical approach and the various challenges surgeons face during the surgery will enable us to provide an adequate interpretation for these studies.
Materials and Methods
1. Explain the steps of cochlear implantation with attention to the surgical approach to the round window/cochlea: a. Cortical mastoidectomy. b. Posterior tympanotomy c. Round window identification and cochleostomy. 2. Describe the pertinent anatomy of T-bone with respect to the surgical approach to the round window/cochlea including degree of mastoid pneumatization, position of the mastoid tegmen/temporal dura, sigmoid sinus position, high riding jugular bulb or dehiscence, and facial nerve course. 3. Provide an easy pictorial description of variants and why we need to evaluate and report them.
Results
N/A
Conclusions
Cochlear implants are used to treat sensorineural hearing loss and preoperative T-bone imaging is an integral part of surgical planning. Aided with a good understanding of the procedure and relevant anatomy as well potential situations which preclude surgery or require modifying standard surgical approaches, we can provide adequate information to our surgical colleagues and improve patient care in general.

1531

Common and Uncommon entities presenting as pineal region mass with histopathology correlation; a case based review.

H Sawhney[1], S Khanpara[2], R Patel[1]

[1]The University of Texas Health Science Center at Houston, Houston, TX, [2]University of Texas MD Anderson Cancer Center, Houston, TX

Purpose

A wide range of neoplastic and non-neoplastic processes can be seen in the pineal region. The common pineal region masses include pineal cyst, pineal germ cell tumors, and pineal parenchymal tumors (pineocytoma, pineoblastoma. Some uncommon masses are also seen in the pineal region including but not limited to pineal region meningioma, pineal metastasis, pineal hemagioblastoma, pineal glial neoplasms etc. An understanding of CT imaging characteristics such as density of the mass lesion, presence and absence of calcification, and the distribution of calcification as well as MRI characteristics such as presence or absence of restricted diffusion, presence or absence of cystic component and the intensity of enhancement can help a radiologist narrow the differential diagnosis and sometimes provide a definitive diagnosis for the clinicians; which can be further helpful for the management and to avoid unnecessary surgery in the setting of pineal germ cell tumor. At the end of our exhibit, the viewer will become familiar with the imaging and histopathologic characteristics, clinical presentation, and help them provide a narrower and more precise differential diagnosis.

Materials and Methods

1. To provide illustrative neuroimaging anatomy of the pineal region. 2. To illustrate key neuroimaging and histopathologic features of common and uncommon pineal region masses as a case based review. 3. To provide a clinically driven and image-rich interactive quiz featuring spectrum of masses involving the pineal region.

Results

We performed a HIPAA-compliant retrospective review of our institution's radiology databases with keywords of "pineal", "masses". Additionally, a review of the current medical literature was performed. The spectrum of masses seen in the pineal region in our institute will be presented with pertinent clinical history, detailed clinical symptoms and exam findings followed by quiz format Neuroimaging presentation with answers/discussion highlighting key features of differentiation between these masses. A brief self-quiz at end will conclude the exhibit.

Conclusions

This exhibit will focus on how imaging characteristics and clinical presentation can be used to narrow the differentials in the pineal region masses.

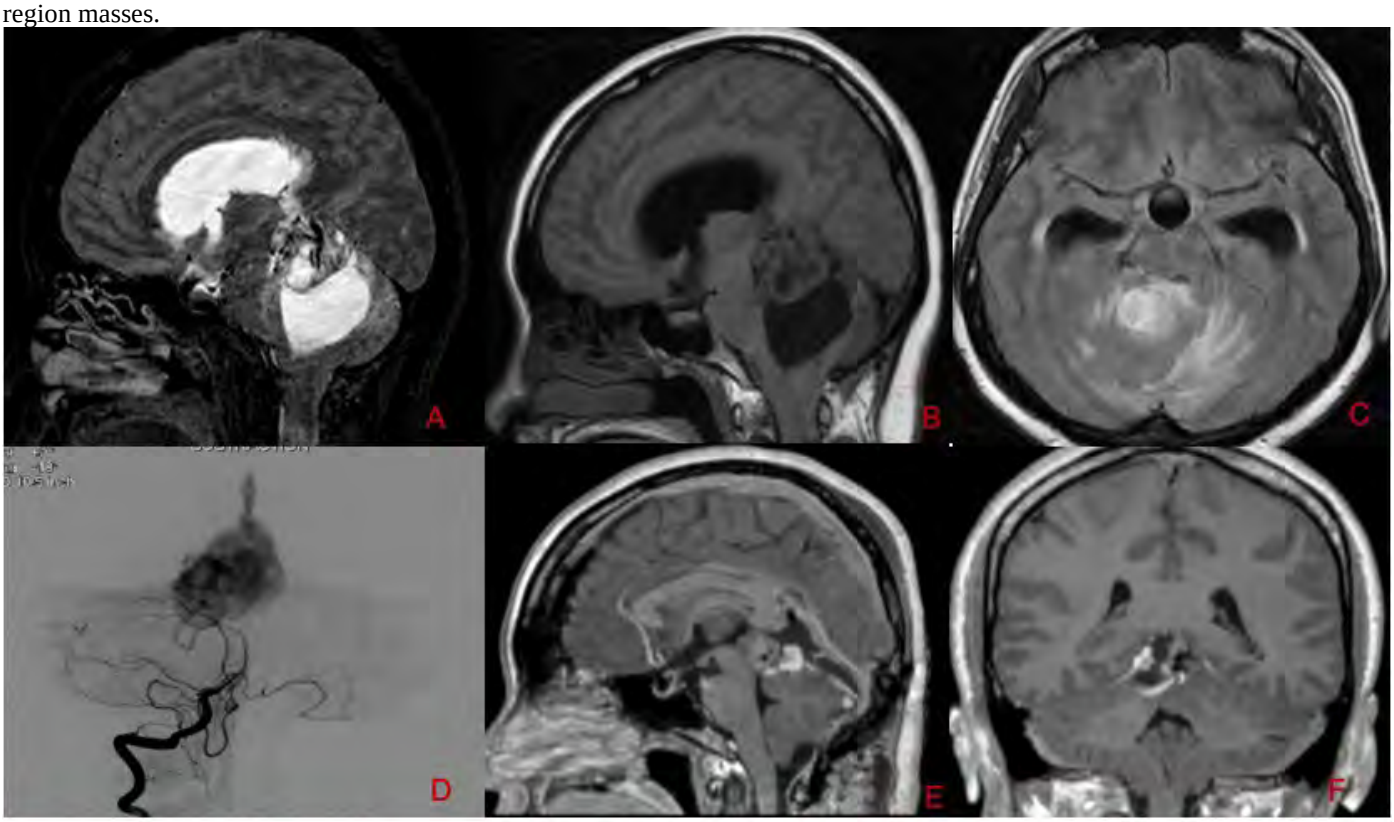

32 years old pregnant female patient presenting with altered mental status. Brain MRI without contrast (A-C) demonstrates a complex solid cystic pineal region mass effacing the 4th ventricle and resulting in obstructed supratentorial hydrocephalus. Angiography co-relation (D) demonstrated intense blush. Post resection MRI with contrast demonstrates subtotal resection of the mass with small residual enhancing nodule within a resection cavity. Histopathology co-relation confirmed the diagnosis of a pineal region hemagioblastoma.

(Filename: TCT_1531_Picture5.jpg)

1142

Common Blind Spots and Interpretive Errors of the upper Aerodigestive Tract Imaging

A Paydar[1], S Saith[2], L Hacein-Bey[3], A Ozturk[4], M Bobinski[3], O Raslan[3], B Haas[5], J CHANG[3], V Ivanovic[6], J Huynh[7], R Assadsangabi[8]

[1]University of Califronia-Davis, Sacramento, CA, [2]UC Davis Medical Center, Redondo Beach, CA, [3]UC Davis, Sacramento, CA, [4]UC Davis Medical Center, Sacramento, CA, Folsom, CA, [5]UC Davis, sacramento, CA, [6]UC Davis Medical Center, Sacramento, CA, [7]University of Cincinnati, Cincinnati, OH, [8]University of California Davis, Sacramento, CA

Purpose

N/A

Materials and Methods

Imaging plays a pivotal role in the diagnosis and staging of many diseases in the aerodigestive tract. A wide variety of pathologies and the anatomic complexity contribute to making this area susceptible to interpretational pitfalls and perceptual errors(1). Recognition of these blind spots in aerodigestive tract may help radiologists in preventing perceptual errors.

Results

We present a case based pictorial review of blind spots and common interpretive errors in the aerodigestive tract. Categorization of blind spots and common interpretive errors will be performed based on review of previous studies, authors' experience, and institutional review of internal and outside reports' misses.

Conclusions

A broad spectrum of pathologies can affect the upper aerodigestive tract from the oral cavity to the upper esophagus which sharing similar imaging features. Misinterpretation of neck findings on imaging is a common problem. The previous studies showed that after reinterpretation by a specialized head and neck radiologist, changes in cancer staging or management occurred in 38%–56% of cases (2,3). There are certain anatomic regions within the neck where a radiologist is more prone to make perceptual errors, called "blind spots" in this review. The aerodigestive tract is one of the most common locations of clinically significant errors (4). The aim of this exhibit is to review common diagnostic errors, provide an outline for blind spots, and present an imaging check list for interpretation of upper aerodigestive tract imaging. These checkpoints can help radiologists prevent errors during routine reporting sessions while maintaining work efficiency and accuracy.

1113

Complications After Radiation Therapy for Skull Base Tumors and Head and Neck Malignancies: Imaging Review and Characteristic Features to Help Differentiate Post Treatment Changes From Tumor Recurrence

N Nagornaya[1], D Lehmkuhl[2], G Saigal[1], R Kuker[3], R Bhatia[1]

[1]Jackson Memorial Hospital/University of Miami, Miami, FL, [2]Jackson Memorial Hospital, Miami, FL, [3]University of Miami Health System/Jackson Memorial Hospital, Miami, FL

Purpose

The aim of this presentation is to present a pictorial review of typical imaging findings of common and uncommon complications after radiation therapy for skull base tumors and neck malignancies, and emphasize important imaging features helpful in differentiating therapy related changes from recurrent malignancy and metastatic disease.

Materials and Methods

To educate radiologists on important imaging features helpful in differentiating therapy related changes from recurrent malignancy and metastatic disease.

Results

Retrospective multimodality (CT, MRI, PET/CT) imaging review evaluated various cases of radiation induced complications in patients that received radiotherapy for head and neck malignancies and skull base tumors. Imaging findings were correlated with pertinent medical and treatment history and pathology.

Conclusions

Results: The most common types of radiotherapy will be discussed followed by a pictorial review of cases of radiation induced complications. We will demonstrate characteristic examples of radiation induced pathology after skull base and neck radiotherapy including cases of osteoradionecrosis of the cervical spine, mandible, skull base, and temporal bone; soft tissue necrosis of the reconstruction flaps, masticator space, and TM joint; chondroradionecrosis of the larynx; and secondary radiation-associated malignancies. Radiation induced intracranial complications after skull base and neck radiation, such as radiation induced cranial neuropathy, cerebral radionecrosis, and radiation induced vasculopathy will also be presented. The essential imaging findings, time of occurrence after radiation exposure, pathophysiology, and relevant clinical history will be discussed in detail. We will highlight imaging characteristics which can be used to help differentiate between radiation induced complications and recurrent or metastatic disease. Conclusion: Although radiation therapy remains a main treatment option, either along or often in conjunction with chemotherapy and surgery in patients with skull base tumors and head and neck malignancies, both local complications and secondary neurotoxicity occur frequently and failure to recognize these complications can lead to poor patient management. Radiologists should not only be aware of these complications, but also be able to differentiate these from recurrent malignancy to help provide optimal patient care and management.

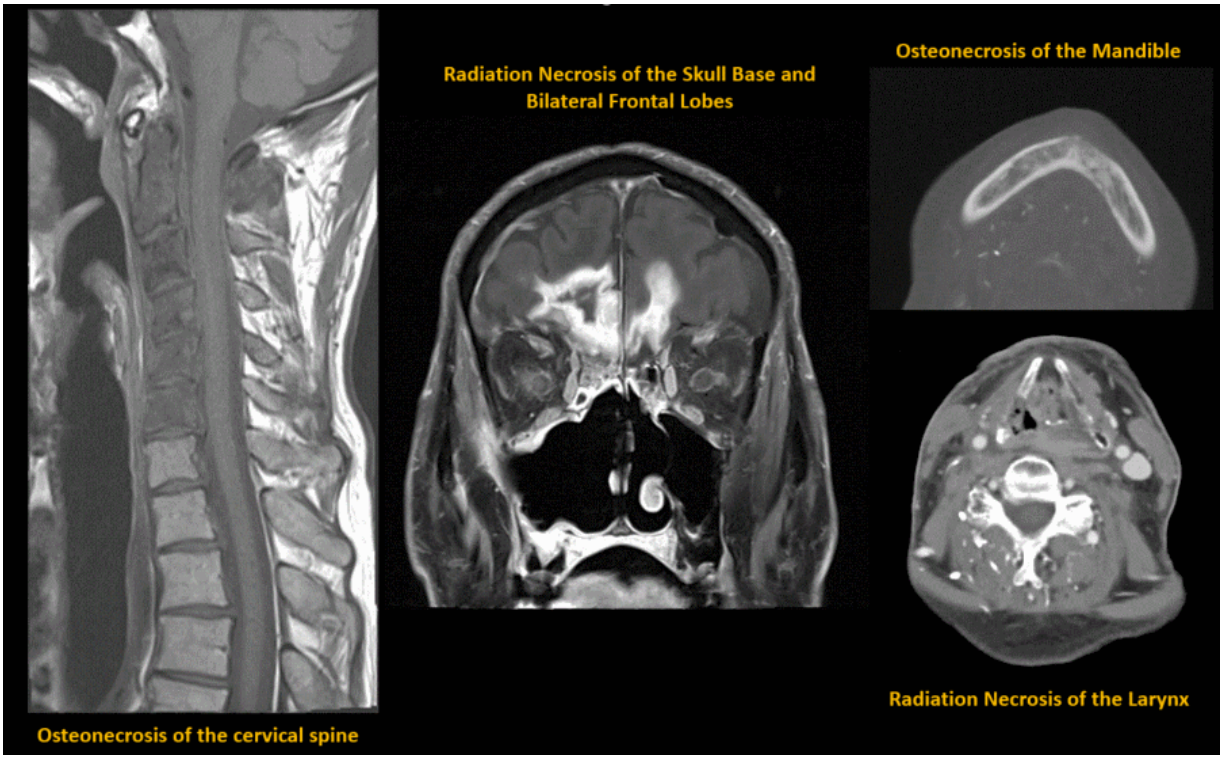

(Filename: TCT_1113_Capture.GIF)

1084

Congenital Cochleovestibular Anomalies in Three Dimensions: Improved Visualization for Accurate Classification

H Bueno[1], E Nimchinsky[2]
[1]Rutgers New Jersey Medical School, Newark, NJ, [2]Rutgers University, Newark, NJ

Purpose

Hearing loss is the most common neonatal sensory abnormality, affecting 1.1 per 1000 newborns (Chen and Oghalai., 2016). 39% of newborns with sensorineural hearing loss (SNHL) have abnormalities on CT or MRI (Mafong et al., 2002)). The nature of these abnormalities will affect treatment options, which include use of hearing aids, cochlear implants, and auditory brainstem implants. An organized approach to the examination of the inner ear allows the reader/interpreter to determine the features that allow for a classification of these abnormalities. In general, insults during earlier embryologic development of the membranous labyrinth from the otic placode will result in more severe features, whereas late insults may result in minimal changes. This sets the stage for a classification of inner ear abnormalities (Sennaroğlu and Bajin, 2017). Accurate characterization and subsequent classification require a thorough understanding of this complex anatomy. This is an area with which trainees frequently struggle, in part due to the complexity of 3-dimensional structures being taught using single-plane images or two-dimensional illustrations. With this in mind, we have collected a series of cases that spans the spectrum of abnormalities, mild to severe, and present interactive 3D renderings of the labyrinth to help conceptualize them. Educational Objectives • Overview of normal inner ear anatomy with CT and MRI and interactive 3D renderings • Present cases ranging from complete labyrinthine aplasia to cochlear aperture abnormalities with corresponding CT images and interactive 3D renderings • The viewer should be able to manipulate the 3D renderings to aid in the conceptualization of these abnormalities

Materials and Methods

N/A

Results

Clinical information was obtained from the medical record. Three-dimensional renderings of the membranous labyrinth were generated from 0.625 mm high resolution slices through the temporal bone. A third party program was utilized to generate 3D objects as STL files to permit interactive manipulation of the objects.

Conclusions

N/A

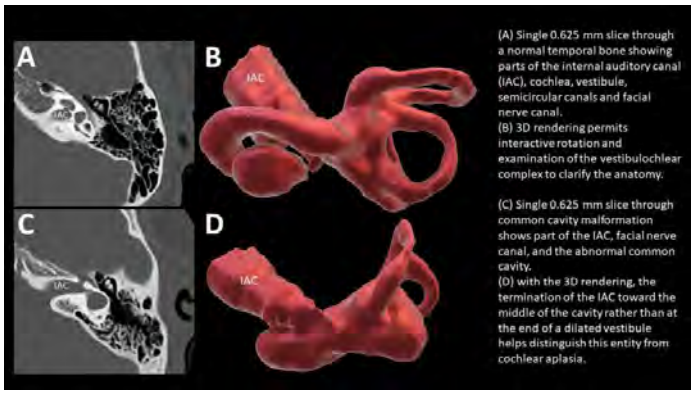

(Filename: TCT_1084_Slide1.JPG)

1132

Contribution Of PET/MRI In Glioma Management: Focus On Amino-Acid Tracers

N Soni[1], J Saini[2], S ELLIKA[3], J Almast[4], R Mangla[5], M Ora[6], S Puri[7], P Rana[8], A JENA[9], S Meyers[10], C Nagaraj[11]

[1]University of Rochester URMC, Rochester, NY, [2]NATIONAL INSTITUTE OF MENTAL HEALTH & NEURO SCIENCES, BANGALORE, India, [3]UNIVERSITY OF ROCHESTER MEDICAL CENTER, ROCHESTER, NY, [4]University of Rochester, Rochester, NY, [5]Upstate Medical University, Syracuse, NY, [6]SGPGIMS, LUCKNOW, Haryana, [7]URMC, Rochester, NY, [8]Indraprastha Apollo Hospitals, New Delhi, New Delhi, DC, [9]Indraprastha Apollo Hospitals, New Delhi, DE, [10]University of Rochester Medical Center, Rochester, NY, [11]National Institute of Mental Health and Neurosciences (NIMHANS), Bengaluru South, Karnataka

Purpose

Differentiation of "tumor progression" and "treatment-related changes" is still challenging, and to date, no single technique provides reliable detection of glioma recurrence. Contrast-enhanced MR with and without perfusion imaging is commonly used for glioma surveillance. Recently, The Response Assessment in Neuro-Oncology working group recommended additional AAs-PET for posttreatment evaluation of brain tumors. The AATs show low gray matter uptake and a high tumor-to-background ratio, better suited for delineating tumor extent, treatment planning, and follow-up. 11C-MET is the most studied and validated AAT. Several studies have reported variable sensitivities (66%–91%) and specificities (60%–100%) to differentiate between TR and RN. [18F] FDOPA is an ideal radiotracer with a longer half-life, high glioma uptake, and a low background signal. FET-PET has shown diagnostic performance similar to FLT and 11C-MET in differentiating benign changes from recurrence. Integrated PET/MRI studies have shown a strong correlation by providing complete anatomic, functional, and metabolic information of tumors at a single point in time.

Materials and Methods

PET/MRI with amino-acid tracers (AATs)-11C-MET, [18F] FET, and [18F] FDOPA has shown significant impacts in gliomas surveillance. This educational exhibit aims to provide a brief introduction of the different PET-tracers with a specific focus on AATs and a practical overview of the clinical applications of AAs-PET/MRI for glioma management, which will be helpful to neuroradiologists.

Results

We will discuss the existing published data and our limited experience about AAs-PET/MRI including their strengths, limitations, challenges, future perspectives, and technical improvements in the setting of posttreatment gliomas.

Conclusions

According to the available data and our experience, it is apparent that the combined use of AAs-PET and perfusion MR imaging improves the overall diagnostic accuracy for earlier detection of recurrence.

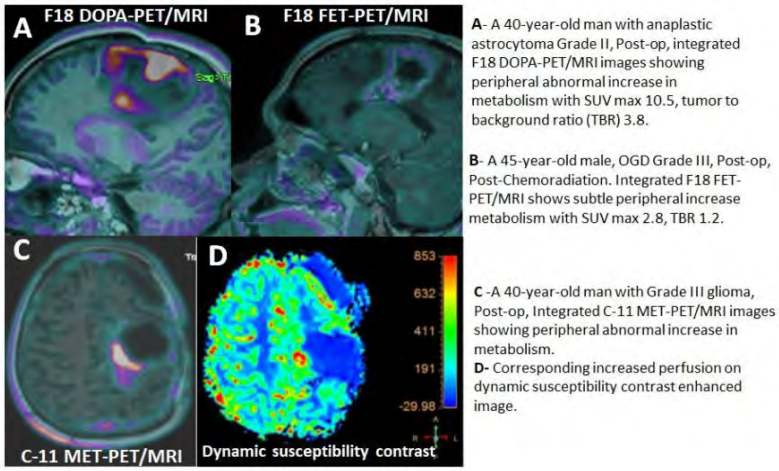

(Filename: TCT_1132_ASNR2022_abstract.jpg)

1009

CPA/IAC Lesion Neuroimaging Review: The Many Faces of Vestibular Schwannomas and Beyond

S Aktan[1], G Carpenter[1], B Ploussard[1], S Ramasamy[1], M Nuru[2], D Anderson[3], A Mallik[1]

[1]Loyola University Medical Center, Maywood, IL, [2]Loyola Medical Center, Chicago, IL, [3]Loyola University Medical Center - Strich School of Medicine, Maywood, IL

Purpose

Cerebellopontine angle (CPA) and internal auditory canal (IAC) lesions are relatively common making up 6-10% of all intra-cranial lesions. The varied imaging appearances of vestibular schwannomas (VS) and the plethora of other possible lesions in this region, however, may create diagnostic difficulty for the radiologist. This interactive presentation will concisely review CPA/IAC lesions, key distinguishing imaging features of these lesions, and allow the learner to test their knowledge with challenge cases. Summary of presentation: We propose an image-rich educational exhibit on CPA/IAC lesions using techniques such as embedded series and click on/off segmentation to take full advantage of the electronic format. The presentation is intended to be beneficial to both trainees and experienced radiologists, and will include multiple pathology proven examples of the varied imaging characteristics of VSs since they are the most common CPA/IAC lesion. There will be a focus on tumor morphology, such as tumor shape and centering at the porus acusticus. Atypical VS features, such as those with cystic components and microhemorrhage will be presented. Pertinent findings that a surgeon would like included in the radiologist's report of a VS, such as the cerebrospinal fluid fundal cap sign, high riding jugular bulb and nerve of origin (if distinguishable), will be included. This presentation will touch on additional VS research topics, such as cochlear FLAIR signal changes to assess hearing preservation. A review of the imaging appearance of CPA meningiomas will also be provided, with a specific focus on the contrast between their appearance and that of VSs. For example, this exhibit will highlight that meningiomas tend to be asymmetric to the porus acusticus, less commonly enter the IAC, may calcify, and can cause hyperostosis of the adjacent bone. Less common CPA lesions will also be exhibited such as aneurysms, lipomas, and epidermoid cysts, as well as CPA mimics such as intra-axial tumors, endolymphatic sac tumors, and cerebellomedullary lesions, with examples provided. The final portion of the exhibit will showcase interactive cases for learners to apply their new knowledge. Educational objectives: 1. Compose a targeted but comprehensive differential diagnosis for CPA/IAC lesions 2. Recognize the imaging features of VSs and other common CPA lesions such as meningiomas 3. Apply this knowledge to make diagnoses in challenge cases

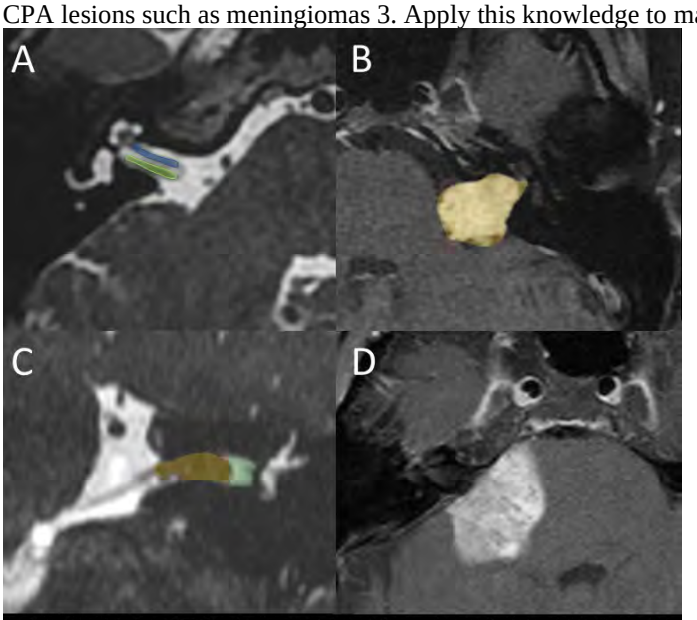

A. Axial FIESTA (fast imaging employing steady state acquisition) of a normal internal auditory canal highlighting the cochlear nerve (blue) and the inferior vestibular nerve (green). B. Axial T1 post contrast with fat saturation demonstrating the classic ice-cream cone shape of a vestibular schwannoma (yellow). C. Coronal FIESTA demonstrating a vestibular schwannoma (yellow) with a cerebrospinal fluid fundal cap (green). D. Axial T1 post contrast with fat saturation demonstrating an enhancing brainstem glioma mimicking a cerebellopontine angle mass.

(Filename: TCT_1009_VSabstractfigure300.jpg)

216

Craniocervical Junction: A Case Based Approach of Ligamentous Injury with Anatomic Review

B Larsen[1], A Svec[2], D Gridley[3]

[1]University of Utah, Cottonwood heights, UT, [2]Creighton University - Arizona, Phoenix, AZ, [3]Creighton University - Arizona, Paradise Valley, AZ

Purpose

Summary: The craniocervical junction contains complex transitional anatomy between the skull base and spine. The craniocervical ligaments providing structural support to this region and protection to critical structures such as the spinal cord, vasculature, and cranial nerves. This exhibit aims to demonstrate ligamentous injury on MRI and review normal anatomy. Objectives: • Identify

craniocervical ligamentous injuries on MRI. • Identify the anatomy that makes up the craniocervical junction. • Understand the importance and function of the craniocervical ligaments.

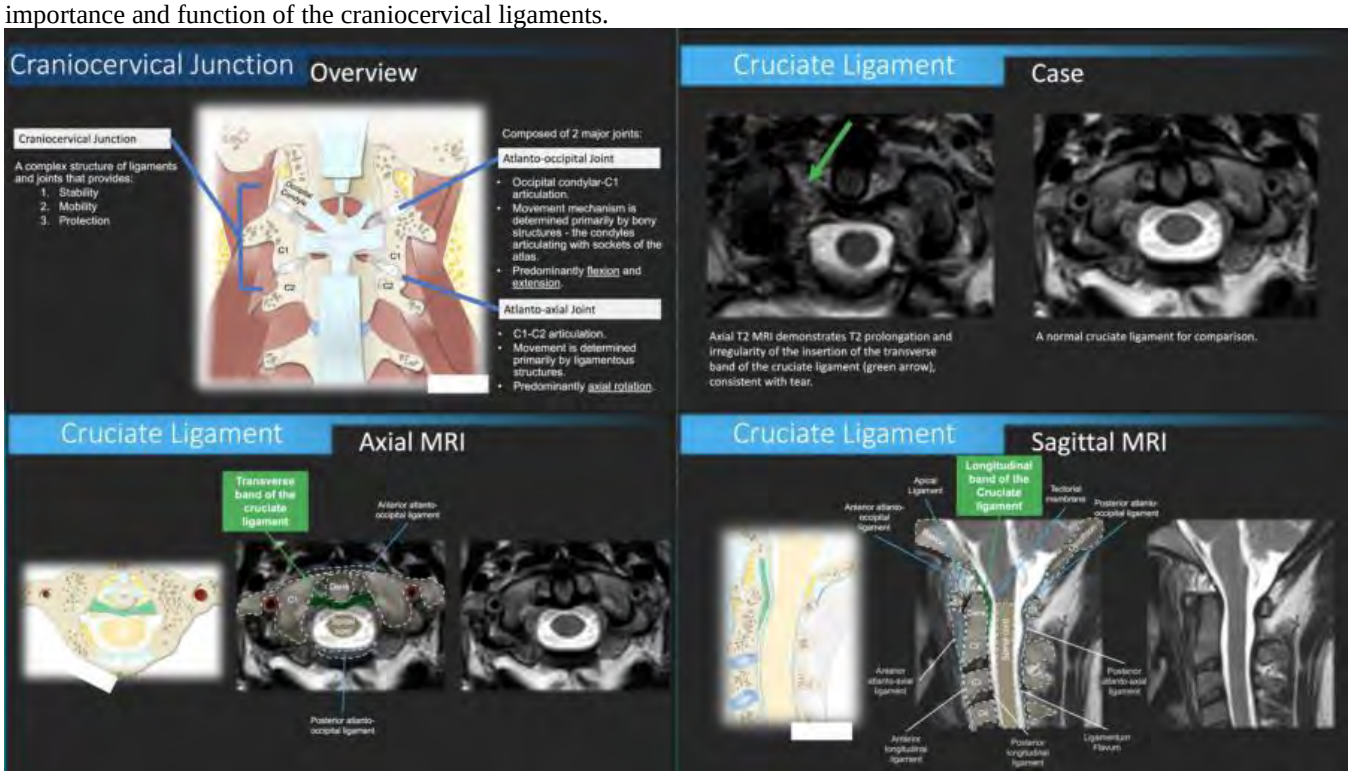

(Filename: TCT_216_ASNRAbstract2022.jpg)

158

Craniopharyngeal Canal Revisited: Role of High Resolution Imaging

A Udare[1], M McClure[2], K Shekdar[3]

[1]Thomas Jefferson University Hospital, Philadelphia, PA, [2]Childrens Hospital of Philadelphia, Philadelphia, PA, [3]Children's Hospital of Philadelphia, Philadelphia, PA

Purpose

Objectives: 1. To understand the complex anatomy and embryogenesis of the craniopharyngeal canal (CPC) and the associated pathologies. 2. To elucidate the role of high-resolution MR imaging in evaluating the CPC anomalies 3. To demonstrate the spectrum of abnormalities associated CPC spectrum and anomalies

Materials and Methods

Learning Points 1. Anatomy and embrogenesis of the craniopharygeal or hypophyseal canal-various theories 2. Different clinical presentations of persistent CPC: pituitary dysfunction, nasopharygeal mass, recurrent meningitis, associated anomalies etc. 3. Anomalies associated with CPC 4. Classification of CPC pathologies 5. MRI sequences and planning: role of 3D SPACE and CISS sequences 6. Correlation with high-resolution skull base CT 7. Overall role of imaging-what the clinician needs to know

Results

Discussion: •Review of the CPC anatomy and embryogenesis to understand the basis of the CPC pathologies and clinical implications. •Role of imaging, in particular high-resolution MRI imaging for assessing the type of CPC and associated anomalies

Conclusions

Diagnosis of the imaging spectrum of persistent craniopharyngeal canal accurately is essential to evaluate lesions requiring surgery, identify patients with potential pituitary dysfunction, and avoid iatrogenic hypopituitarism or CSF leak during surgical resection of nasopharyngeal masses or even nasopharyngeal swab testing for COVID infection.

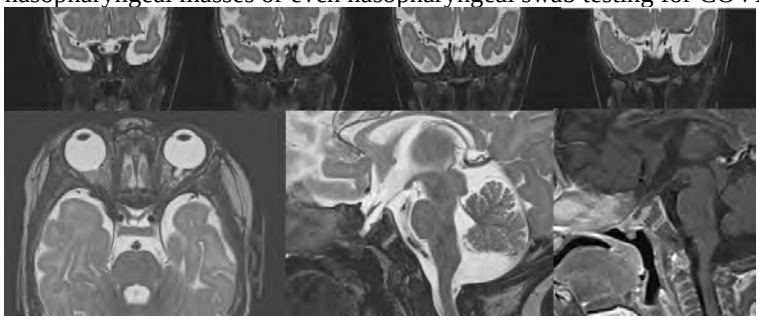
(Filename: TCT_158_CPC.jpg)

586

Craniotomies: A Pictorial Review of What the Radiologist Needs to Know

R Huang[1], C Lee[2], R Cua[2], N Kamal*[3], J Go[1], J Acharya[1]

[1]Keck School of Medicine of USC, Los Angeles, CA, [2]LAC+USC Medical Center, Los Angeles, CA, [3]Vanderbilt University, Nashville, TN

Purpose

Modern neurosurgery has made significant advancements in the last century due deeper understanding of neuroanatomy, innovations in imaging, and development of new neurosurgical techniques. Cranial surgery requires extensive planning and nuanced considerations when developing a tailored treatment plan for a patient. Neurosurgeons must balance multiple factors when developing an operative corridor, including but not limited to, type of lesion, size of lesion, goal of surgery, identification and avoidance of key neurovascular structures, and location of lesion. The cornerstone of a surgical plan is the craniotomy, or bony resection, followed by an intradural trajectory or route. Ultimately, the main goal of neurosurgeons when selecting their approach is to protect the normal anatomy while having sufficient exposure to the target lesion. In this exhibit, we will examine craniotomies from a neurosurgical perspective and demonstrate the various types in a pictorial review. We will review general principles driving neurosurgical decision making regarding cranial approaches. Additionally, we will review the most common cranial approaches, their indications, and the normal imaging appearance. For example, pterional, or frontotemporal, craniotomy is one of the most used surgical approaches for supratentorial lesions along the anterior and middle skull base. A subtemporal craniotomy is typically the preferred for access to the middle cranial fossa. For posterior fossa tumors, a retrosigmoid or suboccipital approach may be used. Finally, we will review some of the most common complications related to craniotomies and their imaging appearance, including but not limited to, hemorrhage, tension pneumocephalus, cerebrospinal fluid (CSF) leak, and infection (abscess, soft tissue infection, osteomyelitis).

Materials and Methods

To review general neurosurgical considerations and rationale when choosing a cranial approach To review the most common neurosurgical craniotomy approaches and their indications To review the normal imaging appearance of the most common craniotomies To review the most common complications related to craniotomies and their imaging appearance

Results

N/A

Conclusions

N/A

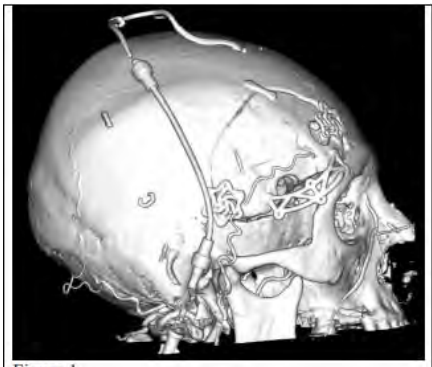

Figure 1.

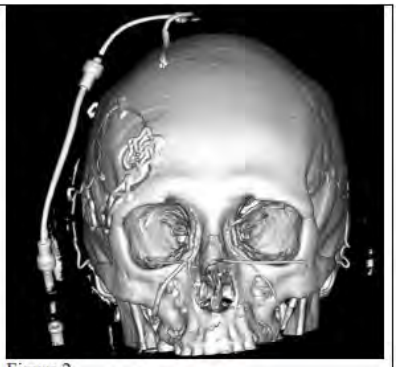

Figure 2.

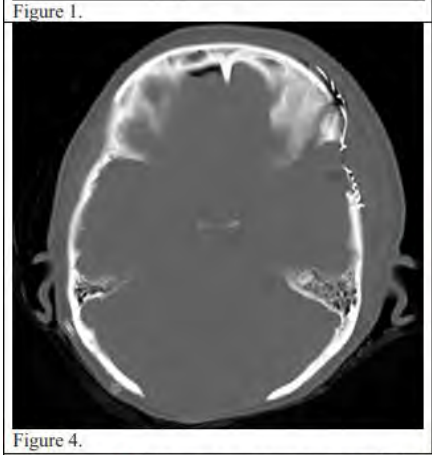

Figure 4.

Figure 3.

Figures 1-4. Clockwise beginning on the top left: (Figures 1-3) Lateral, anterior, and posterior views of a 3D reconstruction of post-operative calvarium performed on 3D post-processing software and (Figure 4) Axial views on bone window through the middle cranial fossa. This patient has a remote history of resected posterior fossa tumor as well as more recent resection of suprasellar mass. Images demonstrate a left pterional cranitomy as well as a suboccipital craniectomy. Also noted a shunt catheter through a left frontal burr hole as well as small volume pneumocephalus.

(Filename: TCT_586_RadImages.JPG)

1231

CSF, you should not be here! How to recognize CSF leak in CT-cisternography and CT-myelography images

M SHIBUYA[1], D Setuguti[2], M Calderaro[3], M Souza[4], R Pincerato[5]

[1]Hospital Samaritano, São Paulo, sao paulo, [2]Hospital Samaritano, São Paulo, Sao Paulo/SP, [3]Hospital Samaritano, sao paulo, sao paulo, [4]Hospital das Clínicas USP, sao paulo, sao paulo, [5]HOSPITAL SAMARITANO SP - UHG BRASIL, São Paulo, SP

Purpose

This pictorial essay aims to demonstrate the main locations and imaging findings of CSF leaks in CT-cisternography and CT-myelography.

Materials and Methods

Recognize the exact location of the CSF leaks in the radiologist's practice is important, once their non-diagnosis and inappropriate treatment lead to an increase in infectious complications, such as meningitis and intracranial abscesses (in cases of CSF leaks in the skull base) in addition to being decisive in the therapeutic success in cases of spinal CSF leaks, especially in refractory cases, with targeted epidural blood patch and surgical repair.

Results

We illustrate in a pictorial essay the main imaging findings of the cranial and spinal cerebrospinal fluid leakage in CT-cisternography and CT-myelography.

Conclusions

Most frequently, CSF leaks at skull base are located in the anterior cranial fossa, and it is necessary to look for extravasation of iodinated contrast especially in the lateral lamella of the cribriform plate. Other sites of bone fragility include the frontal sinus walls, sella turcica and sphenoid sinuses. In spinal CSF leaks, most of them are located in the thoracic spine and thoracolumbar transition, and their appearance varies from patient to patient and depends on the cause of the leak. The extravasation of iodinated contrast may have a broad base along the thecal sac or along the axilla of the nerve root (when related to meningeal diverticula), a extensive epidural CSF collection (associated a ventral dural tear), and, sometimes, associated a contrast medium of a paraspinal vascular structure along the lateral aspect of the vertebral body and early renal contrast on CT-myelography such as in CSF venous fistulas. We encourage radiologists to familiarize with these imaging findings, especially of CSF venous fistulas, which, although rare, have high surgical success rates when diagnosed.

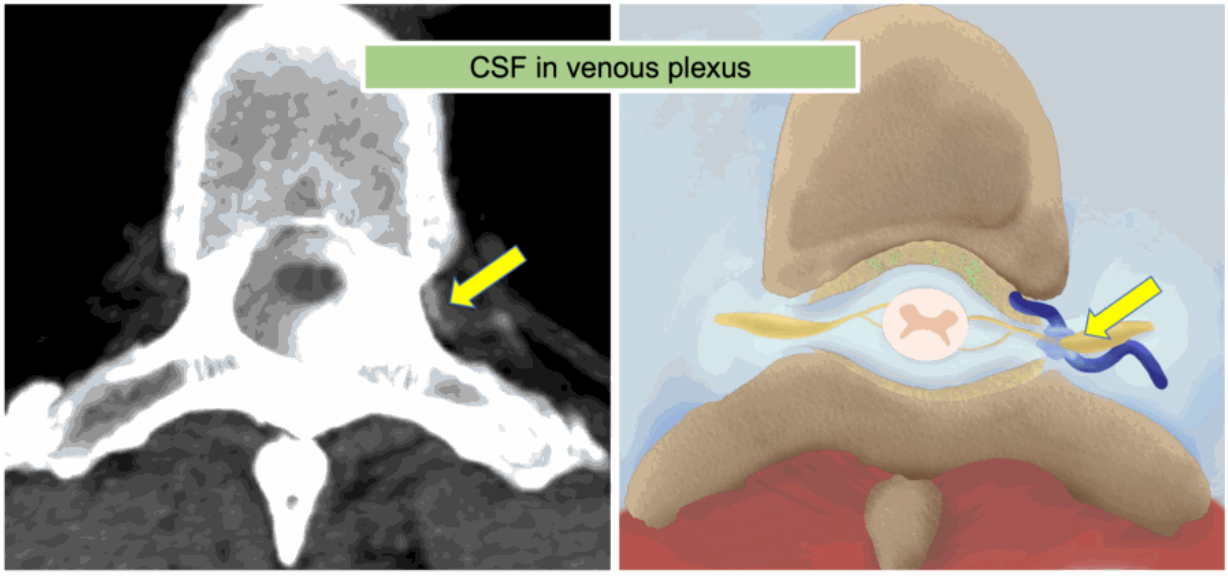

(Filename: TCT_1231_ASNR1.gif)

517

CT versus MR of the ear, when one would be preferred over the other and when they both needed?

A Hussien[1], R Yazdani[2], A Hussain[3]

[1]UT southwestern, Dallas, TX, [2]UT Southwestern, ., Dallas, TX, [3]University of Rochester medical center, Rochester, NY

Purpose

The most common modalities for imaging of the ear and temporal bone are CT and MRI. Each modality has its strengths and limitations. CT imaging provides bone details and MRI shows more soft tissue details. The indications of temporal bone imaging vary from a general question such as hearing loss and tinnitus to a more specific question to look for a mass such as schwannoma or glomus tumor. In this presentation we will shed the light on the various indications of ear imaging, what are the questions need to be answered?, which modality can do best do the job? and when it would be better to do perform both MR and CT to get an accurate answer.

Materials and Methods
In this educational presentation we aim to emphasize the importance of knowing the main or common indications for each ear imaging modality and what needs to be included in the report of the CT or MR of the temporal bone. So the audiences can be aware of each modality's limitations and strengths and have a reliable source for an accurate report that answers the clinician/ surgeon's question
Results
A list of the most common indications for temporal bone/ear imaging will be provided, the preferred modality used for each indication and the most important points need to be included in the report for each entity. We will also include some examples of the subtle findings that can be easy to miss.
Conclusions
It is important to have a clear understanding of the common scenarios and indications of imaging of the temporal bone / ear and the benefits of each modality. It is important to have an easy to review source that can serve as a guide of the important points needed to mention in each temporal bone imaging report and to help the radiologist answer the clinical questions and inquiries about the best modality for each entity.

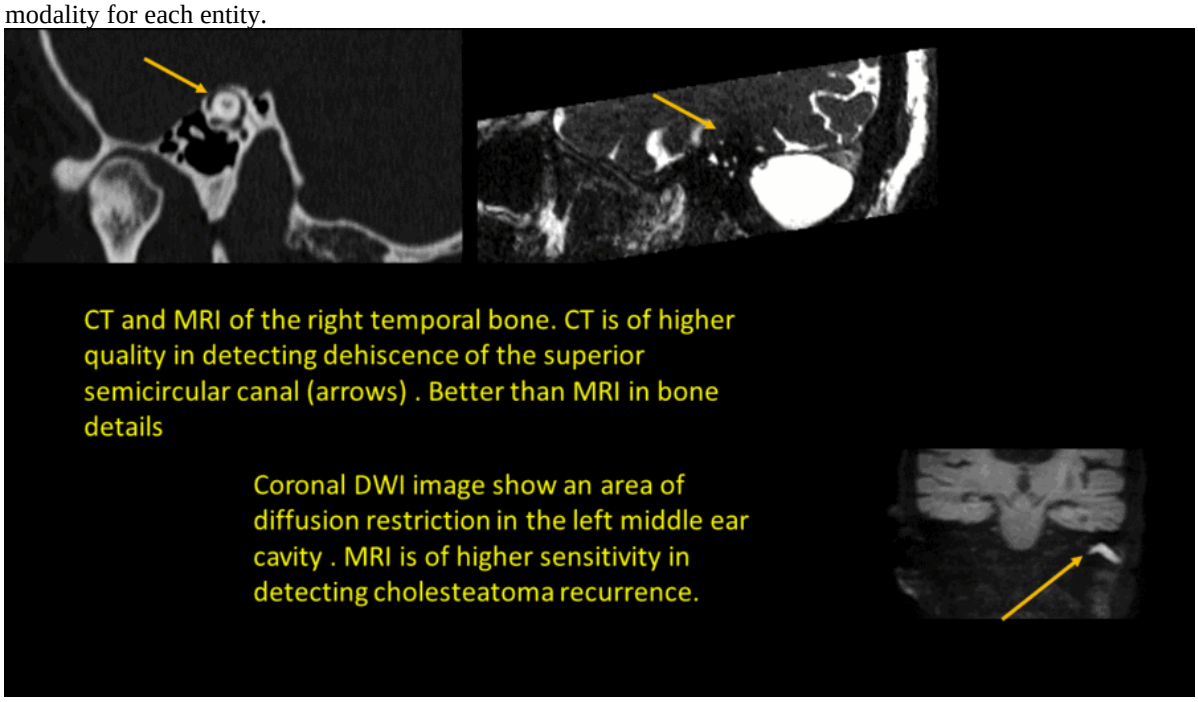

(Filename: TCT_517_Temporalbone.gif)

722
Developing an Eye for Globe Pathologies: A Pictorial Review.
D Yin[1], C LI[1], M Goldberg[1], W CHANG[1], P Annigeri[1]
[1]Allegheny Health Network, Pittsburgh, PA

Purpose
Using a case-based approach, this exhibit will review various common and uncommon pathologies affecting the globe, including their clinical presentations and imaging appearance. Normal anatomy of the globe will also be discussed.
Materials and Methods
It is important to be aware of both common and uncommon processes that can affect the globe as these may be evident not only on dedicated scans of the globe, but also on routine or emergent imaging obtained for other unrelated reasons. An understanding of the complex normal anatomy and the ability to identify pathologic findings allows the neuroradiologist to contribute valuable input to the patient's care and assist our clinical colleagues in triaging the acuity of these findings. The purpose of this educational exhibit is to provide a pictorial review of the normal anatomy of the globe, as well as review the numerous pathologic processes affecting it.
Results
Using representative case files, we will review the anatomy of the globe on CT and MRI. We will review a broad spectrum of common and uncommon pathologies affecting the globe, including: coloboma, staphyloma, ocular trauma, uveitis/scleritis, retinal detachment, choroidal detachment, ocular melanoma, ocular metastasis, silicone migration, and orbital compartment syndrome.
Conclusions
Evaluating globe pathology on imaging requires understanding of the complex normal anatomy and the numerous potential alterations that may occur. This exhibit will provide viewers with an in-depth pictorial review of both common and uncommon pathologies affecting the globe and their associated acuity. Figure: A) Acute right globe rupture with lenticular dislocation (arrow) in the setting of trauma on a non-contrast CT. There is trace retrobulbar hemorrhage as well (dotted arrow). B) Axial T1-weighted MRI showing an intrinsically hyperintense mass in the left globe (arrow), pathologically proven to be a uveal melanoma. C) Axial CT head showing

hyperdense silicone injection in the right globe (arrow) with migration posteriorly into the optic nerve (dotted arrow). D) Non-contrast axial CT of the orbits showing "guitar-pick" deformity of the right globe (arrow) with mild proptosis compatible with orbital compartment syndrome in a patient with sinonasal polyposis with superimposed infection and subperiosteal abscess (not shown).

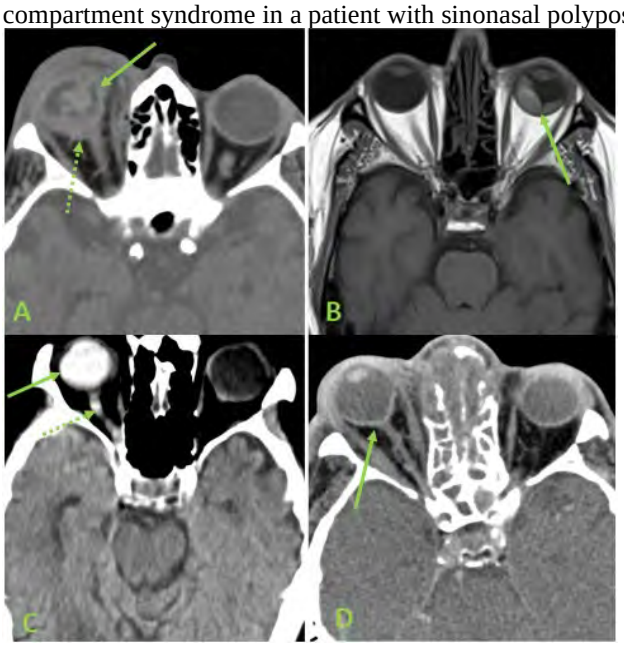

(Filename: TCT_722_globe.jpg)

1456

Differentiating Extracranial Neck Arterial Fenestrations from other Intraluminal Abnormalities

M Macey[1], B Albalooshy[1], J Small[1], A Schmidli[2], J Chang[3]

[1]Lahey Hospital & Medical Center, Burlington, MA, [2]Lahey Clinic, Burlington, MA, [3]Tufts University School of Medicine, Boston, MA

Purpose

Review a spectrum of intraluminal abnormalities involving the extracranial vertebral and carotid arteries, including fenestrations, webs, and dissections. Display selected CTA images of the respective vessel abnormalities, which may present perceptual challenges for the interpreting radiologist. Highlight useful imaging tips and tools to aid in accurate interpretation.

Materials and Methods

Fenestrations and webs are rare congenital abnormalities that can be seen within the extracranial vertebral and carotid arteries. These congenital abnormalities can share imaging characteristics with dissection, making differentiation on CTA difficult at times. Fenestrations are congenital abnormalities that carry little clinical significance, but differentiation from dissection and webs is important. Overtreatment of dissection can impose unnecessary cost and morbidity on patients. On the other hand, failure to identify a vascular web can lead to recurrent ischemic stroke.

Results

Tips to correctly differentiate extracranial neck vascular fenestrations from carotid dissections and webs are presented with the aid of various cases. Fenestrations are the result of incomplete early fetal fusion, characterized as having an extravascular lumen. Fenestrations can be further classified as window, hourglass, or funnel shaped. Similarly, what has often been referred to in the literature as septation, may represent a small aberrant fenestrations. Vascular webs are thin intraluminal membranes, which are often associated with ischemic stroke. Finally, dissections are acquired defects of the vascular intima. The classic CTA findings include a tapering intraluminal narrowing adjacent to the defect, which is secondary to the intimal flap.

Conclusions

It is important for imaging interpreters to be aware of the differentiating features of rare neck vascular fenestrations from the spectrum of other intraluminal abnormalities. These management implications of these varying entities are different. With the appropriate knowledge and interpretive tools, CTA can be used for reliable differentiation.

903

Differentiation Between Recurrent Tumor and Treatment Effect: An Educational Guide to Implementation of Perfusion MRI Fractional Tumor Burden Maps

A Verde[1], M Iv[1], T Massoud[2]

[1]Stanford University, Stanford, CA, [2]Stanford University School of Medicine, Stanford, CA

Materials and Methods

Differentiating recurrent tumor from treatment effect is challenging in brain tumor patients. Dynamic susceptibility contrast (DSC) perfusion MRI (pMRI) is a valuable tool to distinguish hypervascular tumors from hypoperfused radiation necrosis. We created a

clinically useful quantitative fractional tumor burden (FTB) mapping pipeline, which mitigates operator-dependent variability, generates perfusion data for each voxel within an enhancing volume, and outputs quantitative data for monitoring longitudinal changes.

Results

We comprehensively review and present our perfusion pipeline entailing DSC acquisition, postprocessing, and display of FTB maps.

Conclusions

When assessing treated brain tumors, the use of pMRI is critical in determining treatment response versus tumor progression. To optimize DSC acquisition and cerebral blood volume (CBV)/FTB calculation a half-dose preload of contrast agent is administered. The remaining half-dose of gadolinium is used for DSC, which we perform with a low flip angle (30 degrees). Using FDA-cleared software, we generate a T1 difference map of the enhancing tumor volume (from pre- and post-contrast images). Semi-automated segmentation is then performed by an operator (without the need for normalization to the contralateral hemisphere), and output standardized CBV and FTB maps are generated. FTB maps are created by using two defined standardized rCBV (sRCBV) thresholds (1.0 and 1.556): low FTB (sRCBV<1.0), intermediate FTB (sRCBV 1.0-1.556), and high FTB (sRCBV>1.556). Subsequently, voxels within each FTB class are assigned a color (low FTB-blue, intermediate FTB-yellow, high FTB-red) and displayed as a histogram and color-coded map overlaid on T1 postcontrast images. Using these cutoffs, voxels with low and high FTB are helpful to differentiate aggressive tumor from treatment effect. Intermediate FTB is less helpful because it represents varying admixture of both, which is then monitored at follow up imaging. FTB maps help to visualize and quantify tissue perfusion in each voxel of a contrast-enhancing lesion, which can help to distinguish tumor from treatment effects in previously treated brain tumors and has been shown to impact clinical-decision making. This presentation will outline steps for practical development and implementation of a workflow utilizing this clinically useful diagnostic tool.

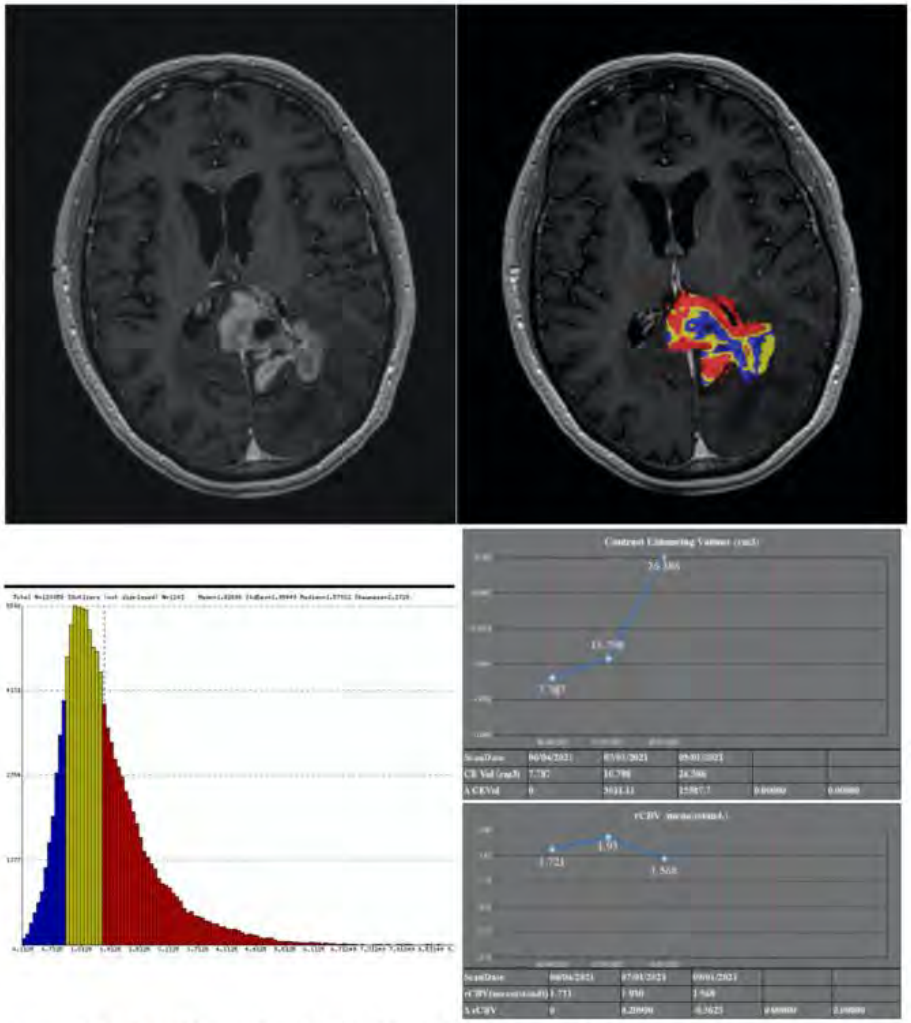

Figure 1. Fractional Tumor Burden (FTB) Pipeline. 61-year-old female with history of GBM status post resection and completion of chemoradiation three months prior, presenting with a recurrent enhancing mass in the treatment bed (**A**). The majority of enhancing voxels consisted of intermediate (yellow) and high (red) FTB (**B**), as confirmed on the histogram (**C**), features that are concerning for recurrent tumor/tumor progression. Longitudinal measurements of contrast enhancing volume and relative cerebral blood volume are shown on the independently generated graph **(D)**.

(Filename: TCT_903_Figure1_FTB_v5.jpg)

1072

Diffusion time is the essential factor for the contrast of diffusion-weighted MR imaging in clinical diagnosis.

M Hori[1]
[1]*Toho University Omori Medical Center, Tokyo, N/A*

Purpose

Diffusion time is an important factor in determining contrast in DWI and diffusion metric values. Neuroradiologists should be careful that the diffusion time of the DWIs they use for their diagnosis is appropriate.

Materials and Methods

Diffusion time is an important factor in determining contrast in diffusion-weighted images (DWIs), yet it is not often considered by neuroradiologists in clinical practice. However, changes in echo time (TE) during diffusion-weighted imaging often alter the diffusion time, resulting in changes in the resulting diffusion-weighted image and quantitative values such as apparent diffusion coefficient (ADC). We provide an educational pictorial and review of the basics of diffusion time and its impact on clinical diffusion magnetic resonance imaging(dMRI) and quantitative diffusion metric values.

Results

We review and demonstrate the basics of diffusion time and multiple DWIs and quantitative maps in clinical cases.

Conclusions

Diffusion time is an important factor in determining contrast in DWI and diffusion metric values. Neuroradiologists should be careful that the diffusion time of the DWIs they use for their diagnosis is appropriate.

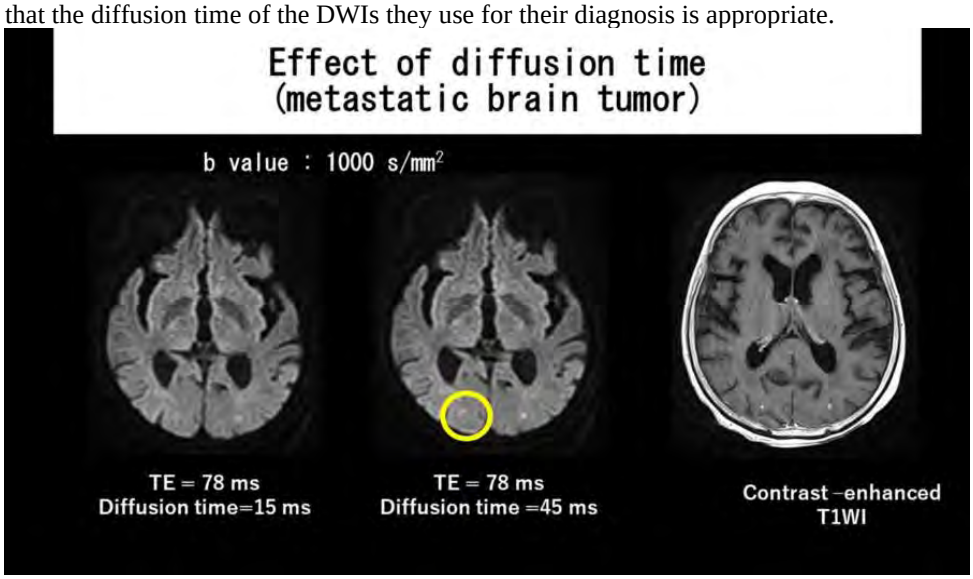

(Filename: TCT_1072_Figure.jpg)

986

Diffusion Weighted Imaging in the Spine: A Magic Key

M Shalaby[1], S Chaker[1], B Jaber[1], A Moawad[1], M Aslam[1], S Kushchayev[2], O Teytelboym[1]
[1]*Mercy Catholic Medical Center, Darby, PA,* [2]*Moffitt Cancer Center, Tampa, FL*

Purpose

Educational Objectives: 1- Illustrate the role of diffusion weighted imaging (DWI) in spine infectious, neoplastic, and inflammatory disease 2- Demonstrate the role of DWI in spine trauma and degenerative disease 3- Emphasize the role of DWI in spinal cord ischemia 4- Highlight the challenges of spine DWI acquisition 5- Discuss technical tips and considerations for protocol optimization for 1.5T and 3T MRI Table of Content: 1- Clinical applications of DWI in common spinal pathologies: -Infectious and inflammatory disease -Primary and metastatic spine tumors -Degenerative disease -Trauma -Spinal cord ischemia -Compression fractures -Demyelinating disease 2- Challenges of spine DWI acquisition 3- Protocol optimization with practical tips for improving spine DWI for 1.5T and 3T MRI

Materials and Methods

N/A

Results

N/A

Conclusions

N/A

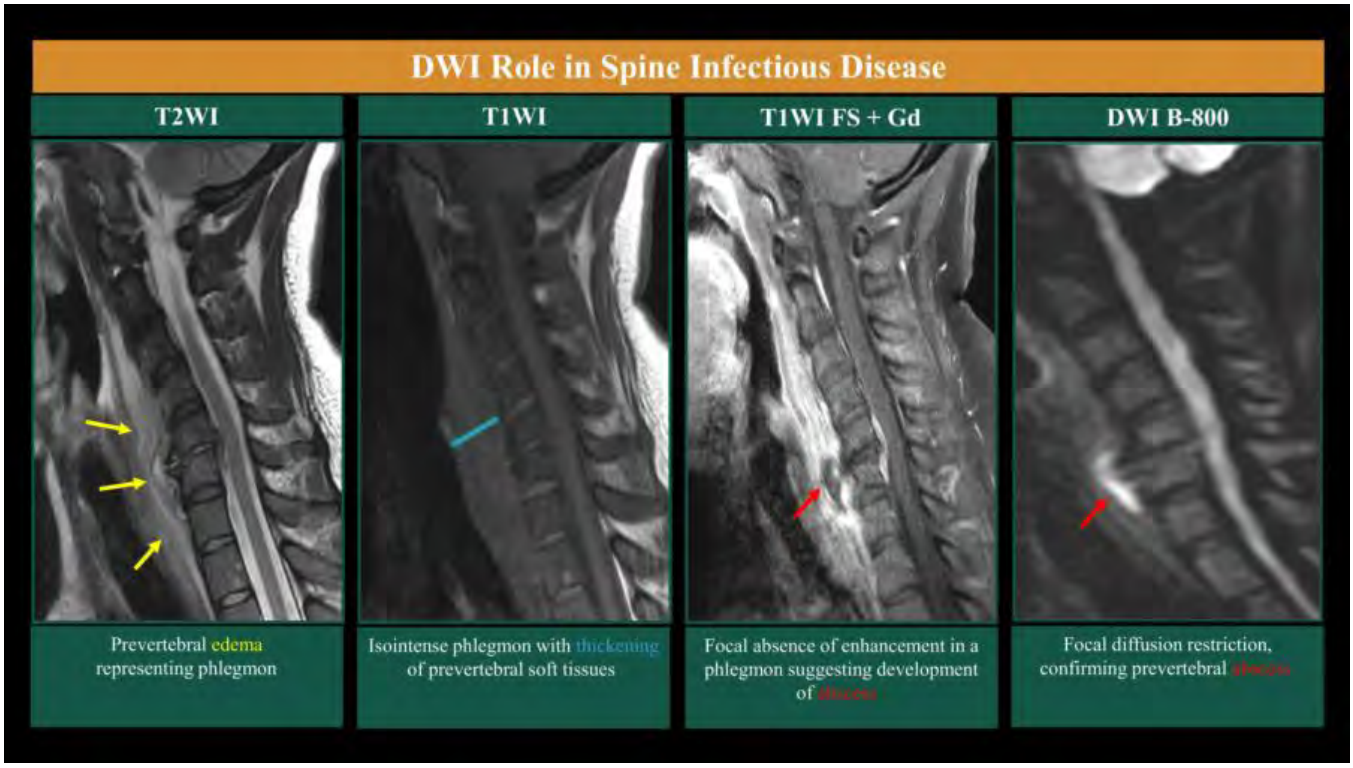

(Filename: TCT_986_DWICasefinal.jpg)

727

Distal Radial Artery (Snuffbox) Access for Neurointerventional Procedures

A Kuhn[1], J Singh[2], F Massari[3], K de Macedo Rodrigues[4], S Puri[5]

[1]N/A, N/A, [2]University of Massachusetts Medical Center, Worcester, MA, [3]UMass, Southborough, MA, [4]Greensboro Radiology, Greensboro, NC, [5]Currently at Univ. of Massachusetts Medical Center., Worcester, MA

Purpose

This educational exhibit will provide viewers with an overview of snuffbox access for neurointerventions. It will discuss important anatomic landmarks and showcase proper access technique. Viewers will learn about pitfalls and managing complications. The exhibit will discuss the importance of patient selection depending on distal radial artery vessel size, procedure to be performed and configuration of the aortic arch with origin of the great vessels. The exhibit will combine text descriptions, tables, photographs/illustrations for better visualization of the content. Case examples will show anonymized ultrasound and fluoroscopic images of patients treated via snuffbox access. Educational Objectives: - To learn a step-by-step approach of distal radial artery vascular access - To understand advantages and limitations of vascular access via the distal radial artery

Materials and Methods

To familiarize the viewer with the newly emerging vascular access site for neurointerventions and to share our experience on access strategy, identification of pitfalls and complication management.

Results

test

Conclusions

Distal radial artery access has gained acceptance as an alternative vascular access for neurointerventions. Knowledge of (vascular) anatomy and proper access/angiographic technique are important for successful interventions via this approach. Awareness of possible complications and ability to mitigate procedural risks, reduces potential harm to patients.

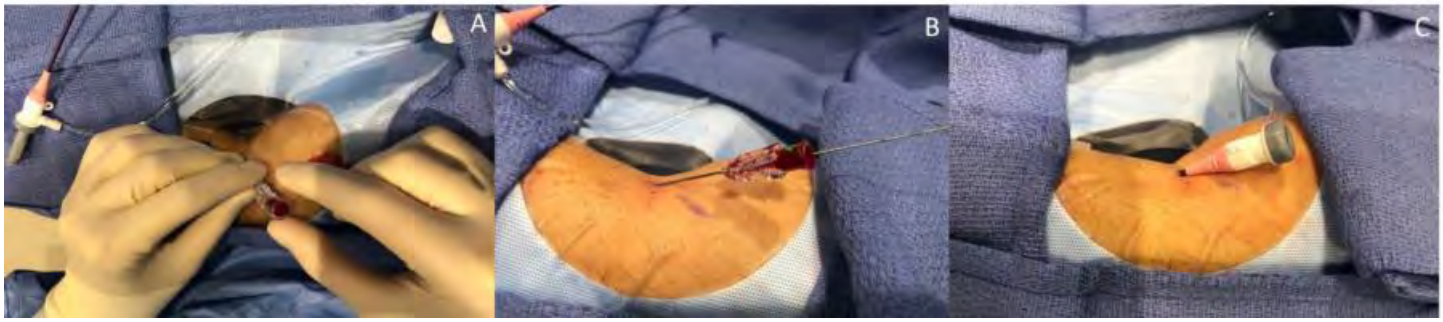

(Filename: TCT_727_Fig6.jpg)

1166

Don't be scared of the skull base: Tips and pearls on how to formulate differential diagnoses of skull base lesions

C Liang[1], C Wishka[2], N Miner[2], E Chu[2], E Kuan[3], E Kuoy[2]

[1]Department of Radiological Sciences, University of California Irvine, Orange, CA, [2]Division of Neuroradiology, Department of Radiological Sciences, University of California Irvine, Orange, CA, [3]Department of Otolaryngology, University of California Irvine, Orange, CA

Purpose

Background information: Skull base foramina are conduits for vital neurological structures and serve as routes of disease spread between the brain and maxillofacial structures. Skull base pathologies encompass a variety of etiologies including, but not limited to, infectious, autoimmune, and neoplastic processes. A fundamental understanding of challenging skull base anatomy is essential for radiologists to accurately characterize disease extent and to formulate a complete differential diagnosis, which can significantly impact clinical treatment. Education Objective/Purpose: After identifying key anatomy, various illustrative benign and malignant skull base pathologies will be reviewed. Imaging tips/pearls will be provided on how to narrow the differential diagnosis and how to distinguish benign from potentially malignant lesions when possible.

Materials and Methods

1. Review key skull base anatomy that are important to diagnosis, surgical planning, and treatment fields. 2. Present a case-based review of key skull base pathologies with an emphasis on image findings that help narrow the differential diagnosis. 3. Reinforce clinically important imaging features of skull base pathologies via interactive imaged-based quiz.

Results

A literature review on skull base lesions was performed. Case examples were obtained from our institutional database to create this case-based educational exhibit.

Conclusions

Table of Contents: Illustrative cases of key skull base pathologies presented in this educational exhibit will include the following: • Encephalocele • Inverted papilloma • Esthesioneuroblastoma • Squamous cell carcinoma • Juvenile nasopharyngeal angiofibroma • Invasive fungal sinusitis • Perineural spread of tumor • Schwannoma • Paraganglioma • Meningioma • Chordoma • Chondrosarcoma Conclusion: Radiologists can significantly aid clinicians in the diagnosis and treatment of skull base pathologies by accurately and completely characterizing their anatomical involvement and using imaging clues to narrow down their differential diagnosis. Figure legends: Figure 1: Chordoma of the clivus Figure 2: Sinonasal chondrosarcoma Figure 3: Schwannoma of left cranial nerve V Figure 4: Inverted papilloma of the left nasal cavity

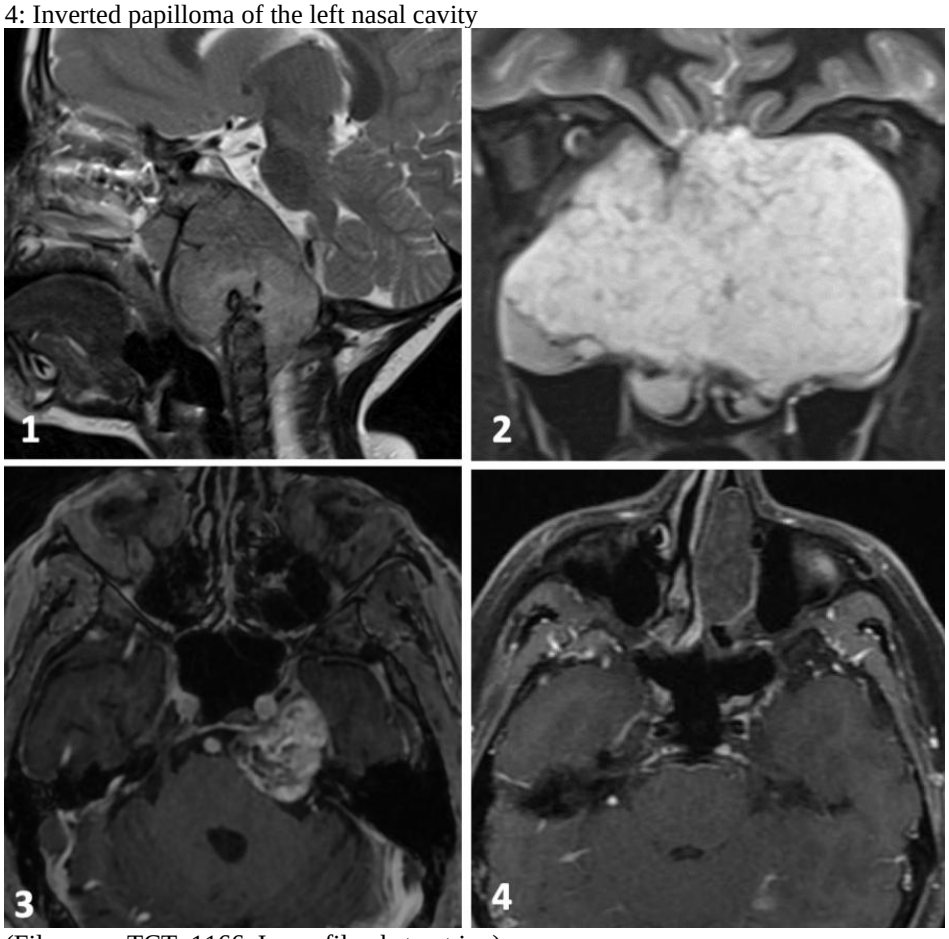

(Filename: TCT_1166_Imagefile-abstract.jpg)

1010

Don´t Be Fooled by "It´s Just Some Lousy Sinusitis..."; There´s a Creepy Tumor There!

A RIELLO[1], B Gherardi[2], a costacurta[3]

[1]Fleury, Rio de Janeiro, Rio de Janeiro, Brasil, RJ, [2]Grupo Fleury, Rio de Janeiro, Rio de Janeiro, [3]Clínica Felippe Mattoso, Rio de Janeiro, Brazil

Purpose

Sinonasal neoplasms are rare, accounting for 3% of head and neck malignancies. Virtually all patients with such tumors will be evaluated with some type of radiologic examination during the course of the disease, and many of them will be misdiagnosed in the beginning of the symptoms. Clinical presentation depends greatly on tumor location and on its invasive components. Generally, those arising in the nasal cavity and ethmoid region present in earlier stages with complaints of nasal congestion and obstruction mimicking sinusitis. Tumors arising in the other sinuses, however, present at later stages, often with signs of invasion and compression of nearby structures, such as facial pain, proptosis and diplopia, headache or neurological symptoms. Computed tomography (CT) and magnetic resonance imaging (MRI) are complementary modalities that excel at demonstrating the location and overall size of such masses, their potential extension, perineural tumor spread and provide a road map for surgical planning.

Materials and Methods

Describe the epidemiology, pathology,clinical manifestations and current treatment strategy of sinonasal tumors. Discuss the important role of imaging in the management of sinonasal tumors.

Results

We present a comprehensive review of Computed Tomography and Magnetic Resonance Imaging features of benign and malignant sinonasal tumors, highlighting important expected and unexpected complications.

Conclusions

Computed Tomography and Magnetic Resonance Imaging are the methods of choice to help distinguishing neoplasms from inflammatory disease and demonstrating tumoral extent and its complications, providing invaluable information for patient therapeutic management.

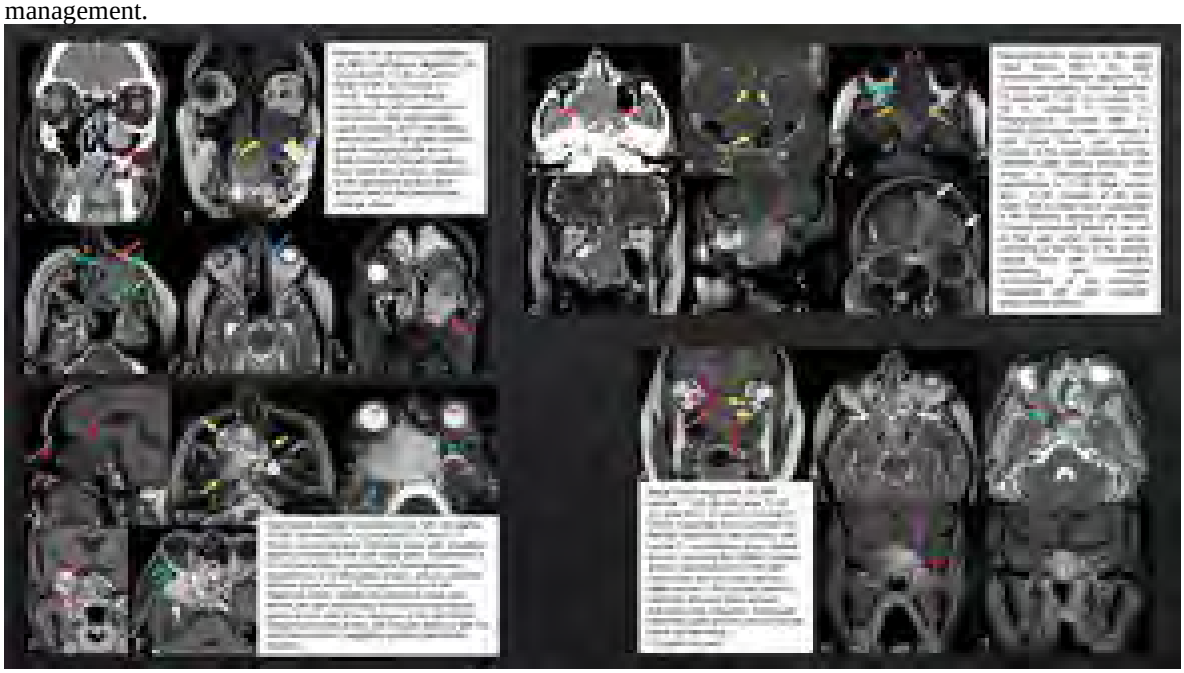

(Filename: TCT_1010_sinonasaltumors.jpg)

211

Don’t Forget to Review Your Teeth!

J Pulito[1], O Intikhab[1], B Griffith[1], J Corrigan[1]

[1]Henry Ford Health System, Detroit, MI

Purpose

Teeth are frequently included in the field of view of imaging studies of the head and neck and the interpreting radiologist should be familiar with the common, and not so common, dental pathologies he or she may encounter. By doing so, the radiologist is able to bring significant and often incidental findings to the attention of the ordering provider, potentially altering patient care. Following this exhibit, radiologists will be able to provide more confident diagnoses and reporting regarding dental abnormalities, ultimately improving patient care.

Materials and Methods
The purpose of this educational exhibit is to provide a review of dental nomenclature and anatomy, imaging techniques, as well as common pathologies and interventions affecting the teeth.
Results
● Using imaging and diagrams, we will review the nomenclature of primary and permanent teeth, as well as the anatomy of the tooth. ● We will discuss various imaging techniques of the teeth and provide examples. ● Using case files, we will review variant anatomy, dental restorations and procedures, dental trauma, dental related infections, as well as both common and uncommon dental tumors and tumor-like lesions.
Conclusions
● Knowing the appropriate nomenclature for the teeth will allow the radiologist to provide an accurate description and location for an affected tooth or teeth, which in turn, will aid the referring physician or dentist to provide appropriate care. ● When trying to diagnose underlying dental pathology, it is essential to know how to image the teeth along with the advantages and disadvantages of each technique. ● Lastly, knowing the common anatomical variations, dental interventions, dental-related infections, and tumor/tumor-like lesions, the radiologist will be able to confidently report the findings and provide an accurate differential diagnosis.

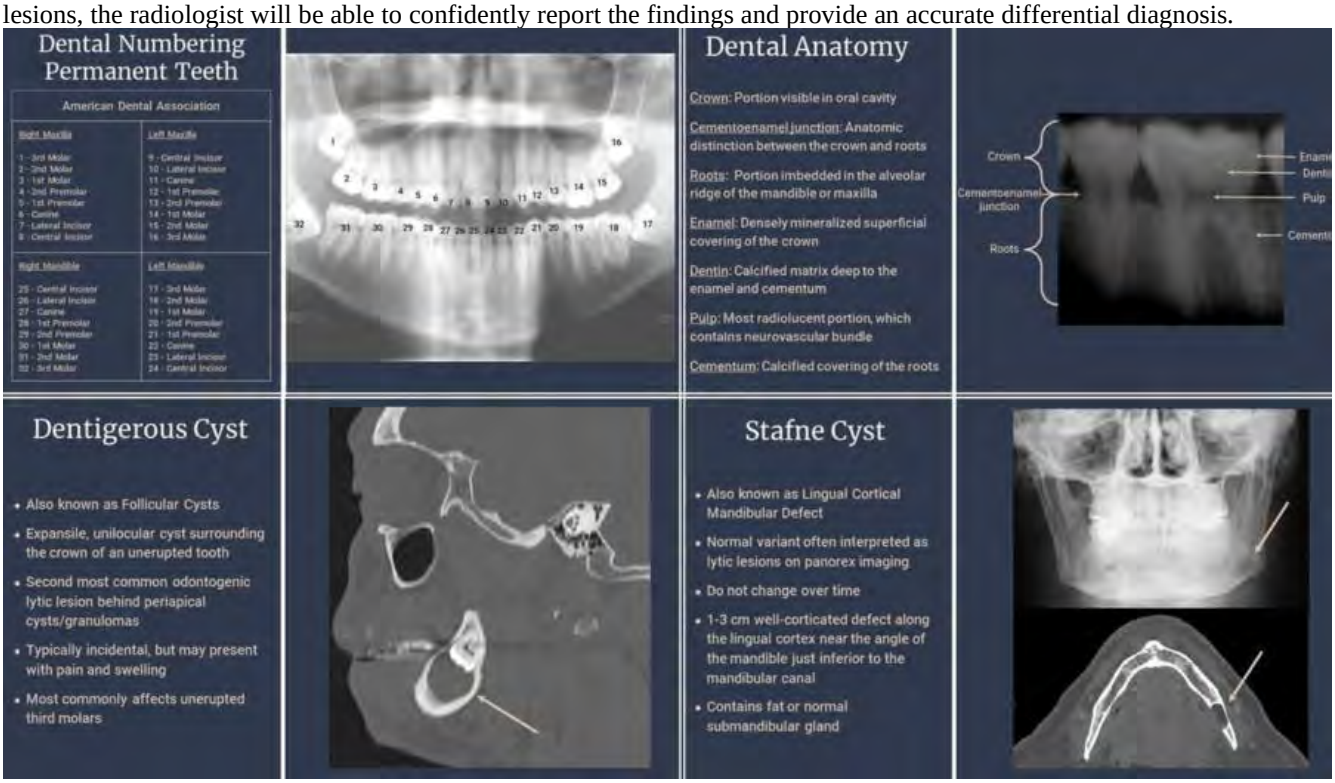

(Filename: TCT_211_Dentalabstract.jpg)

522
Embryonic Process Gone Awry: What a Radiologist Should Know About Neural Tube Defects.
T KALELIOGLU[1], T Rizvi[2]
[1]UVA, C/ville, VA, [2]University of Virginia Health, Charlottesville, VA

Purpose
Neural tube defect (NTD) is general term of congenital malformations affecting the development of the spine, which is seen 1-2 per 1000 births (1). It is usually classified into 2 main categories as open and closed spinal defects which mention if there is a skin covering over the defect or not (2). It is important to make appropriately classification because it effects management and prognosis (3). A definite diagnosis is the most important thing which helps guide effective management planning. Ultrasound is the primary imaging modality for the screening and diagnosis, however MRI is an important imaging tool to classify spinal dysraphism, show associated cranial abnormalities, and is a fundamental study in the presurgical evaluation for in utero repair.
Materials and Methods
1. Review the normal development of spinal cord and spine and reviewing the MRI features of spinal dysraphism. 2. To evaluate the role of MRI in evaluation of spinal dysraphism. To familiarize the radiologists with the spectrum of spinal dysraphism.
Results
The key MRI findings of spinal dysraphism including fetal MRI will be retrospectively reviewed.
Conclusions
High-quality MRI has become a standard tool in evaluating spinal dysraphism, providing a valuable supplement to sonography and helping to guide diagnosis and management. It is important to be familiar with different presentations of this entity to initiate accurate and early treatment.

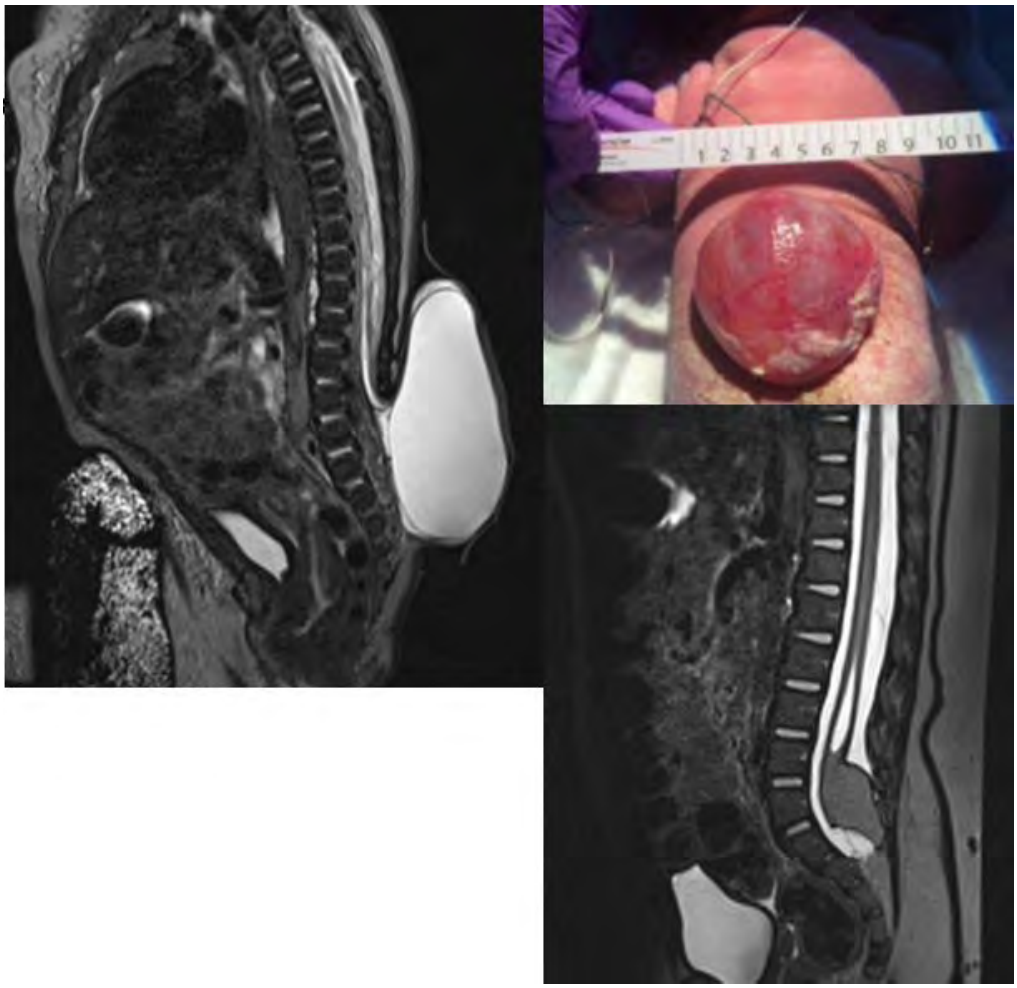

(Filename: TCT_522_IMAGE.jpg)

753

Emergence of Tau PET: Everything You Need to Know

G Cassinelli Petersen[1], M Roytman[2], A FRANCESCHI[3]

[1]Yale School of Medicine, New Haven, CT, [2]Weill Cornell Medicine, New York, NY, [3]Northwell Health, New York, NY

Purpose

Molecular imaging of tauopathies is a newly developing field that has gained particular importance with the recent FDA approval of 18F-flortaucpir in May 2020. EDUCATIONAL OBJECTIVES: • classification of tauopathies according to tau isoform and fibril structure • comparison of 1st and 2nd generation tau PET radiotracers • discussion of clinically relevant off-target binding sites • clinical application of tau PET in different tauopathies

Materials and Methods

To highlight the relevant clinical biochemistry of tau, present binding profiles and recognize pitfalls of the various tau tracers, and delineate the use of tau PET in both Alzheimer's disease (AD) and non-AD tauopathies.

Results

Literature review of the development and validation of 1st and 2nd generation tau tracers both in-vitro and in-vivo, outline the advantages and pitfalls regarding their use in different tauopathies, and provide introductory curriculum for understanding clinically relevant tau biochemistry.

Conclusions

Our educational exhibit introduces the sub-classification of tauopathies according to their predominant tau isoform (3R and/or 4R) and fibril structure (paired helical or straight filaments). We provide a comparison of 1st and 2nd generation tau tracers, focusing on their prototype molecules 18F-flortaucipir and 18F-PI-2620. We compare different binding profiles, focusing on the preferential binding to 3R/4R tau aggregates of flortaucipir and the extended binding profile to non-AD type tau fibrils for PI-2620. We delineate clinically relevant off-target binding sites such as the choroid plexus and substantia nigra, as these pose pitfalls in the assessment of neurodegenerative diseases. Finally, we outline the clinical use of tau PET in different tauopathies. In particular, we emphasize disease staging in AD as it is the spatiotemporal distribution of tau that correlates with progression of symptoms and follows a distinct progressive distribution pattern. We discuss the challenges of imaging non-AD tauopathies, with a focus on progressive supranuclear palsy, corticobasal degeneration, and primary progressive aphasia. In conclusion, molecular imaging of pathological tau aggregates is

a novel and rapidly evolving diagnostic tool, which is poised to enter clinical practice with the expected emergence of tau-targeting dementia therapeutics.

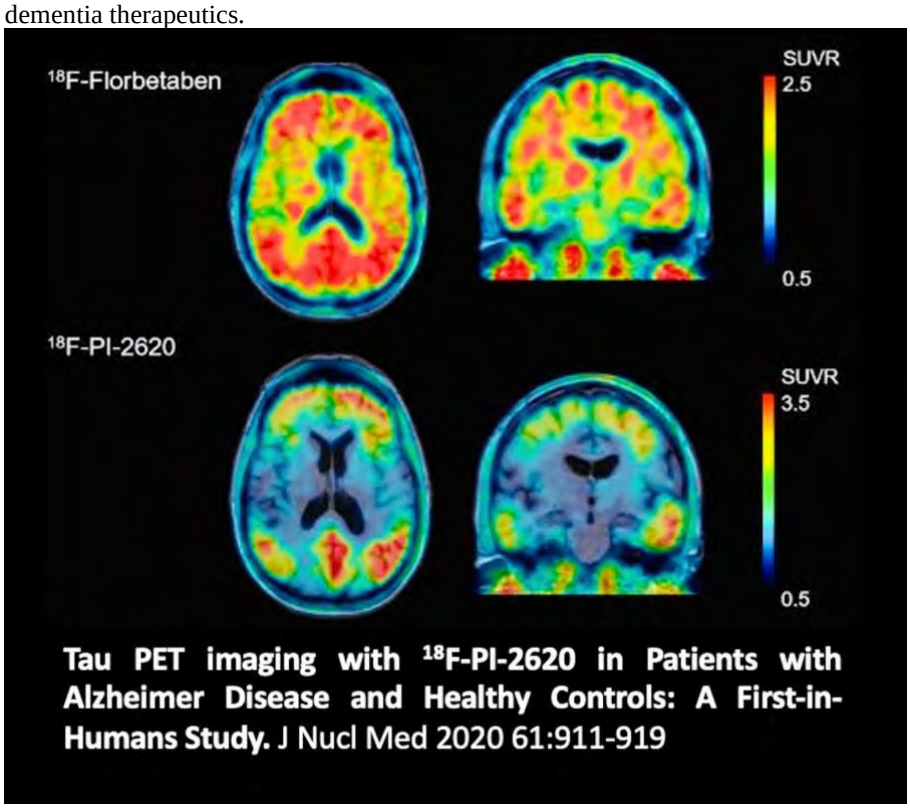

(Filename: TCT_753_ASNRFigure2.jpg)

276

Emerging MR Imaging Features in Multiple Sclerosis

A Rovira[1], C Auger[2]

[1]Hospital Vall d'Hebron, Barcelona, Barcelona, [2]Hospital Universitari Vall d´Hebron, Barcelona, Barcelona

Purpose

This presentation will review recently described MR imaging features in multiple sclerosis, and discuss their pathophysiology and value as a diagnostic and prognostic marker Educational objectives: 1. To learn about new MRI features in multiple sclerosis 2. To understand their diagnostic and prognostic value 3. To know the pathophysiology of these emerging features

Materials and Methods

To learn about new MRI features in multiple sclerosis and their diagnostic and prognostic value.

Results

A review based on literature research and on our experience of different emerging MRI features described in multiple sclerosis.

Conclusions

Although MRI is considered the most important paraclinical tool for establishing an early and accurate diagnosis of MS, it also leads to misdiagnosis in a substantial number of cases, which may result in unnecessary exposure to disease-modifying drugs and costs to healthcare systems. As a consequence, there is an emergent need to identify distinctive MRI features for MS that increase diagnostic specificity in front of other conditions or diseases with similar imaging characteristics. This objective seems to be partially achieved based on the diagnostic value of some relatively novel MR imaging features, such as the central vein and paramagnetic rim signs. The identification of these imaging findings requires the acquisition of T2* or susceptibility-based MRI sequences that, although not routinely performed, are now widely available with clinical scanners. On the other hand, the presence of leptomeningeal enhancement and slowly expanding lesions, although they do not have diagnostic value, they could contribute, together with the presence of the paramagnetic rim sign, to establish the prognosis of the disease Radiologists must be familiar with these emerging MRI features, since they increase the diagnostic specificity of this test, and might contribute to establishing the prognosis of this disease.

281

Emerging Role of Radiomics in Psychiatric Disorders

H Sotoudeh[1], A Sarrami[2], E Sotoudeh[3]

[1]University of Alabama at Birmingham, Birmingham, AL, [2]N/A, Davis, CA, [3]Red Crescent Hospital in Dubai, Dubai, UAE

Purpose

Radiomics is a rapidly evolving research field in radiology. The goal of Radiomics is to capture the hidden features within the medical

images which are beyond the ability of human eyes. This educational exhibit is about the emerging role of Radiomics in diagnosis and management of psychiatric disorders.
Materials and Methods
To review the most recent applications of Radiomics in the psychiatric disorders.
Results
This presentation includes: Radiomics in depression Radiomics in schizophrenia Radiomics in bipolar disorders Radiomics in Attention-deficit/hyperactivity disorder (ADHD) Radiomics in Autism spectrum disorder (ASD)
Conclusions
Radiomics analysis of the psychiatric disorders is still in infancy with scattered published studies, but there are emerging Radiomics applications regarding the early diagnosis, prognosis prediction and treatment response prediction in psychiatric disorders.

638

Endovascular Treatment of Carotid Cavernous Fistulas: An Overview of Different Approaches and Embolic Material

G Vilanilam[1], M Kamran[1], A Amole[1], S Patro[1]
[1]University of Arkansas for Medical Sciences, Little Rock, AR

Purpose
Carotid cavernous fistula (CCF) is an abnormal communication between the carotid system (internal carotid artery or external carotid artery) and the cavernous sinus. CCFs are classified based on: 1. Etiology: Traumatic and spontaneous 2. Angiographic arterial architecture: Direct and indirect 3. Hemodynamic features: High flow and low flow Imaging work up of CCFs: 1. CT: Proptosis and enlargement of the extraocular muscles. 2. CT angiography: Dilatation and enhancement of the superior ophthalmic vein and cavernous sinus. 3. MR angiography: Orbital edema, enlarged pituitary gland, abnormal flow voids in cavernous sinus, dilatation of leptomeningeal and cortical veins (high-flow fistula) 4. Ultrasound doppler: Irregular mosaic flash in the cavernous sinus region, enlarged ophthalmic vein with signal of blood stream and pulsation synchronizing with the pulse, reversed arterialized flow pattern in superior ophthalmic veins. 5. Digital subtraction angiography: Characterization of the size and location, direct or indirect, presence of complete or partial arterial steal phenomenon, evaluation of outflow pathways of the cavernous sinus, collateral circulation, pseudoaneurysms and cavernous sinus varix. Endovascular management: 1. Goal: To occlude the defect/tear/abnormal communication and reduce the pressure in the cavernous sinus. 2. Approach: Trans venous (inferior petrosal sinus, superior ophthalmic vein, facial vein, trans-contralateral cavernous sinus), Trans arterial (stenting of arterial defect/tear and trans arterial coiling/balloon/liquid embolic agent) and direct transorbital puncture of the cavernous sinus through the superior orbital fissure. 3. Endovascular techniques: Embolization (detachable balloon, coils and liquid embolic agents), stent (Flow diverter and covered stent) placement across the fistula and PAO (parent artery occlusion).
Materials and Methods
To describe the etiology, classification, imaging features, clinical presentation and approach to endovascular management of CCFs.
Results
N/A
Conclusions
CCF is an uncommon condition that can be primarily evaluated using CT and MRI and confirmed using DSA. Recognizing imaging features of CCF early can prompt timely management.

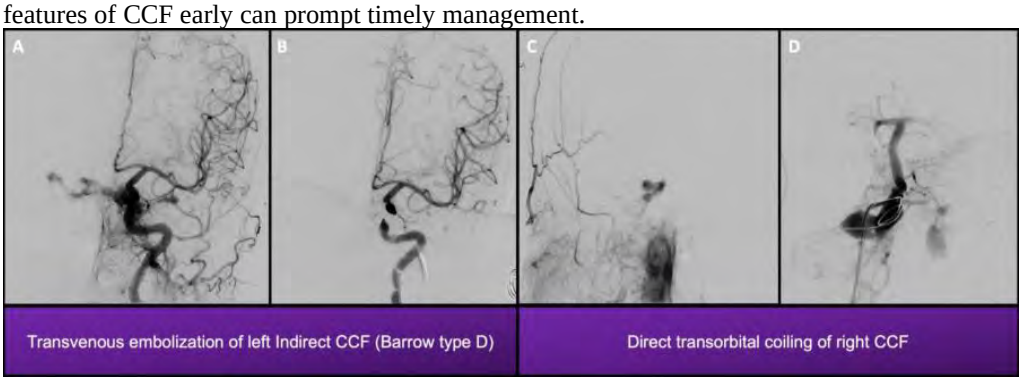

(Filename: TCT_638_CCF_ASNR22.jpg)

439

Enlargement of the Facial Canal: Variants and Underlying Pathology

W Calderon[1], P Puac Polanco[2], J Tortajada[3], C Zamora[4], M Castillo[5], A Rovira[6]
[1]Hospital Universitari Vall d´Hebron, Barcelona, Catalonia, [2]University of Ottawa, Ottawa, ON, [3]Vall d'Hebron University Hospital, Barcelona, Catalonia, [4]UNC Department of Radiology, Chapel Hill, NC, [5]Radiology, Chapel Hill, NC, [6]Hospital Vall d'Hebron, Barcelona, Barcelona

Purpose
Summary: • Background. • Anatomy. • Etiologic classification of facial canal enlargement. • Imaging findings. Objectives: • Illustrate

the anatomy of the facial nerve canal using multimodal imaging. • Describe variants and pathologic entities that cause enlargement of the facial canal(s). • Discuss relevant findings on CT and MRI imaging of facial canal enlargement by various causes.
Materials and Methods
The facial canal is a complex bony structure that houses the cranial nerve VII (CN VII) in its entire intratemporal course. It is divided into four segments from superior to inferior: labyrinthine, geniculate, tympanic, and mastoid. A variety of pathologies can arise within the facial canals resulting in an increase in their size with or without associated osseous dehiscence or erosion. Normal variants may also produce similar findings. Clinical presentation of these patients is nonspecific, including hearing loss and CN VII palsy. CT is the imaging study of choice for bone delineation of the facial canal allowing identification of abnormally enlarged segments. MR imaging is often used to narrow the differential diagnosis of facial canal enlargement. CISS (or its equivalents) and other 3D sequences clearly depict the CN VII segments and are readily available. Our purpose is to review the pathologic and non-pathologic entities causing facial canal enlargement.
Results
We will review the imaging features of entities leading to facial canal enlargement by classifying them into six groups: • Congenital/developmental variants: persistent stapedial artery, branchiootorenal syndrome, congenital cholesteatoma, meningocele, and emissary veins • Primary neoplasms: schwannoma, meningioma, hemangioma, neurofibroma, and paraganglioma • Perineural tumor spread • Metastases • Inflammatory: chronic inflammatory demyelinating polyneuropathy (CIDP) • Trauma: fractures
Conclusions
Facial canal enlargement is an uncommon finding on CT that may require MR imaging characterization. Knowledge of the anatomy of the facial canal and of the imaging spectrum of lesions affecting is essential in establishing a differential diagnosis.

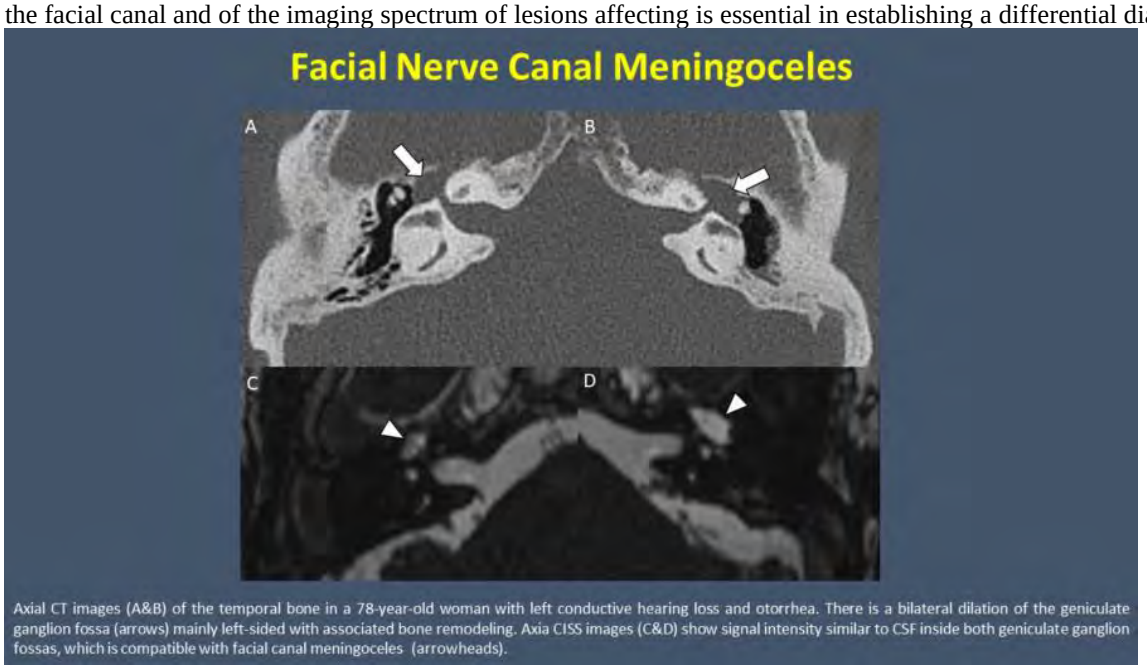

(Filename: TCT_439_FacialCanal.jpg)

733
Epilepsy Imaging and Pitfalls: What the Neuroradiologist Should Know
M Roubakha[1], N Salamon[1]
[1]*University of California Los Angeles, Los Angeles, CA*

Purpose
This educational exhibit will outline the pitfalls and common mistakes of neuroimaging in epilepsy as it provides a pictorial review of common pathologies. The exhibit will also outline how to differentiate findings mimicking real abnormalities with side-by-side comparisons and highlight various techniques to identify differences. 1. To review examples of pitfalls in epilepsy imaging 2. To review common structural variations neuroradiologists should be familiar with 3. To review technical interventions to better understand the pitfalls
Materials and Methods
This educational exhibit will outline the pitfalls of epilepsy imaging. Examples will include, for example, hippocampal sclerosis, focal cortical dysplasia, Sturge-Weber syndrome, various tumors, and vascular malformations. The exhibit will outline various anatomical variants, signal abnormalities, false positives from artifact, and focal cortical dysplasia type III, which can be associated with typical epileptogenic lesions. Recognizing these findings and pitfalls can help precise diagnosis and better surgical planning.
Results
One thousand surgically-proven epilepsy cases at UCLA since 2002 were retrospectively reviewed. Various epilepsy pathologies and imaging representations of pitfalls were selected.

Conclusions
Neuroimaging plays an important role in the diagnosis of epilepsy. Epileptogenic foci may not directly correlate to a given structural abnormality. Cases like focal cortical dysplasia type III should be identified in epilepsy cases as a potential target of surgery. Many pitfalls are false positives and knowing possible anatomical variations is critical. A multimodality approach can help improve diagnostic accuracy in assessing epileptogenic zones. It is important for the neuroradiologist to be familiar with the value of each modality and the imaging features of epilepsy.

479

Epilepsy Imaging and Treatment - What the neuroradiologist should know about pre-surgical evaluation.

S Yang[1], N Salamon[2]
[1]UCLA Medical Center, Los Angeles, CA, [2]University of California Los Angeles, Los Angeles, CA

Purpose
Epilepsy is one of the most common neurological disorders in the world. Neuroimaging is a core component of epilepsy management and has a wide range of applications ranging from identification of pathology to surgical decision making. This educational exhibit will outline the role of imaging in epilepsy as it provides a pictorial review of its common structural pathologies. The exhibit will also outline how to manage non-lesional cases and various therapeutic interventions. 1. To review the role of multimodality imaging in epilepsy pre-surgical evaluation. 2. To review common structural pathologies and their imaging characteristics. 3. To review various therapeutic interventions and their indications.
Materials and Methods
Epilepsy is characterized by a predisposition for recurrent seizures and is a heterogeneous condition with a wide range of etiologies. This educational exhibit will outline the basics of epilepsy pre-surgical assessment. It will describe the various neuroimaging modalities used (i.e., MRI, SPECT, PET, MSI and fMRI) and outline their respective diagnostic value. Further, the exhibit will provide a pictorial review of common structural epileptogenic etiologies. Examples will include conditions such as hippocampal sclerosis, focal cortical dysplasia, polymicrogyria, Tuberous Sclerosis, Sturge Weber syndrome, tumor, infarct, vascular malformations and post-traumatic scar. Lastly, the exhibit will outline various therapeutic interventions, their indications and imaging examples where applicable. These include surgical intervention: hemispherotomy, callosotomy, lesionectomy, or less invasive treatment; such as laser ablation, deep brain stimulation, responsive neurostimulation, and vagal nerve stimulation.
Results
A comprehensive literature review about epilepsy imaging and treatment will be performed. A single institutional retrospective review of over 1000 cases will identify case examples of various pathologies and common therapeutic interventions.
Conclusions
Multiple imaging modalities are used in the assessment of epileptogenic zones and it is important for the neuroradiologist to be familiar with the value of each modality, common structural pathologies of epilepsy, surgical indications as well as the imaging features of post-operative changes.

422

Epileptogenic Lesions Beyond Mesial Temporal Sclerosis

M Oei[1], E Middlebrooks[1]
[1]Mayo Clinic, Jacksonville, FL

Purpose
Epilepsy surgery is highly effective in the subset of patients with a focal imaging abnormality that is convergent with clinical, electrophysiologic, and neuropsychological data, with post-surgical seizure freedom rate of up to 80%. This is two to three times that seen in post-surgical patients without imaging abnormalities. It is therefore important to optimize imaging techniques and scrutinize the imaging studies for potential epileptogenic lesions beyond mesial temporal sclerosis. These include focal cortical dysplasia, gray matter heterotopia, cavernoma, arachnoid pits/encephaloceles. When present, these findings may be subtle, single, multiple, clinically significant, or incidental. Typical imaging characteristics and important associated findings will be discussed. Clinical examples from 7 Tesla and 3 Tesla scans will be presented.
Materials and Methods
Identify potential epileptogenic lesions. Recognize pertinent associated findings.
Results
N/A
Conclusions
N/A

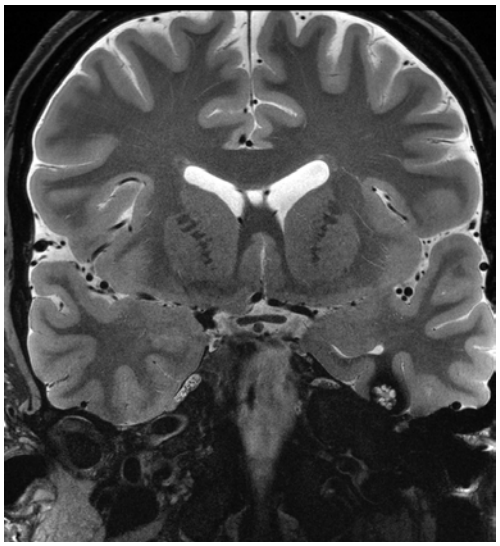
(Filename: TCT_422_7Tcavernoma.jpg)

982

ExtremelyRare Glioma Cases And Their Imaging Findings In Conventional And Advanced Functional MRI Methods

V Katsaros[1]
[1]*National and Kapodistrian University of Athens, Athens, Greece*

Purpose
To demonstrate extremely rare cases of gliomas and their typical imaging features onconventional MRI.To highlight the utmost importance of advanced MRI methods in the evaluation of tumourphenotype and tumour genotype. To evaluate the importance of advanced MRI methods (mainly perfusion andspectroscopy) in post-treatment imaging assessment in cases of tumour progression, pseudo-progression and remission
Materials and Methods
Therapeutic advances in the management of cerebral gliomas demand more precise non-invasive neuroimaging for the diagnosis, therapeutic planning, treatment response and patient outcome prediction. The key pathological features of gliomas include cellularity, invasiveness, mitotic activity, angiogenesis, and necrosis all of which can be detected by different methods of MRI. Hence, atypical characteristics can be misleading over the type of glioma and advanced MRI techniques may add value in discriminating subtypes and are imperative in the clinical routine practice.
Results
Out of more than 1000 cases of gliomas the last 10 years, 9 cases showed histopathologically extremely rare characteristics. All the cases were studied by structural, fMRI, DTI and permeability, as well as perfusion and spectroscopic methods.
Conclusions
We present two cases which proved to be frontal ependymomas, two cases of astroblastomas, one case of gliosarcoma, one case of epithelioid GBM with a prior pathology of pleomorphic xanthoastrocytoma grade III, one case of pleomorphic xanthoastrocytoma grade III , one case of granular cell astrocytoma and finally one case of diffuse whole brain glioma. Some extremely rare cases of brain gliomas share overlapping features depending on their cellularity and aggressiveness and the advanced MRI methods are of utmost importance in the evaluation of tumor phenotype, tumor genotype and post-treatment imaging assessment and monitoring.

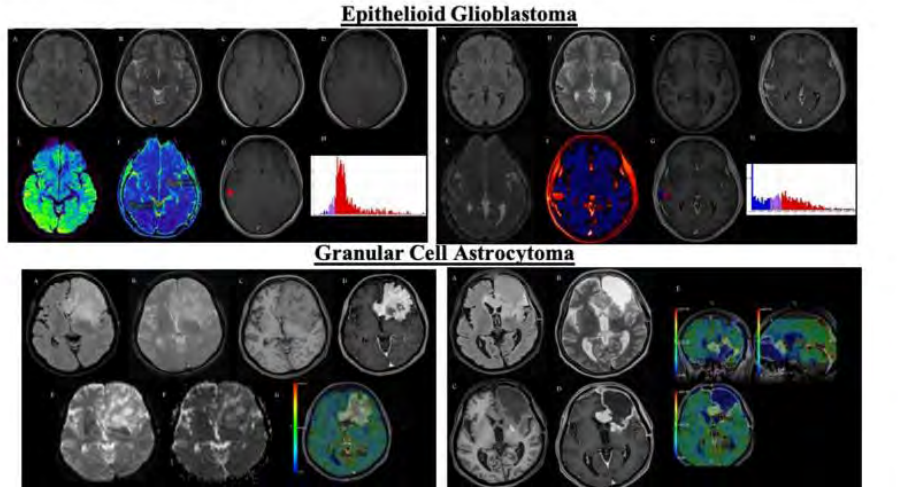

(Filename: TCT_982_RareGliomas.jpg)

954

Facing Orofacial Pain: beyond TMD and Headaches

a costacurta[1]

[1]Clínica Felippe Mattoso, Rio de Janeiro, Brazil

Purpose

Chronic orofacial pain can have a negative effect on the patient's daily activities and quality of life, including sleep, absence from work, or loss of employment. Orofacial pain may be attributed to a variety of disorders including atypical idiopathic facial pain, temporomandibular disorders (TMD), diseases of odontogenic or soft tissue origin, sinus diseases, neuralgia, and headaches. Currently there are no standard radiologic evaluation for patients with orofacial pain since it encompass such a large spectrum of disorders. The evolution and a more widespread use of neuroradiologic intervention, with percutaneous procedures and endoscopic surgery for skull base and pterygopalatine fossa have provided new possibilities in management for difficult cases reinforcing the need for a complete radiologic evaluation before treatment.

Materials and Methods

Temporomandibular joint disorders (TMD) are considered to be the main cause of pain in the orofacial region following pain of odontogenic origin. Nonetheless several causes may be implicated in chronic orofacial pain, often more than one for the same patient, Head and neck innervation is complex. The trigeminal nerve has a crucial role but there are also important nerve anastomosis between the trigeminal, facial, occipital and glossopharyngeal nerves. Many times the patient has already been submitted to a TMJ and a Brain MRI with negative results and needs further investigation. The aim of this presentation is to review the causes of orofacial pain, besides headaches and TMD, guiding the radiologist through the relevant anatomy and establishing a check list from the oral cavity to the skull base.

Results

Discuss the causes of chronic orofacial pain that may be found in a suprahyoid neck, base of skull and posterior fossa exam. Review the pertinent anatomy, focusing on nerve course and "hot spots" for eliciting pain. Establish a check list to rule out disease from the oral cavity to the posterior fossa.

Conclusions

Chronic orofacial pain is a complex diagnosis and may be devastating for an individual´s life with many social implications. Several causes may be implicated, often more than one for the same patient, and the diagnosis and treatment of these conditions are better attained by a multidisciplinary team. In this setting there is a important role for the radiologist, helping the team to tailor an comprehensive radiological investigation, unmasking hidden pathologies or anatomic variations that may impact treatment.

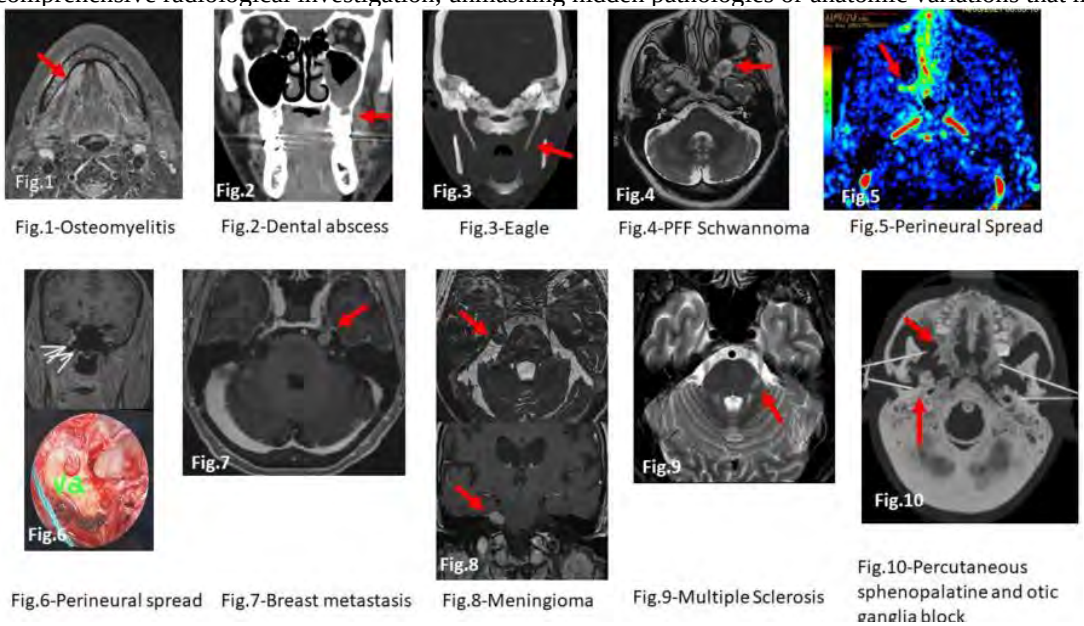

(Filename: TCT_954_DOR1.jpg)

478

Fast Spine MRI: How to Perform Cervical, Thoracic and Lumbar Spine MRI in 30 Minutes

B Jaber[1], S Chaker[2], A Moawad[1], M Shalaby[3], M Aslam[1], O Teytelboym[4]

[1]Mercy Catholic Medical Center, Darby, PA, [2]Mercy Catholic Medical Center, Havertown, PA, [3]Mercy Catholic Medical Center, LANSDOWNE, PA, [4]Mercy Fitzgerald Hospital, Darby, PA

Purpose

Objectives: - Review whole spine MRI indications - Illustrate practical tips to design fast spine MRI protocol on 1.5T and 3T MRI scanners - Fast whole spine MRI protocol - Provide case-based review of common and uncommon pathologies - Review benefits and

pitfalls of fast spine MRI - Highlight the role of fast spine MRI in facilitating ED workflow Summary: - Introductions to fast spine MRI and recent updates - Whole spine MRI advantages and drawbacks - Review the indications for whole spine MRI • Spinal tumors • Acute spinal trauma • Spinal infection • Degenerative spine disease - Practical tips to design the fast spine MRI protocol: How to do it in 30 minutes - 1.5T vs 3T MRI - Fast MRI case-based examples - Fast spine MRI pitfalls and limitations
Materials and Methods
N/A
Results
N/A
Conclusions
N/A

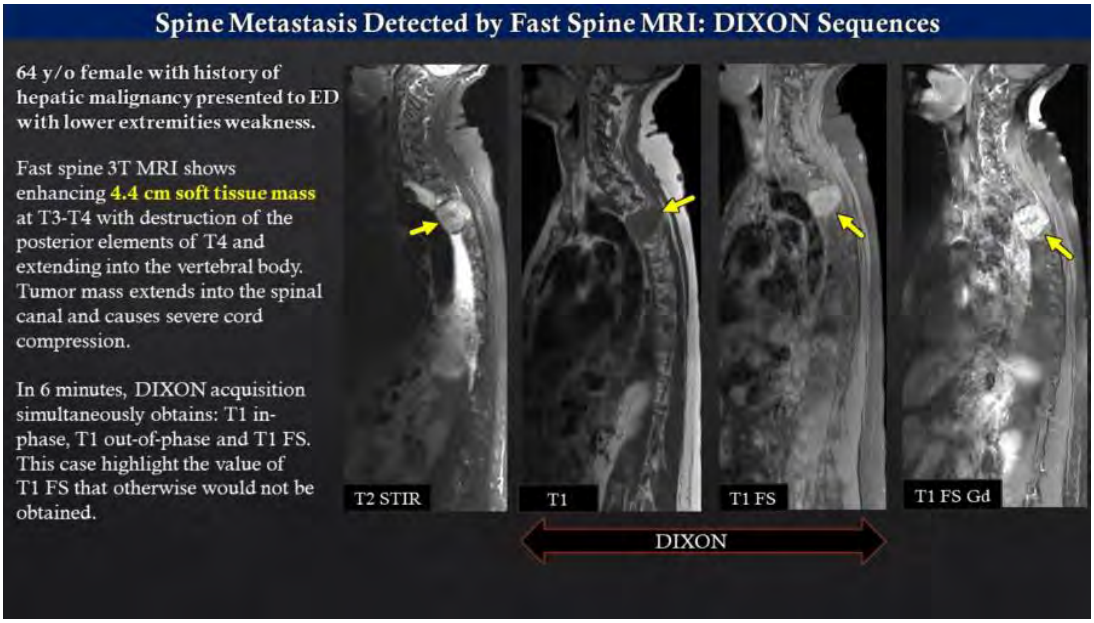

(Filename: TCT_478_Slide1.JPG)

125
Fetal MR Imaging: Common and uncommon central nervous system abnormalities
A Wang[1], J Cole[2], A Singh[2]
[1]University of Texas Health Science Center San Antonio, San Antonio, TX, [2]UT Health San Antonio, San Antonio, TX

Purpose
Recent advancements in fetal MR imaging have resulted in an increased utilization of the modality to diagnose central nervous system abnormalities. Prenatal diagnosis assists the clinician in formulating a treatment plan that can improve the child's quality of life. High quality images have been collected from our tertiary referral center that demonstrate CNS abnormalities such as Chiari malformations, hydrocephalus, callosal abnormalities, cortical malformations and neural tube defects. Our presentation includes information regarding the MR protocol as well as showcases the imaging presentations and clinical associations of these entities. The information is suitable for residents to practicing radiologists. Our educational objectives include: -Learn imaging protocols pertaining to fetal MR -Learn the presentation of routine CNS abnormalities
Materials and Methods
To provide a practical educational exhibit that demonstrates the routine abnormalities of the CNS on fetal MR.
Results
Multiple high quality fetal MR images were collected from our institution which functions as a tertiary referral center for high-risk obstetrics. Cases are appropriately labelled to showcase the pathology. A detailed description of the imaging presentation of the central nervous system abnormalities will accompany each case.
Conclusions
Prenatal diagnosis has profound implications for the treatment and quality of life of children. Learning how CNS abnormalities present on fetal MR can provide a quality service for the referring clinician. In addition, learning the imaging protocols can help optimize scanning at the learner's institution.

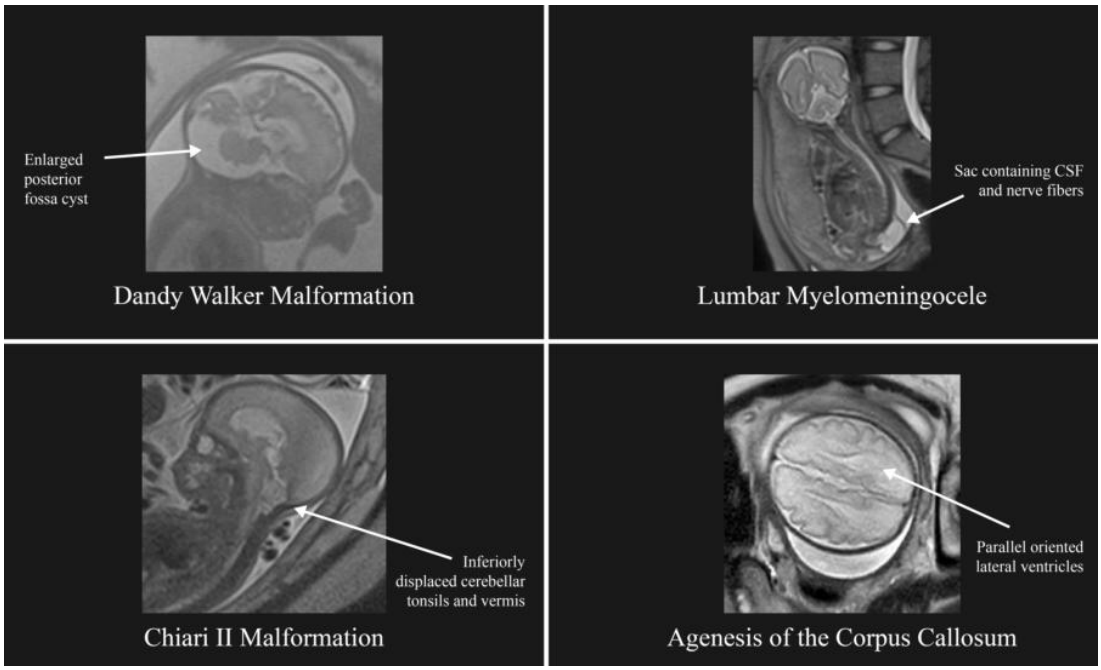

(Filename: TCT_125_Alexv5-01.jpg)

656

Finding What You Are Looking For: Illustrative Primers for Post-operative Devices and Reconstruction in the Head and Neck.

J Junn[1], A Silberzweig[1], A Callen[2], L Eisenmenger[3]
[1]Mount Sinai Hospital Icahn School of Medicine, NYC, NY, [2]University of Colorado, Aurora, CO, [3]University of Wisconsin - Madison, Middleton, WI

Purpose
Radiologic depictions of expected post-operative head and neck devices and surgical reconstructions in the orbit, skull base, temporal bone, and neck. Illustration of less frequently encountered post-operative and post-treatment findings that radiologists need to know.
Materials and Methods
Post-operative images of head and neck can be very challenging even for experienced radiologists. The purpose of this exhibit is to illustrate various head and neck medical devices and surgical techniques, which could be mistaken for pathology or be inadequately assessed if not properly understood. Expected positioning and complications will be highlighted with a case-based review. Patterns of unusual post operative appearances will be described in order to provide the radiologist with an algorithmic approach to these complex cases.
Results
Common surgical approaches to various categories of head and neck pathologies will be described, including illustrative examples of expected and uncommon post-surgical devices. Additionally newer surgical techniques of which many radiologists may not be familiar will be discussed. In the orbits, more common examples will include prosthetic globe, scleral buckling and medial duct implants. In the ear, cochlear implant, stapes implant, and incus interposition grafts will be discussed. Most of the exhibit will be dedicated to post-surgical imaging of the neck, to include thyroid/parathyroid reimplantation, submandibular gland transfer, salivary bypass tubes, wound vac devices, an obturator, and pharynx plugs. These imaging findings will be supplemented by clinical photos of these devices. Finally, unusual post-surgical complications, such as pedicle ossification, will be discussed.
Conclusions
Through this exhibit, viewers will develop an approach to post-surgical cases of the head and neck and be familiar with the expected and uncommon post operative devices and complications in order to achieve an accurate diagnosis and to prevent unnecessary intervention.

603

Function and Fibers – Functional MRI and DTI Fiber Tractography Application in Brain Tumor Resection

M White[1], M Aizenberg[1], D Ellis[1], Y Zhang[1], C Bryant[1]
[1]University of Nebraska Medical Center, Omaha, NE

Purpose
Our presentation will evaluate the pre-operative appearance of fMRI activation and white matter tracts with correlation to the neurological outcomes. Our presentation helps radiologists review the utility and imaging features of fMRI and DTI fiber tractography in brain tumor resection.

Materials and Methods

1) To review the pre-operative appearance of fMRI activations and white matter tracts with correlation to the neurological outcomes, 2)To explain the utility of fMRI and DTI fiber tractography in brain tumor resection.

Results

Analysis of extraaxial, intraaxial, benign and malignant brain tumors included oligodendrogliomas, astrocytomas, ependymomas, meningiomas, AVMS and metastatic tumors. The pre-operative functional status was compared to the post-operative status. Neurological functions and the associated WM tracts evaluated included the vision, language, motor, and sensory systems. mBAND task based FMRI paradigms are discussed in addition to conventional fMRI sequences accelerated with parallel imaging techniques. Resting State FMRI applications are demonstrated and compared to conventional task based fMRI sequences. The effect on white matter tracts by tumors are analyzed by DTI fiber tractography and utilizing color fractional anisotropy maps. Also reviewed are the differential effects of myelination on T2 FLAIR images that demonstrate white matter tract involvement by tumor. The technical difficulties and limitations of fMRI and DTI analysis are demonstrated. The limitations of DTI tractography due to effects of mass effect, edema and infiltrating tumor are outlined.

Conclusions

FMRI and DTI analysis of the functional localization in brain tumor patients adds additional information to the pre-operative knowledge of where the functional tissue are located. Depending upon findings of FMRI & DTI analysis surgical plans potentially are changed from attempting resection to biopsy and a better understanding of the likelihood of specific neurological deficits occurring from surgery are clarified. Preferred distance from functional tissue on fMRI or a tractogram and surgical resection: The greater the distance the better. A 10mm margin is preferred. Functions or white matter tracts demonstrated within tumor resected: Will have neuro deficits. Functions or white matter tracts adjacent to tumor resected: Can result in major neuro deficit but might be minor deficits with recovery.

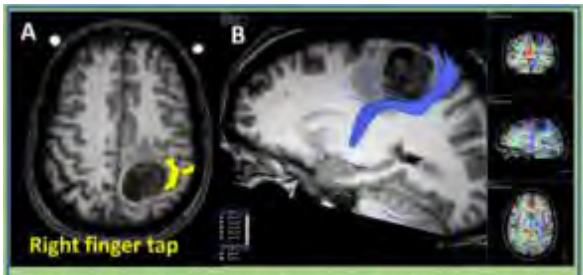

Ependymoma, w/ strange sensations in rt. shoulder & some difficulty utilizing rt. hand.
fMRI (**A**): tumor lies w/l the motor cortex w/ rt. hand finger tap activation at the latl. aspect ( ). (**B**) The fibertracts are distorted by the tumor. The CSTs & TCTs could not be separated. The CSTs appear to be deviated posteriorly w/ the TCTs (blue fibers). No postop motor deficits after GTR w/ awake mapping.

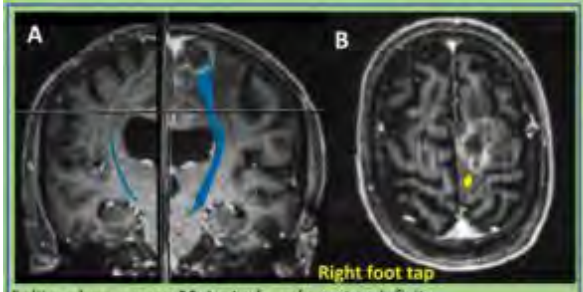

Solitary lung cancer **Metastasis**, w/o motor deficits.
(**A**) The CSTs (blue fibers) on the lt. extends rt. to the mass and then has minimal fibers surrounding the mass. (**B**) The activation map for rt. foot tapping shows an area of activation ( ) adjacent to the posterior medial aspect of the mass.
Weakness in foot and toes after complete resection.

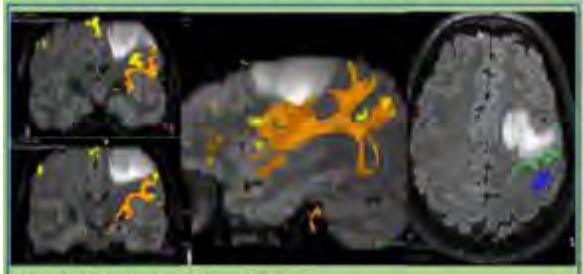

Anaplastic astrocytoma, w/ seizure
Speech areas are laterally and inferior to the mass. are activation areas from word generation. CSTs are at the posterior aspect of the lesion with minimal fibers extending into the lesion (rt. image).
Postop significant expressive aphasia.

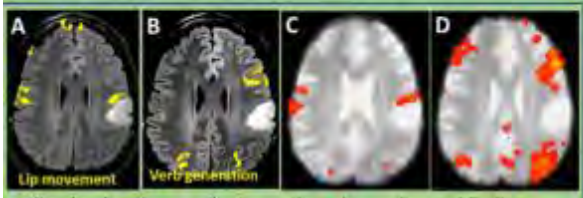

Oligodendroglioma, w/ seizure, slurred speech, word finding difficulty.
FMRI shows the motor gyrus to be rt. at the anterior aspect of the lesion (A). Language activation is seen rather markedly just anterior to and at the superior anterior border of the mass (B). Resting state (RS) fMRI motor activity is also demonstrated at the anterior aspect of the lesion (C). RS language fMRI demonstrates more extensive language network activation than the verb generation alone (D).
Because of the dysarthria during the operation, the patient only underwent a near gross total resection.

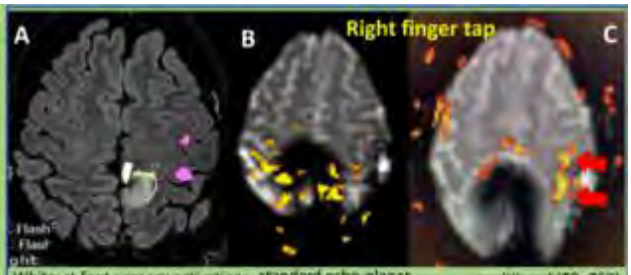

White: rt foot sensory activation; standard echo-planar multiband (TR=760)
Pink: rt hand sensory activation; (TR=3000)
Yellow: TCTs

DNET, w/ new onset seizure.
FMRI (**A**): the mass in the area of the foot sensory function.
Postop fMRI w/ standard technique (**B**) demonstrated no specific activation while the MB4 (C) demonstrated activation in the area of the hand knob (red arrow). The postop metal artifact centrally distorts the image. Potential explanation: the MB4 technique by imaging w/ a shorter TR suffered less distortion of the fMRI signal.
After the operation, the patient developed rt. side sensory deficit.

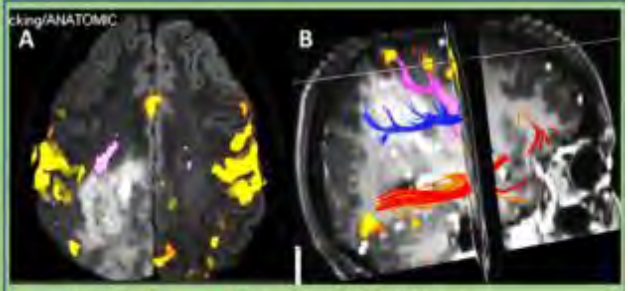

: Lip movement; : CST; : part of arcuate fasciculus;
: optic radiation; : Occipital frontal fasciculus

Oligodendroglioma, w/ upper extremities numbness/tingling
(**A**) The mass extends into the motor strip & invades the hand knob. Lip function ( ) is latl. to the mass. The rt. CS tract is invaded & anteriorly displaced (pink). The sensory gyrus and TCTs are invaded. The anatomy was too distorted to map the TCTs by tractography or sensory fMRI. (**B**) The arcuate fasciculus is invaded and the temporal component doesn't map (dark blue). The optic radiation ( ) and occipital frontal fasciculus are at the inferior aspect of the mass (red).
No obvious neuro deficits after subtotal tumor resection.

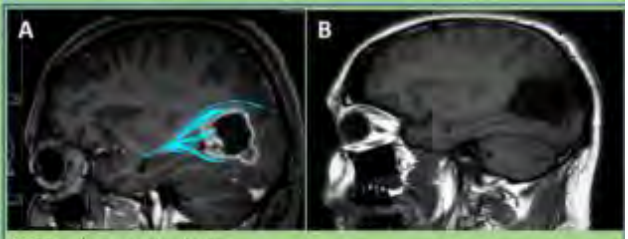

GBM, w/ severe headache.
(A) The optic radiation is split above & below the lesion with no gap btw lesion and the fibertracts (blue) of the optic radiation. No vision loss was present pre-operatively. (B) A gross total resection was achieved. Post-operatively there was a homonymous hemianopsia.

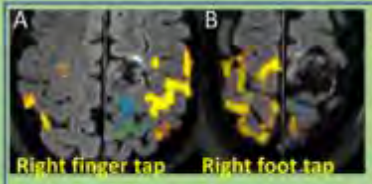

AVM, w/ tinnitus
(A) Right finger tapping is present where expected overlying the left hand knob. The left corticospinal tract is within millimeters of the AVM (blue fibers).
(B) With right foot tapping, the activation is seen in the medial right frontal lobe as well as the medial right parietal lobe. Activation is not seen as expected in the medial left motor strip. The AVM has caused reorganization of the function. On the right foot tap image, some corticospinal fibers aberrantly map to the post-central gyrus.

(Filename: TCT_603_tumorcases.jpg)

228

Geographic Classification of Grey Matter MRI Signal Abnormalities in Patients with Status Epilepticus

S Ferraciolli[1], A Ayres[2], K Nakacima[3], L Ramin[4], L Araujo[5], T Miranda[5], L Lucato[6], C Leite[7], C Zamora[8], M Castillo[9]

[1]InRad - HC- FMUSP, Sao Paulo, -- SELECT --, [2]ICESP- FMUSP, São Paulo, Sao Paulo, [3]InRad-HCFMUSP, São Paulo, São Paulo, [4]University of São Paulo, São Paulo, São Paulo, [5]Inrad, Sao Paulo, Sao Paulo, [6]Instituto de Radiologia, Hospital das Clínicas da Faculdade de Medicina da Universidade de São Paulo, São Paulo, São Paulo, [7]University of São Paulo, Sào Paulo, São Paulo, [8]UNC Department of Radiology, Chapel Hill, NC, [9]Radiology, Chapel Hill, NC

Purpose

In this educational exhibit we describe the geographic spectrum of grey matter MRI signal changes in patients with status epilepticus. We highlight features that suggest this diagnosis, review the pertinent literature, and present a schematic figure summarizing the relevant imaging findings.

Materials and Methods

Our purpose is to review the spectrum of grey matter signal abnormalities that may be seen in patients with status epilepticus and to offer a geographic classification.

Results

For this exhibit we searched the teaching files of two academic institutions for grey matter signal abnormalities on MRI in patients with status epilepticus. We propose a schematic figure summarizing the relevant imaging findings and distribution of signal abnormalities.

Conclusions

Grey matter MRI signal abnormalities in patients with status epilepticus are usually related to neurotoxicity, with cytotoxic/vasogenic edema and increased blood flow due to seizure activity. These alterations may be characterized by hyperintensity on T2/FLAIR, restricted diffusion, leptomeningeal/gyriform post contrast enhancement and increased perfusion in the ictal/peri-ictal phase. The main structures involved are cerebral cortex, thalamus, mesial temporal regions (including hippocampi) and occasionally cerebellum. The distribution of signal abnormalities can be unilateral or bilateral, with or without involvement of the thalamus and/or subcortical white matter. Rarely, patients can present with unilateral edema of an entire cerebral hemisphere with variable involvement of the basal ganglia and thalami. There are also delayed postictal alterations, such as focal atrophy and hippocampal sclerosis. Here, we will show cases illustrating the various patterns of grey matter involvement that may be seen on MRI in patients with status epilepticus. We also provide a literature review and propose a geographic classification for the imaging findings.

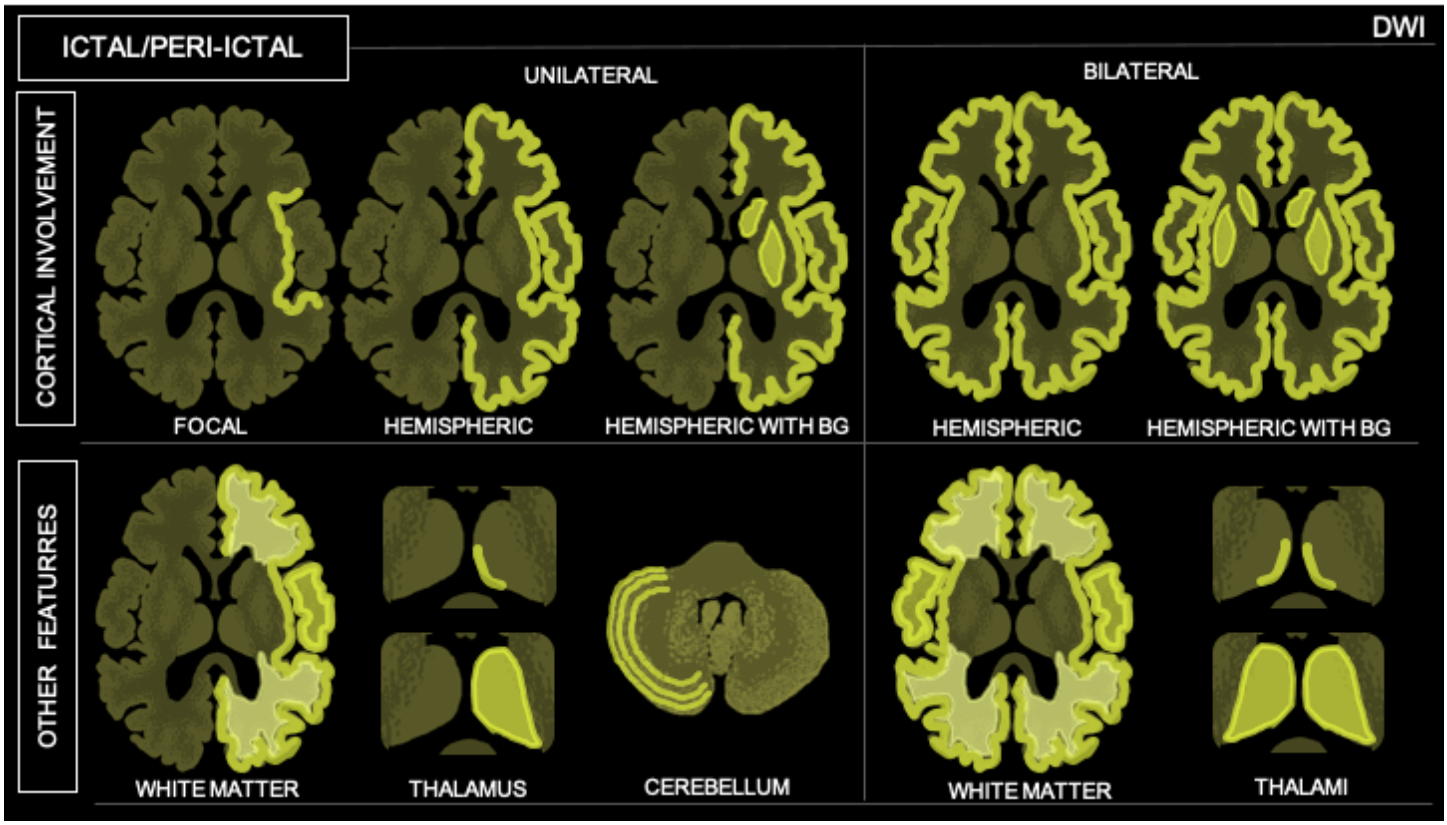

(Filename: TCT_228_ASNR22.gif)

1196

Glioblastoma Physiognomies : Case Series on Unusual Imaging Characteristics

F Mubarak[1]

[1]*Aga Khan University, Karachi, HI*

Purpose

Glioblastoma is an aggressive primary central nervous system tumour that usually has a poor prognosis. Generally, the typical imaging features are easily recognisable, but the behaviour of glioblastoma (GBM) can often be unusual.Several variations and heterogeneity in GBM appearance have been known to occur. Even innocuous-looking foci, cystic lesions, meningeal-based pathology, intraventricular and infra-tentorial masses, multifocal/multicentric lesions and spinal cord abnormalities may represent GBM. Aim to highlight the atypical characteristics of glioblastoma, clarify their importance and list the potential mimickers. Although a definitive diagnosis in these rare cases of GBM warrants histopathological confirmation, an overview of the many imaging aspects may help make an early diagnosis. We will also share histopathology of lesions side by side.

Materials and Methods

We present a series of twelve patients with histologically proven glioblastoma in unusual locations and with atypical features on magnetic resonance imaging.

Results

We present a series of twelve patients with histologically proven glioblastoma in unusual locations and with atypical features on magnetic resonance imaging.

Conclusions

The behaviour of GBMs is unusual with regards to the heterogeneity of its appearance on imaging. In approximately 13% of cases, GBM may presentas multifocal or multicentric masses (more than two lesions, including leptomeningeal dissemination), dis-tant (second lesion non-contiguous with primary lesion) or diffuse disease.Infra-tentorial GBMs are infrequent, and the behaviour of the tumour is differ-ent in this region.5In this pictorial essay, we review the unusual locations and atypical neuroimaging featuresof pathologically proven GBMs, with a primary focuson adult cases. However, of note, there are also other atypical presentations such as early-stage GBM and exclusive paediatric GBM, which unfortunately go beyond the scope of this exhibit.

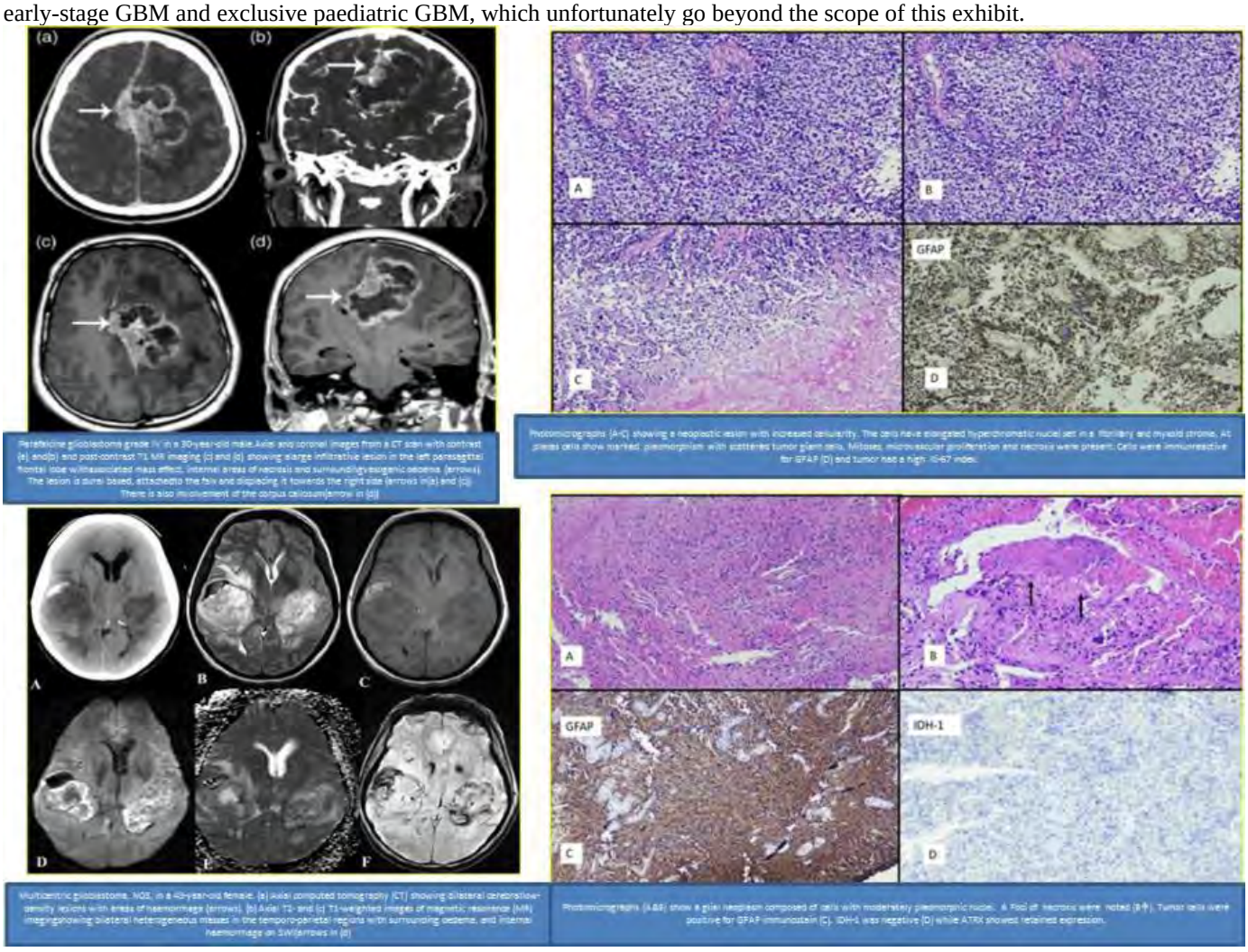

(Filename: TCT_1196_ASNR300wecompresscom.jpg)

301

Gliosarcoma: Pictorial Overview of Presentation, Management, and Outcomes

P Kay[1], J Nickerson[1]

[1]*Oregon Health and Science University, Portland, OR*

Purpose

The exhibit will display seven individual cases of gliosarcoma, along with MRI imaging, history, management, and outcomes of each case. The educational objectives are to recognize different presentations of gliosarcoma, understand the limitations and need for further exploration of the current standard of care, and introduce novel interventions currently being developed.

Materials and Methods

The purpose of this educational exhibit is to present a case series and pictorial review of gliosarcoma in order to better understand its characteristics including diagnosis, current/future interventions, and outcomes.

Results

Seven gliosarcoma patients from a single institution were treated with standard tumor resection followed by radiotherapy and adjuvant temozolomide. These patients were identified and retrospectively evaluated by querying the OHSU Radiology Search Engine (1) for gliosarcoma. Clinical presentation, tumor characteristics, as well as outcomes were obtained via retrospective analysis of medical records and MRI imaging.

Conclusions

Gliosarcomas are rare and highly malignant grade IV variants of glioblastomas that are radiographically similar to glioblastomas despite their additional sarcomatous component. Due to the rarity of the disease, there is conflicting evidence regarding relative prognosis and optimal therapy. Currently, management of gliosarcomas employs the same standardized treatment as conventional glioblastomas which includes: resection, radiotherapy, and adjuvant temozolomide chemotherapy (2). Seven cases will be presented including patient history, MRI images, tumor management, and outcomes in order to review and better understand characteristics of gliosarcoma (see summary table and example images).

Case #	Age/Sex	Tumor Location	Outcome Post-Resection
1	53 F	R temporal lobe	Continued monitoring with recent evidence of disease progression 6 months post-resection
2	18 M	Occipital lobe	No evidence of recurrent disease 4 years post-resection
3	59 F	R frontal lobe	No evidence of disease progression 11 years post-resection
4	52 M	L temporal lobe	Stable disease 4 years post-resection
5	79 M	R frontal lobe	Deceased 2 months post-resection
6	61 F	R parietal lobe	Deceased 1 year post-resection
7	62 M	L temporal lobe	Deceased 9 months post-resection

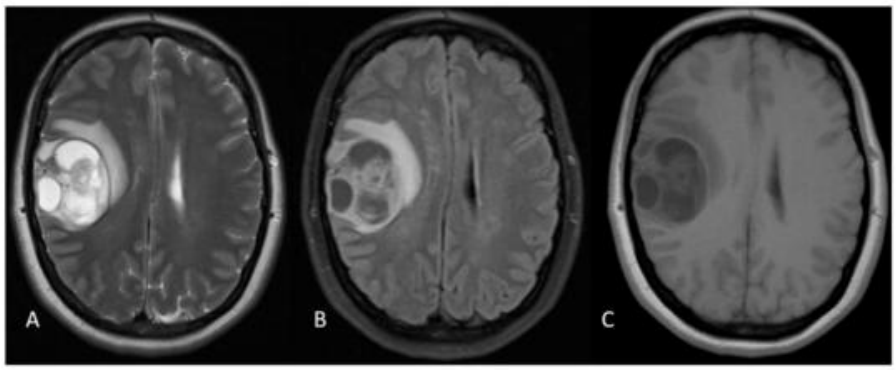

(Filename: TCT_301_ASNRAbstractImages.jpg)

783

Guillain Barre´ Syndrome following COVID-19 vaccination: A systematic review of case reports and case series

N Shaheen[1]

[1]*Alexandria Faculty of Medicine, Alexandria, - None -*

Purpose

Background: Guillain barre syndrome(GBS) has been recently associated with COVID-19 disease. Usually, GBS cases are associated with immune stimulation and reported after taking different vaccines, however, there is no confirmed evidence that this is a causal association. In this systematic review, we are investigating cases of GBS that have been reported following the COVID-19 vaccination.

Materials and Methods

Purpose: Further research is needed to assess all neurological side effects of COVID-19 vaccines such as GBS which was reported after other vaccines like swine influenza vaccine, older formulations of the rabies vaccine, oral polio vaccine, and tetanus toxoid-containing vaccines.

Results

Methods: Based on PRISMA guidelines, we searched five databases (PubMed, Google Scholar, Ovid, Web of Science, and Scopus databases) for studies on COVID-19 vaccination and GBS on August 7, 2021. To conduct our analysis, we divided the GBS variants into two groups acute inflammatory demyelinating polyneuropathy and non-acute inflammatory demyelinating polyneuropathy(AIDP and non-AIDP) and compared the two groups with mEGOS and other clinical presentation

Conclusions

Results: The systematic review resulted in 129 cases included in 15 studies. Of the 15 studies, 14 studies had 29 cases. Ten of 29 were of the AIDP variant, 17 were non-AIDP(one case had MFS variant, one AMAN variant, and 15 cases of BFP variant). The majority of the cases has received the one-dose Johnson and Johnson vaccine. The mean age of GBS cases after COVID-19 vaccination was 58 years. The average time for the appearance of GBS symptoms following vaccination was 14.4 days. Most of the cases (40%) of patients belonged to Brighton level 3 outlining maximum diagnostic certainty of patients with GBS. Conclusion: In this systematic review, a temporal association of GBS following COVID-19 vaccination has been reported in 129 cases especially after receiving the one-dose Johnson and Johnson vaccine

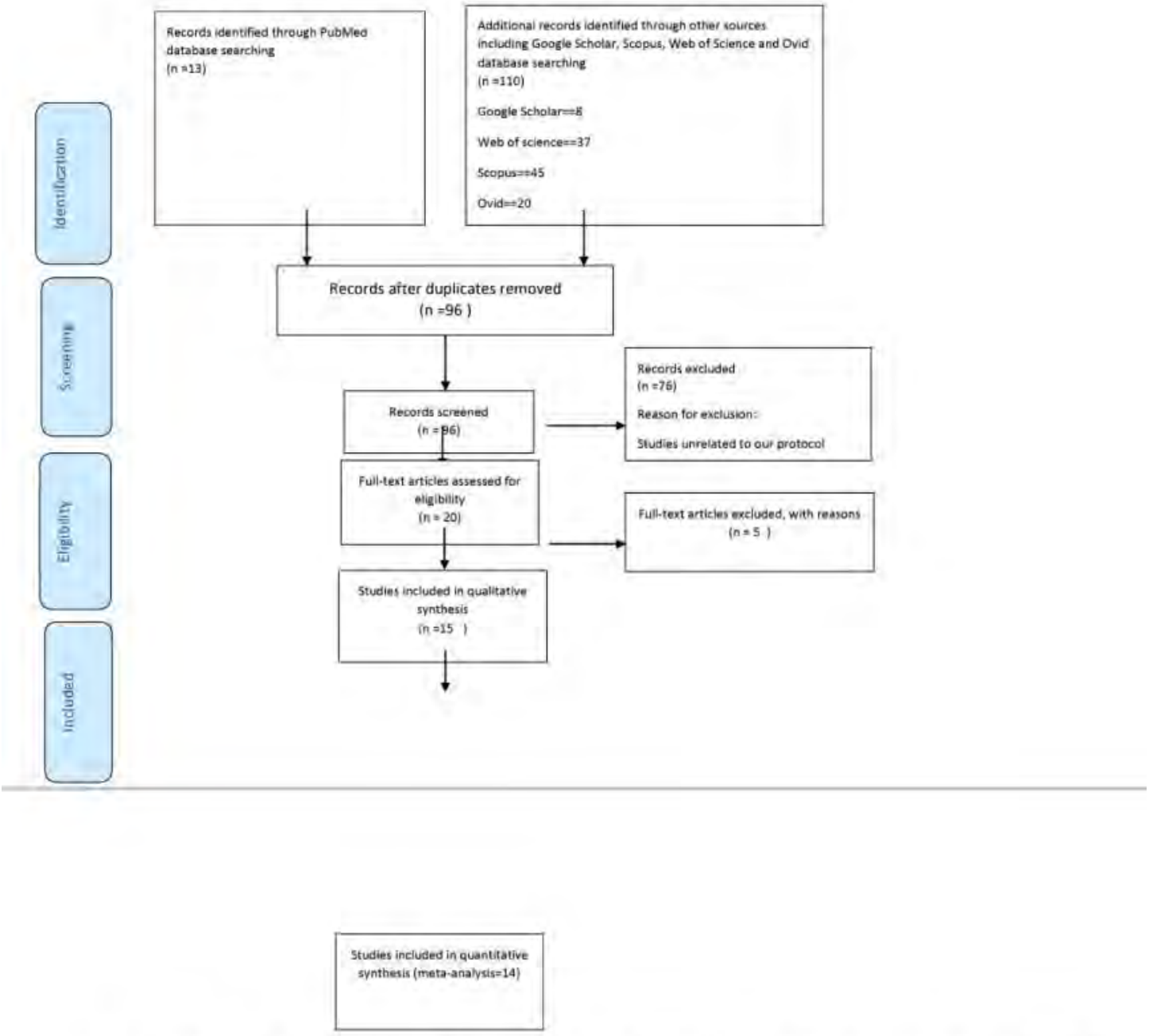

Figure 1. PRISMA flow diagram of systemic review. The flow diagram depicts the flow of information through the different phases of the systematic review. It maps out the number of records identified, included and excluded.

(Filename: TCT_783_Screenshot_20211116-035509_AdobeAcrobat.jpg)

770

Hydrocephalus: a new perspective

L Morales Cifuentes[1], C Singh Boscán[2]

[1]Hospital Universitario San Ignacio, Bogotá, Bogotá, [2]Hospital Universitario San Ignacio, Bogota, Bogotá

Purpose

The classification and definition of hydrocephalus has been debated for the past 90 years. Currently the most accepted definition is active distension of the cerebral ventricular system resulting from inadequate passage of cerebrospinal fluid from the point of origin in the lateral ventricles to the site of absorption into the systemic circulation. There is a classic model of circulation proposed more than a century ago, where hydrocephalus is caused by a discrepancy between the amount of cerebrospinal fluid produced and absorbed.

However, recent studies show that the pathophysiology is more complex than previously thought, and the most accepted model is that of the osmotic gradient and the glymphatic system. Teaching points: - Understand the current definitions. - Define the latest concepts on the pathophysiology of the disease. - Specify the role of the different diagnostic imaging modalities. - Describe the different classifications. - Through an anatomical approach, know the most relevant pathologies and their most representative characteristics. - Explain the different therapeutic approaches and their most important complications. - Illustrate the imaging findings of normal pressure hydrocephalus and its pathophysiology.
Materials and Methods
Understand the newest concepts on the disease, its pathophysiology, imaging findings and workup of patients with hydrocephalus.
Results
A Thorough literature search was made, using Google scholar and Pubmed data bases. With selection of further articles for review of the available and most recent literature on the subject. The majority of cases used to illustrate the findings were collected at our institution, Hospital Universitario San Ignacio.
Conclusions
- Hydrocephalus as a complex and multi- pathology in its pathophysiology. - Fundamental role of the glymphatic system and aquaporins in cerebrospinal fluid absorption. - Hyperacute form of presentation endangers the patient's life, so it is important its adequate recognition. - There are new magnetic resonance sequences, which allow a better diagnostic approach. - Third ventriculostomy is a surgical alternative to ventriculo-peritoneal shunt with better survival. - Normal pressure hydrocephalus is a cause of reversible dementia, so it is important to learn to recognize its findings in images and how to differentiate it from obstructive hydrocephalus.

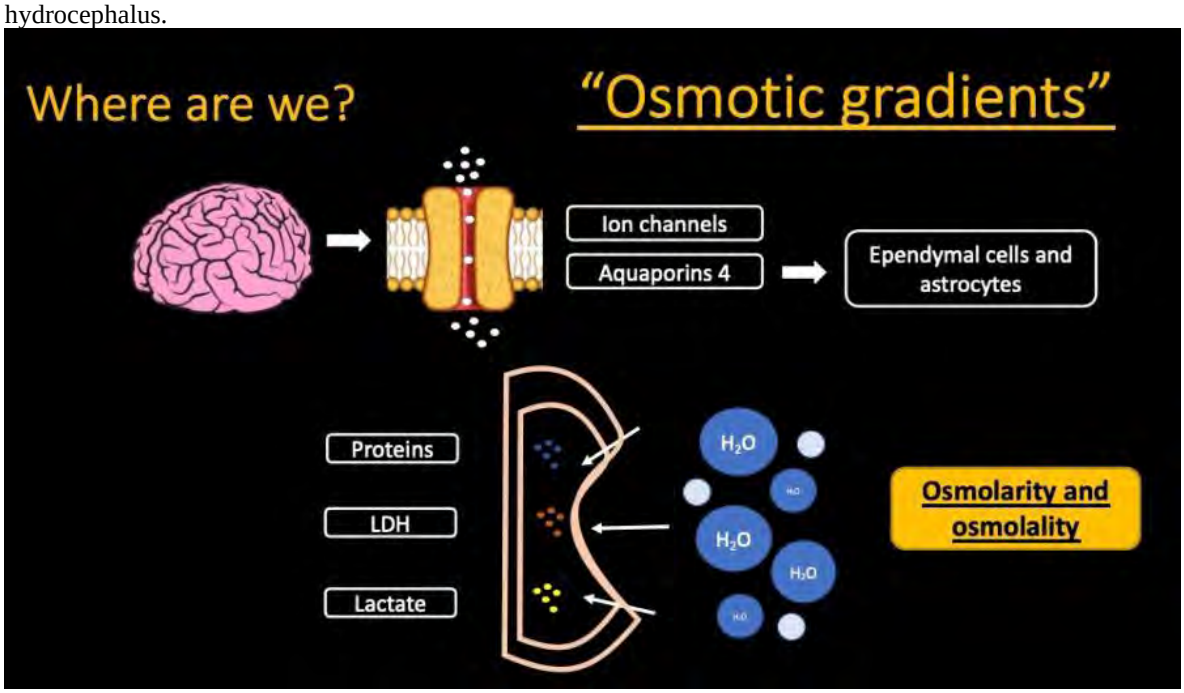

(Filename: TCT_770_Hidrocefalia.jpg)

887

If These Walls Could Talk: Intracranial Vessel Wall Imaging for Acute Ischemic Stroke

A Peret[1], A Spahic[1], A Kuner[1], J Manunga[2], W Chang[3], J Junn[4], K Johnson[1], L Eisenmenger[1]
[1]University of Wisconsin-Madison, Madison, WI, [2]Minneapolis Heart Institute, Minneapolis, MN, [3]Allegheny Health Network, Pittsburgh, PA, [4]Mount Sinai Hospital Icahn School of Medicine, New York City, NY

Purpose
Outline the MRI sequences used for intracranial vessel wall imaging and explore the radiological findings depicted in intracranial atherosclerotic plaques. Review the most recent evidence on vessel wall imaging characterization of intracranial atherosclerotic plaques and the relationship with acute ischemic stroke. Explore future directions of intracranial vessel wall imaging in defining imaging biomarkers for ischemic stroke and guiding patient management.
Materials and Methods
Approximately 800,000 acute ischemic stroke (AIS) events occur annually in the United States. AIS is associated with a high mortality with about 5.5 million deaths worldwide each year and close to 50% of patients with long-term disability. Intracranial vessel wall imaging (VWI) is a powerful and promising MRI technique that allows for the evaluation of intracranial atherosclerotic disease (ICAD), a major cause of AIS. The purpose of this exhibit is to present the current evidence on the relationship between the imaging features provided by VWI and the characterization of ICAD lesions for the diagnosis of AIS.
Results
This exhibit will introduce the methodology of VWI along with the main imaging features encountered in ICAD. A literature-based

discussion on the relationship between these findings and AIS will be proposed with a focus on risk assessment, diagnosis, and patient management.

Conclusions

Conventional imaging techniques (CTA, MRA) only focus on the vessel lumen instead of the origin of vessel pathology itself, the vessel wall. Alternatively, intracranial VWI is able to depict abnormalities in the arterial wall, characterizing early ICAD lesions even in the absence of stenosis. VWI could provide valuable imaging biomarkers in AIS risk assessment and diagnosis. Recently, a considerable interest in VWI for the evaluation of ICAD and AIS has emerged. To this date, the highest level of evidence lies in 3 meta-analyses, showing that several biomarkers, such as arterial wall enhancement (Fig 1), positive remodeling, plaque hyperintensity in T1-weighted imaging, and plaque surface irregularity have a good predictive value in identifying plaques responsible for AIS. Moreover, VWI of asymptomatic plaques could help identify unstable plaques and evaluate for the risk of future AIS event. In conclusion, VWI provides promising imaging biomarkers that could, jointly with conventional imaging, help diagnose stroke of unclear origin, identify plaques responsible for stroke, and predict risk of AIS event.

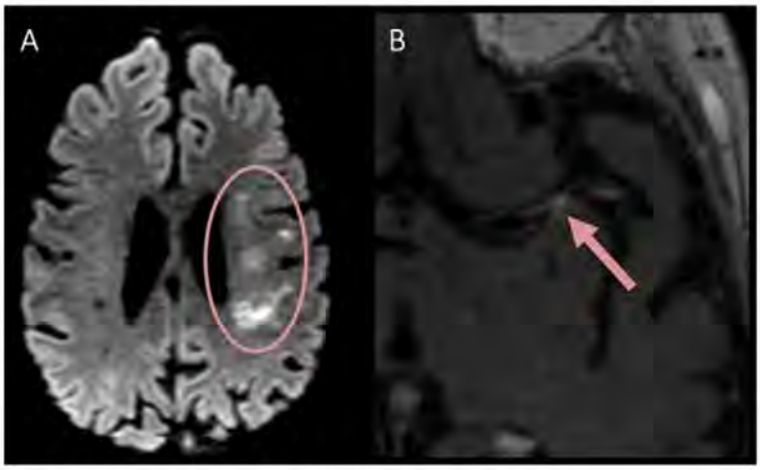

Figure 1 - Acute ischemic stroke of unclear origin.
In this patient, diffusion-weighted imaging shows restricted diffusion within the white matter of the left hemisphere, consistent with acute ischemia. (A). Contrast-enhanced vessel wall imaging shows enhancement of the wall of the left middle cerebral artery (B), corresponding to the most likely culprit atherosclerotic plaque.

(Filename: TCT_887_Abstract_ED_ICVWI_stroke_figure.jpg)

1127

Imaging Characteristics and Prognostic Indicators of Fetal Neck Pathologies

A Kerpel[1], N Shaheen[1], E Bass[1], M Matheus[2]
[1]The Medical University of South Carolina, Charleston, SC, [2]MUSC, Charleston, SC

Purpose

The herein presentation expects to improve awareness, description, and identification of fetal neck pathologies to all radiologists involved in perinatal head and neck imaging with an illustrative and instructive approach.

Materials and Methods

The past decade showed marked improvement in the field of maternal fetal medicine which increasingly utilizes a multidisciplinary approach in perinatal care for complicated and high-risk pregnancies. Fetal imaging allowing for diagnosis of in utero pathologies and evaluating for anatomic prognostic indicators provide a significant benefit to the multidisciplinary team. Dependence upon fetal MRI diagnostic accuracy has summarily increased. This presentation aims to illustrate the most characteristic imaging findings for fetal neck pathologies, discuss some of the more useful prognostic anatomic indexes, and highlight possible pitfalls which may influence perinatal care and delivery plans.

Results

Using a series of illustrative fetal MRI and US cases from our educational imaging files we will show the most characteristic imaging features of fetal neck congenital abnormalities and masses. Sheba Medical CenterPrognostic anatomic indexes such as jaw index, inferior facial angle (IFA), frontal nasomental angle (FNMA), and tracheoesophageal displacement index (TEDI) will be also illustrated and discussed.

Conclusions

Our cases in conjunction with review of the current literature will organize and clarify the differential diagnosis for fetal neck pathologies, revealing the importance of select prognostic indexes to positively influence perinatal care.

1270

Imaging Characteristics of Neurologic Associated Movement Disorders

J Van Dyke[1], J Gupta[2], D Casey[3], N Gupta[2]

[1]LSUHSC New Orleans, New Orleans, LA, [2]Tulane University School of Medicine, New Orleans, LA, [3]Louisiana State University Health Sciences Center, New Orleans, LA

Purpose

Radiologic imaging can provide early recognition and confidence in diagnosis of multiple neurologic movement disorders. Numerous movement disorders have been described to have both sensitive and specific imaging appearances. Imaging has also been described as a tool to follow progression of certain neurologic movement disorders. For example, MRI has been show to reveal the timeline of neurologic structural changes in premanifest to manifest Huntington disease (1), of which the recognition may lead to clinically significant outcomes throughout the course of the disease. Additional other imaging characteristics of known movement disorders have been described in the literature. Included in these disorders is Parkinson's disease, in which both MRI and nuclear imaging can play a role in determining the correct diagnosis, and the severity of structural compromise and relative loss of function in the substantia nigra. Nuclear medicine plays a key role in diagnosis with DAT scan (2). Numerous other movement disorders have relatively unique radiologic appearances, which will be further explored in the exhibit. (3) The objective of this exhibit is to focus on imaging patterns of movement disorders, both common and uncommon. The project will serve as a pictorial review focusing on key imaging throughout multiple modalities including MRI, CT and Nuclear medicine. Learning Objectives: · Review typical imaging characteristics of relatively common movement disorders. · Recognize typical clinical presentation via cases seen at our institution. · Review course of disease, as well as prognosis and general treatment. · Serve as a concise review of imagining patterns in movement disorders for trainees and practicing radiologists.

Materials and Methods

N/A

Results

N/A

Conclusions

N/A

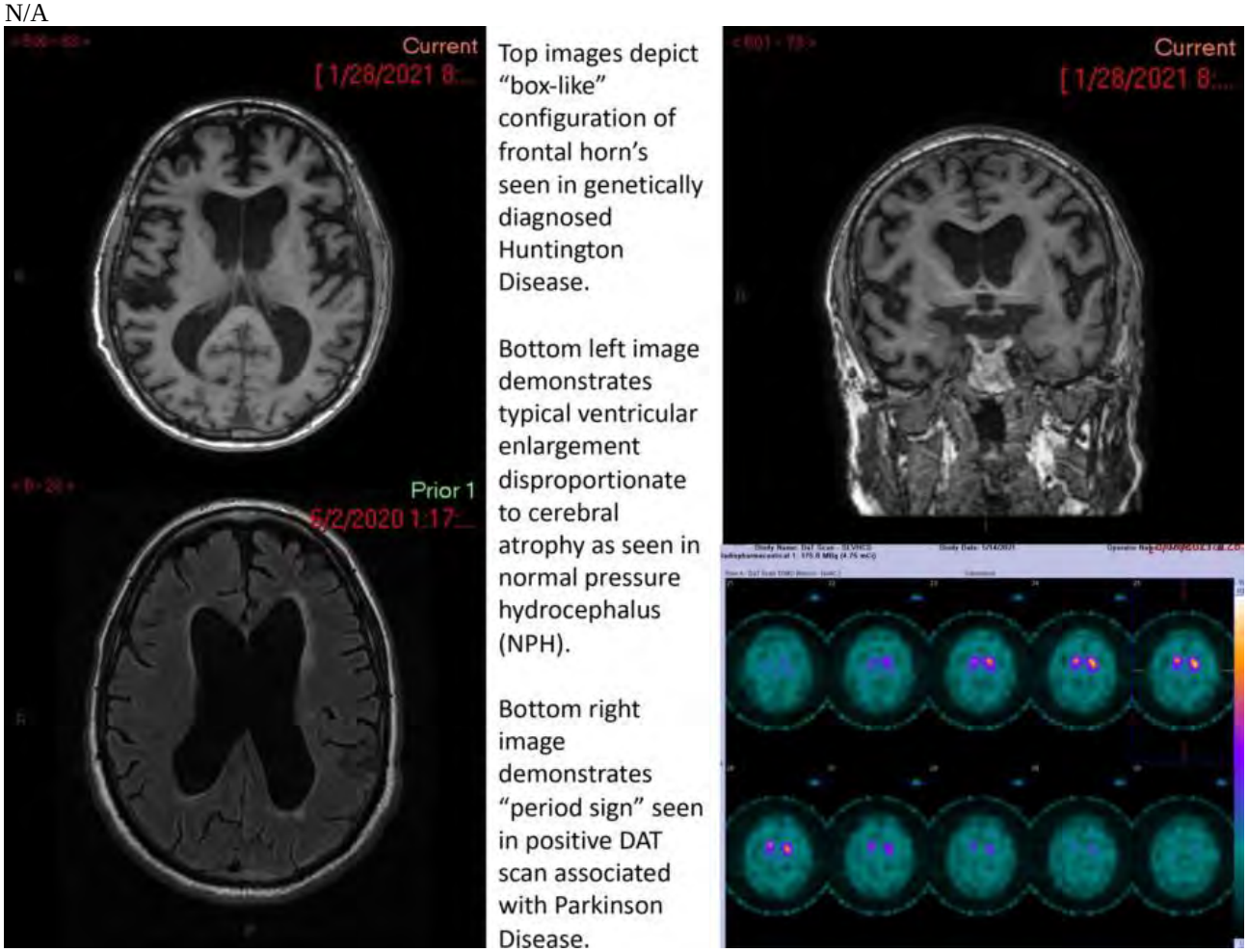

(Filename: TCT_1270_ASNRJPG2.jpg)

1553

Imaging Diagnosis and Treatment Selection for Brain Tumors in the Era of Molecular Therapeutics

S Vagvala[1], J Guenette[2], C Jaimes[3], R Huang[4]

[1]Brigham and Women's Hospital/Harvard University, Boston, MA, [2]Brigham and Women's Hospital - Department of Radiology, Boston, MA, [3]Boston Children's Hospital, BOSTON, MA, [4]Brigham and Women's Hospital, Boston, MA

Purpose

In the current era of oncologic molecular analysis of neural axis tumors, there has been a greater impetus to non-invasively predict molecular markers in order to guide therapy and prognostication. Imaging technologies have become essential in this regard. This exhibit will outline currently known important molecular markers, their associated imaging features, and the accuracy of those features. Traditionally, the histologic characteristics of tumors dominated classification and grading schema. However, 2016 and most recent 2021 updates to the World Health Organization (WHO) classification of central nervous system (CNS) tumors have uniquely integrated molecular parameters into the classification and in certain instances has emphasized them above histologic features.1 The most notable changes involved diffuse infiltrative gliomas with regards to isocitrate dehydrogenase (IDH) and 1p19q codeletion statuses. As a testament to the growing reliance on molecular status, if a tumor's histologic phenotype is discordant with that of the genotype, it is the genotype that determines diagnosis and subsequent treatment.1 The importance of predicting these molecular statuses has prompted considerable research into predictive imaging correlates not only for IDH and 1p19q statuses, but also for other biomarkers including methylguanine-DNA methyltransferase (MGMT) promotor methylation, epidermal growth factor receptor (EGFR) amplification and mutation, histone H3F3A gene (K27M mutations), fibroblast growth factor receptor 3-transforming acidic coiled-coil containing protein (FGFR3-TACC3) fusions, and BRAF mutations.2 Currently, the vast majority of CNS tumors require tissue sampling to discern their molecular/genomic landscape. However, growing research has shown the powerful role imaging can play in non-invasively and accurately detecting the molecular signature of these tumors and helping to select patients who may benefit from novel therapies. This educational exhibit will highlight the powerful role of imaging in patient selection for treatment regimens of several primary brain tumors including diffuse glioma, medulloblastoma and BRAF mutant tumors.

Materials and Methods

N/A

Results

N/A

Conclusions

N/A

1543

Imaging evidence and recommendations for traumatic brain injuries: advanced neuro and neurovascular imaging techniques

A Lee[1]

[1]Soonchunhyang University Bucheon Hospital, Bucheonsi, Korea, Republic of

Purpose

Traumatic brain injury (TBI) is a major health and socio-economic problem worldwide that mainly affects young adults. Neuroimaging plays a critical role in the diagnosis and evaluation of patients with TBI. Some patients with mild TBI have variable neurological symptoms. In such patients, computed tomography (CT) and magnetic resonance imaging (MRI) can present normal findings. Advanced imaging techniques, such as diffusion tensor imaging (DTI), magnetic resonance spectroscopy (MRS), perfusion weighted imaging (PWI), or functional MRI, can reveal abnormalities that are not detected using conventional imaging methods.

Materials and Methods

Here, we briefly review current neuroimaging for TBI and survey advanced imaging techniques in terms of structural and functional aspects, which include a few promising areas of TBI research.

Results

The recent advanced neuroimaging methods for TBI are categorized as structural or functional biomarker techniques. This article reviews advanced traumatic neuroimaging regarding these two categories. 1. Structural Imaging - Microhemorrhage Susceptibility-Weighted Imaging (SWI) - Brain Contusion 3D thin-section T2/ T2-FLAIR imaging Diffusion-Weighted Imaging (DWI) - Brain atrophy 3D isotopic T1WI 2. Advanced Imaging - Diffusion-Tensor Imaging (DTI) - Magnetic resonance spectroscopy (MRS) - Perfusion Weighted Imaging (PWI) - Functional MRI

Conclusions

Conclusion TBI is a major health problem worldwide. In the future, the clinical use of advanced neuroimaging methods that specialize in delineating hemorrhages, white matter fiber tracks, ischemia, and blood-brain barrier disruption should ensure standardized approaches to image acquisition and analysis, improve prognostic accuracy, and facilitate the development of new therapies.

A

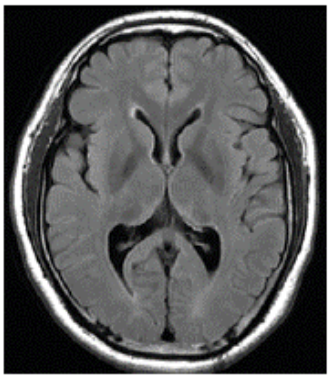

B

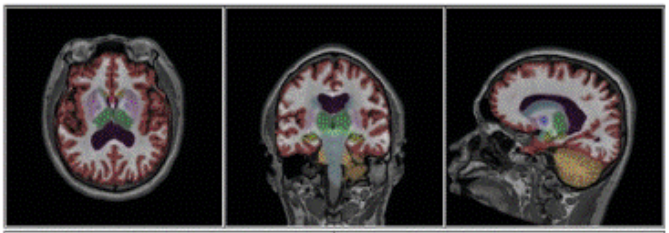

Intracranial Volume (ICV) (cm³)			1742.90		
Brain Structure	LH Volume (cm³)	LH Volume (% of ICV)	RH Volume (cm³)	RH Volume (% of ICV)	Asymmetry Index (%)*
Forebrain Parenchyma	610.14	35.01	611.44	35.08	-0.21
Cortical Gray Matter	282.94	16.23	291.21	16.71	-2.88
Superior Lateral Ventricle	29.23	1.68	33.20	1.90	-12.71
Inferior Lateral Ventricle	0.88	0.05	0.83	0.05	5.88
Hippocampus	4.44	0.25	4.59	0.26	-3.23
Amygdala	1.90	0.11	1.75	0.10	8.43
Caudate	5.52	0.32	6.50	0.37	-16.21
Putamen	6.97	0.40	6.78	0.39	2.72
Pallidum	0.86	0.05	0.80	0.05	7.71
Thalamus	8.67	0.50	8.11	0.47	6.66
Cerebellum	76.32	4.38	75.00	4.30	1.75

*The Asymmetry Index is defined as the percentage difference between left and right volumes divided by their mean.

C

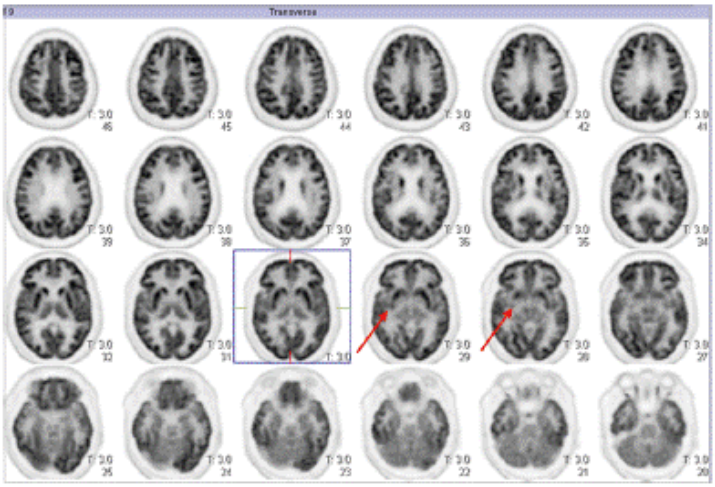

D

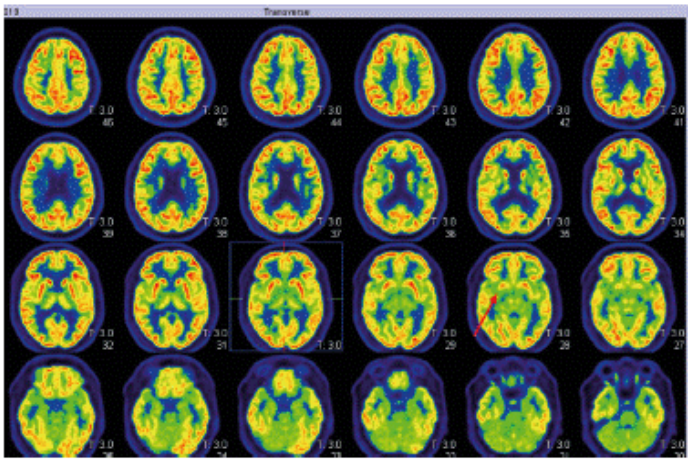

(Filename: TCT_1543_TBI.gif)

890

Imaging features of Balamuthia Amebic Encephalitis

J Baal[1], S Cha[2]

[1]UCSF, San Francisco, CA, [2]University of California San Francisco, San Francisco, CA

Purpose

Balamuthia mandrillaris is a free-living, ubiquitous amoeba, which can cause a rare, usually fatal meningoencephalitis in both immunocompetent and immunocompromised individuals. Since the early 1990s, over 200 cases worldwide have been reported. The imaging findings in Balamuthia encephalitis is often nonspecific and can overlap with other infectious entities such as bacterial, viral or parasitic meningoencephalitis as well as neoplastic entities such as high grade glioma or intracranial metastasis. Educational Objectives: I. Presentation of four cases from our institution, including clinical presentation and a series of associated imaging findings. II. Diagram summarizing the most common imaging findings seen in Balamuthia encephalitis from a comprehensive search of the current literature. III. Brief self-assessment

Materials and Methods

The purpose of this study is to present the imaging features of confirmed cases of Balamuthia encephalitis from our institution, review the current literature for the most common imaging findings seen in this entity, and highlight key imaging features that can aid in diagnosis.

Results

In an image-rich format, various MR imaging patterns of Balamuthia encephalitis from our patient group will be presented in this interactive digital educational exhibit. A summary of the most common imaging characteristics observed in confirmed cases of Balamuthia amebic encephalitis from a systematic review of the current literature will be presented. At the conclusion of the exhibit, a brief self-assessment quiz will be presented for reinforcement of major teaching points.

Conclusions
Although imaging features of Balamuthia encephalitis have been considered nonspecific, this exhibit will highlight key imaging features that can aid in identifying this serious infection early and promptly using MR imaging.

144

Imaging Features To Predict MGMT Promoter Methylation Status In Patients With Glioblastoma

A Nada[1], M Baqar[1], E Mahmoud[2], E Mahdi[1], H Ahsan[1], C LEIVA-SALINAS[1], J Cousins[1]
[1]University of Missouri Healthcare, Columbia, MO, [2]National Cancer Institute, Cairo University, Cairo, Cairo

Purpose
1. Discuss the role of MGMT promoter methylation status. 2. Demonstrate the impact of MGMT promoter methylation status on patients' outcomes. 3. Illustrate the pathogenesis of pseudoprogression and its association to MGMT promoter methylation status. 4. Describe different imaging features to predict MGMT promoter methylation status. 5. Discuss potential value of radiomics to evaluate MGMT promoter methylation status.
Materials and Methods
Our purpose is to demonstrate various described imaging features that can predict MGMT promoter methylation status with the impact on the patients outcome.
Results
1. Discuss the role of MGMT promoter methylation status: role in DNA repair, difference between methylated and unmethylated, impact on DNA repair and relationship to chemotherapeutic agents e.g. temozolamide. 2. Explain the impact of MGMT promoter methylation status on the prognosis and outcome in patients with GBM: how methylated MGMT promoter correlates with good outcome. 3. Illustrate the incidence and prevalence of pseudoprogression phenomenon in methylated MGMT promoter with explanation of underlying pathophysiology. 4.Discuss various MR imaging features to predict MGMT promoter methylation status. 5. Demonstrate radiomic based features to evaluate MGMT promoter methylation status. 6. Demonstrate impact of MGMT promoter methylation status to guide clinical decision making.
Conclusions
Prognosis of glioblastoma with the development of pseudoprogression phenomenon is strongly related to MGMT promoter methylation status. Prediction of Suggested imaging features can point into

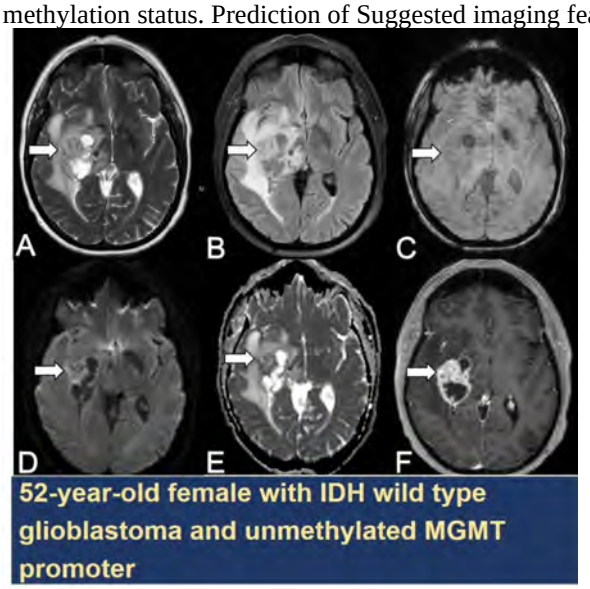

(Filename: TCT_144_GBMunmethylatedMGMTpromoter.jpg)

396

Imaging Findings of Rhino-oculo-cerebral Mucormycosis

V Agarwal[1], A Batra[2], P Bharti[1]
[1]Christian Medical College, Ludhiana, Punjab, India, [2]Christian Medical College, Ludhiana, Punjab

Purpose
Rhino-oculo-cerebral mucormycosis is a life-threatening infection caused by saprophytic fungi seen almost exclusively in immunocompromised patients. Recently we saw a huge surge in the number of Coronavirus disease (COVID-19)-associated mucormycosis. The objective of this study was to describe the imaging findings in patients with rhino-oculo-cerebral mucormycosis.
Materials and Methods
To describe the imaging findings in patients with rhino-oculo-cerebral mucormycosis.
Results
We evaluated the case records of 45 patients with biopsy/culture proven invasive rhino-oculo-cerebral mucormycosis. Computed

Tomography (CT) and/or Magnetic Resonance Imaging (MRI) images were retrieved from the Picture Archiving and Communication System (PACS) and analyzed. Statistical analysis was performed using descriptive statistics.
Conclusions
CT and MR imaging evaluated in biopsy proven 45 patients of mucormycosis showed predominant involvement of the maxillary (40, 89%), ethmoid (38, 84%)and sphenoid (34, 75%) sinuses. Extension to the orbit (subperiosteal / extraconal) (34, 75%) and face (premaxillary fat) (38, 84%) preceded involvement of the deep skull base (6, 13%) and brain (5, 11%). "Black Turbinate" sign was seen in 34 (75%) patients. 2 patients had vascular complications (Left cavernous ICA pseudoaneurysm and right cavernous ICA occlusion). Bone erosion was seen less often (16, 35%). CT showed minimally enhancing hypodense soft tissue thickening as the predominant finding in involved areas, while MRI showed T2 predominantly hypo intense soft tissue thickening and heterogeneous post contrast enhancement as the main finding.

1510

Imaging in Temporal Bone Emergencies beyond Acute Trauma!

D Pinto[1], A Pulido[2], A Zalis[2], N Robertson[2], R Bhatia[3], N Nagornaya[3]
[1]Jackson Memorial Hospital, Miller school of medicine, Miami, FL, [2]University of Miami/Jackson Memorial Hospital, Miami, FL, [3]Jackson Memorial Hospital/University of Miami, Miami, FL

Purpose
This presentation includes a wide spectrum of temporal bone emergencies with a focus on infections and its complications. List of educational objectives: After reviewing this presentation the reader should 1) Be able to identify and differentiate between common non-traumatic temporal bone emergencies on imaging. 2) Be able to identify the role of MRI in imaging temporal bone pathology Structure of the presentation: *List of educational objectives: *Anatomy of the temporal bone *HRCT of the temporal bone – approach and structured reporting. *Importance of MRI in temporal bone imaging *Represented cases include: Infections External ear: Malignant otitis externa Middle ear: a) Suppurative otitis media b) Coalescent mastoiditis c) Petrous apicitis Inner ear: Membranous labyrinthitis Complication of infections: Temporal bone and skull base osteomyelitis Bezolds abscess Dural venous sinus thrombosis CSF leak Nerve pathology: a) Bell's palsy b) Herpes-Zoster Oticus Tumors: Glomus tumor causing obstruction
Materials and Methods
Temporal bone emergencies present with potentially high morbidity. They have a diverse appearance on imaging and have immense potential for developing complications. We aim to provide a structured format for accurately diagnosing non-traumatic temporal bone emergencies and to differentiate them from other entities.
Results
A search through the database of 2 health systems for temporal bone emergencies yielded a large number of patients with emergency pathology. We present a series of cases illustrating the approach to temporal bone emergencies other than trauma.
Conclusions
Temporal bone emergencies are not limited to just trauma. Both CT and MRI have their utility in the evaluation of the temporal bone. Using a step-by- step approach introduced by this structured case discussion should help the reader develop a strong method to analyze temporal bone emergencies.

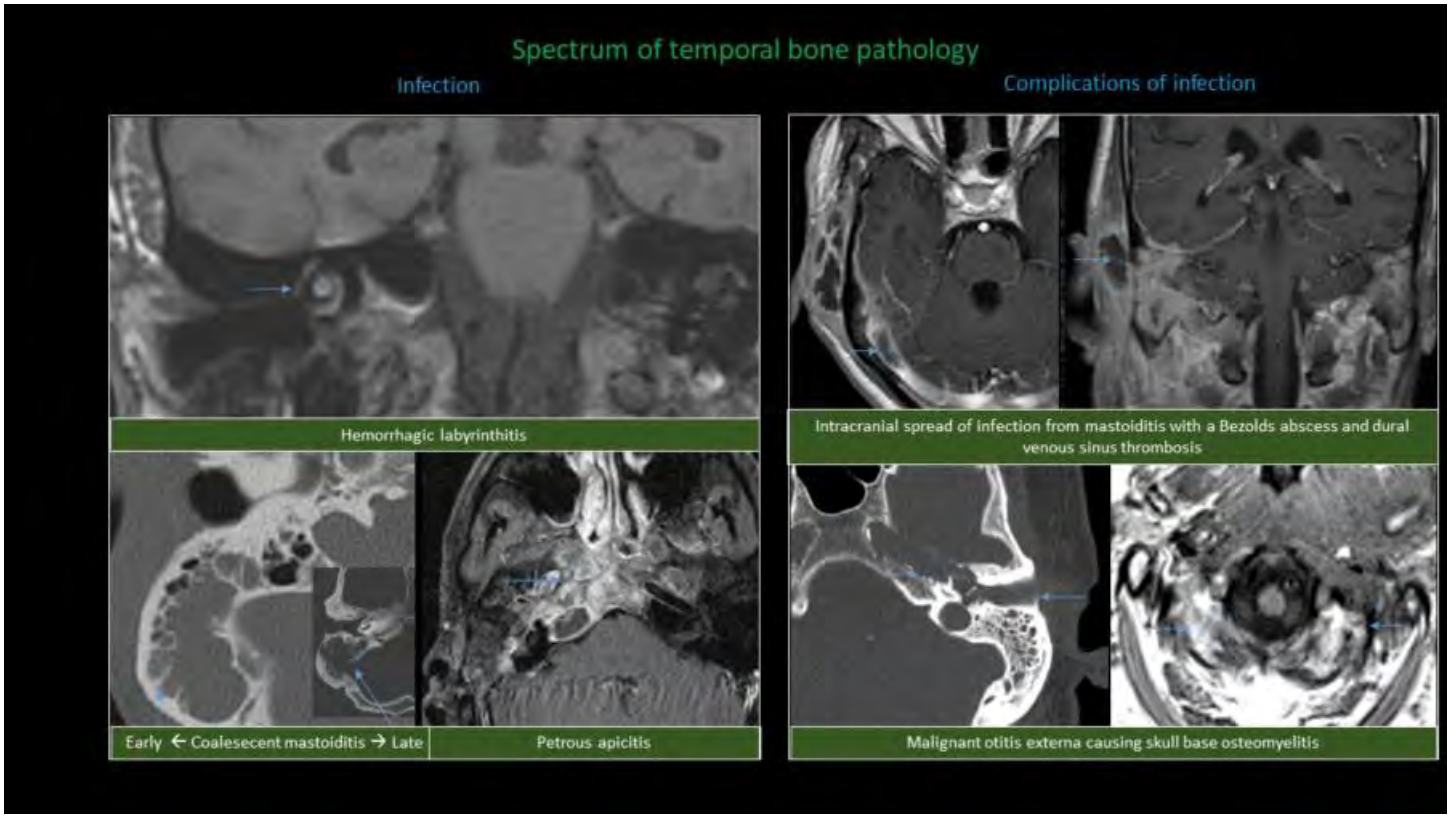

(Filename: TCT_1510_TEmporalboneemergenciespresentation300x300x300.jpg)

1340

Imaging in Tympanosclerosis

M McHugh[1], Y Lau[2], A Herwadkar[3]

[1]Salford Royal Foundation Trust, Manchester, United Kingdom, [2]Salford Royal NHS Foundation Trust, Salford, Manchester, [3]Salford Royal NHS Foundation Trust, Northern Care Alliance, Greater Manchester Neurosciences Centre, Salford, Salford

Purpose

Tympanosclerosis (TS) is a commonly recognized condition characterized by an abnormal formation of calcified deposits in the middle ear, tympanic membrane and mastoid air cells. This typically occurs in response to inflammatory middle ear pathology.[1] This may cause conductive hearing loss. High resolution multi-detector CT is the preferred modality used in imaging of TS.[2] Learning objectives: 1. Define TS and summarise the epidemiology, pathophysiology and clinical manifestations. 2. Understand the role of cross-sectional imaging. 3. Diagnostic features of TS on CT, with consideration of alternative middle ear pathologies.

Materials and Methods

The purpose of this educational exhibit is to demonstrate typical imaging features seen in TS, using a series of case-studies.

Results

We present a retrospective review of the CT imaging findings in a variety of cases that have presented with conductive hearing loss through our audiological department at our tertiary centre over a period of ten years. Patients with known or proven cholesteatomas and previous surgery were excluded from the analysis. Scans were performed using a 64 slice multi-detector CT scanner. Imaging was acquired in 0.625 mm axial sections and thin multiplanar reconstructions were carried out in all cases in various planes to evaluate the tympanic cavity. These scans and associated MR scans were interpreted by a neuro-radiologist with over 14 years of experience in temporal bone imaging.

Conclusions

TS typically presents as high-density or calcific foci within the tympanic membrane or middle ear cavity and can be associated with a small tympanic cavity with hypo-pneumatisation. These are seen as areas of increased density on the ossicles, suspensory ligaments and muscle tendons. Imaging reveals focal or diffuse calcified plaques, distortion of normal ossicular anatomy, or web-like calcified hyperdense plaques on the tympanic membrane. In chronic conditions, ossicular fixation was observed. The commonest site of involvement was in the attic with incudo-malleolal joint fixation. This was followed by affection of stapes, crura and the foot plate. Non-calcified opacities can be difficult to distinguish from granulation tissue and cholesteatomas. Typical location and ossicular erosions are seen in both conditions. TS can result in a false positive finding of diffusion restriction on a non-echo planar diffusion MR imaging, mimicking a cholesteatoma. Multiple imaging modalities in combination with clinical findings may be recommended.

1413

Imaging Manifestations and Complications of Neurosarcoidosis

A El-Araby[1], V Andreu Arasa[1], O Sakai[2]

[1]Boston Medical Center, Boston, MA, [2]Boston Medical Center, Boston University School of Medicine, Boston, MA

Purpose

Sarcoidosis is an idiopathic multisystem disease characterized by formation of non-caseating granulomas. It may involve any part of the nervous system and its coverings, with a clinical presentation and imaging findings that mimic a broad spectrum disease. Imaging serves an essential role in evaluation of neurosarcoidosis by localizing disease involvement, predicting clinical symptoms, monitoring the course of disease, and assessing treatment response. Nervous system involvement, neurosarcoidosis, can occur in both patients with or without systemic sarcoidosis. Additionally, patients with neurosarcoidosis may be either symptomatic or asymotimatic. As neurologic symptoms may be the presenting symptoms, this often prompts the imaging of patients not yet diagnosed with sarcoidosis and thus highlights the importance of being familiar with the imaging manifestations of neurosarcoidosis. Of equal importance is familiarity with the complications of sarcoidosis and its treatments, which are notable for infection. Neruosarcoidosis may affect any part of the nervous system including the meninges (pachymeninges and leptomeninges), CNS parenchyma, or cranial nerves. Pachymeningeal disease involves dural enhancement, and thickening or nodularity. Leptomeningeal involvement presents also as enhancement, which however, may be gyriform, interdigitating at sulci, perivascular spaces, or portions of the brain at the skull base. The pituitary gland, infundibulum, hypothalamus and cranial nerves may be involved as pat of leptomeningeal disease or in isolation. Reported to be the most common, parenchymal involvement is diverse in its imaging features, may present as T2 signal abnormality or enhancing nodules and masses. Likewise, the spinal cord may be involved.

Materials and Methods

N/A

Results

We retrospectively reviewed the neurological clinical signs and symptoms, and imaging findings of the patients seen in our Sarcoid clinic from May 2020 to September 2021.

Conclusions

Amongst the patients that were reviewed, imaging abnormalities were noted to involve meninges, brain parenchyma, pituitary/hypothalamus, cranial nerves, and spinal cord. Neurosarcoidosis is a disease with many imaging patterns of involvement, generally involving the pachymeninges, leptomeninges, brain parenchyma, and spinal cord. Recognition of the imaging manifestations is critical in preventing delayed diagnoses, correlating and predicting clinical signs and symptoms, and evaluating treatment and guiding clinical management.

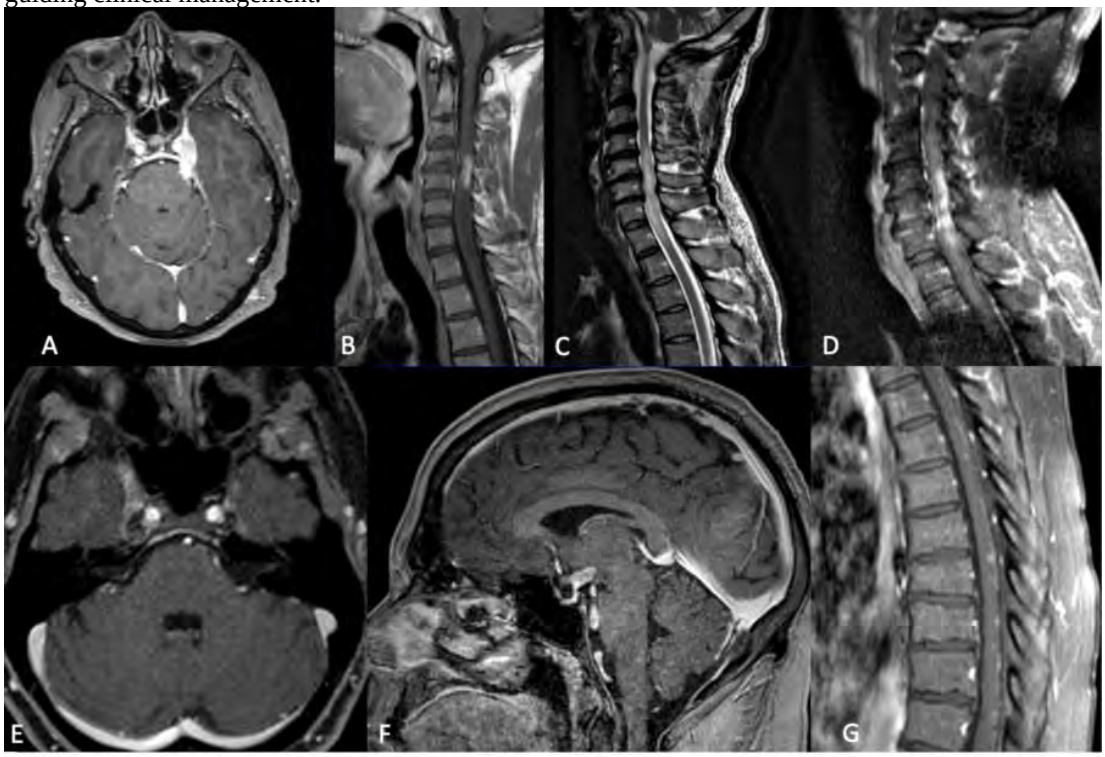

A) 67 year-old Hispanic woman with trigeminal neuralgia distribution of pain, imaging reveals marked thickening and enhancement of the left trigeminal nerve extending to the trigeminal ganglion. B) 31 year-old hispanic man with ascending weakness and paresthesias affecting lower and upper extremities, imaging reveals a segment of abnormal enhancement in the cervical spinal cord at C4-C5. Of note, additional findings of disc disease at the same level. C) 48 year-old African American man with lower extremity weakness and spasticity, imaging of cervical spine reveals abnormal intramedullary T2 hyperintensity with patchy enhancement (image D). E) 45 year-old Caucasian woman with left facial palsy, imaging reveals enhancement of the left facial nerve. F) 50 year-old Hispanic man evaluated tor low testosterone levels, imaging reveals abnormal hypothalamic enhancement. G) 52 year-old Caucasian woman with lower extremity and lower trunk paresthesias, imaging reveals diffuse leptomeningeal nodular enhancement best demonstrated along the posterior cord.

(Filename: TCT_1413_El-Araby_Neurosarcoidosis.jpg)

1436

Imaging Neurological Emergencies: Beyond Trauma and Stroke.

M Drake-Pérez[1]

[1]Hospital Universitario Marqués de Valdecilla, Santander, NE

Purpose

Imaging techniques available at the Emergency Department will be discussed. Five different clinical scenarios will be listed: coma, seizure, headache, fever and neurological deficit (other than stroke). Clinical description, imaging indications, radiological findings and differential diagnosis will be addressed for each of them. List of educational objectives: • Discuss the different possible diagnosis for neurological emergencies, apart from trauma and stroke. • Review the imaging indications. • Highlight the role of non-enhanced CT in the emergency setting.

Materials and Methods

NA

Results

NA

Conclusions

NA

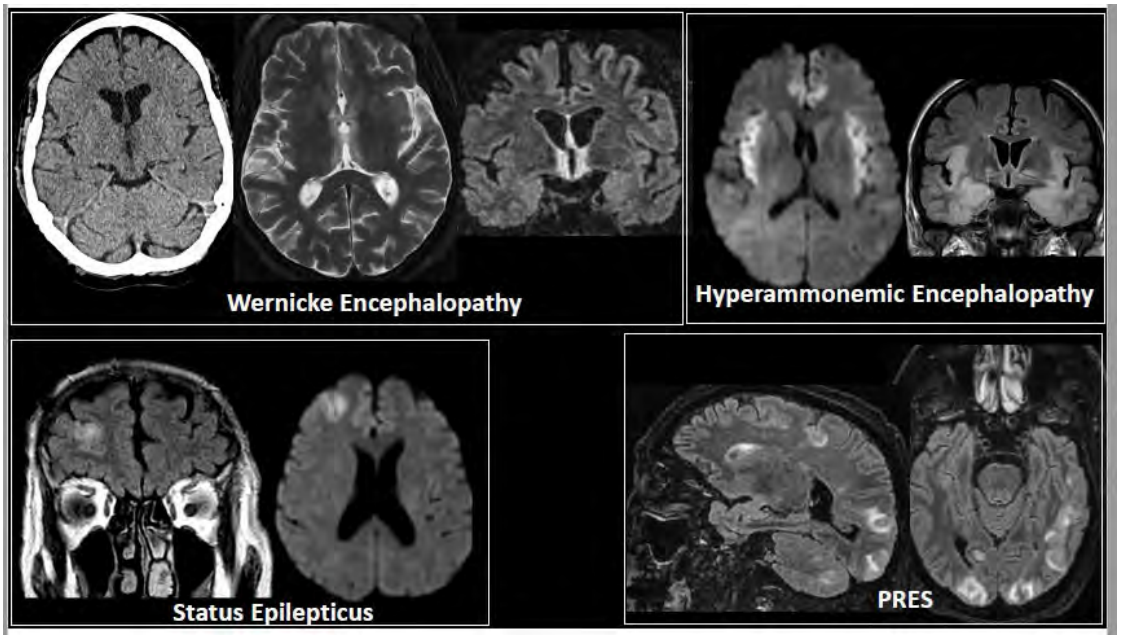

(Filename: TCT_1436_Sinttulo.jpg)

1331

Imaging of Charcot Spine: A Multi-modality Review of Spinal Neuroarthropathy and its Mimics.

Y Lau[1], M McHugh[2], A Herwadkar[3]

[1]Salford Royal NHS Foundation Trust, Manchester, United Kingdom, [2]Salford Royal Foundation Trust, Manchester, United Kingdom, [3]Salford Royal NHS Foundation Trust, Northern Care Alliance, Greater Manchester Neurosciences Centre, Salford, Salford

Purpose

1. Understand the pathophysiology and clinical presentation of spinal neuroarthropathy (SNA). 2. Recognise the classic diagnostic features (6Ds), as depicted in plain films, CT and MR imaging. 3. To be conscious of the common differentials of SNA and features used to distinguish them.

Materials and Methods

Spinal neuroarthropathy (SNA), also known as Charcot spine, is a rare progressive destructive condition caused by a loss of proprioception and pain. While first described as a complication of neurosyphilis[1], SNA is now most commonly recognised as a sequelae of traumatic cord injury[2]. Rarely, cases have also been reported in diabetes, multiple sclerosis and syringomyelia[3]. In the absence of afferent sensation, inherent neuromuscular protective mechanisms fail- resulting in repetitive microtrauma to the disco-vertebral unit. Unfortunately, due to the existing neurological deficits in these patients, early symptoms can be minimal causing SNA to present in its later stages[3]. The process of SNA begins with soft tissue and osseous inflammation, eventually progressing to disorganised bony regeneration[3]. Thus, it is important to recognise and correlate different modalities of imaging when assessing for SNA. Additionally, it is recognised that there is considerable overlap between features of SNA and other pathological spinal processes[3]. Therefore, identifying the radiological features that separate SNA from its mimics is key.

Results
We present cases of patients with SNA that attended our tertiary centre over a period of ten years, demonstrating the initial neurological insult and subsequent changes in the imaging manifestation. Patients' plain film, CT and MR imaging were retrospectively reviewed for the 6Ds of SNA, which are increase in density, bony destruction, disorganization, spinal dislocation of normal anatomy, presence of debris and joint distension.
Conclusions
Typical imaging features of SNA involve all the joints between adjacent segments, affecting both the anterior disco-vertebral junction and posterior elements. Severe disorganization with dislocation, loss of normal anatomy, paraspinal soft tissue masses and heterotopic ossification are also commonly seen. Some common mimics of SNA include infection, pseudoarthrosis in adjacent segments following spinal fixation and haemodialysis related spondyloarthropathy. Imaging along with clinical context is key in the differentiation between these conditions.

1006

Imaging of Migraine: Current and Emerging Approaches

D Phung[1], S Pinto[2], B Chou[1], W Xu[1], A Lerner[1], N Sheikh-Bahaei[1]
[1]Keck School of Medicine of the University of Southern California, Los Angeles, CA, [2]Children's Hospital of Los Angeles, Los Angeles, CA

Purpose
Migraine is a common disorder with incompletely understood complex pathophysiology which underlies its varying clinical presentation including those with and without aura or other neurologic symptoms. While imaging has traditionally been used to exclude other etiologies for migraine symptoms, the ongoing development of advanced MRI techniques has provided new avenues of research for both diagnosis and elucidation of this heterogeneous disease process. Arterial spin labeling (ASL) perfusion changes have been found to correlate with preictal neurologic symptoms. Diffusion tensor imaging (DTI) and functional MRI (fMRI) have been used to study the many changes in functional connectivity that occur in the various types of migraine. Here we present a comprehensive review of the current and emerging MR imaging approaches for migraine evaluation. Content Organization: • Migraine Background o Diagnosis o Types including those with and without aura, chronic versus episodic, hemiplegic migraine, vestibular migraine, and retinal migraine o Pathophysiology • Current Clinical Role of Imaging o Excluding secondary causes of headache and migraine mimics o Discussing the discrepancies in the current literature on migraine imaging and potential explanations for conflicting results • Pictorial Review of structural MRI Findings o Volumetric changes o White matter T2/FLAIR hyperintensities o Prominent Perivascular Spaces o Changes on susceptibility weighted images such as cerebral microhemorrhages, asymmetrical venous dilatation, and superficial siderosis. • Pictorial Review of Advanced Imaging Approaches o ASL Perfusion and temporal relationship with symptoms o DTI o fMRI • Future Directions for Research and utility of ultra-high field MRI in migraine imaging After viewing this exhibit the participant will: 1. Recognize the various types of migraine 2. Understand the role of imaging for migraine and the associated findings which may vary with migraine type 3. Appreciate the role of advanced imaging techniques under investigation
Materials and Methods
1. Review the diagnostic criteria and types of migraine 2. Review the classic MR imaging findings associated with migraine 3. Present the evolving roles of ASL perfusion, DTI, and fMRI
Results
N/A
Conclusions
N/A

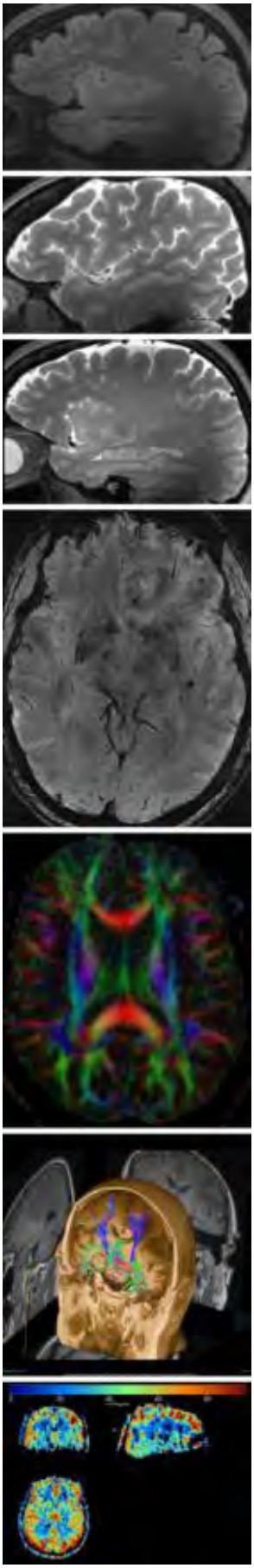

(Filename: TCT_1006_MigraineImagingPanorama.jpg)

781

Imaging of the Brachial Plexus Anatomy and Pathologies: Back to the Roots (…Trunks, Divisions, Cords, and Branches)

G Vilanilam[1], R Ramakrishnaiah[2], S Vattoth[1], M Kumar[1], R Van Hemert[1], M Mian[1], S Sharma[1], A Amole[1], S Patro[1]

[1]University of Arkansas for Medical Sciences, Little Rock, AR, [2]Univ of Arkansas for Medical Sciences, Little Rock, AR

Purpose

The brachial plexus is a complex anatomic component originating from the ventral rami of the lower cervical nerve roots from C5 to C8 and upper thoracic spinal nerve roots from T1, providing sensory and motor innervation to the upper extremities. The various imaging techniques used to evaluate brachial plexus normal anatomy and pathologies include CT and MRI. Imaging modalities: CT: To assess for external compressive etiologies such as hematoma and mass lesion, osseus anomalies such as cervical rib and vertebral body erosion. Suboptimal modality to evaluate individual nerves. CT angiography and venography: To assess for thoracic outlet syndrome using arms-up and arms-down positioning. CT myelography: To assess for root avulsions. MRI primary sequences: To assess nerves, muscle atrophy, and anatomic relationships (T1-weighted non–fat-suppressed sequence). To assess neurovascular signal abnormality, soft tissue, and muscular edema (T2-weighted fat-suppressed sequence). To assess the course of the nerves (maximum intensity projections and curvilinear reconstructions). MRI advanced sequences: 3D STIR SPACE sequence, 3D heavily T2-weighted MR myelography sequences (balanced SSFP=CISS 3D, True FISP 3D, bFFE, FIESTA), and the diffusion-weighted (DW) neurography sequence with fiber tracking reconstruction (tractography). The commonly encountered neuropathies discussed in this exhibit are: 1. Post traumatic brachial plexus root avulsion and pseudomeningocele 2. Nerve sheath tumors 3. Invasion from adjacent tumor 4. Brachial plexus neuritis

Materials and Methods

The purpose of this educational exhibit is: 1. To learn the imaging features of the normal brachial plexus using CT and high-resolution MRI with special sequences. 2. To familiarize the radiologist with the imaging features of commonly encountered brachial plexus lesions.

Results

N/A

Conclusions

The brachial plexus is a complex structure that can be challenging to image and manage. Multimodality imaging is used to confirm and localize sites of involvement, to assess for underlying structural or neoplastic pathologies, and to assist in preoperative planning. Familiarity with the imaging appearance of normal anatomy and pathologies of the brachial plexus is vital for radiologic evaluation of this structure.

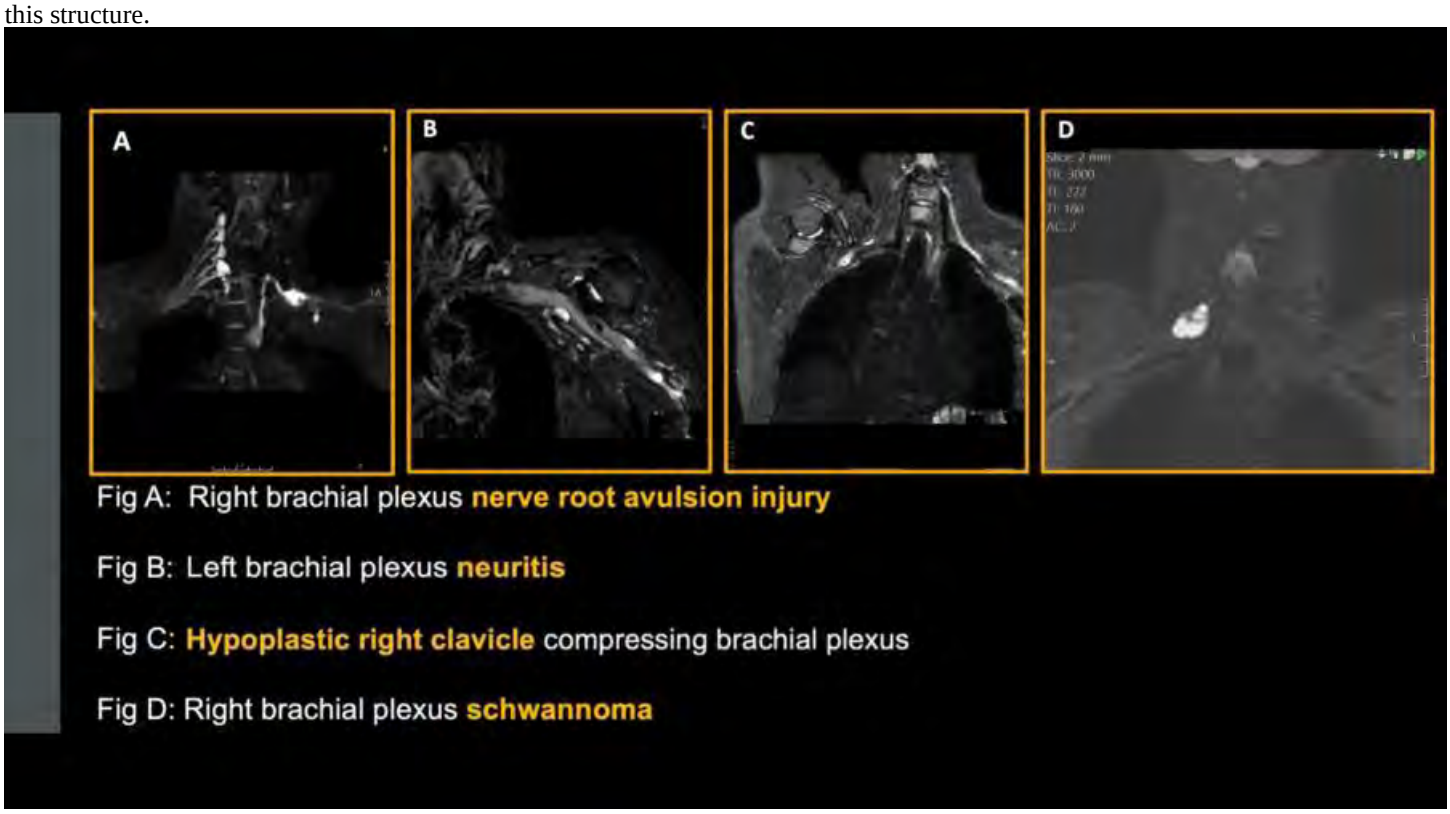

(Filename: TCT_781_Brachialplexus_ASNR22.jpg)

817

Imaging of the sella turcica

B Asenjo Garcia[1], M Vidal-Denis[1], F Nagib Raya[2], M Arraez Sanchez[1], C Arraez Manrique[1], S Maraver-Selfa[1], I Gonzalez Molero[1], A Pérez-Lara[3]

[1]Hospital Regional Universitario de Málaga, MALAGA, Malaga, [2]Hospital Regional Universitario de Málaga, Malaga, Malaga, [3]Hospital Regional Universitario de Málaga, Málaga, Malaga

Purpose

There are a wide variety of entities that involve the sella turcica, leading to an extensive differential diagnosis. Moreover, the postoperative imaging assessment of sellar lesions can be challenging and requires specific training. EDUCATIONAL OBJECTIVES: - Provide a practical differential diagnosis of sellar lesions based on imaging characteristics. - Review the most significant anatomic structures of the sella turcica for presurgical planning. - Describe the most frequent postoperative and post treatment changes involving the sella turcica.

Materials and Methods

There are a wide variety of entities that involve the sella turcica, leading to an extensive differential diagnosis. Moreover, the postoperative imaging assessment of sellar lesions can be challenging and requires specific training. The purpose of this work is to provide a practical differential diagnosis of lesions involving the sella turcica based on imaging and clinical features. In addition, anatomical structures that are significant for presurgical planning are reviewed. A postoperative imaging pictorial essay is provided describing pearls and pitfalls to differentiate between residual lesions and expected postsurgical changes.

Results

A retrospective review of sellar lesions was performed. Imaging MRI and CT features are described, and key radiological findings are highlighted in each case.

Conclusions

Classic cases of sellar lesions are shown, including primary and secondary pituitary tumors, infundibular entities, inflammatory and congenital lesions, extraglandular tumors and cysts. Moreover, critical anatomical structures for presurgical planning are demonstrated. Postoperative transsphenoidal changes including scarring, hemorrhage, haemostatic and surgical material are also shown, as well as drug-induced changes especially in conservative treatment of micro and macroadenomas. Key features to differentiate these changes from residual lesions are provided. The sella turcica is a complex anatomic structure that can be affected by multiple entities. Familiarity with the imaging features of different lesions and with normal postsurgical and post treatment changes is essential to achieve an accurate differential diagnosis.

302

Imaging Review of Labyrinthitis

S Dyer[1], A Madhavan[2], J Lane[2]

[1]MAYO CLINIC, Rochester, MN, [2]Mayo Clinic, Rochester, MN

Purpose

Summary: 1. Background and etiologies of labyrinthitis. 2. Typical work-up and our institution's imaging protocol for labyrinthitis. 3. Case examples of acute, subacute, and chronic labyrinthitis (jpeg for examples, additional case examples and etiologies would be included in final presentation). 4. Mimics of labyrinthitis and other causes of labyrinthine signal abnormality on MRI. Learning Objectives: 1. Describe appropriate imaging techniques for evaluating labyrinthitis. 2. Recognize and describe the radiographic findings in acute, subacute, and chronic labyrinthitis. 3. Recognize pitfalls in the radiographic assessment for labyrinthitis. 4. Recognize and describe alternative diagnoses that can mimic labyrinthitis.

Materials and Methods

Describe appropriate imaging techniques for evaluating labyrinthitis.

Results

N/A

Conclusions

N/A

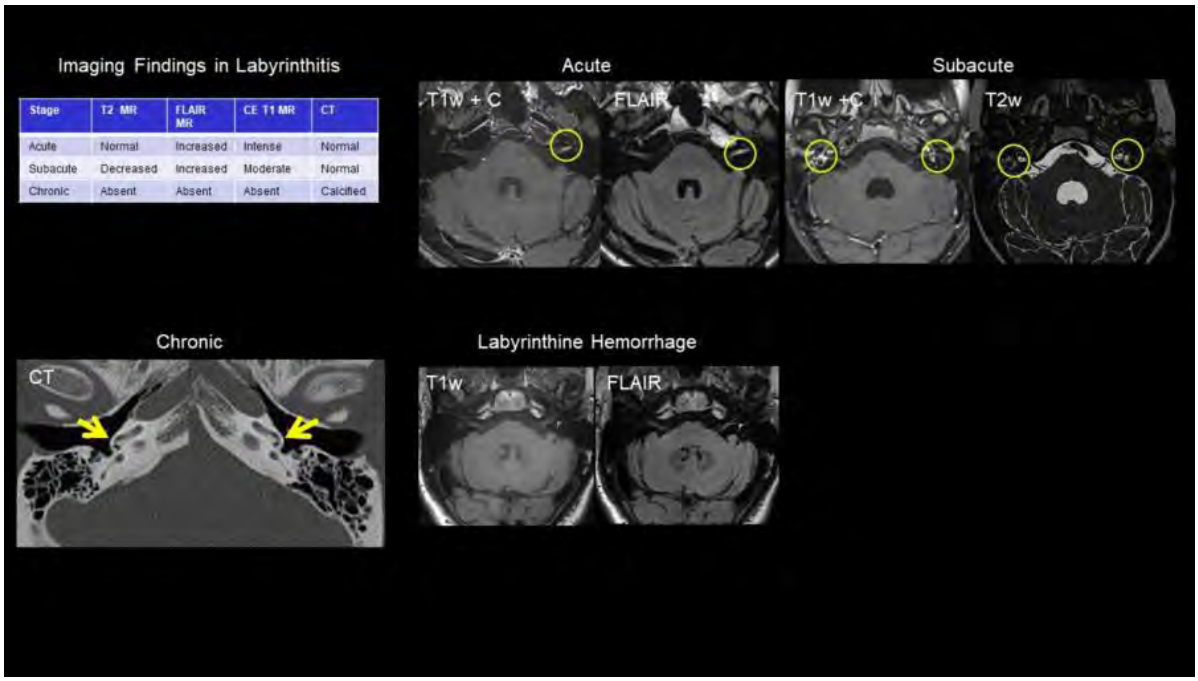

(Filename: TCT_302_Labyrinthitis.jpg)

826

Imaging Spectrum of Diffuse Leptomeningeal Glioneuronal Tumors (DLGNT)

S Kandemirli[1], J Starkey[2], P Watal[3], T Moritani[4], S Sato[5]

[1]University of Iowa, Iowa city, IA, [2]Oregan Health & Science University, Porland, OR, [3]N/A, N/A, [4]University of Michigan, Ann Arbor, MI, [5]University of Iowa, iowa city, IA

Purpose

- Diffuse leptomeningeal glioneuronal tumor was a recently defined tumor subtype in the 2016 World Health Organization classification of brain tumors. - Herein, we will demonstrate the typical as well as not so typical imaging findings of diffuse leptomeningeal glioneuronal tumors. We will also include imaging findings of different entities in the differential list. - Typical imaging findings include thick, basilar leptomeningeal enhancement, subpial cysts, cranial nerve involvement, hydrocephalus, parenchymal or non-parenchymal spinal cord involvement.

Materials and Methods

-To report the imaging findings of diffuse leptomeningeal glioneuronal tumors (a collection of 8 cases) -To report helpful clues for a correct differential diagnosis

Results

*Table of Contents/Outline: 1) Introduction and outline 2) Why the name? 3) Review of glia and DLGNT histology. 4) Epidemiology. 5) Patient presentation. 6) Imaging findings, common and uncommon, brain and spine. 7) Pathological findings, including histology and genetics, WHO 2016 Classification. 8) DDx. 9) Treatments. 10) Summary.

Conclusions

DLGNTs are often histologically low grade with indolent behaviors. Optimal treatment is not established due to rarity of this tumor but include resection, radiation therapy, and/or chemotherapy.

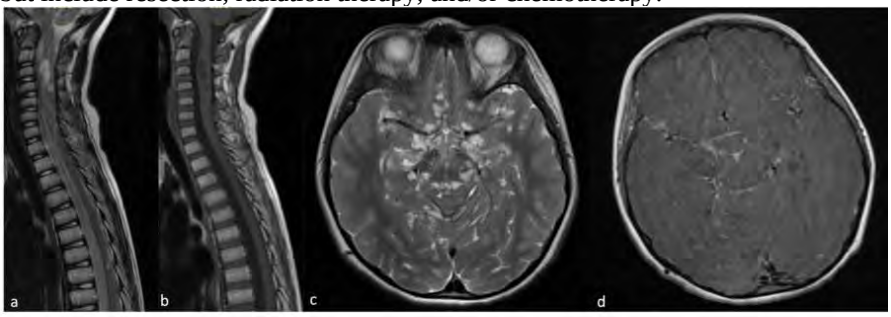

DLGNT with a cystic cervical spinal cord lesion (a, b). T2-WI (c) and post-contrast T1 (d) images at basal cisterns show the typical diffuse "cyst-like" leptomeningeal surfaces with post-contrast enhancement.

(Filename: TCT_826_dlgnt.jpg)

568

Imaging Spectrum of Intracranial Meningioma Variants

M Ali[1], K Dammeyer[1], B Griffith[1], J Corrigan[1], S Patel[1]
[1]Henry Ford Health System, Detroit, MI

Purpose

Meningiomas are the most common non-glial tumor of the central nervous system, typically occurring in the brain and spine. While most meningiomas have a typical imaging appearance, some meningioma subtypes have imaging features that can make it challenging for radiologists to make a straight forward diagnosis. Additionally, although predominantly benign, there are aggressive meningioma variants that can have a more malignant course. Upon completion of this educational exhibit, the learner will become familiar with the imaging features of intracranial meningiomas, including some of the unique features of a variety of WHO Grade I subtypes, as well as of the more aggressive WHO Grade II and III variants.

Materials and Methods

The purpose of this exhibit is to provide a pictorial review of the imaging features of intracranial meningiomas with an emphasis on unique features of the various subtypes.

Results

• Review the WHO classification of meningiomas, including the subtypes of WHO Grade I meningiomas, as well as the atypical (Grade II) and malignant (Grade III) variants. • Review the common imaging features of a typical meningioma, including on CT, MRI, and DSA. • Review imaging features that can help distinguish the histologic meningioma subtypes including the various typical meningioma subtypes such as secretory (Fig 1) and angiomatous (Fig 2), as well as more aggressive atypical (Fig 3) and malignant (Fig 4) meningiomas.

Conclusions

Meningiomas are the most common extra-axial tumor of the central nervous system and are frequently encountered in practice. While most meningiomas demonstrate a characteristic imaging appearance, some may demonstrate atypical or aggressive features. Radiologists must not only be familiar with the imaging characteristics of a classic meningioma, but must also be aware of uncommon imaging features that may suggest a less common histologic subtype or more aggressive variant. This knowledge will help provide important information to the clinician that will help in preoperative planning and determining overall prognosis.

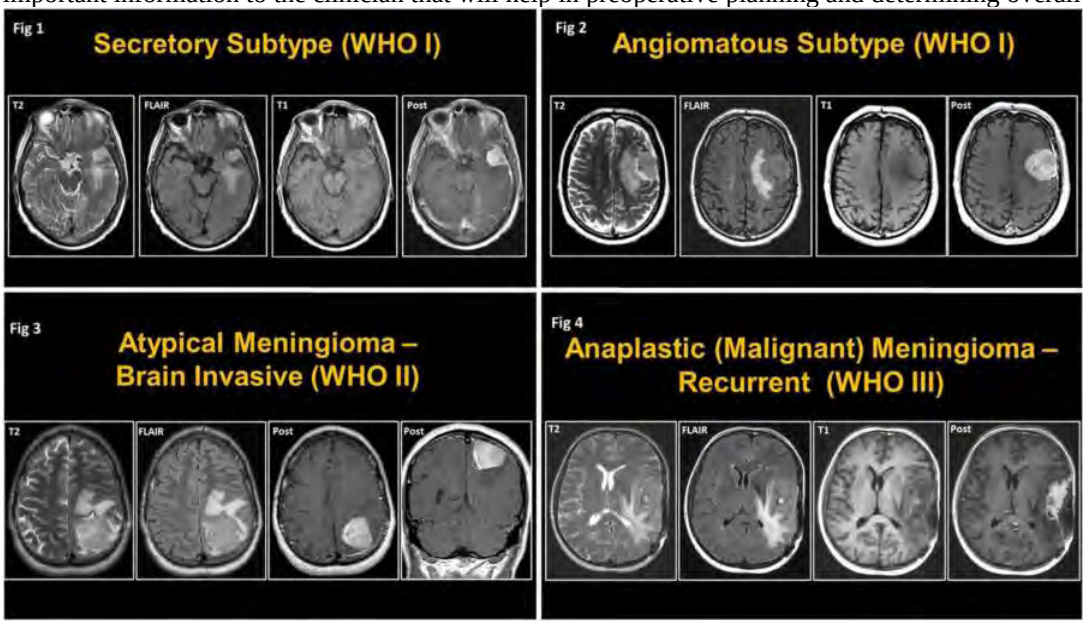

(Filename: TCT_568_meningiomasabstractfigure.jpg)

1260

Imaging Tips and Traps for Diagnosing Sinonasal Tumors

K Calaro[1], A Jay[2], R Thakkar[2]
[1]Howard University College of Medicine, Washington, DC, [2]Medstar Georgetown University Hospital, Washington, DC

Purpose

This exhibit will describe the normal anatomy and the differential diagnosis for multiple sinonasal tumors on CT and MRI. Furthermore, we will discuss salient imaging characteristics to narrow diagnostics and use multiple imaging examples to illustrate tips and traps on diagnosing sinonasal tumors.

Materials and Methods

The paranasal sinuses and nasal cavity are home to diverse neoplasia, both benign and malignant. These lesions are often difficult to

diagnose due to the overlapping of associated presenting symptoms. Imaging strategy and management depend on an accurate diagnosis. The purpose of this abstract is to provide tips and traps for diagnosing sinonasal tumors on imaging.
Results
We performed a retrospective search utilizing our institutional-wide radiology report search engine, yielding studies imaging the sinonasal pathologies. Both CT and MRI images, as well as clinical documents were reviewed.
Conclusions
Sinonasal tumors have common presenting symptoms. It is important to know anatomical variants which can mimic pathology. Imaging is critical to provide narrow differential diagnoses and guide management.

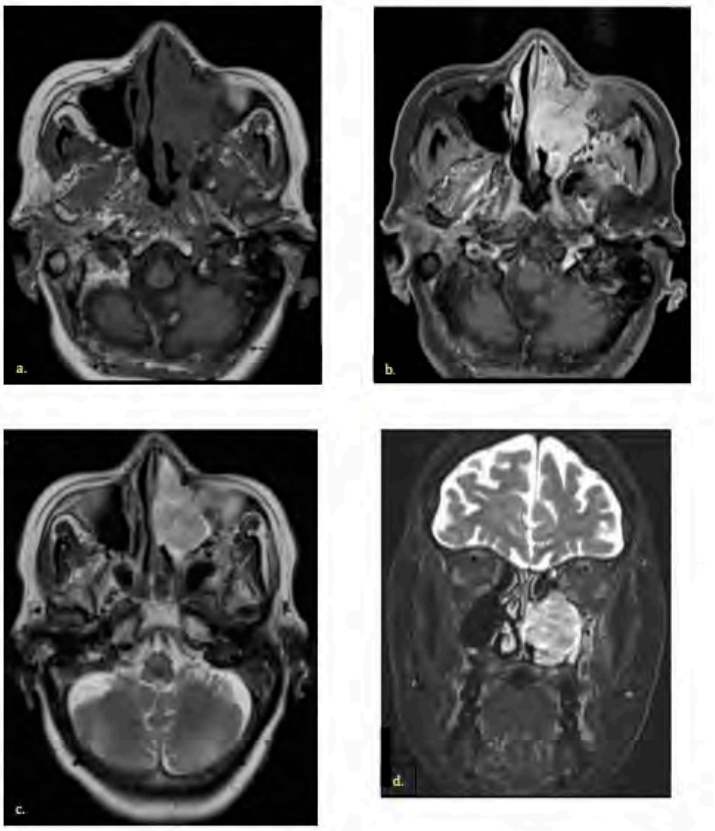

Inverted papilloma. On axial (a) pre-contrast T1 weighted sequence, there is a lobulated soft tissue density isointense mass in the left nasal cavity extending into the left maxillary sinus. It shows homogenous enhancement on axial (b) post contrast t1 weighted sequence. On axial (c) and coronal (d) T2- weighted sequence the mass is hyperintense with alternating hypointense lines giving characteristic "cerebriform pattern."

(Filename: TCT_1260_SinonasalTumorsImagesFinal.jpg)

1124

Immunomediated Encephalitis: Update on Physiopathology and Keys for Prompt Diagnosis

A Hilario[1], E Salvador[2], P Martin Medina[2], A Martinez de Aragon[2]
[1]Universitary Hospital 12 de Octubre, Madrid, Spain, [2]Hospital 12 de Octubre, Madrid, Madrid, SPAIN

Purpose
To describe different autoimmune responses of cell-surface and intracellular antigens. To evaluate antibodies that are markers of paraneoplastic neurological syndromes. To review the main antibody subtypes, their clinical characteristics and main imaging features.
Materials and Methods
Potential triggers of autoimmune encephalitides are tumors and viral encephalitis. Autoimmune response is initiated by antigens released by the viral destruction of neurons, by tumors, or by unknown origin. Antibodies bind to extracellular epitopes of cell-surface and cause reversible neuronal dysfunction. The disorders most frequently recognized are anti-NMDAR and limbic encephalitis.
Results
Anti-NMDAR encephalitis affects children and young adults. Up to 58% of affected female patients have an ovarian teratoma. Progression of symptoms include orofacial and limb dyskinesias, decreased level of consciousness and autonomic instability. Brain MRI is abnormal in 30% showing increased signal involving the cortical, subcortical, or cerebellar regions. Limbic encephalitis occurs in patients older than 45 years and symptoms include behavioral changes and inability to form new memories. MRI demonstrates hyperintensity in the medial aspect of the temporal lobes. LGI1 account for the majority of cases of limbic encephalitis and underlying

tumor is rare. Paraneoplastic encephalitides affects older patients and have a poor response to immunotherapy. Immune response is mediated by T cells and B antibodies directed against onconeuronal antigens. Antibodies anti-Hu, Anti-Ma2, Anti-Ri and Anti-Yo are markers of paraneoplastic neurological syndromes. Young men with testicular tumors often associate antibodies against the Ma2 protein. Limbic encephalitis can also have an onconeuronal origin, associated with anti-Hu antibodies, which, in 80% of cases, are associated with small cell lung carcinoma. Paraneoplastic cerebellar degeneration is associated with anti-Yo antibodies, and in 90% of cases, with a gynecological, ovarian or breast carcinoma. In adults, opsoclonus myoclonus syndrome is paraneoplastic in 39% of cases, and we should rule out anti-Ri antibodies, which are a good predictor of breast carcinoma.
Conclusions
We provide some usefull radiologic and clinical information that will allow us to become familiar with the different types of these encephalitis including anti-NMDAR and limbic encephalitis (LGI1 , paraneoplastic encephalitides and opsoclonus myoclonus syndrome)

712

In a blink of an eye: Computed Tomography in ocular trauma in children

T Guarilha[1], J Parente Goulart[2], J Tagliaferri e Paletta[2], T Kobayashi[2], S Monteiro[2], M Borri[3]
[1]UNIFESP, São Paulo, Indianópolis, [2]UNIFESP, sao paulo, Vila Clementino, [3]Federal University of Sao Paulo-Fleury Group-Hospital Sao Luiz-Rede d'Or, São Paulo, SP

Purpose
Eye trauma is a significant cause of blindness and visual deficits therefore an urgent ophthalmologic evaluation is needed. Imaging examination aids in the expanded assessment of the region and provides information that is limited in clinical examination.
Materials and Methods
The purpose of this work is to review and exemplify the main tomographic findings in the different mechanisms of ocular trauma, in order to demonstrate the importance of this method in the differential diagnosis of these injuries.
Results
Computed tomography (CT) images of illustrative cases of ocular urgencies and traumatic emergencies in children, obtained from cases available in the institution's own file, are demonstrated and discussed.
Conclusions
CT is the modality of choice for the initial assessment of a traumatic injury to the globe, especially when a foreign body is suspected. Some imaging aspects that can be found are: fracture, dislocation or subluxation of the lens, signs of hyphema, rupture of the eyeball, among others. It is also important to carry out the evaluation of the brain parenchyma, as some trauma mechanisms go beyond the orbital limit, causing intracranial injuries. Eye injuries are frequent in emergency room care, with a high prevalence related to trauma. The main mechanisms include accidents with sharp objects, stiletto, knife, stone, and firearms. It is necessary to have a good knowledge of the anatomy of the eyeball in order to accurately identify and describe the lesions found, helping in the proper treatment. Eye trauma is a major cause of admission to pediatric hospitals, and is a significant cause of blindness and vision deficits. Early assessment associated with familiarity with the types of eye lesions and imaging characteristics on computed tomography are crucial to make an accurate diagnosis and guide treatment, acting together to prevent unfavorable outcomes.

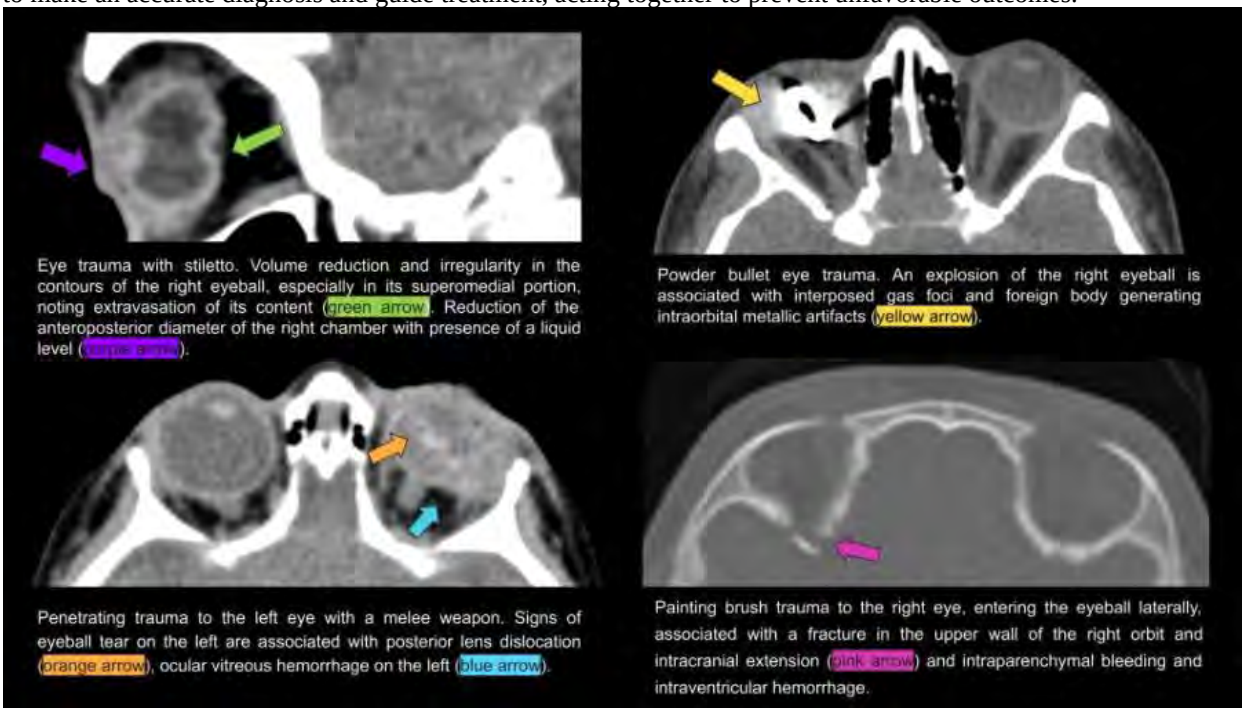

(Filename: TCT_712_inablinkofaneye.jpg)

123

In a Blink of an Eye: Evaluation of Emergent Proptosis

E Fourgas[1], T Singh[1], G Mongelluzzo[2], P Manickam[3], J Sodergren[1]
[1]Geisinger Health System, Wilkes Barre, PA, [2]Radiology, Danville, PA, [3]Geisinger, Danville, PA

Purpose

Since proptosis is common in the ER setting, it is important to review imaging features that can distinguish its many etiologies and guide clinical management. We will present cases in the infectious, inflammatory, traumatic and vascular categories with the following objectives: 1. Discuss the imaging features of orbital cellulitis, its complications and mimickers. 2. Distinguish between retrobulbar and subperiosteal hematomas. 3. Review the role of imaging in the management of orbital compartment syndrome, a surgical emergency. 4. Recognize changes within vascular malformations which can lead to abrupt worsening of proptosis. 5. Illustrate compressive optic neuropathy as an acute presentation of chronic conditions.

Materials and Methods

N/A

Results

CT and MR imaging of 15 patients from our institution were reviewed.

Conclusions

The infection category will include complications of orbital cellulitis such as subperiosteal abscess, intracranial infection and thrombosis of the superior ophthalmic vein and cavernous sinus. Cases of endophthalmitis, dacryocystitis and infected chalazion will be discussed. A frontal sinus pyomucocele rupturing into the subperiosteal space of the superior orbit will be shown. An intracranial epidural abscess after craniectomy with secondary extension into the orbit will also be illustrated. The inflammatory disease category will include cases of diffuse idiopathic orbital inflammatory syndrome, orbital myositis in Crohn's disease and compressive optic neuropathy in a patient with thyroid eye disease. CT images of a retrobulbar hematoma due to penetrating trauma and a rare subperiosteal hematoma after a fall will be discussed. Vascular lesions such a carotid cavernous fistula and interval hemorrhage within vascular malformations will be shown. The clinical and imaging findings in a patient with orbital compartment syndrome shortly after blaspheroplasty will be discussed. The radiologist can distinguish between orbital cellulitis, idiopathic inflammation, carotid cavernous fistula and endophthalmitis when their clinical and imaging presentations overlap. Hemorrhage in a venous varix or venolymphatic malformation can lead to abrupt worsening of long standing proptosis. Since orbital compartment syndrome, endophthalmitis and compressive optic neuropathy are sight threatening ophthalmologic emergencies, prompt imaging and communication is paramount.

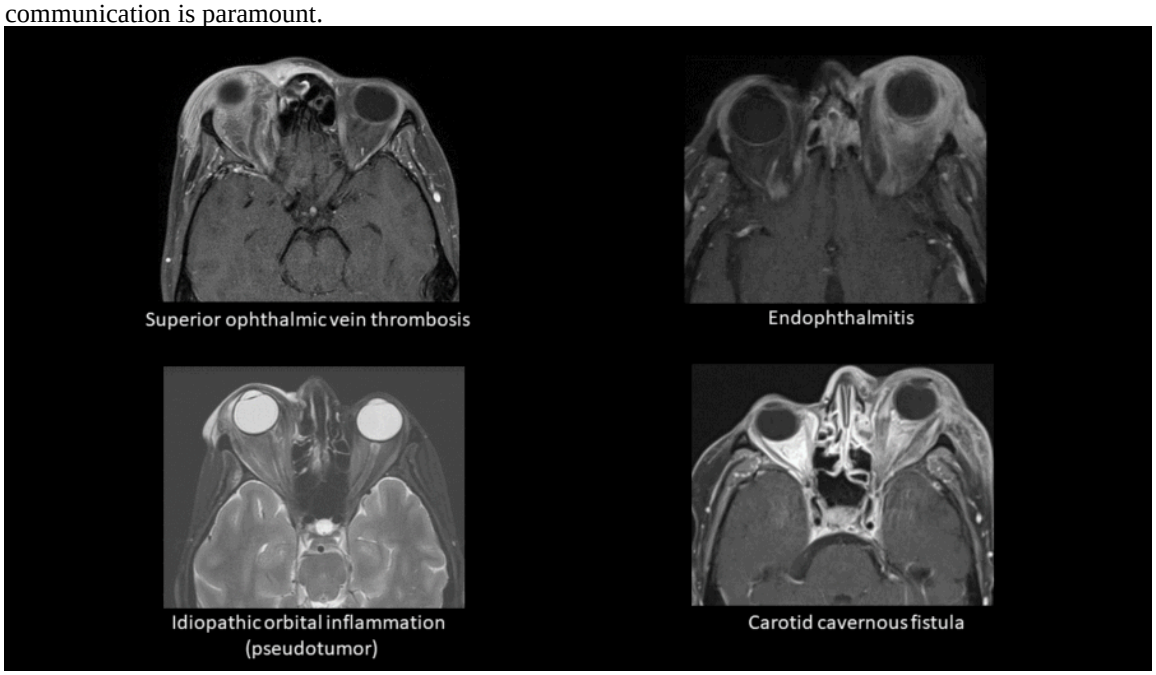

(Filename: TCT_123_Slide1.GIF)

1280

Incomplete Partition Type ll: A review of Critical Findings for the Radiologist.

N Paruk[1], R Wiggins[2]
[1]N/A, N/A, [2]University of Utah Health Sciences Center, SALT LAKE CITY, UT

Purpose

This image rich educational exhibit will review the critical imaging points of Incomplete Partition Type ll. This exhibit will review

normal inner ear anatomy and then review the imaging spectrum of Incomplete Partition inner ear abnormalities. Critical check points on imaging will be reviewed and highlighted for the leaner.
Materials and Methods
To demonstrate IP–II as the cause of sensorineural hearing loss in a 19-year-old, and use this case to review the critical imaging points that radiologists need to know for evaluation of Incomplete Partition cases, including normal inner ear anatomy.
Results
Case presentation and review of critical inner ear normal anatomy and IP-II subtle abnormalities.
Conclusions
Incomplete partition Type II is often described as two main components: Cochlear incomplete partition, and large vestibular aqueduct. The cochlear incomplete partition is secondary to a deficient interscalar septum between the middle and apical turns of the cochlea. The large vestibular aqueduct is described as the enlarged endolymphatic duct and sac. IP-II is considered the most commonly found imaging abnormality in pediatric cases of sensorineural hearing loss (SNHL), however it is often a subtle, easily missed imaging abnormality that is not well known to most radiologists. These patients may present with an acquired SNHL or mixed hearing loss, or a fluctuating or progressive SNHL from this congenital cause, precipitated from relatively mild trauma. The critical imaging findings in these subtle cases focus on the cochlea and endolymphatic duct and sac. The absent ISS between the middle and apical turns results in a smooth external contour between these turns posterolaterally, resulting in what is often referred to as the "baseball hat" appearance of the cochlea. This results in asymmetric scalar chambers and is often associated with a small or absent modiolus. The vestibular aqueduct and endolymphatic sac is typically either enlarged, or borderline large and flared posteriorly, but are rarely normal on close examination. The combination of IP-II and LVA has historically been referred to as the "Mondini anomaly". After interacting with this exhibit, the learner will have reviewed the breadth of Incomplete Partition imaging features and be able to provide valuable insight to neuro-otologists and referring clinicians.

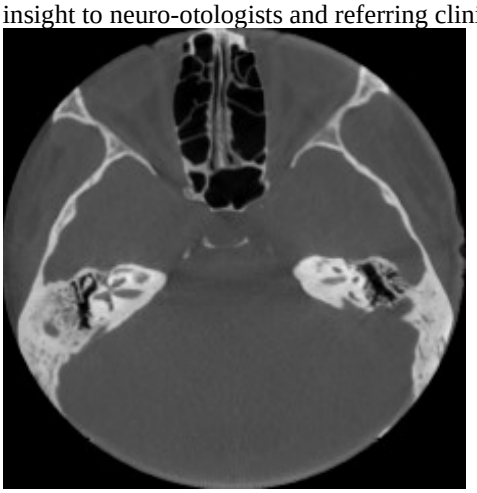
(Filename: TCT_1280_Picture2.jpg)

1114

Incorporation of Perfusion Protocols for Tumor Differentiation and Analysis of Post-Treatment Changes into Busy Clinical Practice

L Jekel[1], H Shooli[2], L Bell[3], J Ivanidze[4], A FRANCESCHI[5], I Ikuta[6], S Abi Fadel[7], R Bronen[6], A Malhotra[8], A Abou Karam[9], M Johnson[10], B Scheffler[11], M Aboian[7]
[1]Yale School of Medicine, New Haven, CT, [2]Brain Tumor Research Group, Yale University School of medicine, New Haven, CT, [3]Genentech Inc., South San Francisco , CA, [4]Weill Cornell Medicine Radiology, Larchmont, NY, [5]Northwell Health, New York, NY, [6]Yale University School of Medicine, New Haven, CT, [7]Yale University, Woodbridge, CT, [8]Yale University School of Medicine, New Canaan, CT, [9]Yale Medicine, New Haven, CT, [10]Yale University, New Haven, CT, [11]University Hospital Essen, Essen, Northrhine-Westphalia

Purpose
1. To present background information on MR perfusion techniques 2. To highlight the utility of different perfusion protocols in diagnosis of CNS tumors and post-treatment changes 3. To address the challenges in implementation of multiple perfusion protocols and key points for optimization in clinical practice
Materials and Methods
Gliomas/glioblastomas (GBM), brain metastases (BM) and primary CNS lymphomas (PCNSL) are among the most common differential diagnoses for enhancing intracranial mass. Differentiation of these tumors, as well as treatment response assessment, can be a diagnostic challenge, even for experienced neuroradiologists. Perfusion MRI has been proposed to address this, although there are inter-institutional variations in perfusion protocols and heterogeneity in implementation into clinical routine. This educational exhibit outlines the relevance of perfusion MR for differential diagnoses of glioma/GBM, BM and PCNSL, as well as for for evaluation of treated tumors, and sheds light on key points to consider for application of different perfusion protocols into clinical routine.

Results
We reviewed the literature for pertinent studies reporting on MR perfusion imaging in this field. Upon integrating these findings with our experience in clinical practice within a tertiary academic hospital and two other institutions, we formulated key points for clinical implementation.
Conclusions
This educational exhibit provides summary information on the main perfusion techniques, on how they reflect properties of tumor biology, i.e. vascularity and vessel permeability, and on how that knowledge can improve tumor differentiation. We review different protocols with particular focus on DSC perfusion for optimal PSR versus rCBV measurement. We underline challenges in optimization of perfusion imaging tailored to tertiary hospitals, which include gadolinium deposition, double bolus protocols, and additional acquisition time. We discuss the variety of image post-processing methods and vendors, as well as internal threshold generation for quantitative metrics in research and clinical applications. Finally, we address the critical need for standardization of perfusion protocols and highlight a community-drive initiative that aims at supporting the clinical translation of perfusion: OSIPI. In conclusion, perfusion MRI provides incremental value for patient management, however choice of appropriate protocols and use of standardized methods are critical for optimum results.

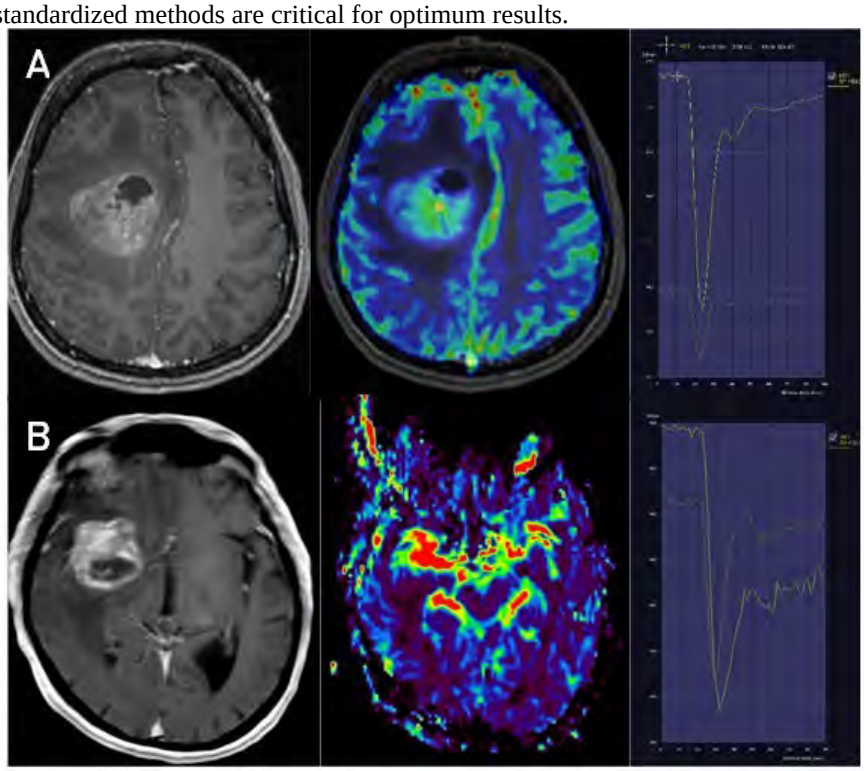

Figure 1: Imaging of two brain tumors on contrast-enhanced T1-weighted sequence and on a DSC perfusion map. The rightmost panel shows the peak signal intensity recovery (PSR) curve, a hemodynamic metric derived from the DSC perfusion map. (A) shows a glioblastoma (GBM). Note that after first pass of contrast agent signal intensity almost returns to baseline. (B) shows metastatic gastric adenocarcinoma. After contrast passage signal intensity remains below baseline, indicating leakage of blood brain barrier, as typically seen in BM.

(Filename: TCT_1114_FigureASNRPerfusionEducationalExhibit.jpg)

1079
Infectious Ring Enhancing Lesions of the Brain. MRI Clues for Diagnosis.
J GOMEZ MUGA[1]
[1]*HOSPITAL UNIVERSITARIO BASURTO, Bilbao, BIZKAIA*

Purpose
Central nervous system (CNS) infections are an emerging health problem with poor prognosis if treatment is not adequate. Establishing a correct diagnosis is necessary to quickly start the appropriate treatment. This is a real challenge for the radiologist, as it frequently requires a multidisciplinary approach. Although radiographic differentiation of the cause of the intracranial abnormality is difficult and often nonspecific, certain clues may help differentiate the etiology of the infection.
Materials and Methods
Review the imaging findings of infectious ring enhancing lesions of the brain with particular emphasis on those signs that can provide a specific diagnosis.

Results
We review different examples of intracranial infections in a case-based format. -. Pyogenic abscess. -. Fungal abscess. -. Tuberculoma. -. Toxoplasmosis. -. Cysticercosis.
Conclusions
In infectious ring enhancing lesions there are characteristic imaging findings and radiological signs that can provide a specific diagnosis.

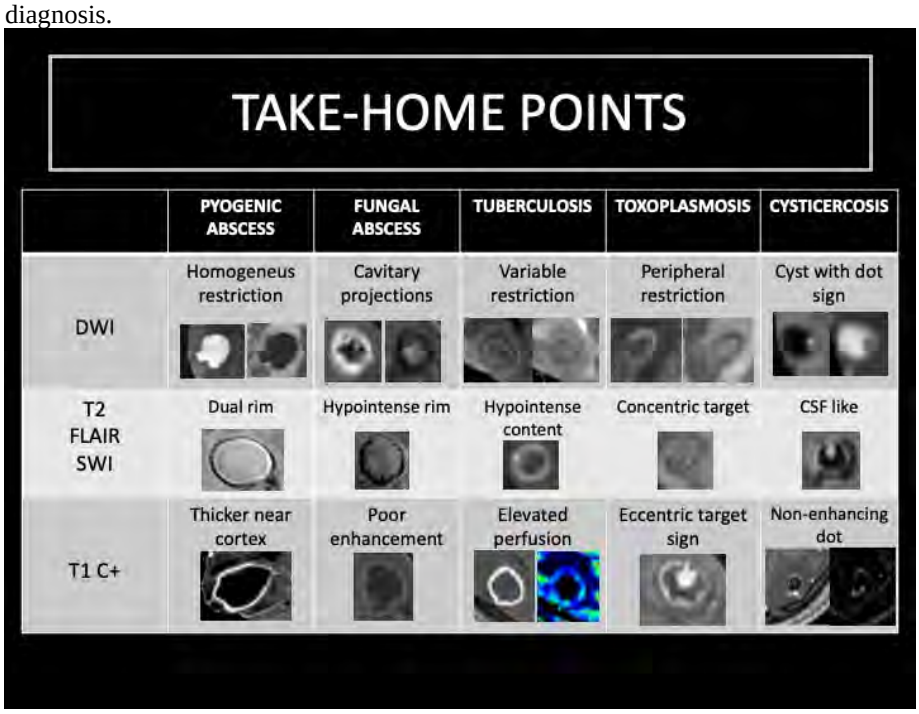

(Filename: TCT_1079_TAKEHOMEPOINTS.jpg)

998
Interpreting Cerebral Digital Subtraction Angiography – A Primer for the Diagnostic Neuroradiologist
C Chung[1], E Raz[1], M Shapiro[1], M Hagiwara[1]
[1]NYU Langone Health, New York, NY

Purpose
Summary: With continued advances in noninvasive neurovascular imaging techniques and limited interest in interventional neuroradiology sub-specialization amongst diagnostic neuroradiology trainees, exposure to and hands-on participation in catheter-based digital subtraction angiography (DSA) and neuroendovascular interventions may be less emphasized in contemporary diagnostic neuroradiology training and practice scope. Nonetheless, as DSA remains the gold standard for diagnosis of cerebrovascular pathologies and indications for neuroendovascular interventions continue to expand, basic understanding of cerebral DSA and neuroendovascular interventions remains crucial for accurate interpretation of noninvasive neurovascular imaging. This exhibit aims to equip the diagnostic neuroradiologist with a framework for understanding and interpreting cerebral DSA images obtained for diagnostic and interventional purposes. The discussion will focus on the head and neck (as opposed to the spine) and artery-based pathologies. The typical diagnostic cerebral angiogram imaging protocol and techniques including imaging views, vessels interrogated, 2D and 3D rotational angiographic techniques will be outlined. A review of angiographic cerebrovascular anatomy, both normal and variant, and the angiographic appearance of cerebrovascular pathologies (such as acute stroke, aneurysm, vascular malformation, dissection, vasculitis) will be provided. The dynamic multiphasic nature of catheter-based cerebral angiography will be highlighted to demonstrate how cerebral hemodynamics is altered in disease states. Intraprocedural deployment and postprocedural appearance of common neuroendovascular treatment devices will be illustrated via case-based review. Correlation with non-invasive imaging will be provided. Educational Objectives: 1. Outline the imaging protocol and techniques of a diagnostic cerebral angiogram. 2. Review angiographic appearance of normal and variant cerebrovascular anatomy and cerebrovascular pathologies. 3. Highlight the temporal resolution of catheter-based angiography and cerebral hemodynamics alterations in cerebrovascular pathologies.
Materials and Methods
N/A
Results
N/A
Conclusions
N/A

408

Introduction to Preoperative Paranasal Sinus Anatomy and Interpretation

D Vargas-Zapata[1], B Tantiwongkosi[1], P Kesava[1], A Singh[1], J Lally[1]
[1]UT Health San Antonio, San Antonio, TX

Purpose

Educational objectives: - Review of the basic functional paranasal sinus and drainage pathway anatomy - Staging of disease and dictation using the Lund-Mackay scoring system - Identify and classify anatomic variants of the sinuses, drainage pathways, skull base, and nasal cavity structures important for pre-operative planning and surgical risk reduction - Describe commonly encountered obstructive and non-obstructive imaging patterns of paranasal sinus inflammatory disease - Recognition of "red flag" imaging findings to prompt further clinical evaluation or contrast enhanced imaging to investigate for underlying malignancy or aggressive infection

Materials and Methods

Summary of contents: • Introduction • Maxillary sinus anatomy o Walls, recesses, ostia, infraorbital canal, and teeth • Frontal sinus anatomy o Tables, ostia, floor, and lacrimal bone • Ethmoid air cells anatomy: o Basal lamella of the middle turbinate, fovea ethmoidalis & cribriform plate • Sphenoid sinus anatomy o Sphenoid face & planum sphenoidale, optic strut & anterior clinoid process, carotid canal, pterygoid process & plates o Associated foramina and recesses (including optic canal, superior orbital fissure, foramen rotundum, vidian canal and pterygoid recesses) • Ostiomeatal unit anatomy o Drainage pathway of the maxillary sinus, frontal sinus, and anterior ethmoid air cells o Maxillary sinus ostium, infundibulum, hiatus semilunaris, and middle meatus o Frontal sinus recess component o Importance of the uncinate process and ethmoid bulla • Sphenoethmoidal recess o Drainage pathways of the sphenoid sinus & posterior ethmoid air cells o Important landmarks • Lund-Mackay score o Utility for pre-operative assessment, staging, & risk stratification in chronic rhinosinusitis

Results

• Anatomic variants o Maxillary sinus and OMU ♣ Infraorbital ethmoid air cells, infraorbital canal, hypoplasia/atelectasis, and odontogenic sinusitis o Frontal sinus and recess ♣ Inter-frontal air cells, uncinate process attachments, middle turbinate variants, and frontal sinus recess variants o Ethmoid air cells ♣ Cribiform plate and fovea ethmoidalis position, anterior ethmoid artery notch and supraorbital ethmoid air cells & lamina papyracea o Sphenoid sinuses ♣ Patterns of pneumatization, carotid & optic canal relationship, and onodi air cells. o Nasal cavity ♣ Septal deviation, turbinate hypertrophy, and turbinate variants

Conclusions

• Chronic sinusitis • Red flags for neoplasm or aggressive infection • Conclusion

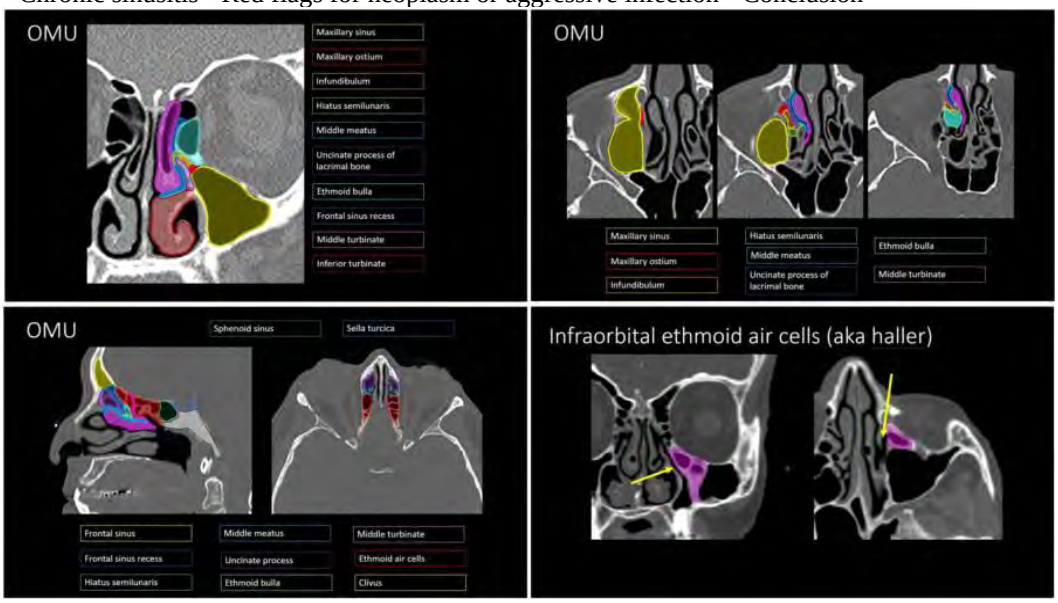

(Filename: TCT_408_SInusJPEG300DPIjpg.jpg)

1028

Invasive Fungal Rhinosinusitis: Imaging findings and complications

A Miranda Merchak[1], A Schilling[2]
[1]Hospital Barros Luco, Santiago, Chile, [2]Universidad Mayor, Santiago, Chile

Purpose

Fungal rhinosinusitis encompasses a wide variety of clinical manifestations, from mild to rapidly progressive and fatal infectious conditions. Although colonization of the airway by fungal microorganisms, mainly Mucor, is frequent, the vast majority of patients do not develop infectious symptoms secondary to fungal rhinosinusitis. It is of utmost importance to determine non-invasive methods to evaluate populations at risk for symptoms suggestive of acute IFRS, in order to have a diagnostic suspicion and early treatment. In this presentation, we will review some of the most common findings in computed tomography and magnetic resonance imaging of the

paranasal sinuses, as well as their usefulness as a diagnostic tool for this pathology. Objectives: Definition of the disease Diagnosis and CT and MRI findings Complications Conclusions
Materials and Methods
To compare the diagnostic utility of computed tomography and magnetic resonance imaging of the paranasal sinuses in the diagnosis of invasive fungal rhinosinusitis.
Results
Series of cases.
Conclusions
Fungal Rhinosinusitis encompasses a wide range of clinical manifestations, from mild to rapidly progressive and fatal infectious conditions. Complications that can be associated with this condition are: Orbital: The most frequent focus of extension of RSFI, being the first cause in children and the third cause of unilateral proptosis in adults. Intracranial: Infrequent complications with high mortality rate, due to direct extension and/or retrograde thrombophlebitis. They are more frequent in adolescents and young adults; and include meningitis, abscesses (epidural, subdural, intracerebral) and venous sinus thrombosis (cavernous, superior sagittal). The main findings on CT scan of the paranasal sinuses are unilateral sinus opacity and thickening of the sinus mucosa in the floor and lateral nasal wall. In the paranasal sinuses MRI it can be observed nasal cavity occupation, obliteration and/or infiltration of perianthral fat, lack of enhancement of turbinates, NPC and soft tissues, bone dehiscence, inflammatory changes in orbital adipose tissue or extra ocular muscles, leptomeningeal enhancement. It has been postulated that MRI is better than CT for screening of acute IFRS, while the latter would have a greater benefit in evaluating late imaging findings (bone erosions), treatment planning and intra-operative guidance.

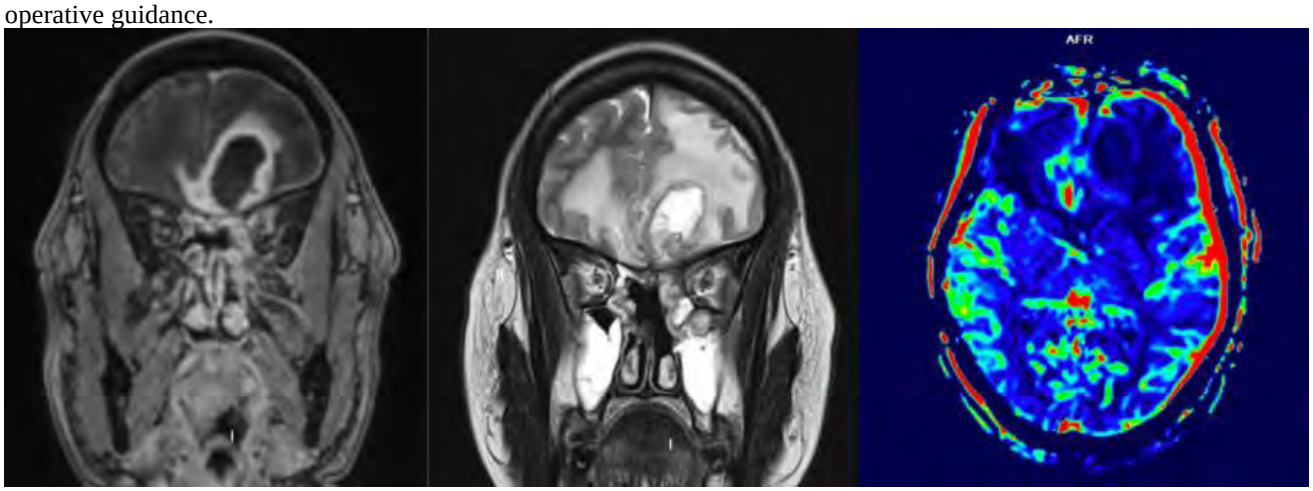

(Filename: TCT_1028_Imagen1.jpg)

427

Isolated Sublingual Gland Abnormalities: A Neuroimaging Pictorial and Educational Review

M Shahrzad[1], W Mu[1], K Seifert[1], E Tranvinh[1], M Wintermark[1], S Hashmi[1], T Massoud[1]
[1]Stanford University School of Medicine, Stanford, CA

Purpose
The sublingual glands (SLGs) are the smallest of the major salivary glands. The SLGs have a low incidence of malignant cancers (<5% of salivary gland tumors) and have 1% of sialolithiasis cases. Therefore diagnostic confusion may arise when these common diseases target the SLGs alone, or other focal pathologies appear in the SLGs. The imaging of SLG abnormalities is generally under-recognized in clinical practice and the radiological literature. We provide a pictorial and educational review of isolated SLG abnormalities.
Materials and Methods
We comprehensively review the imaging findings of SLG lesions, and categorize these by etiology.
Results
We first review imaging anatomy of the SLG and the ducts of Bartholin and Rivinus. CT, MRI, and FDG PET can visualize SLG focal abnormalities. Congenital anomalies include ipsilateral SLG hypertrophy with an atrophic ipsilateral submandibular gland or a contralateral SLG. The SLG may herniate through a boutonniere defect in mylohyoid. SLG bacterial or viral sialadenitis may occur in the elderly where sialolithiasis may rarely be confined to the SLG. Ranulas are pseudocysts of saliva leaking from a damaged SLG, found above or below (plunging) mylohyoid. They may form after SLG infection or trauma, e.g. during dental implant surgery. SLG tumors are asymptomatic swellings in the anterior floor of mouth. However, 15% of malignancies cause pain and loss of tongue sensation (CNV3). CT/MRI can help differentiate a primary SLG from a floor of mouth lesion; important because an early-stage SLG tumor may be removed alone instead of wide excision and floor of mouth reconstruction. Isolated SLG masses are 90% malignant, e.g. adenoid cystic, mucoepidermoid, or acinic cell carcinoma; usually an invasive heterogeneous mass with enhancement. We illustrate other isolated SLG malignancies that have been reported, e.g. lymphoepithelial, neuroendocrine, or NUT midline carcinomas, and lymphoma. SLG benign mixed tumor is a discrete lesion with T2/STIR high signal and homogeneous enhancement.

Other reported SLG benign tumors include: Schwannoma, neurofibroma, solitary fibrous tumor, basal cell adenoma, intraductal papilloma, and hemangioma. Langerhans cell histiocytosis and amyloidosis also affect the SLGs.
Conclusions
Accurate identification of uncommon focal abnormalities of the SLGs is important in clinical decision making prior to treatment. This presentation will aid in neuroimaging interpretation and understanding of isolated SLG diseases to aid in patient management.

747

It's All in the Stem: A Review of Pontine Lesions

J Ortiz-Cruz[1], A Sharma[2]
[1]University of Michigan Department of Radiology, Ann Arbor, MI, [2]University of Michigan, Ann Arbor, MI

Purpose
Discuss pontine anatomy and differential diagnosis of signal abnormalities: Anatomy: Pontine cranial nerve nuclei and white matter tracts Tumors: Diffuse midline glioma, H3 K27-altered, pilocytic astrocytomas, brain metastasis Ischemia: Acute ischemia, lacunar infarcts, small vessel disease changes Vascular: Capillary telangiectasias, vasculitis Demyelination: Multiple Sclerosis, Osmotic demyelination syndrome Trauma: Diffuse axonal injury, Duret hemorrhage Dementia: Parkinsonian, Multiple system atrophy Infectious/Metabolic/Misc: Medication Toxicity, Posterior reversible encephalopathy syndrome (PRES) Ages: pediatric and adult patients Modalities: T1, T2, FLAIR, post Gad, DWI, SWI, Perfusion
Materials and Methods
Not uncommonly, radiologists are faced with signal abnormalities within the pons, including T2 prolongation, abnormal enhancement, internal susceptibility, and diffusion restriction. We seek to describe the signal abnormalities of multiple lesions within the pontine region using multiple modalities, their relation to adjacent cranial nerve nuclei and white matter tracts, and generate a differential diagnosis.
Results
1. Literature review of conditions causing pontine signal alterations. 2. Select multiple cases (patient identifiers will be removed) from our database spanning several hospitals to show representative cases using multiple modalities.
Conclusions
Pontine lesions have a broad differential diagnosis. This differential includes tumors, vascular etiologies, demyelinating conditions, inflammatory changes, among others. We seek to use clinical history and MR findings to develop a differential diagnosis. Tumors in this region include the classic diffuse midline glioma, H3 K27-altered, which tends to manifest in children and carry a poor prognosis, other tumors that can manifest in the pons include pilocytic astrocytomas and metastasis. Ischemic changes include worrisome causes like acute ischemia to less serious chronic small vessel disease changes. Vascular etiologies include the relatively common capillary telangiectasias as well as sequelae from vasculitides. Demyelination causes are also seen not uncommonly involving the pons, such as multiple sclerosis and in osmotic demyelination syndrome. Trauma can also have pontine sequelae. Other more complex etiologies can also affect the pons such as PRES, a more complex etiology associated with hypertension in many cases. Finally, infectious and metabolic etiologies can also cause pontine changes.

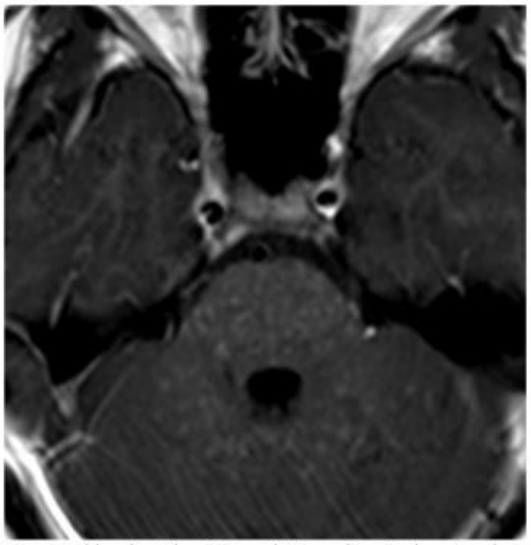

11-year-old male with a 1.5-year history of unsteady gait and frequent falls. T1W post contrast image shows multiple punctate and patchy regions of contrast enhancement centered around the pons and brachium pontis regions. This enhancement completely resolved after steroid therapy. Findings consistent with Chronic lymphocytic inflammation with pontine perivascular enhancement responsive to steroids (CLIPPERS).

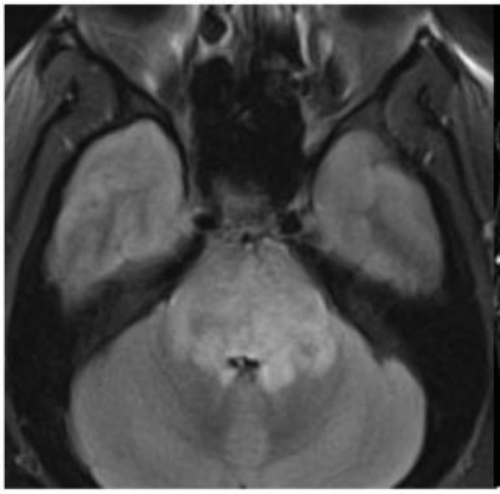

48-year-old female patient with headaches, weakness, and uveitis. History of oral and genital ulceration. Case demonstrates diffuse prominent heterogeneous FLAIR hyperintensities within the pons, sequelae of Behcet's disease, an auto-inflammatory disorder.

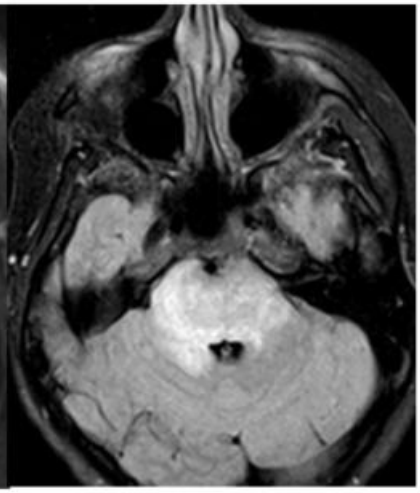

32-year-old female patient with history of headaches for 1 month with FLAIR hyperintensities at the pons (the rest of the parenchyma was unremarkable). Four weeks follow up showed complete resolution. Case was determined to be PRES (central variant).

(Filename: TCT_747_PontineAbstractFinalImages.jpg)

984

It´s a Cervical Mass but it is not a Lymph Node:a Pictorial review

a costacurta[1]

[1]Clínica Felippe Mattoso, Rio de Janeiro, Brazil

Purpose

Cervical mass is a common referral to the radiology department and a source of major concern to the patient. The differential diagnosis for the examining physician is broad, and radiologic evaluation is often requested. Very often it represents lymphadenopathy, enlarged lymph nodes related to malignancy of the head and neck, mostly squamous cell carcinoma of the pharynx. In these cases the radiologist will focus on finding and staging a primary tumor. However there is a number of other conditions, benign as well as malignant, presenting as a cervical mass in adults. The first goal of the radiologic evaluation is to confirm the presence of a mass, typically a soft tissue mass, since other conditions may simulate disease, and once it is done to try to characterize the tumor, narrowing down the differential diagnosis, and assessing the extent of the lesion

Materials and Methods

Cervical mass in adults encompass a wide spectrum of diseases. Patient´s clinical history, mass consistency, pattern of growth and location are all helpful clues to the diagnosis, but imaging is often necessary. Advances in imaging have provided the radiologist with new tools that can add important information regarding soft tissue mass, distinguishing benign process from more aggressive lesions requiring biopsy or surgery. In this review we intend to discuss tumor mimic conditions, benign and malignant soft tissue masses and imaging characteristics that may narrow the differential diagnosis,

Results

Discussion and illustration of the wide spectrum of etiologies presenting as cervical mass in adults, from tumor mimic condition like masseter hypertrophy and inflammmatory diseases to benign and malignant soft tissue tumors. Review CT and MRI findings, highlighting characteristic aspects and benefits of each technique.

Conclusions

Soft tissue cervical mass is a common complaint in daily practice for the head and neck radiologist. Although lymphadenomegalies are very frequent it is important to acknowledge that there are several other causes of cervical mass. Ct and MRI can help characterize these entities an narrow down the differential diagnosis.

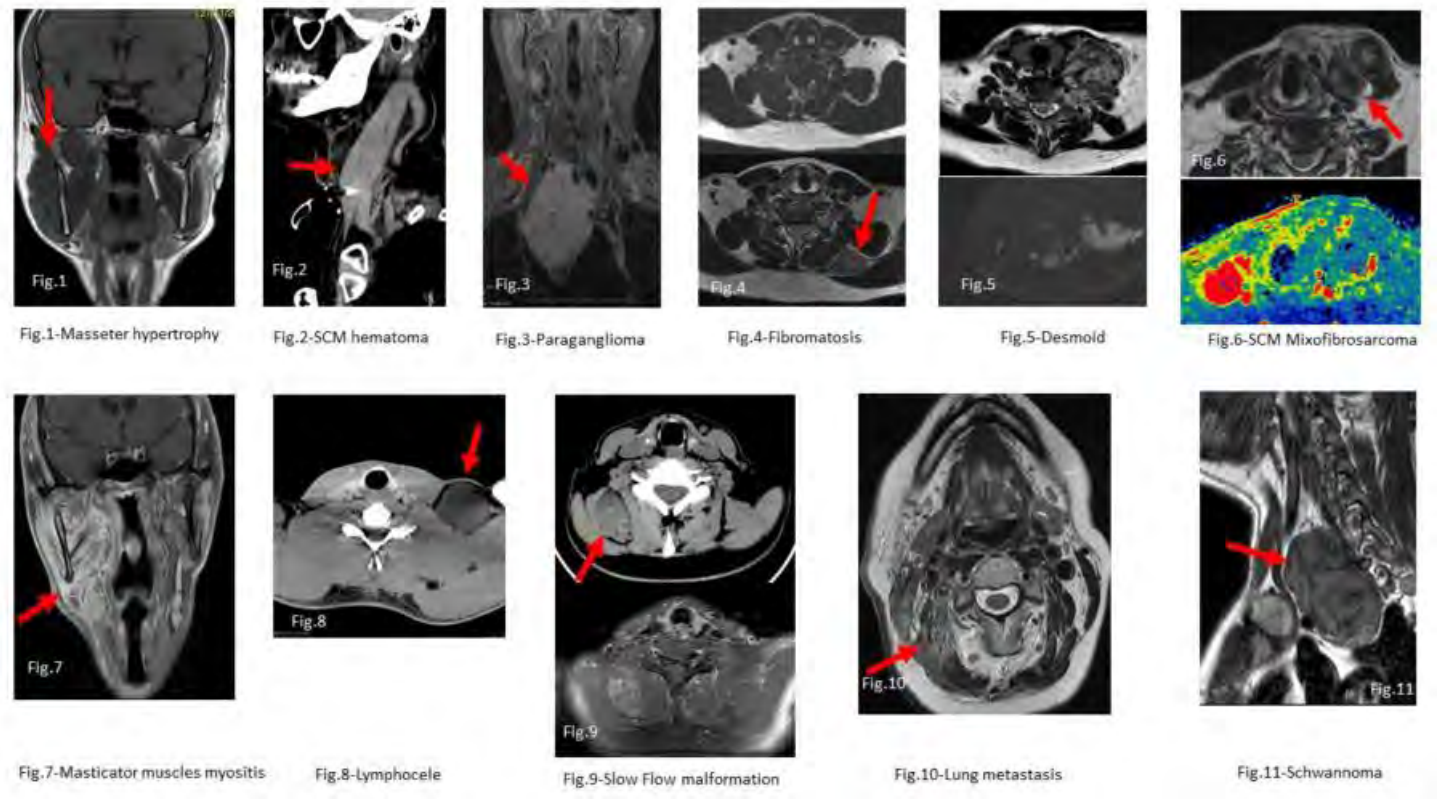

(Filename: TCT_984_cervicalmass.jpg)

876

It's Time to Embrace Hybrid Imaging in Gliomas: A Bench-to-Bedside Tutorial on Amino Acid PET/MRI

H Shooli[1], M Assadi[2], A Nabavizadeh[3], A FRANCESCHI[4], M Aboian[1]

[1]Brain Tumor Research Group, Department of Radiology, Yale University School of Medicine, New Haven, CT, [2]Persian Gulf Nuclear Medicine Research Center, Bushehr University of Medical Science, Iran, Bushehr, Bushehr province, [3]Uinersity of Pennsylvania, Philadelphia, PA, [4]Northwell Health, New York, NY

Purpose

Hybrid imaging is the combination of structural and functional imaging modalities. Positron emission tomography/magnetic resonance (PET/MR) imaging is a subset of hybrid imaging that has an unparalleled value in glioma imaging. Among different types of PET/MRI, amino acid PET/MRI has an established added value in glioma imaging. However, this modality is still underrepresented in the neuroradiology community and is yet to be fully utilized in the clinical setting. Therefore, we have prepared a comprehensive tutorial on this topic with the following learning objectives: • Hybrid PET/MRI in glioma imaging • Amino acid PET/MRI allows for metabolic imaging in gliomas • Clinical indications recommended by joint EANM/EANO/RANO/SNMMI guideline, followed by case presentation • Clinical usefulness of amino acid PET tracers through review of meta-analyses

Materials and Methods

This educational exhibition aims to provide a review of amino acid PET/MRI from molecular principles to updated clinical applications and future perspectives.

Results

This educational exhibition is designed based on an extensive literature search of hybrid imaging in glioma, with a focus on amino acid PET/MRI. We discuss molecular principles that provide basic insight into hybrid amino acid PET/MRI. Then, we review clinical applications of amino acid PET/MRI through a case series presentation that depicts usefulness of this modality in clinical practice. Finally, we outline future perspectives and potential of amino acid PET/MRI for non-invasive characterization of gliomas.

Conclusions

11C-methionine (11C-MET), O-(2-18F--fluoroethyl)-L-tyrosine (18F-FET), and L-3, 4-dihydroxy-6-[18F]fluorophenylalanine (18F-DOPA) are are commonly used amino acid PET tracers for brain tumor assessment. More recently, 18F-fluciclovine is emerging as a novel amino acid PET tracer with great potential in glioma imaging. Then, we review clinical indications for amino acid PET/MRI recommended by EANM/EANO/RANO/SNMMI guideline for glioma imaging. This guideline indicates that amino acid PET/MRI is ready for incorporation into clinical practice, which is followed by a case series presentation. We also discuss principles of dynamic PET with a clinical case. Finally, we assess the added value of hybrid amino acid PET/MRI through review of meta-analyses available in the literature. In conclusion, amino acid PET/MRI is clinically indicated (according to EANM/EANO/RANO/SNMMI guideline) with established added value for glioma imaging in clinical setting.

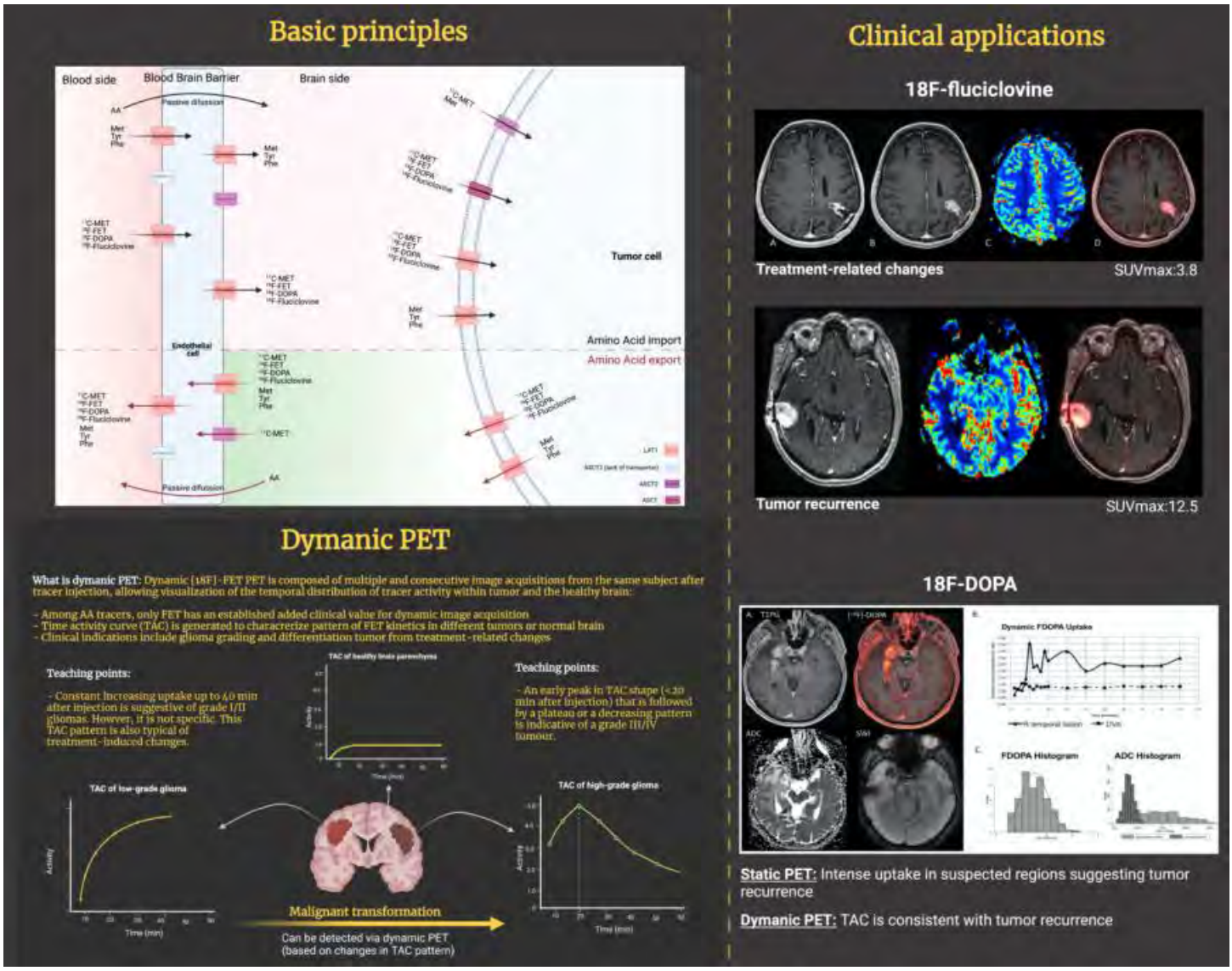

(Filename: TCT_876_AminAcid-ASNR-2022-FInal.jpg)

578

Jaws: Mandibular Lesions in Head and Neck Imaging

R Biswas[1], G Michael[1], O Sergev[1], S Jun[2], M Raden[1], J Felder[1]

[1]Staten Island University Hospital, Staten Island, NY, [2]Northwell Staten Island University Hospital, Staten Island, NY

Purpose

In this educational poster, we provide a pictorial review of common and uncommon mandibular/jaw lesions. We highlight their salient imaging characteristics across multiple modalities, pathophysiologic etiologies, and clinical presentations or associations that can help guide the radiologist to a more focused differential diagnosis.

Materials and Methods

Mandibular lesions encompass an important spectrum of diseases within head and neck imaging. The gamut of mandibular lesions can often feel unfamiliar to both training and experienced radiologists. As such, accurate diagnosis of these lesions can often be challenging. Cystic and solid mandibular lesions can be the result of numerous pathophysiologic processes and can be broadly classified as odontogenic versus non-odontogenic or benign versus malignant. Examples of these entities include odontomas, ameloblastomas, periapical cysts, dentigerous cysts, osteosclerosis, osteomas, fibrous dysplasia, and Pagets disease.

Results

N/A

Conclusions

The imaging diagnosis of mandibular lesions can be challenging to both training and experienced radiologists. A detailed understanding of the imaging characteristics of mandibular lesions and their clinical presentation can help neuroradiologists focus their differential diagnosis, accurately classify lesions, and better guide their clinical management.

631

Laryngeal Ultrasound Imaging in the Evaluation of Vocal Fold Mobility Impairment (VFMI) in Pediatric Patients

H Tran[1], T Huisman[2], N Desai[3], J Ongkasuwan[1]

[1]Baylor College of Medicine, Houston, TX, [2]Texas Children's Hospital and Baylor College of Medicine, Houston, TX, [3]Texas Children's Hospital, Sugar Land, TX

Purpose

To introduce clinical application of laryngeal ultrasound in the evaluation of vocal fold mobility impairment of pediatric patients to neuroradiologists.

Materials and Methods

This educational exhibit reviews the acquisition techniques for laryngeal ultrasound and how to quantitatively and qualitatively diagnose vocal fold mobility impairment in pediatric patients.

Results

n/a

Conclusions

Recent Findings: Laryngeal ultrasound has a sensitivity of 84% and specificity of 95% for noninvasive, nonsedated identification of VFMI when compared with flexible nasolaryngoscopy. It has replaced flexible nasolaryngoscopy as a first-line screening tool for evaluation of laryngeal dysfunction at our quarternary children's hospital. Additionally, during the ongoing viral pandemic, laryngeal ultrasound has provided a measure of relief and protection for our clinicians by reducing unnecessary potential exposure to COVID-19. Qualitatively, asymmetric movement of the vocal folds (particularly the arytenoid cartilages), abnormal position of the affected vocal fold with more internally rotated and paramedian location when compared to the contralateral one and presence of hyperechoic air band of glottis rima during phonation or crying provide the most important clues for the presence of VFMI. Quantitatively, measurement of vocal fold-arytenoid angle in abduction is most predictive of symmetry and movement. Conclusion: Clinical application of laryngeal ultrasound for evaluation of VFMI is tremendous and underutilized by many clinicians. Laryngeal ultrasound should be considered as a first-line screening tool for assessment of laryngeal dysfunction.

1507

Lesion Localization in Neuro-Ophthalmology for Efferent Visual Pathways Disorders: Classic Ophthalmological Exam and Neuroimaging Correlates

R Patel[1], H Sawhney[1], S Khanpara[2], A Kamali[1], R Samant[1]

[1]The University of Texas Health Science Center at Houston, Houston, TX, [2]University of Texas MD Anderson Cancer Center, Houston, TX

Purpose

A wide range of neurologic conditions can involve the efferent visual pathway. An understanding of common neurologic presentations of efferent visual pathway defects can help the neuroradiologist in targeting their search pattern to specific areas of interest that may otherwise go undetected. A good neuro-ophthalmological clinical evaluation followed expert neuroimaging evaluation by Radiologist is crucial in determining lesion localization, appropriate diagnosis and its management. At the end of the exhibit, the viewer will become familiar with common clinical presentation, key neuro-ophthalmological findings for Efferent Visual Pathway disorders and able to localize anatomical regions of interest for neuroimaging.

Materials and Methods

1. To illustrate detailed anatomy and function of the efferent visual pathway. 2. To provide a clinically driven and image-rich interactive quiz featuring spectrum of pathologic conditions involving the efferent visual pathway.

Results

All cases related to efferent visual pathway defects will be presented with pertinent clinical history, detailed neuro-ophthalmology examination findings followed by quiz format Neuroimaging presentation with answers/discussion highlighting neuroanatomical region of interest and the relationship between the location of the lesion and the neuro-ophthalmology examination findings. A brief self-quiz at end will conclude the exhibit.

Conclusions

Neuro-ophthalmology is an interdisciplinary field which includes ophthalmology, neurology, and radiology to determine the visual implications of neurologic disorders. The efferent visual system consists of the brainstem oculomotor nuclei (Supranuclear, Internuclear input), cranial nerves responsible for ocular movement (cranial nerves III, IV, and VI), sympathetic/parasympathetic fibers of the ciliary ganglion, and extra-ocular muscles. Imaging locations of disease are classified as brainstem, cisternal, cavernous sinus, and orbital. Clinical examination signs may reveal cranial nerves (3rd/4th/6th) palsies, vertical gaze palsy, gaze-evoked nystagmus, internuclear ophthalmoplegia, and Horner's syndrome which help the neuro-ophthalmologist to localize anatomical regions of interest for imaging. Radiologist adds value not only by recognizing pathologic imaging features, but also by understanding the clinical examination findings that may result from what they observe, and likewise using findings from the clinical exam as a guide to accurately localize pathologic lesions.

1288

Lesions in the Thalamus and Basal Ganglia: A Resident's Guide Case-Based

K CANCELA[1], A Alves Fonseca[2], E Naves[3], R Pincerato[4], A Salgado[5]

[1]Hospital Samaritano Higienópolis, São Paulo, Brazil, [2]Santa Casa de São Paulo / DASA / United Health Group, São Paulo, São Paulo, [3]Hospital Israelita Albert Einstein, São Paulo, NY, [4]HOSPITAL SAMARITANO SP - UHG BRASIL, São Paulo, SP, [5]Hospital Samariano Higiopolis, São Paulo, São Paulo

Purpose

The basal ganglia and thalamus are structures composed of deep gray matter that can be the site of development of a wide etiologic variety of pathologies, which can demonstrate specific diagnostic clues through imaging methods. The objectives of this exhibit are to review the anatomy of the thalamus and basal ganglia, including their anatomical boundaries, vascularization characteristics, and normal CT and MRI findings. Also, discuss and illustrate the main imaging patterns of these differential diagnoses.

Materials and Methods

The main thalamic and basal ganglia lesions can be vascular, metabolic, traumatic, tumor, inflammatory, infectious, among others. The image pattern of each of these etiologies can be fundamental in complementing and clarifying the diagnosis. The purpose of this work is to carry out an assessment of these lesions, identifying the spatial, quantitative, parity and temporal distribution, in addition to detecting individual characteristics, correlating them with other possible associated findings, helping to narrow the differential diagnoses. As an example, symmetrical and bilateral lesions can speak in favor of metabolic disturbances as well as intoxications. Focal lesions, in turn, can refer to infectious or tumor lesions.

Results

Therefore, after analyzing the digital teaching files of our institution, we are going to describe the diagnostic scenarios through illustrative cases, focusing on typical image patterns, including topographical correlations, unexpected findings and warning signs that aid in the diagnosis.

Conclusions

Imaging methods are essential in the context of basal ganglia and thalamic lesions, since the recognition of imaging patterns of these pathologies can provide subsidies to prevent misinterpretations, aiding the decision-making of assistant physicians, as well as assisting in the follow-up . This pictorial essay provides a practical approach to understanding these lesions, according to their locations and characteristics, bringing together specific types of pathologies.

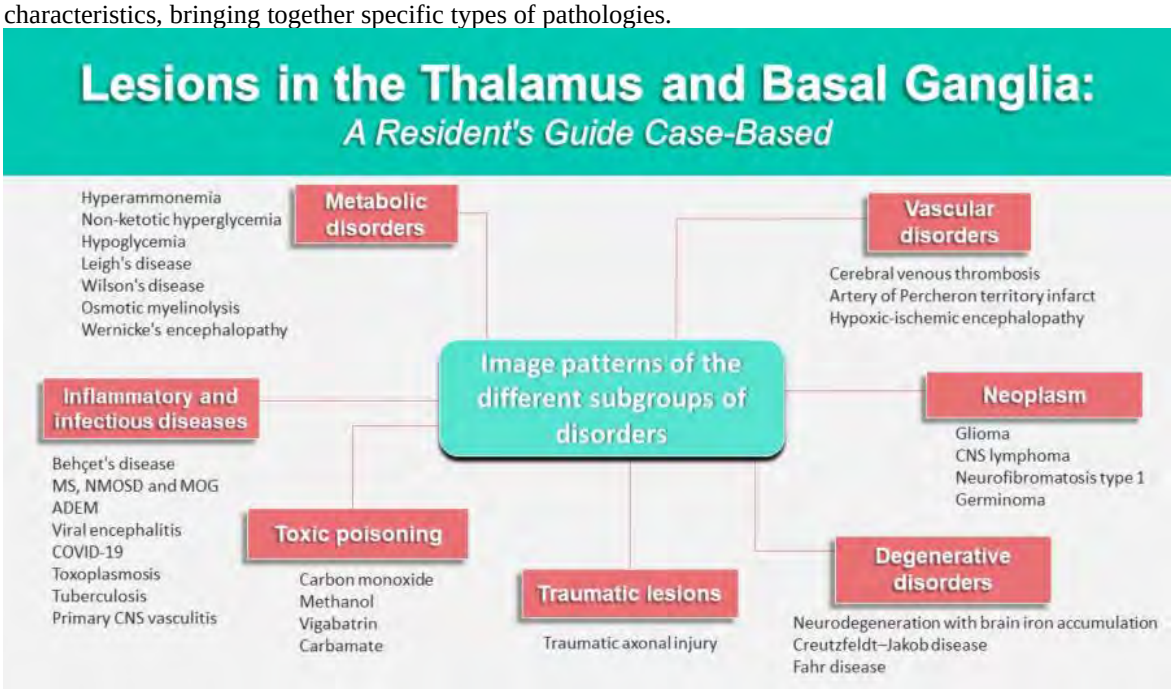

(Filename: TCT_1288_Slide1.JPG)

1116

Lesions of the Orbit: What the Radiologist Needs to Know

D Lehmkuhl[1], N Nagornaya[2], R Bhatia[2]

[1]Jackson Memorial Hospital, Miami, FL, [2]Jackson Memorial Hospital/University of Miami, Miami, FL

Purpose

The aim of this educational exhibit is to present a comprehensive overview of orbital masses. Emphasis will be made to incorporate unique imaging features, common locations, and patient symptomatology to guide appropriate follow-up and therapy.

Materials and Methods

To review the differential diagnosis in orbital lesions and to illustrate common imaging findings.

Results
Numerous cases of either pathology proven orbital lesions or pathognomonic lesions by imaging were reviewed with MRI, CT and/or digital subtraction angiography to describe the common imaging features of various ophthalmic pathologies. In addition, patient clinical history and laboratory findings when appropriate will be discussed to help enhance the differential diagnosis.
Conclusions
Results: This educational exhibit will commence with a short review of orbital anatomy. The presentation will then display an imaging review of vascular malformations, benign neoplastic, malignant neoplastic, infectious, and inflammatory lesions that occur within the orbit. Examples include but are not limited to: Dural arteriovenous fistulas, metastatic disease, fibrous tumors, lymphoma, meningiomas, schwannomas, rhabodmyosarcomas, and histiocytic lesions. Relevant imaging features of each of these lesions will be examined along with relevant clinical history. Conclusion: Orbital pathologies can be difficult to diagnose accurately prospectively. However, with the use of salient imaging findings and clinical history, the radiologist should be able to narrow the differential diagnosis for proper management of the disease.

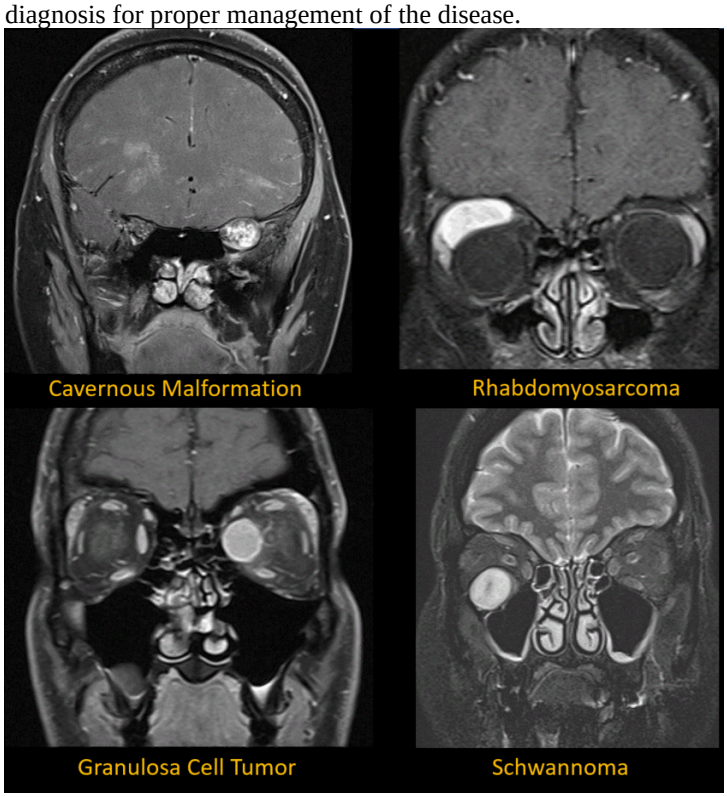

(Filename: TCT_1116_Capture2.GIF)

179
Let's Not Forget the Importance of Imaging: The Current State of Radiologic Dementia Evaluation
M Quinn[1], H ROWLEY[2], K Johnson[3], S Johnson[4], T Betthauser[4], L Eisenmenger[5]
[1]McGaw Medical Center of Northwestern University, Chicago, IL, [2]UW-Madison, Madison, WI, [3]University of Madison - Wisconsin, Madison, WI, [4]University of Wisconsin School of Medicine and Public Health, Madison, WI, [5]University of Wisconsin - Madison, Middleton, WI

Purpose
• Describe complementary structural and molecular imaging techniques available in the evaluation of cognitive impairment • Demonstrate the imaging findings of neurodegenerative disorders by modality • Present recently developed molecular imaging techniques and future directions
Materials and Methods
Dementia is responsible for a high societal, individual, and economic burden with Alzheimer's disease (AD) being the most common type and the only leading cause of death whose prevalence continues to grow. The potential impact of lifestyle, development of targeted therapies, and the need to further study disease pathophysiology make diagnosis before cognitive decline vitally important. The purpose of this exhibit is to familiarize the learner with the available modalities and features supporting the diagnosis of neurodegenerative disorders, in order to facilitate early and accurate diagnosis.
Results
This presentation will describe the current imaging modalities and techniques used in the imaging of dementia. Typical features of neurodegenerative diseases will be illustrated and compared using case-based examples. Finally, we will highlight more advanced approaches currently under investigation.

Conclusions

Antemortem diagnosis of AD has rapidly progressed in the past decade. Structural imaging enables the radiologist to suggest patterns of dementia based on CT or MRI. AD pathology classically follows the Braak staging pattern. In contrast, involvement of the frontotemporal regions suggests FTD and abnormality of the occipital lobe is typical for Lewy body dementia. There are many other classic structural findings that can suggest certain diagnoses, such as hummingbird sign in progressive supranuclear palsy. Neurodegeneration can also be measured in key regions before structural changes using FDG PET. New targeted molecular imaging can be used in diagnosis and staging. AD is defined using the A (amyloid), T (tau), and N (neurodegeneration) framework, which provides a guide for differential diagnosis of suspected dementia. In addition to ATN biomarkers, advanced MRI techniques such as 4D flow and blood brain barrier imaging allow investigation of the relationship of vascular disease and dementia. In conclusion, neuroradiology is moving the field of dementia imaging towards the era of imaging-based diagnosis, disease monitoring, and clinical research. This presentation hopes to help familiarize the learner with this rapidly progressing field of study.

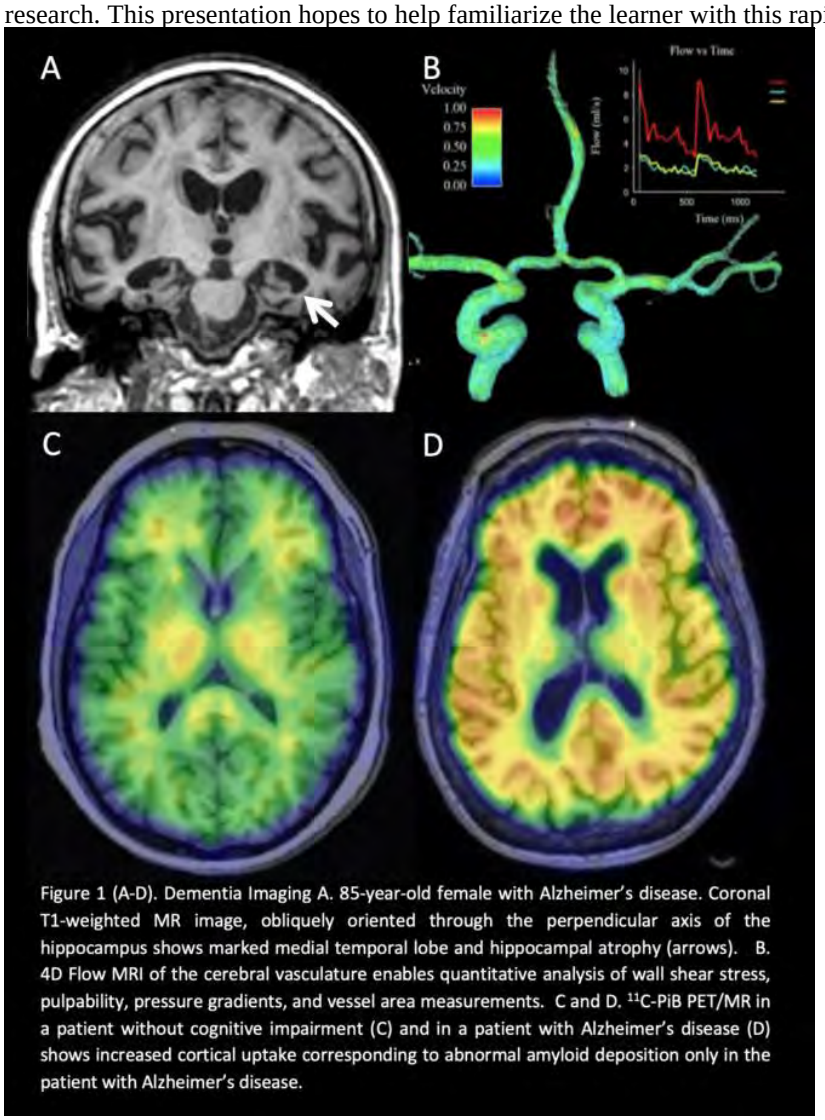

Figure 1 (A-D). Dementia Imaging A. 85-year-old female with Alzheimer's disease. Coronal T1-weighted MR image, obliquely oriented through the perpendicular axis of the hippocampus shows marked medial temporal lobe and hippocampal atrophy (arrows). B. 4D Flow MRI of the cerebral vasculature enables quantitative analysis of wall shear stress, pulpability, pressure gradients, and vessel area measurements. C and D. ^{11}C-PiB PET/MR in a patient without cognitive impairment (C) and in a patient with Alzheimer's disease (D) shows increased cortical uptake corresponding to abnormal amyloid deposition only in the patient with Alzheimer's disease.

(Filename: TCT_179_DementiaImagingAbtractFigure2022.jpg)

215

Magnetic Resonance-Guided High-Intensity Focused Ultrasound: Current Applications and Future Directions

S Majumdar[1], L Ledbetter[1], N Salamon[1]

[1]*University of California Los Angeles, David Geffen School of Medicine, Los Angeles, CA*

Purpose

1. Introduction to MR-Guided High Intensity Focused Ultrasound (MR-HIFU) and schematic of technique 2. Detailed review of current applications of HIFU and relevant anatomy targets for: a) Essential Tremor (ET) - Anatomic Targets: Ventral Intermediate Nucleus of the Thalamus; Growing interest in posterior subthalamic area - History of Medically-Refractory ET Interventions: Radiofrequency Ablation, Stereotactic Surgery, Deep Brain Stimulation, Gamma Knife Radiosurgery - Evolution from early HIFU studies to establishment of MR-HIFU as FDA approved therapy for ET. b) Parkinson's Disease - Anatomic Targets: Pallidothalamic Tracts - Role of HIFU and summary of existing literature c) Neuropathic Pain 3. Future directions and investigative applications of MR-HIFU will be discussed for several entities, such as neuro-oncology and epilepsy, among others. 4. Complications of MR-HIFU

Objectives: 1) Provide practicing neuroradiologists and trainees with a comprehensive review of existing literature on current neurologic applications of MR-HIFU and the relevant anatomic targets for each disease entity discussed. 2) Discuss investigative applications and future directions for MR-HIFU. 3) Review the possible complications of MR-HIFU in order to promote safe practices and informed use of this relatively newer intervention.
Materials and Methods
Please see Objectives section above.
Results
A comprehensive literature review using peer-reviewed medical and scientific journals was performed. Relevant topics included background and mechanism of MR-HIFU, current established applications, investigative applications, and complications of treatment.
Conclusions
MR-HIFU is a quickly evolving technology which has transformed the landscape of neurointervention. The applications of this technology are well-established for certain conditions such as essential tremor and parkinsonian tremor. Several other neurologic applications are under investigation with highly promising potential. This exhibit aims to encourage neuroradiologists and trainees to engage with this exciting technology and continue to push forward the boundaries of the field.

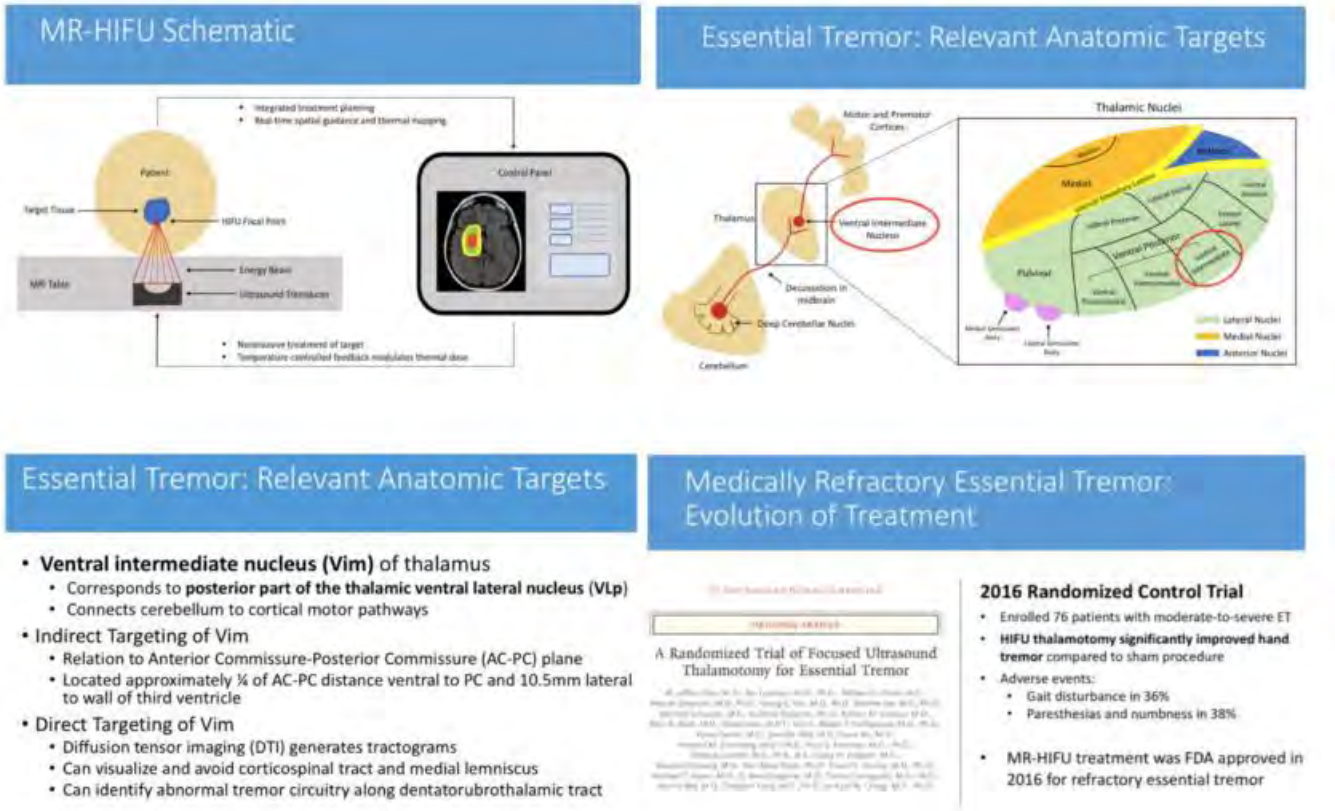

(Filename: TCT_215_HIFUGraphics.jpg)

676
Masses and Mas(s)querades: How to Differentiate Intracranial Malignancy from its Common Mimics
D Shlensky[1], A Srinivasan[1], A Capizzano[1], G Shah[2], F Rivas-Rodriguez[1]
[1]University of Michigan, Ann Arbor, MI, [2]Univ. Michigan Health System, Ann Arbor, MI

Purpose
After this presentation, the viewer should be able to: 1. Identify common intracranial pathology that can masquerade as malignancy. 2. Describe imaging features and clinical history which can suggest a lesion is a tumor mimic, rather than true neoplasm. 3. Understand how advanced imaging modalities, including diffusion weighted imaging, MR spectroscopy, and MR perfusion can help with troubleshooting in the diagnosis of intracranial lesions. 4. Apply the aforementioned to clinical practice with an end goal to improve diagnostic accuracy and patient care.
Materials and Methods
Intracranial masses are frequently encountered in radiologic practice, but do not always represent malignancy. Several pathologies can mimic malignancy including infection, demyelination, hemorrhage, vascular lesions, radiation necrosis, giant perivascular spaces, and infarction. Unfortunately, both imaging and clinical history can be nonspecific, leaving the radiologist "in the dark" about the correct diagnosis. Luckily, several imaging features can help distinguish a lesion as a masquerader of malignancy. These include T1 characteristics (in particular a gyriform distribution), T2 rim appearance, homogeneous restricted diffusion, leading edge of restricted

diffusion, incomplete rim enhancement, perfusion characteristics, and metabolites at MR spectroscopy. Clinical history is also an important adjunct to imaging features and can guide a differential, including immunocompromised state, family history, travel history, recent infection, and acuity of symptom onset. Coming to a correct imaging diagnosis prior to management is essential, as incorrect diagnosis results in suboptimal therapy and the possibility of unnecessary invasive procedures. Several cases will be presented, systematically exploring the imaging and clinical features which can help the reader recognize tumor mimics when they appear.
Results
N/A
Conclusions
When an intracranial lesion is encountered, systematically consider the features described in this presentation to reduce the risk of misdiagnosis. Applying knowledge of clinical and imaging features of tumor mimics can improve diagnostic accuracy, and guide recommendations for further imaging workup.

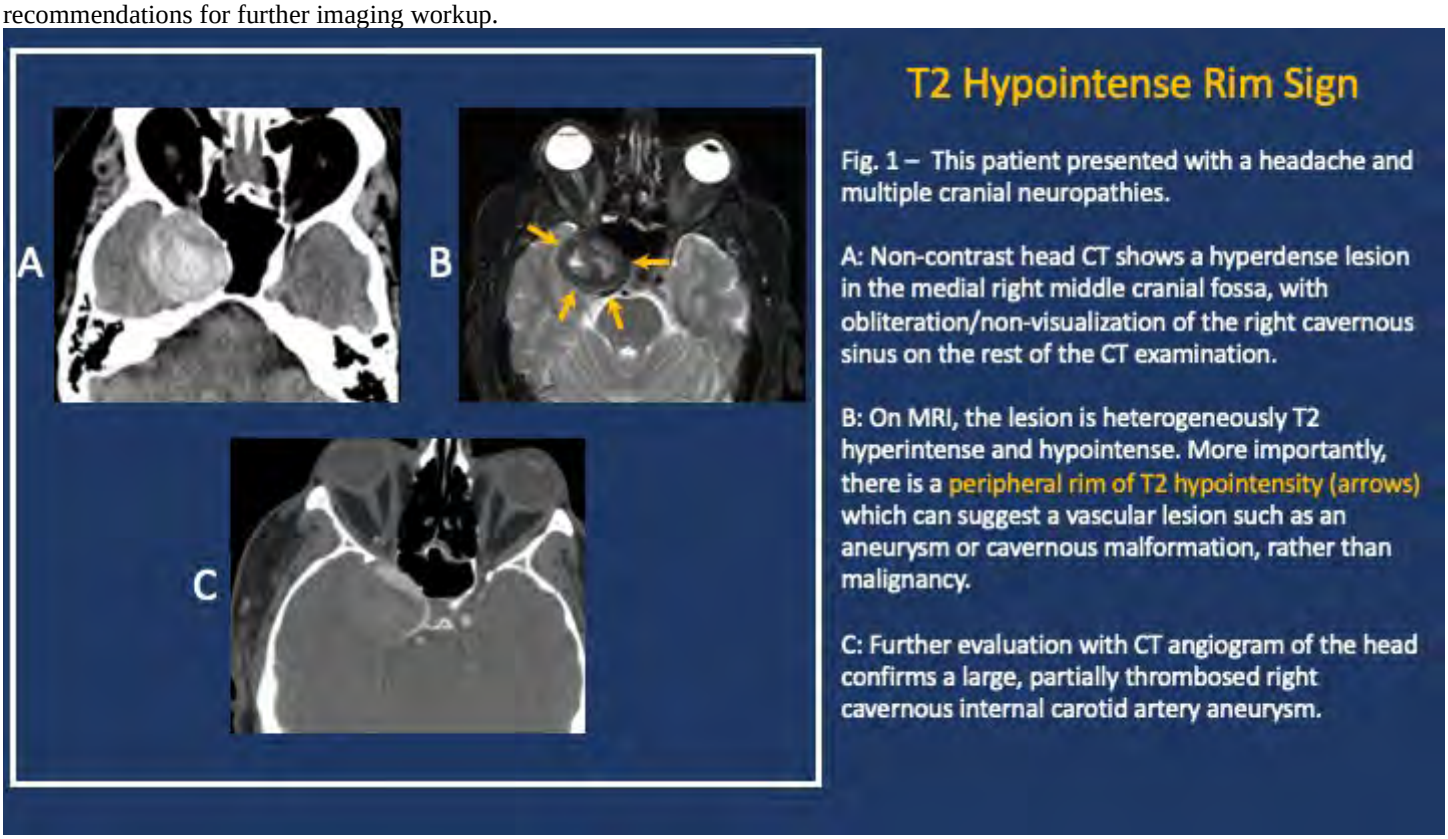

(Filename: TCT_676_masqueraderfinal.jpg)

674
Melanoma you are Checkmate: Targeted Therapy, Immunotherapy and New Imaging Frontiers
S Bhuta[1], A Prabhu[2], M Dzienis[2]
[1]Gold Coast University Hospital & Griffith University School of Medicine, Gold Coast, QLD, [2]Gold Coast University Hospital, Gold Coast, QLD

Purpose
1. To describe role of multimodality imaging in evaluation of treatment response of Metastatic Melanoma(MM) to CNS, head and neck and associated drug, radiation therapy related complications. 2. To illustrate how imaging findings alter oncologic therapy options and decision making in multidisciplinary team or tumour boards. 3. Need for Neuroradiologist to be aware of various treatment regimens to construct a valuable imaging report
Materials and Methods
Metastatic Melanoma(MM) is rampant in Australia and if not detected and treated early carries a poor prognosis. There is a need for appropriate and timely management of this rapidly progressive disease. Treatment options include immuno, targeted, radio therapy and surgical resection. Baseline and follow up imaging of CNS, head and neck, post treatment has a key role to assess treatment response which in turn influences class of drug therapy and management options
Results
All patients with confirmed diagnosis of MM underwent a staging whole body PET CT and MRI of the brain, spine, head and neck as per the diagnosis of primary and extent of metastasis. BRAF status was known for each patient. MRI was performed on 3T system with IV Gadolinium. These cases were discussed in Neurooncology tumour boards. Detailed patient history, clinical records, treatment regimens, radiotherapy, surgical notes, oncology treatment plans of targeted therapy, immunotherapy and access to clinical trials was collated.

Conclusions
The signature of MM on MRI is hyperintensity on T1, hypointense on T2, blooming on SWI. Intracranial disease maybe hemorrhagic and multiple in nature, large intracranial deposits are often debulked surgically followed by radiotherapy of operative bed. Multiple treatment options are available for patients with MM. Immune checkpoint inhibitors like Ipilimumab target CTLA4 axis, Nivolumab and Pembrolizumab block PD-1. Immunotherapy has slow and stable response,2 months to see a response with a 50% response rate. Targeted therapy works through BRAF tyrosine kinase inhibitors like Vemurafenib and Dabrafenib inhibit the downstream activated MAPK. Their response is rapid but short lasting,60% response rate seen in BRAF mutation only(fig). These therapies also have complications like, optic neuritis(fig), PRES etc. Stereotactic Radiosurgery is valuable in treating up to 6-8 lesions and Whole Brain Radiotherapy is reserved for symptomatic management. Imaging is pivotal in assessing treatment response, lesion number, size, and patient prognosis.

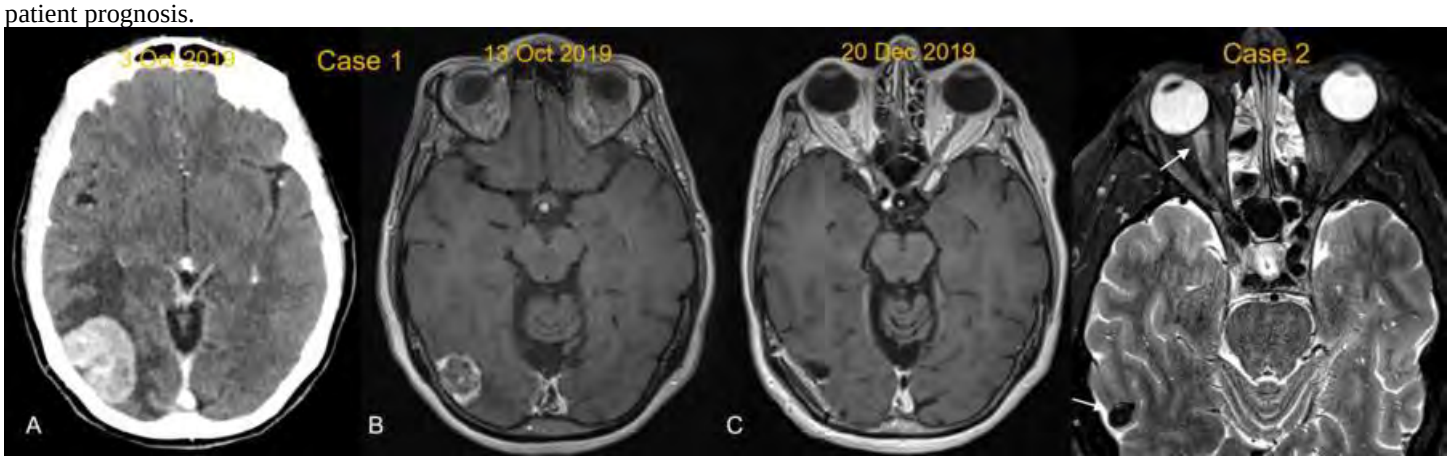

(Filename: TCT_674_Melanoma.jpg)

1015

Meningiomas Mimics: Tips and Tricks on Differential Diagnosis.

G Bandeira[1], I Alves[2], L Godoy[1], A Ayres[3], C Rimkus[4], G dos Santos[5], M MARTIN[4], C Leite[6], L Lucato[4]
[1]Instituto de Radiologia da Universidade de São Paulo, Sao Paulo, Sao Paulo, [2]Hospital Sírio-Libanês, São Paulo, São Paulo, [3]Instituto de Radiologia da Universidade de São Paulo, São Paulo, Sao Paulo, [4]Instituto de Radiologia da Universidade de São Paulo, São Paulo, São Paulo, [5]Instituto de Radiologia da Universidade de São Paulo, Sao Paulo, São Paulo, [6]Instituto de Radiologia da Universidade de São Paulo, Sào Paulo, São Paulo

Purpose
Introduction Extra-axial lesions and their cells of origin Imaging findings: Intra-axial x extra-axial lesions Meningiomas: suggestive signs Meningiomas mimics: red flags Illustrative cases of meningiomas mimics Conclusion Take-home messages References The purpose of this exhibit is: To describe the histology of the meninges and other tissues that cover the brain, recalling the main presumed cells of origin for extra-axial lesions. To illustrate the radiological signs that differentiate intra and extra-axial intracranial lesions: cerebrospinal fluid interface, stacking gyri, claw sign and feeding vessels patterns. To recognize the meningioma imaging findings: contrast enhancement pattern,feeding vessels patterns, dural tail, hyperostosis, calcification. To recognize the main red flags related to meningioma mimics: marked T2 hypointensity, marked T2 hyperintensity, bone erosion and dural displacement sign. To illustrate with cases of meningioma mimics.
Materials and Methods
The purpose of this exhibition is to review the image features of meningiomas and their main mimics.
Results
For this educational exhibit we searched the teaching files of two academic institutions for meningioma and meningioma mimics.
Conclusions
Meningiomas are the most common extra-axial tumors. Several intra-axial and extra-axial masses can mimic meningiomas on imaging. The knowledge of the histology of the meninges and other coverings of the brain is useful for understanding the main extra-axial lesions. The radiologist should be familiar with the typical imaging findings related to meningioma, as well as the main red flags related to meningioma mimics. The preoperative suggestion of a non-meningoendothelial tumor or other extra-axial lesion by the radiologist is useful for neurosurgeons and may impact surgical planning and, consequently, postoperative results.

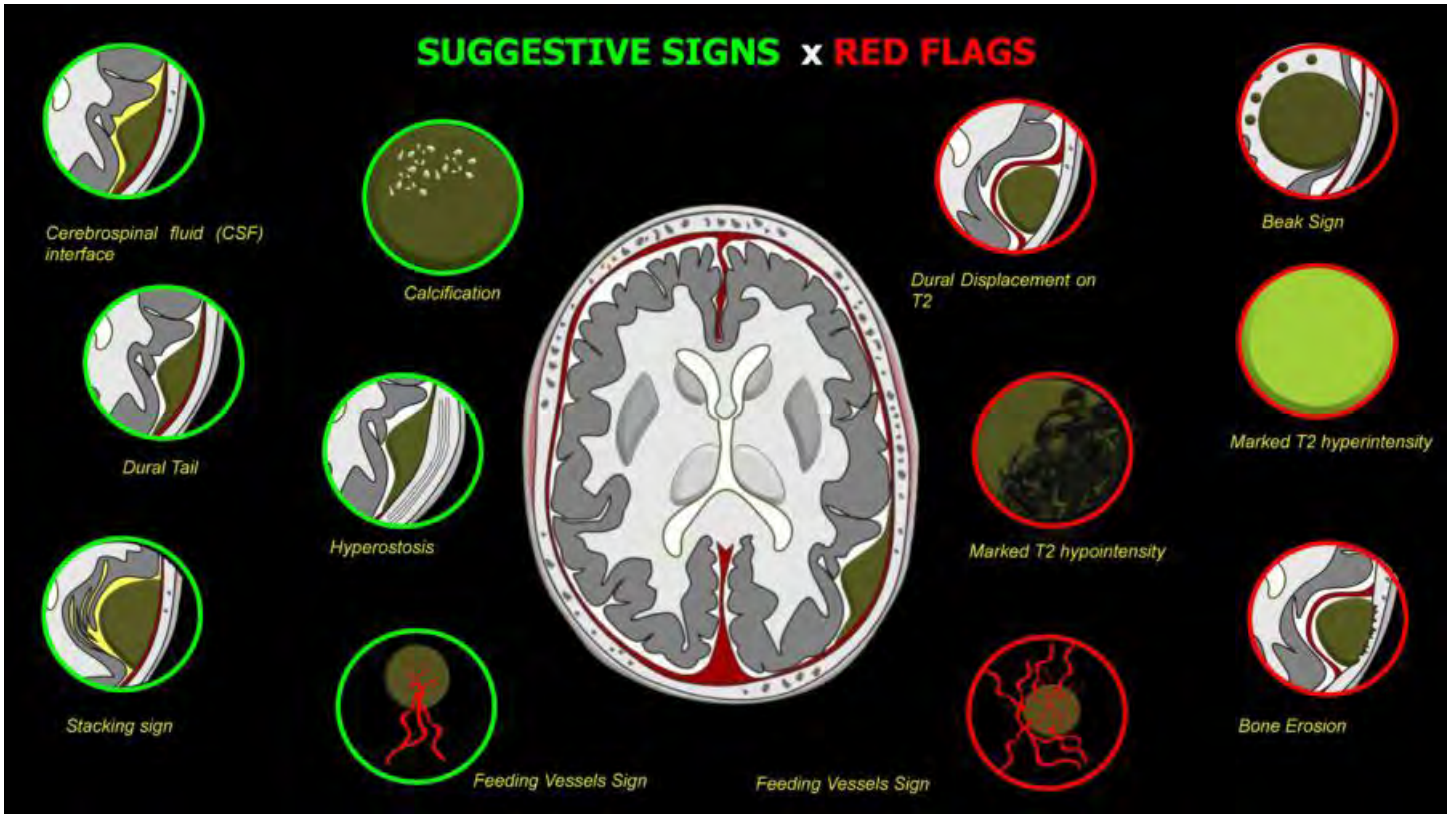

(Filename: TCT_1015_ASNRMENINGIOMASMIMICS.jpg)

1328

Mild Traumatic brain injury (mTBI) - Emerging Pathophysiological Insights From Recent Human and Animal Molecular Imaging Studies.

T Sulehria[1], M Hadi[1], C Ng[1]
[1]*University of Louisville, Louisville, KY*

Purpose

1. Understand current definition and management of mild TBI 2. Current clinical imaging performed for mild TBI 3. Overview of several molecular imaging tracers that have been used in both clinical and animal models of TBI and their results 4. Enhance understanding of new horizons in our understanding and imaging of mild TBI

Materials and Methods

This educational presentation will provide a review of current clinical imaging performed for mild traumatic brain imaging, and will discuss several molecular imaging tracers that are being studied in human and animal models for detection of mild TBI and their proposed or known pathophysiologic mechanisms of localization. FDG-PET imaging aside, several PET tracers quantifying perfusion, tissue hypoxia, amyloid, proteins such as 18kd-TSPO are discussed with the pathophsyiologic rationale and results from clinical and animal studies.

Results

N/A

Conclusions

Different PET tracers show great promise as potential diagnostic tools for mTBI, however, the sensitivity and specificity of these methods for mTBI remain to be determined.

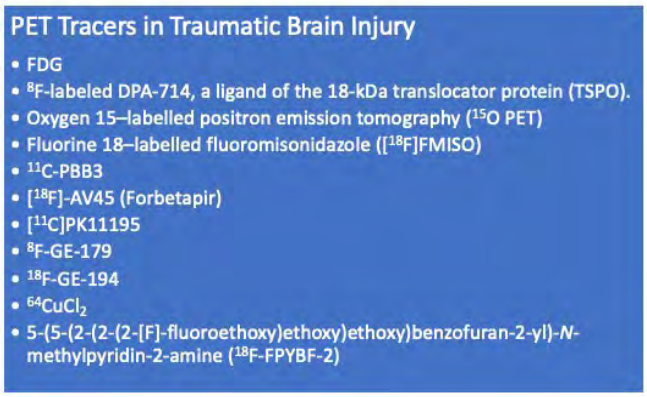

(Filename: TCT_1328_MildTBI.jpg)

905

Missed Opportunities: Acute Stroke Presenting as Altered Mental Status.

M Konner[1], I Boniece[2], A Khorsandi[3], M Starc[4]

[1]Mt. Sinai West, New York, NY, [2]Mt. Sinai Beth Israel, New York, NY, [3]New York Eye and Ear Infirmary of Mount Sinai, New York, NY, [4]Mount Sinai Hospital System, new york, NY

Purpose

Case-based pictorial and educational review of presentations of "Altered Mental Status" secondary to stroke to aid in efficient diagnosis, interpretation, and clinical management.

Materials and Methods

Stroke is the second leading cause of death and major cause of morbidity worldwide. Rapid diagnosis of stroke is crucial to optimal management, and atypical presentations may confound or delay diagnosis. A pictorial and educational review of presentations of "Altered Mental Status" secondary to stroke is compiled to aid in efficient diagnosis, interpretation, and clinical management.

Results

We compile a case-based review of patients that initially presented to a comprehensive stroke center emergency department with altered mental status and were subsequently found to have imaging findings consistent with acute stroke. We contrast these atypical presentations with common stroke syndromes and highlight the need for clinical and imaging accuracy. Lastly, we will review treatment options and effect on management in these unusual presentations in the acute setting. Our presentation synthesizes clinical data from the electronic medical record including initial presenting symptoms, suspected alternate diagnoses, clinical confounders, as well as clinical course and interventions. We illustrate the full spectrum of stroke imaging, including CT, MRI, CTA/MRA, perfusion, and catheter angiography.

Conclusions

Our review highlights atypical presenting symptoms including transient global amnesia, aphasia, acute alteration in baseline mental status, and other nonspecific changes in behavior. Key pitfalls potentially leading to delays in diagnosis are emphasized. Additional atypical stroke syndromes such as blurry vision, headache, nausea and hearing loss are also linked to radiographic findings. Acute stroke can present in a variety of ways including stroke mimics and atypical presentations. Our goal is to spotlight the importance of remaining vigilant to diagnose stroke in cases presenting as 'Altered Mental Status'. Failure to swiftly diagnose stroke often results in a delay in time sensitive interventions and adverse patient outcomes. Radiologists have a duty to rid any bias and recognize unexpected pathology on imaging, thereby aiding our clinical colleagues who may be misled by atypical symptoms.

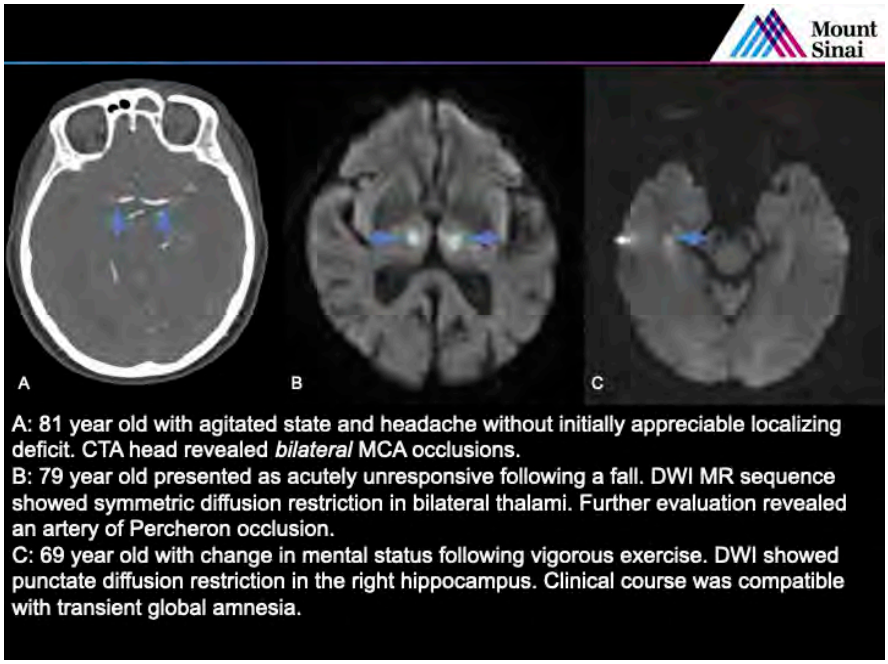

(Filename: TCT_905_ASNRpicsFINAL.jpg)

334

Mitochondrial Disorders in Children: a Comprehensive Introduction for Radiologists and Neuroradiologists alike

T Huisman[1], S Kralik[1], N Desai[1], B Serrallach[1], G Orman[1]
[1]*Texas Children's Hospital and Baylor College of Medicine, Houston, TX*

Purpose

Mitochondrial disorders represent a diverse and complex group of entities typified by defective energy metabolism (1-5). Multiple systems may be affected including the central nervous system, skeletal muscles, kidneys and liver. High-end neuroimaging plays a pivotal role in establishing diagnosis, narrowing differential diagnosis, monitoring disease progression and predicting prognosis. The characteristics of anatomical and functional MRI including MR spectroscopy (1H MRS) are often highly suggestive of a mitochondrial disorder; unfortunately, in many cases the wide variability of involved metabolic processes prevent a more specific sub-classification.

Materials and Methods

The goal is to combine relevant biochemical/metabolic facts and correlate them with key imaging findings. Further, illustrative mitochondrial disorders [including Leigh's disease, Kearns Sayre syndrome, Mitochondrial Encephalopathy, LActic acidosis and Stroke-like lesions (MELAS), and POLG related disorders (POLGRD)] will be presented to familiarize the (neuro)radiologist with pediatric mitochondrial disorders.

Results

N/A

Conclusions

Pathognomonic patterns of imaging findings may be observed which depend on region specific energy requirements, distribution and density of receptors and neurotransmitters, stage of brain development as well as affinity for certain toxins to mention a few (1-5). Cortical gray matter involvement is frequently encountered and typically presents with seizures and encephalopathy. In the acute stage, cortical swelling with restricted diffusion in a nonvascular distribution involving the visual, auditory and somatosensory cortex may be seen. On follow-up, cortical necrosis and subsequent volume loss with atrophy is typically seen. Cortical involvement is typically seen in mtDNA disorders, MELAS as well as POLG1, and Kearns Sayre syndrome. Lactate is commonly seen on 1H-MRS at 1.3 ppm both in abnormal and in normal appearing cortical gray matter. Deep gray matter involvement typically presents with extrapyramidal findings, dystonia and chorea. Typically, T2/FLAIR hyperintensity with matching restricted diffusion is seen in the acute phase involving the globi pallidi, striate nuclei, thalami, and dentate nuclei. White matter involvement may also be observed and typically presents clinically with pyramidal signs, spasticity and hyperreflexia. On initial imaging, T2/FLAIR hyperintensity with matching restricted diffusion is seen, which may evolve into a cystic leukoencephalopathy on follow-up imaging.

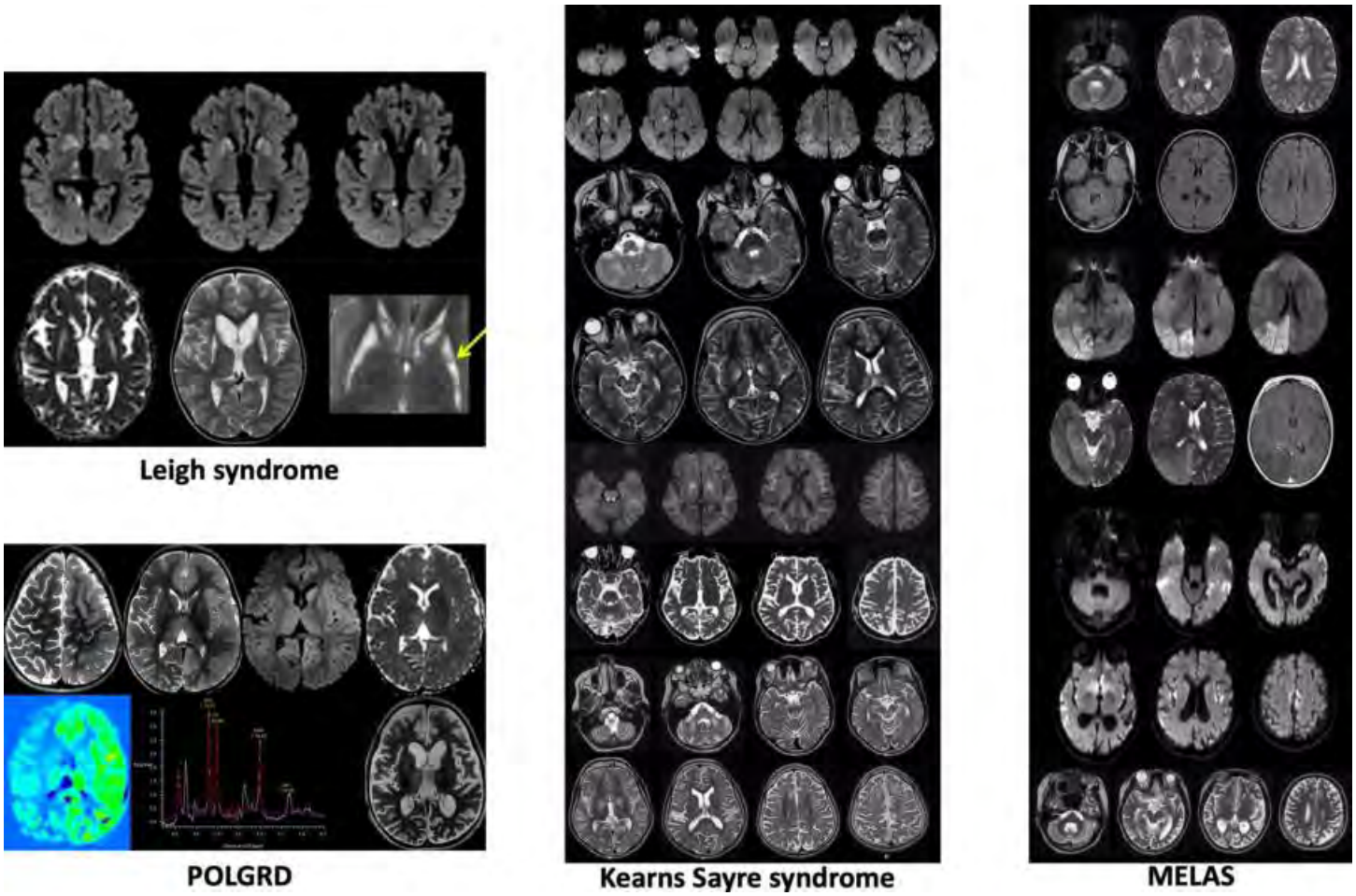

(Filename: TCT_334_mitochondrial-diseases-huisman_300.jpg)

464

Modern Carotid Artery Imaging: CT and MRI Techniques

S Chaker[1], A Moawad[1], B Jaber[1], M Aslam[1], M Shalaby[1], O Teytelboym[1]
[1]*Mercy Catholic Medical Center, Darby, PA*

Purpose

Carotid artery stenosis has been identified as the culprit in up to 20% of ischemic strokes. Traditionally, evaluation of carotid atherosclerosis focused on the degree of luminal narrowing. Advanced CT and MRI techniques have improved assessment of luminal stenosis and offer improved risk stratification of the atherosclerotic plaque/vessel wall.

Materials and Methods

Atherosclerotic plaque formation is a complex, dynamic process involving histopathological changes and vessel wall remodeling. Ultrasound provides convenient hemodynamic evaluation of carotid artery narrowing but in the event of stroke, MRI and CT are used to comprehensively evaluate the intra- and extracranial circulation. Along with CTA and MRA, advanced techniques in vessel wall imaging can help identify high risk plaques. In this abstract, we illustrate the utility of advanced CT and MR imaging in evaluating carotid atherosclerosis and the associated clinical implications.

Results

- Examine the pathophysiology of carotid artery atherosclerosis - Illustrate advanced carotid CT and MR imaging techniques and protocols - Explore the utility of advanced MRI and dual energy CT imaging techniques for carotid vessel wall imaging - Explore carotid plaque imaging features and discuss implications - Discuss future directions of carotid imaging

Conclusions

Carotid stenosis assessment with advanced CT and MRI techniques enhances accuracy, streamlines clinical workflow, and offers plaque rupture risk assessment. Thus, advanced imaging techniques offer many opportunities to add value in guiding medical/surgical therapy.

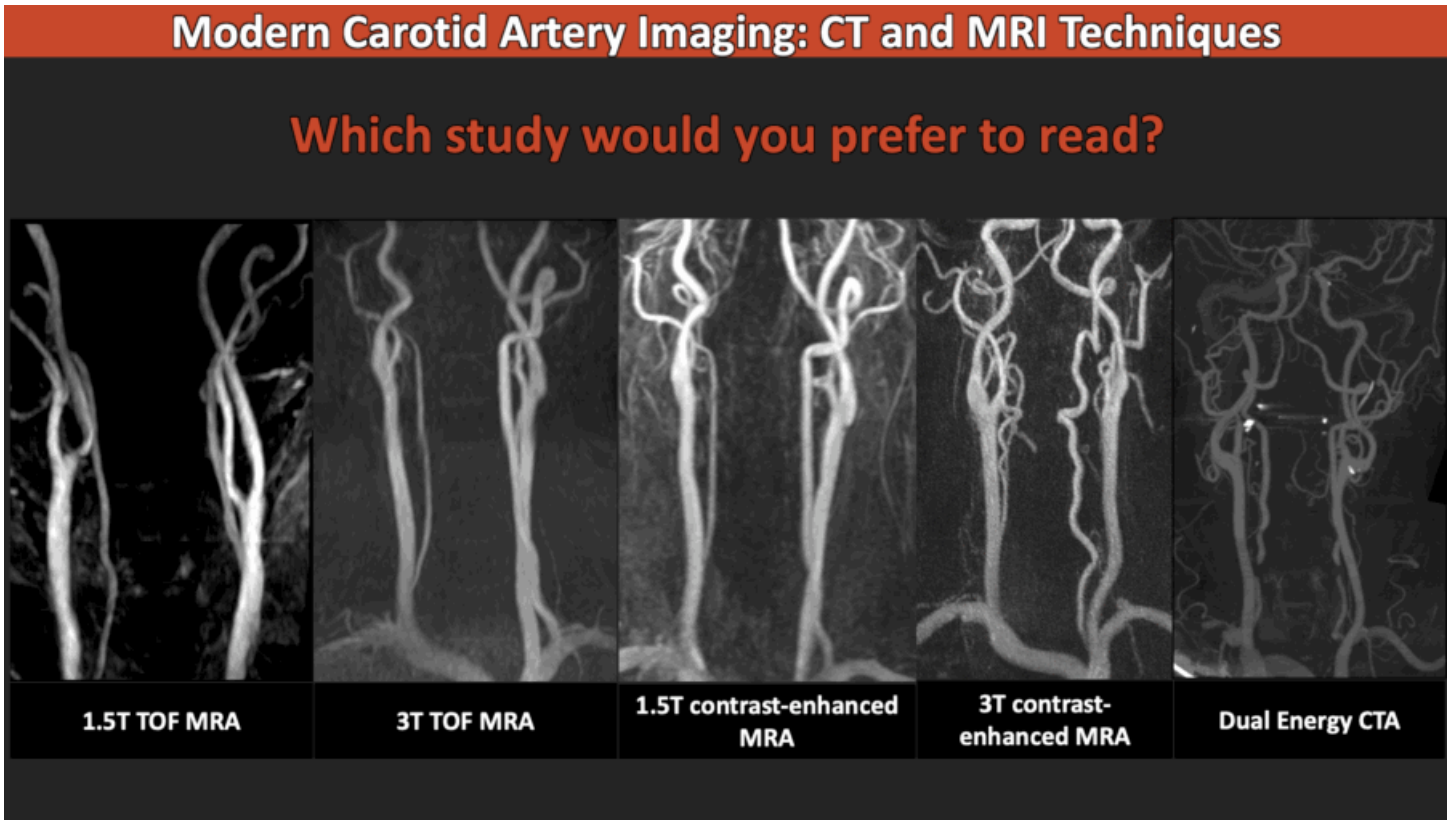

(Filename: TCT_464_Carotid.gif)

1426

Molecular Imaging for differential diagnosis of Parkinsonian Syndromes

R Hernández Ramírez[1], J Chavez Torres[2], R Suazo Aguero[3], A Barrientos-Priego[4], N Ramírez Pedraza[4], G Romero Sanchez[5], B Abundiz Lopez[3], D Cardosa Cisneros[3], Q Pitalua Cortes[3], E Izquierdo Echavarri[3]

[1]INSTITUTO NACIONAL DE CIENCIAS MEDICAS Y DE NUTRICION SALVADOR ZUBIRAN, Mexico, Ciudad de México, [2]Instituto Nacional de Ciencias Médicas y Nutrición Salvador Zubiran, Mexico City , Mexico, [3]Medica Sur, Mexico City, Mexico City, [4]Instituto Nacional de CIencias Medicas y Nutrición Salvador Zubiran, Mexico City, Mexico, [5]Instituto Nacional de Ciencias Médicas y Nutrición Salvado Zubirán, Mexico City, Mexico

Purpose

To demonstrate the utility of molecular imaging for differential diagnosis of Parkinsonian Syndromes. To show different radiotracers and its molecular targets. To explain the different patterns in Atypical Parkinsonism.

Materials and Methods

Parkinsonism syndrome is a frequent alteration among the elderly, it is characterized by a combination of rigidity, resting tremor, bradykinesia, loss of postural reflexes and gait impairment. Parkinsonism can be a clinical manifestation of hereditary and nonhereditary neurodegenerative diseases, differential diagnoses include Idiopathic Parkinson's disease (IPD) and Atypical Parkinsonian Syndromes (APS), but it can also be secondary to multiple causes including structural, pharmacological, toxic, or traumatic events1.

Results

Synapse at a dopaminergic neuron showing the presynaptic terminal (blue) and the postsynaptic terminal (orange). Dopamine is created in the presynaptic neuron and get into vesicles by vesicular monoamine transporters (VMAT), which release the dopamine molecules into the synapse, where it can interact with dopamine receptors (D1 and D2). Dopamine can then either be degraded by catechol-O- methyltransferase or get back into the presynaptic neuron and be recycled through the dopamine transporter. The target of binding is dopamine transporter (DAT), identifying this way dopaminergic neurons2. IPD is a frequent diagnosis in the elderly, but only about 75% of parkinsonian patients have proven IPD at autopsy. The most common alternative diagnosis is one of atypical parkinsonian syndromes, such as Multiple System Atrophy (MSA), Progressive Supranuclear Palsy (PSP) and Corticobasal Degeneration (CBD)3. SPECT and PET are nuclear medicine techniques that yield images of the striatal dopaminergic system. These require previous injection of radiotracers, and their striatal uptake differs depending on the radiotracer used. Presynaptic radiotracers evaluate the presynaptic neurons, these radiopharmaceuticals have affinity for molecules which participate in the synthesis of dopamine and dopamine transporters4.

Conclusions

Patients with essential tremor have normal uptake with presynaptical radiotracers. Presynaptic is not suitable for differentiating the various neurodegenerative parkinsonian syndromes (IPS, MSA, PSP, CBD) from each other. 18F-FDG-PET can differentiate typical

from atypical parkinsonian syndromes and discriminate among atypical parkinsonian syndromes (MSA, PSP and CBS) with high sensitivity and specificity, 75% and 90%, respectively5.

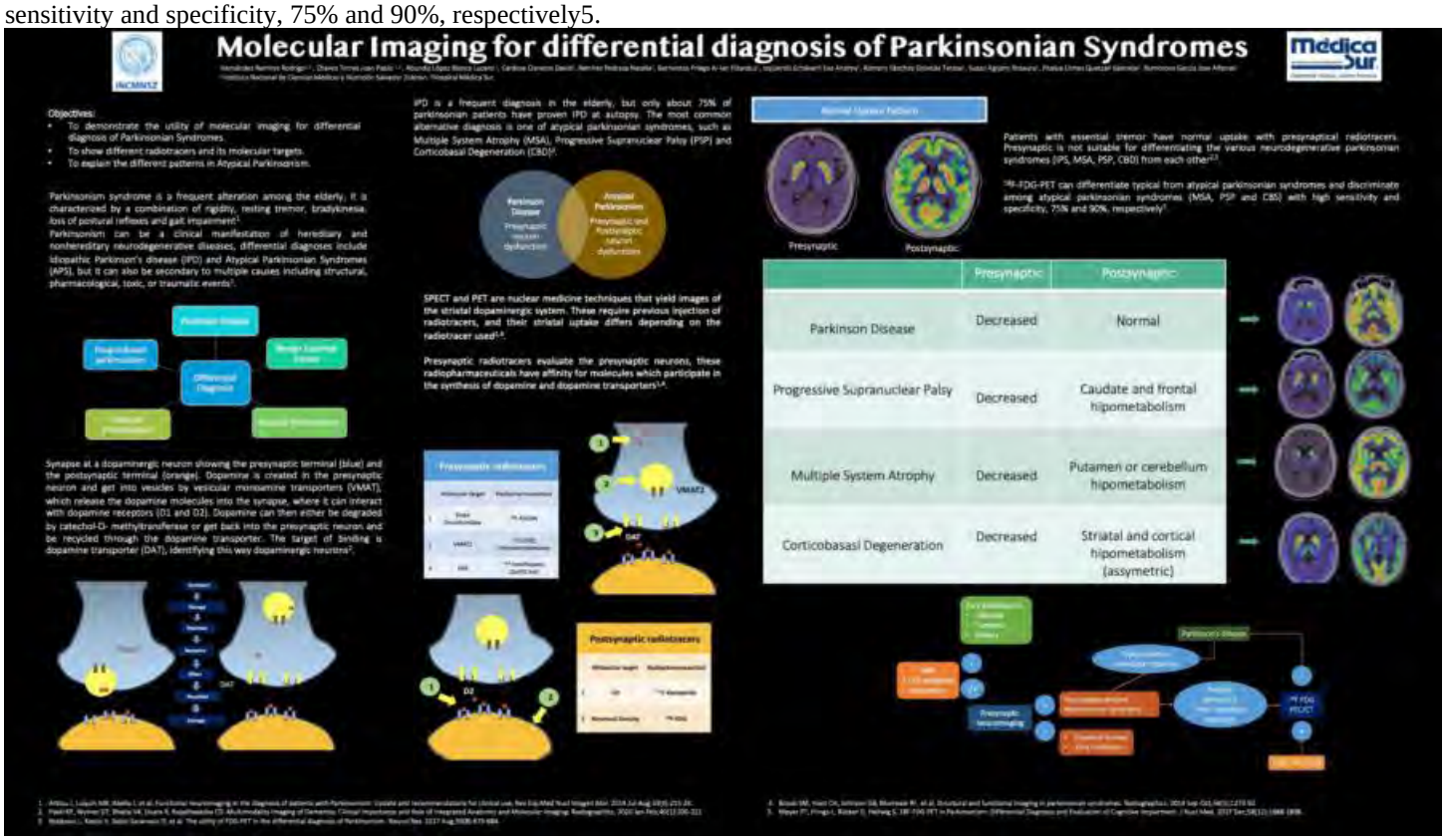

(Filename: TCT_1426_PARKINSONISMABSTRACTASR2022.jpg)

1182

Molecular Imaging in Patients with Dementia: Beyond the Alzheimer Disease

S Kooraki[1], A Catellanos[1], S Parhizgar[2], C Ni[3], D Davila[4], C Jude[1], N Menon[5]

[1]University of California, Los Angeles, Los Angeles, CA, [2]UCLA, Los Angeles, CA, [3]Olive view- UCLA medical center, Sylmar, CA, [4]UCLA Olive view, Sylmar, CA, [5]University of California Los Angeles/Greater Los Angeles VA, Los Angeles, CA

Purpose

Summary: Brain F-18 FDG PET/CT is being clinically used in patients with symptoms of dementia for diagnosis of Alzheimer disease and its differentiation from other less common neurodegenerative diseases. This exhibit will review the patterns of altered glucose metabolism in brain F-18 FDG PET/CT and the use of other molecular tracers in a variety of non-Alzheimer neurodegenerative diseases, in correlation with patients' clinical presentation. The indications for using molecular imaging studies and their potential impact on patient management and treatment will be discussed. Finally, the most recent guidelines and algorithms for interpretation of brain F-18 FDG PET/CT in neurodegenerative diseases will be presented. Educational Objectives: - Review the clinical Indications for acquiring brain F-18 FDG PET/CT - Discuss the use of other molecular tracers other than F-18 FDG (e.g. I-123 Ioflupane, I-123 MIBG, F-18-based amyloid agents) in patients with symptoms of dementia - Describe the differentiation of neurodegenerative diseases based on the patterns of altered glucose metabolism in correlation with clinical findings - Develop a strategy for interpretation of F-18 FDG PET/CT in patients with suspected dementia

Materials and Methods

This case-based presentation aims to describe the patterns of altered glucose metabolism in brain F-18 FDG PET/CT and the use of other molecular tracers in a variety of non-Alzheimer entities including posterior-dominant (Lewy body dementia, posterior cortical atrophy), anterior-dominant (Behavioral variant frontotemporal dementia, subtypes of primary progressive aphasia including semantic, non-fluent and logopenic variants), and miscellaneous (progressive supranuclear palsy, corticobasal degeneration) neurodegenerative diseases, in correlation with patients' clinical presentation.

Results

A case-based algorithmic approach will be formulated to describe FDG PET/CT findings in non-Alzheimer neurodegenerative disease.

Conclusions

A strategy should be developed for the interpretation of F-18 FDG PET/CT in patients with suspected dementia of non-Alzheimer type. Patterns of metabolism in posterior cingulate gyrus, occipital and frontal lobes; the presence of a distinct unilateral involvement; and a history of vision or language disorder are most helpful for drawing a diagnosis. An MIBG scan or an I-123 Ioflupane scan can be used in patients suspected of having Lewy body dementia or other parkinsonian-like disorders.

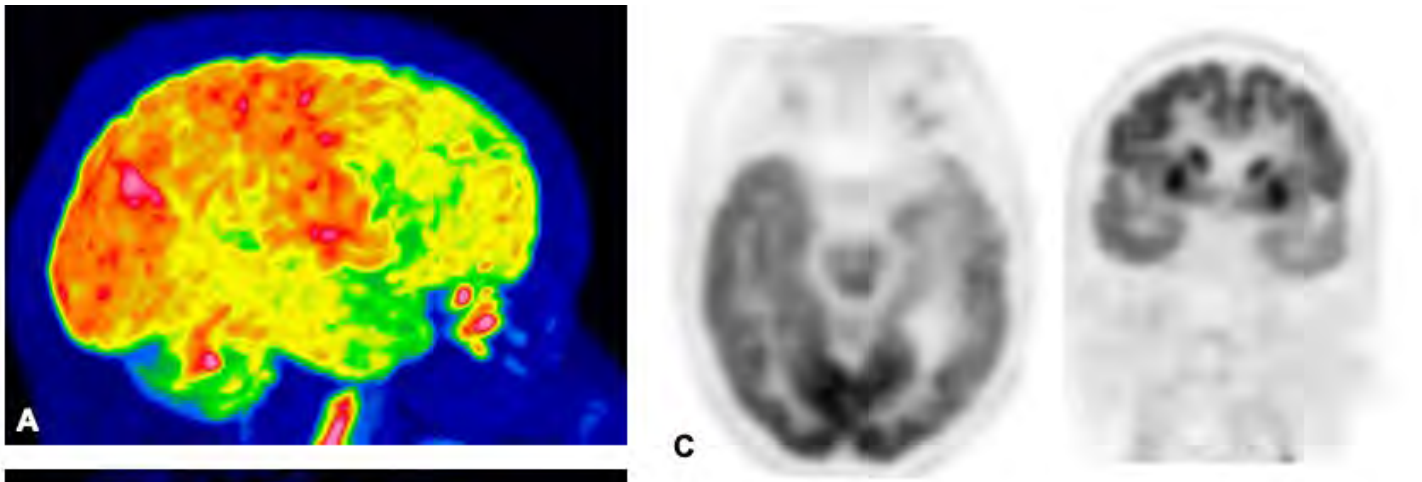

(A) Fused sagittal F-18-FDG PET/CT in a 81-year-old male with behavioral disturbance and memory decline shows hypometabolism in frontal and temporal lobes, in favor of behavioral-variant Frontotemporal Dementia (bvFTD). (B) Fused sagittal F-18-FDG PET/CT in a 75-year-old male with executive function decline, upper limb rigidity and REM sleep behavioral disorder shows decreased metabolism in occipital, and less prominently in parietal and temporal lobes, compatible with Lewy Body Dementia (DLB). (C) Axial F-18-FDG PET images of a 91-year-old female with progressive language dysfunction and amnestic dementia shows relatively decreased asymmetric FDG activity in the left anterior temporal lobe, in favor of Semantic Dementia.

(Filename: TCT_1182_Figure1.jpg)

1478

Movement Disorders: a pictorial review of imaging features

M Chan[1], A Chen[2]
[1]University of Toronto, Toronto, Ontario, [2]N/A, N/A

Purpose

Summary: Movement disorders represent a group of neurodegenerative disorders defined by either abnormal increased or decreased movements. In this educational exhibit, we aim to present the key imaging features for common and uncommon movement disorders encountered in neuroradiology practice. An overview of underlying pathophysiology and the role of imaging in aiding diagnosis and informing treatment strategies for these disorders will be also provided. The imaging findings of common and uncommon primary movement disorders will be discussed, including Parkinsonism, Parkinson's' plus syndromes and hereditary degenerative disorders such as NBIA, Huntington's disease, and Wilson's disease. Educational Objectives: • To discuss the imaging approach to Parkinsonism. • To discuss imaging features of Parkinson plus syndromes - PSP, MSA, and CBD. • To discuss an imaging approach to hemifacial spasm.

Materials and Methods

Teaching Points: • To discuss the imaging approach to Parkinsonism. • To discuss imaging features of Parkinson plus syndromes - PSP, MSA, and CBD. • To discuss an imaging approach to hemifacial spasm.

Results

Summary: Movement disorders represent a group of neurodegenerative disorders defined by either abnormal increased or decreased movements. In this educational exhibit, we aim to present the key imaging features for common and uncommon movement disorders encountered in neuroradiology practice. An overview of underlying pathophysiology and the role of imaging in aiding diagnosis and informing treatment strategies for these disorders will be also provided. The imaging findings of common and uncommon primary movement disorders will be discussed, including Parkinsonism, Parkinson's' plus syndromes and hereditary degenerative disorders such as NBIA, Huntington's disease, and Wilson's disease. Educational Objectives: • To discuss the imaging approach to Parkinsonism. • To discuss imaging features of Parkinson plus syndromes - PSP, MSA, and CBD. • To discuss an imaging approach to hemifacial spasm.

Conclusions
Teaching Points: • To discuss the imaging approach to Parkinsonism. • To discuss imaging features of Parkinson plus syndromes - PSP, MSA, and CBD. • To discuss an imaging approach to hemifacial spasm.

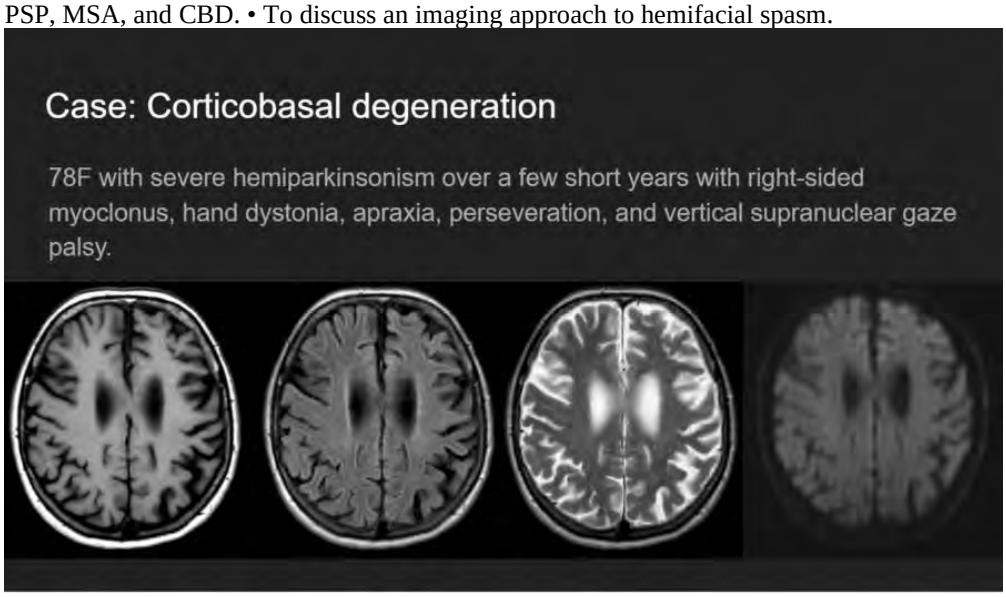

(Filename: TCT_1478_Capture.JPG)

347

Multimodal Imaging of Typical and Atypical Findings of Solitary Fibrous Tumor in the Brain, Head and Neck and Spine, with Pathological Correlation.

T Lin[1], T Moritani[1], S Camelo-Piragua[1], J Kim[1], M Kurokawa[1], R Kurokawa[1]
[1]University of Michigan, Ann Arbor, MI

Purpose
1, Solitary fibrous tumor (SFT) and hemangiopericytoma (HPC) were previously categorized as a single entity under the WHO 2016 classification of tumors of the central nervous system. In the upcoming WHO 2021 classification, the term "hemangiopericytoma" has been retired, and the neoplasm is now termed solely as "solitary fibrous tumor." SFT is further subdivided into grades 1-3, via order of increasing aggressivity on histopathology. 2. SFT mimic meningiomas, metastasis or other tumors on imaging. Typical distinguishing characteristics for SFT include a narrow dural attachment, associated osseous destruction, mixed cellular and fibrous mass with or without bubbly cystic component, and lack of calcification. 3. Preoperative differentiation between SFT from meningioma is critical. Grade 3 SFT has the highest recurrence rate and frequently metastasize outside the central nervous system (CNS). 4. Multimodal techniques which include susceptibility, diffusion, and perfusion weighted imaging (SWI, DWI and PWI), MR spectroscopy, and PET may offer clues when diagnosing atypical cases of SFT.
Materials and Methods
The purpose of this educational exhibit is to elucidate the key multimodality imaging findings and clinical pearls for SFT. Most importantly, we plan to highlight the typical/atypical findings and locations of SFT, while also providing a targeted differential diagnosis.
Results
The materials include approximately 100 cases of SFT in the brain, head and neck and spine with histopathological confirmation. Imaging modalities include CT, MRI including SWI, DWI and PWI, MR spectroscopy, PET and angiogram.
Conclusions
This exhibit illustrates multimodal techniques in the diagnosis of typical and atypical SFT with histopathological correlation. We showcase typical imaging findings for SFT, which include a non-calcified supratentorial mass with a narrow dural-based attachment. Atypical cases involving the orbit, sinonasal cavity, intraventricular space, and spine are challenging to diagnose. Different techniques have been employed to help characterize atypical SFT. MR spectroscopy may be used to non-invasively determine the tumor's cellular characteristics; we present a case of intraventricular SFT that demonstrated abnormal increased mobile lipid and choline peaks, and decreased NAA. Combination of ADC, PWI, and SWI can be used to distinguish SFT from meningioma. Predominately low signal on T2-weighted images may also be a potential SFT distinguishing feature.

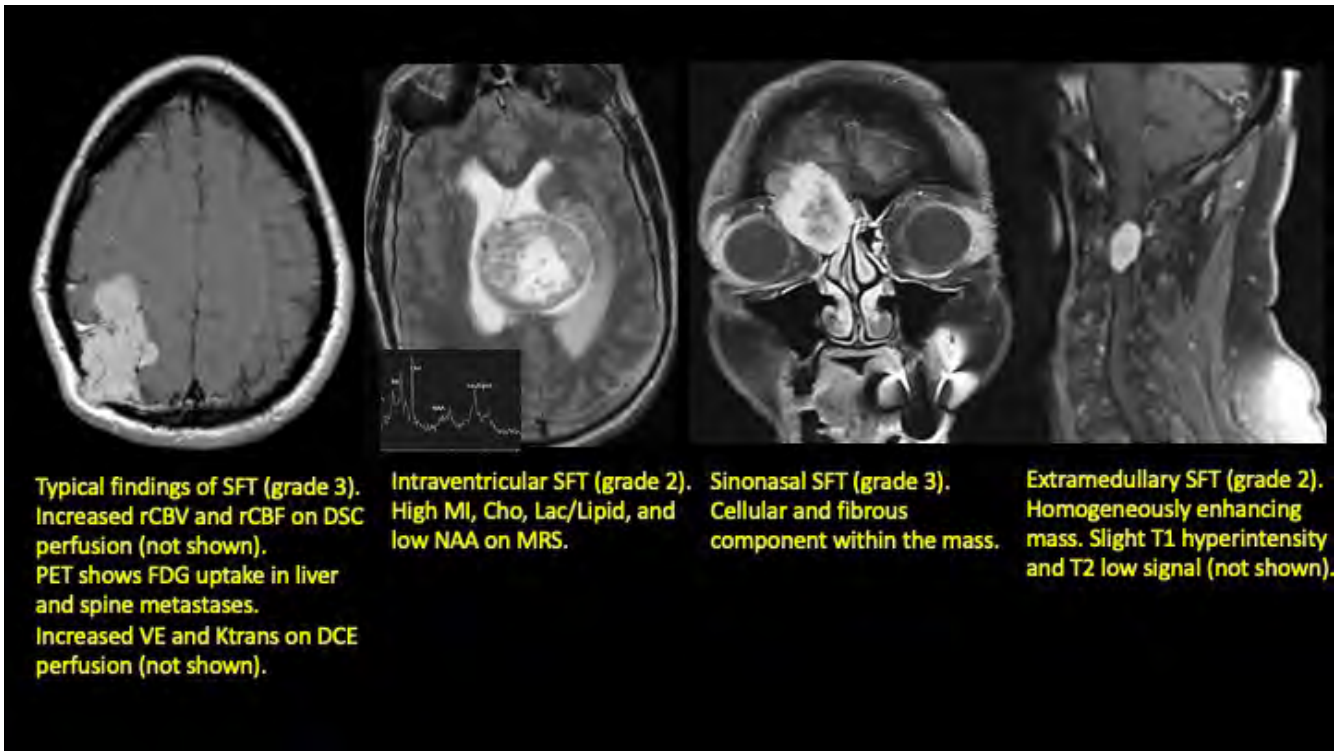

(Filename: TCT_347_SFTASNR.jpg)

217

Multimodality Imaging of Typical and Atypical Pilocytic Astrocytomas with Pathological Correlation

J Ortiz-Cruz[1], T Moritani[2], S Camelo-Piragua[2], R Kurokawa[2], M Kurokawa[2]
[1]University of Michigan Department of Radiology, Ann Arbor, MI, [2]University of Michigan, Ann Arbor, MI

Purpose

Genetic and oncogenic pathways of tumor development of pilocytic astrocytoma (PA) with or without NF1 Pathology: microcystic change, myxoid degeneration, Rosenthal fiber, pilocytic variants such as diffuse variant or pilomyxoid astrocytoma Modalities: CT, MRI, diffusion, perfusion (DSC and DCE), APTw, MR spectroscopy, and PET. Age: pediatric versus adult findings Typical findings: Well-defined infratentorial cystic lesion with enhancing mural nodule and supratentorial enhancing mass, with facilitated diffusion, typical perfusion pattern, or increased APTw. Atypical findings: unusual locations, non-enhancing, exophytic, hemorrhagic, or multicenteric/dissemination, with relatively low ADC value or atypical perfusion pattern.

Materials and Methods

The purpose is to discuss genetics and pathology of this tumor as well as typical and atypical imaging characteristics seen in multiple modalities.

Results

1. Literature review. 2. Select multiple cases (patient identifiers will be removed) from our database spanning several hospitals to show typical and atypical pilocytic astrocytomas in multiple modalities.

Conclusions

Pilocytic astrocytoma (PA) is the most common glial tumor in children and young adults. Histologically, PA is characterized by spindled cells, elongated bipolar cells, granular bodies, Rosenthal fibers and myxoid/microcystic changes. The cerebellum optic pathway including the hypothalamus are common location. Uncommon locations include the cerebral hemisphere, thalamus and brainstem. Cerebellar PA is classically demonstrates a large cystic component with enhancing mural nodule. It can present as a heterogeneous mass with solid and cystic components or a completely solid lesion. The mass commonly is T1 iso to hypointense and T2 hyperintense. CT and SWI (phase) can differentiate calcifications and hemorrhage in the mass. PAs classically demonstrate high ADC values, while high grade gliomas and embryonal tumors show lower ADC. However, there are relatively wide range of ADC values in PAs. Similarly, PAs have low rCBV and rCBF and high K2 on DSC, and low VP, high VE, and partially high Ktrans on DCE, when compared to high grade astrocytomas. MRS often show increased choline and lactate peak which can be a pitfall of the diagnosis. Finally, APT maps often show high values for PA even this is low grade tumor. Differential diagnosis of pilocytic astrocytoma is extensive that includes other circumscribed, diffuse low or high grade gliomas, glioneuronal/neuronal, ependymal and embryonal tumors.

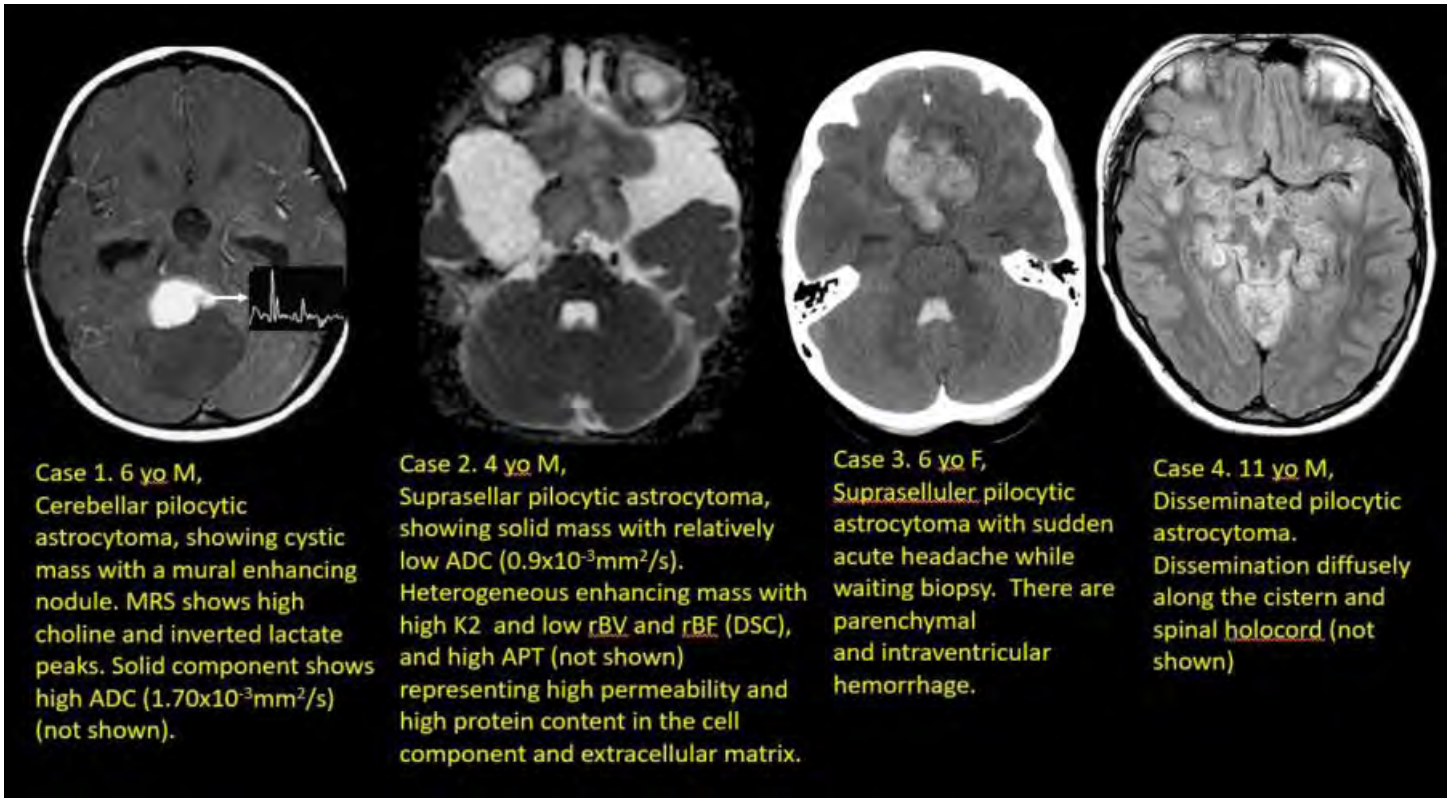

(Filename: TCT_217_PAImages.jpg)

1160

Neoplastic Cauda Equina Syndrome: A Neuroimaging Based Review with Anatomical and Clinical Correlation

T Mujtaba[1], S Ali[2]
[1]University of Chicago, Woodridge, IL, [2]University of Chicago, Chicago, IL

Purpose

Cauda equina syndrome can be a neurological emergency with clinical presentation resulting from dysfunction of the cauda equina nerve roots. The signs and symptoms can be variable and mirror the neuroanatomical complexity of the conus medullaris and cauda equina nerve roots as well as the time course of the underlying pathology. Low back pain is the most common feature followed by motor symptoms and clinical signs of lower motor neuron deficits, depressed deep tendon reflexes in the lower limbs, and muscle wasting with chronic compression. Sensory dysfunction and genitourinary abnormalities includes saddle anesthesia, paresthesia, and dysesthesias as well as urinary retention, overflow incontinence, and sometimes loss of anal sphincter tone or constipation. On imaging involvement of the various lumbar ventral and dorsal roots as well as peripheral nerve roots from the sacral segments of the nerve roots can be seen, often times sequentially as the disease progresses and can provide a better understanding of the progression of clinical signs and symptoms. Many etiologies exist for cauda equina syndrome and include degenerative disc disease, neoplasms, trauma, infection, and other inflammatory processes. In this educational exhibit we focus on neoplastic invasion of the cauda equina nerve roots. We will discuss the complexity of the anatomy of the cauda equina nerve roots and conus medullaris through schematics, discuss the presenting clinical symptoms and neurological exam findings on a series of patients with cauda equina syndrome, and demonstrate the imaging correlation of these patients. We will also review the differentials and imaging features for a variety of primary intraspinal and metastatic spine tumors which can produce cauda equina syndrome.

Materials and Methods

Cauda equina syndrome can be a neurological emergency with clinical presentation resulting from dysfunction of the cauda equina nerve roots. The signs and symptoms can be variable and mirror the neuroanatomical complexity of the conus medullaris and cauda equina nerve roots as well as the time course of the underlying pathology.

Results

We will discuss the anatomy of the cauda equina nerve roots and conus medullaris through schematics, discuss the presenting clinical symptoms and neurological exam findings on a series of patients with cauda equina syndrome, and demonstrate the imaging correlation of these patients.

Conclusions

In this educational exhibit we focus on neoplastic invasion of the cauda equina nerve roots.

1428

Neuoroimaging Features of Myelin Oligodendrocyte Glycoprotein (MOG) Antibody–Associated Disease in the Adolescent and Adult Patient.

F Torres[1], S Sampson[2], M Sanders[3], E Wong[4], M Wang[4], J DeBacker[1]

[1]Kaiser Permanente, Los Angeles Medical Center, Los Angeles, CA, [2]Kaiser Permanente Los Angeles Medical Center, Los Angeles, CA, [3]Kaiser Permanente, School of Medicine, LOS ANGELES, CA, [4]Kaiser Permanente, Los Angeles Medical Center, LOS ANGELES, CA

Purpose

Myelin oligodendrocyte glycoprotein antibody disease (MOGAD) is a relatively recently characterized syndrome predominantly affecting the optic nerves and brain, and less commonly the spinal cord. Although imaging findings often overlap with other demyelinating diseases such as neuromyelitis optica spectrum disorder and multiple sclerosis, there are certain unique neuroimaging features that can help aid in the diagnosis of MOGAD. We hope to review the unique neuroimaging findings of MOGAD in hopes of aiding the neuroradiologist and treating clinicians in the challenging process to diagnose, differentiate, and treat the challenging spectrum of clinical presentations of MOGAD.

Materials and Methods

Review the unique spectrum of neuroimaging features of seropositive myelin oligodendrocyte glycoprotein antibody disease (MOGAD) within the optic nerves, brain, and spinal cord. We will also present mimics of this disease entity including NMOSD, ADEM, and MS.

Results

All patients were diagnosed with the serum biomarker MOG antibody. A total of 12 seropositive MOGAD patients imaging features will be utilized in this educational review. A total of 4 patients are between the ages of 12-17 and a total of 8 patients are over 21 years of age.

Conclusions

MOGAD involvement of the optic nerves was the most commonly identified clinical presentation in the adult patient, with both optic nerve and perioptic nerve enhancement, predominantly involving the anterior aspect of the optic pathway. The lesions involving the optic nerve was slightly longer than typical MS ON and yet shorter than in NMOSD. MOGAD involvement of the cerebrum was the most unique imaging feature, in particular within the adolescent, where the imaging findings and clinical presentation was often similar to ADEM. Cerebral imaging findings included relatively medium to large geographic areas of cortical and subcortical edema, with a slight subcortical predominance. T2 FLAIR hyperintense signal was also noted along the adjacent cerebral sulci/subarachnoid space. Contrast enhancement included linearly-oriented, irregular and stippled subcortical location within the supratentorial brain with variable leptomeningeal involvement.

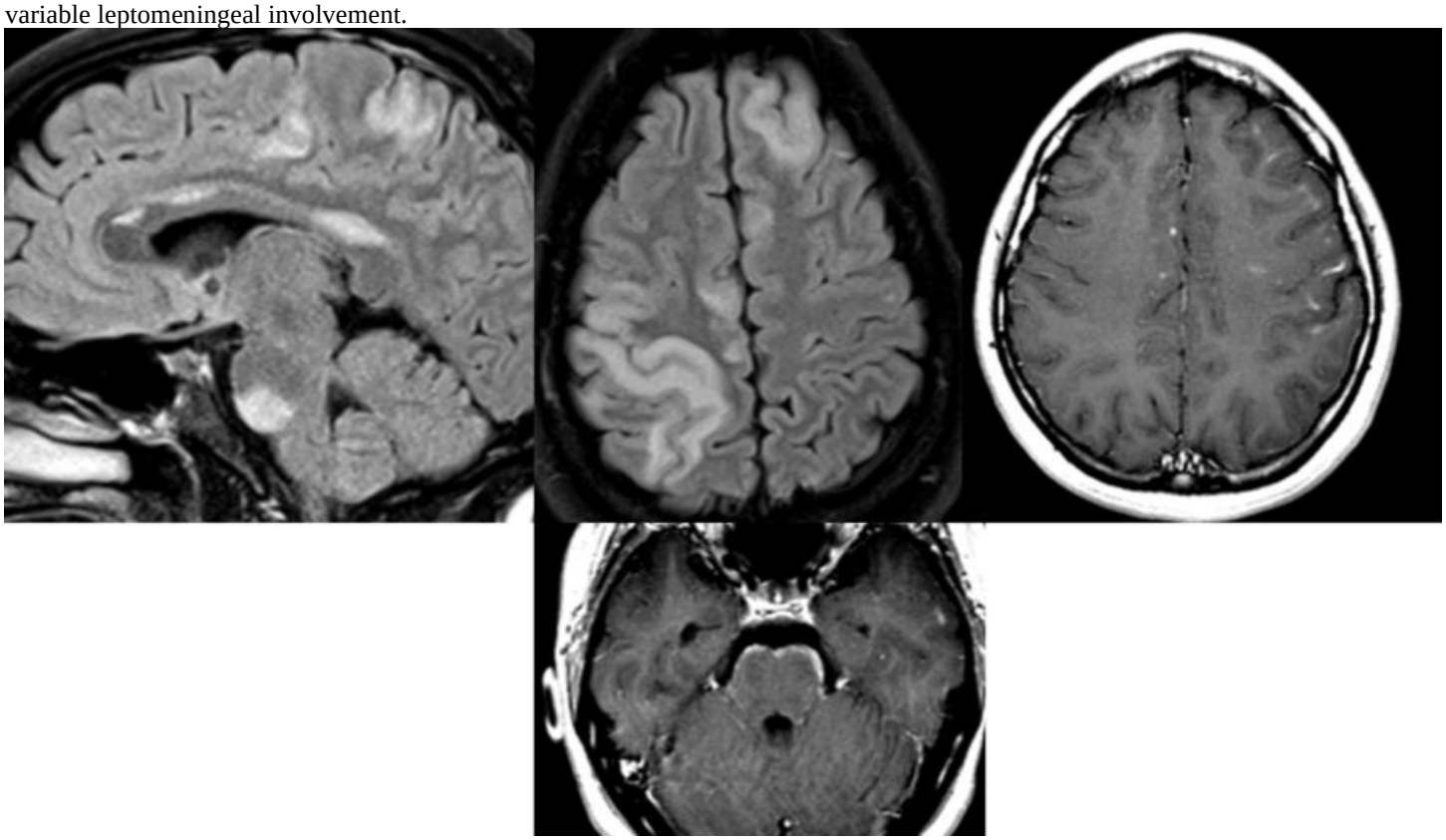

(Filename: TCT_1428_MOGADabstractimages.jpg)

935

Neurocristopathies: Embryology, Pathophysiology, and Imaging Manifestations in the Head and Neck

E Zamora[1], C Zamora[2]

[1]Montefiore Medical Center, Bronx, NY, [2]UNC Department of Radiology, Chapel Hill, NC

Purpose

This presentation will include a collection of cases illustrating neurocristopathies in the head and neck. NCC embryogenesis is a complex process necessary for specialized tissue formation in multiple systems. Dysgenetic malformations or neoplasms can result from congenital or sporadic mutations in specific genes. Understanding the underlying pathophysiologic mechanisms is essential for imaging interpretation.

Materials and Methods

Familiarize the reader with neural crest cell (NCC) embryology and underlying pathophysiologic mechanisms leading to dysgenetic and neoplastic neurocristopathies (NCPs) as well as their imaging manifestations in the head and neck.

Results

This image-rich educational exhibit will include a collection of illustrations and cases from two academic institutions. Cases will be categorized into dysgenetic, neoplastic, and combined NCPs, and subcategorized by NCC lineages involved.

Conclusions

NCCs arise from the dorsal neural tube and differentiate into specialized cells in multiple systems(1). NCPs result from mutations leading to dysgenesis and abnormal migration or differentiation of NCCs(2). Clinical manifestations vary widely based on the NCC lineages involved (e.g., cranial, vagal). Mutations affecting cranial NCCs (i.e. pharyngeal clefts, arches, and pouches), such as Goldenhar and Treacher Collins Syndromes, can lead to prototypic facial dysostoses (e.g., hemifacial microsomia) or skull base abnormalities (e.g., stenosis/atresia of external auditory canals), among other manifestations(3,4). TBX1 and CHD7 gene mutations (e.g., 22q11.2, CHARGE Syndromes) can alter migration of NCCs of cranial/vagal origin and thus affect multiple organ systems. CHD7 mutations, for example, are associated with inner ear anomalies (e.g., vestibular/cochlear dysplasia, hypoplasia of CNVIII) leading to sensorineural hearing loss. Neurocutaneous melanosis can involve all NCC lineages and lead to leptomeningeal melanocytic deposition and increased risk for melanoma. Brain MRI can be used for screening of melanocytic cell infiltration in perivascular spaces(5). Lastly, NCC-related malignancies can result from sporadic or congenital/familial mutations (e.g., VHL, SDHx, RET) including melanoma, neuroblastoma, or paragangliomas. In conclusion, sporadic or congenital mutations in crucial genes can lead to malformations and neoplasms based on NCC lineage involvement. Understanding the underlying pathophysiologic mechanisms is essential for imaging interpretation.

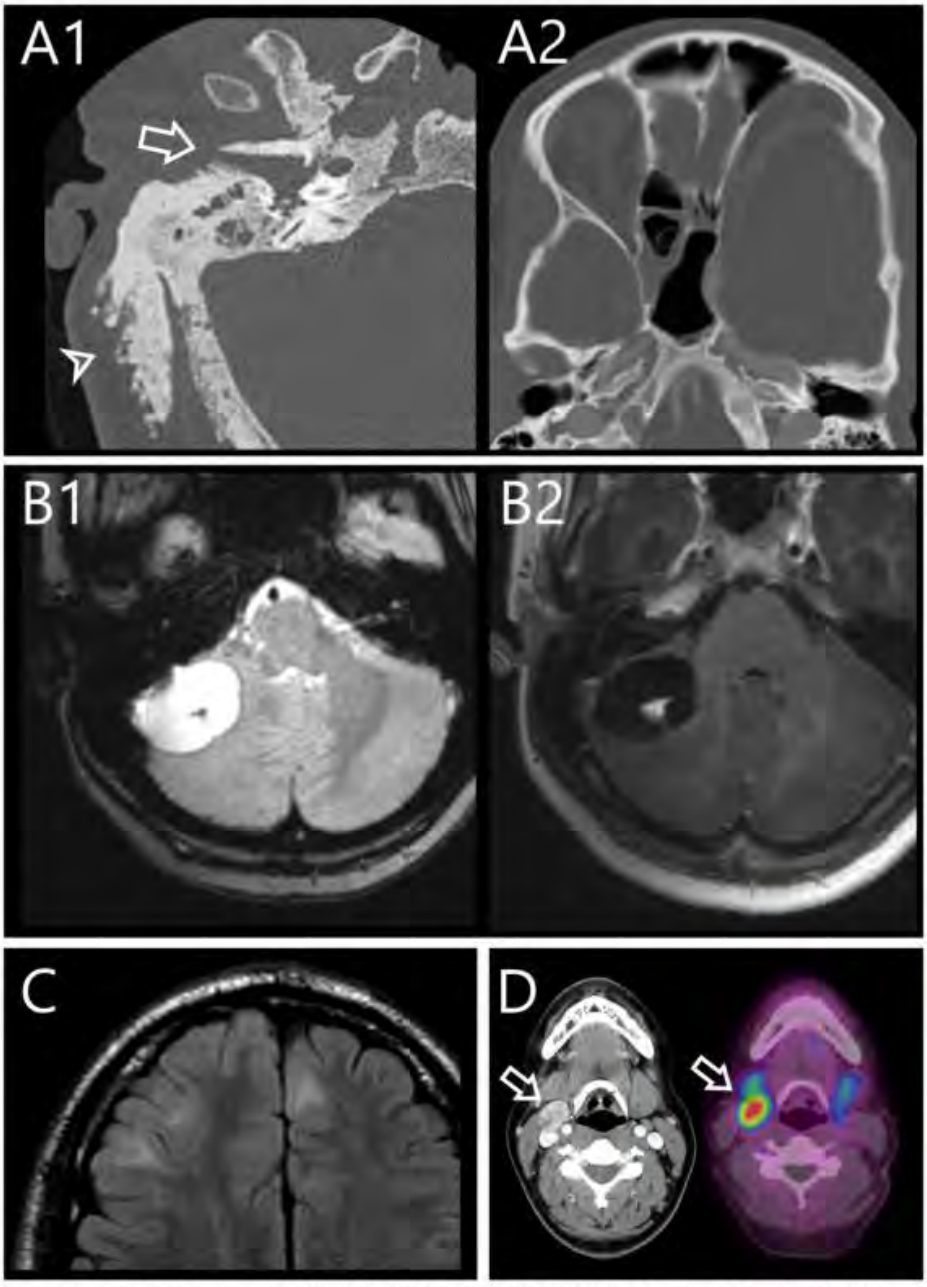

Legends: Images of select neurocristopathies affecting the head and neck. (A1) Axial CT images show stenosis of the right external auditory canal (arrow) and a large right mastoid exostosis (arrowhead) in a patient with Gorlin Syndrome. (A2) Axial CT showing left sphenoid wing dysplasia in a patient with neurofibromatosis type 1 (5-10% incidence in NF1). (B1-B2) Axial brain MRI in patient with Von Hippel Lindau, showing a T2-hyperintense, partially cystic lesion in the right cerebellum with an avidly enhancing nodule consistent with a hemangioblastoma (B1). (C) Axial T2/FLAIR brain MRI showing cortical tubers as hyperintense lesions in a patient with tuberous sclerosis. (D) Axial CT and 68Ga-DOTATATE PET/CT, respectively, showing an intensely avid heterogeneous right carotid space mass consistent with glomus tumor.

(Filename: TCT_935_Neurocristopathiesfinalimage.jpg)

1368

Neurodegenerative Disorders with a Focus on the Spectrum of Movement Disorders: Correlation between Anatomical Findings, Common Imaging Characteristics, and Clinical Presentations with an Introduction to Future Imaging Applications.

N Freedman[1], X Wu[2], B Weinberg[1], S Miocinovic[1], P Testini[1]
[1]Emory University, Atlanta, GA, [2]EMORY UNIV SCHOOL OF MEDICINE, ATLANTA, GA

Purpose

Movement disorders are within the spectrum of neurodegenerative disorders. In addition to the wide variety of imaging findings that can be seen across the spectrum of movement disorders, are the vast differences amongst the clinical findings with how these patients present to their clinicians. The objectives of this educational exhibit are the following: • To review common and uncommon movement disorder imaging features on MRI, with other modalities such as nuclear medicine imaging, including DAT scan and

FDG/PET, where appropriate. • To review the important anatomical structures affected in each of these diagnoses that one should be aware of when reviewing imaging for these patients and planning for surgical intervention, such as for DBS implantation. • To introduce the clinical presentations of actual patients with various movement disorders and include pictures and videos where appropriate. • To create an algorithm to understand the progression of how various movement disorders are diagnosed and when imaging is commonly indicated. • To provide a brief introduction to the future of imaging in movement disorders and possibly developing standardized institution based specific protocols with additional sequences for evaluation of certain suspected disorders.
Materials and Methods
The purpose of this educational exhibit is to provide a review of the important anatomy involved in movement disorders, evaluate the imaging characteristics of these findings and how they change over time, and correlate the imaging characteristics with the clinical presentation of patients diagnosed with these disorders.
Results
A review of radiological signs and findings for movement disorders will be performed to include but not limited to: Parkinson disease, progressive supranuclear palsy, multiple system atrophy, amyotrophic lateral sclerosis, Huntington's disease, various ataxias, variant Creutzfeldt-Jakob disease, Lance Adams syndrome, corticobasal degeneration, neurodegeneration with brain iron accumulation, and Wilson's disease. Various radiologic and patient specific images and videos of a variety of patients with movement disorders at our institution will be featured.
Conclusions
Imaging performed for the evaluation of movement disorders is not always revealing, but sometimes, we as radiologists, are not aware of what findings are important to comment on in our reports for the neurologist or surgeon. A foundation for seeing patient presentations would be beneficial in order to improve our reports and understanding.

955

Neuroimaging Characteristics of Gliosarcoma

P BAISHYA[1], M Bhat[2], K Kulanthaivelu[3]
[1]NATIONAL INSTITUTE OF MENTAL HEALTH AND NEUROSCIENCES (NIMHANS), BENGALURU, KARNATAKA, [2]National Institute of Mental Health and Neurosciences, Bangalore, Karnataka, [3]National Instituite of Mental Health and Neurosciences, Bangalore, Karnataka

Purpose
Gliosarcoma (GSM) and Glioblastoma (GBM) has similar epidemiology and natural history with much overlap of their clinical and radiological features (1). Compared to GBM, GSM's have worse prognosis (2). Multi-parametric MRI may help to identify imaging characteristics of Gliosarcoma.
Materials and Methods
We aim to analyze MRI imaging findings of GSM and to identify its distinct imaging characteristics which may help in its differentiation from Glioblastoma.
Results
Retrospective analysis of 17 cases of histopathologically proven cases of Gliosarcoma were included in this study. MRI imaging characteristics of GSM were evaluated by a Neuroradiology fellow for T1, T2 signals, diffusion and perfusion characteristics, presence of hemorrhage, pattern of enhancement and presence of dural / pial involvement and extracranial extension. Immunohistochemical characteristics of these tumors were reviewed for IDH mutation.
Conclusions
A total of 17 histopathologically proven cases of Gliosarcoma were included in this study, out of which 16 were denovo Gliosarcoma and 1 was secondary Gliosarcoma. 7 men and 10 women with a mean age of 59 years (range 27–74) defined the case cohort. Temporal lobe (n=10) involvement was most frequent followed by frontal lobe. All these lesions measured more than 4 cm and dural contact/ invasion was present in all the cases, however none of the tumors showed extra-cranial extension. Dural invasion was also found in these cases on histopathological examination of the resected tumors. Hemorrhagic areas constituting more than 50% of the lesion on SWI was seen in all the cases. All these lesions showed diffusion restriction of the solid components and irregular peripheral enhancement suggesting necrotic core of the lesion. Dynamic Susceptibility contrast (DSC) perfusion was done in 10 cases and increased perfusion was seen in the solid components of all these cases. Magnetic Resonance Spectroscopy (MRS) was done in 5 cases. In all these cases, NAA was reduced with increased choline, lipid lactate was increased in 3 cases. Immunohistochemistry (IHC) for IDH mutation was done in 13 cases and IDH was negative in all of them. Conclusions Dural invasion and significant hemorrhage can be considered as a imaging feature characteristic of Gliosarcoma. Imaging features of a peripherally based large lesion showing significant hemorrhage and dural involvement may be helpful in differentiating it from other tumors, particularly GBM.

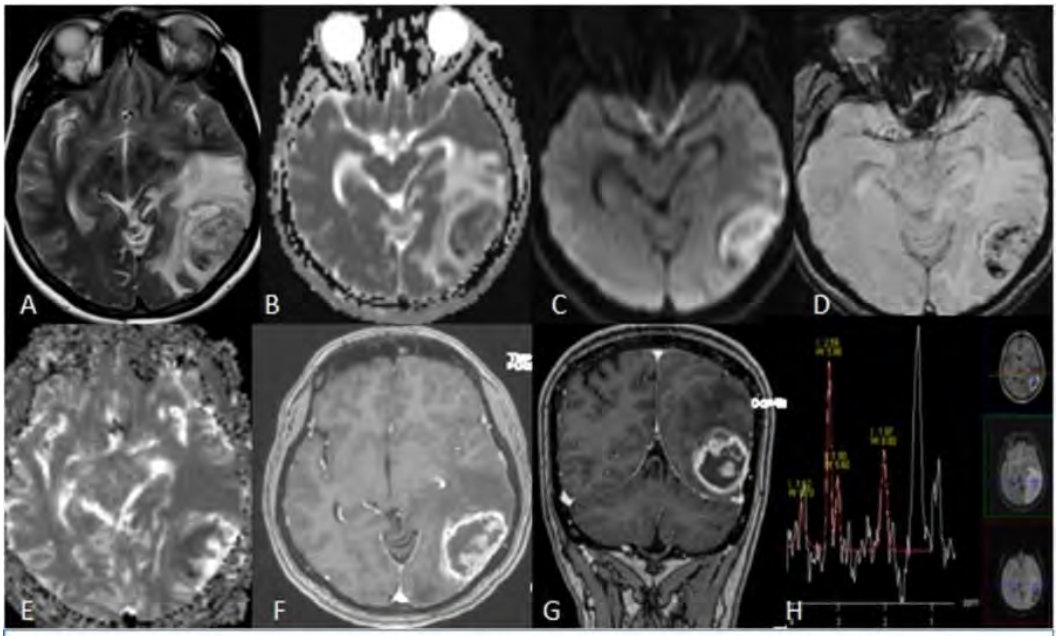

Figure showing the imaging features of Gliosarcoma. T2 hypointense (A) mass lesion in left temporoparietal lobe with diffusion restriction (B,C), SWI (D) signal loss with increased perfusion on CBV maps (E), peripheral contrast enhancement (F,G) and large lipid lactate peak on MRS (H)

(Filename: TCT_955_gliosmri300.jpg)

1033

Neuroimaging in an imaging platform in the autopsy room: CT, 7T MRI and pathological correlation.

G Bandeira[1], I Alves[2], V Paes[3], P Saldiva[3], L Lucato[1], C Leite[1], M MARTIN[1]

[1]Instituto de Radiologia, Hospital das Clínicas da Faculdade de Medicina da Universidade de São Paulo, Sao Paulo, SP, [2]Hospital Sírio-Libanês, Sao Paulo, SP, [3]Hospital das Clínicas da Faculdade de Medicina da Universidade de São Paulo, Sao Paulo, SP

Purpose

Introduction The ex vivo human brain MRI protocols for post-mortem imaging Correlation between post-mortem brain MRI and neuropathological finding Particularities of post-mortem 7 Tesla brain MRI Illustrative cases of post-mortem 7 Tesla brain MRI with neuropathological correlation Take-home messages Conclusion References The purpose of this exhibition is to review the imaging findings of the ex vivo human brain with neuropathological correlation.

Materials and Methods

The purpose of this exhibit is: To illustrate the role of neuroimaging in the autopsy room. To review the particularities of post mortem neuroimaging. To illustrate cases of post-mortem 7 Tesla brain MRI with neuropathological correlation.

Results

For this educational exhibit we selected educational cases from the teaching files of our institution.

Conclusions

Post mortem magnetic resonance imaging (MRI) studies on the human brain are of great interest to facilitate the connection between functional and anatomical information available from MRI in vivo and neuroanatomical knowledge available from histology/immunocytochemistry. However, post mortem brain tissue does not have the same physical properties as in vivo tissue, and therefore MRI approaches need to be adjusted accordingly Typical post-mortem brain findings and challenges include: different T1, T2 and ADC due to a combination of factors like lower temperature and decomposition (that can be affected by post-mortem interval, ambient etc); loss of grey–white matter differentiation mainly on CT, but with some blurring on MRI, due to fluid shift and cerebral autolysis; drastically different susceptibility-weighted image due to a darker vessel signal mainly related to blood stasis (which is even more exacerbated in 7T imaging); gas appearing linked to putrefaction; no intravenous contrast administration (although post-mortem angiography might be done in wich case brain enhancement might be normally expected); hyperdensity (or clot signal on MRI) of the dural venous sinuses, sometimes in a dependent position; increase in brain volume and loss of definition of sulci, that may be due to a combination of vasogenic and cytotoxic edema, and may be more pronounced in death with prolonged duration of the agonal state, leading to a longer hypoxic state, than in acute death; and in more advanced deterioration "softening" of brain tissue and settling of the tissue against the dependent part of the skull.

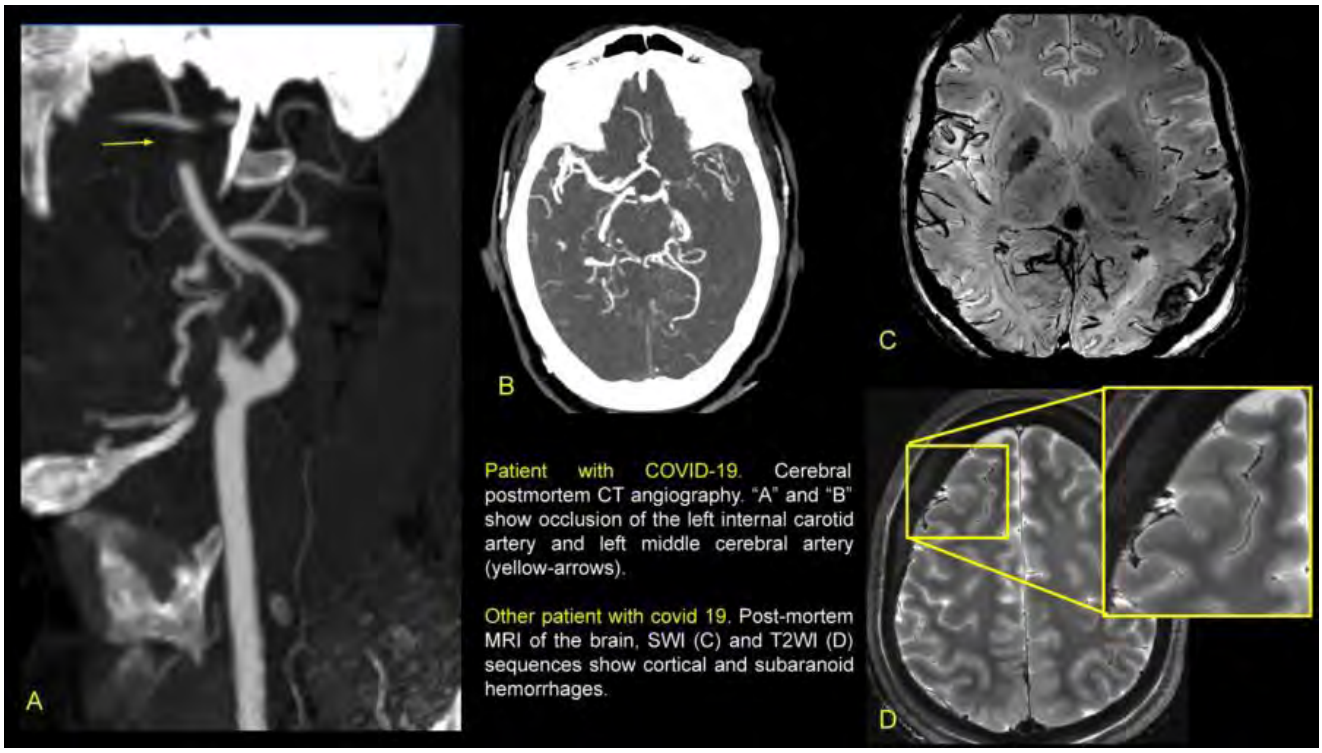

(Filename: TCT_1033_pisa.jpg)

988

Neuroimaging in Oncologic Emergencies: What Radiologists Need to Know and Oncologists Want to Know

P Rabiei[1], J Choi[2], J McCarty[1], S Calle[2], K Learned[2]

[1]The University of Texas Health Science Center at Houston, Houston, TX, [2]The University of Texas MD Anderson Cancer Center, Houston, TX

Purpose

To increase awareness of the imaging features of the oncologic related acute CNS involvement

Materials and Methods

Neuro-oncologic emergencies are potentially morbid or life-threatening events that could be related to the underlying disease or complications of therapy. It is critical for radiologists to recognize the alarming imaging features of emergent conditions in cancer patients to help appropriate management. In this exhibit, we present educational and interesting cases of neuro-oncologic emergencies and we highlight the keywords in recognition of these pathologies

Results

Several CT and MR images are collected on the cancer patients who presented to our health institution with oncologic related emergent conditions. The cases include postoperative complications, osteonecrosis, laryngeal chondronecrosis, carotid blowout syndrome, infection in immunocompromised oncologic patients, cord compression, and stroke in oncologic patients. Critical imaging findings of each image are annotated and described. Keywords in prompt and accurate interpretation of imaging features in neuro oncologic emergencies are provided. Radiological features to distinguish the tumor from treatment complications are explored. Figure (1) demonstrates a few examples of our cases, while the entire collection will be presented in the final exhibit. Image (A) shows lytic cortical destruction (arrows) with sequestration (*) of the clivus and left petrous apex consistent with osteonecrosis in a patient with a history of recurrent nasopharyngeal carcinoma, treated with chemoradiation therapy. The irregular caliber of the left petrous ICA (circle) raised the concern for pseudoaneurysm which was confirmed with digital subtraction angiography on the image (B). The image (C) demonstrates acute invasive fungal sinusitis in an immunosuppressed lymphoma patient as depicted by non-enhancing "black turbinate sign" of the right sinus (*), orbital edema, proptosis, with fungal invasion into the cavernous sinus (arrow). Image (D) shows layering debris in the enlarged ventricles (*) and abnormal FLAIR signals (arrows) on postoperative axial brain MR image of a patient with clival chordoma, indicative of meningitis, ventriculitis, and obstructive hydrocephalus.

Conclusions

It is imperative for radiologists to be aware of imaging features of neuro-oncology emergencies and possible complications of chemoradiation therapy to identify the acute findings, provide relevant differential diagnoses, and help clinicians to timely manage complex cases.

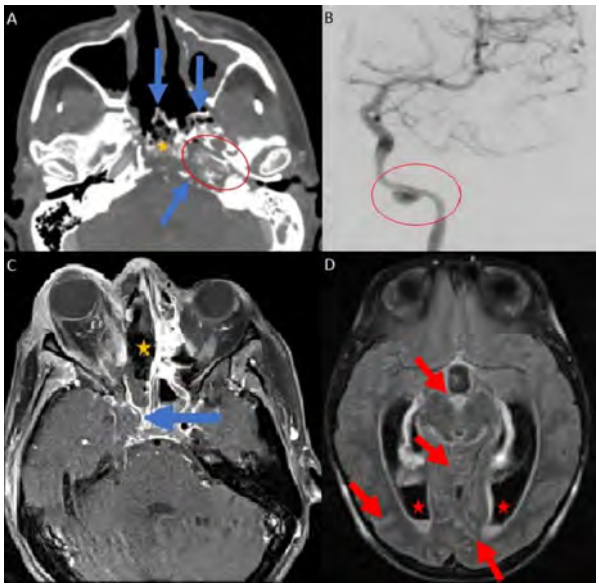

(Filename: TCT_988_Figure1.jpg)

741

Neuroimaging in Pregnancy and the Postpartum Period

A Spiro[1], A Weyer[2]

[1]University of Pittsburgh Medical Center, Pittsburgh, PA, [2]University of Pittsburgh, Pittsburgh, PA

Purpose

• Review imaging safety and recommendations regarding the use of CT, MRI, iodinated contrast, and gadolinium-based contrast agents during pregnancy • Demonstrate imaging findings of vascular pathologies during pregnancy including cortical and dural venous thrombosis, stroke, preeclampsia/eclampsia – posterior reversible encephalopathy syndrome, aneurysm growth, and postpartum cerebral angiopathy • Illustrate imaging findings of intra-axial and extra-axial tumor growth during pregnancy and Wernicke encephalopathy secondary to hyperemesis gravidarum • Discuss and present physiologic and pathologic imaging appearances of the pituitary gland during pregnancy and the postpartum period including physiologic hypertrophy, adenoma growth, apoplexy, and Sheehan's syndrome

Materials and Methods

Multiple physiologic changes during pregnancy and the post-partum period can cause an exacerbation of preexisting neurologic conditions or the onset of new neurological disorders. Neurological disorders during this time period can manifest with changes to the intracranial arterial and venous vasculature, brain parenchyma, preexisting tumors, and pituitary gland. Imaging is often critical in differentiating acute disorders requiring immediate intervention from benign or less urgent conditions. We present a review of neuroimaging in pregnancy and the postpartum period with illustrations of both common and rare conditions and a discussion of imaging safety.

Results

N/A

Conclusions

A range of benign and pathologic neurologic conditions may be associated with pregnancy and the postpartum state. Familiarity with the imaging manifestations of these conditions will allow the radiologist to recommend the appropriate imaging modality and make the correct diagnosis to improve the outcome of the mother and fetus.

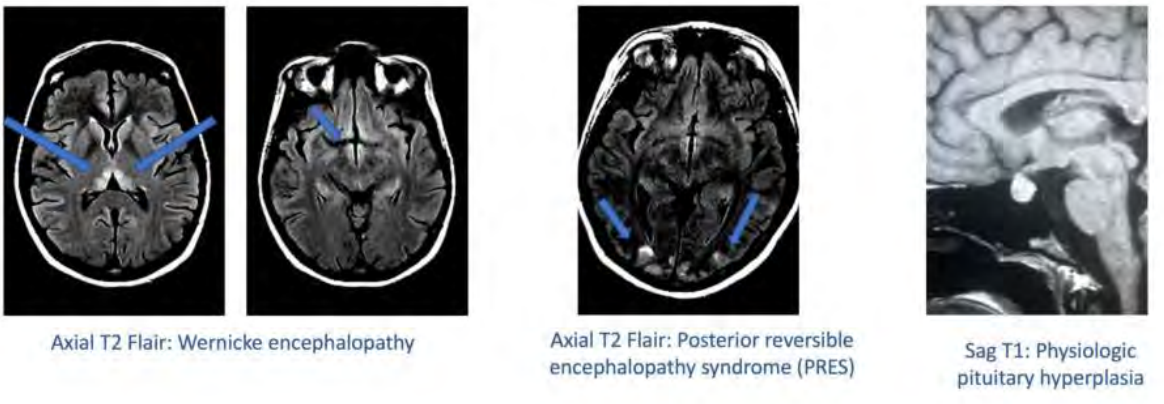

(Filename: TCT_741_ImagesFinal.jpg)

1174

Neuroimaging of Pediatric Epilepsy - A Step-by-step Guide to Multimodality Approach

I Shaikh[1], G Singh[2], K Brock[2], J Matthews[2], A Vaysberg[2], T Bahramipour[2]

[1]Rutgers New Jersey Medical School, Newark, NJ, [2]Newark Beth Israel Medical Center, Newark, NJ

Purpose

Objectives: 1. Patients presenting with new-onset seizure frequently undergo imaging in order to rule out acute conditions (e.g., stroke), anatomic abnormalities, and malignancy [1]. Anatomic abnormalities may include scar tissue from prior brain insults, benign space-occupying lesions, and developmental defects, which may be associated with genetic syndromes. High-resolution MRI is the preferred modality in delineating such defects. 2. When no substantive lesion is identified on MRI, careful evaluation using a variety of post-processing techniques may be indicated to identify potential subtle abnormalities. Further evaluation with PET may identify an epileptic focus or allow for further analysis via intracranial electroencephalography (EEG) [2]. 3. Malformations of cortical development (MCDs) result in abnormal neuronal migration and are frequently associated with epilepsy [3]. These include polymicrogyria, lissencephaly, and schizencephaly (Figure 1A). 4. Neurocutaneous disorders are frequently associated with epilepsy. Seizures are especially commonly seen in tuberous sclerosis (TSC), Sturge-Weber syndrome (SWS), and neurofibromatosis type 1 (NF1) [2]. MCDs and intracranial tumors are common causes of seizure activity in SWS and NF1, respectively. In TSC, benign hamartomatous lesions known as tubers, commonly serve as epileptogenic foci (Figure 1B). Summary: Brain imaging in seizure patients is crucial for detecting anatomic abnormalities and surgical planning. MRI plays an important role in structural brain imaging and can be combined with PET for better delineation of seizure foci. Imaging may provide clues for diagnosis of MCDs or neurocutaneous syndromes.

Materials and Methods

Epilepsy is a severely debilitating disorder characterized by abnormal brain activity and recurrent unprovoked seizures. Along with EEG, imaging plays a pivotal role in diagnosis and management of epilepsy. In addition to identifying potentially epileptogenic foci, imaging allows for surgical planning in patients that fail medical management or have symptoms related to mass effect. Characteristic imaging findings also play a vital role in the diagnosis of various genetic syndromes.

Results

We examined recent MRI studies at our institution for patients with seizure disorder. We highlighted notable intracranial anatomic abnormalities that were likely to be associated with clinical presentation.

Conclusions

N/A

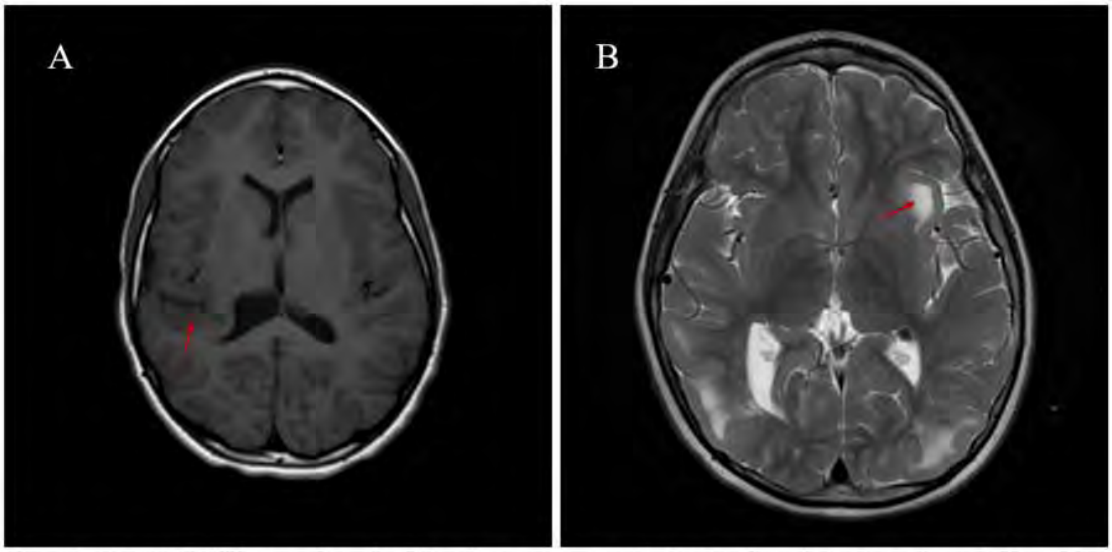

Figure 1: (A) on axial T1 MRI, a tract of irregular, thickened gray matter is seen extending from the cortical surface to the occipital horn of the right lateral ventricle (arrow) with dimpling on the surface of the right lateral ventricle consistent with closed lip type schizencephaly; (B) on axial T2 MRI of a pediatric patient with tuberous sclerosis, a hyperintense cortical tuber is seen in the left perisylvian cortex (arrow).

(Filename: TCT_1174_Epi.jpg)

1375

Neuroimaging of Pediatric Glial Tumors: Updates from 2021 WHO CNS Tumor Classification

O Simsek[1], A Bhatia[2], S Sotardi[2], A Vossough[2], E Schwartz[2]

[1]Dr. Abdurrahman Yurtaslan Ankara Oncology Training and Research Hospital, Ankara, Turkey, [2]Children's Hospital of Philadelphia, Philadelphia, PA

Purpose

Neuroimaging of Pediatric Glial Tumors: Updates from 2021 WHO CNS Tumor Classification Educational Objectives The purpose of the exhibit is to: • Review the updated 2021 WHO classification for pediatric glial tumors. • Describe the imaging features of new glial

tumor types and subtypes with imaging examples. • Develop a practical approach to the diagnosis of pediatric glial tumors based on the 2021 WHO Classification of CNS tumors with interactive flowcharts. Summary The term "glial tumor" encompasses a large, heterogeneous group of tumors originating from glial cells, which demonstrate different neuropathologic and radiological features (1). While early classifications of glial tumors were based on histological features, the integration of molecular and genetic markers into classification models have dramatically improved our understanding and ability to treat Central Nervous System (CNS) tumors (2). The 2021 update of the World Health Organization Classification of CNS Tumors demonstrates the continued evolution of tumor classification, with several important changes, including new and altered naming of tumors and their subtypes. For example, pediatric and adult tumors have been differentiated for the first time (3). Furthermore, ependymomas are now primarily divided into three types according to their localization. Given these significant differences in WHO terminology and grading changes, an update to the neuroradiology community is critical to ensure current and standardized practices. This educational exhibit will assist neuroradiologists in understanding the 2021 WHO classification. In this exhibit, we present interactive flowcharts emphasizing key features to facilitate understanding of the changes to glial tumor nomenclature.
Materials and Methods
N/A
Results
N/A
Conclusions
N/A

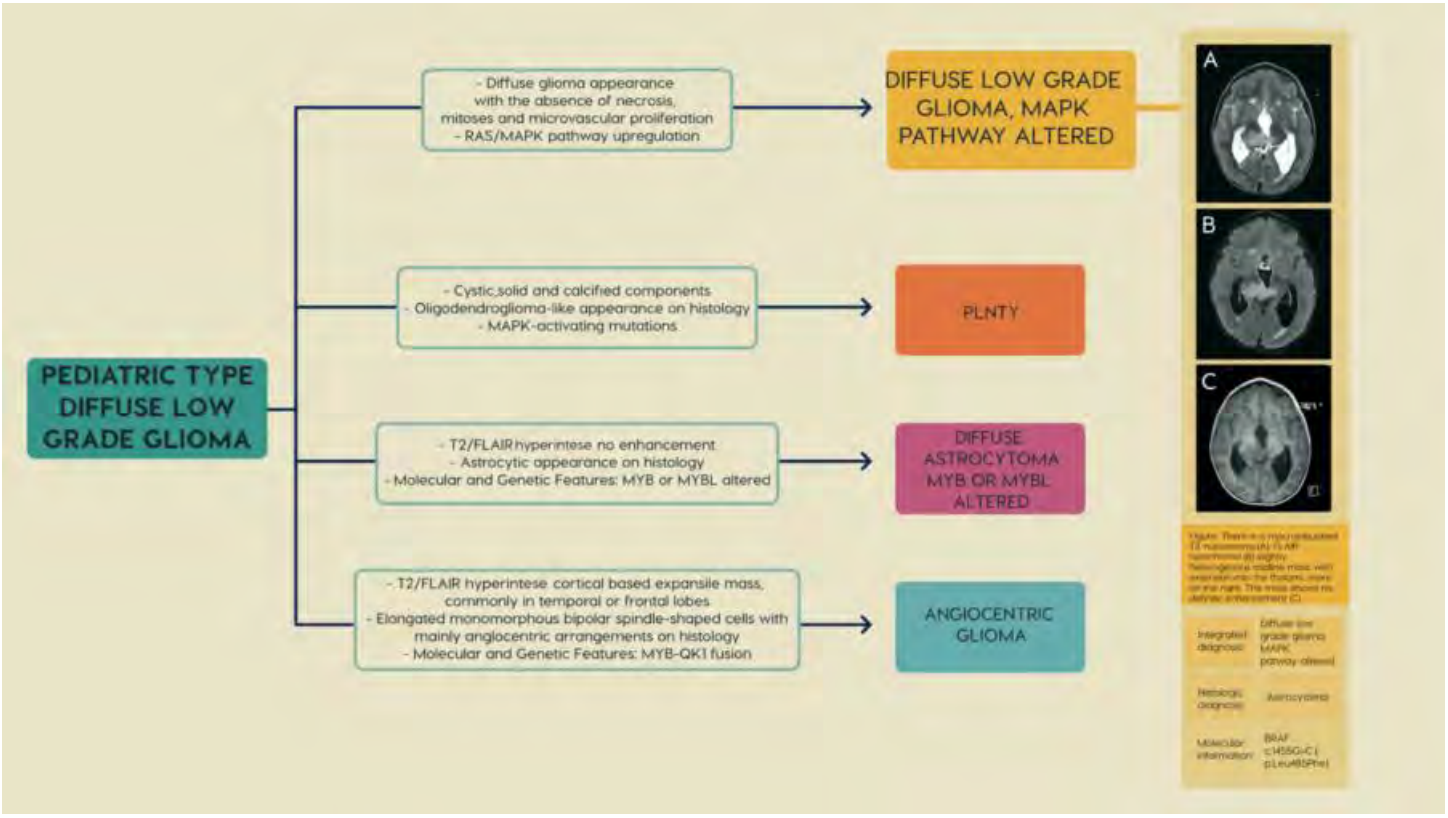

(Filename: TCT_1375_WHO2021.jpg)

1259
Neuroimaging of Pediatric Glioneuronal and Neuronal Tumors, with Updates from 2021 WHO CNS Tumor Classification
O Simsek[1], A Bhatia[2], S Sotardi[2], E Schwartz[2], A Vossough[2]
[1]Dr. Abdurrahman Yurtaslan Ankara Oncology Training and Research Hospital, Ankara, Turkey, [2]Children's Hospital of Philadelphia, Philadelphia, PA

Purpose
Educational Objectives: The purpose of the exhibit is to: • Discuss WHO 2021 CNS tumor classification of glioneuronal and neuronal tumors with interactive flowcharts • Review pediatric glioneuronal and neuronal tumors with case examples enriched with illustrations • Emphasize pearls in imaging of glioneuronal and neuronal tumors Summary: Glioneuronal and neuronal CNS tumors are relatively more common in the pediatric than the adult population and generally portend a good prognosis. Although seizures are the most common clinical presentation of tumors in this group, clinical and imaging features can vary. Glioneuronal and neuronal tumors should be considered in the differential diagnosis of patients presenting with a brain tumor, especially in children and young adults (1,2). Significant changes in the WHO 2021 CNS tumor classification have resulted in the addition of three new tumors, including one provisional tumor entity (3). This exhibit will review imaging and salient clinical findings characteristic of glioneuronal and neuronal

tumor diagnoses. These teaching points will be highlighted with multiple imaging examples and educational illustrations in the light of recent changes in literature.
Materials and Methods
N/A
Results
N/A
Conclusions
N/A

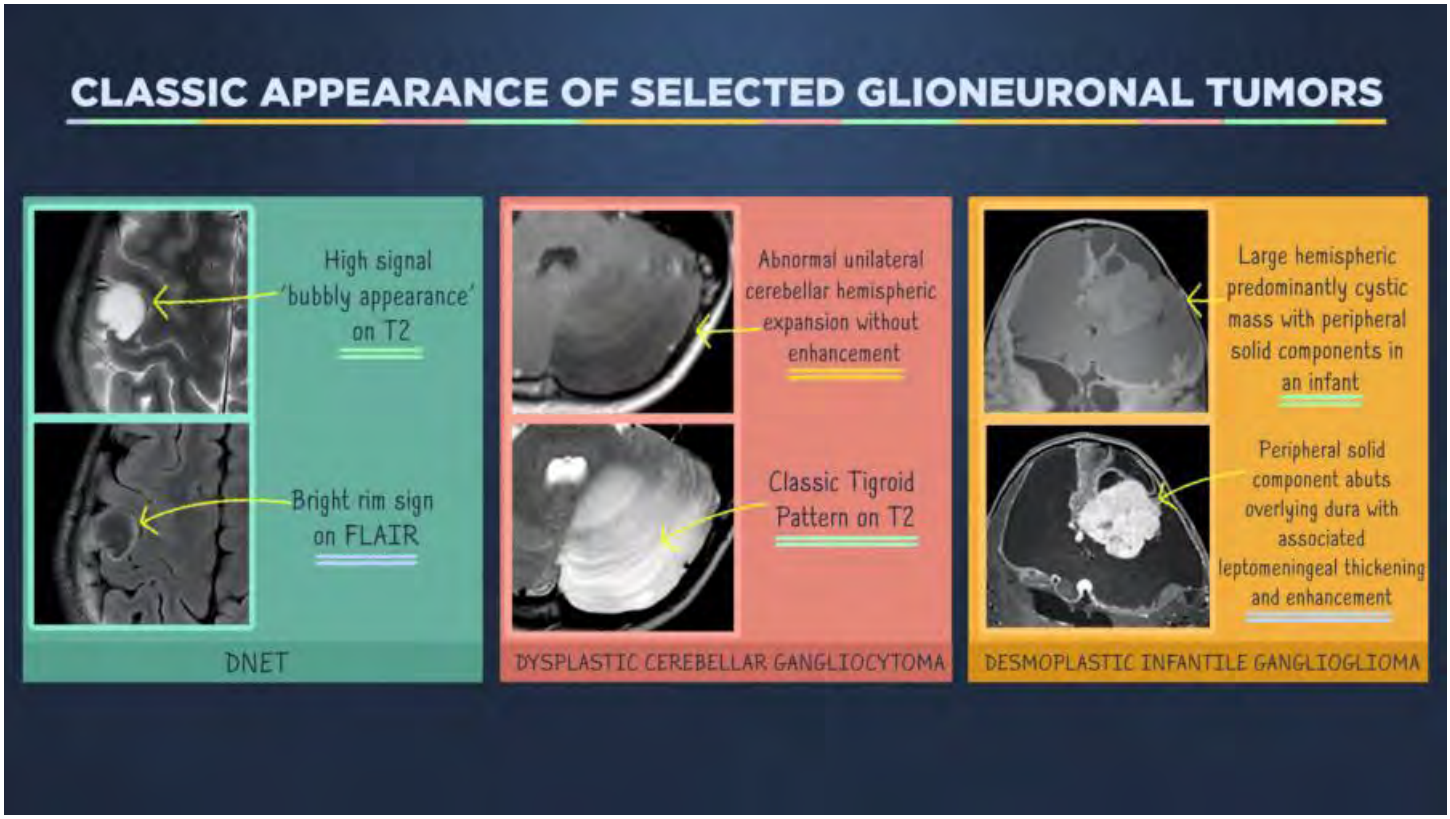

(Filename: TCT_1259_Glioneuronal-image.jpg)

269
Neuroimaging of Pediatric Histiocytic Disorders
K Patel[1], M RYAN[2], N Wadhwani[3], A Jaju[2]
[1]Department of Neuroradiology, Northwestern University Feinberg School of Medicine, Chicago, IL, [2]Department of Medical Imaging, Ann and Robert H Lurie Children's Hospital of Chicago, Chicago, IL, [3]Department of Pathology, Ann and Robert H Lurie Children's Hospital of Chicago, Chicago, IL

Purpose
Histiocytic disorders in the pediatric population encompass a large group of multisystem diseases with variable CNS involvement, arising from an overproduction of WBC, specifically histiocytes, resulting in organ injury and neoplastic evolution. These can have a range of manifestations, and are subclassified according to the type of histiocyte: dendritic cell, macrophage-related, and malignant histiocytic disorders. Langerhans cell histiocytosis, a dendritic cell disorder, is the commonest and best described entity, however the neuroimaging descriptions of the less common entities are sparse. The aim of this exhibit is to provide a comprehensive review of the spectrum of imaging findings in the brain, head and neck, and spine in patients with histiocytic disorders, along with correlating histopathological slides, clinical context, and prognostic information. Below is a brief discussion of major entities that will be discussed with illustrative imaging: Langerhans cell histiocytosis (LCH) most commonly involves the hypothalamic-pituitary axis, but can also involve the meninges, choroid plexus and pineal gland. Parenchymal involvement is usually in the form of neurodegeneration, predominantly in the basal ganglia and dentate nuclei, or less commonly leukoencephalopathy-like changes. Juvenile xanthogranuloma (JXG) typically affects infants and young children with a cutaneous presentation, and CNS involvement is rare, although can manifest as solitary or multiple extra-axial masses, cranial or spinal nerve root involvement, and rarely parenchymal changes. Hemophagocytic lymphohistiocytosis (HLH) can be primary or secondary and CNS involvement can precede systemic findings. Patterns of parenchymal involvement include multifocal supra- and infratentorial lesions, predominantly brainstem, or predominantly cerebellar involvement. Enhancement is seen in over 50% and calcifications are common. Rosai-Dorfman disease (RDD) also known as sinus histiocytosis with massive lymphadenopathy, commonly presents with painless cervical lymphadenopathy, but extranodal involvement can occur, particularly in the orbits and the nasal cavity. Intracranial and spinal disease

is rare, although can manifest as extra-axial masses mimicking meningiomas. ALK-positive histiocytosis: A recently described and rare systemic histiocytic proliferation of infancy. CNS involvement can be in the form of diffusion restricting and enhancing parenchymal masses.
Materials and Methods
N/A
Results
N/A
Conclusions
N/A

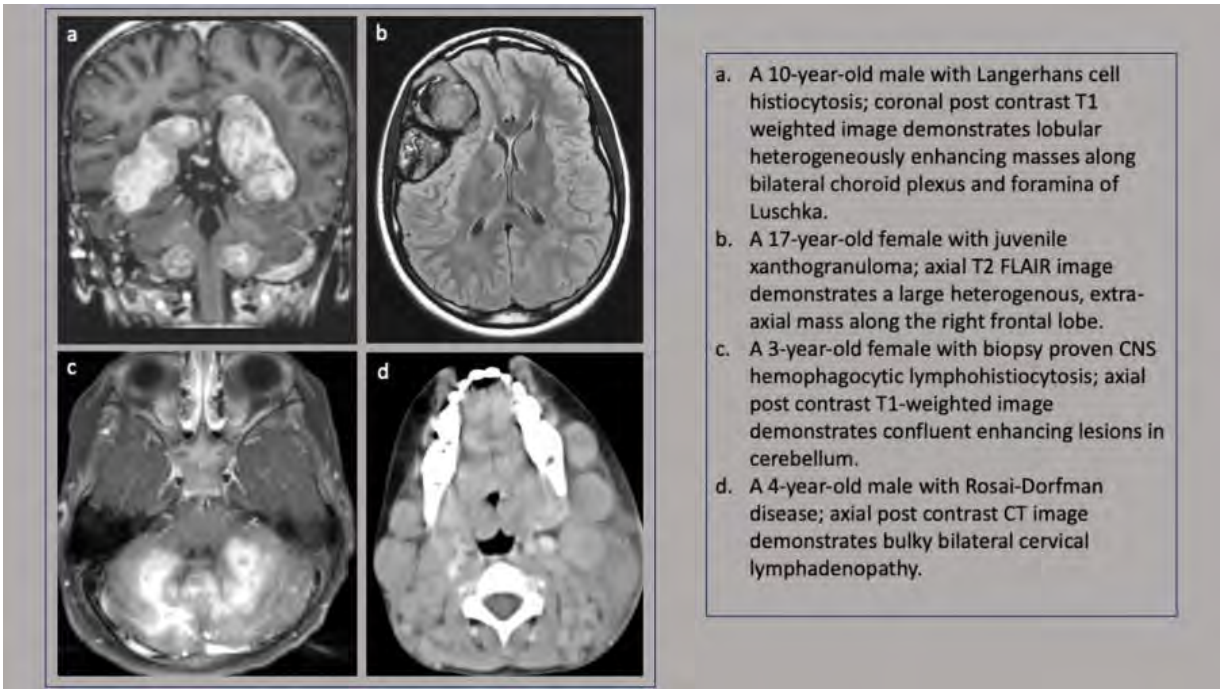

(Filename: TCT_269_PediatricHistiocytosis.jpg)

917

Neuroimaging of Primary Progressive Aphasia: An Educational Review

M Siao[1], M Roytman[2], G Chiang[2], S Pahlajani[3], M Aboian[4], A FRANCESCHI[5], J Ivanidze[2], M Salgado[6]
[1]Tri-Institutional MD-PhD Program, Weill Cornell Medicine, New York, NY, [2]Department of Radiology, Weill Cornell Medicine, New York, NY, [3]Department of Neurology, Weill Cornell Medicine, New York, NY, [4]Department of Radiology and Biomedical Imaging, Yale School of Medicine, New Haven, CT, [5]Department of Radiology, Donald and Barbara Zucker School of Medicine at Hofstra/Northwell Health, Manhasset, NY, [6]New York Presbyterian Brooklyn Methodist, Brooklyn, NY

Purpose
Primary progressive aphasia (PPA) is a clinical syndrome that is characterized by gradually worsening language impairment and categorized into three recognized variants, each with distinct presentations and specific imaging features. PPA continues to evolve as a disease entity, with description of the logopenic variant emerging in 2004 and establishment of current diagnostic consensus criteria in 2011 [1-4]. For a substantial fraction of patients, the presentation eludes classification according to clinical diagnostic criteria; furthermore, disease may progress to include other neurodegenerative syndromes [3-5]. Neuroimaging plays an essential role in the diagnosis of PPA and continues to shape understanding of this rare disease. This exhibit will review the classification of the variants of PPA, including clinical and pathological correlates, and will emphasize key findings on structural and molecular neuroimaging. Learning Objectives I. Introduction: Clinical presentation and epidemiology of PPA II. Diagnostic criteria of the three disease variants: nonfluent, or agrammatic, variant (nfvPPA); semantic variant (svPPA), and logopenic variant PPA (lvPPA) a. Clinical criteria; overview of presentations that do not neatly fit criteria or that include other neurodegenerative syndromes b. Imaging criteria; sensitivity and specificity c. Pathologic criteria III. Clinical cases: a pictorial review of features specific to each variant of PPA a. Typical left hemispheric findings on structural imaging and on [18F]-FDG PET imaging b. Analogous findings in right-sided disease c. Awareness of the utility of imaging with PET radiotracers related to underlying pathologic correlates, e.g. amyloid PET in lvPPA.
Materials and Methods
-
Results
We review the imaging findings of clinical cases representative of the three variants of PPA. Supplementary cases will accompany the exhibit for self-assessment of major educational goals.

Conclusions
This educational exhibit will provide fundamental knowledge of structural and molecular imaging findings specific to the diagnosis of each nfvPPA, svPPA, and lvPPA. It will also provide familiarity with clinical and pathologic correlates, as well as targeted PET imaging approaches based on underlying disease processes. Improving understanding of PPA variants and their radiological features is key to elucidating the neurologic substrate of language and neurodegeneration and to improving outcomes for those affected by this uncommon incompletely understood disease.

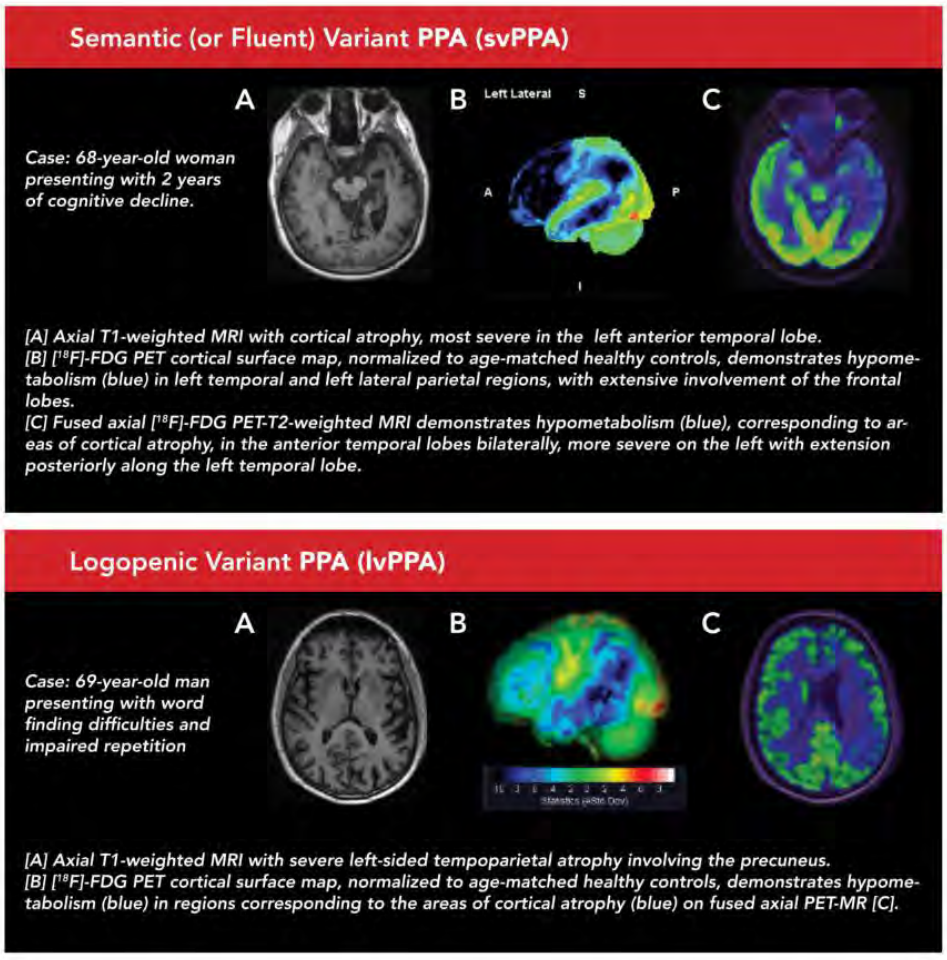

(Filename: TCT_917_asnr-1115b.jpg)

266
Neuroimaging of Synucleinopathies
S Kanekar[1], A Locke[2]
[1]Hershey Medical Center, Hershey, PA, [2]Penn State, Hershey, PA

Purpose
To discuss the neuroinflammation and imaging features of Synucleinopathies.
Materials and Methods
To discuss the imaging findings with clinical, CSF and neurogenetic correlates of synucleinopathies.
Results
We retrospectively studied 173 patients from our PACS system that had clinical and imaging findings correlating with synucleinopathies. All the patients underwent routine MRI of the brain. Twenty five percentage of the patient also had DATA scan. 110 patients also had CSF examination. All studies were read by two neuroradiologist. These findings were correlated with the clinical findings, biochemical and CSF analysis. 161 patients had a follows up MRI which were compared with prior scans for stability, progression or resolution of the abnormality.
Conclusions
For better understanding of synucleinopathies and for the purpose of this exhibit we classified them into: DBL (Lewy bodies); MSA-P (Glial cytoplasmic inclusions); PD (Substantia nigra, Lewi bodes); MSA-C (Glial cytoplasmic inclusions-cerebellum) and PAF (Lewy bodies – sympathetic ganglia). In this exhibit we give an algorithmic approach to imaging of synucleinopathies with diagnostic pearl to the specific diagnosis.

1045

Neuroimaging Spectrum of Compressive Non-Neoplastic Myelopathy

A Dearden[1], J Ghannam[1], A Wang[1], A Krishnan[1]
[1]William Beaumont Hospital, Royal Oak, MI

Purpose

Compressive non-neoplastic spinal cord lesions represent a broad spectrum of neurologic disease processes contributing to back pain and neuropathy, including traumatic, inflammatory/infectious, degenerative, and metastatic etiologies. Compressive cord lesions are optimally evaluated with high-field strength magnet MRI with and without contrast. Differential diagnoses for cord lesions are inherently broad due to the nonspecific nature of increased intramedullary signal on T2-weighted images seen with many cord pathologies. However, differentiating features such as degree of cord expansion, enhancement characteristics, and extramedullary findings can provide additional information to refine the differential diagnosis. In this exhibit, we present representative cases of compressive non-neoplastic spinal cord lesions from our institutional archive, outlined accordingly: traumatic (traumatic spondylolisthesis with cord contusion, epidural hematoma), infectious/inflammatory (epidural abscess), degenerative (disk herniation, spinal stenosis), and metastatic (osseous metastasis with cord compression). These cases will be presented according to our institutional protocol: sagittal T1, sagittal T2, sagittal STIR, axial T2*, axial T2, axial T1 without and with contrast, and diffusion weighted imaging. Each case will include brief literature review with discussion points. Objectives -Review common spinal cord lesions under the category of compressive, non-neoplastic. -Characterize compressive non-neoplastic cord lesions according to anatomic distribution, MRI signal characteristics, enhancement patterns, and relationship to symptom onset and clinical presentation.

Materials and Methods

N/A

Results

N/A

Conclusions

Disease processes relating to compressive non-neoplastic spinal cord lesions are numerous and often difficult to delineate from one another. A thorough knowledge of pathologies within this category, along with key imaging findings to differentiate these pathologies, can aid the radiologist in developing a practical and accurate differential diagnosis, ultimately leading to better patient outcomes.

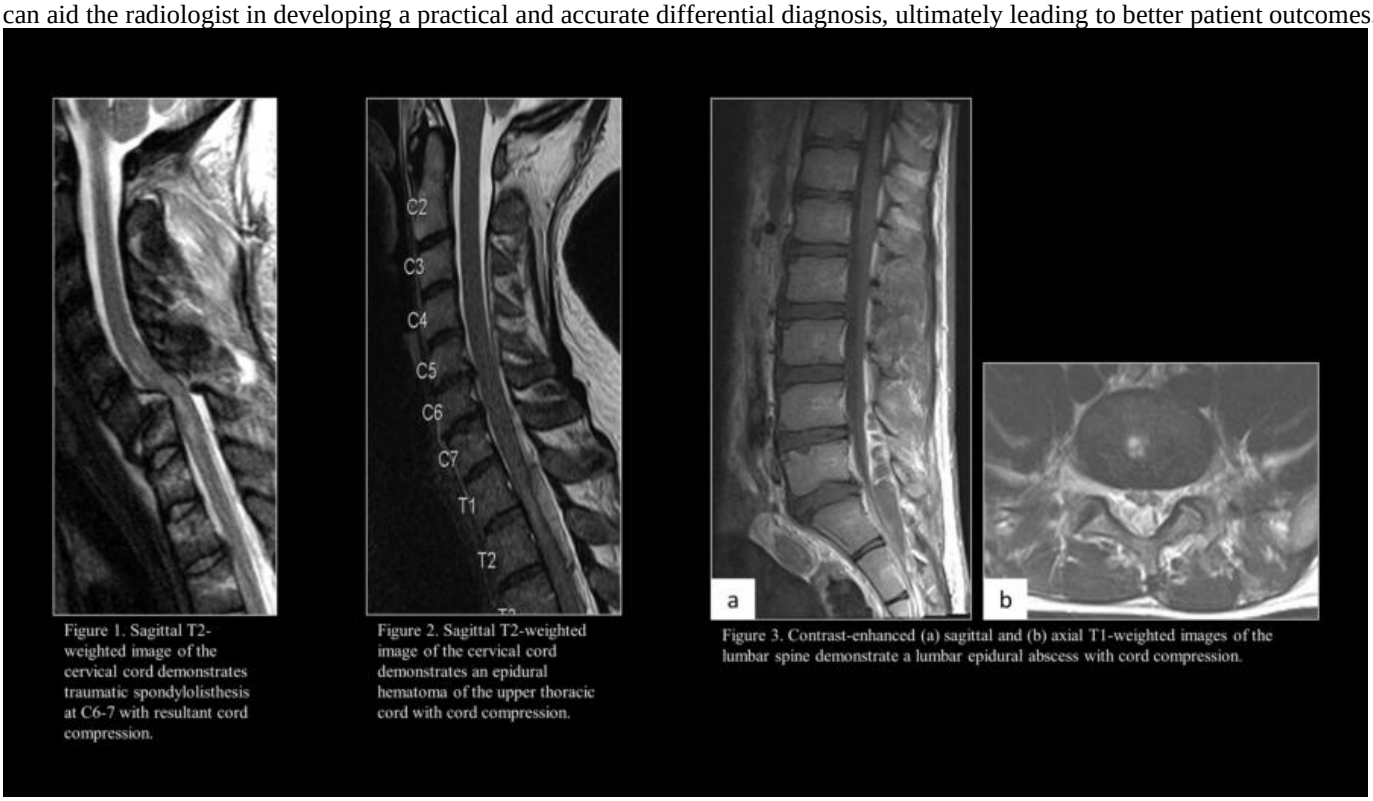

Figure 1. Sagittal T2-weighted image of the cervical cord demonstrates traumatic spondylolisthesis at C6-7 with resultant cord compression.

Figure 2. Sagittal T2-weighted image of the cervical cord demonstrates an epidural hematoma of the upper thoracic cord with cord compression.

Figure 3. Contrast-enhanced (a) sagittal and (b) axial T1-weighted images of the lumbar spine demonstrate a lumbar epidural abscess with cord compression.

(Filename: TCT_1045_compressiveMyelopathyFinal.jpg)

891

Neuroimaging Spectrum of Non-Compressive Non-Neoplastic Myelopathy

J Ghannam[1], A Dearden[1], R Joshi[1], A Wang[1], K Barry[2]
[1]William Beaumont Hospital, Royal Oak, MI, [2]Beaumont Health, Royal Oak, MI

Purpose

Non-compressive, non-neoplastic spinal cord lesions represent a broad range of disease processes and entities. Most commonly, spinal

cord lesions demonstrate T2 signal abnormality on magnetic resonance imaging, a relatively nonspecific finding requiring a variety of differentiating factors to build an accurate differential diagnosis (1). Additionally, many disease entities have significant overlapping features on MRI, rendering it difficult to separate diagnoses and guide management (2). The combination of signal characteristics on MRI, timing of clinical presentation, degree of cord expansion, and contrast enhancement patterns can provide improved differentiation between disease entities. The purpose of this exhibit is to educate the viewer on radiographic findings of non-compressive, non-neoplastic spinal cord lesions, including common and rare clinical and radiological presentations. Building an accurate and complete differential diagnosis can aid in guiding therapy and preventing additional unnecessary work-up.
Materials and Methods
1. To review common pathologies of non-compressive, non-neoplastic spinal cord lesions. 2. Characterize lesions based on anatomic distribution, signal intensity pattern, contrast enhancement, and their relationship to clinical onset and presentation. 3. Identify common pitfalls when imaging non-compressive, non-neoplastic spinal cord lesions.
Results
This exhibit will include presentations of non-compressive non-neoplastic spinal cord lesions and the distinguishing factors on magnetic resonance imaging, with CT and angiographic correlation as well. Cases will include congenital causes, demyelinating disease, longitudinally extensive transverse myelitis (ADEM, Anti-MOG), vascular disease (cord edema, cavernous cord infarction, AV fistula, etc.), post-traumatic etiologies, inflammatory/infectious disease, demyelinating disease, and metabolic myelopathy (vitamin B12 deficiency). Literature review and discussion points will accompany each case presentation in the respective categories.
Conclusions
Multiple clinical presentations of non-neoplastic spinal cord lesions exist, which have unique radiological findings. Familiarity with the neuroimaging findings within the non-compressive pathologic spectrum of non-neoplastic myelopathy can provide timely diagnoses to facilitate appropriate management and improve clinical outcomes.

(Filename: TCT_891_NeuroimagingSpectrumofNonneoplasticNoncompressiveMyelopathy.jpg)

386
Neuroophthalmologic Imaging of Papilledema
E Kim[1]
[1]*Ewha Womans University Mokdong Hospital, Seoul, Korea, Republic of*

Purpose
Papilledema is optic disc swelling that is caused by increased intracranial pressure (ICP) due to any cause. Early recognition of papilledema and elevated ICP is of important for ensuring restoration of vision. Noninvasive imaging of papilledema includes ophthalmologic tests such as ophthalmoscopy, visual field test and optic coherent tomography (OCT), orbital ultrasound (US), CT, and MRI examination. Neuroophthalmologic imaging of papilledema will be presented in a variety of medical condition including idiopathic intracranial hypertension, intracranial hemorrhage, etc.
Materials and Methods
In order to accurately diagnose papilledema at an early stage, it is necessary to understand not only imaging findings such as orbital US, CT, and MRI, but also ophthalmic examinations such as fundus examination, visual field examination, and OCT. Therefore, we

intend to review common neuroophthalmologic imaging findings of papilledema and try to understand the pathophysiology of papilledema through various cases of idiopathic intracranial hypertension and intracranial hemorrhage.
Results
We will review neuroophthalmologic imaging findings in patients with increased ICP, and diagnose papilledema early in patients with increased ICP by comparing the optic nerve size and optic nerve sheath size in normal subjects and IICP patients on orbit US and MRI.
Conclusions
Ophthalmoscopic finding of papilledema is blurring of optic disc margins and elevated optic disc. Orbital US shows increased optic nerve sheath width in patients with papilledema. MR imaging findings of papilledema are enlargement of the optic nerve sheath, flattening of the posterior sclera, protrusion of the optic papilla into the globe, and tortuosity of the optic nerve including smear sign. Ancillary findings on MR imaging for papilledema include empty sella and enlargement of oculomotor cistern. Papilloma are serious warning sign for elevated ICP and potential loss of vision in a variety of clinical settings. MR imaging may facilitate detection of papilledema before fundoscopic examination may indicate elevated ICP.

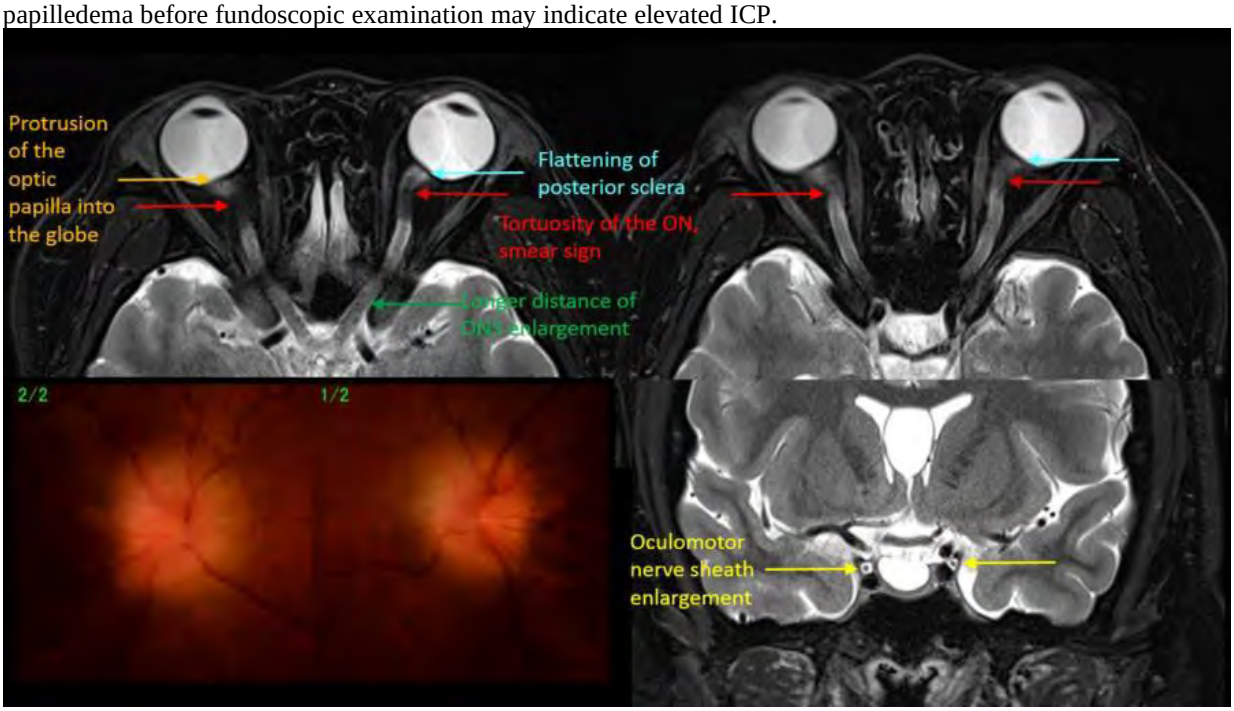

(Filename: TCT_386_31femalewithidiopathicintracranialhypertension.JPG)

518

Neuroradiologic Emergencies: Who You Gonna Call?

J Benjamin[1], A Jain[2], B Comora[3], O Schoeck[4], J Li[5], B Devenney[6], c chan[7]
[1]Einstein Medical Center Philadelphia, Philadelphia, PA, [2]Einstein Medical Center, Philadelphia, PA, [3]Einstein Healthcare Network, Philadelphia, PA, [4]Einstein medical center, Philadelphia, PA, [5]Einstein Healthcare Network, Wayne, PA, [6]Einstein Medical Center Montgomery, East Norriton, PA, [7]Einstein Heathcare Network, Philadelphia, PA

Purpose
We will present pathologies of the head and neck, brain, and spine requiring emergent intervention in the categories of trauma, vascular, and infection. We will also present cases with patterns of mass effect and herniation patterns that require emergent neurosurgical consult. -Review important pathologies of the head and neck requiring emergent intervention. -Review important pathologies of the spine requiring emergent decompression. -Discuss vascular and infectious pathologies of the brain requiring emergent intervention. -Review patterns of mass effect and herniation patterns of the brain requiring emergent decompression using a case-based approach.
Materials and Methods
Misinterpreting or delaying neuroradiologic diagnoses that require emergent surgical and interventional radiologic intervention can lead to permanent neurological disability and death. Therefore, it is crucial for radiologists and radiologists in training to recognize these diagnoses promptly in order to attain appropriate consults for efficient patient management.
Results
We will present pathologies in the following categories based on etiology: trauma (including cases of laryngotracheal separation, temporal bone fractures involving the intratemporal facial canal, spine fractures with cord compression, and cerebrovascular injuries), vascular (including cases of ruptured aneurysms and AV malformations, and strokes with large vessel occlusion), infections (including cases of invasive fungal sinusitis, intraparenchymal abscesses, large epidural abscesses causing cord compression, peritonsillar abscesses with airway compromise and large retropharyngeal abscesses). We will also present cases with patterns of mass effect that

require emergent neurosurgical consults, including cases of paradoxical brain herniation and other herniation patterns that require emergent decompression, tension pneumocephalus, and acute hydrocephalus.
Conclusions
It is fundamental for a radiologist and radiologist in training to be able to identify pathologies that require emergent surgical and interventional radiologic intervention. Our electronic exhibit will provide a concise guide through these many diverse pathologies in order to help clinicians determine cases that may require urgent versus emergent intervention. Identifying pertinent imaging findings of diagnoses that require emergent surgical and interventional radiologic intervention promptly will lead to improved patient care and management by preventing permanent neurological disability and death.

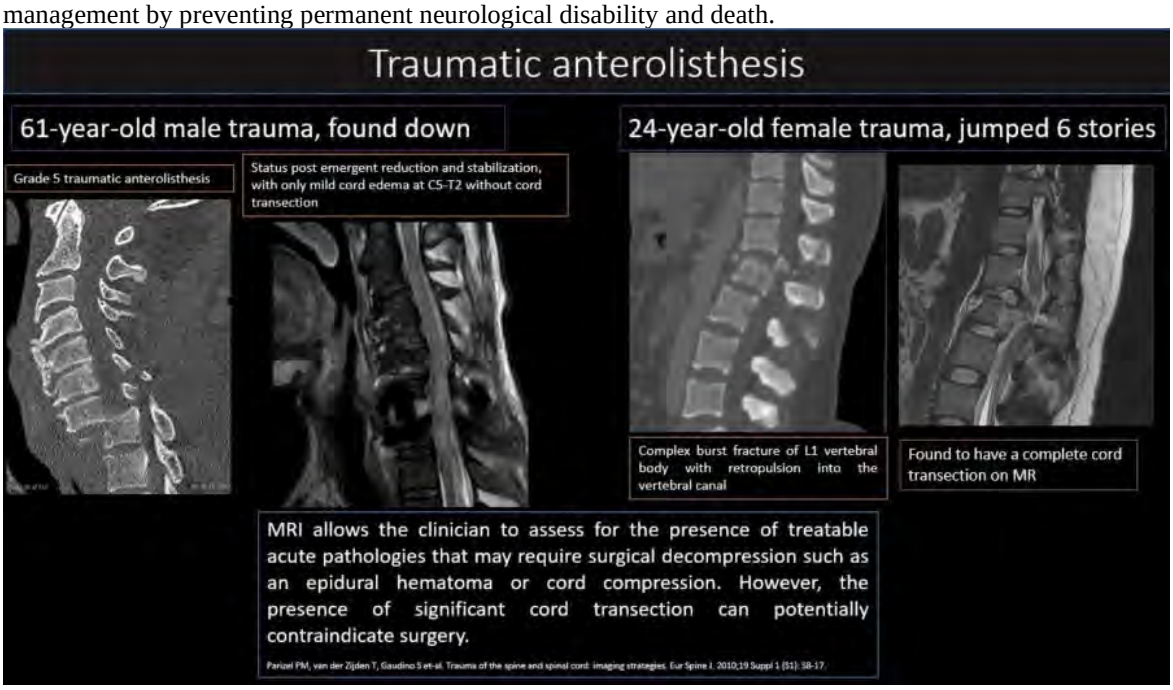

(Filename: TCT_518_Slide2.jpg)

579
Neuroradiologic Manifestations of Erdheim-Chester Disease
A Nayab[1], A Madhavan[1], A Nagelschneider[2], L Eckel[1], J VERDOORN[1]
[1]Mayo Clinic, Rochester, MN, [2]Mayo Clinic-Rochester, Rochester, MN

Purpose
Erdheim-Chester disease (ECD) is a rare non-Langerhans cell histiocytic multisystem disorder. Clinical presentation is nonspecific with ongoing symptomatology for months to years before a diagnosis is made. Objective of this study is to assess central nervous system (CNS) sites and patterns of involvement in ECD.
Materials and Methods
Purpose of this educational exhibit is to highlight the neuroradiologic manifestations that can be seen initially in the course of Erdheim-Chester Disease (ECD) possibly pointing toward the diagnosis.
Results
Retrospective observational study of ten patients seen between 2006 and 2020 at our institute. We assessed gender, symptomatology, age of symptom onset and age at diagnosis, neuroradiological manifestations, and radiological response to treatment.
Conclusions
Results: CNS sites and pattern(s) of involvement were assessed. Site-wise nine out of ten patients had involvement of cerebellum with the most common pattern being bilateral irregular T2/FLAIR hyperintense lesions spanning the middle or less commonly the superior cerebellar peduncles and dentate and peri-dentate regions. The degree of enhancement varied with symptomatology, worsening with progressive symptoms and vice versa. Other less commonly involved sites included the spinal cord and orbits. The hypothalamus and pituitary stalk were involved in two cases. Isolated longstanding leptomeningeal enhancement across the neuraxis was seen in one case. A mass-like cerebellar lesion was seen in one case. The most common presenting symptom was headache, followed by imbalance, vertigo and diplopia. Other less common neurologic symptoms included sensory symptoms such as extremity weakness and paresthesias, and loss of vision. One case was neurologically silent yet demonstrated cerebellar lesions. None of the cases had ECD as the primary working diagnosis at the time of initial neuroradiologic imaging. Mean age at diagnosis was 52.7 years. The mean time between initial presentation and diagnosis was 5.6 years. Radiologic response to treatment was noted in all but one case. Conclusion: Intra-axial findings of patchy T2 hyperintense signal abnormalities in the cerebellum (dentate peri-dentate regions) were common to nine out of ten cases in our study possibly making it a neuroimaging manifestation pointing toward the diagnosis of ECD in the correct clinical setting as that may be how the disease initially presents.

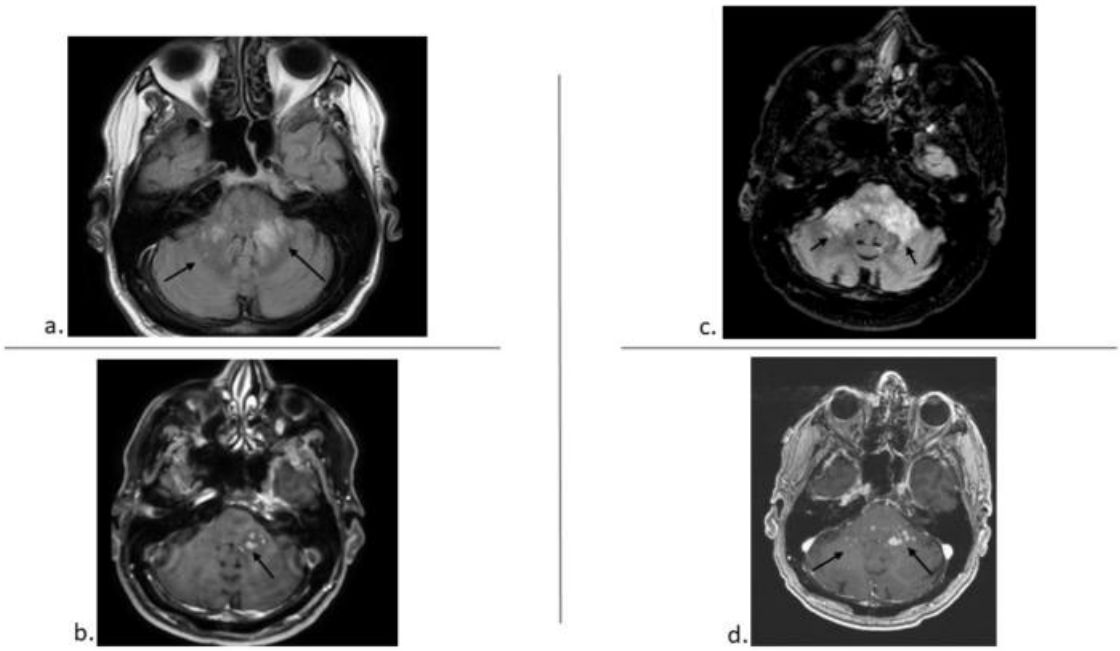

61-year-old male patient with three-year history of vertigo, imbalance and occasional right leg weakness. Findings on brain MRI were present long before the definitive diagnosis of ECD.
Fig. a-b: MRI Brain on presentation shows T2/FLAIR hyperintense signal in middle cerebellar peduncles and medial cerebellar hemispheres (dentate and peri-dentate regions) with corresponding minimal patchy enhancement.
Fig. c-d: Later in the course of disease before definitive diagnosis, progression of abnormalities in the cerebellum seen on T2/FLAIR sequence with corresponding increase in enhancement.

(Filename: TCT_579_Presentation1.jpg)

957

Neuroradiology Artificial Intelligence (AI) in Practice

A Tejani[1], K Raj[1], A Agarwal[1], F F[1]
[1]*UT Southwestern Medical Center, Dallas, TX*

Purpose

Educational Objectives: The purpose of this presentation is to: 1. Provide an update on the current spectrum of artificial intelligence (AI) applications in neuroradiology, highlighting diagnostic and non-diagnostic use cases from clinical practice. 2. Demonstrate the benefits of integrating AI applications in neuroradiology, including improved diagnostic capabilities and workflow efficiency, citing key performance indicators (KPIs). 3. Review limitations and pitfalls of AI applications, using specific examples from clinical cases. 4. Discuss potential improvements in current AI applications and future use cases. Presentation Summary: · Introduction o Basics of machine learning o Diagnostic versus non-diagnostic use cases o Timeline of AI in neuroradiology · Case-guided review of AI applications in practice o Workflow optimization (i.e., worklist prioritization) o Computer vision tasks (i.e., segmentation, quantification) -Intracranial hemorrhage -Cerebrovascular accidents (RAPID/CT perfusion) -Cervical spine trauma -Tumor imaging (i.e., tumor genomics, treatment monitoring) -Neurodegenerative disorders (i.e., amyloid imaging, quantification of atrophy) o Image post-processing/reconstruction (i.e., artifact correction, dose reduction, resolution enhancement) · Case-guided failure analysis · Barriers to AI expansion within neuroradiology · Future use cases and potential challenges to workflow integration

Materials and Methods

N/A

Results

N/A

Conclusions

N/A

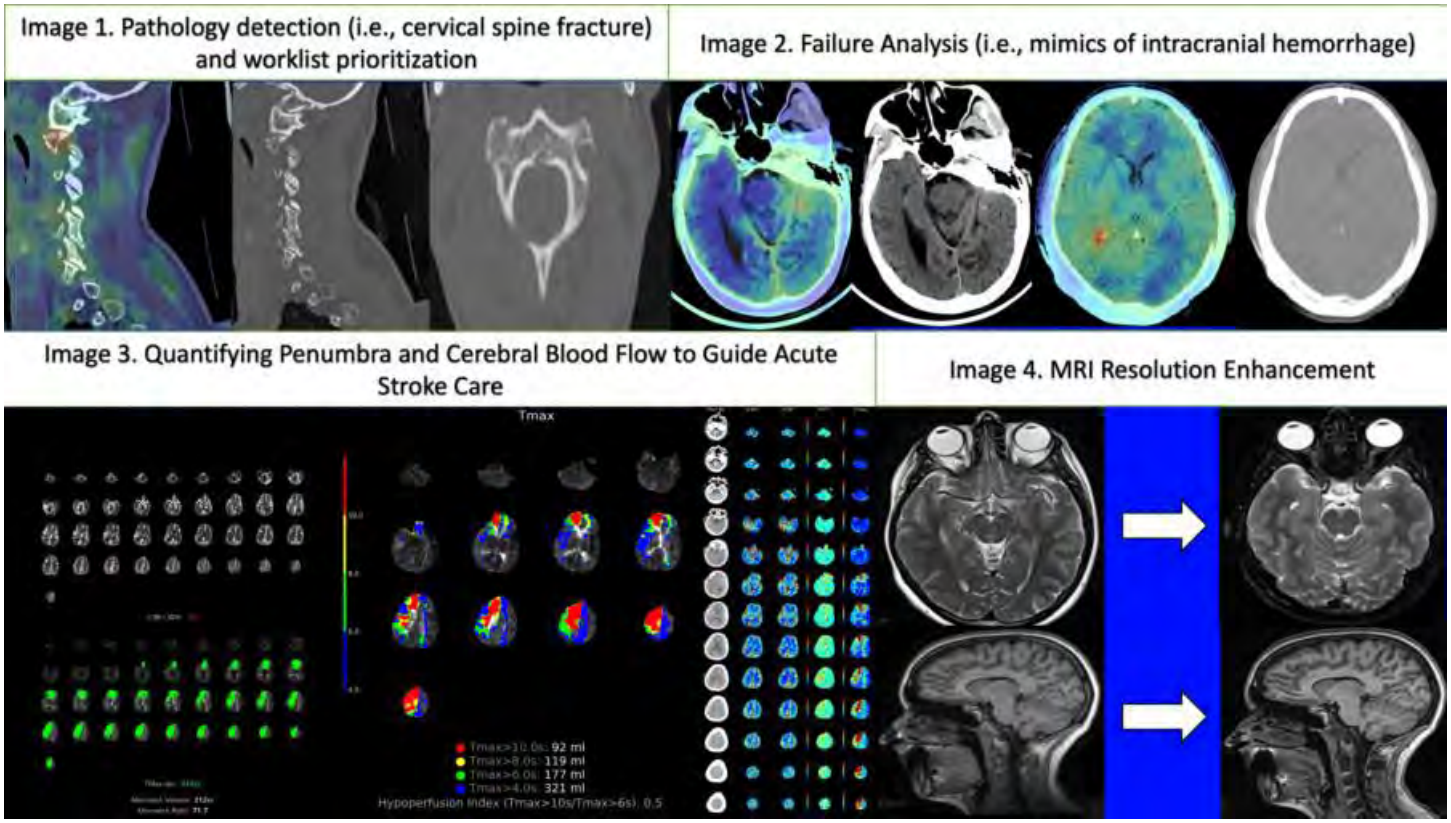

(Filename: TCT_957_ASNR22.jpg)

883

Neurotoxoplasmosis vs CNS Lymphoma in Immunosuppressed Patients: Place Your Bets!

G Romero Sanchez[1], A Pérez-Lara[2], J Ortiz Jimenez[3], R HERNANDEZ RAMIREZ[1], E Chiquete Anaya[1]

[1]Instituto Nacional de Ciencias Médicas y Nutrición Salvado Zubirán, Mexico City, Mexico, [2]Hospital Regional Universitario de Málaga, Málaga, Malaga, [3]Queen's University, Kingston, Ontario

Purpose

To review the main imaging findings of Neurotoxoplasmosis and CNS lymphoma To categorize the imaging findings in typical and atypical To describe the usefulness of PWI, MRS and and PET-CT/SPECT-CT in the differential diagnosis between neurotoxoplasmosis and CNS lymphoma

Materials and Methods

Radiological distinction between neurotoxoplasmosis and CNS lymphoma may be challenging in immunocompromised patients. Advanced imaging sequences such as perfusion weighted imaging (PWI) and spectroscopy can be useful to differentiate between both entities, decreasing the number of unnecessary brain biopsies. Therefore, recognition of the specific imaging findings of each entity is crucial. In this exhibit, we illustrate the typical and atypical findings of both pathologies on MRI, PET/CT and SPECT/CT imaging in immunocompromised patients.

Results

We comprehensively review the imaging findings of neurotoxoplasmosis and CNS lymphoma and categorize them in typical and atypical findings, highlighting the key features that can help to achieve an accurate diagnosis.

Conclusions

We first describe the most frequent imaging findings of each entity. Subsequently, we review the atypical findings that may potentially lead to diagnosis pitfalls. We describe the usefulness of PWI and PET-CT/SPECT-CT in the differential diagnosis between neurotoxoplasmosis and CNS lymphoma. Finally, we present different imaging examples of cases from our institutions describing the key findings that can be helpful to differentiate between both entities. The knowledge of the specific imaging features of neurotoxoplasmosis and CNS lymphoma is important to differentiate both entities, avoiding unnecessary surgical procedures and providing an early diagnosis for appropriate management of these patients.

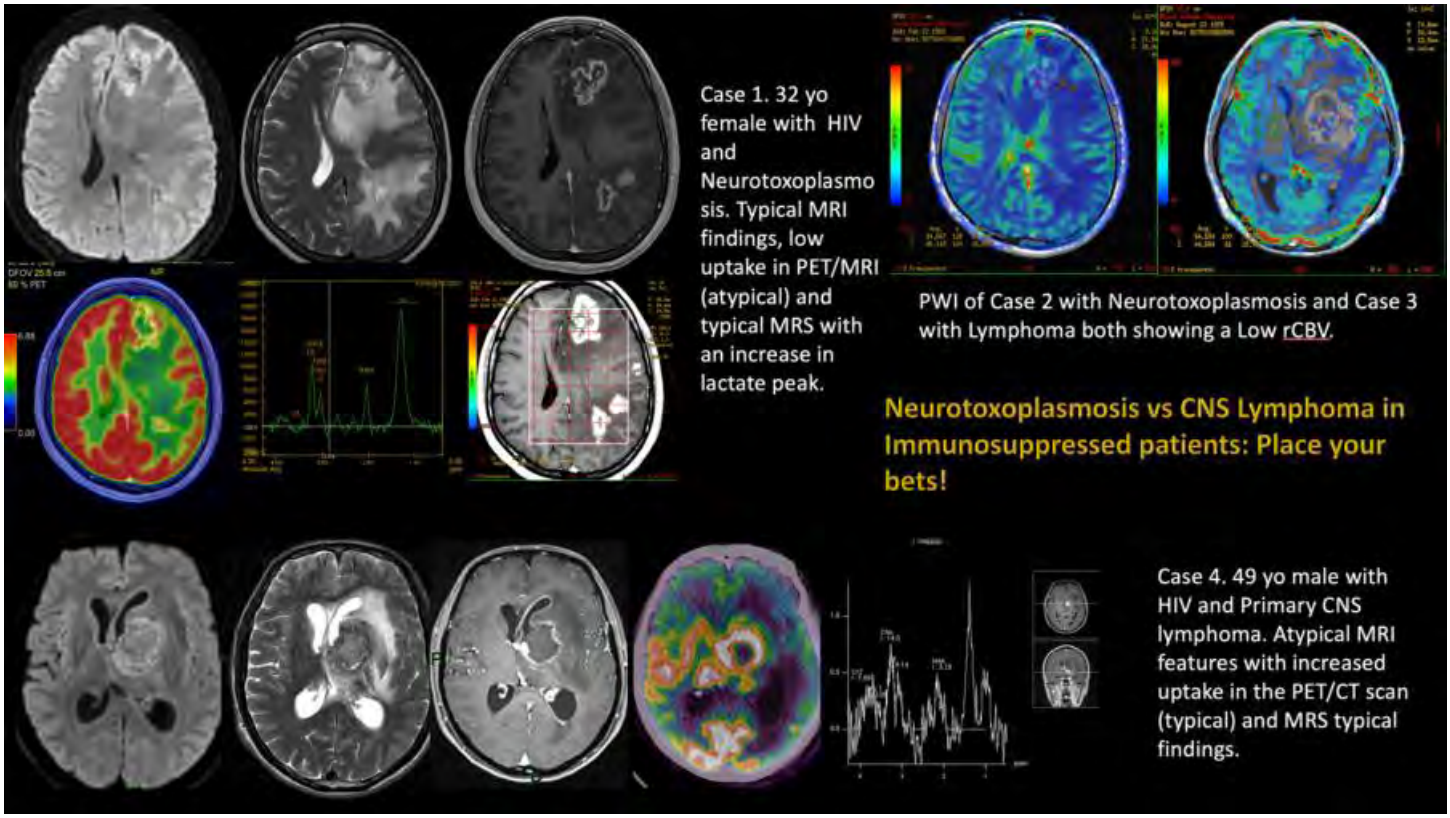

(Filename: TCT_883_asnrImageLN.jpg)

1302

Neurovascular Injury Related to COVID-19: Common and Uncommon Findings

K CANCELA[1], A Alves Fonseca[2], T Iutaka[3], E Naves[4], A Salgado[5], R Pincerato[6]

[1]Hospital Samaritano Higienópolis, São Paulo, Brazil, [2]Santa Casa de São Paulo / DASA / United Health Group, São Paulo, São Paulo, [3]Hospital Samaritano Higienópolis - UHG, São Paulo, São Paulo, [4]Hospital Israelita Albert Einstein, São Paulo, NY, [5]Hospital Samariano Higiopolis, São Paulo, São Paulo, [6]HOSPITAL SAMARITANO SP - UHG BRASIL, São Paulo, SP

Purpose

Coronavirus is a virus with the main target in the human respiratory system. Incubation period of approximately 5 days and the most common symptoms: asymptomatic, fever, cough, fatigue, headache, hemoptysis and dyspnea. More severe cases evaluate with pneumonia, acute respiratory distress syndrome, acute heart problems and multi-organ failure. With this work, we want to review the neurovascular involvement related to COVID-19, discuss the physiopathology of neurovascular injury related to COVID-19 and describe and demonstrate through clinical cases, the main clinical and imaging scenarios of common and uncommon findings of COVID-19-related neurovascular injury, including ischemic stroke, hemorrhages, hypoxic-ischemic injury, cerebral venous thrombosis, spinal cord ischemia and posterior reversible encephalopathy syndrome

Materials and Methods

The mechanisms of involvement of the central nervous system are most commonly related to indirect neurological complications, with cerebrovascular disease resulting from SIRS with pulmonary, renal, hepatic and cardiovascular damage. The symptoms observed are focal deficits, mental confusion and seizures. In relation to direct neurological damage, which are rarer, we have as an example the involvement of the nasal epithelium and olfactory bulb. In addition, we have post-infectious complications, with misdirected host immune response, with mimicry of myelin protein, when patients can evolve with encephalitis, acute disseminated encephalomyelitis and Guillain-Barré. Our purpose was to bring together some illustrative cases of these conditions.

Results

After reviewing our institution's digital teaching files, we selected some illustrative cases to address COVID-19 diagnostic scenarios, focusing on typical imaging patterns and where possible, evolutions of these cases.

Conclusions

Vascular diseases were the most common in the COVID-19 scenario. Ischemic stroke, hemorrhages, thrombosis, PRES and cerebral vasoconstriction were found. Other less common patterns are caused by direct virus damage as a meningitis, encephalitis and myelitis. It is noteworthy that PCR in LCR is rarely positive. In addition, there is the possibility of treatment-related complications.

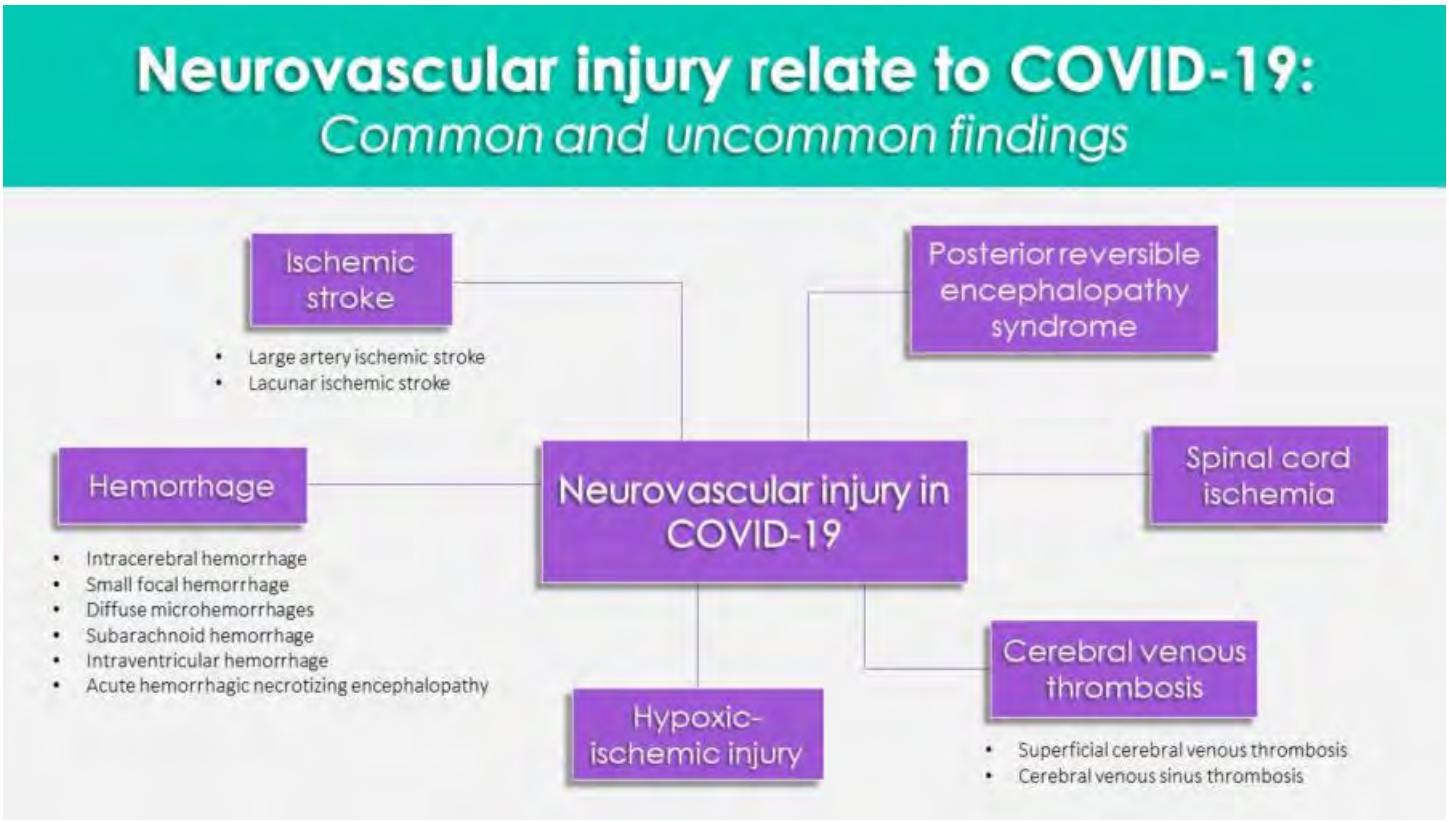

(Filename: TCT_1302_Slide1.JPG)

415

NIGROSOME I: ANATOMY, VARIANTS, AND PATHOLOGIES

D Santos[1], R Leite[2], M Soldatelli[3], B Inada[4], T Morimoto[5], N Hatano[6], L do Amaral[7], S Omar[8], C Campos[4], V Marussi[9]

[1]BP - Hospital Beneficência Portuguesa de São Paulo, São Paulo, São Paulo, [2]Hospital Beneficência Portuguesa de São Paulo, São Paulo, Brazil, [3]Beneficência Portuguesa de São Paulo, São Paulo, Brazil, [4]BP - A Beneficência Portuguesa de São Paulo, São Paulo, SP, [5]Hospital BP, São Paulo, SP, [6]BP - A Beneficência Portuguesa de São Paulo, Sao Paulo, Sao Paulo, [7]Beneficiência Portuguesa, São Paulo, SP, [8]Beneficência Portuguesa de São Paulo, São Paulo, São Paulo, [9]Beneficência Portuguesa Hospital, Sao Paulo, Sao Paulo

Purpose

Parkinson's disease is a clinically heterogeneous chronic progressive neurodegenerative disease with loss of dopaminergic neurons in Nigrosome 1 (N1). Nigrosomes are small clusters of dopaminergic cells within the substance nigra. Five nigrosomes have been described with the largest labeled as N1, located in the posterior third of the substantia nigra. The objectives of this electronic exhibit are: - to revisit the anatomical definition of the N1 region using schematic illustrations and imaging MRI; - to illustrate the anatomical variants of the N1; - to exhibit parkinsonism diagnostic algorithm; - provide imaging findings of various patients who presented with parkinsonism.

Materials and Methods

The purpose of this exhibit is to help the readers to determine the presence or absence of an abnormality in the N1 and establish diagnostic reasoning in cases of parkinsonism.

Results

We performed an extensive literature review and retrospective analysis of parkinsonism cases from our service.

Conclusions

The N1 is the key structure in the midbrain that is very important in movement disorders, particularly those associated with parkinsonism. Interpreting the N1 sign can be difficult because it can take many forms but the high-resolution data and clear characterization of the N1 appearance help to make that decision easier.

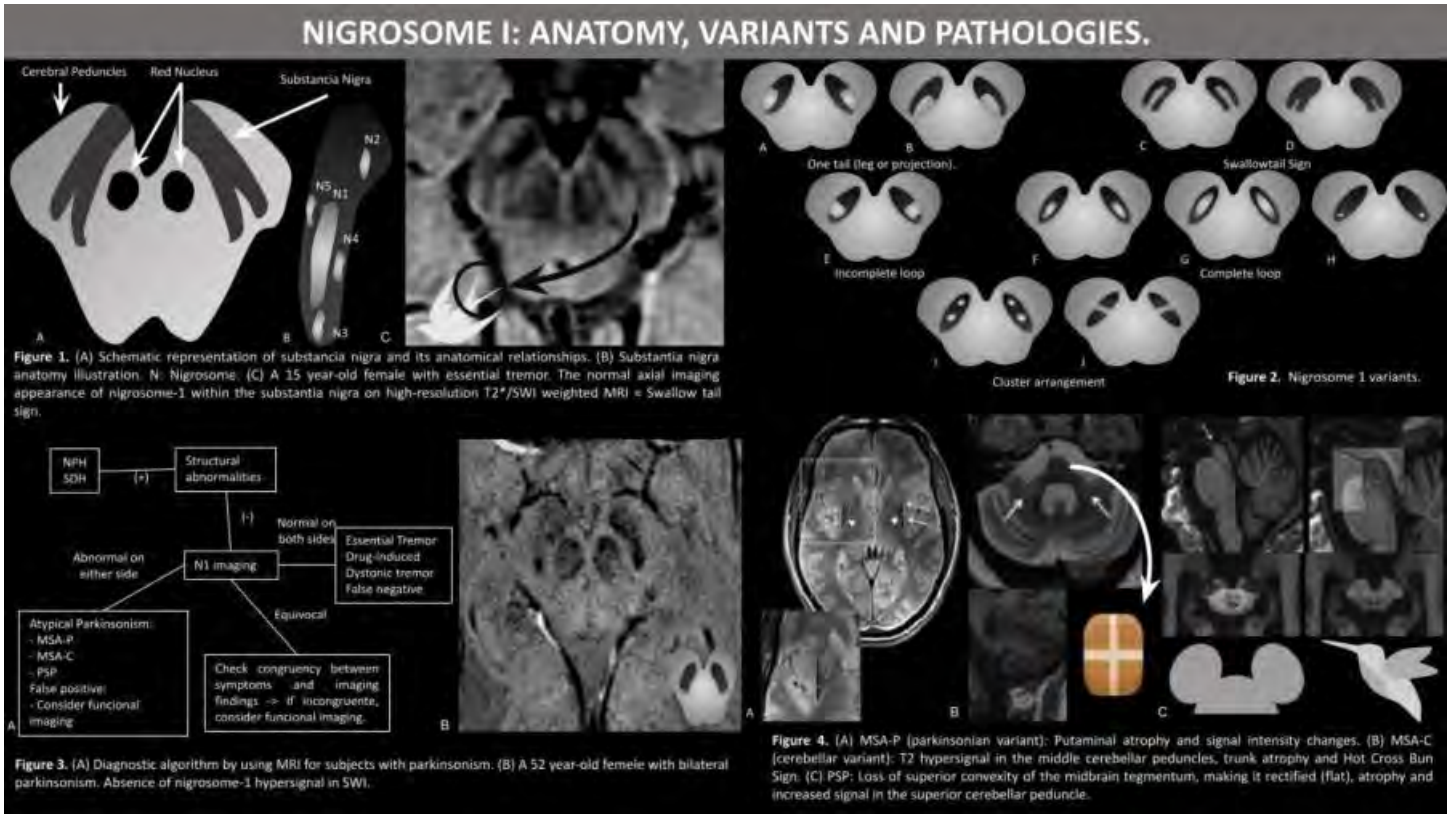

(Filename: TCT_415_nigrossomo11pptx.jpg)

265

Non-Oncologic Applications of Radiomics in Neuroradiology

H Sotoudeh[1], A Sarrami[2], g roberson[1], O Shafaat[3], Z Saadatpour[1], A Rezaei[1], A Babaei Jandaghi[4], A Singhal[1], E Sotoudeh[5], M Tanwar[1]

[1]University of Alabama at Birmingham, Birmingham, AL, [2]N/A, Davis, CA, [3]The Russell H. Morgan Department of Radiology and Radiological Science, Johns Hopkins University, Baltimore, USA, [4]University Health Network, Mount Sinai Hospital and women's College Hospital, Toronto, Ontario, [5]Red crescent Hospital in Dubai, Dubai, UAE

Purpose

Oncologic applications of radiomics are widely applied. However, radiomics is not limited to tumoral analysis, and any digital medical images can benefit from radiomics analysis. This presentation is about the emerging role of radiomics in non-oncologic neurological disorders (ischemic strokes, hemorrhagic stroke, cerebral aneurysms, and demyelinating disorders).

Materials and Methods

To review the emerging role of Radiomics in non-oncological neurology disorders.

Results

This educational exhibit includes: Radiomics in Ischemic Stroke Radiomics in Infarction detection Radiomics in Thrombosis characterization Radiomics in Identification of high-risk carotid plaque Radiomics in Prediction of malignant middle cerebral infarction Radiomics in Intracranial Hemorrhage Radiomics in Prediction of enlarging hematoma Radiomics in Neoplastic versus Non-neoplastic Intracranial Hemorrhages Radiomics in Intracranial Aneurysm Radiomics in Neuroinflammatory and Demyelination Disorders

Conclusions

The preliminary results about the applications of radiomics in non-oncologic neurological disorders are promising. In future, some of the mentioned applications in this exhibit may be a part of standard of care in non-oncological neurological disorders.

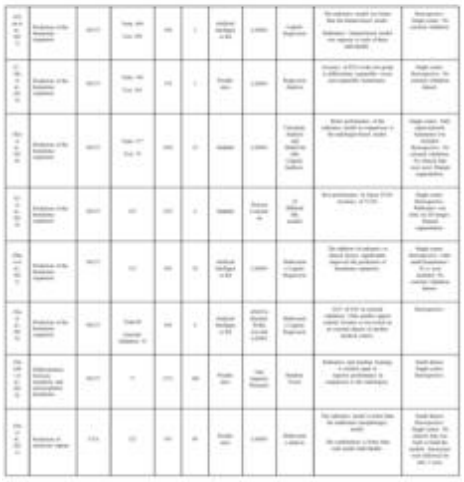

(Filename: TCT_265_Merged_document.jpg)

1100

Non-traumatic Emergencies of the Optic Nerve and Surrounding Areas – What a Radiologist Must Know!

D Pinto[1], R Quencer[2], R Howse[3], J Manov[4], N Nagornaya[5], G Saigal[5]

[1]Jackson Memorial Hospital, Miller school of medicine, Miami, FL, [2]University of Miami, Coral Gables, FL, [3]University of Miami/Jackson Memorial Hospital, Miami, FL, [4]University of Miami, Miami Beach, FL, [5]Jackson Memorial Hospital/University of Miami, Miami, FL

Purpose

We present imaging of orbital emergencies affecting the optic nerve encompassing inflammatory conditions, infections and vascular etiologies, as well as mimics of emergency conditions. Educational objectives: To help the radiologist interpret orbital emergencies with a focus on emergencies involving or potentially involving the optic nerve. To emphasize the importance of technique in emergency evaluation of the orbits. Structure of the presentation: *List of educational objectives: *Importance of MR techniques in orbital imaging – dedicated orbital imaging is required in most cases. *How to evaluate the orbit with structured reporting *Represented cases include: Inflammation: a) Papillitis, b) Optic neuritis – different patterns of enhancement due to multiple sclerosis versus vasculitis, Optic neuritis in Hashimoto's thyroiditis and NMO c) Optic peri-neuritis - due to Giant cell arteritis, sarcoidosis, anti-MOG antibody associated demyelination. Infection: a) Invasive fugal sinusitis causing orbital cellulitis and optic nerve infarct b) COVID patient with bilateral optic neuritis c) Cat-scratch fever. Vascular: Ophthalmic artery aneurysm Toxic: Methotrexate toxicity Mimics of emergencies a) Idiopathic orbital inflammation b) Idiopathic intracranial hypertension c) Normal vascular enhancement mimicking peri-neuritis.

Materials and Methods

Orbital emergencies often present after-hours. Accurate reports with as short as possible turnaround times are critical for high quality health-care delivery especially when the optic nerve is involved. This presentation aims to provide a structure for accurately diagnosing non-traumatic orbital emergencies with a focus on optic nerve involvement.

Results

A search through the database of 2 health systems for stat requests for orbital MR imaging resulted in the identification of optic nerve involvement due to various etiologies. This allowed the creation of guidelines to aid in the rapid and accurate image interpretation of such cases.

Conclusions

The findings in optic nerve emergencies may be subtle; however, by using a structured approach and adhering to effective imaging protocols a fast and accurate diagnosis will be facilitated. Also the various patterns of involvement of the optic nerve will help differentiate between etiologies.

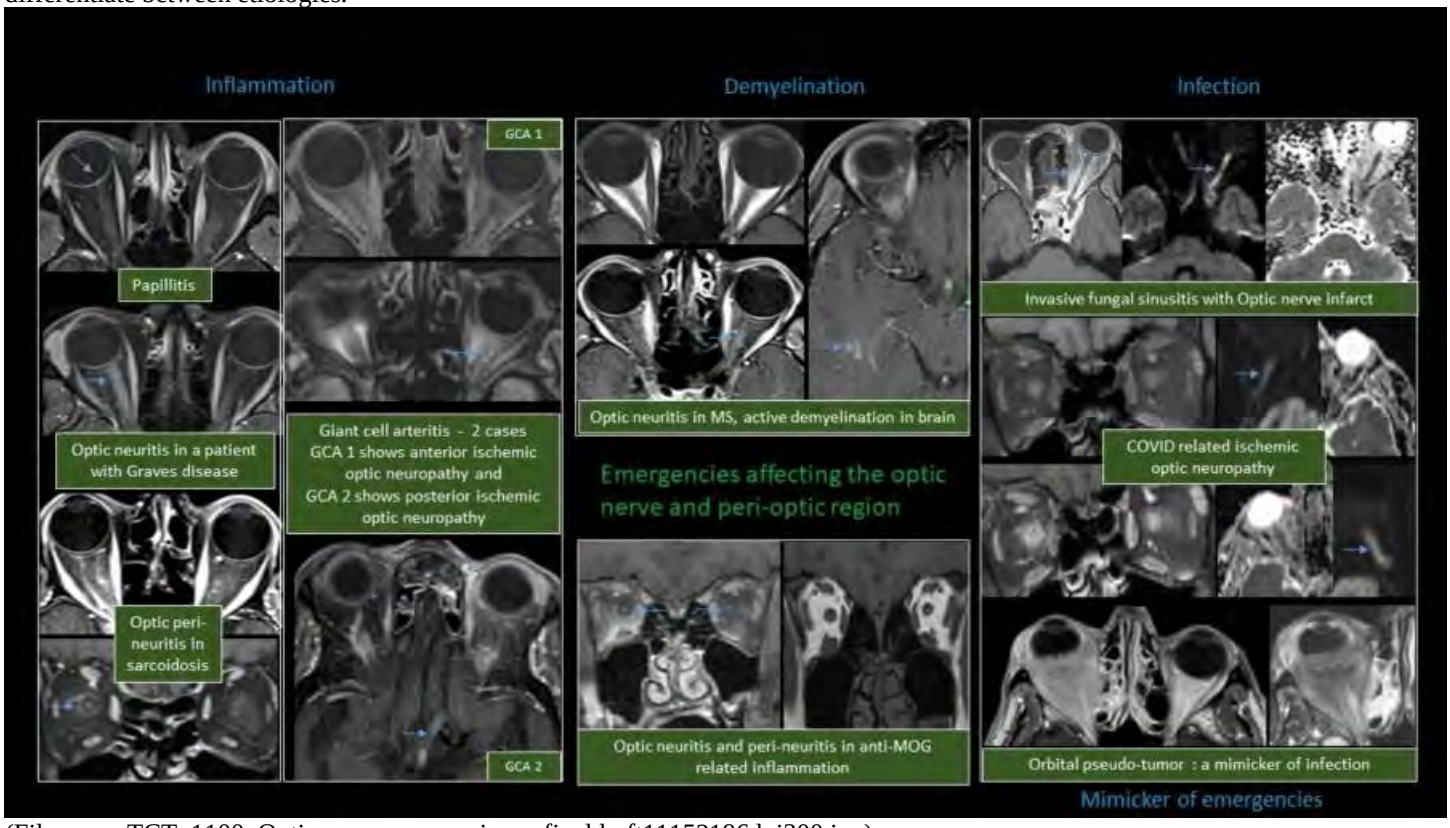

(Filename: TCT_1100_Opticnerveemergenciesprefinaldraft11152196dpi300.jpg)

1538

Nose, Brain and the Perfumer's Art: A Neuroradiological Guide to the Olfactory System and How Scent Makers Tap into our Deepest Memories and Emotions

S Lev[1], C Ekhator[2], M Gelbman[3]

[1]Nassau University Medical Center, East Meadow, NY, [2]New York Institute of Technology College of Osteopathic Medicine, Greenvale, NY, [3]Maimonides Medical Center, Brooklyn, NY

Purpose

The olfactory system, the most primitive of our sensory tracts, extends from the nasal passages to the ancient olfactory cortex. It includes the frontal cortex, limbic system, parahippocampal gyrus and thalamus. The anatomical structures involved with the perception of smell are associated with memories, emotions and even colors. Inhalation of specific aromachemicals precipitates an olfactory journey, the key to any successful perfume. Fragrances, volatile chemical compounds that humans perceive when the molecules attach to the cilia of olfactory receptors in the nasal cavity, trigger an extraordinary cascade of chemical and electrical events. Cognitive recognition of a particular scent occurs only after the deepest parts of our brain have been stimulated. The entire sensory apparatus is susceptible to a variety of injuries, with devastating consequences. Objectives: 1. To appreciate how perfumers design fragrances to excite certain parts of our brain, and learn about the role of modern imaging (eg. fMRI) in exploring and elucidating these sensory pathways and structures. 2. To understand the evolution and anatomy of the human olfactory system. 3. To illustrate how a wide range of pathologies, occurring anywhere along the olfactory system, can alter or eliminate the sense of smell.

Materials and Methods

To review the olfactory system and the pathologies which may affect it. To highlight how fragrances and modern imaging techniques have enhanced our understanding of our sense of smell.

Results

We illustrate assorted radiology studies from our Level I trauma center to highlight the range of pathologies affecting the olfactory system. We review anatomy, an imaging approach, and how scents trigger specific parts of the brain.

Conclusions

The olfactory system is prehistoric, and permits us to obtain environmental information, such as signs of danger or sources of pleasure. Studies have shown that olfactory stimulation by fragrances produces changes in body physiology. Diseases affecting smell occur both intra- and extra-cranially. Congenital, traumatic and neurodegenerative entities are culprits. Sinus disease (neoplasms and inflammatory) can limit access of aromas to the nasal vault. Traumatic injury may damage the cribiform plate and inferior frontal lobes. Alzheimer's, MS, Parkinson's disease, HIV infection, epilepsy and schizophrenia have been reported to reduce our sense of smell. Localizing olfactory pathology presents a challenge to the radiologist.

1314

Not Just Bridging veins! Middle Meningeal Artery Embolization For Chronic Subdural Hematoma.

T Sulehria[1], M Hadi[1], D Ding[2]

[1]Department of Radiology, University of Louisville, Louisville, KY, [2]Department of Neurological Surgery, University of Louisville, Louisville, KY

Purpose

1. Recognize pathophysiology of CSDH 2. Overview of cerebral angiogram of MMA pre- and post-embolization 3. Efficacy of MMA embolization in CSDH 4. Complications of MMA embolization.

Materials and Methods

This educational presentation will provide an overview of pathophysiology of chronic subdural hematomas(CSDH) and middle meningeal artery (MMA) embolization for treatment of recalcitrant CSDH. This is counterintuitive to classic teaching that limits the role of MMA to epidural hematomas and attributes subdural hemorrhages to rupture of bridging veins instead. The formation and growth of chronic subdural hematoma (CSDH) is complex. Histological analysis of surgical specimens suggests that topologically a subdural hematoma is really "intradural", with the split happening at the dural border cell layer rather than at the dura mater-arachnoid junction. This triggers healing responses that include dural border cell proliferation, granulation tissue formation, and macrophage infiltration. Local inflammation is thought to contribute to CSDH formation and leads to hyperfibrinolysis of clots and production of angiogenic factors, which induce neovascularization and bleeding from fragile capillaries within CSDH membranes. It has been proposed that these capillaries might be in vascular contiguity with the MMA. Hence the MMA is not a passive spectator separated by dura from an underlying subdural hematoma but plays an important role in maintaining and propagating CSDH. Venous hemorrhage of classical teaching would be expected to be rapidly self-limiting in a confined space. Growth of CSDH is rather a combination of ongoing inflammation and angiogenesis with resultant exudation and hemorrhage, and this is supported by imaging, advanced microscopy, and molecular biology studies. Based on these mechanisms, various nonsurgical treatments have been proposed, but their effect is limited to selected patient groups. Therefore, surgical hematoma removal is the primary option in most CSDHs. Surgery is effective in relieving mass effect but does not change the underlying pathophysiologic mechanisms, and recurrence or growth occurs. In theory, embolization of the MMA limits blood flow to CSDH membranes, directly controls bleeding from the CSDH membrane, and through ischemia, control and calm the release of inflammatory mediators, and eventually promotes spontaneous resolution of CSDH.

Results
N/A
Conclusions
MMA embolization has a positive therapeutic effect on CSDH and may complement conventional surgical treatment.

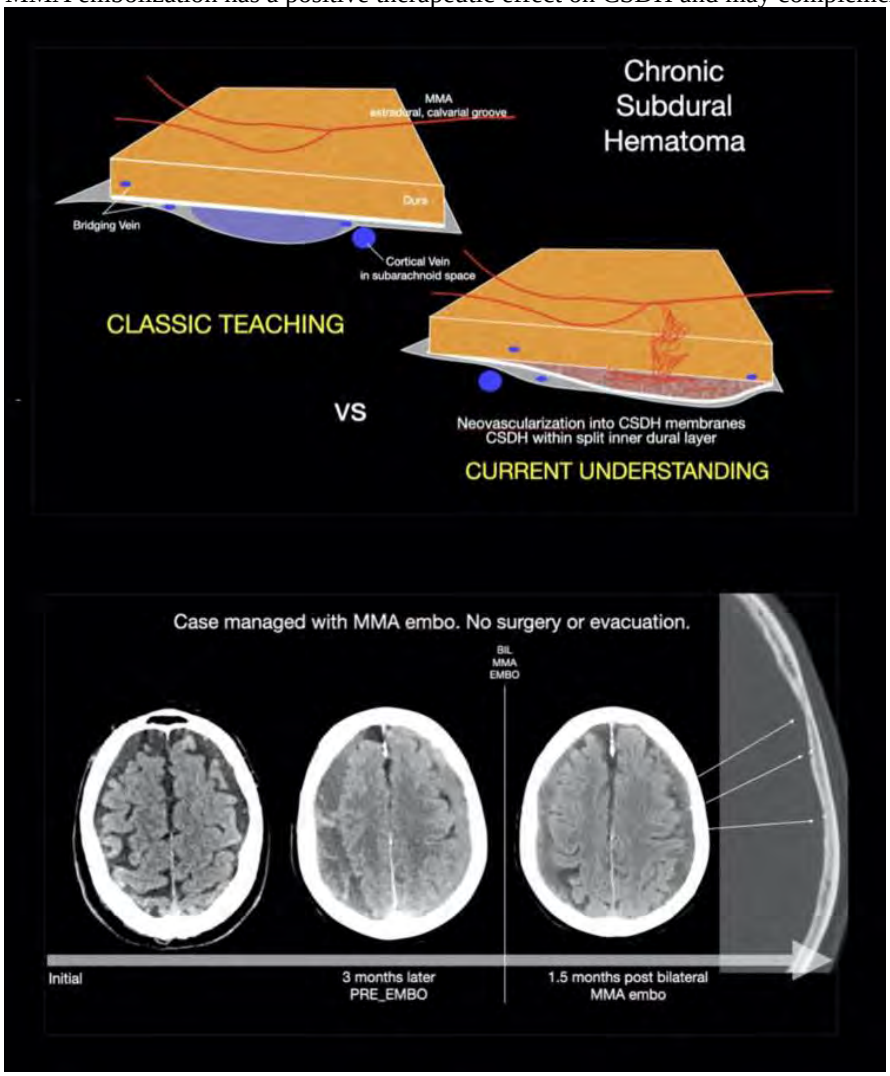

(Filename: TCT_1314_ASNRMMAEmbolization.jpg)

320
Orbital Lymphoma - A Review of the Imaging and Clinical Manifestations
D Wang[1], A Karandikar[2], P Doshi[3], S Patel[4], B Griffith[3]
[1]Henry Ford Hospital, West Bloomfield, MI, [2]Henry Ford Hospital, Detroit, MI, [3]Henry Ford Health System, Detroit, MI, [4]HENRY FORD HOSPITAL, DETROIT, MI

Purpose
Lymphoma is the most common malignant orbital tumor and can involve any part of the orbit. Because of its broad range of imaging appearances, lymphoma is difficult to differentiate from the many other pathologic processes involving the orbit. Using institutional cases, this exhibit will: • Review the imaging appearance of the normal orbital anatomy and adjacent structures. • Review the varied imaging appearances of orbital lymphoma, including extraocular muscle involvement (Fig. 1), diffuse infiltrative form (Fig. 2), anterior orbital involvement (Fig. 3), and lacrimal gland involvement (Fig. 4). • Review the imaging appearance and clinical presentations of differential considerations, including IgG4-related disease, idiopathic orbital inflammation, orbital sarcoidosis, thyroid ophthalmopathy, and orbital metastasis.
Materials and Methods
The purpose of this educational exhibit is to review the spectrum of imaging and clinical manifestations of orbital lymphoma with attention given to those features that can help to differentiate it from other orbital pathologies.
Results
Orbital lymphoma represents 5-10% of orbital masses. While most commonly involving the lacrimal gland, orbital lymphoma can involve any part of the orbit, including the anterior extraconal orbit, conjunctiva, and extraocular muscles, and can also present with a

diffuse infiltrative form. While physical examination can lateralize the lesion, cross-sectional imaging is required to characterize the lesion, evaluate disease extent, and supplement clinical assessment beyond the physical examination. Using cases from our institution, this exhibit will review a variety of imaging and clinical manifestations of orbital lymphoma along with cases of other similar appearing pathologies

Conclusions

Orbital lymphoma is a heterogeneous malignancy that can have a variety of imaging and clinical manifestations. While cross-sectional imaging is an essential tool in the diagnosis and management of orbital lymphoma, neuroradiologists must be aware of the various imaging features of orbital lymphoma in order to help differentiate it from the other pathologies that can have similar presentations and appearances.

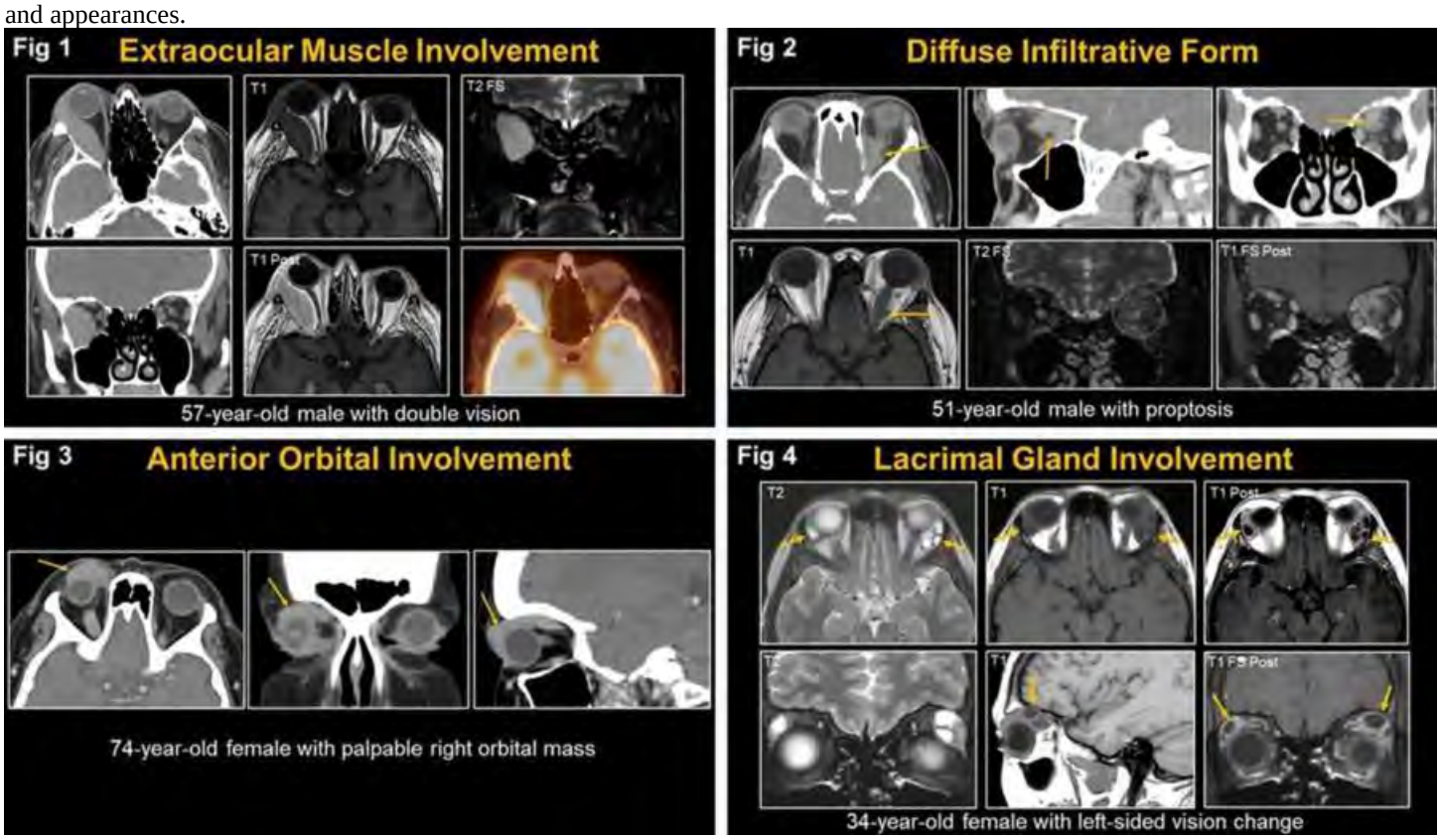

(Filename: TCT_320_Abstractfigure.jpg)

429

Ortner's Cardiovocal Syndrome and Other Neck Vascular Etiologies of Vocal Cord Dysfunction: A Neuroimaging Review

D Sivacharan Gaddam[1], K Seifert[1], A Khalaf[1], M Penta[2], M Wintermark[1], S Hashmi[1], T Massoud[1]

[1]Stanford University School of Medicine, Stanford, CA, [2]N/A, N/A

Purpose

Dysphonia may follow partial or complete vocal cord paralysis (VCP) after damage to the recurrent laryngeal nerves (RLNs). Most VCPs are postoperative or due to malignancy. Dysphonia owing to cardiac and vascular causes is uncommon but should be considered because an early imaging diagnosis is critical; the culprit abnormality can carry a higher risk than the dysphonia itself. Ortner's or cardiovocal syndrome (CVS) is dysphonia from left RLN (LRLN) palsy due to nerve compression by enlarged cardiovascular structures at the aortopulmonary window. Nowadays this term includes dysphonia from all vascular causes affecting the RLNs. These entities are under-recognized in clinical practice and the radiological literature. We present an educational review of vascular causes of dysphonia, and discuss the anatomical basis for clinical and neuroimaging findings.

Materials and Methods

We comprehensively review the imaging findings in vascular etiologies of VCP.

Results

We first review CT/MRI of normal VCs and VCP. We then discuss the anatomical course of the RLNs. They innervate all intrinsic laryngeal muscles (except cricothyroid) for vocalization. The RLNs branch from the vagus nerves (CN10) at different levels on the right and left. In particular, the LRLN is longer and branches then hooks under the arch of aorta, posterior to the ligamentum arteriosum. Hence, neck and chest CT/MRI should be obtained for all patients with LRLN palsy to include the entire nerve course. In 1897 Ortner described patient dysphonia from severe mitral stenosis with enlarged left atrium compressing the LRLN. The term CVS was introduced in 1958. We illustrate the cardiac causes of CVS, including congenital heart diseases, mitral valve disorders, and adult disorders including pulmonary hypertension, aneurysms, and post cardiac procedures. We also review reported neck vascular causes of dysphonia. These may either cause VCP, e.g. cervical internal carotid artery aneurysms compressing CN10 in the carotid sheath, or

follow ischemic damage to the anterior bronchoesophageal artery supplying LRLN, and the inferior thyroideal artery supplying RRLN during root of neck surgery. Another reported mechanism of dysphonia is VC infiltration by a laryngeal AVM.
Conclusions
Early neuroimaging is essential to detect common causes of VCP but it is important for radiologists to also consider cardiac/vascular etiologies in the neck and thorax. This presentation will aid in imaging interpretation of these conditions to improve patient management.

448

Overview of 2-HG MR Spectroscopy for Evaluation of Isocitrate Dehydrogenase Mutant Brain Tumors

I Mark[1], Y Li[2], S Cha[2]
[1]UCSF, San Francisco, CA, [2]University of California San Francisco, San Francisco, CA

Purpose
Noninvasive imaging diagnosis of isocitrate dehydrogenase (IDH) mutant gliomas may have high impact on clinical management and therapeutic decision making. The gain of function of an IDH mutation leads to the reduction of alpha ketoglutarate and accumulation of 2-Hydroxyglutarate (2HG). This oncometabolite can be identified on MR spectroscopy (MRS) at a peak at 2.25 ppm. The ability to diagnose IDH-mutant gliomas can significantly alter patient management in several keys ways. First, the imaging appearance of low grade IDH mutant tumors often does not have the ominous findings of IDH wild type tumors such as central necrosis, enhancement, and reduced diffusion, but rather than can appear as mass-like T2/FLAIR signal. This means that there is imaging overlap with inflammatory and other non-neoplastic conditions. The ability to suggest an IDH mutant tumor may alter the treatment and the decision to perform a biopsy. Second, these IDH mutant tumors and their mimics can occur in eloquent regions of the brain that could lead to significant neurological deficits if a biopsy is performed. Having a greater degree of confidence in whether a lesion is a tumor or tumor mimic may alter the decision to biopsy sites with a high risk of neurological deficit development. Third, the technique of MRS has the potential to quantify 2HG peaks. With wider clinical use of targeted therapies for IDH mutant gliomas, serial 2HG imaging could potentially be used to monitor treatment response.
Materials and Methods
The purpose of this educational exhibit is to provide an overview of 2HG MRS for the evaluation of IDH mutant brain tumors, describe the implementation process from the perspective of a single institution, and to provide multiple imaging examples highlighting the utility and potential pitfalls.
Results
Retrospective review of 2HG MRS from a single institution.
Conclusions
2HG is an important oncometabolite that can assist with the predicting diagnosis and prognosis of low grade gliomas. This is an emerging tool that is important for neuroradiologists to become familiar with.

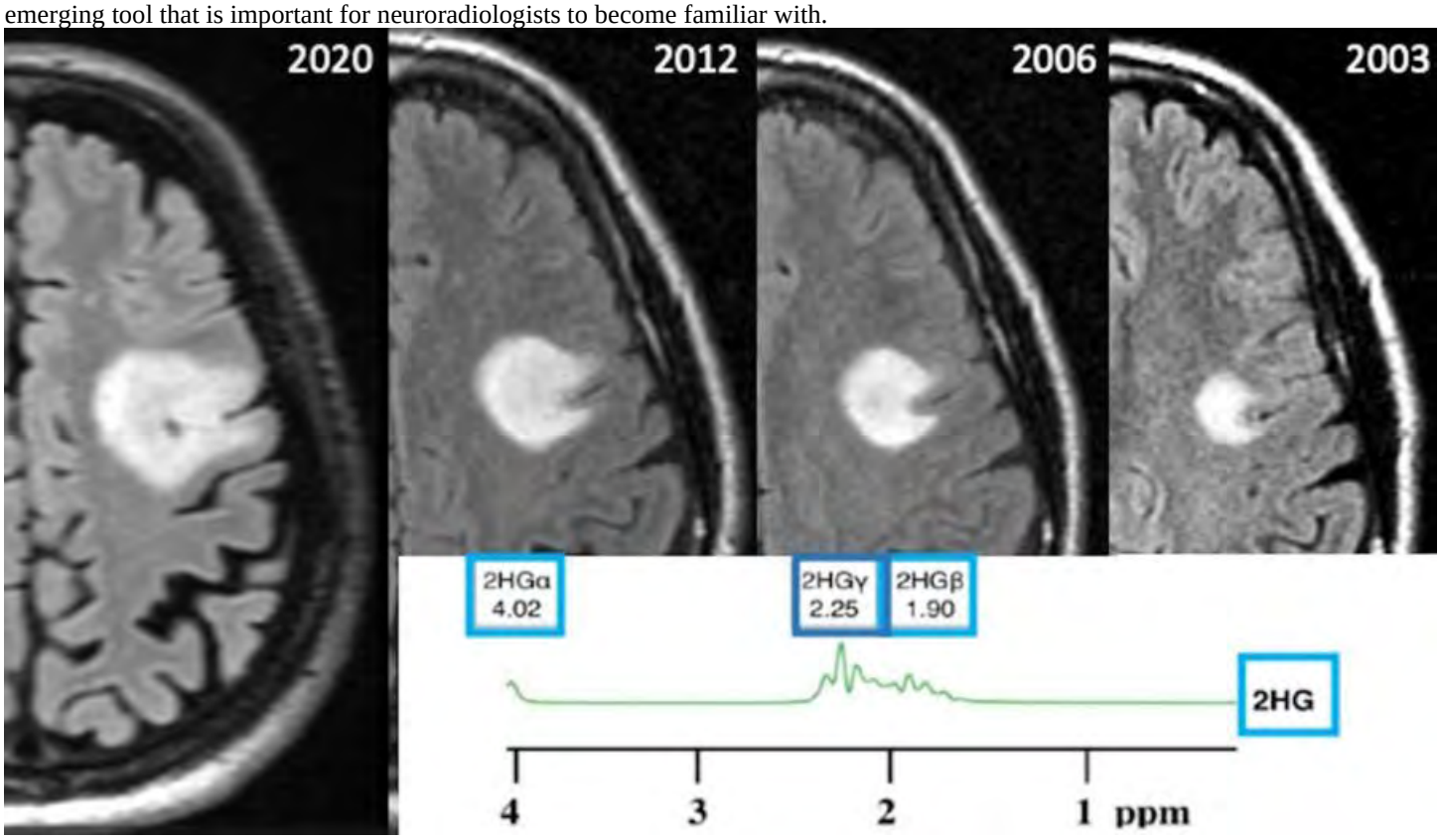

(Filename: TCT_448_2HGMRSASNRabstractimage.jpg)

845

Paracoccidioidomycosis: Central Nervous System Imaging Findings

A Carvalho[1], T Guarilha[2], M Oliveira[3], M Albacete[4], A SANTOS[5]

[1]Universidade Federal de Sao Paulo, Sao Paulo, Brazil, [2]UNIFESP, São Paulo, Indianópolis, [3]Hospital das Clínicas da Faculdade de Medicina de Ribeirão Preto, Ribeirão Preto, São Paulo, [4]Hospital das Clinicas de Ribeirão Preto, ribeirão preto, São Paulo, [5]University of São Paulo, Ribeirão Preto, São Paulo

Purpose

The present study aims to demonstrate the main imaging findings seen in the central nervous system in cases of infection by Paracoccidioides brasiliensis, a fungal agent, endemic in some areas of Brazil.

Materials and Methods

To enable radiologists to understand and interpret MRI common findings in this not so common pathology which can become an important differential diagnosis in specific cases.

Results

Cases from our own service will be reviewed to demonstrate the aspects most frequently identified in computed tomography and magnetic resonance, including advanced resonance sequences, such as perfusion and spectroscopy.

Conclusions

Paracoccidioidomycosis is a granulomatous disease of systemic presentation most commonly found in South American countries. Its transmission is related to the inhalation of fungal spores, mainly in rural patients. Although involvement by the disease occurs largely in the lungs and in the reticuloendothelial system, various manifestations are described, such as intestinal and bone manifestations, as well as central nervous system involvement, the main topic of this study. Frequent neurological symptoms include intracranial hypertension, headache, seizures and cranial nerve palsy. In imaging exams two forms of involvement are currently described: pseudotumoral and meningeal, the first being the most common. On computed tomography, hyper or hypoattenuating lesions may be observed, with annular or nodular enhancement. On magnetic resonance imaging, the lesions usually present with a predominance of hypointense T1 and T2, with annular or nodular enhancement, and the appearance of multiple grouped cysts may be seen, in addition to diffusion restriction and a double halo appearance in the SWI (susceptibility weighted imaging), also seen in pyogenic abscesses. In advanced sequences, spectroscopy shows a lipid peak and NAA reduction while perfusion shows rCBV reduction in T2 and slow and gradual T1 perfusion in DCE (dynamic contrast-enhanced) images. Reports of cases of paracoccidioidomycosis have increased in recent years with globalization, and recent studies show the importance of considering this diagnosis when the patient presents with specific risk factors and epidemiological criteria.

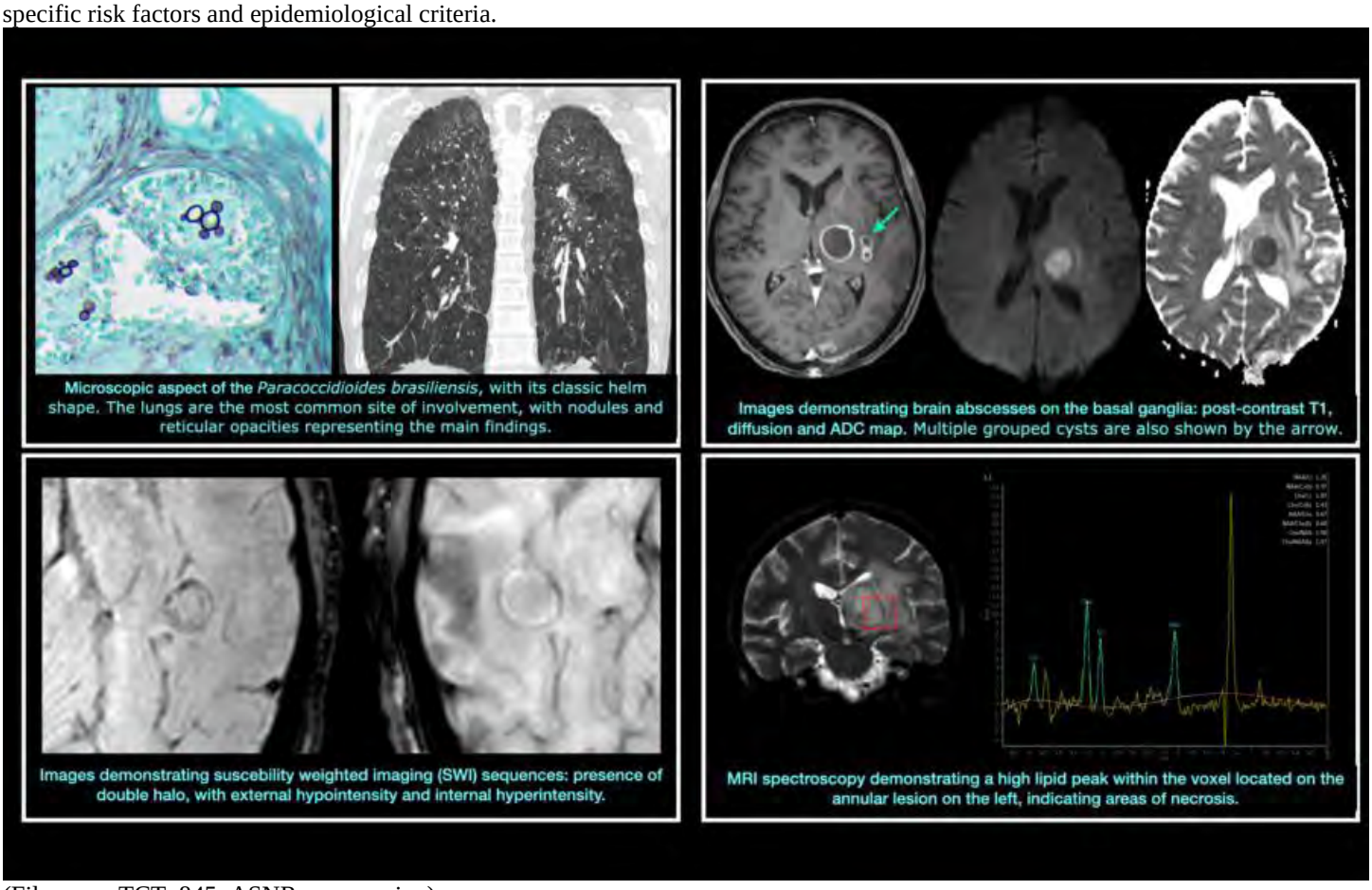

(Filename: TCT_845_ASNRparacoco.jpg)

592

Parathyroid Imaging: The 4th Dimension (CT) and Beyond

P Mazaheri[1], D Oppenheimer[2]

[1]Mallinckrodt Institute of Radiology, St. Louis, MO, [2]University of Rochester Medical Center, Rochester, NY

Purpose

Primary hyperparathyroidism (PHPT) is a common endocrinopathy caused by overproduction of parathyroid hormone, usually secondary to a single hyperfunctioning parathyroid adenoma or less commonly multiple adenomatous or hyperplastic parathyroid glands. The gold standard treatment for parathyroid adenoma is minimally invasive parathyroidectomy, which requires accurate pre-operative localization using diagnostic imaging to identify the abnormal gland(s). Imaging evaluation of PHPT often involves the use of sonography and Tc99m Sestamibi. 4-dimensional computed tomography (4DCT) has more recently emerged as a useful tool in the diagnostic assessment of PHPT, particularly in cases with equivocal or inconclusive results on sonography or sestabmibi, and after previous neck surgery or failed neck exploration. This electronic exhibit will review the anatomy of the parathyroid glands, discuss the role of imaging in PHPT, review the imaging findings of parathyroid disease on sonography, sestimibi and 4DCT, and discuss mimics and pitfalls in the interpretation of imaging studies in PHPT, with an emphasis on the use of 4DCT.

Materials and Methods

N/A

Results

N/A

Conclusions

N/A

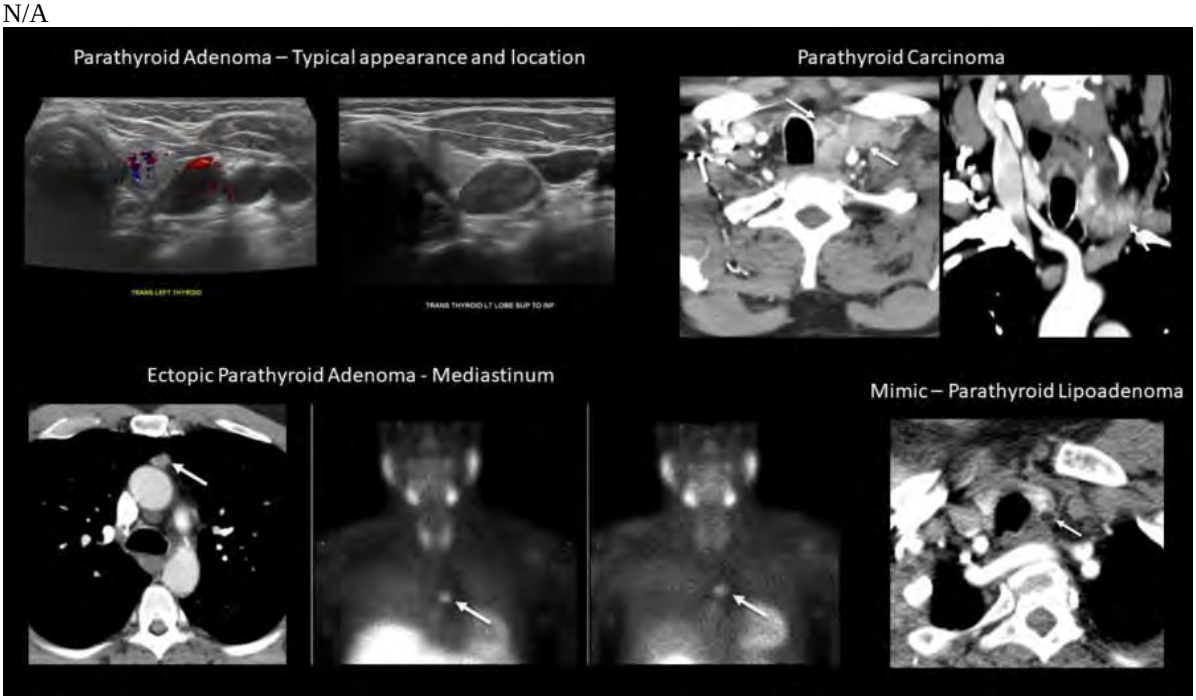

(Filename: TCT_592_ASNRabstract-Images.jpg)

1263

Parry Romberg Syndrome and Morphea En Coup de Sabre: What Radiologists Should know.

D Nunes[1], B Olivetti[1], C da Silva[2], D Fragoso[3], C Toyama[2], D Borges[4], R Gomes[1], E Gebrim[1], C Leite[5]

[1]University of São Paulo, São Paulo, São Paulo, [2]HCFMUSP - BRAZIL, São Paulo, São Paulo, [3]Instituto de Radiologia da Universidade de São Paulo, São Paulo, São Paulo, [4]Ipiranga Hospital, São Paulo, São Paulo, [5]University of São Paulo, Sào Paulo, São Paulo

Purpose

Parry Romberg syndrome (PRS), also called as progressive facial hemiatrophy (PFA), progressive hemifacial atrophy (PHA) and idiopathic hemifacial atrophy, is a rare and insidious acquired disease with hemiatrophy of the face, that characteristically involves the skin and subcutaneous connective tissues and may progress to the muscles, cartilage, and osseous structures. There is involvement of the central nervous system structures in up to 20% of patients. PRS has unknown etiology, but trauma, autoimmunity, infection, and autonomic dysregulation have all been suggested. It is often regarded as a subtype of localized scleroderma. Historically, a debate existed whether PRS is a form of linear scleroderma, called morphea en coup de sabre (ECDS), or whether these conditions are inherently different processes or appear on a spectrum. Currently, it is generally accepted that both diseases exist on a spectrum of localized scleroderma and often coexist. The majority of patients have initial manifestations in the first two decades of life and the

typical course of PRS is slow progression over 2-20 years and eventually reaching quiescence. Objectives: Literature review of the nomenclature, pathogenesis, imaging and treatment of these diseases.

Materials and Methods

• To teach radiologists about recognition of the imaging patterns of Parry Romberg Syndrome (Progressive hemifacial atrophy) and morphea en coup de sabre deformity, using CT and MRI imaging of the brain and head and neck. • Literature review of the nomenclature, pathogenesis and treatment of these diseases

Results

We retrospectively collected and anonymized cases of our institution, and described the manifestations of the diseases.

Conclusions

Typical facial imaging findings are different degrees of hemifacial atrophy with obliteration of fat planes, ipsilateral deviation of the aerodigestive tract, and enophthalmos due to loss of retrobulbar fat, without abnormal CT attenuation or MR signal. Typical brain findings are ipsilateral linear or discrete subcortical calcifications in the frontal lobe, white matter hypoattenuation on CT and hyperintense T2 signal on MRI, ipsilateral microhemorrhages and infarcts and ipsilateral focal or hemispheric brain atrophy. The proper radiology evaluation of multiple tissues of the face and brain contributes for proper diagnosis, differential diagnosis, treatment planning and monitoring disease progression and posttreatment response of localized scleroderma, Parry Romberg Syndrome and en coup de sabre lesion.

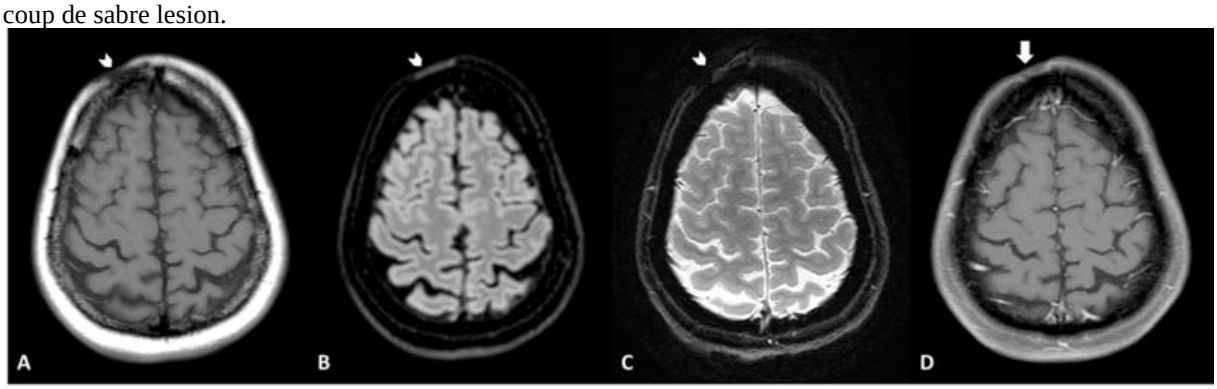

Fig. 1: MR images of a 45 year-old woman with linear scleroderma *en coup de sabre* without Parry Romberg Syndrome. Axial T1 (A), FLAIR (B) and GRE (C) weighted MR image demonstrate right frontal atrophy of the skin and subcutaneous fat (arrow head). D, Axial enhanced T1-weighted MR image demonstrates mild enhancement of skin and subcutaneous fat (thick arrow). There is no involvement of the central nervous system.

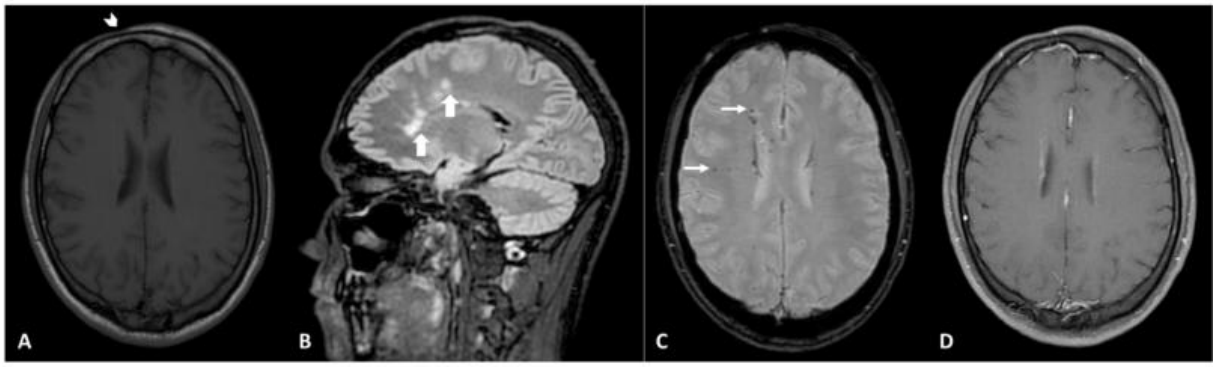

Fig. 2: MR images of a 36 year-old man with linear scleroderma. A, Axial T1-weighted MR image demonstrates right atrophy of the skin and subcutaneous fat (arrow head). B, Sagital FLAIR image demonstrates abnormal hyperintensity of the white matter in the right frontal corona radiata (thick arrow). C, Axial susceptibility-weighted image demonstrates innumerable punctate foci of susceptibility throughout the right cerebral hemisphere (thin arrows). D, Axial enhanced T1-weighted MR image does not demonstrate anomalous enhancement of skin and brain.

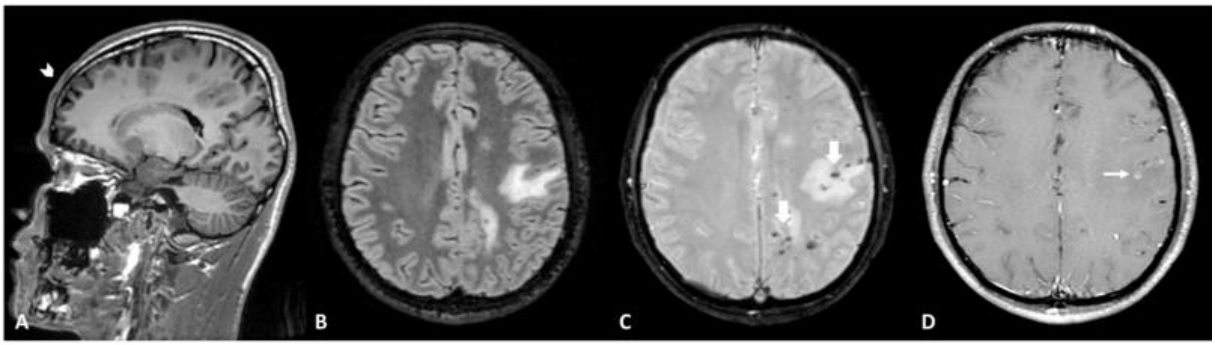

Fig. 3: MR images of a 29 year-old man with linear scleroderma *en coup de sabre* associated with Parry Romberg Syndrome. Sagital T1-weighted MR image (A) demonstrates right hemifacial atrophy primarily involving the skin and subcutaneous fat (arrow head). Axial FLAIR (B) and susceptibility-weighted (C) images demonstrate abnormal hyperintensity of the left frontal and parietal subcortical white matter with innumerable punctate foci of susceptibility (thick arrow), respectively. Axial enhanced T1-weighted MR image (D) demonstrates left frontal subcortical white matter lesion with enhancement (thin arrow).

(Filename: TCT_1263_Figure.jpg)

1534

Pearl and Pitfalls in Arterial Spin-Labelling MR imaging (ASL-MRI) in Various Intracranial Pathologic Condition

A Lee[1]

[1]Soonchunhyang University Bucheon Hospital, Bucheonsi, Korea, Republic of

Purpose

1) DSC-MRI versus ASL: In favor of ASL 2) ASL provides absolute quantification 3) ASL is totally non-invasive (no exogenous contrast agent), allows for repeated measurements in one subject 4) ASL is less sensitive to susceptibility artifacts 5) ASL is useful also outside the brain

Materials and Methods

1. To introduce the concept of Arterial Spin-Labeling Magnetic Resonance Imaging (ASL-MRI). 2. To present the category-based findings (CBF) of ASL-MRI for various conditions of the central nervous system (CNS) 3. To compare the findings of ASL-MRI with those of Dynamic Susceptibility Contrast Magnetic Resonance Imaging (DSC-MRI) 4. To summarize the ASL-MRI appearances based on relative CBF values and analyze the reason for the discrepancy between ASL-MRI and DSC-MRI.

Results

1. Explanation of the scheme of the perfusion imaging acquisition by ASL-MRI. 2. Presentation of the CBF of ASL-MRI in various conditions of the CNS: (1) stroke, (2) tumor, (3) infection, (4) seizure, (5) congenital disorder (Sturge–Weber Syndrome, Neurofibromatosis), and (5) other miscellaneous conditions (brain death, diffuse hypoxic injury, etc.) 3. Summation of the ASL-MRI appearances based on relative CBF values. 4. Explanation of partial discrepancy in findings of ASL-MRI and DSC-MRI.

Conclusions

Conclusion - Recent technical and post processing advances make ASL available for routine clinical practice. - Though several limitation and pitfall of ASL perfusion, can be implemented successfully into a routine clinical neuroimaging protocol and can accurately demonstrate alterations in brain perfusion.

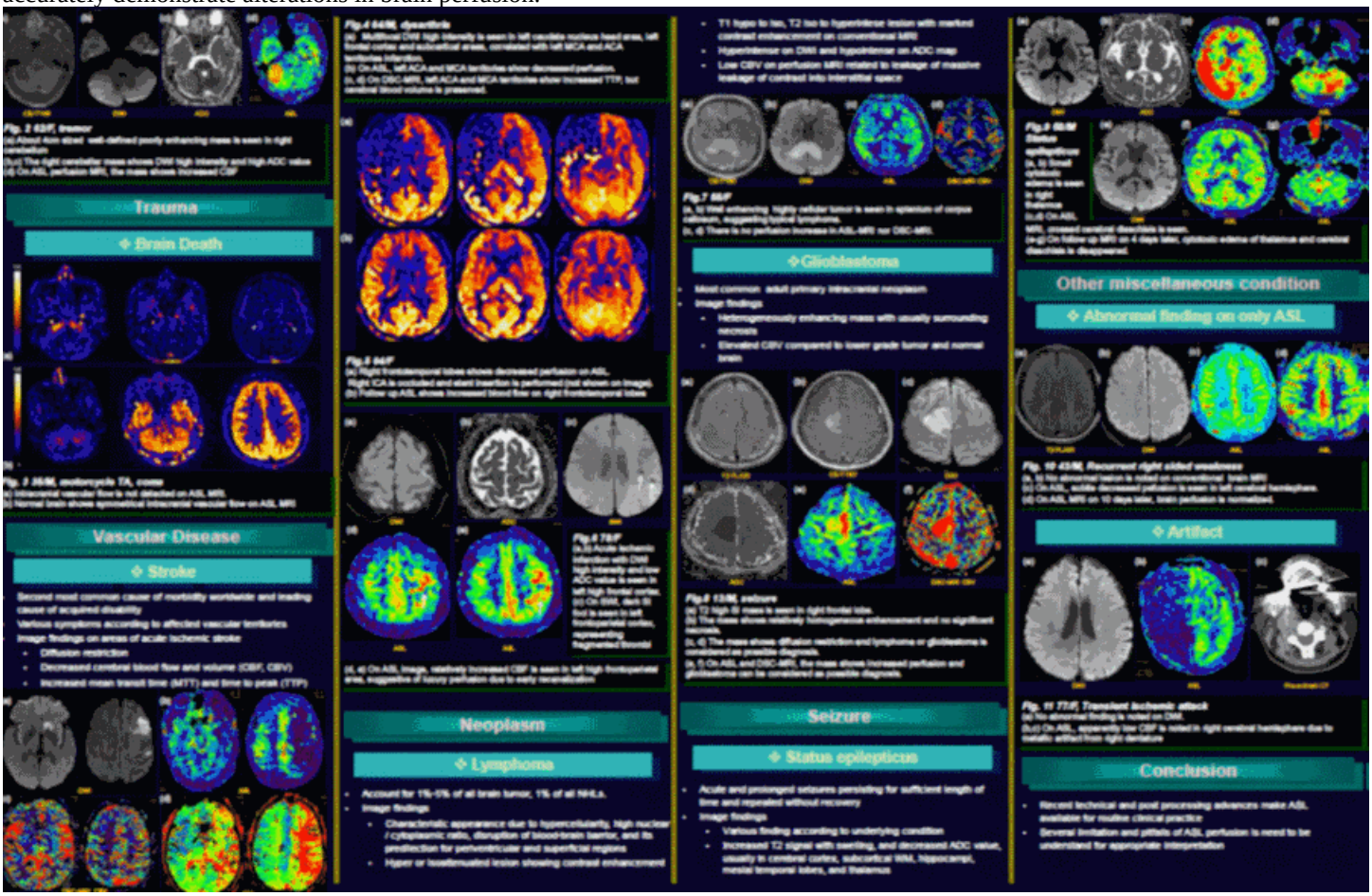

(Filename: TCT_1534_ASLvarious.gif)

780

Pearls and Pitfalls in Interpreting Images for IDH Wildtype and Mutant Glioma through Conventional and Advanced MR Technique

M LEE[1], F Sanvito[2], A Hagiwara[3], N Cho[3], B Ellingson[2], N Salamon[4]

[1]UNIVERSITY OF CALIFORNIA LOS ANGELES, Los Angeles, CA, [2]University of California, Los Angeles, Los Angeles, CA, [3]David Geffen School of Medicine at UCLA, Los Angeles, CA, [4]University of California Los Angeles, Los Angeles, CA

Purpose
- Overview of isocitrate dehydrogenase genotyping with underlying pathophysiology and clinical prognosis - Review similarities and differences of conventional and advanced MR imaging features of IDH wildtype and mutant glioma - Identify potential pearls and pitfalls when interpreting the images, especially in the setting of determinizing true progression from pseudoprogression - Introduce novel MRI techniques using new biomarkers that can be helpful to distinguish IDH wildtype and mutant tumors
Materials and Methods
After viewing this exhibit, the reader will be familiar with genetic basis of IDH mutation status in gliomas and its clinical relevance. The reader will also learn imaging features that can help differentiate IDH wildtype from IDH mutant tumors, and the pearls and pitfalls to assess treatment response accurately.
Results
- Overview of the isocitrate dehydrogenase (IDH) genotyping • Isocitrate dehydrogenase (IDH): enzyme normally involved in tricarboxylic acid (TCA) cycle ♣ Mutation in IDH leads to reprogramming of cellular metabolism and interferes with DNA methylation • Clinical significance ♣ IDH mutant with better response to chemoradiation and longer survival than wildtype - Similarities and differences of MR imaging features of IDH wildtype and mutant glioma • Location ♣ IDH mutant with frontal lobe predominance • Enhancement pattern ♣ IDH mutant often with no or decreased enhancement • T2W/FLAIR ♣ T2-FLAIR mismatch sign • Diffusion-weighted imaging ♣ Minimum ADC and relative ADC were significantly higher in IDH mutated grade II and III astrocytomas than in IDH wild-type tumors • Perfusion-weighted imaging with focus on DSC and ASL technique - Potential pearls and pitfalls when interpreting the images, especially in the setting of treatment response - Novel MRI techniques using new biomarkers • pH- and oxygen-sensitive MR imaging technique ♣ IDH mutant tumor reprograms metabolism to rely less on glycolysis, causing decreased acidity and decreased hypoxia compared to wildtype tumors
Conclusions
Genotyping of gliomas for IDH status has become essential aspect of clinical practice. Conventional and advanced MRI techniques including diffusion and perfusion-weighted imaging can provide valuable information to distinguish between IDH mutant and wildtype gliomas. But just as importantly, MRI is essential for evaluating treatment effects and differentiating recurrent tumors from pseudoprogression or radiation necrosis.

247
Pediatric Neuro 101: Top thirty diagnosis based on Sagittal T1
N Supakul[1], I Wu[2]
[1]Riley Hospital for Children, Indiana University school of Medicine, Indianapolis, IN, [2]Indiana Unversity, Carmel, IN

Purpose
This educational poster aims to provide a systemic approach for the trainees and neuroradiologists when reading pediatric MRI studies. Sagittal T1 sequence is a key anatomical image, that provides more than 80% of diagnosis.
Materials and Methods
• To review normal anatomy and basic embryonal development on sagittal T1 brain MRI • To demonstrate 6 steps imaging checklist in pediatric brain MRI • To highlight 30 pathologies based on 6 step imaging checklists with key imaging findings
Results
Table of Contents: 1. Normal anatomy on sagittal T1 brain MRI 2. 6 Steps imaging checklists including: 1) Foramen magnum 2) Midbrain, pons and medulla oblongata 3) Posterior fossa 4) Pituitary gland, pituitary stalk, and hypothalamus 5) Pineal gland and tectum 6) Corpus callosum 3. Basic embryonal development of the key structures will be displayed including development of the pituitary gland, corpus callosum and posterior fossa. 4. Differential diagnosis with key imaging findings on each step will be demonstrated. 1) Foramen magnum: Chiari I malformation, intracranial hypotension 2) Midbrain, pons and medulla: Intracranial hypotension, Pontine tegmental cap dysplasia, "Kinked brainstem", Pontocerebellar hypoplasia 3) Posterior fossa: Dandy Walker malformation, Mega cisterna magna, Blake pouch cyst, Chiari II (or III) malformation, Arachnoid cyst, Pituitary gland, pituitary stalk and hypothalamus: Intracranial hypertension, Pars intermediate cyst, Rathke cleft cyst, Ectopic posterior pituitary gland with septo-optic dysplasia spectrum, Thickening of pituitary stalk with top 3 differential diagnosis based on age group, Hypothalamic hamartoma, Kallman syndrome, Craniophyarngioma 4) Pineal gland and tectum: Pineal cyst, Pinealoblastoma, Pinealocytoma, Germinoma, Tectal plate glioma, Cerebral aqueduct stenosis. 5) Corpus callosum: Corpus callosal agenesis or dysgenesis, Holoprosencephaly spectrum 5. Challenging cases
Conclusions
1. Sagittal T1 image is a key anatomical image for brain MRI particularly in pediatric patients which many pathologies are related to developmental anomaly. 2. Understanding the embryonal development of the key structures (pituitary gland, corpus callosum and posterior fossa) is crucial to get a correct diagnosis. 3. It is important to have a step by step approach and imaging checklist on each step to recognize characteristic imaging findings and guide for further evaluation.

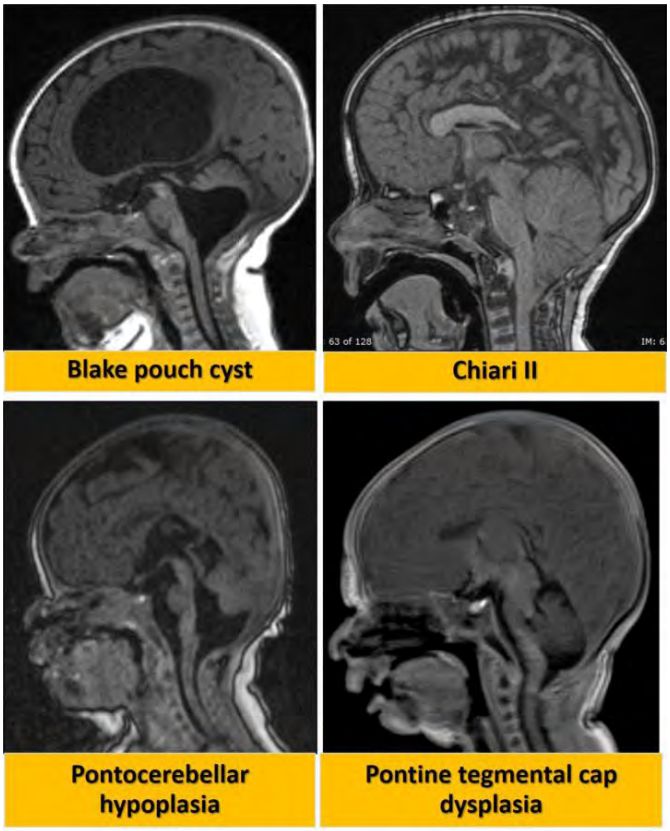

(Filename: TCT_247_SagittalT1.jpg)

961

Pediatric Neurovascular Abnormalities – A Pictorial Essay

I Alves[1], A Vieira[1], C ALVES[2], G Bandeira[3], C Amancio[1], M Docema[1], D Delgado[1], H Lee[1], S Ferraciolli[4], L Lucato[5], C Leite[6], M MARTIN[1]

[1]Hospital Sírio-Libanês, São Paulo, São Paulo, [2]Children's Hospital of Philadelphia, Philadelphia, PA, [3]Faculadde de Medicina da Universisdae de São Paulo, Sao Paulo, Sao Paulo, [4]InRad - HC- FMUSP, São Paulo, São Paulo, [5]Instituto de Radiologia, Hospital das Clínicas da Faculdade de Medicina da Universidade de São Paulo, São Paulo, São Paulo, [6]University of São Paulo, Sào Paulo, São Paulo

Purpose

The neurovascular diseases is much less common in children than in adults and it corresponds a small part of pediatric pathologies. This group of diseases is heterogeneous, including pathologies of genetic origin to idiopathic ones, they can be classified according to their vascular etiology in arterial, venous and arteriovenous disease. It has a several clinical presentations and varied management. Although many of these diseases are rare, they should be included in the differential diagnosis of strokes and hemorrhages. Because of this high complexity and variety of pathologies, the diagnosis becomes a challenge and the radiologist must be aware of the main imaging characteristics to assist the most appropriate approach. So, the main objective of this exhibit is to illustrate in a didatic way these vast group of pathology, review the intracranial vascular anatomy and highlight the imaging features of each pathology.

Materials and Methods

The purpose of this study is to: - To show in an educational and systematic way the childhood neurovascular diseases - To classify the pediatric vascular pathologies in different etiology groups based on genetic and pathophysiological mechanisms - To illustrate with imaging presentation the main etiology groups and highlight the key imaging findings that help the differential diagnoses among the etiologic groups

Results

We will illustrate in a pictorial essay based on cases and original drawings, vascular anatomy of the central nervous system and the main characteristics of images of pediatric neurovascular diseases.

Conclusions

Pediatric neurovascular diseases are rare and have a varied clinical presentation, just as the management of these diseases is diverse. Therefore, due to the vast form of presentation of these diseases we propose to present in a grouped and didactic way these pathologies to facilitate the radiological reasoning and the diagnosis according to the imaging findings and clinical presentation.

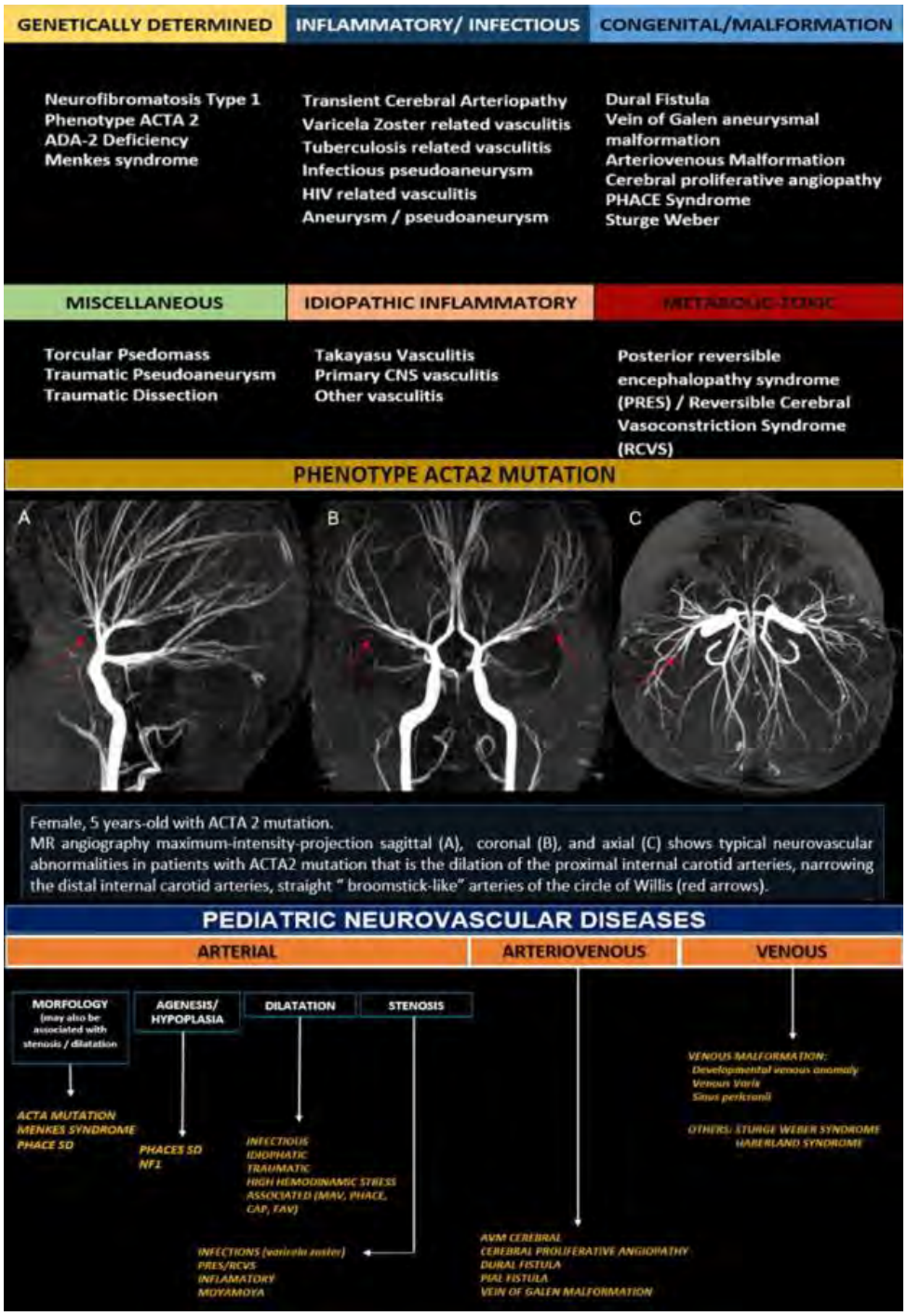

(Filename: TCT_961_5.jpg)

1169

Pediatric Spinal Lesions: Ultrasound and MRI Correlation

K Gupta[1], J Becker[1], T Chandra[2], U Udayasankar[1]
[1]University of Arizona, Tucson, AZ, [2]Nemours Children's Healthcare System, Orlando, FL

Purpose

N/A

Materials and Methods

A wide variety of pathologies can involve the spine in the pediatric age group. The wide availability of ultrasound, lack of need for sedation and its lack of ionizing radiation makes it a first line modality for evaluation of spine in children. MRI provides the ability to evaluate these lesions further and facilitates pre-surgical planning. In this educational exhibit we review the clinical indications, technique and protocol for ultrasound and MRI and discuss the normal anatomy, frequently encountered variants and pathology of the lumbosacral spine in neonates and young infants with ultrasound and MRI correlation.

Results
Using several case-based examples, we will provide an overview of anatomy of the pediatric spine, as seen on ultrasound and MRI. We will also illustrate normal variants that are often misinterpreted, such as ventriculus terminalis, filar cyst, pseudo-sinus tract and transient dilatation of the central canal. Pathological processes that involve the spine will also be illustrated with ultrasound and MRI.
Conclusions
Result: Proper identification of the vertebral levels is crucial for determining the position of the conus medullaris. We will discuss different methods by which vertebral levels can be identified on ultrasound. Ultrasound is very useful for evaluation of pathological processes such as tethered cord, spinal dysraphism, spinal lipoma, diastometamyelia and dermal sinus tract etc. Some of these pathologies are subsequently assessed by MRI. We will provide MRI correlation with ultrasound with case-based examples. We will also briefly discuss the technique of ultrasound guided lumbar puncture with illustrative examples. Conclusion: With its recent advances, the accuracy of ultrasound is comparable to MRI, which remains the gold standard. Knowledge of spinal anatomy and variants on ultrasound enables radiologists to guide clinical colleagues when follow up imaging or MRI is needed and to appropriately guide patient management.

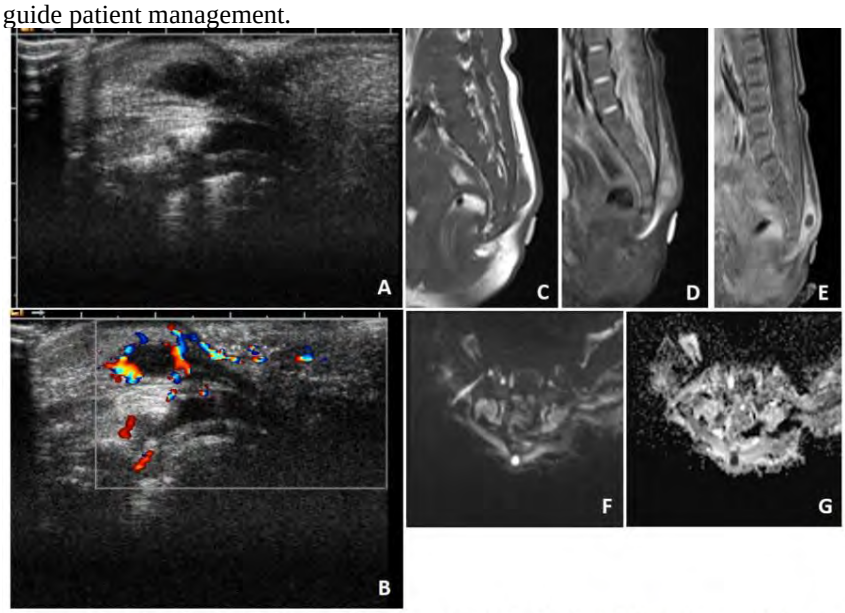

Figure showing the radiological findings of infected pilonidal sinus. A and B are the axial gray scale ultrasound and color doppler image of the tailbone depicting a cystic collection with color flow in the periphery. C to E is mid-sagittal MRI showing fluid filled rim enhancing tubular fistulous track. F and G demonstrate the sinus tract in axial plane with central restricted diffusion, in keeping with an abscess.

(Filename: TCT_1169_Image.jpg)

1026

Pediatric Supratentorial Brain Tumors: The 2021 World Health Organization Classification

G Bandeira[1], L TEIXEIRA[1], I Alves[2], L Bezerra[1], L Godoy[3], C Rimkus[1], A Ayres[1], S Ferraciolli[1], G dos Santos[1], M MARTIN[1], C Leite[1], L Lucato[1]

[1]Instituto de Radiologia da Universidade de São Paulo, São Paulo, SP, [2]Hospital Sírio-Libanês, São Paulo, SP, [3]Faculdade de Medicina da Universidade de São Paulo- FMUSP, São Paulo, SP

Purpose
Introduction Oncogenesis in CNS Main tumor pathways involved in supratentorial tumors in pediatric patients The 2021 WHO Classification of Tumors of the Central Nervous System Genetic and molecular profiles of hemispheric and midline pediatric supratentorial tumors and radiogenomics Illustrative cases of pediatric supratentorial brain tumors Take-home messages Conclusion References The purpose of this exhibition is to review the 2021 WHO classification of supratentorial brain tumors in pediatric patients.
Materials and Methods
The purpose of this exhibit is: To review the oncogenesis of primary brain tumors. To understand the main molecular pathways involved in pediatric supratentorial brain tumors. To integrate the knowledge of the oncogenesis with the new molecular parameters of fifth edition of the WHO Classification of Tumors of the Central Nervous System. To review the applications of radiogenomics (phenotypic and the genotypic key features) of midline and hemispheric pediatric type supratentorial tumors.
Results
For this educational exhibit we searched the teaching files of two academic institutions for supratentorial brain tumor in pediatric patients.

Conclusions
Central Nervous system (CNS) tumors continue representing a significant source of morbidity and mortality in the pediatric population and over half of pediatric CNS tumors arise in supratentorial region. The fifth edition of the WHO Classification of Tumors of the Central Nervous System (WHO CNS5) was updated in 2021 and included new molecular diagnostic parameters to many supratentorial pediatric tumors. The knowledge of the oncogenesis of primary supratentorial brain tumors is useful for understanding the WHO CNS5. The radiologist should be familiar with the new classification of supratentorial brain tumors in pediatric patients, as well as the advances in radiogenomics related to this group of tumors.

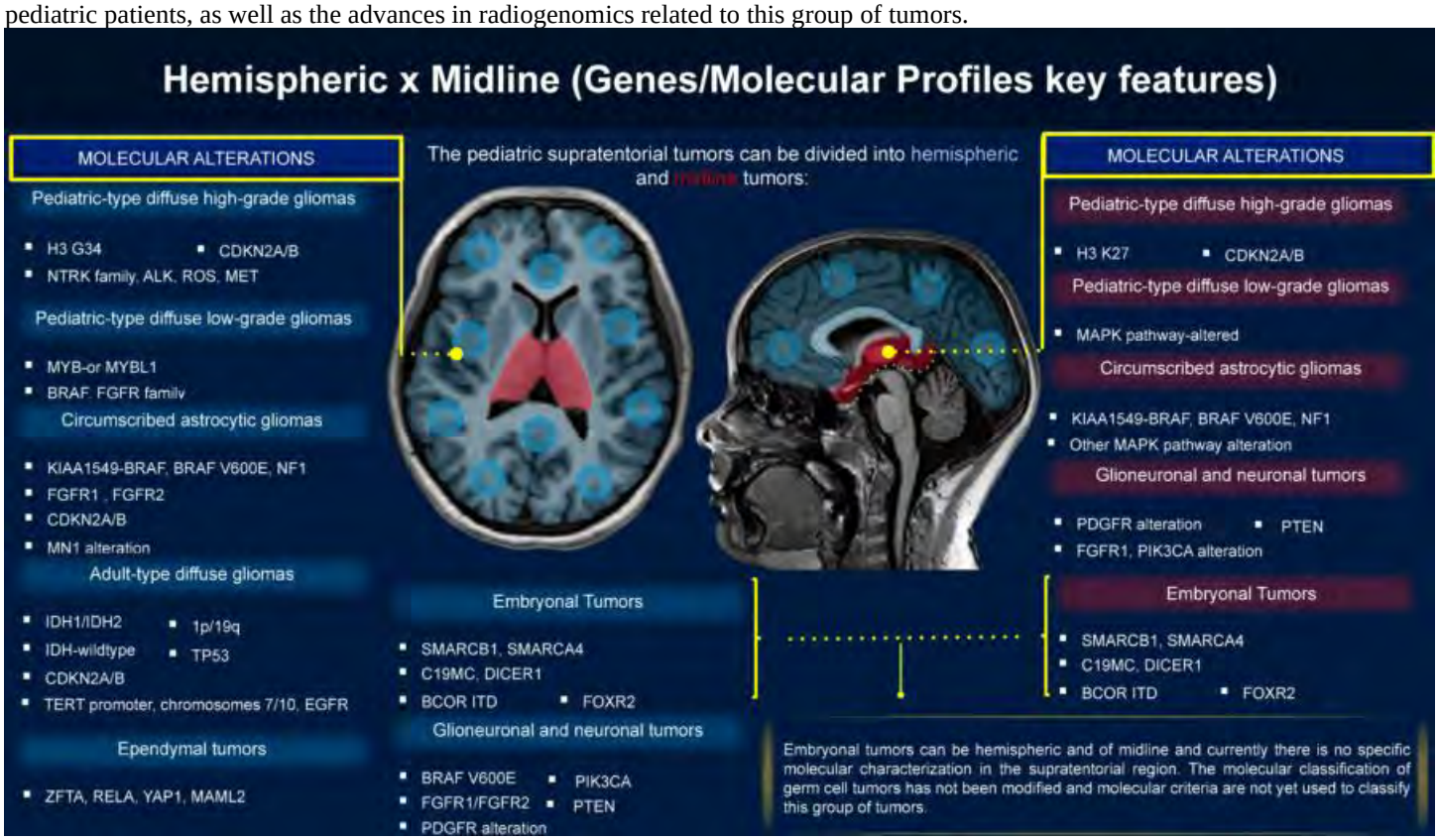

(Filename: TCT_1026_SUPRATENTORIAISPEDIATRICOSASNR.jpg)

166
Perfusion Confusion: Technical and Interpretive Pitfalls of Automated CT Perfusion for Acute Stroke
V Jain[1], M Ma[1]
[1]*Santa Clara Valley Medical Center, San Jose, CA*

Purpose
Based on the DAWN and DEFUSE-III trials, 2018 AHA guidelines extended the thrombectomy treatment window for ischemic stroke to 6-24 hours, and hence opened opportunity for CT perfusion (CTP) use within 24 hours for selected patients. In the past 3 years, automated CTP analysis has developed a dominant role in clinical practice far beyond comprehensive stroke centers. Given the time-sensitivity and importance of accurate imaging results for stroke management, the radiologist must be able to quickly recognize common errors and navigate dilemmas encountered in CTP use. Educational Objectives: 1. Recognize technical pitfalls in the acquisition and processing of CTP images. 2. Identify methods to prevent and address such quality control issues. 3. Understand interpretive pitfalls leading to under- or overestimation of ischemic tissue. 4. Use clinical information and anatomical evaluation to recognize mimics of stroke.
Materials and Methods
This presentation offers a case-based review of common difficulties encountered in CTP analysis for acute stroke. It also provides strategies to help the radiologist address such pitfalls.
Results
Automated CTP analysis by RapidAI was integrated into acute stroke imaging protocols. 446 cases performed 2020-2021 were retrospectively reviewed in the context of clinical information, non-contrast CT data, and MRI data. Examples of technical and interpretive issues were collected.
Conclusions
Multiple technical pitfalls of automated CTP analysis are seen in clinical practice, with distinct routes for prevention and amelioration. Regarding patient positioning, head tilt may mimic pathology, while motion degrades perfusion data. Limited slab coverage may miss infarct beyond the field of view. Contrast bolus flow abnormalities range from patient-related factors to procedural issues. At post-processing, poor selection of arterial input and venous output functions can also cause errors. For accurate interpretation, it is crucial

to be familiar with various pathologies and with the limitations of CTP. For example, small or very early infarcts may be undetectable, and reperfusion by collaterals may reduce apparent infarct size. Chronic infarcts and chronic stenosis must be distinguished from acute infarcts. Various mimics, from seizures to anatomic variants, must be considered based on clinical context and review of CTA and CTP source images. To guide treatment as part of a stroke care team, the radiologist must be able to navigate the challenges of increasingly frequent CTP use.

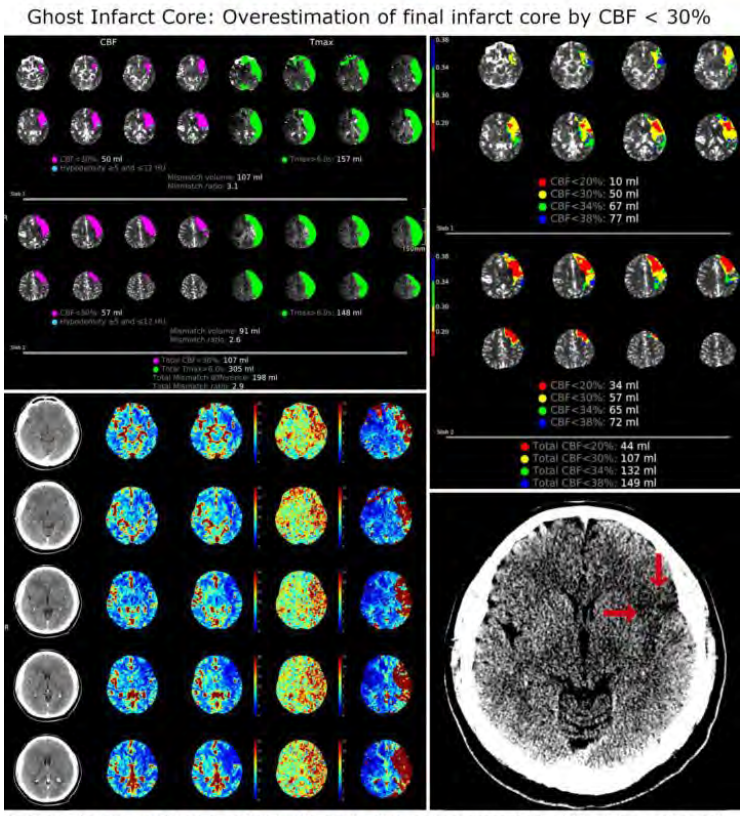

CTP and follow-up CT on a patient with acute stroke who presented within 1 hour of onset. Left: RapidAI CTP analysis shows estimated infarct core of 107 mL and mismatch volume of 198 mL. The area of prolonged Tmax correlates with the area of prolonged MTT. Right: On follow-up CT head, the area of infarct at the left operculum and insula (red arrows) more closely matches the area on CTP with CBF < 20% rather than CBF < 30%.

(Filename: TCT_166_GhostInfarctCore3.jpg)

742

Perinatal Stroke as it is: Updates, insights and challenges.

A Server Alonso[1], A Latysheva[1], B Nedregaard[1], A Roennestad[1], L Heiberg[1], P Marthinsen[1]
[1]*Oslo University Hospital, Oslo, Oslo*

Purpose

The aim of this educational exhibit is: 1. To provide an update on the current knowledge of the role of neuroimaging in diagnosis and long-term prognosis of perinatal stroke diseases, highlighting their similarities and distinctions in etiology and outcome. 2. List and describe the six types of perinatal stroke on the basis of clinical presentation and neuroimaging findings. 3. To establish and discuss a neuroimaging pathway for suspected neonatal stroke. 4. To understand the disease-specific pathophysiology and further discuss the microglial role in perinatal arterial stroke.

Materials and Methods

N/A

Results

We reviewed MRI findings in neonates and fetuses with perinatal stroke. These cases include 1) acute symptomatic perinatal stroke: neonatal arterial ischemic stroke (NAIS), neonatal hemorrhagic stroke (NHS), neonatal cerebral sinovenous thrombosis (CSVT); 2) presumed perinatal ischemic stroke: arterial presumed ischemic stroke (APPIS), periventricular venous infarction (PVI), presumed perinatal hemorrhagic stroke (PPHS).

Conclusions

Diagnosing perinatal stroke can be challenging because of its nonspecific presentation. MRI is performed to confirm a diagnosis of perinatal stroke, for defining the extent of tissue involvement, to determine a potential etiology (maternal, intrapartum and neonatal risk factors), suggest the timing of the insult, exclude stroke mimics, follow stroke evolution, help in treatment decisions, and for the prediction of outcome. We discuss the suggested neuroimaging pathway for suspected neonatal stroke subtypes and review the core recommended sequences (DWI, SWI, T1 and T2-weighted imaging, MRA and MRV, more novel sequences as pCASL; rarely,

catheter angiography), as well as the utility of follow-up imaging. We also discuss the pathophysiology and the neuroimaging features of neonatal subpial hemorrhage with underlying cerebral infarct, an entity that is underreported and poorly understood. We further discuss the potential mechanisms of brain injury and repair unique to the newborn brain, including new insights in the role of microglia as a key cell target for neuroprotection in perinatal brain injuries. Conclusion: There are six different types of perinatal stroke disease based on neuroimaging and clinical presentation. Neuroimaging is essential for making the correct diagnosis and will continue to be an essential component of patient management in concert with clinicians. This will provide the best possible outcomes for neonates affected by perinatal stroke.

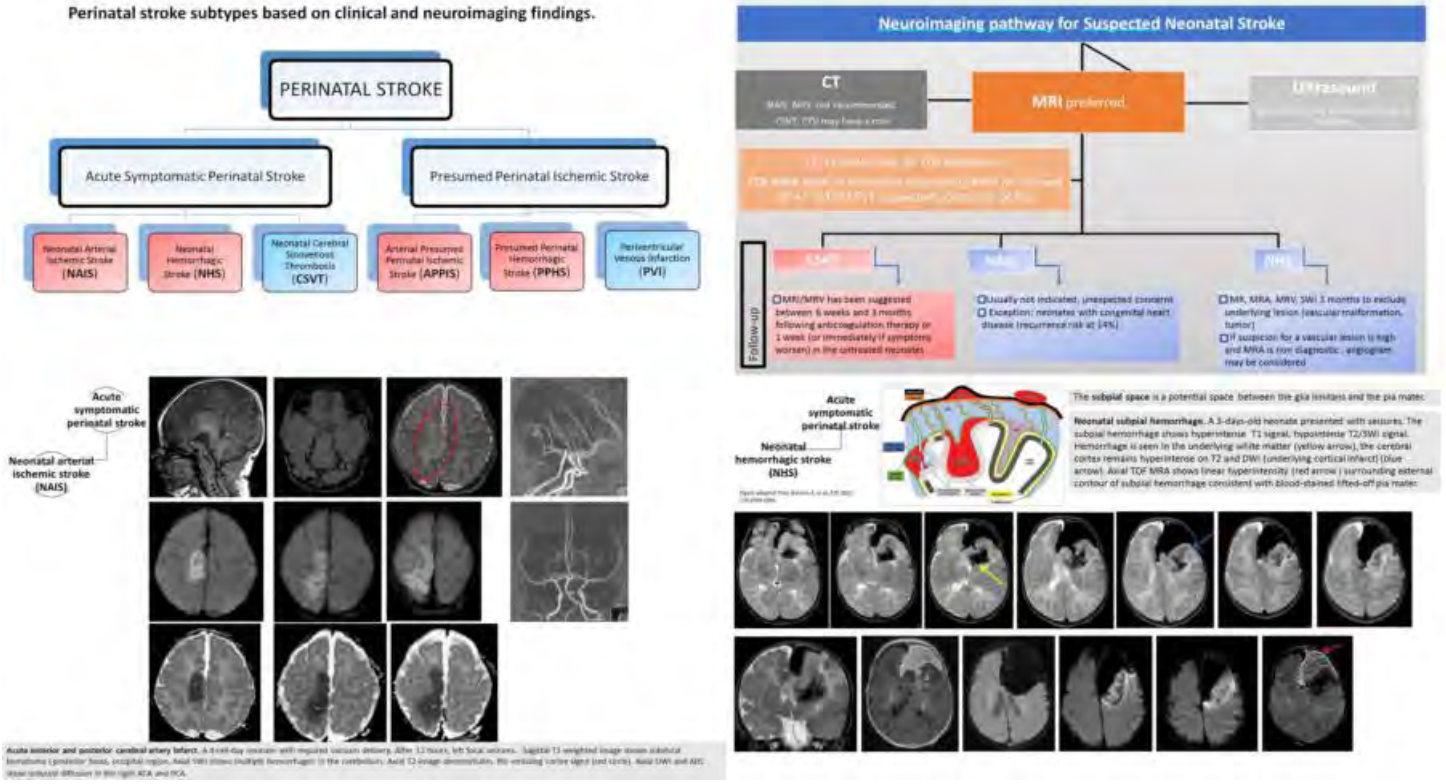

(Filename: TCT_742_Perinatalstroke_images_ver2.jpg)

502

Perivascular Spaces: Microanatomy, Homeostasis, and Pathophysiologic Mechanisms of Disease.

E Zamora[1], C Zamora[2]

[1]Montefiore Medical Center, Bronx, NY, [2]UNC Department of Radiology, Chapel Hill, NC

Purpose

As part of the glymphatic system, the perivascular spaces serve an important role in cerebral homeostasis. They also constitute important routes for the spread of inflammatory and neoplastic processes and are an imaging marker of neurodegenerative disorders. Perivascular spaces can rarely be large and tumefactive mimicking neoplasia in some patients. At the end of this exhibit, the reader will be familiar with the microstructure of the perivascular spaces (PVS) and glymphatic system, their role in homeostasis, and the pathophysiologic mechanisms leading to imaging findings.

Materials and Methods

To familiarize the reader with the microstructure of the perivascular spaces (PVS) and glymphatic system, their role in homeostasis, and the pathophysiologic mechanisms leading to diagnostic findings on MRI.

Results

This will be an image-rich educational exhibit based on a collection of illustrative cases from two academic institutions. Etiologies will be categorized into inflammatory, infectious, structural/traumatic, congenital, and neoplastic.

Conclusions

PVS are microscopic fluid-filled pial-lined structures surrounding small blood vessels in the brain. As part of the glymphatic system, they have a crucial role in homeostasis and clearance of cellular waste products. (1, 2) It is believed that REM sleep serves an important role in PVS waste clearance (3). In neurocognitive disorders, cognitive decline has been associated with visualization of PVS in the centrum semiovale in Alzheimer's disease, and basal ganglia in Parkinson's disease. (4) Enlarged PVS are also imaging markers of cerebral amyloid angiopathy and are a recognized feature of mucopolysaccharidoses. The glymphatic system is believed to play a key role in inflammation and antigen processing. Infectious conditions such as neurosyphilis, cryptococcosis, or neuroborreliosis may manifest with perivascular lymphocytic infiltration. Similarly, inflammatory conditions can present with multifocal involvement (e.g., neurosarcoidosis or multiple sclerosis), while others have a tendency to be more localized (e.g.,

CLIPPERS).(5) Less commonly, vasculitides and neoplasia may spread via PVS. Finally, although PVS can present with an atypical tumefactive appearance that may simulate neoplasia, their location and imaging characteristics allow an adequate diagnosis in most situations.

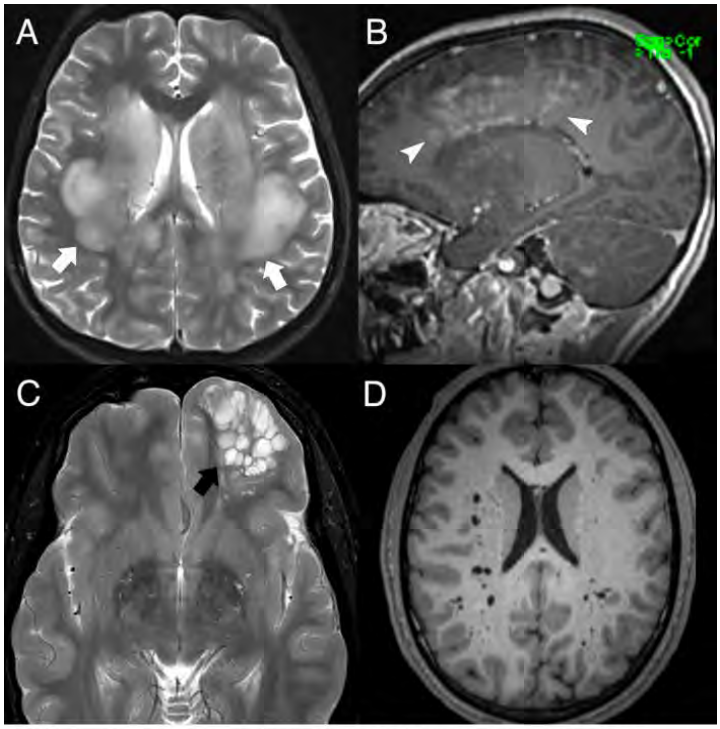

(A, B) Anti-myelin oligodendrocyte glycoprotein (anti-MOG) encephalitis: Axial T2-weighted image **(A)** in a 10-year-old female presenting with cognitive decline and ataxia demonstrates bilateral, mildly tumefactive white matter signal abnormalities (white arrows). Sagittal postcontrast T1-weighted image in the same patient **(B)** shows inflammatory changes with radial linear enhancement along the perivascular spaces (white arrowheads). **(C)** Giant tumefactive perivascular space mimicking tumor in a different patient: Axial T2 image shows a multicystic appearing mass in the left frontal lobe (black arrow). **(D)** Hunter syndrome in a different patient: Axial noncontrast T1 demonstrates prominent perivascular spaces in the deep and subcortical white matter as well as corpus callosum.

(Filename: TCT_502_abstractfigure.jpg)

902

PET and MRI for Assessment of Radiation-induced Cognitive Decline

T Verma[1], H Shooli[2], D Ramakrishnan[3], A FRANCESCHI[4], M Aboian[5]

[1]Yale School of Medicine, Ossining, NY, [2]Department of Radiology and Biomedical Imaging, Yale University School of Medicine, New Haven, CT, [3]Yale School of Medicine, Las Vegas, NV, [4]Northwell Health, New York, NY, [5]Yale University, Woodbridge, CT

Purpose

Radiation-induced cognitive dysfunction has been demonstrated in 50-90% of brain tumor patients receiving radiotherapy. The affected cognitive functions include learning, memory, processing speed, attention, and executive function. Previously undetected signs of irradiation damage can translate to long term and potentially permanent effects. In order to better elucidate the mechanisms of radiation-induced cognitive decline, we performed a literature review on the various methods used to study this phenomenon in clinical and pre-clinical studies.

Materials and Methods

We sought to discuss the various methods used for the assessment of cognitive decline as a result of brain tumor radiotherapy.

Results

Using PubMed, we performed a literature review with the following key terms: cognitive decline, MRI, PET, and synaptic density. We identified 5 articles. This review was focused on MRI methods, PET methods and tracers, cognitive testing in humans and rodents, and pathologic measures of synaptic density.

Conclusions

Our educational exhibit describes methods by which identify or quantify cognitive decline in brain tumor patients as a result of brain tumor radiotherapy. We discuss the neurocognitive tests for attention and processing speed, memory, and executive function that are standardized for clinical use. We also explore the effectiveness of various imaging methods in quantifying cognitive decline through the measurement of several structural and molecular parameters, including white matter damage through Diffusion Tensor Imaging (DTI), cerebral microbleeds through longitudinal MRI, as well as volumetric measurements of brain volume via quantitative MRI. Finally, we describe FDG-PET methods for determining the level of neurosynaptic activity and SV2A for studying synaptic density

loss in neurodegeneration. Overall, We present a variety of PET and MRI methods for studying radiation-induced cognitive decline as well as describe their respective results in clinical and pre-clinical studies.

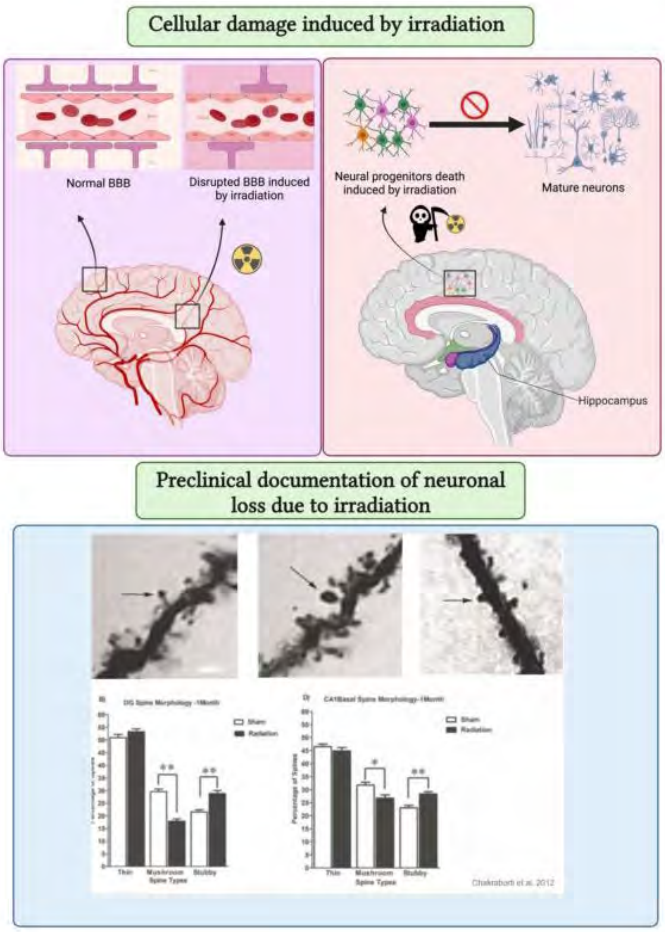

(Filename: TCT_902_ASNR2022Figure.jpg)

570

Photorealistic depiction of intracranial tumors using cinematic rendering of volumetric MRI data for pre-surgical planning and patient education.

D Lakhani[1], A Al-Hallak[1], A Tarabishy[1], G Deib[1]
[1]*West Virginia University, Morgantown, WV*

Purpose

Implication of Cinematic Rendering in: 1. Assess spatial relationship of tumor with surrounding cortex, vascular structure and surface landmarks, for optimal pre-operative planning, in 3 dimensional space 2. Assess intrinsic characteristics and component of tumor in 3 dimensional space 3. Assess peri-tumoral brain parenchyma

Materials and Methods

Cinematic Rendering (CR) incorporates a complex lightening model that allows for the creation of photorealistic models from the reconstruction of isotropic 3D imaging data, by utilizing a complex algorithm [1,2]. The purpose of this study was to assess implications of Cinematic Rendering in Neuroimaging with focus on intracranial tumors and pre-surgical planning utilizing MRI data. Whilst CR algorithm has mostly been used to depict CT data, its use in depicting the brain utilizing MRI data is not well documented in the literature [1-3].

Results

We present 3D reconstructed images on series of cases with intracranial tumor. Isotropic, high-resolution volumetric T1 MPRAGE 3T MRI images on all patients with intracranial tumor were collected. 3D Cinematic Rendering was performed utilizing "Anatomy Education Siemens, Munich, Germany". The goal was to enable a comprehensive understanding of relationship of brain tumor with an individual patient's cortical surface anatomy, dural-based structures and scalp landmarks for optimal pre-surgical planning.

Conclusions

In a series of cases with intracranial tumors, we observed that users can accentuate the appearance of structures by changing the display settings on the CR reconstructions utilizing MRI data. Consequently, visualization of cortex to white matter, brain surface to vessels, subarachnoid space to cortex and skull to intracranial structures can be optimized. Layers of the overlying soft tissue can be progressively removed to provide a comprehensive assessment of the entirety of the region of interest in our case brain tumor. CR

models can be enlarged, rotated and shifted arbitrarily. In the context of the brain surface, there are several benefits to utilizing this technology. Complex, small structures can be demonstrated in very high detail. The depth and architecture of the sulci can be better appreciated than on traditional imaging modalities. With appropriate display settings, the relationship of the cortical surface to the adjacent vasculature can also be delineated.

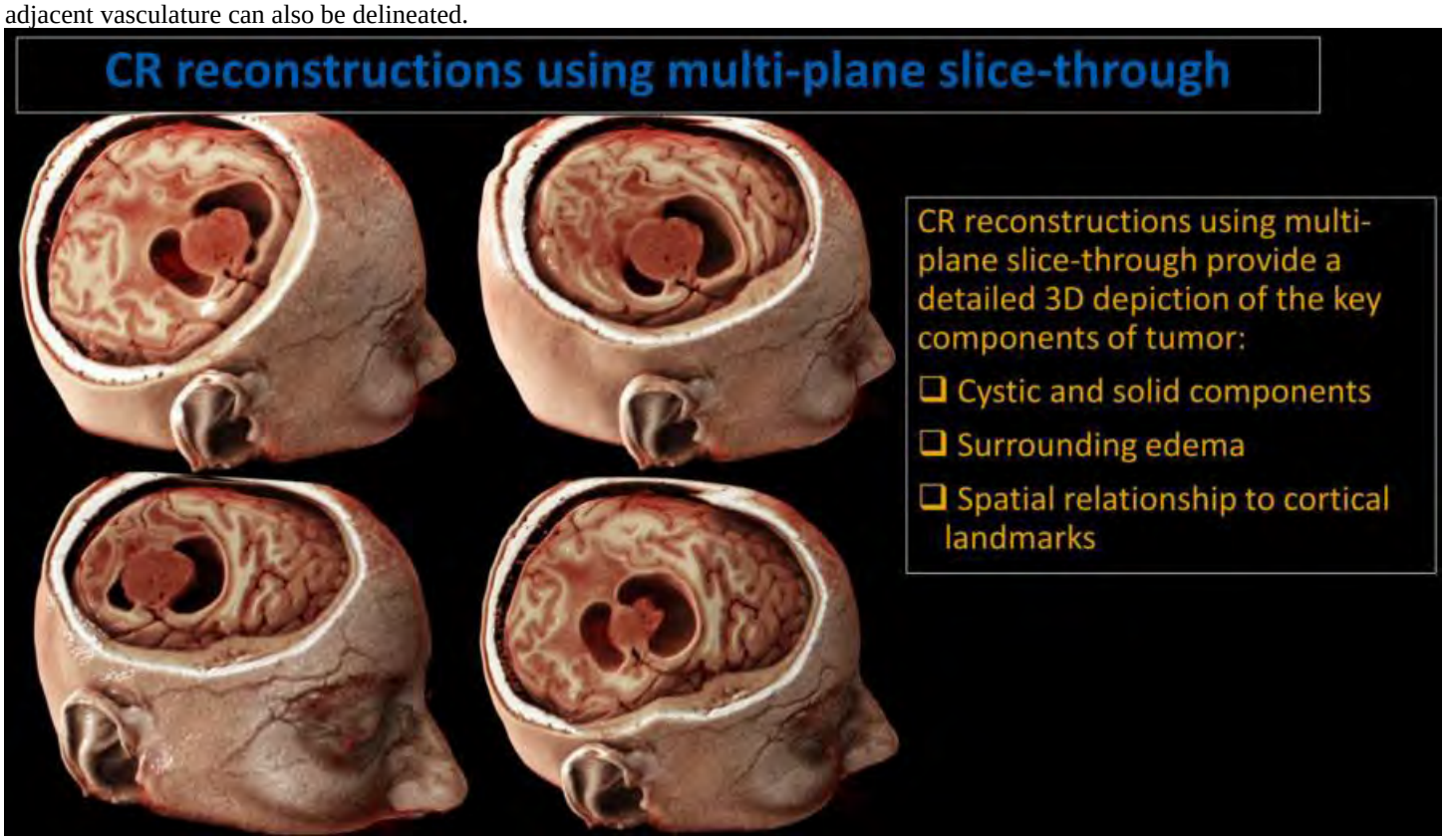

(Filename: TCT_570_2021111ASNR.jpg)

1449

Pictorial Review of Cervical Arterial Variant Anatomy: A Radiologist's Guide

C Wheeler[1], H Sotoudeh[1], A Singhal[1]
[1]University of Alabama at Birmingham School of Medicine, Department of Radiology, Birmingham, AL

Purpose

This exhibit will discuss a systematic methodology that takes into account: 1) Origin; 2) Number; 3) Morphology (diameter, tortuosity); 4) Branching Pattern (for carotid arteries); and 5) Transforaminal Entry Level (for vertebral arteries). A pictorial review will be presented with imaging examples of anomalous origin, duplication, aberrant branching, etc. • Discuss a systematic approach for evaluating variant cervical arterial anatomy and its clinical relevance. • Display a pictorial review illustrating variant anatomy, including but not limited to a case series.

Materials and Methods

Given expanding neuroimaging volumes, the advent of advanced neuroimaging techniques such as vessel wall imaging, and developments in neurointerventional therapy, detection of cervical arterial variants will only become more frequent in the future. A foundational understanding of common vascular anatomic variants is critical for head and neck radiologists. These arterial variants are often detected incidentally and can easily be overlooked or misinterpreted for congenital absence. Without preoperative awareness, surgical planning will be deficient, leading to potentially fatal cerebrovascular ligation or injury. Variants can also be at high risk for traumatic injury and predispose patients to cerebrovascular disease or aneurysm formation.

Results

A retrospective analysis of a case series will be performed at an institutional level.

Conclusions

This pictorial review contains examples of but is not limited to: • Duplicated vertebral artery origin arising as third aortic arch branch with transforaminal entry superior to native artery • Single anomalous vertebral artery origin arising from proximal ECA with entry at C1 level • Duplicated vertebral artery V3 segment • Hypoplastic vertebral artery V4 segment terminating as PICA • Congenital absence of cervical/intracranial ICA with hypoplastic/absent carotid canal • Aberrant ascending pharyngeal artery branch arising from right ICA • Early CCA bifurcation just distal to brachiocephalic artery origin with prominent ECA and diminutive cervical ICA • Non-bifurcating CCA providing cervical ICA • Persistent stapedial artery • Aberrant ICA • Retropharyngeal ICA A solid grasp of common variant anatomy is crucial for diagnostic radiologists to accurately interpret these studies and for endovascular interventionalists to

successfully perform angiography. Awareness empowers clinicians and surgeons to preemptively evade complications and maintain quality patient care.

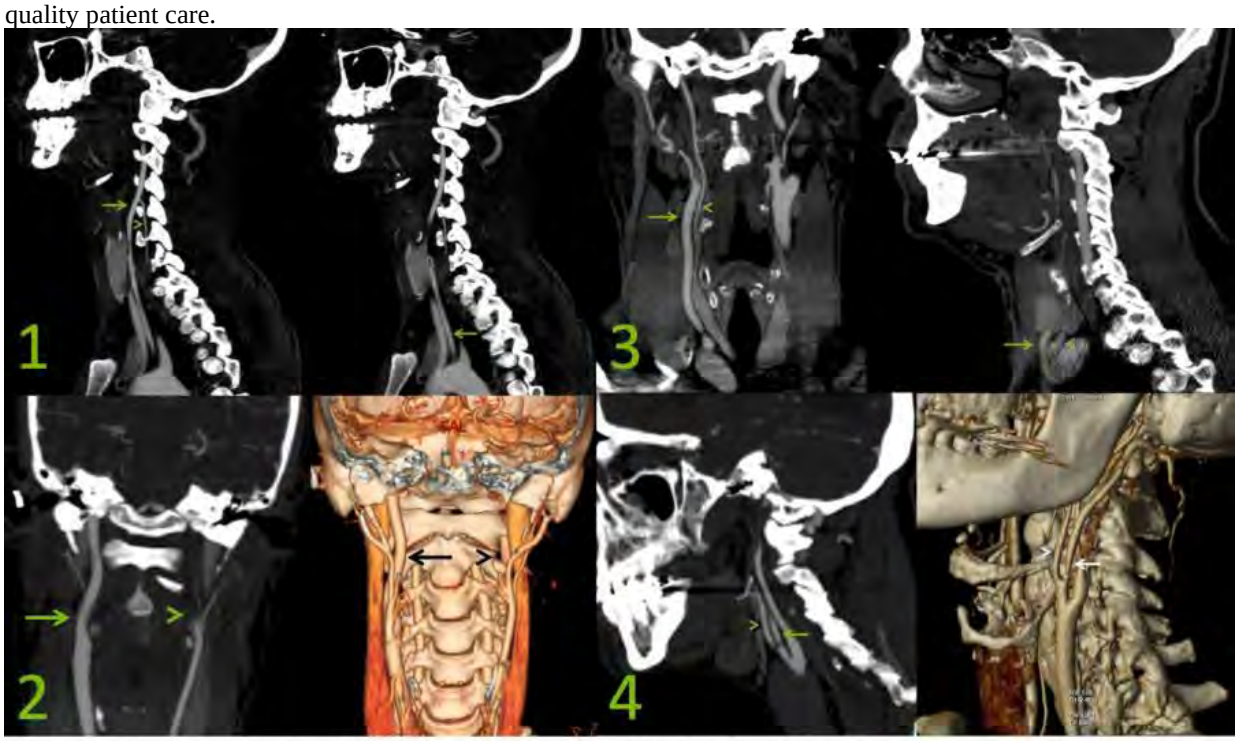

Figure 1. (a, b) Sagittal MIP reformations (a, b) of a CT angiogram demonstrate a duplicated left vertebral artery origin arising directly from the aortic arch as the third arch branch with transforaminal entry at the C4-5 level.

Figure 2. (a, b) Coronal MIP reformation (a) and 3D reconstruction (b) of a CT angiogram demonstrate congenital absence of the left ICA (arrowhead) compared to the right (arrow).

Figure 3. (a, b) Coronal (a) and sagittal (b) MIP reformations demonstrate early CCA bifurcation just distal to brachiocephalic artery origin with prominent ECA (arrow) and diminutive cervical ICA (arrowhead).

Figure 4. (a, b) Sagittal MIP reformation (a) and 3D reconstruction (b) of a CT angiogram demonstrate an anomalous left vertebral artery (arrow) arising directly from the proximal left ECA (arrowhead) with entry at the C1 level.

(Filename: TCT_1449_ASNR22EducationalExhibitCervicalVascularVariantsAbstractLegend.jpg)

389

Pitfalls of CT Perfusion for Endovascular Thrombectomy

Y TSAI[1]

[1]*CHANG-GUNG MEMORIAL HOSPITAL, CHIAYI CITY 600, CHIAYI CITY*

Purpose

Educational objectives: 1. To describe the features of a technically adequate automatic CT perfusion report. 2. To review the technical acquisition parameters for CT perfusion. 3. To discuss the reasons and findings of unreliable automatic CT perfusion results using real-world examples.

Materials and Methods

Brain perfusion imaging, especially the CT perfusion (CTP), has been applied in several clinical trials of endovascular therapy for acute ischemic stroke patients. It is necessary to understand the basics of perfusion acquisition, quantification, interpretation and most importantly, the limitations of automated CT perfusion which may result in misclassification of brain tissue and subsequently inappropriate decision. This educational exhibit aims to highlight the pitfalls of automated CTP along with practical pearls to address the common challenges.

Results

We retrospectively reviewed the automated CTP imaging perfomred in our stroke center from Mar. 2019 through Sep. 2021. CT scans were all performed within 24 hours after stroke onset. All CT images were acquired from a 320 slices CT scanner (Aquilion ONE, Cannon medical system, Japan) and sent to a networked computer running fully-automated Rapid Processing of Perfusion and Diffusion (RAPID, iSchemaView, Menlo Park, CA) software for postprocessing of cerebral blood flow (CBF), cerebral blood volume (CBV), mean transit time, time to maximum residue function (Tmax), and time to drain maps.

Conclusions

A total of 238 stroke patients with CTP imaging were reviewed. Unreliable CTP maps were mostly due to patient factors, technical flaws or core/penumbra volume measurement errors. (Table 1) To avoid mis-interpretation of the automatic CTP results, a standardized checklist is recommended. Stroke clinician must be familiar with the standards of quality maps outputted by the automatic CTP software including motion estimation, arterial input function (AIF) and venous output function (VOF) locations and the time- intensity curve. Summary maps of Tmax, CBV and CBF thresholds should also be checked, especially for patients who early

reperfusion or chronic stenosis/occlusion are suspected and for patients who receive intravenous thrombolysis. Bilateral cerebral perfusion deficits or illogical large mismatch are always crus for unreliable perfusion maps. Most important of all, thickening about clinical presentation while we interpret the automatic CTP results and try to find out the reasons of discrepancies between them.

Table 1. Where are the doubtful CTP maps come from?

Patent factors	Technical flaws	Core/penumbra misclassification
• Motion • Poor cardiac output • Atrial fibrillation • Arrhythmias • Aortic dissection	• Poor contrast bolus • Inadequate IV access • Inadequate AIF/VOF selection	• Perfusion thresholds • Chronic stenosis/occlusion • Early reperfusion • White matter diseases • Skull base, inferior temporal and posterior fossa artifacts

(Filename: TCT_389_2021-10-26111458.jpg)

441

Pituitary Adenoma and What Else - Tumors and Mimics of Sellar/Parasellar Regions

P Noone[1], S Hung[2], V Jewells[3], M Castillo[4], E Harris[5]

[1]University of North Carolina Medical Center, Chapel Hill, NC, [2]University of North Carolina School of Medicine, Chapel Hill, NC, [3]UNC, Chapel Hill, NC, [4]Radiology, Chapel Hill, NC, [5]University of North Carolina, Chapel Hill, NC

Purpose

This exhibit will present a variety of lesions and pathologies of the sellar and parasellar regions including neoplastic and non-neoplastic etiologies with additional input with regards to the endocrinologist's and surgeon's perspective. By the end of the exhibit, the reader will be able to provide an accurate and clinically relevant differential diagnosis based on the imaging appearance of these pathologies.

Materials and Methods

Our purpose is to review the imaging appearances of a variety of lesions and pathologies involving the sellar/parasellar and hypothalamic regions and provide relevant differential diagnoses. Additionally, complications of these sellar/parasellar pathologies will be described.

Results

This educational exhibit consists of a wide variety of cases (pathology proven when available) from our institution and a literature review. We will present a variety of pathologies, complications and relevant post-treatment changes.

Conclusions

Owing to the diverse range of tissue types in the sellar/parasellar region, a broad range of pathologies may affect this location. Pathologies included in this review include neoplastic etiologies (pituitary micro- and macroadenoma), complications of various neoplasias (cavernous sinus invasion with discussion of the Knosp classification system, optic chiasm and optic tract edema), post treatment appearance, anatomic/congenital variants of the sellar region (persistent craniopharyngeal canal, ectopic pituitary gland), inflammatory pathologies that may mimic tumors/neoplasia (hypophysitis, lymphocytic hypereosinophilia, granulomatous disease). Due to its proximity to other structures of the head and neck, invasion of the sellar region by other tumors is also an important consideration and will be included in this review (cordoma, glomus jugulare paraganglioma, chondrosarcoma). Discussion of differential diagnoses for these lesions and etiologies is also included in this talk. Pathologies are described in Figure 1.

Sellar/parasellar lesions can have broad imaging differential diagnoses, and it is important for the radiologist to be aware of the different appearance of their possible complications, as well as relevant post-treatment changes.

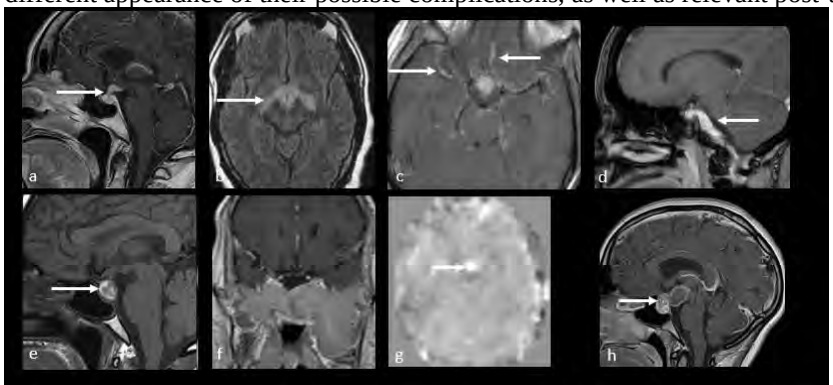

Fig 1. (a) Thickening and enhancement of the infundibulum in lymphocytic hypereosinophilia syndrome. (b) Pituitary macroadenoma with edema of the optic tracts. (c) Sarcoid involving the pituitary/sella with nodular leptomeningeal disease. (d) Glomus jugulare tumor with extension to the sella. (e) Heterogeneous T1 signal consistent with pituitary apoplexy following ibrutinib therapy. (f) Giant adenoma with marked invasion of surrounding structures and skull base. (g) Precocious puberty with increased perfusion of pituitary on ASL images. (h) Adamantinomatous craniopharyngioma.

(Filename: TCT_441_Figurev4.jpg)

663

Post-Operative Findings in the Enucleated Orbit: Pearls and Pitfalls in Patients Treated for Retinoblastoma

J Manov[1], S Maloney[2], G Saigal[3]

[1]Jackson Memorial Hospital, Miami, FL, [2]University of Miami, Miami, FL, [3]Jackson Memorial Hospital/University of Miami, Miami, FL

Purpose

This presentation entails a review of multiple examples of abnormal findings in the orbit of patients enucleated for retinoblastoma. While retinoblastoma is the most common ocular malignancy of childhood, care is concentrated at referral centers and many imagers may be unfamiliar with post-treatment findings, especially enucleation which is increasingly rarely utilized. Our aim is to show the gamut of appearances and findings in the orbit after enucleation to allow imagers to familiarize themselves with the appearance of the enucleated orbit so that they can better communicate with clinicians. Objectives include: -Description and examples of fibrovascular ingrowth in orbital prostheses -Description and examples of common findings at the optic nerve after enucleation -Description and examples of other sites of abnormal enhancement after enucleation. -Provide an example of the appearance of actual recurrence in the orbit

Materials and Methods

Despite advances, there remain children who require enucleation for the treatment of aggressive retinoblastoma. Though retinoblastoma is the most common ocular malignancy of children, care is concentrated at referral centers. The aim of this presentation is to familiarize imagers with the array of post-operative findings in this population to allow better clarity when communicating with clinicians.

Results

Cases of enucleated retinoblastoma patients from the University of Miami and Jackson Memorial Hospital PACS systems were reviewed for illustrative examples.

Conclusions

The array of findings in the post-enucleation orbit of retinoblastoma patients is diverse and easily conflated with pathological recurrence, with which the spectrum of expected post-operative findings significantly overlap. The presentation reviews these findings and provides illustrative examples for imagers unfamiliar with this patient population. While abnormal orbital enhancement is common in the orbit after enucleation, such findings are likely unrelated to tumor recurrence, which has a distinct appearance in our experience and as reported in the literature.

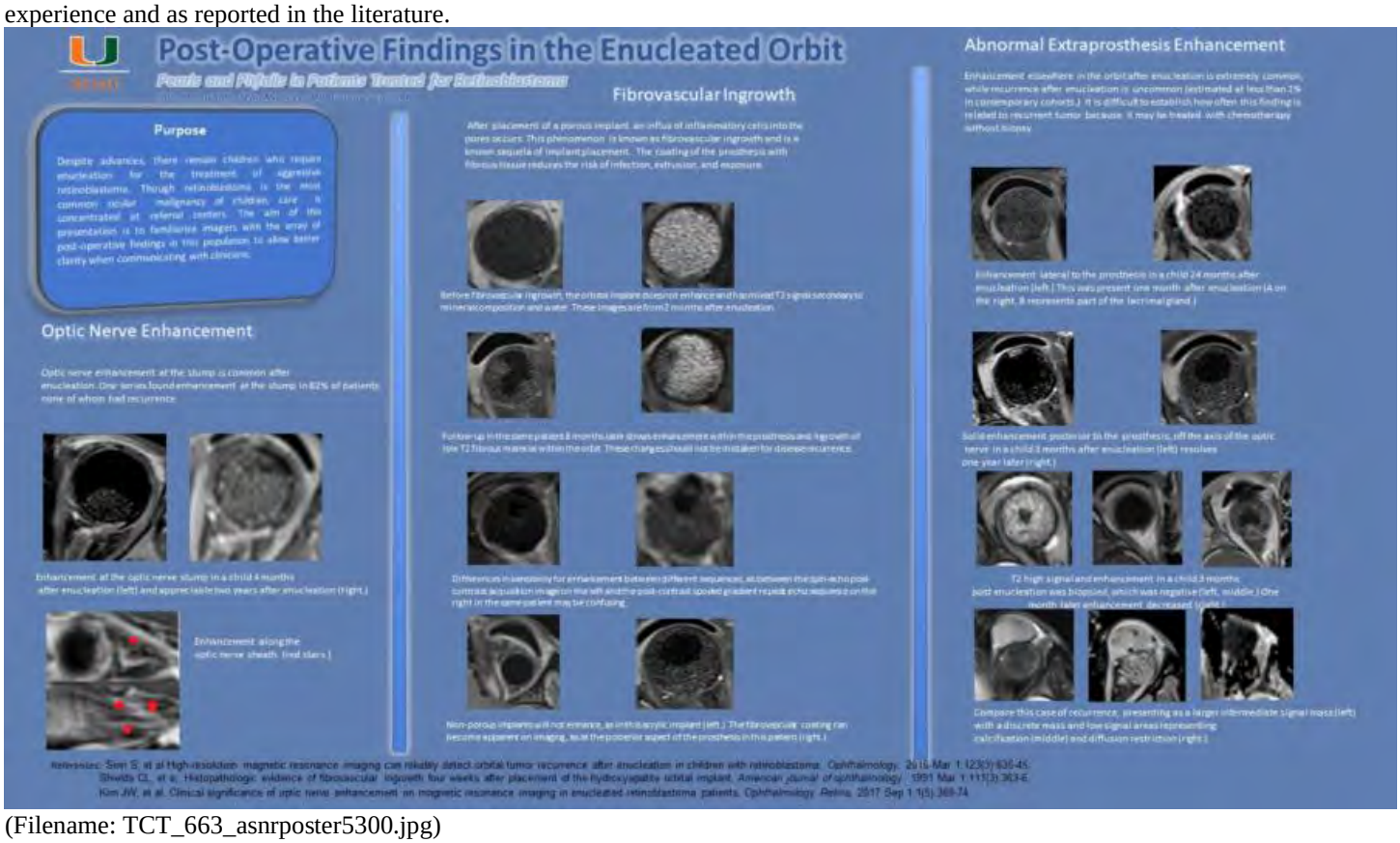

(Filename: TCT_663_asnrposter5300.jpg)

860

Postpartum Maternal Neurological Complications of Pregnancy

A Roth[1], J Mutambuze[1], S Lehnert[1], R Radhakrishnan[1], N Koontz[1]
[1]Indiana University School of Medicine, Indianapolis, IN

Purpose

The substantial physiological changes of pregnancy and transition through puerperium may result in numerous neurological complications manifesting in the postpartum period, of which many represent medical emergencies. Our objectives for this education exhibit are to: 1) provide neuroradiologists with an image-rich, comprehensive review of the salient pathophysiology of these neurological complications, 2) to highlight the typical multimodality imaging appearance of these entities, and 3) to detail imaging recommendations, protocol considerations, and current guidelines for the use of contrast material in breastfeeding mothers.

Materials and Methods

We provide a comprehensive review of neurological complications of pregnancy that may manifest in the postpartum period. We describe multimodality imaging findings, typical locations of pathology, appropriate differential diagnoses, diagnostic pitfalls, and imaging considerations specific for postpartum women.

Results

We performed an IRB-approved, HIPAA-compliant retrospective review the electronic medical record, radiology information system (RIS), and picture archiving and communication system (PACS) at our institution for illustrative cases of neurological complications of pregnancy manifesting in the postpartum period, highlighting multimodality imaging findings involving the brain, spine, and head & neck. We also performed a literature review.

Conclusions

Physiological changes of pregnancy, physical stresses of labor, and certain therapeutic interventions during the peripartum period exert tremendous stresses on a mother's body, which increases the prevalence of several neurological disorders. Etiologies are sundry, but may include neurovascular conditions, hormone-mediated changes, biomechanical alterations, iatrogenic injury, infectious etiologies, and endocrine disorders, many of which share interrelated and overlapping pathoetiologies. While some of these conditions may be diagnosed clinically, imaging plays a critical role in the workup and triage of these disorders, many of which are emergent, life-threatening conditions. CT and MRI are the primary imaging modalities for most of these disorders with conventional angiography reserved as an adjunct modality for some of the neurovascular disorders. Current evidence supports the judicious use of iodinated and gadolinium-based contrast agents in breastfeeding mothers, which is considered to be safe for both mother and baby.

1467

Potentially Reversible Versus Typically Irreversible Encephalopathic Disorders, and those In-Between

N Nagornaya[1], N Ezuddin[2], G Saigal[3], A McKinney[3], R Bhatia[3]
[1]Jackson Memorial Hospital/University of Miami, Miami, FL, [2]University of Miami/Jackson Memorial Hospital, Miami, FL, [3]University of Miami, Miami, FL

Purpose

· Recognize the imaging features of the common encephalopathic syndromes. · Understand the pathophysiology of the various disease processes. · Discuss differentiating features between particular toxic, metabolic and autoimmune disorders, and various encephalitides. · Formulate a differential diagnosis based on the clinical history, topographical distribution and pattern on imaging (particularly MRI) to narrow the differential diagnosis.

Materials and Methods

Encephalopathic syndromes can present as a diagnostic dilemma to clinicians and radiologists due to myriad of pathologic causes, nonspecific imaging findings, and often overlapping imaging appearances. The goal of this presentation is to present a pictorial review of typical imaging appearances of encephalopathic syndromes in 3 different categories: reversible, potentially reversible, and typically irreversible.

Results

A search through the database of 2 health systems for "encephalopathy" yielded a large number of patients with acute encephalopathic syndromes. Imaging findings were correlated with pertinent medical and treatment history and pathology. We will present a retrospective review of typical imaging findings of common encephalopathic syndromes emphasizing that that some of these syndromes have overlapping clinical and radiologic features, also affecting their severity and outcomes.

Conclusions

We present a review of various encephalopathic syndromes. We propose to group these encephalopathic syndromes under 3 categories: reversible, potentially reversible, and typically irreversible. The reversible encephalopathic syndromes include infectious and neoplastic and autoimmune mediated etiologies, RCVS, TGA and seizure related and Wernicke's encephalopathy. The partially reversible entities can be alcohol related, PRES, radiation therapy and metabolic encephalopathies and some drug overdosages. The overlapping group of reversible and irreversible encephalopathic symptoms can be due to osmotic demyelination, diabetic encephalopathies, toxic exposures including solvents, drugs and poisons. Lastly, hypoxic ischemic injury is one of the most common causes of the irreversible acute encephalopathic syndromes. MRI plays an important role in the diagnosis and management of patient's presenting with encephalopathic syndromes. Accurate interpretation of the findings together with a detailed clinical history may help identify the cause of injury which allows for the best therapeutic options and clinical outcome.

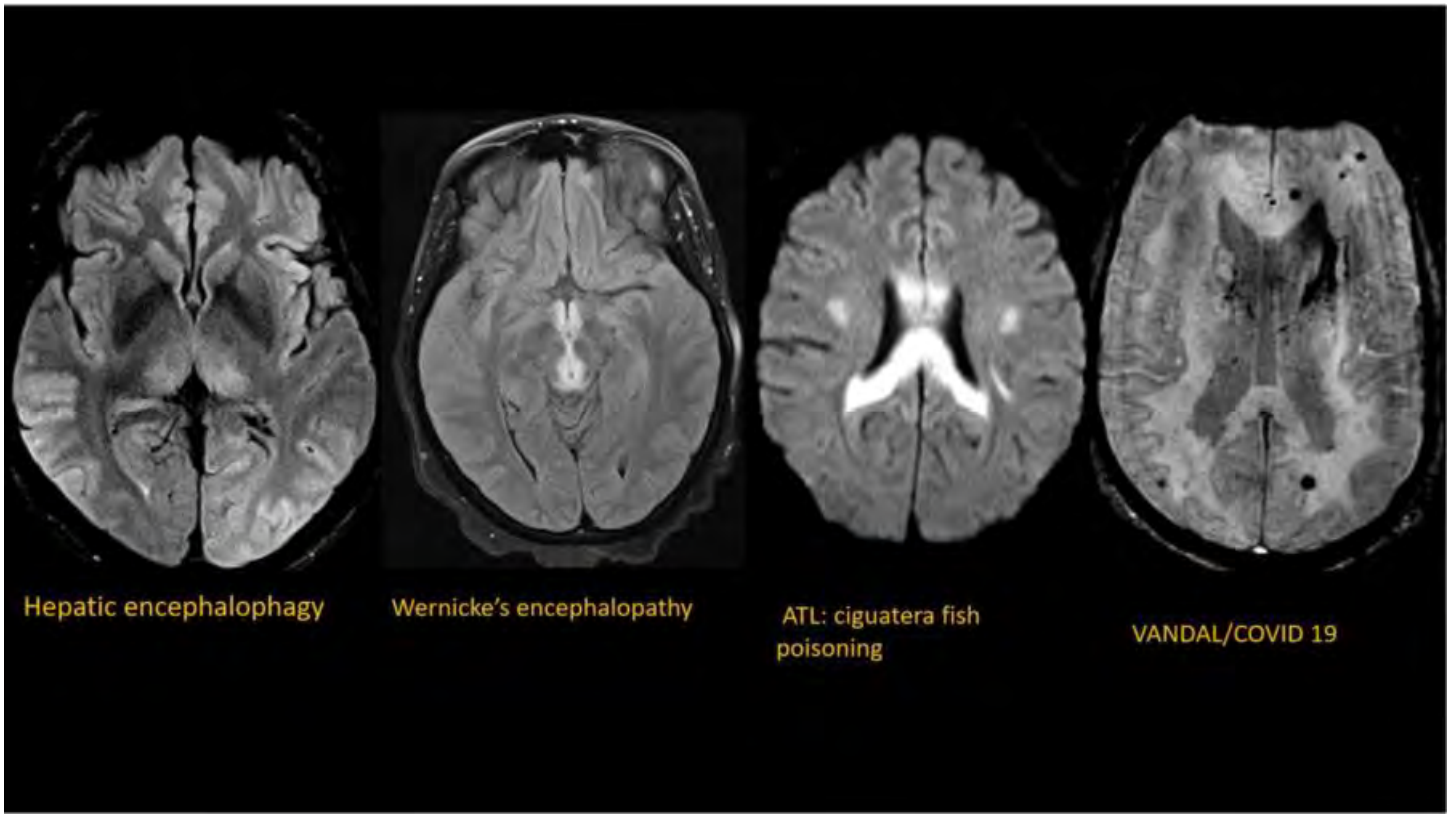

(Filename: TCT_1467_ASNR2021.jpg)

469

Practical Applications of CT Perfusion

E Tang[1], A Remunda[1], B Frate[1], S PATEL[2], B Scott[1], S Ifthikharuddin[1]
[1]Rochester Regional Health, Rochester, NY, [2]ROCHESTER GENERAL HOSPITAL, ROCHESTER, NY

Purpose

This is a case-based educational exhibit highlighting various artifacts, challenging scenarios, and stroke mimics encountered in the interpretation of conventional and AI-generated CT brain perfusion maps in the setting of acute stroke.

Materials and Methods

CT perfusion is increasingly utilized in the workup of acute cerebral ischemia, and serves a vital role in treatment decision-making. Recent work has culminated in an FDA-approved software for artificial intelligence driven generation of perfusion maps. We aim to familiarize the reader with common artifacts and stroke mimics which could potentially lead to diagnostic errors when interpreting both conventional and AI-generated perfusion maps.

Results

We will present interesting CT perfusion cases from a large community-based comprehensive stroke center, with corresponding NCCT, CTA, MR/MRA, and conventional angiographic images where relevant.

Conclusions

CT perfusion technique, including clinically relevant physics, will be reviewed. Normal perfusion maps and various patterns and stages of cerebral ischemia will be illustrated. Cases demonstrating various technical artifacts including patient motion, suboptimal bolus timing, and anomalous selection of arterial inflow or venous outflow will be shown. Finally, challenging perfusion scenarios will be highlighted, such as subacute infarcts, vasospasm, and anatomic variations, as well as acute stroke mimics such as migraines, seizures, and tumor. In the evaluation of acute cerebral ischemia, CT perfusion serves as a prominent adjuvant imaging tool for patient selection for acute stroke intervention. Artificial intelligence software is playing an increasing role, and will likely play a more integral role in the future. Familiarity with and understanding of common artifacts and stroke mimics encountered in the interpretation of CT perfusion is important for trainees, general radiologists, and neuroradiologists involved in the care of the acute stroke patient.

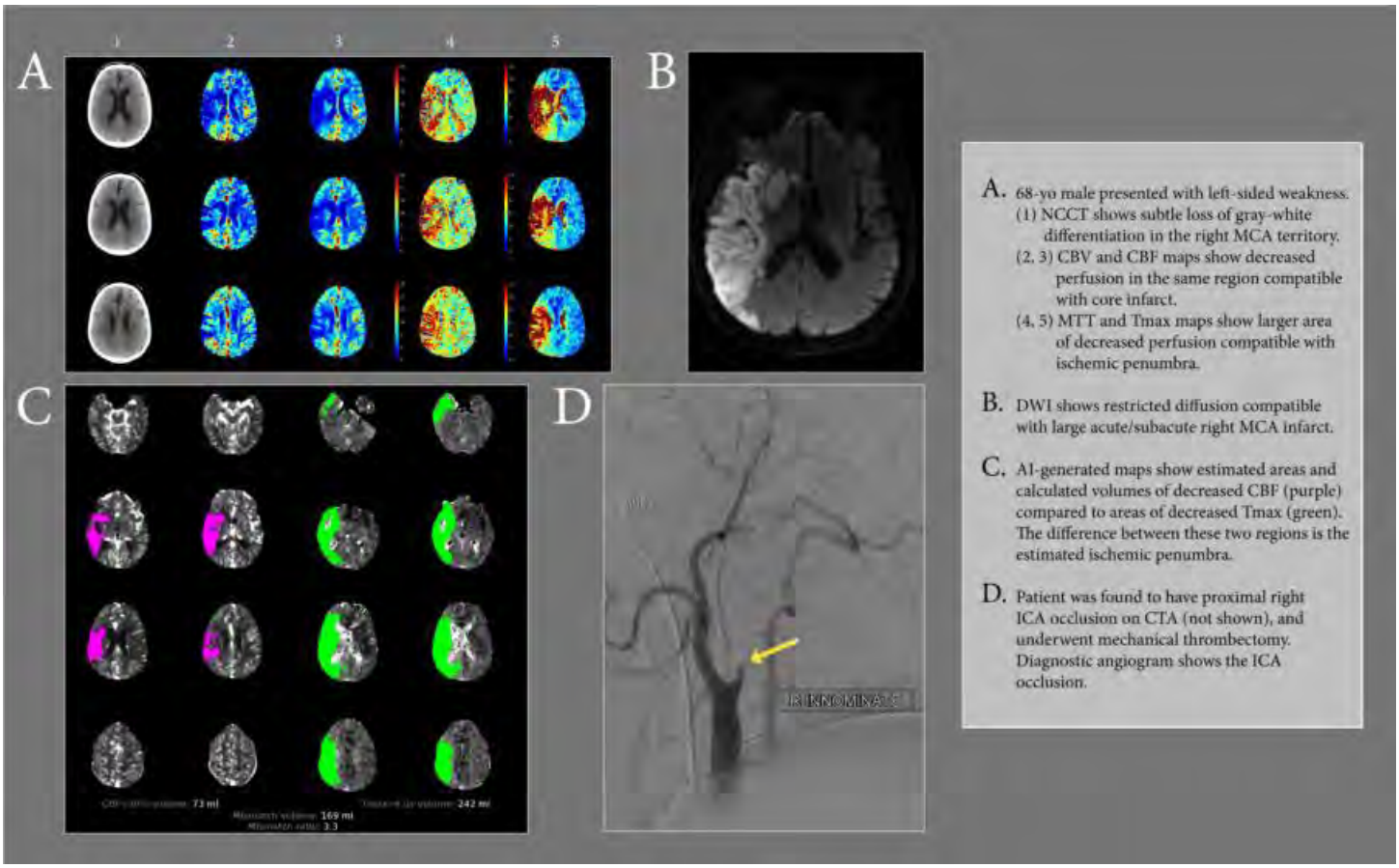

(Filename: TCT_469_Abstractv3.jpg)

497

Prediction of Meningioma Sub-types Using Qualitative Assessment of Fractional Anisotropy Maps.

S Jabeen[1], K Kulanthaivelu[1], J Saini[1]
[1]*NATIONAL INSTITUTE OF MENTAL HEALTH AND NEUROSCIENCES, Bangalore, KARNATAKA*

Purpose
Surgical management of meningioma depend on their histopathological subtype, certain subtypes having higher recurrence rates (1). Fractional anisotropy (FA), a component of Diffusion Tensor Imaging (DTI), represents the directional asymmetry of diffusion and is affected by microstructural changes (2).
Materials and Methods
In this study we explore the role of FA maps in predicting the histopathological subtypes of meningioma using a qualitative ordinal scale.
Results
Retrospective analysis of pre-operative MRI of 98 cases of histopathologically proven subtypes of meningothelial, chordoid, transitional, fibroblastic, microcystic, angiomatous and atypical meningioma was done. FA maps were evaluated by two blinded observers. An ordinal scale of 1 to 4 was used to grade the degree of fractional anisotropy in each lesion. Grade 1 was assigned to those tumors which were nearly dark and grade 4 to those which were nearly bright. Values of 2 and 3 were assigned to tumors which were predominantly dark with patchy bright areas and predominantly bright with scattered dark areas respectively.
Conclusions
Out of 98 cases, 9 were meningothelial/15 transitional/14 chordoid/ 8 angiomatous/15 microcystic/17 fibroblastic/18 atypical meningiomas. Interobserver reliability was excellent with an intraclass correlation coefficient of 0.92. Intergroup comparison revealed significantly low FA grade in microcystic/ angiomatous/ transitional meningioma compared to meningothelial / chordoid/ fibroblastic/ atypical meningioma with transitional being a relatively heterogeneous subgroup compared to the former two. While all fibroblastic meningiomas showed high FA grade, it is relatively non-specific since several grade 3 and 4 meningiomas were also seen among meningothelial/chordoid/atypical subtypes. Qualitative grading of FA maps is useful in predicting the meningioma subtype. Low FA is characteristically seen in microcystic and angiomatous variants. High FA within the tumor although a consistent feature of Fibroblastic variant, is nonspecific

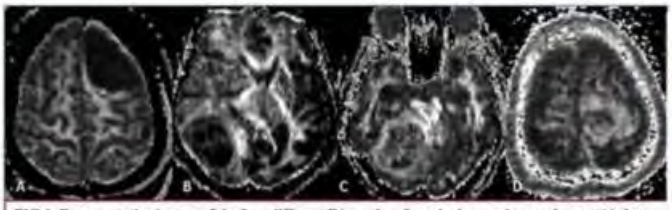

FIG:1 Representative images of the four different FA grades of meningioma subtypes. Image (A) shows the lesion in the left frontal convexity to be almost completely dark, representative of FA grade 1. Image (B) shows few bright areas (<50%) within the right parietal convexity tumor, depicting FA grade of 2. Image (C) shows >50% bright areas within the lesion in right cerebellopontine angle corresponding to FA grade of 3. Image (D) shows the lesion in left frontal convexity to be almost bright representing FA grade 4 lesion.

Table 2: Table showing the intraclass correlation co-efficient (ICC) between two observers

	Intraclass Correlation	95% Confidence Interval		F Test with True Value 0			
		Lower bound	Upper bound	Value	df1	df2	Sig
Single Measures	.859	.796	.903	13.139	97	97	.000
Average measures	.924	.886	.949	13.139	97	97	.000

Table 1: Table showing the FA grade of different meningioma subtypes

MENINGIOMA SUBTYPE	GRADE 1	GRADE 2	GRADE 3	GRADE 4
Meningothelial	1	2	6	0
Transitional	1	8	6	0
Chordoid	2	4	8	0
Angiomatous	4	3	1	0
Microcystic	9	6	0	0
Fibroblastic	0	1	11	5
Atypical	0	6	12	2

Table 3: Table showing pair wise comparison of FA grade amongst different subtypes of meningioma

	Adjusted p value						
SUBTYPE	Meningothelial	Transitional	Microcystic	Chordoid	Angiomatous	Fibroblastic	Atypical
Meningothelial	-	1.000	.027	1.000	.504	1.000	1.000
Transitional	1.000	-	.103	1.000	1.000	.042	1.000
Microcystic	.027	.103	-	.026	1.000	.000	.000
Chordoid	1.000	1.000	.026	-	.727	.223	1.000
Angiomatous	.504	1.000	1.000	.727	-	.000	.029
Fibroblastic	1.000	.042	.000	.223	.000	-	1.000
Atypical	1.000	1.000	.000	1.000	.029	1.000	-

(Filename: TCT_497_faasnrnew300.jpg)

1062

Primary cilia and neuroimaging of ciliopathy

K Ando[1], R Ishikura[1], S Ishikawa[2], A Yoshida[2], S Oka[2], J Fujimoto[2], Y Yamamoto[2], S Kono[2], O Koji[2], M Watanabe[2], R Sakaguchi[2], S Arizono[2], T Suga[2], S Kanao[2]

[1]Kobe City Medical Center General Hospital, Kobe, Hyogo, [2]Kobe city medical center general hospital, Kobe, Hyogo

Purpose

Primary cilia are non-motile cilia that exist one by one in living cells. Primary cilia act like an antenna that conveys various information to cells. As a result, primary cilia are involved in cell proliferation, differentiation, and migration and maintenance of morphology and function of organs. Ciliopathy due to the abnormality causes various abnormalities throughout the body. In the central nervous system, cerebellar vermis hypoplasia (molar tooth sign: MTS) is specific, but other nonspecific abnormalities such as agenesis of the corpus callosum, polymicrogyria, encephalocele, hydrocephalus, and hypothalamic hamartoma may also be seen. Of course, ciliopathy also causes various abnormalities throughout the body: Situs inverses, renal cyst and nephron fistula, hepatic cyst and liver fibrosis, polydactyly, osteodysplasia, obesity, and decreased gonad function are observed. In ciliopathy, these signs are mixed in various combinations and The diagnosis of the disease group is not always clear. In this educational exhibition, we will describe the structure and function of primary cilia, the characteristics clinical manifestations of ciliopathy, and the neuroradiological findings of typical ciliopathy including Joubert syndrome related disease, oral-facial-digital syndrome, Meckel syndrome, acrocallosal syndrome. When you see polysyndactyly, retinopathy, polycystic kidney, nephronophthisis, or liver fibrosis along with MTS or other brain imaging findings such as agenesis of corpus callosum, polymicrogyria, encephalocele, hydrocephalus, and hypothalamic hamartoma, there is a high possibility of ciliopathy. Also if there is MTS on CT or MRI, systemic examination of the body should be considered. Learning objectives are: 1. Understand the structure and role of Primary cilia. 2. Understand the disease types of ciliopathy. 3. Understand the characteristics of neuroimaging findings of ciliopathy. 4. Understand the characteristic findings of systemic ciliopathy.

Materials and Methods

N/A

Results

N/A

Conclusions

N/A

1044

Quantitative Susceptibility Mapping (QSM) as a Novel Technique for Detection and Localisation of Cranial Dural Arteriovenous Fistulae (CdAVF).

S Jabeen[1], V Lanka[2], S Peer[3], J Saini[4], C Prasad[5], K Kulanthaivelu[5]

[1]Sher-i-Kashmir Institute of Medical sciences, Srinagar, India, [2]National Institute of mental health and neurosciences, Bengaluru, Karnataka, [3]National Instituite of Mental Health and Neurosciences, Bangalore, India, [4]NATIONAL INSTITUTE OF MENTAL HEALTH & NEURO SCIENCES, BANGALORE, India, [5]National Instituite of Mental Health and Neurosciences, Bangalore, Karnataka

Purpose

Cranial dural arteriovenous fistula (CdAVF) is difficult to diagnose in a background of chronic cerebral venous thrombosis (CCVT) as the imaging features are alike on conventional MRI. Quantitative Susceptibility Mapping (QSM) is a novel post-processing technique which adopts unfiltered phase data from a gradient echo sequence with multiple echoes to quantify magnetic susceptibility. In this technical note, we aim to highlight the potential of QSM in the diagnosis and localisation of CdAVF. Arterial Spin Labelling (ASL), as an adjunct offering a deeper hemodynamic insight into CdAVF pathophysiology is elucidated. The scope of QSM as an alluring modality and the vital complementary information of ASL for non-invasive detection of C-DAVF has been exemplified in this proof-of-principle case-series. QSM findings mirror the hemodynamic observations on DSA which has been succinctly demonstrated. While by no means a guideline, this case series illustrates the feasibility and rationale for investigating QSM in the diagnosis and prognosis of C-dAVFs in a large-scale study.

Materials and Methods

To highlight the utility of QSM with ASL as novel, non-invasive imaging techniques in the diagnosis, localisation and follow-up of cranial dAVF especially in a background of chronic CVT.

Results

IMAGING TECHNIQUE Seven patients with CCVT underwent imaging on a 3 Tesla scanner. In addition to routine sequences, a multi-echo gradient echo sequence was acquired, the raw data from which was used to generate the quantitative susceptibility map. Pulsed pseudocontinuous 3D ASL was obtained. Automated postprocessing of the ASL data was performed on the imaging console. A 6-vessel cerebral digital subtraction angiogram was acquired using the standard technique. The above imaging protocol was repeated post-embolization in cases with dAVF.

Conclusions

CASES: Four cases with dAVF showed an unequivocal susceptibility gradient in the involved sinus with spin trapping on ASL. The changes resolved postembolisation in case 1 (fig 1). In three cases, QSM ruled out a dAVF by demonstrating lack of susceptibility changes in the dural sinuses. The same was confirmed on DSA.

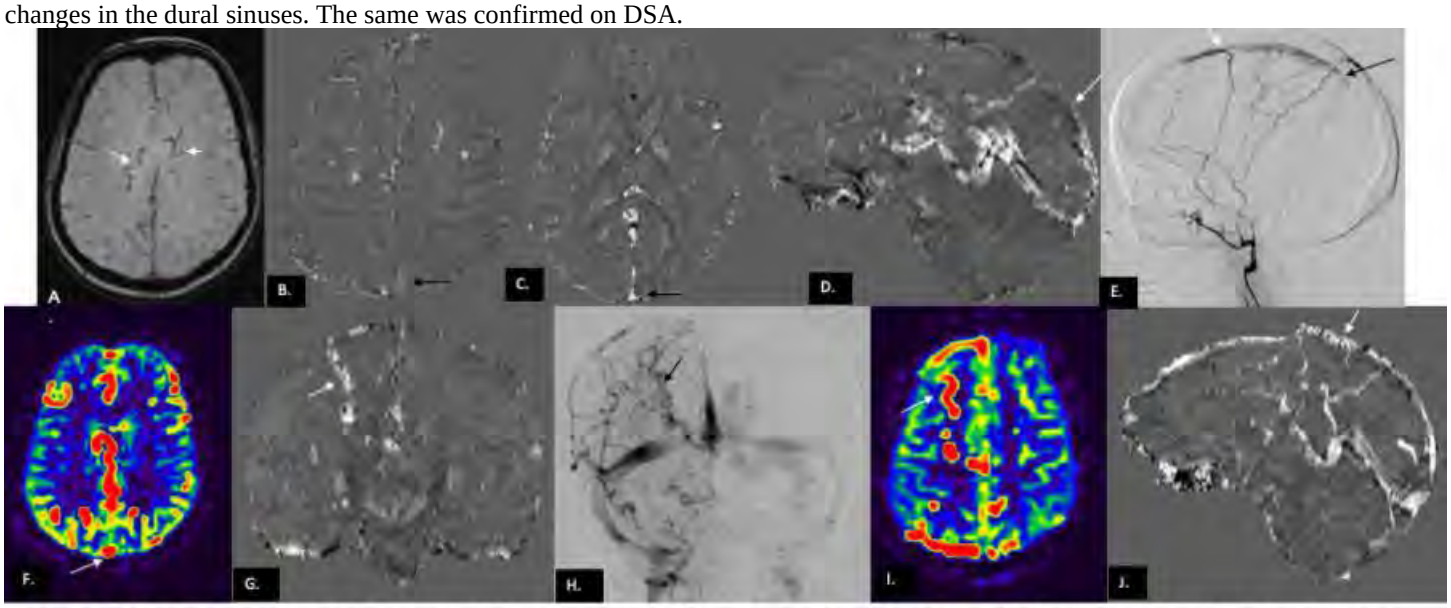

FIGURE 1: **dAVF in background of CVT**: 25 year old female with old H/O CVT and relentless loss of vision with CSF rhinorrhea: SWI (A) shows dilated tortuous veins in bilateral centrum semiovale (white arrows). Axial QSM (B,C) shows decreased signal intensity of the middle third of SSS (black arrow in B) S/O reduced susceptibility compared to the normal bright signal in the posterior third of the sinus (arrow in C). Sagittal reformat of QSM (D) shows the signal intensity gradient in the SSS with transition at the junction of the posterior one third and middle two third of the sinus (white arrow) suggesting a dAVF involving the SSS localized distal to the posterior one third of the sinus. Lateral view of right internal maxillary artery injection (E) confirms dAVF involving the anterior one third of the SSS (white arrow) with feeders from the middle meningeal artery. Note reflux into the middle third of the sinus. The flow gradient in the SSS nearly matches the susceptibility gradient seen on QSM with transition shown by black arrow . ASL (F) shows transit artefact in the SSS (white arrow). Coronal reformat of QSM (G) shows bright signal in one of the right sided cortical veins (arrow) suggestive of venous congestion. AP view of right ICA angiogram (H) shows a congested vein in the capillary phase (black arrow) corresponding to the vein seen on QSM (arrow in G). Also note spin trapping in the vein on ASL (arrow in I).Sagittal reformat of QSM following embolization (J) shows return of normal susceptibility in the middle third of the sinus (arrow). The anterior third is not visible due to presence of onyx. Compare with D.

(Filename: TCT_1044_Picture1.jpg)

278

Radiomics in Neurodegenerative Disorders

H Sotoudeh[1], Z Saadatpour[1], A Rezaei[1], O Shafaat[2], A Sarrami[3], g roberson[1], E Sotoudeh[4], A Singhal[1], M Tanwar[1]
[1]University of Alabama at Birmingham, Birmingham, AL, [2]Johns Hopkins University School of Medicine, Baltimore, MD, [3]N/A, Davis, CA, [4]Red Crescent Hospital in Dubai, Dubai, UAE

Purpose

Traditionally, radiologists use a limited number of imaging features for diagnosis formulation (lesion size, density, lesion border, enhancement). In contrast, radiomics can easily use many more quantitative features to predict and capture specific medical information. So far, the most common application of radiomics in regards to oncologic imaging is for the prediction of histopathology, tumor grading, genetic mutations, prediction of treatment response, the chance of recurrence, and patients' survival. However, the application of radiomics is not limited to oncologic imaging, and it can essentially be implemented in any clinical condition. In this educational exhibit the emerging role of Radiomics in neurodegenerative disorders are discussed.

Materials and Methods

To present the role of Radiomics in neurodegenerative disorders.

Results

In presentation includes: 1. Radiomics in White matter disease 2.Radiomics in Alzheimer's Disease 3. Radiomics in Parkinsonism disorders Parkinson Disease Multiple system atrophy (MSA)

Conclusions

Radiomics is an emerging research field in radiology and may open new doors for medical imaging by extracting image information hidden to the radiologists' eyes. The preliminary results about the applications of radiomics in neurodegenerative disorders are promising. However, this field is still in its infancy, and many challenges must be resolved before achieving clinical application.

(Filename: TCT_278_table-1-ngd-final_DDSjqSAt.jpg)

1029

RB-RECIST Criteria Assessment of Retinoblastoma with MRI Correlation after Intraarterial Treatment

S Turk[1], B Guneri Beser[2], T Moritani[3], H Demirci[3], N Chaudhary[3]
[1]University of Michigan, Ann arbor, MI, [2]University of Michigan, ANN ARBOR, MI, [3]University of Michigan, Ann Arbor, MI

Purpose

After reviewing this exhibit, the reader will be familiar with the complementary roles of ultrasound, MRI, diffusion weighted imaging in evaluating tumor response and post treatment affects after intraarterial treatment of retinoblastoma.

Materials and Methods

• Highlight the role of MRI and diffusion weighted imaging in the evaluation of retinoblastoma treatment response • Discuss the ultrasound and MRI correlation of the different treatment response types of retinoblastoma • Discuss the pearls and pitfalls in interpreting ultrasound and MRI

Results

Overview of imaging characteristics of retinoblastoma after intraarterial treatment with emphasis on ultrasound- MRI correlation of the RB-RECIST criteria assessment. Discuss type 0-IV tumor regression patterns with MRI correlate. Discuss the role of diffusion

weighted imaging in discrimination of treatment affect and tumor progression. The role of MRI in evaluation of extraocular extension, optic nerve invasion, post-treatment complications and intracranial abnormalities.
Conclusions
MRI techniques add value to treatment response assessment in retinoblastoma. Tumor grading, differentiation of post-treatment affects and tumor progression, assessment of post treatment complications, and evaluations of other intracranial abnormalities are further characterized with MRI. Pitfalls and accuracy of different imaging technics differs but complement each other when used together.

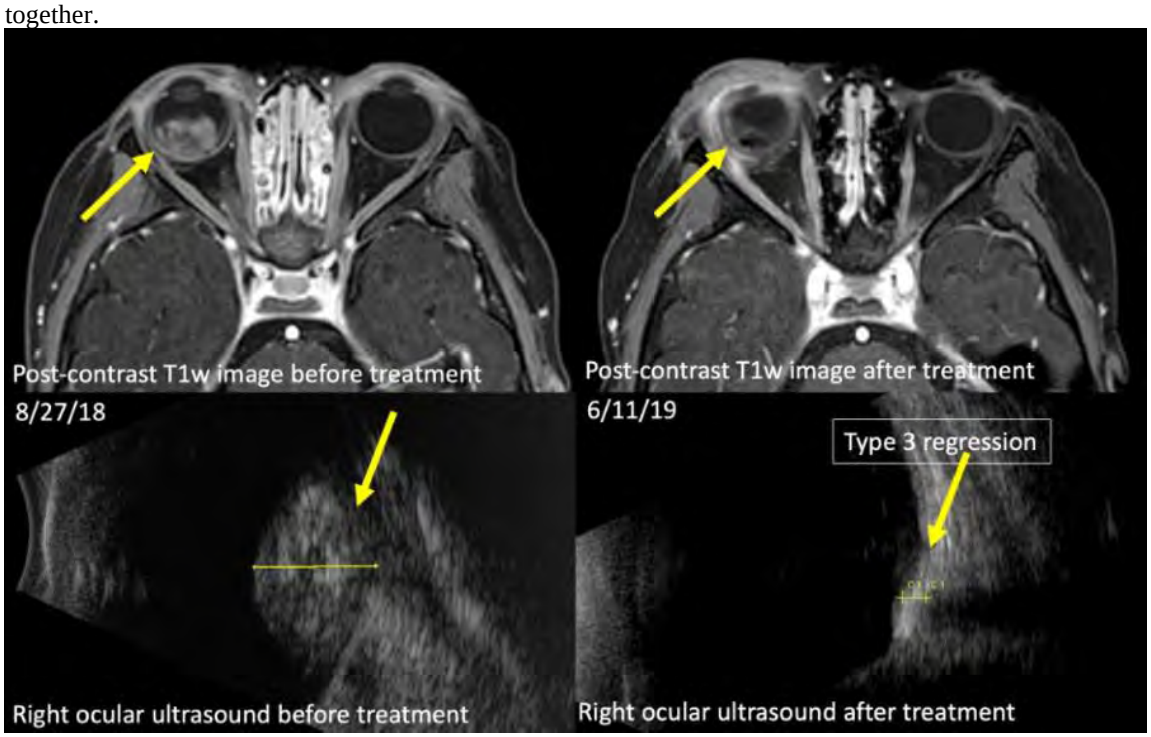

(Filename: TCT_1029_Picture11.jpg)

562
Review of Head & Neck Neuroendocrine Tumors with Emphasis on Contemporary Imaging and Treatment Techniques
B Damadian[1], S Scharf[1], D Shatzkes[1]
[1]*Lenox Hill Hospital, New York, NY*

Purpose
The category of neuroendocrine tumors (NETs) includes a wide variety of rare neoplasms that express somatostatin receptors. NETs in the head & neck (H&N) include esthesioneuroblastomas, paragangliomas, mucosal melanomas, carcinoids and medullary thyroid carcinomas. Recent advances in radionuclide somatostatin receptor target imaging, in particular the increasing utilization of DOTATATE PET/CT, have greatly facilitated detection of tumor recurrence and multiplicity. Our objectives are to: -Review cross-sectional and radionuclide imaging appearance of some of the more common H&N NETs -Illustrate the utilization of DOTATATE PET/CT for detection of local, regional nodal and distant metastatic disease, as well as multiple sites of paraganglioma -Introduce the emerging radionuclide-based treatment options for refractory H&N NETs using representative cases
Materials and Methods
To review the cross-sectional and radionuclide imaging appearance of H&N NETs, with emphasis on DOTATATE-based imaging and treatment options.
Results
Utilizing the relevant literature, a broad overview of the category of NETs is reviewed, as well as the available imaging options. Cases of H&N NETs are presented with representative CT, MRI and radionuclide images. Utilization of DOTATATE PET/CT for the detection of local, regional nodal and distant metastases is illustrated. Case presentations of refractory esthesioneuroblastoma treated with 177Lu-DOTATATE are included.
Conclusions
Contemporary imaging of NETs in the H&N includes both conventional cross-sectional imaging as well as radionuclide imaging that exploits the presence of somatostatin receptors on this diverse group of tumors. DOTATATE PET/CT has emerged as an important modality for the detection of tumor recurrence and multiplicity, with emerging utilization of radiolabeled DOTATATE for the treatment of refractory disease.

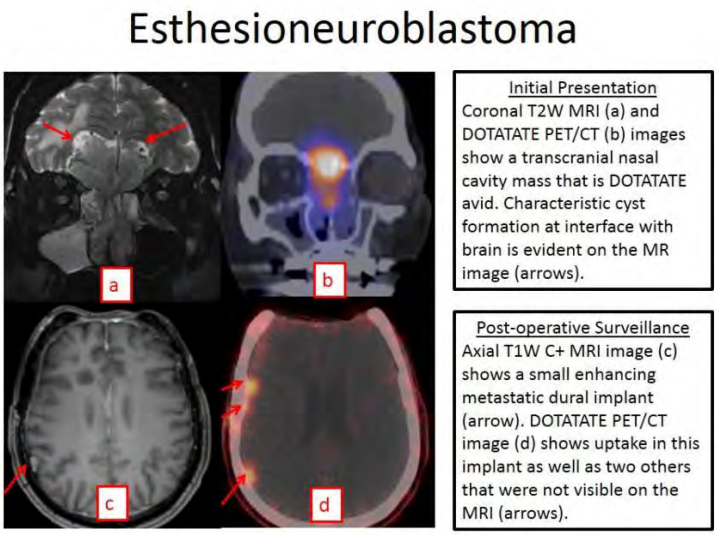

(Filename: TCT_562_NETASNR2021.jpg)

944

Role of Cerebro-Spinal Fluid (CSF) in Tumor Spread; Imaging, Therapeutic Implications and Advances.

A Moawad[1], B Jaber[1], M Aslam[1], M Shalaby[1], S Chaker[1], S Kushchayev[2], O Teytelboym[1]
[1]Mercy Catholic Medical Center, Darby, PA, [2]Moffitt Cancer Center, Tampa, FL

Purpose

- Demonstrate the circulation of Cerebro-spinal fluid (CSF) with highlighting the newly discovered pathways; Glymphatic and meningeal lymphatic routes - Illustrate the different routes for tumors to reach CSF - Highlight the spectrum of neoplastic diseases with high predilection of CSF involvement - Introduce commonly used imaging modalities to diagnose CSF involvement in tumors in both clinical and research settings - Highlight recent advances in laboratory methods to diagnose early CSF involvement in cancer patients - Introduce therapeutic implications of tumor spread to CSF

Materials and Methods

Table of content: - Introduction of CSF circulation and recent updates. - Demonstration of different routes of tumor cells to access CSF and leptomeninges * Glymphatic system. * Meningeal lymphatic system. * Arterial circulation through arachnoid villi. * Perineural route through cranial nerves. * lymphatics and veins through dura and arachnoid sleeves of spinal nerves. * Direct spread from brain or skull. - Types of tumors involving CSF and leptomeninges. - Diagnosis of CSF involvement in malignant neoplasms * Imaging # Contrast enhanced MRI brain # Radio-isotope CSF cisternography # MRI CSF flowcytometry * Glymphatic pathway imaging: # Transcranial mesoscopic imaging # Two photon microscopy # Fluorescent enhanced laser microscopy # Intrathecal contrast enhanced MRI * Laboratory: # Flow cytometry # DNA studies # Liquid biopsy * Leptomeningeal biopsy - Therapeutic implications of CSF tumor spread * Chemotherapy; either Intra-thecal or systemic * Radiotherapy; Whole brain radiotherapy * Treatment response using EANO/ESMO guidelines.

Results

NA

Conclusions

NA

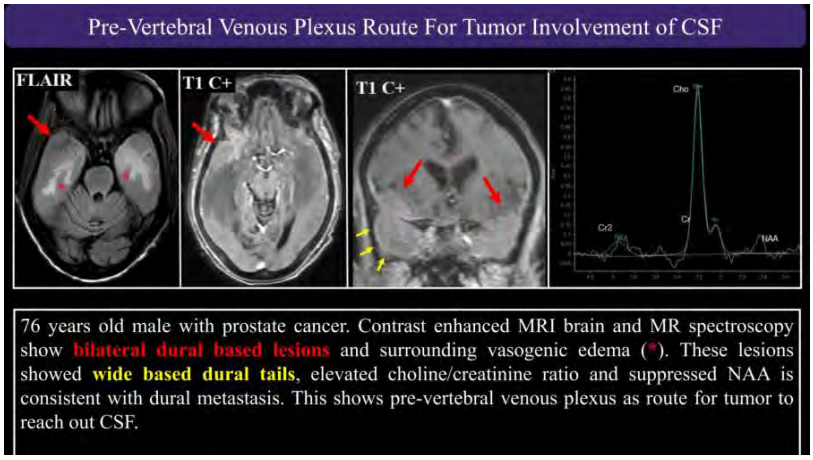

(Filename: TCT_944_Presentation1-3.jpg)

1053

Role of MRI to map anatomical and pathological relation and pathways to cavernous sinus and para cavernous areas

Z Khan[1], B Yawar Faiz[2], H Rana[2]

[1]Shifa International Hospital, Islamabad, [2]Shifa International Hospital Islamabad, Islamabad, Islamabad

Purpose

We reviewed the anatomy and clinical features of diseases involving the cavernous sinus. The cavernous sinus is in relation with various surrounding structures and different pathologic conditions that can occur there can be classified into (a) neoplastic, (b) vascular, (c) infective or inflammatory, or (d) miscellaneous lesions. This comprehensive pictorial review will show normal imaging of cavernous sinus, imaging features of various pathologic conditions affecting the cavernous sinus (CS) and highlight radiologic findings and important differentiating characteristics.

Materials and Methods

To simplify the complex anatomy of the cavernous sinus and illustrate MRI findings of various cavernous sinus lesions.

Results

In this article, the cavernous sinus lesions encountered in our institution during a 10-year period are reviewed and examined by using fat-suppressed contrast-enhanced 3D fast gradient-echo MR imaging. Two radiologists reviewed images on PACS, regarding the normal anatomy and various pathologic conditions which will be presented as pictorial review.

Conclusions

MRI has become essential tool for the evaluation of the tumors and non-neoplasic processes affecting the cavernous sinus as it allows better visualization of the lesions and surrounding structures involvement.

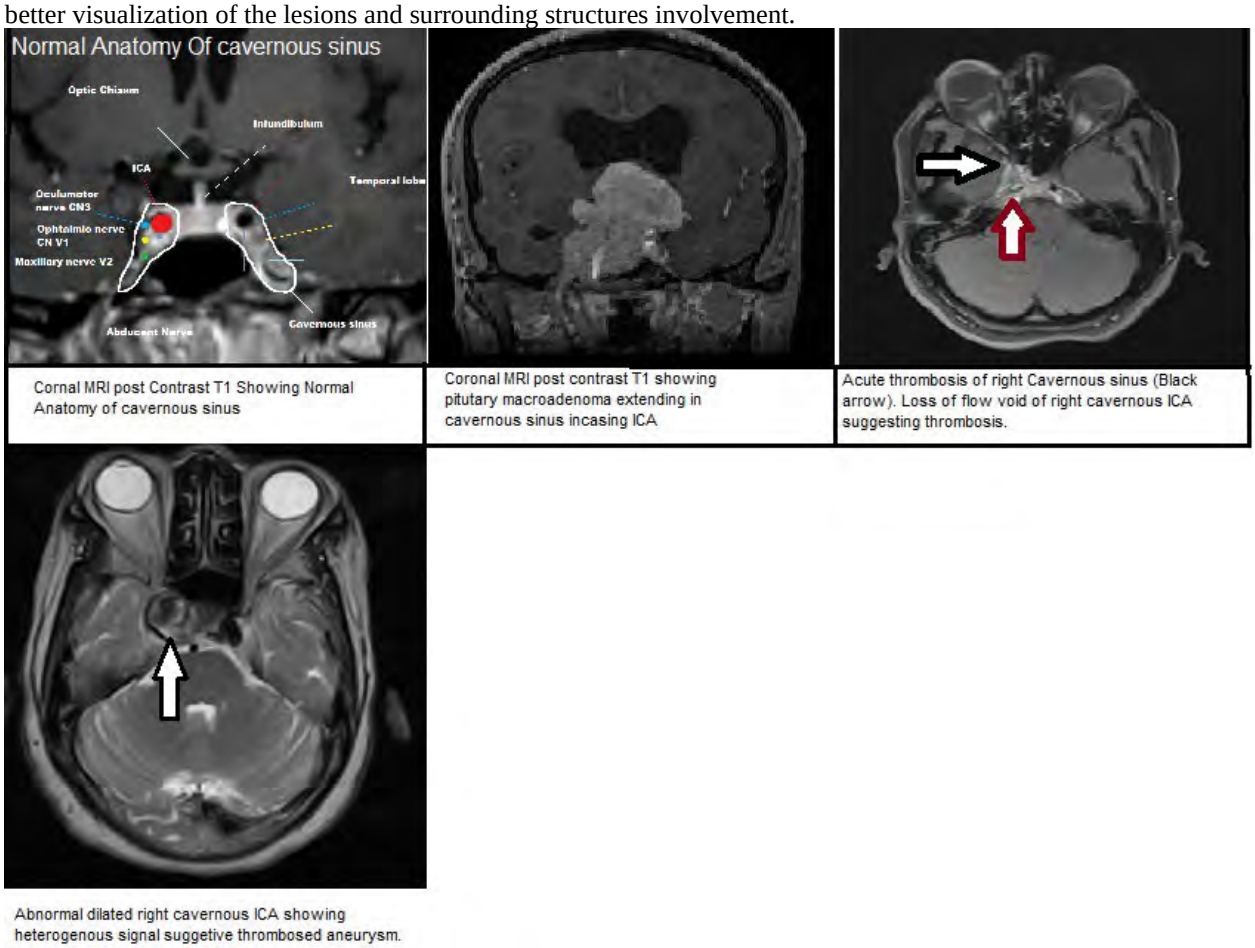

(Filename: TCT_1053_cavernoussinuscases.jpg)

378

Secondary CNS Lymphoma–What Oncologists Want to Know

K Sudanagunta[1], S Goyal[2], N Mehta-Shah[1], N Bartlett[1], M Ponisio[1], M Goyal[1]

[1]Washington University School of Medicine, St. Louis, MO, [2]Saint Louis University School of Medicine, St. Louis, MO

Purpose

Secondary involvement of the central nervous system (CNS) by lymphoma is relatively uncommon but has substantial management implications including the use of treatments that crosses the blood brain barrier and consolidative transplant. Frequency of involvement depends on various features of the lymphoma including histological subtype, cytogenetic features, clinical risk factors,

stage and location of the disease. The type of involvement also varies, ranging from subtle leptomeningeal disease to frank parenchymal masses. Neuroradiologists play a critical role in establishing the absence or presence of CNS involvement. Thus, it is important to understand what defines CNS involvement, its various manifestations, potential mimics, and the accuracy of imaging compared to other diagnostic tests including cerebrospinal fluid testing and biopsy. Here we will provide a pictorial review to highlight these aspects of secondary CNS lymphoma. Relevant imaging modalities, including CT, MRI and F-18 FDG-PET will be discussed, including their value in staging, restaging, and monitoring response to treatment. Effects of CNS involvement upon management will be discussed, particularly in relation to imaging findings. LEARNING OBJECTIVES: 1. Illustrate CT, MRI, and F-18 FDG-PET imaging features of secondary CNS lymphoma, including post-treatment changes on follow-up imaging 2. Understand the role of CSF testing and biopsy in determining CNS involvement 3. Describe potential mimics of secondary CNS lymphoma 4. Describe the effects of CNS involvement upon management decisions SUMMARY: This educational exhibit will inform neuroradiologists on the diagnosis of secondary CNS lymphoma and the key information most relevant to the oncologist with regards to disease management

Materials and Methods

N/A

Results

N/A

Conclusions

N/A

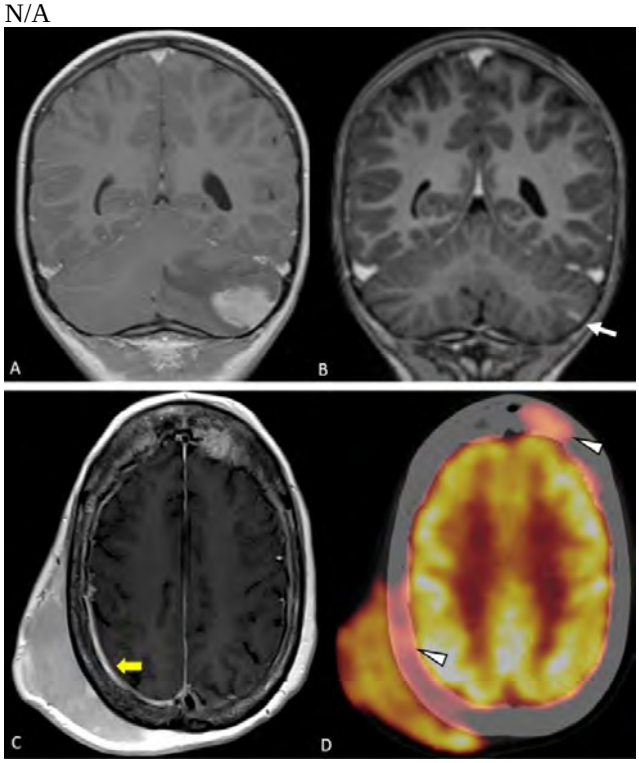

(Filename: TCT_378_Picture13.jpg)

1504

Series of Easy-to-Overlook Cases to Illustrate the Importance of Adhering to a Search Pattern in Neuroradiology

T Nguyen[1], A Hussien[2]

[1]University of Texas Southwestern Medical Center, Dallas, TX, [2]UT southwestern, Dallas, TX

Purpose

The educational exhibit illustrates series of easy-to-overlook cases with the aim to help Radiology trainees consolidate and consistently follow their Neuroradiology search pattern.

Materials and Methods

Search pattern is essential to the workflow of radiologists to maintain a thorough and consistent approach in interpreting studies. The purpose of this educational exhibit is to illustrate the importance of maintaining and adhering to a search pattern, specifically in Neuroradiology. For trainees, consistently following a search pattern will help improve diagnostic accuracy. This is especially critical in Neuroradiology, where abnormalities can be extremely subtle yet carry significant clinical impact.

Results

Through a series of cases, we aim to illustrate findings that often get overlooked if a search pattern is not followed consistently. For example, tendency to focus only along the course of the arteries in the CT Head and Neck Angiogram can lead to missing venous thrombosis, soft tissue injuries, or mass. Additionally, using maximum intensity projection (MIP) can be helpful to detect vasospasm

in CT or MR Head and Neck Angiogram. Extra-axial hemorrhage and extra-cranial mass can be missed if not using appropriate windowing. Furthermore, osseous injuries such as occipital condyle fractures, transverse process fractures, and perched facets are often only apparent on one plane, which highlights the significance of using multiplanar reformats.
Conclusions
Radiology search pattern is developed and hone overtime through learning, reviewing, and encountering cases. We hope that this educational exhibit will provide examples of easy-to-overlook cases to help radiology trainees consolidate and consistently follow their Neuroradiology search pattern.

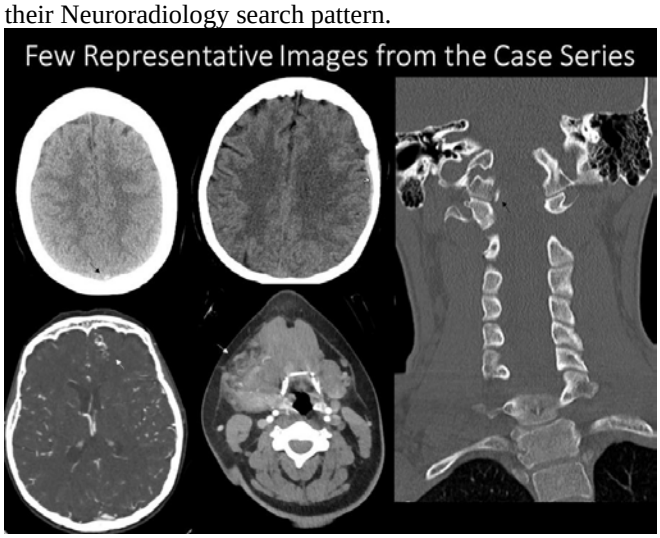

(Filename: TCT_1504_RepresentativeImages.jpg)

406

Sex-Differences of Cervical Carotid and Intracranial Atherosclerosis

I Bhatt[1], B Cucchiara[2], L Loevner[2], J Song[2]
[1]Drexel University College of Medicine, Philadelphia, PA, [2]University of Pennsylvania, Philadelphia, PA

Purpose
N/A
Materials and Methods
To review histologic and radiologic sex-differences of cervical carotid and intracranial plaque composition and identify knowledge gaps.
Results
We reviewed the pathology, radiology, and neurology literature on sex-differences in cervical carotid and intracranial atherosclerosis.
Conclusions
Carotid arteries: A population health study of 6420 participants who underwent carotid ultrasound evaluation showed males have a higher prevalence than females of carotid plaque until the 8th decade of life. A linear increase until 65 years was reported in males, whereas females showed an inflection point in the 5th decade after which the prevalence exceeded males (Fig 1A). Histologic analyses of 450 consecutive carotid endarterectomy specimens from asymptomatic and symptomatic patients showed females are more likely to have a fibrous and less atheromatous plaque phenotype compared to males accounting for age, stenosis degree, cardiovascular risk factors and clinical presentation (Fig 1B). Several MRI studies indicate that asymptomatic carotid arteries with ≤50% stenosis show an association between male sex and a higher volume of intraplaque hemorrhage and thin/ruptured fibrous caps adjusting for age and cardiovascular risk factors (Fig 1C). When stratified by age, carotid plaque in postmenopausal females show an increased prevalence of IPH approaching that of males. Intracranial arteries: Little is known about sex-differences in the prevalence and composition of intracranial atherosclerosis (ICAS). An autopsy study from 1968 studied ICAS lesions from 5033 consecutive autopsies and showed a higher frequency of ICAS lesions in males than females between the 4th to 6th decades. By the 9th decade, females showed more lesions than males (Fig 1D). The authors reported ICAS lesions were histologically more complex and stenotic in males than females until the 8th decade after which females revealed more stenotic lesions. The literature on sex-differences in ICAS composition is sparse apart from a CTA study reporting no significant sex-difference among symptomatic patients in the volumes of intracranial internal carotid and vertebrobasilar artery calcifications adjusting for age and cardiovascular risk factors. Understanding sex-differences will help elucidate disease mechanisms and influence approaches to care and outcomes. Compared to cervical carotid atherosclerosis, less is known about sex-differences in the composition of intracranial atherosclerosis.

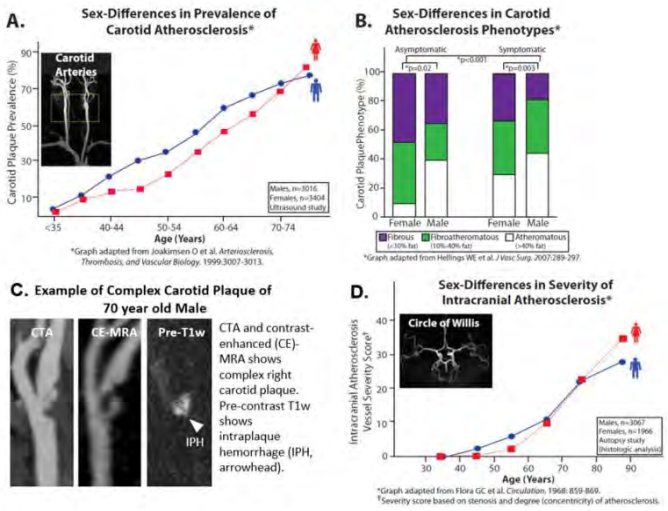

(Filename: TCT_406_ASNRAbstract111521.jpg)

1356

Sinus CT - Standardized Imaging Protocol to Eliminate Need for Repeat Scan for Operative Planning

E Monahan[1], D Zander[1]

[1]*University of Colorado, Aurora, CO*

Purpose

This exhibit will catalog and review the imaging protocols required for the most commonly used available surgical navigation systems. The goal is to determine which protocol requirements for multiple surgical navigation systems can be adapted into a unified standard imaging protocol that could be used by the greatest number of proprietary navigation systems as well as upfront diagnosis, preventing the need for a dedicated guidance scan.

Materials and Methods

Identify and catalog the most common imaging protocol requirements for available surgical navigation systems to adapt into a standard protocol.

Results

Compile list of manufacturers of surgical navigation systems approved within the United States for use in sinus surgery. Identify imaging protocols required for these navigation systems. Then adapt the common requirements into a standard protocol that can be used for both initial diagnosis and operative planning.

Conclusions

Imaging work up leading to sinus surgery often requires two distinct CT studies to be performed - one for initial diagnosis and a second for procedural guidance. This results in increased radiation exposure for the patient and increased cost to the medical system.1 These two issues have been identified, although local practice differences and preferences have limited the ability of a standard imaging protocol that could be used both for initial diagnostic imaging and surgical navigation. By compiling a list of required protocols for several of the most widely used surgical navigation systems, the most commonly required protocol parameters have been identified. Stryker, Medtronic, Brainlab and General Electric surgical navigation systems are some of the more widely used surgical navigation systems included. We hope that our education exhibit will serve as a resource for imaging parameters for these proprietary systems as well as provide a sample CT Sinus protocol that can be ordered by clinicians when surgical intervention is anticipated.

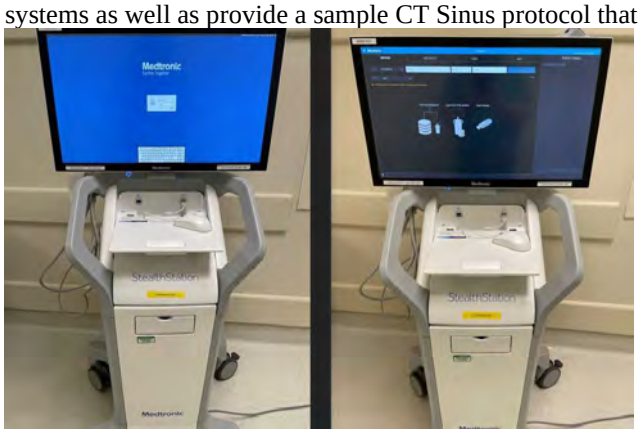

(Filename: TCT_1356_MedtronicStealthStation.jpg)

1043

Skull Base Osteomyelitis: Main imaging findings for the diagnostic suspicion

A Miranda Merchak[1], A Schilling[2]
[1]Hospital Barros Luco, Santiago, Chile, [2]Universidad Mayor, Santiago, Chile

Purpose

Skull Base Osteomyelitis (SBO) is an uncommon pathology with diverse clinical manifestations, which can lead to fatal scenarios in case of late diagnosis and/or treatment. An infectious extension from a primary focus (auditory canal, mastoid, teeth, nasal sinuses) through Havers' system to a secondary focus (skull base) has been proposed as pathogenesis. Dissemination secondary to trauma, surgery and hematogenous route have been reported but are infrequent. It is classified according to frequency in: Typical SBO: Older adult patients with a history of diabetes mellitus with central inflammatory/infectious process resulting from a primary auditory complication (necrotizing eternal otitis eterna). It usually involves the temporal bone. Atypical SBO: Inflammatory/infectious involvement predominantly in the sphenoid and/or occipital bone, with absence of a history of otitis externa and presence of initial symptoms associated with headache as the only symptom, with eventual development of cranial nerve neuropathies. It is a pathology with nonspecific initial symptoms with multiple differential diagnoses, so it is essential to develop an early suspicion in at-risk populations and to have access to a diagnostic protocol that allows confirmation and appropriate treatment. Objectives: Definition of the disease Diagnostic on CT and MRI Complications Conclusions

Materials and Methods

To compare the diagnostic utility of computed tomography of the ears and magnetic resonance imaging of the brain in the diagnosis of skull base osteomyelitis.

Results

A series of cases are presented.

Conclusions

Skull Base Osteomyelitis is an infrequent pathology with diverse clinical manifestations and multiple differential diagnoses. Brain MRI is the best radiological method with good discrimination of soft tissue alterations and intracranial involvement. The findings are focal or diffuse hypointensity of skull base bone marrow in T1, T2-STIR hyperintensity, bone enhancement, exocranial soft tissue infiltration, signs of otitis. Ear CT allows an accurate evaluation of bone components (medullary expansion, sclerosis, cortical discontinuities, bone sequestrations) and their destructive processes/remodeling. Definitive diagnosis requires histopathological confirmation complemented by bacterial/fungal cultures. Late diagnosis and treatment leads to increased mortality and risk of complications such as chronic cranial nerve dysfunction, cavernous sinus thrombosis, meningeal and brain parenchymal extension.

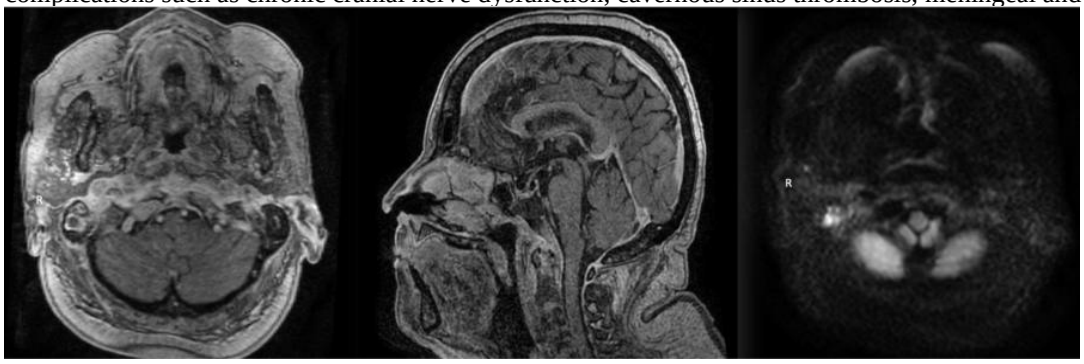

(Filename: TCT_1043_Imagen2.jpg)

746

So You Want to Shorten the Time of MRI Protocols While Preserving the Quality? A Comparison of Time-Efficient MR Techniques and Critical Details to Consider

M von Reppert[1], H Shooli[2], I Ikuta[3], S Abi Fadel[3], A Malhotra[3], A Abou Karam[3], W Zucconi[3], M Johnson[3], A Mahajan[3], F Jiang[3], P Kokeny[4], S Sethi[5], E Haacke[5], M Aboian[3]
[1]Brain Tumor Research Group, Yale School of Medicine, New Haven, CT, [2]Bushehr University of Medical Sciences, Bushehr, Iran, [3]Department of Radiology, Yale School of Medicine, New Haven, CT, [4]SpinTech, Inc., Bingham Farms, MI, [5]Wayne State University, Detroit, MI

Purpose

There is a critical need to develop time-efficient workflows in clinical neuroradiology practice, resulting in decreased use of anesthesia in pediatric neuroimaging and development of rapid screening protocols for applications such as stroke. We review different methods for shortening MRI acquisition time including Synthetic MRI, artificial intelligence-based image reconstruction and rapid multi-echo multi-contrast techniques such as Strategically Acquired Gradient Echo (STAGE) imaging. We aim to describe the basic principles of these methods with a focus on what a neuroradiologist needs to know before implementing them into clinical practice.

Materials and Methods

N/A

Results
We review the literature of different time-shortening image reconstruction approaches and their applications to clinical practice. We evaluate different commercial vendors that provide these services, as well as our experience in implementing them in our own clinical practice.
Conclusions
MAGnetic resonance image Compilation (MAGiC) as an example of synthetic MRI, AI-based image reconstruction and STAGE are approaches that have gained increasing attention in recent years for their ability to improve patient throughput by reducing overall acquisition time and, as for STAGE and MAGiC, to provide quantitative information and enhanced contrasts. Our educational exhibit provides detailed information of the current published literature on novel time-shortening MRI protocols such as MAGiC and STAGE through comparison of these protocols. We also highlight the conceptual difference of these protocols to AI-based image reconstruction and focus on implications for clinical use. We present a case-based review of the application of STAGE rapid imaging technique into tertiary clinical practice in a cohort of stroke, brain tumor and pediatric patients on 1.5T and 3T MRI. Our initial implementation scan times for 2mm slice thickness ranged from under 7 minutes at 3T and 9 minutes at 1.5T, and were decreased to under 5 minutes at 3T and 7 minutes at 1.5T. We also discuss the potential of providing quantitative reports of microbleed number by anatomical location and where it affected radiological interpretation of imaging. Among our cases, there was a distribution of 0-16 foci measured with 100% of the scanned cases providing the anatomy-based quantitative reports. We present a compelling case to help gain a better understanding of these techniques prior to their incorporation into clinical practice.

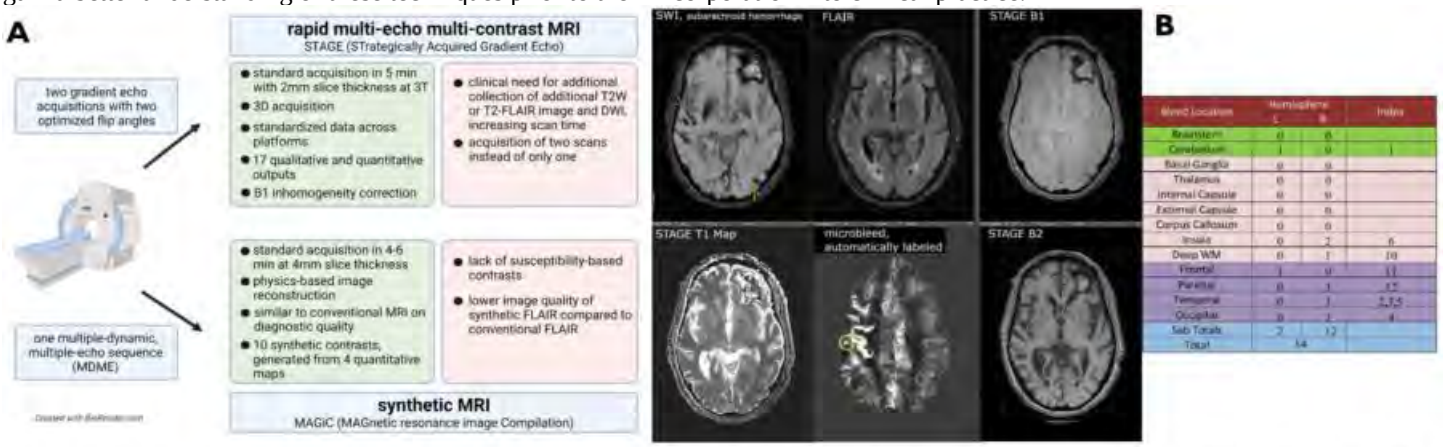

Fig. 1: A) Comparison of rapid multi-echo multi-contrast- and synthetic MRI acquisitions; B) representation of images obtained on a patient with acute stroke and multiple microbleeds using STAGE-MRI, output format for automated reporting of microbleeds.
(Filename: TCT_746_final-mri_comparison_graphic.jpg)

927
Something Smells Fishy: Imaging of Sinonasal Masses and Multidisciplinary Approach
S Bhuta[1], K Huang[2]
[1]Gold Coast University Hospital & Griffith University School of Medicine, Gold Coast, QLD, [2]Gold Coast University Hospital, Gold Coast, QLD

Purpose
Sinonasal neoplasms are broadly classified as either epithelial or mesenchymal. Among sinonasal malignancies, squamous cell carcinoma (SCC) accounts for approximately 80%.These cancers of the paranasal sinuses are clinically silent and in nearly all cases, have already become large with invasion of surrounding organs at the time of the initial examination. CT and MRI are complimentary with PET-CT in accurate tumor staging and in assessing resectability.
Materials and Methods
1) To characterize sinonasal mass lesions with multimodality imaging and how hi-resolution imaging influences TNM staging and surgical management. 2) Understanding complex anatomy of the region and key imaging points that dicate surgical outcomes.
Results
All the patients were referred by the Otorhinolaryngology Department with biopsy proven sinonasal masses and discussed at tumor boards. Clinical presentation, nasal endoscopy findings, imaging findings and histopathology were compiled whenever applicable. Patients underwent CT/Spectral CT, 3T MRI and PET-CT for staging.
Conclusions
Contrast enhanced CT identifies key involvement of nasal septum, intracranial extension(fig) and or origin in the paranasal sinuses. Bony erosion is always a marker of malignant mass .SCC is more aggressive, often has central necrosis and prominent bone destruction. Contrast-enhanced fat-suppressed T1-weighted images are useful in identifying perineural, dural, orbital and intracranial invasion. MR findings of cribriform plate involvement, perineural spread and brain invasion can often deem a patient inoperable. Diffusion restriction indicates hypercellularity and is seen in lymphoma and plasmacytoma. Plasmacytoma tends to be more

heterogenous than NHL, with moderate T1 intensity. Both plasmacytoma and NHL tend to have lower ADC than SCC. Melanoma tends to occur in the nasal septum and turbinate with a hemorrhagic component. Lymph nodal involvement and distant metastatic disease on PET-CT(fig) are all vital parameters in decision making in tumor boards. MR is also reliable in post-operative period and tumor surveillance. Although the radiological differentiation of sinonasal malignancies is very difficult the tumor location, growth pattern into adjacent bone, tumor homogeneity, internal signal intensity, contrast enhancement pattern, and DWI with ADC measurement may facilitate an adequate diagnosis and influence surgical management v/s chemo-radiotherapy decision making algorithms and patient prognosis.

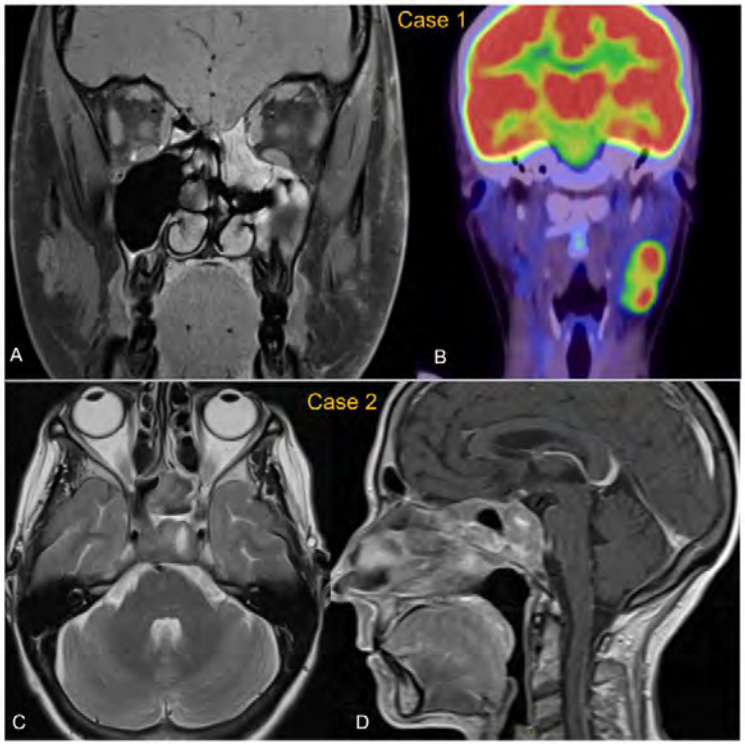

(Filename: TCT_927_SNCase.jpg)

340

Spectrum of Monogenetic CNS Vasculopathy in Children: An imaging Review

N Gupta[1], N Wilson[2]

[1]CHEO Univ of Ottawa, Ottawa, Ontario, [2]CHEO, Ottawa, Ontario

Purpose

Pediatric CNS vasculitis (PCV) is a heterogeneous group of disorders with multifactorial etiology but shared pathogenesis. In children and young adults with cerebral vascular disorders, rare genetic & sporadic mutations should also be considered in the differential of CNS vasculopathies. Imaging findings can be very variable but few of these mutations show characteristic imaging features vital to the specific diagnosis that can guide the specific management in these children. Family history may help to identify the cause, and genetic evaluation is required for confirmation.

Materials and Methods

1. Review the current literature of rare genetic causes of CNS vasculitis in children. 2. Describe the vascular and parenchymal imaging findings in various genetic pediatric CNS vasculitis 3. Discuss the role of conventional imaging modalities and advanced imaging sequences in the diagnosis and prognosis of cerebral vasculitis.

Results

1. Comprehensive discussion of the various monogenetic disease resulting in CNS vasculitis in children like Neurofibromatosis, smooth muscle cell dysfunction - ACTA2 and vascular basement membrane - COL4A1. 2. Identify and familiarize with the salient imaging features of rare genetic Paediatric CNS vasculitis that could help in the diagnosis and to narrow the differentials. 3. Propose a stepwise Clinico-radiological evaluation rare genetic Paediatric CNS vasculitis that could help in guiding the appropriate treatment

Conclusions

The purpose of this exhibit is to outline the rare monogenetic causes of CNS vascular disorder in children with a broad review of the literature. We will also describe the specific vascular and parenchymal neuroimaging findings associated with each entity to facilitate precise diagnosis. We would focus on the role of combined clinical and radiological approaches in arriving at the final diagnosis along with lab evaluation and genetic workup.

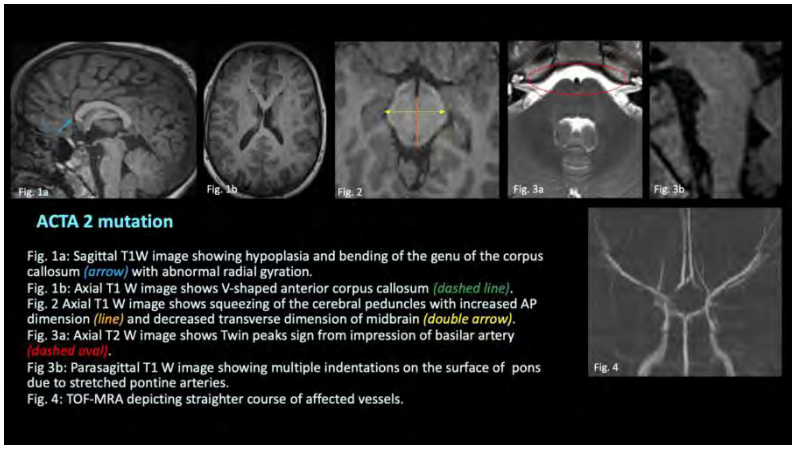

(Filename: TCT_340_ASNR22JPEG.jpg)

1299

Spectrum of Neuroimaging Features of Histiocytosis in Children

O Simsek[1], J Moon[2], K Spagnolo[3], S Clifford[3], C ALVES[3], M Santi-Vicini[3], K Shekdar[3]

[1]Dr Abdurrahman Yurtaslan Ankara Oncology Training and Research Hospiital, Ankara, Turkey, [2]Temple University Hospital, North Wales, PA, [3]Children's Hospital of Philadelphia, Philadelphia, PA

Purpose

Learning Objectives: Purpose of this exhibit is to: • Review neuroimaging findings of Langerhans and non-Langerhans cell histiocytosis in children with illustrative case examples • Highlight imaging pearls and pitfalls for rare subtypes of histiocytosis • Review imaging literature on histiocytosis including summary of WHO 2021 updates of CNS histiocytic tumors Summary: Histiocytosis syndromes, characterized by abnormal accumulation and infiltration of histiocytes (1). In 2016, the WHO central nervous system (CNS) tumor classification divided histiocytosis syndromes into five main groups – L, C, R, M, and H groups (1). The 2021 WHO CNS tumor classification includes only the histiocytic tumor entities that occur relatively often in the CNS or entities that have special histological or molecular features when they occur in the CNS (2). LCH is one of the most common histiocytosis affecting the pediatric population (1). LCH lesions involving the calvarium, facial bones, skull base, vertebrae and pituitary gland are common. Brain parenchymal lesions of LCH are rare and show variable imaging features, with or without mass-like configuration (1,3). From the non LCH group, CNS involvement in children is more often seen seen in Juvenile Xanthogranuloma (JXG) and Hemophagocytic lymphohistiocytosis (HLH) and extracranial involvement in the form of cervical lymphadenopathy is seen in Rosai-Dorfman disease (RDD) (2). Lesions of LCH and non LCH disorders can vary from single lesions to multiple lesions of CNS and extra CNS organs. In this exhibit we present illustrative cases of common LCH and few rare non LCH histiocytosis in pediatric patients and summarize the characteristic neuroimaging findings.

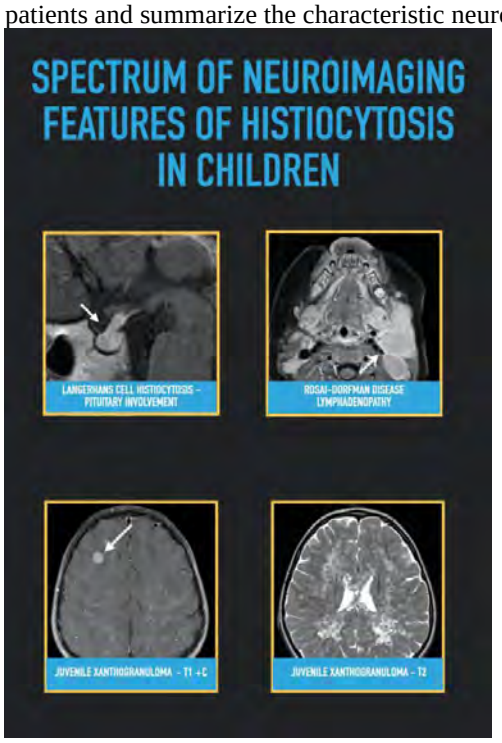

(Filename: TCT_1299_Histiocytosis-image.jpg)

438

Spinocerebellar Degeneration: A systematic differential diagnosis based on cerebellar functional anatomy

K Sato[1], K Kamagata[1], Y Saito[2], W Uchida[2], J Kikuta[1], Y Ikenouchi[1], M Suzuki[3], A Wada[1], S Aoki[1]

[1]Juntendo University, Tokyo, Japan, [2]Juntendo University School of Medicine, Tokyo, Japan, [3]Juntendo University Urayasu Hospital, Urayasu-city, Chiba

Purpose

Spinocerebellar degeneration (SCD) includes various progressive diseases presenting ataxia due to degeneration of the cerebellum and brainstem. Differential diagnosis of SCD on MRI is often difficult since imaging findings are subtle and overlapping among several diseases. It is known that the cerebellar phylogenetic origins are related to symptoms and degeneration patterns of SCD. Knowledge of cerebellar functional anatomy related to phylogenetic origins could simplify differential diagnosis of SCD.

Materials and Methods

In this presentation, we will review how to make better differential diagnosis of SCD with MRI. In addition, we will show recent research regarding cerebellar functional anatomy.

Results

We will review the followings. (1) pathogeneses of SCD (2) differential diagnosis flow of SCD (3) cerebellar functional anatomy related to phylogenetic origins (4) recent research of cerebellar functional anatomy as part of brain connectivity.

Conclusions

[Results] (1) SCD includes various pathogeneses; hereditary diseases such as spinocerebellar ataxia (SCA), dentatorubral-pallidoluysian atrophy (DRPLA), or Friedreich's ataxia (FRDA) and sporadic diseases such as multiple system atrophy (MSA) or secondary ataxia. (2) For differential diagnosis with MRI, neuroradiologists need to precisely evaluate atrophy pattern and abnormal signal intensities of the brain. Clinical information and knowledge of cerebellar functional anatomy are helpful for systematic differential diagnosis. (3) The cerebellum has three regions derived from different phylogenetic origins; the vestibulocerebellum, the spinocerebellum, and the cerebrocerebellum. They are related to the efferent and afferent pathways of the cerebellum connecting to the brainstem, spine, and cerebrum. Therefore, degeneration of each region causes different symptoms. (4) Recent research have demonstrated that the cerebellar function extends to non-motor domains such as working memory or emotion. Advanced structural/ diffusion analyses and connectivity-based parcellation with/without artificial intelligence (AI) have revealed the importance of cerebellar functional anatomy as part of brain connectivity. [Conclusion] Neuroradiologists can make differential diagnosis of SCD systemically based on cerebellar functional anatomy. Knowledge of phylogenetic origins related to the pathways connecting to other regions of the brain would help to understand cerebellar functional anatomy.

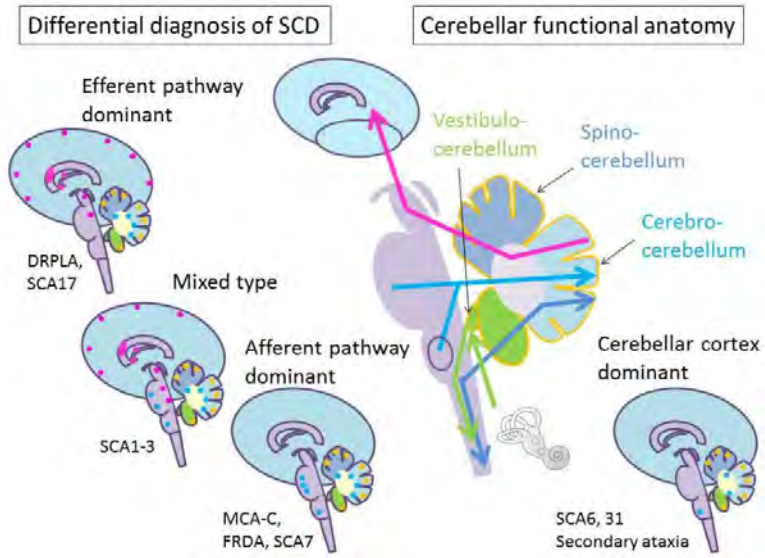

(Filename: TCT_438_ASNR2022_figure.jpg)

893

State-Of-The-Art Imaging of Intracranial Blood

M Aslam[1], S Chaker[2], M Shalaby[3], A Moawad[4], B Jaber[1], O Teytelboym[1]

[1]Mercy Catholic Medical Center, Darby, PA, [2]Mercy Catholic Medical Center, Havertown, PA, [3]Mercy Catholic Medical Center, LANSDOWNE, PA, [4]Mercy Catholic medical center, Darby, PA

Purpose

Summary: This exhibit will illustrate the applications of modern techniques including Dual Energy CT (DECT) automated reformats and novel susceptibility weighted image (SWI) MRI sequence to detect intracranial hemorrhage; and tips and tricks to differentiate paramagnetic blood from diamagnetic calcifications. Sound knowledge of novel neuroimaging techniques enhances diagnostic accuracy. Educational objectives: 1. Pictorial review of the applications of modern Dual Energy CT reformats to detect intracranial

blood such as bone removal reformat, virtual non-contrast and iodine overlay maps. 2. Pictorial review of the applications of novel high spatial resolution, susceptibility weighted image (SWI) MR sequence in the detection of intracranial blood. 3. Pros and cons of SWI and GRE MRI sequences. 4. Applications of phase mask MRI sequence to differentiate blood from dystrophic calcifications.
Materials and Methods
N/A
Results
N/A
Conclusions
N/A

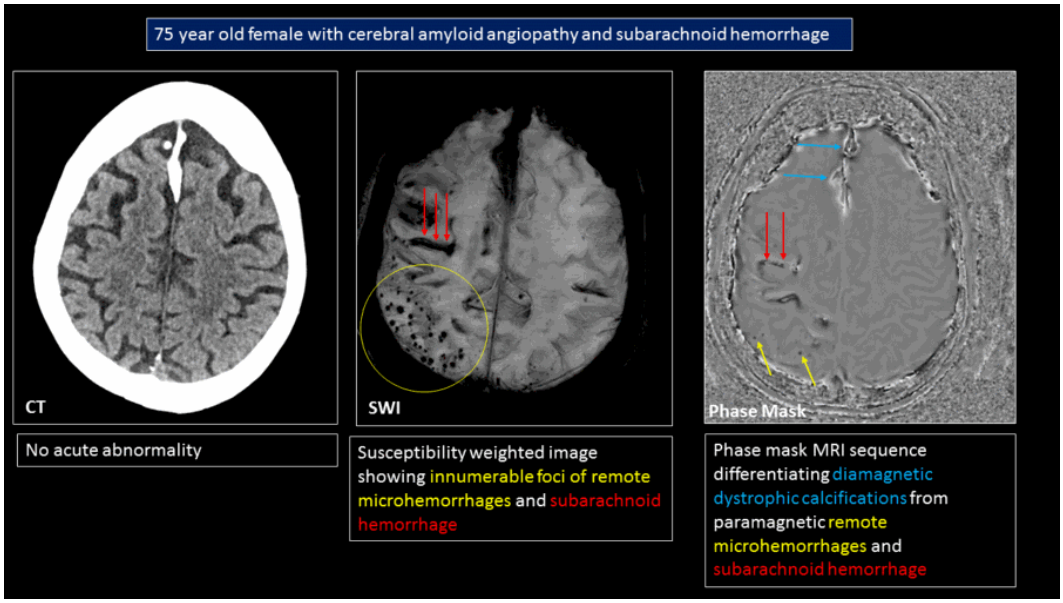

(Filename: TCT_893_ASNR2022.gif)

683

Stones, Bones, Groans, and Psychiatric Overtones: a Pictorial Review of Parathyroid Adenomas

A Rashad[1], T Do[1], N Gupta[1], J Gupta[2]
[1]Department of Radiology, Tulane University School of Medicine, New Orleans, LA, [2]Department of Radiology, New Orleans VA Medical Center, New Orleans, LA

Purpose
• Review embryologic origin and anatomy of parathyroid adenomas • Describe the epidemiology, pathophysiology, and symptoms of primary hyperparathyroidism • Recognize the key clinical and diagnostic features of primary hyperparathyroidism • Define characteristic ultrasound, scintigraphy, CT, and MRI findings of parathyroid adenomas • Discuss the role of imaging in preoperative evaluation of primary hyperparathyroidism
Materials and Methods
The most common cause of primary hyperparathyroidism is by benign overgrowth, or adenomas, of the parathyroid glands. Diagnosis of primary hyperparathyroidism is made with concurrent findings of elevated serum calcium and serum parathyroid hormone. Management options include medications such as cinacalcet and hormone replacement therapy, or definitive surgical excision through conventional or minimally invasive approaches. Imaging is performed during surgical planning for preoperative localization.
Results
N/A
Conclusions
Though most parathyroid adenomas are located immediately posterior or inferior to the thyroid gland, some can present in ectopic locations, most commonly in the mediastinum or carotid sheath. Ultrasound and scintigraphy have traditionally been favored imaging modalities to evaluate parathyroid adenomas, but recent evidence has shown that 4D computed tomography (CT) demonstrates equivalent or superior accuracy in localization when compared to more traditional modalities. In this presentation, we will delineate characteristic imaging findings of ultrasound, scintigraphy, CT, and magnetic resonance imaging (MRI) of parathyroid adenomas in a pictorial review, as well as describe five unusual presentations. Additionally, we will review the interpretation of 4D CT images and their technical considerations. The imaging modalities used to evaluate parathyroid adenomas continue to vary depending on multiple factors including surgeon preference, radiologist expertise, and availability. Though 4D CT has been shown in some studies to have equivalent or superior preoperative localization compared to other modalities, more prospective studies are needed before 4D CT can be widely adopted.

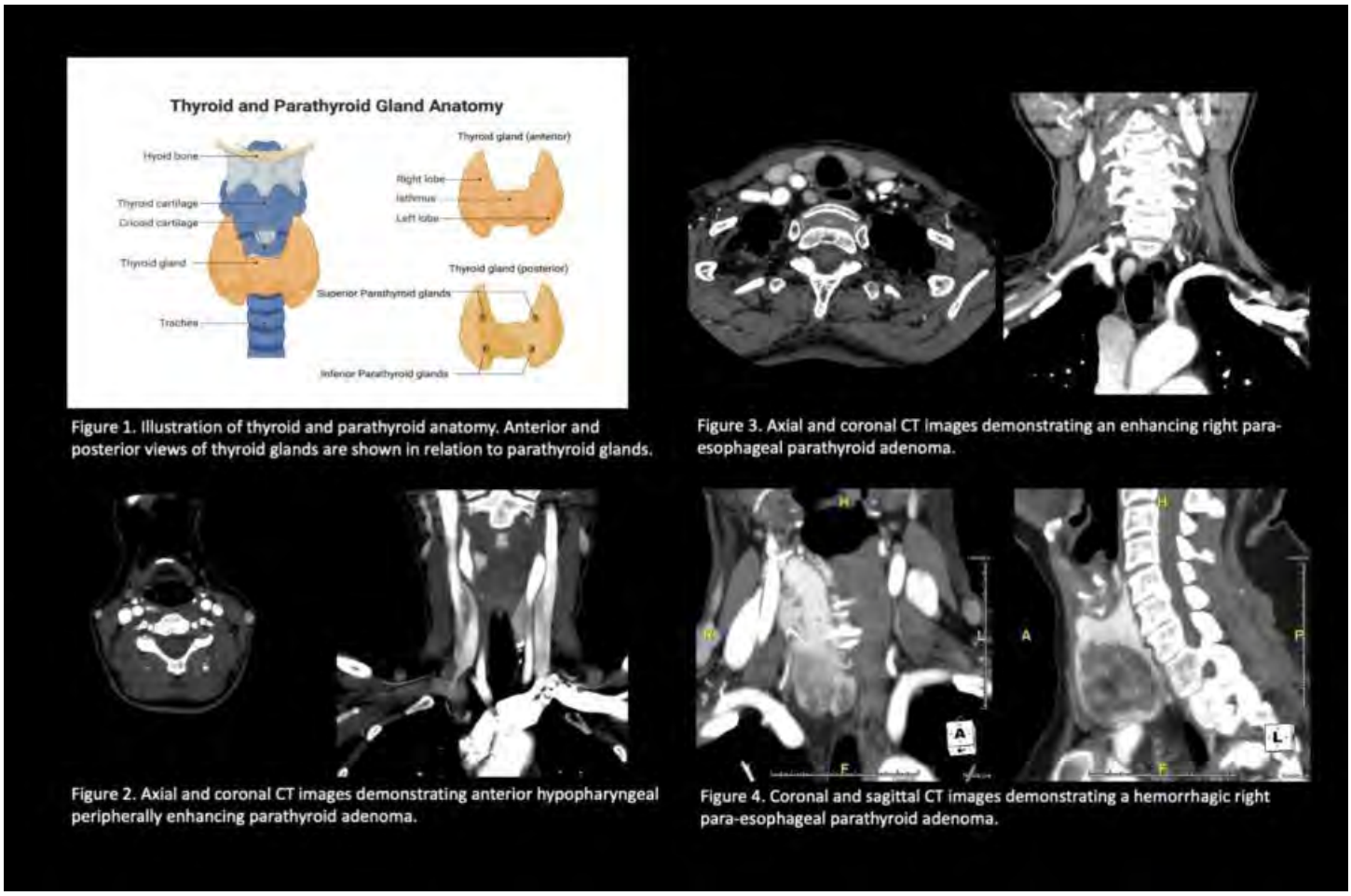

(Filename: TCT_683_ASNRParathyroidAdenomasEE.jpg)

317

Stuck in the Middle? A Pictorial Review of Pathological Processes Affecting the Corpus Callosum

S Saith[1], O Raslan[1], L Hacein-Bey[1], A Paydar[1], M Bobinski[1], R Assadsangabi[1], V Ivanovic[1], A Ozturk[1]
[1]UC Davis Medical Center, Sacramento, CA

Purpose

- Briefly review the embryological development, anatomy, and function of the corpus callosum - Review imaging features of lesions of the corpus callosum by using a case-based approach

Materials and Methods

The corpus callosum (CC), a highway of dense white matter tracts, is the major interhemispheric connection in the brain. A wide spectrum of common and uncommon pathologies involves the CC. We review imaging findings and key clinical features of a wide variety of pathologies of the CC.

Results

We retrospectively evaluated brain MRI studies from our PACS system with cases of corpus callosum pathologies to form this educational exhibit. The exhibit is organized as follows: 1) Brief review of embryology, anatomy, and function of CC 2) Presentation of CC pathologies subdivided according to etiology: - Congenital Anomalies - Trauma - Vascular - Neoplastic - Demyelinating Disease - Leukodystrophy - Infection/Inflammation - Toxic/Metabolic

Conclusions

CC is the largest commissural white matter bundle in the brain with a wide range of pathologies, some with characteristic clinical presentations and many with unique features at imaging. Diagnosis of callosal lesions or anomalies plays a critical role in clinical management. The cases in this educational exhibit illustrate key imaging features of various common and uncommon pathologies involving the corpus callosum, with an emphasis on relevant clinical presentations and key imaging features to narrow the differential diagnosis.

Stuck in the Middle?
A Pictural Review of Pathological Processes Affecting the Corpus Callosum

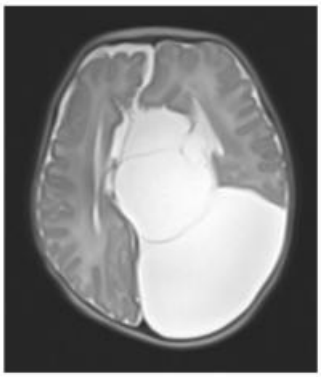

Figure 1. Callosal Agenesis and large interhemispheric cyst.

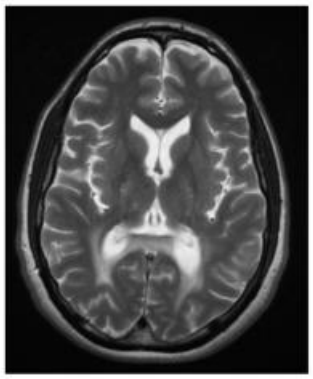

Figure 2. CSFR-1 Adult-onset leukodystrophy.

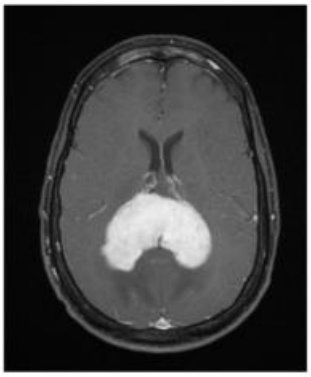

Figure 3. Lymphoma.

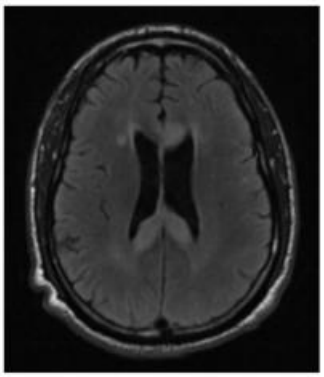

Figure 4. Marchiafavi-Bignami disease.

(Filename: TCT_317_CCfigures.jpg)

1125

Subsequent Neoplasms Involving the CNS in Survivors of Childhood, Adolescent and Young Adult Cancer and Related Lesions

N Sabin[1]

[1]St. Jude Children's Research Hospital, Memphis, TN

Purpose

The number of survivors of childhood, adolescent and young adult (CAYA) cancer continues to grow with over 80% of this group becoming long-term survivors. These individuals are at risk for morbidity and mortality resulting primarily from the treatments they received for their malignancies and have an increased risk for developing subsequent CNS neoplasms, a particularly impactful late effect of of cancer treatment, compared to the general population. This exhibit reviews the imaging appearances of subsequent CNS neoplasms in CAYA cancer survivors and subsequent neoplasms in immediately adjacent anatomic regions as well as imaging mimics of subsequent CNS neoplasms. Finally, recent recommendations from the International Late Effects of Childhood Cancer Guideline Harmonization Group regarding imaging surveillance for subsequent CNS neoplasms in these survivors are presented. Educational Objectives: 1. Discuss the risk factors for subsequent CNS neoplasms in CAYA cancer survivors and the types of neoplasms that are most prevalent in this group as well as considerations for survivors with cancer predisposition syndromes. 2. Review the imaging appearances of subsequent CNS neoplasms in CAYA cancer survivors as well as subsequent neoplasms that occur in immediately adjacent anatomic regions. 3. Describe the appearances of imaging mimics of subsequent CNS neoplasms in survivors of CAYA cancer. 4. Discuss the recommendations for imaging surveillance for subsequent CNS neoplasms in CAYA cancer survivors contained in a recent systematic review by the International Late Effects of Childhood Cancer Guideline Harmonization Group.

Materials and Methods

The purpose of this exhibit is to describe the types of neoplasms seen in survivors of childhood, adolescent, and young adult (CAYA) cancer, show examples of these tumors and review the risk factors for subsequent neoplasms in this survivor group. The exhibit also presents the appearance of imaging mimics of subsequent CNS neoplasms and the findings and recommendations of a recent systematic review by the International Late Effects of Childhood Cancer Guideline Harmonization Group regarding imaging surveillance for subsequent CNS neoplasms in CAYA cancer survivors.

Results

N/A

Conclusions

N/A

1153

Substantia Nigra: Going Beyond Parkinsonian Pathologies

G Curaudeau[1], A Capizzano[1], R Kurokawa[1], M Kurokawa[1], J Kim[1], T Moritani[1]
[1]*University of Michigan, Ann Arbor, MI*

Purpose

Highlight important components of substantia nigra (SN) which may contribute to variability of disease, including anatomic, physiologic and functional components. Leverage unique cases in order to shed light on the differences in pathologies, beyond the typical Parkinson (PD) and Parkinson like diseases.

Materials and Methods

To highlight the anatomic foundations (pars compacta, pars reticulata), review the physiologic substrate (neuromelanin in dopaminergic neurons)(1), and unravel the intertwined functional pathways that lead to various pathologies. To go beyond the imaging findings of PD, and expose the spectrum of primary and secondary degeneration, mitochondrial disease, Wilson disease, viral infection, and drug-induced pathologies that impact the SN.

Results

Correlating a focused literature review with a broad sampling of cases collected from our local hospitals in the University of Michigan system. Specifically, showing multiple cases, with clinically relevant information, in parallel to help outline differentiating factors. Our materials encompass the spectrum of primary degeneration (2) (Parkinson-like disease, multiple system atrophy, progressive supranuclear palsy) and secondary degeneration (striato-nigral pathway) from infarction/hemorrhage, mitochondrial disease (MELAS (3), Leigh, Kearn-Sayre syndrome), neurodegeneration with brain iron accumulation (NBIA) such as beta-propeller protein-associated neurodegeneration (BPAN) (4), Wilson disease, viral infection (West Nile, Japanese, Rabies encephalitis), and drug-induced (vigabatrin, drug abuse) pathologies that impact the SN.

Conclusions

Substantia Nigra (SN) lies at the crossroads of many functional pathways, yet, it's importance is often overlooked. Historically, clinical manifestations of PD and Parkinsonian like diseases have furthered our understanding of the SN. Yet, as our imaging capabilities evolve, our insight of the anatomic, functional and physiologic basis for disease in this area also expands. As our general sensitivity improves with higher resolution MR technologies, our ability to resolve pathologies in the SN will continue to expand. This abstract seeks to demystify anatomic, physiologic and functional aspects of the SN in order to go beyond identification of PD, in order to provide a more specific differential of diseases.

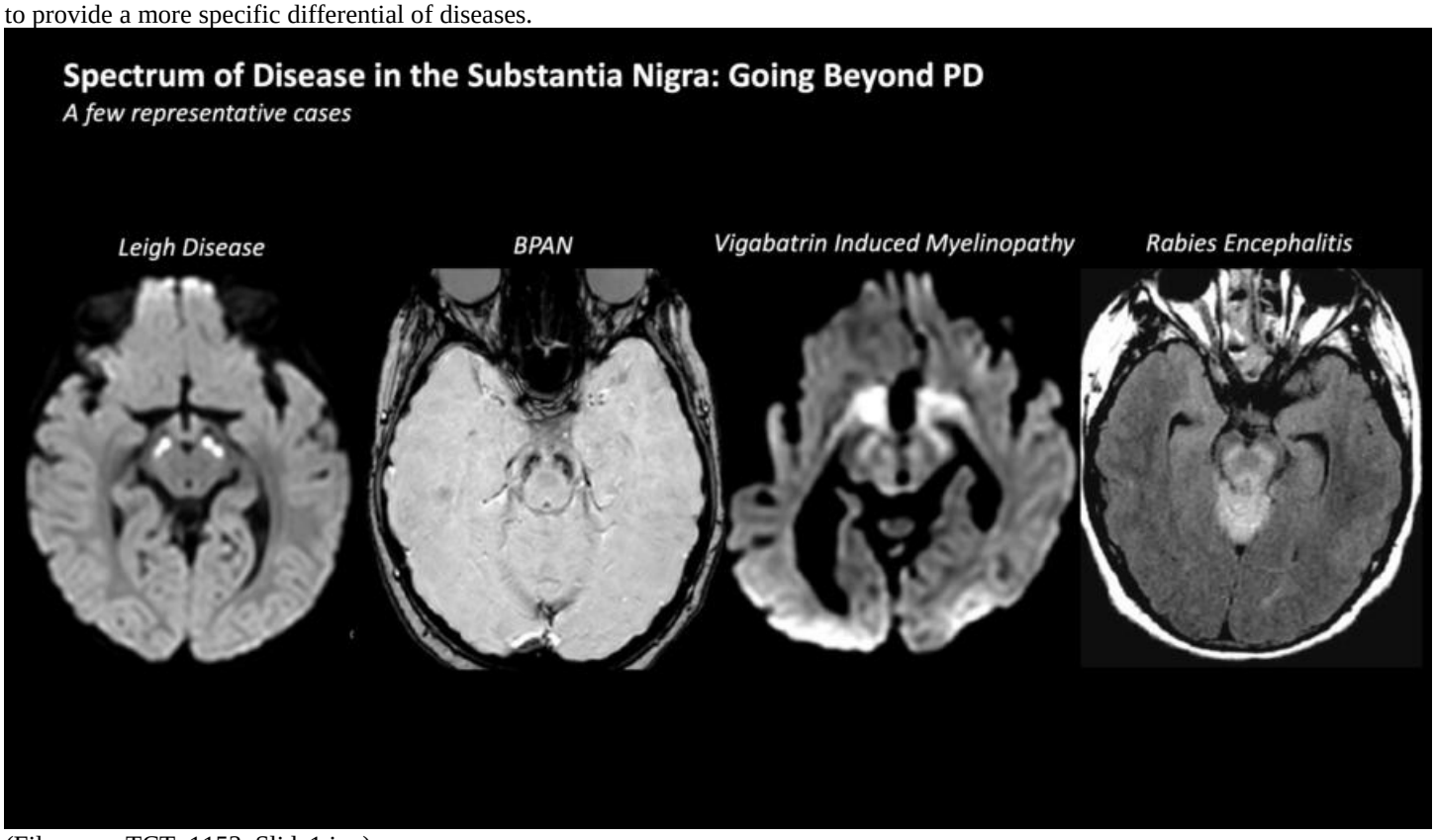

(Filename: TCT_1153_Slide1.jpg)

500

Successful fusion versus pseudoarthrosis after spinal instrumentation: More than meets the eye

J Benson[1], V Lehman[1], N Murthy[1], J Wald[1], A Sebastian[1], F Diehn[1]
[1]Mayo Clinic, Rochester, MN

Purpose

To review the common, and uncommon, imaging manifestations of pseudoarthrosis after instrumentation of the spine.

Materials and Methods

The last few decades have witnessed a substantial increase in the rate of instrumented spinal operations performed in the United States, and worldwide. This is related to a number of factors: diagnostic imaging techniques have improved, there is better understanding of the biomechanical properties of the spine, the number of spinal fixation devices has increased, and new alternatives to bone grafting materials have been developed. Still, nonunion at instrumented segments remains a common post-operative complication. Most radiologists are familiar with the fundamental imaging findings of arthrodesis in a post-operative spine. Nevertheless, accurate identification of successful fusion in an instrumented spine is surprisingly complex. Despite the commonplace of these procedures, there is a surprising lack of consensus for both performing and interpreting post-operative imaging. The purpose of this exhibit is to review what a radiologist needs to know about the imaging of arthrodesis and pseudoarthrosis, including expected post-operative changes and complications, with attention to some of the more nuanced and subtle findings.

Results

This is an education review of the nuanced imaging of instrumented spinal fusion versus pseudoarthrosis.

Conclusions

Assessment of arthrodesis in an instrumented spine is notoriously difficult and necessitates evaluation of both primary and secondary signs of nonunion to accurately diagnose pseudoarthrosis. Although spine instrumentation and fusion are commonly performed, there continues to be a lack of consensus guidelines defining a successful fusion on post-operative imaging. Currently available criteria are often overly simplistic and fail to recognize the complexity of imaging manifestations of arthrodesis and pseudoarthrosis. Evaluation of instrumented spinal fusion requires scrutiny of images across multiple modalities – particularly CT and dynamic radiographs, and a full understanding of the secondary signs of micro-motion across an instrumented segment.

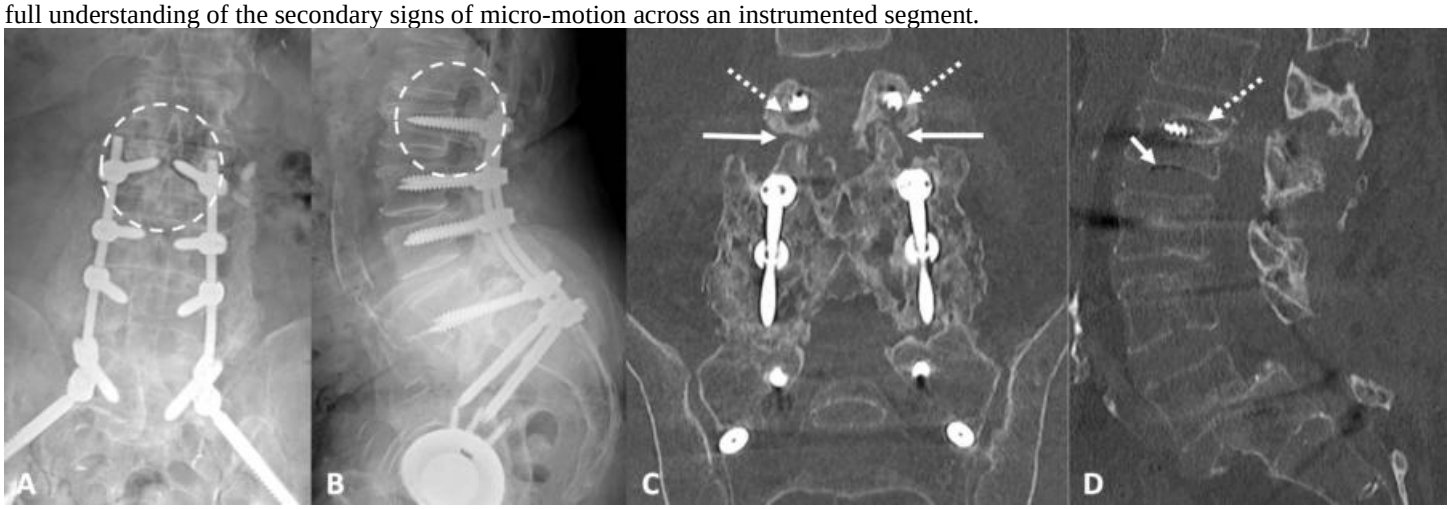

(Filename: TCT_500_Figure8jpeg.jpg)

109

Surgical Landmines in T-Bone: What Every Radiologist Should Report in a Pre-Operative CT

S Sharma[1], V Gautam[2]
[1]Mayo Clinic, Scottsdale, AZ, [2]Synergy Radiology Associates, Houston, TX

Purpose

'The eye sees only what the mind knows'. The temporal bone is a complicated part of head and neck. There are many important surgical landmarks in the T-bone such as position of jugular bulb, position of sigmoid sinus and relative position of tegmen tympani that must be assessed on every temporal bone CT. More so if a mastoidectomy, either canal up or down, is contemplated. It is extremely easy to get overwhelmed with the convoluted anatomy and fail to note an important anatomic variant which may prove to be disastrous to our ENT surgeons if they discover that in the OR. Therefore, it is extremely important for radiologists to incorporate these landmarks in our search pattern and examine and include them in our reports.

Materials and Methods

1. Describe the pertinent anatomy of T-bone with respect to important surgical landmarks. 2. Provide easy pictorial description of why it is important for us to evaluate these structures. 3. Present a format in which these can be incorporated in every T-bone CT report.

Results

N/A

Conclusions
There are a few important structures in the temporal bone that must be assessed on every CT of the temporal bone, especially if a surgery is contemplated. It is of utmost importance to know what to look for as 'The eye sees only what the mind knows'. Aided with a good understanding of what can prove to be a surgical landmine for our surgical colleagues, we can make ourselves better radiologists and serve our patients well.

630

Take a Walk on the Wild Side: CNS Manifestations of Zoonotic Infections

I Tan[1], R Griesbach[1], J Sturgis[2], J Whisenant[3], H ROWLEY[1], T Kennedy[1]
[1]University of Wisconsin School of Medicine and Public Health, Dept. of Radiology, Madison, WI, [2]University of Wisconsin School of Medicine and Public Health, Dept. of Neurology, Madison, WI, [3]University of Wisconsin–Madison, Madison, WI

Purpose
OBJECTIVES 1. Describe the epidemiological characteristics of zoonotic infections with CNS manifestations, including the geographic distributions, routes of transmission, and patient risk factors. 2. Review the pathogeneses and clinical presentations of zoonotic infections with CNS manifestations. 3. Showcase the typical CNS imaging findings of zoonotic infections and review their differential considerations. SUMMARY Overview: A zoonotic infection is caused by an agent transmitted from an animal reservoir to humans, via direct spread from another vertebrate or via indirect spread through an arthropod vector. 60% of all infections are zoonotic, highlighting the importance of recognizing their clinical presentations and imaging findings. West Nile Neuroinvasive Disease: Disease is caused by West Nile virus, of the Flaviviridae family. The distribution of infection is widespread throughout parts of Europe, South Asia, the Middle East, Australia, and the Americas. In the US, most infections occur in temperate climates in August and early September (90%). Birds serve as the reservoir host for West Nile virus. Mosquitoes serve as the vector and transmit the virus to humans and other non-avian vertebrates. Following a mosquito bite, the virus replicates in the spleen and regional lymphoid tissue resulting in viremia, which peaks 2-4 days after infection. In less than 1% of infected persons, viremia leads to dissemination to the CNS, via an unknown mechanism. Once in the CNS, the virus demonstrates specific neurotropism for basal ganglia, thalamus, and brainstem neurons, as well as anterior horn cells in the spinal cord. Patients with CNS infection present clinically with encephalitis, meningoencephalitis, or acute flaccid paralysis. Typical MRI findings are bilateral T2/FLAIR hyperintensity — sometimes with enhancement and/or diffusion restriction — in multiple deep brain structures, most commonly the medial thalamus, substantia nigra, and mesial temporal lobe. Differential considerations include infection by other Flaviviridae, ischemia/infarction, autoimmune encephalitis, Creutzfeldt-Jakob disease, organophosphate poisoning, hypoglycemic encephalopathy, and lymphoma. Remainder of Exhibit: We will also present and discuss the epidemiological characteristics, pathogeneses, clinical presentations, radiologic findings, and differential considerations of eastern equine encephalitis, neurocysticercosis, toxoplasmosis, and Lyme disease.

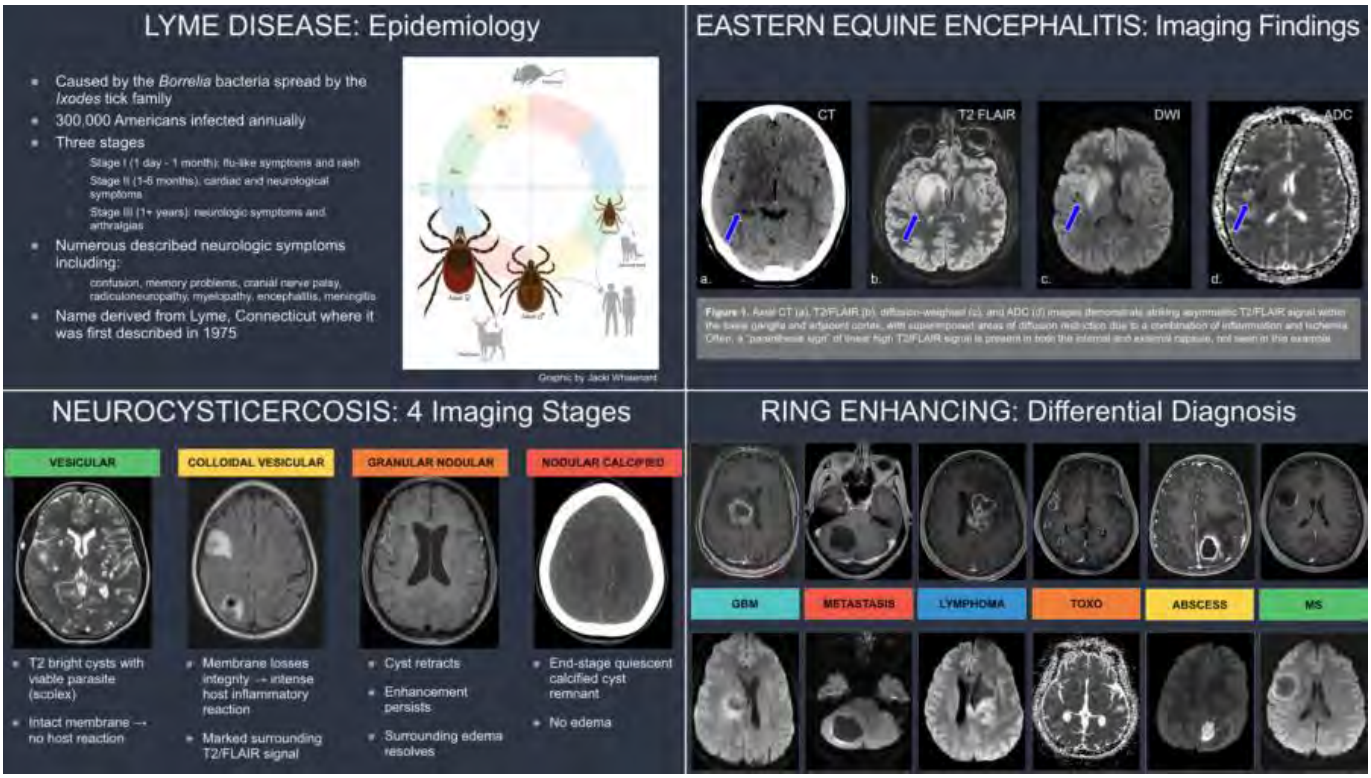

(Filename: TCT_630_6251.jpg)

943

Technical Perspective of CT Perfusion (CTP) Pitfalls and Tips for Troubleshooting

A Moawad[1], M Aslam[1], S Chaker[1], B Jaber[1], M Shalaby[1], S Kushchayev[2], O Teytelboym[1]
[1]Mercy Catholic Medical Center, Darby, PA, [2]Moffitt Cancer Center, Tampa, FL

Purpose

-Illustrate the acquisition protocols for CTP in stroke patients -Introduce the perfusion parameters and thresholds for identifying core infarction and penumbra -Review image processing algorithms -Demonstrate workflow for post processing software - Case based review of technical pitfalls of CT perfusion processing and acquisition

Materials and Methods

N/A

Results

Table of content: - Introduction of CTP acquisition and its parameters - Diagnostic criteria for stroke/penumbra and threshold for each parameter - Different types of image processing * Maximum slope technique * Deconvolution - General workflow for automated post-processing - Technical pitfalls during acquisition * Patient motion - Effect of patient inter-scan motion on image registration - Streak artifact as a result of intra-scan motion - Motion correction algorithms * Head position - Perfusion asymmetry due to head tilt - Types of technical pitfalls in CTP processing * Different CT perfusion thresholds for infarction * Image alignment and registration pitfalls - Skull stripping and brain segmentation algorithm * Arterial inflow (AIF) selection pitfalls - Arteries to use an input - Criteria of correctly selected AIF - Troubleshooting AIF selection *Region of interest (ROI) selection pitfalls - Optimum position of the venous ROI - Troubleshooting ROI selection * Time attenuation curves (TAC) pitfalls - Normal characteristics of the TAC - Bolus arrival time and first moment time - Curve Truncation

Conclusions

NA

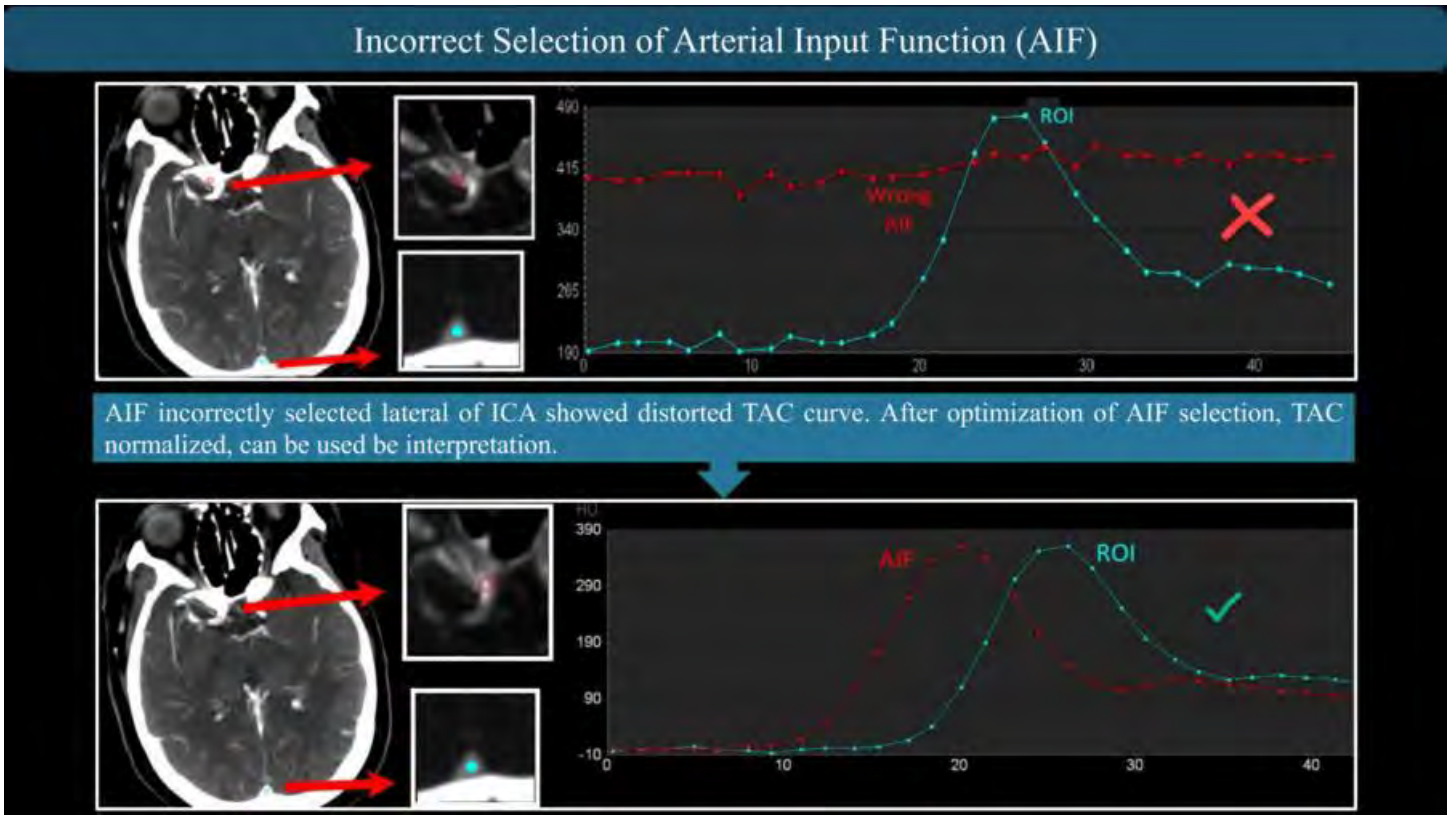

(Filename: TCT_943_Presentation1-2.jpg)

547

Temporal Lobe Abnormalities: The Hallmark for the Diagnosis

G Silva[1], N Calixto[1], F Assunção[1], L Martins[1], L Freitas[2], T Scoppetta[1]
[1]Hospital São Camilo/Grupo Fleury, São Paulo, SP, [2]Hospital São Camilo, São Paulo, SP

Purpose

Various diseases manifest with lesions in the temporal lobes. Common clinical presentations include seizures, dementia, and memory impairment, followed by a spectrum of behavioral disturbances. Brain MRI findings improved our ability to make more-specific diagnoses. The pattern of lesion distribution and the associated imaging findings can narrow the spectrum of differential diagnoses and

suggest a specific pathology. The goal of this digital paper is to demonstrate the magnetic resonance imaging (MRI) changes in temporal lobe abnormalities, classify into specific group and propose a diagnostic workflow.
Materials and Methods
- Review the temporal lobe embryology and anatomy; - Pictorial review of the diseases with distinct temporal lobe findings; - To emphasize the decisive imaging features for the diagnosis and propose a diagnostic workflow.
Results
We performed a retrospective and descriptive study of brain MRI of patients with temporal lobe abnormalities performed at our service.
Conclusions
Classification of MRI imaging findings into specific groups may help provide a more focused differential diagnosis of various pathologies that affect the temporal lobe.

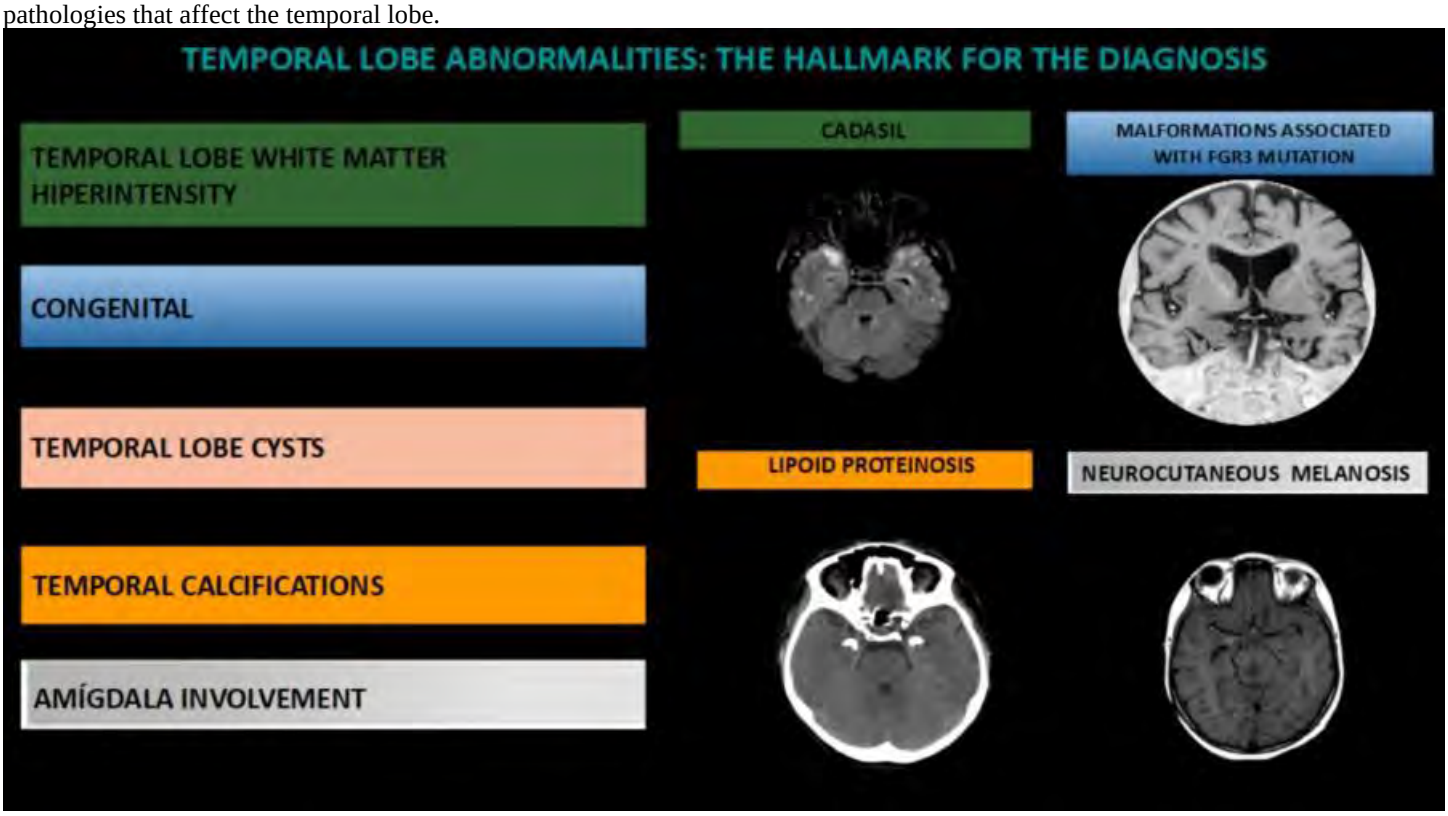

(Filename: TCT_547_temporallobeabnormalities-thahallmarkforthediagnosis.jpg)

1293
Teratomas of the Brain, Spine and Head/Neck: Imaging Appearances
W Calderon[1], P Puac Polanco[2], C Auger[3], K Jonguitud[4], J Balderrama[5], C Zamora[6], M Castillo[7], A Rovira[8]
[1]Hospital Universitari Vall d´Hebron, Barcelona, Catalonia, [2]University of Ottawa, Ottawa, ON, [3]Hospital Vall d´Hebron, Barcelona, Barcelona, [4]National Institute of Neurology and Neurosurgery, Mexico City, Mexico City, [5]Instituto Nacional de Neurología y Neurocirugía, Mexico city, Mexico city, [6]UNC Department of Radiology, Chapel Hill, NC, [7]Radiology, Chapel Hill, NC, [8]Hospital Vall d'Hebron, Barcelona, Barcelona

Purpose
Summary: • Background. • Locations: intracranial, spine and head/neck. • Imaging features. • Complications. Objectives: • Illustrate the different imaging appearances of teratomas in the brain, spine and head/neck. • Discuss their locations and associated complications. • Understand the usefulness of CT and MRI in the diagnosis and characterization of teratomas.
Materials and Methods
Intracranial and spine teratomas, as well as those in the head and neck, are rare tumors that originate from all three embryonic germ layers (ectoderm, mesoderm, endoderm). They can be classified depending on their differentiation as mature, immature, and teratoma with malignant transformation. Clinical manifestations vary according to location and size. Intracranial teratomas are usually located in the midline, generally in the pineal and suprasellar regions, and represent more than two-thirds of brain tumors diagnosed before birth. In the spine, teratomas can occur at any level and compartment (extradural, intradural, or intramedullary). Characteristically, all show distinct components with fat, calcification, and soft-tissue attenuation on CT. Predominantly cystic teratomas also occur. MRI offers better characterization of these tumors and detection of their complications. In this exhibit, we review the typical and atypical imaging features and complications of teratomas in the brain, spine, and head/neck.

Results
We will discuss typical and unusual appearances of teratomas on CT and MRI approaching them by location: • Intracranial: congenital, midline, and off-midline location • Spine: intramedullary, intradural extramedullary, and extradural • Head & Neck
Conclusions
Teratomas are found in the brain, spine, and head/neck. Recognizing their appearances on CT and MRI is useful for the diagnosis and for differentiating them from other lesions.

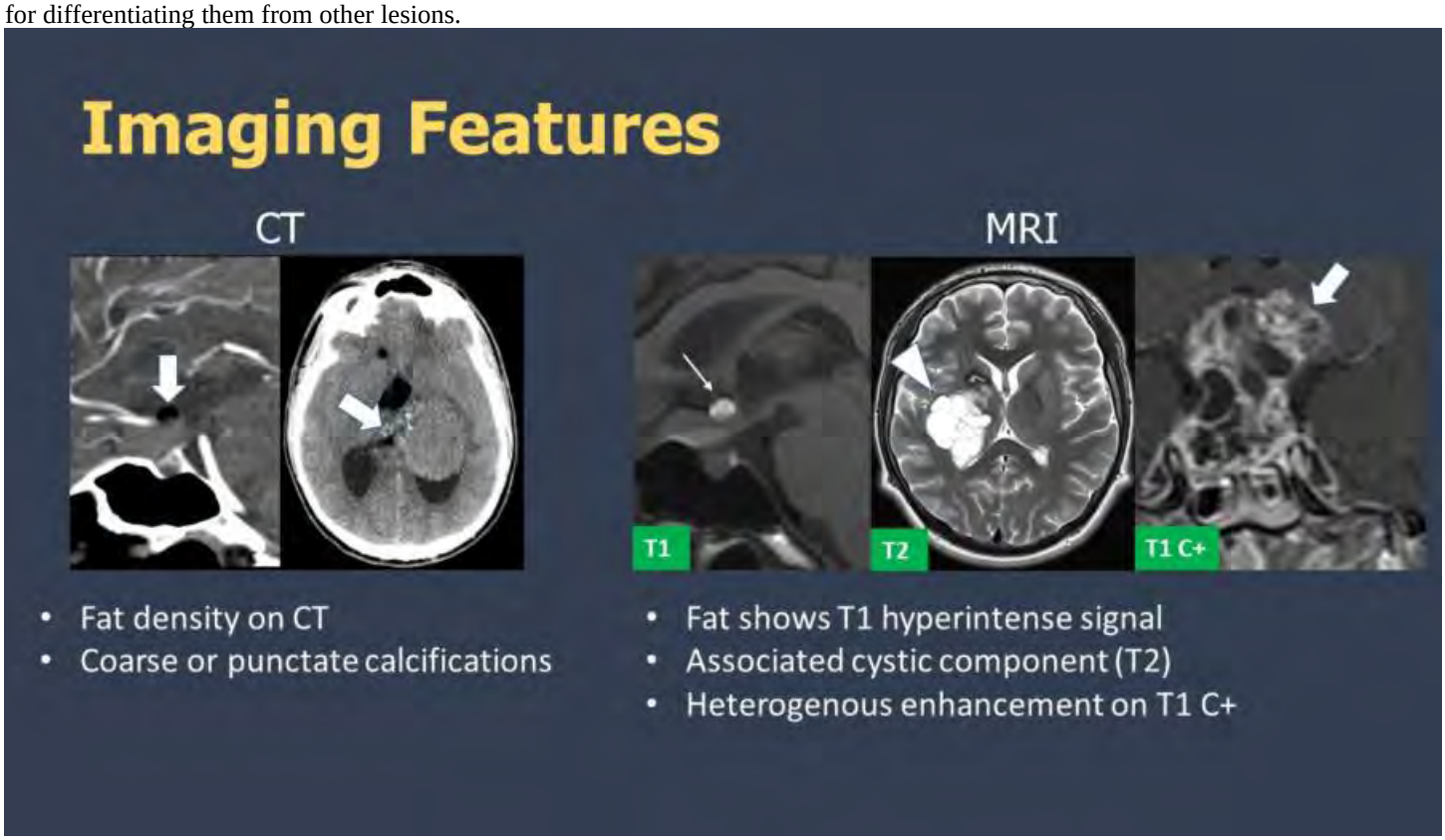

(Filename: TCT_1293_Teratomas_ASNR.jpg)

284
The 2021 WHO Classification of CNS Tumors: Key Updates to Adult-type Tumor Classification for the Radiologist
M Cousar[1], M Nasrallah[1], L Bagley[1]
[1]*Hospital of the University of Pennsylvania, Philadelphia, PA*

Purpose
The 2021 WHO Classification of CNS Tumors introduces substantial changes to the classification of brain and spinal tumors. It is important for the neuroradiologist to become familiar with these changes. Objectives: 1. Summarize the changes in the WHO 2021 tumor classification that are of particular relevance to the radiologist 2. Discuss the increasing importance of molecular genetics in the classification system 3. Demonstrate key imaging features of new entities in the adult population
Materials and Methods
The primary goals of this educational exhibit are to introduce the significant changes to CNS tumor classification and to identify characteristic features of new tumors.
Results
We will use the recently published WHO 2021 update as a framework for this educational exhibit. Anticipated topics for the exhibit include: 1. Changes to CNS tumor grading 2. Astrocytoma versus glioblastoma, with discussion of relevant molecular markers 3. Explain layered reporting of tumor pathology 4. Discuss tumor nomenclature, with emphasis on simplifying names to reduce confusion We have also collected cases of newly-classified tumors in adult patients from our institution. We will demonstrate key imaging features with radiologic-pathologic correlation of select entities, including the following: 1. Astrocytoma, IDH-mutant 2. Diffuse midline glioma, H3 K27-altered 3. Diffuse hemispheric glioma, H3 G34-mutant 4. Posterior fossa ependymoma (PFA/PFB) 5. Multinodular and vacuolating neuronal tumor (MVNT) 6. Solitary fibrous tumor 7. Myxoid Glioneuronal Tumor
Conclusions
After completing this educational exhibit, the radiologist should be able to recognize the typical imaging appearances of newly recognized adult-type tumors. Additionally, by developing a working knowledge of key tumor molecular markers, layered reporting, and revised nomenclature, the radiologist will better understand tumor behaviors and prognoses. This will allow for more effective communication between radiology, pathology, and the clinical teams.

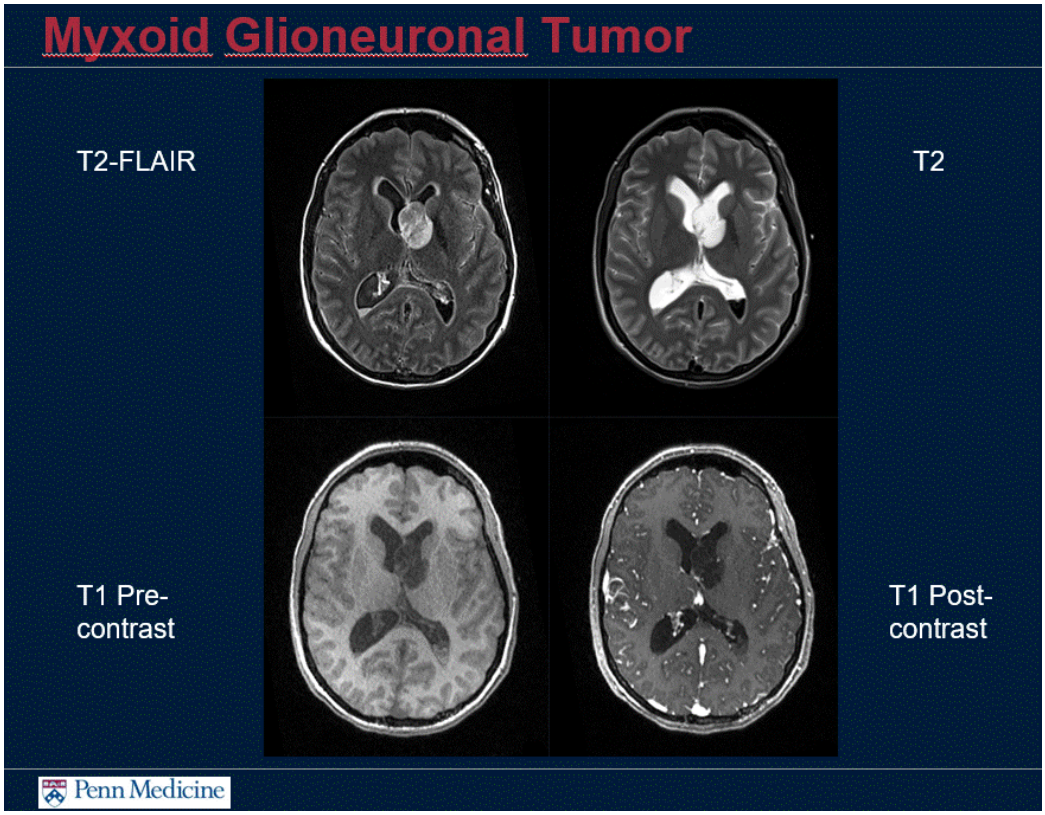

(Filename: TCT_284_MyxoidGlioneuronalTumor.gif)

763

The Art of Making the Easy Things Easy and the Hard Things Possible: Head and Neck Tumor Recurrence Imaging

C Parra-Farinas[1], L Alshafai[1]
[1]*University of Toronto, Toronto, Ontario*

Purpose

Background Recurrent head and neck cancer prompt diagnosis is the essence of successful salvage treatment. The imaging appearance of recurrence is challenging. Full awareness of such imaging features and understanding the limitations lead to a crucial change in the course of the disease. This educational exhibit will elucidate the well and lesser known imaging patterns of head and neck tumor recurrence.

Materials and Methods

Educational Goals To develop a practical approach on why, where, and how to look for head and neck tumor recurrence. 1. Why: To detect the clinically blind or difficult spots to early identify the recurrent disease. 2. Where: To localize the common locations of recurrent cancer taking into account the expected treatment changes. 3. How: To develop a systematic method to identify the imaging patterns of tumor recurrence in order to distinguish these from the treatment changes and potential related complications.

Results

Key Findings Cancer recurrence may not be evident clinically in the early stages. Posttreatment surveillance imaging plays a critical role in detecting recurrence and optimizing salvage therapy. As the treatments have evolved, so have the consequences of these therapies. The various approaches to surgical management, radiotherapy, chemotherapy, and immunotherapy conclude in an altered anatomy and tissue distortion and frequently define a new radiologic baseline that may complicate the interpretation. The patterns of tumor recurrence and their differential diagnosis (DD) are as follows: 1. Necrotic/ulcerative lesion. DD: Abscess, postoperative hemorrhage, venous thrombosis. 2. Cystic lesion. DD: Hemorrhage, laryngocele, lymphocele, mucocele, seroma, sialocele. 3. Solid/enhancing/infiltrative lesion. DD: Radiation/surgical changes, vascular lesion. 4. Perineural spread. Radiation changes, surgical changes. 5. Aggressive bony process. DD: Erosive (acute osteomyelitis, hardware loosening, radiation induced osteosarcoma, osteoradionecrosis), sclerotic (chronic osteomyelitis, healing fracture, radiation osteitis). 6. Aggressive cartilaginous process. DD: Erosive (radiation chondronecrosis, radiation induced chondrosarcoma), sclerotic (healing fracture, radiation changes). 7. Mixed patterns.

Conclusions

Conclusion To understand and recognize the patterns of head and neck cancer recurrence is vital to achieve salvage treatment. Using a systematic approach (why, where, how), the head and neck tumor recurrence can become easier to diagnose and characterize.

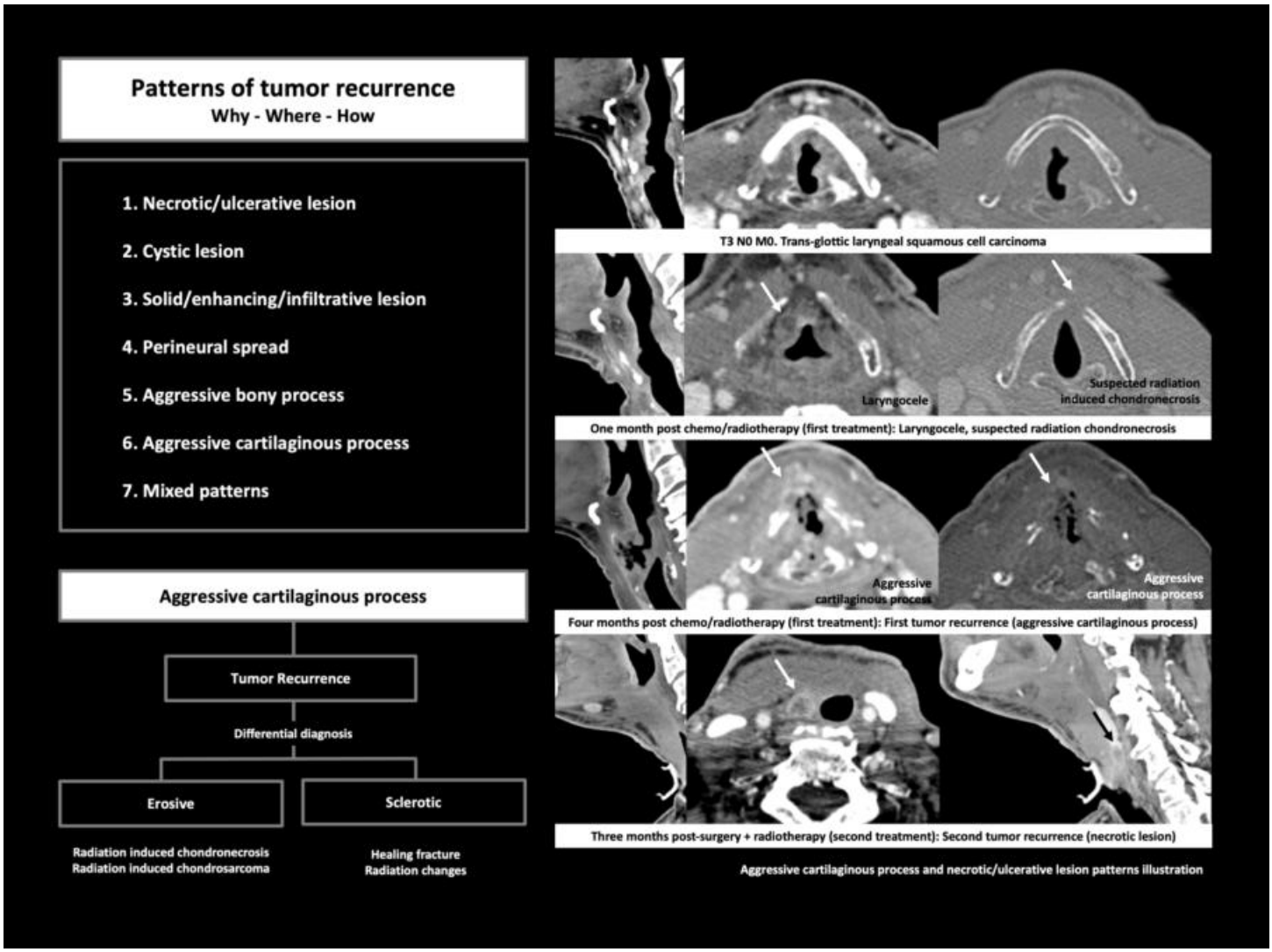

(Filename: TCT_763_CPF_ASNR2022.jpg)

315

The Basal Ganglia - Anatomy & Pathology

S Yang[1], N Salamon[2]

[1]UCLA Medical Center, Los Angeles, CA, [2]University of California Los Angeles, Los Angeles, CA

Purpose

The basal ganglia are a collection of subcortical nuclei involved primarily in motor control/learning, behavior, and emotions. The major nuclei include the striatum (caudate, putamen and nucleus accumbens), globus pallidus, substantia nigra and the subthalamic nucleus. This educational exhibit will review the structural and vascular anatomy of the basal ganglia and attempt to summarize its complex functional role in the context of clinical disease. 1. To review the anatomy of the basal ganglia on multiplanar imaging. 2. To provide a pictorial review of common basal ganglia pathologies. 3. To develop a basic understanding of the function of the basal ganglia in the context of clinical disease.

Materials and Methods

Disease of the basal ganglia are associated with an astounding range of behavioral dysfunction and have long captured the fascination of clinicians around the world. Due to its multicomponent anatomy and complex functional role in motor control, cognition, behavior and memory, the basal ganglia can be one of the most challenging brain structures to understand. This educational exhibit will outline the basic structural and vascular anatomy of the basal ganglia in the context of multiplanar imaging. Once the 3-dimensional anatomy is understood, the major functional loops (motor, prefrontal and limbic) through the basal ganglia will be summarized. The exhibit will also present a pictorial review outlining the imaging characteristics of common basal ganglia pathologies. Examples will include toxicities (i.e., carbon monoxide poisoning), metabolic diseases (i.e., liver dysfunction, Wilson disease, etc), vascular processes (i.e., lacunar infarcts and deep cerebral venous thrombosis), neurodegenerative diseases (i.e., Parkinson, Huntington's disease, etc) as well as neoplasms (i.e., Neurofibromatosis type 1). In the context of pathology, the functional role of the basal ganglia will be reviewed.

Results
A comprehensive literature review will be performed about the anatomy and functional role of the basal ganglia. A single institutional retrospective review will identify cases that demonstrate common pathologies.
Conclusions
The basal ganglia are an anatomically and functionally complex collection of subcortical nuclei. By reviewing the anatomy and summarizing its major functional roles, this educational exhibit will help students, residents and fellows expand their fund of knowledge about the basal ganglia in the context of the imaging and clinical manifestation of common pathologies.

1505

The Bleeding Edge: An Exploration of the Classic and Less Common Presentations of Subpial Hemorrhage

D Martin[1], A Sarma[1], S PRUTHI[2]
[1]Vanderbilt University Medical Center, Nashville, TN, [2]VANDERBILT UNIVERSITY, Nashville, TN

Purpose
Subpial hemorrhages (SPH) are a rare entity that almost exclusively arises in the neonatal or infantile population. SPH refers to blood products that are retained deep to the pia mater but superficial to the cortical surface. Unlike it's more common extra-axial relatives, SPH typically only arises in a younger population, where the pia has not yet fully fused to the cortical surface, creating a theoretical potential space that is not present in the adult population. This limited patient population makes the diagnosis unfamiliar with most practitioners who do not regularly read pediatric neuroradiology imaging. The etiology of SPH is controversial, and several different theories of their origin exist, including birth trauma or subpial venous infarct.
Materials and Methods
The goal of this presentation is to educate the audience about the anatomy and pathophysiology of the subpial space. Regardless of a practioner's familiarity with pediatric imaging, the close association between SPH and neonatal trauma and infarction makes it an extremely important finding for the clinician to recognize. By presenting a review of SPH as well as several examples of common and less common findings associated with them, it is our hope that our audience will come away with a better understanding of the phenomenon, and be better equipped to diagnose them when encountered in practice.
Results
Multiple cases of SPH acquired over the last several years at our institution will be reviewed and presented. A number of common or "classic" features of SPH are illustrated in this presentation including local restriction of blood products, adjacent cortical diffusion restriction, and preference for temporal involvement. In addition, we have come across a few characteristics that are less commonly mentioned in the literature that, nonetheless, seem common within our cases, including lack of infarct, multifocal or atypical location, or very large size.
Conclusions
SPH is a rare pediatric entity with an unclear etiology. Due to the association of this finding with neonatal infarction, it is essential that radiologists of all specialities have some familiarity with SPH. While some characteristics are commonly seen in SPH, we have also encountered less classical associations that seem to arise with relative frequency within our cases. It is our goal that a review of this entity and a presentation of the spectrum of its imaging properties will aid radiologists' familiarity with such findings and build confidence in diagnosis.

262

The Compartmental Approach to Petrous Anatomy and Pathology

M Tawfik-Helika[1], K Gad[2], M Mahfouz[3], W Allaham[4], R Tsitovah[5], J Colombani[4], C Vacher[4]
[1]Aseer central hospital, Abha, KSA, [2]Ibn Sina hospital, Salmiya, Select a State.., [3]Cairo university, Cairo, Cairo, [4]Beaujon hospital, Clichy, Clichy, [5]CHUJRA Antananarivo Madagascar, Antananarivo, Madagascar

Purpose
Objectives - Learn the four petrous compartments: mucosal (Eustachian tube, middle ear and mastoid antrum), cutaneous (external auditory canal), neural (otic capsule) and vascular (internal carotid artery). - Learn segmentation of the pyramid - Identify densities of different contents - Identify structures based on location and density - Use the map to learn details (superimposed on the map), such as middle ear, otic capsule, air cells and facial nerve segments and branches - Use location to create differential diagnosis lists Summary: Introduction Anatomical plan General identification roadmap Modified reconstruction planes and generated sections Applications
Materials and Methods
Learning petrous anatomy through a new approach to allow faster learning. The contents are divided into compartments and then use of special planes of reconstruction to show the anatomical relations in terms of position. After explaining topographic position of main elements, details can be explained such as facial nerve segments and branches. Then, from anatomy, pathology differential diagnosis can be listed based on location i.e., compartmental pathology.
Results
N/A
Conclusions
N/A

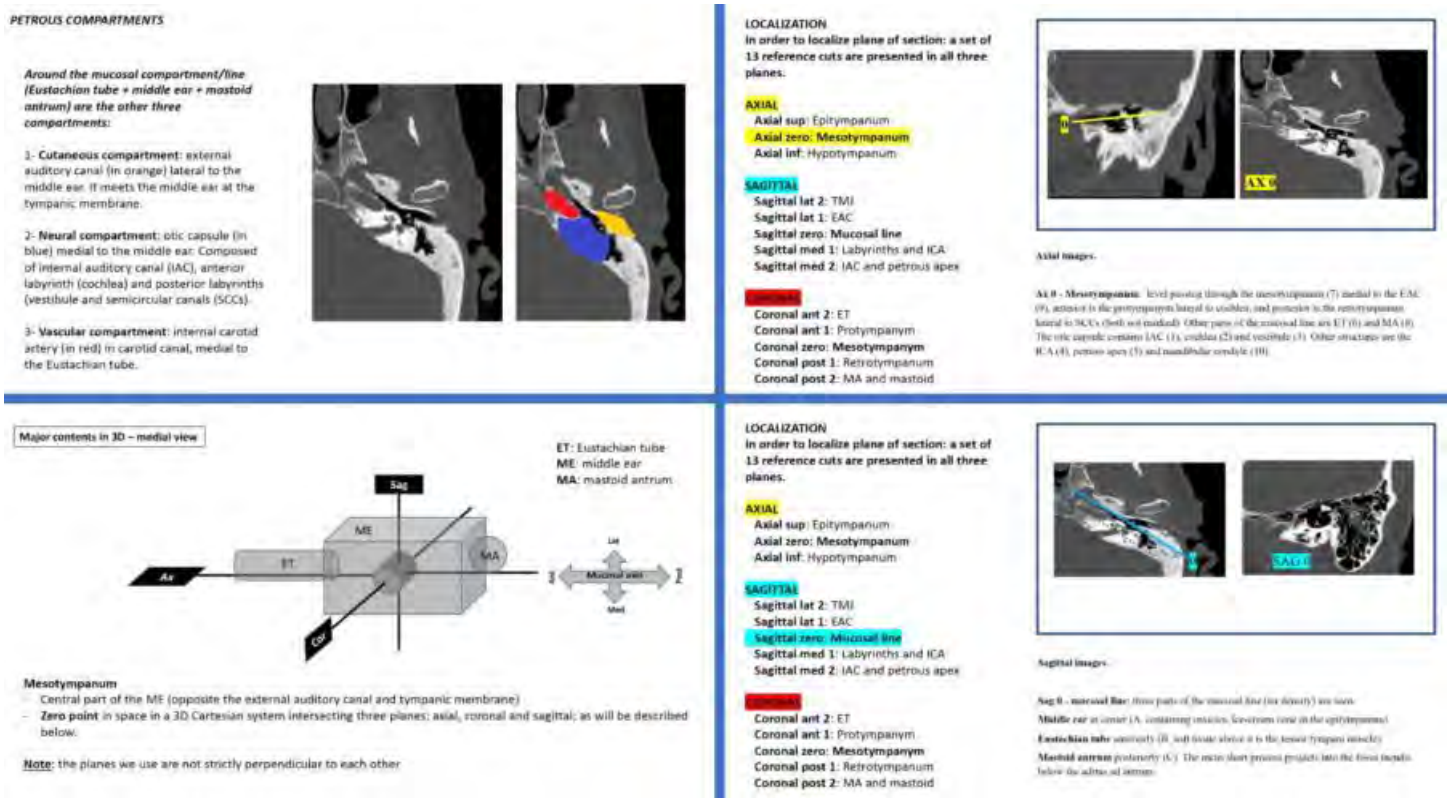

(Filename: TCT_262_ASNRnew.jpg)

1088

The Evolution of Endoscopic Endonasal Approach and the Role of Neuroradiologists

J Rongo[1], K Traylor[1]
[1]*UPMC, Pittsburgh, PA*

Purpose

• Define and illustrate the typical endoscopic expanded endonasal approach (EEA). • Illustrate the midline expansion of EEA to treat suprasellar, anterior skull base, and clival tumors. • Illustrate the lateral expansion of EEA to treat lesions in the middle cranial fossa, cavernous sinus, petrous apex, and orbit. • Focus on radiologic features and important anatomic landmarks critical for surgical planning.

Materials and Methods

Endoscopic endonasal transsphenoidal surgery is a popular surgical approach for the treatment of most sellar tumors. This is because of the ideal relationship of the sphenoid bone to the sphenoid sinus and pituitary gland. More recently, extended approaches have expanded the indications for transsphenoidal surgery. These techniques offer significant advantages over traditional approaches by facilitating greater access to challenging tumors and providing open surgical corridors to once previously considered unresectable lesions.

Results

Not Applicable

Conclusions

At the University of Pittsburgh Medical Center, otolaryngologists and neurosurgeons work collaboratively to transform the traditional function of endoscopic endonasal approach surgery. Just in the past decade, transsphenoidal surgery at UPMC has evolved with the advent of multiple ground breaking approaches including: transcavernous, transorbital, and transmaxillary routes to treat anterior, middle, and posterior skull base pathologies. We will illustrate examples of various midline and lateral extensions to this technique and include a pictorial review of commonly treated skull base pathologies utilizing these novel surgical approaches. We will also review how neuroradiologists can play an important role in the preoperative planning and provide surgical direction by identifying important landmarks and neurovascular structures.

672

The Evolving Landscape of Post-Therapy Imaging in High Grade Gliomas: A Novel Algorithm In Neuro-oncology MR Workflow

A Mahammedi[1], A Vagal[2], M Gaskill-Shipley[1]
[1]University Of Cincinnati, CINCINNATI, OH, [2]University Of Cincinnati Medical Center, Cincinnati, OH

Purpose

• Review important points in the evolution of treatment options in high grade gliomas (HGG) • Review the current management guidelines for HGG • Discuss key concepts of pathophysiologic mechanisms and MRI features of pseudoprogression vs pseudoresponse vs radiation necrosis • Discuss evolution of treatment response criteria in HGG with more focus on Response Assessment in Neuro-Oncology (RANO Criteria) • Propose a novel algorithm in neuro-oncology workflow for treated gliomas • Discuss emerging therapies in GBM: Laser-Induced Thermal Therapy (LITT) Vaccine & Immune-base therapy Tumor-treating fields (TTF)

Materials and Methods

By the end of the presentation participants should be able to: - Be familiar with the evolution of multiple treatment options in HGG - Be familiar with the current management/imaging guidelines of HGG - Understand key concepts of pathophysiologic mechanisms and MRI features of pseudoprogression vs pseudoresponse vs radiation necrosis - Understand treatment response criteria in HGG with more focus on Response Assessment in Neuro-Oncology (RANO Criteria) - Share our proposed novel algorithm in neuro-oncology workflow for treated gliomas

Results

• Neuroimaging features of treated gliomas are important and complex • Both post-treatment change and recurrence have similar imaging characteristics, presenting a diagnostic challenge • Multiple terms need to be understood in order to arrive at the correct diagnosis • Clinical information including tumor markers are also key to understand expected patient prognosis • This exhibit will review the evolution of treatment options in high grade gliomas (HGG). We also propose a simplified algorithm in neuro-oncology workflow for treated gliomas that can offer a more practical diagnostic approach

Conclusions

• No single predictor can distinguish pseudophenoma on conventional MR • Advanced multiparametric imaging techniques are promising but require prospective trials. • No reliable imaging methods, but best diagnosed with follow-up MRIs • The distinction between of pseudoprogression, pseudoresponse, and radiation necrosis is not a dichotomous; most of the time there is a mix of tumor and post-treatment change! We try to determine which is dominant, as it affects treatment

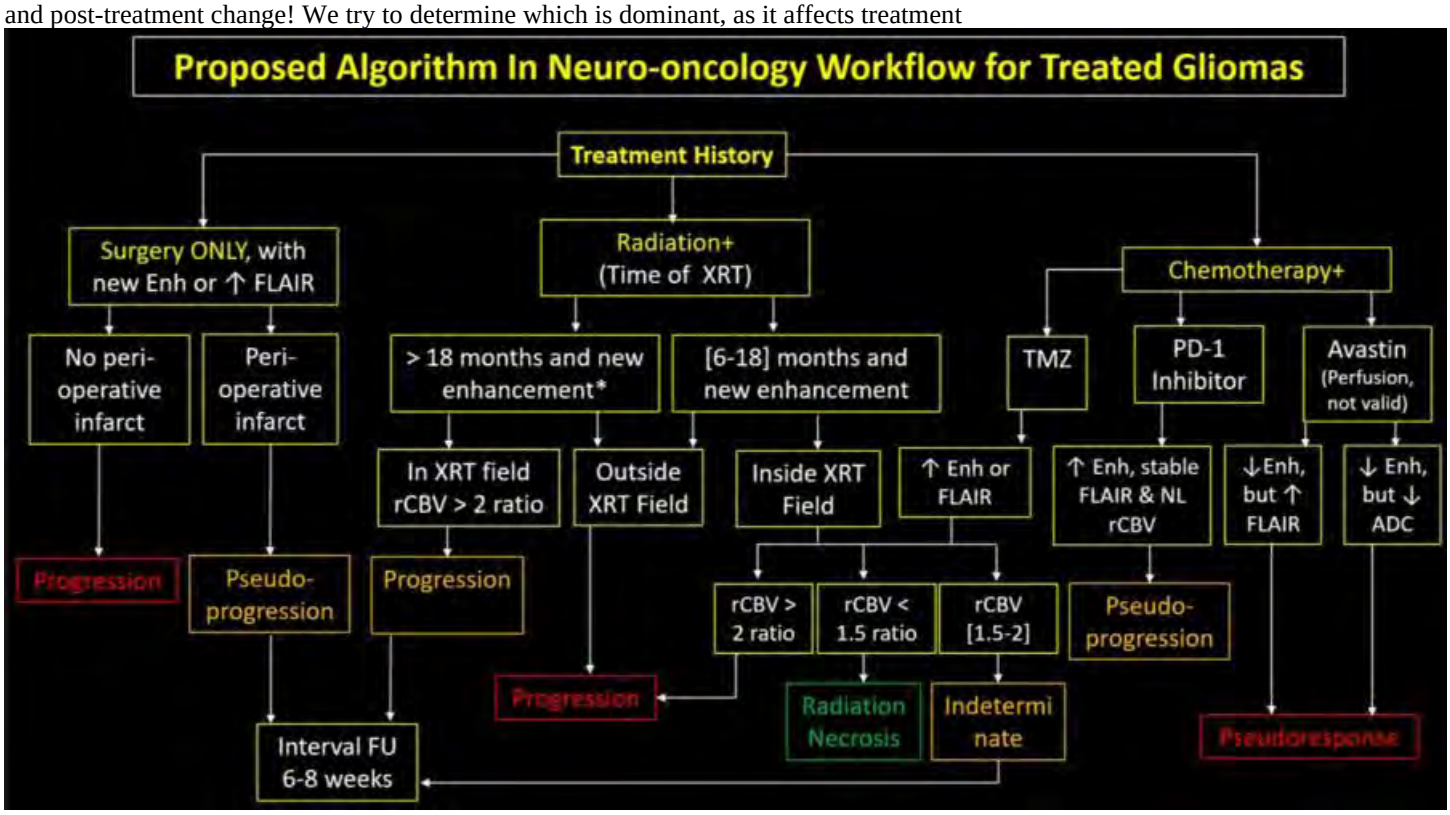

(Filename: TCT_672_ASNR22pic.jpg)

1438

The Forgotten Foramen: A Radiologist's Guide to Foramen Lacerum

C Wheeler[1], O Hamki[2], H Sotoudeh[1], S Gaddamanugu[3]

[1]University of Alabama at Birmingham School of Medicine, Department of Radiology, Birmingham, AL, [2]University of Alabama at Birmingham School of Medicine, Birmingham, AL, [3]Veterans Affairs Medical Center, Birmingham, AL

Purpose

This exhibit will cover: ● Anatomy: Display a pictorial review of foramen lacerum and clinically relevant structures on neuroimaging. ● Pathology: Discuss a case series illustrating a variety of lesions at foramen lacerum, including congenital, vascular, traumatic, infectious, and neoplastic manifestations. Educational Objectives: ● Identify normal neuroanatomy of the foramen lacerum and adjacent structures. ● Emphasize and orient radiologists to analyze the foramen in certain pathologies. ● Recognize characteristic imaging features of common laceral pathologies. ● Understand how pathologies centered at or near the foramen lacerum spread to other areas in the skull base.

Materials and Methods

Foramen lacerum remains a neglected foramen at the skull base. However, this foramen at the central skull base appears at the crossroads of several critical structures. The internal carotid artery with its sympathetic nerve plexus courses along the roof of foramen lacerum. Perineural tumor spread from sinonasal malignancies and nasopharyngeal carcinoma frequently enters this foramen. Primary skull base tumors within the sphenoid, occipital and temporal bone encroach upon this area. The foramina lacera can also become involved in skull base infections, vascular, traumatic and inflammatory conditions. Secondary complications of the internal carotid artery are frequently encountered due to its proximal location.

Results

A retrospective analysis of approximately 175 cases will be performed at an institutional level.

Conclusions

A select number of high-yield cases will be presented to demonstrate a broad spectrum of laceral pathology, ranging from developmental, vascular, posttraumatic, infectious, and oncological manifestations. By honing the radiologist's fund of anatomical knowledge, clinical acumen, and diagnostic checklist on routine brain imaging, this exhibit can improve accurate interpretation and quality of patient care by minimizing errors of perception. Figure Legend: Figure 1. Coronal postcontrast fat-saturated T1 image demonstrates a right-sided nasopharyngeal carcinoma, extending into foramen lacerum and abutting the inferior wall of the right ICA.

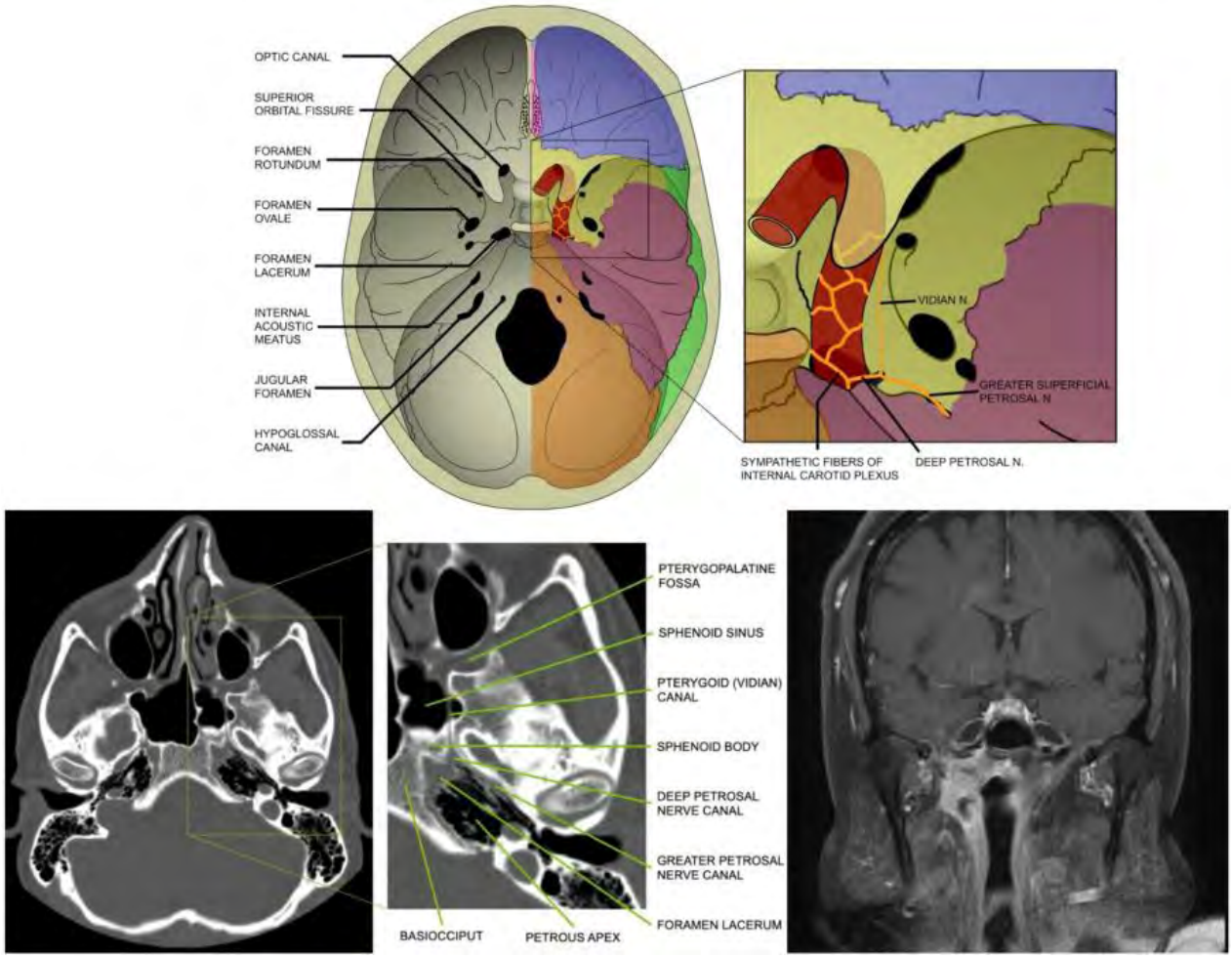

(Filename: TCT_1438_ASNR22EducationalExhibitForamenLacerumFigure1.jpg)

190

The Future of Radiology Resident Education: Lessons Learned from the COVID-19 Pandemic

J Cole[1], A Wang[2], A Singh[1]

[1]UT Health San Antonio, San Antonio, TX, [2]University of Texas Health Science Center San Antonio, San Antonio, TX

Purpose

The Coronavirus Disease 2019 (COVID-19) pandemic dramatically changed radiology graduate medical education in the United States. In particular, the implementation of social distancing forced departments to completely restructure traditional approaches to learning. Whether in the reading room for read outs or in the conference room for didactic sessions, new tools and resources were tested in an effort to preserve both education and safety. Our institution's large department, with between 8-12 residents per year of training, has been utilizing virtual platforms in place of in person didactic lectures. Additionally, we have integrated audience response systems as a method to help maintain resident participation and engagement. In the reading room, our PACS has a built in "collaborator" tool which serves as a HIPPA compliant method of communication. This tool also allows participants to send screenshots of images, in addition to links which let residents remotely view an attendings workstation. Looking forward to a post-COVID residency environment, we plan to retain virtual teaching methods which proved beneficial in conjunction with previously used approaches to learning. Our educational objectives include: -Identify barriers to virtual education in radiology -Discuss methods used to circumvent such barriers in order to maintain a quality educational environment -Provide a framework for the future integration of virtual learning tools

Materials and Methods

To provide a practical educational exhibit that helps radiology residencies choose virtual resources and learning pathways that could prove beneficial for future teaching.

Results

Feedback from residents, fellows, and attendings at our institution. Additionally, we will provide figures which explain specific tools and platforms used for virtual learning.

Conclusions

Our institution has adapted to the need for both high quality resident education and public safety in the era of COVID-19. While this is still an on-going pandemic, we are planning for a future in which social distancing restrictions are lifted. We will incorporate virtual learning methods which proved useful in order to enhance resident education.

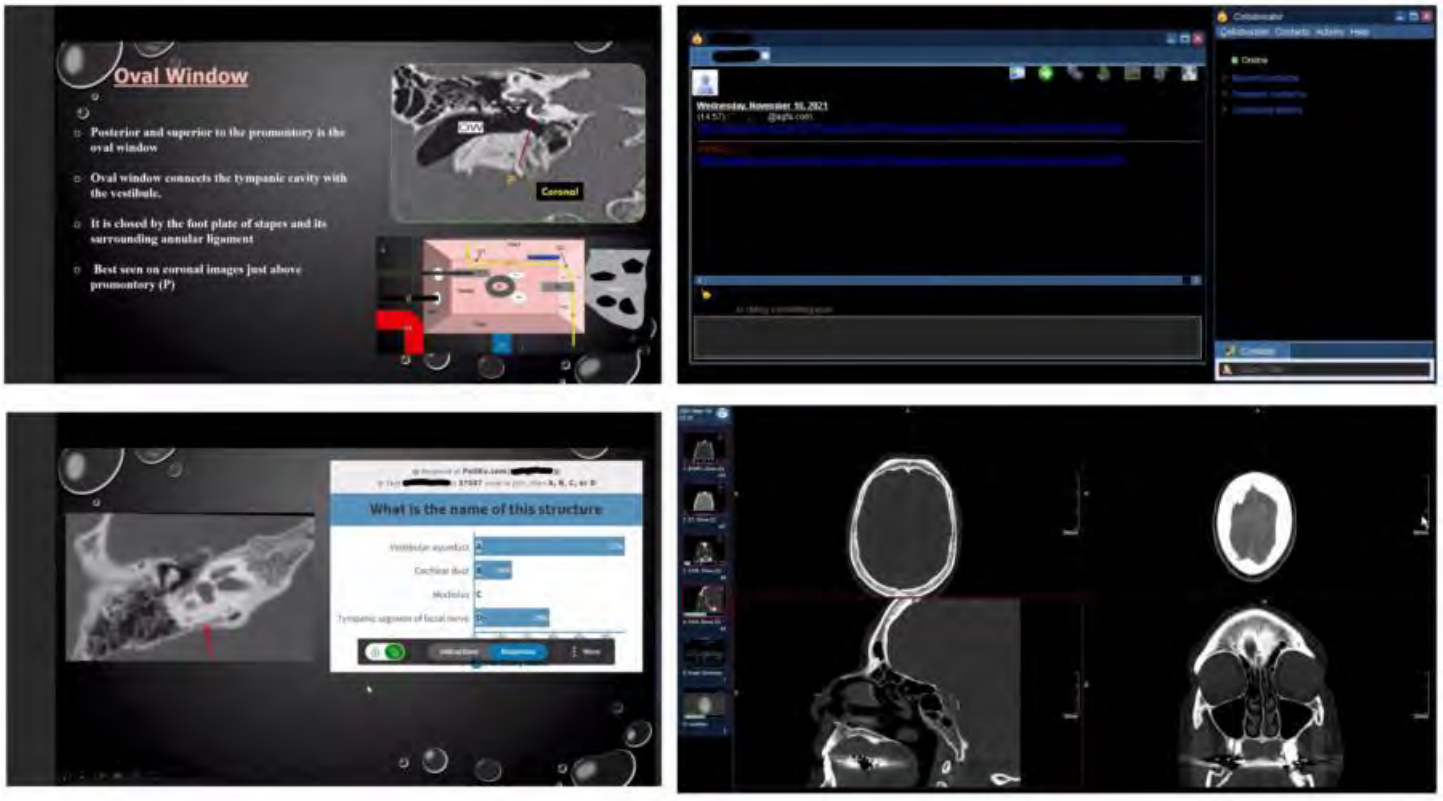

(Filename: TCT_190_ASNR.jpg)

1237

The Great Imitator: A Pattern Based Approach to Neurosarcoidosis

C Kendall[1], K Soderlund[1], J Junn[2], A Rauschecker[3]

[1]Naval Medical Center Portsmouth, Portsmouth, VA, [2]Mount Sinai Hospital Icahn School of Medicine, NYC, NY, [3]UCSF Radiology, Mill Valley, CA

Purpose

To understand the varied neuroimaging features of sarcoidosis involving the brain, head/neck, and spine utilizing a compartmental approach and focused search pattern.

Materials and Methods

Sarcoidosis is a systemic inflammatory disease of uncertain etiology which is characterized the presence of noncaseating granulomas on histopathology. While involvement of the lungs and lymphatics are the hallmarks of the disease, CNS involvement is not uncommon, occurring in 25-50% of cases in autopsy series. With the increased availability and quality of MRI, neurosarcoidosis can be detected earlier and with greater sensitivity. While imaging features of neurosarcoidosis are nonspecific, a high clinical index of suspicion and association of neuroimaging findings with multisystem involvement can increase the confidence of the radiologist in placing neurosarcoidosis high on a differential diagnosis.

Results

In this educational exhibit, we will discuss the extensive and varied imaging features of neurosarcoidosis. Within the brain, we will show parenchymal, pachymeningeal, and leptomeningeal manifestations of neurosarcoidosis, as well as involvement of the optic nerves and sella region. Within the spine, we will show examples of intramedullary disease as well as leptomeningeal and pachymeningeal sarcoidosis. Head and neck manifestations of sarcoidosis in this exhibit will feature examples of sarcoidosis involving the lymph nodes, orbits, and lacrimal glands. Finally, we will show examples of lung and other "corner findings" which might be encountered by neuroradiologists. Clinical aspects of neurosarcoidosis such as laboratory and CSF analysis will be discussed. We will conclude by summarizing our findings and proposing a search pattern for patients with suspected or known neurosarcoidosis.

Conclusions

After viewing this educational exhibit, radiologists will have a greater knowledge of the neuroimaging features of sarcoidosis and be better able to integrate them in the context of clinical, laboratory, and multisystem imaging findings to construct a high value interpretation of neuroimaging studies in patients with suspected sarcoidosis.

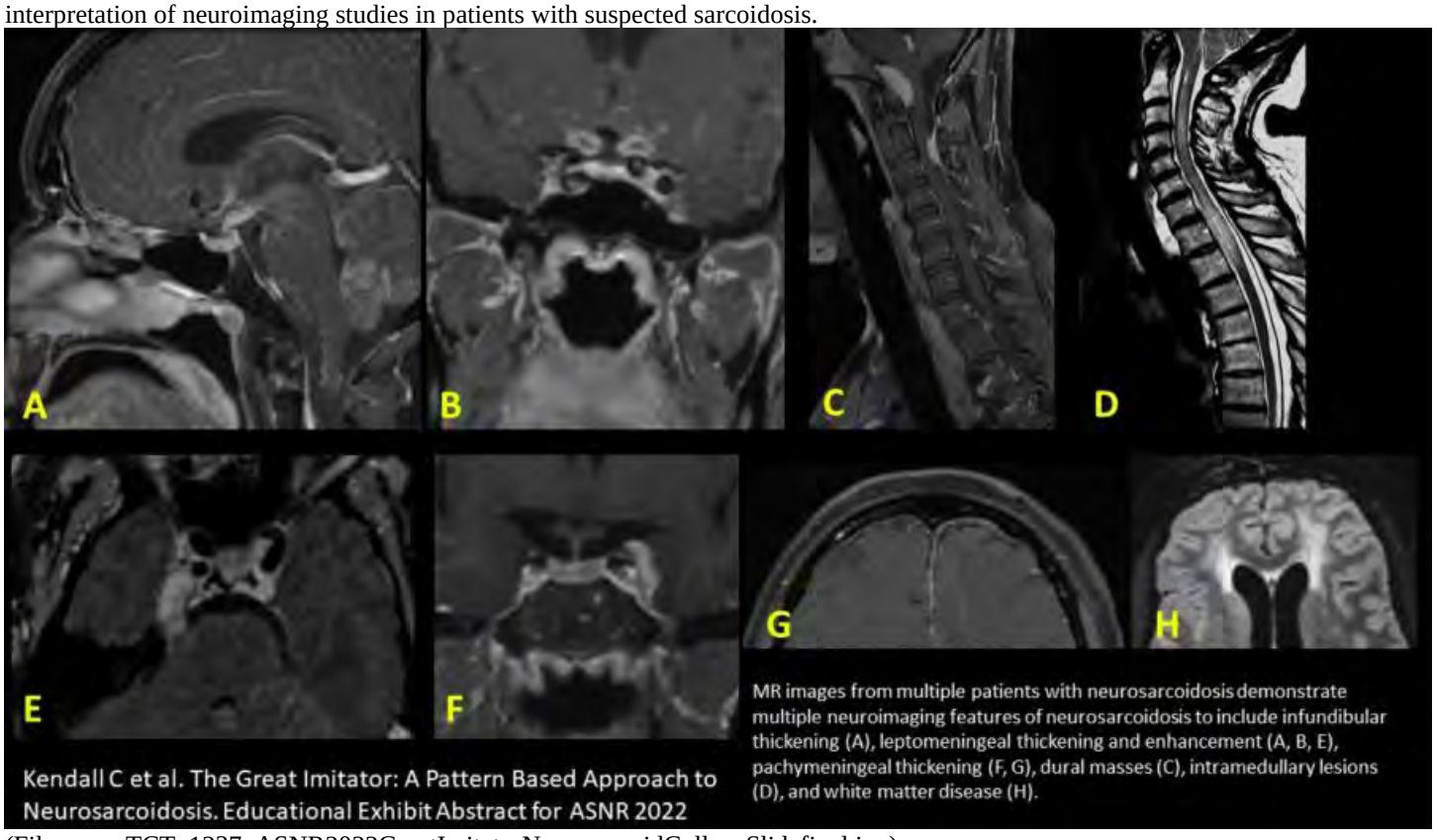

(Filename: TCT_1237_ASNR2022GreatImitatorNeurosarcoidCollageSlidefinal.jpg)

640

The land of tears: A Pictorial review of the lacrimal apparatus radiological anatomy and pathologies

M Alabdulkareem[1], Z Akhtar[1], S Hamid[1], U Chaudhry[1], H Al jadiry[1], K Hsieh[1], J Heymann[1], T Shestopalova[1]
[1]*University of Texas Medical Branch, Galveston, TX*

Purpose

The aim of this exhibit is to familiarize the reader with the normal radiological anatomy of this important system and to discuss the various local and systemic pathologies that can affect it. We start with reviewing the normal radiological anatomy of the lacrimal apparatus with focus on the important anatomical structures displayed in the CT and MRI(1, 2). This is followed by reviewing the common local and systemic pathologies affecting this area with examples. This includes various infectious, inflammatory and neoplastic processes with different imaging presentations. (Fig. 1-2)(3-5). A literature review will be performed for common pathologies and various imaging modalities used for assessing this region with emphasis on the advantages and disadvantages of each modality, including some older and newer techniques.

Materials and Methods

The lacrimal apparatus is somewhat of an overlooked topic when it comes to literature and radiology. Yet it plays a critical role in physiology and has a wide spectrum of pathologies that can affect it.

Results

Orbital imaging studies (such as: MRI, CT and PET scan) performed over the past five years at University of Texas Medical Branch were reviewed by the authors with emphasis on the lacrimal apparatus. Correlation with pathology were performed for selective cases.

Conclusions

It is our hope that with this exhibit the reader will become more familiar with the lacrimal apparatus anatomy and pathologies. This can in turn lead to increased comfort when interpreting cases and recognizing pathologies encountered in the region, leading to better advice to our clinical partners and better patient care.

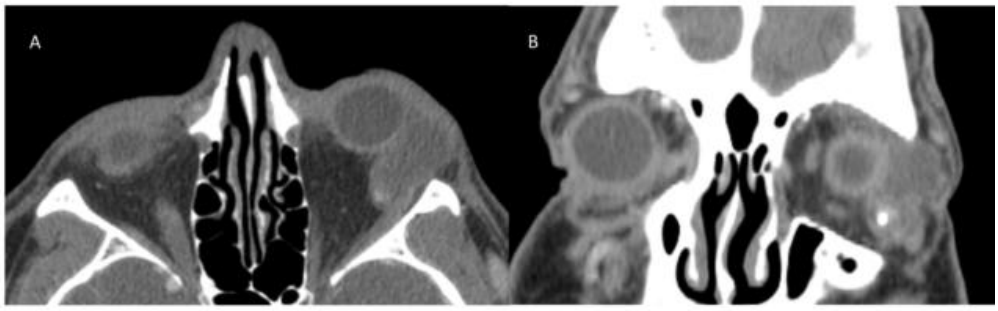

Figure 1. Venous malformation involving the left lacrimal gland and orbit. A and B. Orbital CT shows cystic soft tissue mass involving the left lacrimal gland as well as the extra and intraconal compartment of the left orbit. It has few punctate calcifications, consistent with phleboliths.

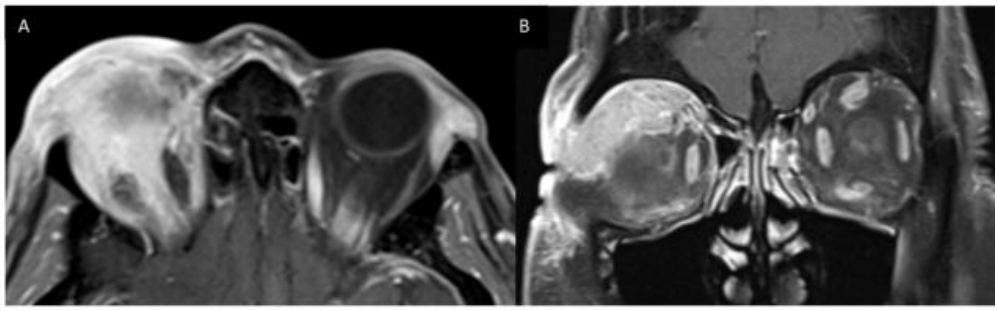

Figure 2: Bilateral Orbital Sarcoidosis. A and B. Coronal and axial post-contrast T1WI fat sat images show Infiltrative enhancing mass involving superior and lateral extraconal spaces of the right orbit. It is infiltrating the right lacrimal gland and extending into the upper eyelid. There is thickening and enhancement of the left lacrimal gland as well. In addition, there is perineural enhancement of the right optic nerve.

(Filename: TCT_640_ASNRlacrimal.jpg)

157

The MRI Appearance of Myloglossus

L Lin[1], F Syed[2]
[1]University of Michigan Hospital, Ann Arbor, MI, [2]VA Ann Arbor Healthcare System, Ann Arbor, MI

Purpose

The extrinsic and intrinsic muscles of the tongue form a complex network to produce all the movements of the tongue. The typical anatomic configuration of the extrinsic tongue muscles consists of genioglossus, hyoglossus, styloglossus, and palatoglossus. Additional extrinsic muscles that have been reported are amigdaloglossus, pharyngoglossus, chondroglossus, and myloglossus. We describe the MRI appearance of the myloglossus, which was incidentally discovered on imaging performed for head and neck cancer evaluation. We also summarize historical literature describing the myloglossus, its function, and potential implications for imaging.

Materials and Methods

N/A

Results

N/A

Conclusions

The myloglossus is best seen on a non-fat saturated sequence (figure 1). This muscle originates at the angle of the mandible and inserts into the tongue between the styloglossus and hyoglossus (figure 2). There are several variations of this muscle reported in the literature. C. H. Hallett first described this muscle as a variation of the styloglossus receiving additional fibers from the angle of the mandible in 1849. Later, J. Wood describes this as a separate muscle, present unilaterally on the left in a single subject in 1866. There are additional reports of the myloglossus present occasionally in the setting of absent styloglossus. The function of this muscle is to act antagonistically to contralateral muscles and synergistically with the palatoglossus in upward movement of the tongue. Although reports of this muscle are rare, a recent cadaveric dissection case series report this muscle to be present in the majority of subjects. On imaging studies, the myloglossus is not commonly seen, and this may be due to small size of the muscle. However, this muscle may be recognized with increasing use of high-resolution imaging, particularly involving head and neck cancer evaluation and follow up. As an extrinsic muscle of the tongue, it is important to identify and evaluate the myloglossus because invasion of the muscle can affect staging of the tumor. Larger studies are needed to further define its role potential role in staging.

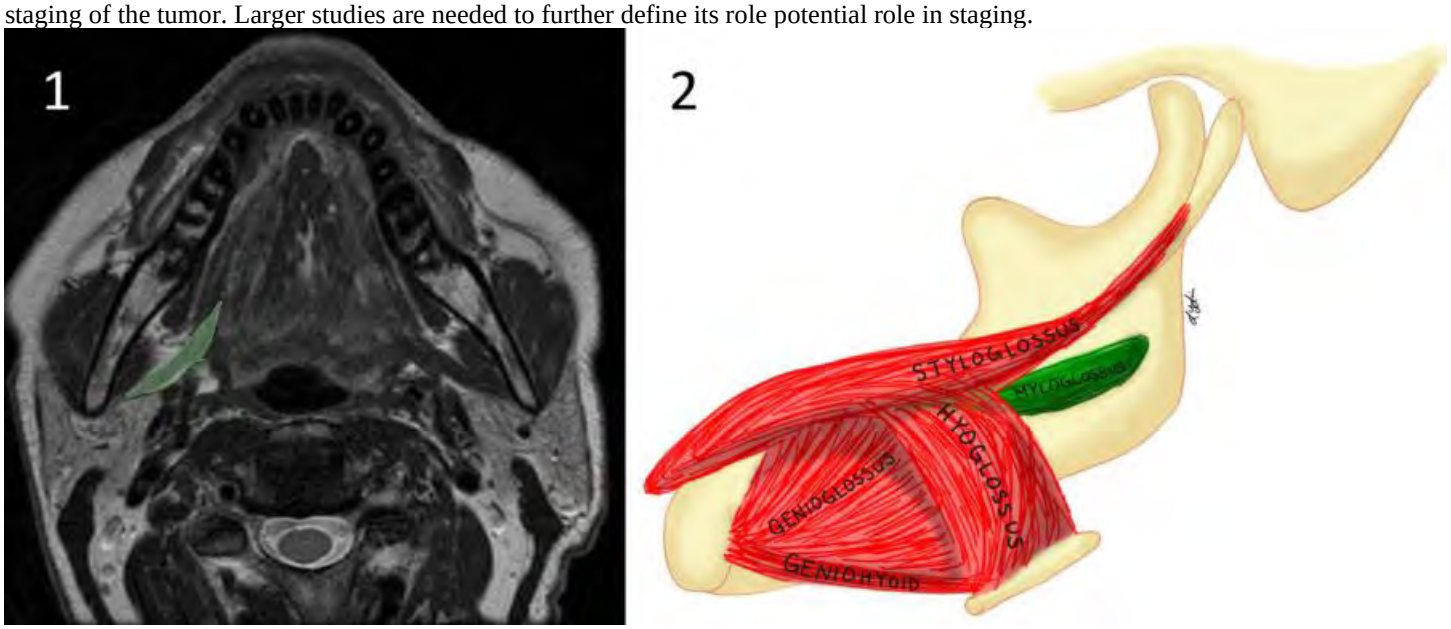

(Filename: TCT_157_ASNR.jpg)

195

The New WHO 2021 Classification of Gliomas: an Imaging Approach.

A Mamere[1], R Fernandes[1], R Fava[1], L Feltrin[1], R ROSSINI[1], E Mamere[2], A Freitas Secaf[1], G Teixeira[1]
[1]Barretos Cancer Hospital, Barretos, SP, [2]Universidade Federal do Rio Grande do Norte - UFRN, Natal, RN

Purpose

In recent years, molecular biomarkers have gained importance in the diagnosis and classification of these tumors, mainly due to the observation of their different biological behavior and prognosis. The classification proposed in 2016 already incorporated the description of molecular biomarkers of a few central nervous system (CNS) neoplasms. In 2021, a new recommendation was released for the classification of these tumors, in which the molecular characteristics of various neoplasms were incorporated. Regarding gliomas, the main changes were the division into adult and pediatric-types, the combination of histological and molecular classifications, the recognition of new entities, the revision of the nomenclature and the abolition of grade modifier terms, such as "anaplastic".

Materials and Methods
To show the recommendations of the new World Health Organization 2021 (WHO 2021) classification for adult and pediatric gliomas and the main modifications concerning the previous one (WHO 2016), exemplified by imaging, histopathological and molecular findings of patients followed at our institution.
Results
Presentation and discussion of the main recommendations of the new WHO 2021 classification for gliomas, based on the medical images and molecular features of adult and pediatric patients with gliomas.
Conclusions
It is important that neuroradiologists are familiarized with the new classification of CNS tumors, so that they can use this knowledge in evaluating and reporting medical images of patients with glioma.

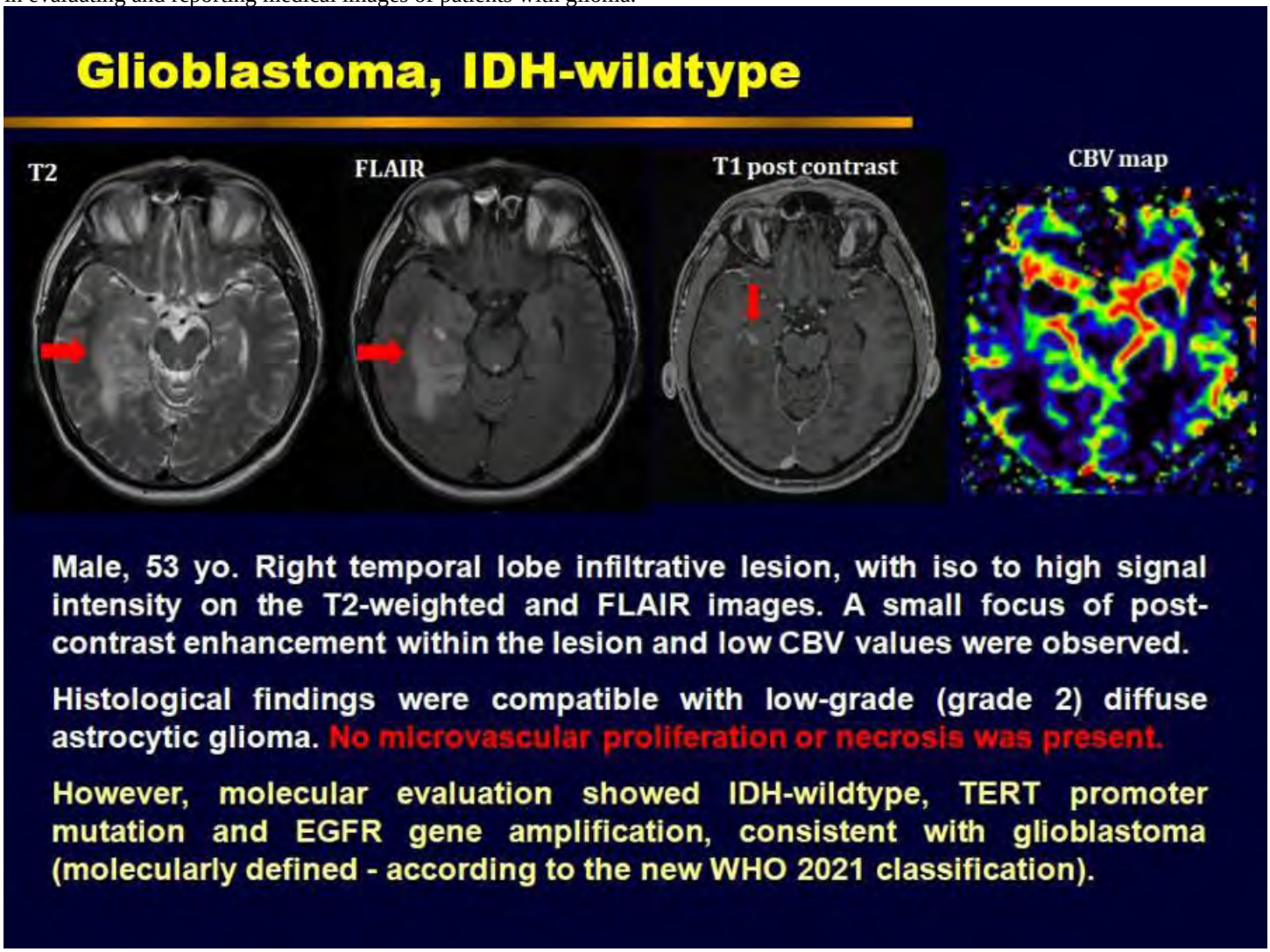

(Filename: TCT_195_6.jpg)

581
The Onus on the Conus: A Neuroimaging Spectrum of Conus Medullaris Pathologies
A Dearden[1], J Ghannam[1], A Wang[1], A Krishnan[1]
[1]*William Beaumont Hospital, Royal Oak, MI*

Purpose
The conus medullaris is the tapered, cone-shaped end of the distal thoracic spinal cord, normally terminating near the L1-2 intervertebral disc space. As a junction between the cord and the cauda equina nerve roots, the conus can present with common cord pathologies in atypical presentations, as well as present with unique, complex pathologies found nowhere else in the cord. The conus is optimally evaluated with MRI of the lumbar spine before and after the administration of contrast medium. Accurate diagnosis of lesions within the conus is complicated by the nonspecific nature of increased intramedullary signal on T2-weighted MRI imaging, inherent with many cord pathologies. However, enhancement characteristics, degree of cord edema, and extramedullary findings can provide additional information to narrow the differential diagnosis. The onus is thus on the radiologist to develop a cogent differential diagnosis for optimal patient care. In this exhibit, we present representative cases of conus medullaris lesions from our institutional

archive, outlined accordingly: congenital (caudal regression syndrome, Chiari Two with tethered cord and lipomyelomeningocele, diastematomyelia), primary neoplastic (myxopapillary ependymoma, anaplastic astrocytoma, teratoma, lipoma), secondary neoplastic (metastatic breast cancer), infectious/inflammatory (Guillan-Barré Syndrome, vincristine neuritis), and vascular (conus infarct). We will also include rare pathologies, including conus infantile hemangioma, conus plasmacytic neoplasm, conus intramedullary arachnoid cyst, and hydromyelia of the terminal ventricle. Each case will include brief literature review with discussion points. After reviewing this exhibit, the participant should be able to: 1. Recognize the normal and pathological MRI appearance of the conus medullaris. 2. Develop a practical differential diagnosis for a conus medullaris lesion based on MRI signal characteristics, enhancement pattern, and relationship to clinical presentation.

Materials and Methods

N/A

Results

N/A

Conclusions

As a junction between the thoracic cord and the cauda equina nerve roots, the conus medullaris can present with common and unique cord pathologies. Pathologies within the cord are numerous, often complex, and difficult to delineate from each other. Thus, a thorough knowledge of the pathologies that can present in the conus medullaris is necessary to help the radiologist develop an accurate differential diagnosis, ultimately leading to better patient outcomes.

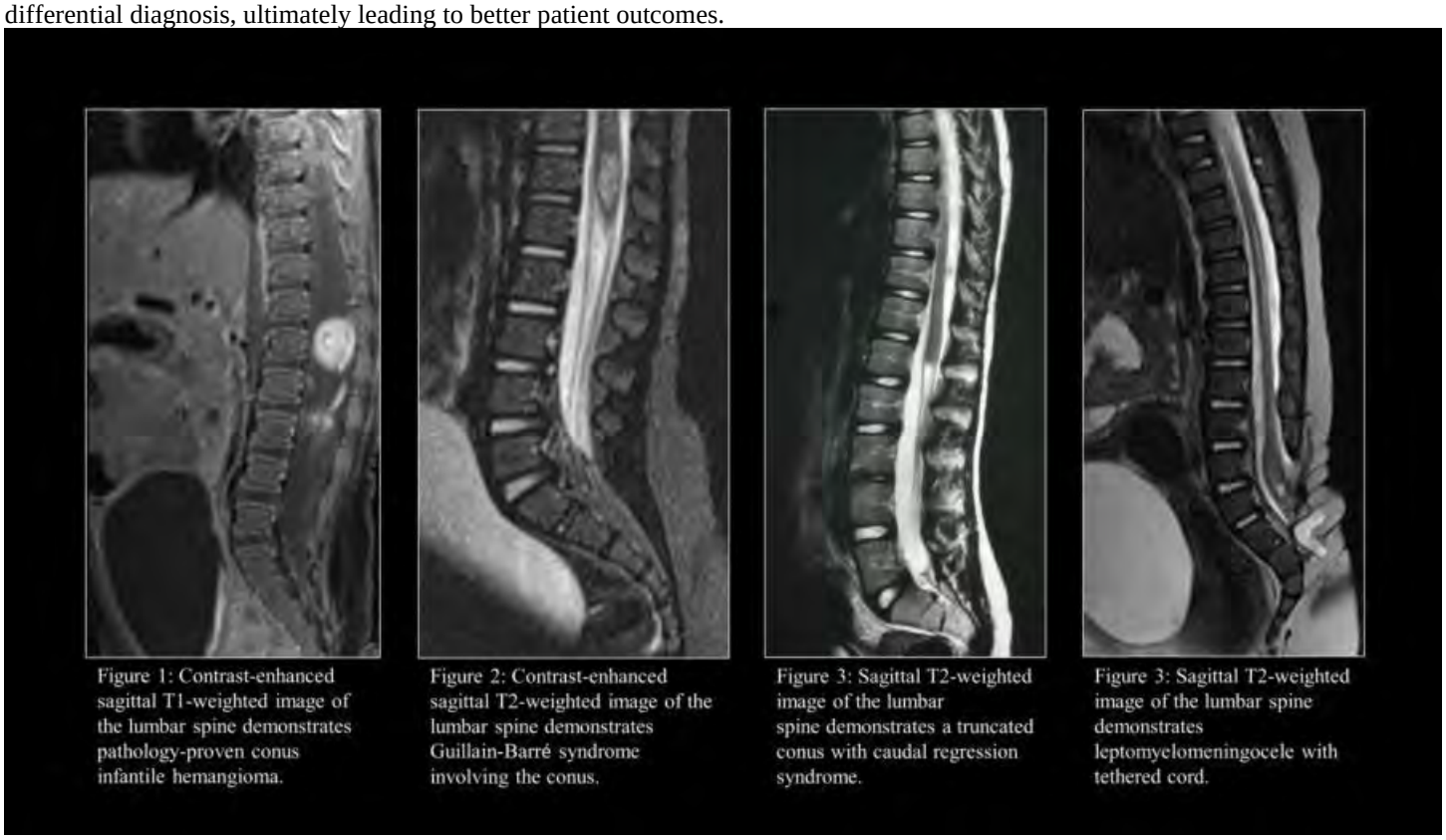

(Filename: TCT_581_conus_masterGraphicFile.jpg)

1039

The Otodystrophies: What the Radiologist Needs to Know

G Bandeira[1], H Tames[1], C Toyama[1], R Gomes[1], E Gebrim[1]
[1]*University of São Paulo, São Paulo, Brazil*

Purpose

Summary Introduction Anatomy and development of the temporal bone Pathophysiology and imaging findings of the main otodystrophies: Otosclerosis Paget's disease Fibrous dysplasia Osteogenesis imperfecta Osteopetrosis Progressive diaphyseal dysplasia (Camurati–Engelmann dysplasia) Van Buchem disease Others Differential diagnoses Incomplete endochondral ossification of the otic capsule Ossicular chain fixation and tympanoesclerosis Otosyphilis Ossicular chain malformation X-linked hypophosphatasia Take-home messages Conclusion References The purpose of this exhibition is to review the imaging findings of the otodystrophies and their main differential diagnoses.

Materials and Methods

The purpose of this exhibit is: To review the anatomy and development of the temporal bone. To recognize the imaging findings of the main otodystrophies. To recognize the main differential diagnosis of otodystrophies. To illustrate the main parameters to be reported in the preoperative and postoperative evaluation of these disorders.

Results
For this educational exhibit we searched the teaching files of our institution for otodystrophies and their main differential diagnoses.
Conclusions
The otodystrophies are a group of disorders that affect the temporal bone and the otic capsule. Otospongiosis, also known as otosclerosis, is a disease that is unique to the otic capsule. Other otodystrophies, unlike otosclerosis, affect not only the otic capsule but other areas of the temporal bone as well, in addition to involving other bones of the body. The radiologist must be familiar with the imaging findings related to otodystrophies and their main mimics, as well as the main parameters to be reported in the preoperative and postoperative evaluation of these disorders.

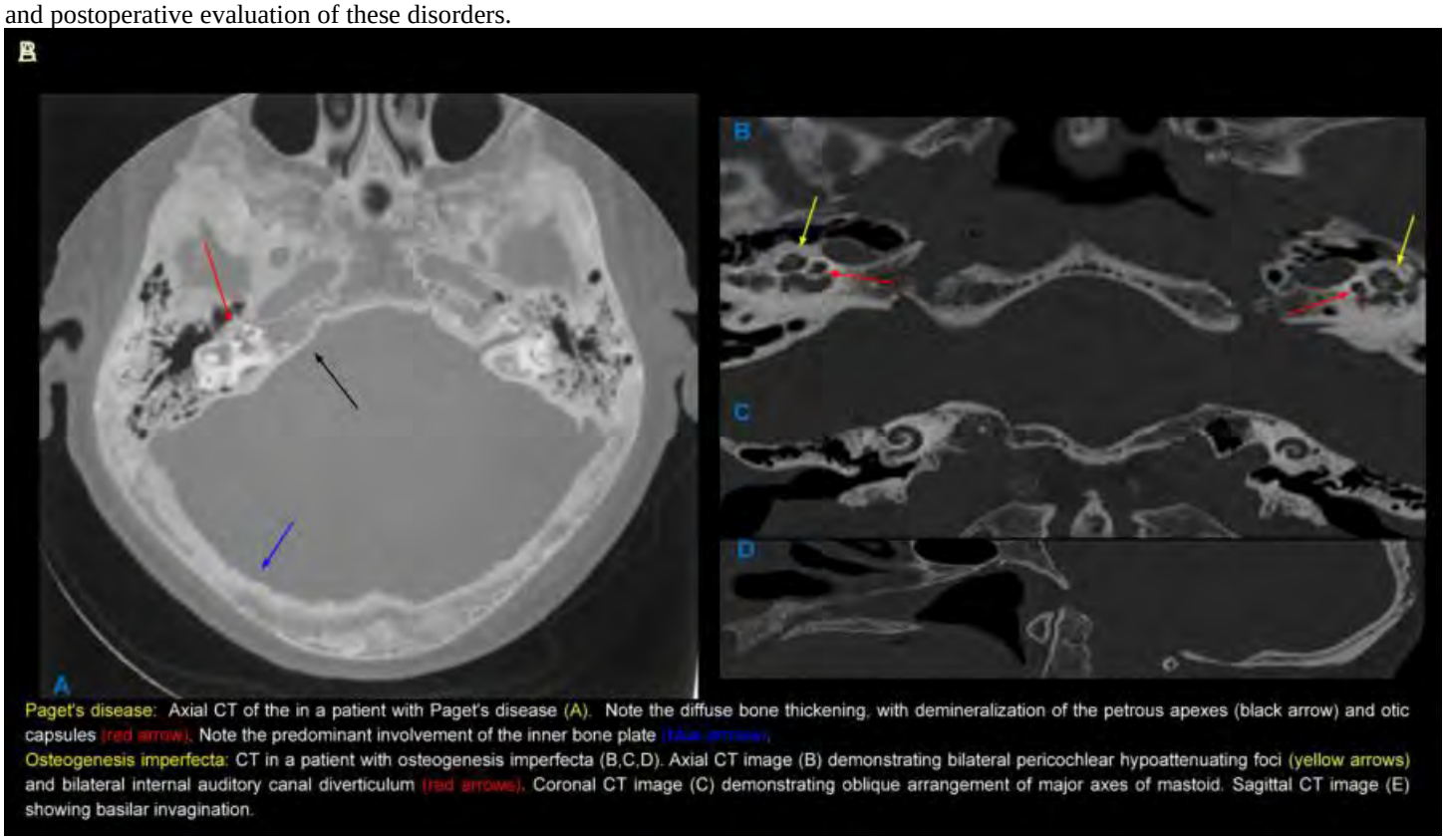

(Filename: TCT_1039_OTODISTROFIASASNR2.jpg)

1398
The Phakomatoses: Review of Neuroimaging and Update on Molecular Features
L Ramin[1], M Carletto[1], C Colombo[2], A Pasquarelli[2], S Ferraciolli[3], L Lucato[4]
[1]Ultra-X, São José do Rio Preto, São Paulo, [2]Ultra-X, São José do Rio Preto, SP, [3]InRad - HC- FMUSP, Sao Paulo, -- SELECT -- , [4]Instituto de Radiologia, Hospital das Clínicas da Faculdade de Medicina da Universidade de São Paulo, São Paulo, São Paulo

Purpose
Phakomatoses, also known as neurocutaneous disorders, comprise a vast number of entities that predominantly affect structures originated from the ectoderm such as the central nervous system and the skin, but also the mesoderm, particularly the vascular system. MR imaging is widely used for the characterization of brain and spinal lesions associated with these disorders. Their molecular genetic aspects are being understood which have brought on interest in these conditions. Objectives: Review features that should prompt consideration of a neurocutaneous syndrome. Highlight the imaging features of the neurocutaneous syndromes, from the most common to the rare ones. Outline the diagnostic criteria for the neurocutaneous syndrome. Correlate to the currently known molecular characteristics of each neurocutaneous syndrome.
Materials and Methods
We review the clinical features, current pathogenesis, and modern neuroimaging findings of the neurocutaneous syndrome from the most common (neurofibromatosis, tuberous sclerosis, Sturge-Weber syndrome and von Hippel-Lindau) to the uncommon ones (such as the melanophakomatoses, vascular phakomatoses, and other rare neurocutaneous syndromes like encephalocraniocutaneous lipomatosis).
Results
We selected didactic and representative neuroimaging features of neurocutaneous syndromes from cases of our institution.
Conclusions
Imaging plays an important role in screening, early identification of abnormalities, advice genetic testing and follow-up of lesions in neurocutaneous syndromes. Radiologists should be familiar with these syndromes to guide appropriate treatment and prognosis.

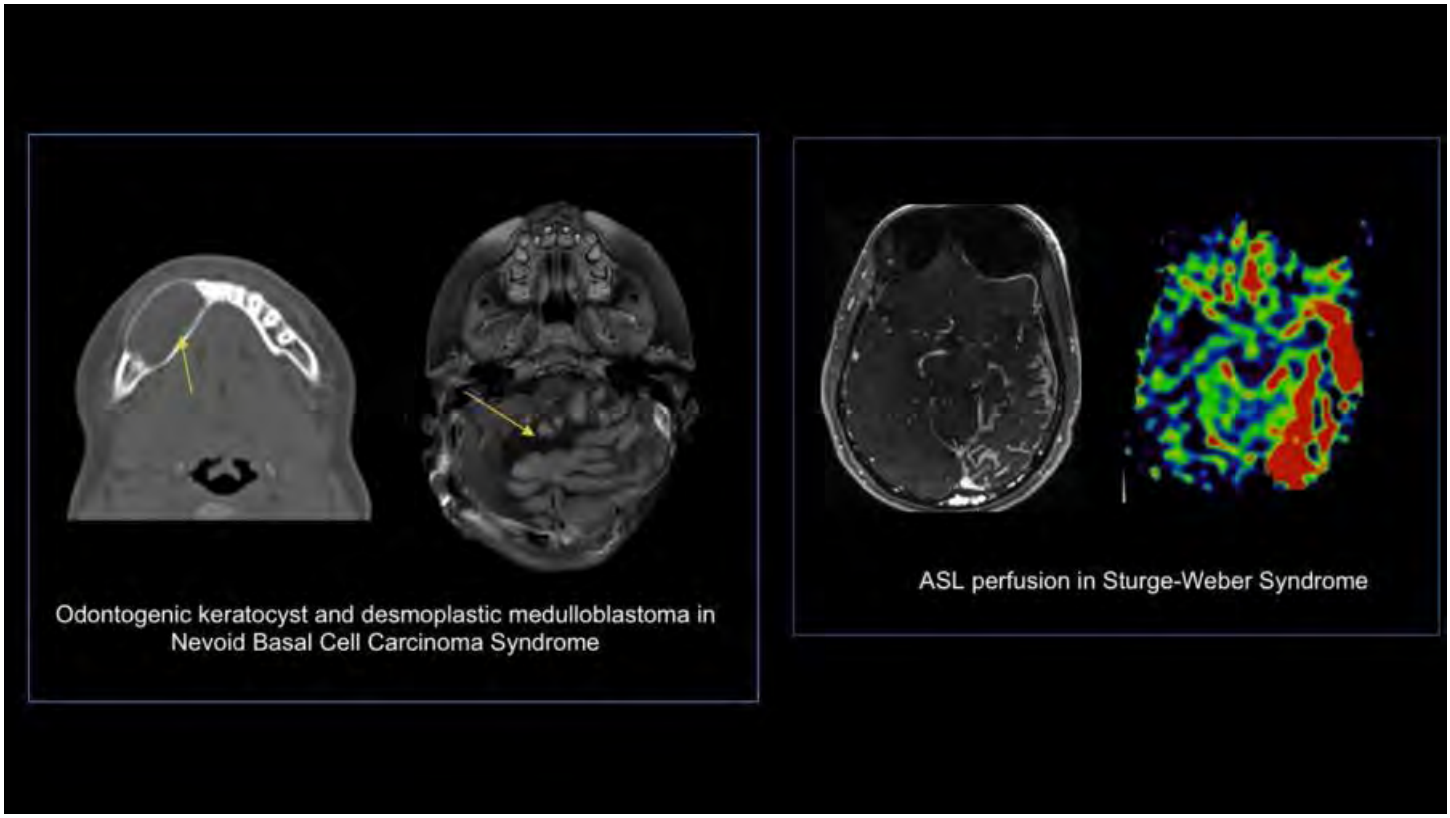

(Filename: TCT_1398_ASNR.jpg)

1337

The Pitfalls of Automated Perfusion Imaging of the Brain

S Alamro[1], N Almarek[1], M Nicolas-Jilwan[2]

[1]King Faisal Specialist Hospital and Research Centre, Riyadh, N/A, [2]King Faisal Specialist Hospital and Research Centre, Riyadh, Saudi Arabia

Purpose

We present several of the most common pitfalls of automated perfusion imaging of the brain. The objectives of the presentation are: 1. To develop a systematic approach in reviewing automated perfusion CT studies of patients with acute ischemic stroke. 2. To identify the most common pitfalls.

Materials and Methods

Automated perfusion CT imaging is increasingly used for the selection of patients with acute ischemic stroke for endovascular thrombectomy. Despite major recent improvements, the technique remains flawed with significant pitfalls. We highlight the most common of these, with a special emphasis on a systematic approach that allows their prompt identification and accurate interpretation of these studies.

Results

We selected CT perfusion studies of six patients presenting with acute ischemic stroke. These encompass the most commonly encountered pitfalls of this technique, including truncation of the perfusion curves, inadequate placement of the arterial input function, the effect of head motion as well as the perfusion alterations secondary to chronic carotid stenosis and chronic infarction. We also included a case that underscores the frequently unreliable estimation of the infarct core and mismatch volumes by the software based on its threshold values, and the utmost importance of interpreting these in conjunction with all other available data (including head CT, CTA and perfusion color maps).

Conclusions

Although Automated Perfusion CT imaging is considered a robust modality for the triage of acute ischemic stroke patients, it has multiple potential drawbacks, frequently encountered in clinical practice. Knowledge of these and a systematic review of the study are crucial to optimize patient selection for reperfusion therapy.

730

The Post-Op Spine - What Could Go Wrong? A Case Based Review of Complications

P Manickam[1], T Ly[2], E Fourgas[3]

[1]Geisinger, Danville, PA, [2]Geisinger Medical Center, Danville, PA, [3]Geisinger Health System, Wilkes Barre, PA

Purpose
Evaluation of the postoperative spine can be a challenging task, however, is standard in our day to day practice. It is imperative for neuroradiologists to be aware of routine findings following surgery, such that pathologies of the postoperative spine and paraspinal soft tissues can be recognized. Knowledge of the patient's surgical history and clinical symptoms is critical. Additionally, understanding of surgical approaches and the utilized surgical hardware is necessary to provide value in our interpretations.
Objectives: Discuss expected immediate and delayed findings in the postoperative spine. Conduct a case based review of implant related complications - including implant malposition, hardware failure, adjacent segment disease, and pseudarthrosis. Review pathologies at the surgical site not immediately related to instrumentation - including post-operative fluid collections, infection, distinguishing recurrent disc herniation from scar, arachnoiditis, and spinal stenosis. Highlight complications related to surgical approaches in the cervical and thoracolumbar spine. This provides an excellent opportunity to review vulnerable anatomical structures based on the surgical approach. Review techniques to optimize image quality of the instrumented spine - including modification of imaging parameters, single energy reconstruction algorithms, dual energy acquisition, and post-processing techniques.
Materials and Methods
To review a broad spectrum of complications associated with the postoperative spine. Furthermore, techniques to optimize image quality of the instrumented spine will be reviewed.
Results
We will review imaging of relevant cases from a tertiary care center.
Conclusions
Given the complex nature of evaluation of the instrumented spine, a thorough understanding of the spectrum of expected and unexpected postoperative findings is imperative. Intimate knowledge of patients' surgical histories, the utilized instrumentation, and surgical approach is necessary to provide accurate interpretations to assist our surgical colleagues.

1032
The Role of APTw, fMRI, and DTI in Preoperative Planning
S Turk[1], J Kim[2], J Bapuraj[3], T Moritani[2], G Shah[4]
[1]University of Michigan, Ann arbor, MI, [2]University of Michigan, Ann Arbor, MI, [3]University Of Michigan, Ann Arbor, MI, [4]Univ. Michigan Health System, Ann Arbor, MI

Purpose
After viewing this exhibit, the reader will be familiar with the complementary roles of APTw, fMRI, DTI, PWI in preoperative brain tumor evaluation: their imaging features, assessment of treatment effects/response, artifacts and other pearls and pitfalls.
Materials and Methods
• Highlight the role of amide proton transfer weighted (APTw) imaging for preoperative planning of the brain tumors • Discuss the potential of using APTw imaging in the assessment of peritumoral invasion • Discuss the potential of using APTw imaging in assessing treatment response and discrimination of true tumor progression from pseudoprogression • Discuss the pearls and pitfalls in interpreting APTw, fMRI, DTI, PWI
Results
Overview of imaging characteristics of brain tumors with emphasis on APTw in conjunction with fMRI, DTI and PWI for preoperative planning. Demonstrate cases of tumor progression versus treatment effects, peritumoral invasion, and genetic mutation correlation APT, PWI, DWI parameters with the role of fMRI and DTI.
Conclusions
Advanced MRI techniques add value to conventional imaging sequences in the assessment of brain tumors. Tumor grade prediction, peritumoral invasion assessment, differentiation of true tumor progression from pseudoprogression, and genetic mutation prediction are discussed based on the combination of APTw, fMRI, DTI, and perfusion weighted imaging. Necrosis, hemorrhage, calcification, and extracellular matrix can affect the signal intensity in APT, fMRI, DTI and perfusion weighted imaging differently. Pitfalls and accuracy of each advanced imaging methods differs.

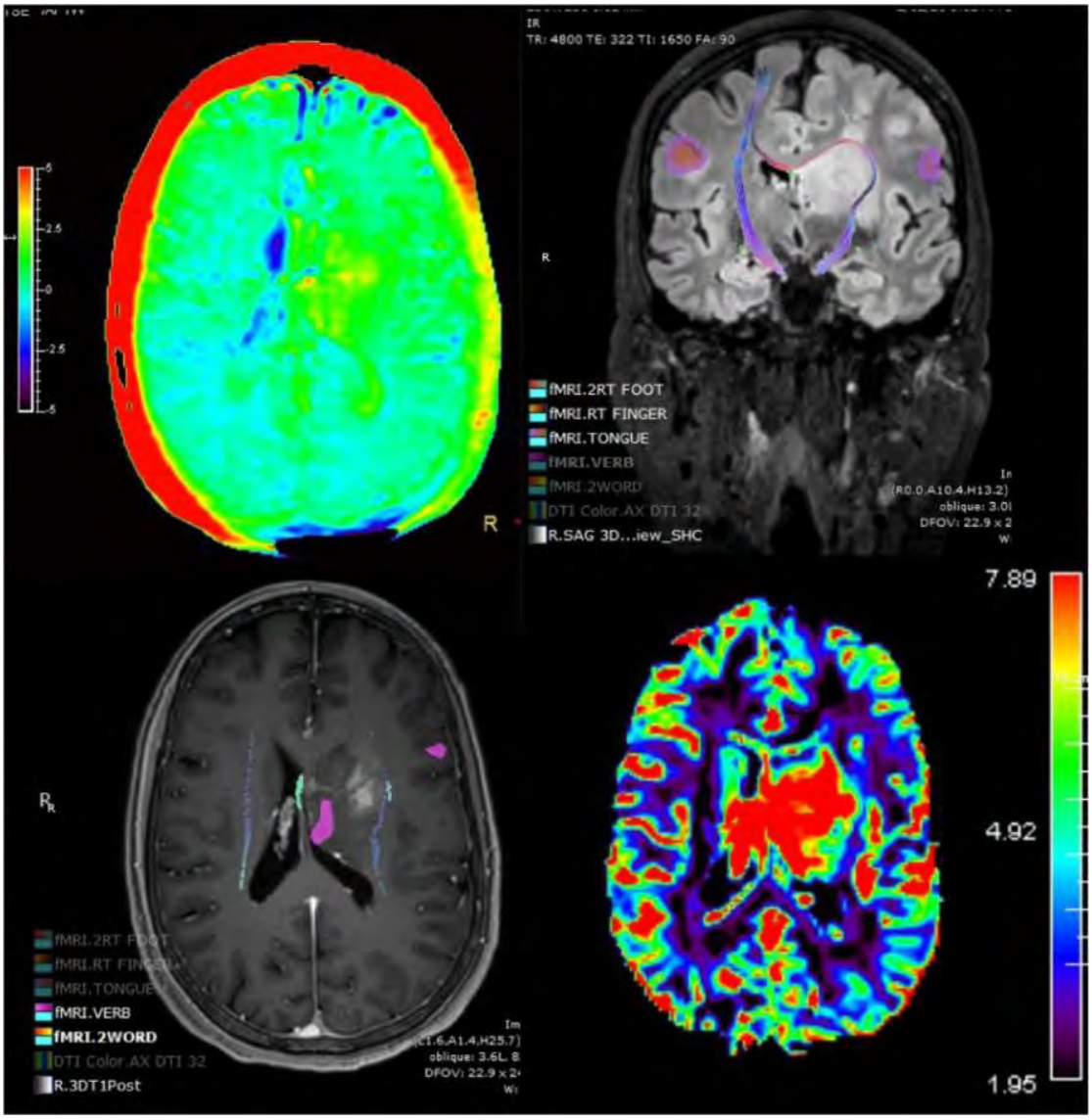

(Filename: TCT_1032_Picture2.jpg)

428

The Role of Neuroimaging in Aid of Minimally Invasive Functional Neurosurgical Procedures: A Pictorial and Educational Review

E van Staalduinen[1], A Khalaf[1], M Shahrzad[1], S Dhawan[1], M Zeineh[2], S Hashmi[1], M Wintermark[1], T Massoud[1]
[1]Stanford University School of Medicine, Stanford, CA, [2]Stanford, Stanford, CA

Purpose

Functional neurosurgery (FNS) aims to restore patient function using open surgery or minimally invasive interventions. FNS is clinically beneficial for epilepsy, movement disorders, and chronic pain. There are 4 primary ablative FNS approaches: stereotactic radiosurgery, radiofrequency thermal ablation, MRI-guided laser interstitial thermal therapy, and MRI-guided focused ultrasound (MRgFUS). Neuroimaging plays a vital role in pre-operative stereotactic planning of minimally invasive interventions, intra-operative guidance, and post-operative detection of procedure complications. We will review the large repertoire of neuroimaging techniques that support different methods to accomplish minimally invasive FNS.

Materials and Methods

We review the principles of minimally invasive FNS procedures, and discuss CT and structural/advanced MRI techniques in support of these interventions.

Results

FNS neuromodulation regulates neural circuits by electrical stimulation. Deep brain stimulation (DBS) is a common neuromodulation procedure approved primarily to treat Parkinson's disease (PD), essential tremor, and epilepsy. MRgFUS may be used for similar indications. We will first discuss techniques for epilepsy treatment, including controlled laser thermal ablation of the amygdala and hippocampus monitored by intraoperative MR thermography. Vagus nerve stimulation and responsive neurostimulation aim to reduce seizures. For PD and essential tremor, DBS entails stereotactic electrode placement into nodes of the cortico-basal ganglia-

thalamocortical loop, e.g. subthalamic nucleus and globus pallidus interna. The ventral intermediate nucleus is an effective target for PD and essential tremor. DBS of the pedunculopontine nucleus may be used to treat gait freezing in PD. We illustrate specific MRI sequences to depict these deep brain targets and plan procedures. We also review CT/MRI appearances of technical and hemorrhagic complications of DBS electrode placements. Regarding pain management we will illustrate the imaging relevant to percutaneous rhizotomy for trigeminal neuralgia, occipital nerve stimulation for occipital neuralgia, and spinal cord stimulation for intractable low back and leg pain.
Conclusions
Accurate targeting of brain structures is crucial for optimal clinical outcomes of FNS. This presentation will aid in understanding current and ongoing neuroimaging advancements for FNS targeting, including the use of ultrahigh magnetic field strengths and new MRI acquisition for improved patient outcomes.

209

The Spectrum of Intracranial Cerebrovascular Lesions on Conventional T2-weighted Images

M Tanwar[1], A Haneef Mohamed[1], J Jones[2], H Sotoudeh[3]
[1]University of Alabama at Birmingham, Birmingham, AL, [2]University of Alabama at Birmingham, Birmigham, AL, [3]UAB, Birmingham, AL

Purpose
1. Cerebrovascular lesions are a major cause of mortality and morbidity in neurological medicine. 2. Magnetic resonance imaging (MRI) of the brain has become widely available and performed for many indications, such as headache, malignancy, multiple sclerosis, trauma, stroke, cerebrovascular disease, and others. Conventional non-contrast T2-weighted images are routinely acquired in almost all brain protocols. 3. T2-weighted images should be assessed for incidental cerebrovascular lesions, irrespective of the primary indication.
Materials and Methods
To familiarize neuroradiologists with the typical appearance of large intracranial cerebrovascular lesions on conventional T2-weighted images.
Results
Review of case material from a single institution, with accompanying literature review.
Conclusions
Results: Vascular structures typically demonstrate a low signal flow-void on the T2-weighted images. In our experience, large cerebrovascular abnormalities are easily visible to a typical neuroradiologist. We hereby present the spectrum of the imaging appearance of various intracranial cerebrovascular lesions on routine non-contrast T2-weighted MRI. These include: Aneurysm, Arteriovenous malformation, Arteriovenous fistula, Arterial occlusion, Capillary telangiectasia, Cavernous malformation, Developmental venous anomaly, Dural venous thrombosis, Moyamoya, Proliferative angiopathy. Conclusion: MRI of the brain has been implemented to evaluate multiple intracranial pathologies. Non-contrast T2-weighted images are acquired as a routine sequence in almost all neuroimaging protocols. It is not uncommon to encounter various cerebrovascular lesions incidentally on brain imaging. Neuroradiologists should evaluate the routine T2-weighted images for incidental cerebrovascular lesions, irrespective of the primary indication of the study.

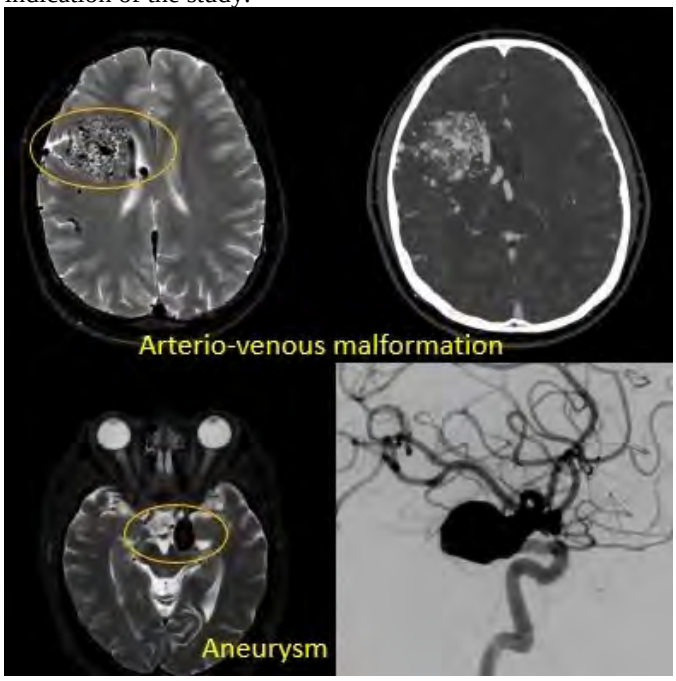

(Filename: TCT_209_ASNR.jpg)

1465

The Spine is the Tree of Life: A Radiographic Review of Spinal Injuries in Athletes

S Lev[1], C Ekhator[2], S Tiu[1], M Gelbman[3]
[1]Nassau University Medical Center, East Meadow, NY, [2]New York Institute of Technology College of Osteopathic Medicine, Greenvale, NY, [3]Maimonides Medical Center, Brooklyn, NY

Purpose

The particular demands of each sport determine the types of injuries sustained. Mechanisms of spinal injuries include hyperextension, hyperflexion, axial loading distraction, torsion and rotational forces. 1. To emphasize the importance of understanding the unique mechanical forces, both acute and long-term, contributing to adverse outcomes for each activity. These injuries can range from chronic back pain to catastrophic events. 2. To discuss the heightened susceptibility to trauma in the pediatric age group and in those with pre-existing congenital conditions.

Materials and Methods

To demonstrate the wide range of spinal injuries occurring to athletes participating in diverse sports. The radiologist can hone his or her search pattern according to common patterns of injury.

Results

We examined the imaging studies of professional and amateur (including "weekend warriors") athletes during the past ten years who presented to the ED of our Level I trauma center. We organized our cases by activity, highlighting type, mechanism and acuity of injury. We also discuss special considerations in the pediatric cohort predisposing to trauma.

Conclusions

Rotatory forces tend to result in dislocation while compressive forces result in fractures. The T-L junction is especially susceptible during high-energy impact. Chronic spine injuries result from repetitive loading, as in golf and rowing. Athletes with congenital stenosis have increased risk of injury even after minor trauma. Suspected injury to the cord, nerve roots or ligaments necessitates urgent MR. Activities may be more solo-based (e.g. running, gymnastics, dancing, surfing) or team-related (e.g. football, soccer, hockey, baseball and basketball). Gymnasts need a high degree of flexibility and may present with hyperextension injuries (eg. facet dislocation), as well as compression fractures. Cervical spine injuries are common in athletes participating in contact and collision sports, like football. Linemen are prone to lower lumbar disc herniations and spondylolysis. Non-contact injuries, like avulsions, result from sudden changes in direction. Hockey injuries are mainly cervical, and may occur when checked from behind. Snowboarding injuries involve failed jumps and subsequent axial loads. Competition as a motivating factor concurrently increases the risk of spinal injuries in children and adolescents. The radiologist plays a crucial role in expeditiously identifying injuries and can help with management, such as determining return to play.

383

The Vomer Bone and Vomerovaginal Canals: A Pictorial and Educational Review of Neuroimaging Anatomy and Pathology

W Mu[1], S Tedla[1], D Sivacharan Gaddam[1], H Dahmoush[1], M Wintermark[1], S Hashmi[1], T Massoud[1]
[1]Stanford University School of Medicine, Stanford, CA

Purpose

The vomer (Latin for plowshare) is a small, thin, midline bone that occupies and divides the nasal cavity, forming the posteroinferior part of the nasal septum. Vomer bone (VB) anatomy is important in surgical procedures on the hard palate and transnasal endoscopic skull base procedures, and can also be involved in many pathological conditions. Anatomy of the vomerovaginal canals (VVCs) relative to the sphenoid sinus is also relevant to endoscopic trans-sphenoidal surgeries. Thus, a thorough neuroimaging understanding of the VB is essential. We provide a pictorial and educational review of normal VB, its variants, and changes induced by different focal pathologies that are underreported in the radiological literature.

Materials and Methods

We comprehensively review the imaging findings of the normal and pathological VB and VVCs.

Results

We first review the imaging anatomy of the VB and VVCs. VB articulates inferiorly with the maxillae and palatines, superiorly with the sphenoid, and anterosuperiorly with the ethmoid and septal cartilage. Each VVC lies medial to the palatovaginal canal and is formed between a VB wing, sphenoid body and the medially directed vaginal process of the sphenoid. VVC transmits the sphenopalatine vessels. Next we discuss VB congenital or acquired pathology and imaging correlates. VB agenesis is a rare anomaly, as is a persistent buccopharyngeal membrane involving the posterior VB. The VB may be wide in bony choanal atresia. Incomplete VB ossification may lead to perforations, or VB may not fuse with the palatal shelves. Most VB shape variations play a part in nasal septum deviation. Rarely, the sphenoid sinus pneumatizes the vomer. Iatrogenic imaging changes include partial VB resection following transsphenoidal procedures, various osteotomies or VB flap repairs for cleft palate, and construction of a large uni-neochoana in repairing choanal atresia. We will also illustrate examples of focal VB changes with trauma (fractures or after septoplasty), cocaine-induced destruction, focal infection (e.g. mucormycosis), hemangioma, fibrous dysplasia, and tumors that range from benign to malignant, e.g. chondroma, myxoma, hamartoma, extracranial craniopharyngioma, teratoma, and chondrosarcoma (an MRI enhancing tumor with calcified tumor matrix).

Conclusions
We review the neuroimaging features of the normal VB and its pathological changes. This knowledge aids patient management especially in preoperative planning and postoperative interpretation of surgical and endoscopic treatments.

591

Thoracic Radiology for the Neuroradiologist

N Stabo[1], R Griesbach[1], J Kanne[1], G AVEY[2]
[1]UW-Hospitals and Clinics, Madison, WI, [2]University of Wisconsin, Madison, WI

Purpose
This presentation will demonstrate a variety of image rich cases with both neurologic and thoracic imaging findings visible within the standard field of view of a study including the head and neck. When viewed in conjunction, the thoracic and neurologic findings inform the interpretation of one another, narrowing the differential diagnosis. Educational objectives: -To illustrate the importance of the neuroradiologist having a sound working knowledge of thoracic radiologic findings, particularly those related to neurologic diagnoses. -To showcase examples of thoracic pathologies with findings visible on routine neurologic imaging studies.
Materials and Methods
Purpose: Between 2007 and 2017, utilization of neuroradiological imaging in the emergency department increased 72% including a 1300% increase for CT angiograms of the neck and a 1011% increase in CT angiograms of the head and neck (AJR 2021). The standard field of view for CT angiograms of the neck includes the aortic arch and the upper lobes of the lungs. Therefore, neuroradiologists need to be comfortable with thoracic radiological findings, particularly those with neurologic manifestations. This exhibit demonstrates entities having both thoracic and neurologic imaging findings, which in conjunction, inform interpretation of one another. Additionally, this work illustrates a variety of common and notable thoracic pathologies visible on routine neurological imaging studies.
Results
Materials/Methods: Using case logs and an electronic search of reports from the institutional PACS, a selection of cases of diagnoses with both neurological and thoracic imaging manifestations were selected. An institutional review board waiver was obtained for this project.
Conclusions
Results: A variety of cases were reviewed, including cases of sarcoidosis, granulomatosis with polyangiitis, immune reconstitution inflammatory syndrome, and nocardiosis. In each case presented, the neurological finding when viewed on its own is nonspecific with a broad differential diagnosis. However, when viewed in conjunction with the correctly interpreted thoracic finding(s), the differential diagnosis is considerably narrowed. Conclusion: Working knowledge of thoracic radiologic findings can help inform the interpretation of associated neuroimaging findings. As shown here, multiple neurological diagnoses have an otherwise broad differential diagnosis, which can be significantly narrowed when viewed in conjunction with their respective associated thoracic findings.

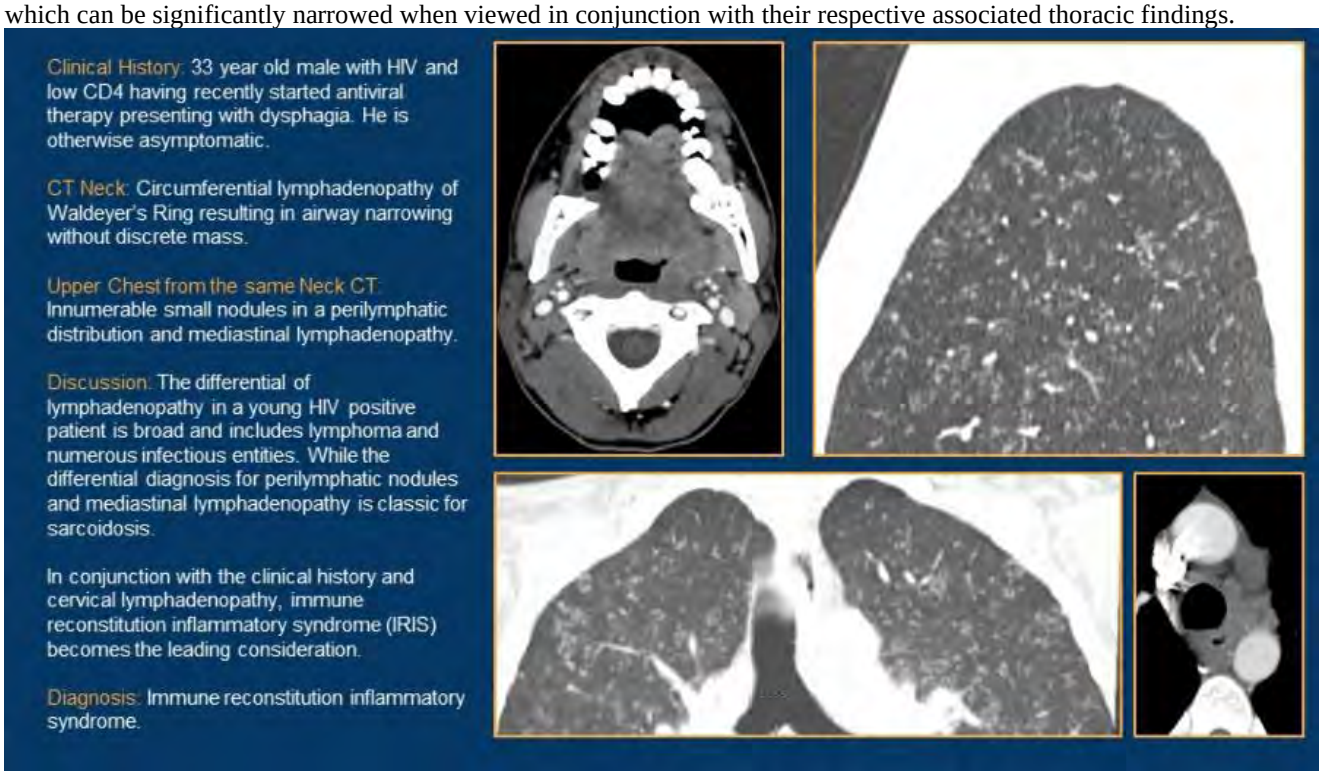

(Filename: TCT_591_ThoracicRadiologyfortheNeuroradiologist.jpg)

1148

Orbital Emergencies: A Pictorial Structured Approach to Orbital Emergencies.

R Kuhnlein[1], A Kerpel[2], M Spampinato[3], M Matheus[3]

[1]MUSC, Morgantown, WV, [2]The Medical University of South Carolina, Charleston, SC, [3]MUSC, Charleston, SC

Purpose

Present a systematic approach to the evaluation of emergent orbital pathology will enable the radiologist to formulate a prompt diagnosis, resulting in a positive impact on patient care.

Materials and Methods

Cross-sectional imaging plays a key role in the assessment of emergent traumatic and non-traumatic orbital pathology. We will provide a detailed review on the radiological interpretation of orbital emergencies using educational cases from our teaching files.

Results

Our didactic exhibit will include: 1. A discussion of orbital anatomy utilizing CT and MRI imaging; 2. A pictorial review of traumatic orbital emergencies; 3. A pictorial review of non-traumatic orbital emergencies.

Conclusions

Orbital emergencies are important diagnoses that need to be immediately recognized by the interpreting radiologist. Imaging plays a key role in the evaluation of orbital trauma, since clinical evaluation may be hindered by facial soft tissue injury and altered mental status of the patient. Non-contrast CT is the modality of choice in the setting of trauma. Patients are also seen in the emergency department for a variety of non-traumatic conditions leading to loss of vision, diplopia, ophthalmoplegia, ocular pain, orbital bruit, proptosis, or enophthalmos. Contrast-enhanced CT or MRI are effective in differentiating among non-traumatic orbital disease processes. We will provide a pictorial review of orbital traumatic and non-traumatic emergencies that the radiologist must be familiar with. Pathologic processes reviewed will include orbital skeletal trauma, lens injury, open globe injury, orbital foreign body, vascular orbital pathology, papilledema, orbital infection and inflammatory conditions, among other common and less common orbital emergencies. Summary/Conclusion: Our pictorial exhibit will highlight the importance of cross-sectional imaging in the diagnosis of common and uncommon orbital emergencies. A systematic approach to the evaluation of emergent orbital pathology will enable the radiologist to formulate a prompt diagnosis, resulting in a positive impact on patient care.

1086

Translation of AI Models into Clinical Neuroradiology Practice - From Concepts to Routinely Used Clinical Tools

S Merkaj[1], C Atkins[1], M von Reppert[2], M Lin[3], J Cavallo[1], I Tocino[1], M Aboian[4]

[1]Yale School of Medicine, New Haven, CT, [2]Brain Tumor Research Group, Yale School of Medicine, New Haven, CT, [3]Yale University School of Medicine and Visage Imaging, Inc., New Haven, CT, [4]Yale University, Woodbridge, CT

Purpose

We review different approaches to implementation of AI image analysis algorithms into clinical practice, which include home grown software, companies such as Aidoc, research PACS Flywheel, and clinical/research PACS hybrids such as Visage. We focus on workflow implementation models and on the interface of their implementation into clinical practice including algorithms embedded into PACS and algorithms which provide information along-side of PACS.

Materials and Methods

Our educational exhibit describes fundamental informatics concepts that are critical to understanding of how to incorporate AI into clinical practice. We present detailed information of past and current informatics approaches for AI implementation that help radiologists tailor their acute studies' reading time and provide detailed reports that are critical for precision approaches in oncology. We provide schema for how to evaluate providers of AI technology and apply this information to the clinical practice within individual hospitals.

Results

We reviewed the literature and available company information for the available AI image analysis software through website search, press releases, and our hospital's experience with various AI algorithm implementations including industry-academic collaborations.

Conclusions

There are various approaches to implement AI algorithms into clinical practice. First, some methods work in parallel/in the background to clinical PACS and provide notifications in real time as studies are generated. This pipeline alerts the radiologist to studies containing critical and urgent findings like intracranial bleeds, large vessel occlusions, etc., allowing for a prioritized finalization of critical reads. Other approaches include AI-based image processing such as quantification of susceptibility foci on SWI, thus providing reports of anatomic quantification of microbleeds in real time. PACS-based approaches include research and clinical software that enable incorporation of AI algorithms within, ideally, the same PACS interface as what is used in the clinic. These algorithms can be implemented for regional volumetric segmentations of organs or research approaches for brain tumor segmentation. These technologies are actively improved by physician feedback and correction, and if the research and clinical PACS systems are the same, there can be accelerated translation from concept to code and easier adoption. Ultimately, all these methods improve diagnostic efficiency and accuracy.

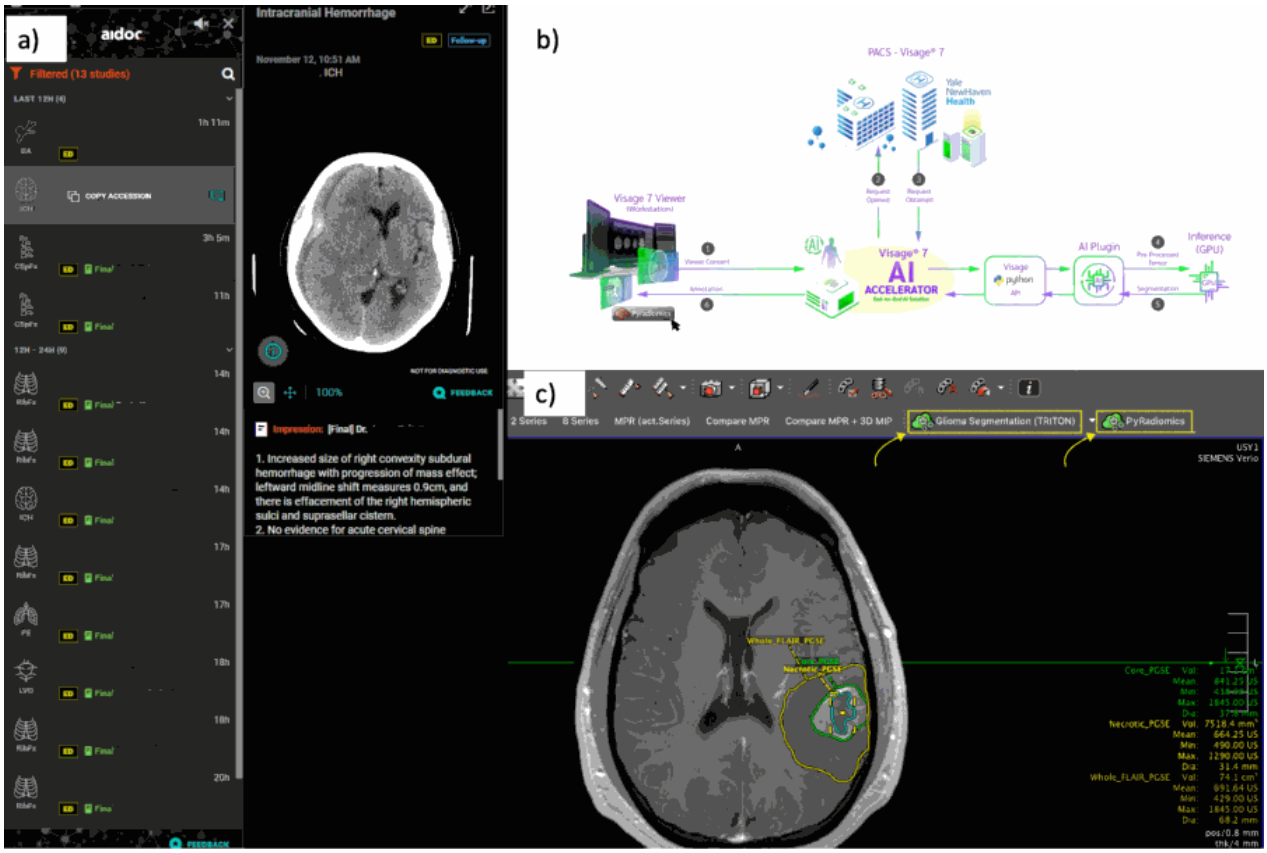

Figure 1: a) Example of study presentation in Aidoc. b) PACS-integrated workflow from Visage 7. c) Example of study presentation in Visage 7, PACS-integrated features include natively embedded automated AI Glioma Segmentation and PyRadiomics feature extraction.

(Filename: TCT_1086_Figure.gif)

548

Traumatic Mid Face and Skull Base Fractures – Radiologist's Role in Guiding Surgical Management and Predicting Complications.

T Min[1], X Wu[2], M Zygmont[1], R Peterson[3]

[1]Emory University, Atlanta, GA, [2]EMORY UNIV SCHOOL OF MEDICINE, ATLANTA, GA, [3]EMORY UNIVERSITY SCHOOL OF MEDICINE, NORCROSS, GA

Purpose

Educational objectives: -Review imaging findings of mid-face and skull base fractures -Review indications for surgery and goals of surgical management -Review complications/common collateral injury in mid-face and skull base fractures -Understand the most efficient and effective approach to reporting mid-face and skull base fractures Presentation outline: -Mid-face fractures – LeFort, ZMC, NOE, orbital blowout -Skull base fractures – anterior, central, lateral, posterior -Indications for surgery – airway compromise, vascular injury, vision, hearing, cranial nerve injury, mal-occlusion, cosmetic -Goals of surgical management -Complications – hemorrhage, infection, stroke, loss of function, CSF leak -Key items to include in report

Materials and Methods

Traumatic mid-face and skull base fractures often involve fracture lines extending through multiple structures, which can lead to reports containing extensive listing of every fractured structure. Although this approach can serve the purpose of being complete, it may not be the most efficient and effective reporting approach for guiding management decision. Attempts at efficient reporting of mid-face and skull base fractures include categorization of fractures into recognized patterns – i.e., LeFort, ZMC or NOE for mid-face fractures, and otic capsule-sparing or otic capsule-violating for skull base fractures. However, simply reporting the fracture pattern may not be sufficient for guiding clinical management, and some level of feature description is necessary. For example, temporal bone fracture with bone fragment extending into the facial canal requires urgent surgical exploration to prevent permanent loss of facial nerve function1, whereas nondisplaced temporal bone fracture sparing the otic capsule and facial nerve canal may not require any surgical treatment at all.

Results

-Review of published articles on the topic of traumatic mid-face/skull-base fractures, their surgical management and complications. -Review of institutional medical records for illustrative cases.

Conclusions

When reporting traumatic mid-face and skull base fractures require, describing the clinically relevant key features of the fractures can

efficiently guide surgical management. Additionally, knowledge of specific injury areas that predispose patients to long-term complications can lead to appropriate preventative measures.

995

Turn Your Gaze to This: Causes and Patterns of Abnormal CNIII Enhancement.

Z Dymon[1], L Kolli[1], A KLEIN[1], D Smullen[1], D O'Neill[1], M Agarwal[1]
[1]Medical College of Wisconsin, Milwaukee, WI

Purpose
Approach: 1. Anatomy of CNIII will be reviewed 2. Causes of CNIII enhancement will be reviewed 3. Appropriate teaching cases will be shown for reinforcement
Materials and Methods
The purpose of this educational exhibit is to review the anatomy, and the causes and patterns of abnormal CN III enhancement.
Results
N/A
Conclusions
Findings/Discussion: The oculomotor nerve (CNIII) arises from the ventral aspect of the midbrain, runs within the lateral interpeduncular cistern and traverses within the superior aspect of the lateral wall of the cavernous sinus before it enters the orbit within the superior orbital fissure. Abnormal enhancement of CNIII can be due to primary involvement of the nerve by pathologies such as schwannoma; due to involvement by adjacent pathology such as cavernous sinus lymphoma or pituitary adenoma, direct involvement by midbrain GBM; or could be due to secondary involvement by infective processes such as meningitis and Lyme disease, or neoplastic processes such as leptomeningeal metastatic disease. Attention to pattern of enhancement, and correlation with other imaging findings, lab work and history can help in getting to an accurate diagnosis. In this review we will describe these imaging findings using interesting case examples.

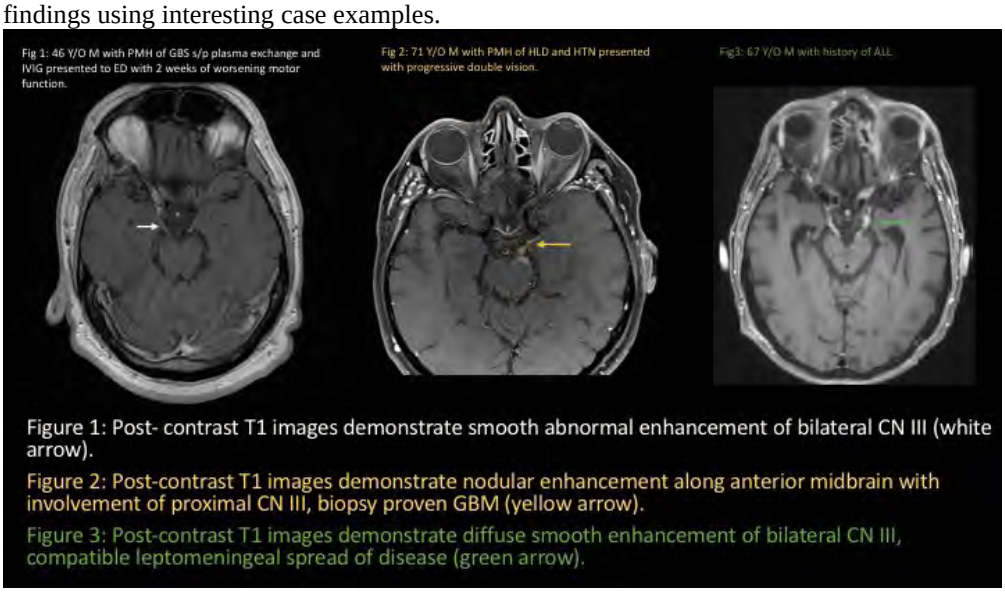

(Filename: TCT_995_CNIIIenhancment.jpg)

476

Typical and Atypical Imaging Pattern of Progressive Multifocal Leukoencephalopathy

N Soni[1], S ELLIKA[2], J Almast[3], R Mangla[4], A Hussien[5], S Meyers[6]
[1]University of Rochester URMC, Rochester, NY, [2]UNIVERSITY OF ROCHESTER MEDICAL CENTER, ROCHESTER, NY, [3]University of Rochester, Rochester, NY, [4]Upstate Medical University, Syracuse, NY, [5]UT southwestern, Dallas, TX, [6]University of Rochester Medical Center, Rochester, NY

Purpose
PML represents a severe demyelinating disorder of the brain caused by the John Cunningham virus (JCV) reactivation during immunosuppression. PML affects individuals with HIV infection, hematologic diseases, solid-organ transplants, and treated with immunomodulatory medications [such as patients treated with natalizumab for multiple sclerosis (MS), rituximab for lymphoma, and efalizumab for psoriasis]. PML–Immune Reconstitution Inflammatory Syndrome (IRIS) is an acute, clinical deterioration of the symptoms, frequently encountered in HIV-positive (on antiretroviral therapy) and HIV-negative (natalizumab-treated MS) patients. JC Virus Granule Cell Neuronopathy (GCN) has been identified in natalizumab-treated MS patients where JCV destroys cerebellar granule cell neurons, resulting in cerebellar atrophy, gait ataxia, and incoordination. For a definite diagnosis, a positive CSF PCR of JCV in addition to compatible clinical and radiological findings is mandatory. In the absence of JCV detection in CSF, brain biopsy should be considered.

Materials and Methods
Progressive multifocal leukoencephalopathy (PML) manifests with a broad spectrum of clinical and imaging features. This exhibit will describe the typical and atypical imaging patterns on conventional MRI, including susceptibility, diffusion, and MR spectroscopy in primary diagnosis and follow-up PML.
Results
In this two-center observational cohort study, we will retrospectively analyze all the consecutive patients with a confirmed diagnosis of PML by medical records with a particular focus on imaging patterns, including advanced-MR techniques. According to the Consensus Statement of the American Academy of Neurology Neuroinfectious disease, only patients with a definitive, probable, or possible diagnosis of PML will be enrolled.
Conclusions
The prognosis of PML remains poor, so early diagnosis is critical to restoring the patient's immune status, preventing rapid neurological deterioration, and improving survival. MRI is the most sensitive diagnostic tool in detecting asymptomatic PML lesions. PML lesions are typically multiple white-matter lesions that frequently involve U-fibers and are rarely associated with mass effect and enhancement. Atypical PML lesions include enhancing unifocal and miliary patterns, primarily seen in natalizumab-associated PML and inflammatory PML-IRIS. Natalizumab-associated PML can affect all deep grey matter structures, thalamus and dentate nucleus.

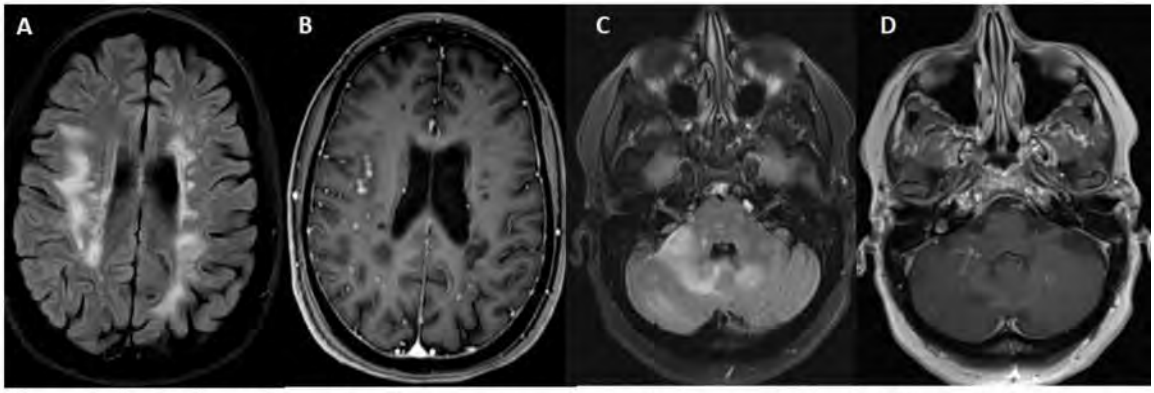

Example of natalizumab-associated progressive multifocal leukoencephalopathy (PML) – PML lesions involving the supratentorial subcortical white matter and cerebellar hemispheres affecting also the dentate nucleus. PML lesions involve U-fibers and appear are hyprintense on FLAIR (A,C) with associated punctate enhancement.

(Filename: TCT_476_ASNR_PML.jpg)

766

Uncertainty Estimation for Deep Learning in Neuroimaging: Primer for Neuroradiologists to Know Their Algorithms' Blind Spots

M von Reppert[1], T Zeevi[2], S Merkaj[1], J Onofrey[2], L Staib[3], M Aboian[2]
[1]Brain Tumor Research Group, Yale School of Medicine, New Haven, CT, [2]Department of Radiology and Biomedical Imaging, Yale School of Medicine, New Haven, CT, [3]Department of Biomedical Engineering, Yale School of Engineering and Applied Science, New Haven, CT

Purpose
We provide an overview of the concept of estimating uncertainty in Deep Learning (DL) and describe the main underlying principles behind different approaches for uncertainty estimation. We focus on its application to practical tasks in neuroimaging, such as segmentation and glioma grade prediction, and discuss how measures for uncertainty have the potential to make the implementation of DL into clinical neuroradiology practice more reliable.
Materials and Methods
N/A
Results
We review the literature on different applications of DL uncertainty estimation in the medical field with particular regard to neuroimaging. We also provide an introductory curriculum for understanding different sources of uncertainty in neuroimaging and quantification.
Conclusions
Our educational exhibit describes fundamental concepts in uncertainty estimation that are critical to understand when applying novel algorithms to neuroradiology data, such as aleatoric and epistemic uncertainty as well as the difference between likelihood, prediction probability and confidence of an algorithm. While the overall diagnostic performance of a Deep Learning prediction model (e.g. for the prediction of glioma grade) can be similar for different model configurations, the individual predictions within that same cohort may vary. This seems to be at odds with the trend towards Personalized Medicine and the clinical need to make reliable decisions for each individual. Our exhibit reviews the current ways to navigate the dilemma of uncertain model predictions in a clinical setting and provides different approaches for making DL-aided classification more transparent.

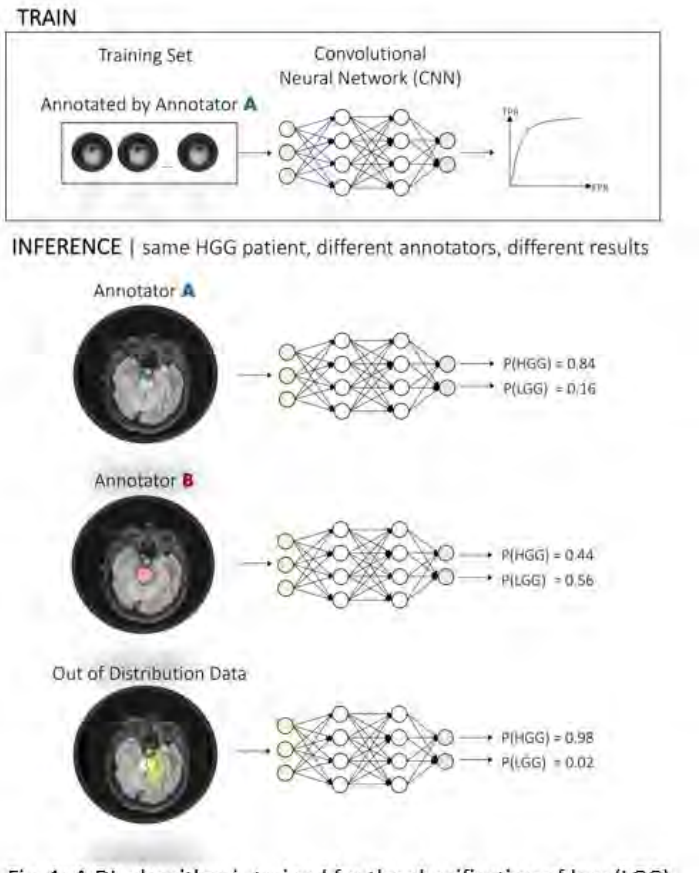

Fig. 1: A DL-algorithm is trained for the classification of low (LGG)- vs. high grade glioma (HGG) on data that was annotated by Annotator A. Precise (Annotator A), noisy (Annotator B) and out-of-distribution segmentation is performed on an unseen HGG, followed by grade prediction by the DL model.

(Filename: TCT_766_us_final.JPG)

200
Understanding Deep Learning Networks Made Easy
J Nguyen[1], A Rashad[1], J Gupta[1], A Yu[1]
[1]Tulane University School of Medicine, New Orleans, LA

Purpose
SUMMARY: Deep learning is a subset of machine learning that mimics the workings of the human thought process. Deep learning utilizes a hierarchical level of artificial neural networks built with artificial neuron nodes connected together to form a topological layer network. The hierarchical neural network reflects the algorithm of the network in processing the data. Deep learning algorithms propagate data through multiple network layers, each of which passes the data to the next layer. Deep learning algorithm is capable of learning from the input data to improve its performance through the utilization of Backward Propagation with method of Steepest Descent to minimize the error of the output. The presentation plans to accomplish the following objectives: • To describe the general principle artificial intelligence • To discuss the concept of machine learning and deep learning • To discuss the architecture of a neural network and its elements, including the "artificial neurons", and network layers. • To explain the concept of activation function, Forward Propagation/Backward Propagation. • To describe the concept of Cost Function and Steepest Descent to minimize the output error in the process of improving the performance of the network. • To explain the training and learning process of a deep neural network
Materials and Methods
This exhibit will provide a succinct tutorial of deep learning without complex mathematics. The radiologist will learn the concept of an artificial neuron, a core unit of a deep learning neural network. The radiologist will learn the construction of a hierarchical neural network. The radiologist will comprehend the concept of Forward Propagation and Backward Propagation that enable the network to learn from the dataset and minimize the error of the output. Method of Steepest Descent will be illustrated to aid in the understanding of improving the performance of the network.
Results
N/A

Conclusions
Deep learning is a machine learning technique that teaches computers to do what comes naturally to humans: learn by example. Deep learning is a key behind technology such as medical imaging, computer vision, natural language processing, etc. Deep learning models can achieve high accuracy, sometimes exceeding human-level performance. Following the tutorial, the radiologist will be familiar with the theory of deep neural networks; giving the radiologist a strong knowledge base to further explore advanced applications of deep learning in radiological imaging

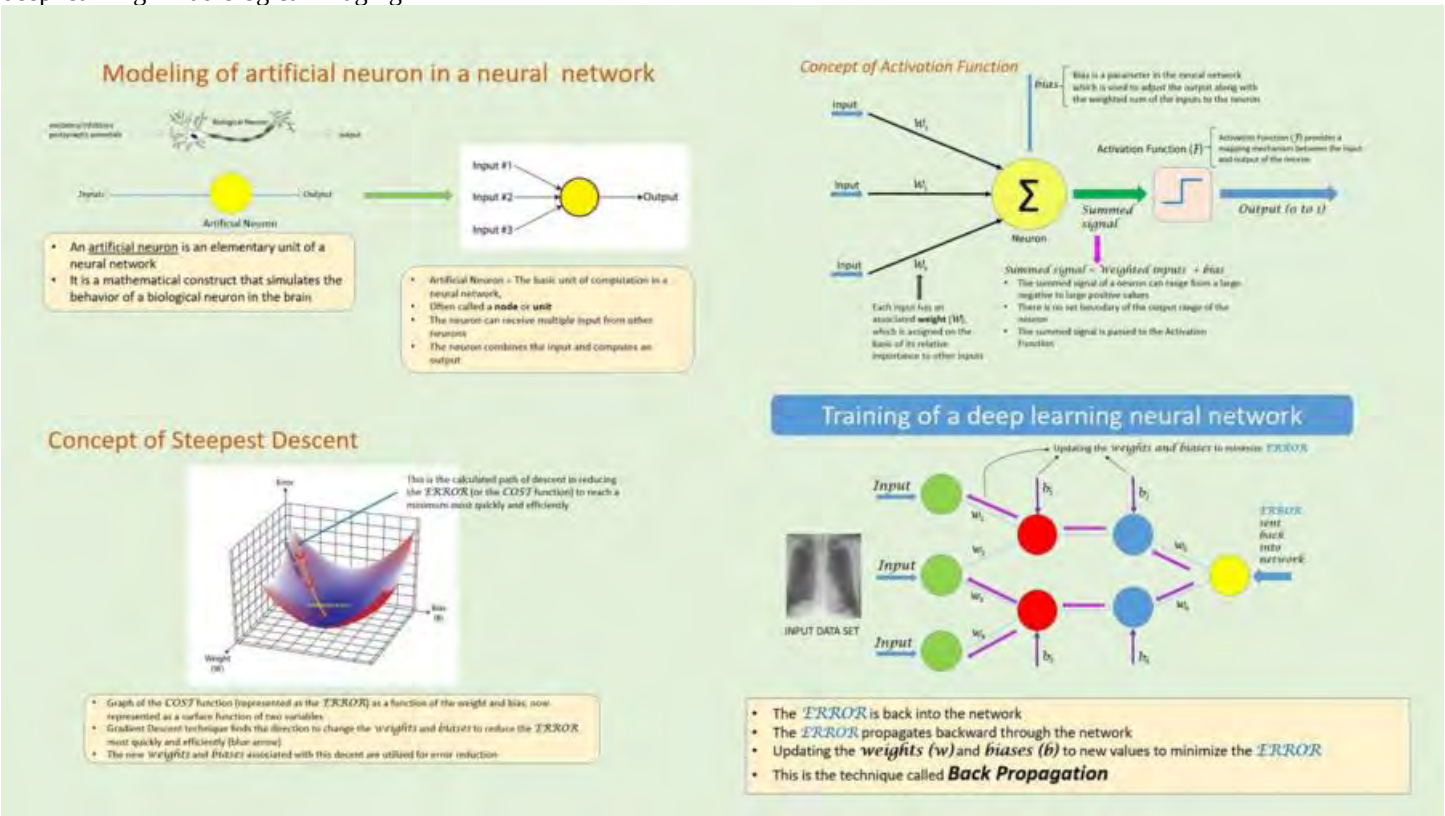

(Filename: TCT_200_ASNRpicture1.jpg)

112
Unusual Entities Involving the Cavernous Sinuses
S Edelman[1], C Zamora[2], M Castillo[3]
[1]University of North Carolina, Chapel Hill, NC, [2]UNC Department of Radiology, Chapel Hill, NC, [3]Radiology, Chapel Hill, NC

Purpose
Common lesions involving the cavernous sinuses include meningioma and schwannoma. However, there are many other lesions and conditions, including some with uncommon histology, that may also involve the cavernous sinuses. Here we present some of these uncommon entities and offer ways to suggest their diagnosis. At the end of this exhibit the reader should able to understand relevant imaging and clinical features of various unusual lesions that may arise in the cavernous sinus.
Materials and Methods
Common lesions involving the cavernous sinuses include meningioma and schwannoma. However, there are many other lesions and conditions, including some with uncommon histology, that may also involve the cavernous sinuses. Here we present some of these uncommon entities and offer ways to suggest their diagnosis.
Results
We searched our teaching files and collected cases of patients who presented with unusual lesions and other conditions involving the cavernous sinus. This search included all cases with proven diagnosis who were imaged using MRI.
Conclusions
Findings/Discussion Many of the entities presented have unique features on MRI that can be used to suggest a definitive diagnosis. These features will be highlighted in this exhibit. We will classify these entities into major groups as follows: A. Vascular: completely and partially thrombosed aneurysm, ICA agenesis, venous thrombosis. B. Malignant: metastases, lymphoma, leukemia, peri-neural spread, malignant neurofibroma, chondrosarcoma, Rosai-Dorfman disease, malignant neuroendocrine tumor. C. Benign: hemangioma, lipoma, epidermoid, cystic and hemorrhagic schwannoma, chordoma, NF-1, meningocele. D. Inflammatory/infectious: pseudotumor, pyogenic abscess, invasive fungi. Summary/Conclusion Entities presented in this exhibit are uncommon in the cavernous sinuses but need to be included in the differential diagnosis of lesions in this region. However, many of them present unique MRI features which allow the radiologist to often suggest a definitive diagnosis.

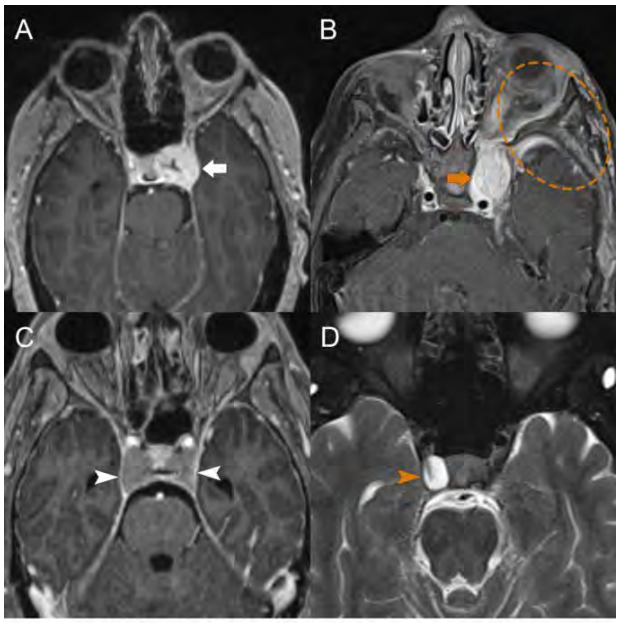

Figure. (A) Axial post-contrast T1 shows an expansile and avidly-enhancing hemangioma in the left cavernous sinus (white arrow). **(B)** Different patient with NF-1. Axial post-contrast T1 demonstrates an enhancing neurofibroma in the left cavernous sinus (orange arrow) as well as sphenoid wing dysplasia (oval). **(C)** Axial post-contrast T1 in a different patient with acute myeloid leukemia shows hypoenhancing masses in the cavernous sinuses (white arrowheads). **(D)** Axial T2 demonstrates a CSF-filled structure in the right cavernous sinus compatible with a meningocele (orange arrowhead).

(Filename: TCT_112_figwithlegend.jpg)

116

Up-to-date in Pediatrics Brain Tumors following WHO 2021 Classification

F Chutivanidchayakul[1], T Sananmuang[2]

[1]Department of radiology, Faculty of medicine Ramathibodi Hospital, Mahidol University, Bangkok, Thailand, [2]Department of radiology, Faculty of medicine Ramathibodi Hospital, Mahidol University, bangkok, Bangkok

Purpose

N/A

Materials and Methods

Review pediatric primary brain tumor types (Gliomas, glioneuronal tumors, and neuronal tumors) based on the new fifth edition of WHO Classification Tumors of the Central Nervous System (CNS)

Results

This exhibit aims to demonstrate the update in pediatrics brain tumor classification on the subgroups of (1) gliomas, (2) embryonal cell tumors, (3) ependymal tumors, and (4) neuronal and mixed neuronal-glial tumors. With this recently fifth edition, the precise diagnosis requires molecular characterization and the integration of histopathological and molecular information.

Conclusions

The 2021 fifth edition introduces major changes that advance the role of molecular diagnostics in CNS tumors, particularly in pediatrics gliomas. New families of tumor types are added to the classification as the pediatrics-type diffuse high-grade gliomas and pediatrics-type diffuse low-grade gliomas, using molecular work-up to characterize and subtype tumor. The term "glioblastoma" is no longer used in the pediatrics-type neoplasm. There are also some newly recognized tumor types in the low-grade gliomas subtype such as PLNTY, which appears as a well-circumscribed, heterogeneous mass with central calcification and cystic component. For embryonal cell tumors, they can be easily classified as medulloblastoma and other CNS embryonal tumors. The 2021 WHO classification modifies the medulloblastoma with 4 molecular groups (Wingless (WNT)-activated, Sonic hedgehog (SHH)-activated , Group 3, and Group 4) as well as combined morphologic types (classic, desmoplastic/nodular, medulloblastoma with extensive nodularity and large cell/anaplastic) into one section mentioned as Medulloblastoma histologically defined. Each molecular subgroup affects specific patient demographics and is associated with different clinical outcomes. In ependymal tumors, there has been classified with histopathological, molecular features and anatomic side (supratentorial, posterior fossa and spinal cord) with biologically distinct entities that have different cells of origin. The two main subgroups of supratentorial ependymomas are characterized by fusions on chromosome 11 (ZFTA fusion-positive and YAP1 fusion-positive). There are two subgroups of infratentorial ependymoma (posterior fossa A and B). Spinal ependymoma is rare in children and comprises two groups (classic and myxopapillary). Neuronal and mixed neuronal-glial tumors are uncommon tumors. Three new types have been added, DGONC; Myxoid glioneuronal tumor; and MVNT.

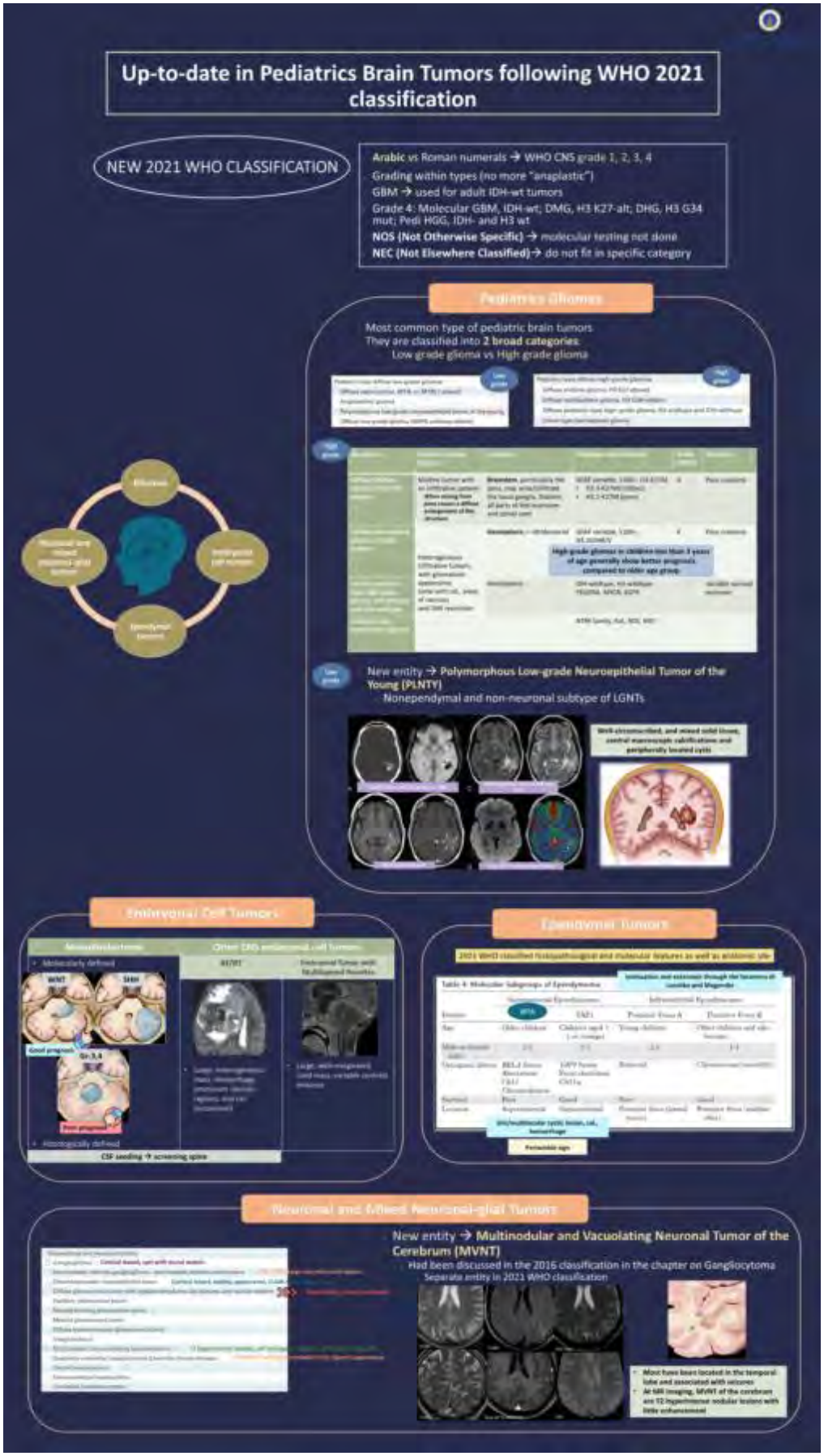

(Filename: TCT_116_updatepediatricsbraintumor.jpg)

1495

Utility of Current and Emerging Molecular Imaging Techniques in Evaluating Various Degenerative Dementias

D Lee[1]
[1]*Staten Island University Hospital, Staten Island, NY*

Purpose

Summary of planned presentation -This educational presentation seeks to discuss the ongoing developments in the role of molecular imaging in diagnosing and managing degenerative dementias. -Introduction and discussion of degenerative dementias such as alzheimer's, frontotemporal lobar degeneration, and lewy body dementia. -History of the role of imaging in diagnosing degenerative dementias and managing these patients -Discuss development and role of molecular imaging techniques in patients with degenerative dementias, as well as case presentations with image examples -Early workup and diagnosis of degenerative dementias leads to prompt management List of educational objectives -Discuss the clinical presentation and pathophysiology of various degenerative dementias including alzheimer's, frontotemporal lobar dementia, lewy body dementia, and vascular dementia. -Discuss CT and MR imaging findings and molecular imaging findings in various degenerative dementias -Describe various current and emerging molecular imaging techniques and their current role in evaluating various degenerative dementias

Materials and Methods

Provide an educational overview of emerging molecular imaging techniques and their utility in evaluating various degenerative dementias.

Results

Not applicable.

Conclusions

Not applicable.

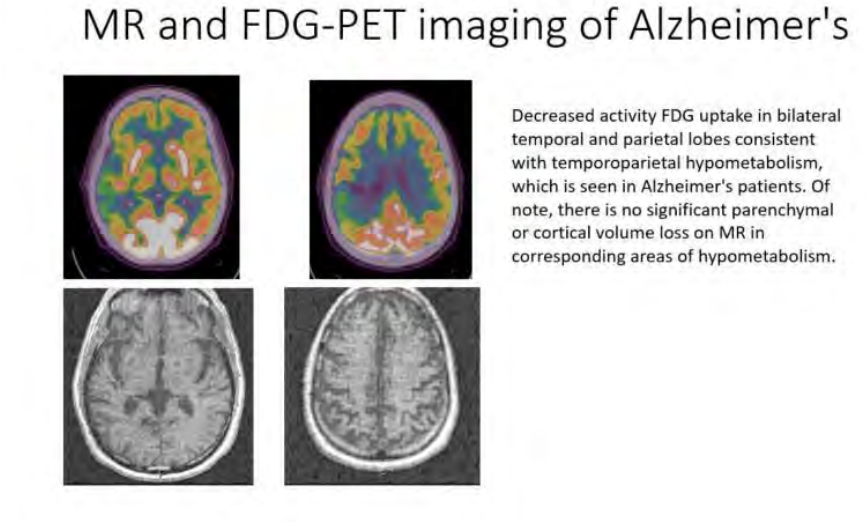

(Filename: TCT_1495_JPEG.jpg)

533

Utility of Dynamic Contrast-Enhanced and Dynamic Susceptibility Contrast-Enhanced MR Perfusion Imaging for Infratentorial Extra-Axial Solid Tumors

Y Ota[1], E Liao[1], A Capizzano[1], A Baba[1], R Kurokawa[1], M Kurokawa[1], A Srinivasan[1]
[1]*University of Michigan, Ann Arbor, MI*

Purpose

DCE-MRI and DSC-MRI can provide additional value for the differentiation of infratentorial extra-axial tumors when typical imaging findings are absent or overlap, and can be used for the assessment of post-treatment effect.

Materials and Methods

- Highlight physics of DCE-MRI/DSC-MRI and the application of DCE-MRI for clinical workup - Present common and uncommon tumors based on each extra-axial space, with emphasis on DCE-MRI/DSC-MRI - Present examples of evaluation for post-treatment effect based on DCE-MRI/DSC-MRI

Results

Infratentorial extra-axial tumors - Cerebellopontine angle/temporal bone: Schwannoma, paraganglioma, meningioma - Jugular foramen: paraganglioma, schwannoma, meningioma, chondrosarcoma, chordoma - Foramen magnum/clivus: meningioma, metastasis, plasmacytoma, paraganglioma - Interpeduncular cistern: schwannoma, meningioma DCE-MRI/DSC-MRI findings and conventional MR findings of each tumor Application of DCE-MRI/DSC-MRI for treatment effect

Conclusions
- Conventional MRI can show typical findings for each tumor, however imaging findings are not always specific, and can be absent or overlap. - DCE-MRI/DSC-MRI can help to differentiate various tumors, and can be moreover used for the assessment of post-treatment effect.

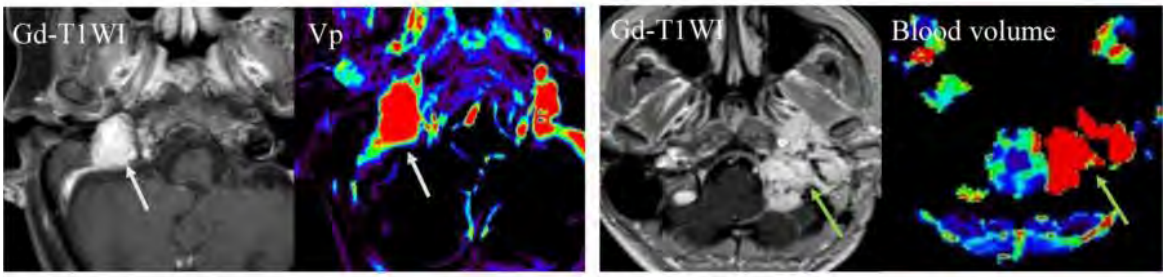

- DCE-MRI with conventional imaging assessment for 76-year-old female with right jugular paraganglioma.
- There is a heterogeneously enhancing mass in the right jugular foramen.
- Vp calculated from a time intensity curve shows 0.66.

- DSC-MRI with conventional imaging assessment for a 24-year-old female with right jugular paraganglioma.
- There is a heterogeneously enhancing mass in the left jugular foramen.
- Blood volume shows 15.66.

(Filename: TCT_533_Revised_ASNR2022education-page-001.jpg)

431

Vertebral Artery Compression Syndromes of the Medulla Oblongata: A Review of Neuroimaging-Neurological Correlations

A Khalaf[1], M Shahrzad[1], E van Staalduinen[1], N Telischak[1], S Hashmi[1], M Wintermark[1], T Massoud[1]
[1]*Stanford University School of Medicine, Stanford, CA*

Purpose
Vertebrobasilar dolichoectasia (VBD) or tortuous vertebral arteries (VA) may asymptomatically abut or compress the medulla oblongata (MO). VA-MO conflicts are seen in 8-25% of asymptomatic patients on CT and MRI. Uncommon symptomatic VA-MO conflicts, first reported in 1985, result in "VA compression syndromes" that are under-recognized in clinical practice and the radiological literature. MRI plays an important complementary role in differentiating asymptomatic from symptomatic VA compression of MO. We provide an educational review of VA-MO conflicts on neuroimaging, and discuss MO anatomy as the basis for mechanisms of different clinical VA compression syndromes.
Materials and Methods
We review and correlate MRI findings of VA-MO conflicts with neurological presentations of VA compression syndromes, and classify these according to neuroanatomy.
Results
We first review normal cross sectional anatomy of the MO. VA-MO compression symptoms are usually unilateral, slowly progressive, and transient or permanent, with poor correlation between clinical stigmata and degree of VA-MO conflict. Compressions affect the anterolateral MO surface more than the MO tegmentum, and symptoms reflect corticospinal tract compromise below the pyramidal decussation (ipsilateral long tract signs), or above it (contralateral signs). Other localizations correlate with MO structures: lateral pyramidal fibers, spinothalamic tracts, vestibular nuclei, lower cranial nerves or nucleus ambiguous, cochlear nuclei or exiting CN8, and CN9 and CN10 nerve root entry zones. As symptomatic conflicts are uncommon, other brain lesions must be ruled out on standard MRI. To consider VA compression syndrome, there should be imaging evidence, symptoms, and positive functional brainstem testing. MRI, including FIESTA/CISS, can reveal VA-MO conflicts and possible MO T2 hyperintensity from ischemia or Wallerian degeneration. Brainstem DTI can better reveal displacement/compression of the pyramidal tracts, and any postoperative changes after micro¬vascular decompression and repositioning of the ectatic VA. Lastly, giant VA aneurysms compressing MO are rare and carry a poor prognosis.
Conclusions
Symptomatic VA compression syndrome is uncommon but important to recognize as patients are often misdiagnosed and it can be reversed by surgery. Advanced neuroimaging can help inform the clinical decision that a VA-MO conflict may be symptomatic. This presentation will aid in neuroimaging interpretation of these conflicts to improve patient management.

629

Vertebral Artery Pathology: A Review of Diagnosis and Angiographic Intervention

R Joshi[1], A Abbas[1], J Wilseck[1]
[1]Beaumont Health, Royal Oak, MI

Purpose

The vertebral arteries are a critical component of the spinal and posterior intracranial circulation. Their associated pathologies are wide ranging including traumatic and congenital causes. Given the profound impact on patient management and outcomes, a careful evaluation of the vertebral artery with a firm understanding of normal anatomy is required to properly rule out pathology. This educational exhibit will provide an overview of the normal anatomy of the vertebral arteries and a case-based review of a large spectrum of their pathologies, including traumatic, spontaneous, iatrogenic, and congenital. Utilization of various imaging modalities including, CTA, MRA, angiography, and ultrasound will be discussed. Finally, discussion of available treatment options for these pathologies will be addressed. List of Educational Objectives: - Overview the normal anatomy of the vertebral arteries throughout their cervical and intracranial course. - Provide a case-based overview of a wide range of pathologies involving the vertebral arteries. - Discuss the associated clinical presentations of these pathologies and how imaging can guide management and affect the clinical course. - Cover the various diagnostic modalities available to evaluate the vertebral arteries and the appropriate indications for utilization. - Discuss available treatment options and indications for treatment.

Materials and Methods

N/A

Results

N/A

Conclusions

N/A

393

Vertebral Artery Variants: Embryology and Clinical Significance

H Bueno[1], E Nimchinsky[2]
[1]Rutgers New Jersey Medical School, Newark, NJ, [2]Rutgers University, Newark, NJ

Purpose

A basic understanding of anatomic variations of the vertebral arteries and their branches is critical for the detection and reporting of clinically significant findings on diagnostic and preoperative CTA and MRA imaging of the head and neck. Clinically significant variants may be unusually vulnerable to injury, or compress adjacent structures. Others may be associated with other vascular anomalies, and should therefore prompt careful search. Several longitudinal and segmental anastomotic pathways exist which may compensate for abnormalities, whether congenital or acquired, in the normal flow pattern of the vertebrobasilar system, and their recruitment may result in predictable variant patterns, explaining otherwise confusing anatomic configurations.

Materials and Methods

The purpose of this Exhibit is to describe the development of the vertebral arterial system with the goal to explain the variants most commonly encountered in clinical practice. In addition, the clinical impact, if any, of these variants are addressed in the context of their particular anatomic relationships.

Results

The examples presented in this Exhibit were accrued during the course of normal neuroimaging in our Level 1 trauma and Comprehensive Stroke centers. The radiologists had no influence on whether or how the scans were performed, and this was a strictly retrospective study. CT angiograms of the neck or neck/head were performed according to our standard protocol, with bolus tracking, and 3D reformates and volume rendered reformats were generated from the original dataset. MRI of the cervical spine and brain were also performed according to our standard protocols on a 1.5T scanner.

Conclusions

Development of the vertebral arteries: 1. early development of the great vessels 2. segmental anatomy 3. carotid-vertebrobasilar anastomoses Specific variants and clinical relevance: 1. abnormal origin 2. abnormal entrance to transverse foramen 3. duplications 4. fenestrations 5. loops 6. PICA variants 7. persistent carotid-vertebrobasilar anastomoses

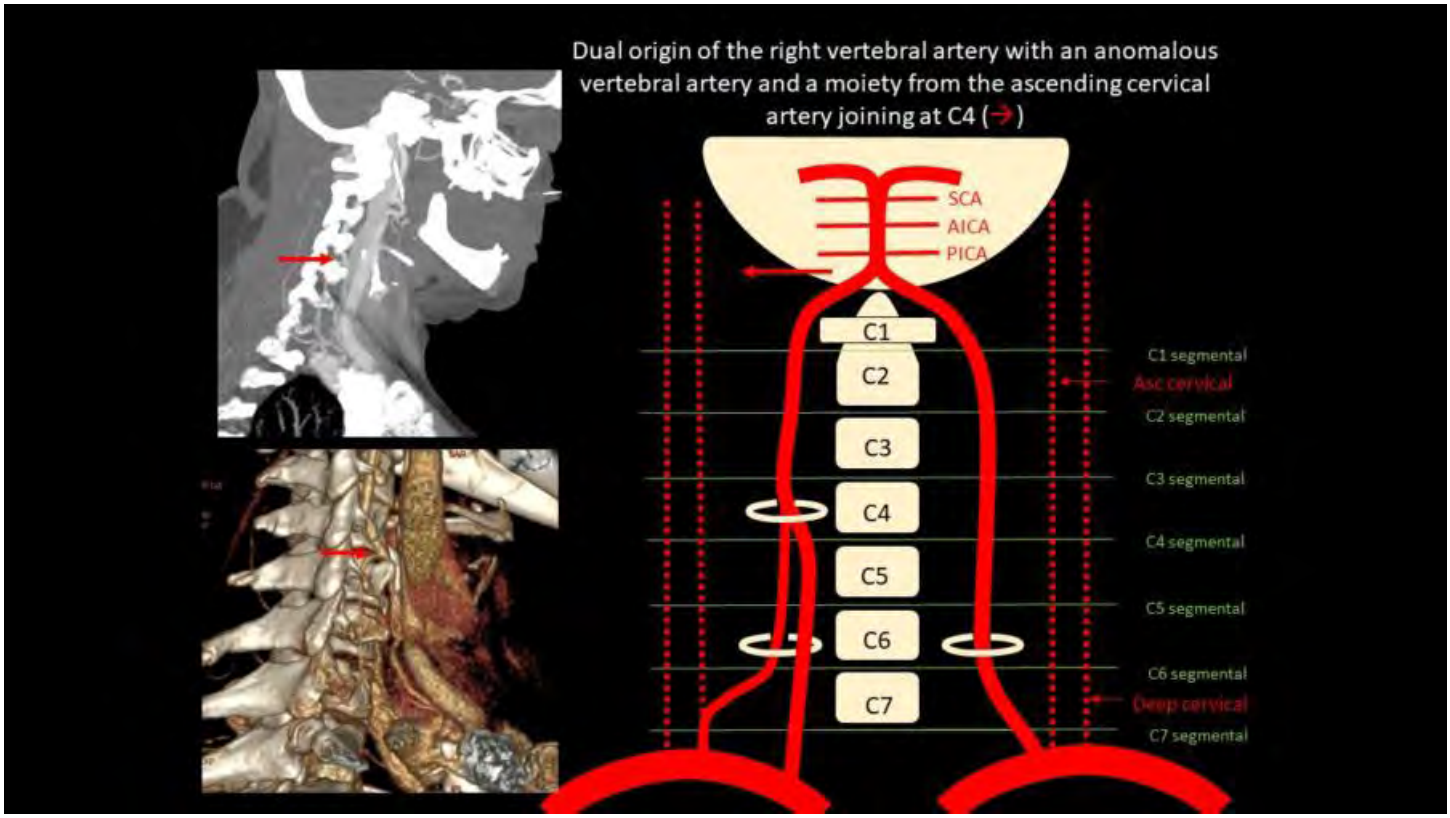

(Filename: TCT_393_vertArtASNR2022.jpg)

604

What is MR Elastography in neuroradiology - application and challenges.

A Ong[1], Z Winchester[1], N Salamon[1]
[1]*University of California Los Angeles, Los Angeles, CA*

Purpose

SUMMARY OF PLANNED PRESENTATION: Magnetic Resonance Elastography (MRE) is a cutting edge, non-invasive, advanced imaging technique that can generate images with high spatial resolution and can allow for the determination of the elastic modulus of tissue in vivo.1 Since its inception, published studies have explored many potential clinical applications on various body parts, with the best documented application to emerge being the use of MRE to assess liver disease.2 Only recently though has this modality been applied to the brain. In our presentation, we will highlight the current applications and possible future directions of MRE in neuroradiology. Brain stiffness has been shown to be sensitive to both physiological and pathological processes. Decreasing brain stiffness has been associated with normal aging as well as neurocognitive disorders such as multiple sclerosis and dementia.3 Increase brain parenchymal elasticity has been linked to processes that increase intracranial pressure such as normal pressure hydrocephalus and jugular venous compression.3,4 Certain intracranial tumors have also been associated with increased brain stiffness such as gliomas, schwannomas, and meningiomas.3,5 Last, our preliminary data suggests that focal cortical dysplasia is also associated with increased elasticity. MRE is an imaging technique that can have superior sensitivity compared to conventional techniques, due to the intrinsically high dynamic range.3 Only recently though has this modality been turned to the neurological axis. Given the promising early data, MRE has the potential to become highly relevant in the clinical setting in the near future. LIST OF EDUCATIONAL OBJECTIVES: 1. Explain the principles behind MRE, shear wave generation, and image acquisition. 2. Current applications of MRE in neuroradiology: literature review. a. Tumors such as meningiomas, pituitary adenomas, vestibular schwannomas, gliomas b. Normal pressure hydrocephalus c. Focal cortical dysplasia d. Altered cranial venous drainage during jugular vein compression e. Normal brain aging and neurodegenerative conditions f. Demyelinating disease 3. Future direction of MRE in neuroradiology.

Materials and Methods

None

Results

None

Conclusions

None

976

What Lies Beneath the Eagle: An Imaging Review of Hypoglossal Canal Lesions.

I Haq[1], S Patro[1], M Mian[1], S Sharma[1], P Reddy[1], S Vattoth[1], M Kumar[1], R Van Hemert[1], R Ramakrishnaiah[1], G Vilanilam[2], J Moore[3], R Mcallister[1]

[1]Division of Neuroradiology, Department of Radiology, University of Arkansas for Medical Sciences, Little Rock, AR, [2]University of Arkansas for Medical Sciences, Little Rock, AR, [3]UAMS, Little Rock, AR

Purpose

1. Understanding the development, course, and function of the hypoglossal nerve 2. Outlining the anatomy of the posterior skull base including the hypoglossal canal. 3. Reviewing imaging features of lesions involving the hypoglossal canal and nerve as well as clinical presentation and managment.

Materials and Methods

To demonstrate the imaging characteristics of various lesions that involve either the hypoglossal nerve and/or hypoglossal canal, as well as to explore the clinical presentation and treatment options.

Results

Retrospective single-center review of lesions involving the hypoglossal nerve and canal as well as the premedullary cistern characterized by CT and MRI.

Conclusions

We reviewed multiple different lesions abutting and extending into the canal and/or involving the hypoglossal nerve. The lesions ranged from hypoglossal schwannomas/mengiomas to juxta-articular cysts to metastasis and dural arteriovenous fistulas. Expectedly, lesions predominantly involving the medullary cistern showed avid enhancement, while cystic lesions outside the dura tend to show peripheral enhancement. The action of the hypoglossal nerve is entirely motor which is why classical abnormalities tend to lead to imbalanced action of the genioglossus muscles causing tongue deviation toward the weak side. The patients referred at our institution varied with clinical presentation, with some lesions being incidental in asymptomatic patients. Other patients presented with asymmetric facial fullness and pain, with vascular lesions such as dural arteriovenous fistula and glomus lesions presenting with asymmetric pulsatile tinnitus. Additionally, we had a patient referred to us with dysarthria and dysphagia with classical left sided tongue weakness with Imaging demonstrating a cystic lesion within the prevertebral space medial to the hypoglossal canal without frank invasion but with imaging showing left sided tongue atrophy. Given that the hypoglossal canal poses difficulty for biopsy due its location along posterior skull base, a combination of imaging findings and clinical history is key in determining diagnoses for appropriate patient care.

(Filename: TCT_976_Merged_document.jpg)

369

What's So Hard About Convolutional Neural Networks: A Primer For Radiologists

J Nguyen[1]

[1]*Tulane University School of Medicine, New Orleans, LA*

Purpose

A convolutional neural network (CNN) is a class of deep learning neural networks, which have practical applications in radiologic imaging. CNN is constructed with artificial neurons connected together to form building blocks which include an input layer, hidden layers and an output layer. CNNs employ a mathematical operation called convolution for extracting features from the input image. CNNs can take in an input image, assign importance to various aspects/features in the image and be able to differentiate one from the other. The presentation plans to accomplish the following objectives: • To describe the structure and operation of an "artificial neuron" in a neural network. • To discuss the basic architecture of a deep learning neural network including the input, hidden and output layers. • To describe the architecture of a Convolutional Neural Network (CNN). • To explain the intuitive meaning of mathematical convolution. • To discuss how a convolutional neural network can extract features of an image though the Convolution Layer, Rectified Linear Unit Layer (ReLU), and Pooling. • To explain how a convolutional neural network can classify an image through the Fully Connected Layer and Softmax function. • To describe an intuitive design of a Convolutional Neural Network, with the integration of the feature extraction and image classification components.

Materials and Methods

This exhibit will provide a concise tutorial of CNNs without complex mathematics. The radiologist will learn the fundamental architecture of a Convolutional Neural Network (CNN). The concept of mathematical convolution for image feature extraction will be intuitively explained. The radiologist will learn the conceptual design of CNN with the integration of the feature extraction and image classification components. A self-assessment quiz is available at the end for assessment of material comprehension.

Results

N/A

Conclusions

Convolutional neural network (CNN) has become a dominant artificial intelligence technology in radiology. CNN is constructed to automatically and adaptively learn the spatial hierarchies of features by using image feature extraction of classification building blocks. CNN can perform radiologic task such as classification, segmentation, and detection. After the completion of this tutorial, the radiologist will have a firm conceptual knowledge of CNN; giving the radiologist a firm foundation to further explore advanced applications of CNN in radiologic imaging

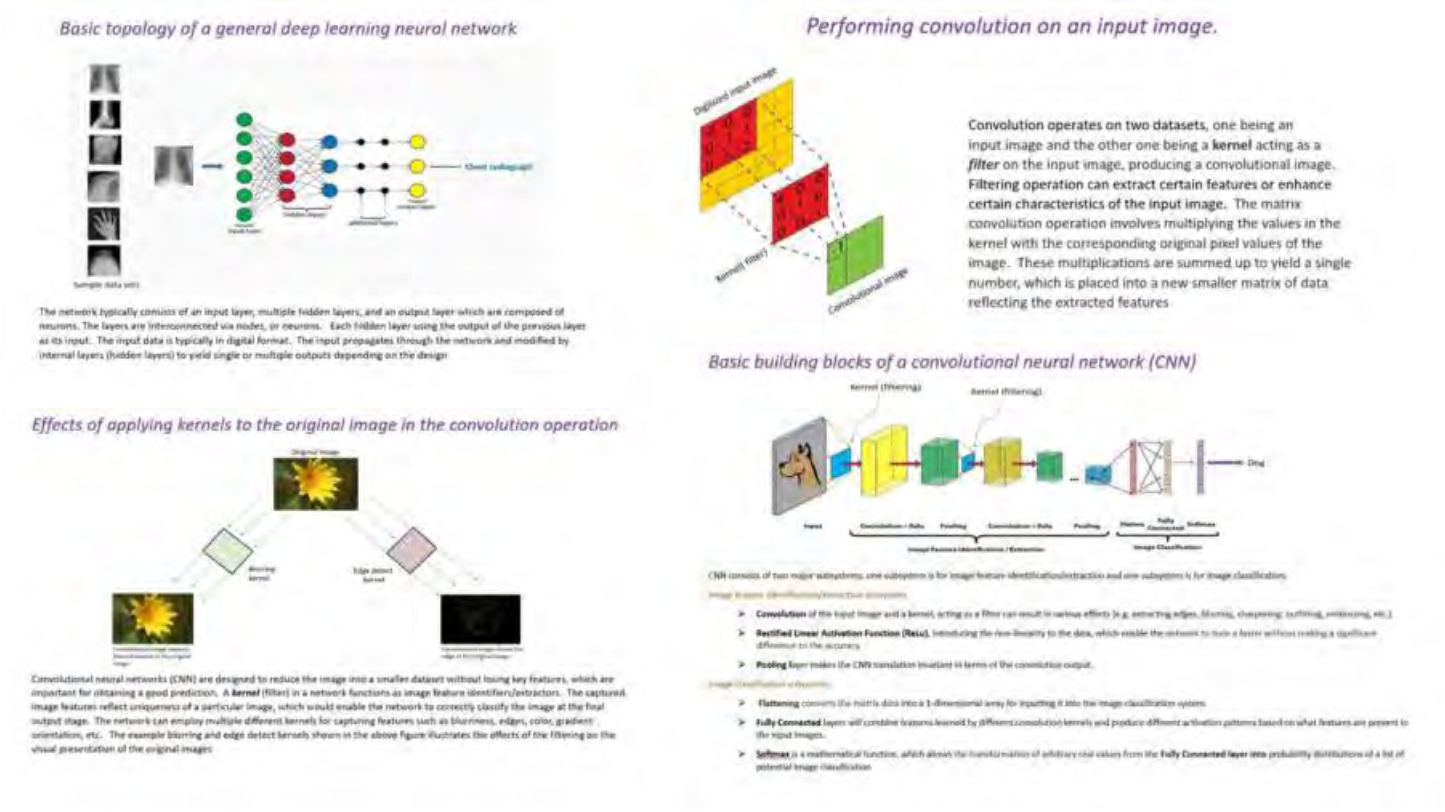

(Filename: TCT_369_ASNRPIc1.jpg)

162

Won't Get Fooled Again. Extrapituitary Mimickers and Pseudo Lesions within the Sella and Parasellar Region.

S Kelly[1], S Genet[2], M Keiper[1], D Zander[2], J Cramer[1]

[1]University of Nebraska Medical Center, Omaha, NE, [2]University of Colorado, Aurora, CO

Purpose

This education exhibit will present a collaborative case series of non-pituitary sellar lesions that can mimic pituitary pathology. Most of our cases presented will be of uncommon but important entities for the interpreting radiologist to recognize to avoid potential pitfalls. Many of the cases chosen will be ones that either were initially misinterpreted or puzzled the neuroradiologist at our institutions. Our goal is for our audience to advance their knowledge of sellar and parasellar lesions with specific attention to more uncommon findings and potential pitfalls to avoid diagnostic misinterpretation.

Materials and Methods

N/A

Results

This exhibit is intended to serve as a collection of interesting cases including uncommon pathology, atypical appearances of common lesions, and anatomic variation in the sellar and parasellar region. The exhibit will go beyond simply highlighting our unique cases. Each example will highlight similarities and differences with other more common lesions in the same region and how to avoid a potential misdiagnosis. We will include key points to making the correct diagnosis as well as clues to help narrow the differential. Additionally, an epidemiological summary, radiologic findings, clinical implications and follow up recommendations will be included when applicable.

Conclusions

The sella and surrounding area is a complex anatomical region and serves as a location for numerous pathologies. Often, radiologists are able to make a fairly narrow differential of lesions in this region based on prevalence, location and imaging characteristics. However, definitive diagnosis often requires major operative intervention putting a patient at significant risk for potential no touch lesions. More extensive knowledge of disease processes in the sellar region is essential in improving patient safety and referring clinician confidence in radiology interpretations. With this in mind, we hope that our education exhibit will highlight uncommon and unusual diseases and appearances in this region to minimize radiologist uncertainty, misdiagnosis and unnecessary intervention and follow-up imaging.

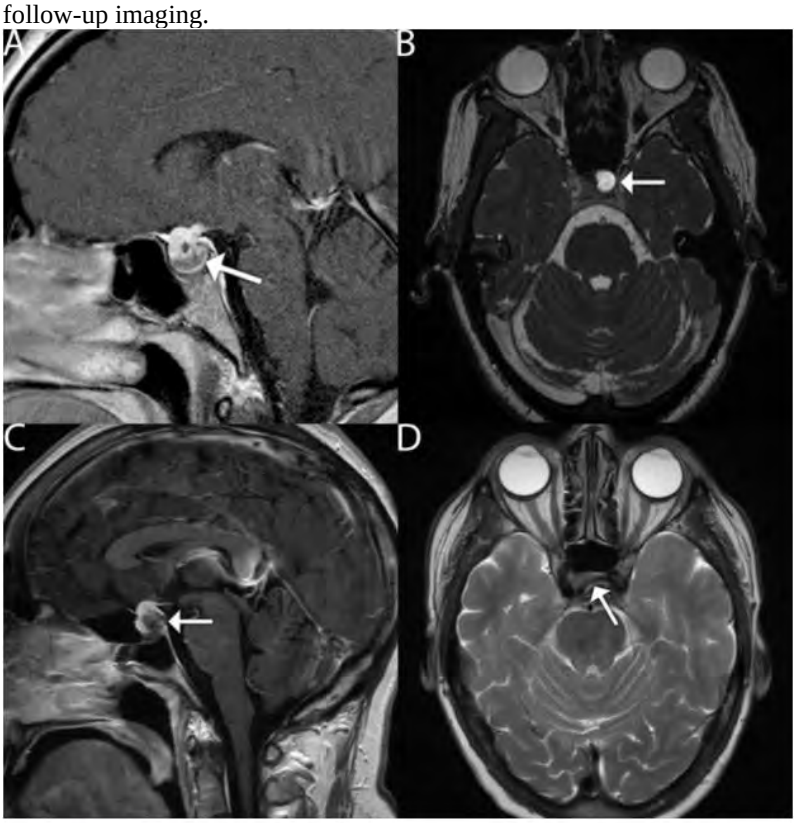

A. Sellar Meningioma
B. Sellar Arachnoid Cyst
C. Dorsum Sellae Osteochondroma
D. Aberrant Artery Coursing Through the Inferior Sella

(Filename: TCT_162_4x4montagewithtext.JPG)

970

"Stroke-Alert" CT Perfusion Primer: Everything You Need to Know to Read Your First Case

M Shalaby[1], A Moawad[1], B Jaber[1], S Chaker[1], M Aslam[1], S Kushchayev[2], O Teytelboym[1]

[1]Mercy Catholic Medical Center, Darby, PA, [2]Moffitt Cancer Center, Tampa, FL

Purpose

Educational Objectives: 1- Discuss the principles of CT perfusion (CTP) 2- Explore qualitative and quantitative approaches to CTP interpretation 3- Highlight the limitations of CT perfusion 4- Demonstrate various clinical situations that may mimic stroke Table of Content: 1- CT perfusion parameters and tissue attenuation curve 2- Typical presentations of stroke CT perfusion -Ischemic penumbra -Complete infarct -Small core infarction, large ischemic penumbra -Large core infarct, small ischemic penumbra 3- False Negative CT perfusion -Lacunar infarcts -Watershed infarcts -Luxury perfusion -"Ictal and Postictal" phases of seizure 4-False positive CT perfusion -Anatomical variants, anomalies and malformations -Transient ischemic attack -Cervical arterial stenosis -Cerebral venous thrombosis -Head tilt -Vasospasm -Migraine -"Interictal" Seizure 5- CT perfusion analysis Qualitative approach Quantitative approach

Materials and Methods

N/A

Results

N/A

Conclusions

N/A

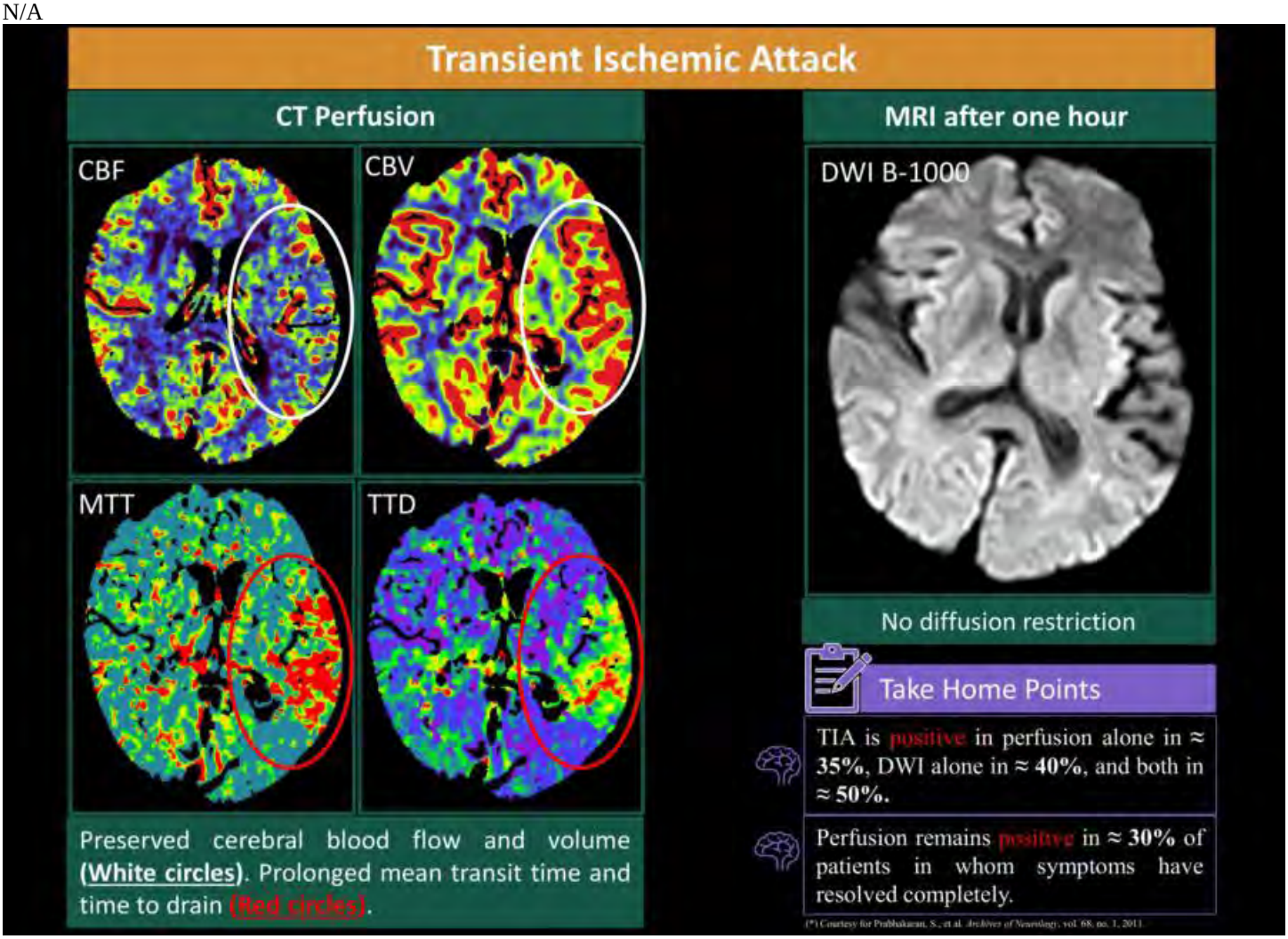

(Filename: TCT_970_PerfusioncaseFinal.jpg)